



Center of Excellence for Explosive Detection, Mitigation and Response

Center of Excellence for Explosive Detection, Mitigation and Response

A Department of Homeland Security

Center of Excellence

University of Rhode Island (URI);

California Institute of Technology

Purdue University

New Mexico State University

University of Illinois

Florida International University

Hebrew University, Jerusalem Israel

Weizmann Institute of Science

Fifth Annual Report

July 2012-July 2013

DHS agreement number: 2008-ST-061-ED0002

Table of Contents

<i>Introduction</i>	5
<i>Characterization</i>	
Factors Influencing TATP and DADP Formation (Part 2) Jimmie Oxley & James Smith (URI)	8
Factors Influencing TATP and DADP Formation (Part 3) Jimmie Oxley & James Smith (URI)	45
Characterization of HME Steve Son (Purdue)	54
Detonation Failure Characterization of HME Steve Son (Purdue)	66
Hot dense liquid TNT decomposition Ronnie Kosloff (Hebrew UJI)	90
Enhanced Sensitivity of Condensed Phase Nitroaromatic Explosives Ronnie Kosloff (Hebrew UJI) & Yehuda Zeiri (BGU)	119
Development of Simulants of Hydrogen Peroxide Based Explosives for use by Canine and IMS Detectors Jose Almirall (FIU)	158
Calibration of PSPME Using Controlled Vapor Generation Followed by IMS Detection Jose Almirall (FIU)	161
<i>Detection</i>	
Optical Chemical Sensors using Nanocomposites from Porous Silicon Photonic Crystals & Sensory Polymers William Euler (URI)	181
Fluorescent Species Formed by the Reaction of Trinitroaromatics with N,N- Dimethylformamide and Peroxide William Euler (URI)	189
A Fluorometric Sensing Array for the Detection of Military Explosives and IED Materials William Euler (URI)	219
Light Trapping to Amplify Metal Enhanced Fluorescence with Application for Sensing TNT	226

William Euler (URI)	
A Persistent Surveillance Technique for the Detection of Explosives and Explosive Precursors Otto Gregory (URI)	234
Solution-Based Direct Readout SERS Method for Detection Radha Narayanan (URI)	303
Solution-based Direct Readout Surface Enhanced Raman Spectroscopic Detection of Ultra-Low Levels of Thiamin with Dogbone Shaped Gold Nanoparticles Radha Narayanan (URI)	310
Gold Nanorods as Surface Enhanced Raman Spectroscopy Substrates for Sensitive and Selective Detection of Ultra-Low Levels of Dithiocarbamate Pesticides Radha Narayanan (URI)	316
Nanocantilever Chemical Vapor Sensors Coated with Localized Rubbery and Glassy Polymer Brush Films Nate Lewis (Cal Tech)	322
Supplementary Information	349

Mitigation

Development of Structural Steel with Higher Blast Resistance H. Ghonem (URI)	354
Time-dependent Deformation of Low Carbon Steel at Elevated Temperatures H. Ghonem and Otto Gregory	365
Simulation of Viscoplastic Deformation of Low Carbon Steel Structures at Elevated Temperatures H. Ghonem (URI)	375
Deformation Criterion of Low Carbon Steel Subjected to High Speed Impacts H. Ghonem, C-E. Rousseau and Otto Gregory	384
Deformation Characteristics of Low Carbon Steel Subjected to Dynamic Impact Loading H. Ghonem, C-E. Rousseau and Otto Gregory	391
Self-Healing Concrete Arijit Bose (URI)	401

Polyurea/Polyurethane Microcapsules Based Self Healing Concrete Arijit Bose (URI)	404
Structural Response to Non-ideal Explosions J. E. Shepherd (California Institute of Technology)	524
Experimental Investigation of Blast Mitigation for Target Protection Steve Son (Purdue University)	529
Self Healing Materials for Autonomic Mitigation of Blast Damage Nancy R. Sottos (U of Illinois)	554
Stress Attenuation by Means of Particulates C-E. Rouseau	566
Development of Novel Composite Materials & Structures for Blast Mitigation Arun Shukla (URI)	574

Center of Excellence Explosives Fifth Annual Report

The goal of this CoE in Explosives is to mitigate the worldwide explosive threat, both today and in the future. To reach that goal, URI has maintained four thrust areas Characterization, Detection, Mitigation, and Education. In addition, one project was designated as Engage to Excellence (E-2-E).

Characterization

For the present and near term, studies in the thrust area are aimed at physical characterization of novel explosives and explosives signatures, along with determination of thermal stability and sensitivity. This information is available to the community within weeks by publication on the URI Explosive Database, journal publication, and classes. Beyond that is the need to understand the mechanism of material formation and destruction with the goal of hindering or facilitating these events. Looking to the future we believe it is high priority to identify and prioritize the list of potential threats. Therefore, we are taking two approaches to identifying potential explosives—a comprehensive theoretical approach which involves prediction of physical properties and hazards and an experimental approach. Enhanced sample collection is addressed both by an experimental approach based on microextraction for the capture of extremely small quantities of the volatile compounds and a survey of potential materials using atomic force microscopy (1.1 - 1.8).

Detection

Progress continues towards development of sensors that are sensitive, selective and able to detect trace levels of explosives. A number of novel sensors are being developed. The sensors employ two orthogonal spectral techniques; surface enhanced Raman scattering (SERS) and metal enhanced fluorescence (MEF). Due to the light absorbing properties of TNT and its quenching capabilities the MEF component was shown to be particularly sensitive to TNT. Another approach is detecting explosive vapors via use of a nanocantilever. The response of these sensors is due to two mechanisms; one that affects mass accumulation to the sensor and another that affects its stiffness. Modeling studies suggest that the response of the nanocantilever to vapor appears to be due more by change in the sensor spring constant rather than accumulation of mass. Also investigated are nanoparticle chemiresistor sensors. Applications of organic capping groups impart electrical conductivity to the films on these sensors. "Shaper-less" standoff remote detection from distance of up to 50 meters has been demonstrated using femtosecond pulses shaped by a photonic crystal filter. The fundamental behavior of ions in ion mobility spectrometers (IMS) continues to be studied. To this end a kinetic dual shutter IMS with a gas chromatograph interface was constructed. This instrument successfully characterized ion lifetimes, energies, and kinetics of decomposition of gas phase ions of energetic materials. Studies are in progress on as many explosives in the nitro-alkane and nitro-aromatic family as possible (2.1 - 2.10)

Mitigation

In the mitigation thrust area approach is diverse from technologies that mitigate the effect of the blast to new sandwich compounds and functionally graded materials that more readily withstand blast. New metrics of assessing material stress as well as non-ideal explosive events are under

development. Already to the commercialization stage are techniques for manufacturing self-healing materials polymers and cements (3.1 - 3.12).

Engage to Excellence

An outstanding success has been achieved in our **E-2-E** project —the development of a new steel with a significantly high blast resistance. This has been accomplished through a systematic numerical/analytical/experimental approach carried out by Professor Hamouda Ghonem and his research group over four years of funding. First, they established metrics for rating the residual strength of steel under post blast conditions. For this purpose, they built an advanced gas gun capable of delivering a blast pressure of 25 GPa at 1000 m/s. Joining this unique gas gun with Split-Hopkinson Pressure Bar and ECAP severe plastic deformation system, blast testing of steel with different microstructures and compositions could be routinely accomplished in the URI-Mechanics of Materials Research lab. These testing facilities coupled with numerical simulation techniques are used to develop pre-strained steel with a blast resistance up to 12 GPa of blast pressure as opposed to that of present steels which is best assessed as 4 GPa. These efforts in the DHS Center have been assisted by FM Global and US Steel. The application significance of this steel is its potential in retrofitting of tunnels and doming of nuclear reactors with a steel fiber mesh to act as self-sustained blast protection shields. (3.1 – 3.5)

Education

Our work in this field to date is as follows. Each University project in the Center supports one or more graduate students. This is their best learning experience. Undergraduates are also supported on the projects as their class schedules permit. In addition, URI has a traveling magic shows for elementary and junior high students. For three summers we hosted Minority Scholars and for the last four summers we have hosted high school science teachers. In the summer of 2012 our Center supported eight high school teachers to conduct research at University of Rhode Island (URI). Four teachers of physics were placed in URI engineering departments; and another four, in the URI chemistry department. The teachers worked fulltime for 8-10 weeks. They were required to prepare a poster and give a brief presentation of their work at the end of their tenure. The purpose of this program is to provide high school teachers with an opportunity to gain research experiences they can take back to the classrooms.

In the calendar year 2012 seventeen professional classes were offered, providing training for over 300 professionals with new titles (red on Table) offered every year. Also new in 2012 were week-long courses with lecture and labs (marked in green on the following Table) most of them aimed at the TSA explosive specialists. Since May we have offered 4 weeks of such classes and trained 48 TSA explosive specialists as well as NYPD forensic lab personnel. The next NYPD class will be offered next week.

Class	DATES	#	Class	2009	#	Class	2010	#students	Class	2011	#students	Class	2012	#students
Stumpneck	Feb 17-19	30	APL Fundamentals	Feb 4-6	10	Fundamentals Edwards	Jan 19-21	26	Terrorism	Apr 26-27	18	Stability	Jan 18-19	16
Pic-Managers	April 23	21	Picatinny Hazard	Feb 17-19	26	Fundamentals Picatinny	Feb 1-3	25	Fundamentals	May 3-5	37	Air Blast	Feb 14-16	10
APL JHU	Apr 29-May 1	30	Picatinny Combust	Feb 22-23	29	Hazards Ottawa, CA	Feb 3-5	13	Combustion	May 9-10	18	Fundamentals	Feb 27-29	25
URI	May 6-8	38	Picatinny Protoco	Apr 23-24	20	Fundamentals ABQ	Feb 17-19	9	Insensitive Mun	May 10-11	26	Nanoenergetics	Mar 12-13	15
Kansas City Plant	Jul 15-19	6	Pic Air Blast	Apr 27-29	19	Hazards ABQ	Feb 17-19	11	Det'n & DDT	June 7-9	20	Firing Trains	Apr 10-12	13
Andrews Materials	Aug 11-14	32	Pic HE Material C	May 12-14	16	Warheads Picatinny	Feb 24-26	26	Mat'l Response	July 21-22	15	Fundamentals	Apr 24-25	42
Indian Head	Aug 18-22	30	Picatinny Fundam	June 23-25	22	Materials Response, CA	Mar 22-23	15	Protocols	Aug 2-3	16	Fundamentals	May 1-3	38
Picatinny Protocol	Sep 22-23	25	URI Fundamentals	May 5-7	44	Air Blast Ottawa, CA	Mar 24-26	13	Det'n & DDT	Sept 6-8	35	Warhead Mech.	May 8-10	13
Picatinny Fundam	Sep 24-26	23	Valcartier	May 26-28	17	Terrorism Issues	April 25-26	40	Dynamic Diagn	Sep 28-29	15	NYPD Analysis	May 7-18	9
Pic Diagnostics	Oct 20-21	24	Crane, IN	Jun 1-3	16	Safety Protocols	Apr 28-29	25	TOTAL	TOTAL	200	TSABAO	May 21-25	24
Picatinny Fundam	Oct 22-24	24	Picatinny DDT	Jul 28-30	23	Fundamentals	May 4-6	26				Fundamentals	July 17-18	18
DHS Fundamentals	Nov 24-26	20	Picatinny	Aug 3-4	16	Nanomaterials	May 25-26	20				Dugway	July 7-10	7
Picatinny Analysis	Dec 2-3	23	Ottawa	Sep 8-10	16	Pyrotechnics	June 7-11	28				TSABAO	Aug 20-24	22
	TOTAL	326	Materials Respor	Sep 29-30	23	Fundamentals	July 26-28	24				Pic Protocols	Sept 10-11	12
			Components	Oct 27-29	25	HE Materials Characteriz	Sept 16-18	19				TSABAO	Sept 17-21	22
			Environmental	Nov 4-5	26	Unintended Ignition	Oct 20-22	19				Warheads, Alb.	Nov. 6-8	25
			TOTAL	TOTAL	348	TOTAL	TOTAL	339				Standoff Detection	Dec 12-13,	18
												TOTALS	TOTALS	329

Factors Influencing Triacetone Triperoxide (TATP) and Diacetone Diperoxide (DADP) Formation: Part 2

Jimmie C. Oxley* ; James L. Smith; Lucus Steinkamp; Guang Zhang

*^aUniversity of Rhode Island,
Chemistry Department
51 Lower College Road
Kingston, RI 02881
joxley@chm.uri.edu

Abstract

A comprehensive mechanistic study regarding acetone peroxides reveals that water has a profound effect on the formation of the solid cyclic peroxides, TATP and DADP. The identification and rate of occurrence of reaction intermediates as well as compositions of the final products offer explanation for previously reported results indicating that acid type and hydrogen peroxide concentration affect the acid catalyzed reaction between acetone and hydrogen peroxide. A kinetics study of the decomposition of TATP revealed the effects of water and alcohols. They generally retard conversion of TATP to DADP and leads to complete decomposition of TATP by acid. A mechanism is proposed for the production of TATP and DADP.

Keywords: Triacetone triperoxide (TATP), Diacetone diperoxide (DADP), Product Formation, Product Decomposition, Mechanism, Kinetics

1. Introduction

Organic peroxides are often used as polymerization catalysts or bleaching agents [1-3]. However, a few with high ratios of peroxide functionality to ketone have found use as illicit explosives [4]. We have previously reported attempts to prevent synthesis of TATP in improvised settings [5]. That work pointed out a need for a detailed mechanistic study. Some of the questions of interest in TATP formation/destruction were conditions under which TATP and DADP form, mechanisms of formation and destruction and whether DADP could be formed directly or only through a TATP intermediate. These questions were addressed by identifying intermediates by gas chromatography/mass spectrometry (GC/MS), liquid chromatography/mass spectrometry (LC/MS) at high mass resolution and $^1\text{H}/^{13}\text{C}$ nuclear magnetic resonance spectroscopy (NMR). Intermediates were monitored during formation and destruction experiments to elucidate mechanisms.

2. Experimental Section

2.1 Reagents and Chemicals

HPLC-grade solvents, deuterated acetone (99.8 wt% d), and acids trifluoroacetic (99 wt%), nitric (70wt%), hydrochloric (37 wt%) and sulfuric (98wt%) were obtained from Fisher Scientific; deuterated acetonitrile, from Cambridge Isotopes Lab. Syntheses of TATP and DADP were previously reported [5]. For synthesis of deuterium-labeled TATP d^6 acetone was used. Precipitates were filtered, rinsed with water, dried under aspiration 30 minutes and recrystallized in methanol. Final products were analyzed by GC/MS, GC/uECD, ^1H NMR and ^{13}C NMR. Anhydrous hydrogen peroxide was prepared by dissolving 20 g of L-serine in 20 mL 65 wt% hydrogen peroxide.⁶ To confirm its concentration, the hydrogen peroxide was dissolved in acetonitrile (ACN) and titrated with 0.25N potassium permanaganate.

2.2 GC/MS Method

An Agilent 6890 gas chromatograph with 5973 mass selective detector (GC/MS) was used with inlet in splitless mode at 110°C, with purge flow 20 mL/min at 0.5 min, total helium flow of 24.1 mL/min and a Varian VF-200MS column (15m, 0.25 mm inner diameter, 0.25 µm film) under constant helium flow (1.5 mL/min). Oven temperature was held at 40°C for 2 minutes, ramped 10°C/min to 70°C, then 20°C/min to 220°C; post-run oven was held 3 min at 310°C. Transfer line, MS detector source, and quadrupole were held at 150°C, 150°C, and 106°C, respectively. Chemical ionization used anhydrous ammonia.

2.2.1 TATP Formation (GC/MS): All reagents were chilled to 0°C. Hydrogen peroxide (HP) (67 wt%, 0.47 g, 9.3 mmol) in 10 mL acetonitrile was stirred in a round bottom flask while sulfuric acid (0.95 g, 96.5 wt%, 9.3 mmol) and then acetone (0.54 g, 9.3 mmol) were added dropwise. Periodically, 100 µL of the solution was removed, placed in 1 mL CH₂Cl₂, and rinsed with 3 wt% sodium bicarbonate. Organic layer was dried over MgSO₄ and analyzed by GC/MS.

2.2.2 Effect of water (GC/MS): Acetone and HP were mixed and chilled to 0°C. Water was mixed with sulfuric or hydrochloric acid, chilled to 0°C, and added dropwise to the acetone/HP mixture keeping the temperature below 5°C. The ratio of HP:acetone:acid was maintained at 1:1:1 (8.6 mmol). Once all acid was added the mixture was removed from the ice water bath and allowed to stir at room temperature 24 hours; resulting products were analyzed by GC/MS.

2.2.3 TATP Destruction (GC/MS): TATP (100 mg) was placed in a 40 mL vial; and 5 mL solvent, added. In a second 40 mL vial 200 µL 96.5 wt% sulfuric acid was added to a solvent/water mix of total volume 5 mL. Both vials were equilibrated at 45°C. Once equilibrated, the two solutions were mixed. At intervals 100 µL aliquots were removed, quenched as above (2.2.1) and analyzed by GC/MS. TATP and DADP were quantified by external calibration.

2.2.4 Acetone Exchange Reactions (GC/MS): TATP was stirred at room temperature with 2.6 mmol sulfuric acid in aqueous ethanol spiked with d^6 acetone (16.4 mmol). After 24 hours the TATP had not completely dissolved, but a small aliquot of solution were analyzed by GC/MS for acetone exchange by identification of presence or absence of deuterium containing fragments. Similar experiments involving ACN, methanol or chloroform/TFA as solvent were conducted.

2.3 LC/MS Method

Certain experiments identified intermediates by liquid chromatography/mass spectrometry at high mass resolution (LC/MS). The Thermo Scientific Exactive Orbitrap MS was operated in positive ion mode using atmospheric pressure chemical ionization (APCI). Decomposition was minimized during analysis by setting the vaporizer at 175°C and capillary at 125°C. Discharge current was 5 μ A; the sheath gas and auxiliary gas operated at 25 and 10 arbitrary units, respectively. The LC was ramped from 70/30 methanol/ammonium acetate (4mM) in water to 15/85 methanol/ ammonium acetate (4 mM) in 5.5 minutes followed by a 30 second hold. The eluent was returned to 70/30 methanol/ ammonium acetate and held for 4 minutes. Resolution was set to high (50,000 at 2 Hz), and the maximum injection time was 250 ms.

2.3.1 TATP Formation (LC/MS): Acetone and HP (67 wt%) mixtures were prepared as molar ratios of 1:1, 2:1 and 1:2 and held at room temperature (r.t.) without stirring. For LC/MS analysis 100 μ L of each mixture was diluted to 1 mL with methanol.

2.3.2 d^6 -Acetone Insertion into Proteo-TATP (LC/MS): At room temperature, stirred solution of TATP (222mg, 1.0 mmols) and d^6 -acetone (75 μ L, 1.0 mmols) in 10 mL ACN, methanol or chloroform was added trifluoroacetic acid (TFA, 150 μ L, 2.0 mmols). Every 24 hours, 0.5mL of the mixture was removed and diluted to 1.5mL total volume for LC/MS analysis.

2.4 Nuclear Magnetic Resonance (NMR) Method

A Bruker Avance III nuclear magnetic resonance (NMR) spectrometer with 7.1 Tesla magnet was used for all NMR experiments. Kinetic experiments, at 15°C (288K), monitored ^1H -spectra every 5 minutes (including scanning time) for up to 17 hours or daily for up to four days. Following the kinetics experiments, the samples were neutralized with excess sodium bicarbonate and either diluted by the identical solvent, sans-deuterium, and analyzed by GC/MS or returned to an NMR tube for subsequent analysis. 2-D NMR experiments: HSQC (heteronuclear single quantum coherence) and HMBC (heteronuclear multi-bond coherence) were performed. The ^1H (300 MHz) and ^{13}C (75 MHz) chemical shifts corresponding to all species present in the formation and decomposition of TATP reaction mixtures were obtained. NMR samples were then analyzed by GC/MS.

2.4.1 Formation of TATP/DADP (NMR): In a 10 mL vial, HP (1 mL, 65 wt%, 24.6 mmols) was mixed with acetone (1.9 mL, 25.8 mmols); 100 μL of the mixture was transferred into an NMR tube with 1.2 mL CD_3CN . Trifluoroacetic acid (TFA) (20-80 μL , 0.26-1.04 mmols) and trace of tetramethylsilane (TMS for calibration and quantification) were added.

2.4.2 Decomposition of TATP or DADP (NMR): TATP (45 mg, 0.2 mmols) was dissolved in deuterated solvent (0.6 mL CD_2Cl_2 , 1.0 mL CDCl_3 or 1.2 mL CD_3CN), transferred to 5mm NMR tube, and acid added [TFA (20-100 μL , 0.26-1.3 mmols), sulfuric (10-20 μL , 0.18-0.36 mmols) or hydrochloric acid (10 μL , 0.12 mmols)]. DADP (29mg, 0.2 mmols) dissolved in CDCl_3 (1mL) was decomposed with TFA (60-100 μL , 0.78-1.3mmols) or sulfuric acid (10 μL , 0.18 mmols).

2.4.3 Acetone Exchange Without Acid (NMR): In 5 mm NMR tubes with 100 μL CH_2Cl_2 , TATP (111 mg, 0.5 mM) and 1 mL d^6 -acetone or d^{18} -TATP (120 mg, 0.5 mM), 0.9 mL acetone, and 100 μL d^6 acetone (for lock) were sealed and stored at room temperature for a week.

2.4.4 Acetone Exchange Reactions (NMR): To d^{18} -TATP (48mg, 0.2mmols) in 1.2 mL CD_3CN or 1.0 mL $CDCl_3$ was added 50 μ L (0.68 mmols) or 40 μ L (0.55 mmols) acetone, respectively. The solution was transferred to an NMR tube and TFA (20-40 μ L, 0.26-0.52 mmols) was added.

2.4.5 1,3-Dichloroacetone insertion into Proteo-TATP and d^{18} -TATP (NMR): A tenth millimole TATP (22 mg) or d^{18} -TATP (25 mg) was dissolved in 1.2 mL CD_3CN ; 1,3-dichloroacetone, 1,1-dichloroacetone (42 mg, 0.3 mmols) or monochloroacetone (27 μ L, 0.3 mmols) was added, and the solution placed in a 5mm NMR tube. TFA (40 μ L, 0.54 mmols) was added.

3.0 Results and Discussion

3.1 Formation of TATP with acid

Previous studies have shown that the best yield of TATP is obtained from a 1:1 mole ratio of acetone and hydrogen peroxide [5,7]. When using an acid catalyst such as hydrochloric or sulfuric acid a white precipitate is quickly formed that can be washed and re-crystallized yielding high purity TATP, DADP or a mixture of the two [5,8]. To fully understand the mechanism of TATP and DADP formation it was necessary to conduct experiments using a co-solvent that would prevent precipitation from solution and not interfere with the analysis of the products and intermediates. Using GC/MS and NMR, TATP, DADP and intermediate species were observed and monitored over time. Figure 1 shows the progress of a typical reaction under highly acidic conditions by monitoring TATP and DADP by GC/MS. Initially the concentration of TATP rises sharply while that of DADP rises more gradually and levels off. The newly formed TATP undergoes decomposition in the presence of 1 molar equivalent of acid while DADP does not. Under less acidic conditions (3.5:3.5:1 HP:acetone:sulfuric acid) TATP concentration reached a maximum, remained constant for several days, and then gradually decreased as DADP

concentration continually increased. DADP is the final product if TATP cannot precipitate from solution. In agreement with NMR data, upon increasing the amount of acid added, a faster rise to equilibrium was observed as well as a higher equilibrium concentration of TATP in solution. The decomposition of TATP also occurred more rapidly with increased amounts of acid, and water, itself, had an effect. Figure 2 shows that when the molar ratios of acetone, hydrogen peroxide and acid are kept constant (9.3 mmol) added water and reduced acid slows the rate of formation of both TATP and DADP and appears to suppress DADP formation more significantly. With minimal water present the rate of formation for TATP and DADP are at a maximum although TATP is still the major product observed early in the reaction.

<Figure 1>

<Figure 2>

3.2 Formation of TATP with no acid

GC/MS analysis of the products when 70 wt% hydrogen peroxide (HP) and acetone were mixed highlighted the importance of the ratios. When HP was in excess 5:1 over acetone more TATP was produced than DADP. When the ratio of HP to acetone was adjusted from 5:1 to 1:1 and then to 1:5, the total amount of solid product decreased and the amount of DADP increased relative to TATP. The reaction between HP (70 wt%) and acetone without acid was monitored for up to 14 days. A number of peaks appeared in ^1H NMR and ^{13}C spectra as well as in GC/MS chromatogram/spectra. Assignments of intermediates by NMR and GC/MS are given in Table 1. Acetone and 70% HP were combined in ratios 1:1, 1:10 (mostly HP) and 10:1 (excess acetone) in 0.6 mL d^3 acetonitrile and monitored by ^1H NMR and ^{13}C NMR for 14 days. The relative reaction progress in terms of proton resonances (as large, medium, small or tiny peaks) is given in the right columns of Table 1. On day zero there were two prominent methyl resonances in the

^1H NMR (Table 1): one at 2.1 ppm, assigned to the methyl protons of acetone and the other at 1.38 ppm attributed to 2-hydroxy-2-hydroperoxypropane (I) (Figure 3 shows structures of intermediates) [9]. The acetone resonance shifted to slightly higher ppm with moderate to excessive amounts of HP. This was taken as evidence for protonation of acetone by HP. By day 4 the 1:1 and 10:1 HP:acetone (i.e. moderate to large amounts of HP) samples exhibited an additional methyl resonance at 1.44 ppm in ^1H NMR which was assigned to a dimeric species where two molecules of acetone were linked by a peroxide functionality. By that time the protonated acetone species had decreased substantially with increasing reaction intermediates.

The larger chemical shift range of the ^{13}C NMR spectrum offered better peak separation with changes in carbon functionality. On day zero for the sample with excess acetone, resonances were observed at 24 ppm in the methyl region and 102 ppm in the carbonyl region. These were assigned to species with hydroxy terminal groups. On day zero of the samples with excess HP, peaks were seen at 20 ppm in the methyl region and at 109 ppm in the carbonyl region. These were assigned to species with terminal hydroperoxy groups. In the ^{13}C NMR spectrum of the sample of 1:1 HP:acetone, the resonance associated with the methyl groups of 2-hydroxy-2-hydroperoxypropane (I) and the 2,2-dihydroperoxypropane (II) were observed at 20 and 24 ppm, respectively, as well as in the carbonyl region at 102 and 109, respectively. With daily monitoring, new ^{13}C resonances were observed in the methyl region: four between 20-21 ppm and three between 24-25 ppm. One at ~21 ppm is known to be TATP. On day zero 2-hydroxy-2-hydroperoxypropane (I) was at a maximum but diminished over time. The ^{13}C resonances of TATP (107.8 ppm CO) and DADP (108.7 ppm CO) did not become discernible until day 5, although their presence was detected on day 1 using GC/MS (Table 1).

In order to validate proton and carbon assignments, 2D NMR experiments were performed: HSQC (heteronuclear single quantum coherence) correlated to methyl and heteronuclear multi-bond coherence (HMBC) correlated to carbonyls. Chemical ionization GC/MS analyses, with ammonia reagent gas, were performed on the aged NMR solutions to confirm assignments of NMR resonances. Reasonable NMR resonances with corresponding masses, relative abundance of species, and chemical intuition were used to formulate assignments shown in Table 1.

<Table 1>

We had shown that solutions of acetone/HP without added acid contained several intermediates, and LC/MS confirmed the presence of longer chain oligomers and cyclic species (Fig. 3) [10]. Species with terminal peroxide functionalities are favored, and increasing amount of HP enhances their formation. Only TATP and DADP precipitated under reaction conditions where acid was present and when no co-solvent was employed. In the absence of acid, solid TATP precipitated when the samples were aged at room temperature for up to two months. The asymmetric peroxides and longer chain oligomers were not observed by GC/MS, but using LC/MS they were observed in trace amounts.

<Figure 3>

3.3 Acetone Exchange in TATP

Experiments were conducted to determine if a new molecule of acetone could insert into an intact TATP ring. Deuterated acetone (d^6 -acetone) was stirred with h^{18} -TATP and monitored daily for seven days by GC/MS. Similarly, d^{18} -TATP was monitored in h^6 -acetone by 1H NMR, typically for days; afterwards the solution was examined by GC/MS. GC/MS results indicated 1, 2, and 3 molecules of d^6 -acetone were incorporated into h^{18} -TATP and 1 or 2 molecules of d^6 -

acetone into h^{12} -DADP in the presence of acid (Table 2). However, when no acid was added, 1H NMR indicated no insertion of acetone; the proton resonances of the methyl groups in h^{18} -TATP (1.43 ppm) showed no decrease in intensity though followed for 7 days in d^6 -acetone. Likewise the resonance of h^6 -acetone (2.1 ppm) containing dissolved d^{18} -TATP indicated no decrease in intensity over a 7 day period. Without acid, neither exchange nor synthesis of fresh TATP nor DADP was observed.

Exchange studies with chlorinated acetone were performed. d^{18} -Substituted TATP or proteo-TATP was stirred with 1,3-dichloroacetone in ACN with a five-fold excess of TFA. GC/MS analysis after d^{18} TATP and TFA had been stirred with dichloroacetone in ACN 17 hr showed d^{12} DADP, 1,3-dichloroacetone, and dichloro-TATP. While d^{12} -DADP was formed, presumably from opening of the d^{18} TATP-ring, no chloro-substitution into DADP was observed. Furthermore, the GC/MS fragmentation pattern as well as the quartet in the 1H NMR spectrum suggested only singly substituted TATP (i.e. 1,3-dichloroacetone) was formed. Neither tetrachloro-DADP nor hexachloro-TATP was observed, suggesting their formation may be sterically hindered. Interestingly, no incorporation of 1,1 dichloroacetone nor monochloroacetone was observed (1H , ^{13}C , GC/MS) even in the presence of acid (Table 3). Nevertheless, the observation of dichloro-substituted TATP indicates ring opening and re-closing does occur.

<Table 2>

3.4 Rate of TATP Formation

1H NMR was used to monitor the one-to-one reaction of acetone and HP (25 mmol each) at 15°C using 20, 40 or 80 μ L of trifluoroacetic acid (TFA) (0.27, 0.54, 1.07 mmol). The reaction was monitored by taking spectra every 5 minutes (including scan time) for up to 17 hours (1020 min) (Figure 4 shows typical NMR data). After 200 minutes the methyl protons of TATP were

clearly visible (as opposed to three days without acid). DADP protons only were barely visible after 800 minutes and were still faint at 1.35 and 1.79 ppm in the 1020 minute spectrum. The most abundant intermediates in the acid catalyzed reactions observed by NMR and GC/MS were 2,2-dihydroperoxypropane (II) and 2,2'-dihydroperoxy-2,2'-diisopropylperoxide (V). Although 2-hydroxy-2-hydroperoxypropane (I) was most abundant when there was no acid catalyst, formation of 2,2-dihydroperoxypropane (II) was favored under acidic conditions [7,11]. TATP formation was greatly accelerated by addition of acid; yet acid also caused TATP decomposition, as evident from following ^1H NMR resonance of TATP (1.42 ppm) when treated with various volumes of TFA (Figure 5). Monitoring TATP formation reactions by GC/MS showed the effect of the strength of acid as well as type of acid used. Compared to a mixture of acetone and HP with no added acid, concentrated sulfuric acid greatly enhanced the rate of formation of TATP as well as its decomposition to DADP. Reducing the concentration of the sulfuric acid, while maintaining a 1 molar equivalent acid, slowed TATP formation and significantly inhibited its decomposition to DADP. This observation suggested that water played a role. Concentrated HCl contains significantly more water than concentrated H_2SO_4 . When water was added to sulfuric acid so that the water content in the acetone/HP mix was the same as when HCl was used, the rates of TATP formation with either acid were comparable. Use of nitric acid did not result in the same observed rate of formation, but nitric acid is the weakest of the strong acids used in these experiments. Use of weak acids such as citric acid and TFA resulted in dramatically slower rates of TATP formation (Fig. 6), although TFA was still capable of decomposing TATP.

<Figure 4>

<Figure 5>

3.5 Effect of Water

Previously reported results indicate that a change in the concentration of acid and hydrogen peroxide can dramatically affect the outcome of TATP syntheses [5]. Dilute reagents result in poor yield of solid products, and concentrated reagents in the presence of higher acid loadings result in increased DADP formation. Water appears to play an important role in the synthesis. In an attempt to understand how water affects DADP versus TATP formation, several syntheses were attempted using 30 wt% and 50 wt% HP, acetone and concentrated sulfuric or hydrochloric acid. The ratios of the three reagents were maintained at 1:1:1 (8.6 mmol scale), but excess water, over that contributed by the reagents, was added (Table 3, Fig. 6). At the lowest levels of added water, the white solid formed was 100% DADP. At the highest levels of added water, the white solid precipitating was 100% TATP [12]. When the acid added was HCl, only a small amount of DADP was observed; this is attributed to the large amount of water (63wt%) in HCl. This phenomenon can be explained by the tendency of 2-hydroxy-2-hydroperoxypropane to disproportionate to 2,2-dihydroperoxypropane (II) and acetone in aqueous media [9]. The formation of the dihydroperoxy species appears to be a key step in TATP formation.

<Table 3>

<Figure 6>

3.6 Effect of Solvent and Temperature

To probe whether order of reactant addition had an effect on formation of TATP vs. DADP, it was varied (Table 4). The final precipitates, as well as in-situ products, were monitored by extracting aliquots of the reaction at intervals during reagent addition and analyzing by GC/MS. There were no notable differences in the final products obtained regardless of whether the acid was added first to the acetone, to the HP, or to both together (cf. exp. 1 to 3, Table 4) [8]. Only

when acid was the last reagent added did the reaction proceed slow enough for an intermediate, 2,2'-dihydroperoxy-2,2'-diisopropylperoxide (V) to be observed along with both cyclic peroxides (exp. 3); otherwise, only the cyclic peroxide(s) were seen. The final product of the hydrogen peroxide/acetone mixture varied markedly with solvent; acetonitrile favored formation of DADP at 0°C, while alcohols favored TATP (cf. exp.1 with 1*, Table 4). The effect of temperature has been discussed by others without agreement [8,11,13]. Generally, TATP is favored at lower temperatures, but the effect of temperature can be manipulated by other factors such as solvent. While DADP was the major solid product in ACN at 0°C, at lower temperatures even in ACN, TATP was favored (cf. 1 to 1' and 3 to 3', Table 4). When TFA was substituted for sulfuric acid (exp 1'') no precipitate formed within the same time interval as previous reactions (~30 minutes).

<Table 4>

3.7 Rate of TATP Decomposition

The decomposition of TATP by acid in CD₃CN or CDCl₃ was monitored by ¹H NMR. In ACN and CDCl₃ decomposition of TATP was pseudo-first order and formed DADP and acetone (Table 5). Quantifying TATP formation kinetics was more difficult due to formation of a number of intermediates, but initial formation rates of TATP in ACN are estimated in Table 5. Data suggests that at very high concentrations of acid, TATP is destroyed as fast as it is formed, and destruction of TATP in ACN leads to the formation of DADP (Tables 4 & 6). As TATP decomposed to DADP and acetone, other intermediates could be observed by ¹H NMR in d³-ACN. In ACN, 2,2'-dihydroperoxy-2,2'-diisopropylperoxide (V) and 2,2-dihydroperoxypropane (II) were observed as intermediates, whereas in CDCl₃ only 2,2'-dihydroperoxy-2,2'-

diisoproylperoxide (V) was observed. NMR and MS data suggests these intermediates are identical to those observed in formation experiments (Table 1).

<Table 5>

Table 6 emphasizes the effect of water and solvent on TATP decomposition. Not only did water slow the decomposition, but it also appeared to retard conversion of TATP to DADP. Table 6 shows the pseudo first-order rate constants for TATP destruction in ACN and various alcohols. When concentrated sulfuric acid was added to a TATP ACN solution, the rate of disappearance of TATP was very high, and DADP was the end product. With added water the reaction was slowed significantly, and only trace amounts of DADP were observed. When concentrated sulfuric acid was added to a TATP alcohol solution, the destruction of TATP was slower than in neat ACN, and only trace amounts of DADP were observed. Destruction of TATP was slower in alcohols with greater reactivity towards concentrated sulfuric acid, i.e. isopropanol or t-butanol. Methanol showed the highest rate of TATP destruction followed by ethanol, n-propanol and isopropanol. When t-butanol was used, an anomalous effect was observed. The reaction proceeded very quickly to a mixture of TATP and DADP and ceased. The decomposition of TATP by 37 wt% HCl generated some DADP, but the amount was very small compared with other acids (TFA SA) and chlorinated acetone species were detected.

<Table 6>

3.8 Mechanism

A proposed mechanism for the production of TATP and DADP is given in Figure 7. In a reaction between HP and acetone without acid catalyst, 2-hydroxy-2-hydroperoxypropane (I) was observed in high quantities soon after mixing. When acid was added 2,2-dihydroperoxypropane (II) was the primary species observed shortly after mixing [11]. Symmetric species,

where two acetones are linked by a peroxide linkage, 2,2'-dihydroxy-2,2'-diisopropylperoxide (III) and 2,2'-dihydroperoxy-2,2'-diisopropylperoxide (V) were also observed, but at later reaction times. The asymmetric species similar to 2-hydroxy-2'-hydroperoxy-2,2'-diisopropylperoxide (IV) were not directly observed by NMR or GC/MS and only trace amounts were observed using LC/MS. We speculate that when these are formed the hydroxyl group exchanges with a hydroperoxy group, or they rapidly convert to DADP and TATP, respectively [7]. The effect of water is apparent at this point. When water content is low, 2-hydroxy-2-hydroperoxypropane (I) can be protonated facilitating formation of (IV) and a pathway to cyclization forming DADP. When water content is high, disproportionation of (I) becomes favored resulting in the formation of the dihydroperoxy species (II) and, ultimately, the formation of TATP [9]. Under high water conditions, water, itself, is protonated; and the overall reaction proceeds more slowly. Alcohol solvents also become involved in this competition for protonation. Formation reactions performed in methanol or ethanol under highly acidic conditions produced almost 100% TATP versus the same reactions performed in acetonitrile which produced 90 to 98% DADP (Table 4).

Destruction of TATP results in the formation of 2,2'-dihydroperoxy-2,2'-diisopropyl peroxide (V) and acetone [14]. Depending upon the solvent used 2,2-dihydroperoxypropane (II) may also be observed. Under destruction conditions, the presence of water or alcohol retards TATP loss and prevents the formation of DADP. The retarding effect of water and alcohol can be attributed to the intermediate species competing with the solvent for protonation. The lack of DADP formation can be attributed to the solubility of the intermediates in more polar and protic solvents. Under mildly acidic conditions the opening of the TATP ring is reversible and

incorporation of a new acetone molecule is possible, or decomposition to DADP may occur, explaining the presence of deuterated DADP in addition to deuterated TATP.

<Figure 7>

4.0 Conclusions

We have reported that the synthesis of TATP is achieved in best yield by use of a 1 to 1 molar ratio of HP to acetone with modest amounts of acid (10-50 mole %). However, acid catalyzes TATP synthesis and decomposition, especially at high acid levels. Herein we examine the intermediates of the acetone/HP reaction and the rates of formation and destruction of TATP and postulate a mechanistic pathway. The oxidation of acetone by HP occurs whether or not acid is added; it is dramatically slower without acid, taking weeks and months to precipitate TATP and DADP [15]. Other linear and even cyclic peroxides have been observed in the reaction solution, but only TATP and DADP precipitate out due to their low solubility in aqueous media. If an organic solvent is present, TATP does not precipitate out of solution and, in the presence of acid, converts to DADP. Whether or not acid is present as soon as HP and acetone are mixed 2-hydroxy-2-hydroperoxypropane (I) forms. This then proceeds to form 2-hydroxy-2'-hydroperoxy-2,2'-diisopropylperoxide (IV) (the precursor to DADP) or 2,2'-dihydroperoxy-2,2'-diisopropylperoxide (V) (the precursor to TATP) depending on whether water content in the reaction mix is low or high, respectively. Water, which comes into the reaction via the acid and the HP, slows the formation of TATP and DADP, DADP most dramatically. Indeed, the same effect is observed when alcohol, which like water is susceptible to protonation, is added to the reaction mixture.

Under nearly anhydrous conditions sulfuric acid and trifluoroacetic acid decompose TATP in a pseudo first-order fashion to DADP. Under mildly acidic conditions the TATP ring

opens to form 2,2'-dihydroperoxy-2,2'-diisopropylperoxide (V) and acetone; this may re-cyclize with a new acetone molecule or further decompose to DADP and other smaller molecules. This point is important for the formation and destruction of TATP. Under destruction conditions it confirms that the process does not proceed to any appreciable extent via radical intermediates. The presence of the dihydroperoxy intermediates observed during destruction or under milder insertion conditions can only be rationalized by an ionic mechanism where acetone is removed leaving hydroperoxy species [14]. The presence of completely substituted TATP also implies one of two things: the TATP molecule opens and equilibrium with the intermediates is reestablished or the ring continues to open and reclose allowing all acetone molecules to be replaced with their deuterated counterparts. Both these possibilities seem reasonable; which dominates may depend upon the solvent. Regarding formation, the insertion of acetone seems to indicate that (V) reacts with acetone to form the asymmetric hydroxy hydroperoxy trimeric species, prior to cyclizing to TATP. This supports the claim that the asymmetric species are short-lived intermediates leading to the cyclic peroxide products.

5. References

1. Graham, S.R., Hodgson, R., Vechot, L., Essa, M.I., Calorimetric Studies on The Thermal Stability of Methyl Ethyl Ketone Peroxides (MEKP) Formulations., Process Safety and Environmental Protection, 2011, 89, 424-433.
2. Lin, Y.F., Tseng, J.M., Wu, T.C., Shu, C.M., Effects of Acetone on Methyl Ethyl Ketone Peroxide Runaway Reaction., Journal of Hazardous Materials, 2008, 153, 1071-77.
3. Jia, X., Wu, Y., Liu, P., Effects of Flour Bleaching Agent on Mice Liver Antioxidant Status and ATPases., Environmental Toxicology and Pharmacology, 2011, 31, 479-484.
4. Encyclopedia of Explosives and Related Items Vol 1 Fedoroff, Ed; Picatinny Arsenal, NJ 1960 A41 and Vol 7, Kaye, Ed; Picatinny Arsenal, NJ 1975 H79
5. Oxley, J.C.; Smith, J.L.; Bowden, P.; Ryan Rettinger "Factors Influencing TATP and DADP Formation: Part I" Propellants, Explosives, Pyrotechnics, submitted
6. Wolanov Y., Ovadia, L., Churakov, A. V., Medvedev, A. G., Novotortsev, V. M., Prikhodchenko, P. V., Preparation of Pure Hydrogen Peroxide and Anhydrous Peroxide Solutions From Crystalline Serine Perhydrate. Tetrahedron, 2010, 66, 5130-5133.
7. McCullough, Ketone-Derived Peroxides. Part 1. Synthetic Methods. J. Chem. Res. Synopses, 1980, 2, 601-627.
8. Matyas, R., Pachman, J., Study of TATP: Influence of Reaction Conditions on Product Composition., Propellants, Explosives, Pyrotechnics, 2010, 35, 31-37.
9. Sauer, M.C.V., Edwards, J.O., "Reactions of Acetone and Hydrogen Peroxide. I. The Primary Adduct," J. Phys. Chem., 1971, 75, 3004-3011. *ibid* Reactions of Acetone and Hydrogen Peroxide. II. Higher Adducts., J. Phys. Chem., 1972, 76, 1283-1287.
10. Sigman, M.E., Clark, C.D., Caiano, T., Mullen, R., Analysis of Triacetone Triperoxide (TATP) and TATP Synthetic Intermediates By Electrospray Ionization Mass Spectrometry., Rapid Communication in Mass Spectrometry, 2008, 22, 84-90.
11. Story, P. R., Lee, B., Bishop, C. E., Denson, D. D., Busch, P., Macrocyclic Synthesis. II. Cyclohexanone Peroxides., J. Org. Chem., 1970, 35, 3059-3062.
12. Sanderson, J. R., Zeiler, A. G., Wilterdink, R. J., An Improved Synthesis of Dicyclohexylidene Diperoxide., J. Org. Chem., 1975, 40, 2239-2241.
13. Pena, A. J., Pacheco-Londoño, L. P., Figueroa, J., Rivera-Montalvo, L. A., Román-Velazquez, F. R., Hernández-Rivera, S. P., Characterization and Differentiation of High Energy Cyclic Organic Peroxides by GC/FT-IR, GC-MS, FT-IR and Raman Microscopy., Proc. Of SPIE, 5778, 347-358.

14. Armitt, D., Zimmermann, P., Ellis-Steinborn, S., Gas Chromatography/Mass Spectrometry Analysis of Triacetone Triperoxide (TATP) Degradation Products., *Rapid Commun. Mass Spectrom.*, 2008, 22, 950-958.
15. Wilson S.A.; Brady, J.E.; Smith, J.L.; Oxley, J.C. The Risk of Mixing Dilute Hydrogen Peroxide and Acetone Solutions *J of Chemical Health & Safety*, **2012**, 19(2), 27-33.

List of Figures

Figure 1. GC/MS Data 1:1:1 (9.3 mmol) of 65%HP to acetone to 96.5% sulfuric acid at 0°C

Figure 2. GC/MS data shows effect of varying the mole ratio of acid and the concentration of acid and hydrogen peroxide. Increasing the water content slows the rate of formation of TATP.

Figure 3. Products of HP/acetone reaction as observed by LC/MS

Figure 4. Formation of TATP followed by ^1H NMR using 40 uL TFA

Figure 5. Formation of TATP followed by ^1H NMR 20, 40, & 80 uL TFA

Figure 6. Rate of TATP Formation with 8.6 mmol each HP-Acetone-Acid vs Water

Figure 7. Mechanism for Synthesis of TATP and DADP

Figure 1

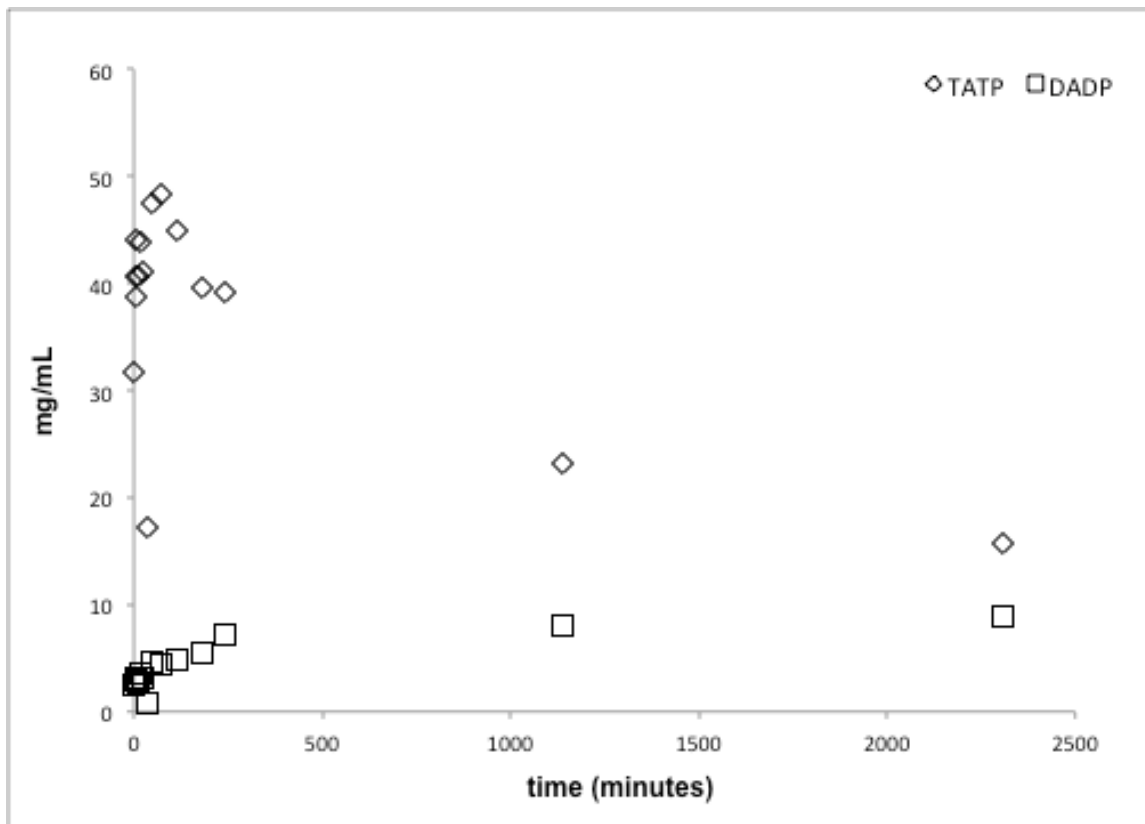


Figure 1. GC/MS Data 1:1:1 (9.3 mmol) of 65%HP to acetone to 96.5% sulfuric acid at 0°C

Figure 2

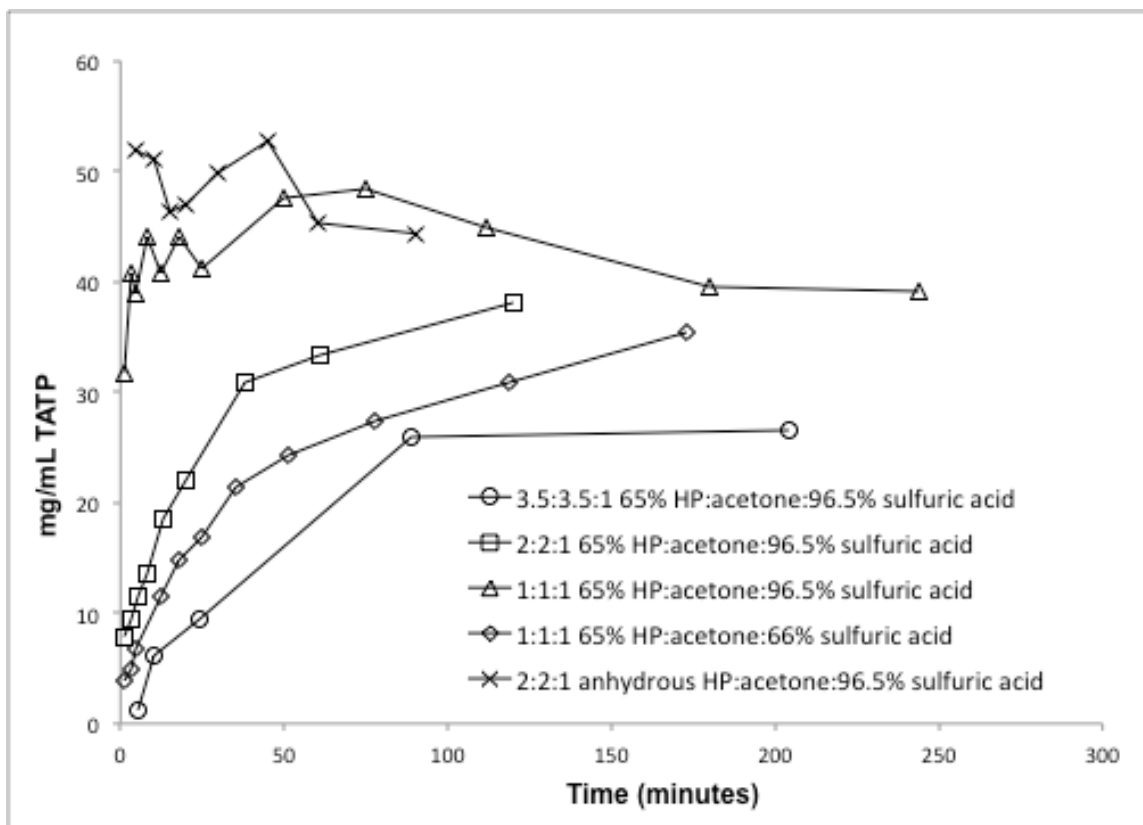
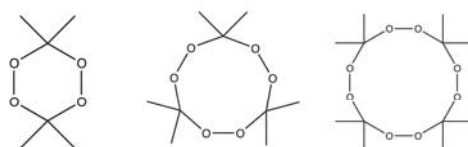


Figure 2. GC/MS data shows effect of varying the mole ratio of acid and the concentration of acid and hydrogen peroxide. Increasing the water content slows the rate of formation of TATP.

Figure 3

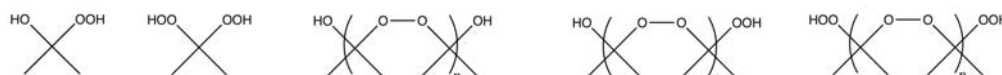
Cyclic acetone peroxides



166	240	314
L	H	M

m/z
relative abundance

Linear acetone peroxides



n =	1	1	2,3,4,5,6	2,3,4	2,3,4,5,6
m/z	110	126	168,242,316,390,464	184, 258,332	200, 274, 348, 422, 496
relative	L	H	L,T,T,T,T	T,T,T	H, H, H, M, T

Figure 3. Products of HP/acetone reaction as observed by LC/MS

Figure 4

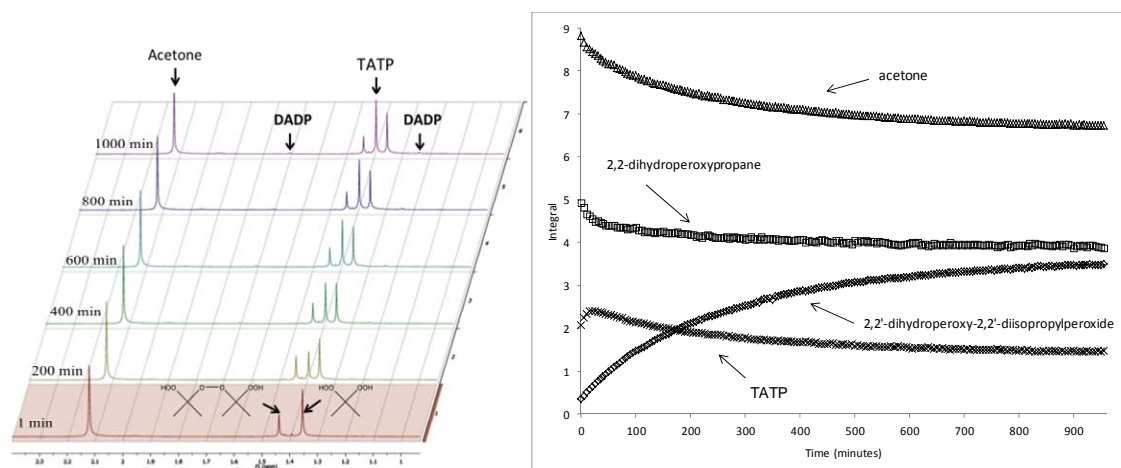


Figure 4. Formation of TATP followed by ^1H NMR using 40 μL TFA

Figure 5

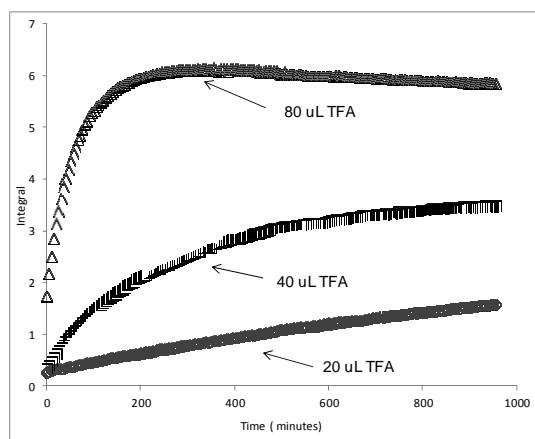


Figure 5. Formation of TATP followed by ^1H NMR 20, 40, & 80 uL TFA

Figure 6

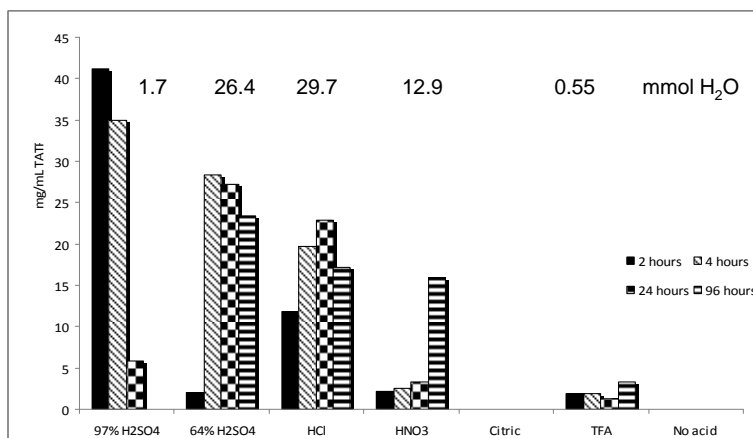


Figure 6. Rate of TATP Formation with 8.6 mmol each HP-Acetone-Acid vs Water

Figure 7

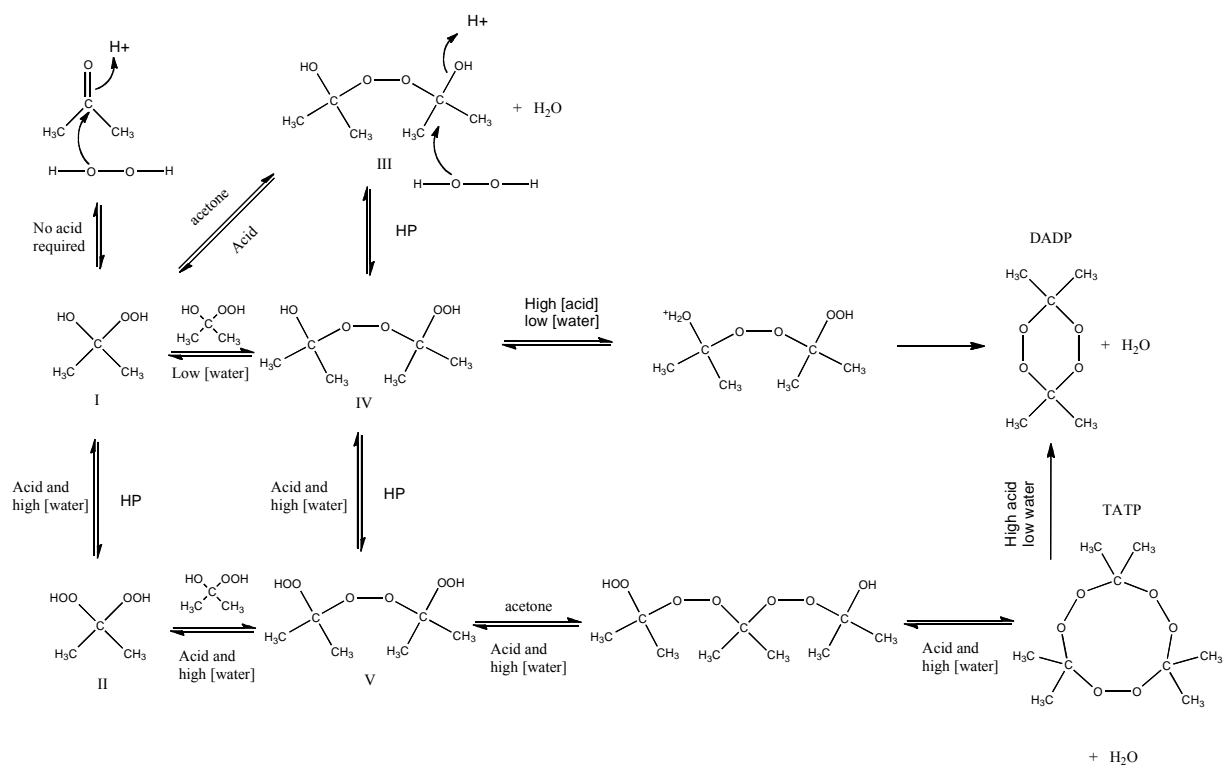


Figure 7. Mechanism for Synthesis of TATP and DADP

List of Tables

Table 1: GC/MS & NMR Assignments for Various Products of Acetone/HP reaction

Table 2: Acid catalyzed insertion of labeled acetone into TATP

Table 3: Acetone, HP, Acid, 1:1:1 (8.6 mmol each) & Varied H₂O

Table 4: GC/MS Analysis of Cyclic Peroxide Products vs HP/Acetone Reaction Conditions

Table 5: First order rate constants obtained from ¹H NMR at 288K following destruction of 45mg (0.203 mmol) TATP with acid or TATP formation from 100 uL acetone & HP (1.36mmol; 1:1 ratio) & TFA in 1.2mL d³-CH₃CN

Table 6: GC/MS monitoring of TATP (100 mg, 045 mol) + H₂SO₄ (96.5 wt%, 200 uL, 3.6 mmol)

Table 1: GC/MS & NMR Resonance Assignments & Relative Abundance by Days of Reaction

1:1 HP:acetone no acid, in acetonitrile		CI mass spectrum		¹ H NMR	¹³ C NMR	¹³ C NMR	Relative NMR abundance on day							
		mass	amount	(CH ₃) ppm	(CH ₃) ppm	(CO) ppm	0	1	3	5	7	10	12	14
I	2,2-hydroxy hydroperoxy propane	92.1	s	1.38	24.2	102.4	L	L	M	M	S	S	S	S
II	2,2-dihydroperoxy propane	108.1	m	1.38	20.2	109.4	M	L	L	L	L	L	L	L
III	2,2'-dihydroxy-2,2'-diisopropyl peroxide	150.2	m	1.44	24.66	102.5	T	S	S	S	S	S	S	S
IV	2,2'-hydroxy hydroperoxy-2,2'-diisopropyl peroxide	166.2	--		uncertain									
V	2,2'-dihydroperoxy-2,2'-diisopropyl peroxide	182.2	l	1.44	20.5	109	T	M	M	M	L	L	L	L
	TATP (3,3,6,6,9,9-hexamethyl-1,2,4,5,7,8-hexoxonane)	222.2	vary	1.42	20.97	107.8	T	S	S	S	S	S	S	S
	DADP (3,3,6,6-tetramethyl-1,2,4,5-tetroxonane)	148.2	vary	1.35, 1.79	20.8, 21.1	108.7				T	T	T	S	S
	acetone			2.1	31	209	L	L	L	L	L	L	L	L
	dihydroxy trimer	224.3	s											
	hydroxy hydroperoxy trimer	240.3	--											
	dihydroperoxy trimer	256.3	m											

* CI with NH₃, M+1, M+18 were observed & for compound I M+35.

L = large; M = medium; S= small; T= tiny

Table 2: Acid catalyzed insertion of labeled acetone into TATP

Labeled Acetone Insertion of TATP at 15°C for 17 hours

Experiment	Solvent	mL Solvent	Acid	μ L Acid	mmols Acid	mg TATP	mmol TATP	Ratio Acid:TATP	μ L Acetone	mmols acetone	Ratio acetone : TATP	Analysis	TATP	DADP
h^6-Acetone + d^{18}-TATP 288K														
h^0 -acetone + d^{18} -TATP	CD ₃ CN	1.2	TFA	30,40	0.40,0.54	48	0.20	2.0, 2.7	50	0.68	3.40	¹ H-NMR	insertion	insertion
h^5 -acetone + d^{18} -TATP	CDCl ₃	1.0	TFA	20,30	0.27,0.40	48	0.20	1.3,2.0	40	0.54	2.72	¹ H-NMR	insertion	insertion
h^5 -acetone + d^{18} -TATP	d^6 & h^6 acetone	1.0	none	0	0	120	0.50	--	900	12.2	24.5	¹ H-NMR LC/MS	no insertion 7 days	no insertion 7 days
d^6-Acetone + h^{18}-TATP Reaction for 7 days 298K														
d^6 -acetone + h^{18} -TATP	d^6 acetone	1.0	none	0	0	111	0.50	--	1000	13.6	27.2	¹ H-NMR LC/MS	no insertion 7 days	no insertion 7 days
d^6 -Acetone + h^{18} -TATP	acetone+ water or EtOH	10	sulfuric	140	2.6	222	1.0	2.6	1200	16.4	16.4	GC/MS	d^6 TATP, TATP after 24 hr	d^{12} DADP, d^6 DADP & DADP+other in 48h
d^6 -Acetone + h^{18} -TATP	CH ₃ OH, ACN, or CHCl ₃	10	TFA	150	2.01	222	0.92	2.2	75	1.02	1.1	LC/MS	d^6 , d^{12} , d^{18} TATP observed	insertion, d^{12} DADP major, d^6 DADP but no parent ion
ChloroAcetone + d^{18} & h^{18}-TATP 288K (dichloroacetone is a solid)														
1,3 dichloro acetone + d^{18} -TATP	CD ₃ CN	1.2	TFA	40	0.54	22	0.10	5.4	42 mg	0.33	3.3	¹ H-NMR & GC/MS	1 dichloro in TATP	no insertion
1,3 dichloro acetone + h^{18} -TATP	CD ₃ CN	1.2	TFA	40	0.54	22	0.10	5.4	42 mg	0.33	3.3	¹ H-NMR & GC/MS	1 dichloro in TATP	no insertion
1,1 dichloro acetone + h^{18} -TATP	CD ₃ CN	1.2	TFA	40	0.54	22	0.10	5.4	42 mg	0.33	3.3	GC/MS	no insertion	no insertion
monochloro acetone + h^{18} -TATP	CD ₃ CN	1.2	TFA	40	0.54	22	0.10	5.4	27	0.33	3.3	GC/MS	no insertion	no insertion
1,3 dichloro acetone + h^{18} -TATP	CD ₃ CN	1.2	none	0	0	22	0.10	0	42 mg	0.33	3.3	GC/MS	no insertion	no insertion

Table 3: Acetone, HP, Acid, 1:1:1 (8.6 mmol each) & Varied H₂O
 Acetone (0.5 g), HP, Acid (1:1:1) (8.6 mmol each)

water (mL)	yield (mg)	% yield	% TATP	% DADP
50% HP (0.586 g), 96.5% H ₂ SO ₄ (0.876g)				
0.25	308	48.3	0	100
0.5	246	38.6	7.6	92
0.75	348	54.6	81	19
1	378	59.3	100	0
30% HP (0.976 g), 96.5% H ₂ SO ₄ (0.876g)				
	218	34	11	89
0.25	140	22	72	28
0.5	265	42	72	28
0.75	161	25	89	11
30% HP (0.976 g), 37% HCl (0.85g)				
	92.1	14	81	0
0.25	98.7	15	83	0
0.5	92.2	14	87	0
0.75	99.3	16	94	0

Table 4: GC/MS Analysis of Cyclic Peroxide Products vs HP/Acetone Reaction Conditions

exp	Order of Reactant Addition			Conditions		crude yield	in situ products	% Final Product analysis		
	HP (66.8%)	acetone	sulfuric acid (96.5%)	solvent	temp			TATP	DADP	GC
(repeat)	2.7g, 54mmol	3.0g, 51mmol	10.4g, 102mmol	ACN (mL)	°C	gram				
1 (3)	1	3	2	30	0	2.6	TATP/DADP	--	98	uECD
2 (2)	3	1	2	30	0	3.1	DADP	--	100	uECD
3 (1)	2	1	3	30	0	3.1	TATP/dimer/DADP	--	87	MS
2'	3	1	2	30	-20	3.0	TATP/DADP	7	77	MS
1'	1	3	2	30	-25	3.3	TATP/dimer/DADP	67	22	MS
	1.5g, 26mmol	1.5g, 26mmol	5.24g, 51mmol							
3'	2	1	3	15	-40	1.7	TATP/dimer/DADP	93	1	MS
1*	1	3	2	15 EtOH	0	1.0	n/a	98	--	uECD
1*	1	3	2	15 MeOH	0	0.8	n/a	100	--	MS
1'	1	3	2	15	-40	1.8	TATP/DADP	90	1	MS
1"	1	3	2 TFA (99%, 5.8g)	15 ACN	0		dimer->TATP, DADP		no ppt	

Table 5: First order rate constants obtained from ^1H NMR at 288K following destruction of 45mg (0.203 mmol) TATP with acid or TATP formation from 100 uL acetone & HP (1.36mmol; 1:1 ratio) & TFA in 1.2mL $\text{d}^3\text{-CH}_3\text{CN}$

TATP Formation & Destruction Monitored by ^1H NMR

Acid	uL	mmol acid	Rate Constant (s^{-1})
Decomposition of TATP (45mg, 0.2 mmol) in Chloroform			
TFA	30	0.392	1.50E-05
TFA	40	0.522	1.83E-05
TFA	60	0.784	6.67E-05
TFA	80	1.045	2.48E-04
SA	10	0.188	2.17E-05
SA	15	0.281	3.00E-05
SA	20	0.375	6.17E-05
Decomposition of TATP (45 mg, 0.2mmol) in Acetonitrile			
TFA	60	0.784	1.17E-05
TFA	100	1.306	3.50E-05
Decomposition of DADP (29 mg) in Chloroform			
SA	10	0.188	3.67E-05
Formation of TATP (45mg, 0.2mmol) in Acetonitrile			
TFA	20	0.261	1.75E-04
TFA	40	0.522	4.83E-04
TFA	80	1.045	4.83E-04

Table 6: GC/MS monitoring of TATP (100 mg, 045 mol) + H2SO4 (96.5 wt%, 200 uL, 3.6 mmol)

GC/MS monitoring of TATP Decomposition (298K)
TATP (100 mg, 045 mmol) + H2SO4 (96.5wt%, 200 uL, 3.6 mmol)

Solvent (10 mL)	k (sec ⁻¹)	Result
Acetonitrile	2.41E-03	DADP
90:10 acetonitrile:water	1.81E-04	no DADP
80:20 acetonitrile:water	4.74E-05	no DADP
70:30 acetonitrile:water	1.82E-05	no DADP
Methanol	1.98E-03	no DADP
90:10 methnaol:water	2.13E-04	no DADP
80:20 methanol:water	2.96E-04	no DADP
Ethanol	6.43E-04	no DADP
90:10 ethanol:water	8.63E-05	no DADP
80:20 ethanol:water	1.46E-04	no DADP
70:30 ethanol:water	2.00E-04	no DADP
n-propanol	2.96E-04	no DADP
90:10 n-propanol:water	1.72E-05	no DADP
isopropanol	8.86E-05	no DADP
90:10 isopropanol:water	2.88E-05	no DADP
80:20 isopropanol:water	1.01E-04	no DADP
70:30 isopropanol:water	6.96E-05	no DADP
t-butanol	n/a	DADP/TATP
90:10 t-butanol:water	n/a	DADP/TATP

*Reaction in t- butanol quickly converted some of the TATP to DADP but further change in concentrations was not observed. **Reaction in neat ACN used only 20 uL acid

**Factors Influencing Triacetone Triperoxide (TATP) and
Diacetone Diperoxide (DADP) Formation: Part 3**
Jimmie C. Oxley* ; James L. Smith; Joseph E. Brady, IV; Lucus Steinkamp

*^aUniversity of Rhode Island,
Chemistry Department
51 Lower College Road
Kingston, RI 02881
joxley@chm.uri.edu

Abstract

Acid catalyzes the formation of triacetone triperoxide (TATP) from acetone and hydrogen peroxide, but acid also destroys TATP, and, under certain conditions, converts it to diacetone diperoxide (DADP). Strong acid reacts so quickly with TATP that it can explode. We found that the use of dilute acid reduces the rate of decomposition almost too much for the purpose of gentle destruction. However, combining the use of weak acid with slightly solvated TATP made the destruction of TATP proceed at a reasonable rate. The variables of acid type, concentration, solvent and ratios thereof have been explored, along with kinetics, in an attempt to provide a safe fieldable technique for gently destroying this homemade primary explosive.

1. Introduction

The hazardous nature of peroxides is well established; however, those with multiple peroxide functionalities, such as triacetone triperoxide (TATP), diacetone diperoxide (DADP), or hexamethylene triperoxide diamine (HMTD), can be explosive (Fig. 1). They are impractical as explosives and are not used by legitimate military groups because they are too shock and heat sensitive. They are attractive to terrorists because synthesis is straightforward, requiring only a few easily obtained ingredients. Peroxide explosives were employed as initiators by would-be-bombers Ahmed Ressam (Dec. 1999), Richard Reid (Dec. 2001), and Umar Abdulmutallab (Dec 2009). They also have proven to be effective as the main charges in Palestinian bombs and the July 2005 London bombs. This paper discusses methods to gently degrade peroxide explosives chemically, at room temperature.

Currently, the safest way to dispose of illegal explosives is to blow-in-place. This procedure keeps law enforcement from handling and transporting highly sensitive materials. However, because the peroxide explosives are frequently found in high-population density areas, blow-in-place protocols are impractical. In recent years there have been many examples of finds of illicit explosives where law enforcement went to extreme measures to destroy on the premises. For example, in November 2010 at a rented house in Escondido, CA was found “the largest amount of certain homemade explosives ever found in a single U.S. location. Nearly every room was packed with piles of explosive material...six mason jars with highly unstable hexamethylene triperoxide diamine, or HMTD...” Controlled burn of the house was deemed the only safe way to handle the disposal.¹

The goal of this work was to find a safe, effective, field-usable method for destroying TATP. Few publications have addressed this issue; two have suggested copper and tin salts to effect destruction at elevated temperature;^{2,3} one used mineral acids and elevated temperature.⁴ These articles were used as the starting point in a search for a room-temperature, chemical destruction method for peroxides. We sought an all-liquid chemical solution that could be

sprayed over solid peroxide stashes or in which peroxide saturated materials could be immersed and the peroxide would quiescently be destroyed within hours without further handling. We sought a chemical solution that could destroy either TATP or HMTD so that the white illicit explosive would not require prior characterization. At a lab-scale of milligrams we found concentrated sulfuric acid effectively destroyed TATP; however, on scale-up to even 1 gram, the heat released in the reaction caused a violent and rapid release of energy, perhaps detonation.⁵

TATP is made by the reaction of acetone and hydrogen peroxide. Under the right conditions those two reagents slowly form TATP at room temperature.^{6,8} However, when synthesis of TATP is desired, the controlled addition of acid is used. With too much acid or too high a temperature the reaction can form mainly DADP, or the heat of the reaction of TATP with acid can initiate detonation. Herein we explore the region where acid can be used to affect quiescent decomposition of TATP. This work mainly focuses on the destruction of 0.5 g or 3g quantities of solid TATP, but kinetics are also reported on solutions of TATP. Field tests were also performed on 500g quantities of TATP and 500mg of HMTD.

2.0 Experimental Section

2.1 Synthesis of TATP and DADP

TATP and DADP were prepared in our laboratory.⁷⁻⁹ TATP was prepared by stirring 7 g 50% hydrogen peroxide and 5.8 grams acetone in a cold bath (< -5°C) while 0.5 mL of HCl (18% m/m) was slowly added. The mixture was held at -14°C overnight (14-18 hours). Water was added to the mixture; it was filtered; and the precipitate was rinsed with copious amounts of water. Crude yield was 5 g (67.6%) with melting point 88-92°C; recrystallization from hot methanol yielded a white, finely divided crystalline product, melting point 94-95°C.

DADP was prepared by adding concentrated sulfuric acid (10.7 g, 96%, 105 mmol) with stirring to a cold (< 3°C) acetonitrile solution of hydrogen peroxide (3.00 g, 70%, 62 mmol). Acetone (2.9 g, 50 mmol) and acetonitrile (10 mL) were combined and chilled (~ 0°C). The acetone mixture was added drop-wise to the hydrogen peroxide mixture while the temperature was maintained between -4 and 4°C, and the mixture was allowed to stir for 90 minutes, during which time a white precipitate formed. The precipitate was collected by vacuum filtration and rinsed with copious amounts of cold water. The crude solid (2.9 g, 76% yield) had a melting point of 131-132°C and was recrystallized from ethyl acetate.

2.2 Destruction of TATP

For the destruction, 500 mg (2.25 mmol) of the recrystallized TATP was placed in clear 40 mL glass vials and moisten with 0.5, 1, 2, or 4 mL solvent. This was followed by addition of 0.5, 1, 2, 3, 4, 5, 9 mL of acids in varying concentrations. More than 600 individual experiments were performed. All mixtures were allowed to react at room temperature uncovered for 2-24 h before extraction with 10 mL dichloromethane (solubility of TATP at room temperature ~ 1g/4mL), rinsing with 3 mL distilled water followed by 3 mL of 1% Na₂CO₃. The organic layer was dried over anhydrous magnesium sulfate and analyzed via gas chromatography with mass selective detector (GC/MS). Each analytical run began with a series of five or more authentic TATP samples ranging in concentration from 10-10,000 µg/mL. These samples were used to monitor instrument response and plot a calibration curve.

An Agilent 6890 GC with Agilent 5973i MSD detector was used. The inlet was operated with a 5:1 split at 150°C. The column was an HP-5MS (30m x 0.25mm x 250µm), operated in constant flow mode with a flow rate of 1.5 mL/min and average velocity of 45 cm/sec. The

transfer line for the GC to the MS was held at 250°C for the duration of the run. The oven was held at 50°C for two minutes before ramping to 200°C at a rate of 10°C/min. The MS had a solvent delay of 2 minutes and scanned from 14-500 m/z.

2.3 Kinetics for Destruction of TATP

Solutions of TATP (5 mL) were measured into 40 mL screw-top vials. In a separate vial solutions of acid and solvent (5 mL total) were measured. The solutions were equilibrated at the experimental temperature, in a water bath or GC oven. After equilibration, the 5 mL solution of acid was poured into the 5mL TATP solution, and the mixture was held at constant temperature for the duration of the experiment. At recorded time intervals, an aliquot of the reaction mixture was removed by syringe, placed in a separate 15 mL vial containing dichloromethane (DCM), rinsed with 2 to 3 mL of 3% NaHCO₃, followed by a rinse with distilled water, removing the aqueous layer each time. The organic layer was dried over a small amount of MgSO₄ (anhydrous) and transferred to a GC vial for quantification of remaining TATP.

For destruction of solid TATP with aqueous acid 5 mg TATP was placed into a 16 mL screw cap vial; and 1 mL acid, added. At recorded intervals the reaction was quenched by addition of ~3 mL 3 wt% sodium bicarbonate followed by 5 mL DCM. The aqueous layer was discarded; a second rinse with bicarbonate was performed; and a third with distilled water. The organic layer was dried over anhydrous magnesium sulfate and analyzed by GC/MS.

To quantify TATP an Agilent 6890 gas chromatograph with 5973 mass selective detector (GC/MS) was used. The inlet temperature was 110°C and total flow of 24.1 mL/min (helium carrier gas). Inlet was operated in splitless mode, with a purge flow of 20 mL/min at 0.5 minutes. A 15 m Varian VF-200MS column with 0.25 mm inner diameter and 0.25 µm film thickness was operated under constant flow condition at 1.5 mL/min. The oven program was initial temperature of 40°C with a 2 minutes hold followed by a 10°C/min ramp to 70°C, a 20°C/min ramp to 220°C and a post-run at 310°C for 3 minutes. The transfer line temperature was 250°C and the mass selective detector source and quadrupole temperatures were 230°C and 150°C, respectively. Electron impact ionization was used.

2.4 Heat Release

Heat released during the reaction of acid on dissolved TATP was measured using a Thermal Hazards Technologies micro-calorimeter. To calibrate the instrument two amber GC vials containing 1 mL reagent alcohol were placed in the sample and reference positions of the instrument. In calibration mode the number of pulses was set to 3; the pulse size, to 300 mJ; the pulse interval, to 300 seconds; and the lead time, to 30 seconds; samples were stirred at 200 rpm. To determine the heat of mixing between sulfuric acid and reagent alcohol, the instrument was set to collection mode with an experimental duration of 1000 seconds. A modified acid injection method was designed to accommodate the corrosive nature of strong acids. A glass capillary syringe needle was attached to a 1 mL plastic syringe. The syringe was primed to remove excess air and reduce dead volume, and the desired mass of acid was pulled into the syringe. Once a stable baseline was achieved, data collection began followed by manual injection of acid into alcohol. To determine heat released during the reaction between acid and TATP, the steps described above were followed using 1 mL of a 40 mg/mL TATP/ alcohol solution in the sample position and an experimental duration of 50,000 seconds.

2.5 Product ID

The type and concentration of acid used to destroy TATP determined the progress of reaction and the reaction products. Experiments, in duplicate, were conducted to examine the effect of acid type. TATP (500 mg) and 1 mL of 50% water/alcohol were combined (the alcohol

was ethanol or isopropanol). To this mixture was added 2 mL of sulfuric acid (65%), hydrochloric acid (36%), nitric acid (70%), phosphoric acid (85%), methanesulfonic acid (99%), boron trifluoride (48% in diethyl ether), trifluoroacetic acid (99%), or perchloric acid (99%). WARNING In one experiment, addition of nitric acid resulted in a violent fuming reaction. The mixtures were allowed to react for 3 hours before extracting as described above. Products were identified by comparing the mass spectra to authentic samples of TATP and DADP or by spectral matching to the NIST database. The relative amounts of each material in solution are expressed as a percentage of the total chromatographic signal.

3.0 Results & Discussion

Relative rates of TATP Decomposition with Acid: Mineral acid, an inexpensive liquid applied as a spray or mist, could be the perfect field approach to destroying TATP. However, the addition of some concentrated acids to solid TATP (3 g) resulted in detonation (3 mL 80% or 98% sulfuric) or violent decomposition (98% sulfuric with alcohol-wet or diesel-wet TATP) while with more dilute acid the reaction appeared non-existent. To avoid the potentially violent reactions, experiments were designed to screen different solvent and acid combinations. TATP destruction did not occur with bases, but many acids, even BF₃, destroyed TATP to some extent. A survey of acids was performed, both with alcohol wetted TATP (Table 1) and with neat TATP (Table 2). Note that decomposition is faster with HCl than with H₂SO₄, though the molar concentrations were roughly the same, and decomposition is much faster in solution with lower concentrations of acid than is necessary to decompose the solid (Table 3).

Table 1: Percent alcohol-wet TATP remaining (from 0.5 g) after acid treatment [TATP DADP031213] (1:2 is solvent to acid ratio)

Solvent	MeSO ₃ H	HClO ₄	HCl 36%	H ₂ SO ₄ 65%	HNO ₃ 70%	TFA CF ₃ CO ₂ H	BF ₃	H ₃ PO ₄	CH ₃ CO ₂ H
3h IPA EtOH 50%	1:2 0%	1:2 0%	1:2 9-0%	1:2 37-30%	1:2 0%	1:2 1-0%	1:2 0%	1:2 83-75%	2:2, 2:3 100%
24h toluene	1:0.5 43%	1:0.5 violent	0.5:2 36%	0.5:1 73%	1:0.5 0%				
pK _a	-13	-8	-6.3	-3	-1.64	0.23		2.15	4.75

Table 2: Decomposition Rate Constant of Solid TATP (5 mg) at 22°C with 1 mL aqueous acid [TATP DADP031213]

H ₂ SO ₄	wt%	k(sec ⁻¹)	HCl	wt%	k(sec ⁻¹)	HNO ₃	wt%	k(sec ⁻¹)	HClO ₄	wt%	k(sec ⁻¹)
16M	89	7.1E-03									
14M	82	1.9E-03				13M	60	1.8E-02			
12M	74	8.8E-04	12M	37	1.4E-03						
10M	64	1.9E-04	10M	32	2.6E-04	10M	49	2.4E-03	9.3M	61	7.9E-03
8.1M	54	9.8E-05	8.8M	28	1.8E-04	8.1M	41	1.5E-04	8.4M	58	1.7E-03
4.7M	34	2.7E-05	5.4M	18	1.3E-05						

Table 3: Decomposition Rate Constants for Dissolved TATP with Aqueous Acid
 $\text{rate}(\text{mg/s}) = k \cdot \text{solubility}$ [Excel TATP DADP031213]

Temperature 22C						Temperature 45C					
TATP (mg)	Acid (3.7 mmol)	Solvent (10 mL)	k (s ⁻¹)	Solubility (mg/mL)	Rate (mg/sec)	TATP (mg)	Acid (3.7 mmol)	Solvent (10 mL)	k (s ⁻¹)	Solubility (mg/mL)	Rate (mg/sec)
100	97%*	Acetonitrile (ACN)	1.4E-01	125	1.8E+01	100	97%	Ethanol (EtOH)	6.4E-04	143	9.2E-02
100	97%	90:10 ACN:H ₂ O	1.8E-04	105	1.9E-02	100	97%	90:10 EtOH:H ₂ O	8.6E-05	123	1.1E-02
100	97%	80:20 ACN:H ₂ O	4.7E-05	49	2.3E-03	100	97%	80:20 EtOH:H ₂ O	1.5E-04	76.9	1.1E-02
100	97%	70:30 ACN:H ₂ O	1.8E-05	44	8.0E-04	100	97%	70:30 EtOH:H ₂ O	2.0E-04	51.4	1.0E-02
7.5	97%	50:50 ACN:H ₂ O	7.4E-05	11.1	8.2E-04	7.5	97%	50:50 EtOH:H ₂ O	3.0E-04	13.2	4.0E-03
7.5	37%	Acetonitrile	2.0E-04	125	2.5E-02	100	97%	n-propanol (n-PrOH)	3.0E-04	188	5.6E-02
7.5	37%	50:50 ACN:H ₂ O	9.9E-05	11.1	1.1E-03	100	97%	90:10 n-PrOH:H ₂ O	1.7E-05	141	2.4E-03
7.5	18%	Acetonitrile	4.8E-04	125	6.0E-02	100	97%	Isopropanol (i-PrOH)	8.9E-05	217	1.9E-02
7.5	18%	50:50 ACN:H ₂ O	1.1E-04	11.1	1.2E-03	100	97%	90:10 i-PrOH:H ₂ O	2.9E-05	155	4.5E-03
7.5	97%	Methanol (MeOH)	5.2E-04	35.7	1.9E-02	100	97%	80:20 i-PrOH:H ₂ O	2.3E-05	109	2.5E-03
7.5	97%	50:50 MeOH:H ₂ O	5.6E-05	1.45	8.0E-05	100	97%	70:30 i-PrOH:H ₂ O	7.0E-05	69	4.8E-03
7.5	65%	Methanol	4.7E-05	35.7	1.7E-03	7.5	97%	50:50 i-PrOH:H ₂ O	2.5E-04	24.0	6.0E-03
7.5	65%	50:50 MeOH:H ₂ O	5.3E-05	1.45	7.7E-05	100	97%	Methanol	2.0E-03	80	1.6E-01
7.5	35%	Methanol	6.7E-05	35.7	2.4E-03	100	97%	90:10 MeOH:H ₂ O	2.1E-04	57.6	1.2E-02
7.5	35%	50:50 MeOH:H ₂ O	3.7E-05	1.45	5.3E-05	100	97%	80:20 MeOH:H ₂ O	3.0E-04	33.3	9.9E-03
7.5	37%	Methanol	1.7E-04	35.7	6.0E-03	7.5	97%	60:40 MeOH:H ₂ O	8.8E-04	12.7	1.1E-02
7.5	37%	50:50 MeOH:H ₂ O	5.8E-05	1.45	8.4E-05	7.5	97%	50:50 MeOH:H ₂ O	9.7E-04	5.99	5.8E-03
7.5	18%	Methanol	2.4E-04	35.7	8.6E-03	100	97%	t-butanol (t-BuOH)	acid reacts preferentially with t-butanol		
7.5	18%	50:50 MeOH:H ₂ O	6.3E-05	1.45	9.1E-05	100	97%	90:10 t-BuOH:H ₂ O			

*20 uL 96.5wt% H₂SO₄ [18.2M] 65%= 65wt% H₂SO₄ [10.2M] 37% = 37 wt% HCl [12.2M]
 97% = 96.5wt% H₂SO₄ [18.2M] 35%= 35wt% H₂SO₄ [4.5M] 18% = 18wt% HCl [5.4M]

We previously noted that water content affected the ratio of TATP/DADP precipitates when synthesizing TATP.⁸ Now we note water effects the rate of decomposition as well as the decomposition products. Water, entering the reaction with the acid, and in some cases with the solvent, slows the rate of TATP decomposition (Table 3). Solubility is part of the effect. While TATP was soluble in the alcohols and acetonitrile used it is essentially insoluble in water, yet the acid can more freely dissociate in water. The highest observed decomposition rate constant was for TATP in acetonitrile with no water, and in that solvent TATP converted to DADP. This

conversion was not observed in alcohol solvents, nor when water was added to acetonitrile. Furthermore, use of an alcohol solvent or addition of water markedly slowed the decomposition of TATP. Similar observations were noted when using alcohols as co-solvents in TATP formation reactions.⁸ The rate of TATP decomposition was dependent on the type of alcohol. TATP decomposed faster in primary alcohols (MeOH > EtOH > n-PrOH) than in isopropanol, a secondary alcohol. Tertiary butyl alcohol reacts preferentially with acid rather than TATP forming 2,2,4,6,6-pentamethyl-3-heptene, a condensation product of alcohol with sulfuric acid.

The rate constants for TATP decomposition in alcohol are at a maximum in pure alcohol but pass through a minimum as the amount of water increases. The formation of alcohol/water complexes were shown to have a significant impact upon protonation of organic acids and bases and is attributed to preferential solubility by water or the organic solvent depending on the nature of the substance.¹⁰⁻¹² Table 3 shows the solubility of TATP in the various solvents. If rate (mg/sec) were calculated from the product of the rate constant and solubility (assuming solvent-wetted solid TATP maintains a film of saturated solution), the decreased solubility negates (Table 3, far right columns) the effect of increasing rate constants with increasing water content.

We found that TATP reacted violently with concentrated sulfuric acid, but decomposed extremely slowly when the concentration was diluted to 65wt%. As an alternative to using strong acid to decompose TATP, partial dissolution of the TATP was used. TATP is soluble in most organic solvents, but complete dissolution of large quantities found in the field would be impractical. Instead of attempting to dissolve TATP, just enough solvent to wet the TATP was applied. The dissolved TATP surface layer was available for faster decomposition than the solid TATP so that more dilute aqueous acid could cause its decomposition without instant explosion. In addition, the solvent may have served as somewhat of a heat sink. Postulating a coating effect for the organic solvent means that volume of the organic liquid as well as surface area of the TATP must be considered in any attempt to scale-up these reactions.

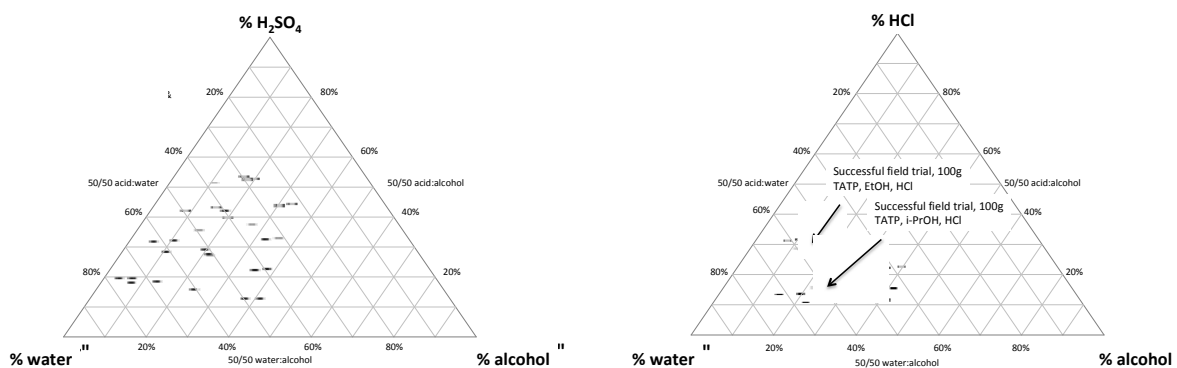


Fig. 1: Ternary diagram of destruction of 500 mg TATP wetted with alcohol (ethanol or isopropanol), water and acid (left H₂SO₄, 24hr; or right HCl, 7 hr). [ternary ppt]

Figure 1 represents attempts to decompose 500 mg TATP using the method outlined in section 2.2. The ternary diagrams express the percentage by weight of water, alcohol and acid present in the experiments. Note that the percentage does not represent the concentration of solvent or acid added but is the percentage after all components in the composition are accounted for. Success was defined as 0-25% of the TATP remained after sitting together overnight (17 to 24 hours). Some important trends emerge which support the kinetics experiments where TATP decomposed in solution. Hydrochloric acid appears to be more effective at decomposing TATP than sulfuric

acid. Increased amounts of water, reduced quantities of organic solvent and reduced amounts of acid slow the decomposition to an extent that decomposition overnight was incomplete (i.e. more than 50% TATP remaining). Using acetone, ethylene glycol, and ethyl acetate as the wetting agents, similar trends were observed. Hydrochloric acid is more effective than sulfuric acid; more water reduced the rate of decomposition, while more solvent and more acid increased that rate. Using sulfuric acid with ethylene glycol wetting-agent, did not destroy TATP; probably because of the reactivity of ethylene glycol with sulfuric acid. Although TATP was soluble in i-octane, toluene and diesel (Table 4), many of these experiments failed to destroy TATP, possibly due to the immiscibility of the aqueous acids with these solvents.

Table 4: Milliliters Solvent Required to Dissolve 100 mg TATP at Room Temperature

	acetone	diesel	EtAc	i-octane	toluene	EtOH(100%)	EtOH(50%)	i-PrOH	i-PrOH(50%)	water
average	1.0	3.0	1.2	2.1	0.8	3.0	62.2	3.8	40.2	14-16 ppm ⁶
sd	0.5	1.0	0.2	0.5	0.2	0.8	7.4	1.2	3.5	
rsd(%)	44	33	14	23	20	26	12	33	9	

Products

TATP was observed to convert to DADP in pure acetonitrile or chloroform (Table 3). When water or other protic species were present, DADP formation was not favored. Not every acid was compatible with the organic solvent used. The addition of methylsulfonic acid (MSA), BF₃, or HClO₄ resulted in instant and violent boiling of the solutions, and the solutions quickly turned from white to brownish-black. GC/MS analysis of the resulting extracts gave only a weak signal, suggesting that TATP had decomposed to relatively small molecules such as acetone and other smaller intermediate that volatilized away.^{8,13} DADP was formed to some extent by most of the acids, but acid was applied in molar excess, which favors conversion of TATP to DADP.^{8,14} Since all reactions were allowed to progress at room temperature for the same length of time, (3 hours), the amount of DADP observed was directly related to the rate of TATP decomposition in each acid. Minor amounts of species tentatively identified as peroxy-acetone species (Table 5) were observed. DADP is also decomposed by the acid but at a much slower rate than TATP.

Table 5: Conversion of TATP (2.25mmol,500 mg) to DADP Alcohol in 3h at 25°C [TATP DADP031213]

acid	pKa	conc M	mmol	TATP	DADP	R-OOH's peroxy	Other Products
conc HCl (36%)	-6	12	24	0-20%	2-5%	0.7-2%	chlorinated acetones (73-97%)
conc HNO ₃ (70%)	-1.64	16	32	0.1-0.2%	81-92%	0.1-0.5%	R-ONO, R-ONO ₂ (8-17%)
conc TFA (98%)	0.23	13	26	0.1-1%	99-100%	0.1-0.2%	none identified
H ₂ SO ₄ (65%)	-3.6	10	24	47-48%	48-50%	2-5%	none identified
H ₃ PO ₄	2.15	15	29	83-87%	13-17%	0.2-2%	none identified

HCl destruction of TATP produced various chlorinated acetones (1,1-dichloroacetone, 1,1,1-trichloroacetone, 1,3-dichloroacetone, and 1,1,3,3-tetrachloroacetone) and little (2-5%) DADP. It is possible that in the highly oxidizing reaction environment chloroacetones and peroxy fragments may have resulted from DADP decomposition.¹³ On the other hand a direct decomposition route from TATP to the chloroacetones cannot be ruled out. We have reported the insertion of chloroacetone into TATP under less oxidizing conditions.⁸ Although the primary decomposition product of nitric acid (70%) on TATP was DADP, methyl nitrate and a fragment

assigned as an organic nitrite were observed. The presence of methyl nitrate suggests that a radical decomposition pathway, as previously suggested.¹⁵

Decomposition Mechanism

All the strong acids decompose TATP, but rates (Table 1) and final products (Table 5) differ. If a protic species, e.g. water or alcohol, is present with TATP, is protonated then attacked at the peroxide group. If no water is present, the conjugate base of the acid, e.g. chloride or nitrate attacks the hydroperoxy end of the opened TATP. Acetone is lost and DADP is formed. Figure 3 illustrates these alternate routes. The formation of chlorinated acetones and nitrate esters (Table 5) supports this hypothesis.

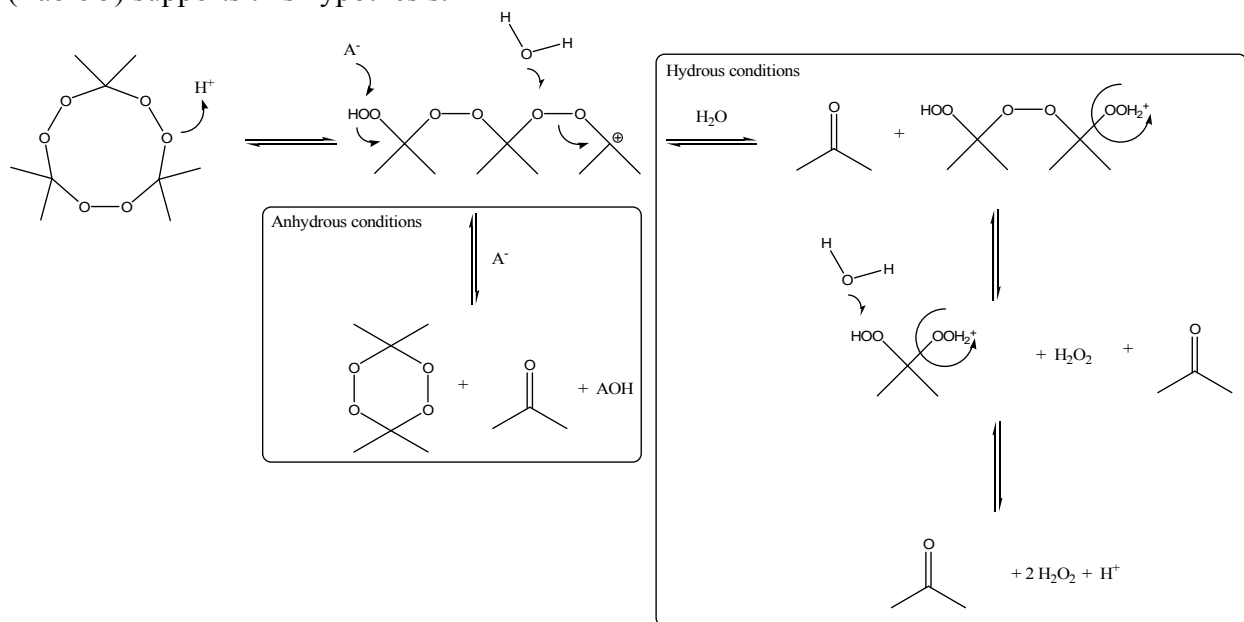


Fig. 3: TATP Decomposition by Acid with and without Water Present

Calorimetry: During calorimetry experiments when 65 wt% H₂SO₄ was added to (40 mg/mL) alcohol solutions of TATP, no reaction was observed until the solution was raised to 50°C. At that temperature the reaction started within a few minutes. The experiment was repeated using 80 wt% sulfuric acid. Within a few minutes heat release was visible and after about 11 hours it appeared to be complete. Duplicate experiments were run using sulfuric, hydrochloric and nitric acids taking care to deliver similar quantities of water while delivering the same number of moles of acid because previous work had shown that water affects the formation and destruction of TATP⁸. Under the same conditions hydrochloric acid resulted in a faster reaction but with less heat released overall than tests using nitric or sulfuric acid. Figure 4 shows the calorimetry traces and the heat release observed for each of the duplicate experiments.

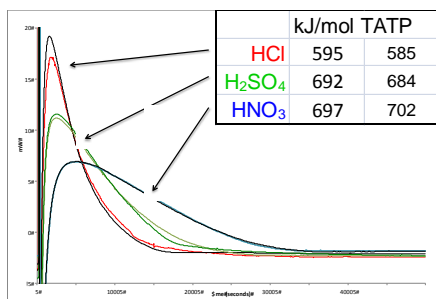


Fig. 4: Calorimetry trace acid added to ethanol (1 mL) solution of 40 mg TATP[TATPuRC.ppt]

Scaleup

When the 500 mg tests were scaled to 3 g TATP wetted with 3 g alcohol, the acid (3mL) was added remotely. When the acid was concentrated HCl (36%), the decomposition went quiescently; when it was 90% sulfuric acid, the reaction was violent (see Figure 5). Scaling to 100 g of TATP, 100 mL of solvent was used and 400 mL hydrochloric acid (see labeled data points in Figure 1). The alcohol was added to a 4 L beaker containing the TATP; the TATP absorbed this amount of solvent without noticeable wetting. The acid was added all at once, remotely (in an outdoor area). Results are shown in Table 6. Scaling up further will require carefully maintaining a balance between the wetting solvent, the acid, and the volume of TATP.

Table 6: TATP (100g) Destruction Tests

date	solvent	solvent mL	acid	acid mL	time to destruction
12/14/10	acetone 50%		HCl 36%		
12/14/10	EtOH 50%	200	HCl 36%	400	20 min
4/21/11	IPA 50%	200	HCl 36%	400	2h 20 min
4/21/11	IPA 50%	100	HCl 36%	400	3 h



Fig. 5 TATP (3g) violently reacting with acid

Conclusions

TATP can be destroyed quiescently under certain conditions. Using aqueous acids alone may result in a successful decomposition attempt, but the rate of decomposition is unreasonably slow when concentrations are low and becomes exponentially faster as the concentration of acid increases. This is problematic since the exothermic decomposition could potentially go into thermal runaway and lead to detonation. For example, concentrated sulfuric acid (>80 wt%) successfully decomposed small quantities (< 50 mg) of TATP but caused detonation of a larger quantity (> 3g).

The key to controlling the acid destruction of TATP is maintaining a balance between the wetting solvent, the acid, and the water brought in with the acid and with the solvent. It is the uncontrolled release of heat during TATP destruction that results in explosion. In employing a wetting solvent, it must be one in which TATP has some solubility and the chosen acid is miscible. There is a balance among the solvent, water and acid that can be visualized in the ternary diagrams (Fig. 1). The organic solvent/wetting agent makes a thin layer of solvated TATP accessible to the acid. Depending on the solvent, it may or may not support dissociation of the acid. The water ameliorates the solubility of TATP in the solvent, but it ensures dissociation of the acid. Water slows the decomposition of TATP, but slows its conversion to DADP more so. The balance among constituents is illustrated in ternary diagrams (Fig. 1). Generally, systems which successfully destroyed TATP overnight were one-to-one water-to-solvent or two-to-one. Both water and the solvent could be considered to supply a heat sink for TATP decomposition.

The ternary diagrams (Fig 1) suggest that the optimum ratio of water, solvent and acid may vary depending on the acid. TATP decomposes faster with hydrochloric acid and nitric acid than with sulfuric of about comparable molarity. The same decomposition mechanism is postulated (Fig. 3), but the attack of the different conjugate bases on the hydroperoxy end results

in different decomposition products. We prefer using hydrochloric acid when gentle destruction of TATP is desired though it reacts faster than sulfuric acid, the heat release is significantly lower. Hydrochloric acid and alcohol wetting agent have gently destroyed TATP on the 100 gram scale. Prediction of the actual outcome is still challenging since there are numerous potential variables that cannot be accounted for in a laboratory setting, but this work serves as a guideline for decomposing TATP when blowing-in-place or transporting to a remote location is not a viable option. It is recommended that addition of chemicals be done remotely.

References

1. KTLA News 11:53 a.m. PST, Dec 11, 2010 & . Feb 2, 2011 CBS 8 (KFMB)
2. Bellamy, A.J. "Triacetone Triperoxide: Its Chemical Destruction" *J. Forensic Sci.*, **1999**, *44*(3),603-8.
3. Costantini, M. "Destruction of Acetone Peroxides" U.S. Patent 5,003,109; Mar. 26, **1991**.
4. Matyas, R. "Chemical Decomposition of Triacetone Triperoxide and Hexamethylene triperoxide diamide Nitrem Symposium, Pardubice, CZ, **2004**, 241-247.
5. Oxley, J.C.; Smith, J.L.; Huang, J.; Luo, W. "Destruction of Peroxide Explosives" *J Forensic Sci.* **2009**, *54*(5), 1029-1033.
6. Oxley, J.C.; Wilson, S.A.; Brady, J.E. Smith, J.L.; "Risk of Mixing Dilute Hydrogen Peroxide and Acetone Solutions" *J Chemical Health & Safety* **2012**, *19*(2), 27-33.
7. Oxley, J.C.; Smith, J.L.; Bowden, P.; Ryan Rettinger "Factors Influencing TATP and DADP Formation: Part I," *Propellants, Explosives, Pyrotechnics*, accepted
8. Oxley, J.C.; Smith, J.L.; Steinkamp, L.; Zhang, G. "Factors Influencing TATP and DADP Formation: Part II," *Propellants, Explosives, Pyrotechnics*, submitted.
9. McCullough, K.J.; Morgan, A.R.; Nonhebel, D.C.; Pauson, P.L., Ketones-derived Peroxides. Part. I. Synthetic Methods. *J. Chem. Res. Synop.* **1981**, *2*, 34-36.
10. Canals, I.; Portal, J. A.; Bosch, E.; Roses, M. Retention of Ionizable Compounds on HPLC. 4. Mobile-Phase pH Measurement in Methanol/Water. *Anal. Chem.*, 2000, *72*, 1802-1809.
11. Rived, F.; Canals, I.; Bosch, E.; Roses, M. Acidity in Methanol-Water. *Analytical Chimica Acta*, 2001, *439*, 315-333.
12. Katz, E. D.; Ogan, K.; Scott, R. P. W. Distribution of A Solute Between Two Phases. *Journal of Chromatography*, 1986, *352*, 67-90.
13. Armitt, D.; Zimmerman, P.; Ellis-Steinborner, S. "Gas chromatography/mass spectrometry analysis of triacetone triperoxide (TATP) degradation products" *Rapid Communications in Mass Spectrometry*, **2008**, *22*(7), 950-958.
14. Matyas, R.; Pachman, J.; Ang, H.-G. "Study of TATP: Spontaneous Transformation of TATP to DADP" *Propellants, Explosives and Pyrotechnics* **2008**, *33*, 89-91
15. Oxley, J.C.; Smith, J.L.; Chen, H.; Cioffi, E. "Decomposition of Multi-Peroxidic Compounds: Part II: Hexamethylene Triperoxide Diamine (HMTD)" *Thermochemica Acta* **2002**, *388*(1-2), 215-225.

Characterization of Homemade Explosives (HMEs)

S. F. Son (PI), L. J. Groven, R. S. Janesheski, P. J. Renslow, and D. E. Kittell

School of Mechanical Engineering, Purdue University

West Lafayette, Indiana

April, 2013

1. Objectives

The goal of this experimental work is to characterize homemade explosives (many are often non-ideal explosives) on a small-scale. The need of characterized explosives that could be used in threats has seen an increase due to the constituent materials used and relatively low costs that allow terrorist to obtain and use them. In contrast to military and DOE explosives the characterization of these materials is severely lacking. A significant challenge is there is an insignificant amount of experimental data available due to the large-scale setup that is required for characterization. The main restraint is due to the large critical diameters needed to sustain a steady detonation in a non-ideal explosive. We are developing and performing small-scale experiments (grams) in tubes with small diameters relative to the expected critical diameter and anticipating unsteady detonations that are likely to fail in many cases. Using microwave interferometry, a highly time resolved profile of the location of the detonation front is measured. The failure dynamics measured with the interferometer allows for the characterization of the non-ideal explosive over a wide parameter space (from overdriven to failure). A simulation of the experimental results is being pursued using CTH, a shock physics hydrocode, to calibrate a reaction model of the non-ideal explosive. The small-scale nature of the experiment allows for various parameters to be changed quickly that include chemical composition, non-ideal explosive density, and confiner thickness. The final goal of this work is to demonstrate that the calibrated model obtained from the small-scale experiment calibration is able to predict the results of large-scale experiment. Specifically, our goals this period are to: 1) Characterize a wider variety of AN-based HMEs on a small-scale. 2) Develop higher fidelity data analysis techniques (wavelet decomposition). 3) Compare experimental data to CTH simulations. We were also able to secure grant for a \$5000 computer to do these simulations from Zink Corporation.

2. Summary

A unique method for characterizing HME explosives on a small-scale has been achieved and extended to more materials (see Fig. 2.1). This experiment has also been successful at evaluating the relative detonability of different mixtures with only a few grams of material. Successful experiments have been performed using the microwave interferometer to measure the detonation front's position profile of non-ideal explosives. Different compositions of AN with either diesel fuel, mineral oil, or sugar have been used as non-ideal explosives. The failure dynamics between the compositions were measurably different. The amount of fuel in the non-ideal explosive affected the distance the detonation was able to sustain itself as well as the rate at which it decreased in velocity and eventually reached complete failure. Experiments showed different failure dynamics among a single composition when the thickness of the confinement was changed. It was seen that lateral losses of energy occur in the thin-walled confiners and reduces the reaction zones ability to sustain the detonation. The thick-walled confiner sees minimal deformation, which allows for the much slower rate of deceleration of the detonation front as it is failing.

This year we applied this to a wide variety of additional AN-based explosives and will add to this data set in the remaining time. We have also greatly improved the experiment by eliminating noise issues to a significant extent and applied state of the art data analysis using wavelet decomposition. This has shown significant improvement in the data quality.

Modeling of the non-ideal explosives is well underway using CTH. Working simulations have been developed and parameters are currently being tuned to fit the experimental data. Once the data has been fit, the calibrated model will then be compared to results reported from large scale experiments. We have identified a material that has sufficient large scale data and also an existing CTH model. We will be applying the experiment and model to this material.

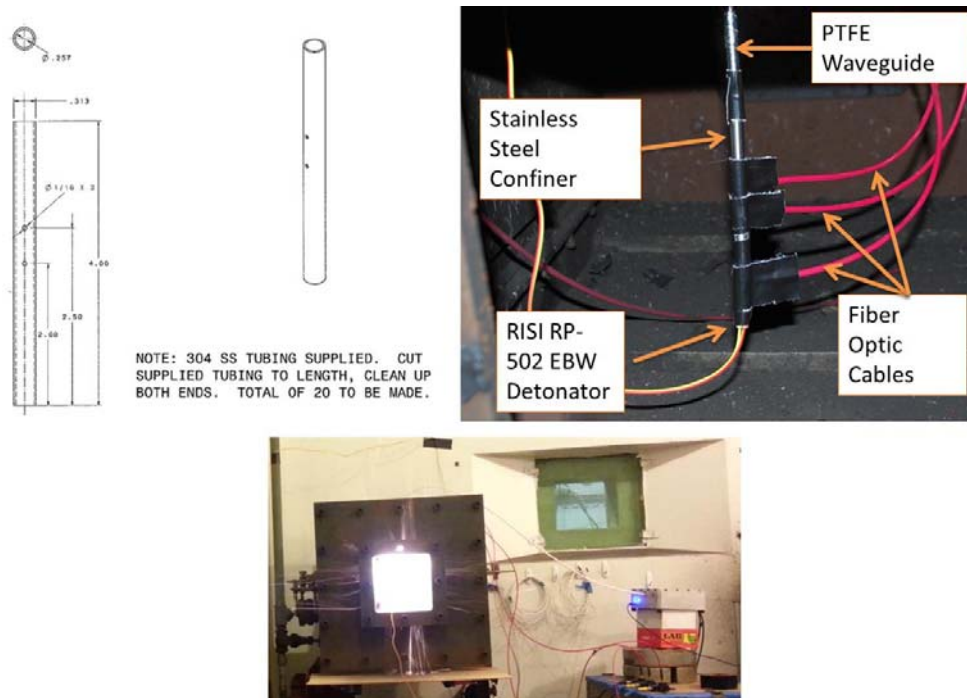


Figure 2.1. Drawing of the confiner in units of inches (upper left); packed confiner instrumented and ready for testing (upper right); sealed frag box and detonation event is occurring (bottom).

3. Accomplishments

Our specific accomplishments this period are summarized below:

- a. Improved the quality of the data collected and the analysis technique (wavelet).
- b. Showed that for ANFO made from Kinepak, 2wt.% FO has the slowest detonation failure (strongest propagation) than 4, 5, and 10wt.% FO.
 - o Kinepak is packaged with small amount of paraffin wax and this might explain why stoichiometric 5wt.% FO has a faster detonation failure.
- c. Results indicate that for a fixed confinement and diameter, different fuel mass percents determine when the detonation will fail.
 - o Until failure under these conditions all samples have nearly identical frequency (velocity and position) histories.
- d. Systematically tested 6 AN-based HMEs using our technique.
- e. Observed that wavelet technique has the ability to determine point of detonation failure and potentially shock decoupling.

- f. Found that ideal explosive (Primasheet) experimental data matches best with PETN EOS and burn model in CTH.
- g. Demonstrated that CTH can predict a detonation failure location paving the way for experiment validation with TATB (a non-ideal explosive that is well-characterized).
- h. Obtained a \$5000 grant for the purchase of a computer to do these calculations.

4. Details

The following reviews much of the recent work accomplished. A chapter and journal article, from this funding, will also be sent with this report.

4.1 Data collection and wavelet transforms

Using a battery pack to power the microwave interferometer and by carefully shielding the experiment through equipment placement and metal foils, the quality of the experimental data was improved as shown in Figure 4.1.

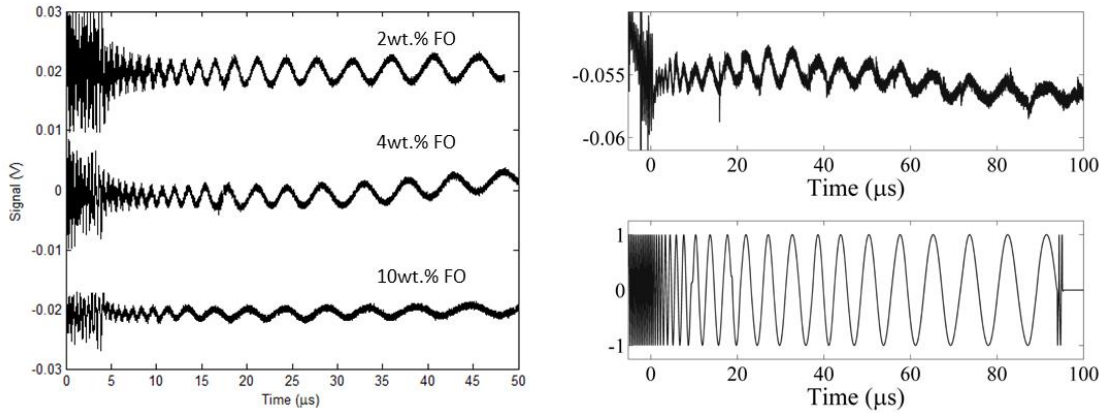


Figure 4.1. Clean data after switching to the battery pack (left) and original data plus filtering result (right).

Instead of using the quadrature method – which relies on taking the inverse tangent of two noisy signals – a wavelet analysis was selected to calculate the instantaneous frequency of the primary signal without any need to filter the data. Instantaneous frequency is related to the speed of the propagating wave by the equation,

$$v = \frac{\lambda}{2} f,$$

where the wavelength, λ , is related to the average dielectric constant that the microwave signal sees as it travels down the waveguide and into the ideal and non-ideal explosives. It is approximately constant but has a discontinuity as the leading shock passes from the ideal to the non-ideal explosive. If λ is constant then the leading shock position may be found from simple integration

$$x = \frac{\lambda}{2} \int_0^t f dt.$$

Because integration is used instead of differentiation, the position data has improved resolution; hence unlike the other technique numerical differentiation of experimental data is avoided.

A wavelet transform can extract instantaneous frequencies (linearly related to velocity of the wave) and do it more effectively than a short time Fourier transform (STFT). Wavelet transforms utilize mother wavelet basis functions that must be carefully adjusted so that the desired frequency-time resolution is achieved. An example of a normalized scalogram (method of displaying wavelet transform output) for an ANFO test is shown below in Figure 4.2.

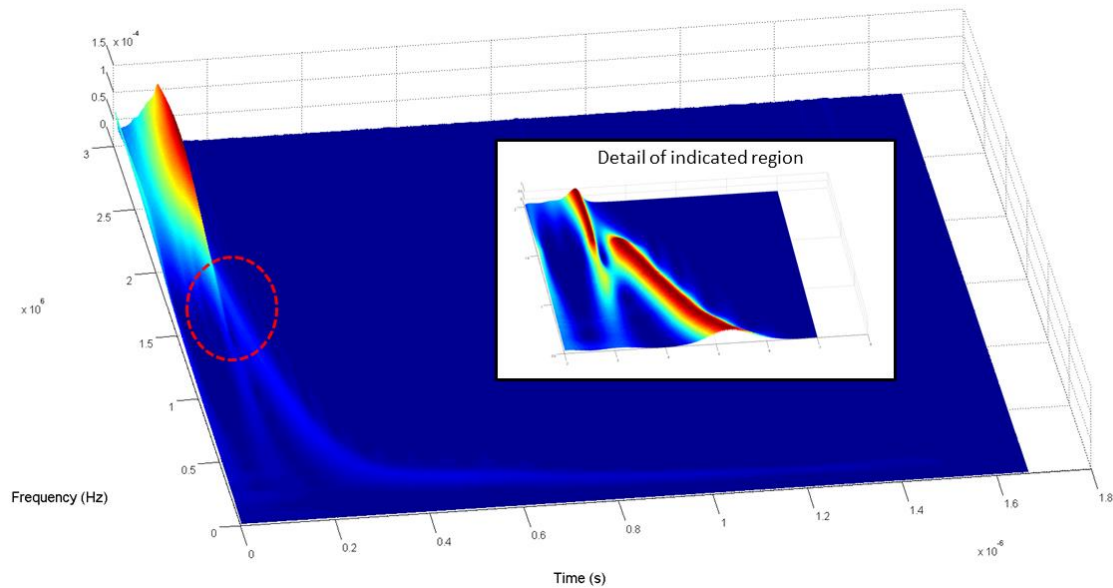


Figure 4.2. Time-frequency wavelet transform data for 10wt.% ANFO shown in a normalized scalogram; additional settings were used to enhance the level of detail in the transition region from the ideal to the non-ideal explosive.

Wavelet transforms have the ability to provide high-fidelity resolution and may be capable of detecting quick and subtle changes to shock velocity, such as a potential velocity hiccups during the transition between the ideal and non-ideal explosive. For characterizing the strength of the detonation in different compositions of non-ideal explosives, this analysis technique is effective. Shown below in Figure 4.3 are velocity/frequency profiles for 2, 4/5, and 10 wt.% ANFO for both wavelet and quadrature analyses (see also Figure 4.4). Using quadrature there is not much distinction between the different cases, while in the frequency-time plots it is clear to see that 2wt.% ANFO has the strongest detonation. This is in some ways unexpected because the stoichiometric ratio for ANFO is closer to 5wt.%. One possible explanation is that the AN used (Kinepak) has a light coating of paraffin wax, which might also react as fuel.

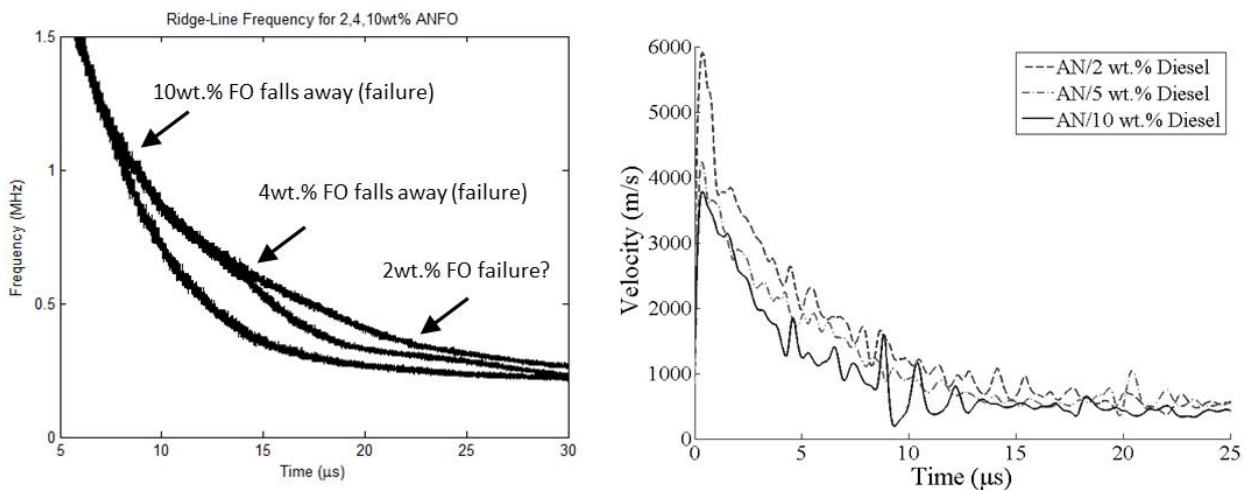


Figure 4.3. Comparison of wavelet analysis technique (left) to the quadrature analysis (right). Note: frequency is proportional to true velocity; however, the constant of proportionality is discontinuous and has not been calibrated past the shock decoupling point. 1.5 MHz corresponds roughly to 4000 m/s.

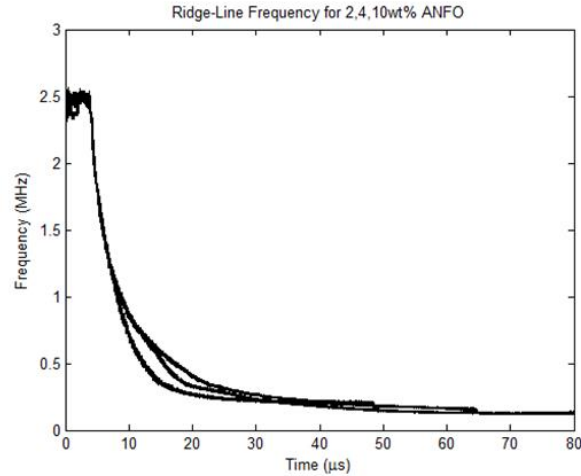


Figure 4.4. Frequency (directly related to velocity) data corresponding to 2, 4, and 10wt.% ANFO shown for the whole duration of the test (ideal and non-ideal explosives).

4.2 AN-based explosives with alternate fuels

A total of six different fuels were mixed at stoichiometric conditions that were calculated for pure AN: glycine, diesel, paraffin, urea, citric acid, and sugar. All fuels are relatively accessible to terrorists and could easily be incorporated into improvised, non-ideal explosives. In small quantities, the sensitivities of these mixtures are very low and this is shown in Table 1; average post experiment sample lengths are also shown in Table 4.1.

Figures 4.5 to 4.8 summarize the results obtained. From the results it is observed that there are only subtle differences between each of the stoichiometric fuels. It is difficult to determine a shock decoupling point, but it is possible to rank these combinations in order of strongest to weakest detonation according to frequency (velocity) and the post experiment confiner lengths. From each of the metrics applied we can summarize these results as follows:

By Confiner Length:

Glycine > Diesel > Urea & Citric Acid > Paraffin > Sugar

By Unreacted Explosive Length:

Diesel > Glycine & Citric Acid > Paraffin > Urea > Sugar

By Velocity (Frequency):

Glycine > Diesel > Paraffin > Urea > Citric Acid > Sugar

Our results do indicate that a variety of fuels with AN can be used with only minor changes in detonation properties.

Table 4.1. Stoichiometric fuel wt.%, measured sensitivity, and post experiment sample lengths for AN-based explosives. Sensitivity limits are the maximum available stimuli for each test, respectively.

Fuel	Stoic. Fuel wt. %	BAM Friction Test	ESD Sensitivity	Drop Weight Impact	Est. Length of Confiner Bottom to Failure Point (cm)	Avg. Length of Unreacted Material (cm)
Glycine	17.25	> 360 N	> 1.02 J	> 213 cm	2.87	1.63
Diesel	5.56	> 360 N	> 1.02 J	> 213 cm	3.05	1.55
Paraffin	5.47	> 360 N	> 1.02 J	> 213 cm	3.51	1.83
Urea	20.01	> 360 N	> 1.02 J	> 213 cm	3.48	1.98
Citric Acid	22.58	> 360 N	> 1.02 J	> 213 cm	3.48	1.63
Sugar	15.12	> 360 N	> 1.02 J	> 213 cm	3.63	2.13

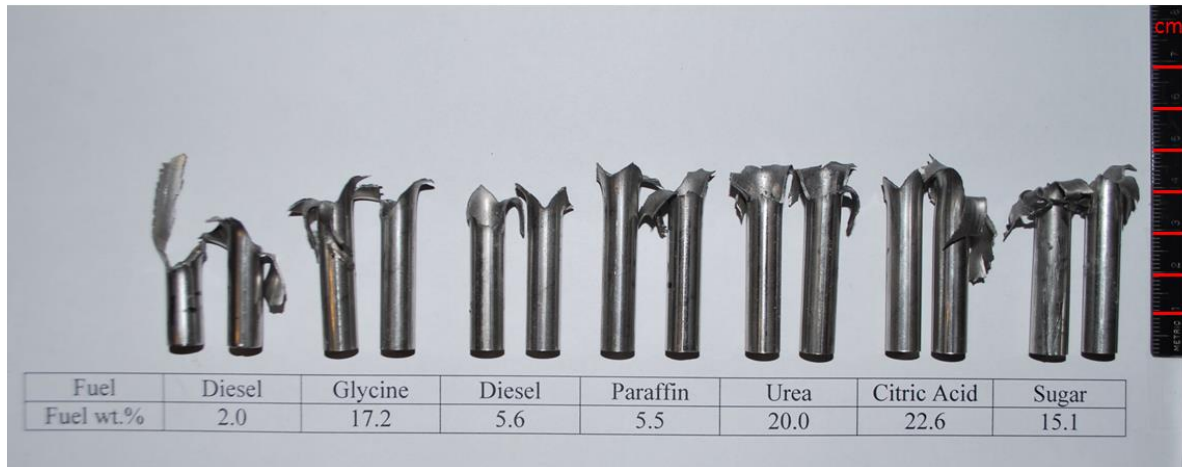


Figure 4.5. Post experiment images of the sample confiners with fuel type and wt.% indicated. 2wt.% diesel is included as a comparison because it has shown the strongest detonation during the testing.

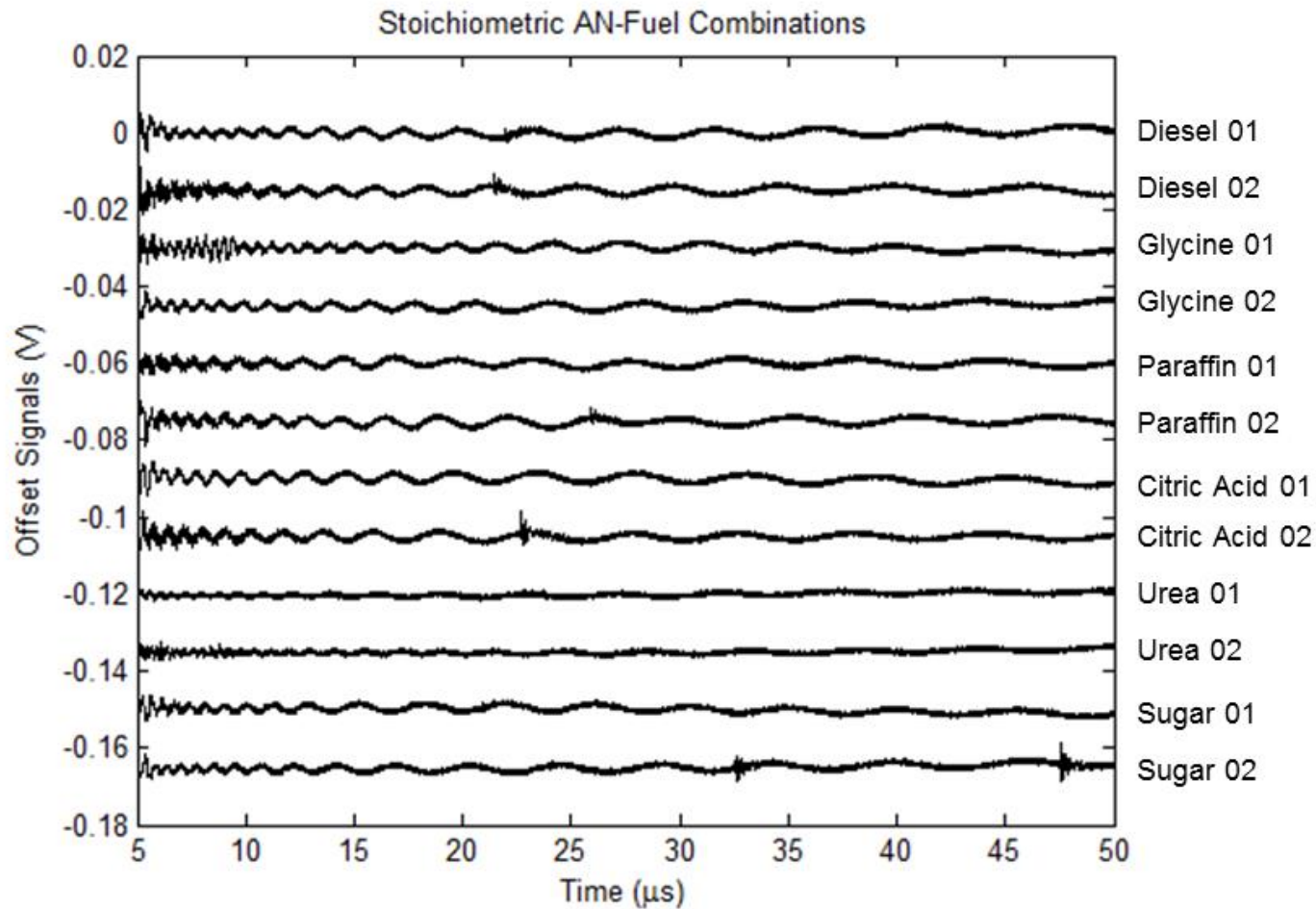


Figure 4.6. Overview of the microwave signal recorded for the different stoichiometric AN-based explosives.

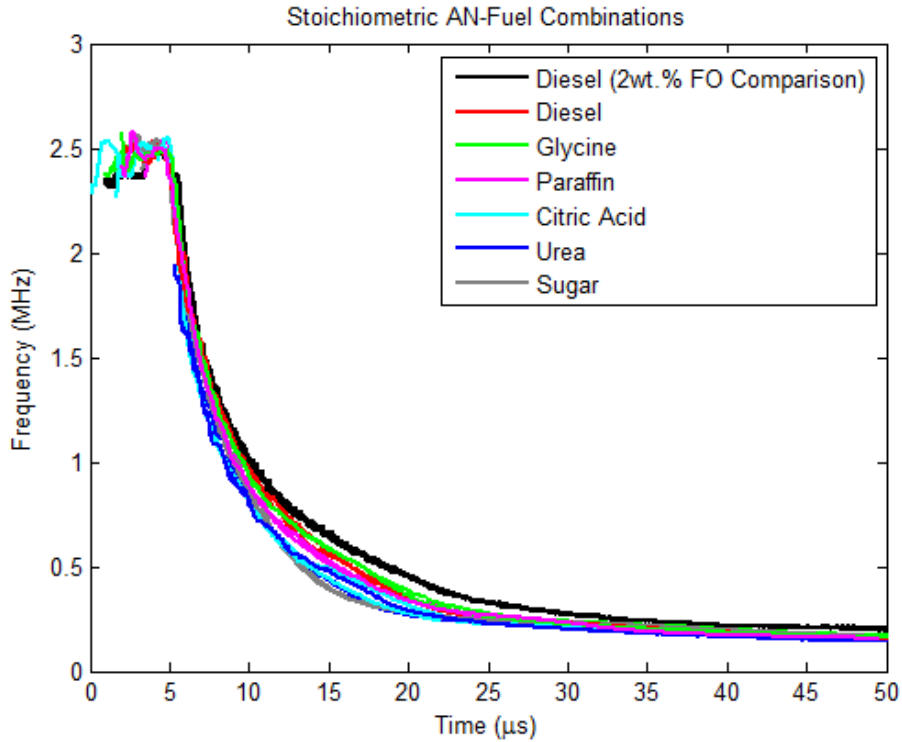


Figure 4.7. Frequency (velocity) data for stoichiometric combinations of AN-based explosives. Only one leg of the quadrature signal was needed to produce these curves.

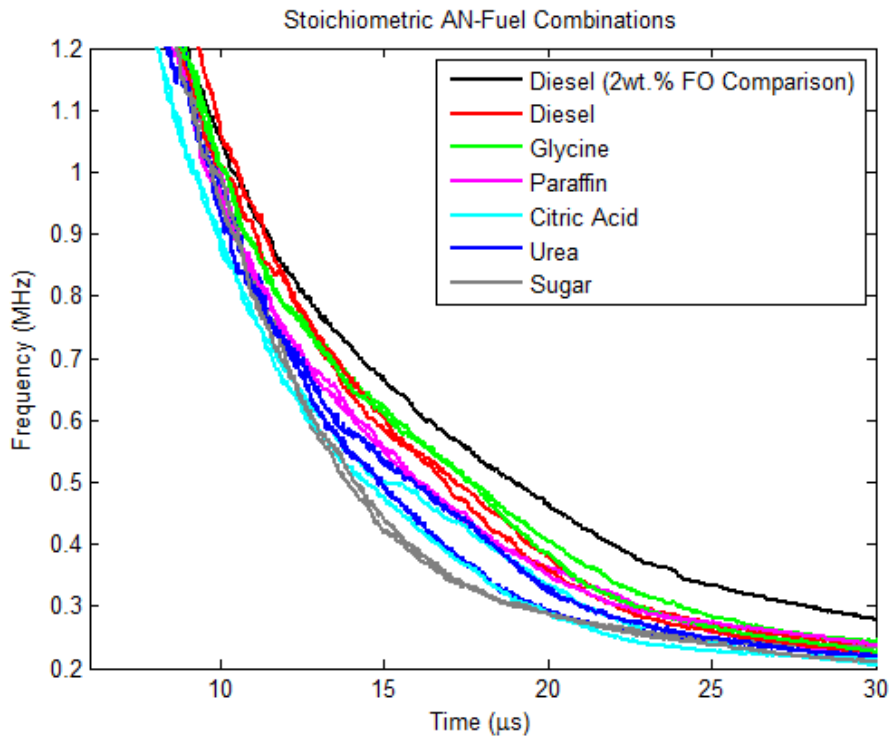


Figure 4.8. Detail for the detonation failure region shown in Figure 3.

From the results it is observed that there are only subtle differences between each of the stoichiometric fuels. It is difficult to determine a shock decoupling point, but it is possible to rank these combinations in order of strongest to weakest detonation according to frequency (velocity) and the post experiment confiner lengths.

4.3 CTH simulation results

Simulating the experiment in CTH requires an initiation mechanism and a robust model for each explosive. Explosives models are composed of an equation of state for both the detonation products and unreacted explosive as well as an expression for the chemical kinetics within the reaction zone. Calibration of these models is not trivial and few models exist for non-ideal explosives, especially over the wide variety of chemical formulations and material properties. As a first step, a model was built for the RP-502 detonator and then a pre-built model was selected to best match the detonation speed of the ideal explosive (Primasheet). Simulation output is shown in Figure 4.9 and calibration curves in Figure 4.10. The best available model for the ideal explosive is PETN (Primasheet 1000 is composed of nominally 63% PETN by mass).

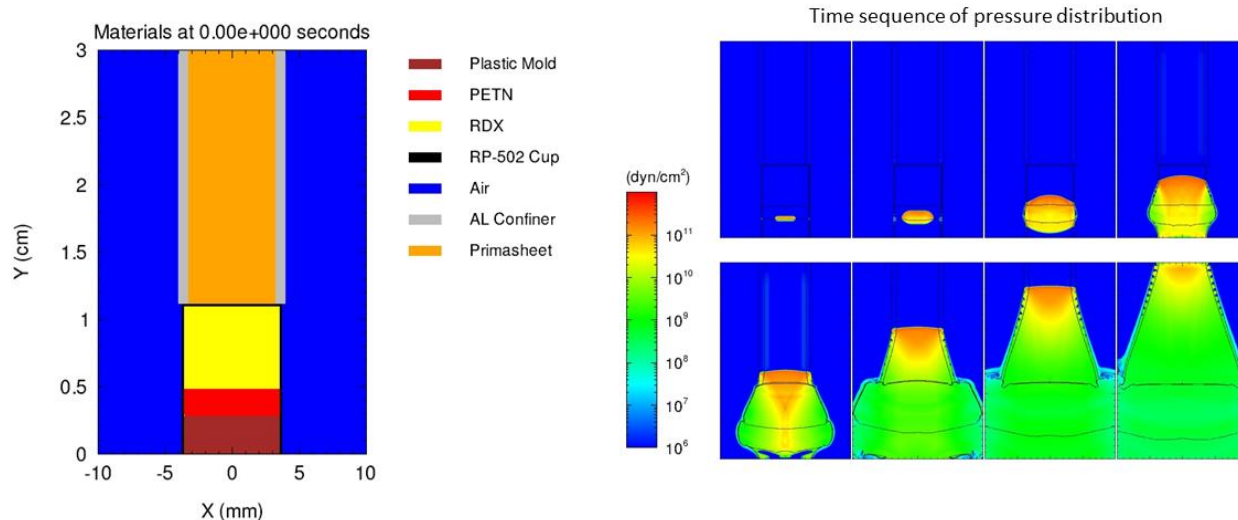


Figure 4.9. Simulation output of the RP-502 detonator initiating a ¼-inch dia. confiner packed with a mock-up of the ideal explosive.

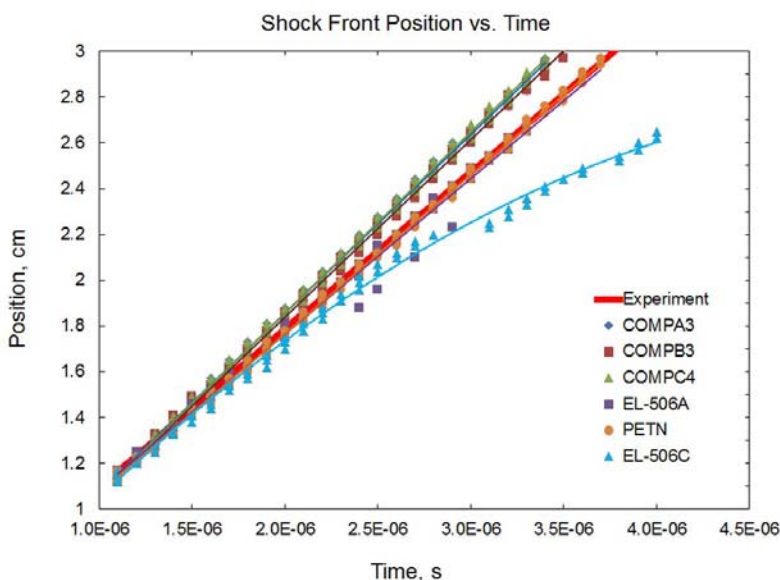


Figure 4.10. Simulation and experimental data for the shock front position throughout the ideal explosive; several different pre-build explosive models in CTH have been tested to simulate Primasheet 1000.

Having calibrated and developed a working model for the detonator and the ideal explosive, no suitable model was available for the AN-based compositions. In attempting to simulate detonation failure, PBX 9502 (a TATB based explosive) was selected because of its non-ideal nature and well-established EOS. In an unconfined configuration, it was found that PBX 9502 fails to propagate a detonation for charge diameters between 6-7mm. The detonation failure is marked by a decoupling of the shock wave with the reaction zone, and this is depicted in Figure 4.11. In order to illustrate how CTH can simulate detonation failure and produce comparable results to those obtained from the experiment, the position of the pressure, reaction, and temperature fronts for a confined and unconfined cylinder of PBX 9502 is shown below in Figure 4.12.

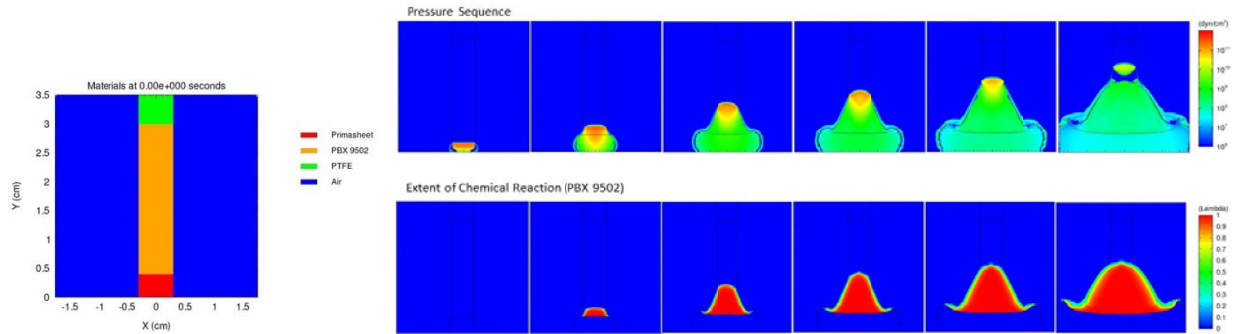


Figure 4.11. Detonation failure in an unconfined 6mm dia. Cylinder of PBX 9502 initiated by an ideal explosive. Images show how the chemical reaction front thickens and separates from the leading shock.

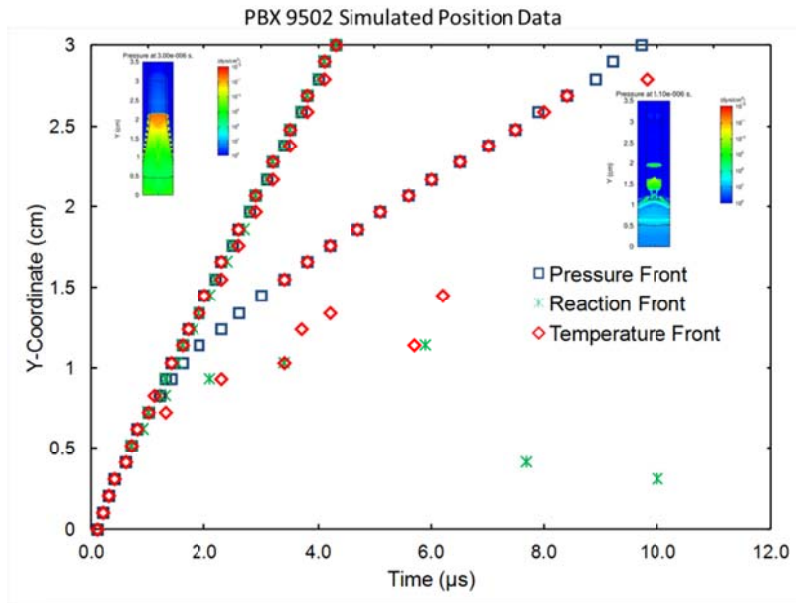


Figure 4.12. Simulated position data for the leading pressure, reaction, and temperature fronts in confined and unconfined PBX 9502 (4mm dia.).

5. Students Supported

David E. Kittell

We leveraged a Fellowship student, P. J. Renslow, who is a Sandia National Laboratory employee on a Sandia Fellowship.



Fig. 5.1. David Kittell (standing) and Peter Renslow performing a HME characterization experiment.

6. Conference & Journal Publications

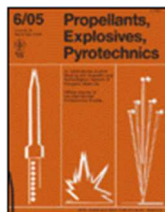
- Paper submitted for publication (in review). We have also published a book chapter. Both will be submitted with this report.

7. Future Directions

Our future directions are summarized as follows:

- Implement shock pins with fiber optics to calibrate signal through detonation failure and shock decoupling.
- Complete AN-based explosives using the following fuels at various stoichiometries for:
 - Sugar
 - Citric Acid
 - Urea
 - Glycine
 - Paraffin
- Obtain experimental results for ANFO with different particle sizes / size distributions and stoichiometry (NOT using Kinepak) to look for more trends to be correlated with wavelet analysis
- Increase the thin walled confiner diameter to slow down detonation failure and accentuate the differences between chemical formulations.
- Obtain experimental data for TATB in order to validate simulation output from CTH.

8. Appendix: Paper in review and published chapter are sent in separate files.



DETONATION FAILURE CHARACTERIZATION OF HOME MADE EXPLOSIVES

Journal:	<i>Propellants, Explosives, Pyrotechnics</i>
Manuscript ID:	Draft
Wiley - Manuscript type:	Full Paper
Date Submitted by the Author:	n/a
Complete List of Authors:	Janesheski, Robert; Purdue University, School of Mechanical Engineering Groven, Lori; Purdue University, School of Mechanical Engineering Son, Steven; Purdue University, School of Mechanical Engineering
Keywords:	ammonium nitrate, homemade explosives, microwave interferometry, detonation failure, shockwave

SCHOLARONE™
Manuscripts

Full Paper

DOI: 10.1002/prop.201((full DOI will be filled in by the editorial staff))

DETONATION FAILURE CHARACTERIZATION
OF HOME MADE EXPLOSIVESRobert S. Janesheski, Lori J. Groven, and Steven F. Son^[a]

Abstract: Typically characterizing home made explosives (HMEs) requires many large scale experiments, which is prohibitive given the large number of materials in use. A small scale experiment has been developed to characterize HMEs such as ammonium nitrate-fuel oil mixtures. A microwave interferometer is applied to small scale confined transient experiments, yielding time resolved characterization of a failing detonation that is initiated with an ideal explosive booster charge. Experiments were performed with ammonium nitrate and two fuel compositions (diesel fuel and mineral oil). It was observed that the failure dynamics were influenced by factors such as the chemical composition, confiner thickness, and applied shock wave strength. Thin steel walled confiners with 0.71 mm wall thickness experienced detonation failure and decoupling of the shock wave from the reaction zone. Confiners with a wall thickness of 34.9 mm showed a decrease in propagation speed and a steady reactive wave was achieved. Varying the applied shock strength by using an attenuator showed corresponding changes in the initial overdriven reactive wave velocity in the HMEs. The distance to detonation failure was also shown to depend on the attenuator length when thin wall confinement was used. This experimental method is shown to be repeatable and can be performed with little required material (about 2 grams). The data obtained could be useful to model development and validation, as well as quantifying detonability of materials.

Keywords: home made explosives, ammonium nitrate, microwave interferometry, detonation failure, shockwave

1 Introduction

There is a strong need for characterizing, modelling, and understanding home made explosives (HMEs) as their availability and low cost makes them terrorist accessible [1-5]. In order to more adequately mitigate and respond to these threats, characterization coupled with modelling of HMEs has become of the utmost importance. Presently, the lack of detailed experimental data has limited the development of reactive models for HMEs. This is especially challenging because of the wide variety in HME compositions and typically expensive, large scale experiments currently applied.

A large critical diameter is a characteristic associated with many HMEs due to a thick reaction zone. An explosive with a large critical diameter is also termed a non-ideal high explosive. Ammonium nitrate (AN), a typical HME component, has a critical diameter of 100 mm when confined in a steel tube that is loosely packed [6]. When fuel is added to AN, it has been shown that the critical diameter can vary from 10 mm with fine AN particles to 50 mm with coarse AN particles [7]. It is evident that many parameters such as AN particle size, confiner diameter, packing, and confiner thickness have an effect on the detonability of HMEs [2-4]. However, the wide range of HME compositions makes large scale characterization of every composition prohibitive.

A steady detonation experiment is the conventional approach for detonation property measurement such as velocity, reaction zone length, and detonation front curvature [5]. Producing a steady detonation with a HME requires a large amount of material, on the order of kilograms, in order to satisfy the critical diameter constraint. It is evident that small scale experiments are highly desirable and the ability

to assess detonability with small samples is also a critical need.

Transient data also provides rich data sets for model validation. The large scale required to sustain a detonation in HMEs has also made it a challenge to perform transient measurements, such as deflagration to detonation transition (DDT) [8] or shock initiation [9]. Shock initiation measurements have been used for the calibration of parameters for reaction models [9], such as Forest-Fire [10] and ignition and growth [11], typically used for ideal explosives.

The data available involving transient measurement during a reactive wave transition (including detonation failure) for HMEs is very limited. However, some work has been performed to fit equation of state (EOS) parameters for HMEs using high pressure x-ray diffraction and gas gun-driven plate impact experiments [12]. Reaction and growth modelling parameters have also been measured with HMEs by using a hybrid Hopkinson bar experiment (modified plate impact experiment) [13]. The need for an experimental technique to study the transient dynamics of a HME remains, especially if the experiment can span a wide parameter space. A small scale transient experiment would be especially useful to modellers and could provide valuable qualitative insight as well.

Microwave interferometry has been used as a non-intrusive measurement for burning rates of propellants [14] and for the study of the detonation of ideal

[a] RS Janesheski, LJ Groven, SF Son
School of Mechanical Engineering
Purdue University
500 N. Allison Rd., West Lafayette IN 47907
E-mail: sson@purdue.edu

DETONATION FAILURE CHARACTERIZATION
OF HOME MADE EXPLOSIVES

explosives including tetryl [15], trinitrotoluene (TNT), Pentolite, Amatol, and even Tritonal (an aluminized explosive) [16]. Low power microwaves have been used to develop interference signals produced from reflection off of the reactive wave front. The position and velocity of the reactive wave can then be calculated non-intrusively from the interference signal. The spatial and temporal resolution of the technique is dependent on the wavelength of the microwave system. Over the years, the technique has been refined and wavelengths have decreased from 3 cm [16] to 2 mm [17] resulting in increased accuracy. It also has been shown that a single experiment can measure the regression rate of propellants as a function of pressure [18] in a slowly pressurizing experiment. Since the technique is applicable to both deflagration and detonation, it has also been used to characterize the highly transient deflagration-to-detonation transition (DDT) of ideal explosives [8]. Therefore, this diagnostic tool could be applied to detonation failure in HMEs.

It is noted here for clarity that the term “detonation” is only applicable to a steady reactive wave involving a shock. Here, we use the term “detonation failure” to refer to the transient reactive wave process where the reaction zone decouples from the leading shock wave. We use the term “reactive wave” to refer to the transient front observed.

The objective of this work is to develop a small scale experiment to characterize HMEs in a detonation failure experiment using a microwave interferometer. This could provide a broad range of parameter space for model validation or calibration, as well as provide a quick screening tool and increase the understanding of the reactive dynamics. Material composition, various confinement properties, and leading shock strength can also be investigated to quantify the effects on the failing detonation through HMEs.

2 EXPERIMENTAL PROCEDURE

2.1 Materials and Equipment

The HMEs used in this work consisted of ammonium nitrate (AN) mixed with various fuels. Kinepak™ ammonium nitrate produced by SEC, Orica Manufacturing Company, was used. Sizing of the AN was conducted with a Malvern Mastersizer with hexane as the dispersing medium. The material is trimodal with a mean volume diameter of ~200 μm and $d(50)$ of ~175 μm . Various weight percentages of diesel and mineral oil were mixed with AN as the fuels of interest. In these experiments, 2 to 2.5 g of HME was required. The HME mixtures characterized in this work include AN with 2, 5 and 10 wt.% diesel fuel as well as AN with 2 and 15 wt.% mineral oil. The explosives were pressed within the confiner in increments to yield uniform density throughout the length of the sample. Depending on the compositions being pressed, 0.25 g increments were pressed to lengths that ranged from 5 to 10 mm. Samples ranged

from 60% TMD for compositions with 2 wt.% fuel up to 70% TMD for compositions with 15 wt.% fuel. Approximately 1.9 g of Primasheet 1000 (an ideal explosive with 63% PETN qualified to MIL-PRF-46676) was used to develop a steady detonation into the HME. A Teledyne Risi, Inc. RP-502 detonator was used to initiate the detonation in the Primasheet.

Three confinement conditions were used that included very weak confinement (polypropylene tube with a wall thickness of 0.2 mm and I.D. of 6.95 mm), thin-wall confinement (304 stainless steel tube with 0.71 mm wall thickness and I.D. of 6.53 mm) and thick-wall confinement (1018 steel tube with a wall thickness of 34.9 mm and I.D. of 6.35 mm). To study the effect of applied shock strength leading into the HMEs, poly(methyl methacrylate) (PMMA) attenuators with thicknesses ranging from 1 to 8 mm were used.

A custom built microwave interferometer was used to produce time-resolved position measurements of the reactive front, or shock wave. The microwave system produced microwaves with a frequency of 35 GHz and a free space vacuum wavelength of 8.6 mm. The output signal from the microwave interferometer was recorded with a 500 MHz sampling rate using a Tektronix DPO4034 Digital Oscilloscope. Microwave transmission to the sample was made possible by an expendable 6.35 mm O.D. cylindrical Teflon™ waveguide. The location of the reactive wave within the confiners was verified with a fiber optic system consisting of patch cables (Thorlabs, Inc. M34L02) having a 600 μm core diameter and DET10A photo-detectors (Thorlabs, Inc.) with a 1 ns rise time.

2.2 Experimental Configuration

The experimental configuration within the confiner is shown in Fig. 1. Detonation begins with the detonator initiating a steady detonation through the ideal explosive. When present, a PMMA attenuator transmits a shock wave to the HME. The baseline configuration is to have no PMMA attenuator. When the attenuator was omitted, the ideal and HMEs were placed together to allow for the steady detonation developed by the ideal explosive to transition to the HME. Due to the inner diameter of the confiner being below the critical diameter for the HME, the initial overdriven reactive wave weakens and decelerates in the HME.

<Figure 1>

The waveguide was placed on the opposite end of the detonator in the confiner tube as shown in Fig. 2. The explosives and PMMA attenuator are dielectric mediums, allowing for transmission of the microwave signal from the waveguide. Reflection of the microwave signal occurs with the presence of a dielectric discontinuity caused by an ionizing reaction zone or a shock wave [19, 20]. A fiber optic cable was located at the interface of the detonator/ideal explosive to trigger the oscilloscope. A second fiber optic cable was placed at the ideal/HME interface. A

DETONATION FAILURE CHARACTERIZATION
OF HOME MADE EXPLOSIVES

third location was either at 1.5 cm away from the ideal/non-ideal interface into the HME for in situ interference signal calibration or at the end of the confiner to verify that a reactive wave was sustained through the entire length of the HME.

<Figure 2>

2.3 Microwave Interferometry Technique

As previously mentioned microwaves are partially reflected off of the reactive wave, a shock wave, or other dielectric discontinuity. The reflected signal is mixed with the reference signal to produce an interference signal.

The frequency of the interference signal is proportional to the velocity. The position can be determined using the zero-axis crossing method [19] with

$$x(t) = \frac{\lambda_I N(t)}{2}, \quad (1)$$

where x is the position, λ_I is the wavelength of the interference signal through the medium, and N is the number wavelengths present at a specified time. The spatial resolution is limited to half the wavelength of the interference signal. The interference signal advancing in phase by 2π indicates that the reactive wave has advanced in position a distance equivalent to the wavelength of the interference signal.

Higher spatial resolution can be obtained between each zero-axis crossing using the quadrature method [21]. The microwave interferometer can be designed to output a second signal shifted 90 degrees from the interference signal using a quadrature mixer. The two output signals are then combined to calculate the position using,

$$x(t) = \frac{\lambda_I}{4\pi} \tan^{-1} \frac{V_2(t)}{V_1(t)}, \quad (2)$$

where V_1 is the interference signal and V_2 is the 90 degree shifted interference signal. The arctangent function is pieced together to yield a continuous position.

In practice the raw data from each experiment was also filtered and normalized before Eqn. 2 was applied. Low-pass and high pass filters were implemented using MATLAB® to reduce the low frequency shifts that were observed and remove high frequency noise. Normalization of the signal from -1 to 1 also allows for an improved visual representation of the frequency (reactive wave front velocity) as a function of time.

Each method requires knowledge of the wavelength of the interference signal for the material being measured. This could be calculated from dielectric constant values, however here this was calibrated in situ using fiber optic cables at two known locations of the medium. The wavelength is found using

$$\lambda_I = \frac{L}{N} = \frac{2x}{N}, \quad (3)$$

where L is the total distance the microwave travels from one fiber optic cable to the next, N is the number of wavelengths that are present in the interference signal between the time the fiber optics were triggered, and x is the length between the fiber optic cables. The number of wavelengths present can be found by producing a Lissajous diagram with both quadrature signals between the time intervals indicated by the fiber optics. Since both signals are in quadrature, one full revolution of the data in the Lissajous curve represents advancement in phase by one wavelength. Fractions of a wavelength are then calculated by calculating the phase angle of an incomplete revolution for more accuracy.

A numerical differentiation method by Fast Fourier Transform (FFT) [22] was used to calculate the velocity of the front from position measurements. This method reduces error produced during numerical differentiation associated with experimental data.

2.4 Numerical Predictions

The Chapman-Jouguet (C-J) pressures were predicted for a range of compositions using CHEETAH 6.0 with the standard equation of state product library [23]. Compositions for investigation were selected based on the predicted C-J pressure; assuming that the failure dynamics of these HMEs would correlate to the predicted C-J pressures and detonation energy. A density of 100% of the theoretical was assumed.

3 Results and Discussion

The results from a typical test are shown first and the analysis steps illustrated. Figure 3 shows raw data (top) and the filtered/normalized data of the interference signal (bottom) for an experiment with AN/10 wt.% diesel fuel. The signal prior to $t=0$ is the measurement of the detonation front as it propagates through the ideal explosive. It is seen in the normalized data (bottom of Fig. 3) that a constant frequency is present during this time, representing a steady detonation through the ideal explosive.

<Figure3>

At $t=0$, the shock reaches the HME. The frequency of the interference signal then decreases as a function of time, capturing the reactive wave front slowing as the detonation fails.

The position and velocity of the front is calculated and shown in Fig. 4 with the position (top) and the velocity (bottom). A constant slope of the position (top of Fig. 4 at early times) as well as a nearly constant velocity (bottom of Fig. 4) is shown through the ideal explosive prior to $t=0$, as expected. At $t=0$, the

DETONATION FAILURE CHARACTERIZATION
OF HOME MADE EXPLOSIVES

measured position no longer has a constant slope as a function of time. A concave-down curve is seen indicating a decelerating reactive wave as a function of time. A decelerating reactive wave is also evident in the bottom plot of Fig. 4 (velocity) as the reactive wave slows. This trend shows the non-ideal reactive wave weakening during propagation through the sample. The plots in Fig. 4 illustrate the ability of microwave interferometry to measure the entire dynamic process.

<Figure 4>

3.1 Verification

It is important to verify that measurements made using the microwave interferometer with HMEs were indeed of a reactive wave front and not of a shock or compaction wave of the material. To distinguish between a signal produced by reflection from a decoupled shock wave and a reactive wave, experiments with an inert material were also considered.

Data was collected using a thick-walled confiner with compositions consisting of non-iodized table salt/2 wt.% mineral oil (inert) and AN/2 wt.% mineral oil (HME) for comparison. The interference signal produced from the salt/2 wt.% mineral oil is shown in the top of Fig. 5. The amplitude of the interference signal stays approximately constant for the duration of the measurement. When compared to the signal for AN/2 wt.% mineral oil there is a clear difference; the amplitude does not remain constant and increases generally as a function of time as shown in Fig. 5 (bottom).

<Figure 5>

It was previously noted that the amplitude of the interference signal has no effect on the measurement of position. However, the amplitude can provide an indication of whether a decoupled (inert) shock wave or reactive wave is causing the reflection of the microwave signal as there is a generally a difference in the interference signal amplitude of an inert material and HME. Previous work has shown that for inert material the reflections due to a shock wave produced constant amplitudes and are caused by dielectric discontinuities from compaction (density changes) [19]. It has also been shown that in reflections from a reactive wave the signal amplitude will tend to steadily increase due to ionization effects [20]. The increasing amplitude indicates that a reaction is occurring within the HME.

The higher frequency signal of the HME in Fig. 5 also indicates that the wave is traveling at a faster rate compared to the shock wave within the inert material. The amplitude of the interference signal cuts off much sooner in time for the signal from the HME when compared to the inert material because the end of the confiner is reached much sooner. Fiber optic cables placed near the end of the confiner indicated that a

reaction zone was present as emitted light was measured. As anticipated, no emission of light was recorded with the inert material (top of Fig. 5). A few oscillations of the interference signal are seen after the fiber optic triggers for AN/2 wt.% mineral oil, which occurred due to the waveguide being forced out of the confiner as the reactive wave reached the end of the HME. However, beyond the end of the tube the data is not relevant.

3.2 Experimental Accuracy

All subsequent results reported are only of the HME as the steady detonation leading to the attenuator or HME interface for each experiment was the same. Four experiments were performed using thin wall confiners with each composition of 2 and 10 wt.% diesel fuel to determine the accuracy of the microwave interferometry method during detonation failure. The mean position along with the standard deviation of AN/2 wt.% diesel fuel is shown in Fig.6. Maximum standard deviations calculated were +/-1.1 mm for AN/2 wt.% diesel fuel and +/-2.5 mm for AN/10 wt.% diesel fuel. It is noted that the standard deviation was observed to be the largest near the end of the HME's position record. The increased standard deviation can be explained by the method used to calculate the position from the interference signal. Specifically, the advancement in position of the front calculated for each time step compounds error, which therefore results in maximum deviation occurring near the end of the measurement.

<Figure 6>

3.3 Thin-walled Confinement with AN/Diesel Compositions

A typical position vs. velocity result with AN/2 wt.% diesel fuel is shown in Fig. 7. Two distinct slopes are observed. The initial slope is the weakening of the overdriven reactive wave as it travels through the AN/2 wt.% diesel fuel composition. The second velocity slope is less steep. The location of the interception of the two slopes is defined as the location at which the reactive wave fails and measurement of a decoupled shock wave begins. The location is indicated in Fig. 7. This is analogous to analysis of shock initiation to determine run-to-detonation, and here this could perhaps be termed a run-to-failure measure. It is not meant to be a precise measure of the point of failure, but rather is a systematic way to obtain a single parameter from an experiment. This value and the entire position-time trace are useful for model comparison.

The velocity oscillation may correspond to a pulsating, failing detonation (reactive wave). It is noted that once the shock wave decouples from the reaction, two microwave signals will be reflected and measured by the interferometer (one of reflection off of the reaction front and the other off of the shock wave). We do see some indications of this in the data, however

*DETONATION FAILURE CHARACTERIZATION
OF HOME MADE EXPLOSIVES*

the current method of processing the data did not allow for extracting the reaction front data from the mixed interference signal. Perhaps future work could analyze these results in order to separate the two signals and allow the relative velocities between the decaying reaction front and the shock wave to be determined although this is not a trivial task because after the shock the dielectric constant increases because the bed density is higher, effectively changing the wavelength.

<Figure 7>

The stoichiometric mixture of AN/diesel fuel was calculated to consist of 5.56 wt.% diesel fuel. Predictions using CHEETAH, shown in Fig. 8, indicate that the C-J energy is largest at the stoichiometric composition (near 5 wt.% diesel fuel). A higher C-J energy correlates to larger detonation energy available to support a reactive wave. The additional energy released from the stoichiometric mixture should allow for the reaction front to be sustained further through the HME.

<Figure8>

Measurements of the location within the HME where detonation fails and decoupling of the shock wave occurs (run-to-failure distance) are shown for compositions of AN with 2, 5, and 10 wt.% diesel fuel in Table 1 for thin wall confiners. It is shown in Table 1 that the mixture consisting of AN/5 wt.% diesel sustained a reactive wave the furthest into the HME. It is shown that the fuel lean (2 wt.% diesel) and fuel rich (10 wt.% diesel) were not able to sustain the reactive wave through the tube. Consequently, we see that they run-to-failure. Measurements appear to be consistent with the idea that higher calculated C-J pressures (or energy) tends to lead to a longer run-to-failure distance.

<Table 1>

For failed propagations, unreacted HME was recovered and was observed to be compacted due to the shock wave. The recovered samples after the experiments verified that the detonation failed in the HME. Obviously, deflagration also failed as would be expected for these materials in this configuration. All thin wall confinement experiments were consistent with complete failure. When the reactive wave fails the shock wave decouples and decreases in speed without the energy from the reaction zone, eventually weakening to the point where no deformation of the thin-wall confiner occurs. An example of a recovered thin walled steel confiner is shown in Fig. 9.

<Figure 9>

The remaining lengths of the recovered confiners were measured and were approximately 3.9, 4.0, and 4.4

cm long for AN with 2, 5, and 10 wt.% diesel fuel respectively. The recovered confiners show that deformation occurred further through the confiners for mixtures closest to stoichiometric. It is noted that these measurements are approximate and the microwave interferometer measurements are viewed as being more reliable.

3.4 Thin-walled Confinement with AN/Mineral Oil Compositions

A similar relationship was seen when diesel fuel was replaced with mineral oil (MO). Velocity slope intercepts were used to determine the location of the reactive wave failure (run-to-failure) in the same way previously shown for AN/diesel fuel. Increasing the fuel percentage decreased how far the failing detonation could sustain itself through the HME, shown in Fig. 10.

<Figure 10>

The AN/2 wt.% MO composition sustained the reactive front through 3.9 cm of HME while the AN/15 wt.% composition only sustained the reactive front for 2.5 cm, as shown in Table 2. Assuming that mineral oil is similar in composition to diesel fuel, it was shown that a mixture closer to the stoichiometric composition (2 wt.% MO) sustained the reactive wave further, much like what was previously observed for diesel fuel.

<Table 2>

3.5 Various Confinement Conditions with AN/2 wt.% Mineral Oil

Different failure dynamics are observed when the material composition is held constant and the confinement conditions are changed. Figure 11 shows the reactive front velocity as it travels through AN/2 wt.% mineral oil for various confinement conditions. The condition emulating no confinement (thin plastic tube) showed deceleration of the overdriven reactive front much more rapidly when compared to the other confinement conditions. The radial loss of energy is greatest with conditions of little confinement and the failing reactive wave does not continue beyond 2 cm of the HME.

The difference in the failure dynamics for different confinement is due to energy loss from the reaction zone. In the thin wall confiners, there are more significant lateral losses due to plastic deformation and expansion. With sizing of the HME below the critical diameter, the energy loss due to plastic deformation of the confiner can surpass the amount of energy supplied to the leading shock by the reaction zone. The reactive front weakens until the reactive wave can no longer be sustained and the shock wave decouples from the reaction zone.

DETONATION FAILURE CHARACTERIZATION
OF HOME MADE EXPLOSIVES

Unlike with thin wall confinement, the velocity of the thick wall confiner never dropped below 1000 m/s. The transition zone for a decoupled shock wave seen with the thin wall confinements was not evident with the thick wall confinements. This indicates that although the reactive wave is weakening, with a decreasing velocity, complete failure never occurs for thick walled confinements although the propagation speed is far from CJ, as might be expected.

The amount of deformation that occurs within the thick wall confiner should depend on the amount of energy lost from the reaction zone. Energy is required to result in expansion of the confiner. Measuring the amount of deformation that occurred after the HME reactive front would verify whether or not a reactive front (approaching a steady detonation) occurred through the entire length of the confiner.

<Figure 11>

The thick-wall confinements were cut in half to produce one side that would allow for the measurement of the inner diameter, as seen in the bottom of Fig. 12, to determine the expansion from the original diameter of 6.35 mm occurred. Inner diameter measurements (top of Fig. 12) showed that a coupled reactive wave occurred through the entire length of AN/2 wt.% mineral oil, as the measured I.D. never dropped below 6.46 mm. The fiber optic cable placed at the end of the HME in the thick wall confiner was also triggered indicating that a luminous reaction occurred through the entirety of the sample.

Previous work has shown that energy lost due to expansion of the confiner can be distributed in front of the detonation by pressure waves when the sound speed of the confiner is larger than the velocity of the explosive [24]. The speed of sound for steel is 5790 m/s [25]. The reactive wave front velocities measured in this work propagated at values below the sound speed of the steel confinements, allowing for the energy lost due to deformation of the confinements to be distributed in front of the detonation front. The transported energy into the walls could of course have an effect on the reactive wave velocity. It was also shown by Jackson et al. [24] that when energy transport within the confiner occurs, increasing the confiner thickness increases the detonation velocity of ammonium nitrate-fuel oil. In this work, increasing confinement thickness showed a similar trend as the sustainment of the reactive wave was shown to increase. Consequently, simulations of these data should certainly account for confiner wall thickness and wall material properties.

<Figure 12>

3.6 Effect of Attenuator Thickness with AN/2 wt. % Diesel Fuel

Experiments were performed using PMMA attenuators in thin and thick wall confinements with various attenuator thicknesses. These experiments allow for examination

of the transient dynamics as applied shock strength is varied. The strength of the shock wave transmitted to the HME (AN/2 wt.% diesel fuel) is dependent on the thickness of the attenuator. Thicker attenuators result in weaker applied shock waves. The weaker shock waves should lower initial reactive wave velocities in the HMEs. Associated with the weaker shock waves across the attenuator is an increase in curvature to the reaction front that leads to a two-dimensional shock initiation. However, this complexity is still acceptable for the purpose of these experiments due to the ability of simulations to replicate two-dimensional reaction zone curvature for rate law calibration. The use of an attenuator can also allow for the run-to-failure distance to be obtained as a function of attenuation when thin wall confinements are used, similar to "Pop-plots" for shock initiation.

3.6.1 Thick wall Confinement

Using thick wall confinement with AN/2 wt.% diesel fuel, attenuators 2, 4, and 8 mm thick were used along with a base case without attenuation. As shown in Fig. 13, the velocity without an attenuator produced a higher initial wave velocity. Using the 2 mm thick attenuator reduced the initial reactive wave velocity, but the deceleration is seen to be similar to the deceleration without an attenuator. Increasing the attenuator thickness to 4 mm showed very little difference compared to the 2 mm case. It could be expected that a lower initiating reactive wave velocity would be observed with a slightly thicker attenuator. However, the additional 2 mm thickness of the attenuator may not have as large of an effect on the leading shock strength compared to just the effect of having the presence of the attenuator of any thickness due to impedance mismatching effects. With a doubling of the attenuator thickness to 8 mm from 4 mm, the largest decrease in initiating reactive wave velocity is seen. However, the deceleration of the reactive wave in all three cases has a common slope indicating that the dynamics occurring (specifically the losses in energy to deformation of the confiner walls) are similar. The key difference is that the initial reactive wave velocity is dependent on the incoming shock wave strength (attenuator thickness), which was expected.

Results for all cases show a nearly steady wave velocity near 2000 m/s (Fig. 13). The steady detonation velocity was calculated using CHEETAH to be 1865 m/s for AN/2 wt.% diesel. With the thick wall confinement, a steady wave may therefore be sustainable. The fiber optic cables placed at the end of the confinements indicated that a reactive wave propagated through the entire HME sample. Consequently, there was no recovery of unreacted HME for any of the thick wall confinement experiments.

DETONATION FAILURE CHARACTERIZATION
OF HOME MADE EXPLOSIVES

<Figure 13>

3.6.2 Thin wall Confinement

Experiments were also conducted in thin wall confiners. Attenuators of different thicknesses (0, 1, 4, and 8 mm) were used with a HME composition of AN/2 wt.% diesel fuel. Decreased leading reactive wave velocities were observed with thicker attenuators similar to thick wall confinement experiments. The deceleration of the reaction front was similar between each case, with the difference in leading velocity proportional to the transmitted shock strength. As observed in previous results with thin wall confinement, complete failure of the reactive wave occurred along with the decoupling of a shock wave. A run-to-failure (RTF) distance is observed to depend on the attenuator thickness (leading shock strength), as shown in Fig. 14. The case without an attenuator was able to sustain the reaction the furthest through the HME, while the cases with attenuation showed a linear relationship between the RTF distance and the attenuator thickness. The RTF plot could be beneficial for calibrating a model of AN/2 wt.% diesel fuel in a thin wall confiner. Again, the large drop from no attenuator to a thin attenuator is attributed to impedance mismatch effects.

<Figure 14>

4 Conclusion

A unique method has been developed to characterize the failure dynamics of HMEs with small sample sizes. The experimental work presented could be used for calibration of models using hydrocodes such as Sandia's CTH [26] or other shock physics code. The calibrated models could then be compared to large scale data for validation. If successful, it would show that this small scale experimental technique can be used for the characterization of HMEs and still be valid for large scale configurations. Regardless, this experiment is useful for improving the understanding of detonation failure in HMEs.

Experiments have been performed using AN with diesel fuel and mineral oil. High resolution spatial measurements of the position and velocity were attained indicating factors such as chemical composition, confiner thickness, and initiating shock wave strength all affect the detonation failure dynamics. Thin wall experiments showed that stoichiometric compositions sustained a coupled reactive wave (approaching a steady detonation) further through the HMEs. Various confinement conditions used with AN/2 wt.% mineral oil showed how confinement had an effect on sustaining a coupled reactive wave (approaching a steady detonation) through a HME. Complete failure of the detonation was accompanied by a decoupling shock

wave with thin wall confinement. It was shown that the thick wall confiner sustained the reactive wave through the entire length of HME by limiting the lateral loss of energy compared to the thin wall confiners and likely propagating energy ahead of the shock wave. Many other combinations of materials can also now be quickly and conveniently be considered.

The strength of the shock wave transmitted to the HME corresponded to the resulting initial reactive wave speed. In thin wall confinement, it was shown that the run-to-failure distance increased as the attenuator length decreased. Higher initiating shock strengths yielded additional energy for sustaining the reactive wave further into the HME. This experimental technique shows potential to reduce the time and cost required to dynamically characterize HMEs and rapidly characterize a variety of materials and confinement conditions over a broad parameter space. It is a useful tool for assessing the detonability of HMEs with only a few grams of material.

Acknowledgements

This project was funded by the Department of Homeland Security through the Center of Excellence for Explosive Detection, Mitigation, and Response under award number 080409/0002251. Discussions with Dr. Blaine Asay were also very useful.

References

- [1] W. M. Howard, L. E. Fried, P. C. Souers, Modeling of Non-Ideal Aluminized Explosives, *AIP Conference Proceedings*, **2000**, 505.1 p. 389.
- [2] A. Miyake, H. Echigoya, H. Kobayashi, T. Ogawa, K. Katoh, S. Kubota, Y. Wada, Non-Ideal Detonation Properties of Ammonium Nitrate and Activated Carbon Mixtures, *Int. J. Mod. Phys. B*, **2008**, 22.9-11, p. 1319-1324.
- [3] S. I. Jackson, C. B. Kiyanda, M. Short, Experimental Observations of Detonation in Ammonium-nitrate-fuel-oil (ANFO) Surrounded by a High-sound-speed, Shockless, Aluminum Confiner, *Proceedings of the Combustion Institute*, **2011**, 33.2 p. 2219-2226.
- [4] A. Miyake, K. Takahara, T. Ogawa, Y. Ogata, Y. Wada, H. Arai, Influence of Physical Properties of Ammonium Nitrate on the Detonation Behavior of ANFO, *Journal of Loss Prevention in the Process Industries*, **2001**, 14.6, p. 533-538.
- [5] F. W. Sandstrom, R. L. Abernathy, M. G. Leone, M. L. Banks, Diameter Effect and Detonation Front Curvature of Ideal and Non-ideal Explosives, *AIP Conference Proceedings*, **2000**, 505 p. 825-828.
- [6] B. M. Dobratz, *LLNL handbook of explosives*, Report UCRL-52997, Lawrence Livermore National Laboratory, Livermore, CA, USA, **1981** (updated **1985**).
- [7] C. H. Johansson, P. A. Persson, in: *Detonics of High Explosives*, Academic Press, London, **1970**.
- [8] N. J. Burnside, S. F. Son, B. W. Asay, P. M. Dickson, Deflagration to Detonation Experiments

DETONATION FAILURE CHARACTERIZATION
OF HOME MADE EXPLOSIVES

- in Granular HMX, *1997 Joint Army, Navy, NASA, Air Force (JANNAF) CS/propulsion systems hazards subcommittee meeting*, West Palm Beach, FL, USA, **1997**.
- [9] E. L. Lee, C. M. Tarver, Phenomenological Model of Shock Initiation in Heterogeneous Explosives, *Phys. Fluids.*, **1980**, *23*, p. 2362–272.
- [10] R. Menikoff, M. S. Shaw, Review of the Forest fire Model for High Explosives, *Combustion Theory and Modeling*, **2008**, *12.3* p. 569-604.
- [11] R. Menikoff, M. S. Shaw, Reactive Burn Models and Ignition & Growth Concept, *EPJ Web of Conferences*, **2010**, *10*, p. 00003.
- [12] D. L. Robbins, S. A. Sheffield, D. M. Dattelbaum, N. Velisavljevic, D. B. Stahl, Equation of State of Ammonium Nitrate, *AIP Conference Proceedings*, **2009**, *1195*, p. 552–555.
- [13] E. J. Cart, R. H. Granholm, V. S. Joshi, H. W. Sandusky, R. J. Lee, Measurement of Ignition and Reaction Parameters in Non-Ideal Energetic Materials, *AIP Conference Proceedings*, **2006**, *845* p. 1045–1048.
- [14] V. S. Bozic, D. D. Blagojevic, B. A. Anicin, Measurement System for Determining Solid Rocket Propellant Burning Rate using Reflection Microwave Interferometry, *J. Propulsion and Power*, **1997**, *13.4*, p. 457-462.
- [15] G. F. Cawsey, J. L. Farrands, S. Thomas, Observations of Detonation in Solid Explosives by Microwave Interferometry, *Proceedings - Royal Society. Mathematical, Physical and Engineering Sciences*, **1958**, *248.1255* p. 499-521.
- [16] M. A. Cook, R. L. Doran, G. J. Morris, Measurement of Detonation Velocity by Doppler Effect at 3-centimeter Wavelength, *J. Appl. Phys.*, **1955**, *26.4*, p. 426-428.
- [17] V. E. Zarko, D. V. Vdovin, V.V. Perov, Methodical Problems of Solid-Propellant Burning-rate Measurements Using Microwaves, *Comb. Explosion, and Shock Waves*, **2000**, *36.1*, p. 62-71.
- [18] B. A. Anicin, B. Jojic, D. Blagojevic, M. Adzic, V. Milosavljevic, Flame Plasma and the Microwave Determination of Solid-Propellant Regression Rates, *Combust. Flame*, **1986**, *64.3* p. 309-319.
- [19] A. D. Krall, B. C. Glancy, H. W. Sandusky, Microwave Interferometry of Shock Waves .1. Unreacting Porous-media, *J. Appl. Phys.*, **1993**, *74.10*, p. 6322-6327.
- [20] B. C. Glancy, A. D. Krall and H. W. Sandusky, Microwave Interferometry of Shock Waves .2. Reacting Porous-media, *J. Appl. Phys.*, **1993**, *74.10*, p. 6328-6334.
- [21] N. Burnside, Deflagration to Detonation Transition in Granular HMX, *MS thesis*, Brigham Young University, Provo, UT, USA, **1999**.
- [22] R. D. Levie, S. Sarangapani, P. Czekaj, Numerical Differentiation by Fourier Transformation as Applied to Electrochemical Interfacial Tension Data, *Anal. Chem.*, **1978**, *50*, p. 110-115.
- [23] L. E. Fried, W. M. Howard, P. C. Souers, *Cheetah 6.0 User's Manual*, Lawrence Livermore National Laboratory, Livermore, CA, USA, **2010**.
- [24] S. I. Jackson, C. B. Kiyanda, M. Short, Precursor Detonation Wave Development in ANFO Due to Aluminum Confinement, *14th International Detonation Symposium*, Coeur d'Alene, Idaho, USA, **2009**.
- [25] *CRC Handbook of Chemistry and Physics, 90th ed.*, CRC Press, Boca Raton, FL., **2009**.
- [26] D. A. Crawford, A. L. Brundage, E. N. Harstad, E. S. Hertel, Jr., R. G. Schmitt, S. C. Schumacher, J. S. Simmons, *CTH User's Manual and Input Instruction*, Sandia National Laboratories, Albuquerque, NM, USA, **2011**.

Full Paper

C. Author, B. Coauthor

Tables

TABLE 1. Failure position and velocity measured at the location of the velocity slope intercepts for various AN/diesel fuel compositions.

Diesel Fuel (wt.%)	Position (cm)	Velocity (m/s)
2	2.7	760
5	3.2	850
10	2.9	640

TABLE 2. Failure position and velocity measured at the location of the velocity slope intercepts for various AN/mineral oil compositions.

Mineral Oil (wt.%)	Position (cm)	Velocity (m/s)
2	3.9	910
15	2.5	980

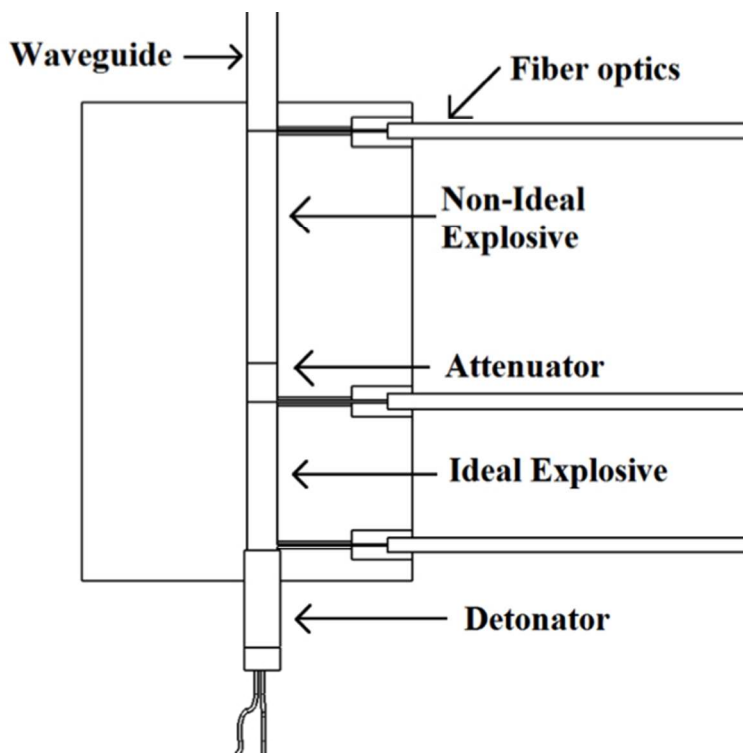


FIG. 1. Cross-section of confiner showing location of the detonator, ideal explosive, non-ideal explosive, PMMA attenuator, waveguide, and fiber optics.

282x211mm (72 x 72 DPI)

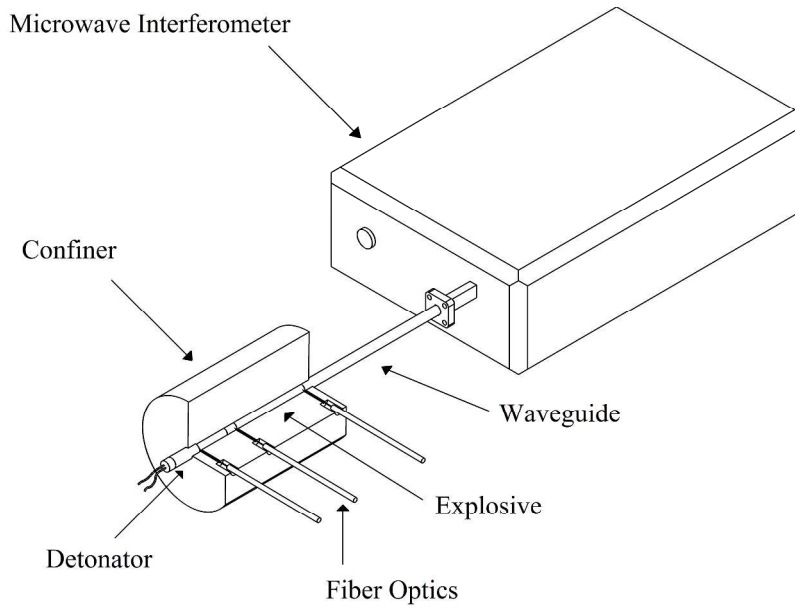


FIG. 2. Schematic of the experimental configuration.
1189x841mm (150 x 150 DPI)

View Only

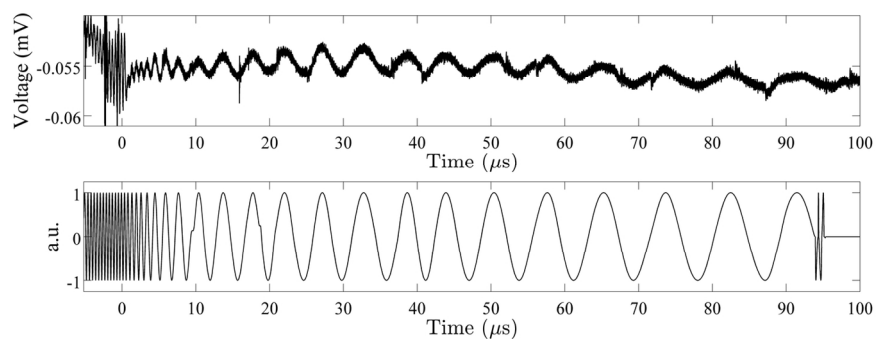


FIG. 3. Raw interference signal (top) and normalized signal (bottom) of detonation through ideal explosive transitioning to AN/10 wt.% diesel ($t = 0$).
142x50mm (300 x 300 DPI)

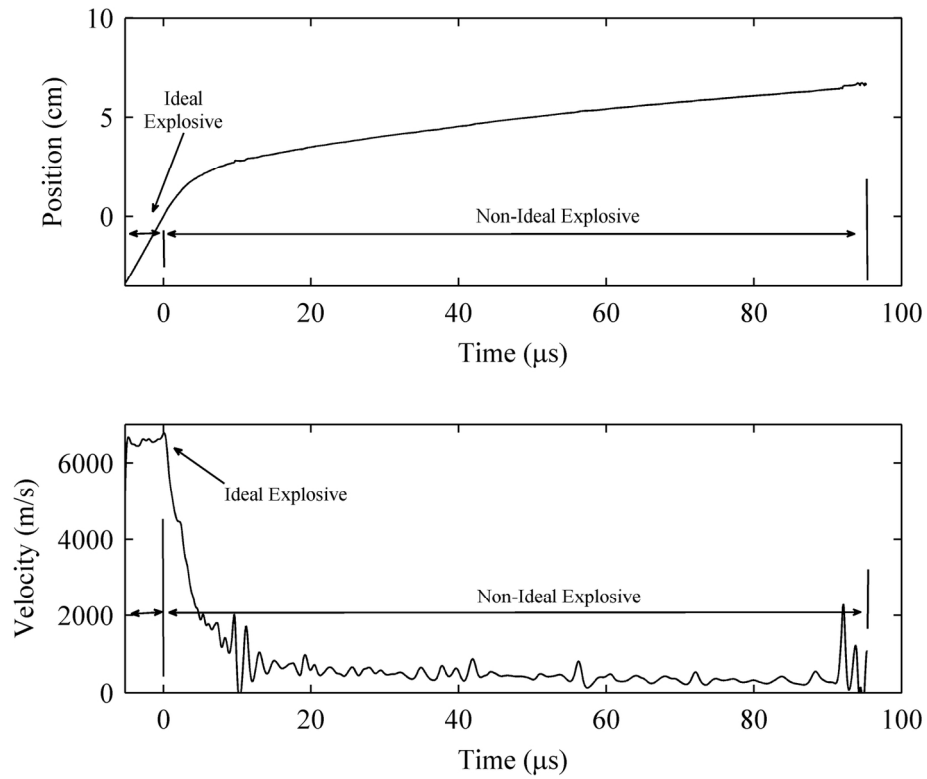


FIG. 4. Position (top) and velocity (bottom) of detonation through ideal explosive transitioning to AN/10 wt.% diesel ($t = 0$), 76x65mm (600 x 600 DPI)

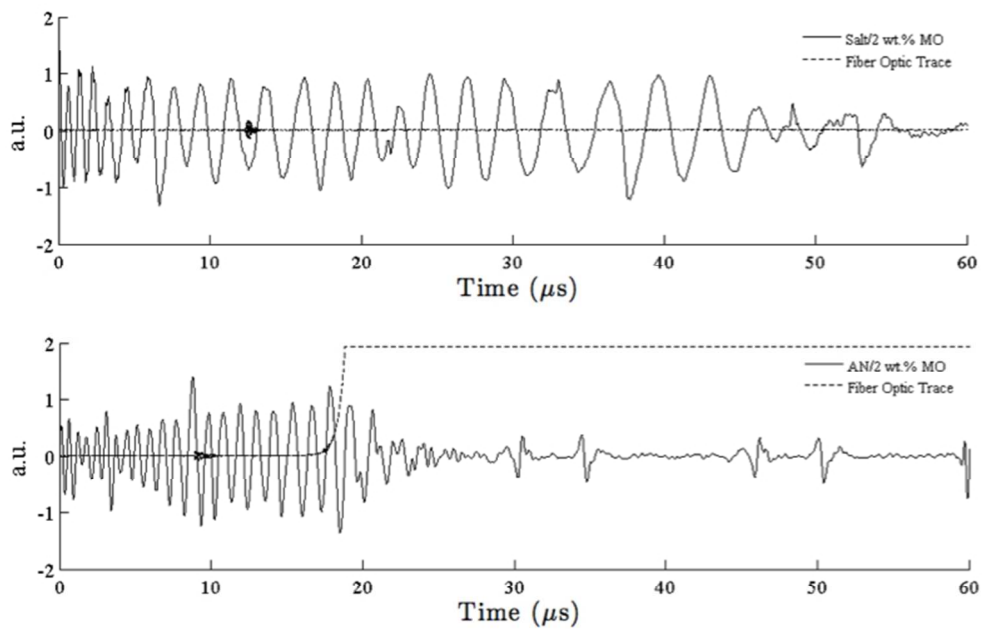


FIG. 5. Interference signal produced due to reflection through salt/2 wt.% mineral oil (top) and AN/2 wt.% mineral oil (bottom).
282x211mm (72 x 72 DPI)

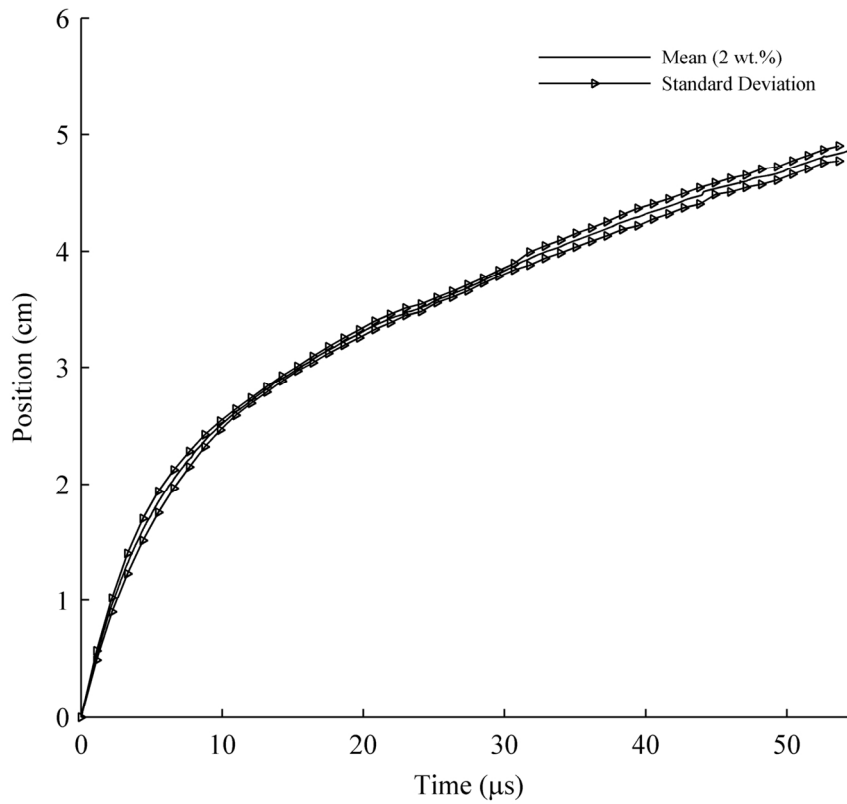


FIG. 6. Result showing the detonation velocity of the detonation front through AN/2 wt.% diesel fuel in thin-wall confiners. 76x65mm (600 x 600 DPI)

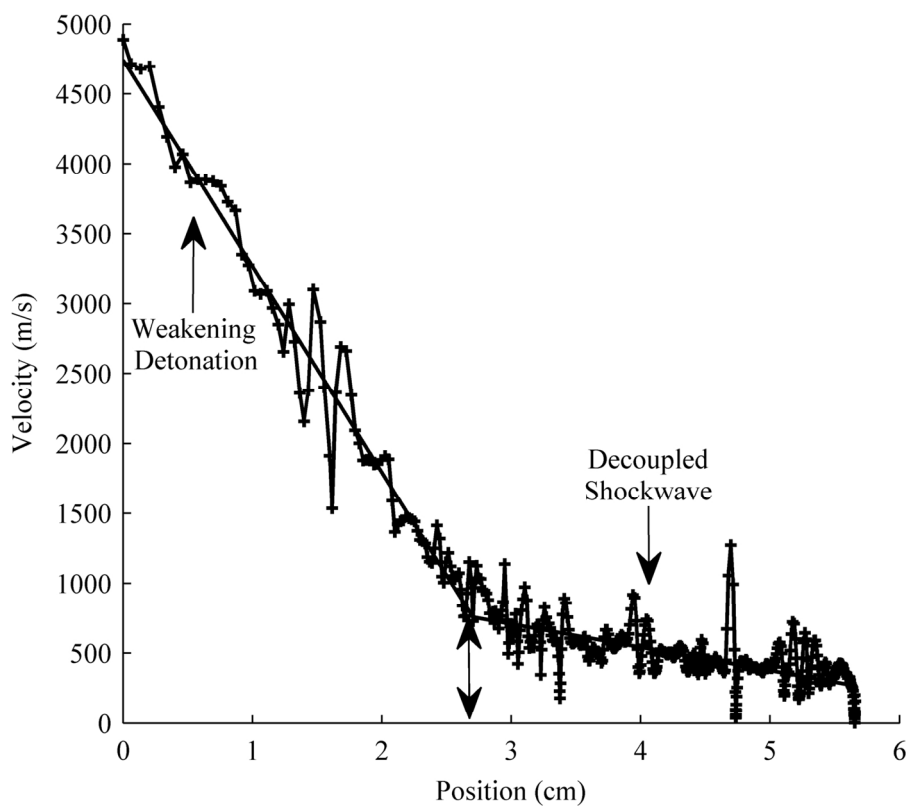


FIG. 7. Wave velocity as a function of position through AN/2 wt.% diesel fuel. 76x65mm (600 x 600 DPI)

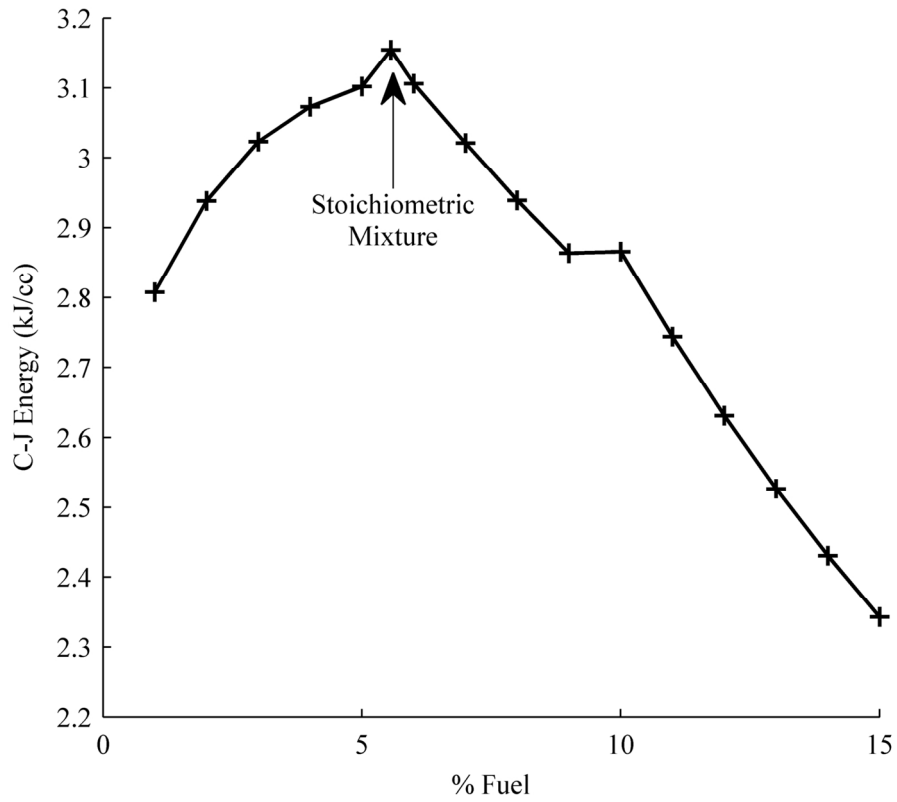


FIG. 8. C-J energy predictions for AN/diesel mixtures at various compositions (100% TMD) using CHEETAH 6.0.
76x65mm (600 x 600 DPI)



FIG. 9. Recovered thin-walled confiner after detonation of a non-ideal explosive fails.

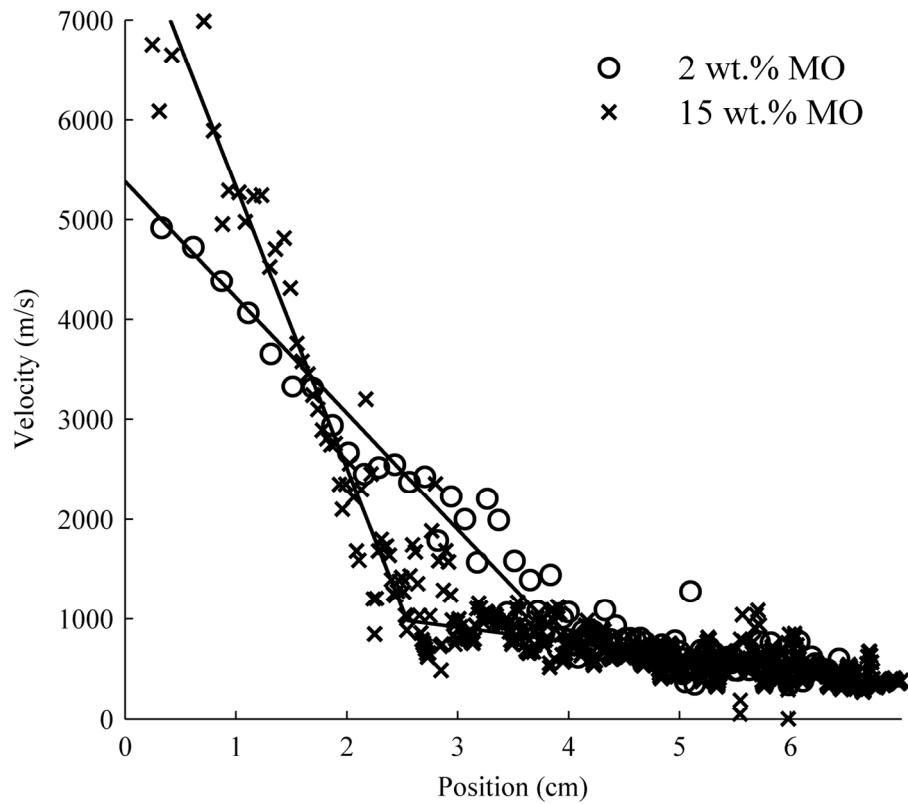


FIG. 10. Results showing the velocity of the detonation front through non-ideal explosives with various mineral oil compositions in thin-wall confiners. 76x65mm (600 x 600 DPI)

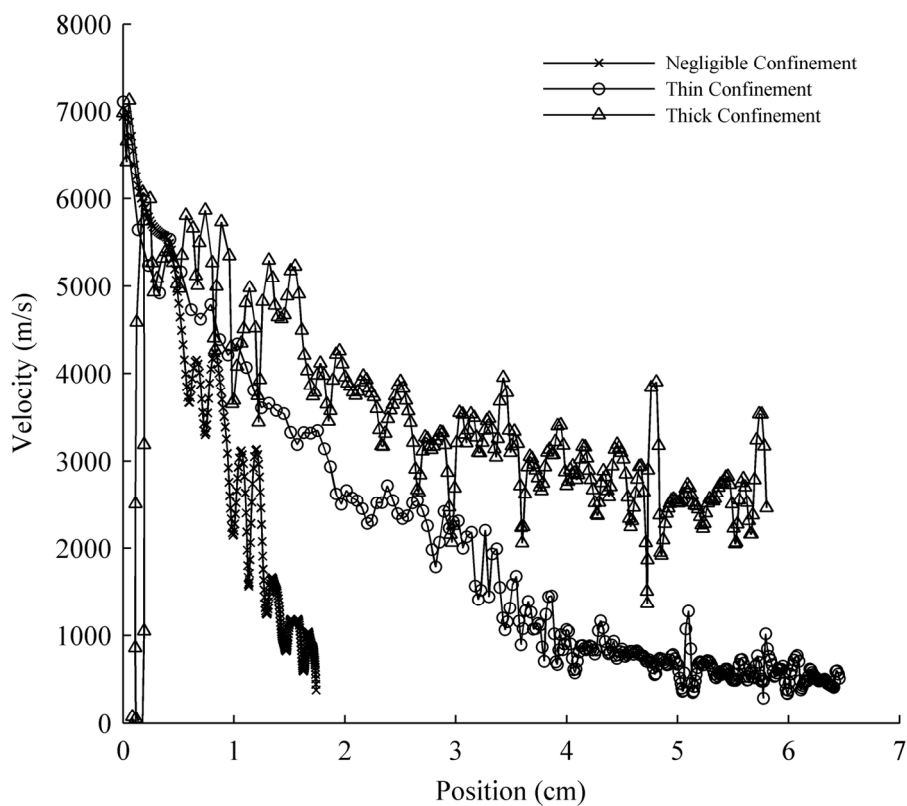


FIG. 11. Results between no confinement, thick confinement, and thin wall confiner using AN/2 wt.% mineral oil showing the velocity as a function of position through the non-ideal explosive. 76x65mm (600 x 600 DPI)

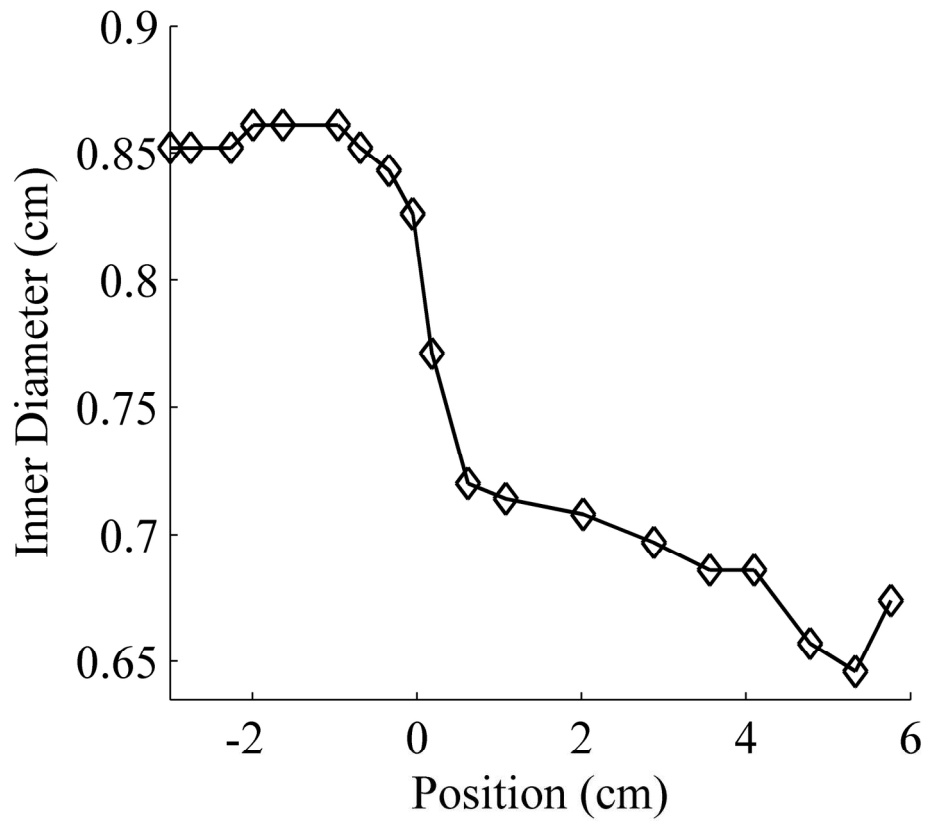


FIG. 12. Measurement of the I.D. of the recovered thick wall confiner (top) where $x=0$ is the location that the detonation transfers to the non-ideal explosive along with the cross-section of the thick-wall confiner cut in half used to measure the inner diameter I.D. (bottom).
87x85mm (600 x 600 DPI)

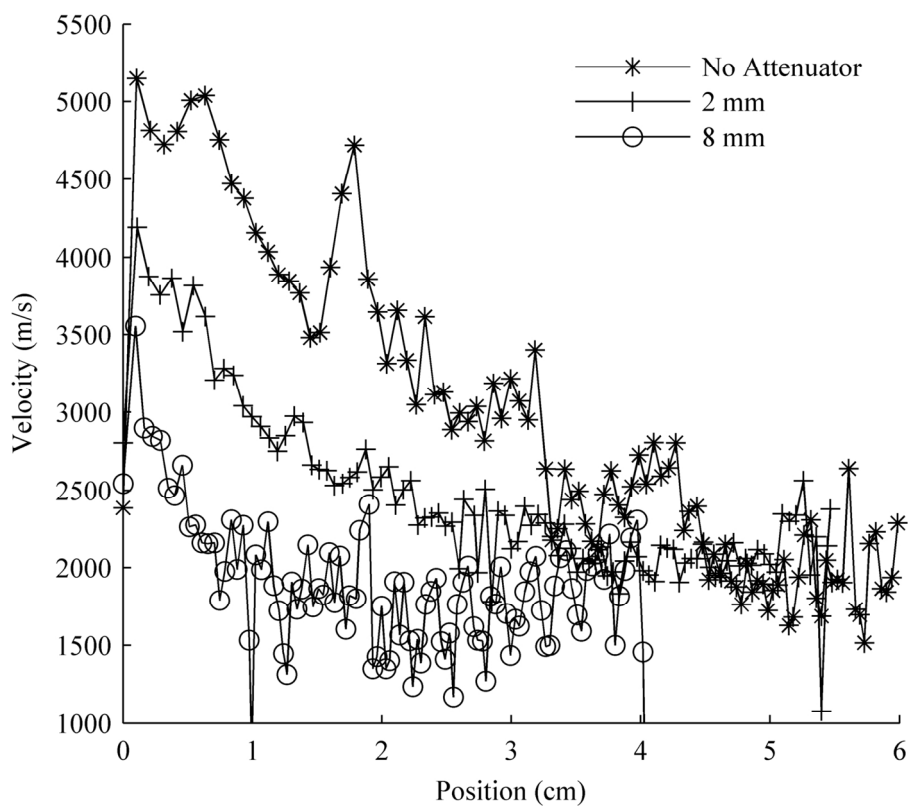


FIG. 13. Results showing velocity of a detonation front through AN/2 wt.% diesel fuel with various attenuator thicknesses to alter the overdriven shock strength in thick-wall confiners. 76x65mm (600 x 600 DPI)

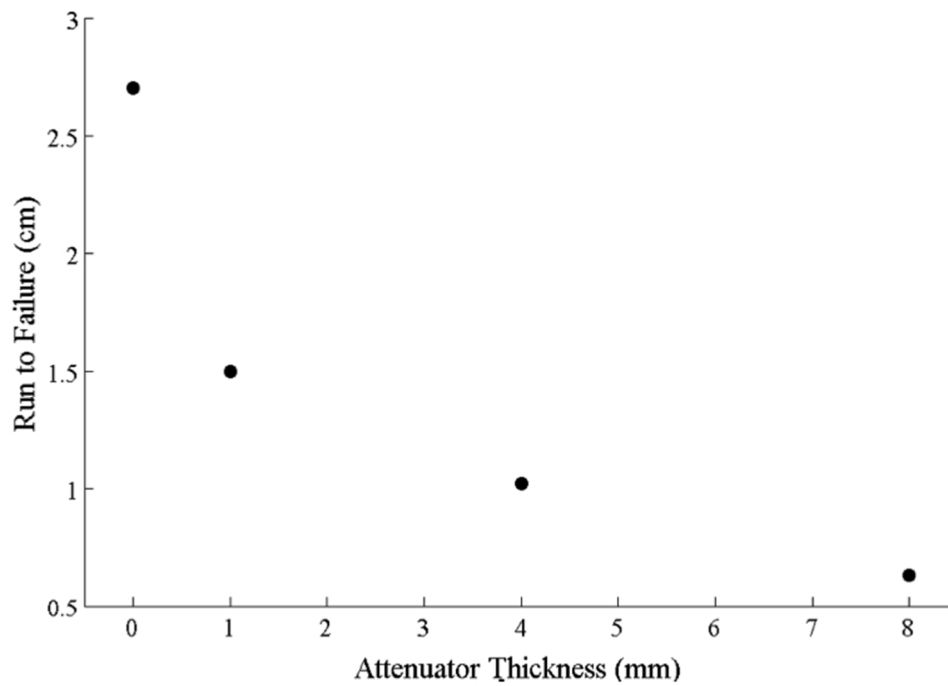


FIG. 14. Run to failure as a function of attenuator thickness in a thin steel wall confiner for AN/2 wt.% diesel fuel.

282x211mm (72 x 72 DPI)

Hot dense liquid TNT decomposition: Fragmentation, kinetics and carbon clusters formation

Naomi Rom¹, Barak Hirshberg¹, Yehuda Zeiri^{3,4}, D. Furman¹, Sergey V. Zybin², William A. Goddard III², and Ronnie Kosloff¹

¹Fritz Haber Research Center for Molecular Dynamics, Hebrew University, Jerusalem 91904, Israel

²Materials and Process Simulation Center, 139-74, California Institute of Technology, Pasadena, California 91125, USA,

³Bio-medical Engineering, Ben Gurion University, Beer-Sheva 84105, Israel

⁴Division of Chemistry, NRCN, P.O. Box 9001 Beer-Sheva 84190, Israel

Abstract – The thermal decomposition mechanism of hot, dense liquid TNT was studied using reactive force field (ReaxFF) molecular dynamics simulations. The decomposition was analyzed from the initial stage through carbon-clusters and stable gaseous production. The density and temperature dependence of these reactions, activation energies and fragments production was studied in details. The initial decomposition reaction is density and temperature dependent: In general, a unimolecular C-N bond scission is dominant at the lower densities (producing NO₂), whereas dimer formation and decomposition to TNT derivatives and smaller gaseous fragments prevails at higher compressions. The carbon-clustering is enhanced when density is increased, while initial gaseous fragments formation is suppressed. Temperature rise, on the other hand, speeds up the production of both clusters and gaseous products. The activation energy for the initial decomposition stage of liquid TNT is ~10 kcal/mole lower than the corresponding gas phase value. Finally, a simple linear growth kinetic model is suggested for describing the clustering process, and gives a very good agreement to simulation results.

Index Terms— TNT, liquid, heat up, compression, Arrhenius, kinetics, fragments, detonation, soot, clusters.

1 INTRODUCTION

Trinitrotoluene (C₇N₃O₆H₅) is an insensitive high explosive (HE) that has wide applications both in industry and military. Due to its low melting point (80°C), it can be easily poured to obtain various shapes, or mixed with other materials. Upon heating above its melting point, TNT melts and reacts as a liquid, therefore studying the properties of liquid TNT are of importance.

Density functional theory (DFT) calculations of TNT unimolecular decomposition along three main reaction routes were performed in [1]. The initial reactions that were studied are:

1. NO₂ homolysis.
2. C-H alpha attack, leading to the formation of 2,4-dinitro-anthranil and water molecule release.
3. NO₂-ONO rearrangement.

The detailed chemical mechanisms and the species created along these reaction paths were presented in [1], as well as the free energies and enthalpies in the temperature range 300K-3500K. At room temperature, the kinetically and thermodynamically favorable unimolecular path is the C-H alpha attack, whereas at 3500K the NO₂ homolysis is dominant. The calculated activation free energies for the reactions 1-3 at 300K are 43.8, 37.7 and 54.9 kcal/mole, whereas at 3500K the corresponding values are -90.6, 60.8, 60.1 kcal/mole [1].

The decomposition of liquid TNT under hydrostatic compression as a function of density is studied at high temperatures using LAMMPS molecular dynamics simulation package [2] with ReaxFF potentials [3, 4] and LG dispersion correction [5]. The evolution of fragments that are formed during the decomposition process of liquid TNT is presented, and the corresponding reaction kinetics is evaluated. As shown below, the initial decomposition reaction path of hot liquid TNT depends on the compression and temperature conditions. Similarly, density dependent initial decomposition mechanisms were seen in the ReaxFF molecular dynamics (MD) simulations of hot, dense liquid nitromethane [6].

Due to the low oxygen content of TNT, soot is formed upon TNT reaction/explosion, as observed in experiments [7]. The formation of soot is common to other HE nitroaromatic substances, such as TATB, and was obtained in previous ReaxFF-MD simulations [8]. The present liquid TNT simulations demonstrate this behavior as well, where large, carbon-rich clusters are formed as the decomposition reaction proceeds. An analysis of the clusters production process and a suggestion of a kinetic model that describes the coagulation mechanism are given for the various conditions studied.

The computational approach is described in Section 2, and the results of the simulations are presented in Section 0. The decay of liquid TNT at high temperatures and compressions is shown and analyzed, starting at the initial decomposition, followed by intermediate fragments formation and finally stable products formation. The clusters analysis and the kinetic model are presented in Section 4, and the conclusions are summarized in Section 5.

2 COMPUTATIONAL APPROACH

The molecular dynamics code that was used in the present liquid TNT simulation with ReaxFF potentials [3, 4] is LAMMPS [2], with LG-corrected potentials [5]. The potential parameters are given in the Supporting Information. In Section 2.1, the enthalpy change calculated with these ReaxFF potentials is compared to DFT values, for two TNT unimolecular decomposition paths.

The ReaxFF-MD simulation cell includes 288 TNT molecules (6048 atoms). The liquid sample preparation, the type of simulations and the decomposition reactions and kinetic analysis are similar to the scheme applied and outlined in details in Ref. 6, excluding the clusters analysis and kinetic modeling (not relevant to NM decomposition). Thus, only the main points that are typical to the present liquid TNT simulations are mentioned in the sections below.

2.1 Single TNT molecule decomposition

The decomposition paths of a single TNT molecule were studied intensively using DFT (see for example [1], [9]). Two unimolecular reactions of TNT were chosen here as study cases for the enthalpy change values calculated using ReaxFF potentials in LAMMPS:

1. $C_7N_3O_6H_5$ (TNT) \rightarrow $C_7N_3O_6H_5$ (ortho-nitril (ONO)-TNT, see FIG. 1).
2. $C_7N_3O_6H_5$ (TNT) \rightarrow $C_7N_2O_4H_5$ + NO_2 (NO_2 homolysis).

The enthalpy change in these reactions is obtained from the potential energy (PE) difference at 0K, between the initial TNT molecule and the energy minimized products. The enthalpy change obtained using ReaxFF potentials is -1.2 and 61.4 kcal/mole, and the DFT results at 298K are -6.6 (-8.1) and 57.0 (58.0) kcal/mole in Ref. [9] ([1]), respectively. The ReaxFF parameters can be further optimized for improved description of TNT decomposition energetics, however this is not within the scope of this paper.

The activation energies calculated for the above reactions are 55 and 44 kcal/mole, respectively [1]. Another decomposition path of TNT molecule in the gas phase is the intra-molecular

hydrogen atom attack, which results in H₂O release. Its calculated activation energy is 43 kcal/mole [1], which is similar to the TNT unimolecular C-N bond break barrier. In Section 3.3 the activation energy of the initial decomposition step of TNT is calculated.

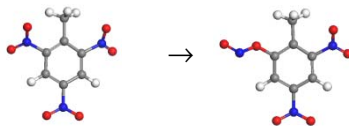


FIG. 1: NO₂ → ONO (nitro-nitril) rearrangement in TNT molecule.

2.2 Sample preparation

The unitcell used for the liquid TNT simulation cell preparation is CSD_CIF_ZZZMUC01[910], with a, b, c = 14.991, 6.077, 20.017 Å (see FIG. 2). First, a 3x6x2 expanded crystal supercell was created and its energy was minimized (see FIG. 3, l.h.s). The supercell has 288 molecules, with a, b, c = 44.730, 36.204, 39.360 Å. Thereafter, the following procedure was applied:

- The supercell volume was increased by 45%, then its energy was minimized, resulting in an optimized geometry.
- The obtained supercell was heated to 500K (well above the TNT melting point - 354K) and thermalized for 10ps.
- The hot cell was heavily compressed (NPT simulation at 1 GPa and 500K, for 30 ps).
- Cooling and decompression was applied (NPT simulation at 1atm and 400K, for 30ps). The calculated mass density of the liquefied sample at the end of the simulation was 1.444gr/cm³ (a, b, c = 47.2714, 38.2609, 41.5961Å), in excellent agreement with the measured density at 373°K: 1.443 gr/cm³ [11].
- The liquid cell was then thermalized (NVT simulation at T=400K, for 2 ps).
- Finally the system state was relaxed (NVE simulation, for 1ps). A typical liquid supercell is shown in FIG. 3 and FIG. 4 (r.h.s).

The time step used in the simulation steps described above was 0.25 fs.

The radial distribution functions (RDF) for the liquid and the solid at 1 atm are presented in FIG. 5. The liquid RDF has smoothed and smeared peaks that are characteristic of a liquid phase. However, some order is preserved in the liquid RDF in the vicinity of the crystal sharp peaks as shown in FIG. 6.

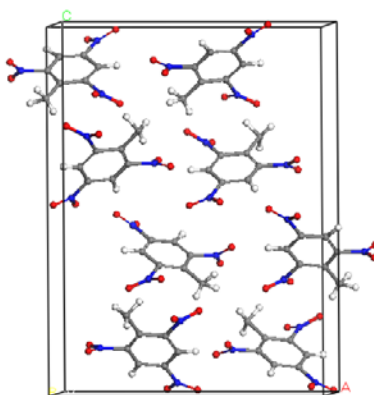


FIG. 2: TNT orthorhombic unitcell [910].

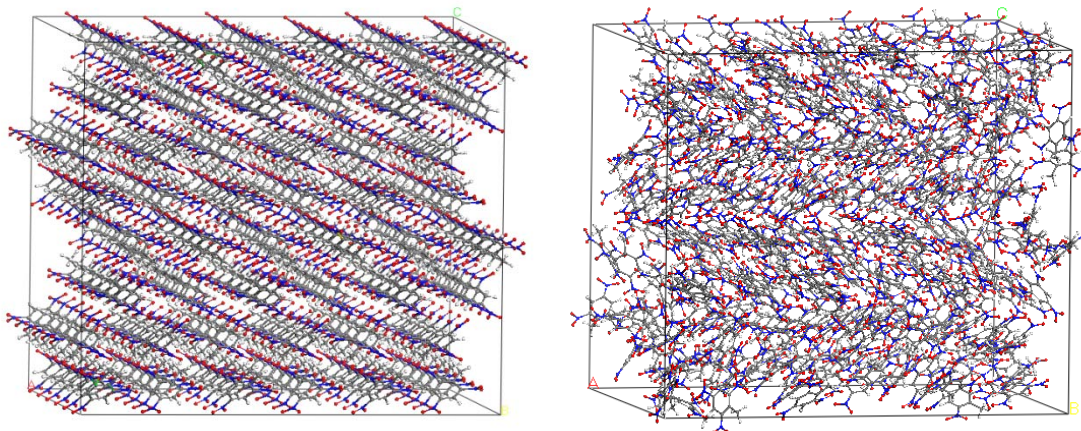


FIG. 3: Energy-minimized TNT Crystal supercell (left) vs. liquid simulation cell (right) at 1atm, 400K.

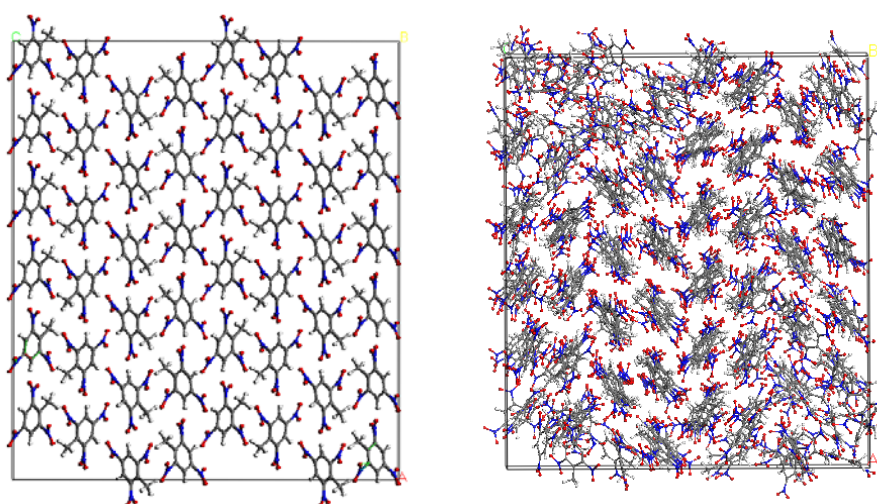


FIG. 4: As FIG. 3, but from a different direction. Some order remains in the liquid cell.

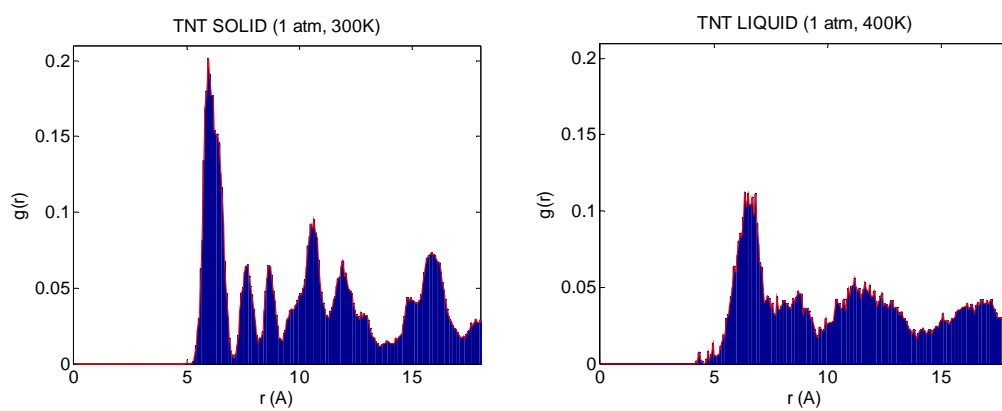


FIG. 5: Radial distribution function for TNT molecules in the solid (left) and liquid (right) phases. Distance units are Å.

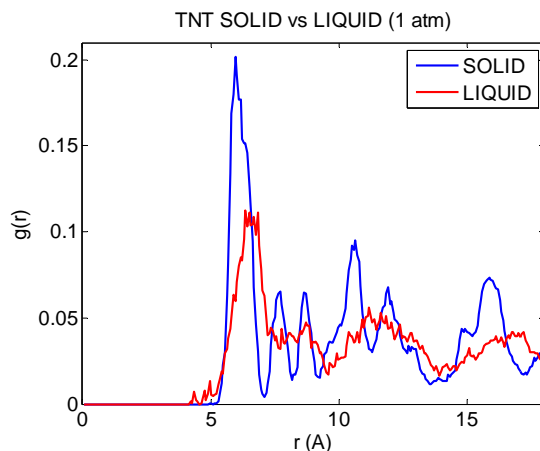


FIG. 6: Comparison between the radial distribution function for TNT solid (300K) and liquid (400K). Distance units are Å

2.3 Liquid compression

In order to obtain liquid at various compressions, the liquid sample prepared by the process described above (at 400K and 1atm) was volumetrically compressed by the desired amount. Then, the compressed liquid cell energy was minimized, until equilibrium positions were obtained. Finally, each compressed liquid cell was thermalized using NVT simulation at 400K, for 5 ps. It is important to note that none of the TNT molecules decomposed during these initial state preparation stages.

The liquid TNT densities obtained are shown in Table 1, corresponding to ambient density, 15% and 30% compression at 400K. The temperatures used in the heat up simulations are 1800K, 2250K, 2750K, and 3500K.

Table 1: Densities, volumes and compressions of the heat up simulation cells.

Mass density [gr/cm ³]	Cell volume, V [Å ³]	Compression, V/V ₀
1.444	75233	1
1.699	63948	0.85
2.063	52663	0.7

2.4 Heat up simulations

Liquid TNT heat up simulations were carried out in two stages: Initially, the sample at a fixed density was heated rapidly (within 100 fs, using time step 0.1 fs) from the initial liquid temperature of 400K to the desired temperature (T_f). Then, NVT simulations were carried out at T_f until the final decomposition products were obtained. The values of T_f used are: 1800K, 2250K, 2700K, and 3500K.

The rapid heating is carried out on a time scale similar to that of a detonation wave passing through the simulation cell (~500 fs). The measured detonation velocity of liquid TNT with initial density 1.472 gr/cm³ is 6.633 ± 0.012 km/sec [12], and the Chapman Jouguet pressure is 182 ± 12 kbar [13]. The time step used in the NVT simulations was 0.25 fs (the energy conservation is similar for simulations with 0.1 and 0.25 fs timesteps). The simulations length varied between 100-200 ps, depending on the reaction rate.

2.5 Thermal kinetic analysis

Fragments formation along the liquid TNT decomposition path is analyzed using an internal

code from the LAMMPS package [2] in the following regimes:

- Initial decomposition (endothermic stage).
- Intermediate reactions and products (exothermic stage).
- Final products formation:
 - o Gaseous products: H_2O , CO_2 , N_2 , H_2 , NH_3 , CO and OH .
 - o Soot (large clusters).

The calculation of liquid TNT decomposition thermal rate constants for the initial and intermediates stages, and for the gaseous products formation stage were calculated using the formalism outlined in our previous study of liquid NM [6]. The soot formation kinetic analysis was made using a linear growth model, as described in Section 4.3.

3 RESULTS: GASEOUS FRAGMENTS FORMATION AND THERMAL RATE CONSTANTS

In this chapter the decay of liquid TNT and the gaseous products formed in ReaxFF-MD simulations at extreme conditions are presented. Thermal rate constants are computed for the decomposition reaction at the initial and intermediate stages from the TNT decay (k_1) and the potential energy decay (k_2), respectively. In particular, the influence of pressure and temperature on the above is studied.

3.1 Liquid TNT initial decay

The time evolution of the amount of TNT molecules, normalized by the initial number of 288 molecules, is presented in FIG. 7, for the different temperatures. The initial, rapid heating stage is not shown in these plots, and it was verified that no decomposition occurred during this period. As seen, the decomposition rate increases when density (compression) increases. The reaction rate increase with compression is expected if the decomposition dynamics is dominated by inter-molecular processes. In contrast, the increase of liquid TNT decomposition rate due to temperature rise is expected both in unimolecular and bi-molecular reactions, since the probability to overcome energy barriers is higher at elevated temperatures. These findings are further discussed in Section 3.4, in relation to the fragments formation at the various conditions.

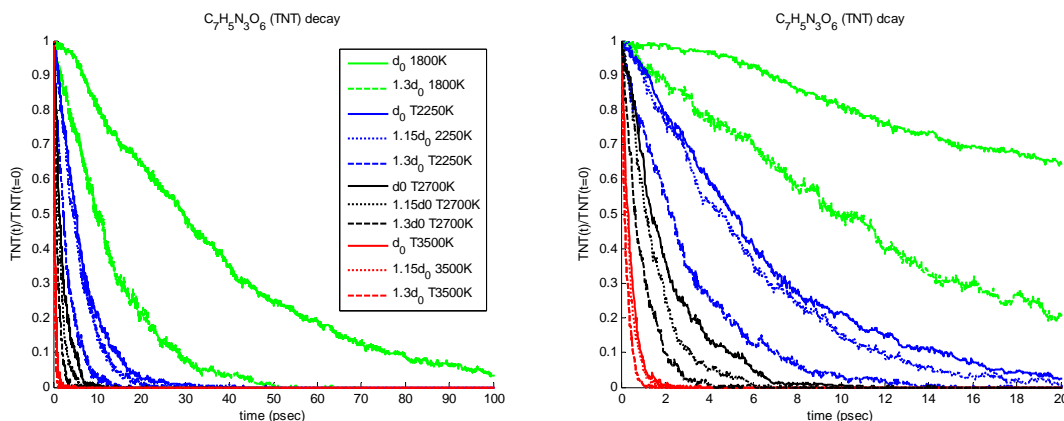


FIG. 7: TNT decay vs. simulation time for various densities and.

3.2 Pressure and potential energy evolution

The time evolution of the total pressure and potential energy as a function of density (see Table 1) is presented in FIG. 8 and FIG. 9. Generally, the pressure increases with temperature and compression. In all cases, the pressure profiles reach an asymptotic limit, but with low (0 and

15%) compression the pressure increases toward the asymptotic value, whereas it decreases as it approach the asymptotic value with 30% compression. This different trend can be explained, as will be demonstrated below in Section 4, by the following reasoning: At low compression, the decomposition of TNT results in the production of large amount of gaseous products. However, at high compression, large clusters are formed, slowing down the gaseous products formation, resulting in a lower pressure.

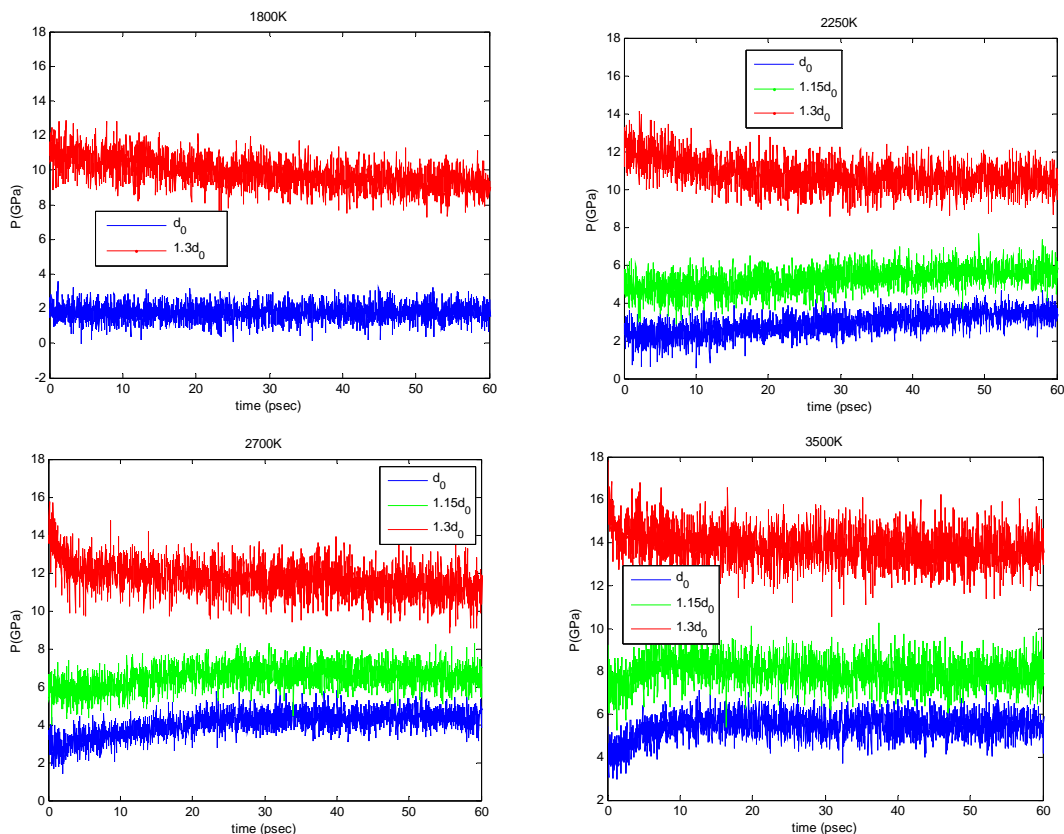


FIG. 8: Pressure as a function of time for various temperatures and compressions.

The variation of the system PE during the decomposition process is presented in FIG. 9. Although the simulations are carried out at a constant temperature (and kinetic energy), energy is consumed and released during the simulation due to chemical bond rupture and formation. The calculated PE profile can be divided into two parts: A short increasing part, which is related to the endothermic initial decomposition step, and a decreasing part, related to the exothermic reactions that take place following the initial part.

The influence of compression on the PE profile is demonstrated in FIG. 9. For all temperature values examined, the asymptotic potential energy value reduces as the compression increases. This means that the final products are more stable at high compressions. This result can be explained by a more effective and complete decomposition of liquid TNT at these high pressures. A second observation is that the energy released (calculated as the difference between the asymptotic value of PE and the barrier energy) is larger at high compressions. In addition, at each temperature shown in FIG. 9, the PE reaches its maximal and asymptotic values faster as compression increases. This is in agreement with the liquid TNT decay rate increase as compression rises (see FIG. 7). The temperature dependence of the PE is presented in FIG. 10 for 30% compression. It is clear that the completion of the liquid TNT decomposition is faster at

higher temperatures. The energy release in the exothermic part of the PE is similar at all temperatures studied, with only $\sim 2\%$ variation between the lowest and highest temperatures.

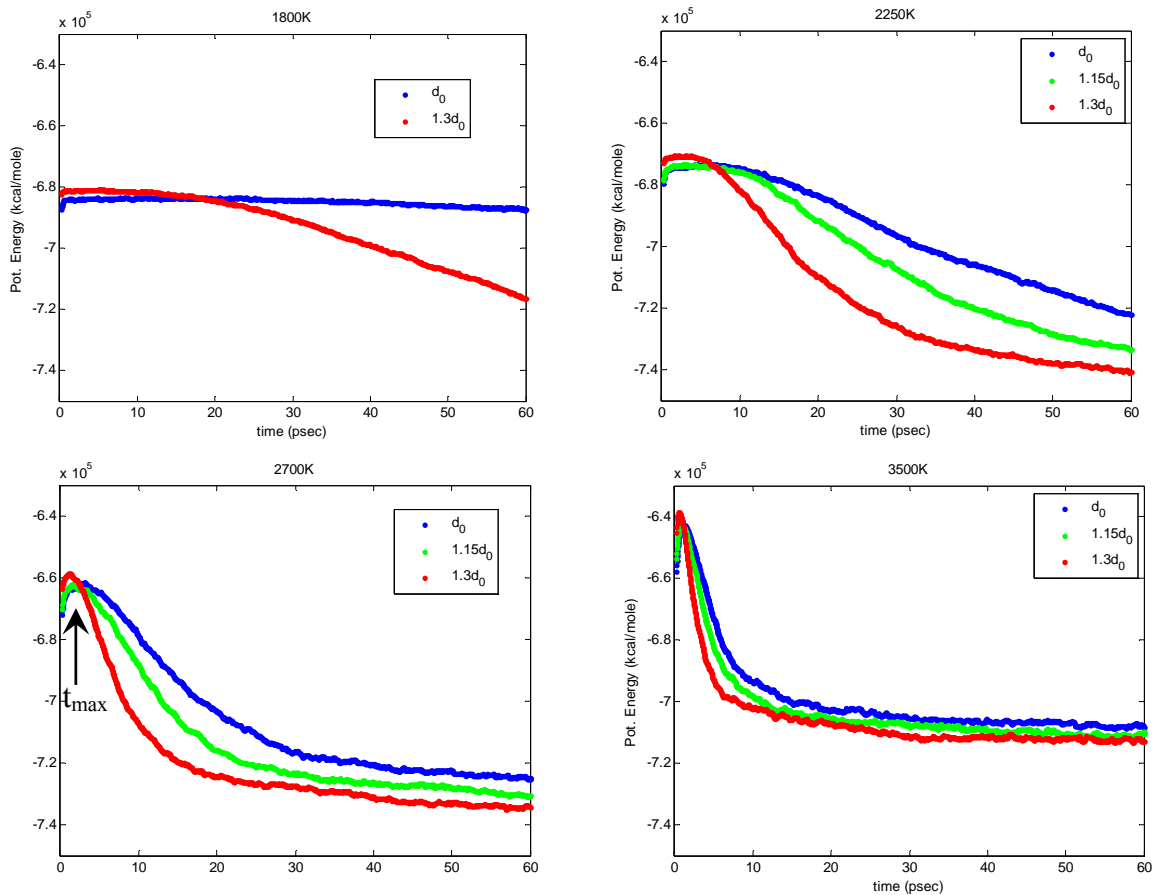


FIG. 9: Potential energy vs. simulation time for various densities, plotted separately per constant temperature simulation (1800-3500K). t_{max} is the PE maximum, separating between the endothermic and exothermic stages in the decomposition reaction of liquid TNT. Energy units are kcal/mole, where “mole” here refers to a mole of simulation cells¹.

¹ In order to change energy units to kcal/mole of TNT molecules, the values in the plots should be divided by 288 (number of molecules/cell).

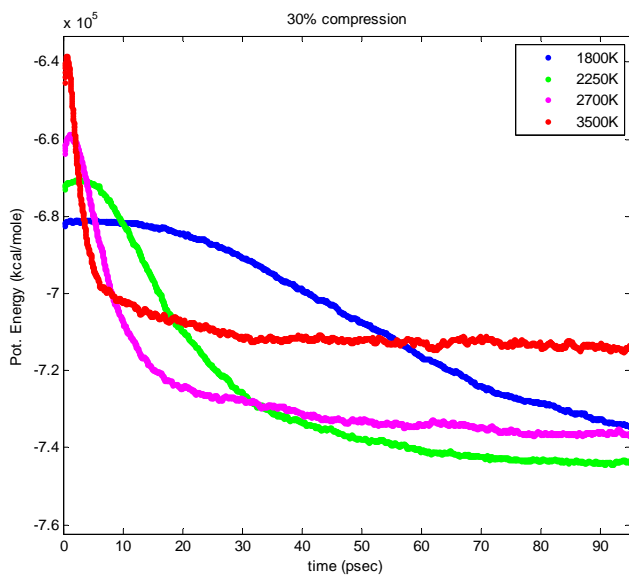


FIG. 10: PE at 30% compression for various temperatures.

3.3 Decomposition reactions rate constants: k_1 and k_2

Rate constants for the initial (k_1) and intermediate (k_2) decomposition stages were calculated by the procedure described in [6]. The first step in the analysis is finding t_{\max} , the time when the maximum value of PE is reached (see FIG. 9). k_1 is obtained by fitting an exponential decay function to the TNT decay curve in the range $[t_0, t_{\max}]$, where t_0 is the time when decomposition begins (note that t_0 does not necessarily resemble the time when the fast heating ends). The value of k_2 is obtained by fitting an exponential decay function to the PE decay in the range $[t_{\max}, t_{\text{end}}]$, where t_{end} denotes the time when all the TNT molecules decomposed. As seen in FIG. 11, t_{\max} decreases with increased compression and temperature, in correlation with the increase of the reaction rate.

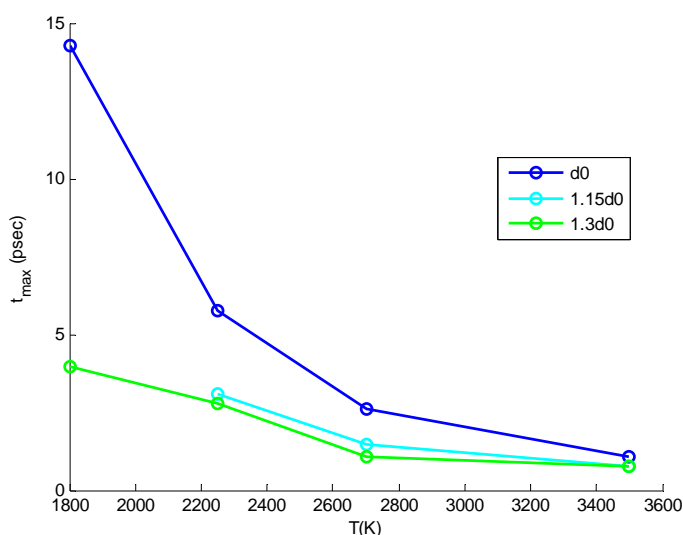


FIG. 11: PE maximum time vs. temperature for various densities. At the lower temperatures PE has a flat top (see FIG. 9) and the accuracy of t_{\max} is reduced.

Arrhenius plots of the rate constants for the initial and intermediate decomposition stages of liquid TNT are shown in FIG. 12. The Arrhenius parameters for k_1 and k_2 are summarized in Table 2 and Table 3, respectively. Both reaction rates increase for higher values of temperature and compression, at the studied ranges. However, it is seen that the activation energy (E_{a1}) of the initial decomposition stage is similar for ambient density and 15% compression cases (the latter is higher by only $\sim 4\%$), while for 30% compression E_{a1} is lower by $\sim 10\%$. This non-monotonic behavior can be explained by an initial decomposition mechanism change that occurs when compression increases from lower compressions to 30%. This point will be further discussed in Section 3.4.

The activation energies obtained for the initial decomposition stage of liquid TNT, at all studied compressions, are lower from the lowest TNT molecule decomposition activation energy in the gas phase (~ 37.7 kcal/mole for the C-H alpha attack reaction [1]).

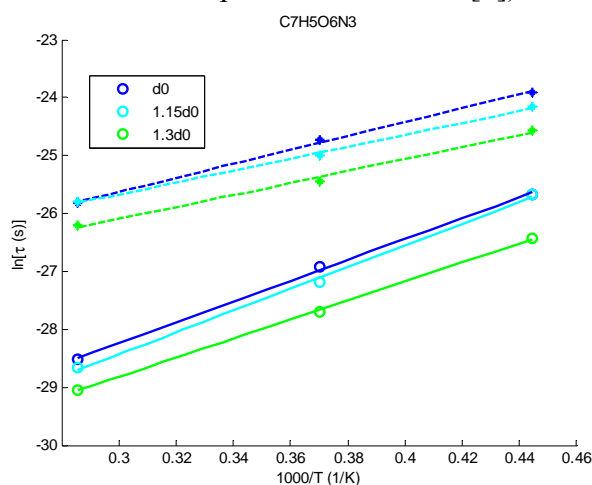


FIG. 12: Arrhenius plots (shown is reaction time, $\tau = 1/k$) for liquid TNT decomposition: (1) initial, endothermic stage (k_1 , full lines); (2) exothermic reactions stage (k_2 , dashed lines), for various densities, in the temperature range 2250K-3500K.

Table 2: Arrhenius parameters fitted to TNT exponential decay rates, $k_1[\rho, T]$, over $[t_0, t_{\max}]$ time interval for various initial compressions (see the corresponding densities in Table 1). Temperature range used: 2250K-3500K

Compression, V/V_0	$\ln(A_0[\text{sec}^{-1}])$	E_a [kcal/mole]
1	33.7	35.8
0.85	34.1	37.3
0.7	33.8	32.7

Table 3: Arrhenius parameters fitted to Potential Energy exponential decay rate, $k_2[\rho, T]$, over $[t_{\max}, t_{\text{end}}]$ time interval for various initial compressions. Temperature range used: 2250K-3500K.

Compression, V/V_0	$\ln(A_0[\text{sec}^{-1}])$	E_a [kcal/mole]
1	29.2	24.0
0.85	28.8	20.5
0.7	29.2	20.5

An effective overall first order decay rate of liquid TNT can be obtained by fitting an exponential decay function to the whole range of TNT decomposition $[t_0, t_{\text{end}}]$. The Arrhenius plot is shown in FIG. 13, compared to the TNT decay rate fitted in the range $[t_0, t_{\text{max}}]$. The Arrhenius parameters for this effective decay rate are presented in Table 4. The effective decay rate is *higher* than the one obtained with the endothermic-stage-only, in all compressions, as can be expected when additional reactions contribute and speed up the TNT decay. In addition, the non-monotonic activation energy change with compression seen in the endothermic-stage-only case (Table 2) is absent in the effective first order decay rate constant (Table 4). This can be understood as the latter is less sensitive to a possible mechanism change in the initial decomposition stage, or to a non-monotonic reactant decay curve. In the case of liquid NM [6], the activation energy calculated in the range $[t_0, t_{\text{max}}]$ was higher by up to 12% from the one calculated between $[t_0, t_{\text{end}}]$ for densities above 30% compression. This is related to a change in the *initial* decomposition mechanism of NM decay when compression increases, which is averaged out when the exponential function fit to the reactant decay is done over the whole decomposition period.

Table 4: Arrhenius parameters fitted to TNT exponential decay rates, $k_1[\rho, T]$, over the region $[t_0, t_{\text{end}}]$ for various initial compressions. Temperatures range: 2250K-3500K.

Compression, V/V_0	$\ln(A_0[\text{sec}^{-1}])$	Ea [kcal/mole]
1	33.4	34.0
0.85	33.5	33.7
0.7	33.6	31.4

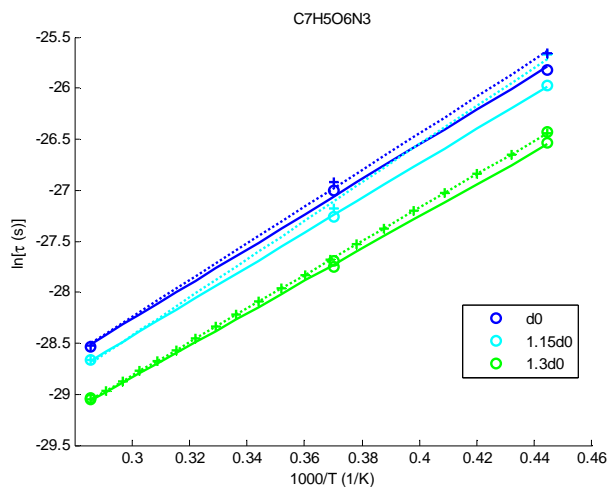


FIG. 13: Arrhenius plots (shown is reaction time, $\tau = 1/k$) for liquid TNT initial decomposition (k_I) for two cases: exponential fit is carried out in the region $[t_0, t_{\text{max}}]$ (dotted lines, +) and $[t_0, t_{\text{end}}]$ (full lines, o), for various densities in the temperature range 2250K-3500K.

An estimate of the temperatures for which liquid TNT decomposition rates are in the vicinity of $k_I=1\text{Hz}$ ($\tau=1\text{sec}$) is made by interpolating the Arrhenius plot (FIG. 12). The temperatures obtained are 530K, 550K and 490K for 0, 15% and 30% compressions, respectively. This implies that when confined TNT is heated to temperatures above $\sim 500\text{K}$ (where TNT is a liquid) it starts to decompose within a time scale of approximately 1 sec. Similarly, for $k_I=0.001\text{Hz}$ the

corresponding interpolated reaction temperatures are 675K, 690K, 615K for 0, 15% and 30% compressions.

3.4 Fragments analysis: Initial and intermediate reactions

The fragments formed in the heat up simulations of liquid TNT were obtained using the fragments analysis code supplied in LAMMPS [2]. The fragments are identified according to the bond order calculated for each pair of atoms with ReaxFF potentials, and the bond order cutoff used in BondFrag (see Supplementary Materials).

The stable products and soot that are produced at later stages of the simulation are analyzed separately in Section 4.

The *initial* fragments formed are presented for ambient density and 30% compression at various temperatures in FIG. 14 - FIG. 19. Only the fragments that reach > 2% of the initial amount of TNT molecules (288) during the simulations are shown. Several observations that can be deduced from the plots are:

- **At T=1800K**, the initial decomposition step involves *TNT-dimer* ($C_{14}H_{10}O_{12}N_6$) creation followed by its instant decomposition, producing the fragments NO_2 , $C_7H_5O_5N_3$ and $C_7H_5O_5N_2$ (see the initial fragmentation in FIG. 14). The amount of these fragments is similar for some period, indicating that they are formed concurrently, via the dimer decomposition reaction. The amount of dimers is very low, which means that its stability is low at 1800K. Note that the length of the correlation between the fragments creation depends on the density: At ambient density this decomposition route lasts for ~ 25 psec (FIG. 14, l.h.s.), whereas with 30% compression the correlation is interrupted after ~ 2.5 psec (FIG. 14, r.h.s.). The correlation ends when other reactions initiate, interfere and compete with this initial reaction path. In FIG. 15, additional initial fragments are shown (TNT derivatives and NO). At the higher compressions, the fragments variety and amount increase.
- **At ambient density and temperature > 1800K**: The initial reaction is a unimolecular decomposition of a TNT molecule via C-N bond scission (see FIG. 16 and FIG. 17, green and cyan colored lines). After some delay, the TNT-dimer ($C_{14}H_{10}O_{12}N_6$) is formed and decomposes, via the route described above, to the fragments NO_2 , $C_7H_5O_5N_3$ and $C_7H_5O_5N_2$ (see FIG. 16 and FIG. 17, green red and black colored lines).
- **At 30% compression:**
 - **3500K > T > 1800K**: Initially the TNT-dimer is formed (see FIG. 16). Then, it decomposes to various TNT and TNT-dimer derivatives and smaller fragments. The major small molecular fragments formed at this stage are NO_2 (of which only a small part is created by a unimolecular C-N bond break in a TNT molecule) and NO, and the dominant TNT derivative is $C_7H_5O_5N_3$. As temperature increases, the variety of derivatives increases.
 - **At T \sim 3500K**: The unimolecular decomposition via C-N bond scission becomes energetically favored at this high temperature and density, and begins the decomposition process of liquid TNT under these conditions. It is closely followed by the dimer creation and decomposition reactions as well as other TNT derivatives formation.

As described in Section 3.3, the activation energies for the initial decomposition stage of liquid TNT demonstrate a non monotonic behavior when compression increases beyond 15% (see Table 2). The fragments analysis discussed above supports this behavior for $T \geq 2250K$: The

initial decomposition reaction of ambient and moderate densities liquid TNT ($\leq 15\%$ compression; fragments for this case are not shown) is the *unimolecular C-N bond scission*, whereas for high compressions ($\geq 30\%$), below 3500K, the *decomposition begins with TNT dimer formation* and decomposition, accompanied by NO_2 release. Apparently, the activation energy for the latter initial decomposition process is lower by $\sim 10\%$.

Comparing the behavior of liquid and gas TNT, it is seen that the unimolecular NO_2 scission is a common initial decomposition mechanism for both gas phase and liquid TNT at lower compressions ($\leq 15\%$) and $T > 1800\text{K}$. However, at lower temperatures the initial decomposition processes in the gas phase is the C-H alpha attack [1], whereas for liquid TNT the dimer formation and decomposition is favored (at all compressions studied). In addition, in contrast to the gas phase and low density liquid TNT initial reactions, the initial decomposition path of 30% compressed liquid TNT in the range $3500\text{K} > T > 1800\text{K}$ is dimer formation and decomposition.

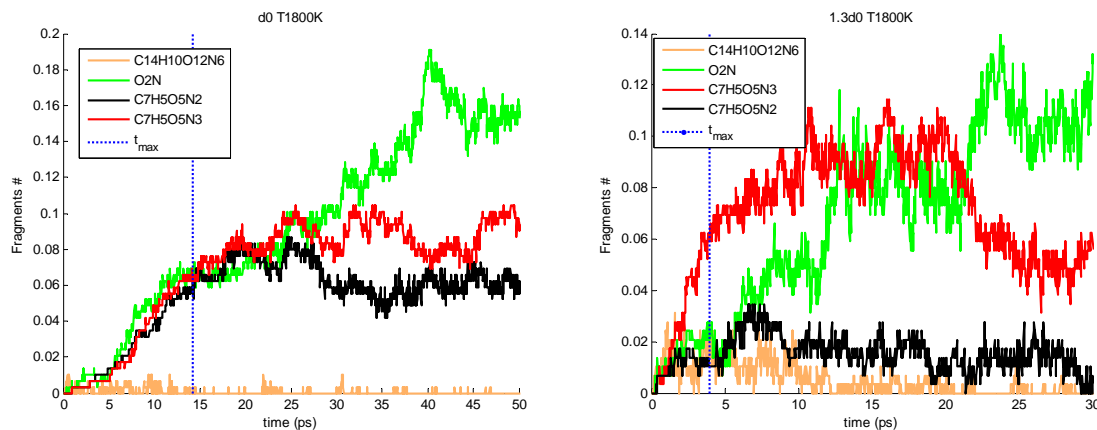


FIG. 14: A comparison between the initial fragments created at ambient density and 30% compression at 1800K.

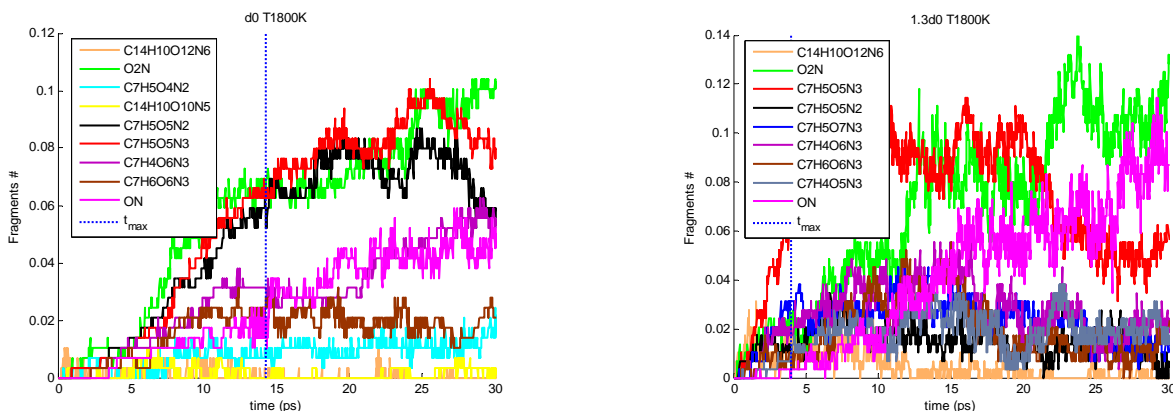


FIG. 15: Additional fragments at 1800K for ambient density (left) and 30% compression (right).

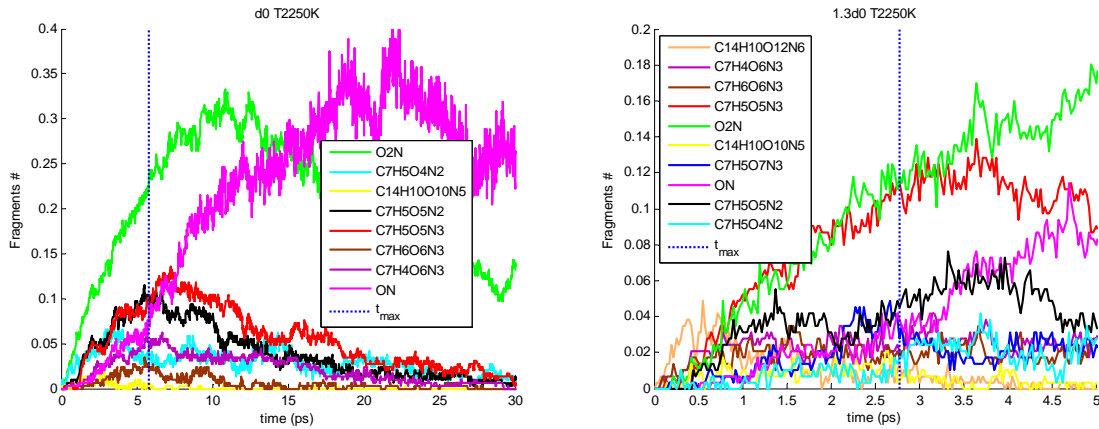


FIG. 16: A comparison between the initial fragments created at ambient density and 30% compression at 2250K.

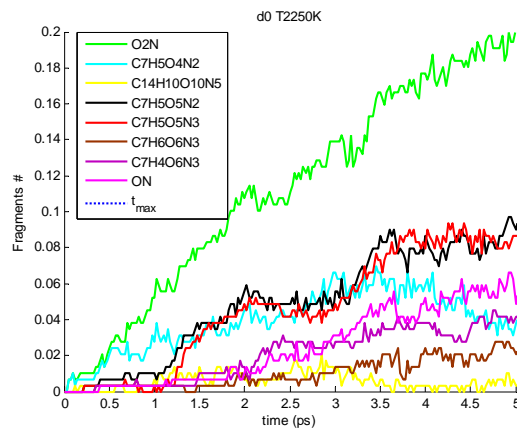


FIG. 17: Blow up of FIG. 16 for ambient density liquid TNT at 2250K, focusing on the initial decomposition reactions: 1. Unimolecular NO_2 release; 2. TNT dimer decomposition, producing $\text{C}_7\text{H}_5\text{O}_5\text{N}_2$, $\text{C}_7\text{H}_5\text{O}_5\text{N}_3$ and NO_2 .

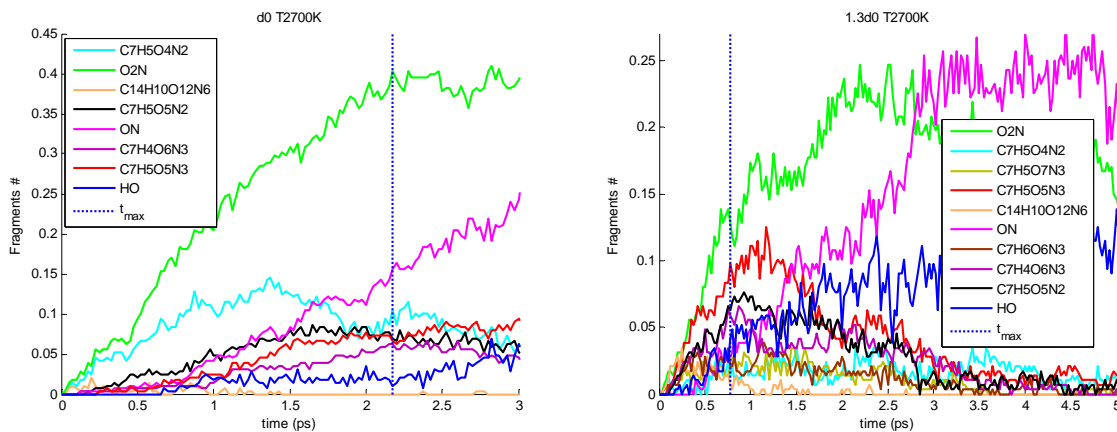


FIG. 18: A comparison between the initial fragments created at ambient density and 30% compression at 2700K.

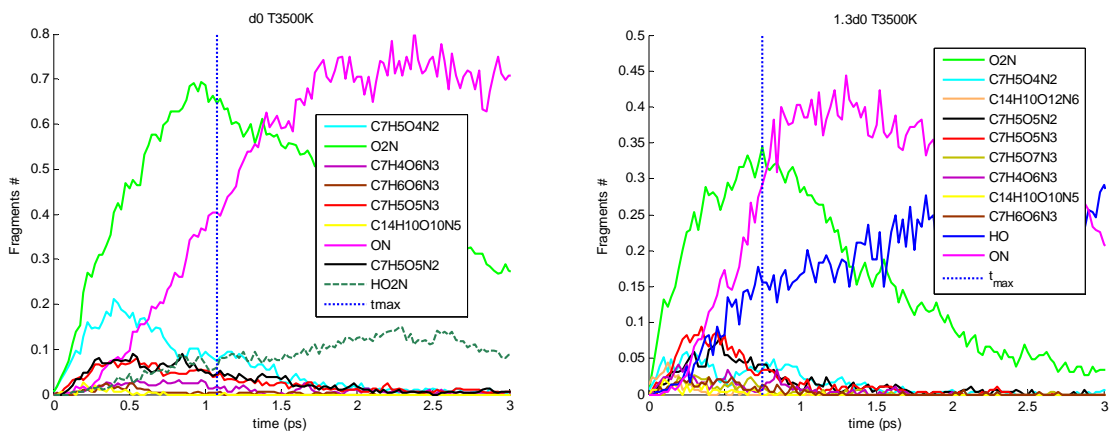


FIG. 19: A comparison between the initial fragments created at ambient density and 30% compression at 3500K.

In FIG. 20 the production of NO_2 and NO is shown for ambient density (left) and for 30% compression (right) at the various temperatures. At all conditions, first NO_2 is formed, thereafter NO . It can be seen that temperature speeds up these small fragments formation, while compression suppresses it. This tendency is in agreement with the enhanced clustering that takes place at high densities, along with reduction in gaseous fragments production, as will be shown in the clusters analysis in Section 4.

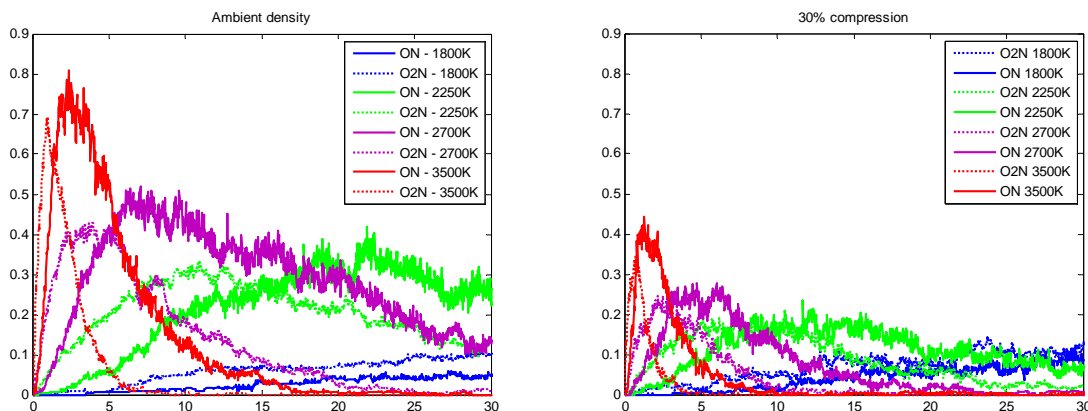


FIG. 20: NO and NO_2 formation at ambient density (left) and 30% compression, at various temperatures.

3.5 Final products analysis: Formation and asymptotic amounts

The main final gaseous products obtained in the thermal decomposition of liquid TNT are: N_2 , H_2 , H_2O , CO_2 , CO , NH_3 and OH . In

Table 5 these fragments asymptotic amounts are given at 3500K. These products evolution with time is shown in FIG. 21 at various temperatures and densities.

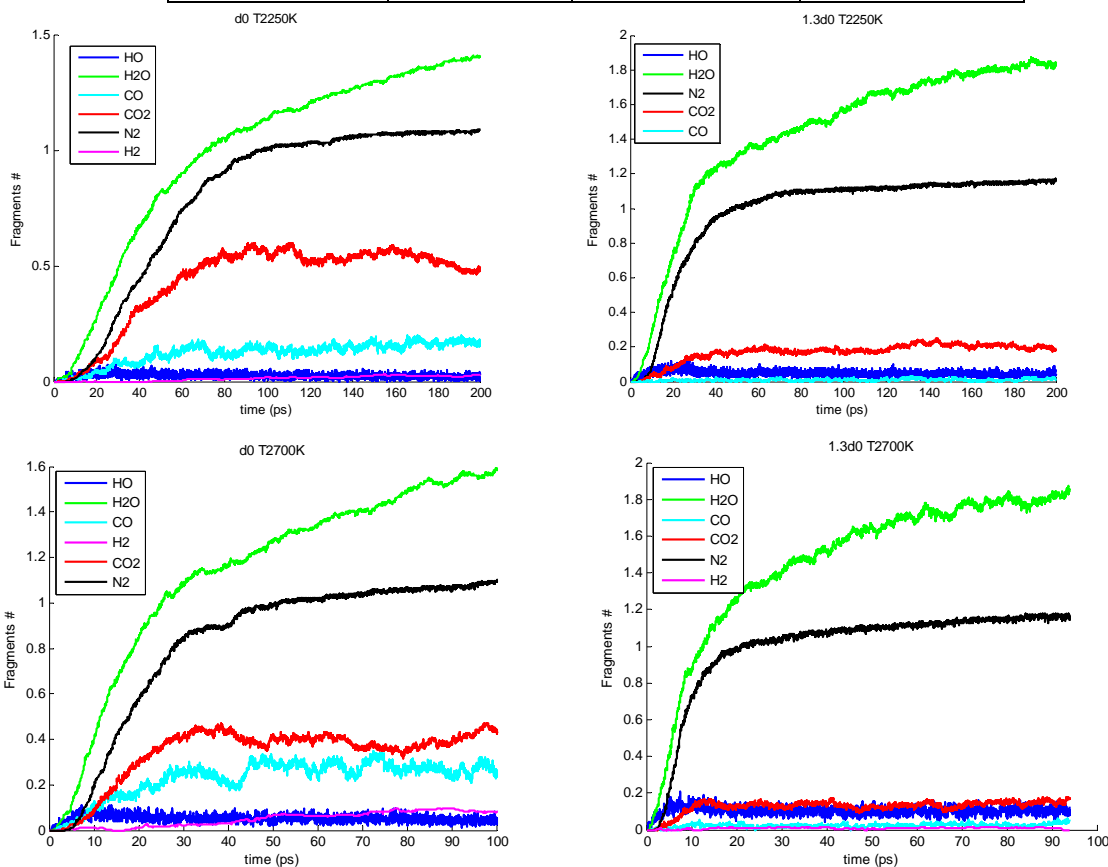
The final amounts of H_2O and N_2 are not very sensitive to the liquid compression (see FIG. 22). On the other hand, the amount of CO_2 and CO reduces with increasing hydrostatic pressure, due to the density-enhanced carbon-clustering (see Section 4). The temperature increase improves the OH and CO production.

The asymptotic amount of the stable gaseous products at various densities, at 3500K, is presented in FIG. 22, in comparison to measured values [15]. A good agreement is obtained for

N_2 and H_2O . The amount of carbon containing gases (CO and CO_2) differs from the measured values (which are higher than the calculated ones), and so do H_2 , NH_3 and OH . This difference is related to the production of soot during the liquid TNT decomposition and the accuracy of this process description by the ReaxFF potentials. The clusters formation directly influences the amount of carbon-containing gases produced, and also the amount of hydrogen-containing gases, as the later depend on the trapping (or caging) of hydrogen atoms within the clusters.

Table 5: Final gaseous products asymptotic amounts, at 3500K and various densities. The values are normalized with respect to the initial amount of TNT molecules.

Fragment	Ambient density	15% compression	30% compression
OH	0.13	0.18	0.27
H_2	0.19	0.07	0.03
H_2O	1.57	1.72	1.66
CO	0.55	0.29	0.09
N_2	1.21	1.27	1.25
CO_2	0.27	0.23	0.15
NH_3	-	-	0.04



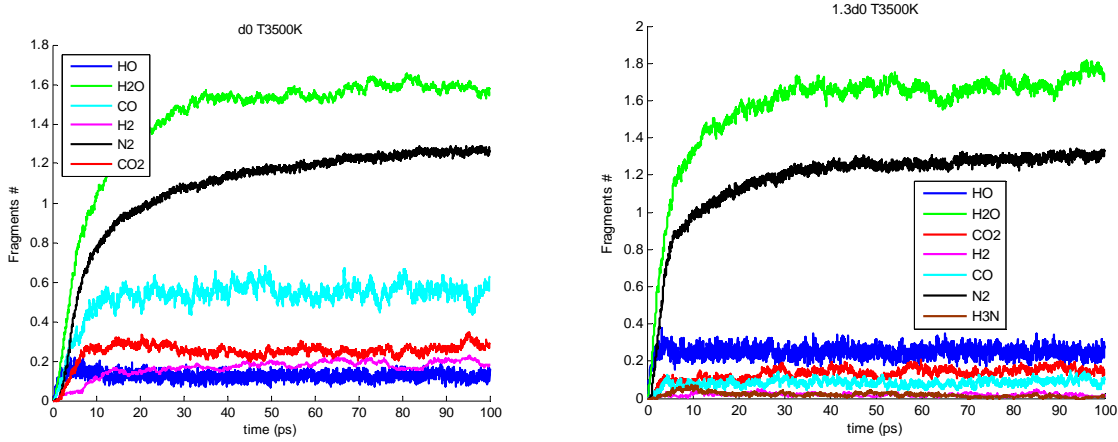


FIG. 21: Final gaseous products creation (solid lines) at various temperatures, for ambient density and 30% compression.

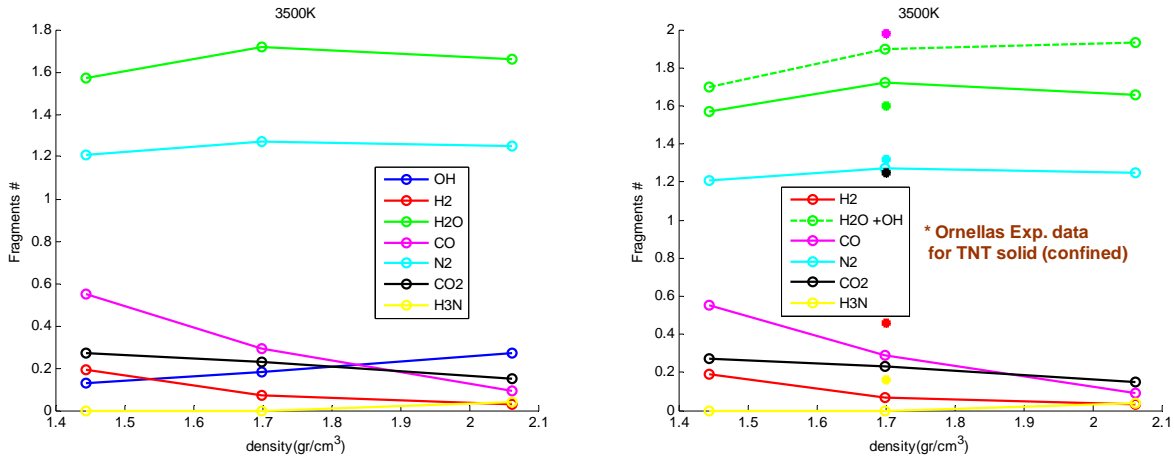


FIG. 22: Final gaseous products amount as a function of density, for liquid TNT decomposition (left). Also shown are (right) the measured fragments amounts (stars) from confined experiments [15].

4 RESULTS: SOOT FORMATION

Carbon clusters formation under pressure in general, and during detonation of high explosives in particular, has been the topic of several theoretical and experimental studies in the past years [8, 16-22]. This soot formation is important as it may have a significant effect on the detonation performance of different explosives, especially ones with negative oxygen balance [8]. Despite the interest, the microscopic details of carbon clustering are yet to be resolved. To the best of our knowledge, this is the first microscopic study of the carbon coagulation process in a hot dense liquid explosive.

In order to study the time dependent clustering in liquid TNT, the time evolution of the average molecular weight (AMW) of clusters with a number of carbon atoms (C) above a minimal value n ($C \geq n$) is analyzed. The AMW is defined as follows:

$$AMW(t; n) = \frac{1}{N_0} \frac{\sum_{i \in C \geq n} MW_i N_i(t)}{\sum_{i \in C \geq n} N_i(t)}$$

Where N_0 is the initial number of TNT molecules in the simulation cell (288), MW_i is the molecular weight of fragment i and $N_i(t)$ is the number of fragments of type i at a given time, t .

The temporal dependence of the AMW during the simulation at 2250K is shown in FIG. 23, for the cases $C \geq 0$, $C \geq 7$, $C \geq 14$ and $C \geq 21$, and two densities (ambient and 30% compression). In all plots below, the AMW is normalized to the weight of a single TNT molecule. The $C \geq 0$ case corresponds to averaging the MW of all carbon-containing fragments in the simulation cell, at each time step. The AMW for $C \geq 7$, $C \geq 14$ and $C \geq 21$ is calculated by averaging over the MW of fragments with at least 7, 14, and 21 carbon atoms (corresponding to TNT molecules and their derivatives, TNT dimers and their derivatives, and trimers and their derivatives, accordingly). Each type of AMWs provides both unique and complementary information:

- The AMW of *all* carbon-containing fragments ($C \geq 0$) in the simulation cell decreases as a function of time, due to the formation of many small carbon containing products (see Section 3.4).
- The time dependence of the AMW of all fragments with $C \geq 7$ initially decreases, due to the detachment of small fragments (e.g., NO_2 and OH) from the original TNT molecules. Thereafter (at ~ 10 ps, in the case shown in FIG. 23 at ambient density), the AMW starts to increase, due to initiation of carbon clustering. This process is density/pressure and temperature dependent, as shown below.
- For AMW with larger clusters ($C \geq 14$, $C \geq 21$) it is seen that they are starting to form at some time, $t_{\text{form}} > 0$, and they continue to grow as the simulation progresses. As can be expected, t_{form} is shorter as the minimal cluster size in the AMW calculation is smaller. Once they are formed, the clusters grow in a similar fashion regardless of their size.

It appears that the clusters grow in a step-wise fashion (see in FIG. 23 the dashed lines marking the steps in AMW for $C \geq 14$ at ambient density). At each step, the clusters grow by approximately a single TNT molecule. This observation will serve as the basis for the kinetic model presented in the following section.

FIG. 23 also shows (r.h.s.) the time evolution of the AMW for 30% compression. A detailed analysis of the pressure influence on the carbon clustering is discussed in Section 4.2. A few observations can be made here: Until ~ 20 psec, the temporal change of AMW is similar to the ambient density case for $C \geq 0$, $C \geq 7$, $C \geq 14$, and $C \geq 21$ (see enlarged plot in FIG. 24). However, unlike the ambient density results, at 30% compression the AMW for $C \geq 7$, $C \geq 14$, and $C \geq 21$ begins to oscillate after clustering begins. In addition, the AMW for $C \geq 0$ and 30% compression shows a non monotonic decay starting at ~ 20 psec as well (see insert plot in FIG. 24). The oscillations are caused by the instability of the large clusters formed, which can be an artifact of the numerical fragments analysis algorithm (not using time-window to average over unstable fragments).

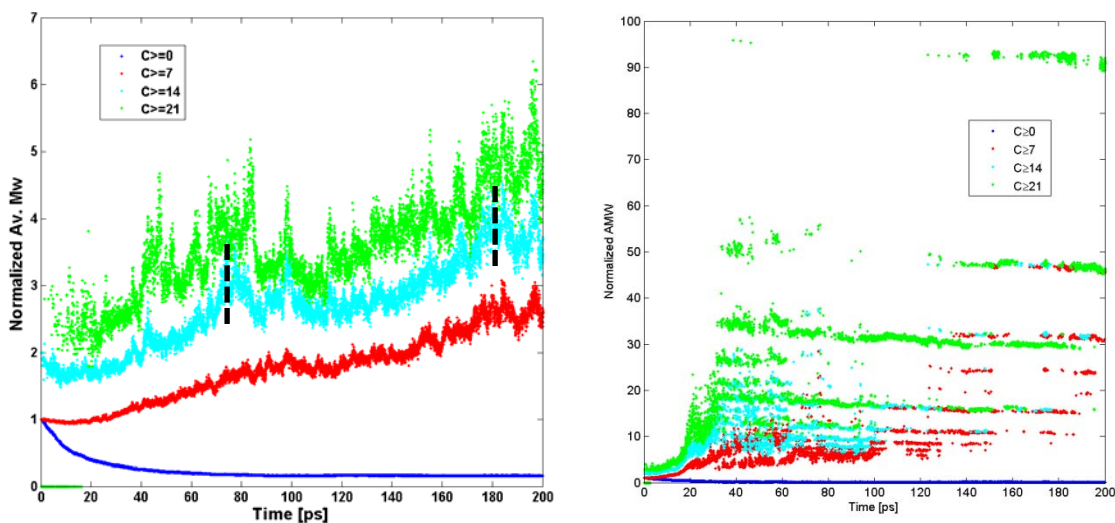


FIG. 23: Average molecular weight (AMW) as a function of time, for fragments with at least C carbon atoms, where $C \geq 0$, $C \geq 7$, $C \geq 14$ and $C \geq 21$. The liquid TNT simulations were done at 2250K for ambient density (l.h.s.) and for 30% compression (r.h.s.).

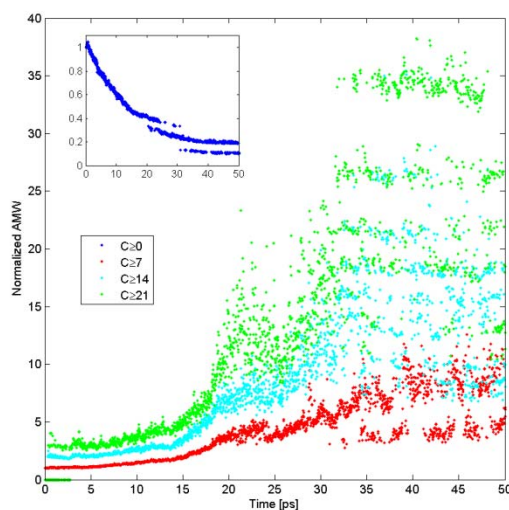


FIG. 24: A blow up of FIG. 23 for 30% compression at 2250K, emphasizing the initial steps of liquid TNT decomposition and clustering. The inner panel shows results for $C \geq 0$ on a different scale, for clarity.

In order to have a complete understanding of carbon clustering it is important to analyze the effect of pressure and temperature on the clusters' growth. It is possible that different pressure and temperature conditions accelerate or decelerate the clustering, or might even result in different mechanisms governing the overall clustering process.

4.1 Temperature effect on clustering

FIG. 25 (l.h.s.) shows the effect of temperature on the AMW at ambient density, for the $C \geq 0$ and $C \geq 7$ cases. In the former, it is seen that the temperature accelerates the decay in the overall AMW, as expected. For the $C \geq 7$ case, the following is observed:

- Initially the AMW decays faster and to smaller values as temperature increases. This can be explained by the fact that as temperature increases, more TNT molecules have enough kinetic energy to overcome the decomposition barrier.
- At later times, it is seen that temperature increase speeds up the clusters formation. In addition, larger clusters are formed at a given time as temperature increases.

This temperature dependence can be understood by the increased mobility of the clusters at high temperatures, which allows them to diffuse and react faster.

The above temperature effect on clustering is observed at higher densities as well, as can be seen in FIG. 25 (r.h.s.) for the 30% compression case and $C \geq 7$. However, the initial decay of the AMW for $C \geq 7$, due to the decomposition of TNT molecules to smaller gaseous fragments, is almost negligible, even at the higher temperatures (see FIG. 26). This suggests that compression suppresses the detachment of small fragments, while clustering becomes favorable. The increased cluster formation is also seen for $C \geq 14$ and $C \geq 21$ (not shown). As explained above, the oscillations that appear in the decay of the AMW for $C \geq 0$ at 30% compression originate from the numerical instability of the clusters formed at that stage.

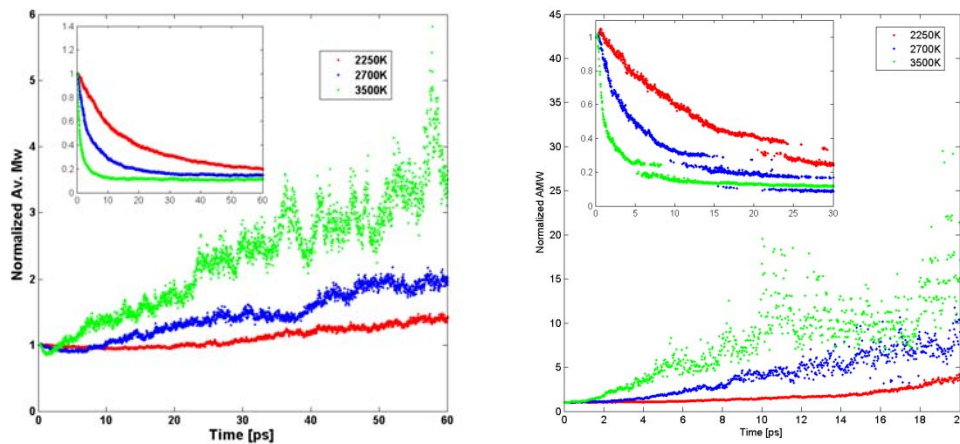


FIG. 25: AMW as a function of time at ambient density (l.h.s.) and 30% compression (r.h.s.) at 2250K, 2700K and 3500K. The results in the main and internal panels are for $C \geq 7$ and $C \geq 0$, respectively.

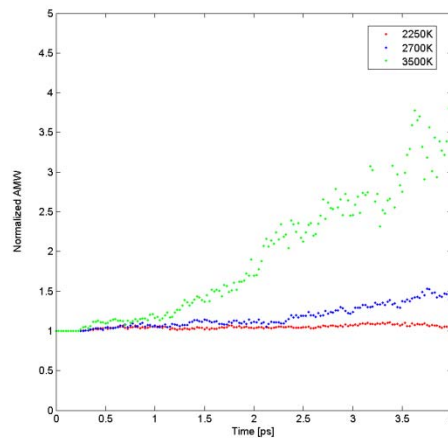


FIG. 26: A blow up of FIG. 25 for 30% compression in the vicinity of the initial decay for $C \geq 7$.

4.2 Pressure effect on clustering

The AMW dependence on compression ($C \geq 0$ and $C \geq 7$) is plotted in FIG. 27 for 2250K (l.h.s.) and 3500K (r.h.s.).

For $C \geq 0$ (inner panels) at both temperatures (2250K, 3500K) it is seen that the AMW reduces monotonically with time for the lower densities (ambient density and 15% compression). However, for 30% compression a non-monotonic behavior is observed. The later behavior is correlated with the instability of clusters discussed above. It seems that the influence of compression on the decay is not significant in the case of $C \geq 0$. This density dependence differs from the one seen in Section 3.1 for the liquid TNT molecules decay (see FIG. 7), where the decay speeds up with compression.

At both temperatures and $C \geq 7$ the clustering is enhanced as density rises: The clusters are formed sooner and reach a higher AMW value, at any given time. As mentioned above, the initial AMW decay for $C \geq 7$ is suppressed when the density increases (see FIG. 28).

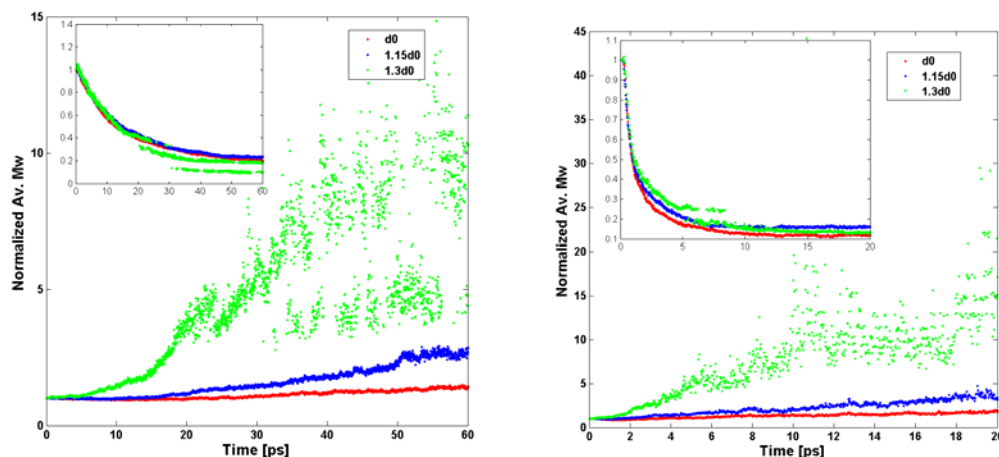


FIG. 27: AMW as a function of time at 2250K (l.h.s.) and 3500K (r.h.s.) for three compression ratios: ambient density, 15% and 30% compression. The results in the main and the internal panels are for $C \geq 7$ and $C \geq 0$, respectively.

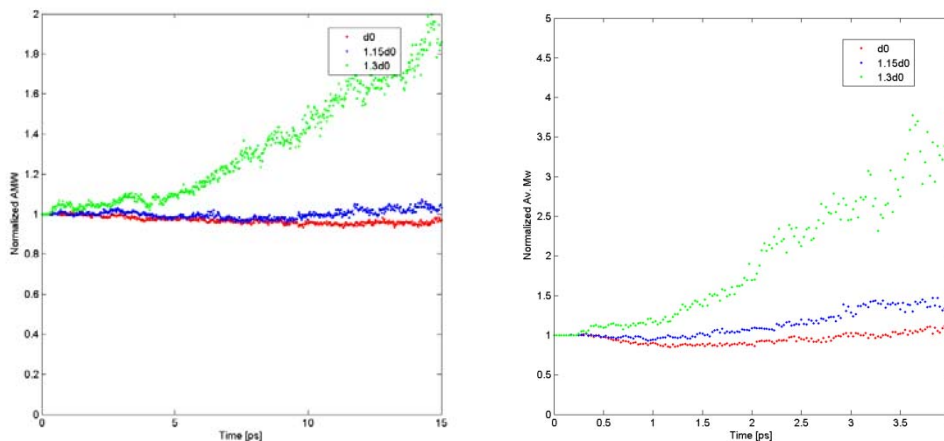
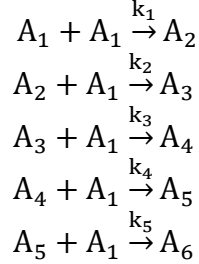


FIG. 28: A blow up of FIG. 27 showing the density dependence of the AMW with $C \geq 7$ in the vicinity of the initial decay, for 2250K (l.h.s.) and 3500K (r.h.s.).

4.3 Kinetic Analysis

A possible mechanism to describe the cluster growth shown in FIG. 23, during liquid TNT decomposition, is a step-wise mechanism, where the cluster size increases by approximately the MW of a single TNT molecule at each step. Such a linear growth model is applied below for the carbon clustering in hot liquid TNT decomposition. The model denotes the building block of the different clusters produced as A_1 , which is defined as all fragments with $6 \leq C \leq 8$ carbon atoms. Generally, A_i is defined as a fragment with $7i-1 \leq C \leq 7i+1$ carbon atoms, where $1 \leq i \leq 6$ (i is an integer). k_i is the rate constant for the reaction between A_i and A_1 , producing A_{i+1} . The kinetic model for the initial five clustering reactions is represented by the following equations:



The kinetic model suggested produces a set of differential equations that cannot be solved analytically. In order to fit this kinetic model to the liquid TNT simulations results, the following numerical scheme is used:

- An initial guess for the rate constants in the above clustering reactions is made.
- The set of five differential equations is numerically solved [14], producing the temporal variation of $A_i(t)$.
- A least-squares fitting to the MD simulation results is performed only for the three smallest clusters (A_1, A_2 and A_3), as for $i \geq 4$ $A_i \sim 0$ is obtained, and the clusters A_1, A_2 , and A_3 are insensitive to the values of A_4 - A_6 .

The quality of fitness of the model, R^2 , is evaluated by:

$$R^2 = 1 - \frac{\sum_{i,j} (N_i^m[t_j] - N_i^s[t_j])^2}{\sum_{i,j} (N_i^m[t_j] - \overline{N_i^s})^2}$$

Where $N_i^{m/s}[t_j]$ is the number of fragments A_i at time t_j , obtained from the kinetic model result (m) or the MD simulation (s). $\overline{N_i^s}$ is the time average of $N_i^s[t_j]$ for a given A_i .

In FIG. 29 and FIG. 30, the linear growth model results are compared to the simulations results for ambient density at 2250K and 3500K, and for 30% compression at 2250K, respectively. It is seen that in general there is a good agreement between the model and the simulation results for the clusters A_1 - A_3 . In particular, the agreement is very good at ambient density (at both temperatures shown in FIG. 29), and is reasonable for the higher compression, which may indicate that a more complex clustering mechanism takes place as density increases. This agreement shows that the carbon clustering reactions and kinetics in hot, dense liquid TNT can be fairly described by the simple linear cluster growth model suggested here.

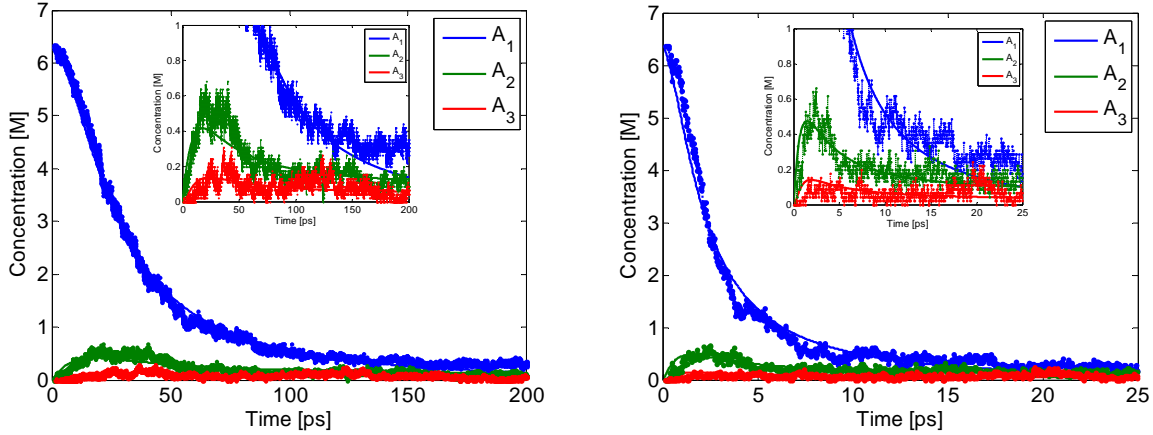


FIG. 29: The temporal evolution of clusters A_1 , A_2 , A_3 concentration (with $6 \leq C \leq 8$, $13 \leq C \leq 15$, $20 \leq C \leq 22$, respectively) at ambient density, in the MD simulation (dashed lines) and in the linear growth kinetic model (full lines). Two temperatures are shown: 2250K (l.h.s.) and 3500K (r.h.s.).

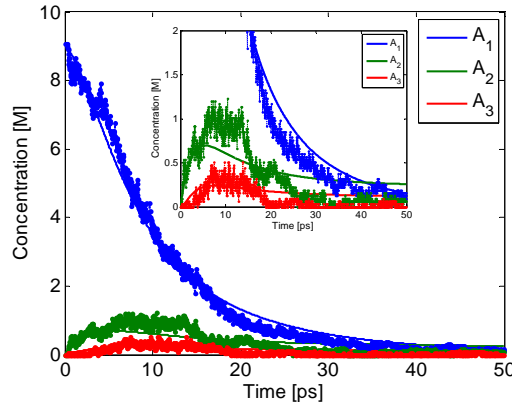


FIG. 30: As FIG. 29, for results at 2250K and 30% compression.

The rate constants k_1 - k_3 obtained for various temperatures and compressions are shown in Table 6. As expected, increasing the temperature and pressure speeds up the clusters formation rate.

Table 6: Rate constants and error estimates calculated with the linear growth kinetic model at various conditions.

T [K]	V/V_0	k_3 [$s^{-1}M^{-1}$]	k_2 [$s^{-1}M^{-1}$]	k_1 [$s^{-1}M^{-1}$]	R^2
2250	1	0.0507	0.0171	0.0017	0.99
2700	1	0.1571	0.0525	0.0049	0.99
3500	1	0.6925	0.2111	0.0246	0.98
2250	0.85	0.0517	0.0205	0.0023	0.98
2250	0.7	0.1109	0.0395	0.0047	0.98

5 CONCLUSIONS

The thermal decomposition of hot, dense liquid TNT was studied using ReaxFF-MD simulations with LAMMPS code. The process was analyzed starting from the initial, endothermic stage, through clusters formation, and reaching stable gaseous products.

A density dependence of the liquid TNT decomposition mechanism was observed:

- Initial reaction: The initial decomposition of ambient density liquid TNT begins with C-N bond scission (NO_2 release), whereas the dominant initial step of compressed liquid TNT is TNT dimer formation and decomposition to TNT derivatives.
- Clusters formation: Carbon clustering increases while the small gases production is suppressed when the pressure and density rise.

The density dependent initial decomposition path has an imprint on the density dependent activation energy. The latter is ~ 10 kcal/mole lower than the lowest gas phase unimolecular TNT decomposition activation energy.

The temperature also influences the reaction path: At low temperatures (1800K), the dimer formation and decomposition is the dominant initial decomposition path for all compressions studied. As temperature increases, the initial reaction path is determined by the liquid density, as described above. In addition, the temperature rise speeds up both the clustering reactions and the small fragments formation.

A linear growth kinetic model was suggested for the clustering process. The model was shown to be in a very good agreement with the simulation results at low compression, and in reasonable agreement for 30% compression and 3500K. At higher densities a more complex model may be required for describing the clustering in liquid TNT.

The stable gases production was calculated and compared with experimental data. A good agreement was obtained for N_2 and H_2O . The amount of carbon-containing gases (CO and CO_2) is under estimated in the simulations. The hydrogen-containing gases (H_2 and NH_3) are also lacking with respect to measurements, but to a lesser extent. This difference is attributed to the inaccurate description of the soot production process in the simulations, since the ReaxFF potentials were not trained for the clustering phenomena, yet.

6 REFERENCES

1. COHEN, R.; ZEIRI, Y.; WURZBERG, E.; KOSLOFF, R. *J. PHYS. CHEM. A* **2007**, *111*, 11074.
2. LAMMPS PACKAGE REFERENCE...
3. VAN DUIN, A. C. T.; DASGUPTA, S.; LORANT, F.; GODDARD, W.A. *J. PHYS. CHEM. A* **2001**, *105*, 9396.
4. VAN DUIN, A. C. T.; STRACHAN, A.; STEWMAN, S.; ZHANG, Q. S.; XU, X.; GODDARD, W. A. *J. PHYS. CHEM. A* **2003**, *107*, 3803.
5. SERGEY LG CORRECTION PAPER...
6. ROM, N; ZYBIN, S. V.; VAN DUIN, A. C. T.; GODDARD, W. A. III; ZEIRI, Y.; KATZ, G.; KOSLOFF, R. *J. PHYS. CHEM. A* **2011**, *115*, 10181.
7. TNT SOOT FORMATION PAPER (EXP)
8. ZHANG, L.; ZYBIN, S. V.; VAN DUIN, A. C. T.; DASGUPTA, S.; GODDARD, W. A.; KOBER, E. M. *J. PHYS. CHEM. A* **2009**, *113*, 10619.
9. CHEN, X. F.; LIU, J. F.; MENG, Z. H.; HAN, K. L. *THEOR CHEM ACC* **2010**, *127*, 327.
10. TNT UNITCELL DATA WAS OBTAINED FROM THE CAMBRIDGE CRYSTALLOGRAPHIC DATA CENTRE, FILE TNT.CIF, DATA_CSD_CIF_ZZZMUC01 (OBTAINED AT ROOM TEMPERATURES 283-303K): CARPER, W.R.; DAVIS, L.P.; EXTINE, M.W., *J. PHYS. CHEM.*, **1982**, *86*, 459.
11. LLNL EXPLOSIVES HANDBOOK – PROPERTIES OF CHEMICAL EXPLOSIVES AND EXPLOSIVE SIMULATIONS, P. 241, 8-33.
12. GARN, W.B., *J. CHEM. PHYS.*, **1959**, *30*, 819.
13. DAVIS, W. C., CRAIG, B. G., RAMSAY, J. B., *PHYS. OF FLUIDS*, **1965**, *8*, 2169.
14. MATLAB REFERENCE
15. ORNELLAS, D. L. *J. PHYS. CHEM.* **1968**, *72*, 2390.
16. VIECELLI, J. A. AND GLOSLI, J. N. S.L. : *J. CHEM. PHYS.*, **2002**, *117*, 11352.
17. *PHYS. CHEM. A*, **2009**, *112*, 10619.
18. CHEVROT, G. , SOLLIER, A. AND PINEAU, N. S.L. : *J. CHEM. PHYS.*, **2012**, *136*, 084506.
19. PINEAU, N. , SOULARD, L. , LOS, J.H. AND FASOLINO, A. S.L. : *J. CHEM. PHYS.*, **2008**, *129*, 024708.
20. LU, Y. , ZHU, Z. AND LIU Z. S.L. : *CARBON*, **2003**, *42*, 361.
21. MCENNIS, C. , DIKMELIK, Y. AND SPICER, J. B. S.L. : *APPLIED SURFACE SCIENCE*, **2007**, *254*, 557.
22. EMELIANOV, A. AND EREMIN, A. S.L. : *SHOCK WAVES*, **2010**, VOL. 20, P. 491.

7 SUPPORTING INFORMATION

7.1 *Cutoff.dic*

```
# Interesting name. This file contains
# the bond-order cut off for each
# pair of ReaxFF elements
C   N   0.3
C   C   0.55
C   O   0.65
C   H   0.4
O   O   0.65
N   O   0.40
O   H   0.4
H   H   0.55
H   N   0.55
N   N   0.55
```

7.2 *ReaxFF parameters*

Reactive MD-force field nitramines (RDX/HMX/TATB/PETN): Strachan, A.; et al. Phys. Rev. Lett. 2003, 91, 098301

```
39      ! Number of general parameters
50.0000 !Overcoordination parameter
9.4514  !Overcoordination parameter
30.0000 !Valency angle conjugation parameter
216.4305 !Triple bond stabilisation parameter
12.4838 !Triple bond stabilisation parameter
0.0000 !C2-correction
1.0701 !Undercoordination parameter
7.5000 !Triple bond stabilisation parameter
11.9083 !Undercoordination parameter
13.3822 !Undercoordination parameter
10.4637 !Triple bond stabilization energy
0.0000 !Lower Taper-radius
10.0000 !Upper Taper-radius
2.8793 !Not used
33.8667 !Valency undercoordination
3.5895 !Valency angle/lone pair parameter
1.0563 !Valency angle
2.0384 !Valency angle parameter
6.1431 !Not used
6.9290 !Double bond/angle parameter
0.0283 !Double bond/angle parameter: overcoord
0.0570 !Double bond/angle parameter: overcoord
-2.4837 !Not used
5.8374 !Torsion/BO parameter
10.0000 !Torsion overcoordination
1.8820 !Torsion overcoordination
-1.2327 !Conjugation 0 (not used)
2.1861 !Conjugation
1.5591 !vdWaals shielding
```

0.0100 !Cutoff for bond order (*100)
 5.2216 !Valency angle conjugation parameter
 3.4021 !Overcoordination parameter
 38.5241 !Overcoordination parameter
 2.1533 !Valency/lone pair parameter
 0.5000 !Not used
 20.0000 !Not used
 5.0000 !Molecular energy (not used)
 2.0000 !Version number
 6.5560 !Valency angle conjugation parameter
 4 !Nr of atoms; cov.r; valency;a.m;Rvdw;Evdw;gammaEEM;cov.r2;#
 alfa;gammavdW;valency;Eunder;Eover;chiEEM;etaEEM;n.u.
 cov.r3;Elp;Heat inc.;n.u.;n.u.;n.u.;n.u.
 ov/un;val1;n.u.;val3,vval4
 C 1.3742 4.0000 12.0000 1.9684 0.1723 0.8712 1.2385 4.0000
 9.4606 2.1346 4.0000 31.0823 79.5548 5.7254 6.9235 0.0000
 1.2104 0.0000 183.7012 5.7419 33.3951 11.9957 0.8563 0.0000
 -2.8983 2.5000 1.0564 4.0000 2.9663 0.0000 0.0000 0.0000
 0.0001 1.9255
 H 0.6867 1.0000 1.0080 1.3525 0.0616 0.8910 -0.1000 1.0000
 9.3858 5.0013 1.0000 0.0000 121.1250 3.8446 10.0839 1.0000
 -0.1000 0.0000 58.4228 3.8461 3.2540 1.0000 1.0698 0.0000
 -15.7683 2.1504 1.0338 1.0000 2.8793 0.0000 0.0000 0.0000
 0.0001 1.4430
 O 1.3142 2.0000 15.9990 1.9741 0.0880 0.8712 1.1139 6.0000
 10.2186 7.7719 4.0000 29.5271 116.0768 8.5000 7.1412 2.0000
 0.9909 14.9473 69.2812 9.1371 1.6258 0.1863 0.9745 0.0000
 -3.5965 2.5000 1.0493 4.0000 2.9225 0.0000 0.0000 0.0000
 623.8417 1.7500
 N 1.2450 3.0000 14.0000 1.9951 0.1088 1.0512 1.1911 5.0000
 9.9303 7.8431 4.0000 32.4758 100.0000 6.7768 6.8035 2.0000
 1.0636 0.1045 128.0119 2.1604 2.9464 2.5181 0.9745 0.0000
 -4.0959 2.0047 1.0183 4.0000 2.8793 0.0000 0.0000 0.0000
 1240.001 1.8300
 10 !Nr of bonds; Edis1;LPpen;n.u.;pbe1;pbo5;13corr;pbo6
 pbe2;pbo3;pbo4;Etrip;pbo1;pbo2;ovcorr
 1 1 141.9346 113.4487 67.6027 0.1554 -0.3045 1.0000 30.4515 0.4283
 0.0801 -0.2113 8.5395 1.0000 -0.0933 6.6967 1.0000 0.0000
 1 2 163.6889 0.0000 0.0000 -0.4525 0.0000 1.0000 6.0000 0.5921
 12.1053 1.0000 0.0000 1.0000 -0.0097 8.6351 0.0000 0.0000
 2 2 169.8421 0.0000 0.0000 -0.3591 0.0000 1.0000 6.0000 0.7503
 9.3119 1.0000 0.0000 1.0000 -0.0169 5.9406 0.0000 0.0000
 1 3 164.0476 117.4881 72.1261 -0.6031 -0.1795 1.0000 14.9755 0.5413
 1.2626 -0.3063 7.0000 1.0000 -0.1588 4.5000 0.0000 0.0000
 3 3 110.4748 155.6441 40.0000 0.1150 -0.1054 1.0000 28.5221 0.2000
 0.9590 -0.2635 8.5715 1.0000 -0.1007 6.8548 1.0000 0.0000
 1 4 130.7147 175.2276 97.2523 -0.0368 -0.4942 1.0000 26.7545 0.5133
 0.3296 -0.3653 7.0000 1.0000 -0.1171 5.1025 1.0000 0.0000
 3 4 85.4950 114.0081 70.1453 0.5778 -0.1070 1.0000 16.6611 0.2339
 0.3474 -0.1948 8.3762 1.0000 -0.1089 5.8148 1.0000 0.0000
 4 4 157.7518 67.1322 160.9732 -0.5869 -0.1824 1.0000 12.0000 0.7136
 0.8204 -0.1657 10.6490 1.0000 -0.0967 4.5976 1.0000 0.0000
 2 3 224.3076 0.0000 0.0000 -0.6280 0.0000 1.0000 6.0000 1.0000
 5.0050 1.0000 0.0000 1.0000 -0.0512 5.1982 0.0000 0.0000
 2 4 212.1772 0.0000 0.0000 -0.3585 0.0000 1.0000 6.0000 0.3316
 10.4316 1.0000 0.0000 1.0000 -0.0658 6.4545 0.0000 0.0000

```

6 ! Nr of off-diagonal terms; Ediss;Ro;gamma;rsigma;rpi;rpi2
1 2 0.0464 1.8296 10.1311 1.0029 -1.0000 -1.0000
2 3 0.0375 1.7275 10.8037 0.8813 -1.0000 -1.0000
2 4 0.0509 1.7672 10.4261 0.9990 -1.0000 -1.0000
1 3 0.1036 1.8869 9.5668 1.3590 1.1099 1.1534
1 4 0.1971 1.7356 10.0734 1.2754 1.2113 1.1172
3 4 0.0535 1.6709 10.8180 1.2968 1.1416 1.0167
42 ! Nr of angles;at1;at2;at3;Thetao,o;ka;kb;pv1;pv2
1 1 1 74.0317 32.2712 0.9501 0.0000 0.1780 10.5736 1.0400
1 1 2 70.6558 14.3658 5.3224 0.0000 0.0058 0.0000 1.0400
2 1 2 76.7339 14.4217 3.3631 0.0000 0.0127 0.0000 1.0400
1 2 2 0.0000 0.0000 6.0000 0.0000 0.0000 0.0000 1.0400
1 2 1 0.0000 3.4110 7.7350 0.0000 0.0000 0.0000 1.0400
2 2 2 0.0000 27.9213 5.8635 0.0000 0.0000 0.0000 1.0400
1 1 3 65.3104 6.3897 7.5000 0.0000 0.2000 10.0000 1.8525
3 1 3 71.9855 28.5708 6.4252 0.0000 0.2000 0.0000 1.8525
1 1 4 65.8892 45.0000 1.6598 0.0000 0.2000 10.0000 1.8525
3 1 4 73.1057 25.8227 4.2145 0.0000 0.2000 0.0000 1.8525
4 1 4 65.8759 40.9838 2.4369 0.0000 0.2000 0.0000 1.8525
2 1 3 56.3039 17.3681 5.3095 0.0000 0.9110 0.0000 1.0400
2 1 4 71.5505 11.1820 3.7129 0.0000 0.9110 0.0000 1.0400
1 2 4 0.0000 0.0019 6.3000 0.0000 0.0000 0.0000 1.0400
1 3 1 72.3642 37.8942 1.1566 0.0000 0.7472 0.0000 1.2639
1 3 3 90.0000 45.0000 0.5719 0.0000 0.7472 0.0000 1.2639
1 3 4 70.4313 14.4055 7.1593 0.0000 0.7472 0.0000 1.2639
3 3 3 83.8833 23.3345 2.3433 -10.0000 0.7472 0.0000 1.2639
3 3 4 84.0407 45.0000 1.0695 0.0000 0.7472 0.0000 1.2639
4 3 4 73.9966 24.4410 5.2760 0.0000 0.7472 0.0000 1.2639
1 3 2 89.1394 37.0874 0.3849 0.0000 3.0000 0.0000 1.2618
2 3 3 80.7068 5.0854 5.7151 0.0000 3.0000 0.0000 1.2618
2 3 4 76.0238 45.0000 0.8637 0.0000 3.0000 0.0000 1.2618
2 3 2 82.3474 13.5165 3.4896 0.0000 0.3596 0.0000 1.3307
1 4 1 68.4330 19.3525 2.1625 0.0000 1.7325 0.0000 1.0440
1 4 3 86.2893 37.5587 1.2660 0.0000 1.7325 0.0000 1.0440
1 4 4 74.2404 12.0547 7.5000 0.0000 1.7325 0.0000 1.0440
3 4 3 78.5566 43.8492 1.3351 -26.1471 1.7325 40.0000 1.0440
3 4 4 77.4239 33.7297 1.7944 -0.9193 1.7325 0.0000 1.0440
4 4 4 64.9107 17.5558 7.5000 0.0000 1.7325 0.0000 1.0440
1 4 2 90.0000 32.0540 0.7195 0.0000 0.5355 0.0000 2.5279
2 4 3 84.1185 45.0000 1.3826 0.0000 0.5355 0.0000 2.5279
2 4 4 78.7133 24.6250 3.8202 0.0000 0.5355 0.0000 2.5279
2 4 2 56.3036 14.1532 3.3914 0.0000 0.2000 0.0000 2.1689
1 2 3 0.0000 0.0019 6.0000 0.0000 0.0000 0.0000 1.0400
1 2 4 0.0000 0.0019 6.0000 0.0000 0.0000 0.0000 1.0400
1 2 5 0.0000 0.0019 6.0000 0.0000 0.0000 0.0000 1.0400
3 2 3 0.0000 0.0019 6.0000 0.0000 0.0000 0.0000 1.0400
3 2 4 0.0000 0.0019 6.0000 0.0000 0.0000 0.0000 1.0400
4 2 4 0.0000 0.0019 6.0000 0.0000 0.0000 0.0000 1.0400
2 2 3 0.0000 0.0019 6.0000 0.0000 0.0000 0.0000 1.0400
2 2 4 0.0000 0.0019 6.0000 0.0000 0.0000 0.0000 1.0400
17 ! Nr of torsions;at1;at2;at3;at4;;V1;V2;V3;V2(BO);vconj;n.u;n
1 1 1 1 0.0000 48.4194 0.3163 -8.6506 -1.7255 0.0000 0.0000
1 1 1 2 0.0000 63.3484 0.2210 -8.8401 -1.8081 0.0000 0.0000
2 1 1 2 0.0000 45.2741 0.4171 -6.9800 -1.2359 0.0000 0.0000
0 1 2 0 0.0000 0.0000 0.0000 0.0000 0.0000 0.0000 0.0000
0 2 2 0 0.0000 0.0000 0.0000 0.0000 0.0000 0.0000 0.0000

```

0	1	3	0	-0.0002	85.8794	0.3236	-3.8134	-2.0000	0.0000	0.0000
0	2	3	0	0.0000	0.1000	0.0200	-2.5415	0.0000	0.0000	0.0000
0	3	3	0	-0.9667	116.4743	0.0002	-4.9422	0.0000	0.0000	0.0000
0	1	4	0	-0.0069	150.0000	0.4891	-7.4921	-2.0000	0.0000	0.0000
0	2	4	0	0.0000	0.1000	0.0200	-2.5415	0.0000	0.0000	0.0000
0	3	4	0	1.6745	56.6301	-0.0008	-4.5064	-2.0000	0.0000	0.0000
0	4	4	0	1.1253	75.3447	0.0080	-9.0000	-2.0000	0.0000	0.0000
0	1	1	0	0.0930	18.5962	0.0002	-9.0000	-1.0000	0.0000	0.0000
4	1	4	4	-2.0000	20.8732	-1.5000	-9.0000	-2.0000	0.0000	0.0000
1	1	3	3	-0.0002	21.5452	0.1727	-9.0000	-2.0000	0.0000	0.0000
1	3	3	1	0.0002	79.3777	-1.5000	-5.2139	-2.0000	0.0000	0.0000
3	1	3	3	-1.3476	22.4932	1.5000	-9.0000	-2.0000	0.0000	0.0000
4	! Nr of hydrogen bonds;at1;at2;at3;Rhb;Dehb;vhb1									
3	2	3		2.0000	-5.0000	3.0000	3.0000			
3	2	4		1.7753	-5.0000	3.0000	3.0000			
4	2	3		1.3884	-5.0000	3.0000	3.0000			
4	2	4		1.6953	-4.0695	3.0000	3.0000			

Enhanced Sensitivity of Condensed Phase Nitroaromatic Explosives: 2,4,6-trinitrotoluene as a model system

^aDavid Furman, ^aRonnie Kosloff, ^aFaina Dubnikova, ^bSergey V. Zybin, ^bWilliam A. Goddard III, ^aNaomi Rom, ^aBarak Hirshberg and ^{*c,d}Yehuda Zeiri

^aFritz Haber Research Center for Molecular Dynamics, Institute of Chemistry, Hebrew University of Jerusalem, Jerusalem 91904, Israel

^bMaterials and Process Simulation Center, California Institute of Technology, Pasadena, California 91125

^cBiomedical Engineering, Ben Gurion University, Beer-Sheva 94105, Israel

^dDivision of Chemistry, NRCN, P.O. Box 9001, Beer-Sheva 84190, Israel

ABSTRACT

A thermal decomposition study of nitroaromatic high explosives based on 2,4,6-trinitrotoluene (TNT) is carried out using reactive molecular dynamics (MD) and electronic structure (DFT) calculations. Dramatic differences with increased decomposition sensitivity of the solid phase compared to an isolated molecule are observed. The activation energy of the homolysis decomposition pathway is reduced by ~ 23 kcal/mol. The reactive MD simulations suggested that bimolecular processes dominate the decomposition process. We then used DFT calculations to study a variety of possible bimolecular pathways. Indeed we discovered bimolecular mechanisms leading to a barrier ~ 23 kcal/mol lower than for the gas phase unimolecular decomposition. The new mechanisms involve (1) a TNT molecule that had lost an H atom from its aromatic ring that promotes breaking an adjacent C-NO₂ bond leading to a new C \equiv C cis benzyne type bond, and (2) Intermolecular H-transfer from the methyl group of one TNT molecule to a NO₂ group on an adjacent TNT molecule and the subsequent formation of HONO and NO products. It is suggested that these mechanisms are responsible for the increased sensitivity observed for condensed phase nitroaromatic explosives as compared to their gas phase sensitivity. The thermal decomposition is simulated using reactive MD up to 400 ps to characterize its kinetics and thermodynamics. In addition, the mechanism and rates of carbon cluster formation are addressed and shown to be composed primarily of sp² carbon, clusters of aromatic rings. It is predicted that these carbon rich clusters are formed in nanosecond timescales, in good agreement to experiments. The pathways discussed here are believed to dominate also the initial decomposition of many aromatic ring based explosives in the condensed phase.

1 Introduction

The technology of chemical explosives is heavily dependent on safe handling. The first industrial production and use of Nitroglycerine by the Noble family in 1863 led to several accidental initiations. Improvement in the science and technology of chemical explosives led to enhanced performance and safety in handling. Nevertheless, considerable uncertainties remain in knowledge of basic properties of many high explosives including the simplest ones. Important characteristics include the thermal decomposition mechanism, the kinetic and thermodynamic properties and the resultant intermediates and final stable products. Understanding these topics can assist in systematic predictions of new high energy molecules, influence feasibility of large-scale synthesis, and lead to a predictive capability based on structure-function relationships.

One of the most important parameters of an explosive is its initiation sensitivity, which in turn depends on complex multiscale phenomena^{1,2,3,4}. It has been known that initiation can occur following minute energy input, much less than that needed for deflagration to occur. Thus, the concept of localized energy regions ("hot spots") was conceived. The hot spot based mechanisms currently accepted are collapse of voids and the shearing of surfaces in the solid^{5,6}. It is clear, though, that chemical reaction kinetics play an important role in the initiation sequence. A slower kinetically regulated rate-controlling step can desensitize the energetic material. The rate at which these slower events take place during the initiation sequence defines the sensitivity of an explosive.

The present study focuses on nitroaromatic compounds such as 2,4,6-trinitrotoluene (TNT), 1,3,5-trinitrobenzene (TNB) and 1,3,5-triamino-2,4,6-trinitrobenzene (TATB) which are all crystalline secondary high explosives. These materials are widespread in civilian and military applications due to their low impact sensitivities.

Recently, numerous experimental^{7,8,9,10} and theoretical^{11,2,12,13} studies were aimed at understanding the initiation mechanisms and detonation properties of high explosives. A number of different experimental techniques have been used, each with its advantages and limitations, leading to discrepancies between reported values of activation energy and rate constants. Moreover, different levels of accuracy in electronic structure calculations show markedly different results^{14,15} and thus invalidate the direct comparison between such studies.

Particular attention should be given to the dramatic differences apparent in reported activation energies for condensed as opposed to the gas phases of some common high explosives. It is well known that the decomposition of some explosives is pressure dependent^{11,16,17}. This implies that one should expect noticeable differences between the gas phase and condensed phase reactions. It is intriguing that some types of explosives show no difference in activation energy, whereas others decompose up to 10 times faster in the condensed phase. Maksimov¹⁸ proposed that intermolecular H-transfer is responsible for the increased decomposition rate of molten TNT in contrast to nitrate esters and nitramines, whose decomposition is faster in the gas phase. Furthermore, in a series of isothermal decompositions in dilute supercritical solutions, Minier et al.¹⁹ found that the rate-controlling step for nitrobenzene and p-nitrotoluene is probably an intermolecular H-transfer. The bimolecular path is also supported by the works of Davis et al.²⁰ with some evidence for intermolecular H-transfer reactions for shock-induced reactions in nitroaromatic compounds. However, this contradicts the works of Brill and James^{10,21} and others^{22,23} claiming the dominant rate-controlling step in nitroaromatic explosives is a unimolecular C-NO₂ homolysis reaction.

Based on reactive MD simulations and DFT calculations we propose and verify bimolecular chemical routes of initiation in condensed phase nitroaromatic explosives. We show that labile hydrogen atoms on the aromatic ring substituents or on the ring itself are mainly responsible for the difference in activation energies between the condensed and gas phases of nitroaromatic high explosives. It is also suggested that this sensitization does not occur in the gas phase and it does not contribute to other types of explosives in the condensed phase including nitramines and nitrate esters. Finally, this study sheds light on later stages of the decomposition process including production of intermediates as well as final stable gases and carbon rich particulates for aromatic explosives in contrast to only small volatile molecules in the case of non-aromatic explosives.

As a model high explosive we have chosen TNT to represent the class of nitroaromatic explosives. TNT molecules consist of a toluene moiety with three NO₂ groups replacing three of the H atoms on the ring. Consequently, there are two types of H atoms: three hydrogen atoms of the methyl group and two remaining hydrogen atoms connected to the aromatic ring. The solid TNT unit cell and typical single crystal structures are illustrated in Fig. 1. This study describes a series of molecular dynamics simulations utilizing the reactive force field, ReaxFF-*lg*, as

implemented in the simulation package LAMMPS²⁴ together with density functional theory calculations using the Gaussian 09²⁵ package. By employing broad ranges of temperature and material compression (1800-3500K and 0-30% volumetric compression) in the reactive molecular dynamics simulations we gain insight into the complex set of physical and chemical processes occurring at these extreme conditions characterizing the reaction zone during TNT detonation. The results are compared to previously published²⁶ DFT investigations.

The rest of the paper is organized as follows: section 2 will describe the technical details of the various computational methods used in this study; section 3 is devoted to a detailed description of the major decomposition mechanisms as elucidated by DFT and MD calculations; section 4 presents an analysis of final decomposition products; section 5 is devoted to description of the thermodynamics and kinetics of the thermal decomposition process; lastly, section 6 provides a short summary of main results and draws conclusions.

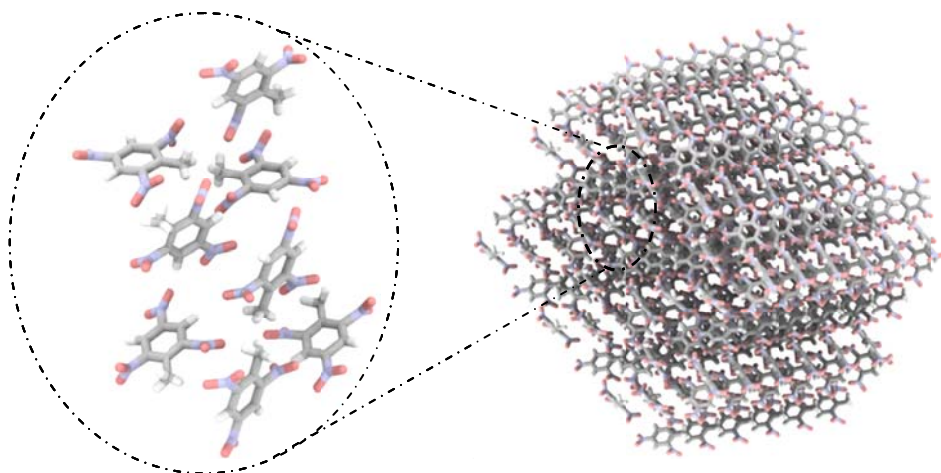


Figure 1: (left) Unit cell of *o*-2,4,6-trinitrotoluene and (right) non-compressed super cell consisting of 288 molecules

2 Computational Details

2.1 ReaxFF- ℓg Reactive Force Field

The reactive force field ReaxFF- ℓg ²⁷ partitions the system energy into a sum of contributions as shown in equation (1)

$$(1) \quad E_{system} = E_{bond} + E_{lp} + E_{over} + E_{under} + E_{val} + E_{pen} + E_{tors} + E_{conj} + E_{H-bond} \\ + E_{vdW} + E_{Coulomb} + E_{\ell g}$$

Generally, the total energy of the system consists of three types: covalent bond order-dependent terms (bonds, angles and torsions), electrostatic forces and van der Waals interactions between all atomic pairs²⁷.

The covalent part is mainly responsible for the reactivity of the force field, describing instantaneous bond formation and rupture events as smooth functions of the interatomic separations for σ , π , and $\pi\pi$ bonds.

$$(2) \quad \begin{aligned} BO'_{ij} &= BO_{ij}^{\sigma} + BO_{ij}^{\pi} + BO_{ij}^{\pi\pi} \\ &= \exp \left[p_{bo1} \left(\frac{r_{ij}}{r_0^{\sigma}} \right)^{pbo2} \right] + \exp \left[p_{bo3} \left(\frac{r_{ij}}{r_0^{\pi}} \right)^{pbo4} \right] \\ &+ \exp \left[p_{bo5} \left(\frac{r_{ij}}{r_0^{\pi\pi}} \right)^{pbo6} \right] \end{aligned}$$

The bond order, BO'_{ij} , in equation (2) is calculated on-the-fly and consecutively corrected with under- and over-coordination terms to attain the correct valency. In addition, ReaxFF- lg accounts for polarization effects by using a geometry-dependent charge equilibration scheme. All parameters are optimized to reproduce QM data. In the present study the nitramines-trained force field was used with low gradient correction for dispersion interactions. The long range correction factor is responsible for a proper description of vdW and London forces between molecules and has been shown to be important in molecular solids. The parameterization is based on a large number of *ab-initio* QM calculations of nitramine and nitroaromatic high energy compounds both at ambient and at extreme conditions^{28,29,11,30}.

We briefly describe here the correction method presented extensively elsewhere²⁷. The proposed method adds a correction factor to the original ReaxFF total energy expression³¹ (Eq. 1) in order to keep the fitted parameters intact, while adding the ability to train a new set of correction parameters so to predict a correct density and heat of sublimation for energetic materials such as PETN, TATB, NM and RDX compared to experimental results. The new energy term introduced is the low-gradient energy term of the form:

$$(3) \quad E_{lg} = - \sum_{ij, i < j}^N \frac{C_{lg,ij}}{r_{ij}^6 + R_{eij}^6}$$

Where r_{ij} is the interatomic distance, R_{eij} is the interatomic equilibrium vdW distance and $C_{lg,ij}$ is the dispersion energy correction parameter for atomic pair i and j .

Although no TNT-specific training was performed, we have ensured that major single molecule unimolecular decomposition pathways and energetics are reproduced with high accuracy compared to previously reported DFT results^{26,32,33} indicating the applicability of the ReaxFF-*lg* force field to nitroaromatic (TATB, TNT) and nitroaminic (RDX, HMX, NM) energetic materials. The obtained crystal density of TNT at ambient conditions was 1.49 gr/cm³ compared to the experimental density of 1.65 gr/cm³. This indicates that the dispersion correction should be increased.

2.2 Reactive Molecular Dynamics of TNT at Extreme Conditions

An initially non-compressed (V_0) super cell of 288 molecules (6048 atoms) was generated using orthorhombic TNT unit cell (see fig. 1) obtained from the Cambridge Crystallographic Data Centre³⁴. The super cell was created by multiplying the a , b and c cell vectors by 3, 6 and 2 respectively to form a cubic shaped super cell. Energy minimization using the conjugate gradient method was employed until convergence of potential energy was reached. Subsequent thermalization with the Berendsen thermostat at 300K for 5ps using a 25fs damping constant was carried out to thermalize the system at room temperature. In order to relax excess pressure another 5ps of isobaric-isothermal (NPT) relaxation was performed using Nose-Hoover barostat at 1atm and 300K with 50fs and 250fs damping constants for temperature and pressure respectively. By the end of this stage we have obtained the relaxed initial super cell (with $V_0 = 7.2 \times 10^3 \text{ \AA}^3$ and crystal density of 1.49 gr/cm³). This initial super cell was used to generate the volumetrically compressed super cells. By shortening lattice parameters for each compressed super cell, we have obtained the $0.9V_0$, $0.8V_0$ and $0.7V_0$ super cells corresponding to 10%, 20% and 30% compression. We have checked that no artificial bond breaking occurred at this stage. To further decrease any artificial stress, the group of compressed super cells was evolved through the micro canonical ensemble (NVE) for an additional 5 ps to get a fully relaxed set of super cells to be used in the decomposition simulation.

The target temperatures at 1800K, 2250K, 2500K, 3000K and 3500K were reached by rapid heating during 100fs. The rapid heating was imposed by rescaling the atomic velocities and maintaining target temperature using a Berendsen thermostat during the rest of the simulation.

Simulation length varied in the range 80-400ps depending on temperature. Lower temperatures needed longer simulation time to achieve chemical equilibrium. The time steps used during thermalization and the rapid heating steps were kept at 0.25fs and 0.1fs respectively. Small time step is essential in reactive simulations where chemical transformations occur and a chemical bond's vibrational frequency is accounted for. During each simulation bond formation and rupture events were monitored. Each possible atomic pair was assigned different cutoff distances to properly identify chemical species. The full set of force field parameters and cutoffs can be found in the supporting information.

2.3 DFT calculations

The calculations were carried out using the Gaussian-09 package²⁵. The PBE1PBE hybrid density functional (also known as PBE0)^{35,35b} was used in conjunction with the Dunning correlation consistent polarized valence double ξ (cc-pVDZ) basis set³⁶. The PBE1PBE functional yields reliable results and is quite economic in computational time requirements for rather large molecular systems as those discussed. The vibrational analysis of the structures was performed at the same level of theory in order to reliably characterize the optimized structures either as local minima or transition states. All the calculated frequencies, the zero point energies and the thermal energies correspond to harmonic approximation. The calculations of intrinsic reaction coordinates (IRC) using internal coordinates were performed in order to examine whether the transition states under consideration connect the expected reactants and products. These calculations were performed for all the transition states at the PBE1PBE level of theory. The basis set used was the same as that used for the stationary point optimizations.

3 Initial Decomposition Mechanisms

The basic mechanisms that govern TNT decomposition were elucidated recently using extensive density functional theory calculations^{26,32}. It was suggested that only unimolecular reactions are kinetically accessible during the passage of a shock wave (~ 6900 m/s) through a characteristic length scale of a unit cell of TNT (10-20Å)^{37,38,39} and that ring fission does not take place until most of the attached substituents are removed^{10,40}. Three major decomposition routes were proposed as the initiating agents of detonation, depending upon temperature and pressure conditions. Starting with $-\text{C}(\text{CH}_3)\text{-C}(\text{NO}_2)\text{-CH-C}(\text{NO}_2)\text{-CH-C}(\text{NO}_2)\text{-}$, we found²⁶

- (1) C-NO₂ homolytic cleavage followed by subsequent C-NO₂ steps forming eventually three NO_{2(g)} molecules and a triradical intermediate $-\text{C}(\text{CH}_3)\text{-C}(\cdot)\text{-CH-C}(\cdot)\text{-CH-C}(\cdot)-$, (C₇H₅O₄N₂)
- (2) C-H attack on the nitro substituent to form 2,4-dinitro-anthranil (DNA_n, C₇H₃O₅N₃) and water and
- (3) Nitro-Nitrite (C-NO₂ → C-ONO) rearrangement followed by O-NO homolytic cleavage and release of NO_(g) for each of the three NO₂ substituents.

It was suggested that above 1700K the dominant pathway is the C-NO₂ homolytic cleavage while the other pathways are negligible.

To assess the influence of bulk environment on the thermal decomposition simulations were carried out at temperatures in the range: 1800K-3500K and compressions: 0-30% for the solid slab with periodic conditions. Fig. 2 shows the time evolution of the major species during the initial TNT decomposition for low and high temperature and pressure conditions.

— NO ₂	— C ₇ H ₆ O ₆ N ₃	— HONO	— C ₁₄ H ₁₀ O ₁₂ N ₆
- - - NO	- - - C ₇ H ₄ O ₆ N ₃	- - - C ₇ H ₄ O ₄ N ₂	— C ₁₄ H ₉ O ₁₂ N ₆
— H ₂ O	— C ₇ H ₅ O ₄ N ₂	— C ₇ H ₅ O ₅ N ₂	- - - C ₇ H ₃ O ₅ N ₃

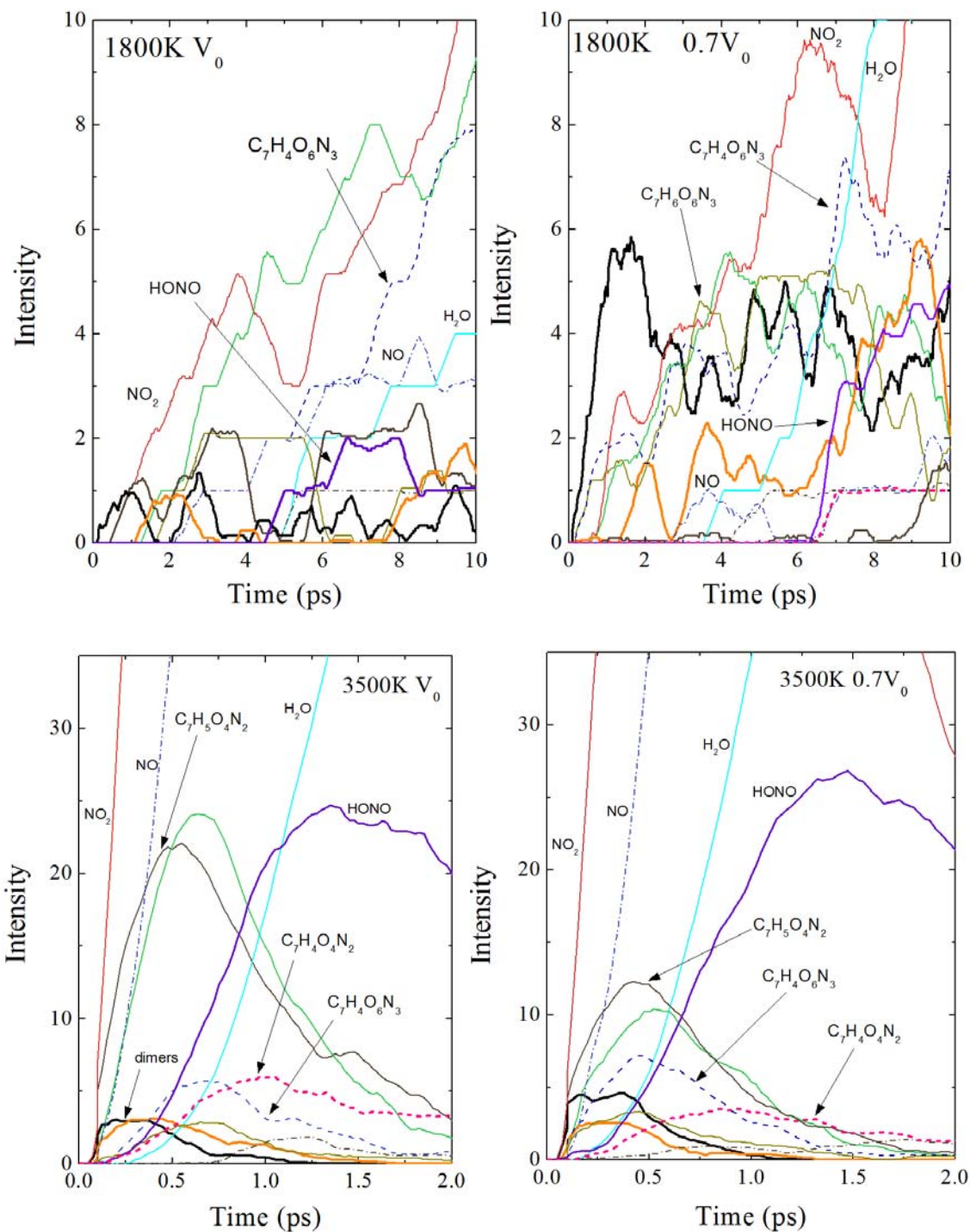


Figure 22: Initial decomposition intermediates following TNT thermal initiation

Fig. 2 shows that the most dominant step of decomposition in all the temperature and compression ranges is cleavage of the NO_2 substituent with production of the highly reactive $[\text{C}(\text{CH}_3)\text{-C}(\cdot)\text{-CH-C}(\text{NO}_2)\text{-CH-C}(\text{NO}_2)]\cdot$ radical ($\text{C}_7\text{H}_5\text{O}_4\text{N}_2$) in agreement with DFT results²⁶. We also find the di- and tri-radicals formed following the 2nd and 3rd NO_2 cleavages though in a

much lesser amount (not shown for clarity). NO begins to appear shortly after NO₂ is produced with significant amounts at high temperatures simultaneously with the formation of the TNT radical, $-\text{C}(\text{CH}_3)\text{-C}(\text{NO}_2)\text{-CH-C}(\text{NO}_2)\text{-CH-C}(\text{O})-$, (C₇H₅O₅N₂). According to DFT and ReaxFF-*lg* calculations both routes become more exergonic at high temperatures. Water molecules and 2,4-dinitro-anthranil (C₇H₃O₅N₃) appear as products at a later stage and evolve with a slower rate.

The ReaxFF-*lg* simulations predict formation of TNT dimers very early in the decomposition with increasing amounts and rates for increased compressions. Their formation and evolution together with bigger clusters is elaborated in section 4.2. Various other radicals are produced during the initial decomposition steps, for example: The bimolecular formation of TNT radicals lacking a hydrogen atom (C₇H₄O₆N₃) and some with an extra hydrogen atom (C₇H₆O₆N₃). We also observe the unimolecular HONO elimination path leading to C₇H₄O₄N₂ at the higher temperatures; however, it is occurring at later stages and with a relatively low intensity. It is clear that the initial steps of condensed phase TNT decomposition are a complex set of bimolecular reactions.

4 Stable products in the Solid Chemical Decomposition

4.1 Stable Final Detonation Gases

The final amounts of the stable gases, normalized by the initial number of TNT molecules, are shown in Fig. 3. Both N₂ and H₂O are relatively insensitive to the wide range of applied temperature and compression values, while the combustion gases, CO and CO₂, seem to behave differently. As the temperature increases the amount of CO₂ diminishes while more CO is produced. We also noticed that higher compressions reduce the production of these gases, suggesting that oxygen is trapped in carbon clusters as will be discussed in section 4.2. Generally, higher temperatures and compressions enhance the production rate of all species. A detailed kinetic study will be presented in section 5.

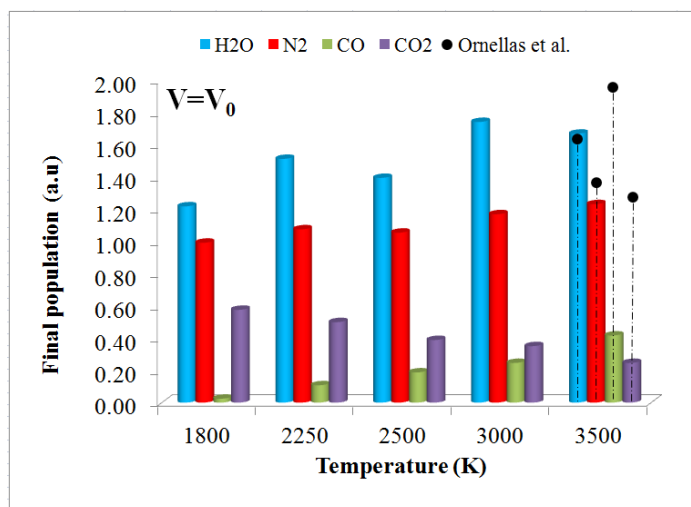


Figure 33: Normalized populations of stable final detonation gases

We compare the final populations for $T=3500\text{K}$ and $d=1.49\text{ gr/cm}^3$ ($V=V_0$), where most secondary reactions reached equilibrium, to available experimental results of calorimetric bomb experiments⁴¹ of TNT with a density $d=1.53\text{ gr/cm}^3$ conducted in vacuum confined environment. Post detonation analysis identified the main detonation gaseous species to be N_2 , H_2O , CO , and CO_2 with relative amounts of 1.32, 1.60, 1.98, and 1.25 respectively. The MD data show that the N_2 and H_2O produced in the MD simulation agrees well with the corresponding experimental values, however, CO and CO_2 deviate quite notably. One should be aware that the experimental measurements of detonation are performed after isentropic expansion and subsequent cooling of the released gases, whereas our results are obtained in NVT ensemble conditions which characterize the reaction zone of the detonation wave. We assume that by performing additional expansion of the systems a higher degree of combustion will be achieved, as was also suggested in a study of TATB detonation¹². This is further supported by our carbon clusters analysis described below.

4.2 Carbon Clusters

Nitroaromatic explosives such as TNT and TATB are known to produce large quantities of soot and carbonaceous clusters.^{12, 42, 43} Recent theoretical studies demonstrated the effect of phase transitions in these clusters, occurring during detonation, to be significant to the explosive performance. Victorov et al. claimed that the graphite-diamond phase transition during TNT detonation wave is responsible for the invalidity of the Chapman Jougeout (CJ) theory for this explosive⁴⁴ since chemical equilibrium implied by the CJ theory is inconsistent with the findings

that the carbon phase change doesn't follow the equilibrium phase diagram. Moreover, experimental data indicates that sp^2 -bonded graphitic solid is present as detonation soot⁴⁵; in contrary to the equilibrium CJ assumption where the carbon phase in the reaction zone is expected to be sp^3 -bonded with a diamond structure. To elucidate the initial steps of cluster formation we followed both the kinetics and variation in carbon hybridization during the simulations in all temperature and pressure conditions. The average number of carbon atoms in large product molecules, $\langle N_C \rangle$, was monitored for all species containing over 100 carbon atoms. Each cluster was weighted by its frequency of appearance at any given time to properly represent relative contribution as is shown in Eq. 4. These results are presented in Fig. 4.

$$(4) \quad \langle N_C \rangle_t = \frac{\sum_{i=1}^{N_{tot}} N_c(t) \cdot I(t)}{N_{tot} \cdot I(t)}$$

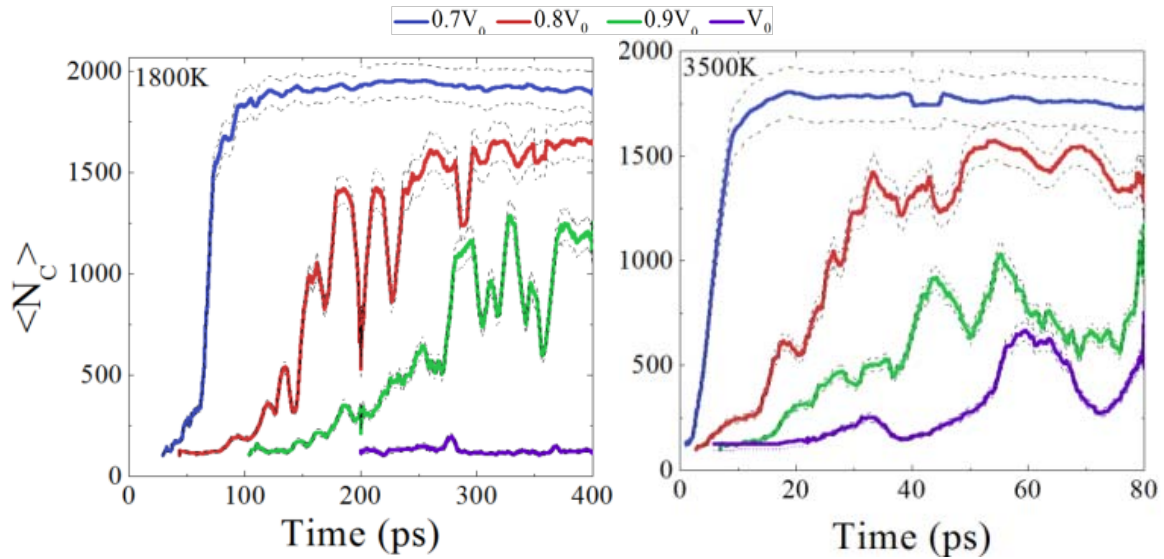


Figure 44: Average number of carbon atoms in a cluster with a size of 100 and above carbon atoms. Dashed lines show addition and subtraction of one standard deviation value.

We noticed (See Fig. 1 in supplementary material) that in the group of carbon clusters having less than 100 atoms, there were ~ 7 carbon atoms in a species for $V=V_0$ at 1800K for the full simulation period. At higher temperatures (3500K) there was a rapid reduction to ~ 4 carbons with initially ~ 7 carbons in a species. At high compressions we noticed a sharp increase to ~ 14 carbon atoms in a species (dimer) and their subsequent disappearance in favor of molecules that contain 2 to 3 carbon atoms. This behavior demonstrates the rapid formation of dimers of TNT molecules and their involvement in the following decomposition steps. This is supported by our

findings in section 4.1 and by Rom et al.³³. These relatively small carbon clusters grow into larger clusters as is shown in Fig. 4 where clusters containing over 100 carbon atoms are time-averaged. Inspection of these results clearly shows that high compressions favor production of larger clusters at a higher rate. In addition, the scatter in the data indicates a transient nature of the clusters. While temperature seems to have a minor influence on the stability of the clusters, we see that they become more stable at high compressions. However, from the kinetic point of view, we find that at 1800K clusters begin to appear at a much later stage than at 3500K. Moreover, the clusters begin to form before the complete decomposition of parent TNT molecules which in all cases undergoes dimerization and agglomeration mechanisms.

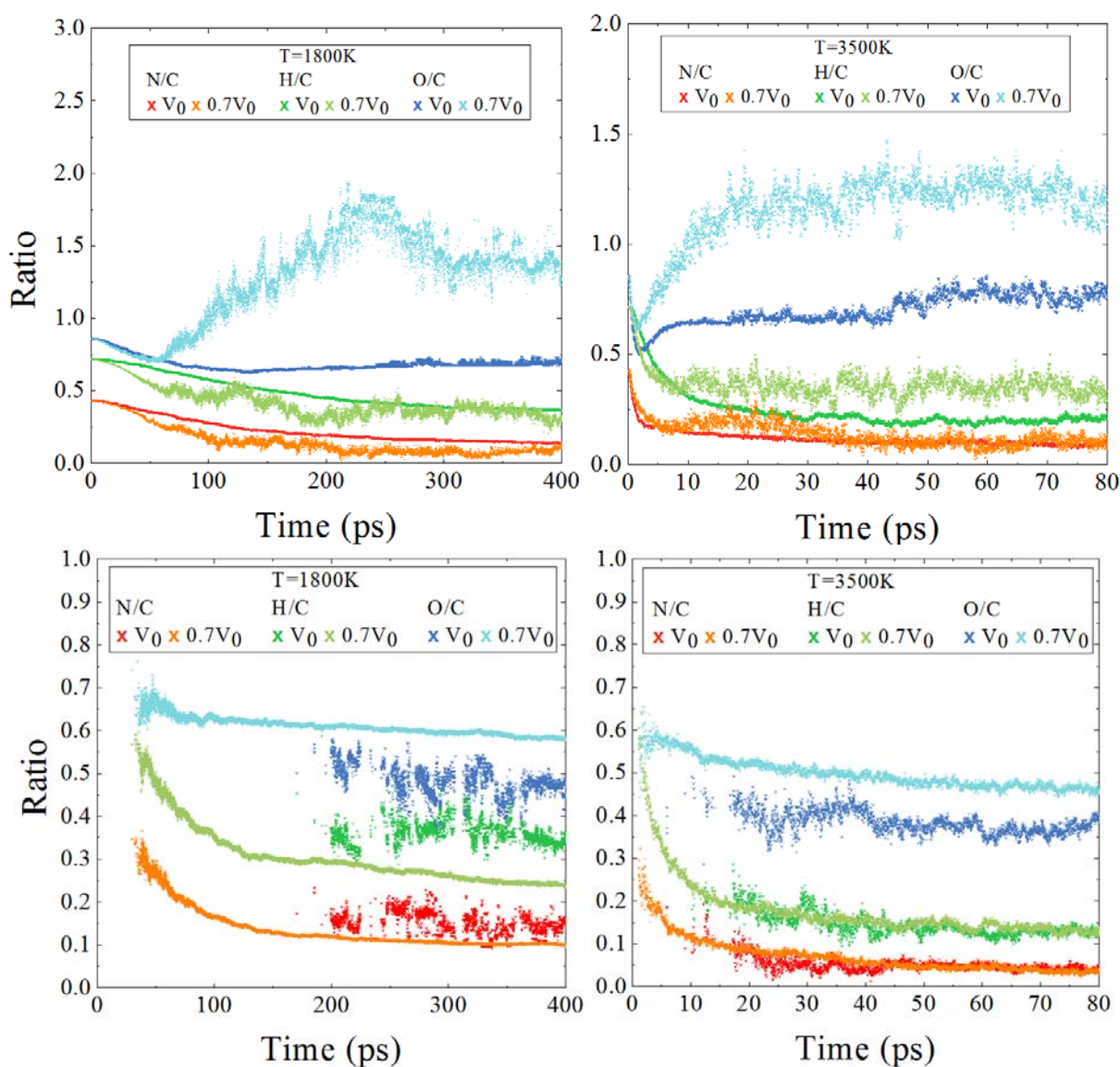


Figure 55: Elemental ratio for clusters with: (top) < 100 carbon atoms and (bottom) > 100 carbon atoms

The data presented in Fig. 5 show the ratio of H, N and O atoms with respect to C atoms in the clusters. The upper row plots belong to clusters having less than 100 carbon atoms. They clearly indicate the uptake of O, N and H atoms into the clusters at high compressions and their stability during the simulation. Interestingly, at high compressions Oxygen is the most abundant species in these clusters with a relative amount of ~ 1.5 times that of carbon itself. Clearly, this behavior is attributed to the production of CO and CO₂ as the main carbon containing gaseous species during the simulations. However, clusters with over 100 carbon atoms are primarily composed of carbon with oxygen being the second abundant atom. These results clearly indicate that a slow reduction in the amount of H, N and O atoms content in the clusters takes place, but significant amounts of oxygen and hydrogen are still trapped in these clusters even at the end of the simulations. The oxygen trapped in these clusters is incapable of further oxidizing them into CO and CO₂ because of the high stability of the clusters in the simulated constant temperature and volume (NVT) conditions. A similar result was recently obtained for shocked and thermally initiated TATB^{43,12}.

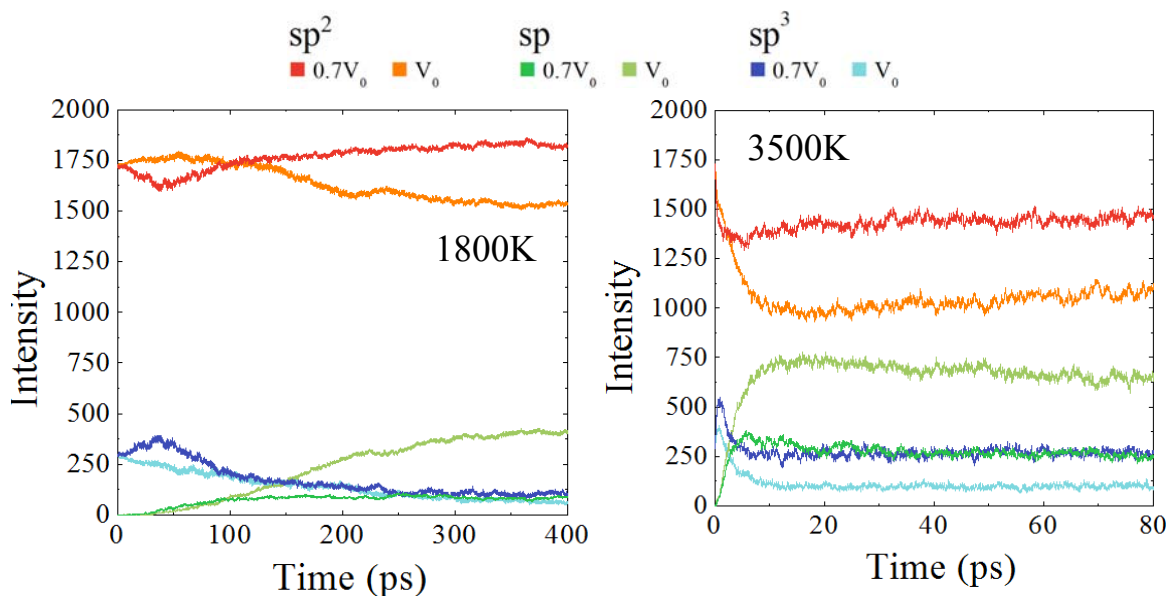


Figure 66: Hybridization of all carbon atoms in the system

To further analyze the bonding nature of carbon in the detonation products, we monitored the hybridization of the carbon atoms in the simulation for the 3500K and 1800K cases for both uncompressed and highly compressed super cells. The system begins with 288 TNT molecules; each one contains 6 sp^2 carbons and 1 sp^3 carbon, thus making a total of 1728 sp^2 carbons and 288 sp^3 carbons in the initial state of the system. The decomposition of the aromatic benzene rings expected to lead to a decrease in the number of sp^2 carbons and an increase in the number of sp^3 carbons associated with the formation of intermediates and final volatile carbon containing molecules. At later stages of the simulations we witness a slow increase in the number of sp^2 carbon atoms that is consistent with the formation of graphite-like carbon clusters. The increase in sp carbons is mainly associated with the production of CO_2 and CO that start to form after ~ 5 ps at $T=3500K$ and $\sim 100ps$ at $T=1800K$ (Fig. 3 top).

At the final stage of the simulation for the highly compressed state ($0.7V_0$) most of the carbon is in the form of carbon clusters with an average size of ~ 1800 carbon atoms (Fig. 4 bottom) in sp^2 hybridization suggesting that the soot is mainly graphite like material. Higher compression and temperature seem to favor production of sp^3 carbon clusters implying a preference of diamond-like structures. According to recent experimental detonation measurements⁴⁶ of pure TNT and TNT/RDX mixtures, the condensed carbon phase exhibited a complex composition, made up of nano diamonds, graphite and amorphous phases. Generally,

the mixture exhibited a larger content of sp^3 carbon (ultrafine diamond). In addition, an X-ray photoelectron spectroscopy analysis showed that only $\sim 12\%$ of the detonation soot in a TNT/RDX (50/50) in N_2 environment is actually in a diamond phase and that graphite accounts for $\sim 71\%$. Our results for the 3500K and $0.7V_0$ conditions reveal a $sp^3:sp^2$ ratio of 1:6 in accordance with the experimentally measured values. It is known that TNT reaction zone is characterized by a very high electrical conductivity^{47,48}. Two possible mechanisms for this anomalous effect were proposed to be (a) thermal emission of electrons from sp^2 carbon complexes and (b) the contact electrical conduction in the presence of carbon complexes dispersed in the large sp^2 matrix formed in the soot. Thus, our calculations provide further indirect evidence for the possibility of electrical conductivity during the detonation of TNT by graphitic carbon complexes.

5 Kinetics and Thermodynamics of Decomposition

5.1 Stable Gaseous Species

The variation of potential energy along the simulation of the system is related to the changes occurring during the decomposition process^{11,12,31}. Hence, evidence for endothermic and exothermic stages is clearly noticeable. The time evolution of the potential energy for the various systems examined is shown in Fig. 7.

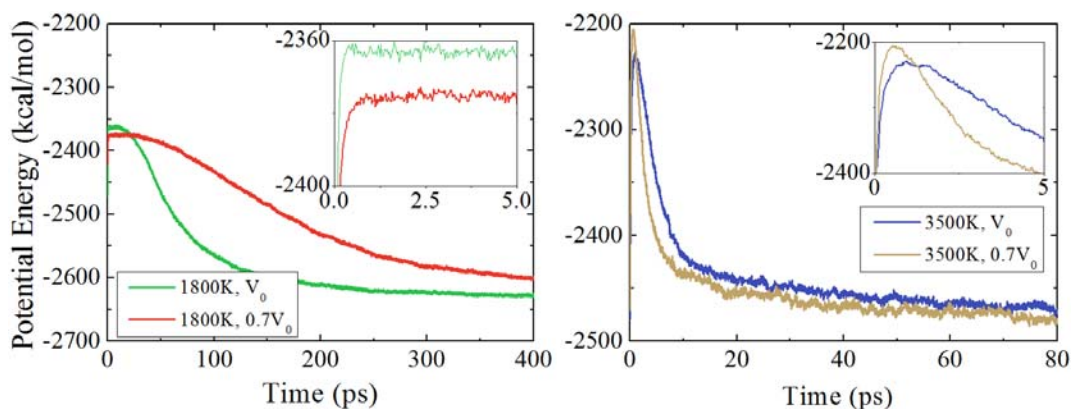


Figure 7: Thermal decomposition potential energy curves for lowest (1800K) and highest (3500K) temperatures for non-compressed (V_0) and 30% compressed ($0.7V_0$) TNT super cell

Inspection of Fig. 7 reveals that in all cases the first stage in the decomposition process is endothermic. This stage corresponds to energy transfer from translational into vibrational modes

of TNT molecules and followed by initiation of the decomposition that involves bond rupture. The maximum obtained in the potential energy profile marks the commencement of exothermic reactions and the formation of a large variety of intermediate species and final products. The time dependence of the potential energy profile starting at the potential energy maximum is fitted to a decaying exponential function $U(t;T,P)$ to extract kinetic and thermodynamic parameters of the exothermic stage in the decomposition process. The exponential function used for the fitting is shown in Eq. 5:

$$(5) \quad U(t;T,P) = U_0 + \Delta Q \cdot \exp\left\{-\frac{t - t_{max}}{\tau_{exo}}\right\}$$

In Eq. 5 U_0 is the asymptotic potential energy of the system (kcal/mol), ΔQ is the exothermicity (cal/g), τ_{exo} is the inverse reaction rate (ps) and t_{max} (ps) is the time when the maximum in the potential energy is obtained ("induction time"). To extract the global endothermic reactions rate constant (τ_{endo}), a 1st order rate model (Eq. 6) was fitted to the TNT decomposition curves (Fig. 3) from $t=0$ up to $t=t_{max}$. Here, N_0 is the initial amount of TNT molecules. The fit quality was high ($R^2 > 0.99$) and is indicative of a dominant unimolecular channel during the period between $t=0$ and $t=t_{max}$. However, as will be demonstrated below, the very initiation of TNT in the condensed phase follows bimolecular reactions which subsequently promote the C-NO₂ unimolecular cleavage. The parameters obtained in these fits are presented in Table 1 in the supplementary material.

$$(6) \quad N(t) = N_0 \cdot \exp\left\{-\frac{t}{\tau_{endo}}\right\}$$

We observed that temperature variation plays a major role in the kinetics of both stages. The rate of the exothermic stage becomes 40 times faster for the non-compressed case when temperature is increased from 1800K to 3500K, and an 80-fold faster kinetics is observed for endothermic stage of TNT decomposition. Compression of the bulk has also a significant effect. For example, 20% volumetrically compressed TNT exhibits a 60% faster exothermic products evolution at 1800K, suggesting that both stages in TNT decomposition are pressure dependent in the compression range examined. The calculated heat released during the exothermic step of compressed crystals, ΔQ , varies in the range 1091.7–1606.7 cal/g where for a density of $d=1.49$ gr/cm³ ($V=V_0$) it is in the range 1091–1304 cal/g. The experimental data yield ΔQ values in the

range 900–930 cal/g⁴⁹ (for $d=1.605 \text{ g/cm}^3$, $T=500\text{--}600\text{K}$), 950 cal/g⁵⁰ (for $d=1.654 \text{ g/cm}^3$, $T=470\text{--}600\text{K}$), and 1082–1128 cal/g for $d=1.66 \text{ gr/cm}^3$ in vacuum confined experiments⁴¹. These values are in good agreement with our results.

To investigate temperature and pressure dependence of the rate constant one can consider the total differential:

$$(7) \quad d \ln k = \left(-\frac{\partial \ln k}{\partial T} \right)_P dT + \left(-\frac{\partial \ln k}{\partial P} \right)_T dP$$

The partial derivatives are easily evaluated using the 1st law of thermodynamics, $dH = dU + pdV + Vdp$ together with the Arrhenius relation⁵¹ $k = Ae^{-\frac{E_a}{RT}}$.

$$(8) \quad \left(\frac{\partial \ln k}{\partial \left(\frac{1}{T} \right)} \right)_P = -\frac{E_a}{R} \quad ; \quad \left(\frac{\partial \ln k}{\partial P} \right)_T = -\frac{\Delta V^\ddagger}{RT}$$

According to Eq. 8, increase in pressure results in faster reaction rates only if the change in activation volume is negative. Conversely, a positive change in activation volume implies a decrease in the reaction rate for increasing pressure. Hence, a unimolecular reaction is expected to have a positive change in activation volume, while a bimolecular reaction will exhibit a negative activation volume^{52,53}.

Plotting the logarithm of inverse reaction rate as a function of average pressure, one can extract the volume of activation, ΔV^\ddagger , from the slope. The calculated average pressures for each compression and temperature and the calculated activation volumes are presented in Table 1.

Table 1: Average pressures and volumes of activation during decomposition

	Average pressure (GPa) 1800K		Average pressure (GPa) 2500K	
V_0	3.04		4.29	
$0.9V_0$	4.38		5.94	
$0.8V_0$	6.70		8.28	
$0.7V_0$	10.53		13.04	
ΔV^\ddagger (cm ³ /mol)	Endo	Exo	Endo	Exo
	-1.94	-2.69	-2.55	-1.66

As can be seen in Table 2 all the changes in activation volumes are negative as is expected from the decreasing magnitudes of the inverse rate constants for increasing compression. The rate constants for both endothermic and exothermic stages represent a complex mixture of many reactions that occur in parallel. According to the calculated values of ΔV^\ddagger both stages are (at least) bimolecular in contrast to the DFT results where a unimolecular rate determining step was suggested for the initial endothermic stage. We could not find any experimental measurements of activation volumes of TNT, however, some data are reported for HMX, RDX and Nitromethane^{16,54,55}. These are: $-5.6 \text{ cm}^3/\text{mol}$ for α -RDX (for 478-508K and 1.3-2.1GPa), $+3.89 \text{ cm}^3/\text{mol}$ for β -RDX (for 508K and 3-7GPa), and $+4.1 \text{ cm}^3/\text{mol}$ (for β -HMX at 558-573K and 3-8GPa). Nitromethane exhibits complex kinetics with several pressure dependent mechanism changes^{11,56,57} and includes both positive and negative volumes of activation⁵⁸. Our calculated values seem to be close in magnitude to the reported values of nitramine explosives and suggest that the global condensed phase TNT thermal decomposition is at least a bimolecular process. This finding is also supported by the initial stages of decomposition presented in Fig. 2 where dimerization and radical formation reactions are found to occur concurrently with NO_2 cleavage. Recently, Zhang et al¹² used ReaxFF to study the thermal decomposition of both β -HMX and TATB. They found that both TATB and β -HMX decompositions are pressure dependent in the range 0-50% compression. Increasing pressure results in a decreased rate of β -HMX decomposition, but leads to an increase in the decomposition rate of TATB. Since TATB and TNT are structurally similar, one would expect them to behave similarly, as is found in here. The activation energies for both stages of the decomposition process were calculated and are presented in Fig. 8.

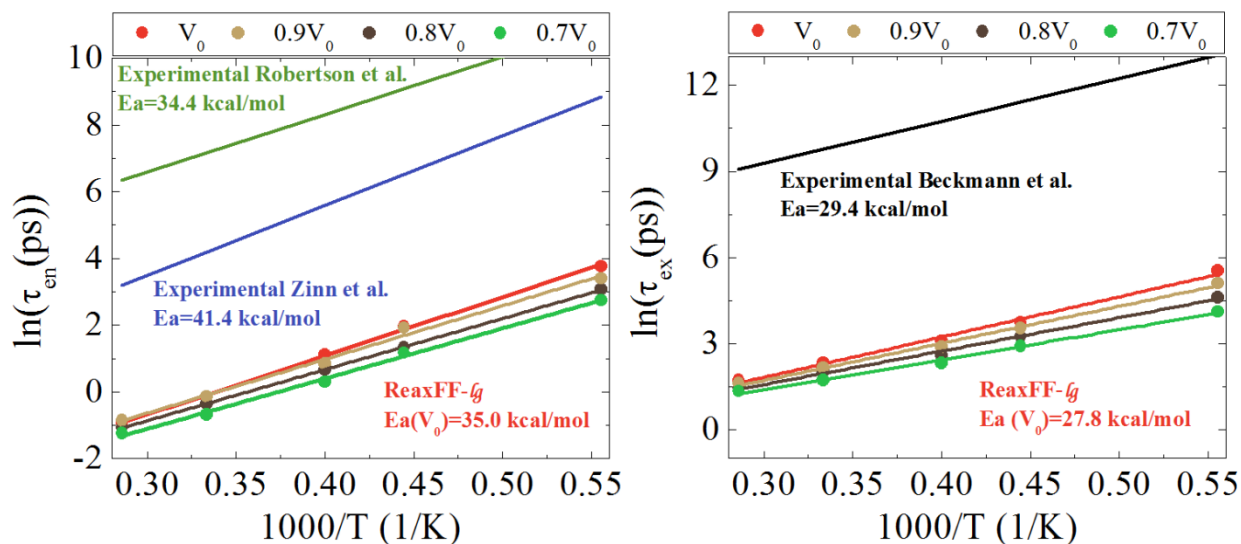


Figure 88: Arrhenius plots for the endothermic (left) and exothermic stages (right) of decomposition. Extrapolations for experimental results of Robertson et al.⁵⁹ (548-583K EG study), Zinn et al.⁶⁰ (571-763K TTX study) and Beckmann et al.²² (518-542K IDSC study) are also shown.

The ReaxFF- \dot{g} predicted activation energies are in excellent agreement with experimental values, although there is a clear discrepancy in the values of the pre-exponential factors, which are up to 2 orders of magnitude larger in the simulations (units: s^{-1}). Possible reason for this discrepancy in pre-factor values is that the simulation cell (6048 atoms) is relatively small and the simulation time scales are relatively short due to computational cost. In addition, surfaces, grain boundaries, and defects are not included in our model. These limitations may prevent full coverage of the phase space for the decomposition process. Besides, additional possible routes can exist at high temperatures and pressures (including charge transfer and excited states) that might lead to complex kinetic behavior including autocatalysis¹⁰, which could invalidate the comparison to extrapolated low temperature measurements. Nonetheless, the slopes of the linear regression analysis allow extracting the activation energies for the stages of the decomposition process at each material compression. These are summarized in Table 2.

Table 2: Activation energies and pre-factors for both stages of TNT thermal decomposition

Stage	Super cell	E_a (kcal/mol)	$\ln[A (s^{-1})]$
Endothermic	V_0	35.0	33.6
	$0.9V_0$	32.0	33.1
	$0.8V_0$	30.4	33.1
	$0.7V_0$	29.9	33.2
	Zinn et al.	41.4	30.4
	Robertson et al.	34.4	26.3
Exothermic	V_0	27.8	30.0
	$0.9V_0$	25.7	29.8
	$0.8V_0$	23.1	29.5
	$0.7V_0$	20.7	29.3
	Beckmann et al.	29.4	22.8

The activation energies represent an effective rate-limiting step for both endothermic and exothermic stages of TNT decomposition. There is a good agreement between the calculated activation energies and the experimental data from different sources and measurement methods. However, DFT calculations for a single TNT molecule unimolecular decomposition predict for C-NO₂ bond rupture an activation energy which is higher by ~23 kcal/mol^{26,32} than the values described above. Inspection of Fig. 2 clearly shows that the initial stage of TNT decomposition involves a dominant NO₂ production, as predicted by the DFT calculation; however, the large discrepancy in the predicted activation energies is unclear. Moreover, the negative ΔV^\ddagger values obtained above suggests that a bimolecular mechanism is responsible for the endothermic stage, also in contradiction with the DFT predictions. An analogous behavior is observed for TATB, a similar nitroaromatic. Some of the reported activation energies for a single molecule of TATB (C-NO₂ bond dissociation energy) lie in the range 69.4-77.2 kcal/mol^{61,62}, while reported activation energies in the condensed phase lie in the range 42.0-60.0 kcal/mol⁶³. However, in the case of RDX, HMX and PETN, three high explosives representing the nitramine and nitrate ester classes, the gas and condensed phases share the same activation energy. The data of activation energies for variety of systems is presented in Table 4. Surprisingly, 1,3,5-trinitrobenzene

(TNB), a nitroaromatic explosive, similar in structure to TATB and TNT, with a missing NH₂ or a CH₃ group, is also characterized by similar activation energies in both phases.

Table 3: Global activation energies of condensed phase nitroaromatic, nitramine and nitrate ester high explosives and unimolecular DFT energy barriers for NO₂ cleavage

Family	Aromatic			Non-aromatic		
	TATB	TNT	TNB	RDX	PETN	HMX
ΔE^\ddagger (kcal/mol)						
Gas phase DFT results	69.4 ⁶¹ , 77.2 ⁶²	61.7	64.0 ⁶¹ , 67.7 ⁶⁴	41.5	46.5	42.8 ⁶²
Condensed phase Experimental results	60.0 ⁵ ; 59.1 ⁶⁵ ; 42.0 ⁶³	34.4 ⁵⁹ , 43.4 ⁴⁷ , 41.4 ⁶⁰	67.3±0.8 ¹⁰	47.1 ⁶³ , 53.6 ⁶⁶	41.83 - 62.86 ^{67,9}	48.47 ⁶⁸ ; 52.7 ⁶⁹
$\Delta(\Delta E^\ddagger)$	+19.6	+21.8	-1.45	-8.8	-5.8	-5.5

A possible explanation for this behavior is proposed and tested by further DFT calculations. The condensed phase allows the formation of a large amount of radical fragments during its initial steps via bimolecular pathways, which in turn can promote further decomposition in a chain-like reaction, whereas in the gas phase this is not likely to occur. We noticed that a major intermediate radical species is a TNT molecule lacking one hydrogen atom (C₇H₄O₆N₃) on the aromatic ring or on the methyl group as was seen in Fig. 2. These species are produced very early in the decomposition, reach a maximum value and then decrease to zero, as these radicals are rapidly consumed by the decomposition process. Thus, we focused on two possible bimolecular decomposition channels consistent with the above findings:

- (1) Homolytic cleavage of NO₂ from a TNT molecule missing an aromatic hydrogen resulting in a neutral radical
- (2) Methylic H-transfer to an NO₂ group on a TNT molecule by an adjacent TNT molecule

In the first case the resultant *ortho* bond cleavage energy was found to be ~23 kcal/mol lower (BDE=38.3 kcal/mol) than the corresponding value for an intact TNT molecule^{1,2}. The H abstraction promotes breaking the adjacent C-NO₂ bond due to the formation of a new C≡C cis benzyne type bond. This value is very close to the reported experimental values and our solid TNT ReaxFF-*lg* calculations (29.9-35.0 kcal/mol). We note that although the reaction for H abstraction from the aromatic ring is quite endothermic (BDE=112.5 kcal/mol) in the unimolecular gas phase case, it could still serve as an initiating and sensitizing channel for C-

NO₂ homolysis and further radical production in the hot and dense environment characterizing TNT reaction zone.

In the second case, we identified three possible routes with significantly lower activation barriers compared to the gas phase (Scheme 1 and Table 2 in the supplementary material). The first step involves methylic H-transfer to an NO₂ group ($E_a=43.0$ kcal/mol) to form C₆H₂(NO₂)₂(NOOH)CH₃[·] and C₆H₂(NO₂)₃CH₂[·]. Subsequently, the former leads to the formation of HONO and 2,4-dinitrotoluene radical (C₆H₂(NO₂)₂CH₃[·]) via 2 transition states (TS2=38.0 kcal/mol and TS3=42.3 kcal/mol). Alternatively, the parent molecule can undergo an isomerization reaction (route 2) to produce NO and 4-methyl-4,5-dinitrophenol (C₆H₂(NO₂)₂(OH)CH₃). Another possibility (route 3) is to begin from C₆H₂(NO₂)₃CH₂[·] to form NO and C₆H₂(NO₂)₂(O)CH₂ with a slightly higher barrier of TS5=47.7 kcal/mol. The calculated activation energies for the different routes are lower by ~20 kcal/mol compared to the gas phase NO₂ unimolecular decomposition channel. Thus, it is asserted that gas phase TNT decomposition is a unimolecular stage where the dominant reaction is the C-NO₂ homolytic cleavage, whereas the condensed phase decomposition is a more complex set of few steps in which bimolecular routes assist further NO₂ production from reactive intermediate radicals. The second route, namely, intermolecular hydrogen transfer, is only possible if available hydrogen atoms are present on the ring substituents (-CH₃, -NH₂). Hence, although TNB is a very similar aromatic explosive to TNT and TATB, its decomposition is not likely to proceed via the above routes but instead lead primarily to unimolecular C-NO₂ homolysis step as evidenced by the similar activation energies for the gas and condensed phases. For non-aromatic explosives, such as RDX and PETN, that have no available hydrogen atoms the decomposition proceeds via unimolecular channels, namely homolytic cleavage of the weakest bond ($\Delta E^\ddagger_{(O-NO_2)}=46.5$ kcal/mol and $\Delta E^\ddagger_{(N-NO_2)}=41.5$ kcal/mol). Therefore, possible bimolecular routes discussed above, such as abstraction of hydrogen atoms and further NO₂ release, become irrelevant as bimolecular reactions are generally much slower. The full set of total energies for all transition states and intermediates including *para* reactions is included (Table 3 in the supporting information).

It is interesting to compare the above findings with possible ionic species that could be responsible for electronic excited state and ionic initiation mechanisms. Recently, Wang et al.⁷⁰ suggested that an intramolecular H-transfer from CH₃ to an *ortho* NO₂ group in TNT is

facilitated by ionization and leads to a decrease in activation energy of ~ 20 kcal/mol. It was additionally suggested by Kuklja et al.¹³ that electronic excitation promoted by lattice defects is a possible initiation mechanism in explosive solids. Thus, to assess the effects of ionization on the decomposition of TNT and related compounds, we calculated the activation energy for the unimolecular C-NO₂ cleavage channel of the radical cation and anion species. We find that ionization lowers the TNT molecule activation barrier by ~ 27 kcal/mol, similar to the routes discussed above. We also find that unlike TNT, the explosives RDX and PETN are prone to immediate decomposition ($\Delta E^\ddagger \sim 0$ kcal/mol) following ionization except for a cationic RDX with $\Delta E^\ddagger = 19.4$ kcal/mol. This implies that the aromaticity of nitroaromatic explosives maintains the stability of the ionic intermediates and neutral radicals and is also an important aspect for the stability of detonation carbon complexes as is further discussed in Section 5.2.

5.2 Carbon Clusters

In order to shed light on the initial rate of carbon clustering in TNT detonation we have calculated rates of formation of carbon clusters found in the simulations. Inspection of Fig. 4 shows that the clustering process is characterized by a rapid stage followed by a slow stage. To quantify the initial rates of formation of carbon clusters ($\tau_1, N_{C0,1}$), we fitted the time evolution plots of the average number of carbon atoms in clusters containing over 100 carbon atoms (Fig. 4) to a simple exponential rate law (Eq. 9), where $\langle N_C \rangle_0$ is the average initial amount of carbon atoms in a cluster.

$$(9) \quad \langle N_C \rangle(t) = \langle N_C \rangle_0 \exp\left(-\frac{t}{\tau}\right)$$

We stress that our simulations are probably too short to describe the clustering phenomena observed at timescales close to the end of a detonation^{42,71,72}, and obviously do not describe the isentropic expansion of the products because of the constant volume conditions in our simulations. Nevertheless, we can gain important insight into longer timescale phenomena occurring at the reaction zone of the detonation wave. Thus, we fit Eq. 6 to the time dependent atomic ratio plot O/C for the case of $0.7V_0$ in Fig. 5 to extract the rate constant for the slow stage ($\tau_2, N_{C0,2}$) of carbon clustering. We choose to follow the oxygen ratio since its relative amount is the largest compared to hydrogen and nitrogen. We have chosen the highly compressed case ($0.7V_0$) to represent the reaction zone of TNT. The fitting parameters are listed in Table 4.

Table 4: Fitted kinetic parameters for carbon clustering process at $0.7V_0$

T (K)	τ_1 (ps)	$N_{0,1}$ (atoms)	τ_2 (ps)	$N_{0,2}$ (ratio)
1800	11.79	2.77	3590.61	0.64
3500	2.38	84.88	368.35	0.55

As can be seen from the rate constants, the initial clustering process is characterized by timescales of tens of picoseconds, whereas the longer rate leads to hundreds and thousands of picoseconds of condensation process. We calculate the time needed to attain a cluster that is mainly composed of carbon atoms with low level of impurities of O, N and H by extracting the time needed to attain a cluster with an O/C ratio of 0.1 from Eq. 6 and using the τ_2 and $N_{0,2}$ rate constants. We obtain this time to be 1.05 ns for 3500K and 10.89 ns for 1800K; both are much longer than our simulations. We note that a recent theoretical study⁷³ of carbon nucleation and growth processes of model carbon systems under pressure at temperatures of 2000-5000K and densities 0.95-3.80 gr/cm^3 showed that the timescales associated with carbon condensation reactions are on the order of tens of nanoseconds, in good agreement with our results, and a similar result (10^{-7} - 10^{-8} s) was suggested by van Thiel and Ree⁴⁵ for detonation of TNT.

6 Summary and Conclusions

A comprehensive study based on ReaxFF-*lj* reactive molecular dynamics and DFT calculations was conducted to understand some major discrepancies in the reported mechanisms of thermal decomposition of nitroaromatic high explosives. TNT was used as a model aromatic explosive in the present study. It was found that the activation energy associated with thermal decomposition of condensed phase TNT is ~ 23 kcal/mol lower than the one expected based on values for the gas phase decomposition. This enhanced sensitivity of the solid exists also in the case of other nitroaromatic high explosives, provided they have labile hydrogen atoms on the aromatic ring or on its substituents. For example, thermal decomposition of condensed phase TATB has an activation energy lower by ~ 19 kcal/mol than expected based on the decomposition of a gas phase molecule. On the other hand, for explosives like TNB, RDX and PETN the activation energies in the condensed phase are almost identical to those of single molecule decomposition. It has been shown that this behavior is due to new bimolecular reaction channels present in the

condensed phase nitroaromatic explosives which promote and sensitize the unimolecular C-NO₂ cleavage channel, including intermolecular H-transfer routes with lower activation barriers compared to the gas phase. The crystalline structure is not essential for these bimolecular routes to be operational as is evident by the fact that liquid TNT exhibits very similar activation energy for thermal decomposition as the solid.³⁸ This findings is in contrast to previous assumptions of unimolecular decomposition of condensed phase TNT. Furthermore, the stability of the aromatic ring, even as a radical, is the main reason for the formation of large, high carbon content, clusters in the case of TNT, TNB and TATB. The sp² nature of the carbon atoms in the post detonation clusters suggest that they are mainly formed by aromatic ring agglomeration. The rate of formation of these clusters was shown to be in the range 0.3-10 ns, in good agreement with experimental data. This behavior is also in contrast to that of RDX, HMX and PETN where the thermal decomposition produces a variety of highly reactive radicals that mostly end in the form of stable products typically with sp³ hybridization and a much smaller amount of carbon clusters produced.

|

7 Acknowledgments

SZ and WAG were supported by the US ONR (N0014-12-1-0538 and N00014-09-1-0634). RK and YZ acknowledge partial support of The Center of Excellence for Explosives Detection, Mitigation and Response, Department of Homeland Security.

8 References

1. Ershov, A. P., Ionization During Detonation of Solid Explosives. *Fizika Goreniya i Vzryva* **1974**, *11*, 938-945.
2. van Duin, A. C.; Zeiri, Y.; Dubnikova, F.; Kosloff, R.; Goddard, W. A., 3rd, Atomistic-scale simulations of the initial chemical events in the thermal initiation of triacetoneperoxide. *J Am Chem Soc* **2005**, *127* (31), 11053-62.
3. Tarver, C. M., What is a shock wave to an explosive molecule? In *12th American Physical Society Topical Conference*, Atlanta, GA., 2001.
4. S. M. Walley, J. E. F. a. M. W. G., Crystal Sensitivities of Energetic Materials. *Materials Science and Technology* **2006**, *22*, 402-413.
5. Tarver, C. M.; Chidester, S. K.; Nichols, A. L., Critical conditions for impact- and shock-induced hot spots in solid explosives. *Journal of Physical Chemistry* **1996**, *100* (14), 5794-5799.
6. An, Q.; Liu, Y.; Zybin, S. V.; Kim, H.; Goddard, W. A., Anisotropic Shock Sensitivity of Cyclotrimethylene Trinitramine (RDX) from Compress-and-Shear Reactive Dynamics. *Journal of Physical Chemistry C* **2012**, *116* (18), 10198-10206.
7. da Silva, G.; Nakamura, N. M.; Iha, K., Kinetic Study of the Thermal Decomposition of Pentaerythritol-Tetranitrate (Petn). *Quimica Nova* **2008**, *31* (8), 2060-U160.
8. Chovancova, M.; Zeman, S., Study of initiation reactivity of some plastic explosives by vacuum stability test and non-isothermal differential thermal analysis. *Thermochimica Acta* **2007**, *460* (1-2), 67-76.
9. Lee, J. S.; Hsu, C. K.; Chang, C. L., A study on the thermal decomposition behaviors of PETN, RDX, HNS and HMX. *Thermochimica Acta* **2002**, *392*, 173-176.
10. Brill, T. B.; James, K. J., Kinetics and mechanisms of thermal decomposition of nitroaromatic explosives. *Chemical Reviews* **1993**, *93* (8), 2667-2692.
11. Rom, N.; Zybin, S. V.; van Duin, A. C.; Goddard, W. A.; Zeiri, Y.; Katz, G.; Kosloff, R., Density-Dependent Liquid Nitromethane Decomposition: Molecular Dynamics Simulations Based on ReaxFF. *J Phys Chem A* **2011**, *115* (36), 10181-202.
12. Zhang, L.; Zybin, S. V.; van Duin, A. C.; Dasgupta, S.; Goddard, W. A., 3rd; Kober, E. M., Carbon cluster formation during thermal decomposition of octahydro-1,3,5,7-tetranitro-1,3,5,7-tetrazocine and 1,3,5-triamino-2,4,6-trinitrobenzene high explosives from ReaxFF reactive molecular dynamics simulations. *J Phys Chem A* **2009**, *113* (40), 10619-40.
13. Kuklja, M. M.; Aduiev, B. P.; Aluker, E. D.; Krashenin, V. I.; Krechetov, A. G.; Mitrofanov, A. Y., Role of electronic excitations in explosive decomposition of solids. *Journal of Applied Physics* **2001**, *89* (7), 4156-4166.
14. Wu, Z. Q.; Kalia, R. K.; Nakano, A.; Vashishta, P., Vibrational and thermodynamic properties of beta-HMX: A first-principles investigation. *J Chem Phys* **2011**, *134* (20).
15. Byrd, E. F. C.; Scuseria, G. E.; Chabalowski, C. F., An ab initio study of solid nitromethane, HMX, RDX, and CL20: Successes and failures of DFT. *J Phys Chem B* **2004**, *108* (35), 13100-13106.

16. Miller, P. J.; Block, S.; Piermarini, G. J., Effects of Pressure on the Thermal-Decomposition Kinetics, Chemical-Reactivity and Phase-Behavior of Rdx. *Combustion and Flame* **1991**, *83* (1-2), 174-184.
17. Piermarini, G. J.; Block, S.; Miller, P. J., Effects of Pressure on the Thermal-Decomposition Rates, Chemical-Reactivity and Phase-Behavior of Hmx, Rdx and Nitromethane. *Chemistry and Physics of Energetic Materials* **1990**, *309*, 391-412.
18. Maksimov, Y. Y., Thermal Dissociation of Aromatic Polynitro Compounds in Vapors. *Zhurnal Fizicheskoi Khimii* **1972**, *46* (7), 1726-&.
19. L. M. Minier, K. R. B. a. J. C. O., Role of Intermolecular Reactions in Thermolysis of Aromatic Nitro Compounds in Supercritical Aromatic Solvents. *J. Org. Chem.* **1991**, *56*, 3306-3314.
20. L. L. Davis, K. R. B., Reactions of Organic Compounds in Explosive-Driven Shock Waves. *J. Phys. Chem.* **1996**, *100*, 18775-18783.
21. James, T. B. B. a. K. J., Thermal Decomposition of Energetic Materials. 62. Reconciliation of the Kinetics and Mechanisms of TNT on the Time Scale from Microseconds to Hours. *J. Phys. Chem.* **1993**, (97), 8759-8763.
22. Beckmann, J. W.; Wilkes, J. S.; Mcguire, R. R., 2,4,6-Trinitrotoluene Thermal-Decomposition - Kinetic-Parameters Determined by Isothermal Differential Scanning Calorimetry Technique. *Thermochimica Acta* **1977**, *19* (1), 111-118.
23. Stevenson, C. D. G., P. M.; Batz, M. L., Evidence of Carbenes in the Explosion Chemistry of Nitroaromatic Anion Radicals. *J. Org. Chem.* **1996**, (61), 5948.
24. (a) Steve, P., Fast Parallel Algorithms for Short-Range Molecular Dynamics. *Journal of Computational Physics* **1995**, *117* (1), 1-19; (b) LAMMPS. <http://lammps.sandia.gov>.
25. Frisch, M. J. T., G. W.; Schlegel, H. B.; Scuseria, G. E.; Robb, M. A.; Cheeseman, J. R.; Scalmani, G.; Barone, V.; Mennucci, B.; Petersson, G. A.; Nakatsuji, H.; Caricato, M.; Li, X.; Hratchian, H. P.; Izmaylov, A. F.; Bloino, J.; Zheng, G.; Sonnenberg, J. L.; Hada, M.; Ehara, M.; Toyota, K.; Fukuda, R.; Hasegawa, J.; Ishida, M.; Nakajima, T.; Honda, Y.; Kitao, O.; Nakai, H.; Vreven, T.; Montgomery, Jr., J. A.; Peralta, J. E.; Ogliaro, F.; Bearpark, M.; Heyd, J. J.; Brothers, E.; Kudin, K. N.; Staroverov, V. N.; Kobayashi, R.; Normand, J.; Raghavachari, K.; Rendell, A.; Burant, J. C.; Iyengar, S. S.; Tomasi, J.; Cossi, M.; Rega, N.; Millam, N. J.; Klene, M.; Knox, J. E.; Cross, J. B.; Bakken, V.; Adamo, C.; Jaramillo, J.; Gomperts, R.; Stratmann, R. E.; Yazyev, O.; Austin, A. J.; Cammi, R.; Pomelli, C.; Ochterski, J. W.; Martin, R. L.; Morokuma, K.; Zakrzewski, V. G.; Voth, G. A.; Salvador, P.; Dannenberg, J. J.; Dapprich, S.; Daniels, A. D.; Farkas, Ö.; Foresman, J. B.; Ortiz, J. V.; Cioslowski, J.; Fox, D. J. *Gaussian 09, Revision A.1*, 2009.
26. Cohen, R.; Zeiri, Y.; Wurzburg, E.; Kosloff, R., Mechanism of thermal unimolecular decomposition of TNT (2,4,6-trinitrotoluene): a DFT study. *J Phys Chem A* **2007**, *111* (43), 11074-83.
27. Liu, L.; Liu, Y.; Zybin, S. V.; Sun, H.; Goddard, W. A., ReaxFF-ig: Correction of the ReaxFF Reactive Force Field for London Dispersion, with Applications to the Equations of State for Energetic Materials. *J Phys Chem A* **2011**, *115* (40), 11016-22.
28. Strachan, A.; van Duin, A. C.; Chakraborty, D.; Dasgupta, S.; Goddard, W. A., 3rd, Shock waves in high-energy materials: the initial chemical events in nitramine RDX. *Phys Rev Lett* **2003**, *91* (9), 098301.
29. Brower, L. L. D. a. K. R., Shock-Initiation Chemistry of Nitroarenes. In *The 10th American Physical Society Topical Conference on Shock Compression of Condensed Matter*, Amhrest, Massachusetts, 27 Jul - 1 Aug 1997; pp 699-702.
30. Zhou, T. T.; Huang, F. L., Effects of defects on thermal decomposition of HMX via ReaxFF molecular dynamics simulations. *J Phys Chem B* **2011**, *115* (2), 278-87.
31. Strachan, A.; Kober, E. M.; van Duin, A. C.; Ongaard, J.; Goddard, W. A., Thermal decomposition of RDX from reactive molecular dynamics. *J Chem Phys* **2005**, *122* (5), 54502.
32. Chen, X.-F.; Liu, J.-F.; Meng, Z.-H.; Han, K.-L., Thermal unimolecular decomposition mechanism of 2,4,6-trinitrotoluene: a first-principles DFT study. *Theoretical Chemistry Accounts: Theory, Computation, and Modeling (Theoretica Chimica Acta)* **2010**, *127* (4), 327-344.

33. Rom, N., Hirshberg, B., Zeiri, Y., Furman, D., Zybin, S.V, Goddard III, W.A, and Kosloff, R., Hot Dense Liquid TNT Decomposition: Fragmentation, Kinetics and Carbon Clusters Formation. *In prep.* **2013**.
34. Cambridge Crystallographic Data Centre. <http://www.ccdc.cam.ac.uk>.
35. (a) Perdew, J. P.; Burke, K.; Ernzerhof, M., Generalized gradient approximation made simple (vol 77, pg 3865, 1996). *Phys Rev Lett* **1997**, *78* (7), 1396-1396; (b) Adamo, C.; Barone, V., Toward reliable density functional methods without adjustable parameters: The PBE0 model. *Journal of Chemical Physics* **1999**, *110* (13), 6158-6170.
36. Dunning, T. H., Gaussian-Basis Sets for Use in Correlated Molecular Calculations .1. The Atoms Boron through Neon and Hydrogen. *Journal of Chemical Physics* **1989**, *90* (2), 1007-1023.
37. Carper, W. R.; Davis, L. P.; Extine, M. W., Molecular-Structure of 2,4,6-Trinitrotoluene. *Journal of Physical Chemistry* **1982**, *86* (4), 459-462.
38. Golovina, N. I.; Titkov, A. N.; Raevskii, A. V.; Atovmyan, L. O., Kinetics and Mechanism of Phase-Transitions in the Crystals of 2,4,6-Trinitrotoluene and Benzotrifuroxane. *Journal of Solid State Chemistry* **1994**, *113* (2), 229-238.
39. Vrcelj, R. M.; Sherwood, J. N.; Kennedy, A. R.; Gallagher, H. G.; Gelbrich, T., Polymorphism in 2-4-6 trinitrotoluene. *Crystal Growth & Design* **2003**, *3* (6), 1027-1032.
40. Singh, G.; Kapoor, I. P. S.; Mannan, S. M.; Tiwari, S. K., Studies on energetic compounds Part XI: Preparation and thermolysis of polynitro organic compounds. *J Hazard Mater* **1999**, *68* (3), 155-178.
41. Ornellas, D. L., Calorimetric Determination of the Heat and Products of Detonation for Explosives: October 1961 to April 1982. **1982**, (UCRL-52821).
42. Chevrot, G.; Sollier, A.; Pineau, N., Molecular dynamics and kinetic study of carbon coagulation in the release wave of detonation products. *Journal of Chemical Physics* **2012**, *136* (8).
43. Manaa, M. R.; Reed, E. J.; Fried, L. E.; Goldman, N., Nitrogen-Rich Heterocycles as Reactivity Retardants in Shocked Insensitive Explosives. *J Am Chem Soc* **2009**, *131* (15), 5483-5487.
44. Victorov, S. B.; Gubin, S. A., A double-front structure of detonation wave as the result of phase transitions. *Shock Waves* **2006**, *15* (2), 113-128.
45. Vanthiel, M.; Ree, F. H., Properties of Carbon Clusters in Tnt Detonation Products - Graphite-Diamond Transition. *Journal of Applied Physics* **1987**, *62* (5), 1761-1767.
46. Chen, P. W.; Huang, F. L.; Yun, S. R., Characterization of the condensed carbon in detonation soot. *Carbon* **2003**, *41* (11), 2093-2099.
47. Satonkina, A. P. E. a. N. P., Investigation of the Reaction Zone in Heterogeneous Explosives Substances Using an Electrical Conductivity Method. *Combustion, Explosion and Shock Waves* **2009**, *45* (2), 205-210.
48. Hayes, B., On the Electrical Conductivity in Detonation Products. In *Proc. 4th Symp. (Int.) on Detonation (White Oak, 1965)*, Office of Naval Research, Washington (1967): 1967; pp 595-601.
49. Tarver, C. M.; McGuire, R. R.; Lee, E. L.; Wrenn, E. W.; Brein, K. R., The thermal decomposition of explosives with full containment in one-dimensional geometries. *Symposium (International) on Combustion* **1979**, *17* (1), 1407-1413.
50. Wemhoff, A. P.; Hsieh, H. *TNT Prout-Tompkins Kinetics Calibration with PSUADE*; UCRL-TR-230194; TRN: US2007222%967; 2007; pp Medium: ED; Size: PDF-file: 40 pages; size: 1.1 Mbytes.
51. Eyring, H., The Activated Complex in Chemical Reactions. *J Chem Phys* **1935**, *3* (2), 107-115.
52. Luft, G.; Recasens, F.; Velo, E., Chapter 3 Kinetic properties at high pressure. In *Industrial Chemistry Library*, Bertuccio, A.; Vetter, G., Eds. Elsevier: 2001; Vol. Volume 9, pp 65-140.
53. Jenner, G., High-pressure mechanistic delineation based on activation volumes. *Journal of Physical Organic Chemistry* **2002**, *15* (1), 1-13.
54. Bulusu, S. N.; North Atlantic Treaty Organization. Scientific Affairs Division., *Chemistry and physics of energetic materials*. Kluwer Academic ;

Sold and distributed in the U.S.A. and Canada by Kluwer Academic: Dordrecht ; Boston

Norwell, MA, U.S.A., 1990; p x, 764 p.

55. Peiris, S. M., *Static compression of energetic materials*. Springer: New York, 2008.
56. Piermarini, G. J.; Block, S.; Miller, P. J., Effects of Pressure on the Thermal-Decomposition Kinetics and Chemical-Reactivity of Nitromethane. *Journal of Physical Chemistry* **1989**, *93* (1), 457-462.
57. Citroni, M.; Bini, R.; Pagliai, M.; Cardini, G.; Schettino, V., Nitromethane Decomposition under High Static Pressure. *Journal of Physical Chemistry B* **2010**, *114* (29), 9420-9428.
58. Svatoopluk Zeman, T. A., Zdenek Friedl, Xue-Hai Ju, Accounts of the New Aspects of Nitromethane Initiation Reactivity. *Central European Journal of Energetic Materials* **2009**, *6* (1), 119-133.
59. Robertson, A. J. B., *Trans. Faraday Soc.* **1948**, (48).
60. Zinn, J., Rogers, R. N., Thermal Initiation of Explosives. *Journal of Physical Chemistry* **1962**, *66* (12), 2646-2653.
61. Rice B. M. , S. S., Owens F. J. , Density functional calculations of bond dissociation energies for NO₂ scission in some nitroaromatic molecules. *Journal of Molecular Structure (Theochem)* **2002**, *583*, 69-72.
62. Wu, C. J., Fried, L. E., First-Principles Study of High Explosive Decomposition Energetics. In *Eleventh International Detonation Symposium*, Snowmass, CO, 1998.
63. McGuire R. R., T. C. M., Chemical Decomposition Models for the Thermal Explosion of Confined HMX, TATB, RDX and TNT Explosives. In *Seventh Symposium (International) on Detonation; Naval Surface Weapons Center NSWC MP Annapolis, MD*, 1981; p 56.
64. Pexa, M.; Friedl, Z., Characterization of C-NO₂ Bonds in Nitroaromatic Compounds: A Bond Disproportionation Approach. *Central European Journal of Energetic Materials* **2010**, *7* (2), 131-144.
65. Rogers, R. N.; Janney, J. L.; Ebinger, M. H., Kinetic-Isotope Effects in Thermal Explosions. *Thermochimica Acta* **1982**, *59* (3), 287-298.
66. Cottrell, T. L.; Graham, T. E.; Reid, T. J., The thermal decomposition of nitromethane. *Transactions of the Faraday Society* **1951**, *47* (0), 584-590.
67. Ng, W. L.; Field, J. E.; Hauser, H. M., Study of Thermal-Decomposition of Pentaerythritol Tetranitrate. *Journal of the Chemical Society-Perkin Transactions 2* **1976**, (6), 637-639.
68. Tarver, C. M.; Tran, T. D., Thermal decomposition models for HMX-based plastic bonded explosives. *Combustion and Flame* **2004**, *137* (1-2), 50-62.
69. Gibbs, R. T., Popolato, A., *LASL explosive property data*. University of California: 1980.
70. Wang, B.; Wright, D.; Cliffl, D.; Haglund, R.; Pantelides, S. T., Ionization-Enhanced Decomposition of 2,4,6-Trinitrotoluene (TNT) Molecules. *Journal of Physical Chemistry A* **2011**, *115* (28), 8142-8146.
71. Viecelli, J. A.; Ree, F. H., Carbon clustering kinetics in detonation wave propagation. *Journal of Applied Physics* **1999**, *86* (1), 237-248.
72. Vitello, P., Fried, L.E., Glaesemann, K.R., Souers, C., Kinetic modeling of slow energy release in non-ideal carbon rich explosives. In *Thirteenth Symposium (International) on Detonation*, Norfolk, 2006; pp 465-475.
73. Pineau, N.; Souldard, L.; Los, J. H.; Fasolino, A., Theoretical study of the nucleation/growth process of carbon clusters under pressure. *Journal of Chemical Physics* **2008**, *129* (2).

Supporting Information

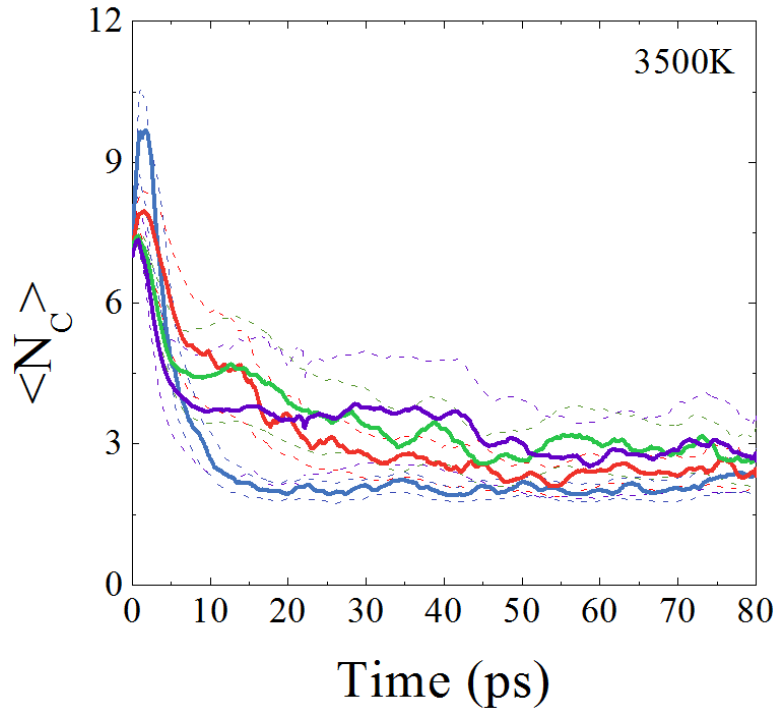
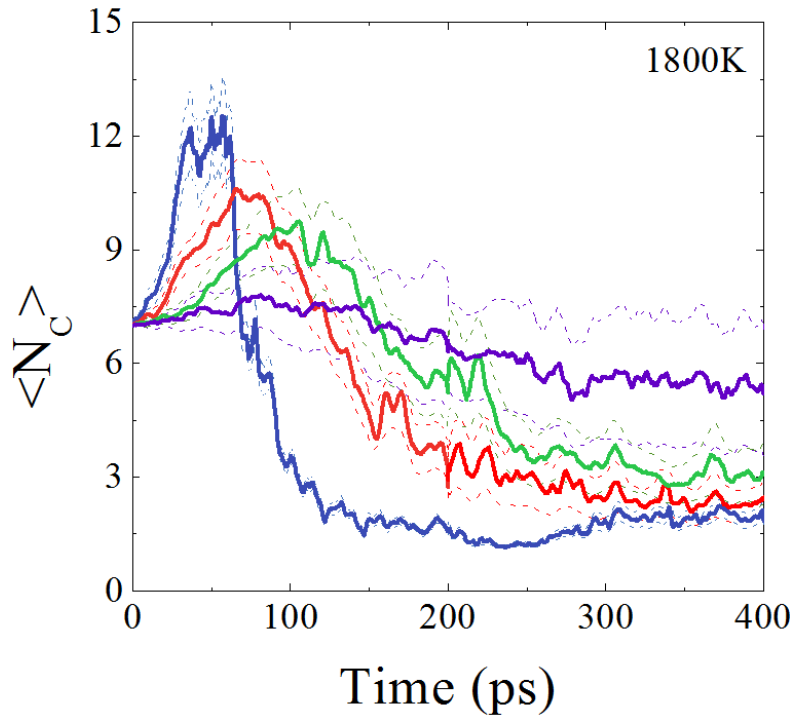


Figure 1: Average number of carbon atoms in a cluster containing up to 100 carbon atoms. Dashed lines show addition and subtraction of one standard deviation value.

Table 5: Parameters obtained by fitting an exponential function to the Potential energy time evolution curve for second stage decomposition (exothermic decay phase) and 1st order rate model to TNT decomposition curves (endothermic step)

T (K)	Super cell volume	τ_{exo} (ps)	ΔQ (cal/g)	t_{max} (ps)	U_0 (kcal/mol)	τ_{endo} (ps)
1800	V_0	256.0	-1304.0	49.8	-2688.4	42.9
2250		41.3	-1144.0	8.0	-2580.1	7.1
2500		22.0	-1092.58	5.3	-2553.3	3.0
3000		10.3	-1091.7	1.7	-2508.0	0.9
3500		5.6	-1095.8	0.7	-2459.5	0.4
1800	$0.9 V_0$	165.1	-1280.8	21.2	-2658.0	30.0
2250		34.2	-1191.4	5.2	-2589.4	6.8
2500		17.7	-1125.8	3.2	-2555.1	2.3
3000		8.6	-1129.4	1.3	-2513.8	0.9
3500		5.0	-1121.2	0.7	-2465.1	0.4
1800	$0.8 V_0$	101.0	-1266.6	11.8	-2639.3	21.5
2250		25.6	-1274.9	3.4	-2597.4	3.7
2500		13.3	-1170.1	2.8	-2561.3	1.9
3000		7.4	-1184.9	0.8	-2520.7	0.7
3500		4.3	-1119.9	0.5	-2467.5	0.3
1800	$0.7 V_0$	60.9	-1250.42	8.4	-2629.4	11.4
2250		18.4	-1370.2	2.4	-2591.1	3.0
2500		10.1	-1244.0	2.3	-2560.9	1.4
3000		5.6	-1514.8	0.8	-2517.3	0.5
3500		3.8	-1606.7	0.04	-2466.2	0.3

Scheme 14. Total energies (kcal/mol) for *ortho* TNT protonation (top part) and decomposition routes of NO₂-protonated TNT (C₆H₂(NO₂)₂(NOOH)CH₃) and TNT with a removed methylic hydrogen (C₆H₂(NO₂)₃CH₂) (bottom part)

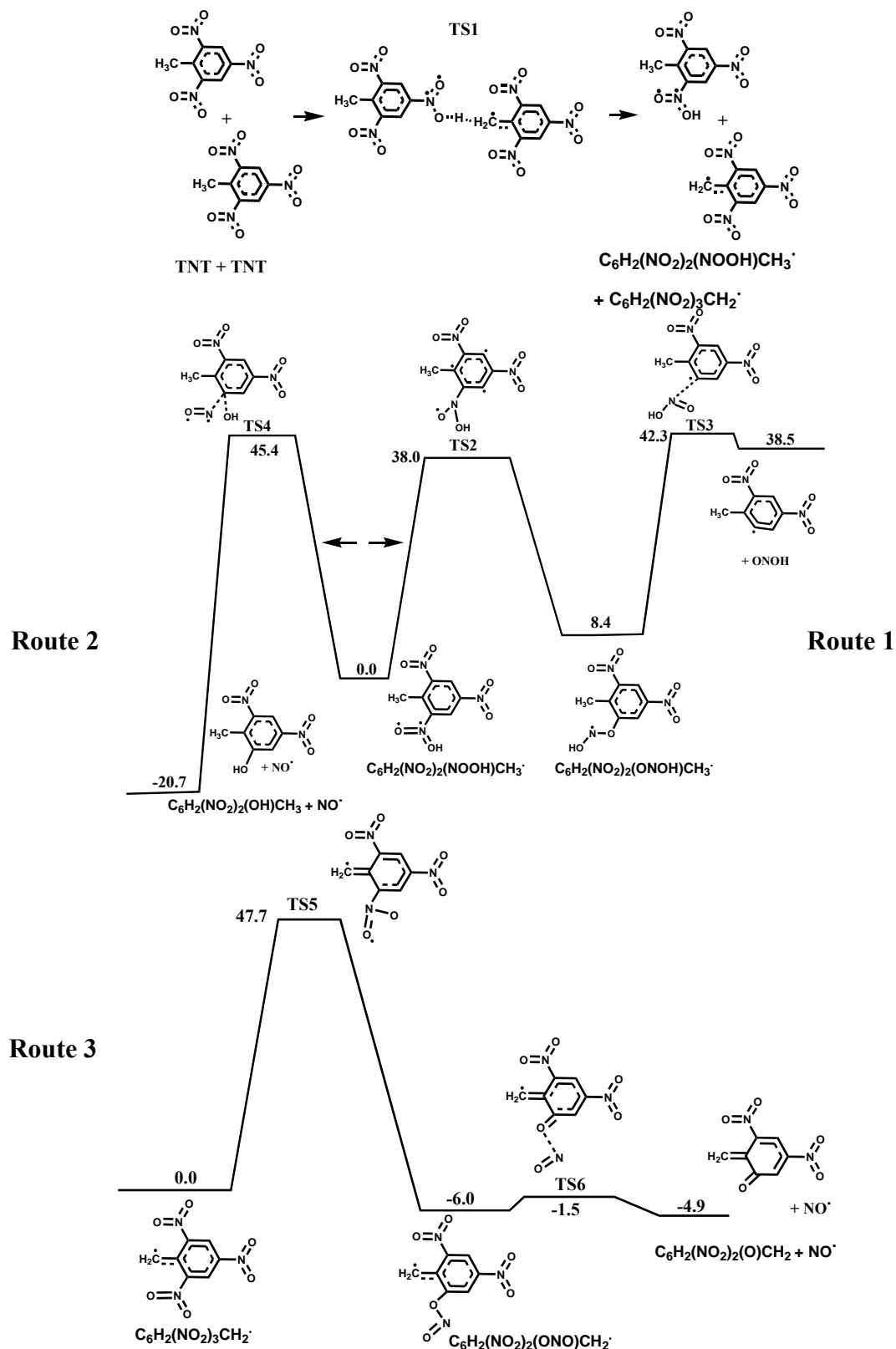


Table 2. Energy barriers and reaction energies, Functional: PBE1PBE, basis set: cc-pVDz, energy values in kcal/mol

Reaction	$\Delta E^\ddagger / \Delta E_{\text{react}}$
TNT... TNT \rightarrow TS1 \rightarrow C ₆ H ₂ (NO ₂) ₂ (NOOH)CH ₃ [•] + C ₆ H ₂ (NO ₂) ₃ CH ₂ [•]	43.0 / 43.6
C ₆ H ₂ (NO ₂) ₂ (NOOH)CH ₃ [•] (ortho)	
C ₆ H ₂ (NO ₂) ₂ (NOOH)CH ₃ [•] \rightarrow TS2 \rightarrow C ₆ H ₂ (NO ₂) ₂ (ONOH)CH ₃ [•]	38.0 / 8.4
C ₆ H ₂ (NO ₂) ₂ (ONOH)CH ₃ [•] \rightarrow TS3 \rightarrow C ₆ H ₂ (NO ₂) ₂ CH ₃ [•] + ONOH	33.9 / 30.1
C ₆ H ₂ (NO ₂) ₂ (NOOH)CH ₃ [•] \rightarrow TS4 \rightarrow C ₆ H ₂ (NO ₂) ₂ (OH)CH ₃ + NO [•]	45.4 / -20.7
C ₆ H ₂ (NO ₂) ₂ (NOOH)CH ₃ [•] (para)	
C ₆ H ₂ (NO ₂) ₂ (NOOH)CH ₃ [•] \rightarrow TS2 \rightarrow C ₆ H ₂ (NO ₂) ₂ (ONOH)CH ₃ [•]	44.2 / 10.2
C ₆ H ₂ (NO ₂) ₂ (ONOH)CH ₃ [•] \rightarrow TS3 \rightarrow C ₆ H ₂ (NO ₂) ₂ CH ₃ [•] + ONOH	35.1 / 34.3
C ₆ H ₂ (NO ₂) ₂ (NOOH)CH ₃ [•] \rightarrow TS4 \rightarrow C ₆ H ₂ (NO ₂) ₂ (OH)CH ₃ + NO [•]	47.8 / -15.8
C ₆ H ₂ (NO ₂) ₃ CH ₂ [•] (ortho)	
C ₆ H ₂ (NO ₂) ₃ CH ₂ [•] \rightarrow TS5 \rightarrow C ₆ H ₂ (NO ₂) ₂ (ONO)CH ₂ [•]	47.7 / -6.0
C ₆ H ₂ (NO ₂) ₂ (ONO)CH ₂ [•] \rightarrow TS6 \rightarrow C ₆ H ₂ (NO ₂) ₂ (O)CH ₂ + NO [•]	4.4 / 1.1
C ₆ H ₂ (NO ₂) ₃ CH ₂ [•] (para)	
C ₆ H ₂ (NO ₂) ₃ CH ₂ [•] \rightarrow TS5 \rightarrow C ₆ H ₂ (NO ₂) ₂ (O)CH ₂ + NO [•]	54.3 / -0.4

Table 3. DFT values of activation energies of NO₂ cleavage from TNT, RDX and PETN. For TNT *ortho* and *para* positions of NO₂ group are with respect to CH₃ group. For RDX the positions are with respect to removed H atom. Asterisk denotes a change in total energy (=bond dissociation energy) in cases where no transition state was found. - No H^{m/ar} indicates a methylic/aromatic hydrogen deficient molecule

Case		ΔE^\ddagger (kcal/mol) <i>ortho / para</i>
#1	TNT → TNT• + NO ₂ •	61.7* / 67.8*
#2	TNT• ⁺ → TNT ⁺ + NO ₂ •	34.4 / 42.1
#3	TNT• ⁻ → TNT ⁻ + NO ₂ •	59.2 / 66.4
#4	TNT-noH ^m → TNT + •TNT_noH ^m + NO ₂ •	59.0 / 89.4*
#5	TNT-noH ^{ar} → TNT + •TNT_noH ^{ar} + NO ₂ •	38.3 / 44.8
#6	RDX → RDX• + NO ₂ •	41.5*
#7	RDX• ⁺ → RDX ⁺ + NO ₂ •	19.4
#8	RDX• ⁻ → RDX ⁻ + NO ₂ •	-0.1
#9	RDX•-noH → RDX-noH + NO ₂ •	2.1 / 29.4
#10	PETN → PETN• + NO ₂ •	46.5*
#11	PETN• ⁺ → PETN ⁺ + NO ₂ •	0.1
#12	PETN• ⁻ → PETN ⁻ + NO ₂ •	0.3
#13	PETN•-noH → PETN•-noH (A) + NO ₂ •	-0.3
#14	PETN•-noH → PETN•-noH (B) + NO ₂ •	20.9

For cases #13 and #14: (A) refers to NO₂ cleavage from the same chain where H is absent and (B) refers to a cleavage from a different chain

ReaxFF-lg force field parameters used in this study:

39 ! Number of general parameters
50.0000 !Overcoordination parameter
9.4514 !Overcoordination parameter
30.0000 !Valency angle conjugation parameter
216.4305 !Triple bond stabilisation parameter
12.4838 !Triple bond stabilisation parameter
0.0000 !C2-correction
1.0701 !Undercoordination parameter
7.5000 !Triple bond stabilisation parameter
11.9083 !Undercoordination parameter
13.3822 !Undercoordination parameter
-10.4637 !Triple bond stabilization energy
0.0000 !Lower Taper-radius
10.0000 !Upper Taper-radius
2.8793 !Not used
33.8667 !Valency undercoordination
3.5895 !Valency angle/lone pair parameter
1.0563 !Valency angle
2.0384 !Valency angle parameter
6.1431 !Not used
6.9290 !Double bond/angle parameter
0.0283 !Double bond/angle parameter: overcoord
0.0570 !Double bond/angle parameter: overcoord
-2.4837 !Not used
5.8374 !Torsion/BO parameter
10.0000 !Torsion overcoordination
1.8820 !Torsion overcoordination
-1.2327 !Conjugation 0 (not used)
2.1861 !Conjugation
1.5591 !vdWaals shielding
0.0100 !Cutoff for bond order (*100)
5.2216 !Valency angle conjugation parameter
3.4021 !Overcoordination parameter
38.5241 !Overcoordination parameter
2.1533 !Valency/lone pair parameter
0.5000 !Not used
20.0000 !Not used
5.0000 !Molecular energy (not used)
2.0000 !Version number
6.5560 !Valency angle conjugation parameter
4 ! Nr of atoms; cov.r; valency;a.m;Rvdw;Evdw;gammaEEM;cov.r2;#
 alfa;gammavdW;valency;Eunder;Eover;chiEEM;etaEEM;n.u.
 cov r3;Elp;Heat inc.;n.u.;n.u.;n.u.;n.u.
 ov/un;val1;n.u.;val3,vval4
C 1.3742 4.0000 12.0000 1.9684 0.1723 0.8712 1.2385 4.0000
9.4606 2.1346 4.0000 31.0823 79.5548 5.7254 6.9235 0.0000
1.2104 0.0000 183.7012 5.7419 33.3951 11.9957 0.8563 0.0000
-2.8983 2.5000 1.0564 4.0000 2.9663 0.0000 0.0000 0.0000
0.0001 1.9255

H 0.6867 1.0000 1.0080 1.3525 0.0616 0.8910 -0.1000 1.0000
9.3858 5.0013 1.0000 0.0000 121.1250 3.8446 10.0839 1.0000
-0.1000 0.0000 58.4228 3.8461 3.2540 1.0000 1.0698 0.0000
-15.7683 2.1504 1.0338 1.0000 2.8793 0.0000 0.0000 0.0000
0.0001 1.4430

O 1.3142 2.0000 15.9990 1.9741 0.0880 0.8712 1.1139 6.0000
10.2186 7.7719 4.0000 29.5271 116.0768 8.5000 7.1412 2.0000
0.9909 14.9473 69.2812 9.1371 1.6258 0.1863 0.9745 0.0000
-3.5965 2.5000 1.0493 4.0000 2.9225 0.0000 0.0000 0.0000
623.8417 1.7500

N 1.2450 3.0000 14.0000 1.9951 0.1088 1.0512 1.1911 5.0000
9.9303 7.8431 4.0000 32.4758 100.0000 6.7768 6.8035 2.0000
1.0636 0.1045 128.0119 2.1604 2.9464 2.5181 0.9745 0.0000
-4.0959 2.0047 1.0183 4.0000 2.8793 0.0000 0.0000 0.0000
1240.001 1.8300

10 ! Nr of bonds; Edis1;LPpen;n.u.;pbe1;pbo5;13corr;pbo6
pbe2;pbo3;pbo4;Etrip;pbo1;pbo2;ovcorr

1 1 141.9346 113.4487 67.6027 0.1554 -0.3045 1.0000 30.4515 0.4283
0.0801 -0.2113 8.5395 1.0000 -0.0933 6.6967 1.0000 0.0000

1 2 163.6889 0.0000 0.0000 -0.4525 0.0000 1.0000 6.0000 0.5921
12.1053 1.0000 0.0000 1.0000 -0.0097 8.6351 0.0000 0.0000

2 2 169.8421 0.0000 0.0000 -0.3591 0.0000 1.0000 6.0000 0.7503
9.3119 1.0000 0.0000 1.0000 -0.0169 5.9406 0.0000 0.0000

1 3 164.0476 117.4881 72.1261 -0.6031 -0.1795 1.0000 14.9755 0.5413
1.2626 -0.3063 7.0000 1.0000 -0.1588 4.5000 0.0000 0.0000

3 3 110.4748 155.6441 40.0000 0.1150 -0.1054 1.0000 28.5221 0.2000
0.9590 -0.2635 8.5715 1.0000 -0.1007 6.8548 1.0000 0.0000

1 4 130.7147 175.2276 97.2523 -0.0368 -0.4942 1.0000 26.7545 0.5133
0.3296 -0.3653 7.0000 1.0000 -0.1171 5.1025 1.0000 0.0000

3 4 85.4950 114.0081 70.1453 0.5778 -0.1070 1.0000 16.6611 0.2339
0.3474 -0.1948 8.3762 1.0000 -0.1089 5.8148 1.0000 0.0000

4 4 157.7518 67.1322 160.9732 -0.5869 -0.1824 1.0000 12.0000 0.7136
0.8204 -0.1657 10.6490 1.0000 -0.0967 4.5976 1.0000 0.0000

2 3 224.3076 0.0000 0.0000 -0.6280 0.0000 1.0000 6.0000 1.0000
5.0050 1.0000 0.0000 1.0000 -0.0512 5.1982 0.0000 0.0000

2 4 212.1772 0.0000 0.0000 -0.3585 0.0000 1.0000 6.0000 0.3316
10.4316 1.0000 0.0000 1.0000 -0.0658 6.4545 0.0000 0.0000

6 ! Nr of off-diagonal terms; Ediss;Ro;gamma;rsigma;rpi;rpi2

1 2 0.0464 1.8296 10.1311 1.0029 -1.0000 -1.0000

2 3 0.0375 1.7275 10.8037 0.8813 -1.0000 -1.0000

2 4 0.0509 1.7672 10.4261 0.9990 -1.0000 -1.0000

1 3 0.1036 1.8869 9.5668 1.3590 1.1099 1.1534

1 4 0.1971 1.7356 10.0734 1.2754 1.2113 1.1172

3 4 0.0535 1.6709 10.8180 1.2968 1.1416 1.0167

42 ! Nr of angles;at1;at2;at3;Thetao;o;ka;kb;pv1;pv2

1 1 1 74.0317 32.2712 0.9501 0.0000 0.1780 10.5736 1.0400

1 1 2 70.6558 14.3658 5.3224 0.0000 0.0058 0.0000 1.0400

2 1 2 76.7339 14.4217 3.3631 0.0000 0.0127 0.0000 1.0400

1 2 2 0.0000 0.0000 6.0000 0.0000 0.0000 0.0000 1.0400

1 2 1 0.0000 3.4110 7.7350 0.0000 0.0000 0.0000 1.0400

2 2 2 0.0000 27.9213 5.8635 0.0000 0.0000 0.0000 1.0400

1	1	3	65.3104	6.3897	7.5000	0.0000	0.2000	10.0000	1.8525	
3	1	3	71.9855	28.5708	6.4252	0.0000	0.2000	0.0000	1.8525	
1	1	4	65.8892	45.0000	1.6598	0.0000	0.2000	10.0000	1.8525	
3	1	4	73.1057	25.8227	4.2145	0.0000	0.2000	0.0000	1.8525	
4	1	4	65.8759	40.9838	2.4369	0.0000	0.2000	0.0000	1.8525	
2	1	3	56.3039	17.3681	5.3095	0.0000	0.9110	0.0000	1.0400	
2	1	4	71.5505	11.1820	3.7129	0.0000	0.9110	0.0000	1.0400	
1	2	4	0.0000	0.0019	6.3000	0.0000	0.0000	0.0000	1.0400	
1	3	1	72.3642	37.8942	1.1566	0.0000	0.7472	0.0000	1.2639	
1	3	3	90.0000	45.0000	0.5719	0.0000	0.7472	0.0000	1.2639	
1	3	4	70.4313	14.4055	7.1593	0.0000	0.7472	0.0000	1.2639	
3	3	3	83.8833	23.3345	2.3433	-10.0000	0.7472	0.0000	1.2639	
3	3	4	84.0407	45.0000	1.0695	0.0000	0.7472	0.0000	1.2639	
4	3	4	73.9966	24.4410	5.2760	0.0000	0.7472	0.0000	1.2639	
1	3	2	89.1394	37.0874	0.3849	0.0000	3.0000	0.0000	1.2618	
2	3	3	80.7068	5.0854	5.7151	0.0000	3.0000	0.0000	1.2618	
2	3	4	76.0238	45.0000	0.8637	0.0000	3.0000	0.0000	1.2618	
2	3	2	82.3474	13.5165	3.4896	0.0000	0.3596	0.0000	1.3307	
1	4	1	68.4330	19.3525	2.1625	0.0000	1.7325	0.0000	1.0440	
1	4	3	86.2893	37.5587	1.2660	0.0000	1.7325	0.0000	1.0440	
1	4	4	74.2404	12.0547	7.5000	0.0000	1.7325	0.0000	1.0440	
3	4	3	78.5566	43.8492	1.3351	-26.1471	1.7325	40.0000	1.0440	
3	4	4	77.4239	33.7297	1.7944	-0.9193	1.7325	0.0000	1.0440	
4	4	4	64.9107	17.5558	7.5000	0.0000	1.7325	0.0000	1.0440	
1	4	2	90.0000	32.0540	0.7195	0.0000	0.5355	0.0000	2.5279	
2	4	3	84.1185	45.0000	1.3826	0.0000	0.5355	0.0000	2.5279	
2	4	4	78.7133	24.6250	3.8202	0.0000	0.5355	0.0000	2.5279	
2	4	2	56.3036	14.1532	3.3914	0.0000	0.2000	0.0000	2.1689	
1	2	3	0.0000	0.0019	6.0000	0.0000	0.0000	0.0000	1.0400	
1	2	4	0.0000	0.0019	6.0000	0.0000	0.0000	0.0000	1.0400	
1	2	5	0.0000	0.0019	6.0000	0.0000	0.0000	0.0000	1.0400	
3	2	3	0.0000	0.0019	6.0000	0.0000	0.0000	0.0000	1.0400	
3	2	4	0.0000	0.0019	6.0000	0.0000	0.0000	0.0000	1.0400	
4	2	4	0.0000	0.0019	6.0000	0.0000	0.0000	0.0000	1.0400	
2	2	3	0.0000	0.0019	6.0000	0.0000	0.0000	0.0000	1.0400	
2	2	4	0.0000	0.0019	6.0000	0.0000	0.0000	0.0000	1.0400	
17	! Nr of torsions;at1;at2;at3;at4;;V1;V2;V3;V2(BO);vconj;n.u;n									
1	1	1	1	0.0000	48.4194	0.3163	-8.6506	-1.7255	0.0000	0.0000
1	1	1	2	0.0000	63.3484	0.2210	-8.8401	-1.8081	0.0000	0.0000
2	1	1	2	0.0000	45.2741	0.4171	-6.9800	-1.2359	0.0000	0.0000
0	1	2	0	0.0000	0.0000	0.0000	0.0000	0.0000	0.0000	0.0000
0	2	2	0	0.0000	0.0000	0.0000	0.0000	0.0000	0.0000	0.0000
0	1	3	0	-0.0002	85.8794	0.3236	-3.8134	-2.0000	0.0000	0.0000
0	2	3	0	0.0000	0.1000	0.0200	-2.5415	0.0000	0.0000	0.0000
0	3	3	0	-0.9667	116.4743	0.0002	-4.9422	0.0000	0.0000	0.0000
0	1	4	0	-0.0069	150.0000	0.4891	-7.4921	-2.0000	0.0000	0.0000
0	2	4	0	0.0000	0.1000	0.0200	-2.5415	0.0000	0.0000	0.0000
0	3	4	0	1.6745	56.6301	-0.0008	-4.5064	-2.0000	0.0000	0.0000
0	4	4	0	1.1253	75.3447	0.0080	-9.0000	-2.0000	0.0000	0.0000
0	1	1	0	0.0930	18.5962	0.0002	-9.0000	-1.0000	0.0000	0.0000
4	1	4	4	-2.0000	20.8732	-1.5000	-9.0000	-2.0000	0.0000	0.0000

1	1	3	3	-0.0002	21.5452	0.1727	-9.0000	-2.0000	0.0000	0.0000
1	3	3	1	0.0002	79.3777	-1.5000	-5.2139	-2.0000	0.0000	0.0000
3	1	3	3	-1.3476	22.4932	1.5000	-9.0000	-2.0000	0.0000	0.0000
4	! Nr of hydrogen bonds;at1;at2;at3;Rhb;Dehb;vhb1									
3	2	3		2.0000	-5.0000	3.0000	3.0000			
3	2	4		1.7753	-5.0000	3.0000	3.0000			
4	2	3		1.3884	-5.0000	3.0000	3.0000			
4	2	4		1.6953	-4.0695	3.0000	3.0000			

Cutoff of bond orders used for post-analysis of molecular species:

C	N	0.3
C	C	0.55
C	O	0.65
C	H	0.4
O	O	0.65
N	O	0.40
O	H	0.4
H	H	0.55
H	N	0.55
N	N	0.55

Development of Simulants of Hydrogen Peroxide Based Explosives for use by Canine and IMS Detectors

José Almirall, Ph.D., *Department of Chemistry and Biochemistry and International Forensic Research Institute, Florida International University, Miami, FL*

I. Objective

The objective of this effort is to develop an improved field instrument system for the detection of explosive odors based on ion mobility spectrometry (IMS). The PI and co-workers have previously described the composition of the volatile and semi-volatile chemical compounds that are characteristic of several drugs of abuse and chemical explosives in order to assist the design and application of canine detection training aids. The PI has also developed **pre-concentration** and **sampling** devices based on Solid Phase Microextraction (SPME) for the capture of extremely small quantities of the volatile compounds (on the order of ng) for subsequent detection using IMS using an in-house developed interface (patent pending). The current effort investigates home-made explosives (HME) detection, particularly explosives based on hydrogen peroxide (HP). This proposal aims to characterize the odor signatures of a set of samples from HP-based explosives, some of which will be provided by the University of Rhode Island Center of Excellence, in order to improve the detection of this threat using IMS instruments. The existing large installed base of > 12,000 IMS instruments make this technology viable as a crime scene detection tool and the already proven use of detection canine teams also makes this approach a viable alternative to instrumental detectors. The project team will continue to characterize the odor signature compounds of HP-based explosives and provide the chemical data to the URI center collaborators. The results will also be used to target compounds that can be used for 1) IMS detection and 2) canine detection. The identification of these compounds will assist future researchers interested in detection of HP-based explosives. Additionally, the effort will continue to develop a planar-SPME device specifically designed and optimized to extract the volatile odor signature compounds associated with HP-based explosives. Finally, the existing IMS operating parameters will be investigated to work towards an unambiguous identification of the target compounds of the HP-based explosives by coupling an IMS instrument with a mass spectrometer of high sensitivity to better investigate the composition of the ion swarms in the IMS experiment. An already existing ESI-IMS-MS instrument in our laboratory will be used in this research along with the more traditional techniques of SPME-GC-MS and SPME-IMS already developed in our lab.

II. Accomplishments

A manuscript describing the results of the analysis of TATP using PSPME coupled to IMS was published in a very good quality analytical chemistry journal (attached).

W Fan, M Young, J Canino, J Smith, J Oxley, and **JR Almirall***, Fast Detection of Triacetone Triperoxide (TATP) from Headspace using Planar Solid Phase Microextraction (PSPME) Coupled to an IMS Detector, *Anal. and Bio. Chem.* **2012**, DOI 10.1007/s00216-012-5878-x.

A second manuscript describing a novel calibration strategy for adsorption of volatiles using a vaporjet generator was submitted to the same journal (JABC) and the reviewers requested minor changes to the manuscript. The revised manuscript was recently submitted for consideration. The manuscript is entitled:

M Young, W Fan, and **JR Almirall***, Calibration of Planar Solid Phase Microextraction (PSPME) Using Controlled Vapor Generation Followed by Ion Mobility Spectrometry (IMS) Detection, *Anal. and Bio. Chem.* **2013**, submitted.

A third manuscript has been completed and will be submitted before the end of April 2013. The manuscript is entitled:

W. Fan and JR Almirall, Fast detection of explosives by using capillary microextractor of volatiles (CMV) coupled with gas chromatography – mass spectrometer (GC-MS).

III. Students Supported

Mimy Young: PhD in Chemistry

Wen Fan: PhD in Chemistry

IV. Conference Presentations

Mimy Young, Anna Raeva, "Development of Receiver Operating Characteristic (ROC) Curves for Explosives Detection for Different Sampling and Detection Techniques." Gordon Research Conferen 2013, May 26-31, 2013 (Les Diablerets, Switzerland).

Anna Raeva Wen Fan, Mimy Young and Jose Almirall, Determination of true and false positive explosives detection rates using planar solid phase microextraction (PSPME) non-contact sampling coupled to ion mobility spectrometry (IMS), Trace Explosives Detection Conference (TED), April 18-12, 2013, Philadelphia, PA.

Wen Fan, Mimy Young and Jose Almirall "Fast Detection of Peroxide Explosives Using Planar Solid Phase Microextraction (PSPME) Coupled to Ion Mobility Spectrometers (IMS)" 2013 Florida International University Scholarly Forum, Mar 25-26, 2013, Miami, FL

Mimy Young, Wen Fan and Jose Almirall "Evaluation and Comparison of Planar Solid Phase Microextraction (PSPME) with Other Substrates for Headspace Sampling of Cocaine and MDMA Coupled to Ion Mobility Spectrometry." FIU Scholarly Forum, March 25-26, 2013 (Miami, FL).

Wen Fan, Mimy Young and Jose Almirall "Fast Detection of Peroxide Explosives Using Planar Solid Phase Microextraction (PSPME) Coupled to Ion Mobility Spectrometers (IMS)" Second Annual Forensic Science Symposium, Mar 14-15, 2013, Miami, FL

Wen Fan, Mimy Young and Jose Almirall "Fast Detection of Peroxide Explosives Using Planar Solid Phase Microextraction (PSPME) Coupled to Ion Mobility Spectrometers (IMS)" International Society of Ion Mobility Spectrometry Conference, July 22-26, 2012, Orlando, FL

Mimy Young, Wen Fan and Jose Almirall "Evaluation and Comparison of Planar Solid Phase Microextraction (PSPME) with Other Substrates for Headspace Sampling of Cocaine and MDMA Coupled to Ion Mobility Spectrometry." International Conference on Ion Mobility Spectrometry, July 22-26, 2012 (Orlando, FL).

April 2012. Field Detection of Hydrogen Peroxide Based Explosives Using SPME-GC-MS and PSPME-IMS, Department of Homeland Security Center of Excellence at the University of Rhode Island, Providence, RI (PA, **Invited Oral**)

March 2012. Rapid Instrumental Detection of Explosives and Drugs in the Field, in New Developments in Forensic Chemistry for use at the Crime Scene and in the Laboratory Symposium, Pittsburgh Conference, Orlando, FL (PA, **Invited Oral** and Symposium Organizer)

February 2012. Field Detection of Drugs and Explosives by SPME-IMS and PSPME-IMS, Forensic Science Without Borders Symposium - NIJ Grantees Meeting, American Academy of Forensic Sciences Meeting, Atlanta, GA (PA, **Invited Oral**)

September 2011. NFSTC Technology Transition Workshop; PSPME for the Analysis of Drugs and Explosives, Largo, FL (PA, **Workshop Organizer**)

June 2011. Performance Evaluation and Calibration of Planar Solid Phase Microextraction (PSPME) Using Vapors of Standards Followed by Ion Mobility Spectrometry (IMS) Detection, Gordon Research Conference on the Analysis of Illicit Substances, Lucca, Italy (PA, Poster)

June 2011. Headspace Profiling of Volatile Compounds from Explosives Using Planar Solid Phase Microextraction (PSPME) Followed by Ion Mobility Spectrometer (IMS) Detection Gordon Research Conference on Illicit Substances, Lucca, Italy (SP, Poster)

June 2011. Fast Detection of Triacetone Triperoxide (TATP) from Headspace using Planar Solid Phase Microextraction (PSPME) Coupled to an Ion Mobility Spectrometer Detector, Gordon Research Conference on Illicit Substances, Lucca, Italy (SP, Poster)

Commercialization Efforts:

The developed PSPME technology has been licensed to Field Forensics Inc. (<http://www.fieldforensics.com>) and marketed as FAST[®] in 2012.

1 **Calibration of Planar Solid Phase**
2 **Microextraction (PSPME) Using Controlled**
3 **Vapor Generation Followed by Ion Mobility**
4 **Spectrometry (IMS) Detection**

5 Mimy Young, Wen Fan, and Jose R. Almirall*

6

7 *Department of Chemistry and Biochemistry and International*

8 *Forensic Research Institute, Florida International University,*

9 *11200 SW 8th St. OE 116A,*

10 *Miami, FL 33199, USA*

11 almirall@fiu.edu

12

13 **Abstract** Planar solid phase microextraction (PSPME) is used as a sampling and preconcentration
14 device for the extraction of volatile chemical compounds found in the headspace above illicit
15 drugs and explosives. The PSPME calibration was accomplished by delivering very small
16 quantities (~ 90 pg) of target analytes onto a heated ceramic to deliver a controlled amount of the
17 standards, in the gas phase, for subsequent collection by the PSPME device. The planar disk
18 geometry allows for the use of commercially available ion mobility spectrometry (IMS)
19 instruments to be used as a detector without further modification. Several volatile chemical
20 compounds found in the headspace above explosives such as diphenylamine (DPA), ethyl
21 centralite (EC), 2,4,6-trinitrotoluene (TNT), 2,4-dinitrotoluene (2,4-DNT) and triacetone
22 triperoxide (TATP) as well as vapors associated with the illicit drugs cocaine (methyl benzoate)
23 and 3,4-methylenedioxymethamphetamine (MDMA) (piperonal) were used to determine the
24 extraction recoveries and the limits of detection of the PSPME coupled with IMS. Limits of
25 detection (LOD) for vapors of explosives TNT, DNT, DPA, and EC using a PSPME substrate as
26 well as vapors associated to illicit drugs methyl benzoate and piperonal resulted in the sub-
27 nanogram to nanogram range (0.5 – 24 ng for explosives and 3 – 14 ng for illicit drugs).
28 Extraction recovery of the PSPME varied from ~7 to ~24% depending on the analyte of interest.

29 **Keywords** *Planar solid phase microextraction (PSPME), Ion mobility spectrometer (IMS),*
30 *explosives, vapor calibration, piezoelectric microdrop printing technology*

31

32 * Corresponding Author

1 Introduction

2 Solid-phase microextraction (SPME) has proven to be a sensitive method for
3 sampling and preconcentration of a wide range of volatile and semi-volatile target
4 analytes in a wide range of applications [1-3] when coupled to a gas
5 chromatograph inlet. Our group has previously reported the utility of sol-gel
6 polydimethylsiloxane (PDMS) coated disks, referred to as planar solid phase
7 microextraction (PSPME), as a sampling and preconcentration device and coupled
8 to the inlet of an ion mobility spectrometer [4,5], offering non-contact vapor
9 preconcentration, rather than direct swabbing of residues offering lower false
10 positive in high throughput environments. The PSPME disk geometry has been
11 shown [6] to offer surface area increases ($> 15,000X$) over the widely accepted
12 solid-phase microextraction resulting in significant improvements in extraction
13 performance and lower sampling times for the same conditions [3,7,8]. The use
14 of this planar disk geometry allows commercial off-the-shelf (COTS) ion mobility
15 spectrometry (IMS) instruments to be used as detectors of the extracted target
16 volatiles without further modification.

17 In order to evaluate the performance of the PSPME device, a means of
18 generating reliable amounts of standards is required. Calibration and quantitation
19 methods for solid phase microextraction (SPME) have been proposed [9,10] as a
20 non-exhaustive extraction due to the low sample volume [9,11], where the phase
21 volume of the SPME fiber is negligible. The improved sensitivity in detectors
22 also increases the demand for sub-nanoliter microdispensing chemical assays and
23 vapor generation. A vapor generator that can accurately deliver trace amounts of
24 volatile organic compounds (VOCs) of explosives and illicit drugs into the
25 headspace will be used to calibrate the newly developed PSPME preconcentration
26 devices.

27 Great efforts have been made to generate consistent vapors of various
28 compounds for landmine determination [12], environmental chemical monitoring
29 [13], explosives detection [14-17] and sensor calibration [18] through the past
30 decades. One technique such as Controlled Odor Mimic Permeation Systems
31 (COMPS) uses a thin plastic film to release vapors generated from the solid
32 compounds into the headspace at a fixed rate [19,20]. Another technique has been
33 developed especially for explosives with low vapor pressure, such as 1,3,5-
34 trinitroperhydro-1,3,5-triazine (RDX), 2,4,6-trinitrotoluene (TNT) and

1 pentaerythritol tetranitrate (PETN) [21]. This explosive vapor generation device
2 has proven to be suitable for generating controlled vapor for explosive analysis at
3 elevated temperatures for low vapor pressure explosives; however, the device
4 requires a large amount of explosive solids to perform the calibration.

5 Piezoelectric nozzles, a similar technology to that used in ink-jet printers, have
6 been used for precise picoliter volume depositions on a surface [18]. Uniform-
7 sized microdrops with well-defined trajectories and known amounts of volume
8 can be delivered by the user in amounts as low as 1 drop to a rapid, steady stream
9 of drops at will [22]. The drop volume can be determined by gravimetric methods
10 as well as by imaging the droplet morphology and dispensing dynamics [23,24].
11 Various piezoelectric delivery devices are currently commercially available for
12 the evaluation of trace detectors in part-per-trillion levels using liquid standards;
13 however, in order to appropriately evaluate a vapor collecting device, a calibrator
14 for generating and extracting vapors is needed. A home-built design by
15 Verkouteren et al. [18,25] from the National Institute of Standards and
16 Technology (NIST) utilizes the technology of the piezoelectric microdispenser
17 with a heated ceramic plate for generating precisely controlled amounts of vapors.
18 Similar to the technology at NIST, a commercial instrument developed by
19 MicroFab Technologies also allows users to generate precise amount of vapors for
20 research purposes. The heating element is set to a temperature above the boiling
21 points of the solvent and the analytes of interest in order to generate the analyte
22 vapors.

23 In this study, a commercial piezoelectric trace vapor generator was used to
24 deliver picoliter quantities of target analyte mass in the form of a vapor, allowing
25 precise control of known amounts of vapors to be released and subsequently
26 extracted by the PSPME, for the evaluation of the mass calibration and extraction
27 performance of vapors in PSPME devices coupled to ion mobility spectrometry
28 (IMS) systems. Compounds of interest include explosives such as 2,4,6-
29 trinitrotoluene (TNT) and triacetone triperoxide (TATP) as well as volatile
30 chemical markers found in smokeless powders such as 2,4-dinitrotoluene (2,4-
31 DNT), diphenylamine (DPA) and ethyl centralite (EC). These volatile chemical
32 compounds provide the identification of smokeless powders which are typically
33 used as improvised explosives [26] and will be used as a model for explosives
34 detection. Reduced mobility, boiling points and vapor pressures for the

1 compounds of interest are listed in Table 1. Signature volatile vapors associated
2 with the illicit drugs cocaine (methyl benzoate) and MDMA (piperonal) were also
3 targeted as volatile chemical markers associated to the illicit drug [27,28]. This
4 evaluation and calibration method can also assist in the fabrication of training aids
5 of illicit drugs and explosives for detector canines.

6 **Experimental**

7 **Instrumentation**

8 A Jetlab[®] 4 (MicroFab Technologies Inc., Plano, Texas) Microdrop printing
9 instrument was used to deliver picoliter volumes of standard solutions on a
10 PSPME device. The VaporJet Calibrator (MicroFab Technologies Inc., Plano,
11 Texas) vapor generator was used to deliver very small quantities of target analyte
12 mass in the form of a vapor, collected by a PSPME device at the opening of the
13 chamber. Both instruments utilize piezoelectric orifice nozzles for delivery of
14 picoliter volumes of standard solutions. For the microdrop printing experiments
15 performed on the JetLab[®] 4, a 60- μ m piezoelectric orifice device was used
16 whereas the vapor generator was configured with a 40- μ m piezoelectric orifice
17 nozzle. Microdrop printing conditions were optimized by using 2-butanol as the
18 solvent to generate reproducible droplets with similar sizes and velocities. In
19 order to properly produce droplets, the fluid was flush with the orifice face by
20 adjusting the backpressure and fluid reservoir. Moreover, the bipolar waveform
21 conditions were also adjusted in order to produce consistent droplets, in which the
22 volume of the droplets was calculated by using the volume of a sphere. This was
23 performed by obtaining several images of the jetting solution in continuous mode
24 using a strobed light-emitting diode (LED) and CCD, measuring the diameter by
25 the number of pixels per mm, as described previously [10]. The average drop
26 volume was observed to be 133 ± 20 pL for the liquid-generating technology and
27 72 ± 20 pL for the vapor-generating technology. Other operating conditions of the
28 vapor generator include the temperature of the heating element which was chosen
29 depending on the solvents' and analytes' boiling point in order to deliver
30 reproducible microdrops without degradation. The boiling points of most of the
31 analytes exceed 100 °C, greater than that of the solvent; however, the vapor
32 pressure of most compounds is sufficiently high at the selected elevated

1 temperature resulting in primarily existing as vapors in the chamber with minor
2 analyte decomposition. Optimization of flow rate was performed for this
3 instrument; however, a flow rate 50 mL min^{-1} was chosen to accommodate the
4 instrument's two physical configurations. Furthermore, the frequency of droplets
5 dispensed was held constant at 300 Hz.

6 Two different physical configurations of the vapor generator instrument were
7 evaluated to optimize the performance for vapor production and collection. The
8 original configuration arranges the microdrop nozzle to generate the microdrops
9 vertically (Figure 1 (a)). A modified configuration was also used in which placed
10 the chamber at a 90° angle where the microdrop nozzle generated microdrops
11 horizontally in order for the vapors to exit from the top of the jetting device
12 (Figure 1 (b)) as proposed in similar technology developed at NIST [18]. Due to
13 the configuration modification, higher droplet velocity was required in the new
14 setup in order to successfully target the droplets onto the heating element,
15 resulting in smaller drop volume. Drop volume for the microdrops produced
16 using the original physical configuration was calculated to be $0.025 \pm 0.003 \mu\text{L s}^{-1}$
17 and the modified physical configuration was calculated to have a drop volume of
18 $0.018 \pm 0.003 \mu\text{L s}^{-1}$.

19 An IONSCAN®-LS (Smiths Detection, Warren, NJ) ion mobility
20 spectrometer was used for the detection of the explosive vapors collected by the
21 PSPME device in either the positive mode or the negative mode. An Itemiser 2
22 IMS (GE Securities, Wilmington, MA) was used for the analysis of the volatile
23 chemical signatures associated with cocaine and MDMA, methyl benzoate and
24 piperonal, respectively, due to the requirement of lower drift tube temperature[2]
25 (80°C) for the targeting compounds. The IMS operating conditions for both
26 commercial instruments are shown in Table 2.

27 **Materials and methods**

28 A planar solid phase microextraction (PSPME) device is an acid-cured glass filter
29 that is spin-coated (Laurell Technologies Co., North Wales, PA) with a sol-gel
30 solution prepared as previously described [5]. The liquid and vapors were
31 deposited onto the PSPME device in triplicates followed by thermal desorption
32 into an IMS system. The compounds detected were quantified by using standard
33 solutions (TATP solution from AccuStandard, New Haven, CT; TNT solution

1 from Cerilliant, Round Rock, TX; DPA, EC, piperonal and 2,4-DNT solid
2 powders from Sigma-Alrich, St. Louis, MO, and Alfa Aesar, Ward Hill, MA; and
3 methyl benzoate (99%) obtained from Aldrich Chemical Company, Inc.,
4 Milwaukee, WI). 2-Butanol (99%, Alrich Chemical Company Co., Inc.,
5 Milwaukee, WI) and methanol of optima grade (Fisher Scientific, Fair Lawn, NJ)
6 were used as the solvents for dilution.

7 The calibration solutions for both technologies were prepared using the
8 certified standard solutions mentioned above and diluted to concentrations
9 ranging from 10-500 ng μL^{-1} in 2-butanol. Other standards in solid form were
10 prepared by dissolving 50 mg with 5 mL of 2-butanol and then further diluting the
11 solution into the desired concentrations. The calibration experiments were
12 performed in triplicates to determine the precision of the delivery.

13 A known amount of target analyte was deposited onto a PSPME surface by
14 triggering known amounts of droplets with known concentration, followed by
15 detection using an IMS. Due to the large solvent (2-butanol) interference
16 responses observed in the GE Itemiser 2 IMS instrument, microdrop printing
17 calibration was performed at higher concentrations for methyl benzoate and
18 piperonal (1000 ng μL^{-1}) to prevent competitive ionization [4,10,29].

19 Vapor quantitative analysis required a period of continuous jetting onto the
20 inserted ceramic heater for establishing consistent droplet generation using the
21 optimized waveform and equilibrium headspace system in the chamber. The
22 vapors exited through the chamber with the assistance of an air flow (10-50 mL
23 min^{-1}) and then were collected using the PSPME device positioned at the opening
24 of the chamber. The amount of vapors generated was determined by jetting at a
25 known frequency for a given time period.

26

27 **Results and Discussion**

28 **VaporJet Optimization**

29 *Dose versus continuous mode*

30 The vapor-generating technology allows two jetting modes, dose mode and
31 continuous mode. Dose mode generates a burst of microdrops onto the heating
32 element and the microdrops are heated and evaporated by a user-defined

1 temperature profile. This operation mode allows a preprogrammed temperature
2 gradient for evaporation of the solvent (T_{evap}) and analyte (T_{vap}) separately which
3 is beneficial for detectors that are sensitive to the analyte solvent. The other
4 mode, continuous mode, vaporizes the droplets in a continuous manner where the
5 heater is set at a constant temperature. A calibration curve was developed in the
6 dose mode using a $100 \text{ ng } \mu\text{L}^{-1}$ TNT solution with different extraction times in
7 comparison to the continuous mode using a $10 \text{ ng } \mu\text{L}^{-1}$ TNT solution (Figure 2).
8 Based on the results, the dose mode was inadequate for the evaluation purpose
9 because of the high RSD observed between experiments in comparison to the
10 RSD values observed in the continuous mode (dose mode resulted with an RSD
11 range of 3-16 whereas continuous mode resulted with a RSD range of 1-13). The
12 poor precision could be caused by co-evaporation of analytes and solvent and loss
13 of signal to the chamber surrounding during the vapor generation period. In
14 addition, constant emission of target odors is required for the simulation of
15 concealed contraband. Thus, experiments thereafter were conducted using the
16 continuous mode.

17 *Steady-state delivery*

18 When using the VaporJet in the continuous mode, a constant delivery of the
19 analyte onto the PSPME device depends on the equilibrium established in the
20 system chamber. A five second extraction was performed at different elapsed
21 times to evaluate when the system reaches a steady state, determined to be after
22 30 minutes of continuous jetting.

23 *Effect of flow rate*

24 Air flow is utilized for the assistance of generated vapors to exit from the
25 chamber. The effect of air flow rates on amount delivered on the PSPME device
26 was monitored by collecting the vapors at the exiting chamber of the vapor
27 generator at different time periods followed by detection with an IMS instrument.
28 Air flow rates of 10 , 30 , and 50 mL min^{-1} were used to optimize the amount of
29 analyte (TNT) delivered (Figure 3). The optimum air flow rate to efficiently
30 assist the vapors to exit from the generating region was determined to be 30 mL
31 min^{-1} since increased flow rates did not result with further improvement in signal.
32 As a result, a minimum flow rate of 30 mL min^{-1} is required for the maximum

1 amount of vapors to exit the chamber. For these studies, a flow rate of 50 mL
2 min^{-1} was used to keep the flow rates consistent based on the instrument's
3 physical configuration.

4 *VaporJet chamber orientation*

5 The physical configuration of the vapor generating instrument was modified by
6 turning the chamber in such a way that the thermal vapors exit the chamber from
7 the desired position (top) rather than the side as done in the original configuration.
8 This configuration was used in previous studies by Verkouteren et al. [25] and a
9 comparison study of the two configurations was investigated.

10 With the modified physical configuration, the velocity of the microdrop
11 generation is increased for the microdrops traveling horizontally to come into
12 contact with the heated ceramic plate and successfully generate vapors. The
13 increase in velocity of the microdrops resulted in greater volume and mass of the
14 analyte delivered on the PSPME compared to the similar extraction time
15 performed as using the original configuration. Figure 4 shows the response
16 curves of TNT on the PSPME using the two different configurations. Although
17 the intensity detected was greater for the modified physical configuration of the
18 vapor generator when extracting the vapors for the same amount of time, the
19 amount of vapors generated in the generating region was also greater for the
20 modified physical configuration. Comparing both configurations shows that the
21 instrument performs similarly regardless which configuration is applied.
22 Accordingly, the following experiments were conducted in the original physical
23 configuration of the vapor generating instrument.

24 **PSPME Desorption Profiles of Volatile Chemical Compounds**

25 *Limit of detection for explosives and their associated volatile compounds*

26 Extraction curves of the explosive vapors were generated by extracting the vapors
27 at different times. The amount of analyte vapors generated by the instrument was
28 determined by calculating the total volume of the microdrops generated from the
29 dispenser at a constant jetting frequency for different extraction times. The
30 response curve was used to calculate the limit of detection (LOD) as well as the
31 precision in the form of relative standard deviation (RSD). The limits of detection

1 for TNT and 2,4-DNT vapors by the vapor generator were noted to be 2.3 ng with
2 an RSD of ~7% and 3.7 ng with an RSD of ~10%, respectively.

3 One desorption was inadequate to completely desorb the DPA and EC when
4 extracted by PSPME due to the presence and alarm for these analytes after
5 subsequent desorption. Multiple desorption of the PSPME allowed for semi-
6 quantitative analysis of the vapors collected via PSPME. As a result, the limit of
7 detection of DPA was 24 ng with RSD value of 12%; the limit of detection for EC
8 was 0.5 ng with a RSD of 8%.

9 Although the vapor generating instrument was capable of producing
10 reproducible vapors for most explosives, this technique is not suitable for
11 thermally labile compounds such as TATP [30]. A comparison of the IMS
12 response curves observed for manually delivering liquid standard solutions of
13 varying concentrations of TATP onto the PSPME and vapors collected on the
14 PSPME via the generated vapors is shown in Figure 5 (a). Decomposition is
15 evident on the IMS plasmagram for vapor extractions using the vapor generator,
16 resulting in decreased signal for similar vapor extraction technique performed by
17 depositing the same amount of TATP in a closed system and extracted for 5
18 minutes (Figure 5 (b)). Furthermore, the ions observed in the IMS instrument
19 result in a signal with a different drift time and detection window (6.73 ms) as
20 well as a more pronounced unidentified decomposition signal (~7.85 ms).

21 *Limits of detection for illicit drugs and their associated volatile signatures*

22 Methyl benzoate and piperonal, the volatile chemical compounds associated with
23 cocaine and MDMA were detected using a different commercial IMS instrument
24 due to user accessibility to be able to modify the drift tube temperature without
25 further modification. Desorption profiles of each analyte were obtained using the
26 vapor generator and the limits of detection for these two analytes were observed
27 as 14 ng (RSD 2%) and 2.8 ng (RSD 10%) for methyl benzoate and piperonal,
28 respectively.

29 In summary, the limits of detection calculated from the generated vapors are
30 higher compared to the liquid standards delivered on the PSPME by microdrop
31 printing which is due to the limitation of only extracting the vapors of the analyte
32 of interest rather than absolute deposition of analyte on the PSPME device. Also,
33 some loss associated with the instrument design could incorporate to the increased

1 detection limits. However, the vapor generator has proven to produce
2 reproducible results with low RSD values (Table 3) from triplicates with the
3 average values of less than 12%. The use of piezoelectric microdrop vapor
4 printing device allows for the determination of the limits of detection of the
5 vapors generated from an explosive or illicit substance by PSPME followed by
6 IMS detection.

7 *PSPME extraction performance evaluation*

8 Calibration curves of the analytes of interest were also generated by using the
9 microdrop generating technology or direct microliter spiking in order to determine
10 the extraction performance of an analyte by PSPME, which is defined as the mass
11 detected divided by the mass available. The use of a microdispenser for delivery
12 of picoliter volumes of analyte allows for a more accurate response of the analyte
13 with no or little interferences caused by solvents [10]. A summary of the limits of
14 detection and RSD values obtained from the microdrop printing are shown in
15 Table 3. The PSPME extraction performance varies for each analyte due to the
16 analyte-phase chemistry selectivity [31]. The coating of the PSPME is a sol-gel
17 based PDMS [5,32] which is widely used for general applications as well as
18 detection of volatile components in explosives and drugs [1,2]. The evaluated
19 extraction performances for the analytes of interest are summarized in Table 3 as
20 well. For most of the analytes associated with explosives, the extraction
21 performance was observed to be ~20%, while diphenylamine showed a much
22 lower recovery (7%) for the first desorption. The lower recovery of the analyte
23 could be caused by the higher partitioning coefficient (K) between the sample and
24 the PSPME coating resulting in lower recovery of the analyte [31,33] as well as
25 loss of analyte between multiple desorption since subsequent desorption were
26 required to fully desorb all the adsorbed DPA and EC vapors. Furthermore,
27 extraction performance for TNT using the two different physical configurations of
28 the instrument allowed further evaluation of the physical configurations of the
29 instrument. Using the original configuration, the recovery of TNT was
30 determined to be ~18% which was slightly higher compared to the modified
31 physical configuration (~15%) recovery of TNT. Thus, similarly to the previous
32 conclusions, both physical configuration for vapor generation of this instrument
33 will result in similar results and the original configuration can be used for further

1 PSPME evaluation studies. For signature compounds associated with illicit drugs,
2 the extraction efficiencies were much higher than the previous calculated
3 extraction efficiencies of explosives and their volatile signature compounds,
4 ~51% for methyl benzoate and ~80% for piperonal. Calibration curves produced
5 by direct spiking of standard solutions on the PSPME surface using a micropipette
6 resulted in decreased responses due to competitive ionization between analytes
7 and solvent [4,10,29] which suppressed the analyte signal. Vapor extractions
8 were done in the presence of very low amount of solvents, which did not suffer
9 from signal suppression. Calibration for methyl benzoate and piperonal were also
10 performed with the microdrop printer using higher concentration solutions onto a
11 PSPME device, resulting in fewer interferences observed from the solvent. From
12 the observed extraction efficiencies for explosives and illicit drugs, the enhanced
13 surface area and phase volume of the PSPME has shown to decrease the sampling
14 time, providing approximately twenty fold increase in extraction performance in
15 comparison to the commercial SPME [5].

16 **Conclusions**

17 Microdrop dispensing devices were used to deliver picoliter quantities of target
18 analyte mass in the form of a vapor and liquid for the calibration and
19 characterization of the planar solid phase microextraction (PSPME) device.
20 Steady-state delivery of analytes in the gaseous phase was achieved after 30
21 minutes of continuous generation of vapors, and the optimum analyte delivery
22 was obtained at minimum gas flow delivery rate of 30 mL min⁻¹. Modifications
23 of the vapor generator were performed in order to allow for the generated vapors
24 to exit from above the generating region in order to simulate vapors of explosives.
25 Since this physical configuration required a faster speed for the microdrops
26 generated, larger volumes were produced and similar microdrop generation
27 efficiencies were obtained for the modified configuration in comparison to the
28 original design.

29 The PSPME devices have been proven to be a universal pre-concentrator for
30 different headspace volatiles above explosives and illicit drugs. By using liquid
31 standards, the PSPME devices were calibrated by vapor generation to deliver
32 precise amounts of the analytes in the form of vapor onto the PSPME surfaces
33 followed by IMS detection. Once the steady state has been reached, the amounts

1 of the headspace compounds extracted on the PSPME devices are directly
2 proportional to the extraction time. The PSPME extraction efficiencies were
3 determined for TNT, DNT, DPA and EC ranging from ~7 to ~24% and for methyl
4 benzoate and piperonal were ~51% and ~80%, respectively. The explosive TATP
5 is a thermally labile chemical and decomposes on the ceramic plate during the
6 vapor generation process; as a result, the extraction performance for this analyte
7 was not obtained in this experiment.

8 In conclusion, the PSPME devices were calibrated using a piezoelectric
9 microdrop printing instrument and evaluated using a vapor generating instrument
10 for different headspace compounds related to both explosives and illicit drugs.
11 The high surface area and phase volume of allow higher capacity for the
12 adsorption of the volatile compounds onto the PSPME surface, resulting in higher
13 extraction efficiencies, as low as ~7% for DPA and as high as ~24% for 2,4-DNT,
14 with low limits of detections ranging as low as ~ 0.5 ng for EC and a maximum of
15 ~ 24 ng for DPA.

16

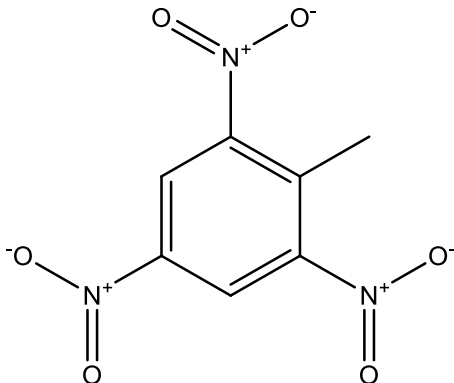
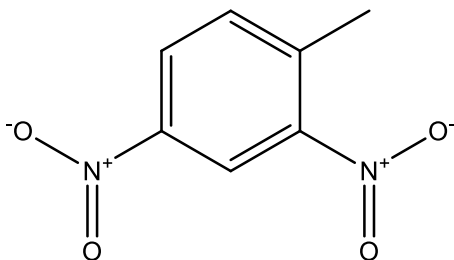
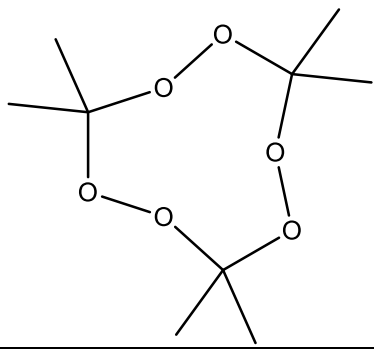
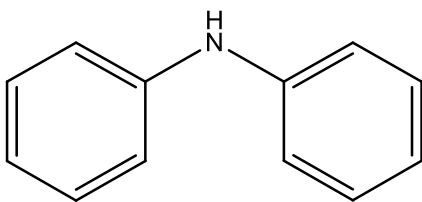
17 **Acknowledgements**

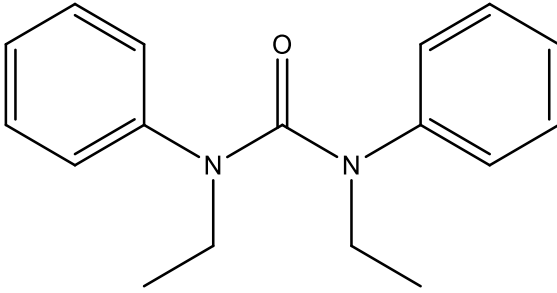
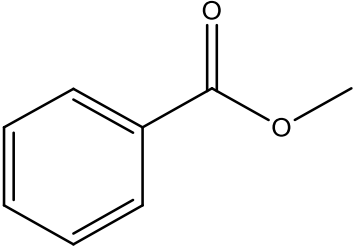
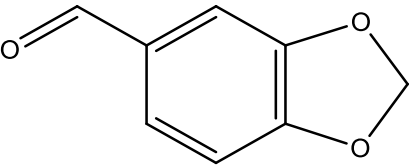
18 The authors would like to thank Dr. Bogdan Antohe for providing the instrument as well as for
19 helpful discussions. This project was supported by a research grant award from the University of
20 Rhode Island and the Dept. of Homeland Security Center of Excellence at the University of Rhode
21 Island. The opinions, findings, and conclusions or recommendations expressed in this publication
22 are those of the authors and do not necessarily reflect those of the Department of Homeland
23 Security.

24

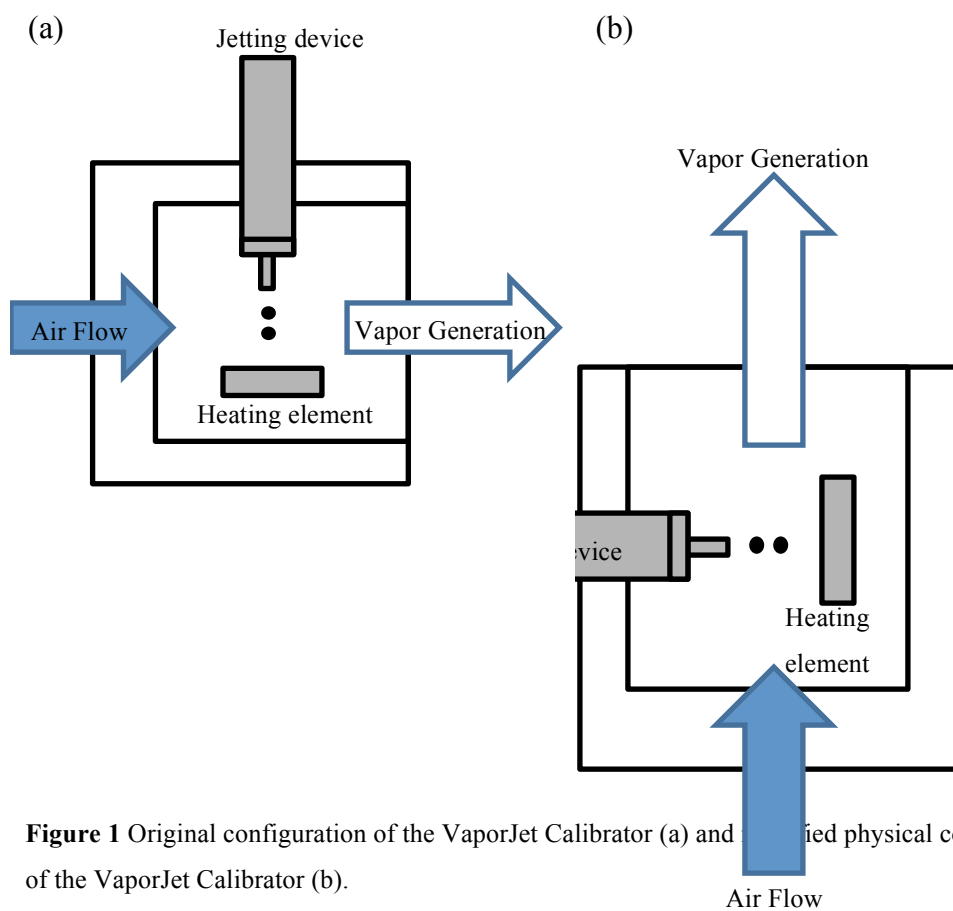
1 Tables and Figures

- 2 **Table 1** Analytes of interest listed with their reduced mobility (K_0), boiling point and vapor
3 pressure (data from MSDS and references [3,19,34]).

Chemical	Structure	K_0 ($\text{cm}^2\text{V}^{-1}\text{s}^{-1}$)	b.p. ($^{\circ}\text{C}$)	Vapor pressure (Torr at 20-25 $^{\circ}\text{C}$)
2,4,6-Trinitrotoluene		1.45	280	3.0×10^{-6}
2,4-Dinitrotoluene		1.57	300	2.1×10^{-4}
Triacetone triperoxide		2.57	97	5.2×10^{-2}
Diphenylamine		1.61	302	2.2×10^{-4}

Ethyl centralite		1.24	325	6.0×10^{-6}
Methyl benzoate		1.55	199	2.5×10^{-1}
Piperonal		1.51	264	1.0×10^{-2}

1
2



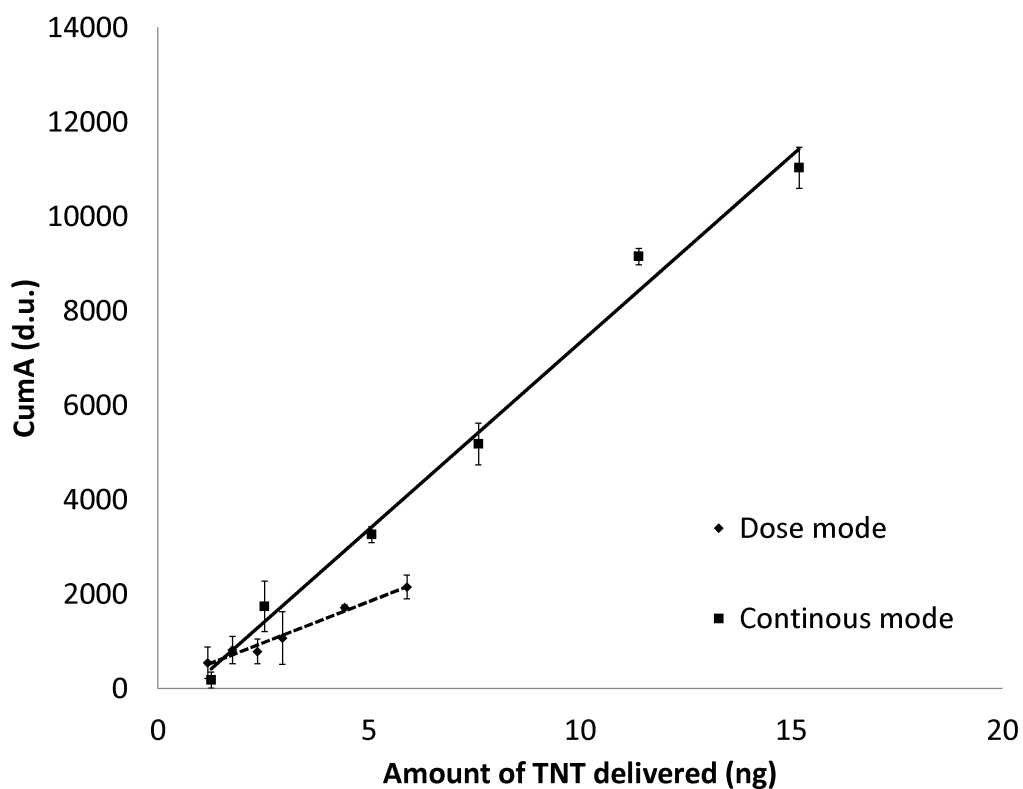
3 **Figure 1** Original configuration of the VaporJet Calibrator (a) and modified physical configuration
4 of the VaporJet Calibrator (b).

5

6 **Table 2** Operating conditions for the IMS instruments used in the experiments.

IMS operating conditions	Smiths Detection IONSCAN®-LS		GE Itemiser 2 IMS	
	Positive (+)	Negative (-)	Positive (+)	Positive (+)
Polarity	Positive (+)	Negative (-)	Positive (+)	Positive (+)
Desorber temperature (°C)	250	300	150	197
Drift tube temperature (°C)	235	115	80	190
Sample flow (mL min ⁻¹)	200	500	500	1000
Drift flow (mL min ⁻¹)	300	350	350	250
Reagent gas	Nicotinamide	Hexachloromethane	Nicotinamide	None
Compounds detected	DPA, TATP, EC	2,4-DNT, TNT	Piperonal	Methyl benzoate

1



2

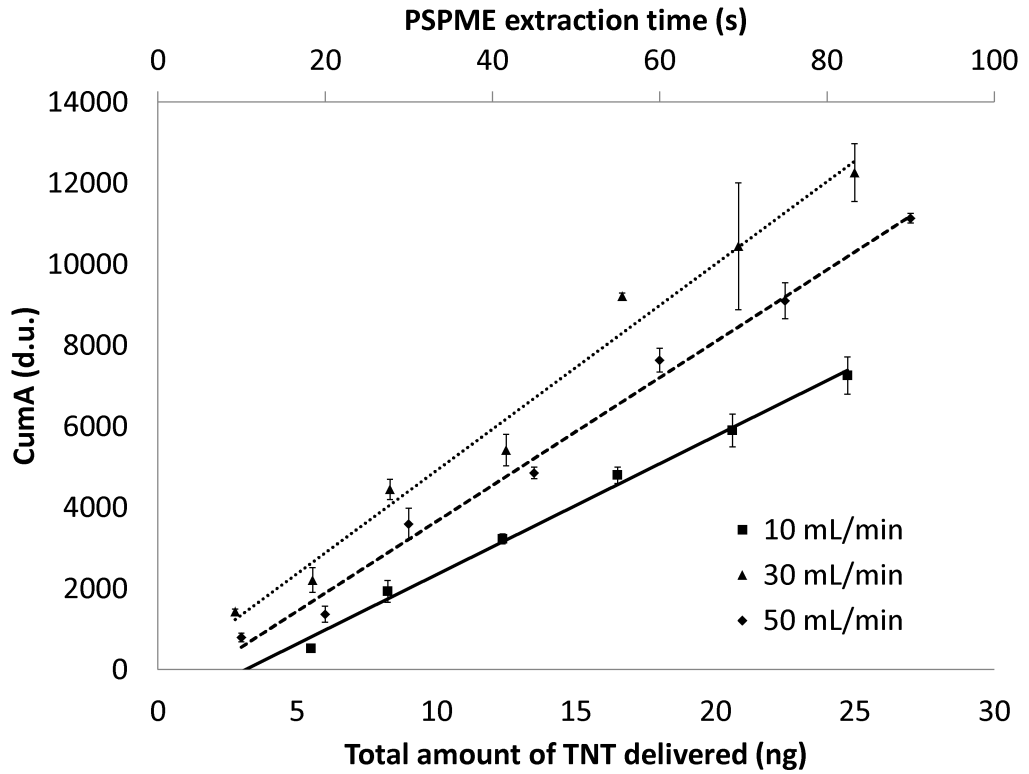
3 **Figure 2** Response curves of TNT in IMS using the dose mode and continuous mode in triplicates.

4 Different amounts of drops of 100 ppm TNT solution (in 2-butanol) were jetted onto the heating

5 element with the programmed profile: $T_{\text{base}} = 25\text{ °C}$, $T_{\text{evap}} = 50\text{ °C}$, $T_{\text{vap}} = 150\text{ °C}$, $T_{\text{clean}} = 300\text{ °C}$.

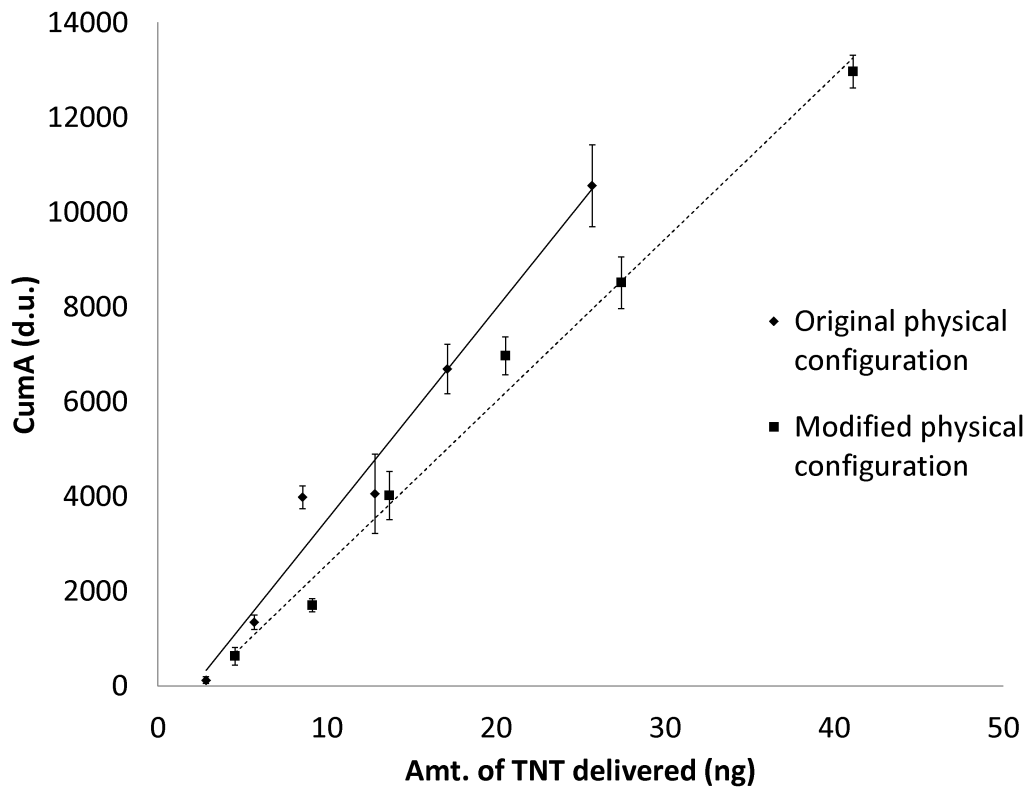
6

7



1
2 **Figure 3** Air flow rate effects on the amounts of analyte delivered (N=3).

3



4
5 **Figure 4** PSPME desorption profiles for TNT using two different VaporJet physical
6 configurations (N=3).

7

1
2
3
4

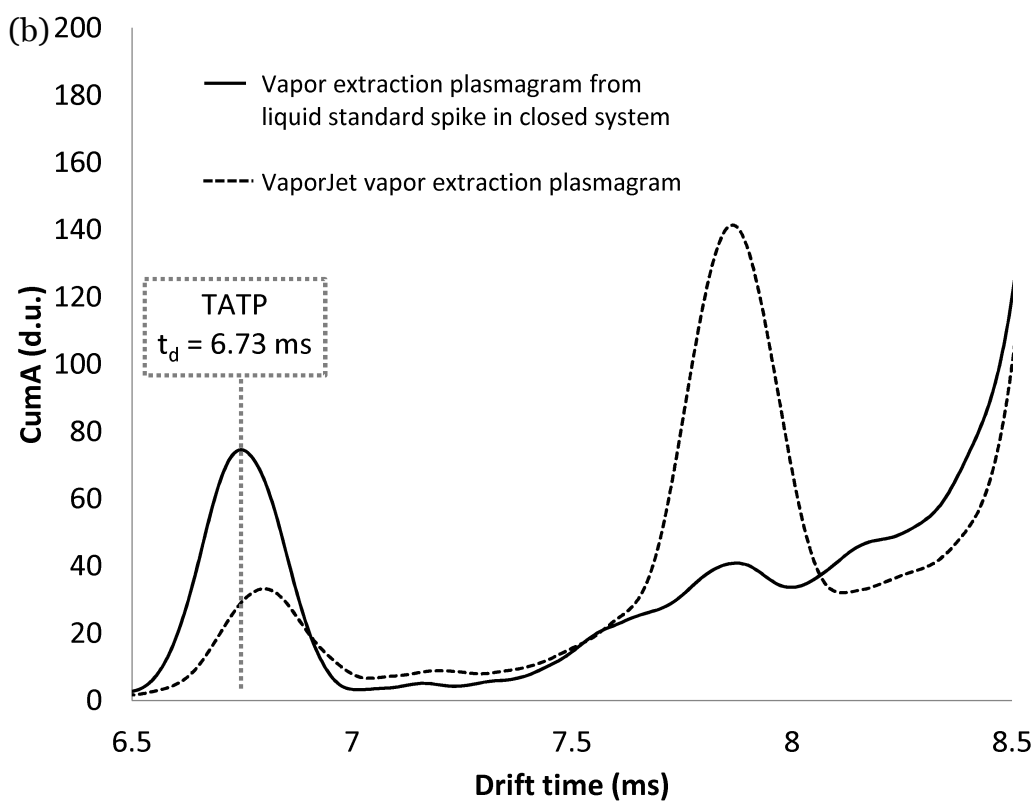
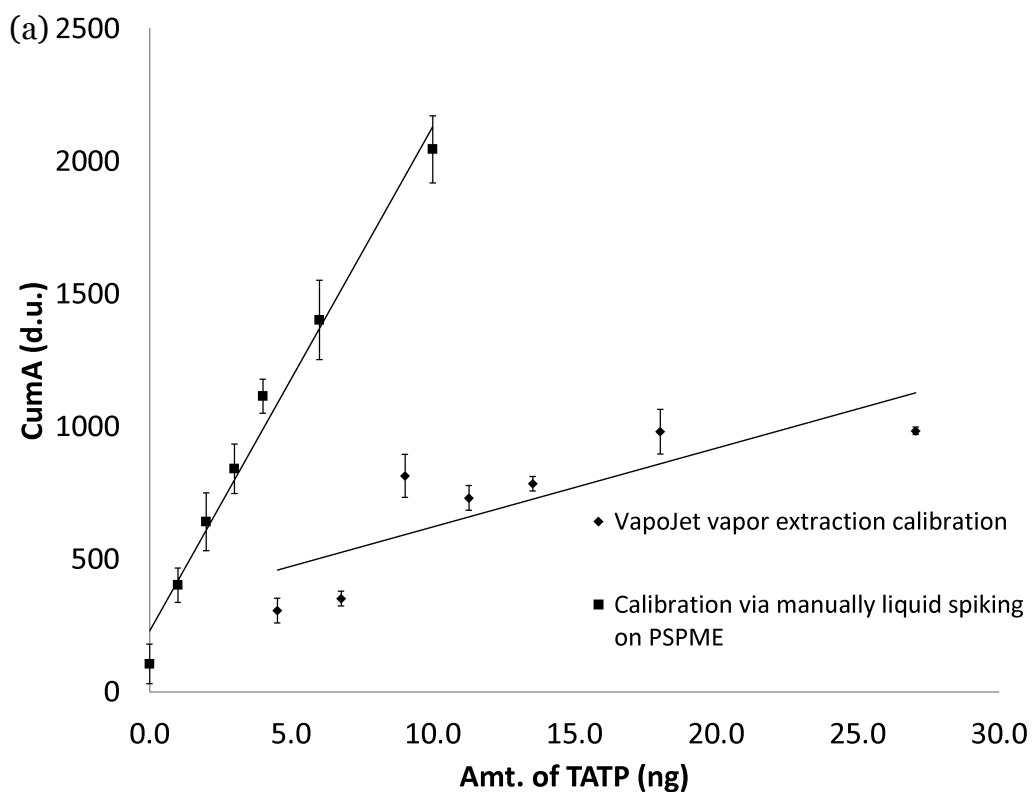


Figure 5 (a) PSPME desorption profiles for TATP from VaporJet vapor extractions and manually

spiking liquid TATP solutions unto the PSPME surface (N=3); (b) IMS plasmagrams of TATP from vapor extractions from liquid deposition on a closed system and VaporJet vapor extractions.

1

2 **Table 3** Limits of detection and precision (as RSD, %) for explosives and illicit drugs from vapor
 3 and liquid calibrations (N=3). (*) Denotes analyte that required calibrations using manual liquid
 4 delivery of standards solution using a micropipette.

Technique	Compound	LOD (ng)	RSD (%)		Extraction Performance (%)
			Range	Average	Average
Vapor generation	TNT	2.3	1-14	7.3	18
	2,4-DNT	3.7	2-22	9.7	24
	DPA	24	5-21	12	7
	TATP	17	1-15	7.6	n/a
	EC	0.5	1-15	7.5	19
	Methyl benzoate	14	1-4	1.7	51
	Piperonal	2.8	2-18	9.5	80
Microdrop printing or manual liquid standard deliver using a micropipette(*)	TNT	0.37	4-50	15	
	2,4-DNT	0.53	6-30	17	
	DPA	10	3-16	10	
	TATP*	1.0	6-17	11	
	EC	0.4	5-56	22	
	Methyl benzoate*	0.5	1-22	9.7	
	Piperonal	4.0	4-21	12	

5

6

7

8

1 References

- 2 1. Lai H, Leung A, Magee M, Almirall J (2010) Identification of volatile chemical signatures from
3 plastic explosives by SPME-GC/MS and detection by ion mobility spectrometry. *Anal Bioanal*
4 *Chem* 396 (8):2997-3007.
- 5 2. Lai H, Guerra P, Joshi M, Almirall JR (2008) Analysis of volatile components of drugs and
6 explosives by solid phase microextraction-ion mobility spectrometry. *Journal of Separation*
7 *Science* 31 (2):402-412.
- 8 3. Lai H, Corbin I, Almirall J (2008) Headspace sampling and detection of cocaine, MDMA, and
9 marijuana via volatile markers in the presence of potential interferences by solid phase
10 microextraction-ion mobility spectrometry (SPME-IMS). *Anal Bioanal Chem* 392 (1):105-113.
- 11 4. Gura S, Guerra-Diaz P, Lai H, Almirall JR (2009) Enhancement in sample collection for the
12 detection of MDMA using a novel planar SPME (PSPME) device coupled to ion mobility
13 spectrometry (IMS). *Drug Testing and Analysis* 1 (7):355-362.
- 14 5. Guerra-Diaz P, Gura S, Almirall JR (2010) Dynamic Planar Solid Phase Microextraction-Ion
15 Mobility Spectrometry for Rapid Field Air Sampling and Analysis of Illicit Drugs and Explosives.
16 *Analytical Chemistry* 82 (7):2826-2835.
- 17 6. Fan W, Young M, Canino J, Smith J, Oxley J, Almirall J (2012) Fast detection of triacetone
18 triperoxide (TATP) from headspace using planar solid-phase microextraction (PSPME) coupled to
19 an IMS detector. *Anal Bioanal Chem* 403 (2):401-408.
- 20 7. Perr JM, Furton KG, Almirall JR (2005) Gas chromatography positive chemical ionization and
21 tandem mass spectrometry for the analysis of organic high explosives. *Talanta* 67 (2):430-436.
- 22 8. Joshi M, Delgado Y, Guerra P, Lai H, Almirall JR (2009) Detection of odor signatures of
23 smokeless powders using solid phase microextraction coupled to an ion mobility spectrometer.
24 *Forensic Science International* 188 (1-3):112-118.
- 25 9. Ai J (1997) Headspace Solid Phase Microextraction. Dynamics and Quantitative Analysis
26 before Reaching a Partition Equilibrium. *Analytical Chemistry* 69 (16):3260-3266.
- 27 10. Gura S, Joshi M, Almirall J (2010) Solid-phase microextraction (SPME) calibration using
28 inkjet microdrop printing for direct loading of known analyte mass on to SPME fibers. *Anal*
29 *Bioanal Chem* 398 (2):1049-1060.
- 30 11. Pawliszyn J (2002) Chapter 13 Solid phase microextraction. In: Pawliszyn J (ed)
31 *Comprehensive Analytical Chemistry*, vol 37. Elsevier, pp 389-477.
- 32 12. Kapoor JC, Kannan GK (2007) Landmine Detection Technologies to Trace Explosive Vapour
33 Detection Techniques. *Defence Science Journal* 57 (6):797-810.
- 34 13. Rana P, Kannan GK, Bhalla R, Kapoor JC (2003) Standardisation of a Vapour Generator for
35 Calibration of Environmental Monitoring Instruments. *Defence Science Journal* 53 (4):415-423.
- 36 14. Eiceman GA, Preston D, Tiano G, Rodriguez J, Parmeter JE (1997) Quantitative calibration of
37 vapor levels of TNT, RDX, and PETN using a diffusion generator with gravimetry and ion
38 mobility spectrometry. *Talanta* 45 (1):57-74.
- 39 15. Davies JP, Blackwood LG, Davis SG, Goodrich LD, Larson RA (1993) Design and calibration
40 of pulsed vapor generators for 2,4,6-trinitrotoluene, cyclo-1,3,5-trimethylene-2,4,6-trinitramine,
41 and pentaerythritol tetranitrate. *Analytical Chemistry* 65 (21):3004-3009.
- 42 16. Moorman M, Robinson A, Manginell RP, Tappan AS, Linker K Microfabricated Chip for
43 Calibration of Field Instruments. In: *Technologies for Homeland Security, 2007 IEEE Conference*
44 *on*, 16-17 May 2007 2007. pp 34-38.
- 45 17. Zhang G, Pitchimani R, Weeks BL (2008) A simple and flexible thin film evaporating device
46 for energetic materials. *Review of Scientific Instruments* 79 (9):096102-096103.
- 47 18. Verkouteren RM, Gillen G, Taylor DW (2006) Piezoelectric trace vapor calibrator. *Review of*
48 *Scientific Instruments* 77 (8):085104-085104-085106.
- 49 19. Harper RJ, Almirall JR, Furton KG (2005) Identification of dominant odor chemicals
50 emanating from explosives for use in developing optimal training aid combinations and mimics for
51 canine detection. *Talanta* 67 (2):313-327.
- 52 20. Macias MS, Guerra-Diaz P, Almirall JR, Furton KG (2010) Detection of piperonal emitted
53 from polymer controlled odor mimic permeation systems utilizing *Canis familiaris* and solid phase
54 microextraction-ion mobility spectrometry. *Forensic Science International* 195 (1-3):132-138.
- 55 21. Bonnot K, Bernhardt P, Hassler D, Baras C, Comet M, Keller Vr, Spitzer D (2010) Tunable
56 Generation and Adsorption of Energetic Compounds in the Vapor Phase at Trace Levels: A Tool
57 for Testing and Developing Sensitive and Selective Substrates for Explosive Detection. *Analytical*
58 *Chemistry* 82 (8):3389-3393.

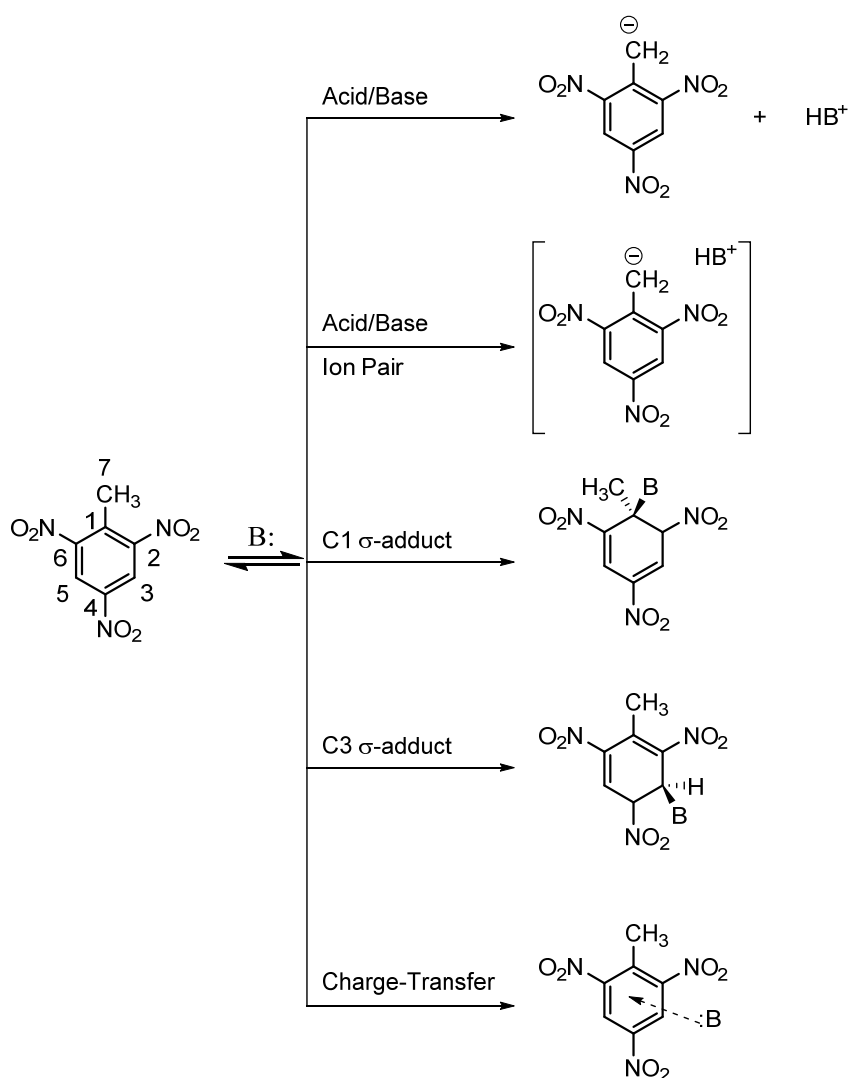
1 22. Lee ER (2003) Microdrop generation. CRC Press, Boca Raton.
2 23. Verkouteren RM, Verkouteren JR (2009) Inkjet Metrology: High-Accuracy Mass
3 Measurements of Microdroplets Produced by a Drop-on-Demand Dispenser. *Analytical Chemistry*
4 81 (20):8577-8584.
5 24. Wu HC, Hwang WS, Lin HJ (2004) Development of a three-dimensional simulation system
6 for micro-inkjet and its experimental verification. *Materials Science and Engineering A* 373 (1-
7 2):268-278.
8 25. Verkouteren M, Staymates M, Fletcher R, MacCrehan B, Staymates J, Anderson J, Najarro M,
9 Brewer T, Gillen G The NIST Inkjet Trace Explosives Vapor Generator. In: *Trace Explosive*
10 *Detection Workshop*, Portland, Oregon, 2011.
11 26. Joshi M, Rigsby K, Almirall JR (2011) Analysis of the headspace composition of smokeless
12 powders using GC-MS, GC- μ ECD and ion mobility spectrometry. *Forensic Science International*
13 208 (1):29-36.
14 27. Furton KG, Hong YC, Hsu YL, Luo T, Rose S, Walton J (2002) Identification of Odor
15 Signature Chemicals in Cocaine Using Solid-Phase Microextraction-Gas Chromatography and
16 Detector-Dog Response to Isolated Compounds Spiked on U.S. Paper Currency. *Journal of*
17 *Chromatographic Science* 40 (3):147-155.
18 28. Lorenzo N, Wan T, Harper R, Hsu Y-L, Chow M, Rose S, Furton K (2003) Laboratory and
19 field experiments used to identify *Canis lupus var. familiaris* active odor signature chemicals from
20 drugs, explosives, and humans. *Anal Bioanal Chem* 376 (8):1212-1224.
21 29. Eiceman G, Karpas Z (2005) *Ion mobility spectrometry*. 2 edn. CRC Press, Boca Raton.
22 30. Oxley JC, Smith JL, Chen H (2002) Decomposition of a Multi-Peroxidic Compound:
23 Triacetone Triperoxide (TATP). *Propellants, Explosives, Pyrotechnics* 27 (4):209-216.
24 31. Wilson CL, Pawliszyn J (2002) *Comprehensive analytical chemistry*. Elsevier.
25 32. Guerra P, Lai H, Almirall JR (2008) Analysis of the volatile chemical markers of explosives
26 using novel solid phase microextraction coupled to ion mobility spectrometry. *Journal of*
27 *Separation Science* 31 (15):2891-2898.
28 33. Gorecki T (1997) Effect of Sample Volume on Quantitative Analysis by Solid-phase
29 Microextraction Part 1. Theoretical Considerations. *Analyst* 122 (10):1079-1086.
30 34. Oxley JC, Smith JL, Shinde K, Moran J (2005) Determination of the Vapor Density of
31 Triacetone Triperoxide (TATP) Using a Gas Chromatography Headspace Technique. *Propellants,*
32 *Explosives, Pyrotechnics* 30 (2):127-130.
33
34

Optical Chemical Sensors using Nanocomposites from Porus Silicon Photonic Crystals and Sensory Polymers. William Euler, URI

Accomplishments

1. *Reactivity of TNT and other nitroaromatics in various solvents*

To determine optimal sensing environments for explosives, several solvent systems were investigated, including tetrahydrofuran (THF), methanol (MeOH), and dimethylformamide (DMF). In all cases it was discovered that a reaction that could be used for optical sensing could be invoked and in all cases water was a critical component to inducing formation of the chromophore.



An investigation of the reaction of amine bases with TNT in THF and MeOH showed that there were several products possible, as shown in Scheme 1.

Scheme 1

Both ^1H NMR and visible absorption spectroscopy showed that both acid-base and σ -adduct formation could occur, depending upon solvent and concentration conditions. For the amines, direct detection via NMR spectroscopy of a small amount of the C1 σ -adduct could be observed for ethyl amine, butyl amine, and diethylamine when the solvent was THF. However, in MeOH only the deprotonation of the methyl group could be detected in the NMR spectra. The visible spectroscopy showed that the primary chromophoric product was the TNT^- anion formed from deprotonation of the methyl group but there also was a second product formed, which was attributed to the σ -adduct. This was true in both THF and MeOH.

A kinetic study was undertaken to better understand the reactivity of TNT with bases in THF and MeOH. For the reaction of TNT with hydroxide, absolute rate constants could be determined for the formation of TNT^- and the σ -adduct, TNT-OH^- . The rate constants were used to estimate equilibrium constants and ΔG° for the reaction between TNT and OH^- : formation of the σ -adduct is 2 orders of magnitude faster than the deprotonation reaction for both solvents but the two products have the same stability in THF while the TNT^- anion is slightly more stable in MeOH.

When TNT is exposed to amine bases no reaction was observed when the dry, neat base was used as the solvent. However, in THF or MeOH, reaction proceeded readily. It was discovered that residual water in the nominally solvents was acting catalytically to promote deprotonation, with observed rate constants 3 – 4 orders of magnitude larger than observed when reacting with hydroxide ion. Although the mechanistic details are yet to be confirmed, the formation of the N-centered σ -adduct appears to proceed by addition to TNT^- .

To help support these conclusions, a computational study was done. A few of the converged structures are shown in Figure 1. All of the amine bases allowed converged structures for TNT^- , C1 σ -adducts, C3 σ -adducts, and charge-transfer (CT) complexes with comparable energies. The

thermodynamic energies of the different reactions showed that in the gas phase formation of σ -adducts was similar in energy to the deprotonation of TNT when the base was hydroxide or methoxide. For the amine bases, none of the reactions were favorable, but the formation of the σ -adducts was less disfavored than deprotonation in the gas phase.

A study was done looking at the effect of solvation by simulating a changing dielectric environment for each reaction. In the case of reaction with hydroxide or methoxide, an increasing dielectric constant reduced the spontaneity of both the deprotonation and σ -adduct formation reactions but never to the point of being disfavored. A more dramatic result was seen with the amine bases. As noted above, in the gas phase all reactions between TNT and amines were disfavored but at higher dielectric constants these reactions become favorable. For example, for reaction with ethylamine, when the dielectric constant exceeds ~ 5 , both deprotonation and σ -adduct formation becomes spontaneous with the C1 σ -adduct being most favored. ΔE continues to become more negative to a dielectric constant of ~ 20 and then levels off. The computational results parallel the experimental observations surprisingly well.

When the solvent system was DMF, no added base was required to observe a reaction. Addition of a crystal of TNT to DMF leads to immediate color formation. The visible spectra for the reactions of TNT and trinitrobenzene (TNB) are shown in Figure 2. The role of water is demonstrated by the increase of intensities of the spectral bands with added water. Analysis of the visible and fluorescence spectra showed that deprotonation and σ -adduct formation was observed for reaction with TNT but only σ -adduct formation occurred for TNB (as necessary, since TNB has no acidic protons).

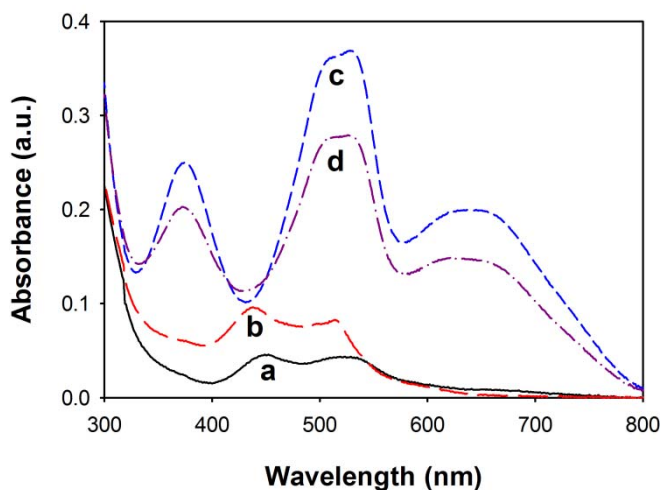


Figure 2. Initial and final absorbance spectra from trinitroaromatics titrated with water in DMF: (a) 7×10^{-5} M TNB in DMF; (b) TNB + 30 μL H_2O in DMF; (c) 1.1×10^{-4} M TNT in DMF; (d) TNT + 30 μL H_2O in DMF.

In the DMF solvent system it was discovered that the *s*-adduct between the trinitroaromatics and DMF was fluorescent, an unexpected result. Deconvolution of the spectra showed that the

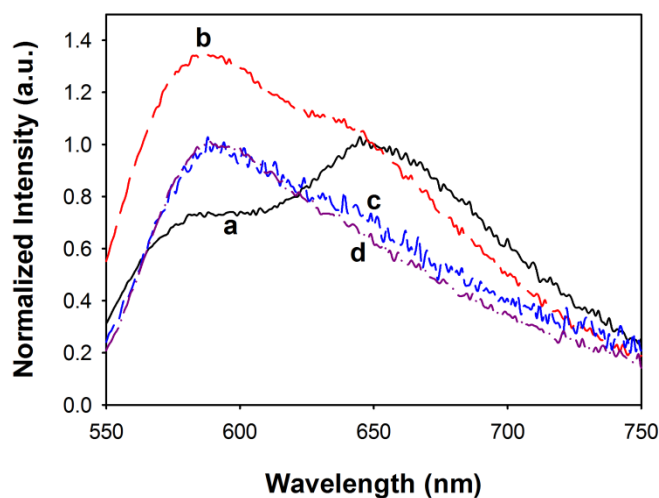


Figure 3. Initial and final emission spectra from trinitroaromatics titrated with water in DMF: (a) 7×10^{-5} M TNB in DMF; (b) TNB + 30 μ L H₂O in DMF; (c) 1.1×10^{-4} M TNT in DMF; (d) TNT + 30 μ L H₂O in DMF. TNB spectra normalized at 650 nm, TNT spectra normalized at 591 nm.

emission arises from both OH⁻ and DMF σ -adducts (B in Scheme 1). This leads to the exciting possibility of developing sensors based on the fluorescence of TNT products directly, rather than the indirect methods currently used.

2. *Fluorescent arrays for detection of explosives.*

A series of common and inexpensive fluorophores were examined to determine their reactivity with a suite of explosives and common impurities found in explosives. The goal was to develop a sensor array that could be used to detect the explosive analytes at a trace level while using pattern recognition techniques to provide unambiguous identification of the detected species. Thus, a series of rhodamine dyes were used as the fluorophores, with the emission maxima spanning the entire visible region. Figure 4 shows the results. Every analyte shows a different pattern of response for the set of fluorophores used. An unexpected result was that some fluorophore/analyte combinations showed fluorescent enhancements rather than the more typical quenching response. Quantum computations were able to help explain the fluorescent enhancements. In most cases where enhancement was observed, the highest occupied molecular orbital (HOMO) of the analyte or analyte reaction product was of nearly the same energy as the lowest unoccupied molecular orbital (LUMO) of the fluorophore. This leads to a resonance condition that allows population of the fluorophore excited state directly from the analyte ground state.

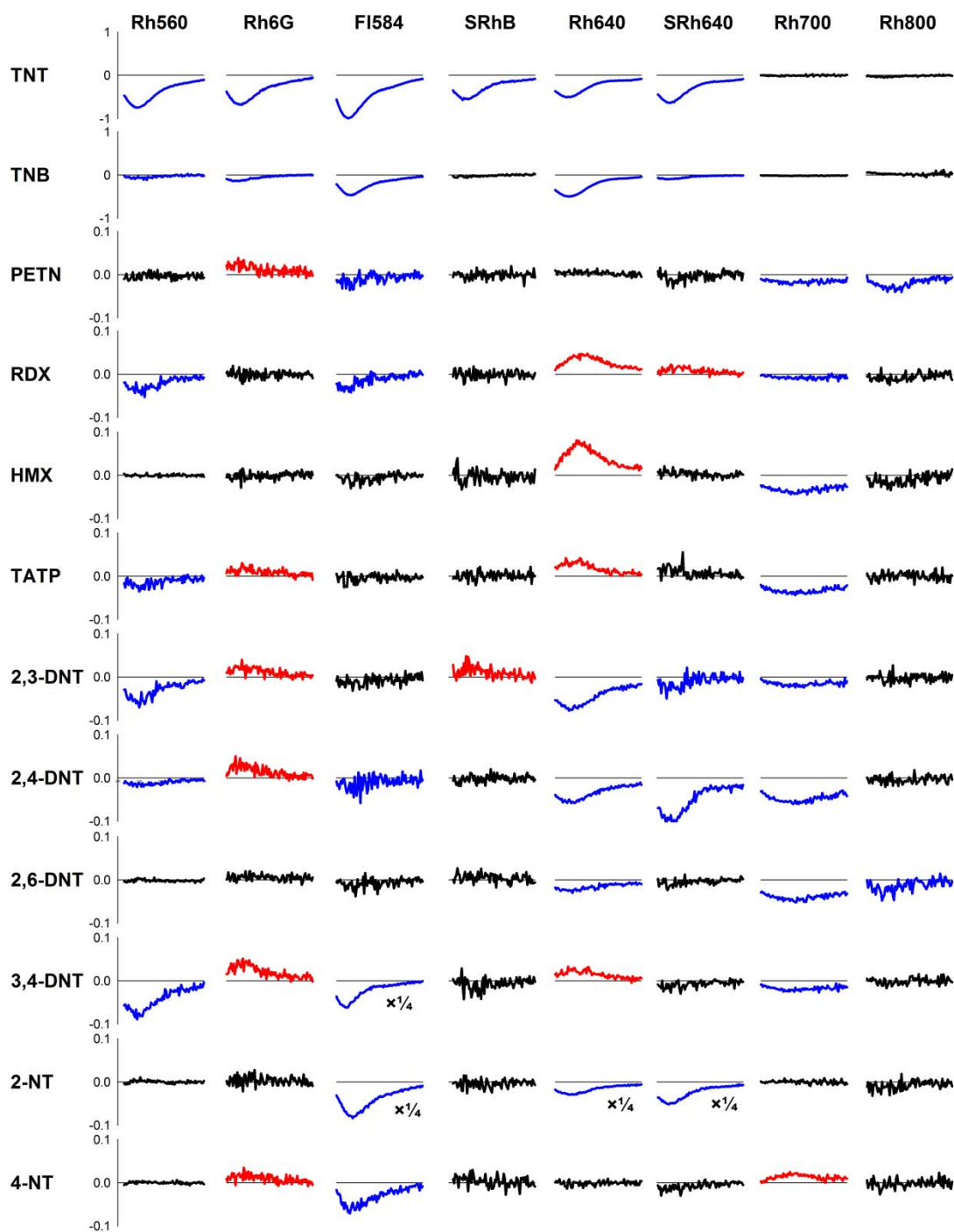


Figure 4. Emission difference spectra for the exposure of explosive analytes to selected fluorophores in DMF solution, normalized to the initial emission maximum. Blue spectra indicate the observed quenching of emission, red spectra indicate the observed enhancement of emission, and black spectra indicate minimal change in emission.

3. *Fluorescence enhancement using polymer thin films*

All of the previously described results pertain to solutions. Ultimately, a sensor that can detect TNT and other explosives in the gas phase is the desired goal. The design plan was to use the fluorophore array described above on a solid substrate and test this against explosive vapors. To further improve the sensitivity, the sensor array was to be designed to take advantage of a technique reported in the literature known as metal enhanced fluorescence (MEF). A MEF structure has a substrate coated with silver or gold nanoparticles, a few nm thick dielectric layer (typically SiO₂), and then the fluorophore. The surface plasmon resonance of the Ag or Au layer provides an electric field enhancement to the fluorophore, which leads to an emission enhancement, typically of about 50.

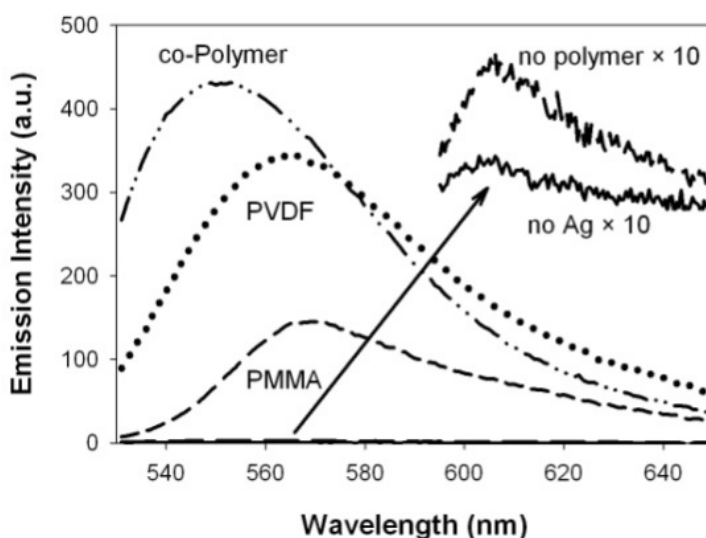


Figure 5. Emission spectra of Rhodamine 6G coated on different polymers cast on a porous Si/Ag substrate. All spectra are normalized to the spectrum with no Ag and no polymer, p-Si/Rh6G (solid line). MEF samples were: no polymer, p-Si/Ag/Rh6G (long dashed); p-Si/Ag/PMMA/Rh6G (short dashes); p-Si/Ag/PVDF/Rh6G (dotted); and p-Si/Ag/co-polymer/Rh6G (dot-dashed). The inset shows the p-Si/Rh6G and p-Si/Ag/Rh6G spectra multiplied by 10.

When preparing the MEF structure we decided to try using a polymer for the dielectric layer, since this would be easier and cheaper to make. To our surprise, the observed fluorescent enhancements were significantly larger than reported in the literature. An example of this is shown in Figure 5. Several different polymers were examined and all showed varying degrees of enhancement. The ordinate in Fig. 5 is the enhancement factor observed based on the intensity of the fluorophore emission with no Ag layer and no dielectric layer. Enhancements about 10 times of those seen with normal MEF were observed.

To test if this enhancement could be used for explosives detection, a sample was made using a fluorophore that is known to quench upon exposure to gas phase TNT, MEH-PPV. The results of this are shown in Figure 6. Two interesting results were observed. First, while an enhancement was seen for MEH-PPV, it was much smaller than observed for Rhodamine 6G, the fluorophore used to obtain the data in Fig. 5. More positively, the time constant for the quenching of the TNT was reduced by an order of magnitude for the MEF structure. The reason for both of these effects is unknown. However, the initial data does show that it is possible to concurrently improve the sensitivity of the measurement and do so in a shorter time.

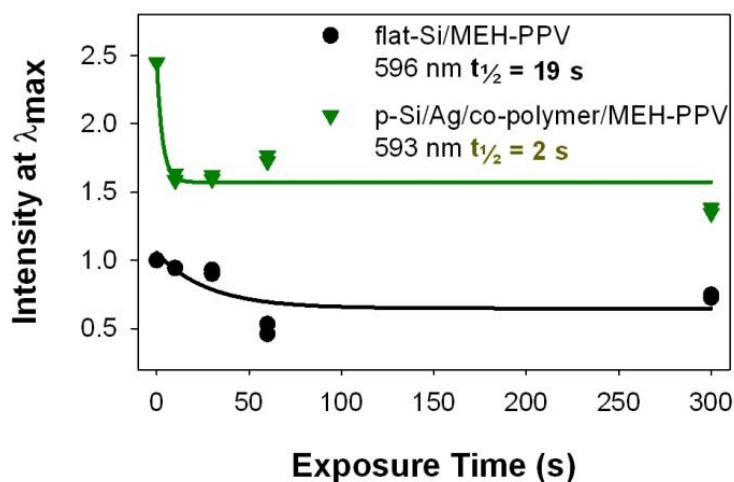


Figure 6. Quenching of MEH-PPV at λ_{\max} (598 nm) upon exposure to TNT. Black circles – flat Si/MEH-PPV; black line – exponential fit with half-life = 19 s; green triangle – p-Si/Ag/co-polymer/ MEH-PPV; green line – exponential fit with half-life 2 s. Intensities are normalized to the flat-Si/MEH-PPV value at $t = 0$ s.

Publications

1. Christopher A. Latendresse, Syrena C. Fernandes, Sangmin You, Hui Qi Zhang, William B. Euler, "Fluorescent Species Formed by Reaction Trinitroaromatics with *N,N*-Dimethylformamide and Hydroxide," *J. Phys. Chem. A* **2013**, *117*, 324 – 332
2. Meredith A. Matoian, Richard Sweetman, Emily C. Hall, Shayna Albanese, William B. Euler, Light Trapping to Amplify Metal Enhanced Fluorescence with Application for Sensing TNT," *J. Fluoresc.*, **2013**, accepted pending corrections.
3. Christopher A. Latendresse, Syrena C. Fernandes, Sangmin You, Hui Qi Zhang, William B. Euler, "A Fluorometric Sensing Array for the Detection of Military Explosives and IED Materials," *Anal. Methods*, **2013**, under review.

4. Christopher A. Latendresse, Syrena C. Fernandes, Sangmin You, William B. Euler, "Comparing the Roles of Hydroxide and Amines in Reactions with TNT," *J. Am. Chem. Soc.*, **2013**, to be submitted.
5. Christopher A. Latendresse, William B. Euler, "Relative Thermodynamics of TNT Reactions Commonly Used for Sensor Applications: Computational Modeling *in vacuo* and in Solution," *J. Am. Chem. Soc.*, **2013**, to be submitted.

Students

Ph.D. Christopher A. Latendresse, May, 2013

M.S. Emily C. Hall, May 2013; Meredith A. Matoian, May 2013.

B.S. Shayna Albanese, December, 2013; Syrena C. Fernandes, May 2013; Alessandra Lonardo, May 2013; Courtney McGowan, May 2013; Sangmin You, May 2016; Hui Qi Zhang, May 2014.



Fluorescent Species Formed by the Reaction of Trinitroaromatics With *N,N*-Dimethylformamide and Hydroxide

*Christopher A. Latendresse, Syrena C. Fernandes, Sangmin You, Hui Qi Zhang, and William B. Euler**

University of Rhode Island Department of Chemistry, 51 Lower College Road, Kingston, RI 02881, USA

ABSTRACT

Trinitrobenzene (TNB) and trinitrotoluene (TNT) react in *N,N*-dimethylformamide (DMF) to form multiple species in solution. Despite structural similarities, electronic spectra show that the reactivity is different for TNB and TNT. In addition to reaction with the DMF solvent, residual water in nominally dry DMF generates sufficient hydroxide for reaction with TNB and TNT. Multiple sigma adducts are formed and observed to be fluorescent, which has not been previously reported. Both TNB and TNT show the capacity to form sigma adducts with hydroxide and DMF, while methyl hydrogens of TNT can be deprotonated by hydroxide.

KEYWORDS: trinitrobenzene (TNB); trinitrotoluene (TNT); Meisenheimer complex.

1. Introduction

Common reactions of nitroaromatic molecules are of interest to the scientific community, especially for the application of explosive detection. Many products of these reactions have absorbances in the visible range, which allow for a multitude of detection approaches including colorimetry^{1,2} and fluorescence methods.³⁻⁸ 2,4,6-Trinitrotoluene (TNT) and 1,3,5-trinitrobenzene (TNB) are perhaps the most studied of the nitroaromatic family, having the highest electron deficiency in their pi system from their three nitro groups; this leaves them the most susceptible to nucleophilic attack, thereby converting the original species with no visible absorbance features to a vibrantly colorful product (commonly referred to as a "Meisenheimer complex"). While TNT and TNB share this type of reactivity, TNT also has acidic hydrogens that can be abstracted to form the TNT anion (TNT⁻).⁹⁻¹² Since both TNT products have absorbances in similar locations in the visible range,^{9,10} and basicity and nucleophilicity tend to go hand in hand, it is a precarious process to be able to differentiate TNT sigma adducts from TNT⁻.

It is commonly believed that nitroaromatics and their nucleophilic substitution products are not fluorescent, and therefore additional mechanisms need to be imposed in order to address their sensing using a fluorescence method. Many sensors rely on the fluorescence quenching of a reporter molecule, where the emission of a selected fluorophore decreases as a function of interacting with an explosive analyte. This process may result from either dynamic or static quenching, but is most often observed as a combination of both mechanisms.¹³⁻¹⁸ Since quenching decreases the observed signal as a function of addition of analyte, these collective mechanisms are commonly referred to as "turn-off" mechanisms.

Another typical approach utilizes absorbance features of an analyte in a resonance energy transfer mechanism (RET). In this mechanism, the excited state of a donor molecule is deactivated by the transfer of energy across space to an acceptor molecule, promoting it to its excited state. Since the mechanism does not necessitate direct contact between donor and acceptor, a sensor developed using RET has the capacity to be more sensitive. If the acceptor is emissive, then the observation is ratiometric with a decrease of donor emission concurrent with an increase in acceptor emission; otherwise, the observation is just a quenching of the donor's emission. Because many explosive analytes do not have visible absorbance features or react under the same conditions, this is also touted as a selectivity parameter to differentiate nitroaromatics. Many proposals in the literature^{3,6-8} use the visible absorbance features of nitroaromatic products to justify their use as a RET acceptor, but since these products lack emissive features the sensing remains a "turn-off" mechanism.

We describe herein the observation of fluorescence emission from TNT and TNB products formed in *N,N*-dimethylformamide (DMF), without addition of any strong base or nucleophile. The competing equilibria are complicated. TNT is observed to react with OH⁻ (present from the trace water in nominally dry DMF) forming the non-emissive TNT⁻ or an emissive sigma adduct with DMF or OH⁻. TNB also shows the ability to form emissive sigma adducts with either DMF or OH⁻. In addition, the emission of TNT adducts may give a long desired method to clarify their abundance from that of TNT⁻. This is the first description of these products as being emissive, with evidence of the formation of products through a reaction with DMF. This work also demonstrates the need to understand the role of even trace amounts of water in working TNT sensors.

2. Materials and Methods

2.1. Materials. TNB was purchased from Fisher Scientific wetted with ca. 40% water with 98.0% purity. Concentrations of TNB solution were thus calculated using a value of 60% TNB solid by mass. TNT was obtained from Drs. Jimmie Oxley and James Smith and was used without further purification. DMF ($\geq 99.5\%$) was purchased from Fisher Scientific and used as received. H₂O (HPLC grade) was purchased from Sigma and used as received. Aqueous 0.1 M NaOH and HCl solutions were purchased from Anachemia.

2.2. Absorbance and Fluorescence Measurements. Absorbance spectra were obtained between 300 and 800 nm on a Perkin-Elmer Lambda 900 UV/Vis/NIR spectrophotometer. Fluorescence spectra were obtained with a Horiba Fluorolog-3, Xe arc lamp excitation source, 3 nm excitation and emission slits for TNB, 5 nm excitation and emission slits for TNT, 0.1 sec integration time, and ambient temperature. TNB and TNT titration emission scans were excited at 446 nm, while additional samples were investigated using excitations every 10 nm from 350 to 600 nm. TNB and TNT excitation scans were monitored at an emission wavelength of 550 and 700 nm.

2.3. Peak Fitting Method. The commercially available software PeakFit© and SigmaPlot© were employed to fit emission spectra to constituent peaks. Initially, spectra were fit with an increasing number of Gaussian peaks with vibrationally related maxima, FWHM (full width at half maximum), and peak intensity until a consistent set of peaks were obtained for each individual spectrum in a given titration. After this, a global fit was undertaken upon all related spectra at the same time using the average initial parameters as a starting point. Converged fits were obtained without unrealistic or inconsistent parameters to support chemical mechanisms.

2.4. Computational Analysis. Spartan '10 computational software¹⁹ was used to propose the relative absorbance maxima for the isomers of [TNT-OH]⁻. Structures were optimized at the HF/6-311+G** level without imaginary vibrational frequencies. TDDFT energies and absorbance spectra were calculated using the converged structures at the B3LYP/6-311+G** level.

3. Results and Discussion

3.1. UV/Vis Absorption

The addition of a few crystals of TNB or TNT into DMF rapidly generates colorful products visible to the naked eye. To monitor these products, a 7×10^{-5} M solution of TNB and a 1.1×10^{-4} M TNT solution were prepared in DMF and immediately observed using absorbance and fluorescence spectroscopy. The initial absorbance spectrum for the TNB solution (Figure 1a) shows maxima at 452 nm and 523 nm, reminiscent of other "Meisenheimer" type adducts reported in literature with a narrow feature around 420 nm and a broader set of features around 500 nm.^{9,10}

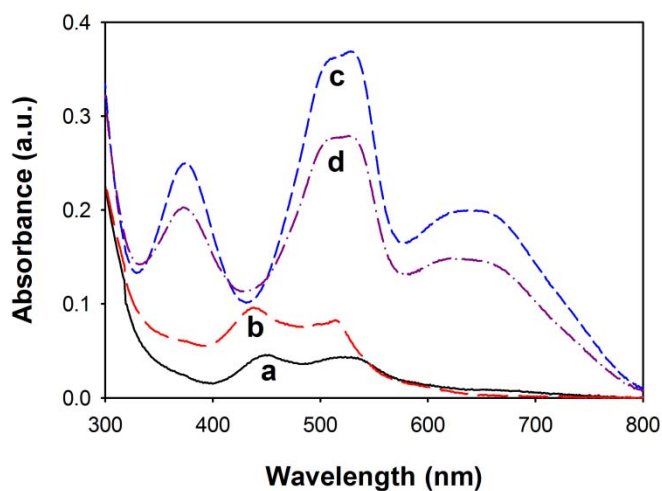


Figure 1. Initial and final absorbance spectra from trinitroaromatics titrated with water in DMF: (a) 7×10^{-5} M TNB in DMF; (b) TNB + 30 μ L H₂O in DMF; (c) 1.1×10^{-4} M TNT in DMF; (d) TNT + 30 μ L H₂O in DMF.

Only two possible products are expected to be formed by TNB, which are sigma adducts with DMF or OH⁻ (TNB-DMF and [TNB-OH]⁻, respectively - see Scheme 1); the absorbance changes observed suggest an equilibrium between the DMF adduct and the hydroxide adduct with free TNB. Titration of water to the TNB solution was done in increments of 5 μ L. The initial concentration of water in the TNB solutions was 6×10^{-4} M due to the availability as a wetted solid, whereas TNT was not pre-wetted. While the autoionization constant of water in DMF is not available, we estimate the initial [OH⁻] in the TNB solutions to be on the order of 10^{-10} M using K_w in pure water as an approximation. The initial [OH⁻] in the TNT solutions will be less than this, as the same amount of water is not carried in by solid addition. Titration of water gives evidence of a tight isosbestic point at 318 nm early in the titration and a second isosbestic point at 475 nm later in the titration (see Supplementary Information, Fig. S1). Addition of water decreases the initial absorbance features at higher wavelengths while increasing the new features at lower wavelengths; after 30 μ L of water are added, new maxima are observed at 438 nm and 514 nm. This likely indicates the indirect conversion of the TNB-DMF adduct to the [TNB-OH]⁻ adduct. The isosbestic point that is well defined at 318 nm represents the loss of UV features of TNB in solution with the rise of an absorbance peak from [TNB-OH]⁻. The late forming isosbestic point at 475 nm shows a decrease in absorbance at higher wavelengths from the loss of TNB-DMF while features at lower wavelength increase from the generation of [TNB-OH]⁻; the late isosbestic point formation may be resultant from a third species that completely disappears after the second addition of water - this may be a dinitrobenzene impurity in the TNB

or a charge-transfer complex that goes below limits of detection. TNB CT complexes have been reported in the literature, with maxima ranging from the UV to the violet end of the visible spectrum.²⁰

To help confirm our assignments, we monitored the absorbance of the TNB solution with the addition of 5 μL of 0.1 M NaOH/H₂O and the addition of 5 μL of 0.1 M HCl/H₂O. Figure 2a shows the absorbance increase from the addition of NaOH and the decrease from the addition of HCl.

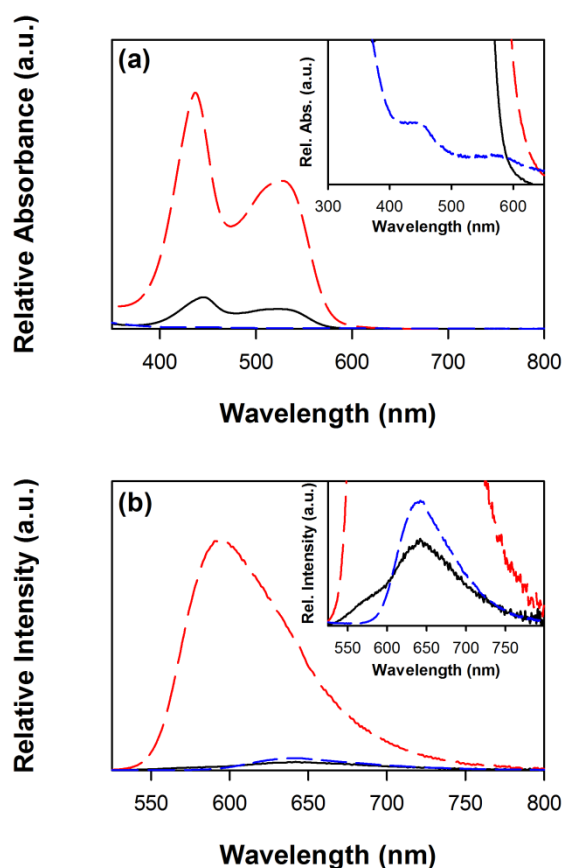


Figure 2. (a) Absorbance spectra and (b) emission spectra resultant from 7×10^{-5} M TNB in DMF (—); + 5 μL of 0.1 M NaOH/H₂O ($[\text{OH}^-]/[\text{TNB}] = 3.6$) (---); + 5 μL of 0.1 M HCl/H₂O ($[\text{H}^+]/[\text{TNB}] = 3.6$) (- - -). Samples were excited at 446 nm. The addition of NaOH increases the concentration of $[\text{TNB-OH}]^-$ in solution, increasing the initial absorbance and emission spectra. The addition of HCl decreases the concentration of $[\text{TNB-OH}]^-$, leaving TNB-DMF as the only observed absorbing and emitting species in the visible range. The insets show the lower intensity features closer to baseline.

The initial spectral shape is retained with the NaOH addition, supporting that the initial spectrum is at least in part resultant from the formation of $[\text{TNB-OH}]^-$. There is a small shift in the absorbance maximum, initially observed at 450 nm shifting to 440 nm. This indicates that there is another absorbing species involved. The addition of HCl helps to clarify this spectrum, as it removes OH^- from solution. Two very weak signals are retained after the acidification, as seen in the inset on Figure 2a. We attribute these features to be from the TNB-DMF adduct, since there is still an overwhelming amount of DMF available that is not protonated. These experiments support our assignments of the generation of $[\text{TNB-OH}]^-$ and TNB-DMF in our titration of water into TNB/DMF solution.

The addition of TNT to DMF shows a very different absorbance spectrum (Figure 1c), suggesting different products. Maxima for this initial spectrum are observed at 375 nm, 509 nm, 529 nm, and 645 nm. Since TNT has acidic methyl protons whereas TNB does not, it is not surprising that this absorbance spectrum has been previously attributed to TNT^- ;⁹⁻¹² in this particular system, hydroxide from ambient water is likely acting as the Brønsted-Lowry base. The addition of water leads to the observation of isosbestic points at 339 nm, 414 nm, and 451 nm (see Supplementary Information Fig. S2), suggesting the contribution of only two absorbing species. This can be explained through the loss of TNT^- and the increase in $[\text{TNT-OH}]^-$, while there is little evidence here to suggest a DMF adduct. If there is a DMF sigma adduct, it either has a low molar absorptivity or the concentration is much lower than that of the corresponding hydroxide adduct. In similar fashion to our TNB experiments, we added 5 μL of 0.1 M NaOH/ H_2O and 5 μL of 0.1 M HCl/ H_2O to our TNT solution to help confirm our spectral assignments. Figure 3a shows the absorbance growth of the TNT/DMF solution with the addition of NaOH, and the decrease of the absorbance spectrum with the addition of HCl.

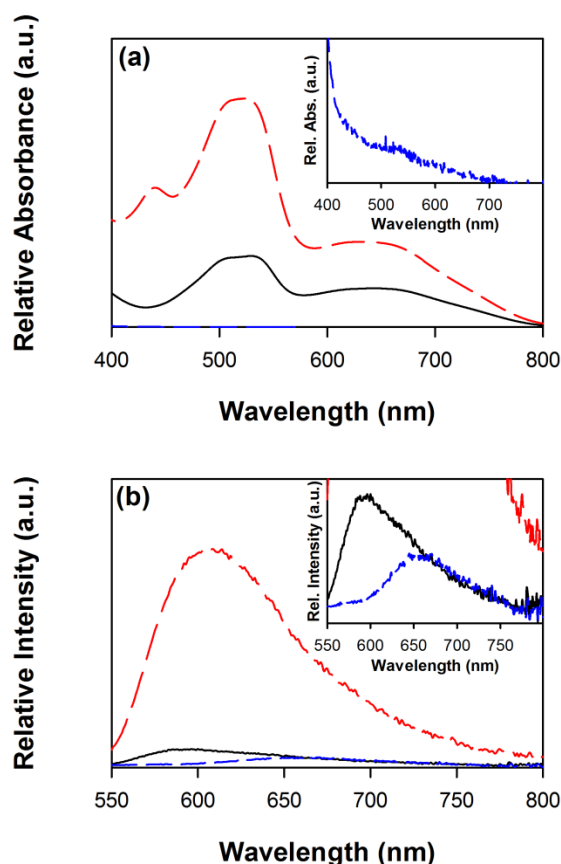
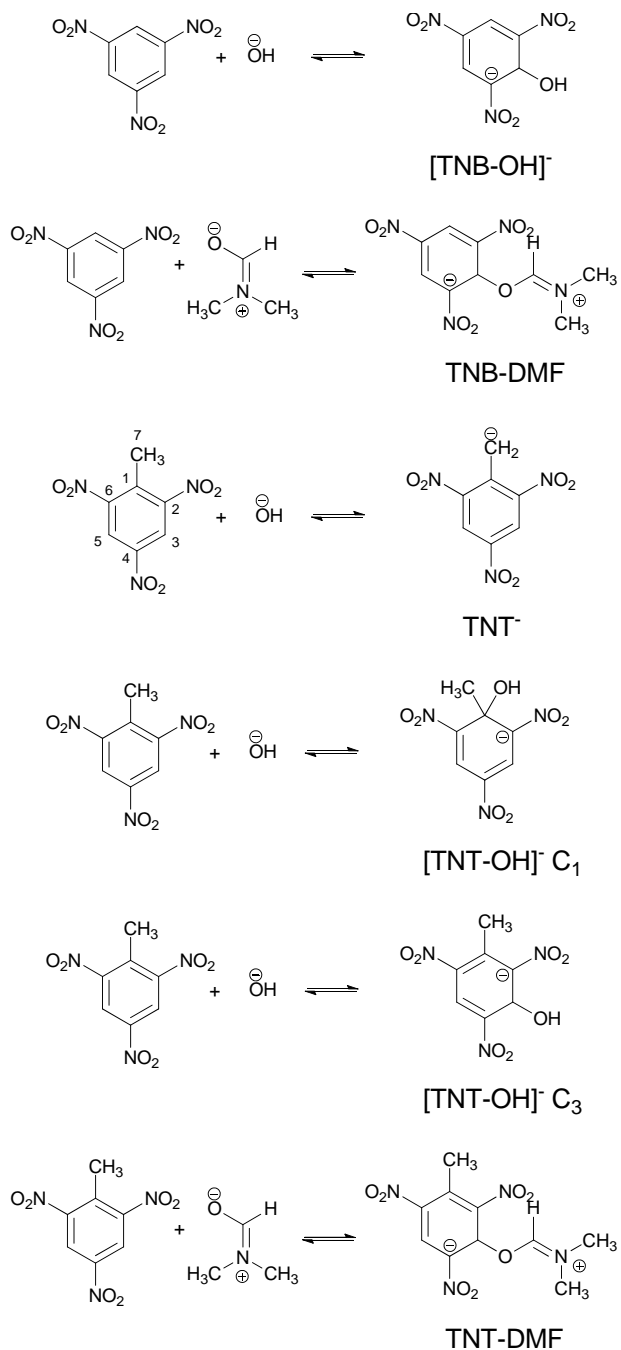


Figure 3. (a) Absorbance spectra and (b) emission spectra resultant from 1.1×10^{-4} M TNT in DMF (—); + 5 μ L of 0.1 M NaOH/H₂O ($[\text{OH}^-]/[\text{TNT}] = 2.3$) (- - -); + 5 μ L of 0.1 M HCl/H₂O ($[\text{H}^+]/[\text{TNT}] = 2.3$) (- - -). Samples were excited at 446 nm. The addition of NaOH increases the concentration of $[\text{TNT-OH}]^-$ in solution, increasing the initial absorbance and emission spectra. The addition of HCl decreases the concentration of $[\text{TNT-OH}]^-$, leaving TNT-DMF as the only observed absorbing and emitting species in the visible range. The insets show the lower intensity features closer to baseline.

As expected, the addition of NaOH created more TNT^- , increasing the absorbance but retaining nearly the same spectral shape throughout the visible range. The new feature at 443 nm comes from the generation of $[\text{TNT-OH}]^-$, where the growth in the water titration occurred. Addition of HCl obliterated the initial absorbance spectrum; this is consistent with the initially observed product being TNT^- , which is fully protonated as the solution is acidified. The inset on Figure 3a shows the baseline, where there is a very small absorbance component remaining. This may indicate a small amount of TNT-DMF that is not affected by HCl addition. Again, these

experiments have helped to support our original assessment that OH^- from the water titration is responsible for the absorbance changes, forming both TNT^- and $[\text{TNT-OH}]^-$ and possibly TNT-DMF. Overall, the absorbance spectra indicate sigma adduct formation for both TNB and TNT along with acid-base reactivity for TNT. The proposed reaction products are summarized in Scheme 1.

Scheme 1. Proposed reactions of TNB/TNT with DMF or OH⁻.



3.2. Emission & Excitation Spectra of TNB Products

Emission spectra were collected for both systems before and after each addition of water in the titration. In the case of TNB, the samples were excited at 446 nm in an effort to observe possible emissions from each species. Figure 4 shows the emission spectra for the initial addition of TNB into DMF and also after the addition of 30 μL H_2O . The initial spectrum has a maximum at 650 nm, which decreases as water is added (see Supplementary Information, Fig. S3), while a new maximum is observed at 586 nm, which increases with the addition of water. In correlation to the absorbance spectra, the initial emission spectrum represents major features of the TNB-DMF adduct, which then gives way to the $[\text{TNB-OH}]^-$ adduct. The previously discussed NaOH and HCl additions support this assignment. Figure 2b shows the emission spectra of the TNB/DMF samples with the addition of NaOH and HCl, excited at 446 nm. We observe increase in emission at 591 nm for TNB + NaOH, indicating this feature to be resultant of the formation of $[\text{TNB-OH}]^-$. This feature overwhelms the spectrum, such that the original feature at 637 nm can no longer be seen. The addition of HCl to the TNB/DMF solution causes a decrease in emission at higher energy, but an increase in emission beyond 600 nm. Combined with our assessment of the absorbance spectra, this indicates the loss of $[\text{TNB-OH}]^-$ concurrent with the increase in TNB-DMF. This is likely the result of the reversion of $[\text{TNB-OH}]^-$ back to free TNB, which then shifts the TNB-DMF formation equilibrium forward.

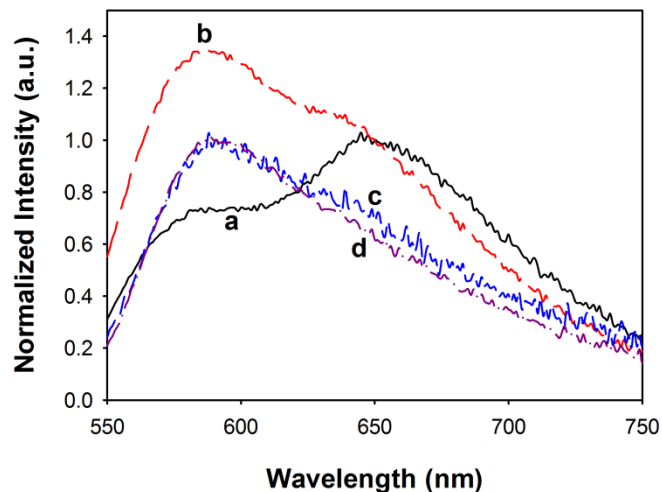


Figure 4. Initial and final emission spectra from trinitroaromatics titrated with water in DMF: (a) 7×10^{-5} M TNB in DMF; (b) TNB + 30 μL H_2O in DMF; (c) 1.1×10^{-4} M TNT in DMF; (d) TNT + 30 μL H_2O in DMF. TNB spectra normalized at 650 nm, TNT spectra normalized at 591 nm.

In an effort to understand the exchange between the emissive species in the titration, a separate pair of samples were prepared with identical concentration of nitroaromatic and water as the final point in the titration. These samples were allowed to equilibrate for one hour before obtaining emission and excitation data. Both sets of emission spectra were fit to a modeled set of Gaussian peaks, based on initial parameters from selective excitation of individual products; the TNB and TNT samples show a unique excitation spectrum for emission at 550 nm and evidence of a separate species at 700 nm emission (see Figure 5).

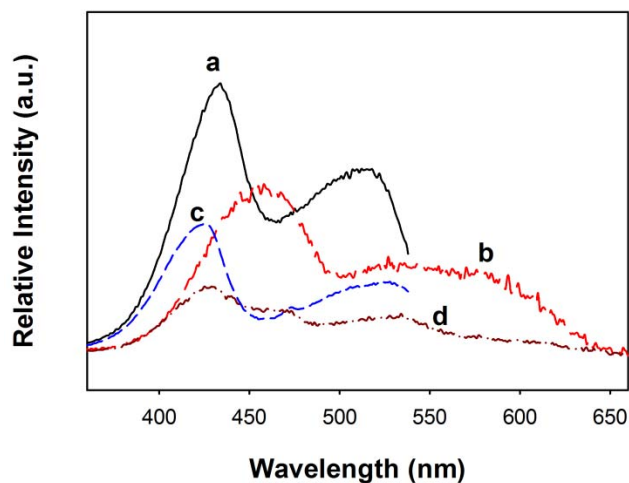


Figure 5. Excitation spectra from trinitroaromatics with water in DMF: 7×10^{-5} M TNB + 30 μ L H₂O in DMF (a) 550 nm emission, (b) 700 nm emission; 1.1×10^{-4} M TNT + 30 μ L H₂O in DMF (c) 550 nm emission, (d) 700 nm emission.

Excitation maxima for the TNB solution are observed at 433 nm and 515 nm for 550 nm emission and 448 nm, 527 nm and 575 nm for 700 nm emission. This corresponds well to the absorbance features described previously, where [TNB-OH]⁻ absorbance and excitation features are blue-shifted relative to TNB-DMF. The maximum observed for TNB-DMF at 527 nm may have slight overlap from a [TNB-OH]⁻ emission contribution at 700 nm. Figure 6a shows the [TNB-OH]⁻ emission spectrum resultant from 390 nm excitation of the TNB sample, indicating that three Gaussian peaks were required for a proper fit. As expected, the emission spectrum is similar in shape only to the lower energy features in the excitation spectrum; this indicates that all emission is occurring from the first electronic excited state.

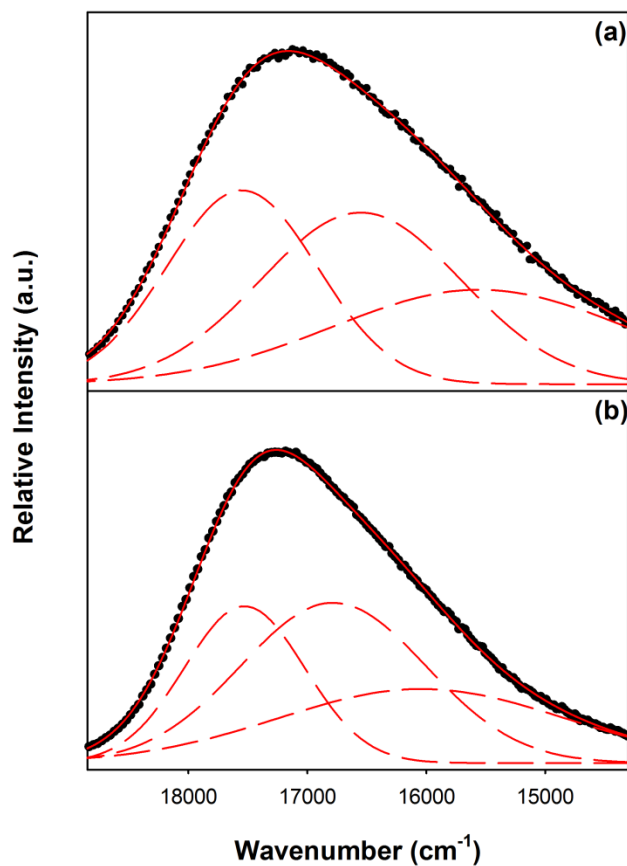


Figure 6. Emission spectra of OH^- adducts fit with a three Gaussian spectrum for initial modeling parameters: (a) 7×10^{-5} M TNB + 30 μL water in DMF, 390 nm excitation; (b) 1.1×10^{-4} M TNT in DMF + 30 μL water, 370 nm excitation. Scatter points represent raw emission data, dashed lines represent constituent Gaussian peaks, and solid lines represent the sum of the Gaussian peaks for the overall modeled spectrum.

The TNB-DMF emission spectrum was observed using an excitation of 600 nm, as seen in Figure 7a modeled with two Gaussian peaks. These sets of peaks were used as initial parameters in the establishment of the overall model, fitting both species' spectra at the same time. An intensity ratio was held between peaks in the same spectrum, normalizing one intensity to the highest energy feature. Since emission generally occurs through transition from the ground vibrational state of the first electronic excited state to an excited vibrational excited state in the ground electronic excited state, the energy spacing between peaks in the same spectrum should

indicate a vibrational mode for the ground state of an emitting species. Due to this, a vibronic energy parameter was included in the equation, separating the peak maxima equally, for partial validation of data fitting. The complete set of parameters accounting for each emissive species in our model can be found in Table 1. The model's equation can be found in Supplementary Information.

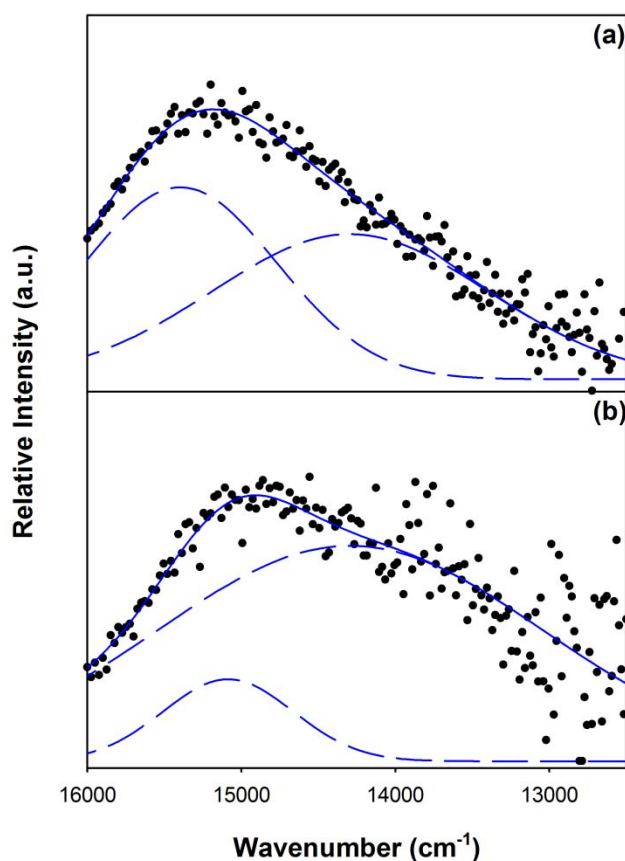


Figure 7. Emission spectra of DMF adducts fit with a two Gaussian spectrum for initial modeling parameters: (a) 7×10^{-5} M TNB + 30 μ L water in DMF, 600 nm excitation; (b) 1.1×10^{-4} M TNT in DMF + 30 μ L water, 600 nm excitation. Scatter points represent raw emission data, dashed lines represent constituent Gaussian peaks, and solid lines represent the sum of the Gaussian peaks for the overall modeled spectrum.

Table 1. Fitting parameters for TNB/TNT emission product spectra.

	Intensity Ratio (a.u.)	Peak max (cm^{-1})	FWHM (cm^{-1})	Vibronic Energy (cm^{-1})
[TNB-OH] ⁻	a ₁ 1*	λ_1 17496 ± 7	FWHM ₁ 640 ± 10	v ₁ 990 ± 10
	a ₂ 0.89 ± 0.02	16510 ± 10	FWHM ₂ 850 ± 10	
	a ₃ 0.49 ± 0.01	15530 ± 20	FWHM ₃ 1220 ± 10	
TNB-DMF	a ₄ 1*	λ_2 15370 ± 30	FWHM ₄ 626 ± 3	v ₂ 1000 ± 30
	a ₅ 0.76 ± 0.02	14370 ± 40	FWHM ₅ 900 ± 20	
[TNT-OH] ⁻ C ₁	a ₁ 1*	λ_1 17317 ± 6	FWHM ₁ 530 ± 30	v ₁ 770 ± 30
	a ₂ 1.04 ± 0.03	16550 ± 30	FWHM ₂ 710 ± 40	
	a ₃ 0.48 ± 0.02	15780 ± 60	FWHM ₃ 1220 ± 40	
TNT-DMF	a ₄ 1*	λ_2 15390 ± 10	FWHM ₄ 440 ± 20	v ₂ 630 ± 20
	a ₅ 2.8 ± 0.9	14760 ± 20	FWHM ₅ 1190 ± 60	
[TNT-OH] ⁻ C ₃	a ₆ 1*	λ_3 17930 ± 20	FWHM ₆ 499 ± 3	N/A

*Normalized in fitting equation

In the assigned [TNB-OH]⁻ spectrum, the energy difference between the two modeled peaks is 990 cm^{-1} , while the difference in the TNB-DMF spectrum is 1000 cm^{-1} . These energies may represent out of plane ring bending modes, formed by the nucleophilic attack. To verify that these modeling parameters are valid, the TNB fitting model was applied to emission data with varying excitation wavelengths. Figure 8a shows emission data excited from 410 to 450 nm with the TNB model overlaid on the raw data. The model clearly applies well to data collected across a range of excitation wavelengths that excite each species in varying quantities.

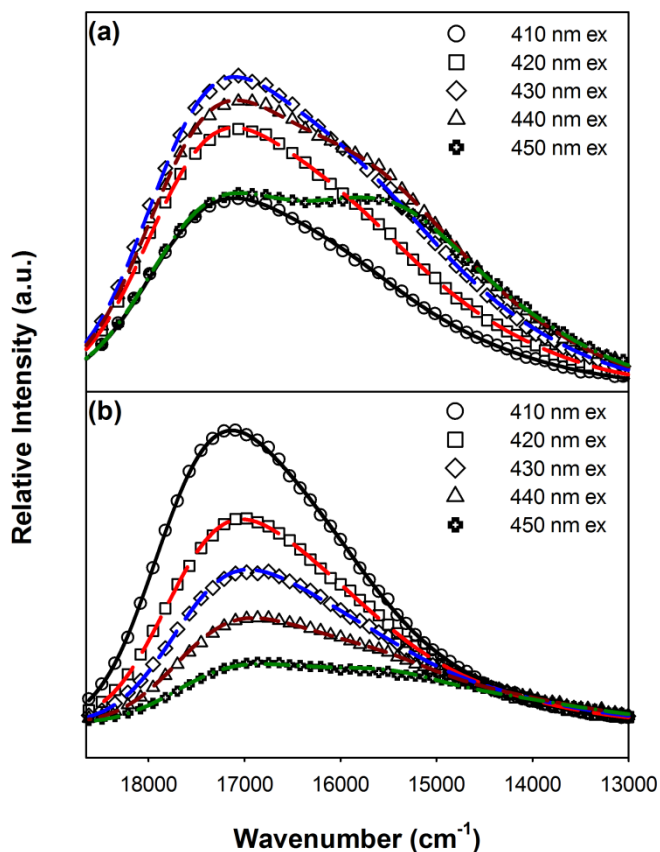


Figure 8. Emission spectra of trinitroaromatics with water in DMF as a function of excitation wavelength (410 to 450 nm excitation): (a) 7×10^{-5} M TNB + 30 μ L water in DMF; (b) 1.1×10^{-4} M TNT in DMF + 30 μ L water. Scatter points represent raw emission data, and lines represent the fit resultant from each established model.

Figure 9 shows emission spectra for the individual species fit to the initial, middle, and final point of the water titration. The two modeled species' spectra fit the overall spectrum very well throughout the titration, indicating the decrease of TNB-DMF relative to $[\text{TNB-OH}]^-$. The entire set of TNB titration spectra with the model fitting can be found in the Supplementary Information (Figure S4). Using these modeled fits, the area under each species' spectrum was calculated at each titration point.

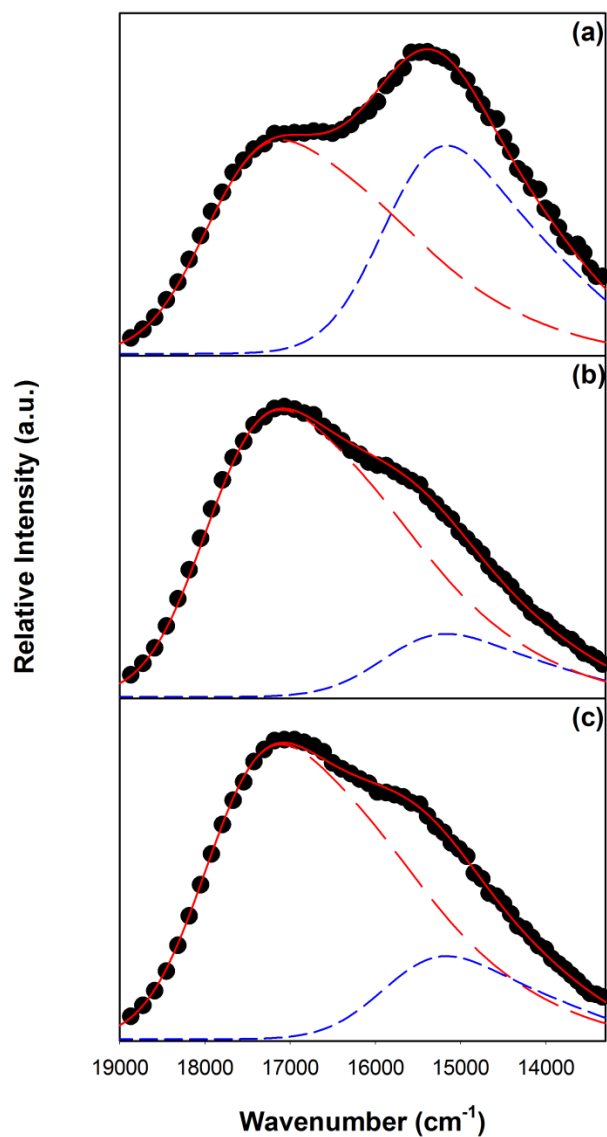


Figure 9. Emission spectra from TNB titration with water in DMF, fit with a two species model for $[\text{TNB-OH}]^-$ (— —) & TNB-DMF (- - -). (a) 7×10^{-5} M TNB in DMF; (b) + 15 μL H_2O ; (c) + 30 μL H_2O . Scatter points represent raw emission data, and lines represent the fit resultant from each established model.

Figure 10 shows the trend of each spectrum's integrated area as a function of the addition of water. The general trend supports our original assessment: $[\text{TNB-OH}]^-$ is observed to increase while TNB-DMF decreases with the addition of water.

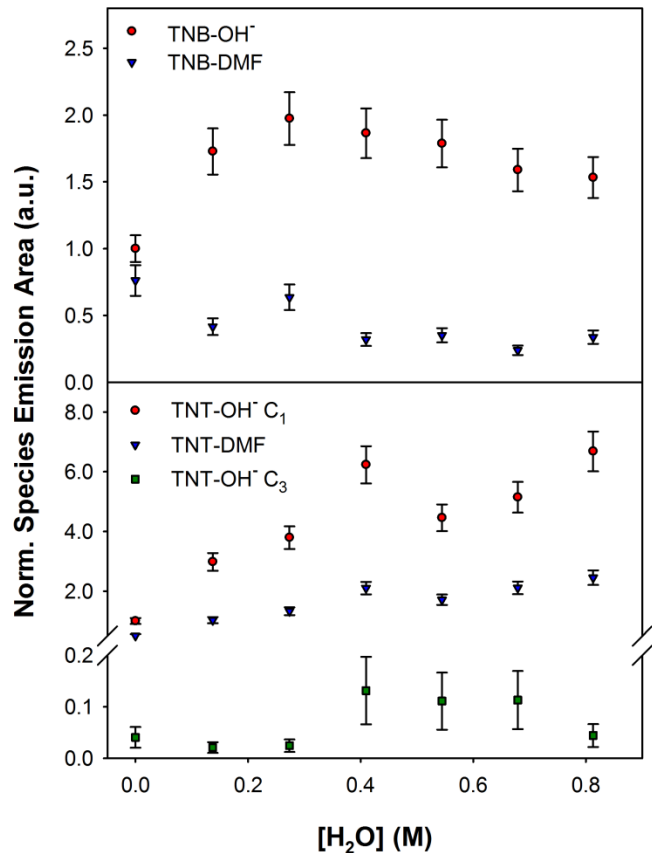


Figure 10. Normalized modeled emission spectrum area as a function of increasing concentration of water.

3.3. Excitation and Emission Spectra of TNT Products

For TNT, the emission spectra of the titration do not show a great deal of shape change (see Supplementary Information S5). Figure 4 shows the normalized emission of the initial TNT solution and after the addition of 30 μ L water, excited at 446 nm. These two spectra appear to be superimposable, however the excitation data in Figure 5 refutes the existence of only one species. In similar fashion to the TNB data, two distinctly different excitation spectra are acquired using 550 nm emission and 700 nm emission. As previously mentioned, the methyl

group on TNT gives additional reactions that TNB cannot exhibit, so identification of emissive species requires caution. Since the emission intensity increases (Supplementary Information Fig. S5) while the absorbance of TNT^- is decreasing, TNT^- cannot be the emissive species. Also, the established TNT^- absorbance spectrum^{9,10} has absorbance at lower energy beyond 700 nm; this rules out TNT^- emitting at higher energy wavelengths. These emission spectra show similarity to the products that are formed from TNB, which does not have the ability to be deprotonated. In addition, Figure 5 shows that the excitation spectra are similar for $[\text{TNB-OH}]^-$ and the TNT product after adding 30 μL of water; with an observed emission at 550 nm, excitation maxima are observed at 424 nm and 526 nm. This supports that this excitation spectrum belongs to one of the possible $[\text{TNT-OH}]^-$ species. Features similar to TNB-DMF are seen for the excitation spectrum at 700 nm emission, with maxima around 460 nm and 590 nm, but are not as pronounced relative to the hydroxide sigma adduct features. Figure 3b shows the emission spectra from the aforementioned addition of NaOH and HCl to the TNT/DMF solution. The addition of NaOH causes a sizable increase in emission at 603 nm, too large of a change to be consistent with the more modest increase in the absorbance of TNT^- . Instead, this is consistent with the magnitude of the absorbance increase seen for $[\text{TNT-OH}]^-$. The addition of HCl to the TNT/DMF solution eliminates the $[\text{TNT-OH}]^-$ emission signal, again by removing hydroxide from the formation equilibrium. The inset on Figure 3b shows a component of the original emission that remains around 655 nm after the acidification, which is consistent with the analogous formation of a DMF adduct, TNT-DMF.

To further understand the TNT reactions, the emission data was also modeled using the same approach as described above. Figure 6b shows the emission spectrum resultant from 370 nm excitation, where only $[\text{TNT-OH}]^-$ is excited. The outcome was a three peak spectrum with

slight differences from the [TNB-OH]⁻ model, which was not able to reasonably fit all spectra in the titration by itself even when allowing for relaxation of initial parameters. TNT-DMF emission peaks were initially fit using a 600 nm excitation (see Figure 7b), and subsequently iterated with the [TNT-OH]⁻ parameters to establish an overall model. It became obvious that there was an additional emitting feature for several reasons. First, the emission maximum appears to shift to higher energy as the excitation shifts to higher energy (see Figure 8b), which was not observed for TNB. Also, the initial fits for [TNT-OH]⁻ and TNT-DMF were unable to account for all of the observed emission data collected between samples excited at varying wavelengths, even when the parameters were allowed to change dramatically. The addition of one extra Gaussian peak at a higher energy maximum than [TNT-OH]⁻ was able to globally satisfy all data without drastically altering the initial [TNT-OH]⁻ and TNT-DMF fits. The complete equation for the TNT model can be found in the Supplementary Information.

The existence of a third species seems to go against the observation of tight isosbestic points, which typically indicate only two absorbing species in solution. TNT⁻ and [TNT-OH]⁻ are well established and clearly evident here. TNT-DMF has been observed through fluorescence, and supported through analogous chemistry to the formation of TNB-DMF. As a third contributing species, we cannot ascertain the magnitude of TNT-DMF's molar absorptivity nor its quantum yield. The addition of another [TNT-OH]⁻ species appears to cloud this even further; however, there are systems that may exhibit isosbestic points with three contributing species. Such a situation can arise in a system with absorbance contributions from a Lewis acid with two binding sites and one Lewis base, where the free acid and each form of the adduct absorb in the same range with different molar extinction coefficients.²¹ In our case, TNT acts as the Lewis acid, which has two binding sites (C₁ & C₃ - see numbering for TNT carbons in

Scheme 1). While TNT does not absorb in the visible range, TNT^- does; the three products of the reaction of TNT with hydroxide (TNT^- , $[\text{TNT-OH}]^- \text{C}_1$, and $[\text{TNT-OH}]^- \text{C}_3$) should therefore still show isosbestic points if TNT-DMF is at or below absorbance detection limits. The question arises as to which form of $[\text{TNT-OH}]^-$ belongs to which modeled spectrum. While Fyfe *et. al.* previously described $[\text{TNT-OCH}_3]^- \text{C}_3$ as the only observable sigma adduct via $^1\text{H NMR}$,⁹ we cannot appropriately correlate this to our measurements without knowing how significantly the sterics affect methoxide attack versus hydroxide attack. We also do not know each species' molar absorptivity and quantum yield. If we estimate that both $[\text{TNT-OH}]^-$ species have molar absorptivities and quantum yields on the same order of magnitude, then the three peak emission spectrum that we initially fit plausibly belongs to $[\text{TNT-OH}]^- \text{C}_1$. Also, TDDFT UV-Vis calculations may support this assignment by projecting the C_3 adduct as having higher energy transitions (Supplementary Information Fig. S6). Absorbance computations at the B3LYP/6-311+G**//HF/6-311+G** level suggest that the HOMO/LUMO gap for the C_1 sigma adduct is of lower energy than the C_3 form. If each hydroxide sigma adduct has a similar Stokes shift, this would assign the higher energy, single peak emission spectrum to $[\text{TNT-OH}]^- \text{C}_3$. The TDDFT calculated absorbance spectrum shows that the maximum for $[\text{TNT-OH}]^- \text{C}_3$ is at about 25 nm shorter wavelength than $[\text{TNT-OH}]^- \text{C}_1$ while the fit emission spectra show a 21 nm difference, giving some quantitative support for the assignments.

Figure 11 shows the initial emission spectrum of the TNT/DMF solution, the addition of 15 μL of water, and addition of 30 μL of water. All spectra in this titration fit well using our established model (full titration fitting can be found in Supplementary Information Fig. S7). The converged parameters for the TNT product emission spectra model can be found in Table 1. The vibronic energy for $[\text{TNT-OH}]^- \text{C}_1$ is 770 cm^{-1} and 630 cm^{-1} for TNT-DMF; these energies may

represent ring bending modes in each respective species. The integrated area of each spectrum as a function of water addition is found in Figure 10. Unlike the trend for TNB, all emissive species are observed to grow as more water is added to the system. This could be an indication that TNT-DMF formation requires $[\text{TNT-OH}]^- \text{C}_3$ as an intermediate with a subsequent $\text{S}_{\text{N}}2$ step.

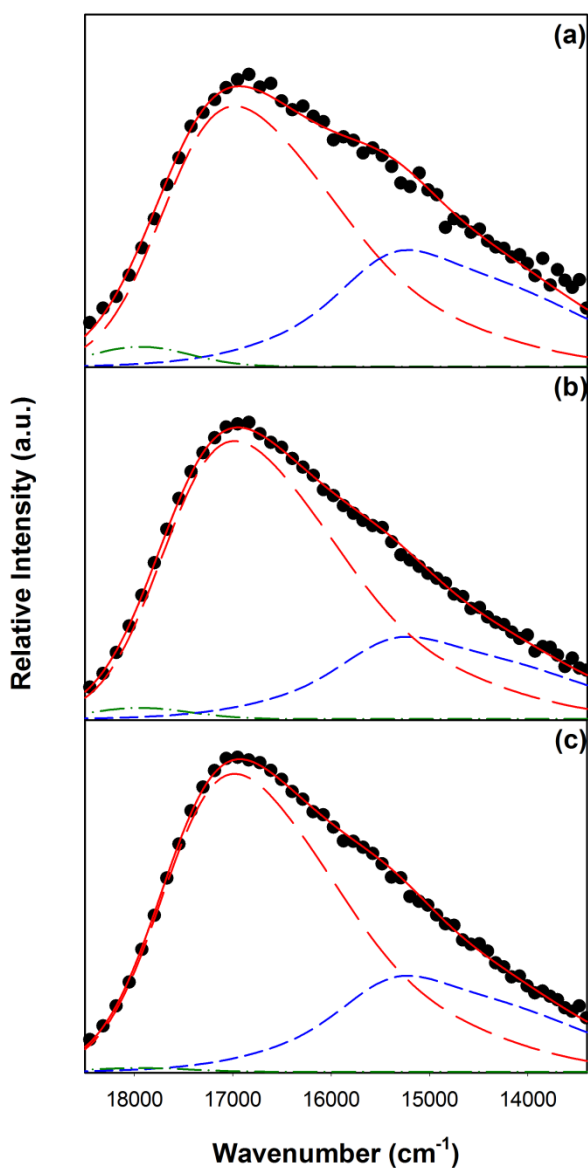


Figure 11. Emission spectra from TNT titration with water in DMF, fit to a three species model for $[\text{TNT-OH}]^- \text{C}_1$ (— — —), TNT-DMF (- - - -), and $[\text{TNT-OH}]^- \text{C}_3$ (- · - · -). (a) 1.1×10^{-4} M TNT in DMF; (b) + 15 μL H_2O ; (c) + 30 μL H_2O .

4. Conclusions

In summary, we have shown that TNB has the capacity to form two sigma adducts in DMF, $[\text{TNB-OH}]^-$ and TNB-DMF, as shown in Scheme 1. Absorbance data for TNB/DMF solutions supports the existence of two species that absorb in the region expected for sigma adducts. Further investigation into excitation and emission data supports the two species. The development of a multi-Gaussian model (with parameters given in Table 1) clarifies the relative quantities of emission from each species, showing the two to be linked by equilibrium. The methyl group of TNT causes different reactivity than TNB. TNT has the ability to form four products in DMF (Scheme 1), leading to spectral differences and similarities which require careful analysis to discern. The major absorbing species, TNT^- , is shown to be non-emissive. Absorbance features consistent with sigma adducts of TNT are observed to grow as a function of water addition. The three possible sigma adducts, $[\text{TNT-OH}]^- \text{C}_1$, $[\text{TNT-OH}]^- \text{C}_3$, and TNT-DMF, all exhibit excitation and emission features that have distinct similarity to their TNB counterparts. A multi-Gaussian model was also established to differentiate the TNT sigma adducts' relative emission (Table 1), showing that all grow together as a function of added water. This is not observed for the TNB sigma adducts, and implies different mechanisms for DMF sigma adduct formation.

This is the first report of fluorescent emission from Meisenheimer adducts of TNB and TNT, with both nitroaromatics capable of nucleophilic attack by hydroxide and the less sterically hindered TNB capable of attack by DMF. All reactions show significant changes within minutes, which allow these reactions to be further explored in the context of sensor development. The emissions may be able to be enhanced by using a resonance energy transfer from a donor

fluorophore with a long excited state lifetime to these adducts as acceptors; this could further amplify this form of a "turn-on" mechanism. Alternatively, a solid state sensor capable of capturing these nitroaromatics through stronger nucleophilic attack may be able to serve in a facile turn-on approach. Future work should compare dinitrotoluene (DNT) emission characteristics to those described here. DNTs are common impurities in TNT, but since DNTs have a much higher vapor pressure than TNT they will each deliver similar amounts in the vapor phase to a sensor. Depending on the relative equilibrium constants for each adduct formation and their relative quantum yield, it may be found that DNTs are more observable in this capacity. In addition, the different reactivity between TNT and TNB means that caution must be used when using TNB as a surrogate for TNT in the development and testing of TNT sensors. Finally, this work shows that TNT sensors are expected to perform differently under wet or humid conditions than under dry conditions. Water can react with nitroaromatics even at trace levels.

ASSOCIATED CONTENT

Supporting Information.

UV/Vis Absorbance spectra, excitation and emission spectra of trinitroaromatics in DMF with water titration. This material is available free of charge via the Internet at <http://pubs.acs.org>.

AUTHOR INFORMATION

Corresponding Author

*Email: weuler@chm.uri.edu

Notes

The authors declare no competing financial interest.

ACKNOWLEDGMENT

We would like to gratefully acknowledge Drs. Jimmie Oxley and James Smith for providing us with TNT. We also thank the Department of Homeland Security ALERT Center for funding.

ABBREVIATIONS

TNB, trinitrobenzene; TNT, trinitrotoluene; DMF, *N,N*-dimethylformamide.

REFERENCES

- (1) Jiang, Y.; Zhao, H.; Zhu, N.; Lin, Y.; Yu, P.; Mao, L. *Angew. Chem. Int. Ed.* **2008**, *47*, 8601-8604.
- (2) Üzer, A.; Erçağ, E.; Apak, R. *For. Sci. Int.* **2008**, 239-243.
- (3) Xia, Y.; Song, L.; Zhu, C. *Anal. Chem.* **2011**, *83*, 1401-1407.
- (4) Chen, Y.; Chen, Z.; He, Y.; Lin, H.; Sheng, P.; Liu, C.; Luo, S.; Cai, Q. *Nanotechnology* **2010**, *21*, 125502-125507.
- (5) Tu, R.; Liu, B.; Wang, Z.; Gao, D.; Wang, F.; Fang, Q.; Zhang, Z. *Anal. Chem.* **2008**, *80*, 3458-3465.

- (6) Gao, D.; Wang, Z.; Liu, B.; Ni, L.; Wu, M.; Zhang, Z. *Anal. Chem.* **2008**, *80*, 8545-8553.
- (7) Fang, Q.; Geng, J.; Liu, B.; Gao, D.; Li, F.; Wang, Z.; Guan, G.; Zhang, Z. *Chem. Eur. J.* **2009**, *15*, 11507-11514.
- (8) Zhang, K.; Zhou, H.; Mei, Q.; Wang, S.; Guan, G.; Liu, R.; Zhang, J.; Zhang, Z. *J. Am. Chem. Soc.* **2011**, *133*, 8424-8427.
- (9) Fyfe, C.; Malkiewich, C.; Damji, S.; Norris, A. *J. Am. Chem. Soc.* **1976**, *98*, 6983-6988.
- (10) Bernasconi, C. *J. Org. Chem.* **1971**, *36*, 1671-1679.
- (11) Shipp, K.; Kaplan, L. *J. Org. Chem.* **1966**, *31*, 857-861.
- (12) Buncel, E.; Norris, A.; Russell, K.; Tucker, R. *J. Am. Chem. Soc.* **1972**, *94*, 1646-1649.
- (13) Lakowicz, J.R. *Principles of Fluorescence Spectroscopy*, third ed., Springer Science, New York, **2006**.
- (14) Rahman, M.; Harmon, H.J. *Spectrochimica Acta A* **2006**, *65*, 901-906.
- (15) Olley, D.A.; Wren, E.J.; Vamvounis, G.; Fernee, M.J.; Wang, X.; Burn, P.L.; Meredith, P.; Shaw, P.E. *Chem. Mater.* **2011**, *23*, 789-794.
- (16) Algarra, M.; Campos, B.B.; Miranda, M.S.; Esteves da Silva, J.C.G. *Talanta*, **2011**, *83*, 1335-1340.
- (17) Thomas III, S.W.; Joly, G.D.; Swager, T.M. *Chem. Rev.* **2007**, *107*, 1339-1386.

- (18) Shi, G.H.; Shang, Z.B.; Wang, Y.; Jin, W.J.; Zhang, T.C. *Spectrochimica Acta A* **2008**, *70*, 247-252.
- (19) *Spartan '10*; Wavefunction, Inc.: Irvine, CA, 2010. Version 1.1.0.
- (20) Foster, R.; Mackie, R.K. *J. Chem. Soc.* **1962**, 3843-3844.
- (21) Drago, R.S. *Physical Methods for Chemists*, second ed., Saunders College Publishing, New York, **1992**.

TOC Graphic



Cite this: DOI: 10.1039/c0xx00000x

www.rsc.org/xxxxxx

ARTICLE TYPE

A Fluorometric Sensing Array for the Detection of Military Explosives and IED Materials

Christopher A. Latendresse^a, Syrena C. Fernandes^a, Sangmin You^a, Hui Qi Zhang^a, and William B. Euler^{*a}

⁵ Received (in XXX, XXX) Xth XXXXXXXXXX 20XX, Accepted Xth XXXXXXXXXX 20XX
DOI: 10.1039/b000000x

A fluorometric sensing array was developed to detect and discern common military explosives and materials used in improvised explosive devices (IEDs). Xanthene-based fluorophores were chosen as reporter molecules and were exposed to explosive analytes in DMF solution. Unique responses were observed for each analyte, with the strongest observed responses resultant from trinitrobenzene (TNB) or trinitrotoluene (TNT) addition. Evidence for substantial electron transfer (ET) between TNB and TNT products and fluorophores was observed. Computational results indicate that anionic trinitroaromatic products are likely donating electrons to cationic fluorophores, leading to an observed enhancement of their emission.

15 Introduction

With the rise in domestic and international terroristic events in the past decade, the scientific community has been pushed by the need to develop rapid and sensitive means of detection of explosive analytes. Explosive sensors have been developed based on a number of methods of detection, including colorimetry,^{1,2} fluorescence,³⁻⁹ mass spectrometry,¹⁰⁻¹² electrochemical,¹³⁻¹⁵ and Surface Enhanced Raman Scattering (SERS),¹⁶⁻¹⁸ among others.

Sensitivity and selectivity remain at the heart of an effective sensor, and while many sensors are able to claim one, most cannot achieve both. Fluorescence sensing benefits from the inherently high sensitivity of contemporary fluorescence instrumentation, which can achieve attomolar detection for molecules with high quantum yields in solution.¹⁹ Additionally, detection limits may be improved by another order of magnitude using metal enhanced fluorescence.^{20,21} Selectivity, although difficult to achieve using a single interactive sensor, can be induced by the use of a sensor array where multiple sensors can be exposed to the same analyte stream and their responses observed together. This “fingerprint” can be read as a function of a specific analyte; whereas one of the sensors may not be able to discern one analyte from another, it is unlikely that two analytes will interact with the multitude of sensors in the exact same fashion.

Perhaps surprisingly, the rhodamine family has not been well explored in the field of explosive detection. Meaney & coworkers investigated the fluorescence quenching of common fluorophores including Rhodamine 6G against nitrobenzene, 4-nitrotoluene and 2,6-dinitrotoluene, but did not explore more contemporarily relevant analytes.⁹ Rhodamines have notoriety as being very strong fluorophores, and were therefore selected to

test as fluorescence reporters against explosive analytes. Rhodamines also have the advantage of possessing visible range excitations and emissions that are not subject to interference by absorbance bands of explosive analytes. The rhodamines investigated in this study were Rhodamine 560 Chloride (Rh560), Rhodamine 6G (Rh6G), Sulforhodamine B (SRhB), Rhodamine 640 Perchlorate (Rh640), Sulforhodamine 640 (SRh640), Rhodamine 700 (Rh700) and Rhodamine 800 (Rh800). Fluorescein 548 (F1548) was also included, as another representative xanthene derivative with a high quantum yield. The structures of the selected fluorophores can be found in Supplementary Information Fig. S1. The analytes exposed to the aforementioned fluorophores were selected based on current military relevance: trinitrobenzene (TNB), trinitrotoluene (TNT), cyclotrimethylenetrinitramine (RDX), and cyclotetramethylenetetranitramine (HMX) are common military grade secondary explosives; pentaerythritoltetranitrate (PETN) and triacetone-triperoxide (TATP) have been used in improvised explosive devices (IEDs) and large scale terrorist events over the past two decades due to their relatively simple synthesis and high output,^{10,11,22} and 2,3-dinitrotoluene (2,3-DNT), 2,4-dinitrotoluene (2,4-DNT), 2,6-dinitrotoluene (2,6-DNT), 3,4-dinitrotoluene (3,4-DNT), 2-nitrotoluene (2-NT) and 4-nitrotoluene (4-NT) are common impurities in crude and refined TNT due to incomplete nitration.²³ Due to the much higher vapor pressures and saturated vapor densities of DNTs and NTs relative to TNT, these species may serve as useful analytes for the implication of TNT sensing. The structures of the explosive analytes can be found in Supplementary Information Fig. S2.

Experimental section

Chemicals and materials

DMF ($\geq 99.5\%$) was purchased from Fisher Scientific and used as received. Rh560, F1548, Rh640, SRh640, Rh700, and Rh800 were purchased from Exciton (Dayton, Ohio) and used as received. Rh6G (99%) was purchased from Acros and used as received. SRhB was purchased from Lambda Physik and used as received. TNT, TATP, PETN, HMX, and RDX were obtained from Drs. Jimmie Oxley and James Smith and were used without further purification. TNB was purchased from Fisher Scientific wetted with ca. 40% water with 98.0% purity; 2,3-DNT (99%), 2,6-DNT (98%), and 3,4-DNT (99%) were purchased from Aldrich; 2,4-DNT (95%) was purchased from Alfa Aesar; and 2-NT (99%) and 4-NT (99%) were purchased from Acros. All were used as received.

Apparatus and Procedure

Fluorophore solutions in DMF were created and diluted to a maximum visible range absorbance of 0.1 abs. units. Solutions of Rh700 and Rh800 were acidified with trifluoroacetic acid (TFA) to prevent photobleaching prior to use. Absorbance data (PerkinElmer Lambda900 UV/Vis/NIR spectrophotometer) and emission data (Horiba Fluorolog-3, Xe arc lamp excitation) were obtained before and after the addition of a few crystals of solid explosive, or the addition of a small drop in the case of 2-NT_(l). Excitation and emission slits were used between 2 and 5 nm, but did not vary between initial and final spectra acquisitions.

Computational Analysis

Spartan '10 computational software²⁴ was used to propose the relative absorbance maxima for the isomers of [TNT-OH]⁻. Structures were optimized at the HF/6-311+G** level without imaginary vibrational frequencies. TDDFT energies and absorbance spectra were calculated using the converged structures at the B3LYP/6-311+G** level.

Results and Discussion

Solutions of fluorophores were prepared in DMF, with absorbance and emission spectra acquired before and after the addition of explosive analyte. Figure 1 shows the absorbances characterizing the initial fluorophore solutions, spanning the visible range. In similar fashion, Figure 2 shows the normalized emission spectra from each initial fluorophore solution, spanning from 530 nm to 800 nm. Pairing absorbance and emission measurements together allows for determination of possible interactions between fluorophore and analyte, as both ground state and excited state profiles are examined.

Figure 3 shows the output of the sensing array, as indicated by emission difference spectra. Note that the ordinate axis for TNB and TNT interactions are set to 100% change in emission. All others are zoomed to 10% for clarity, with a select few zoomed to 40% marked by " $\times 1/4$." The trinitroaromatics, TNB and TNT, both show very strong observed quenching. This is in large part due to the products which they form in DMF, reacting with hydroxide generated by trace amounts of water. Others have previously described the absorbance properties²⁵⁻²⁸ and recently we have described the emission properties of these products;²⁹ both of these factors complicate the observations made here as added variables. TNB and TNT are capable of nucleophilic attack by hydroxide and DMF; in addition, TNT is capable of

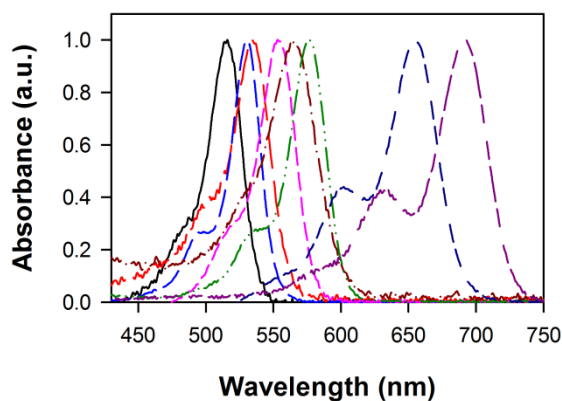


Fig. 1 Absorbance overlay of selected fluorophores in DMF, normalized to visible absorbance maximum. Listed in order of decreasing energy maximum, the fluorophores are Rh560 (—), F1548 (— — —), Rh6G (— — —), SRhB (— — —), Rh640 (— — —), SRh640 (— — —), Rh700 (— — —), Rh800 (— — —).

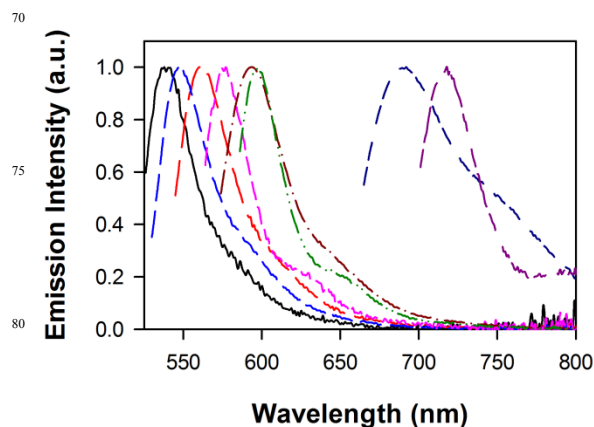


Fig. 2 Emission overlay of selected fluorophores in DMF, normalized to emission maximum. Listed in order of decreasing energy maximum, the fluorophores are Rh560 (—), F1548 (— — —), Rh6G (— — —), SRhB (— — —), Rh640 (— — —), SRh640 (— — —), Rh700 (— — —), Rh800 (— — —).

deprotonation by hydroxide. The resulting strong absorbance features can be seen in Supplementary Information Figs. S3-S6. Consistently, these products are diminished in the observations with Rh700 and Rh800, as these solutions were slightly acidified to inhibit photobleaching during analysis. Since the product formation is reliant on hydroxide in solution, acidification removes hydroxide and shifts the equilibria back towards free TNT or TNB. The formation of these products serves to complicate the interactions with the fluorophores in solution, due to their inner filter effect and possible ground state interactions. Both of these factors will be discussed in greater detail later in the paper.

PETN, RDX, and HMX are all nitroaliphatics, which show a mixture of quenches and enhancements through interactions with the sensing fluorophores. There is no observed change in any fluorophore's absorbance upon these exposures (see Figs. S3-S6), implying that emission changes are only resultant from excited state interactions. Emission decreases are likely resultant from dynamic mechanisms. Increases in emission may result from interactions that either decrease the lifetime of the excited state,

Cite this: DOI: 10.1039/c0xx00000x

www.rsc.org/xxxxxx

ARTICLE TYPE

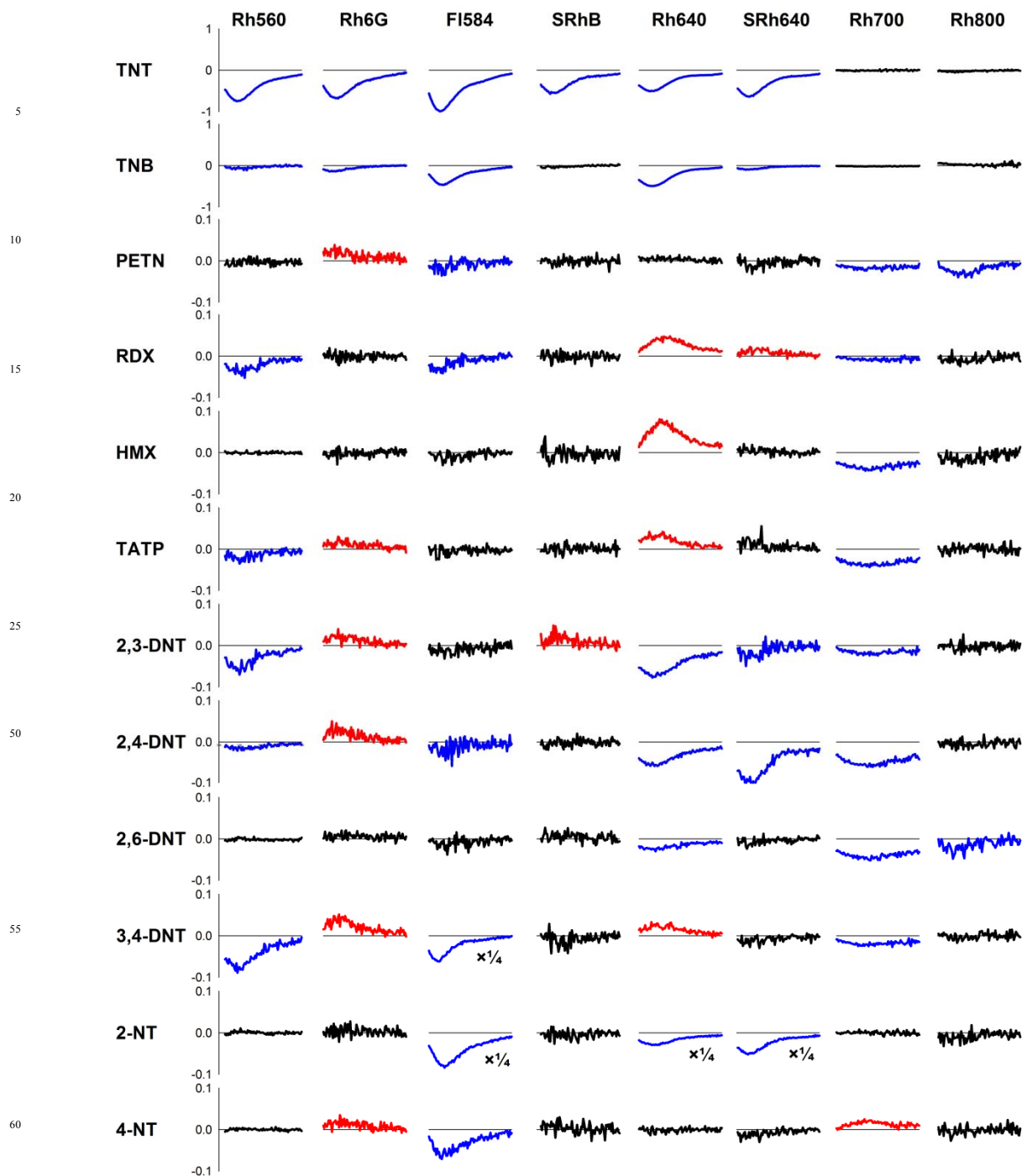


Fig. 3 Emission difference spectra for the exposure of explosive analytes to selected fluorophores in DMF solution, normalized to the initial emission maximum. Blue spectra indicate the observed quenching of emission, red spectra indicate the observed enhancement of emission, and black spectra indicate minimal change in emission. Full absorbance and emission spectra can be found in Supplementary Information Figs. S3-S6.

65

Cite this: DOI: 10.1039/c0xx00000x

www.rsc.org/xxxxxx

ARTICLE TYPE

or perhaps increase the rigidity of the fluorochrome leading to more favorable emission kinetics. Rh640 most strongly shows this capacity here with both RDX and HMX. TATP, the only explored peroxide based explosive, also shows this capacity with Rh640 and Rh6G. Since TATP is known to decompose to H₂O₂ and acetone in the presence of acid,^{30,31} it might be proposed that oxidation of Rh700 and Rh800 might occur by H₂O₂ due to the small amount of TFA in solution. Absorbance measurements do not show this, as there is no change to support such a ground state reaction. Instead, TATP or its decomposition products appear to quench Rh700 through a collisional mechanism.

The DNT isomers that were explored show a range of emission quenching and enhancement, but with fingerprint patterns that differentiate them from the other analytes. DNTs have a similar capacity to TNT to be deprotonated to a varying degree, and the ability to form a sigma complex with hydroxide from ambient water in solution. In some of our additions, absorbance features arise to support this assessment. For example, Fig. S5 shows an increase in absorbance for the addition of 2,4-DNT to SRh640 centered around 650 nm; this absorbance spectrum has been shown previously to be resultant from the deprotonation of 2,4-DNT.³² Likewise, Fig. S4 shows an increase in absorbance for the addition of 3,4-DNT to FI548 between 400 and 500 nm; this would be consistent with the formation of a hydroxide adduct. While these absorbance features contribute to an inner filtering effect, they are minimal compared to those of the TNB or TNT products, which will be described later. In addition, there are observable emission changes for DNT additions that either do not show these absorbance growths or are not fully resultant from an inner filter effect. 3,4-DNT causes a larger decrease in the emission of FI548 than the absorbance growth of its product (Fig. S4). Another example can be found in Fig. S6, where 2,4-DNT causes a dynamic quench to the emission of Rh700, while the absorbance spectrum is unchanged. The NT isomers also show differentiating patterns from each other, and from other analytes. Colorful products similar to those formed by hydroxide reacting with TNT or DNTs are not observed with NTs, and so all observed absorbance spectra remained unchanged upon addition of 2-NT or 4-NT. Dynamic quenching was observed from addition of 2-NT and 4-NT to FI548 (Fig. S4), as well as 2-NT added to Rh640 or SRh640.

One issue with the trinitroaromatic products involves the degree of inner filter effect (IFE) caused by their absorbance. While we observe large quenches in emission, this may not be related to excited state interactions, but rather simple absorbance of emitted photons by other components in solution. To account for this, IFE corrections were done using the following equation:¹⁹

$$F_{corr} = F_{obs} \times 10^{\left(\frac{A_{ex} + A_{em}}{2}\right)}$$

where F_{corr} is the corrected emission intensity, F_{obs} is the observed emission intensity, A_{ex} is the absorbance at the excitation

wavelength, and A_{em} is the absorbance at the emission maximum. Although the DNTs showed some slight evidence of product formation, which were consistent with sigma adduct formation or deprotonation, their absorbance changes were minute and did not have a dramatic impact on the IFE correction calculations. The trinitroaromatic products had massive absorbances, which definitely required corrections; a comparison of observed vs. corrected emission changes can be found in Table 1.

Table 1 Observed percent emission changes compared to inner filter effect corrected changes for fluorophores with addition of TNB or TNT.^a

Fluorophore	TNB obs.	TNB corr.	TNT obs.	TNT corr.
Rh560	-5	5	-75	9
Rh6G	-12	24	-68	23
FI548	-44	-29	-97	-98
SRhB	-5	0	-54	4
Rh640	-44	47	-44	104
SRh640	-9	-2	-64	-4
Rh700	-2	2	-1	1
Rh800	2	2	-4	-6

^a Note that negative changes represent a quench in emission while positive changes represent enhancements in emission.

Once the maximum emissions were corrected using the above equation, the % change was recalculated. We estimate the relative error in the corrected emission change to be between 5-10%. The IFE corrected changes stand in stark contrast to the observed changes, indicating a hidden component of increased emission in the process. For example, the addition of TNT to Rh640 shows an observed quench of 44%. However, given the amount of TNT products that absorb in the visible range, IFE corrections should be applied. If no true collisional or static quenching occur, these corrections should bring the change back to 0%. Instead, the corrected change is calculated to be 104%, indicating a competing interaction that enhances the emission of the fluorophore. A similar effect can be seen for other rhodamine/trinitroaromatic pairings in Table 1, in which the corrected % changes are all more positive than the observed. The exceptions to this are the additions of TNT to FI548, Rh700, and Rh800, which do not change significantly within the estimated error. FI548 especially shows significant quenching with TNT and TNB, which does not appear to be competing with an enhancing phenomenon.

Although we have previously described the emission of TNB and TNT products in DMF,²⁹ there is little shape change in the emission spectra to justify their direct additive role in the calculated increase in emission. TNB reacts with hydroxide from trace water to form the sigma complex TNB-OH⁻, which shows a narrow absorbance feature around 450 nm and a broader absorbance feature around 520 nm. Additional absorbance bands are expected from the TNB-DMF sigma adduct around 650 nm, which we see in varying amounts. TNT is capable of similar

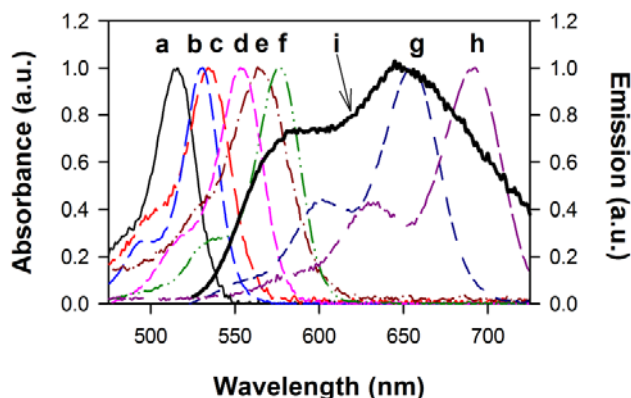


Fig. 4 Normalized absorbance overlay of fluorophores in DMF, compared with the normalized emission of TNB products. Listed in order of decreasing energy maximum, the fluorophores are (a) Rh560 (—), (b) FI548 (— — —), (c) Rh6G (— · — · —), (d) SRhB (— · — · —), (e) Rh640 (— · — · —), (f) SRh640 (— · — · —), (g) Rh700 (— · — · —), (h) Rh800 (— · — · —). The emission spectrum (i), given by the thicker line width, is a composite of the emission of TNB-OH⁻ and TNB-DMF formed in the addition of TNB to DMF solution.

chemistry, by forming two possible TNT-OH⁻ adduct isomers, as well as a DMF adduct; both have been shown to be emissive. TNT is also capable of being deprotonated by OH⁻, forming TNT⁻, but this species is not emissive.

One plausible conclusion is that the increase results from resonance energy transfer (RET). This would result from the excited states of a trinitroaromatic product to donate energy to the fluorophore acceptor, populating their excited states leading to greater emission. Additionally, it appears that the addition of TNT leads to a greater enhancement than the TNB counterparts. While we cannot address RET efficiencies here without knowing the relative amount of each species and lifetimes, it is interesting to note the consistently higher response to TNT. To further investigate the possibility of RET between trinitroaromatic products and the fluorophores, the absorbance spectra of the fluorophore acceptors is compared to the emission spectrum of TNB product donors in DMF solution in Figure 4.

The emission spectrum is comprised of two components, TNB-OH⁻ and TNB-DMF, which emit at a maximum around 580 nm and 650 nm respectively.²⁹ The emission spectrum overlaps best with the absorbance spectra of Rh700 and Rh800, which do not exhibit enhancement when exposed to TNB in DMF. Also, the similar absorbance spectra of Rh640 and SRh640 but different response to TNB do not make sense in the context of RET shown here. In a RET mechanism, it would be expected that both Rh640 and SRh640 would show enhancements, which are not observed. In addition, the concentrations of each species in solution are on the order of 10⁻³ M, which would make the average distance between molecules greater than 100 Å. Given the strong distance dependence in a RET mechanism, this distance is higher than the typical Förster distance exhibited by similar molecules.¹⁹ The poor correlation of the spectral bands of the fluorophores and TNB products and the large intramolecular distances suggest that RET is not the enhancement mechanism.

Other possibilities for an enhanced fluorescence are charge transfer (CT) or electron transfer (ET) mechanisms. A CT complex may be formed if the HOMOs of the TNB or TNT products are close enough in energy to the LUMOs of the sensing

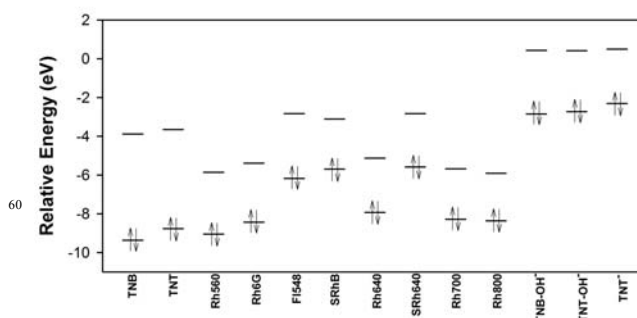


Fig. 5 HOMO/LUMO diagram for energy comparison between sensing fluorophores, trinitroaromatics, and trinitroaromatic products. Relative energies were computed at the B3LYP/6-311+G**//HF/6-311+G** level in vacuum at 298.15 K and 1 atm. Arrows are shown to designate the HOMO.

fluorophores, for a small amount of overlap to occur. If either of the TNB or TNT products have HOMOs of high energy relative to the LUMOs of the fluorophores, ET may justify the enhanced excited state population and subsequent enhanced emission of the fluorophores. To help in our assignment of the mechanism of enhanced emission, molecular orbital energies were calculated. Figure 5 shows the calculated relative energies of the HOMO and LUMO for TNB, TNB-OH⁻, TNT, TNT-OH⁻, TNT⁻, and the sensing fluorophores.

It is clear that there is a dramatic difference between the frontier orbital energies of the free trinitroaromatics, with the transient anionic products (TNT⁻ and the OH⁻ adducts) being of much higher energy. The trinitroaromatic products have HOMOs so high in energy that they are very close to the energy of the LUMOs of some of the modeled fluorophores (eg. FI548, SRh640). This gives plausibility to the formation of a CT complex where the products may donate to the fluorophore. The HOMOs of TNB and TNT are reasonably close in energy to the LUMOs of several of the fluorophores, which indicates the possibility of a trinitroaromatic:fluorophore CT complex formation. However, the energy of this transition would be greater than the HOMO/LUMO gap of all of the fluorophores, suggesting that the CT band would not be in the visible range but rather in the UV. Since the formation of any CT complex would lead to a spectral shift, yet no shift is observed, no significant CT complex formation is occurring.

Photo-induced electron transfer (PET) is unlikely to play a role in our observations in the context of these calculations. Typically, PET causes a quench in emission if electron density is transferred to or away from a fluorophore, as this can lead to structural and lifetime changes.¹⁹ Emission enhancements can be justified through disruption of PET mechanisms, but since our initial solution is comprised of only the fluorophore in DMF this also seems unlikely. The only way that this might be conceived is if DMF is initially quenching the fluorophores, and that the displacement of DMF by explosive molecules in solvation leads to an observed enhancement. Given the relatively low quantity of analyte added relative to the overwhelming amount of DMF solvent, the small addition cannot account for the magnitude of enhancement observed.

In the context of a ground state ET mechanism, TNB and TNT have the lowest calculated HOMO energy of all of the modeled species. This feature as well as their electron deficient character

makes it unlikely that the free trinitroaromatics would donate electrons to the fluorophores. The anionic products have a much higher calculated HOMO energy however, making them more likely electron donors. F1548 and SRh640 have LUMOs that are slightly higher in energy than the HOMOs of TNT⁻ and the OH⁻ adducts, making them poor candidates as electron acceptors. The calculated LUMO of SRhB is lower but still close in energy to the HOMO of the anionic products (within 0.3 eV); this is likely an insufficient energy gap to cause significant ET at ambient temperatures. Rh6G and Rh640 have LUMOs of very similar energy (-5.39 and -5.13 eV respectively), which are about 2.4 eV lower than the HOMO of TNB-OH⁻. Since these two fluorophores show the greatest enhancement with TNB and TNT addition in solution and their relative LUMO energies to TNB-OH⁻ are strikingly similar, electron transfer appears to be the most probable mechanism. The difference in energy is substantial enough to occur without significant reversibility. Rh560, Rh700, and Rh800 have LUMOs of lower energy than Rh6G and Rh640. Rh560 shows a calculated enhancement that is within the estimated error of our approach, and with a LUMO that is 3 eV lower than the HOMO of TNB-OH⁻ the magnitude of the enhancement might be expected to be higher. The correlation of the relative enhancements is beyond the scope of our calculations here, however Rh560 is likely to follow the trend of enhancement shown by Rh6G and Rh640. Rh700 and Rh800 have a difference of about 2.8 eV, but an electron transfer is hindered by the lack of OH⁻ adduct formation in the acidified solution. In these cases, only slight changes in emission are observed after IFE calculations. It is also interesting to note that the three enhanced fluorophores (Rh560, Rh6G, Rh640) happen to all be cationic, whereas the remaining fluorophores (excluding Rh700 and Rh800 for aforementioned reasons) are either neutral in charge or anionic. It is easy to conceive the possible formation of an ion pair between the cationic fluorophores and the anionic trinitroaromatic products. This driving force would bring the species in close proximity to allow ET to occur, without the limitations of diffusion and collision in solution.

Conclusion

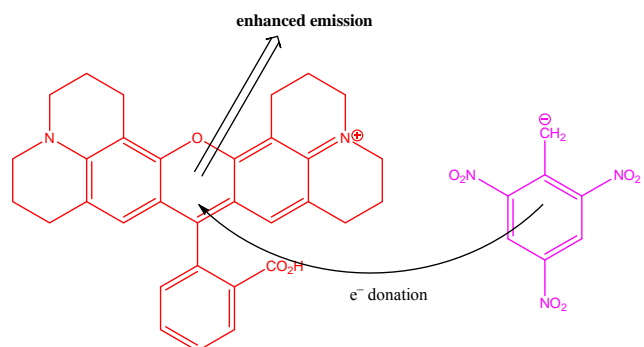
We have investigated a sensing array based on highly fluorescent molecules in DMF solution that shows promise for the detection of explosive analytes. In addition to typical collisional or static quenching, inner filter effect corrections indicate an ET component, which increases the emission of at least two of the fluorescent reporters (Rh6G and Rh640). The findings of ET may have an impact on pre-existing RET based sensors, as the emission of the fluorophores in this study was observed to enhance. The capability of trinitroaromatic products to be involved in ET may influence existing sensors that rely on TNB or TNT as a RET disruptor, leading to a competitive ET mechanism that would decrease the effectiveness of the sensor by diminishing an observed quench in emission. Further studies will be undertaken to expand the set of fluorescent reporter molecules and quantify the interactions with the most significant emission change, as well as experiments to give additional clarification of the ET with trinitroaromatic products.

Notes and references

^a University of Rhode Island, Department of Chemistry, 51 Lower College Road, Kingston, RI, USA. Fax: XX XXXX XXXX; Tel: 401 874 5090; E-mail: weuler@chm.uri.edu

† Electronic Supplementary Information (ESI) available: absorbance and emission spectra for all fluorophore/analyte combinations. See DOI: 10.1039/b000000x/

- 1 Y. Jiang, H. Zhao, N. Zhu, Y. Lin, P. Yu, and L. Mao, *Angew. Chem. Int. Ed.*, 2008, **47**, 8601.
- 2 A. Üzer, E. Erçağ, and R. Apak., *For. Sci. Int.*, 2008, 239.
- 3 Y. Xia, L. Song, and C. Zhu, *Anal. Chem.*, 2011, **83**, 1401.
- 4 Y. Chen, Z. Chen, Y. He, H. Lin, P. Sheng, C. Liu, S. Luo, and Q. Cai, *Nanotechnology*, **2010**, *21*, 125502.
- 5 R. Tu, B. Liu, Z. Wang, D. Gao, F. Wang, Q. Fang, and Z. Zhang, *Anal. Chem.*, 2008, **80**, 3458.
- 6 D. Gao, Z. Wang, B. Liu, L. Ni, M. Wu, and Z. Zhang, *Anal. Chem.*, 2008, **80**, 8545.
- 7 Q. Fang, J. Geng, B. Liu, D. Gao, F. Li, Z. Wang, G. Guan, and Z. Zhang, *Chem. Eur. J.*, 2009, **15**, 11507.
- 8 K. Zhang, H. Zhou, Q. Mei, S. Wang, G. Guan, R. Liu, J. Zhang, and Z. Zhang, *J. Am. Chem. Soc.*, 2011, **133**, 8424.
- 9 M. S. Meaney and V. L. McGuffin, *Anal. Chim. Acta*, 2008, **610**, 57.
- 10 Y. Takada, Y. Suzuki, H. Nagano, M. Sugiyama, E. Nakajima, M. Sugaya, Y. Hashimoto, and M. Sakairi, *IEEE Sensors*, 2012, **12**, 1673.
- 11 J. Kozole, J. Tomlinson-Phillips, J. R. Stairs, J. D. Harper, S. R. Lukow, R. T. Lareau, H. Boudries, H. Lai, and C. S. Brauer, *Talanta*, 2012, **99**, 799.
- 12 P. Sulzer, F. Petersson, B. Agarwal, K. H. Becker, S. Jürschik, T. D. Märk, D. Perry, P. Watts, and C. A. Mayhew, *Anal. Chem.*, 2012, **84**, 4161.
- 13 P. K. Sekhara, E. L. Broshaa, R. Mukundana, K. L. Linkerb, C. Brusseau, and F. H. Garzona, *J. Haz. Mat.*, 2011, **190**, 125.
- 14 M. Y. Ho, N. D'Souza, and P. Migliorato, *Anal. Chem.*, 2012, **84**, 4245.
- 15 R. L. Marple and W. R. LaCourse, *Anal. Chem.*, 2005, **77**, 6709.
- 16 X. Liua, L. Zhaob, H. Shenb, H. Xub, and L. Lua, *Talanta*, 2011, **83**, 1023.
- 17 T. Demeritte, R. Kanchanapally, Z. Fan, A. K. Singh, D. Senapati, M. Dubey, E. Zakarb, and P. C. Ray, *Analyst*, 2012, **137**, 5041.
- 18 P. R. Sajanlal and T. Pradeep, *Nanoscale*, 2012, **4**, 3427.
- 19 J. R. Lakowicz, *Principles of Fluorescence Spectroscopy*, third ed., Springer Science, New York, 2006.
- 20 Y. Wang, Z. Li, H. Li, M. Vukib, D. Xua, and H. Y. Chen, *Biosensors and Bioelectronics*, 2012, **32**, 76.
- 21 H. Li, C. Y. Chen, X. Wei, W. Qiang, Z. Li, Q. Cheng, and D. Xu, *Anal. Chem.*, 2012, **84**, 8656.
- 22 W. Fan, M. Young, J. Canino, J. Smith, J. Oxley, and J. R. Almirall, *Anal. Bioanal. Chem.*, 2012, **403**, 401.
- 23 *Military Explosives*, Dept. of the Army Technical Manual, updated 1990.
- 24 *Spartan '10*; Wavefunction, Inc.: Irvine, CA, 2010. Version 1.1.0.
- 25 C. Fyfe, C. Malkiewich, S. Damji, and A. Norris, *J. Am. Chem. Soc.*, 1976, **98**, 6983.
- 26 C. Bernasconi, *J. Org. Chem.*, 1971, **36**, 1671.
- 27 K. Shipp and L. Kaplan, *J. Org. Chem.*, 1966, **31**, 857.
- 28 E. Bunzel, A. Norris, K. Russell, and R. Tucker, *J. Am. Chem. Soc.*, 1972, **94**, 1646.
- 29 C. A. Latendresse, S. C. Fernandes, S. You, H. Q. Zhang, and W. B. Euler, *J. Phys. Chem. A*, 2013, **117**, 324.
- 30 H. Lin and K. S. Suslick, *J. Am. Chem. Soc.*, 2010, **132**, 15519.
- 31 J. C. Oxley, J. L. Smith, and H. Chen, *Prop., Explos., Pyro.*, 2002, **27**, 209.
- 32 E. J. Olson, T. T. Xiong, C. J. Cramer, and P. Bühlmann, *J. Am. Chem. Soc.*, 2011, **133**, 12858.



Light Trapping to Amplify Metal Enhanced Fluorescence with Application for Sensing TNT

Meredith A. Matoian, Richard Sweetman, Emily C. Hall, Shayna Albanese, William B. Euler*

Department of Chemistry, University of Rhode Island, 51 Lower College Road, Kingston, RI 02881

E-mail: weuler@chm.uri.edu.

Abstract

Metal Enhanced Fluorescence (MEF) typically produces enhancement factors of 10 to 50. By using a polymer layer as the dielectric spacer enhancements as high as 1600 can be observed. The effect occurs with a variety of different polymers and substrates, all of which act to trap light in the dielectric layer. This allows the fabrication of sensors with improved sensitivity as demonstrated for detection of trinitrotoluene (TNT).

Keywords: enhanced fluorescence, polymer layer, light trapping, TNT sensing

Introduction

Exploitation of the plasmon properties of metal nanoparticles is currently of interest. Coupling the electric field created by a plasmon to a molecule on the surface can lead to significant intensity increases in Raman spectra (surface enhanced Raman spectra, SERS) and in fluorescent spectra (metal enhanced fluorescence spectra, MEF).¹⁻⁸ For SERS, typical enhancements can be 10^6 or greater while for MEF the enhancements are more modest, typically $10^1 - 10^2$. We have been interested in using fluorescence methods for the detection of explosives.⁹ A porous silicon (p-Si) substrate is used as the substrate for the fluorophore, which increases the surface area available to the analyte, thereby increasing the sensitivity. We presumed that adding a metal layer to the porous layer the sensitivity could be further improved by taking advantage of MEF. Optimized MEF structures require a dielectric layer between the metal and the fluorophore and when we used a polymer as the dielectric the enhancements increased to $10^2 - 10^3$.

We report here that using a polymer layer between a fluorophore and substrate provides an enhanced emission for a variety of polymers and substrates, including those that do not include a metal layer. The enhancement appears to arise from the ability of the dielectric layer to also act as a light trapping layer, i.e., the light makes a number of bounces between the substrate layer and the fluorophore layer, thereby being confined to the polymer layer. When the substrate contains a layer of silver nanoparticles the MEF effect is amplified cooperatively by the polymer effect. We exploit this effect to demonstrate improved sensitivity for the detection of trinitrotoluene (TNT).

Experimental Section

Silver coated porous silicon substrates, p-Si/Ag, were created by electrochemical etching⁹ and reduction of silver nitrate solution on the freshly etched pores.¹⁰ Flat silicon wafers (p-type <100>, Silicon Quest International) were first cut down to a 4 cm by 4 cm size and mounted in a Teflon etching chamber. An aqueous HF solution (100:100:90 H₂O: EtOH: HF) was poured over the wafer immediately before current was applied. Constant current was applied by a Keithley 2635A SYSTEM sourcemeter using 25 mA/cm² current for 190 seconds. The resulting p-Si had pores with approximately 10 micron diameter.⁹ Freshly etched p-Si samples were then submerged in a 50 mM AgNO₃ solution for 14 min. A chosen polymer was spin-cast on the p-Si/Ag wafer at a rate of 1200 rpm for 45 seconds (acceleration rate 1296 /s/s), followed by drying in a 60 °C oven for 2 min to evaporate residual solvent. Polymer solutions used were 2 % w/v polyvinylidene difluoride, PVDF, in 90/10 (v/v) acetone/dimethyl formamide (DMF) mixture, 3 % w/v [(CH₂CF₂)_{0.65}-(CHFCF₂)_{0.35}]_x, co-polymer, in acetone/DMF, and 5 % w/v polymethylmethacrylate, PMMA, in toluene. 30 μL of the selected fluorophore (6.0×10⁻⁴ M of rhodamine 6G, Rh6G, dissolved in ethanol or 6.5×10⁻⁴ M methoxy-ethylhexyloxypolyphenylenevinylene, MEH-PPV, dissolved in methylene chloride), was applied to the p-Si/Ag/polymer samples and allowed to dry in air to complete the MEF substrates. For samples on flat Si or glass, the same coating procedure for the polymers and fluorophores was followed. The average area of the sample was 3.5 cm²; using the densities of the fluorophores this gave an estimated thickness of 20 nm for Rh6G and 40 nm for MEH-PPV. Substrates were mounted on glass slides to fit the solid sample holder for the Horiba Fluorolog-3 instrument for fluorescence measurements and care was taken to ensure that the same spot was sampled in every measurement. The incidence angle was set to 55° from perpendicular, which was determined to provide the

maximum response. For all measurements reported here, the slit width was set to 1 nm for both the excitation and emission monochromators. Reflection spectra were obtained using an Ocean Optics spectrometer with a reflectance probe at 90° incidence from the sample.

Results and Discussion

Figure 1 shows the emission spectra for rhodamine 6G (Rh6G) on several different substrates designed with a typical MEF structure, i.e. substrate, Ag nanoparticle layer, dielectric layer, and fluorophore. When Rh6G is placed directly on p-Si a weak luminescence is observed with a maximum at 555 nm. When a layer of Ag nanoparticles (~100 – 200 nm thick islands, as estimated by AFM) is placed between the fluorophore and the p-Si the emission intensity increases by a factor of 3, which is typical for MEF with no dielectric layer. Using a transparent polymer as the dielectric spacer, giving a structure of p-Si/Ag/polymer/Rh6G, leads to dramatic enhancements, as shown in Fig. 1 (the spectra are referenced to the maximum of the p-Si/Rh6G sample). These are significantly increased compared to what is usually observed in MEF and is especially unusual since the polymer layers are ~10 – 20 times thicker than the usual dielectric layers used in MEF structures. There are also shifts of the wavelength maximum that are not typically seen in MEF.

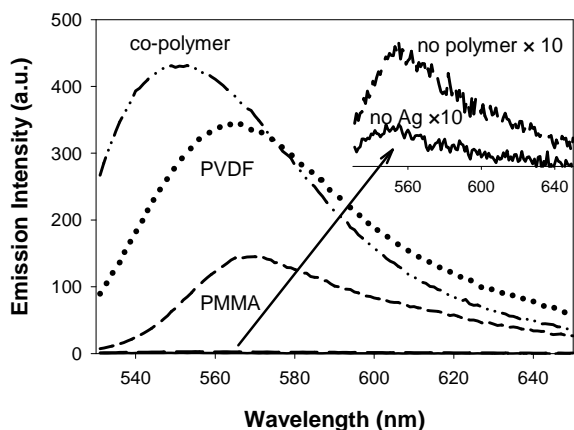


Figure 1. Emission spectra of Rhodamine 6G coated on different polymers cast on a porous Si/Ag substrate. All spectra are referenced to the spectrum with no Ag and no polymer, p-Si/Rh6G (solid line). MEF samples were: no polymer, p-Si/Ag/Rh6G (long dashed); p-Si/Ag/PMMA/Rh6G (short dashes); p-Si/Ag/PVDF/Rh6G (dotted); and p-Si/Ag/co-polymer/Rh6G (dot-dashed). The inset shows the p-Si/Rh6G and p-Si/Ag/Rh6G spectra multiplied by 10. Excitation was at 521 nm and 1 nm slits were used for both the excitation and emission monochromator.

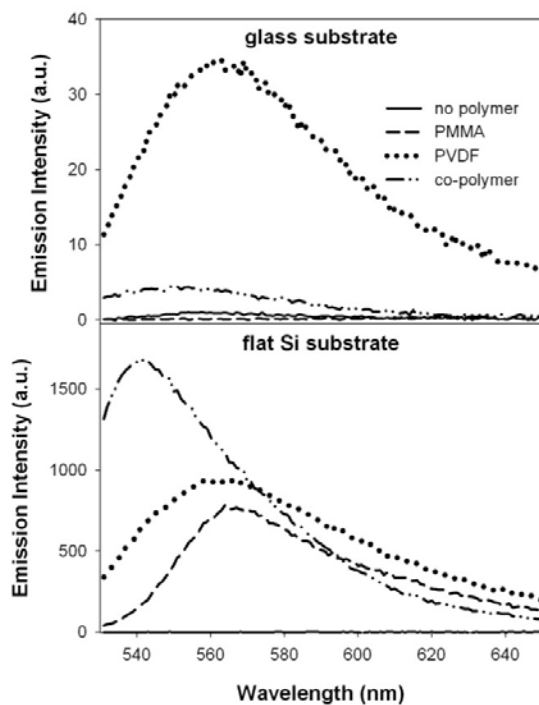


Figure 2. Emission spectra of Rhodamine 6G coated on different polymers cast on a glass substrate (upper) and a flat Si substrate (lower). All spectra are referenced to the spectrum with no polymer (solid line). PMMA (short dashes), PVDF (dotted), and co-polymer (dot-dashed). Excitation was at 521 nm and 1 nm slits were used for both the excitation and emission monochromator.

To test the effect of different substrates, Rh6G was deposited onto polymers spin-cast onto a glass slide and a flat Si wafer. Neither of these substrates contained Ag, yet substantial enhancements were observed as shown in Figure 2. Even with a glass slide substrate there is a modest enhancement, by as much as a factor of ~ 35 for PVDF. When the substrate is flat Si, again with no Ag, the polymers lead to enormous enhancements, as high as 1600 for 0.3 μm thick co-polymer film. On the flat Si substrate there also is noticeable shift of the emission maximum, ranging from 560 nm for PMMA, 550 nm for PVDF, and 540 nm for the co-polymer. When Fabry-Perot modes are coupled to a plasmon resonance the absorption maximum can shift¹¹ and this should affect the emission maximum similarly. However, the flat Si is a semiconductor and is not expected to support a plasmon resonance in the visible region. Further, the observation of some enhancement on a glass substrate rules out any coupling to a plasmon resonance. Another possible explanation for the shift in the emission maxima is the difference in the polarity of each of the polymers. Environmental polarity is

often observed to shift emission maxima in solution and that may contribute to the observed wavelength shift here, as well.

Figure 3 shows the emission spectra for different substrates all spin-cast with a $\sim 0.3 \mu\text{m}$ PVDF film, normalized to Rh6G on glass with no polymer. When the substrate is glass, flat Si, or p-Si the enhancements are all comparable, ~ 400 , relative to the glass substrates, glass/Rh6G. The enhancement more than doubles when Ag is deposited on the p-Si. This shows that the plasmon induced enhancement and the polymer amplification are cooperative.

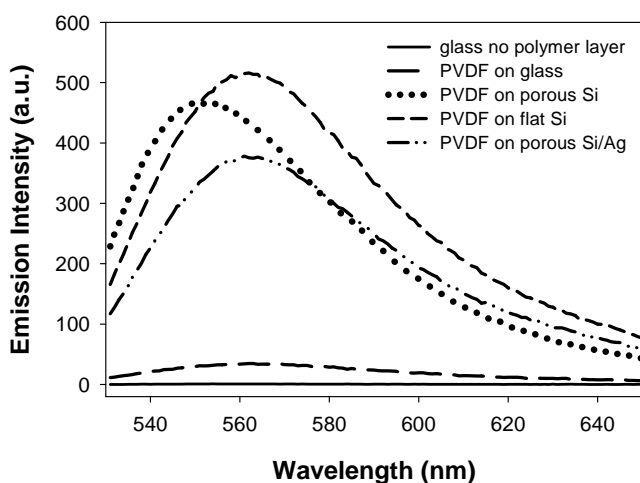


Figure 3. Emission spectra of Rhodamine 6G cast on PVDF with different substrates. All spectra are referenced to Rhodamine 6G cast on glass with no polymer layer (solid line). PVDF on glass (long dashes), PVDF on porous Si (dots), PVDF on flat Si (short dashes), PVDF on Ag coated porous Si (dot-dashed line). Excitation was at 521 nm and 1 nm slits were used for both the excitation and emission monochromator.

One possible explanation for the observed enhancement effect is that the Rh6G is dissolved into the polymer layer when it is deposited. If this were to happen, then there would be less self-quenching from Rh6G and an enhancement. This seems unlikely, however, because the solvent used to dissolve the Rh6G, ethanol, does not dissolve the polymers used here.

Reflection spectra for the various layered structures were measured, as shown in Figure 4. The effect of simply depositing Rh6G onto the substrate is shown in Fig. 4A using flat Si as the reference (using Si as the reference removed the large contribution arising from the Si reflectivity). In the absence of Rh6G, p-Si shows a fringing pattern resulting from the pore structure ($\sim 2 \mu\text{m}$ thick) but the fringing largely disappears when the Ag layer is added,

indicating that the light does not pass through to the p-Si layer. The p-Si shows a resonance at 450 nm while the p-Si/Ag substrate shows minimal reflection throughout the visible region. Upon addition of Rh6G, reflection drops considerably in all cases and does not show any feature that could be assigned to the absorption maximum expected for Rh6G at 521 nm. The featureless response is assigned to diffuse reflection of the rough Rh6G surface since the Rh6G layer is too thin (20 – 40 nm) to exhibit a fringing pattern. Fig. 4B shows the reflection spectra of different polymers, with no Rh6G, coated onto p-Si/Ag. The polymers, which are all transparent, all reduce the reflectivity compared to the bare p-Si/Ag, showing that the polymers trap the light within the polymer layer of the structure.

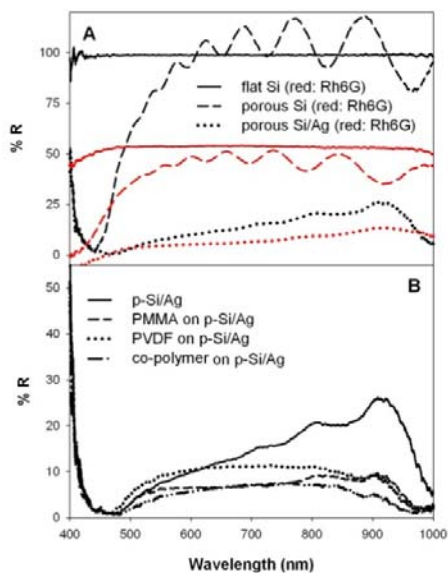


Figure 4. A. Reflection spectra of flat Si substrate (black solid line), flat Si substrate coated with Rhodamine 6G (red solid line), porous Si substrate (black dashed line), porous Si substrate coated with Rhodamine 6G (red dashed line), Ag coated porous Si substrate (black dotted line), and Ag coated porous Silicon substrate coated with Rhodamine 6G (red dotted line). B. Reflection spectra of Ag coated porous Si (solid line), ~310 nm PMMA on Ag/p-Si (dashed line), ~470 nm PVDF on Ag/p-Si (dotted line), and ~150 nm co-polymer on Ag/p-Si.

To test the utility of the enhanced fluorescent signal, samples were prepared using MEH-PPV on flat Si and p-Si/Ag/co-polymer substrates to be used for TNT sensing. MEH-PPV has been previously shown to be effectively quenched by nitroaromatics,⁹ while Rh6G has not been shown to interact with TNT in the gas phase. The p-Si/Ag/co-polymer/MEH-PPV

structure showed a fluorescence enhancement compared to flat-Si/MEH-PPV, but the enhancement at the emission maximum (598 nm) was only about 2.5 times. It is not clear why the enhancement is so much less than observed with Rh6G, but may be related to the overlap of the excitation wavelength (495 nm) and the resonance observed in the p-Si. Some of the excitation light is undoubtedly lost into the tail of the p-Si absorption.

Figure 5 shows the effect of exposing flat-Si/MEH-PPV and p-Si/Ag/co-polymer/MEH-PPV samples to TNT. The decay of the emission maximum is plotted as a function of exposure time to vapors of TNT (formed from the natural vapor pressure of TNT at room temperature, which is in the ppb range¹²). Both samples exhibit a quenching of about 60 % of the initial signal in less than 100 s. For comparison, MEH-PPV coated onto p-Si also shows about a 60 % quench but requires ~300 s to reach this value. Notably, in the p-Si/Ag/co-polymer/MEH-PPV sample this quenching occurs significantly faster: the half-life for the flat-Si/MEH-PPV sample is 19 s while the half-life for the p-Si/Ag/co-polymer/MEH-PPV sample is only 2 s, nearly an order of magnitude improvement.

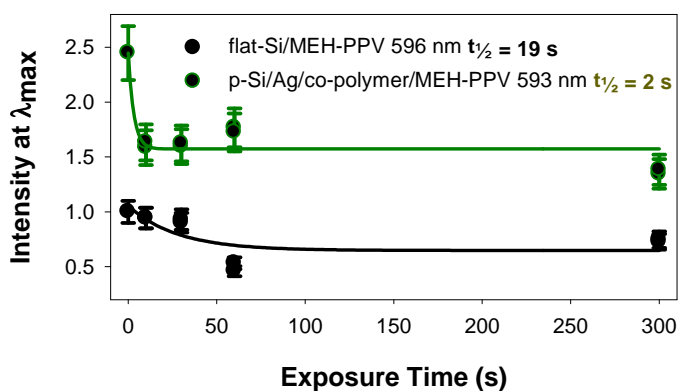


Figure 5. Quenching of MEH-PPV at λ_{\max} (598 nm) upon exposure to TNT. Black circles – flat Si/MEH-PPV; black line – exponential fit with half-life = 19 s; green triangle – p-Si/Ag/co-polymer/ MEH-PPV; green line – exponential fit with half-life 2 s. Intensities are referenced to the flat-Si/MEH-PPV value at $t = 0$ s.

Conclusions

In conclusion, we have shown that by adding a light trapping layer to a MEF structure can increase the fluorescence signal intensity by a factor of several hundred to over 1000. Further, when the light trapping layer is used in a TNT sensor, the exposure time to reach maximum

quenching is reduced, an important quality required for improved sensors. Work to better understand the influence all of the parameters in the structures is underway.

Acknowledgment

We gratefully acknowledge the ALERT Center of Excellence sponsored by the Department of Homeland Security for funding this work.

References

1. Geddes CD, Lakowicz JR (2002) Metal-Enhanced Fluorescence. *J Fluoresc* 12:121 – 129.
2. Geddes CD, Cao H, Gryczynski I, Gryczynski Z, Fang J, Lakowicz JR (2003) Metal-Enhanced Fluorescence (MEF) Due to Silver Colloids on a Planar Surface: Potential Applications of Indocyanine Green to in Vivo Imaging. *J Phys Chem A* 107:3443 – 3449.
3. Parfenov A, Gryczynski I, Malicka J, Geddes CD, Lakowicz JR (2003) Enhanced Fluorescence from Fluorophores on Fractal Silver Surfaces. *J Phys Chem B* 107:8829 – 8833.
4. Lakowicz JR (2005) Radiative decay engineering 5: metal-enhanced fluorescence and plasmon emission. *Anal Biochem* 337:171 – 194.
5. Aslan K, Leonenko Z, Lakowicz JR, Geddes CD (2005) Fast and Slow Deposition of Silver Nanorods on Planar Surfaces: Application to Metal-Enhanced Fluorescence. *J Phys Chem B* 109:3157 – 3162.
6. Deng W, Goldys EM (2012) Plasmonic Approach to Enhanced Fluorescence for Applications in Biotechnology and the Life Sciences. *Langmuir* 28:10152 – 10163.
7. Gill R, Tian L, Somerville WRC, Le Ru EC, van Amerongen H, Subramanian V (2012) Silver Nanoparticle Aggregates as Highly Efficient Plasmonic Antennas for Fluorescent Enhancement. *J Phys Chem C* 116:16687 – 16693.
8. Guzatov DV, Vaschenko SV, Stankevich VV, Lunevich AY, Glukhov YF, Gaponenko SV (2012) Plasmonic Enhancement of Molecular Fluorescence near Silver Nanoparticles: Theory, Modeling, and Experiment. *J Phys Chem C* 116:10723 – 1073.
9. Levitsky IA, Euler WB, Tokranova N, Rose A (2007) Fluorescent Polymer – Porous Silicon Microcavity Devices for Explosives Detection. *Appl Phys Lett* 90:041904/1 – 041904/3.
10. Zeiri L, Rechav K, Porat Z, Zeiri Y (2012) Silver Nanoparticles Deposited on Porous Silicon as a Surface-Enhanced Raman Scattering (SERS) Active Substrate. *Appl Spec* 66:294 – 299
11. Saison-Francioso O, Lévêque G, Akjouj A, Pennec Y, Djafari-Rouhani B, Szunerits S, Boukherroub R (2012) Plasmonic Nanoparticles Array for High-Sensitivity Sensing: A Theoretical Investigation. *J Phys Chem C* 116:17819 – 17827.
12. Oxley, JC, Smith, JL, Luo, W, Brady, J (2009) Determining the Vapor Pressures of Diacetone Diperoxide (DADP), and Hexamethylene Triperoxide Diamine (HMTD). *Propel. Explos. Pyrotech.* 34: 539 – 543.

Persistent Surveillance of Explosives and Explosive Precursors Using an Orthogonal Sensor Platform

**Professor Otto J. Gregory
Department of Chemical Engineering
University of Rhode Island**

Objective: Airports, subways and major transportation hubs have long been targets for terrorists intent on deploying improvised explosive devices or IED's. As such, the early detection of explosives at trace levels for screening purposes or for the direct intervention of potential threats continues to be a priority for the Department of Homeland Security. In response to this very real need, we are developing an orthogonal sensor platform that can uniquely identify threat molecules at trace levels. Using a continuous, passive detection system that exhibits both high sensitivity and selectivity for nitrogen and non-nitrogen based explosives without generating false positives continues to be our primary goal in this project. The ability to detect energetic materials such as TATP at trace concentrations in confined spaces by deploying sensors or sensor arrays that could "sniff" for explosives in relatively confined spaces is particularly important in venues that threaten public safety. We have seen many examples of terrorist acts over the past decade where the early detection of explosives and their precursors could have alerted the travelling public to such potential threats. Compounding the problem is the fact that most of explosives and energetic materials have extremely low vapor pressure. Towards that end, we have successfully detected TATP, ammonium nitrate, 2,6-DNT and diacetone diperoxide (DADP) at trace levels using our sensor platforms and we continue to broaden our range of threat molecules that can be detected.

Project Summary: Our initial focus was the detection of TATP and its precursors at trace levels, which was later expanded to include 2,6-DNT, urea and ammonium nitrate. Since the peroxide based compounds are generally harder to detect than the nitrogen based compounds used in many IED's and that there are some more mature technologies for the detection of nitrogen based explosives, we focused our initial efforts on the compounds related to TATP. We developed a small footprint, robust sensor platform that can reliably detect TATP at the single part per million level without multi-pass and pre-concentration steps. Our thermodynamic based sensor can continuously monitor the environment for explosives and explosive precursors by measuring the heat affect (heat generated or absorbed) associated with the interaction between a catalyst and a target molecule. The technique employs a digital control system which enables a microheater coated with a catalyst, to be thermally scanned over a selected temperature range and the electrical power difference due to catalytic activity (power difference between the target molecule and an inert reference) is measured similar to that in a microcalorimeter.

By minaturizing the sensor platform using MEMS technology, arrays of microheater sensors each coated with different catalysts specifically "tuned" for different threat molecules, it will be possible to uniquely identify target molecules of interest, without false positives. Provided that the energetic materials have sufficient vapor pressure, our thermodynamic based sensor is ideally suited for this purpose. Early indications were that unique signature to threat molecules such as TATP were a result of the catalytic

decomposition of the TATP, since we did not see any evidence of acetone in the output signal of our sensor and the signature closely tracked that of hydrogen peroxide. Further evidence of catalytic decomposition of TATP was provided by the Smith Oxley group at URI, who found that under ambient conditions, TATP decomposes primarily into acetone. Therefore, we believe that the catalytic decomposition of TATP actually provides a more specific reaction “tag” than first thought. Furthermore, the signature generated from our sensor will be used to uniquely characterize target molecules of interest when incorporated into a sensor array comprised of different catalysts, which can further minimize false positives.

To separate the sensor signals of H_2O_2 from TATP, a combinatorial chemistry approach was employed to enhance catalyst selectivity. Combinatorial catalyst libraries were created by “doping” metals such as platinum, palladium and copper into different metal oxides including ZnO , SnO_2 , In_2O_3 and WO_3 . The library based on $Pd-SnO_2$ was the most promising from this point of view and we demonstrated that the nanocomposite catalyst based on $Pd-SnO_2$ could dramatically improve the selectivity and sensitivity of TATP over that of H_2O_2 .

To achieve lower detection limits without sacrificing its excellent selectivity, our thermodynamic sensor platform was combined with a conductometric sensor platform to form an orthogonal sensor that can simultaneously interrogate catalysts exposed to explosive vapors. In doing so, a certain redundancy can be built into the sensor that can reduce the frequency of false positives, a major concern with any passive detection system. As a result of this work, we have successfully identified a number of explosives including 2,6-DNT, ammonia nitrate and TATP using multiple orthogonal sensors.

We have also continued to develop a microelectromechanical system (MEMS) version of the orthogonal sensor to miniaturize its footprint and thus, improve its response time, selectivity and sensitivity. The MEMS version of the sensor will also lower the power requirements, which is beneficial for continuous monitoring purposes should make it compatible for wireless networking capabilities. The smaller footprint also provides the possibility of creating sensor arrays with multiple catalysts and configurations.

Accomplishments: The development of sensor platforms, which could reliably detect those explosives commonly used in IED’s as initiators or the main explosive such as TATP and its precursors, was the primary goal of our research. Since TATP’s precursors (acetone, hydrogen peroxide and a strong acid) are readily available and its preparation is relatively simple, TATP is the explosive of choice for many terrorists. Unlike other explosives, TATP contains neither metallic elements nor nitro groups, and therefore, has no significant absorption in the ultraviolet region and does not fluoresce, making it very difficult to detect with conventional spectroscopy techniques. However, TATP has relatively high vapor pressure and sublimates readily at room temperature, which makes it ideal for vapor phase detection such as ours. Towards that end, we have identified various metal oxide catalysts and developed sensor protocols, as shown in Figure 1(a) and Figure 2) for the detection of TATP at the ppm level.

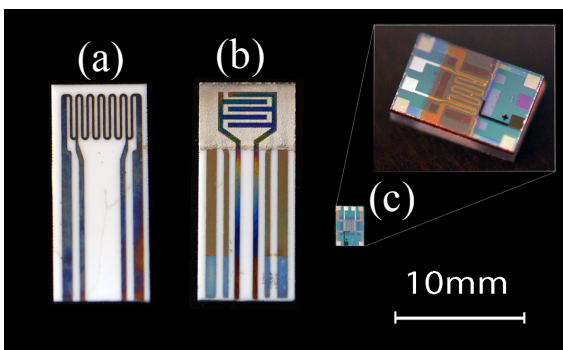


Figure 1. Photograph of our two sensor platforms developed for detection of explosives and explosive precursors: (a) thermodynamic sensor platform, (b) orthogonal sensor platform and (c) MEMS platform.

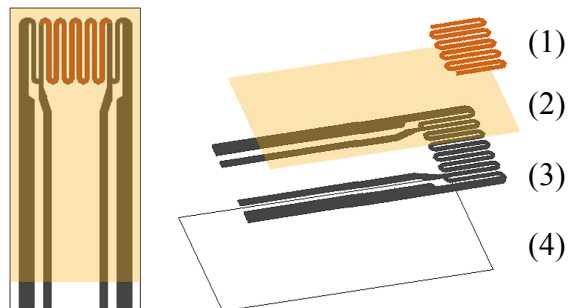


Figure 2. Schematic of thermodynamic sensor platform showing the top view (left) and expanded view (right) of catalyst (1), alumina layer (2), nickel micro-heater (3) and alumina substrate (4).

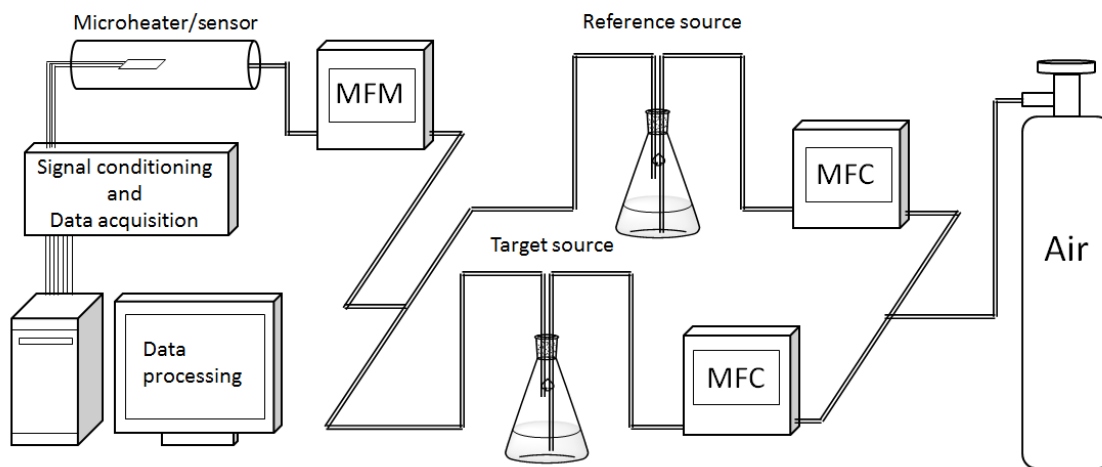


Figure 3. Apparatus used as testbed for the detection of explosive vapors and explosive precursors using a micro-calorimetric sensor.

The response of our sensor to TATP using a number of different catalysts is shown in Figure 4. Here, the responses to $0.685 \mu\text{g/mL}$ TATP as a function of temperature using several catalysts including $\text{WO}_3\text{-TiO}_2$, V_2O_5 , SnO_{2-x} , Nb_2O_3 and ZnO were measured. Each of the five metal oxide catalysts show a unique response as a function of temperature, with features ranging from almost no peak response for Nb_2O_3 to well defined peak responses for ZnO . Since we demonstrated that we can detect hydrogen peroxide at comparable levels using the same metal oxide catalysts, we compared the TATP and peroxide responses to determine if the TATP was decomposing in the vicinity of the microheater as it was being detected. Based on the responses of V_2O_5 and SnO catalysts to TATP and peroxide, it appears that the response of each catalyst to these target molecules occurs at the same temperature and that the signatures have a similar

peak intensity and shape.

From Figure 5, it can be seen that the relative response to acetone is considerably greater than that of H₂O₂, which was consistent with other investigations using thermodynamic based gas sensors for detection. These studies support our findings that significant exothermic heat effects are observed for hydrocarbons. Not only is the magnitude of the response to acetone for Cu₂O significantly greater than that of hydrogen peroxide but it is also of opposite sign, which implies that the sensitivity of our thermodynamic sensor platform to acetone is significantly greater than that of the other products derived from the decomposition of TATP. The fact that there is a sign change in the response signal for this catalyst, adds to the uniqueness of the signature which will ultimately lead to fewer false positives.

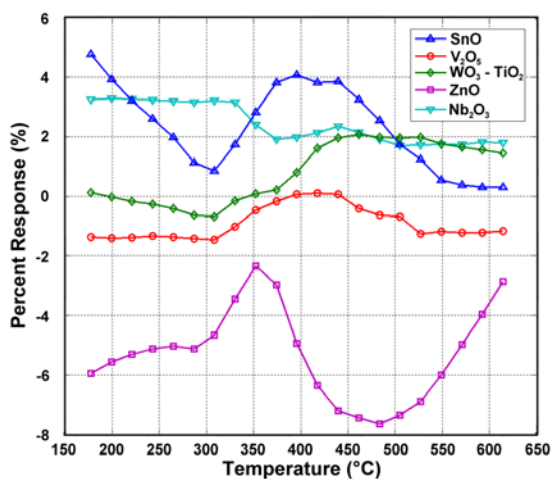


Figure 4. Response of various catalysts to 0.685 µg/mL TATP as a function of temperature.

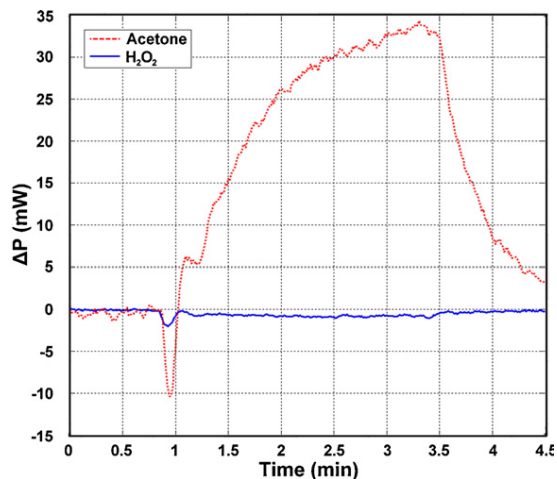


Figure 5. Response of Cu₂O catalyst to acetone and hydrogen peroxide.

We also focused our efforts throughout this research on catalyst development, which was an integral part of the overall sensor project. Even though we successfully demonstrated a thermodynamic based sensor that was capable of detecting TATP at trace levels, we wanted to improve the selectivity between TATP and hydrogen peroxide. Therefore, we incorporated palladium nanoparticles into a SnO₂ catalyst to improve both the sensitivity and selectivity to H₂O₂ over TATP. A Pd-SnO₂ nano-composite catalyst containing 8 wt.% Pd yielded the greatest selectivity (H₂O₂ relative to TATP) as shown in Figure 6. Not only was the selectivity to TATP increased using this approach but the sensitivity to TATP was also increased by more than 60% and the sensitivity to H₂O₂ was increased by more than 160%. As a reference, the selectivity improvement relative to urea was also demonstrated in Figure 6 and a series of concentration tests were completed to determine the effect of concentration of TATP in the vapor phase on the response of a Pd-SnO₂ nanocomposite catalyst. These results are shown in Figure 7. SEM and TEM micrographs of a Pd-SnO₂ nanocomposite catalyst containing 12 wt.% Pd is shown in Figure 8. Microscopy was used to determine the palladium loading in the Pd-SnO₂ nanocomposite catalyst that was developed for optimum selectivity and sensitivity.

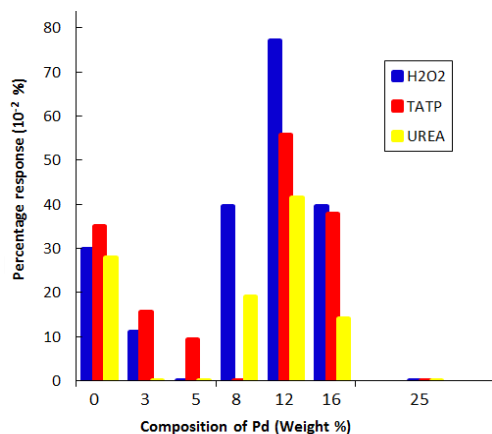


Figure 6. Selectivity of various Pd doped SnO₂ catalysts to H₂O₂, TATP and UREA.

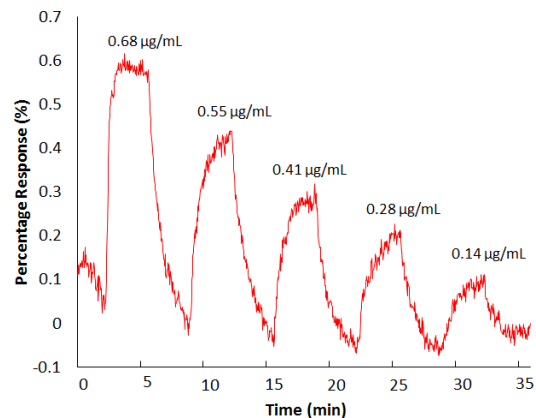


Figure 7. Effect of TATP concentration on the response to Pd-SnO₂ sensor (8 wt.% Pd)

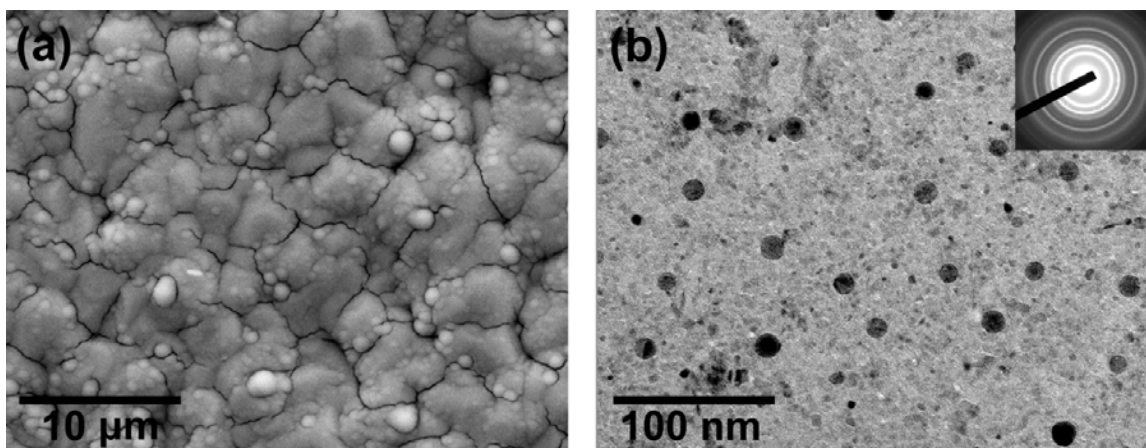


Figure 8. SEM (a) and TEM (b) micrographs of a SnO₂ catalyst with a 12 wt% palladium.

We have also pursued new sensor templates that will ultimately reduce the frequency of false positives, a major concern with any passive detection scheme. Our approach to mitigate false positives was to combine multiple sensor platforms to yield a more unique signature or sensor response. By combining a thermodynamic platform with a conductometric platform, we could effectively interrogate our catalysts (simultaneously) in a single sensor by relying on these very different sensing mechanisms. Most conductometric sensors are highly sensitive to oxidizing and reducing species, but other than that difference, target molecules are not easily identified. Thus, conductometric sensors on their own merit have relatively poor selectivity. Thermodynamic based sensors, however, have much greater selectivity, since target molecules react with a particular catalyst, the sensor can accurately measure these heat effects associated with decomposition and/or decomposition products. Based on this idea, a conductometric platform was successfully paired with a thermodynamic platform to establish an orthogonal sensor, as shown in Figure 1(b) and Figure 9. The orthogonal sensor provides additional redundancy to mitigate false positives and at the same time lowered the detection limit for target molecules.

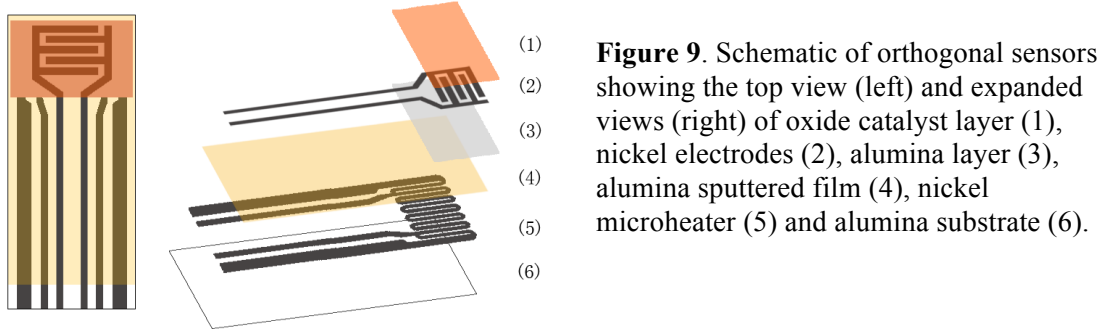


Figure 9. Schematic of orthogonal sensors showing the top view (left) and expanded views (right) of oxide catalyst layer (1), nickel electrodes (2), alumina layer (3), alumina sputtered film (4), nickel microheater (5) and alumina substrate (6).

Figure 10 shows the response of an orthogonal sensor to 0.5 ppm 2,6-DNT using a ZnO catalyst at 410 °C. 2,6-DNT was introduced into system at the 60 second mark and was exposed for 360 seconds as shown in Figure 10 (horizontal axis). Both thermodynamic and conductometric signals indicated a large, rapid response (response time of less than 10 seconds), but appeared to have different time constants: i.e. compared to the conductometric response, thermodynamic response took longer to reach equilibrium. Additional testing of the orthogonal sensor using a SnO₂ catalyst to DNT as a function of vapor concentration was conducted to study the effect of vapor concentration, on recovery time as shown in Figure 11. The thermodynamic response was linear with respect to DNT vapor concentration whereas the conductometric response remained reasonably large as DNT vapor concentration was decreased.

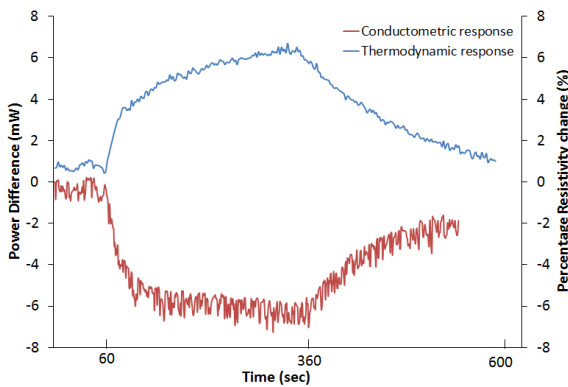


Figure 10. Thermodynamic sensor response (blue) and conductometric sensor response (red) to 2, 6-DNT at 410 °C: ZnO catalyst was simultaneously interrogated using two different platforms in orthogonal sensor.

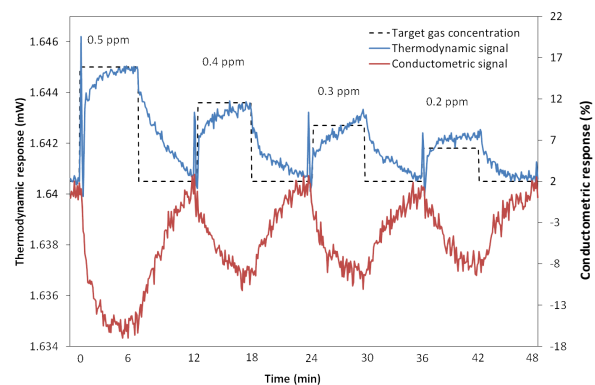


Figure 11. Response of a SnO₂ orthogonal sensor to different concentrations of 2, 6-DNT in the vapor phase at 410 °C.

The conductometric signal of SnO₂ to ammonia nitrate, DNT and TATP vapor as a function of temperature is shown in Figure 12. Sensor response of ammonia nitrate was proportional to temperature and leveled off at high temperatures (>350°C), whereas the TATP signal exhibits a steady response at all temperatures investigated. Sensor response to 2, 6-DNT showed similar behavior (as TATP) but a shallow peak was observed at 280 °C. The differences of response signals were due to the differences in vapor pressure, functional groups and molecular structures of each explosive molecules.

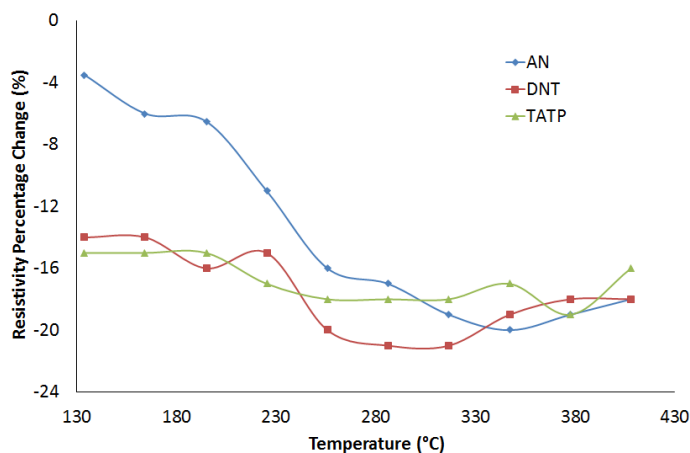


Figure 12. Conductometric sensor response to ammonia nitrate (blue), 2,6-DNT (red) and TATP (green) as a function of temperature using a SnO₂ catalyst.

We have also developed a microelectrochemical (MEMS) based sensor platform that utilizes our novel thermodynamic and conductometric platform on a much smaller scale. A suspended membrane MEMS sensor is being developed both at URI and NUWC to replace the existing solid-state sensor (Figure 1c and Figure 13). Several versions of the device have been fabricated and tested. They show more than a 60% and 90% reduction in power requirement relative to the existing solid-state sensors. Based on our most recent fabrication results, we have reduced the size of the micro-heater platform even further and in the process reduced its thermal mass and power consumption. To fabricate a sensor with the desired characteristics, a silicon wafer was etched to form a thin suspended membrane onto which the microheaters and catalyst are deposited. With this size reduction comes a reduction in power requirements relative to our current sensor platform, leading to an increase in sensitivity to the target molecules of interest and a decrease in response time. The smaller footprints achieved with the MEMS platform also creates the possibility of forming microarrays of sensors; i.e. sensor arrays containing many different catalysts, which will increase selectivity and sensitivity for target explosives while eliminating false positives. Due to the ease of integration, the ability to form large sensor arrays in a fast responding, single pass continuous detection system is feasible. The MEMS platform developed at URI is shown in Figure 1 (c) and has considerable potential for commercialization.

Finally, the most critical part of our detection system for "sniffing" explosives is the acquisition, reduction, and signal processing of the raw data collected from our measurements. When an inert is passed over the sensor, a baseline electrical analog response was generated. When the sensor is exposed to the target molecule, a signal corresponding to the heat effect is measured and recorded. That is, the analog signal is sampled using an A/D converter and the data stored in a text file. To efficiently analyze this data, a graphical user interface (GUI) using MATLAB was developed. This MATLAB code performs the data reduction function. The acquired digitized data typically has over 100,000 sampling points per run. The GUI digitally samples the data and reduces this to between 100 and 2000 data points. It also enables the user to perform some graphical manipulation of the data. Once stored, the data can be easily analyzed or plotted using a broad array of mathematical and graphical tools. A second GUI was developed using MATLAB to perform signal processing. This program loads the original data, reduced data, or reduced data that has been truncated. The data can be digitally

filtered to minimize random noise either using automatic or manual selection controls depending on user input. The program also enables the user to calculate and subtract out any signal drift either automatically or manually. Our high school chemistry and physics teacher, Mr. Anthony Fascia, was largely responsible for this task, which was successfully integrated into our working sensor platform.

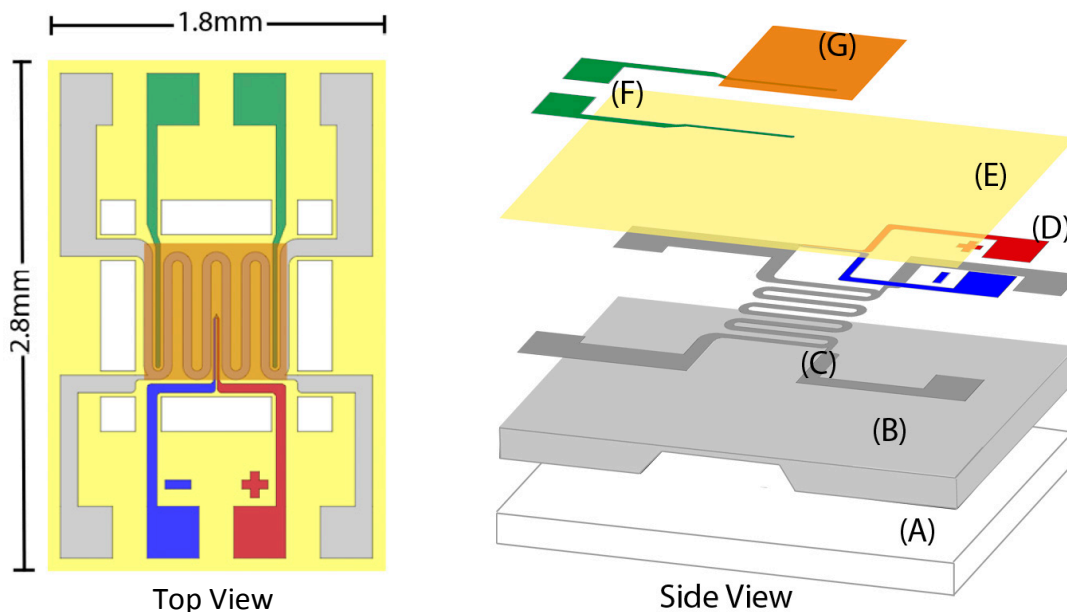


Figure 13. Left is the top view of a URI MEMS sensor and on the right is a side view illustrating the layers including: (A) pyrex glass, (B) silicon wafer with a KOH etched cavity on the underside, (C) platinum microheater, (D) Type K thermocouple, (E) silicon dioxide dielectric layer, (F) platinum conductometric electrodes and (G) a metal oxide catalyst layer placed over the coils of the microheater.

5. Students Supported

Undergraduate Students Supported:

Chemical Engineering Bisola B. Bruno;

Chemical Engineering Ben Jacques

Chemical Engineering Kelly Waterman

Chemical Engineering Caitlin Hurley

Chemical Engineering Dennis Below

Chemical Engineering Matin Amani

Electrical Engineering Fabian Sierra

Graduate Students Supported:

Yun Chu; Chemical Engineering PhD

Dan Mallin; Chemical Engineering MS

Carson Pryde; Chemical Engineering MS

Tom Hilfer; Chemical Engineering MS

Matthew Priest; Chemical Engineering MS

Agust Cote III Electrical Engineering MS

6. Transition Partners

SensorTech, Inc., Savannah, GA and NUWC Middletown, RI

Naval Undersea Warfare Center, Middletown, RI

FLIR-Nomadics, Stillwater, OK

7. Publications / Patents

Y. Chu, D. Mallin, M. Amani, M. Platek, and O.J. Gregory, “Detection of Explosives using Orthogonal Sensor”, submitted to IEEE Sensors.

Y. Chu, D. Mallin, M. Amani, M. Platek, and O.J. Gregory, “Detection of Peroxides Using Pd/SnO₂ Nanocomposite Catalysts”, Sensors and Actuators B Chemical in press.

M. Amani, Y. Chu, K. Waterman, C. Hurley, M. Platek and O.J. Gregory, “Detection of Triacetone Triperoxide (TATP) Using a Thermodynamic Based Gas Sensor”, Sensors and Actuators B: Chemical, Vol. 162, p.7-13 (2012).

K. Maciejewski, Y. Sun, O. J. Gregory and H. Ghonem, “Time-dependent Deformation of Low Carbon Steel at Elevated Temperatures”, Materials Science and Engineering: A, Volume 534, p.147–156 (2012).

W. Visser, Y. Sun, O. Gregory, G. Plume, C-E. Rousseau, H. Ghonem, “Deformation characteristics of low carbon steel subjected to dynamic impact loading”, Material Science and Engineering A, 528, p. 7857– 7866 (2011).

O.J. Gregory, H. Ghonem, M.J. Platek, J. Oxley, J. Smith, M. Downey, C. Cummiskey and E. Bernier, “Microstructural Characterization of Pipe Bomb Fragments”, Materials Characterization, Vol.61, No. 3, p.347-354, (2010).

“A Thermodynamic Based Gas Sensor for the Detection of TATP”, O.J. Gregory, M. Platek, M. Amani and A. Cote, URI Patent disclosure filed 2011.

“An Orthogonal Sensor for the Detection of Explosives”, O.J. Gregory, M. Platek, M. Amani, Daniel Mallin, and Yun Chu, URI Patent disclosure filed 2012.

8. Presentations:

RICC Research to Resilience 2012, Northeastern Univ., Boston, MA, Sep. 2012, “Detection of Explosives Using Multi-technique Sensor”, Y. Chu, D. Mallin, B. Bruno, O.J. Gregory

221st Electrochemical Society Meeting, Seattle, Washington, May 2012, “Catalyst Development for Thermodynamic Based Gas Sensors Using Combinatorial Chemistry”, Y. Chu, C. Hurley, C. Pryde, M. Amani, M. Platek and O.J. Gregory.

RICC Research 2 Reality 2011, Northeastern Univ, Boston, MA, Oct 2011, “Thermodynamic Based Sensors for the Detection of Explosives and Explosive Precursors”, O.J. Gregory

219th Electrochemical Society Meeting, May 2011, Montreal, Canada, “Detection of TATP Using Thermodynamic Based Gas Sensors with Metal Oxide Catalysts”, Y. Chu, K. Waterman, C. Hurley, M. Amani and O.J. Gregory.

IMPLAST 2010-Society of Experimental Mechanics (SEM), Providence, RI, October 2010, “Deformation Criterion of Low Carbon Steel Subjected to High Speed Impacts”, W. Visser, G. Plume, C.E. Rousseau, O. Gregory and H. Ghonem.

Microscopy and Microanalysis 2010, Portland , OR, “Characterization of Pipe Bomb Fragments using Optical Microscopy and Scanning Electron Microscopy”, M.J. Platek, O. J. Gregory, T. Duarte, H. Ghonem, J. Oxley, J. Smith, E. Bernier.



Detection of triacetone triperoxide (TATP) using a thermodynamic based gas sensor

Matin Amani^{a,b}, Yun Chu^a, Kellie L. Waterman^a, Caitlin M. Hurley^a, Michael J. Platek^b, Otto J. Gregory^{a,*}

^a Department of Chemical Engineering, University of Rhode Island, Kingston, RI 02881, USA

^b Department of Electrical Engineering, University of Rhode Island, Kingston, RI 02881, USA

ARTICLE INFO

Article history:

Received 31 July 2011

Received in revised form

22 September 2011

Accepted 6 November 2011

Available online 17 November 2011

Keywords:

Gas sensor

TATP

Hydrogen peroxide

Sputtering

Metal oxide

ABSTRACT

Triacetone triperoxide (TATP) is commonly used in improvised explosive devices (IEDs) due to its relatively simple preparation and readily available precursors. In this study, a small footprint gas sensor utilizing metal oxide catalysts was fabricated and tested, which is capable of detecting the heat of reaction during the catalytic decomposition of TATP. Due to its relatively high vapor pressure compared to other explosives, TATP is an ideal target molecule for this type of gas sensor. TATP and its decomposition products, hydrogen peroxide and acetone were successfully detected using this thermodynamic based sensor platform. Each tested catalyst exhibited a specific response at a given temperature and the detection limit of TATP was determined to be in the range of parts per million. X-ray photoelectron spectroscopy (XPS) was employed to study the oxidation state of selected catalysts prior to and after exposure to the target gases. Morphology of the catalysts in the as-deposited and tested condition was followed using scanning electron microscopy (SEM).

© 2011 Elsevier B.V. All rights reserved.

1. Introduction

Triacetone triperoxide (TATP) has been widely used in IEDs by terrorists, since its precursors (acetone, hydrogen peroxide and a strong acid) are readily available and its preparation is relatively simple. For example, in 2001 a suicide bomber targeted American Airlines with a TATP trigger [1] and it is also believed that TATP was used in the 2005 London subway bombings. Consequently, the reliable detection of TATP using a portable, small footprint sensor continues to draw interest, however, relatively few studies have been published to date.

Unlike many other explosives, TATP contains neither metallic elements nor nitro groups, and therefore, has no significant absorption in the ultraviolet region and does not fluoresce [2]. This makes it very difficult to detect with conventional spectroscopy techniques, especially when combined with its instability and molecular structure. Specifically, the presence of peroxide bonds makes the TATP molecule sensitive to extreme shock, heat and friction, but at the same time this makes it degrade readily. TATP is typically a crystalline solid compound at low temperatures but sublimates readily at room temperature, which makes it an ideal material for vapor phase detection. Several studies have been published on detecting TATP, including ion mobility spectra (IMS) combined with Raman spectrometry, mass spectrometry (MS),

nuclear magnetic resonance (NMR), fluorescence spectroscopy and absorption spectroscopy [3–8]. Each of these detection methods has limitations, which include slow responses and/or low sensitivity [2], and all these techniques require large scale analytical instrumentation which is very difficult to implement at venues where a portable or hand held device is required. TATP analysis by high performance liquid chromatography has been touted as an improved technique, coupled with UV irradiation and electrochemical detection [9], but it still requires considerable analysis time and is not suitable for in situ monitoring under field conditions. Finally, all these techniques are based on the detection of solid TATP and often involve swabbing techniques, thus cannot be used for continuous in situ monitoring. More recently, sensor platforms based on colorimetric sensor arrays have been developed which have detection limits as low as 2 ppb [10]; however, this method is based on a one-time use, swabbing technique, and cannot be used for continuous real time detection. Capua et al. have also recently demonstrated a multisensory array capable of detecting ppb quantities of TATP vapor continuously, in real time [11].

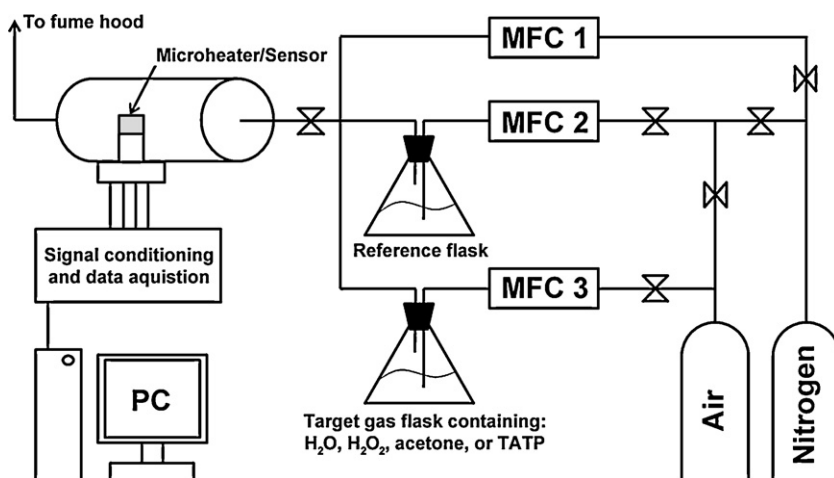
Metal oxide based gas sensors have been extensively studied and have been implemented in several commercial applications, such as O₂ and CO detection in internal combustion engine exhaust systems as well as the detection of other toxic, inflammable gases such as NH₃, NO₂, SO₂ and H₂ at concentrations as low as 1 ppm [12,13]. These sensor platforms also offer several advantages, such as compatibility with conventional CMOS processing, low cost and small dimensions, but have been criticized for their lack of long term stability and poor selectivity. The majority of these platforms

* Corresponding author. Tel.: +1 401 874 2085.

E-mail address: gregory@egr.uri.edu (O.J. Gregory).

Table 1
Sputtering conditions for various metal oxide catalysts.

	Catalyst					
	Cu ₂ O	Cu ₂ O–CuO	SnO _{2-x}	ZnO	V ₂ O ₅	WO ₃ –TiO ₂
Target diameter (mm)	150	150	150	150	125	150
Target material	Cu	CuO	SnO ₂	ZnO	V	W–Ti (90/10)
Power density (W/cm ²)	1.77	1.98	1.98	1.98	2.45	1.77
Voltage (V)	1100	900	1150	950	1600	1400
Gas pressure (Pa)	Ar: 1.1 PaO ₂ : 0.3 Pa	Ar: 1.4 Pa	Ar: 1.4 Pa	Ar: 1.4 Pa	Ar: 1.1 PaO ₂ : 0.3 Pa	Ar: 1.1 PaO ₂ : 0.3 Pa
Deposition rate (μm/h)	0.17	0.9	0.8	1.1	0.06	0.13

Fig. 1. Schematic of apparatus used for the detection of TATP, H₂O₂ and acetone using a thermodynamic gas sensor.

operate by monitoring the changes in the electrical properties of the catalyst due reactions with a target gas [14]. However, these reactions are typically observed at relatively high temperatures, and the electrical properties of the catalyst film tend to vary due to issues such as cracking or sintering of the film. While these issues are still of concern in the thermodynamic sensors described here, the heat effect generated by the catalyst is relatively constant over time compared to the electrical response and provides a more stable response which should provide additional information when coupled with a conductometric sensor.

In order to satisfy the need for a fast and accurate method of continuously screening TATP, extensive efforts have been devoted to developing an innovative and effective sensor platform that is capable of monitoring explosives, such as TATP, in real time [15]. TATP sublimes readily due to its relatively high vapor pressure, and forms a complex vapor upon decomposition [16,17]. Preliminary studies suggest that using our gas sensor platform, TATP has a similar response to hydrogen peroxide, one of its decomposition products, but also exhibits its own characteristic signal. Consequently, by selecting metal oxide catalysts sensitive to the peroxide bonds in TATP, as well as its organic by-products, a reliable sensor with high sensitivity and high selectivity can be produced.

In this study, a thermodynamic based gas sensor was developed for the detection of TATP and its precursors. This sensor measures the heat generated or absorbed by a metal oxide catalyst in the presence of TATP and its decomposition products in air at very low concentrations. The technique employs a digital control system which enables a thin film microheater, coated with a metal oxide catalyst, to be scanned over a selected temperature range. The electrical power difference due to catalytic reaction (power difference between the microheater in air and the microheater in the presence of TATP) was measured as a function of temperature for various metal oxide catalysts. Utilizing arrays of microheaters, each with a different catalyst it was possible to uniquely identify TATP in real time, while simultaneously minimizing false positives.

2. Experimental

2.1. Fabrication of thermodynamic gas sensors

Over a hundred thin film microheaters were fabricated on perforated 96% pure compact alumina substrates using an MRC 822 sputtering system to deposit 2 μm thick nickel films at room temperature. The wafer was then annealed at 900 °C in nitrogen for 5 h to densify and stabilize the electrical resistivity of the nickel films. Various metal oxide catalysts having a nominal thickness of 0.5 μm were then deposited directly over the nickel microheaters using either metal or ceramic targets in a MRC 8667 sputtering system. The detailed sputtering conditions for the deposition of the metal oxide catalysts are listed in Table 1. The sensors were subsequently annealed in air at 650 °C to further improve their stability. Prior to and after testing, the oxidation state of the metal oxide catalysts was characterized using XPS and the morphology of the oxide catalysts was followed using SEM.

2.2. Gas sensor testing apparatus and protocol

A schematic of the test bed used for all the gas sensor experiments is shown in Fig. 1, where multiple Alicat Scientific mass flow controllers were used to mix the target gases at various concentrations while maintaining a constant flow rate of 100 SCCM. H₂O₂ and acetone were introduced into the system by bubbling air through sealed flasks containing the liquid precursors, while TATP was introduced into the system by passing air over filter paper impregnated with nanogram quantities of TATP crystals.¹ The sensors were mounted using a standard DB-9 connector mounted in a 13 mm diameter PVC tube.

¹ Prepared by Professor Jimmie Oxley and Professor James Smith at the University of Rhode Island.

A digital control system employing a LabView program was used to heat the microheaters to a series of predetermined set point temperatures. These temperatures were selected using the temperature coefficient of resistance (TCR) of the nickel film, which was independently calibrated. After the sensor reached equilibrium at each temperature set point, the total power dissipation was recorded for a period of 75 s. The average amount of heat generated or absorbed by the catalyst in the presence of the target gas was calculated as the power required to maintain the sensor at a constant temperature, as well as the percent response which was the fraction of total power generated by the catalyst. These tests were conducted using both a dynamic pulsed gas scheme, where the sensor is initially run in air, followed by 2 min in various concentrations of the target gas, and then run in air again, without changing temperature. Static testing was also performed by determining the power dissipation in air at each temperature, cooling the sensor to room temperature and running again in the target gas at the same temperatures. Using the static test protocol, the sensitivity of electronics and drift in the resistance of the thin film microheaters allow for power differences greater than 8 mW to be reliably detected, while the dynamic response technique allows for power differences as low as 1 mW to be reliably detected.

3. Results and discussion

3.1. Chemical characterization

The oxidation states of the copper oxide catalysts prepared from ceramic and metallic targets were determined by XPS (Fig. 2). In Fig. 2, the Cu 2p spectra of those copper oxide films prepared by reactive sputtering in an Ar/O₂ plasma from a metallic target (dashed line) were compared to copper oxide films prepared by sputtering in an Ar plasma from a CuO target (solid line). The significant difference between the spectra is that the films prepared from ceramic targets contain satellite peaks which are typically found 7–10 eV above the main peaks associated with the copper 2p_{3/2} and 2p_{1/2} electrons, respectively for Cu²⁺ compounds, and correspond to shake-up electrons with 2p3d⁹ character [18]. In this film, the copper 2p_{3/2} and 2p_{1/2} peaks were found at 929.65 and 949.15 eV (Cu⁺), respectively; furthermore, curve fitting of the main 2p_{3/2} peak revealed a second peak with lower amplitude at

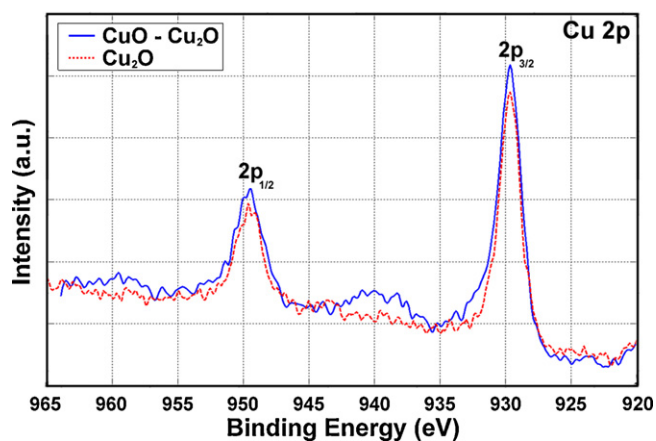


Fig. 2. XPS spectra of Cu₂O films prepared by sputtering in an Ar/O₂ plasma from a metal target and CuO–Cu₂O films prepared by sputtering in an Ar plasma from a CuO target.

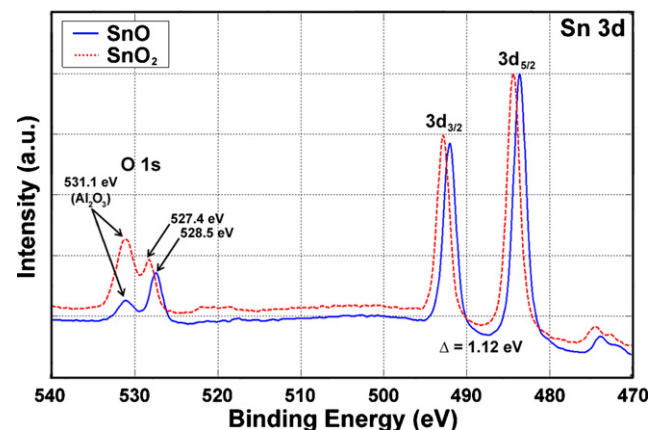


Fig. 3. XPS spectra of stoichiometric SnO₂ films prepared by sputtering in an Ar/O₂ plasma from a ceramic target and non-stoichiometric SnO_{2-x} films prepared by sputtering in an Ar plasma from a SnO₂ target.

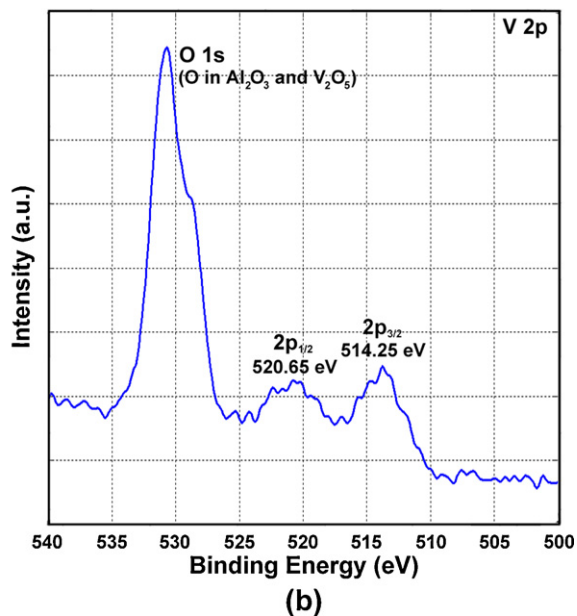
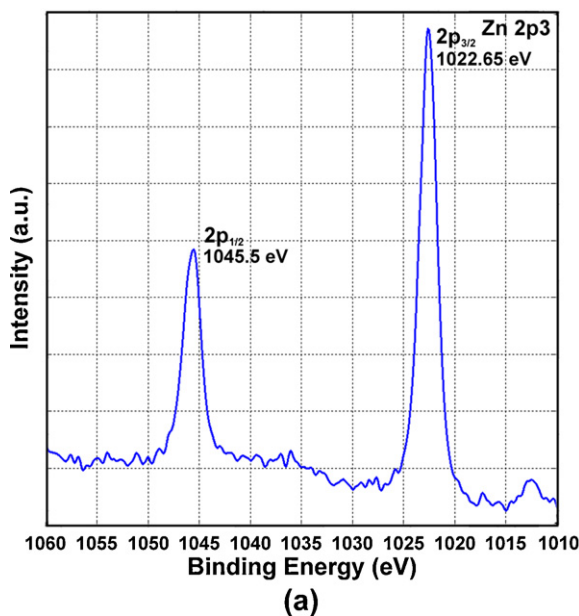


Fig. 4. XPS spectra of (a) ZnO and (b) V₂O₅ films.

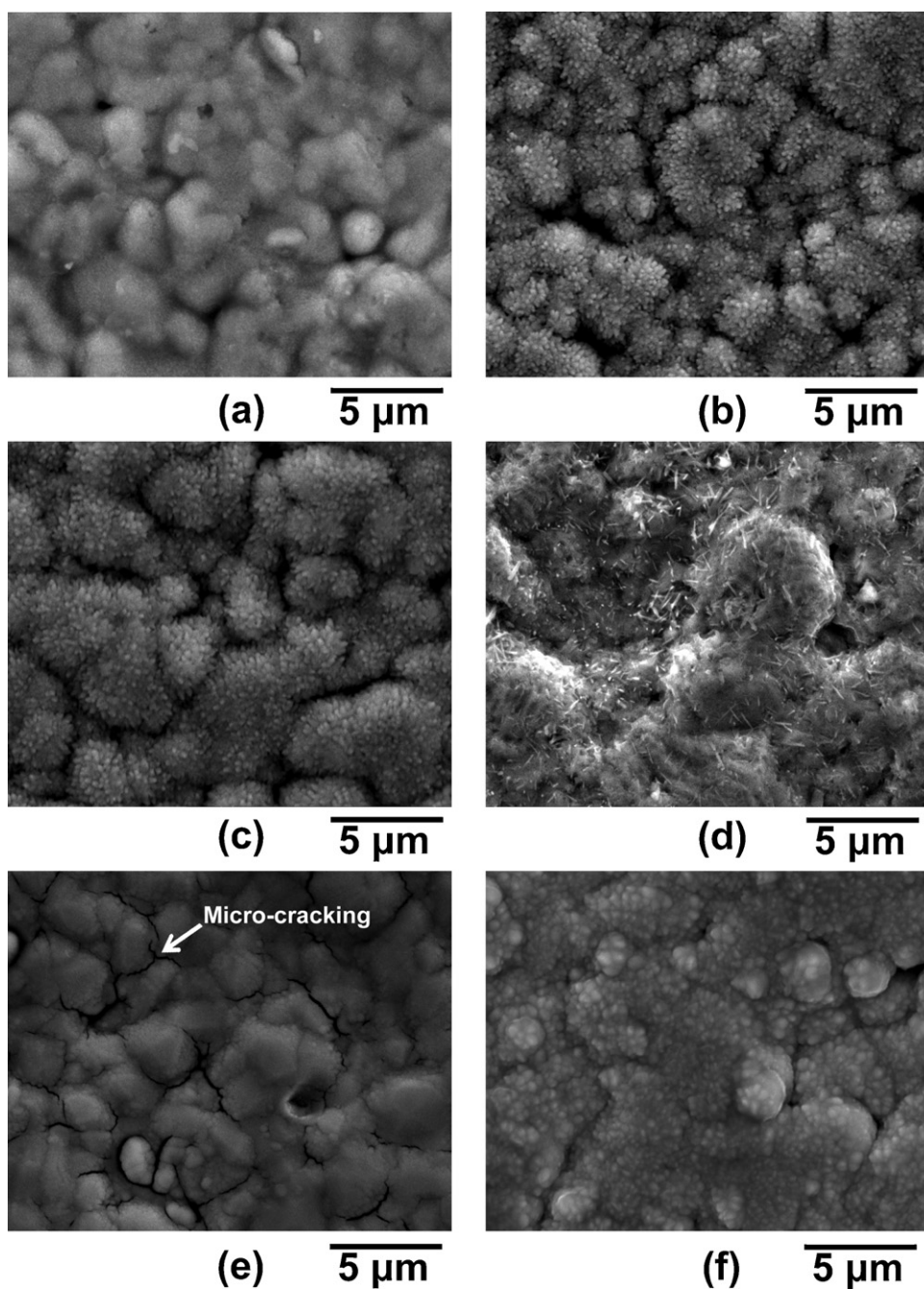


Fig. 5. SEM micrographs of (a) CuO–Cu₂O after testing, Cu₂O (b) before and (c) after testing and (d) V₂O₅, (e) ZnO and (f) SnO_{2-x} after testing.

931 eV (Cu²⁺). The broadening of the 2p_{3/2} peak towards higher binding energies combined with the presence of the satellite peaks suggests that these copper oxide films prepared by sputtering from ceramic targets in an Ar plasma have mixed oxidation states [19]. On the other hand, by sputtering in Ar/O₂ plasma from a metal target, a narrow 2p_{3/2} peak at 929.65 eV was observed and no satellite peaks were present, in the spectra indicating that the film is largely composed of Cu₂O. Non-stoichiometric SnO_{2-x} films were also prepared by sputtering from an oxide target in an argon plasma. A 1.12 eV shift in both the O 1s and the Sn 3d peaks was observed relative to those peaks for a SnO₂ reference film, as shown in Fig. 3. This is consistent with the shift typically described in the literature, for SnO [20]. Fig. 4 shows the XPS spectra of the 3d and 2p electrons in (a) ZnO and (b) V₂O₅. The Zn 2p_{3/2} and 2p_{1/2} peaks were found at 1022.65 eV and 1045.5 eV, respectively. In the spectra for vanadium

oxide, the 2p_{3/2} and 2p_{1/2} core levels were found at 514.25 eV and 520.65 eV, respectively, both of which are in agreement with those values typically observed in ZnO and V₂O₅ films [21,22]. Moreover, no significant shifting of these peaks was observed after testing at a maximum temperature of 650 °C.

3.2. Structural characterization

Fig. 5 shows the microstructure of several oxide catalysts sputtered from metallic and ceramic targets in different Ar/O₂ partial pressures. CuO–Cu₂O films with mixed oxidation states, were sputtered from a ceramic target in argon plasma, and show surfaces devoid of any fine structure. They also exhibit relatively smooth rounded protuberances with minimal surface area, typical of an as-sputtered film (Fig. 5a). However, the Cu₂O films reactively

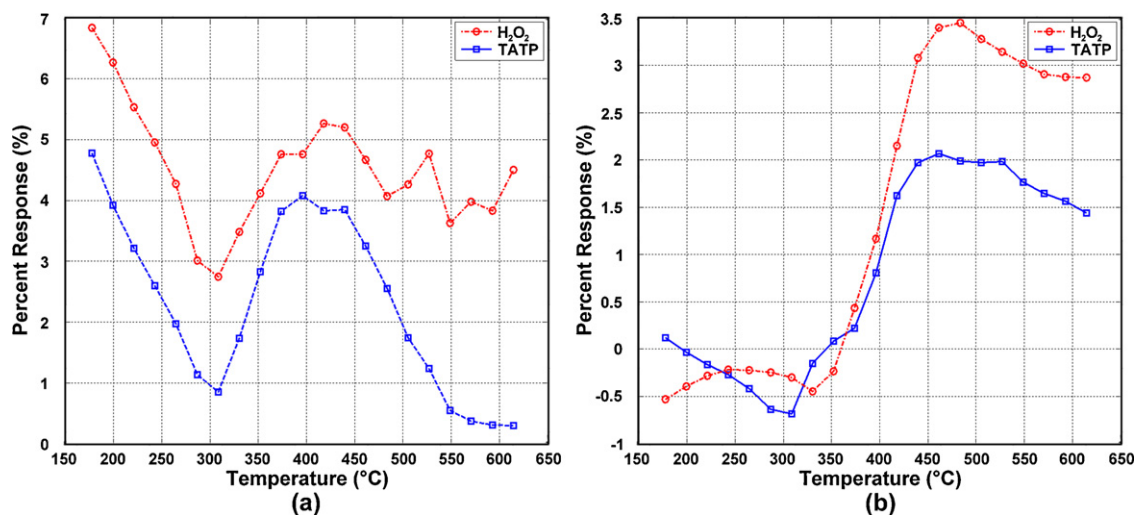


Fig. 6. Percent response in 8 ppm TATP and 9 ppm H₂O₂ as a function of temperature for (a) tin oxide and (b) tungsten oxide catalysts, measured using the static testing approach.

sputtered from a metallic target in Ar/O₂ mixtures, exhibited a microcrystalline surface morphology within the rounded protuberances of the as-deposited films, unlike those films prepared from a ceramic target (Fig. 5b). When this catalyst surface was exposed to various target gases, including H₂O₂ and TATP at a high temperature, there was no apparent change in the fine microstructure but instead an increase in the cluster/grain size was observed (Fig. 5c). The reactively sputtered V₂O₅ catalysts prepared from a metallic vanadium target in an Ar/O₂ plasma (Fig. 5d), revealed the formation of acicular needles as well as a very fine fibrous morphology or nano-hair on the surface of the sensor. The surface area of these very fine microstructural features, associated with reactively sputtered films produced from metallic targets, was estimated to be orders of magnitude greater than that of typical sputtered film morphology. SnO_{2-x} and ZnO films were also deposited from a ceramic target by sputtering in an argon plasma (Fig. 5e and f), and a morphology more similar to that of sputtered CuO–Cu₂O (Fig. 5a) was observed. In the case of SnO_{2-x}, some micro-cracking of the films due to thermal stress due to high temperature testing became apparent over time.

3.3. Gas sensing properties

The responses of a tin oxide catalyst and a tungsten oxide catalyst to TATP and hydrogen peroxide are shown in Fig. 6. Here, the percent response to 8 ppm TATP and 9 ppm H₂O₂ as a function of temperature were measured using the static testing approach. A precipitous drop in the response for tin oxide occurs until a temperature of 300°C, at which point the response increases dramatically as a function of temperature. We believe this is due to the decomposition of TATP by the catalyst, for which the response peaks at 400°C. It should be noted that the response for hydrogen peroxide using the same catalyst has a similar behavior and tracks the TATP response closely. The response of a tungsten oxide catalyst to TATP and hydrogen peroxide is shown in Fig. 6b and has very different characteristics than that of tin oxide. No significant response was observed at temperatures below 380°C, at which point the response then increased dramatically until a maxima was observed at 460°C. As was the case for the tin oxide catalyst, the response of the sensor to H₂O₂ was very similar and closely tracks the TATP response. In both cases the response to hydrogen peroxide was larger in magnitude as might be expected since the decomposition

of the TATP is not complete during the test cycle and the starting concentration of TATP is 8 ppm whereas the starting concentration of H₂O₂ is 9 ppm.

The gas sensor response to TATP using a number of different catalysts is shown in Fig. 7. Here, the response to 8 ppm TATP as a function of temperature using several catalysts including WO₃–TiO₂, V₂O₅, SnO_{2-x}, Nb₂O₃ and ZnO was measured using the static testing approach. Each of the five oxide catalysts show a unique response as a function of temperature, and show features ranging from almost no peak response for Nb₂O₃ to well defined peaks for ZnO. Due to the catalytic decomposition of TATP, it is expected that the target gas consists not only of a mixture of air and TATP vapor, but also contains some H₂O₂ vapor. To verify this, several experiments were undertaken to investigate if TATP is indeed decomposing into H₂O₂ in the vicinity of the catalyst, which is not the primary decomposition product based on a number of related studies. For example, Oxley and Smith [16,17] have determined that acetone and not hydrogen

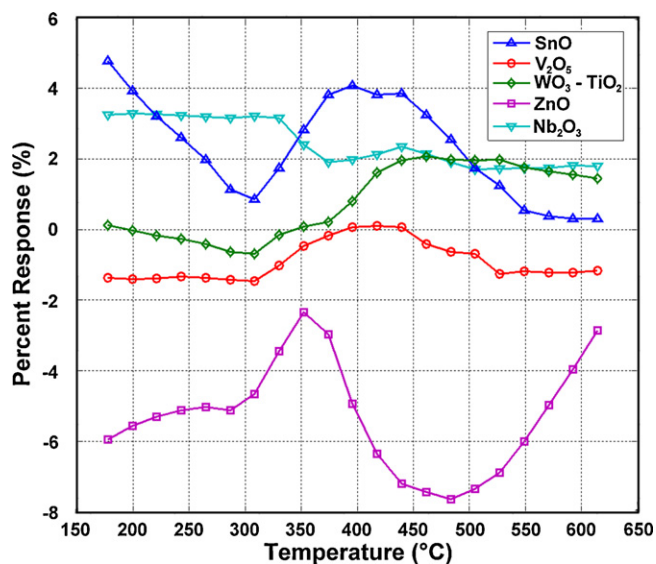


Fig. 7. Response as a function of temperature using several catalysts to detect TATP (8 ppm) including WO₃–TiO₂, V₂O₅, SnO_{2-x} and ZnO, measured using the static testing approach.

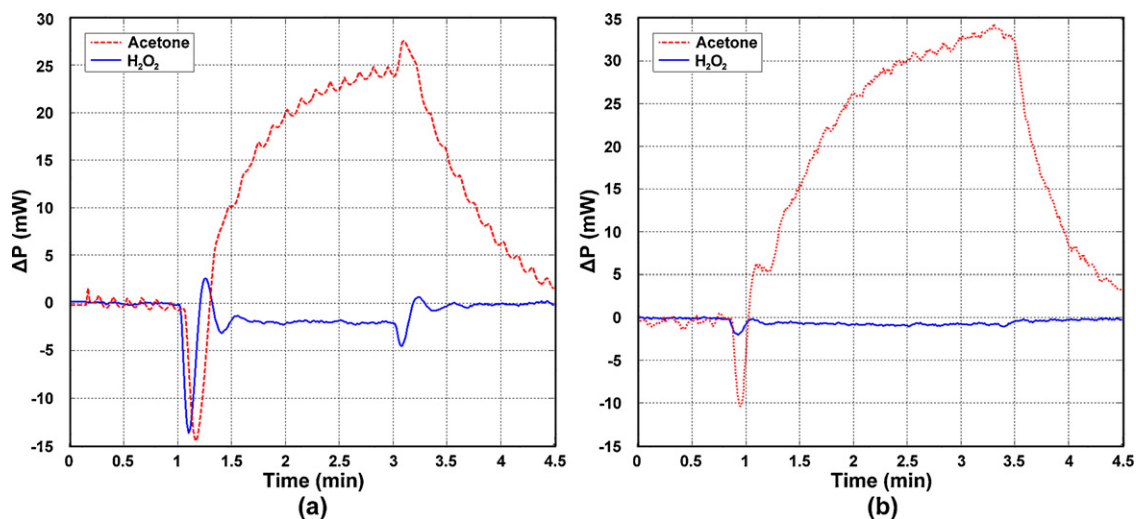


Fig. 8. Response of (a) CuO–Cu₂O and (b) Cu₂O in acetone and H₂O₂ at 330 °C.

peroxide is the predominant decomposition product of high purity TATP in air and they have measured the activation degradation energy and determined the decomposition kinetics for the degradation of TATP.

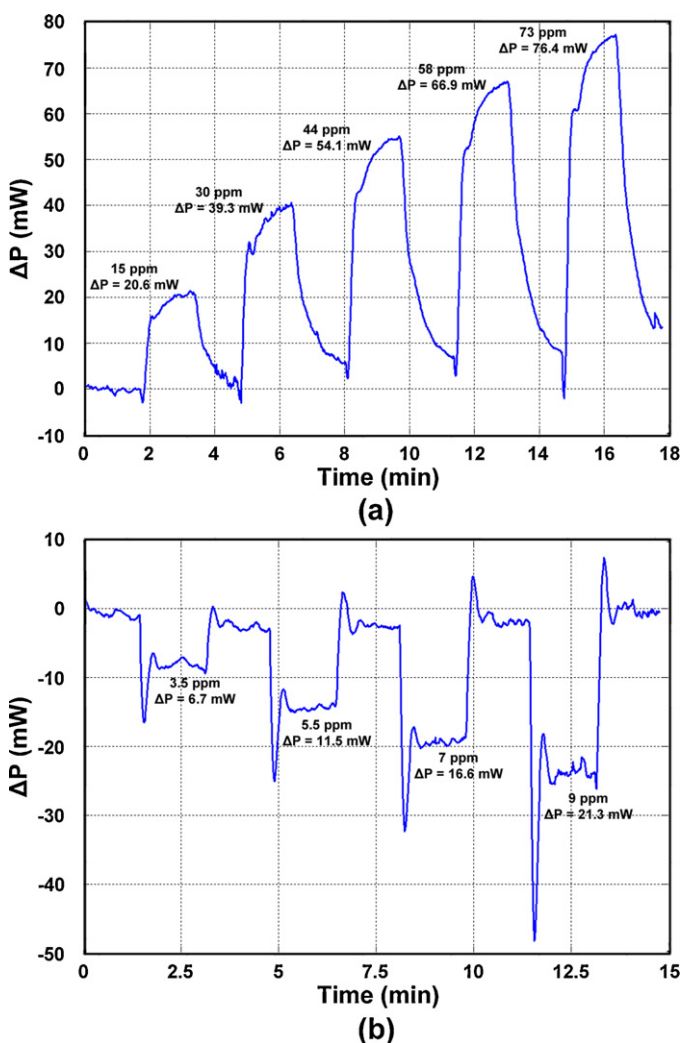


Fig. 9. Response of SnO_{2-x} in several concentrations of (a) acetone and (b) H₂O₂ at 415 °C.

Fig. 8 shows the response of a CuO–Cu₂O and Cu₂O catalyst to 8 ppm acetone and H₂O₂ at 330 °C after a 2-min exposure to the target gas. From this figure it can be seen that the relative response to acetone is considerably greater than that of H₂O₂, which is consistent with other investigations using thermodynamic based gas sensors for detection [23]. These studies support our findings that significant exothermic heat effects are observed for hydrocarbons. Not only is the magnitude of the response to acetone for both CuO–Cu₂O and Cu₂O significantly greater than that of hydrogen peroxide but it is also of opposite sign, which implies that the sensitivity of the thermodynamic sensor platform to acetone is significantly greater than that of the other gaseous products derived from the decomposition of TATP. Furthermore, this figure indicates that CuO–Cu₂O (Fig. 8a) is a more selective catalyst for hydrogen peroxide than that of Cu₂O (Fig. 8b), since both a smaller heat of reaction in the presence of acetone and a more negative heat of reaction for H₂O₂ were observed. All of this suggests that these results can be further improved upon by tailoring the sputtering conditions and thus, the oxidation state of the catalyst films. The effect of acetone and H₂O₂ concentration on the magnitude of the response using tin oxide as the catalyst is shown in Fig. 9, where the temperature was held constant at 415 °C (maximum sensitivity to H₂O₂ and TATP shown in Fig. 6a). Again the responses are of opposite sign, and it was found that the TATP response tracks that of hydrogen peroxide, which can be readily detected at concentrations as low as 3.5 ppm. Based on the results presented in Fig. 9, we should also be able to reliably detect low levels of acetone in the gas stream generated by the decomposition of TATP. Since we do not see any evidence of acetone in the output signal, we can conclude that the TATP is detected as hydrogen peroxide. However, it has also been extensively cited in the literature [16,17] that under ambient conditions TATP primarily decomposes into acetone. Therefore, we believe that we are sensing the catalytic decomposition of TATP, which is a much more specific reaction than the decomposition of TATP to acetone in air ambient, and this specific mechanism should help mitigate false positives using this sensor platform.

4. Conclusion

A small footprint, thermodynamic based gas sensor capable of detecting TATP at ppm levels in air under ambient conditions was demonstrated. This robust sensor platform has the potential of exhibiting the necessary sensitivity, selectivity and response time to be used for the continuous monitoring of TATP and its

precursors. This would be particularly important in closed spaced venues where the public may be exposed to potential threats from IEDs employing TATP as the triggering device. A number of metal oxide catalysts were able to detect TATP using the thermodynamic based gas sensor described within. We have shown that TATP vapor at concentrations of 8 ppm in air can be detected readily using SnO_{2-x} and ZnO catalysts, and its peroxide and acetone precursors were able to be detected at even lower concentrations. Based on our preliminary results, arrays of microheater sensors can be fabricated using multiple catalysts and combining the characteristic response curves to uniquely identify the target molecules of interest. In addition, the current thermodynamic detection scheme can easily be integrated into an existing micro-hotplate based MEMS metal oxide gas sensing platforms by modifying the heater electronics and adding a mass flow controller to eliminate hydrodynamic effects. This can add a second independent variable to minimize false positives and improve long term stability in existing gas sensor systems.

Acknowledgements

The authors wish to thank the Department of Homeland Security Center of Excellence for Explosives Detection, Mitigation and Response and Sensor Tech, Savannah, GA for support of this work. The authors also thank Prof. Jimmy Oxley and Prof. James Smith at the University of Rhode Island for preparation of the TATP samples used throughout the study. The authors would like to acknowledge US Patent #7,329,389 B2, "Sensor Device and Method for Qualitative and Quantitative Analysis of Gas Phase Substances", Feb. 12, 2008, Michael L. Horovitz and Karl L. Anderson upon which some of the preliminary work was based.

References

- [1] F. Dubnikova, R. Kosloff, Y. Zeiri, Z. Karpas, Novel approach to the detection of triacetone triperoxide (TATP), its structure and its complexes with ions, *J. Phys. Chem. A* 106 (19) (2002) 4951–4956.
- [2] I. Cotte-Rodriguez, H. Chen, R.G. Cooks, Rapid trace detection of triacetone triperoxide (TATP) of complexation detections of desorption electrospray ionization, *Chem. Commun.* 5 (2006) 953–955.
- [3] G.A. Buttigieg, A.K. Knight, S. Denson, C. Pommier, M.B. Denton, Characterization of the explosive triacetone triperoxide and detection by ion mobility spectrometry, *Forensic Sci. Int.* 135 (2003) 53–59.
- [4] R. Rasanen, M. Nousiainen, K. Parakorpi, M. Sillanpaa, L. Polari, O. Anttalainen, M. Utriainen, Determination of gas phase triacetone triperoxide with aspiration ion mobility spectrometry and gas chromatography–mass spectrometry, *Anal. Chim. Acta* 623 (2008) 59–65.
- [5] J. Wilkinson, C.T. Konek, J.S. Moran, E.M. Witko, T.M. Korter, Terahertz absorption spectrum of triacetone triperoxide (TATP), *Chem. Phys. Lett.* 478 (2009) 172–174.
- [6] A. Stambouli, A. El Bouri, T. Bouayoun, M.A. Bellimam, Headspace GC/MS detection of TATP traces in post-explosion debris, *Forensic Sci. Int.* 146S (2004) S191–S194.
- [7] C. Mullen, A. Irwin, B.V. Pond, D.L. Huestis, M.J. Coggiola, H. Oser, Detection of explosives and explosives-related compounds by single photon laser ionization time-of-flight mass spectrometry, *Anal. Chem.* 78 (2006) 3807.
- [8] C. Shen, J. Li, H. Han, H. Wang, H. Jiang, Y. Chu, Triacetone triperoxide using low reduced-field proton transfer reaction mass spectrometer, *Int. J. Mass Spectrom.* 285 (2009) 100–103.
- [9] R.S. Ladbeck, U. Karst, Determination of triacetone triperoxide in ambient air, *Anal. Chem.* 482 (2003) 183–188.
- [10] H. Lin, K.S. Suslick, A colorimetric sensor array for detection of triacetone triperoxide vapor, *J. Am. Chem. Soc.* 132 (2010) 15519–15521.
- [11] E. Capua, R. Cao, C.N. Sukenik, R. Naaman, Detection of triacetone triperoxide (TATP) with an array of sensors based on non-specific interactions, *Sens. Actuators B* 140 (2009) 122–127.
- [12] N. Barsan, D. Koziej, U. Weimar, Metal oxide-based gas sensor research: how to? *Sens. Actuators B* 121 (2007) 18–35.
- [13] N.L. Hung, H. Kim, S.K. Hong, D. Kim, Enhancement of CO gas sensing properties of ZnO thin films deposited on self-assembled Au nanodots, *Sens. Actuators B* 151 (2010) 127–132.
- [14] G. Eranna, B. C./Joshi, D.P. Runthala, R.P. Gupta, Oxide materials for development of integrated gas sensors: a comprehensive review, *Crit. Rev. Solid State Mater. Sci.* 29 (2004) 111–188.
- [15] W.H. Zhang, W.D. Zhang, L.Y. Chen, Highly sensitive detection of explosive triacetone triperoxide by an In_2O_3 sensor, *Nanotechnology* 21 (2010) 315502.
- [16] J.C. Oxley, J.L. Smith, K. Shinde, J. Moran, Determination of the vapor density of triacetone triperoxide (TATP) using a gas chromatography headspace technique, *Propellants Explos. Pyrotech.* 30 (2) (2005) 127–130.
- [17] J.C. Oxley, J.L. Smith, H. Chen, Decomposition of a multi-peroxidic compound: triacetone triperoxide (TATP), *Propellants Explos. Pyrotech.* 27 (4) (2002) 209–216.
- [18] W.Y. Yang, W.G. Kim, S.W. Rhee, Radio frequency sputter deposition of single phase cuprous oxide using Cu_2O as a target material and its resistive switching properties, *Thin Solid Films* 517 (2008) 967–971.
- [19] C.I. Pearce, R.A.D. Patrick, D.J. Vaughan, C.M.B. Henderson, G. van der Laan, Copper oxidation state in chalcopyrite: mixed $\text{Cu } d^9$ and d^{10} characteristics, *Geochimica* 70 (2006) 4635–4642.
- [20] S. Hwang, Y.Y. Kim, J.H. Lee, D.K. Seo, J.Y. Lee, H.K. Cho, Irregular electrical conduction types in tin oxide thin films induced by nanoscale phase separation, *Journal of the American Ceramic Society* 95 (1) (2012) 324–332.
- [21] S. Uthanna, T.K. Subramanyam, B.S. Naidu, G.M. Rao, Structure–composition–property dependence of reactive magnetron sputtered ZnO thin films, *Opt. Mater.* 19 (4) (2002) 461–469.
- [22] G. Silversmit, D. Depla, H. Poelman, G.B. Marin, R. Gryse, Determination of the V2p XPS binding energies for different vanadium oxide oxidation states (V^{5+} to V^{0+}), *J. Electron Spectrosc. Relat. Phenom.* 135 (2–3) (2004) 167–175.
- [23] E. Vereshchaginam, R.A.M. Wolters, J.G.E. Gardeniers, Measurement of reaction heats using a polysilicon based microcalorimetric sensor, *Sens. Actuators A* 169 (2) (2011) 308–316.

Biographies

Matin Amani received his B.S. degree in electrical engineering at URI in 2011, and is currently working on his B.S. degree in chemical engineering and M.S. degree in electrical engineering. His research interests include oxide thermoelectrics, nanomaterials, sensors for harsh environments and gas sensors.

Yun Chu received his M.S. degree in chemistry from Beihang University in 2008. He is currently working on his Ph.D. in chemical engineering at URI. His research interests include gas sensors and materials discovery using combinatorial chemistry.

Kellie L. Waterman received her B.S. degree in chemical engineering in 2011, and is in processes of obtaining her M.S. degree at WPI.

Caitlin M. Hurley is a senior undergraduate student studying chemical engineering at URI.

Michael J. Platek received his B.S. degree in physics from Indiana University of PA (1984) and M.S. degree in physics from Wesleyan University (Middletown, CT) (1986). He is the laboratory manager for the URI Sensors and Sensors Technology Partnership. His interests include fabrication as well as characterization of nanomaterials, development of gas sensors, bio-sensors and MEMS.

Otto J. Gregory received his B.S. degrees in chemical engineering and ocean engineering and his M.S. degree in chemical engineering from URI, in 1975 and 1977, respectively and his Ph.D. in engineering from Brown University in 1984. He is currently Distinguished Engineering Professor at URI and Director of the URI Sensors and Surface Technology Partnership. Dr. Gregory has published over 80 peer-reviewed journal articles and filed 25 US patents. His work has largely focused on sensors for harsh environments, wide bandgap semiconductors and chemical sensors, and has been funded by the gas turbine engine industry, NASA, DOE, Air Force, NSF and DHS.



ELSEVIER

available at www.sciencedirect.comwww.elsevier.com/locate/matchar

Microstructural characterization of pipe bomb fragments

Otto Gregory^{a,*}, Jimmie Oxley^c, James Smith^c, Michael Platek^a, Hamouda Ghonem^b,
Evan Bernier^c, Markus Downey^a, Christopher Cumminskey^a

Sensors and Surface Technology Partnership Forensic Science Partnership

^aDepartment of Chemical Engineering, University of Rhode Island, Kingston, RI, 02881, USA

^bDepartment of Mechanical Engineering, University of Rhode Island, Kingston, RI, 02881, USA

^cDepartment of Chemistry, University of Rhode Island, Kingston, RI, 02881, USA

ARTICLE DATA

Article history:

Received 22 May 2009

Received in revised form

17 December 2009

Accepted 22 December 2009

Keywords:

Pipe bomb

High strain rate loading

Steel microstructure

ABSTRACT

Recovered pipe bomb fragments, exploded under controlled conditions, have been characterized using scanning electron microscopy, optical microscopy and microhardness. Specifically, this paper examines the microstructural changes in plain carbon-steel fragments collected after the controlled explosion of galvanized, schedule 40, continuously welded, steel pipes filled with various smokeless powders. A number of microstructural changes were observed in the recovered pipe fragments: deformation of the soft alpha-ferrite grains, deformation of pearlite colonies, twin formation, bands of distorted pearlite colonies, slip bands, and cross-slip bands. These microstructural changes were correlated with the relative energy of the smokeless powder fillers. The energy of the smokeless powder was reflected in a reduction in thickness of the pipe fragments (due to plastic strain prior to fracture) and an increase in microhardness. Moreover, within fragments from a single pipe, there was a radial variation in microhardness, with the microhardness at the outer wall being greater than that at the inner wall. These findings were consistent with the premise that, with the high energy fillers, extensive plastic deformation and wall thinning occurred prior to pipe fracture. Ultimately, the information collected from this investigation will be used to develop a database, where the fragment microstructure and microhardness will be correlated with type of explosive filler and bomb design. Some analyses, specifically wall thinning and microhardness, may aid in field characterization of explosive devices.

© 2009 Elsevier Inc. All rights reserved.

1. Introduction

In the United States, pipe bombs are a common improvised explosive device. Construction is straightforward, and both metal and plastic pipes are readily available. Many of the pipe fillers are propellants which may include black powder, smokeless powder, photo and fireworks powder, and even match heads which can be purchased without special permit [1]. Over the years, law enforcement has developed robust protocols for processing bomb scenes and analytical procedures for identifying explosive residue, but chemical residue is

not always recovered [2,3]. Generally, the recovered fragments are intermixed with a host of metal shards and debris characteristic of the chaotic scene of an explosion. A wealth of forensic information remains unexploited in terms of “metallurgical evidence” found in each pipe fragment. Such evidence is embodied in changes in the microstructure and microhardness of the pipe fragments. Metallurgical changes in armor steels have been extensively studied in order to estimate explosive loadings [4]. The degree of shock loading in plain carbon steel is reflected by pearlite and ferrite grain deformation, twinning, and slip band formation [5]. This study

* Corresponding author. Department of Chemical Engineering, 16 Greenhouse Rd, Kingston, RI, 02881, USA. Tel.: +1 401 874 2085.
E-mail address: gregory@egr.uri.edu (O. Gregory).

attempts to correlate such microstructural features found in recovered steel pipe bomb fragments with the power and quantity of the propellant used, as well as other characteristics of the initial device [6]. The characterization included the application of quantitative stereology techniques to study the microstructural changes that occur in plain carbon-steel pipes due to high strain rate deformation and variations in microhardness obtained under different loading conditions. A correlation between pipe fragment microstructure, microhardness, and wall thinning with the pipes propellant filler may provide clues concerning the relative nature of the propellant in cases where chemical residue is not recovered.

2. Experimental

2.1. Materials/Methods

Commercially available, continuously welded, schedule 40 steel pipes [2 in. I.D. by 12 in. long (5 cm × 30.5 cm)] were used in this investigation. These galvanized AISI 1030 steel pipes nominally contain 0.3% carbon by weight and trace amounts of other impurities. Standard end caps were used at both ends of the threaded pipes and the pipes were usually initiated in a vertical orientation, with the detonator threaded through a hole drilled in the top end cap. To contain the fragments, pipes were initiated in 55-gallon (208.14 L) drums which were mostly filled with either sand or ground cornhusks. A cardboard sleeve was placed around the vertical pipe to ensure there was no direct contact between the pipe and the drum filler. Pipes were filled to volume (i.e. pour density) with black powder or one of the following smokeless powders: WC 870 (DB); IMR-PB (SB); Red Dot (DB); Winchester Action Pistol (DB); Bullseye (DB); where SB and DB indicate single (nitrocellulose) or double-base (nitrocellulose and nitroglycerin) powder, respectively. An improvised formulation made of sodium chlorate and aluminum chips as found in paint was also tested. Nitromethane, a high explosive, was used as a reference material. (Ref. [7] contains additional details related to the experimental procedure used here.)

Over 60 pipes were shot under the controlled conditions described above, and on average 87% of the pipe material was recovered. An effort was made to separate end cap pieces from those of the main body of the pipe, such that only those fragments from the main body of the pipe were selected for the microstructural analysis. Fragments from the end caps were not used in this study because they, and the threaded portion of the steel pipe, were already work hardened prior to use (Fig. 1).

2.2. Pipe Thinning

The extent of plastic deformation prior to fracture was determined by measuring the wall thickness of the fragments in the radial direction using Vernier calipers and comparing these measurements to those from the wall of an unexploded pipe. No special sample preparation was necessary to make these measurements; thus, it may be a field-adaptable technique. By comparing the ratio of the fragment wall thickness to that of the wall thickness of an unexploded pipe (Eq. (1)), the engineering radial strain, or plastic strain, prior to fracture was estimated [8]. A total of 10–40 fragments were analyzed, at least four wall

thickness measurements per fragment, for each type of energetic filler. The seam region of the pipe was avoided because seam edges exhibited less ductility and the reduction in wall thickness was less pronounced than in other locations.

$$(a_0 - a_f) / a_0 = \varepsilon_p \quad (1)$$

where

a_0	initial wall thickness (unexploded)=4.15 mm
a_f	final wall thickness (exploded)
ε_p	plastic strain.

2.3. Microhardness

A Wilson microhardness tester with a 200 g load was used for all microhardness measurements. The measurements were made across the through-thickness of the wall of as-received fragments. This provided considerable insight into the extent of work hardening in the individual fragments as a function of radial position. The procedure required that a series of indentations be made across the fragment through-thickness followed by a measurement of the length of each indentation (L). In this way, the Knoop hardness number (HK) was determined from the indenter load and the indentation length using the equation [9]:

$$HK = 14229 * (P / L^2) \quad (2)$$

where

P	applied load (g)
L	length of indentation in (μm).

2.4. Microscopy

Recovered pipe fragments were prepared for examination by scanning electron microscopy (SEM) and optical microscopy using standard metallographic preparation techniques [5]. A JEOL JSM5900LV SEM equipped with an energy dispersive X-ray analyzer (EDX) was used at magnifications between 200 and 5000× to determine the fine microstructural features and the size of the microhardness indentations. The fragments were sectioned using a water soluble oil-cooled diamond saw so that they would fit into a standard 1.25-inch (3.18 cm) diameter metallurgical mount. The fragments were cut in such a way that the cross section of the pipe wall could be viewed. The sectioned fragments were mounted in an Extex[®] two-part epoxy and polished using Extex[®] silicon carbide polishing discs. Successively finer grit papers were used, starting with 120 grit paper and progressing to 240, 400, 600 and 1200 grit paper. After lapping on the 1200 grit paper, the samples were polished with 3.0 μm and 0.3 μm Extex[®] alumina slurries. To reveal the final microstructure, the fragments were etched for 30–90s in nital (1 vol.% nitric acid (50–70%)/95 vol.% absolute ethanol).

A reflection light microscope (Nikon Optifont 100) with bright-field illumination was used for all optical microscopies. Optical micrographs were captured using a Nikon Digital Sight DS-F11 high definition (5-megapixel CCD) color camera head with a DS-L2 controller operated by Nikon's NIS-Elements (version F2.20)

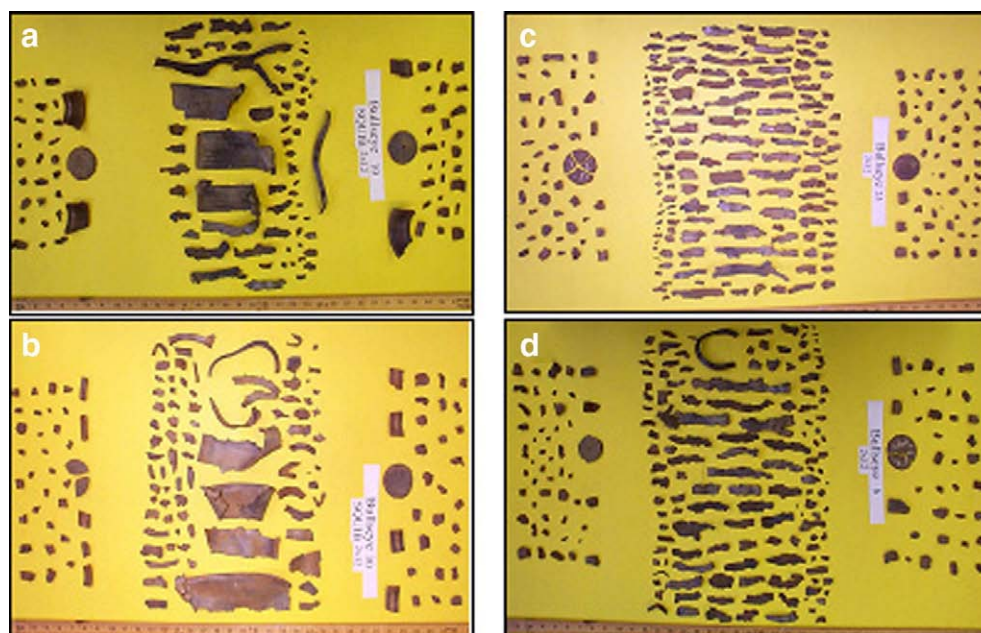


Fig. 1 – Photographs of pipe bomb fragments collected under controlled conditions: a.) Bullseye endcap detonation b.) Bullseye endcap detonation c.) Bullseye center detonation d.) Bullseye center detonation. On average 87% of the pipe material was collected.

software. Depending on the specific microstructural feature being analyzed, quantitative stereology was performed at magnifications of 20 \times , 50 \times , 100 \times or 200 \times [5]. A Sun Spark workstation running Princeton Gamma Tech (PGT) software was used to collect and analyze the images. The extent of plastic deformation in the α -ferrite grains and pearlite colonies, as measured by the aspect ratio in the digitally stored micrographs, was quantified utilizing the PGT metallography module. Deformation of the pearlite colonies was selected to follow the deformation trends instead of the α -ferrite grains because the dark pearlite colonies were more readily distinguished by the software than the light ferrite grains.

3. Results and Discussion

3.1. Thinning

Considerable thinning of the pipe wall was usually observed. Average fragment wall thickness is shown in Fig. 2, along with the associated plastic strain. Reduction in wall thickness was caused by plastic deformation that occurred prior to the rupture of the pipe material during explosion [10]. As the pressure wave propagated through the pipe, the material at the inner wall was placed in compression. This caused the material in the outer wall to expand (deform) biaxially and, as a result, the pipe became thinner and eventually ruptured. This plastic deformation prior to fracture increased as the power of each pipe bomb device increased. For example, black powder, the least powerful propellant in the study, caused the least plastic deformation prior to fracture. The fragments collected from explosions using black powder showed a 25% reduction in thickness, whereas pipes exploded with Bullseye smokeless powder, the most powerful propellant used, showed 61% reduction in wall thickness (Fig. 2).

3.2. Microscopy

Examination of pipe fragments using microscopy revealed specific detail on the extent of plastic deformation and the development of characteristic features in the steel microstructure. Fig. 3 shows the microstructure of an as-received (unexploded) steel pipe which was purposely over-etched (15 vol.% nital). Notice the visible boundaries of the α -ferrite grains (light phase) and the pearlite colonies (dark phase). It is evident from these micrographs that the individual grains are equiaxed, having approximately the same length and width. Scanning electron microscopy was used to observe the fine structure of the pearlite colonies. These colonies consist of alternating plates or lamellae of α -ferrite and cementite (Fe_3C)

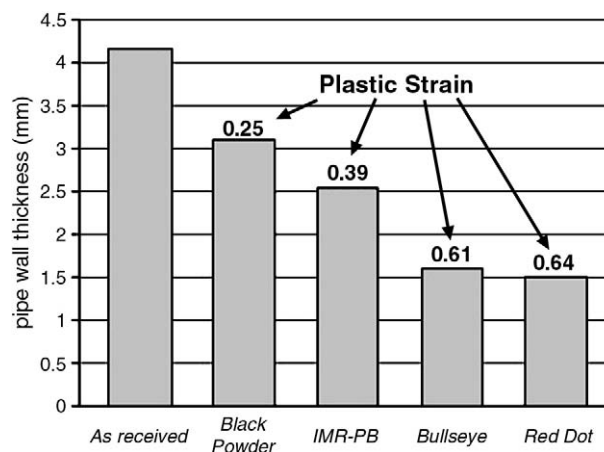


Fig. 2 – Changes in measured wall thickness of pipe bomb fragments as a function of filler (propellant) energy. Note corresponding plastic deformation prior to fracture.

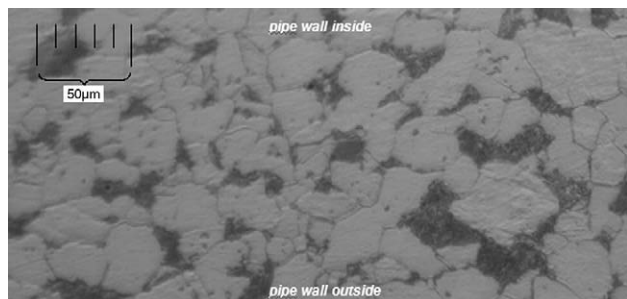


Fig. 3 – Optical micrograph of “as-received” plain carbon-steel pipe (transverse view — 500 \times). The dark phase is pearlite colonies and the light phase is α -ferrite grains. Grain boundaries are clearly visible due to over-etching of the sample (15% nital).

which are responsible for the scattering of visible light and resulting dark contrast of the colonies in the optical micrographs (Fig. 4).

Fig. 5 shows a micrograph of a fragment collected from a pipe filled with black powder. The pearlite colonies and α -ferrite grains are visibly deformed and elongated in the direction of the applied strain. As the power of the propellant filler increased, the deformation of the pearlite became more pronounced. This trend is shown in Fig. 6 for an improvised formulation of NaClO_3/Al . To quantify the extent of pearlite deformation, the average aspect ratio of the pearlite colonies from the various pipe bomb fragments was determined. An aspect ratio close to one represents features that are very symmetrical or equiaxed. The as-received pipe seen in Fig. 3 had average pearlite aspect ratios closer to 2 than 1. The aspect ratios of the pearlite colonies correlate well with the observed plastic deformation prior to pipe fracture. As expected, the more powerful fillers yielded larger pearlite aspect ratios (Fig. 7).

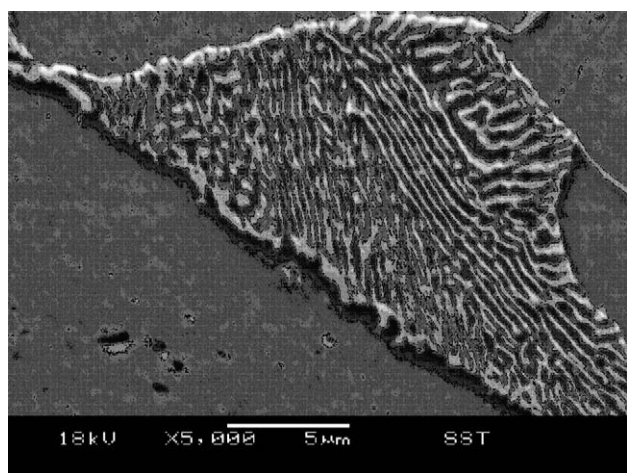


Fig. 4 – SEM micrograph of pearlite colony lamella in a steel pipe (5000 \times). The light phase is cementite (Fe_3C) and the dark phase is α -ferrite. [The lamella appears as a solid black phase in lower magnification micrographs as its structure encourages light scattering.]

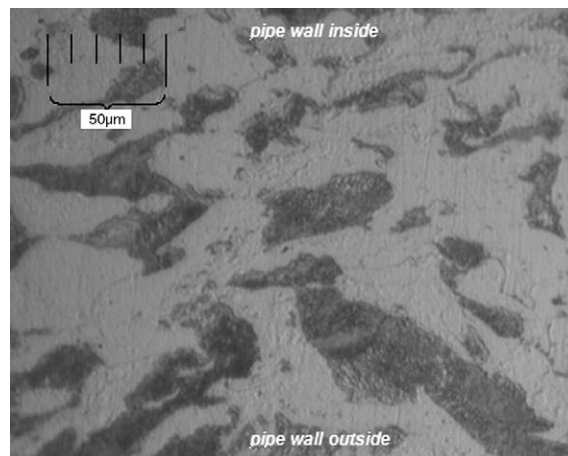


Fig. 5 – Optical micrograph of a recovered steel pipe bomb fragment with black powder used as the filler (transverse view — 200 \times). Note the deformation (elongation) of the pearlite (dark phase) and subsequent change in aspect ratio associated with the pearlite and α -ferrite relative to the as-received pipe (Fig. 4).

In the fragments collected from pipes using high-power fillers, twinning was observed along with elongation of both the α -ferrite grains and pearlite colonies. These characteristics were observed for Winchester Action Pistol 44, Red Dot, IMR-PB, Bullseye, and nitromethane as shown in Figs. 8, 9.A–9.C, 10.A–10.B, 11.A–11.C, and 12.A–12.B respectively. Normally, plastic deformation in body-centered cubic (BCC) metal occurs by slip, but deformation twins can occur in BCC metals and alloys at very low temperatures or at very high strain rates [10,11]. Therefore, the high-power propellants must have produced sufficiently high shock loading (pressure waves) within the walls of the pipe, prior to fracture, to

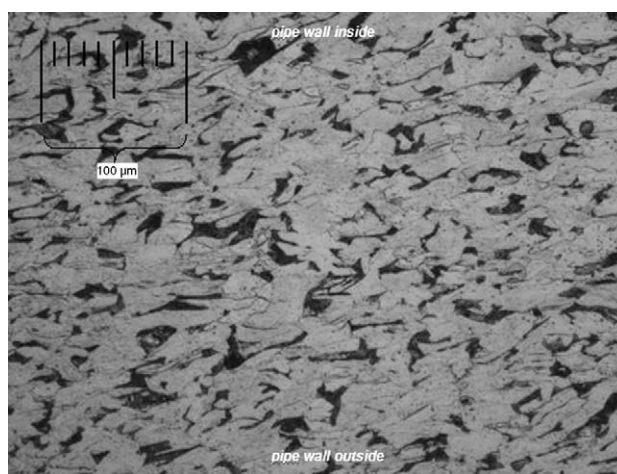


Fig. 6 – Optical micrograph of a recovered steel pipe bomb fragment with NaClO_3/Al used as the filler (200 \times). Note the deformation of the pearlite (dark phase).

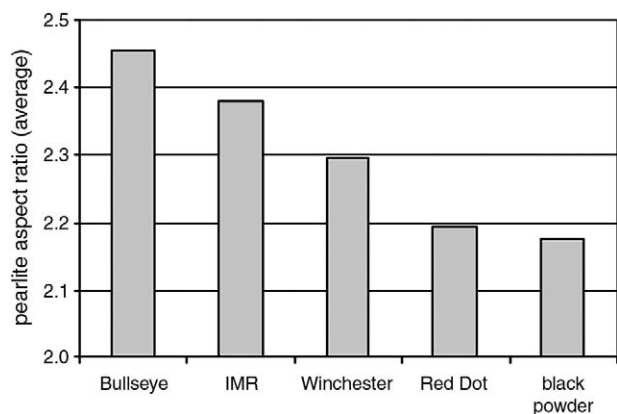


Fig. 7 – Relative plastic deformation of pearlite colonies in collected pipe bomb fragments prior to fracture, as evidenced by the changes in aspect ratio. Note the variation in aspect ratio as a function of filler (propellant) power.

induce twin plane formation in the steel pipe. The twin density was relatively low in most instances where twins were observed, due to random orientation of the pearlite colonies in the starting material. When high-power, high explosive fillers such as nitromethane were employed in this study, additional microstructural features were observed. The pearlite colonies were extremely distorted in continuous bands which extended well beyond a single grain or colony (Figs. 12.A–12.B). Fig. 12.A also reveals the presence of intersecting slip bands, or cross-slip bands, in the steel detonated with nitromethane.

A qualitative representation of the various threshold energy levels associated with the different propellants is shown in Fig. 13. Low-power propellant fillers, such as black powder, released enough energy to deform both the α -ferrite grains and pearlite colonies. Higher-power fillers, such as Winchester or

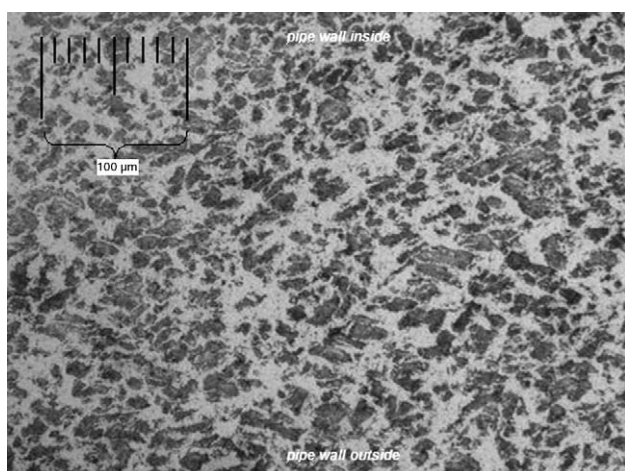


Fig. 8 – Optical micrograph of a recovered pipe bomb fragment with Winchester 44 used as the filler (transverse view — 200×). Note the deformation of the pearlite (dark phase) as well as the presence of twins in the microstructure.

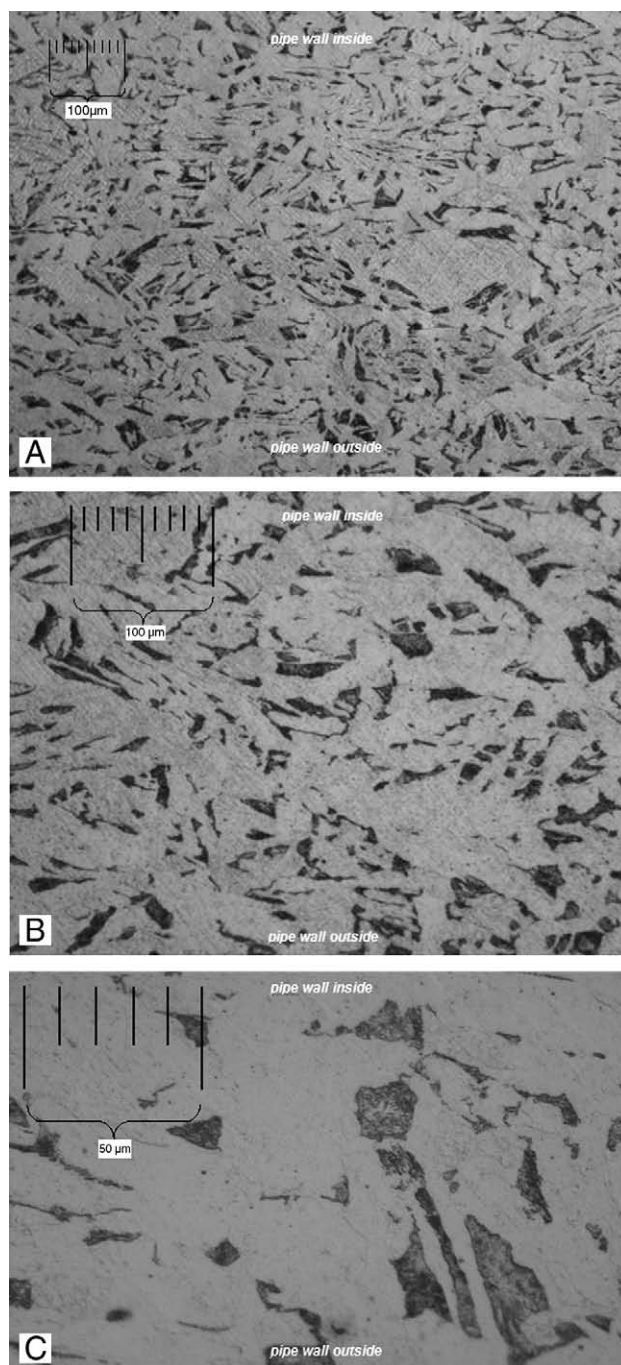


Fig. 9.A – Optical micrograph of a recovered steel pipe bomb fragment with Red Dot used as the filler (transverse view — 100×). Note the heavily deformed pearlite (dark phase). 9.B. Optical micrograph of a recovered steel pipe bomb fragment with Red Dot used as the filler (transverse view — 200×). Note the heavily deformed pearlite (dark phase) as well as the presence of twins in the microstructure. 9.C. Optical micrograph of a recovered steel pipe bomb fragment with Red Dot used as the filler (transverse view — 500×). Expanded view of twinning and deformed pearlite.

Red Dot, showed twin formation in addition to elongation of the pearlite colonies. In the most powerful devices, for example, employing IMR, Bullseye or nitromethane, the pearlite colonies

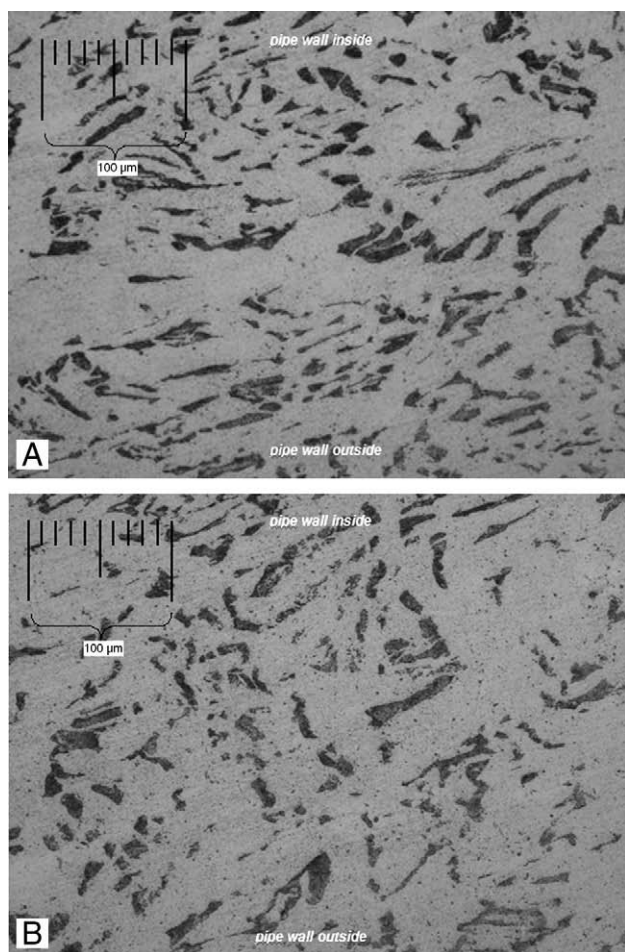


Fig. 10.A – Optical micrograph of a recovered steel pipe bomb fragment with IMR used as the filler (transverse view — 200×). Note the deformation of the pearlite (dark phase) and its overall distortion in continuous bands. **10.B.** Optical micrograph of a recovered steel pipe bomb fragment with IMR used as the filler (transverse view — 200×). Note the deformation of the pearlite (dark phase) as well as the presence of twins in the microstructure.

were severely distorted and formed continuous bands extending beyond a single ferrite grain or pearlite colony. Fragment analysis from the pipe bomb detonated with the only high explosive, nitromethane, showed a significant number of slip bands.

3.3. Microhardness

The observed microstructural changes were accompanied by work hardening of the steel during the high strain rate conditions. The energy of the pressure wave created by the propellant was partially dissipated by the pipe material in the form of work hardening; i.e. the metal at the inner wall was compressed into the outer wall material. Microhardness test results were consistent with the degree of plastic deformation as determined from the physical thinning of the pipe fragment walls. Larger Knoop hardness values were associated with fragments produced from high-power propellants. Every filler

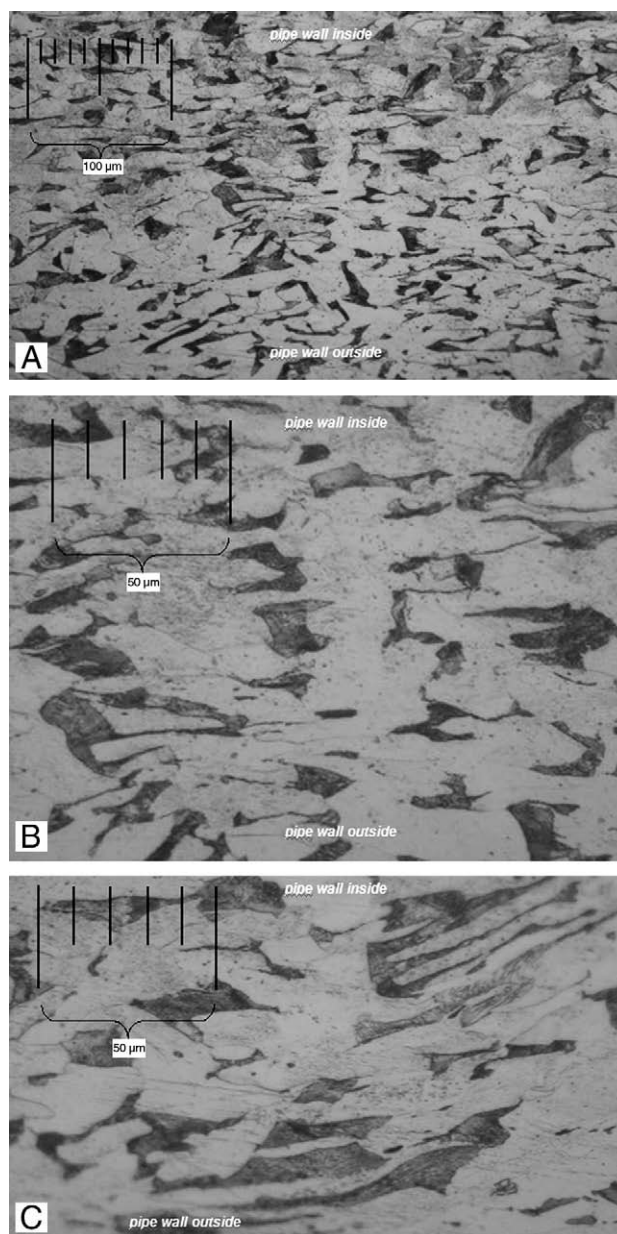


Fig. 11.A – Optical micrograph of a recovered steel pipe bomb fragment with Bullseye used as the filler (transverse view — 200×). Note the heavily deformed pearlite (dark phase) and its overall distortion in continuous bands, as well as the presence of twins in the microstructure. **11.B.** Optical micrograph of a recovered steel pipe bomb fragment with Bullseye used as the filler (transverse view — 500×). Note the heavily deformed pearlite (dark phase) as well as the presence of twins in the microstructure. **11.C.** Optical micrograph of a recovered steel pipe bomb fragment with Bullseye used as the filler (transverse view — 500×). Note the heavily deformed pearlite (dark phase) as well as the presence of twins in the microstructure.

used produced consistent Knoop hardness numbers with standard deviations less than 20 for the five points tested at the three locations tested; inside, middle and outside pipe wall. This result correlates well with the pearlite aspect ratios

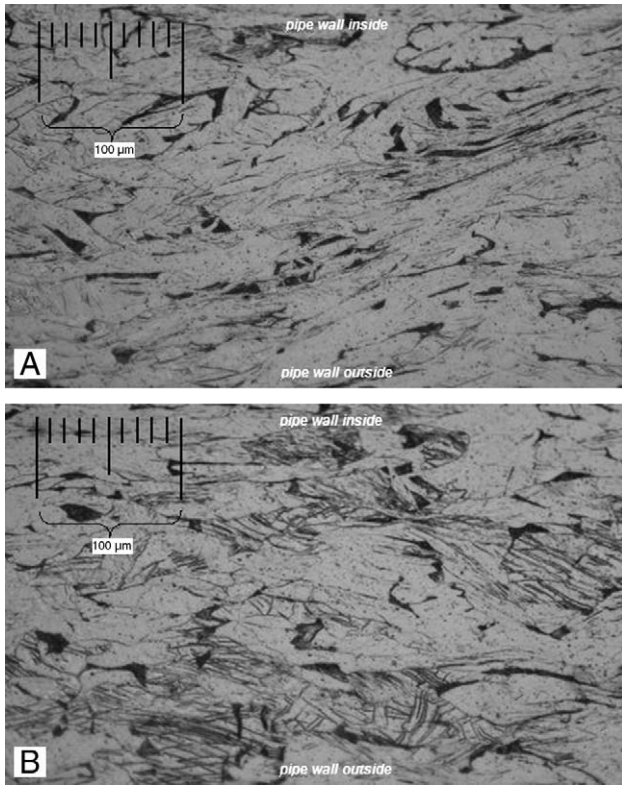


Fig. 12.A – Optical micrograph of a recovered steel pipe bomb fragment with nitromethane used as the propellant (transverse view — 200×). Note the heavily deformed pearlite (dark phase) as well as the presence of slip bands and twins in the microstructure. **12.B.** Optical micrograph of a recovered steel pipe bomb fragment with nitromethane used as the propellant (transverse view — 200×). Note the heavily deformed pearlite (dark phase) as well as the presence of slip bands and twins in the microstructure.

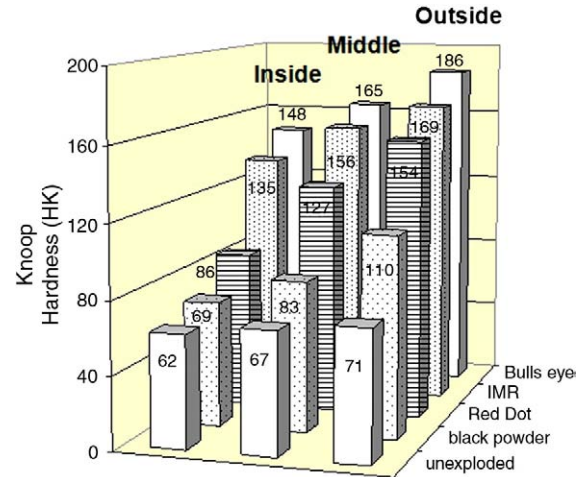


Fig. 14 – Microhardness variations of pipe bomb fragments as a function of radial position; i.e. microhardness variations within the wall of exploded pipes. Note the variation in microhardness with propellant energy.

determined from quantitative stereology, where more powerful explosive devices showed greater pearlite deformation (larger aspect ratios) and greater work hardening (microhardness numbers). A radial variation in microhardness was also observed i.e. microhardness numbers measured at the outer wall of the pipe fragments were typically larger than those measured at the inner wall. Fig. 14 illustrates the change in microhardness as a function of propellant energy and radial position. The work hardening was caused by the propagation of the pressure wave through the pipe wall and was enhanced by the compression of the material from the inner to the outer wall. Thus, the observed work hardening is greater at the outer wall than the inner wall of the pipe.

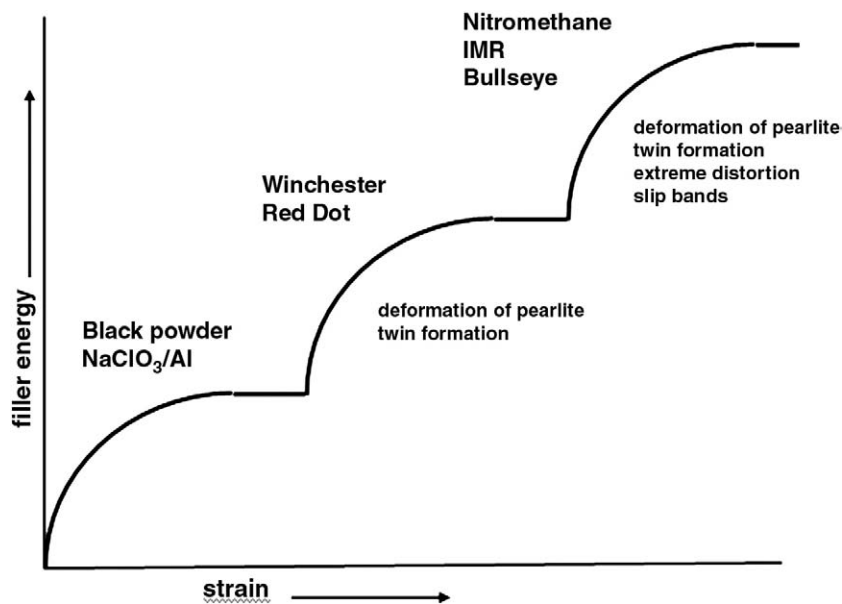


Fig. 13 – Microstructural changes observed in pipe bomb fragments collected after detonation.

4. Conclusions

More powerful, faster burning, propellants produced more plastic deformation in steel pipe bombs prior to fracture than lower power propellants. This can be shown by quantitative stereology and microhardness analysis of the pipe fragments recovered after the explosion. As the power of the propellant filler increased, the extent of work hardening in the pipe fragments also increased, as measured by microhardness. A radial variation in microhardness was observed, with larger Knoop Hardness values at the outer pipe wall than at the inner wall of the pipe fragments. Moreover, the recovered pipe fragments exhibited four distinct changes in microstructure, which also showed a strong correlation with the power of the propellant. The microstructural changes observed in the post-blast pipe fragments include (1) deformation of α -ferrite grains and pearlite colonies as evidenced by changes in aspect ratio, (2) twin formation, (3) distortion of pearlite colonies in continuous bands, and (4) formation of cross-slip bands. Quantitative stereology revealed that the average aspect ratio of the pearlite colonies in the recovered fragments increased with increasing filler energy. This trend was consistent with the work hardening effect determined from microhardness measurements of the fragments.

REFERENCES

- [1] Arson and Explosives Incidents Report; Bureau of Alcohol, Tobacco, and Firearms: Dept. of Treasury: Washington D.C., 1997.
- [2] A Guide for Explosion and Bombing Scene Investigation; J181869; U.S. Department of Justice: June, 2000.
- [3] 25 Ways to Fight Terrorism. Prism — American Society of Engineering Education Journal Feb., 2002, p 27.
- [4] Raftenberg MN, Krause CD. Metallographic observations of armor steel specimens from plates perforated by shaped charge jets. *Int J Imp Eng* 1999;23:757–70.
- [5] Vander-Voort GF. *Metallography, principles and practices*. New York: McGraw Hill Book Co; 1984.
- [6] Walsh GA, Inal OT, Romero VD. A potential metallographic technique for the investigation of pipe bombings. *J Forens Sci* 2003;48(5):945–60.
- [7] Oxley JC, Smith JL, Resende E, Rogers E, Strobel RA, Bender EC. Improvised explosive devices: pipe bombs. *J For Sci* 2001;46(3):87–110.
- [8] Mock W, Holt WH. Fragmentation behavior of Armco Iron and HF-1 steel explosive-filled cylinders. *J Appl Phys* 1983;54(5):2350.
- [9] ASTM E384-00 Test Method for Microindentation Hardness of Materials, American Society for Testing and Materials International, Volume 03.01, W. Conshohocken, PA, 2003.
- [10] Reed-Hill RE. *Physical metallurgy principles*. 3rd ed. Boston, MA: PWS Publishing Co; 1994.
- [11] Callister WD. *Materials science and engineering, an introduction*. 6th ed. Hoboken, NJ: John Wiley and Sons; 1999.

Detection of Peroxides Using Pd/SnO₂ Nanocomposite Catalysts

Yun Chu¹, Daniel Mallin¹, Matin Amani^{1,2},

Michael J. Platek², and Otto J. Gregory^{1*}

Department of Chemical Engineering, University of Rhode Island, Kingston, RI 02881, USA¹

Department of Electrical Engineering, University of Rhode Island, Kingston, RI 02881, USA²

TATP is one of the most frequently used peroxide based explosives in improvised explosive devices (IED's) by terrorists. While TATP and its precursors have previously been detected at the ppm level using a thermodynamic gas sensor platform, most of the catalysts considered for this platform exhibited relatively poor selectivity between hydrogen peroxide and TATP. Transition metals were reported of the capability to improve the sensitivity of metal oxide based gas sensor by modifying the surface energy state of the metal oxide. Therefore, combinatorial chemistry techniques were employed to screen catalysts with various compositions for micro-calorimetric sensor arrays that will ultimately reduce false positives. These nanocomposite catalysts were prepared by incorporating palladium nanoparticles of different loadings in a SnO₂ matrix, such that improved sensitivity and selectivity could be achieved in a single thermodynamic sensor platform. SEM and TEM were employed to study morphology of the catalyst. Oxidation state and crystal structures were identified using XPS and XRD separately.

Key Words: Gas sensor, TATP, hydrogen peroxide, sputtering, SnO₂, Pd

*Corresponding author. Tel.: +1 401 874 2085.

E-mail Address: gregory@egr.uri.edu (O.J.Gregory)

I. Introduction

TATP is a hydrogen peroxide-based compound commonly used as an initiator in improvised explosive devices (IED's) employing PETN and other high explosives due to its ease of manufacture from available precursors and simple preparation [1]. The detection of TATP using bench-scale analytical instrumentation has been readily demonstrated. Specifically, mass spectrometry [2, 3, 4], terahertz absorption spectrometry [5], ion mobility spectrometry [4, 6] and fluorescence spectroscopy [7], exhibit both adequate sensitivity and stability for detection purposes. However, the aforementioned techniques are somewhat limited for field use since they cannot be adapted in a small footprint sensor platform and are not capable of continuous monitoring. This is due in part to the cost, complexity, analysis time and sample preparation associated with these more traditional analytical tools. A low cost, small footprint sensor that exhibits adequate speed, selectivity and sensitivity without false positives is highly desired for field use where continuous monitoring is warranted.

Many investigators have reported on gas sensors employing metal oxide catalysts in a variety of sensor platforms. For example, these catalysts have been used to detect trace levels of toxic gases such as CO, H₂S, H₂ and NO_x [8]. However, a vast majority of the gas sensors employing metal oxide catalyst respond to changes in the electrical properties of the catalyst during exposure to the target gas which can include changes in electrical conductivity or dielectric constant of the metal oxide [10, 11], changes in work function [12, 13] and changes in optical properties of the metal oxide [15, 16]. A number of researchers have also reported that the sensitivity of metal oxide based sensors can be enhanced by a direct exchange of electrons between the oxide semiconductor and heavy metals such as Pd, Au, and Pt. The addition of such metals increases the rate of specific reactions on the surface of oxide crystals due to spill-over

effects or through modification of surface energy states [18, 19]. However, one major disadvantage of the metal oxide gas sensors, as well as all other types of solid-state gas sensors, is their poor selectivity caused by their inability to distinguish between complex target molecules [9]. In a previous study, we demonstrated a gas sensor which was capable of detecting TATP via catalytic decomposition to form hydrogen peroxide. However, these sensors exhibited little or no selectivity between TATP and hydrogen peroxide, making them prone to false positives when other peroxides may exist in the ambient.

In the present study we utilized combinatorial chemistry techniques to screen potential catalysts for enhanced selectivity using a thermodynamic gas sensor platform. The thermodynamic sensor platform employs a digital control system to measure the heat effect associated with the interaction of a target gas molecule with a catalyst deposited onto the surface of a microheater. The heat effect of the catalyst-coated microheater is monitored by thermal scanning from room temperature to 500°C. These characteristic heat affects are measured as the target molecules including TATP, H₂O₂ and acetone were passed over the active sensor element. In this paper, the controlled addition of palladium to a SnO₂ matrix was used to systematically enhance both the sensitivity and selectivity of TATP over H₂O₂.

II. Experimental

2.1 Sensor fabrication and characterization

Thin film nickel micro-heaters having a nominal thickness of 4.5 μm were deposited onto a laser-perforated alumina substrate using a MRC 822 sputtering system. The nickel microheaters were annealed in flowing nitrogen at 900°C for 5 hours to improve the electrical stability and eliminate point defects as a result of the sputtering process. A 1μm thick alumina layer was then deposited over the nickel microheaters to prevent direct electrical shorts between

the Ni heating element and the catalyst layer. The alumina layer was also used to prevent possible interactions with oxygen and other gases present in the atmosphere. A SnO₂/Pd nanocomposite film was then deposited onto the isolated microheater surface which served as the catalyst support. A cutaway view of the various layers comprising the sensor is shown in Figure 1. The nanocomposite catalyst was deposited onto arrays of microheater sensors in an MRC 8667 sputtering machine by co-sputtering from simultaneously energized SnO₂ and Pd targets. This produced a large number of essentially different catalysts with a continuously varying, spatially dependent chemistry. Palladium loadings ranged from 2 wt.% to 25 wt.% in the nanocomposite. Following deposition, the films were annealed at 550°C in an air ambient to promote crystallization and further stabilize the catalysts. The chemical composition and morphology of these catalysts were characterized using scanning electron microscopy (SEM) equipped with energy dispersive x-ray spectroscopy (EDS). The catalysts were also characterized using x-ray diffraction (XRD) and x-ray photoelectron spectroscopy (XPS). Pure tin oxide films were also prepared as catalysts for comparison purposes using the deposition conditions presented in reference [19].

2.2 Testing apparatus and protocol

The flow rate of inert gas (dry air) and target gas was precisely metered into the test chamber using two mass flow controllers and a digital flowmeter, which produced a constant mass flow and allowed precise control over the target gas and inert gas mixtures delivered to the testbed. The desired vapor phase concentration of TATP (e.g. 0.68 µg/ml) was achieved by passing a carrier gas over a piece of filter paper impregnated with high purity TATP crystals maintained at room temperature. When the target molecules were derived from liquid-based chemical solutions such as H₂O, or acetone in deionized water, air was bubbled through the flask

containing dilute solutions to establish an equilibrium partial pressure in the vapor phase. A schematic of the test bed used to evaluate sensor performance is shown in Figure 2.

Catalytic response was determined by measuring the heat affect associated with the interaction of the target molecules with a catalyst using a dynamic testing protocol. The catalyst coated microheater was heated to a series of predetermined temperature set points by controlling the electrical resistance of the microheater, measured via the four point probe method. The temperature coefficient of resistance of the nickel microheater was independently calibrated and verified prior to each test. Gas delivery system and data acquisition system were computer controlled using LabView software. After reaching each target set point temperature, the sensor was allowed to equilibrate for 360 seconds under constant inert gas flow. The target gas was then introduced into the test chamber for 180 seconds and then the reference gas was introduced for 180 seconds before the microheater was ramped to the next temperature set point. The power required to maintain the sensor at a particular temperature was recorded after the target gas was introduced and this temperature was maintained until the start of next step increase in temperature. The heat effect at each temperature set point was measured as by taking the difference in power required to maintain the temperature in the presence of the target gas and the power required to maintain the temperature in the presence of the inert gas. Prior to measuring the sensor response, the background power or drift was subtracted from the sensor response. Typically, all responses smaller than ± 1.0 mW were considered background noise, which was due to small variations in the target and inert gas flow rates, drift in the nickel microheaters and other sources of electrical noise.

III. Results and Discussion

3.1 Chemical characterization and surface morphology

Catalysts incorporating palladium nanoparticles in a tin oxide matrix were characterized by XRD, in both the as-deposited and annealed condition (Figure 3). All of the nanocomposite catalysts, regardless of composition were amorphous in the as-deposited condition and crystalline or partially crystalline after subsequent annealing. Peaks corresponding to the rutile form of SnO₂ were observed in the XRD patterns of the annealed films with no preferred orientation or texture evident. A uniform 2 θ shift of (0.01Å) was also observed for the SnO₂ diffraction peaks relative to the literature value, which was likely caused by substitutional defects [20]. The oxidation states of the nanocomposite catalysts after exposure to hydrogen peroxide and TATP were characterized using XPS. As shown in Figure 4, the XPS spectrum of pure SnO₂ and Pd doped SnO₂ exhibited the same Sn 3d₅ core level peak at 486.5 eV, suggesting that tin was present in +4 oxidation states in both specimens. Pure SnO₂ contains +2 state tin as indicated by the lower intensity and slight shifting of the main peak. The Pd 3d₅ peaks in the 2.2 wt.% nanocomposite were observed at 336.4 eV and 337.5 eV respectively, which is in good agreement with literature values corresponding to palladium in the +2 and +4 states [20-24]. The composition (at.%) was estimated to be 0.17:0.83 based on the peak area. As the palladium doping level was increased to 12 wt.%, metallic palladium started to phase separate and the composition of PdO₂:PdO:Pd became 0.084:0.723:0.193. When the palladium doping level reached 32 wt.%, the metallic component became dominant while the PdO₂ peak disappeared along with the PdO peak. This is because palladium single crystals are more difficult to oxidize and the palladium particles in the SnO₂ are easier to oxidize [22]. This finding is in good agreement with the disappearance of the palladium (220) peak indicated in XRD pattern of the nanocomposite. Finally, the catalyst morphology was followed by both SEM and TEM and is shown in Figure 5. While most of the as-deposited films were featureless, as might be expected

with an amorphous film, extensive micro-cracking was observed in the catalysts after annealing. This was attributed to the large volume change associated with crystallization of the nanocomposite. In addition, as the palladium content in the nanocomposite was increased, the density of micro-cracks diminished and eventually disappeared from the microstructure when palladium loadings greater than 25 wt.% were realized. EDS analysis was used in conjunction with TEM to determine the chemistry of the dark spherical particles observed in the SnO₂ matrix. These palladium particles had an average diameter of 20 nm, and EDS confirmed the presence of palladium in the SnO₂ matrix.

3.2 Gas sensing characteristics

Baseline experiments using an un-doped SnO₂ catalyst at several temperature set points in the presence of 0.68 µg/ml TATP were conducted. Figure 6 illustrates the “off-on-off” protocol used for each run. At temperatures below 240°C, a slightly exothermic reaction was observed at the surface of the SnO₂ catalyst. However, as the temperature was increased, the reaction tended to be endothermic and peaked at 420°C. Accompanying the change in sign of the response was a change in the reaction kinetics, which was apparent from the reduced response time for the exothermic reaction when compared to the endothermic sensor response. Such sign changes are very telling with respect to the uniqueness of the sensor response or signature and along with the magnitude of response can alleviate false positives.

When similar tests were performed using pure SnO₂, the palladium doped catalysts showed very different behavior (response versus temperature curves) when exposed to H₂O₂ compared to TATP as shown in Figure 7. The sensor clearly had a response to TATP at low temperature (185°C – 275°C) and reached maximum at 390°C. However, the catalyst exhibited little or no response to H₂O₂ until 275°C, where a peak response at 455°C was observed. A series

of concentration tests, shown in Figure 8, was performed in both H₂O₂ and TATP to determine the sensitivity and detection limit of the sensor.

Figure 9 shows the magnitude of the heat effect observed in a number of nanocomposite catalysts as a function of palladium loading in the presence of 0.68 µg/ml TATP and 0.225 µg/ml H₂O₂. At palladium loadings less than 8 wt.%, the sensors exhibit a relatively poor response compared to the un-doped SnO₂ catalysts. However, at higher palladium loadings, there was a substantial increase in sensor response, which abruptly decreased when more than 12 wt.% Pd was incorporated into the film. Catalysts with even higher palladium loadings showed almost no response to TATP and H₂O₂. While there was a substantial improvement in the maximum response to the two target molecules at a 12 wt.% palladium loading, the selectivity between these two target molecules was also significantly improved. A nanocomposite catalyst with a 8 wt.% palladium loading yielded the greatest selectivity (H₂O₂ relative to TATP) while a 12 wt.% palladium loading yielded the greatest sensitivity as shown in Figure 9.

IV. Discussion

4.1 Effect of palladium doping rate

The role of Pd in the promotion of sensing ability of metal oxides was discussed in literatures [25-34]. However, variables including doping method [25, 26], loading concentration [26, 27], working temperature [28] and species of analytic gases [29-32] all played important roles in varying its functioning mechanism. In this study, stoichiometric SnO₂ without addition of dopants exhibited higher sensitivity to oxidizing vapors such as H₂O₂ and TATP compared with non-stoichiometric SnO₂. At low Pd loading, Pd atoms diffused uniformly into SnO₂ matrix and formed two possible types of bond: (1) a strong Pd-Sn alloy metallic bond which was

suggested in literature [33] and (2) Pd-O and O-Pd-O ionic bond which were conformed in XPS. The first type of bond reduced the amount of active SnO₂ molecules in unit surface area while the second type of bond seized oxygen atoms from stoichiometric SnO₂ leaving non-stoichiometric SnO₂. This explains the decrease of sensitivity from 0 - 8 wt.% palladium loading. As Pd loading increased, oxygen molecules diffused into the catalyst during annealing processes were insufficient for Pd atoms to form O-Pd-O bonds which caused a disappearance of PdO₂ peak as indicated by XPS in Figure 4(b). Instead, Pd metallic clusters with relatively small size encapsulated in PdO-SnO₂ molecules were formed resulting in the increase of Pd metallic peak [33]. Meanwhile, Sn peak remained a single state as stoichiometric SnO₂ by sharing oxygen atoms from PdO as indicated by XPS in Figure 4(a). This uniform stoichiometric SnO₂ lead to the maximum sensitivity of Pd-SnO₂ sensor at 12 wt.%. When Pd loading continued increasing, the size of Pd cluster increased resulting in a large Pd metallic peak and the active space of SnO₂ were greatly occupied, which caused the second decrease of the sensitivity of the sensors.

4.2 Protocol of TATP identification

As indicated in Figure 9, SnO₂ with 12 wt.% palladium doping rate provided the maximum sensitivity to both TATP and H₂O₂ at 395°C. Thus this 12 wt.% Pd:SnO₂ sensor was selected and maintained at 410°C as an early warning indicator. Once the sensor was triggered by an unknown vapor and received positive signal, further measures were taken to identify the species of such suspicious vapor. The sensor would then be scanned at various temperature setpoint ranged from 150°C to 450°C to collect a profile of signal intensity as a function of temperature. Significant differences between H₂O₂ response and TATP response are their different positive trigger point and their temperature range of peak response, which can be used to detect TATP from H₂O₂. The Pd:SnO₂ nanocomposite with 5 wt.% and 8 wt.% palladium

loading were also employed for the reason that the sensor with 5 wt.% palladium loading only responds to TATP but shows no signal to H₂O₂ while the one with 8 wt.% palladium loading does the opposite. These two sets of sensors provided a certain redundancy in response which helped mitigate false positives.

V. Conclusion

Palladium-tin oxide combinatorial libraries were fabricated by co-sputtering from metal palladium and SnO₂ targets to screen catalysts for the optimal selectivity to TATP. Tin was present in largely the Sn⁴⁺ state while palladium was present in both the Pd²⁺ and Pd⁴⁺ oxidation state. Compared with a pure SnO₂ catalyst, several unique features in the response versus temperature curves were observed for the catalysts that were doped with palladium, which greatly improved the magnitude of responses to both TATP and H₂O₂. Sensors with various palladium doping levels also exhibited very different characteristics to the target molecules: the catalyst with an 8 wt.% palladium loading yielded the greatest selectivity while a 12 wt.% palladium loading provided maximum sensitivity.

Acknowledgements

The authors wish to thank the Department of Homeland Security Center of Excellence for Explosives Detection, Mitigation and Response and Sensor Tech, Savannah GA for support of this work. The authors also thank Prof. Jimmy Oxley and Prof. James Smith at the University of Rhode Island for preparation of the TATP samples used throughout the study.

References

- ¹F. Dubnikova, R. Kosloff, Y. Zeiri, Z. Karpas, “Novel approach to the detection of triacetone triperoxide (TATP), its structure and its complexes with ions”, *J. Phys. Chem. A* 106 (19) (2002) 4951–4956.
- ²I. Cotte-Rodriguez, H. Chen, R. G. Cooks, “Rapid trace detection of triacetone triperoxide (TATP) of complexation detections of desorption electrospray ionization”, *Chemical Communications*, 12 January, 2006
- ³G. A. Buttigieg, A. K. Knight, S. Denson, C. Pommier, M. B. Denton, “Characterization of the explosive triacetone triperoxide and detection by ion mobility spectrometry”, *Forensic Science International* 135 (2003) 53-59
- ⁴R. Rasanen, M. Nousiainen, K. Parakorpi, M. Sillanpaa, L. Polari, O. Anttalainen, M. Utriainen, “Determination of gas phase triacetone triperoxide with aspiration ion mobility spectrometry and gas chromatography-mass spectrometry”, *Analytica Chimica Acta*, 623 (2008) 59-65
- ⁵J. Wilkinson, C. T. Konek, J. S. Moran, E. M. Witko, T. M. Korter, “Terahertz absorption spectrum of triacetone triperoxide (TATP)”, *Chemical Physics Letters*, 478 (2009) 172-174
- ⁶A. Stambouli, A. El Bouri, T. Bouayoun, M. A. Bellimam, “Headspace GC/MS detection of TATP traces in post-explosion debris”, *Forensic Science International*, 146S (2004) S191-S194
- ⁷C. Mullen, A. Irwin, B. V. Pond, D. L. Huestis, M. J. Coggiola, H. Oser, “Detection of explosives and explosives-related compounds by single photon laser ionization time-of-flight mass spectrometry”, *Anal. Chem.* 78 (2006) 3807.
- ⁸C. Shen, J. Li, H. Han, H. Wang, H. Jiang, Y. Chu, “Triacetone triperoxide using low reduced-field proton transfer reaction mass spectrometer”, *International Journal of Mass Spectrometry*, 285 (2009) 100-103

- ⁹R. S. Ladbeck, U. Karst. "Determination of triacetone triperoxide in ambient air", *Anal. Chem.* 482 (2003) 183-188
- ¹⁰N. Barsan, D. Koziej, U. Weimar. "Metal oxide-based gas sensor research: How to?", *Sens. Actuators, B*, 121 (2007) 18-35.
- ¹¹N. L. Hung, H. Kim, S. K. Hong, D. Kim. "Enhancement of CO gas sensing properties of ZnO thin films deposited on self-assembled Au nanodots", *Sens. Actuators, B*, 151 (2010) 127-132.
- ¹²G. Eranna, B. C/ Joshi, D. P. Runthala, R. P. Gupta. "Oxide materials for development of integrated gas sensors: A comprehensive review", *Crit. Rev. Solid State Mater. Sci.*, 29 (2004) 111-188.
- ¹³W. H. Zhang, W. D. Zhang, L. Y. Chen. "Highly sensitive detection of explosive Triacetone triperoxide by an In₂O₃ sensor", *Nanotechnol.*, 21 (2010) 315502.
- ¹⁴J. C. Oxley, J. L. Smith, K. Shinde, J. Moran. "Determination of the Vapor Density of Triacetone Triperoxide (TATP) Using a Gas Chromatography Headspace Technique", *Propellants Explos. Pyrotech.*, 30 [2] (2005) 127-130.
- ¹⁵J. C. Oxley, J. L. Smith, H. Chen. "Decomposition of a Multi-Peroxidic Compound: Triacetone Triperoxide (TATP)", *Propellants Explos. Pyrotech.*, 27 [4] (2002) 209-216.
- ¹⁶W. Y. Yang, W. G. Kim, S. W. Rhee. "Radio frequency sputter deposition of single phase cuprous oxide using Cu₂O as a target material and its resistive switching properties", *Thin Solid Films*, 517 (2008) 967-971.
- ¹⁷C. I. Pearce, R. A. D. Patrick, D. J. Vaughan, C. M. B. Henderson, G. van der Laan. "Copper oxidation state in chalcopyrite: Mixed Cu d^9 and d^{10} characteristics", *Geochimica*, 70 (2006) 4635-4642.

- ¹⁸E. Vereshchaginam, R. A. M. Wolters, J. G. E. Gardeniers. “Measurement of reaction heats using a polysilicon based microcalorimetric sensor”, Sens. Actuators, A , In press.
- ¹⁹M. Amani, Y. Chu, K. L. Waterman, C. M. Hurley, M. J. Platek, O. J. Gregory. “Detection of triacetone triperoxide (TATP) using a thermodynamic based gas sensor”, Sens. Actuators B, 162(2012)7-13.
- ²⁰T. Zhang, L. Liu, Q. Qi, S. Li, G. Lu. “Development of microstructure In/Pd-doped SnO₂ sensor for low level CO detection”, Sensors and Actuators B, 139 (2009) 287-291.
- ²¹V. Jimenez, J. Espinos, A. Gonzalez-Elipe. “Effect of texture and annealing treatments in SnO₂ and Pd/SnO₂ gas sensor materials”, Sensors and Actuators B, 61(1999)23-32.
- ²²T. Skala, K. Veltruska, M. Moroseac, I. Matolinova, A. Cirera, V. Matolin. “Redox process of Pd-SnO₂ system”, Surface Science 566-568(2004)1217-1221.
- ²³R. Tan, Y. Guo, J. Zhao, Y. Li, T. Xu, W. Song. “Synthesis, characterization and gas-sensing properties of Pd-doped SnO₂ nano particles”, Trans. Nonferrous Met. Soc. China 21(2011)1568-1573.
- ²⁴Y. Shen, T. Yamazaki, Z. Liu, D. Meng, T. Kikuta, N. Nakatani, M. Saito, M. Mori. “Microstructure and H₂ gas sensing properties of undoped and Pd-doped SnO₂ nanowires”, Sensors and Actuators B, 135(2009)524-529.
- ²⁵C.B. Lim, S. Oh. “Microstructure evolution and gas sensitivities of Pd-doped SnO₂-based sensor prepared by three different catalyst-addition process”, Sensors and Actuators B 30 (1996) 223-231.
- ²⁶S. Matsushima, T. Maekawa, J. Tamaki, N. Miura, N. Yamazoe. “New methods for supporting palladium on a tin oxide gas sensor”, Sensors and Actuators B, 9 (1992) 71-78.

- ²⁷M. Yuasa, T. Masaki, T. Kida, K. Shimanoe, N. Yamazoe. "Nano-sized PdO loaded SnO₂ nanoparticles by reverse micelle method for highly sensitive CO gas sensor", *Sensors and Actuators B*, 136 (2009) 99-104.
- ²⁸L. Liu, T. Zhang, S. Li, L. Wang, T. Tian. "Preparation, characterization, and gas-sensing properties of Pd-doped In₂O₃ nanofibers", *Materials Letters*, 63 (2009) 1975-1977.
- ²⁹N. Yamazoe, K. Kurokawa, T. Seiyama. "Effects of additives on semiconductor gas sensor", *Sensors and Actuators*, 4 (1983) 283-289.
- ³⁰G. Tournier, C. Pijolat, R. Lalauze, B. Patissier. "Selective detection of CO and CH₄ with gas sensors using SnO₂ doped with palladium", *Sensors and Actuators B*, 26-27 (1995) 24-28.
- ³¹Y.C. Lee, H. Huang, O.K. Tan, M.S. Tse. "Semiconductor gas sensor based on Pd doped SnO₂ nanorod thin films", *Sensors and Actuators B* 132 (2008) 239-242.
- ³²Y. Zhang, Q. Xiang, J. Xu, P. Xu, Q. Pan, F. Li. "Self-assemblies of Pd nanoparticles on the surfaces of single crystal ZnO nanowires for chemical sensors with enhanced performances", *Journal of Material Chemistry*, 19 (2009) 4701-4706.
- ³³N. Tsud, V. Johaneck, I. Stara, K. Veltruska, V. Matolin. "XPS, ISS and TPD of Pd-Sn interactions on Pd-SnO_x systems", *Thin Solid Films* 391 (2001) 204-208
- ³⁴J.Choia, I. Hwanga, S. Kima, J. Parkb, S. Parkb, U. Jeongc, Y. Kangd, J. Leea. "Design of selective gas sensor using electrospun Pd doped SnO₂ hollow nanofibers", *Sensors and Actuators B*, 150 (2010) 191-199

List of Figures

Fig. 1 Schematic of microsensor, showing the top view (a) and expanded view (b) of catalyst layer (1), alumina passivation layer (2), nickel microheater (3) and alumina substrate (4).

Fig. 2 Apparatus used for the detection of TATP, H_2O_2 and acetone using a micro-calorimetric sensor.

Fig. 3 XRD patterns of as-deposited (a) and annealed films with (b) 8 wt.% loading Pd (1), 2.5 wt.% loading Pd (2), and 1 wt.% loading Pd (3) in the Pd:SnO₂ nanocomposite catalyst.

Fig. 4 XPS spectra of Sn 3d doublet for Pd doped and undoped SnO₂ (a), and Pd 3d doublet corresponding to 2.2 wt.% loading Pd, 12 wt.% loading Pd and 38 wt.% loading Pd in the PdSnO₂ nanocomposite(b).

Fig. 5 SEM (a) and TEM (b) micrographs of as-annealed nanocomposite catalyst with a 12 wt.% palladium loading.

Fig. 6 Response of micro-calorimetric sensor to 0.68 $\mu\text{g}/\text{ml}$ TATP using an SnO₂ catalyst thermally scanned to various temperature set points.

Fig. 7 Response of a 12 wt.% Pd nanocomposite catalyst to 0.225 $\mu\text{g}/\text{ml}$ H_2O_2 (a) and 0.68 $\mu\text{g}/\text{ml}$ TATP (b).

Fig. 8 Response of a 12 wt.% Pd nanocomposite to H_2O_2 (a) and TATP (b) as a function of concentration in the vapor phase.

Fig. 9 Response and selectivity of Pd:SnO₂ nanocomposite catalyst with various Pd loadings to H_2O_2 and TATP.

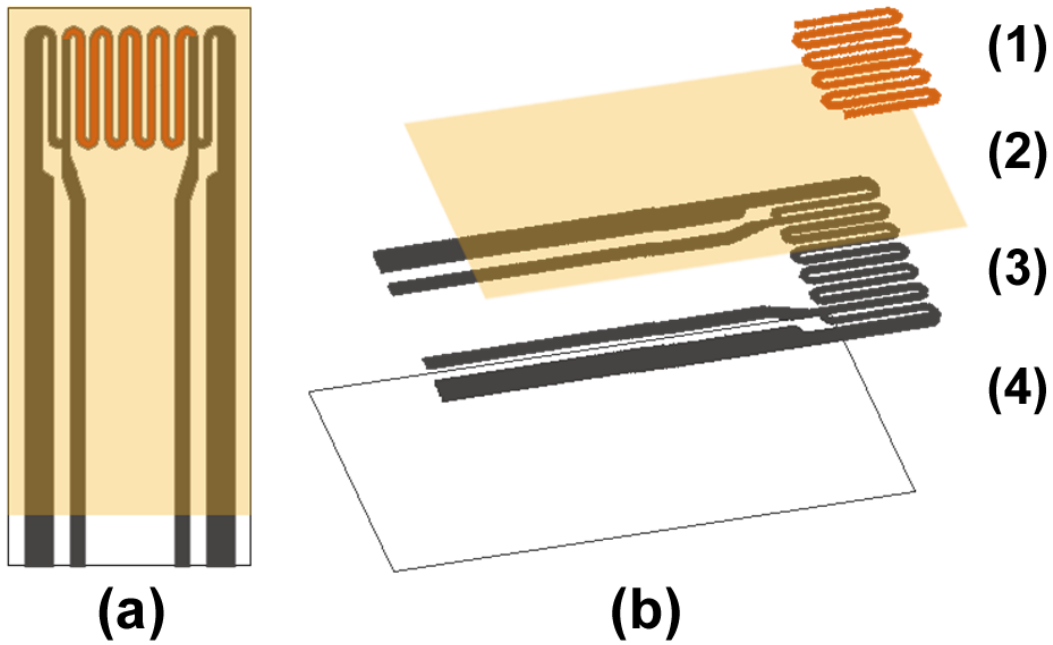


Fig. 1 Schematic of microsensor, showing the top view (a) and expanded view (b) of catalyst layer (1), alumina passivation layer (2), nickel microheater (3) and alumina substrate (4).

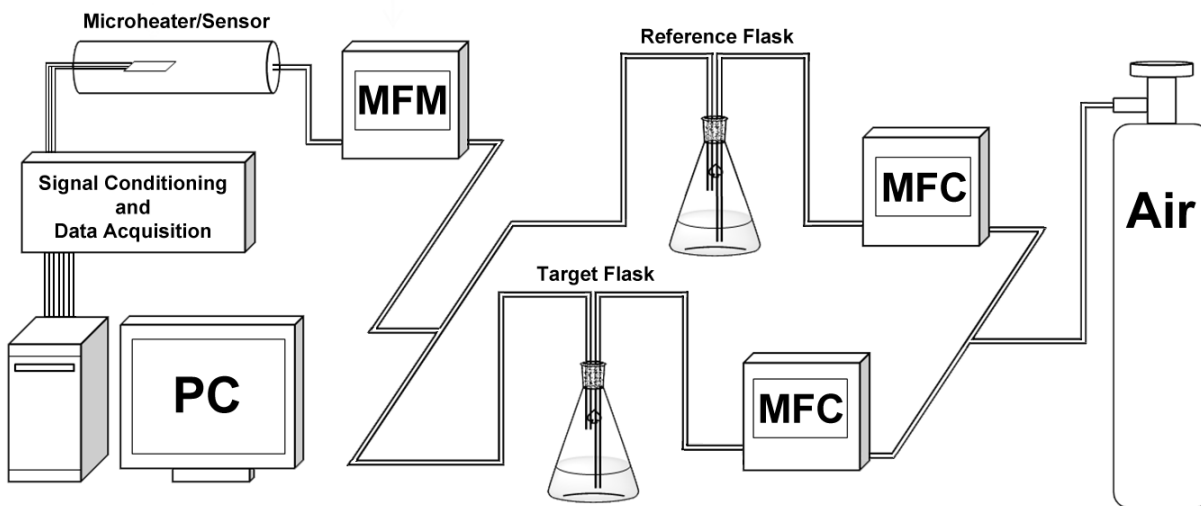


Fig. 2 Apparatus used for the detection of TATP, H_2O_2 and acetone using a micro-calorimetric sensor.

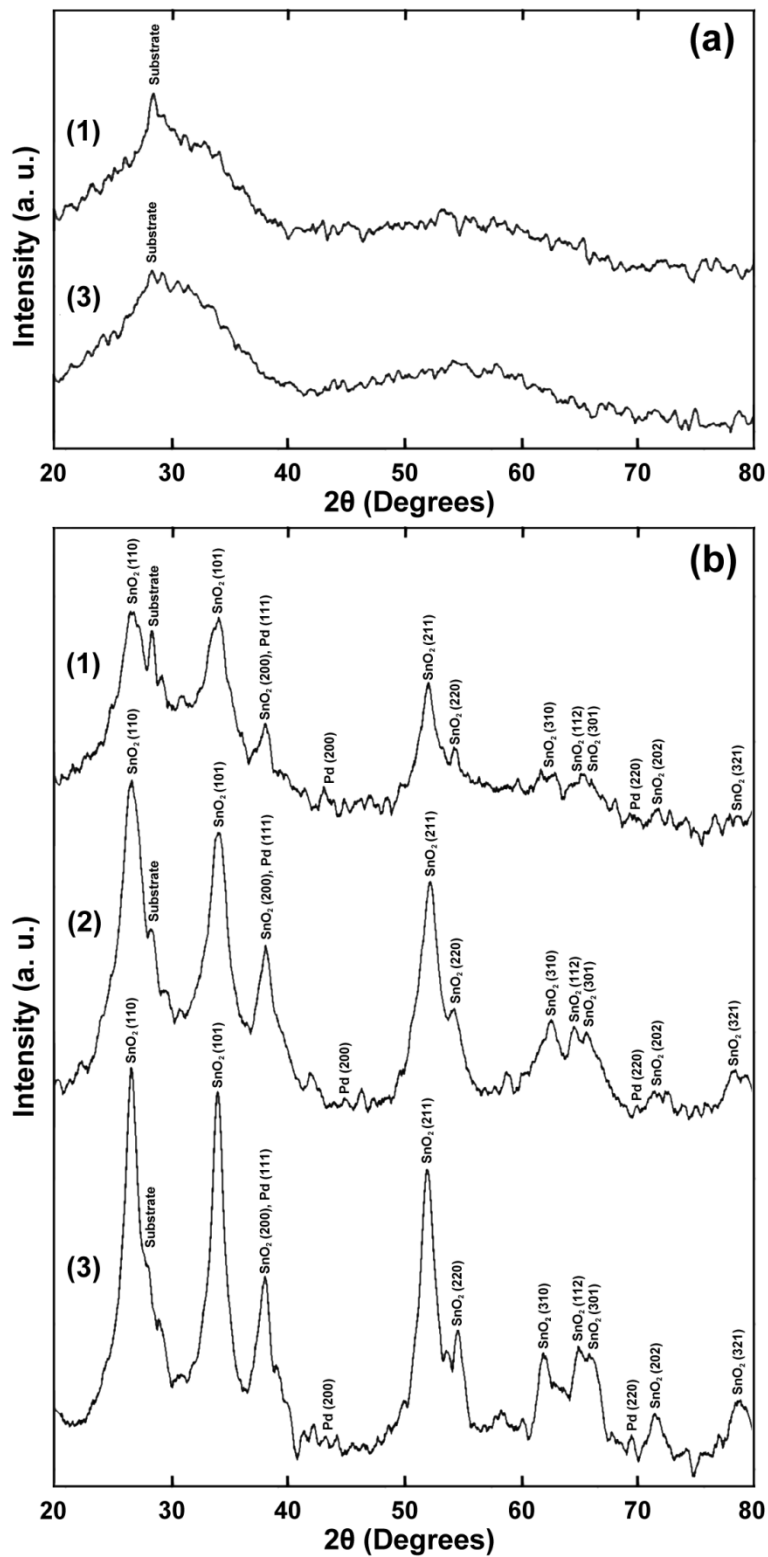


Fig. 3 XRD patterns of as-deposited (a) and annealed films with (b) 8 wt.% loading Pd (1), 2.5 wt.% loading Pd (2), and 1 wt.% loading Pd (3) in the Pd:SnO₂ nanocomposite catalyst.

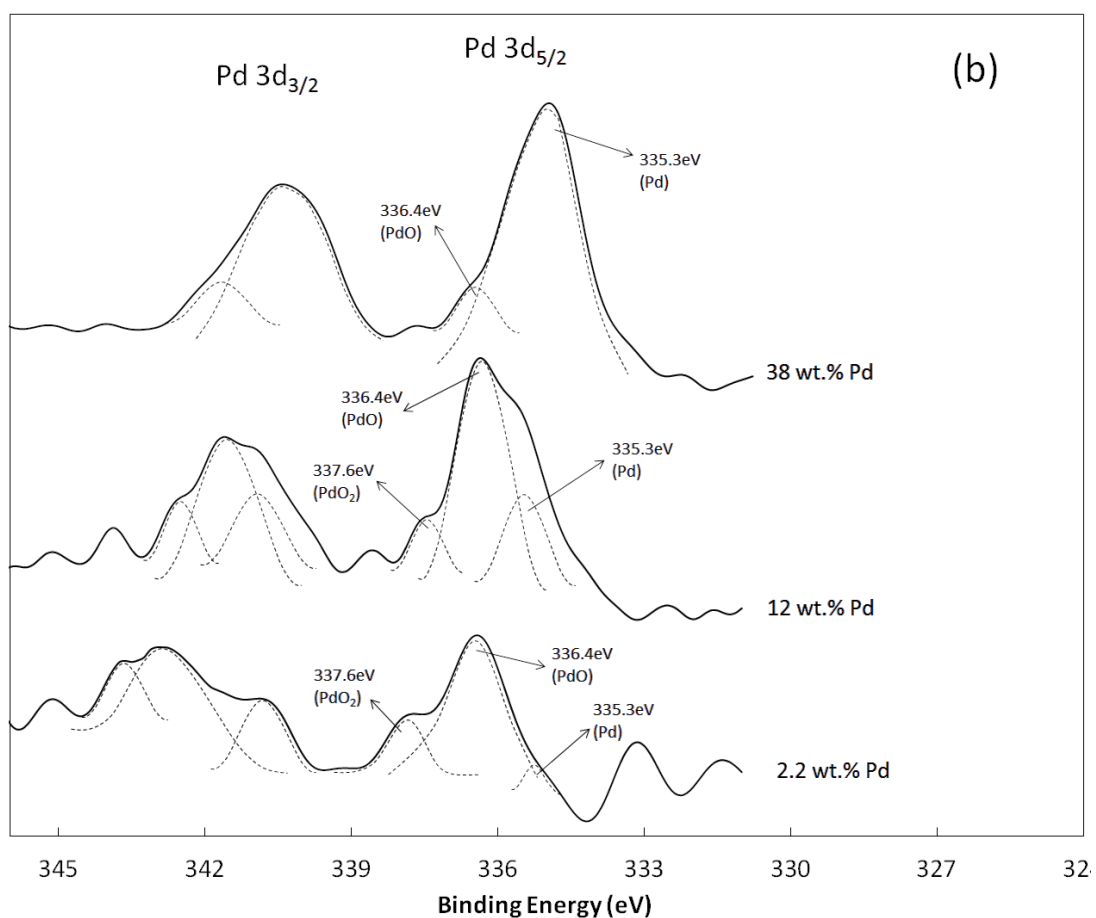
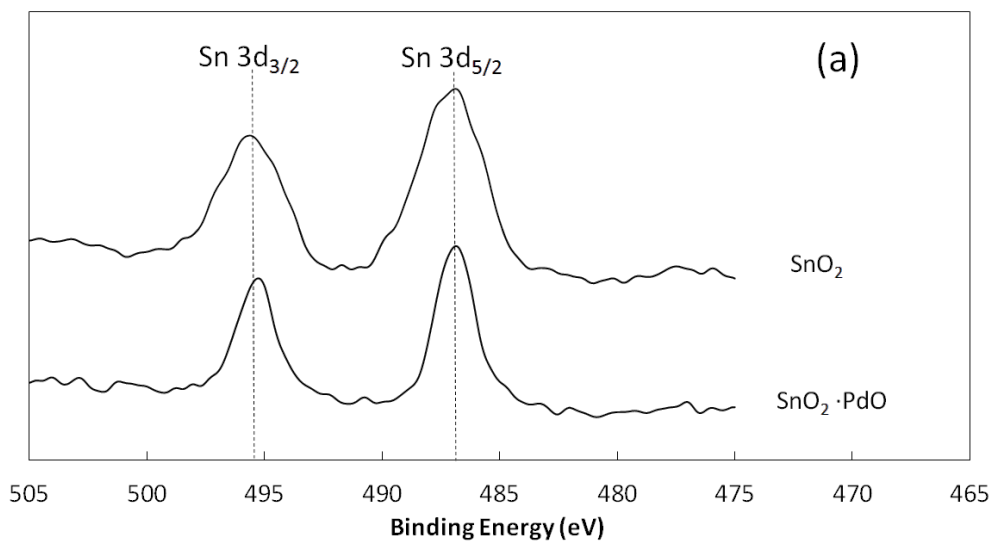


Fig. 4 XPS spectra of Sn 3d doublet for Pd doped and undoped SnO₂ (a), and Pd 3d doublet corresponding to 2.2 wt.% loading Pd, 12 wt.% loading Pd and 38 wt.% loading Pd in the PdSnO₂ nanocomposite(b).

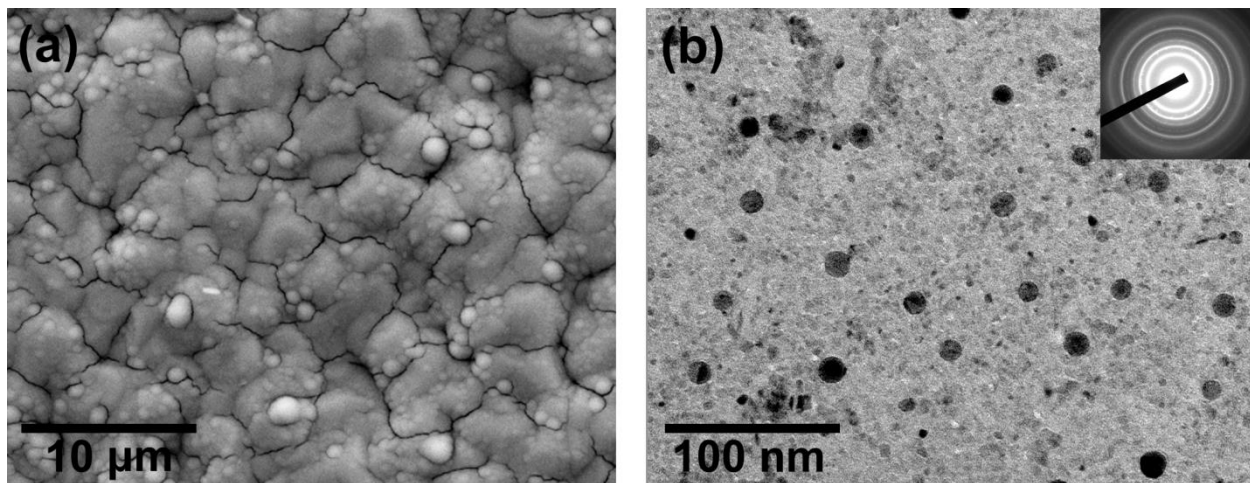


Fig. 5 SEM (a) and TEM (b) micrographs of as-annealed nanocomposite catalyst with a 12 wt.% palladium loading.

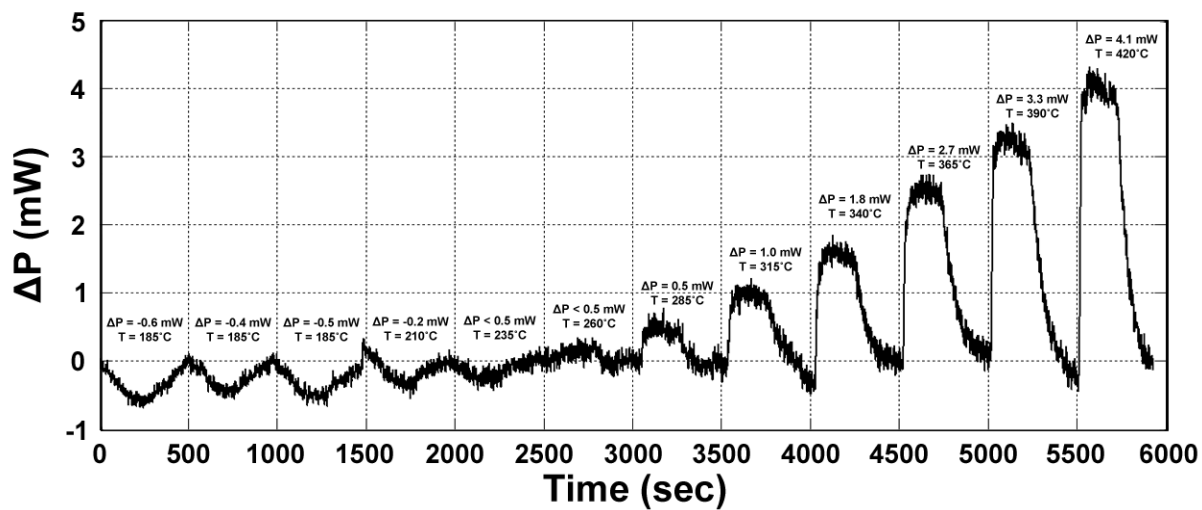
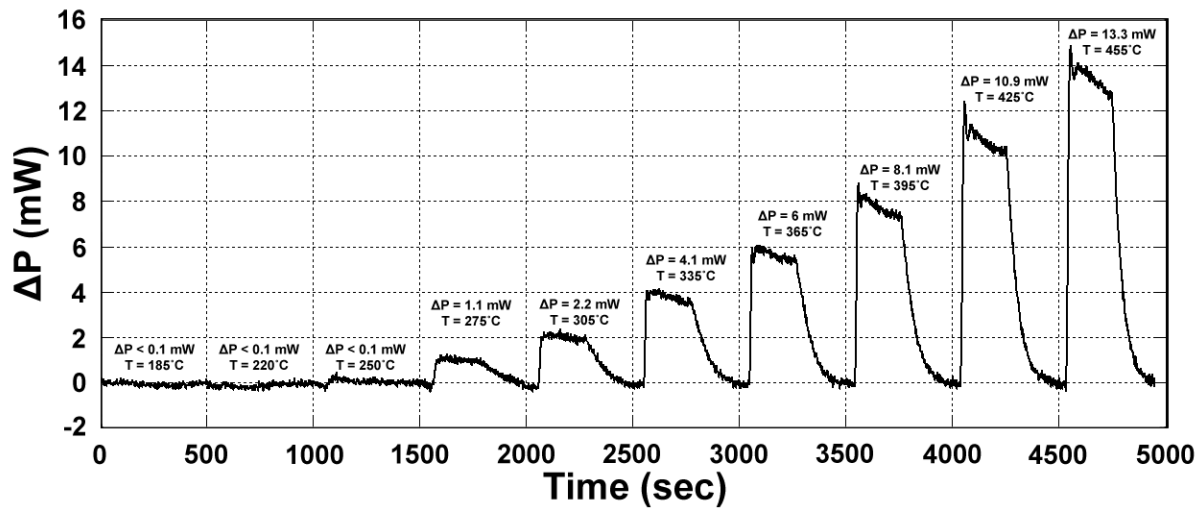
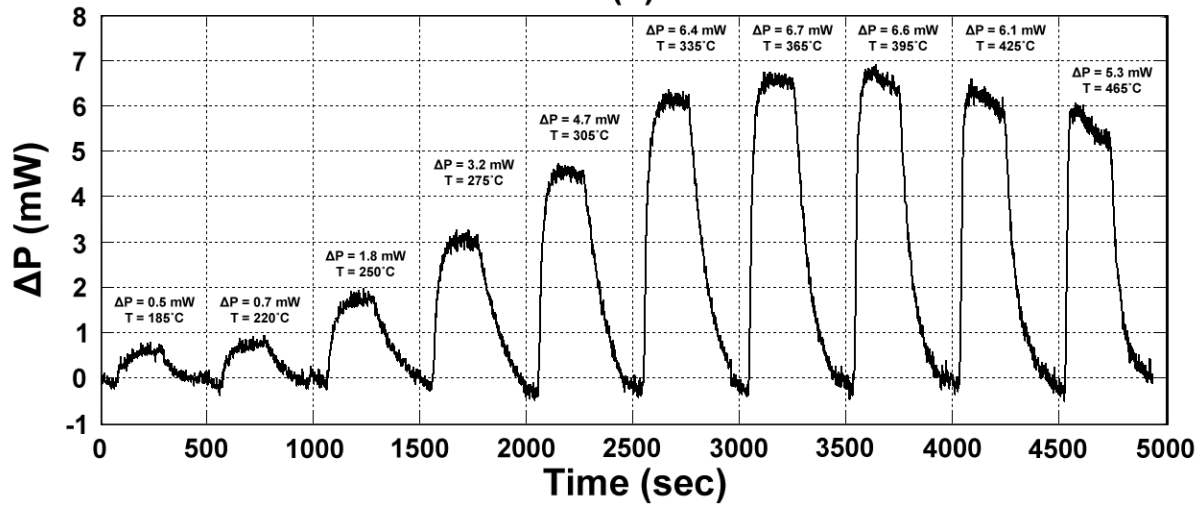


Fig. 6 Response of micro-calorimetric sensor to 0.68 $\mu\text{g/ml}$ TATP using an SnO_2 catalyst thermally scanned to various temperature set points.



(a)



(b)

Fig. 7 Response of a 12 wt.% Pd nanocomposite catalyst to 0.225 µg/ml H₂O₂ (a) and 0.68 µg/ml TATP (b).

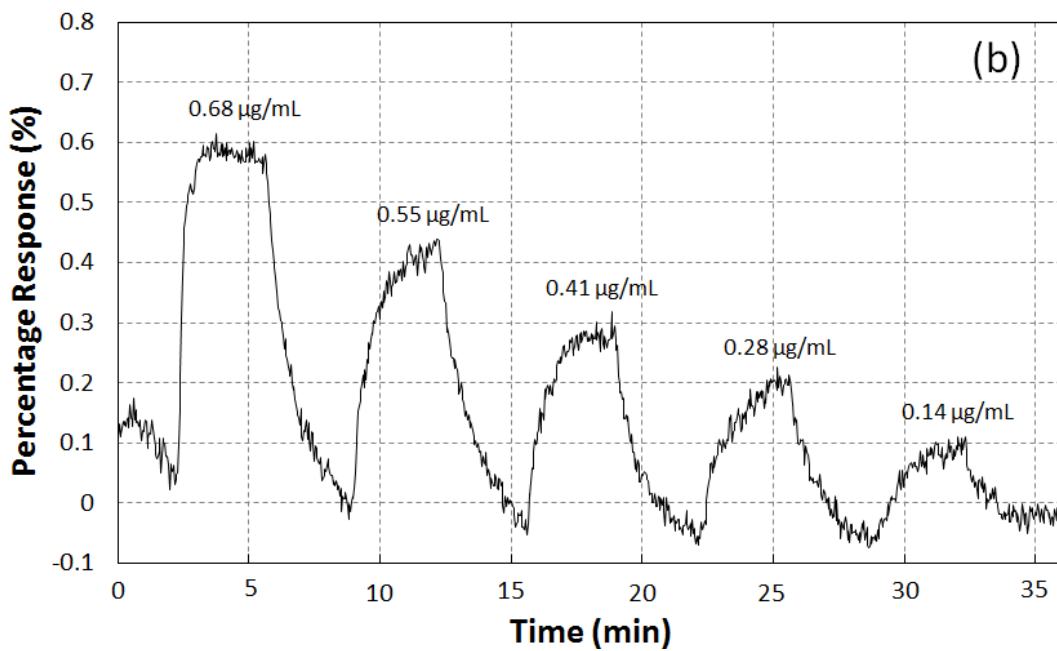
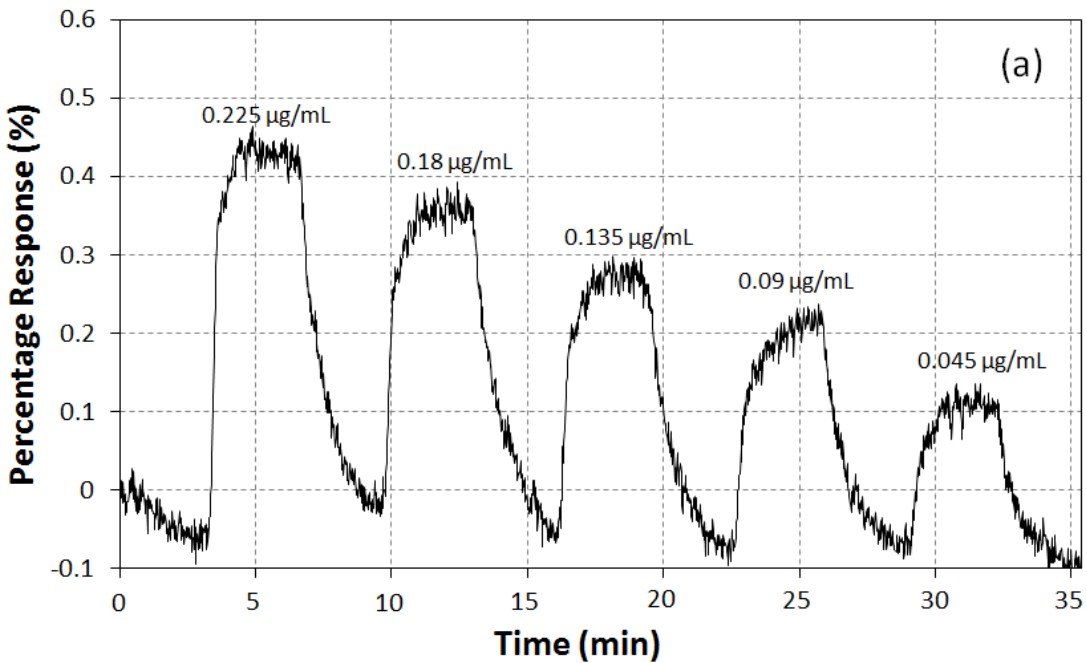


Figure 8. Response of a 12 wt.% Pd nanocomposite to H₂O₂ (a) and TATP (b) as a function of concentration in the vapor phase at 395°C.

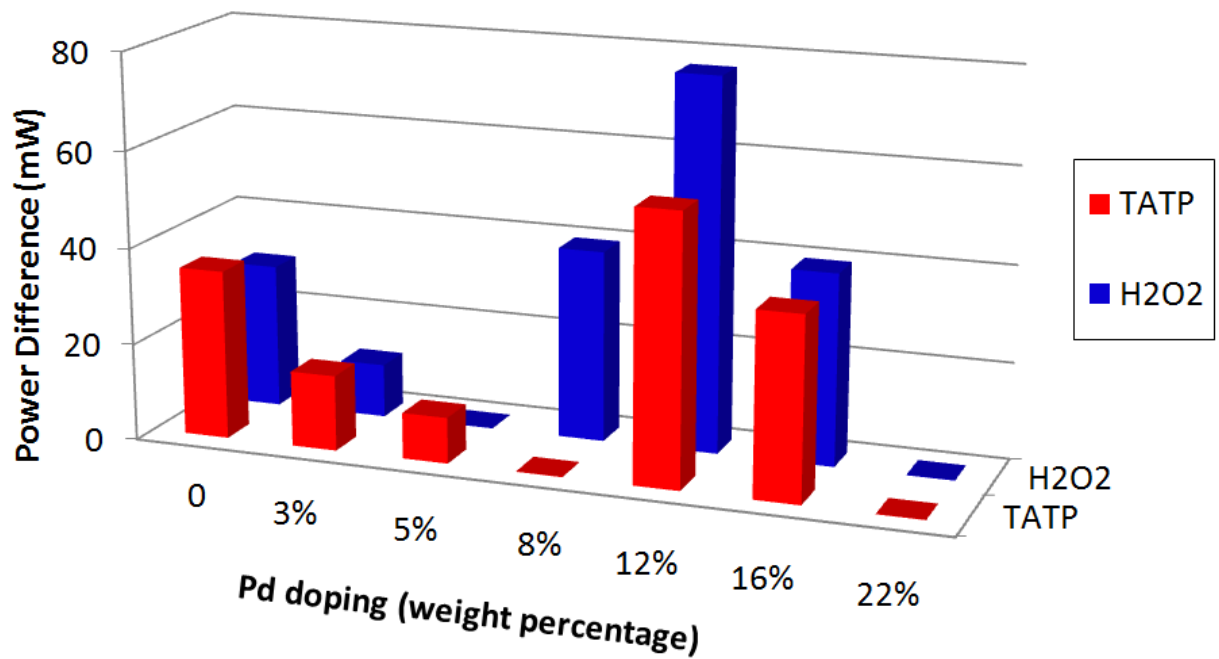


Fig. 9 Response and selectivity of Pd:SnO₂ nanocomposite catalyst with various Pd loadings to H₂O₂ and TATP at 395°C.

Author Biographies

Yun Chu received his B.S. degree in chemistry in Beijing University of Aeronautics and Astronautics in 2008. He is currently working on his Ph.D. in chemical engineering at University of Rhode Island (URI). His research interests include gas sensors, MEMS and catalyst development using nano-materials.

Caitlin M. Hurley received her B.S. degree in chemical engineering and a B.A. degree in French language from the URI in 2012. She is currently working on her Ph.D. at the Institute National Polytechnique de Toulouse through the Commissariat à l'Energie Atomique located in Saclay, France.

Matin Amani received B.S. degrees in electrical and biomedical engineering at URI in 2011, and his B.S. degree in chemical engineering and M.S. degree in electrical engineering in 2012. He is currently working on his Ph.D. in electrical engineering at Oregon State University through the Army Research Laboratory. His research interests include graphene electronics, MIM tunnel diodes, sensors for harsh environments, and gas sensors.

Michael J. Platek received his B.S degree in physics from Indiana University of PA (1984) and M.S. degree in physics from Wesleyan University (Middletown, CT) (1986). He is the laboratory manager for the URI Sensors and Sensors Technology Partnership. His interests include fabrication as well as characterization of nano-materials, development of gas sensors, bio-sensors and MEMS.

Alan J. Davis received his B.S. in Physics and Electrical Engineering, the M.S. degree in Electrical Engineering from the University of Massachusetts, Dartmouth, MA and Ph.D. in Electrical Engineering from the URI, Kingston in 1983, 1985 and 2000, respectively. Dr. Davis is currently employed by the Naval Undersea Warfare Center (NUWC) in Newport, RI. His research interests include MEMS devices/modeling, high speed ROIC development, sigma-delta modulation and mixed signal integrated circuits.

Otto J. Gregory received his B.S. degrees in chemical engineering and ocean engineering and his M.S. degree in chemical engineering from URI, in 1975 and 1977, respectively and his Ph.D. in engineering from Brown University in 1984. He is currently Distinguished Engineering Professor at URI and Director of the URI Sensors and Surface Technology Partnership. Dr. Gregory has published over 80 peer-reviewed journal articles and filed 25 US patents. His work has largely focused on sensors for harsh environments, wide bandgap semiconductors and chemical sensors, and has been funded by the gas turbine engine industry, NASA, DOE, Air Force, NSF and DHS.

Detection of Explosives Using Orthogonal Sensors

Yun Chu¹, Daniel Mallin¹, Matin Amani², Bissolar Bruno¹, Otto J. Gregory^{1*}
Department of Chemical Engineering, University of Rhode Island, Kingston, RI 02881¹

Abstract: An orthogonal detection system comprised of two independent sensing platforms integrated into a single sensor was recently developed to detect trace levels of explosives including TATP, DNT and ammonium nitrate in the vapor phase. The orthogonal sensor consists of a thermodynamic based sensing platform, which measures the heat effect associated with the interaction of specific target molecules with various metal oxide catalyst (ZnO and SnO₂) and a conductometric sensing platform which monitors the electrical conductivity changes of the same catalyst when exposed to the explosive molecules. The experimental results to date indicated that the combined orthogonal sensor was effective in identifying explosives at the ppb level. At the same time, it also provided a certain redundancy in sensor response to help mitigate false positives. The sensor output typically exhibited a linear response as a function of target molecule concentration. XPS was employed to confirm the oxidation state of metal oxides used as catalysts, which were a function of deposition and post deposition heat treatments.

Key words: Thermodynamic, conductometric, explosive detection, metal oxide

1. Introduction

The detection of explosive compounds is a highly significant task for military, industrial and public security purposes. Yet since different types of explosives are composed of various of chemicals and functional groups (e.g. $-\text{NO}_2$, $-\text{ONO}_2$, $-\text{NH}_2$, $-\text{[O-O]-}$, etc.) [1, 2] and since many of such compounds have extremely low vapor pressures [2-5], their detection is a complicated task. Conventional analytical instruments (e.g. infra-red spectroscopy, fluorescence spectroscopy, mass spectroscopy, Terahertz spectroscopy and Raman Spectroscopy) [6-13] have shown excellent reliability and selectivity to trace levels of explosives, especially to explosives containing nitro groups. However, these techniques suffer from limitations like complicated sample preparation, high cost of maintenance, the requirement of skilled operator and the incapability of in situ monitoring. Additionally, well trained canines can react to particular chemicals or even a combination of many smells that make up an explosive [14, 15], but dogs also require extensive training, high maintenance costs, are incapable of working long hours and due to many variables, lack reliability. As a result, an easy to operate, low cost and portable electronic “nose” with continuous and fast screening, high selectivity and sensitivity is needed for explosive detection.

Conductometric gas sensors based on measuring the conductivity changes of semiconducting metal oxides have been widely studied by researchers and scientists due to their excellent gas sensing capability and sensitivity under atmospheric conditions. Metal oxides materials (SnO , SnO_2 , In_2O_3 , WO_3 , TiO_2 , ZrO_2 , etc.) have demonstrated excellent sensitivity toward trace level, simple gas molecules (H_2O , CO , O_2 , O_3 , H_2 , SO_2 , NO_2 , etc.) or even complex explosive compounds [16-21]. The changes in resistivity of metal oxides occur at the adsorption or reaction process of gases on the surface of film, where the free charge carriers are transferred from the

semiconductor to the target gas or vice versa. Gases of the same type, either acceptor gases or donor gases, will cause similar characteristic changes in resistivity, which makes it difficult to determine the interaction at gas/solid interface. Thus, this poor selectivity, due to its sensing mechanism, is a major defect that impedes the application of conductometric sensors [19, 22-25].

In our previous study, a thin film thermodynamic gas sensor which measures the catalytic reaction heat of target gases with relatively high selectivity among different peroxide based compounds and sensitivity to part per million level was demonstrated [26]. To further improve its sensitivity without sacrificing selectivity to different chemical compounds, the thermodynamic sensing platform was combined with conductometric approach. Using these two complimentary techniques simultaneously provides a certain redundancy in response that mitigated the detection of false positives. In this paper, Tin dioxide and zinc oxide were employed to exhibit the sensing ability of this new platform.

2. Experimental

2.1 Fabrication of the combined sensor

Photolithography processes were used to form film patterns shown in Figure 1 onto a 6mm * 5.1mm * 0.5mm alumina substrate. Nickel thin-film micro-heaters with a thickness of 4.5 μm were sputtered using a MRC 822 sputtering system, followed by a nitrogen annealing process to improve electrical stability of the film. A 1 μm alumina insulation layer and 5 μm alumina coating were employed as the passivation layers to prevent the nickel micro-heaters from direct exposure to the gas molecules present in the surrounding atmosphere and prevent electrical

shorts to the marginally conductive catalysts. Nickel electrodes were then deposited to supply constant current through metal oxide catalysts and measure the resistivity change. Metal oxide catalysts (e.g. SnO₂, ZnO, In₂O₃, etc.) were subsequently deposited using a MRC 8667 sputtering system in argon. The catalysts were then annealed at 500°C in nitrogen for 5 hours, densifying the film and eliminating point defects, and then in nitrogen/oxygen atmosphere (volume ratio of 90:10) for 10 minutes to form a stoichiometric metal oxide rich surface over a non-stoichiometric film, for the reason that stoichiometric sensor exhibited maximum sensitivity in thermodynamic signals while conductometric sensor required high conductivity of the film. The oxidation states of the metal oxide as a function of deposition and post deposition heat treatment were studied using X-ray photoelectron spectroscopy (XPS).

2.2 Sensing procedure and data acquisition

A schematic diagram of sensing apparatus is shown in Figure 2. The flow rate of reference gas (dry air) and target gas was precisely metered into the test chamber using two mass flow controllers and a digital flowmeter, which produced a constant mass flow and allowed precise control over the target gas and reference gas mixtures delivered to the sensor. The desired concentration of explosive molecules was achieved by mixing the carrier gas passing over explosive crystals in target source chamber and reference gas at designed flow rate ratios.

Catalytic response and resistivity behavior were measured using a dynamic testing protocol. The catalyst coated microheater was heated to a series of predetermined temperature set points by controlling the electrical resistance of the microheater and correlating to a calibration

curve based on its TCR. Electrical power was used to maintain the temperature while switching from an inert gas to target gas. Change in power was recorded to determine the heat effect associated with the interaction between the explosive molecules and the catalyst. Thermodynamic response was then analyzed by compiling the power differences at different temperature setpoints. Conductivity changes of the catalyst layer were measured simultaneously using a four-point probe method by supplying constant current through metal oxide catalyst while recording voltage applied. The gas delivery system and data acquisition system were computer controlled using LabView software.

Thermodynamic and conductometric response were analyzed by compiling each power signal and resistivity change at different temperature setpoints. After reaching each desired temperature, the sensor was allowed to reach equilibrium for 360 seconds under constant reference gas flow. The target gas was introduced next into the test chamber for 300 seconds, and then switched back to reference gas for another 240 seconds to study the recovery ability of the sensor before the microheater was ramped to the next temperature setpoint. The power change required to maintain the sensor at a particular temperature and resistivity change of semiconductor in presence of target gas were recorded for the entire step. Prior to calculate the sensor response, the reference base line and electrical signal drift were subtracted from the sensor response. Typically, all responses smaller than $\pm 5\%$ were considered background noise, which was due to small variations in the target and inert gas flow rates, drift in the nickel microheaters and other sources of electrical noise. Sensor responses to explosive vapors as a function of target gas concentration were also conducted to study the sensitivity, detection limit, response and recovery time.

3. Results

3.1 Analysis of oxidation state

Oxidation states of catalysts as a function of deposition and post deposition heat treatments were characterized by XPS as shown in Figure 3. Position 1, 2 and 3 represent as annealed surface, approximately 200Å from surface and 600Å from surface of the catalyst, separately. From Figure 3(b), Zn 2p doublets can be observed indicating multiple oxidation states exist at surface of ZnO catalyst due to the annealing processes. Also Zn 2p_{3/2} peaks at position 2 and 3 shift to lower binding energy and appear sharper compared to one at position one, indicating a uniform non-stoichiometric ZnO_{1-x} state. This assumption was confirmed in Figure 3(c) by the disappearance of a ZnO secondary peak at 3s and 3p states and the increase of 3d intensity as a function of sampling position, which verified the transition in oxidation state.

3.2 Explosive sensing characteristics

Figure 4 showed a typical orthogonal signal generated from SnO₂ and ZnO separately in presence of 2, 6-DNT. The sensor was pre-stabilized at 410°C for 15 minutes before data recording. DNT was then introduced into system by 60th second for 360 seconds as shown along the horizontal axis. SnO₂ exhibited the fastest thermodynamic response time of less than 5 seconds whereas its conductometric signal took longest time to reach equilibrium and didn't exhibit clear transition steps when switching gases. However, both thermodynamic and conductometric signal completely recovered to the origin within 5 minutes. Both thermodynamic and conductometric signal of ZnO demonstrated a rapid response time of less than 10 seconds. However, both signals took longer time to reach equilibrium and recover, compared with SnO₂.

The difference of response and recovery time between the two sensing platforms was caused by their sensing mechanism. Thermodynamic platform was measuring the decomposition heat effect which initiated instantly as target gas molecules interact with the surface of catalyst. As new target gas molecules was engaged to decompose, previous molecules had already been depleted. This forms a dynamic equilibrium where reaction rate is the rate-controlling step. Conductometric platform was measuring the charge carrier concentration which was varied by donating or accepting extra charge carriers when target gas adsorbed onto the surface of catalyst and desorbed from the surface. This process also forms a dynamic equilibrium where in this case adsorption rate is the rate-controlling step. Since chemical reaction rate is of magnitude faster than physical adsorption, thermodynamic signal exhibit a faster response and recover time compared with thermodynamic signal.

Orthogonal responses of SnO₂ to 2,6-DNT as a function of DNT vapor concentration at 410°C was shown in Figure 5. Thermodynamic response showed an excellent linear relationship to DNT vapor concentration while conductometric response remained a considerable response magnitude as DNT vapor concentration decreased. Both responses were considered effective and were repeatable when the vapor concentration was diluted into 0.2 ppm.

The conductometric signal of SnO₂ and ZnO to ammonia nitrate, DNT and TATP vapor as a function of temperature is shown in Figure 6. Response magnitude of both catalysts to ammonia nitrate is proportional to temperature at low-mid range and levels off or even decreases. at high temperature range (>350°C), while TATP signal exhibits a steady intensity along all temperature range. 2, 6-DNT shows a similar behavior as TATP but a shallow peak at medium temperature range of 280°C. These differences of response signature were caused by the differences of vapor pressure, functional groups and molecular structures between each explosive

molecule. As a result, all three explosives exhibited their unique orthogonal response signature, which could be used as their characteristic curve in identification of explosives and mitigate false positives.

4 Conclusion

An orthogonal explosive sensing system comprised of two independent sensor platforms was developed and tested. A fast response and recover time was observed in concentration tests, which also demonstrated spare capacity of detection limit in conductometric sensor platform. The sensor output showed a linear relationship to concentration of target vapor concentrations. The experimental results suggested that both sensor platform demonstrated reliable responses to TATP, ammonium nitrate and 2,6-DNT and formed unique signal-temperature curves of each explosive vapor.

References

- [1] K. G. Furton, L. J. Meyers, "The scientific foundation and efficacy of the use of canines as chemical detectors for explosives", *Talanta* 54 (2001) 487.
- [2] S. Singh, "Sensors—An effective approach for the detection of explosives", *Journals of Hazardous Materials* 144 (2007) 15-28
- [3] J. C. Oxley, J. L. Smith, K. Shinde, J. Moran, "Determination of the Vapor Density of Triacetone Triperoxide (TATP) Using A Gas Chromatography Headspace Technique," *Propellants, Explosives, Pyrotechnics*, 30 (2005), 127.
- [4] P. A. Pella, "Measurement of the Vapor Pressure of TNT, 2,4-DNT, 2,6-DNT and EGDN," *Journal of Chemical Thermodynamics*, 1977, 9(4), 301
- [5] B. C. Dionne, D. P. Roundbehrer, E. K. Achter, J. R. Hobbs, D. H. Fine, "Vapor Pressure of Explosives," *Journal of Energetic Materials*, 1986, 4, 447.
- [6] M. W. Todd, R. A. Provencal, T. G. Owano, B. A. Paldus, A. Kachanov, K. L. Vodopyanov, M. Hunter, S. L. Coy, J. I. Steinfeld, J. T. Arnold, "Application of mid-infrared cavity-ringdown spectroscopy to trace explosives vapor detection using a broadly tunable (6-8 μm) optical parametric oscillator", *Applied Physics B*, 75 (2002) 367-376.
- [7] K. J. Albert, D. R. Walt, "High speed fluorescence detection of explosive like vapors", *Analytical Chemistry*, 72 (2000) 1947-1955.
- [8] Z. Takats, I. Cotte-Rodriguez, N. Talaty, H. Chen, R. G. Cooks, "Direct, trace level detection of explosives on ambient surfaces by desorption electrospray ionization mass spectrometry", *Chemical Communications*, 2005, 1950-1952.

- [9] Y. Zhang, X. Ma, S. Zhang, C. Yang, O. Zheng, X. Zhang, "Direct detection of explosives on solid surfaces by low temperature plasma desorption mass spectrometry", *Analyst*, 134 (2009) 176-181.
- [10] M. C. Kemp, "Explosive Detection by Terahertz Spectroscopy- A Bridge Too Far?" *Terahertz Science and Technology, IEEE*, 1 (2011) 282-292.
- [11] M. R. Leahy-Hoppa, M. J. Fitch, R. Osiander, "Terahertz spectroscopy techniques for explosives detection", *Analytical and Bioanalytical Chemistry*, 395 (2009) 247-257.
- [12] I. E. Hayward, T. E. Kirkbride, D. N. Batchelder, R. J. Lacey, "Use of a Fiber Optic Probe for the Detection and Identification of Explosive Materials by Raman Spectroscopy", *Journal of Forensic Sciences*, 40 (1995) 883-334.
- [13] M. Gaft, L. Nagli, "UV gated Raman spectroscopy for standoff detection of explosives", *Optical Materials*, 30 (2008) 1739-1746.
- [14] J. S. Caygilla, F. Davisa, S. P. J. Higson, "Current trends in explosive detection techniques," *Talanta*, 88 (2012) 14-29.
- [15] I. Gazit, J. Terkel, "Explosive detection by sniffer dogs following strenuous physical activity" *Applied Animal Behavior Science*, 81 (2003) 149–161.
- [16] N. Barsan, D. Koziej, U. Weimar, "Metal oxide-based gas sensor research: How to?" *Sensors and Actuators B*, 121 (2007)18-35
- [17] T. Seiyama, A. Kato, K. Fujiishi, M. Nagatani, "A New detector for gaseous components using semiconductive thin films," *Analytical Chemistry*, 34 (1962) 1502-1503.
- [18] J. Barkauskas, "Investigation of conductometric humidity sensors", *Talanta*, 44(1997)1107-1112.
- [19] G. Korotcenkov, B.K. Cho, "Ozone measuring: what can limit application of SnO₂-based conductometric gas sensor?" *Sensors and Actuators B*, 161(2012)28-44.

- [20] S. S. Symanski, S. Bruckenstein, "Conductometric sensor for parts per billion sulfur dioxide determination", *Analytical Chemistry*, 58 (1986) 1771-1777.
- [21] A. Dutta, S. Basu, "Modified metal-insulator-metal (M-I-M) hydrogen gas sensors based on zinc oxide," *Journal of Materials Science: Materials in Electronics*, 6 (1995) 415-418.
- [22] P. Massok, M. Loesch, D. Bertrand, "Comparison for the between two Figaro sensors (TGS 813 and TGS 842) for the detection of methane, in terms of selectivity and long-term stability", *Sensors and Actuators B* 25 (1995) 525-528.
- [23] G. Korotcenkov, B.K. Cho, "Instability of metal oxide based conductometric gas sensors and approaches to stability improvement (short survey)", *Sensors and Actuators B*, 156 (2011) 527-538.
- [24] A. C. Romain, J. Nicolas, "Long term stability of metal oxide-based gas sensors for E-nose environmental applications: an overview", *Sensors and Actuators B* 146 (2010) 502-506.
- [25] I. Sayago, J. Gutierrez, L. Ares, J. I. Robla, M. C. Horrilo, J. Getino, J. Rino, J. A. Agapito, "Long-term reliability of sensors for detection of nitrogen oxides", *Sensors and Actuators B*, 26 (1995) 56-58.
- [26] M. Amani, Y. Chu, K. L. Waterman, C. M. Hurley, M. J. Platek, O. J. Gregory. "Detection of triacetone triperoxide (TATP) using a thermodynamic based gas sensor", *Sensors and Actuators B*, 162(2012)7-13.

Author Biographies

Yun Chu received his B.S. degree in chemistry in Beijing University of Aeronautics and Astronautics in 2008. He is currently working on his Ph.D. in chemical engineering at University of Rhode Island (URI). His research interests include gas sensors, MEMS and catalyst development using nano-materials.

Daniel M. Mallin received his B.S. degree in chemical engineering from URI in 2012. He is currently working on his M.S. degree in chemical engineering at URI. His research interests include gas sensors, MEMS and catalyst development using nano-materials.

Matin Amani received B.S. degrees in electrical and biomedical engineering at URI in 2011, and his B.S. degree in chemical engineering and M.S. degree in electrical engineering in 2012. He is currently working on his Ph.D. in electrical engineering at Oregon State University through the Army Research Laboratory. His research interests include graphene electronics, MIM tunnel diodes, sensors for harsh environments, and gas sensors.

Otto J. Gregory received his B.S. degrees in chemical engineering and ocean engineering and his M.S. degree in chemical engineering from URI, in 1975 and 1977, respectively and his Ph.D. in engineering from Brown University in 1984. He is currently Distinguished Engineering Professor at URI and Director of the URI Sensors and Surface Technology Partnership. Dr. Gregory has published over 80 peer-reviewed journal articles and filed 25 US patents. His work has largely focused on sensors for harsh environments, wide bandgap semiconductors and chemical sensors, and has been funded by the gas turbine engine industry, NASA, DOE, Air Force, NSF and DHS.

List of Figures

Figure 1. Schematic of orthogonal sensor showing the top view (left) and expanded views (right) of the metal oxide catalyst layer (1), nickel electrodes (2), alumina coatings (3-4), nickel microheater (5) and alumina substrate (6).

Figure 2. Apparatus used for TATP, 2,6-DNT and ammonia nitrate detection using orthogonal sensor.

Figure 3. X-ray photoelectron spectra (XPS) results of ZnO catalyst. 3(a) indicates the sampling position in a cross-section diagram of catalyst; Zn 2p states were shown in 3(b) and 3s, 3p and 3d states in 3(c).

Figure 4. Thermodynamic response (blue) and conductometric response (red) to 2, 6-DNT at 410 °C taken simultaneously with SnO₂ (left) and ZnO (right) orthogonal sensor.

Figure 5. Orthogonal response of SnO₂ (where conductometric response is presented in red and thermodynamic response in blue) as a function of 2,6-DNT vapor concentration (black dashed line) at 410°C.

Figure 6. Conductometric response of SnO₂ (left) and ZnO (right) orthogonal sensor to ammonia nitrate (blue), 2,6-DNT (red) and TATP (green) as a function of temperature.

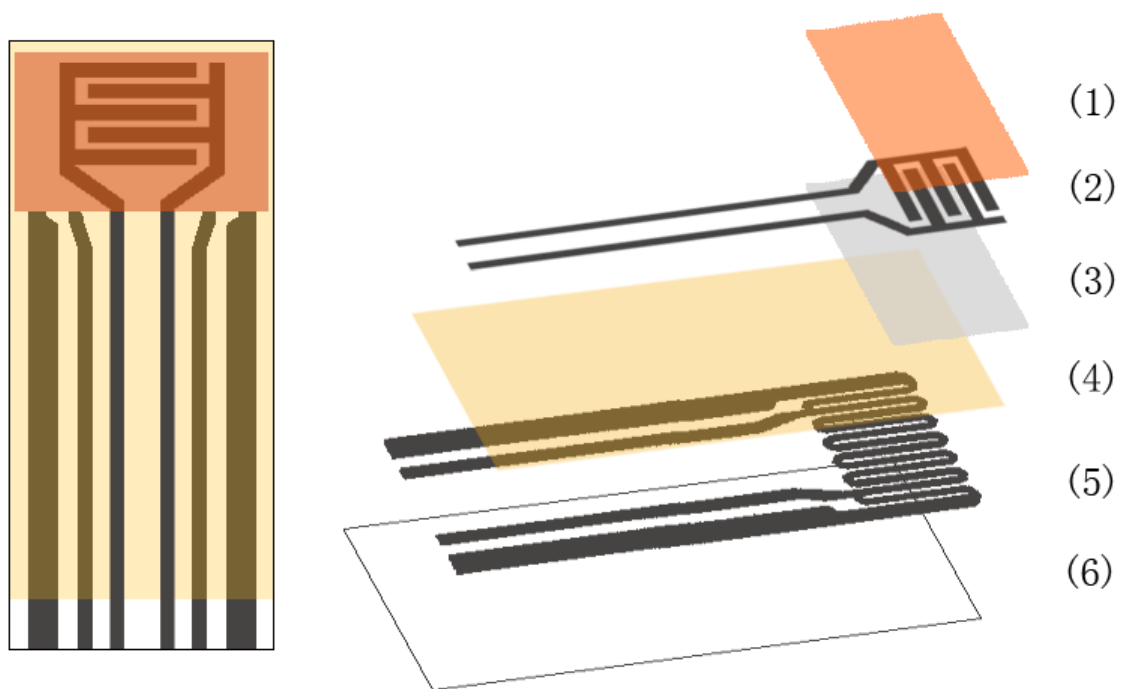


Figure 1. Schematic of orthogonal sensor showing the top view (left) and expanded views (right) of the metal oxide catalyst layer (1), nickel electrodes (2), alumina coatings (3-4), nickel microheater (5) and alumina substrate (6).

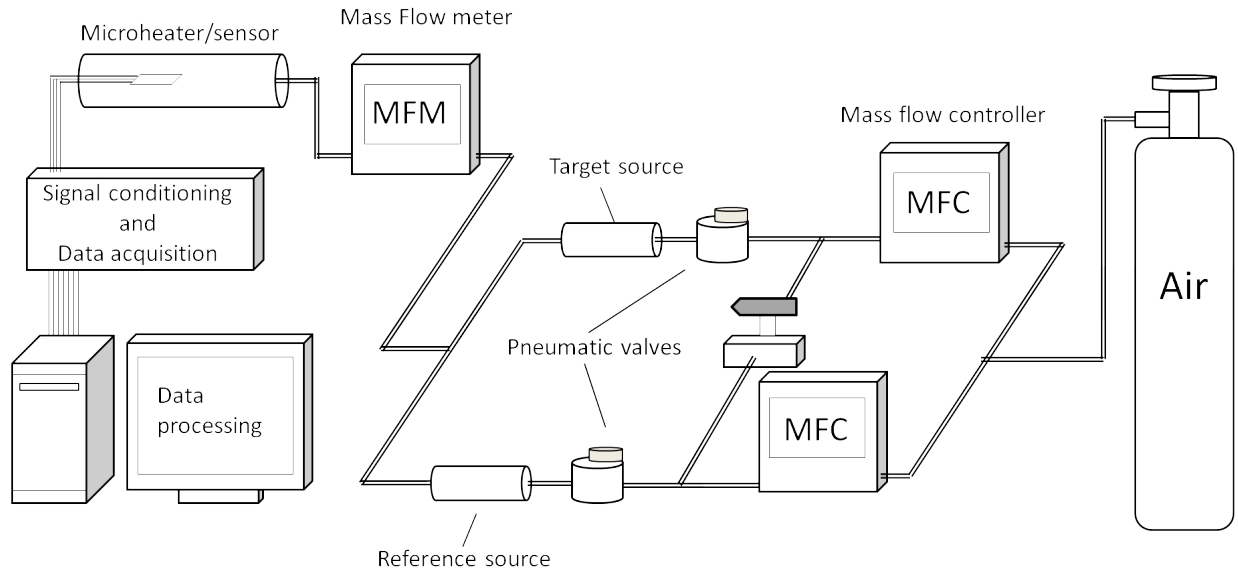


Figure 2. Apparatus used for TATP, 2,6-DNT and ammonia nitrate detection using orthogonal sensor.

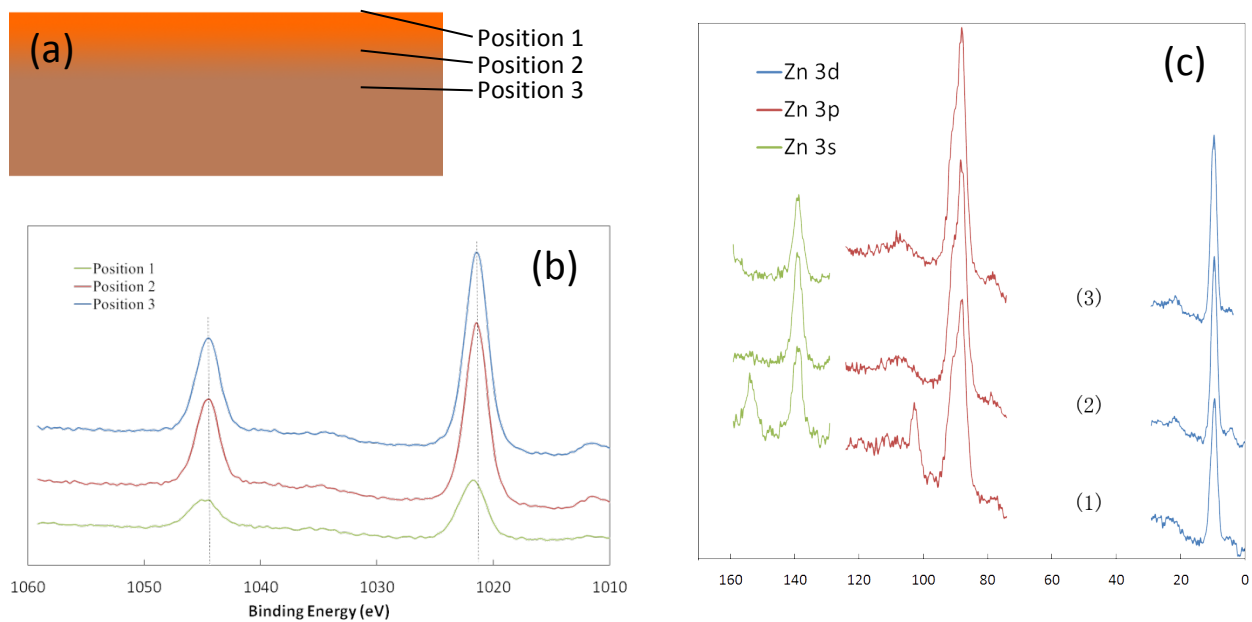


Figure 3. X-ray photoelectron spectra (XPS) results of ZnO catalyst. 3(a) indicates the sampling position in a cross-section diagram of catalyst; Zn 2p states were shown in 3(b) and 3s, 3p and 3d states in 3(c).

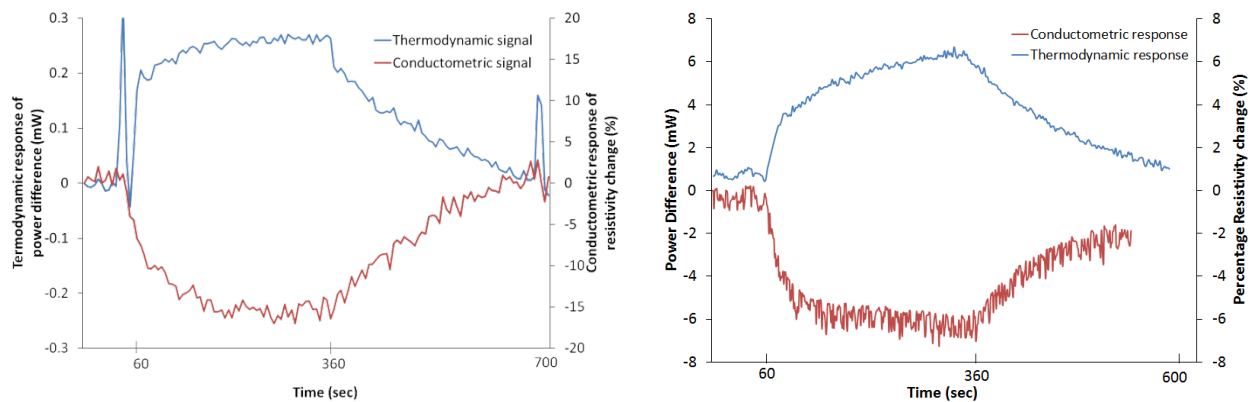


Figure 4. Thermodynamic response (blue) and conductometric response (red) to 2, 6-DNT at 410 °C taken simultaneously with SnO₂ (left) and ZnO (right) orthogonal sensor.

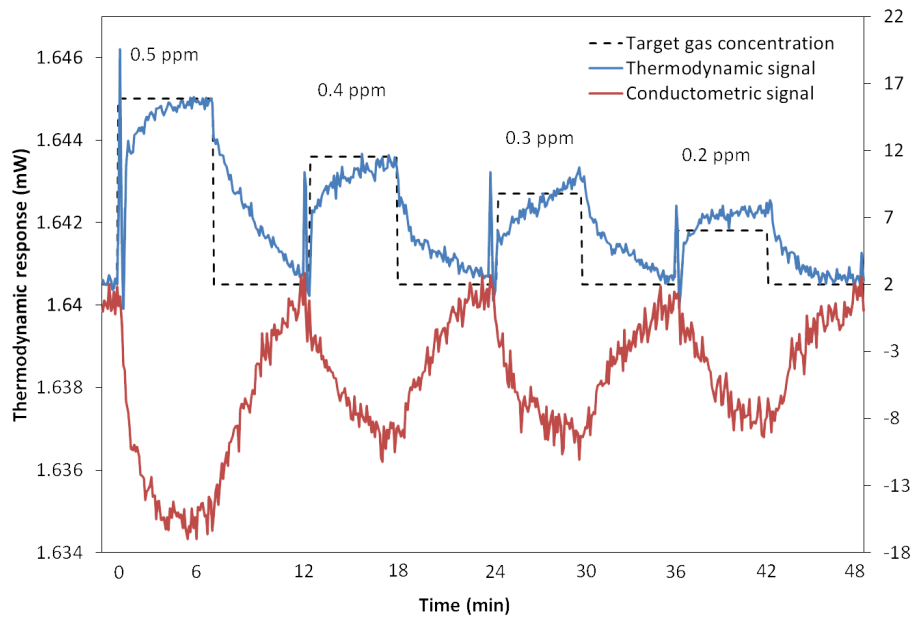


Figure 5. Orthogonal response of SnO₂ (where conductometric response is presented in red and thermodynamic response in blue) as a function of 2,6-DNT vapor concentration (black dashed line) at 410°C.

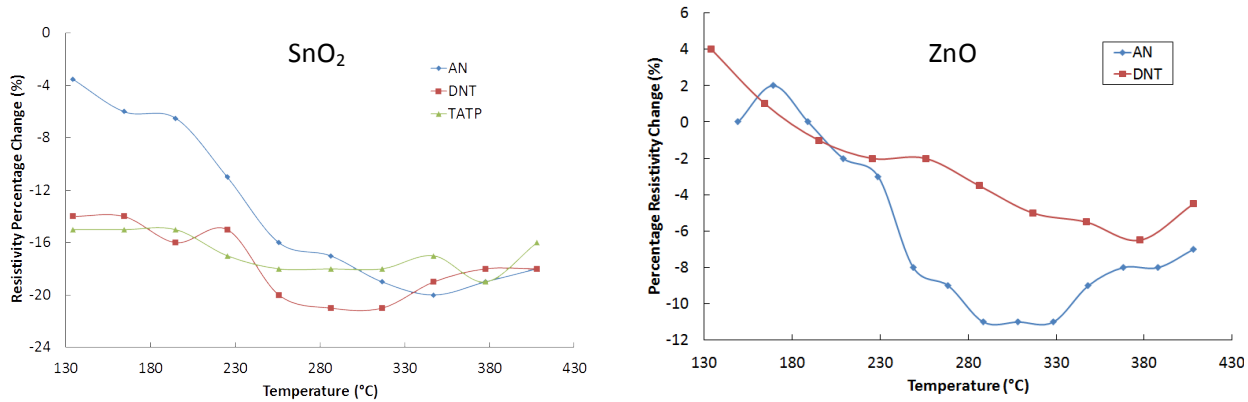


Figure 6. Conductometric response of SnO₂ (left) and ZnO (right) orthogonal sensor to ammonia nitrate (blue), 2,6-DNT (red) and TATP (green) as a function of temperature.

Solution Based Direct Readout SERS Method for Detection of Ultra-Low Levels of Explosives In Complex Matrices

Objective

The overall objective of my research is to use nanoparticles of different shapes as colloidal SERS substrates for a direct readout and solution-based detection of ultra-low levels of different explosives in different matrices

Summary

We have synthesized dogbone shaped gold nanoparticles of two different sizes. The surface plasmon band of the nanoparticles red-shifts with increasing size of the dogbone shaped gold nanoparticles. We have successfully acquired the SERS spectra for nitrobenzenethiol in water and obtained the calibration curve. We have successfully acquired the SERS spectra of nitrobenzenethiol in other complex matrices such as Sprite and hairspray.

Accomplishments

- Successfully synthesized two different sizes of dogbone shaped gold nanoparticles
- Obtained the UV-Visible spectra of the two sizes of dogbone shaped gold nanoparticles
- Acquired the SERS spectra of nitrobenzenethiol in water
- Obtained the calibration curve of nitrobenzenethiol in water
- Acquired the SERS spectra of nitrobenzenethiol in Sprite and hairspray

Details

The dogbone shaped gold nanoparticles is synthesized using the seed-mediated growth method which consists of two steps: preparation of the gold nanoparticle seeds and growth of the seeds in a growth solution. Systematic variation of the concentration of the different components as well as a variety of different synthetic parameters results in gold nanoparticles of different shapes and sizes. We have synthesized two different sizes of dogbone shaped gold nanoparticles. Figure 1 and 2 show the TEM image and size distribution plot for two different sizes of dogbone shaped gold nanoparticles.

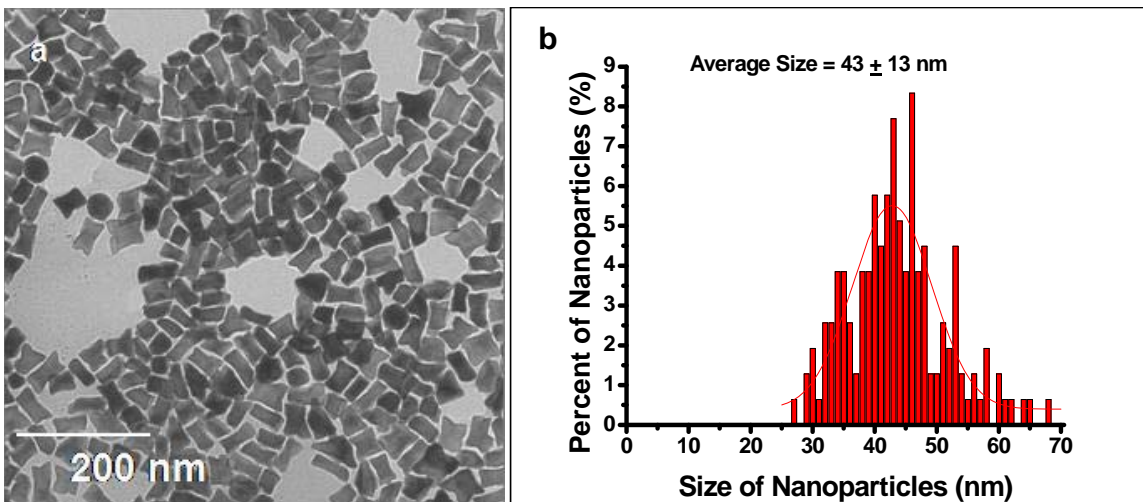


Figure 1. TEM image and size distribution plot of the smaller dogbone shaped gold nanoparticles.

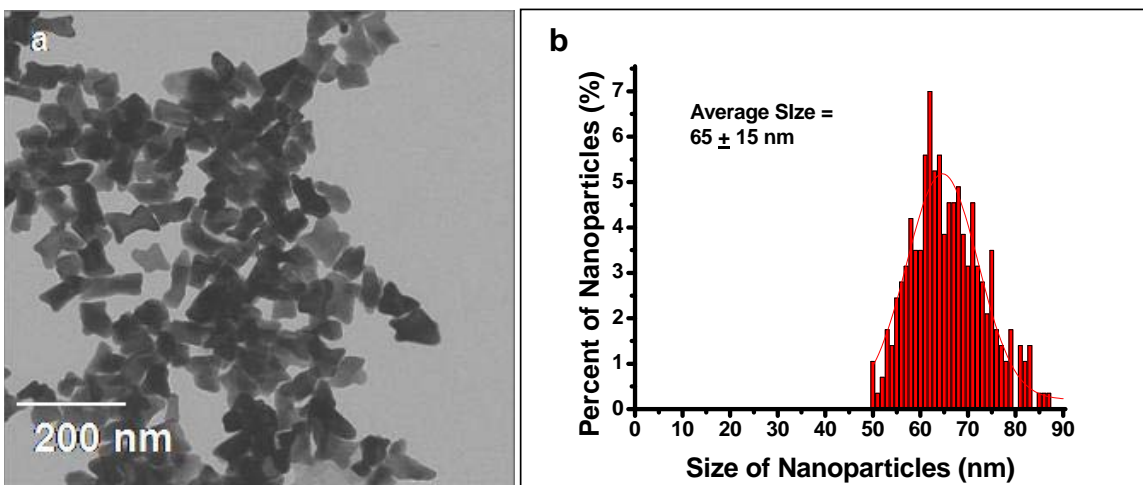


Figure 2. TEM image and size distribution plot of the larger dogbone shaped gold nanoparticles.

We have obtained the UV-Visible spectra of the two different types of dogbone shaped gold nanoparticles. It was observed that the larger dogbone shaped gold nanoparticles result in a higher SPR lambda max which would result in higher SERS enhancements compared to the smaller dogbone shaped gold nanoparticles. Figure 3 and 4 show the UV-Visible spectra of the two types of dogbone shaped gold nanoparticles.

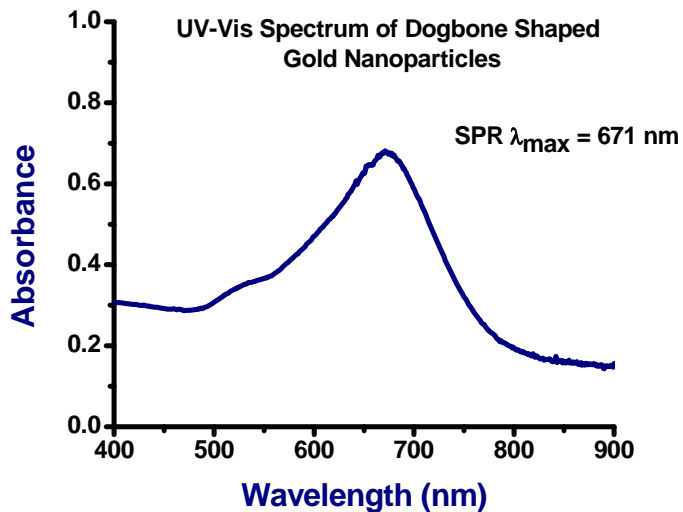


Figure 3. UV-Visible spectra of the smaller dogbone shaped gold nanoparticles

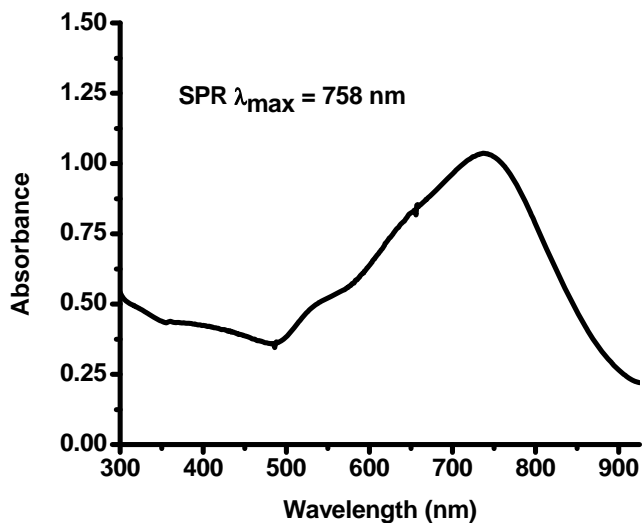


Figure 4. UV-Visible spectra of the larger dogbone shaped gold nanoparticles

We have obtained the SERS spectra of different concentrations of nitrobenzenethiol in water using the larger dogbone shaped gold nanoparticles. Figure 5 shows the SERS spectra of nitrobenzenethiol in water that we have obtained. Figure 6 shows the calibration curve that we have generated for nitrobenzene in water. We also have obtained SERS spectra of nitrobenzenethiol in other complex matrices that would be present in passengers travelling in an airplane. Figure 7 shows the SERS spectra of nitrobenzenethiol in Sprite and Figure 8 shows the SERS spectra of nitrobenzenethiol in hairspray.

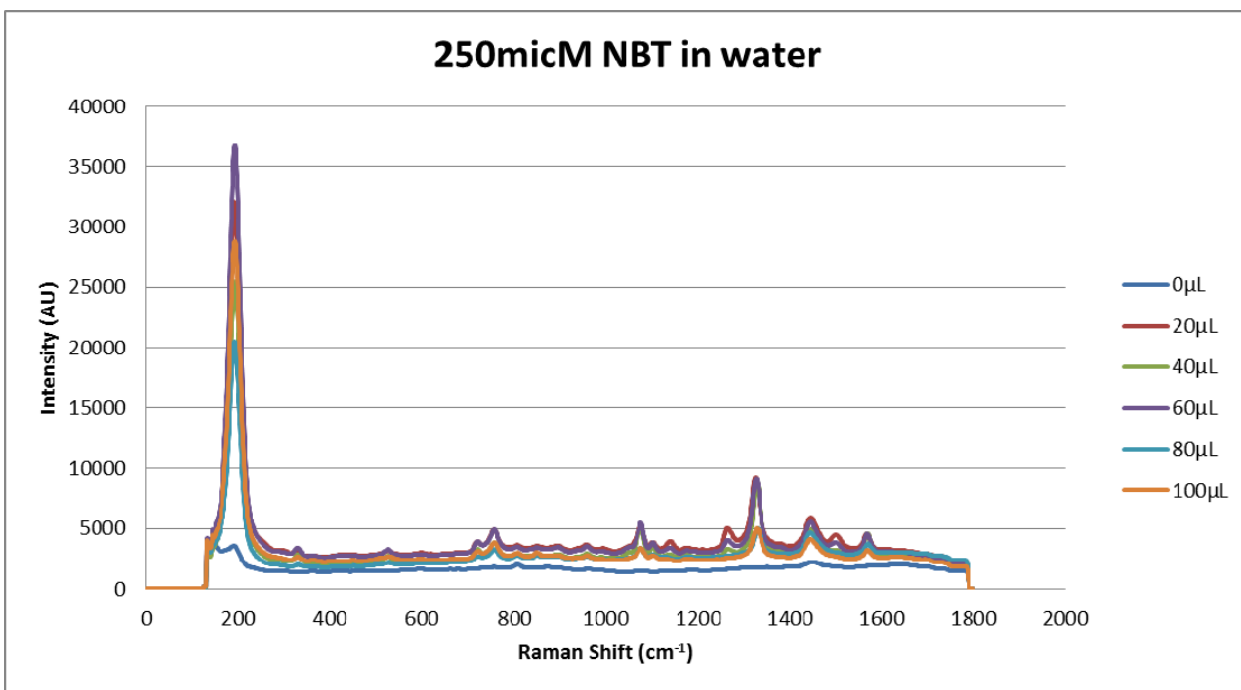


Figure 5. SERS spectra of nitrobenzenethiol in water using the dogbone shaped gold nanoparticles as solution based SERS substrates

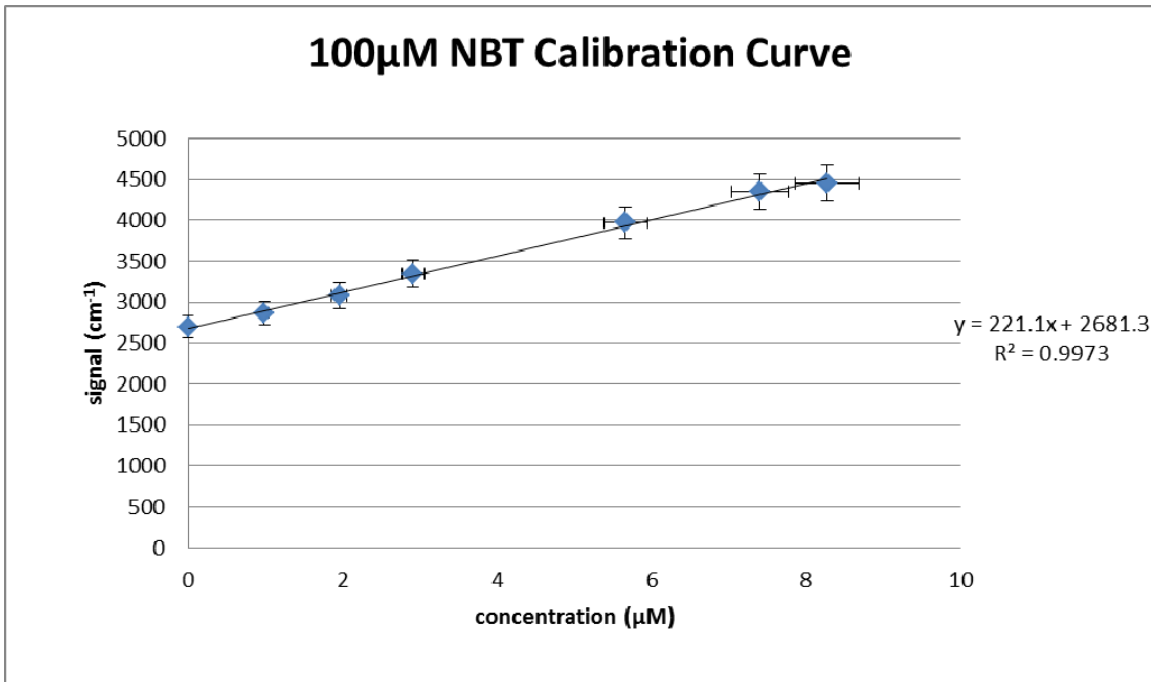


Figure 6. Calibration curve of nitrobenzenethiol in water

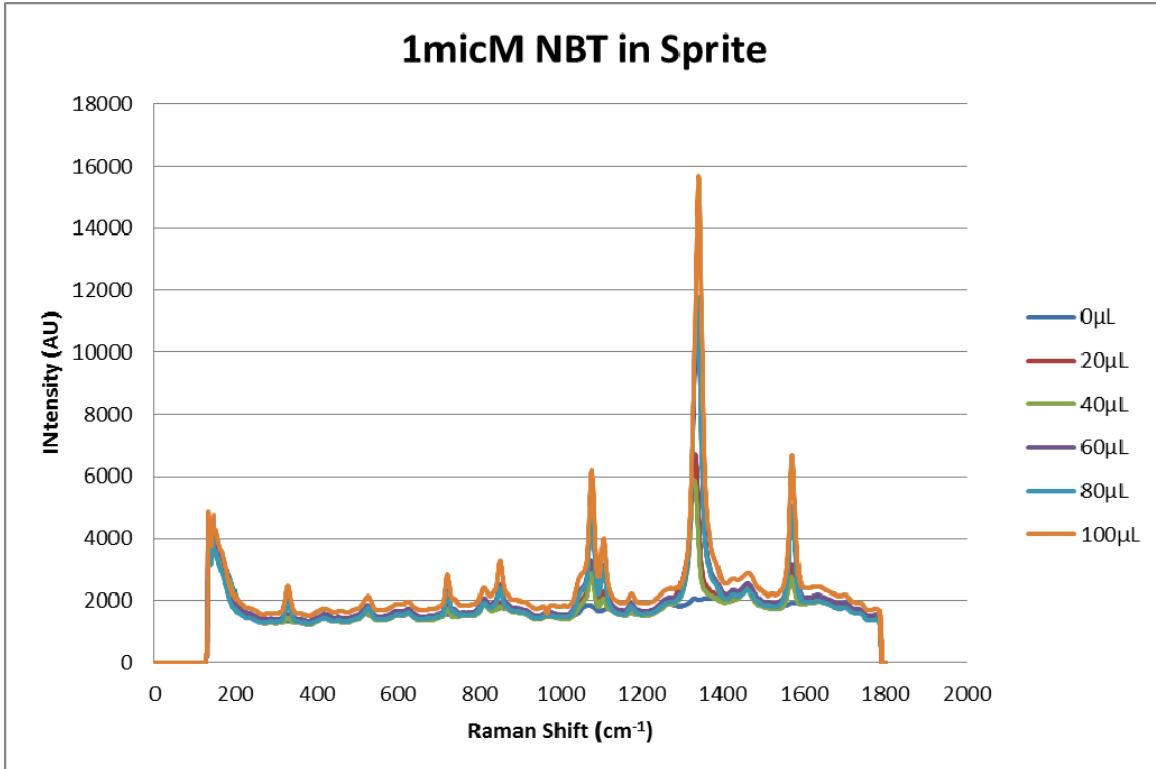


Figure 7. SERS spectra of nitrobenzenethiol in Sprite as the matrix

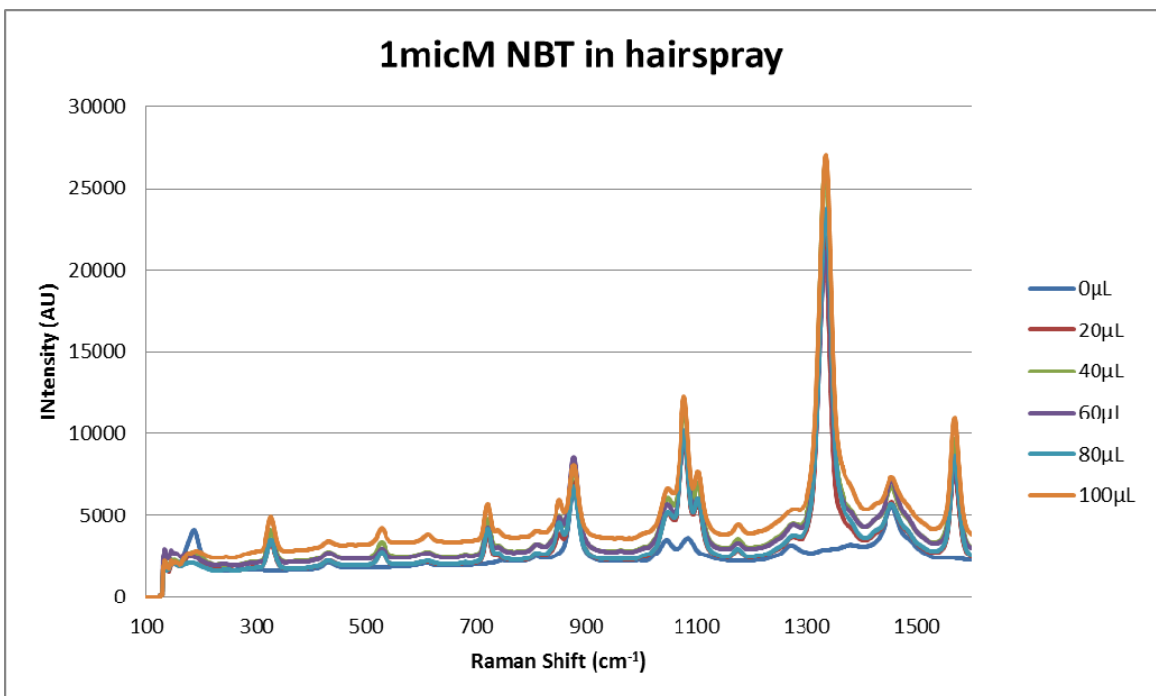


Figure 8. SERS spectra of nitrobenzenethiol in hairspray

Students Supported



Benjamin Saute—Ph.D. student



Allison Alix—undergraduate student

Transition Partners

None.

Publications

1. Saute, B.; Narayanan, R., “Solution-Based Direct Readout Surface Enhanced Raman Spectroscopic (SERS) Detection of Ultra-Low Levels of Thiram with Dogbone-Shaped Gold Nanoparticles”, *Analyst*, **2011**, *136*(3), 527-532.
2. Saute, B.; Premasiri, R., Ziegler, L, Narayanan, R., “Gold Nanorods as Surface Enhanced Raman Spectroscopy Substrates for Sensitive and Selective Detection of

Ultra-Low Levels of Dithiocarbamate Pesticides”, *Analyst*, **2012**, *137(21)*, 5082-5087.

Prsentations

1. URI Explosives Workshop Poster Session, October 7-9, 2009, Kingston, RI, **Poster**, “Metal Nanoparticles of Different Shapes as Colloidal Substrates for Solution-Based SERS Detection of Environmental Pollutants and Explosives”, Benjamin Saute, Nicole Cook, and Radha Narayanan
2. DHS Center Review, March 24-25, 2011, **Poster**, “Nanotechnology for Detection of Ultralow Levels of Explosives”, Benjamin Saute and Radha Narayanan
3. DHS Center Review, April 4-5, 2012, Kingston, RI, **Oral**, “SERS Detection of Explosives with Au Nanoparticles”, Radha Narayanan

Solution-based direct readout surface enhanced Raman spectroscopic (SERS) detection of ultra-low levels of thiram with dogbone shaped gold nanoparticles

Benjamin Saute and Radha Narayanan*

Received 1st August 2010, Accepted 4th November 2010

DOI: 10.1039/c0an00594k

We report the use of two different sizes of dogbone shaped gold nanoparticles as colloidal substrates for surface enhanced Raman spectroscopy (SERS) based detection of ultra-low levels of thiram, a dithiocarbamate fungicide. We demonstrate the ability to use a solution based, direct readout SERS method as a quantitative tool for the detection of ultra-low levels of thiram. The two different sizes of dogbone shaped gold nanoparticles are synthesized by using the seed-mediated growth method and characterized by using UV-visible spectroscopy and transmission electron microscopy (TEM). The smaller dogbone shaped nanoparticles have an average size of 43 ± 13 nm. The larger dogbone shaped gold nanoparticles have an average size of 65 ± 15 nm. The nanoparticle concentration is 1.25×10^{11} nanoparticles per mL for the smaller dogbone shaped gold nanoparticles and is 1.13×10^{11} nanoparticles per mL for the larger dogbone shaped gold nanoparticles. Different concentrations of thiram are allowed to bind to the two different sizes of dogbone shaped gold nanoparticles and the SERS spectra are obtained. From the calibration curve, the limit of detection for thiram is 43.9 ± 6.2 nM when the smaller dogbone shaped gold nanoparticles are used as colloidal SERS substrates. In the case of the larger dogbone shaped gold nanoparticles, the limit of detection for thiram is 11.8 ± 3.2 nM. The lower limit of detection obtained by using the larger dogbone shaped gold nanoparticles as colloidal substrates is due to the lightning rod effect, higher contributions from the electromagnetic enhancement effect, and larger number of surface sites for thiram to bind.

Introduction

Surface-enhanced Raman scattering (SERS) was discovered in 1977 by Van Duyne¹ and by Creighton.² SERS is a phenomenon in which there are greatly enhanced Raman signals when Raman scattering molecules are placed very near or attached onto metal substrates or metal nanoparticles. While of long standing fundamental importance,^{3–6} its potential as a quantitative analytical tool has only recently begun to take place.^{7–10} Some types of quantitative applications of SERS are biological sensing,^{5,11–23} environmental monitoring,^{16,24} trace analysis,²⁴ and explosive and contaminant detection.^{5,24–26} The ability to use SERS as a quantitative analytical tool reflects advances in the ability to reproducibly synthesize and manipulate the size and shape of gold and silver nanoparticles.

The EPA have set maximum concentration limit (MCL) of <1 ng mL⁻¹ for pollutants present in water. As a result, it is necessary to be able to detect ultra-low levels of pesticides, insecticides, fungicides, and other environmental pollutants. SERS has been used for the detection of different types of environmental pollutants.^{27–30} SERS has also been used for the detection of polychlorinated biphenyls (PCBs).^{27–29} Different types of pesticides^{27–34} have also been detected by using SERS. In addition, SERS has been used for the detection of fungicides.^{35–38} It is worth noting that in many of these studies, SERS is used qualitatively for identification of the different pollutants, PCBs,

pesticides and fungicides as well as structural studies on the binding process. In our paper, we use SERS as a quantitative analytical tool for detecting ultra-low levels of thiram, which is a dithiocarbamate fungicide.

SERS has traditionally been conducted with gold and silver substrates as well as colloidal gold and silver nanoparticles. It has been recently shown that using cubic, block, and dogbone shaped gold nanoparticles result in ~ 100 times higher SERS enhancements of 4-mercaptobenzoic acid compared to spherical gold nanoparticles.³⁹ This SERS enhancement has been attributed to the lightning rod effect in which there is greater amount of localized electromagnetic fields at the corners and edges of the nanoparticles.³⁹

We show that we can use two different sizes of dogbone shaped gold nanoparticles as colloidal SERS substrates for quantitative detection of ultralow levels of thiram, which is a dithiocarbamate fungicide. In this paper we demonstrate the ability to use a solution based, direct readout SERS method as a quantitative tool for the detection of ultra-low levels of thiram. In our method, we use two different sizes of dogbone shaped gold nanoparticles as colloidal SERS substrates for a solution based direct readout SERS based detection of ultra-low levels of thiram. Thiram has a disulfide bond which spontaneously breaks upon exposure to the gold nanoparticles and binds to the nanoparticles through the Au–S bond, which is the gold thiolate bond. It was observed that there is a lower limit of detection when the larger dogbone shaped gold nanoparticles are used as colloidal SERS substrates. Different sources that give rise to higher enhancements will also be discussed in the paper.

Department of Chemistry, University of Rhode Island, 51 Lower College Road, Kingston, RI, 02881, USA. E-mail: rnarayanan@chm.uri.edu; Fax: +1 401-874-5072; Tel: +1 401-874-2298

Experimental

Synthesis of two different sizes of dogbone shaped gold nanoparticles

The smaller dogbone shaped gold nanoparticles were synthesized by a slightly modified seed mediated growth method reported previously.^{40–42} This synthesis consists of two distinct steps: preparation of the nanoparticle seeds and preparation of the nanoparticle growth solution. To prepare the seeds, 250 μL of 0.01 M HAuCl_4 is added to a solution containing 4.75 mL deionized water and 5 mL of 0.2 M CTAB. Next, 600 μL of ice-cold 0.01 M NaBH_4 is added to the solution, acting as a rapid reducing agent. The seed solution is allowed to age for approximately one hour. After the seed is aged, the growth solution is prepared. The growth solution consists of 95 mL of 0.1 M CTAB, 800 μL of 0.01 M AgNO_3 , 5 mL of 0.01 M HAuCl_4 , 550 μL of 0.1 M ascorbic acid, and 120 μL of the previously prepared seed solution. After the growth solution is prepared, the jar is left undisturbed overnight to allow the nucleation and growth process to occur. The resulting nanoparticle solution appears navy blue. In the case of the synthesis of larger dogbone shaped nanoparticles, the same type of seed mediated growth method was used and 0.25 M ascorbic acid is used in the growth solution instead of 0.1 M ascorbic acid.

UV-visible spectroscopic characterization

The two different sizes of dogbone shaped gold nanoparticles were characterized by using UV-visible spectroscopy to determine the surface plasmon band λ_{max} of the nanoparticles. The two different sizes of dogbone shaped nanoparticles were filtered by using a 0.22 micron PVDF syringe filter. Two mL of the dogbone shaped gold nanoparticles were placed into a quartz cuvette and placed in the sample holder of the Agilent 8453 diode array UV-visible spectrophotometer. The smaller dogbone shaped nanoparticles have a surface plasmon band λ_{max} of 671 nm and the larger dogbone shaped nanoparticles have a surface plasmon band λ_{max} of 758 nm.

Transmission electron microscopic characterization

TEM characterization allows for determination of the size and shape distributions of our gold nanoparticles. The different sizes of dogbone shaped gold nanoparticles are filtered in the same way as the UV-vis sample preparation. The nanoparticles are then centrifuged twice at 12 000 rpm for 10 minutes each time. This removes excess CTAB that is present in solution. One drop of the filtered and centrifuged nanoparticles is spotted on the TEM grid.

Size distribution analysis

The UTHSCSA ImageTool for Windows—Version 3 image analysis software was used to determine the size distributions of the two different sizes of dogbone shaped gold nanoparticles. The Distance tool in the Analysis pull-down menu is used to measure the number of pixels in the scale bar of the TEM image. Based on the number of pixels for the fixed size associated with the scale bar and measuring the number of pixels for ~ 200

nanoparticles in several TEM images, the size of the dogbone shaped gold nanoparticles can be calculated by dividing the number of pixels for the nanoparticles by the number of pixels of the scale bar and multiplying by the fixed size associated with the scale bar of the TEM image. We then plotted the histogram of % dogbone shaped gold nanoparticles vs. nanoparticle size and obtained a Gaussian fit to the histogram. From the Gaussian fit, we can determine the average size and standard deviation of the dogbone shaped gold nanoparticles.

Surface enhanced Raman spectroscopy (SERS)

The SERS spectra of thiram were obtained by using a Raman Systems R-3000QE Raman spectrometer. The laser excitation wavelength is 785 nm. One mL of the dogbone shaped gold nanoparticles with thiram bound to it is placed in a cuvette. The cuvette is placed in the self-contained dark chamber. The L cap is used since these are solution samples that are being analyzed. A 30 second integration time is used for acquisition of the SERS spectra. The SERS spectra are acquired in the range from 200 to 1800 cm^{-1} .

Results and discussion

There are a few papers in the literature which report the SERS spectra for thiram and discuss the binding modes to silver colloids and gold films.^{43–45} In addition, there has been a paper in which the authors have made assignments of the SERS bands associated with thiram when it is bound to silver colloids.³⁵ We have developed a solution-based direct readout SERS method for quantitative detection of ultralow levels of thiram, which is a dithiocarbamate fungicide. Two different sizes of dogbone shaped gold nanoparticles have been used as colloidal SERS substrates for the detection of thiram.

Synthesis of the two different sizes of dogbone shaped gold nanoparticles

We have synthesized two different sizes of dogbone shaped gold nanoparticles by using the seed-mediated growth method described previously.^{40–42} Fig. 1 shows a representative TEM image of the smaller dogbone shaped gold nanoparticles as well as the size distribution histogram with the average size of the particles. The size distributions were determined by using the ImageTool software. The smaller dogbone shaped gold nanoparticles have an average size of 43 ± 13 nm. The concentration

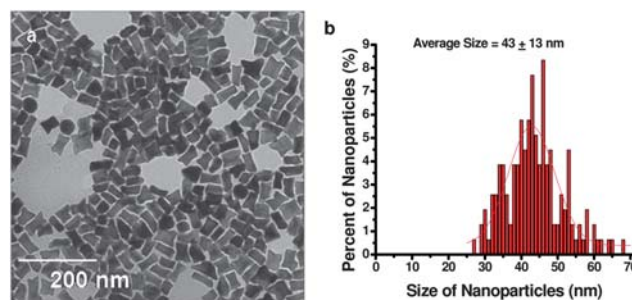


Fig. 1 TEM image of the smaller dogbone shaped gold nanoparticles (a) and size distribution histogram of the nanoparticles (b).

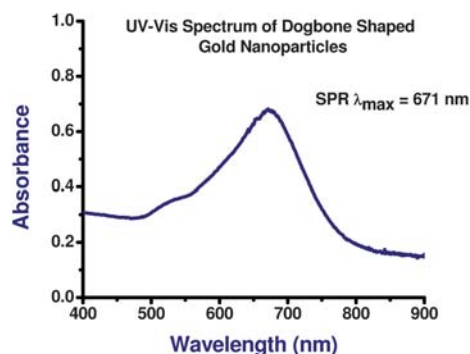


Fig. 2 UV-visible spectrum showing the surface plasmon band λ_{\max} of the smaller dogbone shaped gold nanoparticles.

of the smaller dogbone shaped nanoparticles is calculated to be 1.25×10^{11} nanoparticles per mL. We have also characterized the smaller dogbone shaped gold nanoparticles by using UV-visible spectroscopy to characterize the surface plasmon band λ_{\max} . It can be seen in Fig. 2 that the smaller dogbone shaped gold nanoparticles have a λ_{\max} of 671 nm.

TEM images and size distribution plots were also obtained for the larger dogbone shaped gold nanoparticles. Fig. 3 shows a representative TEM image of the larger dogbone shaped gold nanoparticles as well as the size histogram with the average size of the nanoparticles. The larger dogbone shaped gold nanoparticles have an average size of 65 ± 15 nm. The concentration of the larger dogbone shaped gold nanoparticles is calculated to be 1.13×10^{11} nanoparticles per mL. We have also used UV-visible spectroscopy to obtain the surface plasmon band λ_{\max} . It can be seen in Fig. 4 that the larger dogbone shaped gold nanoparticles have a surface plasmon band λ_{\max} of 758 nm.

The dogbone shaped gold nanoparticles are much more attractive as colloidal SERS substrates compared to the spherical gold nanoparticles since the dogbone shaped gold nanoparticles have surface plasmon bands (671 nm and 758 nm) that are in greater resonance to the laser excitation wavelength. The spherical gold nanoparticles have surface plasmon band in the range between 520 and 560 nm, which are not in good resonance to the laser excitation wavelength. The larger dogbone shaped gold nanoparticles have a surface plasmon band λ_{\max} which is in greater resonance to the laser excitation wavelength than that of the smaller dogbone shaped gold nanoparticles. As a result, we

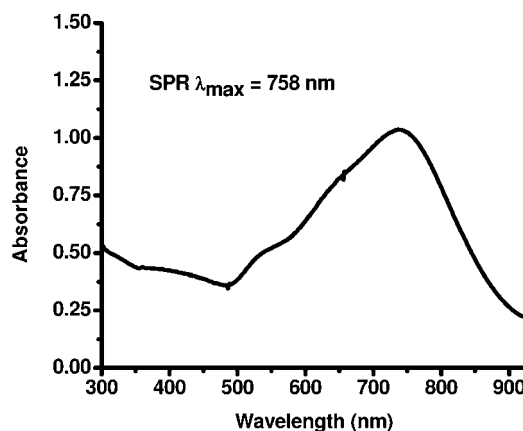


Fig. 4 UV-visible spectrum showing the surface plasmon band λ_{\max} of the larger dogbone shaped gold nanoparticles.

would expect to obtain higher SERS signals using the larger dogbone shaped gold nanoparticles compared to the smaller dogbone shaped gold nanoparticles. This is discussed in more detail later on in the paper.

SERS bands of thiram

There has been a previous study where the SERS spectrum of thiram has been obtained in which the assignments of the different bands has been determined.³⁵ Table 1 shows the SERS peaks that we observe when the thiram is bound to the dogbone

Table 1 Table of the SERS bands associated with thiram^a

SERS band	Assignment ³⁵
339 (vw)	δ (S=CS), δ (CSS)
486 (vw)	δ (CH ₃ NC), ν (C=S)
556 (m)	ν (SS)
755 (vw)	—
928 (m)	ν (CH ₃ N), ν (C=S)
1139 (m)	ρ (CH ₃), ν (CN)
1379 (vs)	δ s(CH ₃), ν (CN)
1444 (m)	δ as(CH ₃)
1508 (m)	ρ (CH ₃), ν (CN)

^a s = strong, w = weak, m = medium, sh = shoulder, v = very, ν = stretching, δ = deformation, ρ = rocking.

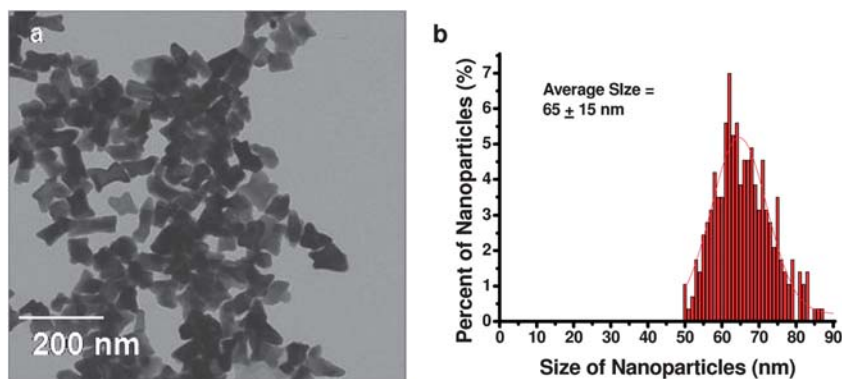


Fig. 3 TEM image of the larger dogbone shaped gold nanoparticles (a) and size distribution histogram of the nanoparticles (b).

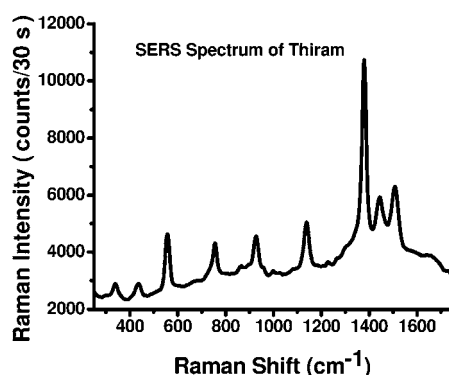


Fig. 5 Example of a SERS spectrum of thiram bound to dogbone shaped gold nanoparticles.

shaped gold nanoparticles and Fig. 5 shows an example of the SERS bands observed when thiram binds to the nanoparticles. There are many peaks in the SERS spectrum of thiram. The strongest peak is at 1379 cm^{-1} which is the CN stretching mode and symmetric CH_3 deformation mode. Since this is the strongest peak in the SERS spectra, this is the band we use for monitoring the SERS intensity as a function of the thiram concentration. The asymmetric CH_3 deformation mode occurs at 1444 cm^{-1} . The CN stretching mode also occurs at 1508 cm^{-1} as well as the rocking CH_3 mode. The CN stretching mode and rocking CH_3 mode also occurs at 1139 cm^{-1} . The stretching CH_3N and $\text{C}=\text{S}$ modes occur at 928 cm^{-1} . The peak at 556 cm^{-1} is associated with the SS stretching mode. The peak at 486 cm^{-1} is due to the CH_3NC deformation and $\text{C}=\text{S}$ stretching modes. The $\text{S}=\text{CS}$ deformation and the CSS deformation occur at 339 cm^{-1} .

SERS calibration curve

Thiram is a dithiocarbamate fungicide which has a disulfide bond. It is known that there is cleavage of the disulfide bond upon exposure to gold nanoparticles or gold substrates.⁴⁶ When the disulfide bond in thiram breaks, it can bind to the dogbone shaped gold nanoparticles *via* the gold thiolate bond. Different concentrations of thiram are added to the dogbone shaped gold nanoparticles and allowed to bind overnight. The SERS spectra were obtained in triplicate sets for different concentrations of thiram that is covalently bound to the smaller dogbone shaped gold nanoparticles. Fig. 6 shows a representative raw SERS spectra as well as the calibration curve of the SERS intensity as a function of the thiram concentration obtained by using the smaller dogbone shaped gold nanoparticles. The error bars represent the standard deviation of the average Raman intensity (counts per 30 s) obtained with three sets of SERS measurement. It can be seen from the linear fit that the SERS measurements are reproducible. The limit of detection (LOD) is determined by first calculating the minimum distinguishable signal which is the average signal of the blank + 3 times the standard deviation of the blank. The minimum distinguishable signal is then plugged into the best-fit equation of the calibration curve to calculate the limit of detection. The limit of detection obtained for thiram by using the smaller dogbone shaped gold nanoparticles is $43.9 \pm 6.2\text{ nM}$.

Fig. 7 shows a representative set of raw SERS spectra from triplicate sets as well as the calibration curve of the SERS

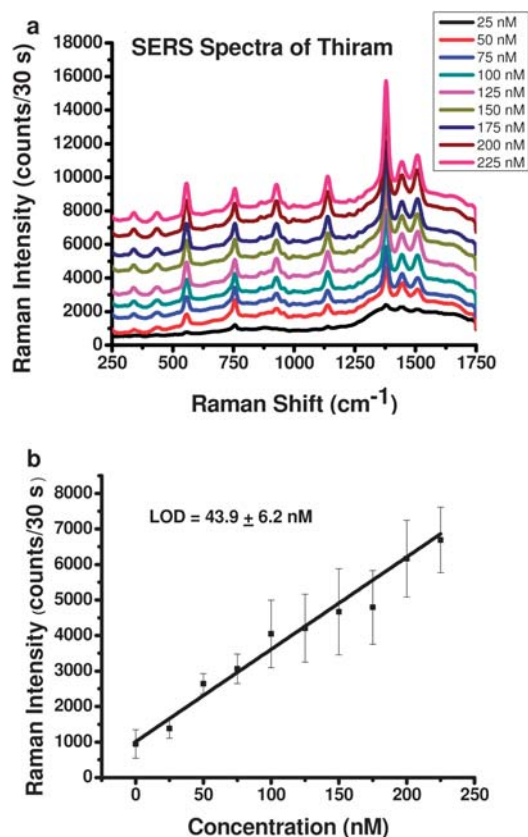


Fig. 6 Raw SERS spectra (a) and SERS calibration curve of SERS intensity with 30 second integration time as a function of the thiram concentration obtained by using the smaller dogbone shaped gold nanoparticles as colloidal SERS substrates (b).

intensity as a function of the thiram concentration obtained by using the larger dogbone shaped gold nanoparticles. The error bars represent the standard deviation of the average Raman intensity (counts per 30 s) obtained with three sets of SERS measurement. It can be seen from the linear fit that the SERS measurements are reproducible. In the case of the larger dogbone shaped Au nanoparticles, the limit of detection is $11.8 \pm 3.2\text{ nM}$. Using the larger dogbone shaped Au nanoparticles as colloidal SERS substrates results in $3.7\times$ lower limit of detection. Several sources that give rise to the higher SERS enhancements are discussed in the next section.

Sources of higher SERS activities

It has been previously shown that cubic, block, and dogbone shaped gold nanoparticles result in $\sim 100\times$ higher SERS enhancements for 4-mercaptobenzoic acid compared to spherical nanoparticles.³⁹ In the case of these nanoparticles, the higher SERS enhancements are attributed to the lightning rod effect. The two types of dogbone shaped gold nanoparticles that we have synthesized have a similar concentration in which the smaller nanoparticles have a concentration of 1.25×10^{11} nanoparticles per mL and the larger dogbone shaped gold nanoparticles have a concentration of 1.13×10^{11} nanoparticles per mL. In the case of our smaller dogbone shaped gold nanoparticles, the source of the SERS enhancement is due to the

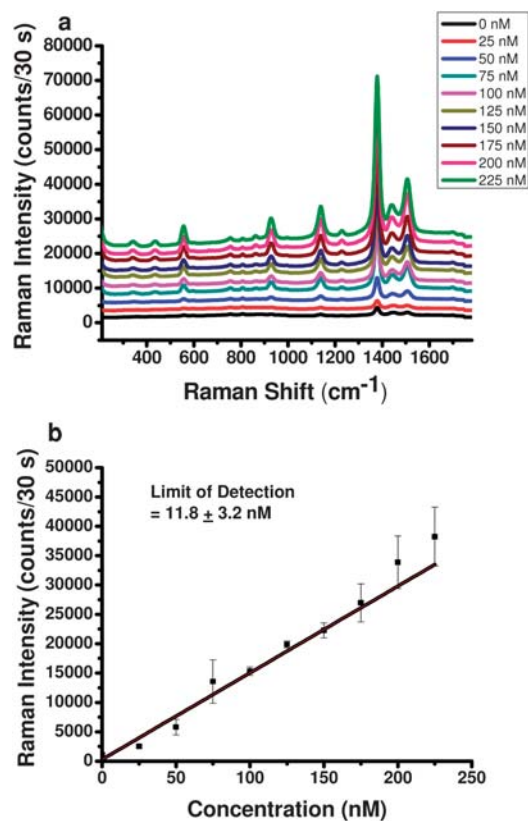


Fig. 7 Raw SERS spectra (a) and SERS calibration curve of SERS intensity with 30 second integration time as a function of the thiram concentration obtained by using the larger dogbone shaped gold nanoparticles as colloidal SERS substrates (b).

lightning rod effect in which there are greater electromagnetic fields at the corners and edges of the nanoparticles. In the case of the larger dogbone shaped gold nanoparticles, in addition to the lightning rod effect, there are much greater contributions from the electromagnetic enhancement effect since the surface plasmon band λ_{max} is 758 nm which is close to the laser excitation wavelength of 785 nm. This gives rise to some of the higher SERS enhancement that is observed. Also, since the surface area of the larger dogbone shaped gold nanoparticles (6276.07 nm²) is larger than the surface area of the smaller dogbone shaped gold nanoparticles (5175.85 nm²) more thiram can bind to the nanoparticle surface resulting in some of the higher enhancements that is observed. Overall, there are higher SERS enhancements and lower limits of detection for thiram observed for the larger dogbone shaped gold nanoparticles. The sources that contribute to the higher SERS enhancements and lower limits of detection observed for the larger dogbone shaped gold nanoparticles are lightning rod effect, surface plasmon band λ_{max} being in much greater resonance to the laser excitation wavelength resulting in greater contributions from the electromagnetic enhancement effect, and more surface sites for thiram to bind to the nanoparticle surface due to a higher surface area.

Conclusions

We have developed a quantitative analytical solution-based direct readout SERS method for detection of thiram which is

a dithiocarbamate fungicide. Two different sizes of dogbone shaped gold nanoparticles are used as colloidal SERS substrates for SERS based detection of thiram. It is observed that using larger dogbone shaped gold nanoparticles results in lower limits of detection compared to using the smaller dogbone shaped gold nanoparticles. The lower limits of detection observed for the larger dogbone shaped gold nanoparticles could be attributed to the lightning rod effect, surface plasmon band λ_{max} being in much greater resonance to the laser excitation wavelength, and more surface sites for thiram to bind. There are higher contributions in the SERS intensities from the electromagnetic enhancement effect.

Acknowledgements

We thank Dr Richard Kingsley at the Electron Microscopy Facility for assistance in acquiring the TEM images. We thank the University of Rhode Island start-up funds, RI-INBRE Pilot Program, as well as the Society for Analytical Chemists of Pittsburgh starter grant for funding of this work.

References

- 1 D. L. Jeanmaire and R. P. VanDuyne, Surface Raman spectro-electrochemistry. Part I. Heterocyclic, aromatic, and aliphatic amines adsorbed on the anodized silver electrode, *J. Electroanal. Chem.*, 1977, **84**, 1.
- 2 M. G. Albrecht and J. A. Creighton, Anomalous intense Raman spectra of pyridine at a silver electrode, *J. Am. Chem. Soc.*, 1977, **99**, 5215.
- 3 M. Moskovits, Surface-enhanced Raman spectroscopy. A brief perspective, *Top. Appl. Phys.*, 2006, **103**, 1.
- 4 J. A. Dieringer, A. D. McFarland, N. C. Shah, D. A. Stuart, A. V. Whitney, C. R. Yonzon, M. A. Young, X. Zhang and R. P. Van Duyne, Surface enhanced Raman spectroscopy: new materials, concepts, characterization tools, and applications, *Faraday Discuss.*, 2006, **132**, 9.
- 5 C. L. Haynes, A. D. McFarland and R. P. VanDuyne, Surface-enhanced Raman spectroscopy, *Anal. Chem.*, 2005, **77**(17), 338A–346A.
- 6 M. Moskovits, Surface-enhanced Raman spectroscopy: a brief retrospective, *J. Raman Spectrosc.*, 2005, **36**(6–7), 485.
- 7 W. E. Smith, K. Faulds and D. Graham, Quantitative surface-enhanced resonance Raman spectroscopy for analysis, *Top. Appl. Phys.*, 2006, **103**, 381.
- 8 C. L. Haynes, C. R. Yonzon, X. Zhang and R. P. VanDuyne, Surface-enhanced Raman sensors: early history and the development of sensors for quantitative biowarefare agent and glucose detection, *J. Raman Spectrosc.*, 2005, **36**(6–7), 471.
- 9 S. C. Pinzaru, I. Pavel, N. Leopold and W. Kiefer, Identification and characterization of pharmaceuticals using Raman and surface-enhanced Raman scattering, *J. Raman Spectrosc.*, 2004, **35**(5), 338.
- 10 T. Vo-Dinh, SERS chemical sensors and biosensors: new tools for environmental and biological analysis, *Sens. Actuators, B*, 1995, **B29**(1–3), 183.
- 11 K. Faulds, W. E. Smith and D. Graham, DNA detection by surface enhanced resonance Raman scattering (SERRS), *Analyst*, 2005, **130**(8), 1125–1131.
- 12 A. E. Grow, L. L. Wood, J. L. Claycomb and P. A. Thompson, New biochip technology for label-free detection of pathogens and their toxins, *J. Microbiol. Methods*, 2003, **53**(2), 221–233.
- 13 K. Kneipp, H. Kneipp, I. Itzkan, R. R. Dasari and M. S. Feld, Surface-enhanced Raman scattering and biophysics, *J. Phys.: Condens. Matter*, 2002, **14**(18), R597–R624.
- 14 A. G. Ryder, Surface enhanced Raman scattering for narcotic detection and applications to chemical biology, *Curr. Opin. Chem. Biol.*, 2005, **9**(5), 489–493.
- 15 Z. Q. Tian, Surface-enhanced Raman spectroscopy: advancements and applications, *J. Raman Spectrosc.*, 2005, **36**(6–7), 466–470.

- 16 T. Vo-Dinh, Surface-enhanced Raman spectroscopy using metallic nanostructures, *TrAC, Trends Anal. Chem.*, 1998, **17**(8–9), 557–582.
- 17 T. Vo-Dinh, D. L. Stokes, in *Surface-Enhanced Raman Scattering (SERS) for Biomedical Diagnostics*, 2003, pp 64/1–64/39.
- 18 T. Vo-Dinh, F. Yan and D. L. Stokes, Plasmonics-based nanostructures for surface-enhanced Raman scattering bioanalysis, *Methods Mol. Biol.*, 2005, **300**, 255–283, Protein Nanotechnology.
- 19 S. Xu, X. Ji, W. Xu, B. Zhao, X. Dou, Y. Bai and Y. Ozaki, Surface-enhanced Raman scattering studies on immunoassay, *J. Biomed. Opt.*, 2005, **10**(3), 031112.
- 20 W. E. Doering, M. E. Piotti, M. J. Natan and R. G. Freeman, *Adv. Mater.*, 2007, **19**(20), 3100.
- 21 R. G. Freeman, W. E. Doering, I. D. Walton, S. G. Penn, G. Davis, F. Wong and M. J. Natan, *Proc. SPIE*, 2005, **5705**, 114.
- 22 S. P. Mulvaney, M. D. Musick, C. D. Keating and M. J. Natan, *Langmuir*, 2003, **19**(11), 4784.
- 23 M. El-Kouedi, C. D. Keating, *Nanobiotechnology*, 2004, p. 429.
- 24 G. A. Baker and D. S. Moore, Progress in plasmonic engineering of surface-enhanced Raman-scattering substrates toward ultra-trace analysis, *Anal. Bioanal. Chem.*, 2005, **382**(8), 1751–1770.
- 25 K. M. Spencer, J. M. Sylvia, P. J. Marren, J. F. Bertone and S. D. Christesen, Surface-enhanced Raman spectroscopy for homeland defense, *Proc. SPIE*, 2004, **5269**, 1–8, Chemical and Biological Point Sensors for Homeland Defense.
- 26 W. E. Smith, P. C. White, C. Rodger and G. Dent, Raman and surface enhanced resonance Raman scattering: applications in forensic science, *Pract. Spectrosc.*, 2001, **28**, 733–748, Handbook of Raman Spectroscopy.
- 27 A. M. Alak and D. Tuan Vo, Surface-enhanced Raman spectrometry of chlorinated pesticides, *Anal. Chim. Acta*, 1988, **206**(1–2), 333–337.
- 28 S. Bonora, M. Di Foggia and M. Iafisco, SERS in the analysis of pesticides (triazinic herbicides), *Chim. Ind.*, 2008, **90**(10), 98–100.
- 29 C. J. Lee, H. J. Kim, M. R. Karim and M. S. Lee, Surface-enhanced Raman spectroscopy of ethephone adsorbed on silver surface, *Bull. Korean Chem. Soc.*, 2006, **27**(4), 545–548.
- 30 D. Lee, S. Lee, G. H. Seong, J. Choo, E. K. Lee, D.-G. Gweon and S. Lee, Quantitative analysis of methyl parathion pesticide in a polydimethylsiloxane microfluidic channel using confocal surface-enhanced Raman spectroscopy, *Appl. Spectrosc.*, 2006, **60**(4), 373–377.
- 31 V. Lee and S. Farquharson, SERS sample vials based on sol-gel process for trace pesticide analysis, *Proc. SPIE*, 2001, **4206**, 140–146, Photonic Detection and Intervention Technologies for Safe Food.
- 32 J. Qiao, G. Zheng and F. Li, Determination of trace pesticide in water by surface enhanced Raman spectroscopy, *Huaxue Tongbao*, 2006, **69**(6), 462–464.
- 33 C. Shende, A. Gift, F. Inscore, P. Maksymiuk and S. Farquharson, Inspection of pesticide residues on food by surface-enhanced raman spectroscopy, *Proc. SPIE*, 2004, **5271**, 28–34, Monitoring Food Safety, Agriculture, and Plant Health.
- 34 C. S. Shende, F. Inscore, A. Gift, P. Maksymiuk and S. Farquharson, Analysis of pesticides on or in fruit by surface-enhanced Raman spectroscopy, *Proc. SPIE*, 2004, **5587**, 170–176, Nondestructive sensing for food Safety, Quality, and Natural Resources.
- 35 J. S. Kang, S. Y. Hwang, C. J. Lee and M. S. Lee, SERS of dithiocarbamate pesticides adsorbed on silver surface; thiram, *Bull. Korean Chem. Soc.*, 2002, **23**(11), 1604–1610.
- 36 M. S. Kim, J. S. Kang, S. B. Park and M. S. Lee, Surface-enhanced Raman spectroscopy of quinomethionate adsorbed on silver colloids, *Bull. Korean Chem. Soc.*, 2003, **24**(5), 633–637.
- 37 S. Sanchez-Cortes, C. Domingo, J. V. Garcia-Ramos and J. A. Aznarez, Surface-enhanced vibrational study (SEIR and SERS) of dithiocarbamate pesticides on gold films, *Langmuir*, 2001, **17**(4), 1157–1162.
- 38 S. Sanchez-Cortes, M. Vasina, O. Francioso and J. V. Garcia-Ramos, Raman and surface-enhanced Raman spectroscopy of dithiocarbamate fungicides, *Vib. Spectrosc.*, 1998, **17**(2), 133–144.
- 39 C. J. Orendorff, A. Gole, T. K. Sau and C. J. Murphy, Surface-enhanced Raman spectroscopy of self-assembled monolayers: sandwich architecture and nanoparticle shape dependence, *Anal. Chem.*, 2005, **77**(10), 3261–3266.
- 40 L. Gou and C. J. Murphy, Fine-tuning the shape of gold nanorods, *Chem. Mater.*, 2005, **17**(14), 3668–3672.
- 41 C. J. Murphy, T. K. Sau, A. M. Gole, C. J. Orendorff, J. Gao, L. Gou, S. E. Hunyadi and T. Li, Anisotropic metal nanoparticles: synthesis, assembly, and optical applications, *J. Phys. Chem. B*, 2005, **109**(29), 13857–13870.
- 42 T. K. Sau and C. J. Murphy, Room temperature, high-yield synthesis of multiple shapes of gold nanoparticles in aqueous solution, *J. Am. Chem. Soc.*, 2004, **126**(28), 8648–8649.
- 43 A. Torreggiani, Z. Jurasekova, M. D'Angelantonio, M. Tamba, J. V. Garcia-Ramos and S. Sanchez-Cortes, Fabrication of Ag nanoparticles by 1-irradiation: application to surface-enhanced Raman spectroscopy of fungicides, *Colloids Surf., A*, 2009, **339**, 60–67.
- 44 S. Sanchez-Cortes, M. Vasina, O. Francioso and J. V. Garcia-Ramos, Raman and surface-enhanced Raman spectroscopy of dithiocarbamate fungicides, *Vib. Spectrosc.*, 1998, **17**, 133–144.
- 45 S. Sanchez-Cortes, C. Domingo, J. V. Garcia-Ramos and J. A. Aznarez, Surface-enhanced vibrational study (SEIR and SERS) of dithiocarbamate pesticides on gold films, *Langmuir*, 2001, **17**, 1157–1162.
- 46 H. A. Biebuyck and G. M. Whitesides, Interchange between monolayers on gold formed from unsymmetrical disulfides and solutions of thiols: evidence for sulfur-sulfur bond cleavage by gold metal, *Langmuir*, 1993, **9**(7), 1766–1770.

Cite this: *Analyst*, 2012, **137**, 5082

www.rsc.org/analyst

PAPER

Gold nanorods as surface enhanced Raman spectroscopy substrates for sensitive and selective detection of ultra-low levels of dithiocarbamate pesticides

Benjamin Saute, Ranjith Premasiri, Lawrence Ziegler and Radha Narayanan*

Received 31st July 2012, Accepted 3rd September 2012

DOI: 10.1039/c2an36047k

We report the use of gold nanorods as solution-based SERS substrates for the detection of ultralow-levels of three different dithiocarbamate fungicides: thiram, ferbam and ziram. Gold nanorods are attractive to use as SERS substrates due to the ability to tune the surface plasmon resonance of the nanoparticles to the laser excitation wavelength of the Raman spectrometer equipped with a 785 nm diode laser. The gold nanorods are synthesized using a seed-mediated growth method and characterized using UV-Visible spectroscopy, zeta potential, and TEM. The gold nanorods have an aspect ratio of 2.19 ± 0.21 and have an average length of 37.81 ± 4.83 nm. SERS spectra are acquired at different concentrations of each fungicide and calibration curves are obtained by monitoring the intensity of the band arising from the $\nu(\text{C-N})$ stretching mode coupled to the symmetric $\delta(\text{CH}_3)$ motion. The limits of detection and limits of quantitation are obtained for each fungicide. The limits of detection are 11.00 ± 0.95 nM, 8.00 ± 1.01 nM, and 4.20 ± 1.22 nM for thiram, ferbam, and ziram respectively. The limits of quantitation are 34.43 ± 0.95 nM, 25.61 ± 1.01 nM, and 12.94 ± 1.22 nM for thiram, ferbam, and ziram respectively. It can be seen that the three different dithiocarbamates can be detected in the low nM range based on the limits of detection that are achieved.

Introduction

Dithiocarbamates are a subclass of carbamate pesticides that are widely used as insecticidal agents on food crops in the US and abroad.¹ Quantitative determination of trace quantities of dithiocarbamates is necessary in order to mitigate potential human exposure *via* pesticide residues left on inadequately washed food items as well as groundwater contamination from agricultural runoff. The focus of this research is on the development of a sensitive and selective sensing platform based on surface enhanced Raman spectroscopy (SERS) in conjunction with multivariate cluster-based data analysis techniques for the sensitive and selective determination of structurally similar dithiocarbamate fungicides, namely, thiram, ferbam and ziram. Data clustering analysis coupled to the output from SERS analysis has been shown to enable the discrimination between similar spectra for bacterial diagnostics²⁻⁴ and as such, the application of the technique to the analysis of thiram, ferbam, and ziram allows for trace-level quantitative determination as well as unambiguous identification of unknown species from comparison with previously constructed SERS libraries.

The frequencies and relative intensities of SERS vibrational bands are sensitive to the nature of the substrate. Gold

nanostructures have been explored extensively as SERS substrates due to their unique size dependent optical and electronic properties.⁵⁻⁸ Of these unique properties of nanoscale gold particles, localized surface plasmon resonance is one of the most widely exploited properties for sensing applications. Excitation of localized surface plasmons (conduction band electrons located at the surface of a nanoparticle) by an external electromagnetic field results in strong light scattering, the appearance of intense absorption bands, and an increase in the magnitude of the local electromagnetic field by several orders of magnitude.⁹ Surface plasmon resonance has been exploited to construct a variety of chemical sensors for analytes including biomolecules,¹⁰ explosives,¹¹ chemical warfare simulants,¹² and environmental pollutants.¹³

Surface enhanced Raman spectroscopy (SERS)¹⁴ is a technique that utilizes the enormous enhancement of the local electric field around a nanoparticle generated by surface plasmon resonance. Since its discovery in 1974,¹⁵ significant research has been conducted toward investigating the mechanism of the enhancement process. It is widely accepted in the literature that SERS operates *via* two distinct mechanisms.¹⁶ The electromagnetic enhancement is considered to be the dominant enhancement process and is a direct result of the amplification of the local electromagnetic field due to localized surface plasmon resonance. The other mechanism underlying SERS enhancement is the chemical enhancement where the excitation of adsorbate electrons creates charge transfer

Department of Chemistry, University of Rhode Island, Kingston, RI, USA, 02881. E-mail: rnarayanan@chm.uri.edu; Fax: +1 401-874-5072; Tel: +1 401-874-2298

states between the metal substrate and an adsorbed molecule.^{17,18} These charge transfer states contribute more strongly to the observed Raman scattering intensity than do adsorbate molecules in their native ground states. The sensitivity afforded by such significant increases in signal intensity makes SERS well suited for a wide variety of analytical applications including detecting anthrax biomarkers,¹² *in vitro*¹⁹ and *in vivo*²⁰ glucose monitoring, monitoring of heterogeneous catalytic reactions²¹ and detection of explosive compounds.²²

One of the major challenges involved with establishing a SERS based analytical method involves fabricating and optimizing the SERS-active substrate. Typically, nanostructures composed of silver and gold are used as SERS substrates due to the fact that these metals can support localized surface plasmon resonance located in the visible region of the spectrum.²³ Although substrates composed of silver nanoparticles are often used in SERS applications,²⁴ gold nanoparticles display several advantageous characteristics including resistance to surface oxidation as well as a red-shifted surface plasmon resonance.²⁵ The shifting of the surface plasmon resonance to lower frequencies is advantageous because it allows for the use of lower energy Raman excitation sources. Lower energy excitation reduces the risk of analyte photobleaching²⁶ and photodegradation²⁷ and allows for the use of inexpensive, commercially available diode laser sources in the red and NIR spectral region.

Previously, our group has demonstrated an analytical method for the quantitative detection of the dithiocarbamate pesticide thiram in solution using SERS.²⁸ In this study, we used dog bone shaped gold nanoparticles stabilized by the cationic surfactant hexadecyltrimethylammonium bromide (CTAB) as SERS substrates. The substrate was characterized by UV-Vis spectroscopy and found to have a surface plasmon resonance located at 671 nm, significantly off-resonance with our instrumental excitation wavelength of 785 nm. These substrates were used to construct a solution based SERS calibration curve and the limit of detection of thiram was calculated to be 43.9 ± 6.2 nM. From this work we hypothesized that utilizing substrates with surface plasmon resonance matching the 785 nm instrumental excitation wavelength should allow for the highest possible enhancement of the local electromagnetic field around the particle and therefore, the lowest possible limits of detection.

Among the various gold nanostructures that have been reported in the literature, gold nanorods are attractive as SERS substrates because the surface plasmon resonance frequency can be tuned as a function of the aspect ratio.²⁹ Typically, gold nanorods are synthesized in the presence of CTAB, a cationic surfactant which assists in the formation of the nanorods by forming micellar templates in solution.³⁰ While the presence of CTAB during nanorod formation is crucial, it remains strongly bound to the surface of the nanorods after synthesis and competes with analytes for binding sites. Reducing the amount of surface bound CTAB is necessary to optimize binding between the analyte and the substrate surface. Cui *et al.*³¹ have published a method for removing surface bound CTAB through treatment of the nanorod solution with HCl at elevated temperatures and we have utilized this method to produce highly active gold nanorod SERS substrates.

In this work, we present the development of an analytical method for the trace analysis of dithiocarbamate pesticides

utilizing SERS. We have expanded the target analytes to include ferbam and ziram, two dithiocarbamate pesticides with structural similarity to thiram. Utilizing CTAB-removed gold nanorods as SERS substrates, we present limits of detection and quantitation for the three target analytes and compare these values to the maximum residue tolerances established by the EPA. In addition to quantitative analysis, we utilize a second derivative based principle component analysis (PCA) clustering technique³² to show how the SERS spectra of these closely related fungicides may be readily identified when compared to a previously generated library (Fig. 1).

Experimental

Gold nanorod synthesis

Gold nanorods were prepared using established synthetic protocols.³³ Briefly, a seed solution is prepared composed of 250 μ L [0.01 M] HAuCl₄, 7.5 mL [0.1 M] CTAB, 1.65 mL H₂O and reduced by the addition of 600 μ L ice-cold [0.01 M] NaBH₄. This solution was allowed to age for one hour while the growth solution is prepared consisting of 47.5 mL [0.1 M] CTAB, 400 μ L [0.01 M] AgNO₃, 2.5 mL [0.01 M] HAuCl₄, and 275 μ L [0.1 M] ascorbic acid. Addition of 60 μ L of the aged seed solution initiates nanorod growth which is allowed to proceed overnight.

The as-synthesized gold nanorods were purified and surface bound CTAB removed using protocols established by Cui *et al.*³¹ Excess CTAB on the surface of the nanorods was removed by centrifuging the nanorod solution at 8000 rpm for 10 minutes, removing the supernatant liquid, and redispersing the collected solid in deionized water. 3.2 μ L [10 M] HCl per mL of particles was added and the solution was heated at 60 °C with stirring for 3 hours to remove surface bound CTAB. The particles were again centrifuged at 8000 rpm for 10 minutes, the supernatant liquid removed, and the remaining solid was redispersed in deionized water.

Characterization of HCl-treated gold nanorods

UV-Vis absorption measurements were acquired using an Agilent 8453 spectrophotometer in plastic cuvettes with 1 cm path length. A Malvern Zetasizer Nano series dynamic light scattering instrument in a dip cell configuration with a plastic cuvette was used to obtain zeta potential measurements. Transmission electron microscopy was performed using a JEOL JEM-2100 TEM operating at 200 kV at 40 000 \times magnification.

SERS sample preparation and instrumentation

One mL of the centrifuged HCl-treated gold nanorod solution was used as the SERS substrate. A known quantity of 10 μ M

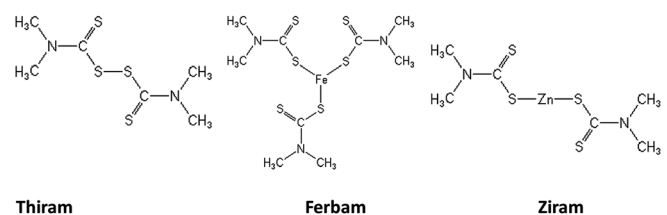


Fig. 1 Chemical structures of dithiocarbamate pesticides analyzed.

analyte stock solution in acetonitrile was added to the substrate and the system was mixed for one hour to allow binding between the analyte and substrate. After binding, SERS measurements were acquired using a Raman Systems R-3000QE system equipped with a 785 nm diode laser excitation source. The excitation light is delivered by a fiber optic probe equipped with a fiber Bragg grating for wavelength isolation. The same fiber optic probe is used to collect the Raman scattered light which is directed to an ultra high sensitive dispersive grating spectrometer and focused on a cooled back-thinned 2D CCD array detector.

“Barcode” principle component analysis

The PCA approach employed here to uniquely distinguish and identify the SERS spectra of these three fungicides that exhibit very similar SERS spectra was previously developed for the detection and identification of vegetative bacterial cells and has been shown to result in enhanced specificity relative to more standard PCA treatments.¹⁸ Briefly, the observed SERS spectra are Fourier filtered to remove the high frequency noise. The normalized filtered SERS spectra are converted to a barcode, *i.e.* a series of zeros and ones, based on the sign of the second derivative of the SERS spectrum as a function of Raman frequency. A minimum value, typically at $\sim 10\%$ of the maximum second derivative value is used as a threshold for the zero (one) assignment. These so-called barcodes are the inputs to a PCA treatment that is carried out with Matlab software routines. The clusters that result from this barcode PCA approach result in improved effective reproducibility and specificity. Identification results from group membership in a barcode PCA cluster. This procedure minimizes background variability while maximizing the more robust spectral features, regions of peaks and valleys, in the observed vibrational spectra.¹⁸

Results and discussion

The main focus of this research was to utilize gold nanorod substrates for the investigation of the limits of detection and quantitation of three structurally similar dithiocarbamate pesticides in solution. Upon synthesis, the gold nanorod substrate was subjected to treatment with HCl at 60 °C in order to remove as

much surface bound CTAB as possible. In order to assess the effectiveness of CTAB removal, zeta potential measurements were made both before and after HCl treatment. Zeta potential can be used to qualitatively assess the stability of the nanoparticle solution by measuring the surface charge on the particle.³⁴ Zeta potential values of ± 40 mV indicate that there is sufficient charge on the surface of the particle to ensure that the solution does not experience aggregation. The value of the zeta potential for the gold nanorod solution was 43 mV immediately following synthesis, indicative of a highly stable substrate solution and 33.4 mV immediately following HCl treatment. This decrease in zeta potential indicates that the overall stability of the substrate solution decreased as a result of HCl treatment and that this decrease in substrate solution stability suggests that there was a decrease in the amount of stabilizing CTAB on the surface of the particle. The decrease in the amount of CTAB present on the particle surface was not sufficient to cause particle aggregation, and the particles remained stable over the course of several days. A decrease in the amount of surface bound CTAB increases the number of free binding sites on the substrate which serves to increase the sensitivity of the SERS method.

Fig. 2 is a TEM image showing the size and shape of the synthesized gold nanorods. The synthesis is successful in producing the desired nanorod shape in high yields with minimal spherical impurities. From this TEM image, we determine the size distribution to be Gaussian with an average nanorod length

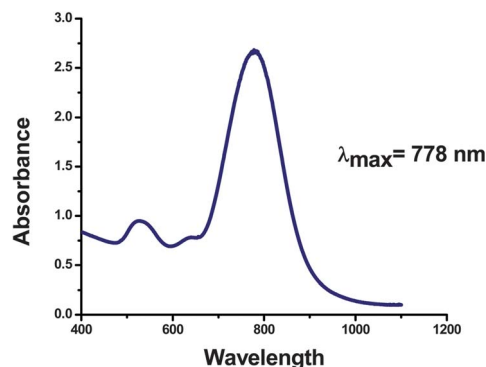


Fig. 3 UV-Vis absorption spectrum of HCl-treated gold nanorods.

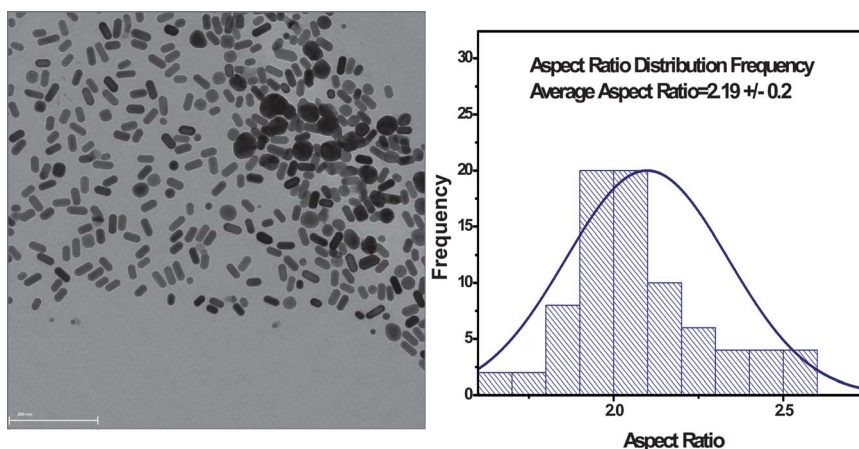


Fig. 2 TEM micrograph and size distribution of gold nanorods.

along the longitudinal axis of 37.81 ± 4.83 nm. Additionally, the aspect ratio is calculated to be 2.19 ± 0.21 . The length of the longitudinal axis is an important parameter when characterizing the gold nanorod substrate because of the sensitivity of the surface plasmon resonance to the size and shape of the substrate. The ability to tune this resonance is paramount to high SERS intensity and, as such, is one of the most important characteristics of an effective SERS substrate.

As can be seen in Fig. 3, the surface plasmon resonance of the synthesized gold nanorod substrate displays two absorption

features. The strong feature centered at 778 nm is due to the resonant propagation of surface plasmons along the longitudinal axis and is highly tunable with the substrate aspect ratio. The weaker absorption feature centered around 540 nm is characteristic of surface plasmons propagating along the transverse axis as well as spherical gold nanoparticle impurities. The Raman spectrometer utilized in this research is equipped with a 785 nm excitation source and as such, it is desirable to synthesize a substrate with surface plasmon resonance located as close as possible to the instrumental excitation wavelength. This ensures

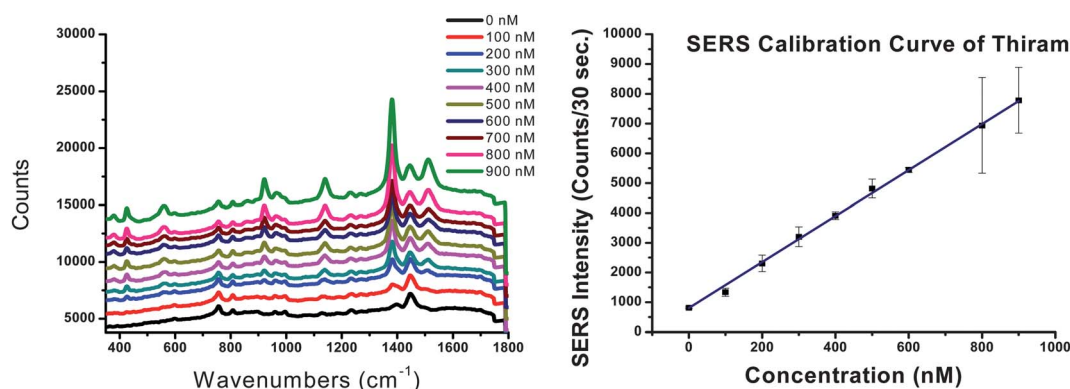


Fig. 4 Surface enhanced Raman spectrum of thiram and calibration curve of SERS intensity vs. concentration (nM). Calibration curve error bars represent the standard deviation of three identical measurements.

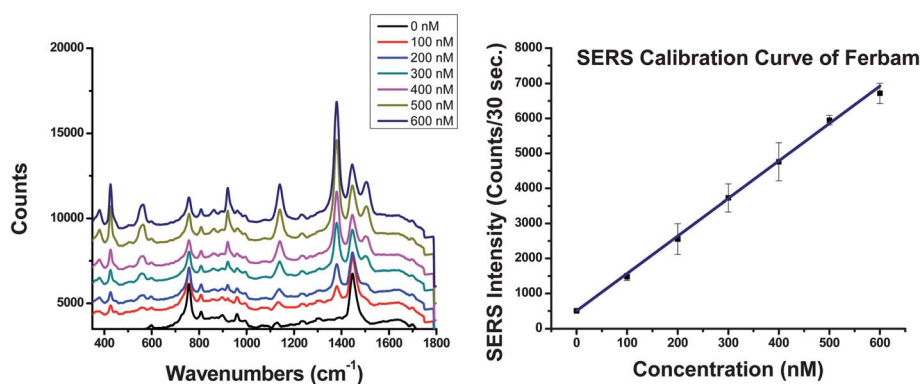


Fig. 5 SERS spectrum of ferbam and corresponding calibration curve. Calibration curve error bars represent the standard deviation of three identical measurements.

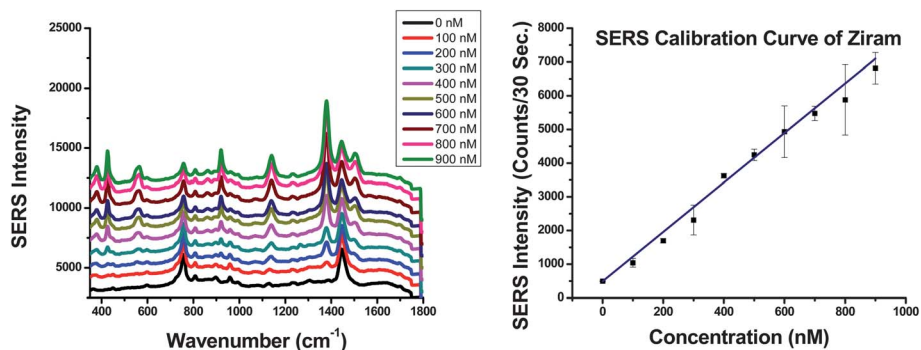


Fig. 6 SERS spectrum of ziram and corresponding calibration curve. Calibration curve error bars represent the standard deviation of three identical measurements.

Table 1 Analytical figures of merit for the quantitative SERS detection of thiram, ferbam, and ziram

Fungicide	R^2	Limit of detection	Limit of quantitation	EPA tolerance
Thiram	0.99872	11.00 ± 0.95 nM	34.43 ± 0.95 nM	16.6 μ M
Ferbam	0.99893	8.00 ± 1.01 nM	25.61 ± 1.01 nM	9.6 μ M
Ziram	0.99073	4.20 ± 1.22 nM	12.94 ± 1.22 nM	22.9 μ M

that conditions for surface plasmon resonance are fulfilled for the maximum number of particles and maximizes the magnitude of the local electric field near the surface of the particle responsible for the SERS effect. Optimizing the surface plasmon resonance of the substrate to the instrumental excitation energy should maximize the observed SERS intensity and afford the lowest detection limits for our analytes of interest. In addition to the surface plasmon resonance location of 778 nm, the UV-Vis absorption spectrum in Fig. 3 shows a narrow absorption band indicating a highly monodisperse substrate morphology.

Fig. 4 shows raw SERS spectra of different concentrations of thiram and the linear calibration curve constructed by monitoring the intensity of the strong 1377 cm^{-1} spectral feature as a function of analyte concentration. An in-depth analysis and assignment of the SERS bands of thiram and ziram adsorbed onto gold and silver colloidal films has been previously reported by Sanchez-Cortes *et al.*³⁵ The monitored band at 1377 cm^{-1} is likely due to the $\nu(\text{C-N})$ stretching coupled to the symmetric $\delta(\text{CH}_3)$ motion and was chosen as the calibration band due to its strong intensity. Fig. 4 shows the SERS spectra (A) and calibration curve (B) obtained for thiram. Similarly, the SERS spectra and calibration curve of ferbam and ziram are shown in Figs. 5 and 6 respectively. Superficially, the spectra for the three dithiocarbamate pesticide analytes show little difference due to their structural similarity and lead to the inference that the orientation of the analyte molecule on the gold nanorod surface is similar for all three pesticides. A 1998 study by Sanchez-Cortes *et al.*³⁶ proposes that upon exposure to a silver nanoparticle sol substrate, spontaneous cleavage of the disulfide bond of thiram occurs producing a dimethyldithiocarbamate ion which assembles onto the substrate surface in a bidentate configuration. Similarly, ferbam and ziram undergo spontaneous cleavage of their metal-sulfur bond to produce the dimethyldithiocarbamate ion which then assembles on the substrate surface. Because these degradation processes produce identical dimethyldithiocarbamate ions, the SERS spectra for the three compounds appear very similar. Any differences in the spectra are assumed to be due to non-degraded analyte molecules adsorbing onto the substrate surface in a monodentate configuration.

Calibration curves were constructed by monitoring the intensity of the spectral feature located at 1377 cm^{-1} as a function of analyte concentration. In order to correct for variations in instrumental noise, the background signal at 1048 cm^{-1} was subtracted from each spectrum. The background-corrected intensity at 1377 cm^{-1} was plotted against the analyte concentration at a minimum of 7 different analyte concentration values. Each point on the calibration curve represents the average value of three identical measurements with error bars representing the standard deviation for each set of measurements.

Table 1 displays calculated limits of detection, limits of quantitation, the correlation coefficient (R^2) for each calibration

curve, and the maximum residue tolerance of each pesticide determined by the US Environmental Protection Agency.³⁷ Limits of detection are calculated by first determining the minimum distinguishable signal using the following expression:

$$S_m = \overline{S_{bl}} + k_{sbl}$$

where S_m is the minimum distinguishable signal, S_{bl} is the Raman signal generated by a blank measurement of the nanorod

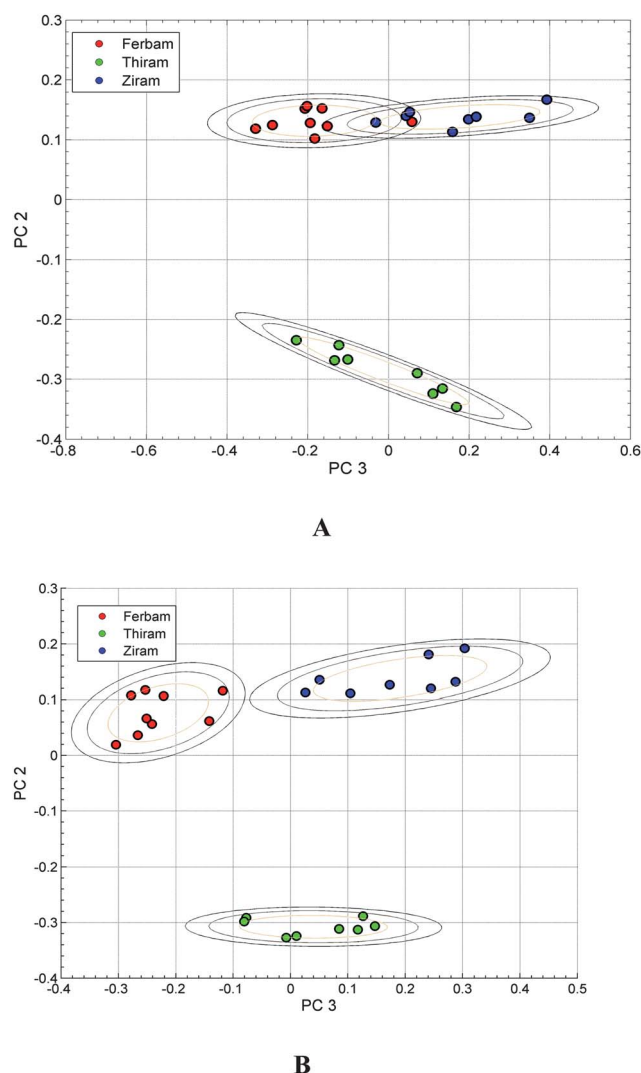


Fig. 7 (A) Principle component analysis (PCA) plot (PC2 vs. PC3) resulting from SERS spectra of ferbam, thiram and ziram in the concentration range of 700–900 nM, (B) analogous PCA 2D plot resulting from SERS spectra of ferbam, thiram and ziram in the concentration range of 700–900 nM based on the second derivative barcode analysis procedure.¹⁸ 2D contours correspond to successive standard deviations for each cluster distribution.

substrate in the absence of the analyte at 1377 cm^{-1} , k is the proportionality constant, and s_{bl} is the standard deviation of k blank measurements. In the case of the limit of detection, the k value is 3, and in the case of the limit of quantitation, the k value is 10. The concentration value is determined by substituting the minimum distinguishable signal to the best fit equation of the calibration curve to determine the limits of detection.

In addition to the sensitivity provided by this SERS approach, fungicide specificity for these three closely related compounds can also be attained by exploiting multivariate data analysis techniques. The results of a principle components analysis (PCA) for SERS spectra of ziram, ferbam, and thiram are shown in Fig. 7A. Three SERS spectra at 700 nM, 800 nM, and 900 nM for each of these three compounds were the input vectors for this PCA analysis. PC2 vs. PC3 is plotted in this figure. These PCs are found to exhibit the most significant variance for a two dimensional plot. The contour rings are the corresponding two dimensional standard deviations for each of the cluster distributions. These fungicide concentrations for the samples analyzed here are all below the minimum current EPA tolerances. Although good clustering is evident in this figure, the clusters corresponding to ziram and ferbam are partially overlapping (Fig. 7A) and thus this spectra based PCA approach could not unequivocally distinguish these two compounds. However, when the inputs to the PCA analysis are the barcodes based on the sign of the second derivatives of the SERS spectra,¹⁸ all three compounds may be unequivocally distinguished based on the separation of their PCA clusters as shown in Fig. 7B. As seen in this figure, the barcode treatment results in ziram and ferbam clusters separating, as judged by the 3 standard deviation contours, in contrast to the spectra inputs (Fig. 7A), at least for this sample dataset. Thus, in addition to high sensitivity, multivariate data analysis can be used to distinguish which of these fungicides are present at environmentally relevant concentrations.

Conclusion

We report a solution-based analytical method for the quantitative determination of three dithiocarbamate pesticides (thiram, ferbam and ziram) in solution utilizing surface enhanced Raman spectroscopy (SERS). Gold nanorods were chosen as SERS substrates due to the ability to easily tune the localized surface plasmon resonance to be in resonance with the instrumental excitation frequency. This solution-based SERS method is highly sensitive with limits of detection in the low ppb range for each investigated fungicide and specificity can be provided by multivariate data analysis techniques. The demonstrated sensitivity coupled with molecule specific structural information afforded by Raman spectroscopy makes this an ideal method for the analysis of dithiocarbamate fungicides.

References

- 1 EPA, U. S., U. S. Government Printing Office, Washington D.C., 2001.
- 2 I. Patel, W. Premasiri, D. Moir and L. Ziegler, *J. Raman Spectrosc.*, 2008, **39**, 1660.
- 3 R. Jarvis, A. Brooker and R. Goodacre, *Faraday Discuss.*, 2006, **132**, 281.
- 4 R. Jarvis and R. Goodacre, *Anal. Chem.*, 2004, **76**, 40.
- 5 W. Rechberger, A. Hohenau, A. Leitner, J. Krenn, B. Lamprecht and F. Ausnegg, *Opt. Commun.*, 2003, **220**, 137.
- 6 P. Jain, K. Lee, I. El-Sayed and M. El-Sayed, *J. Phys. Chem. B*, 2006, **110**, 7238.
- 7 D. Hernandez-Santos, M. Gonzalez-Garcia and A. Costa-Garcia, *Electroanalysis*, 2002, **14**, 1225.
- 8 M. Castaneda, S. Alegret and A. Merkoci, *Electroanalysis*, 2007, **19**, 743.
- 9 E. Hutter and J. Fendler, *Adv. Mater.*, 2004, **16**, 1685.
- 10 M. Mrksich, G. Sigal and G. Whitesides, *Langmuir*, 1995, **11**, 4383.
- 11 M. Riskin, R. Tel-Vered, O. Lioubashevski and I. Willner, *J. Am. Chem. Soc.*, 2009, **131**, 7368.
- 12 X. Zhang, M. Young, O. Lyandres and R. Van Duyne, *J. Am. Chem. Soc.*, 2005, **127**, 4484.
- 13 K. Gobi, M. Sasaki, Y. Shoyama and N. Mirua, *Sens. Actuators, B*, 2003, **89**, 137.
- 14 P. L. Stiles, J. A. Dieringer, N. C. Shah and R. P. Van Duyne, *Annu. Rev. Anal. Chem.*, 2008, **1**, 601.
- 15 J. MacQuillan, J. Jendra and P. Fleischmann, *Chem. Phys. Lett.*, 1974, **26**, 163.
- 16 K. Kelly, E. Coronado, L. Zhao and G. Schatz, *J. Phys. Chem. B*, 1987, **107**, 668.
- 17 S. Morton and L. Jensen, *J. Am. Chem. Soc.*, 2009, **131**, 4090.
- 18 S. Saikin, Y. Chu, D. Rappoport, K. Crozier and A. Aspuru-Guzik, *J. Phys. Chem. Lett.*, 2010, **1**, 2740.
- 19 D. Stuart, C. Yonzon, X. Zhang, O. Lyandres and N. Shah, *Anal. Chem.*, 2005, **77**, 4013.
- 20 D. Stuart, J. Yuen, N. Shah, O. Lyandres and C. Yonzon, *Anal. Chem.*, 2006, **78**, 7211.
- 21 S. Knudsen, M. Mandal, S. Ghosh and T. Pal, *Science*, 2004, **272**, 134.
- 22 J. Sylvia, J. Janni, J. Klein and K. Spencer, *Anal. Chem.*, 2000, **72**, 5834.
- 23 A. Moores and F. Goettmann, *New J. Chem.*, 2006, **30**, 1121.
- 24 W. Doering and S. Nie, *J. Phys. Chem. B*, 2002, **106**, 311.
- 25 K. Lee and M. El-Sayed, *J. Phys. Chem. B*, 2006, **110**, 19220.
- 26 E. Ru, M. Meyer and P. Etchegoin, *J. Phys. Chem. B*, 2006, **110**, 1944.
- 27 K. Myli and V. Grassian, *J. Phys. Chem.*, 1994, **98**, 6237.
- 28 B. Saute and R. Narayanan, *Analyst*, 2011, **136**, 527.
- 29 B. Nikoobahkt, J. Wang and M. El-Sayed, *Chem. Phys. Lett.*, 2002, **366**, 17.
- 30 P. Sisco, A. Alkilany, J. Huang, S. Boulos, J. Yang, D. Chernal, L. Thompson and C. Murphy, *Curr. Opin. Colloid Interface Sci.*, 2011, **16**, 128.
- 31 Z. Wang, S. Zong, J. Yang, C. Song, J. Li and Y. Cui, *Biosens. Bioelectron.*, 2010, **1**, 241.
- 32 W. Premasiri, Y. Gebregziabher and L. Ziegler, *Appl. Spectrosc.*, 2011, **65**, 493.
- 33 C. Johnson, E. Dujardin, S. Davis, C. Murphy and S. Mann, *J. Mater. Chem.*, 2002, **12**, 1765.
- 34 T. Kim, K. Lee, M. Gong and S. Joo, *Langmuir*, 2005, **21**, 9524.
- 35 J. Aznarez, J. Garcia-Ramos, C. Domingo and S. Sanchez-Cortes, *Langmuir*, 2001, **17**, 1157.
- 36 S. Sanchez-Cortes, M. Vasina, O. Francioso and J. Garcia-Ramos, *Vib. Spectrosc.*, 1998, **17**, 133.
- 37 EPA, US Government Printing Office, Washington DC, 2004.

Nanocantilever Chemical Vapor Sensors Coated with Localized Rubbery and Glassy Polymer Brush Films: Sensing Changes in Stiffness

Heather C. McCaig, Edward B. Myers, Derrick Chi, Bruce S. Brunshwig, Nate S. Lewis, and Michael L. Roukes

DRAFT 3 101612

Abstract (250 words)

Highly-miniaturized chemical vapor detection systems, capable of near laboratory-quality analysis, could potentially be deployed widely, for applications in security, environmental monitoring, and disease biomarker detection on exhaled breath. Nanocantilever chemical vapor sensors, when coated with sorptive films, are ideal for such systems because of their ultra-small footprint, high sensitivity, and rapid response time. The deposition of well-controlled sorptive films is critical for optimizing sensor performance and enables the study of complex sensor response mechanisms. Towards this end, thick, uniform, and localized polymer films of poly(methyl methacrylate), poly(methyl acrylate), and poly(n-butyl methacrylate) were grown onto nanocantilevers via surface initiated atom transfer radical polymerization (SI-ATRP). Upon exposure to a series of chemical vapors at a concentration of $0.02 P/P^{\circ}$ (where P is the partial pressure and P° is the saturated vapor pressure) the relative frequency shifts ($\Delta f/f_0$) of SI-ATRP polymer coated nanocantilevers were on the order of $5 - 200 \times 10^5$, two orders of magnitude greater than calculated frequency shift due to mass-loading alone. To determine what section of the nanocantilever contributed the greatest portion of the observed response, polymer films were localized, by a chromium masking and passivation scheme, to selected regions of the nanocantilevers. Vapor sorption on the clamped end resulted in much stronger responses than vapor sorption on the tip, indicating that stiffness change, rather than mass-loading, is the predominant response mechanism. This information could be the key to improving future design and coating parameters for resonant nanocantilever sensors.

Introduction (<1000 words, no heading)

Purpose and significance of work. Put into context of other work. Cite reviews rather than do complete lit rev.

Nanoscale chemical vapor sensors are an essential component of highly-miniaturized chemical detection systems.¹ Such systems have the potential to bring real-time, laboratory quality analysis to handheld devices, impacting fields as diverse as environmental monitoring, homeland security, and medical diagnostics.² A number of microscale chemical vapor sensors

that are compatible with the constraints of miniaturized detection systems have been investigated, including chemiresistors,³⁻⁷ carbon nanotube chemicapacitors,^{8,9} surface acoustic wave (SAW) devices,^{1,10,11} organic thin film transistors,¹² metal oxide nanowires,¹³ and microcantilevers (static and resonating).¹⁴⁻¹⁸ Of these, resonant nanocantilevers, and other nanoelectromechanical systems (NEMS), have been shown to be extremely sensitive to changes in mass,¹⁹⁻²¹ and are able to detect mass loading on the attogram (10^{-18} g) scale in ambient conditions.²²

The response mechanisms governing the behavior of NEMS sensors have been the subject of intense study,²³ and while experimentally observed shifts in resonance frequency are often attributed to mass loading, changes in the sensor's spring constant, especially when the thickness of the sorbed material is close to that of the nanocantilever, also contribute to frequency shifts. In particular, the effect of the modulus of the absorbate on nanocantilever resonant frequency has been observed upon the absorption of self assembled monolayers (SAMs),²⁴ protein,²⁴ and bacterial cells,²⁵ as well as upon the patterning of gold films on cantilevers.²⁶ Similarly, the positive shifts in resonance frequency of gelatin-coated V-shaped microcantilevers upon exposure to water vapor has been attributed to stiffening of the gelatin film.²⁷ Previously, polymers have been deposited on nanocantilevers by dropcasting,^{22,28} (ref cantilever array paper) however, the resulting films were too thin, non-uniform, and irreproducible to draw conclusions about the polymer film's influence on sensor behavior.

One critical challenge that must be overcome to determine the effects of polymer films on the behavior of nanocantilever chemical vapor sensors is the development of a method to coat nanocantilevers, and other NEMS, with thick, uniform, and localized polymer films. Well-defined films composed of polymer brushes can be grown directly from substrates using surface initiated polymerization.²⁹ Polymer brushes are formed when polymer chains are tethered to a substrate in sufficient density that the chains are forced to stretch away from the surface, forming an anisotropic film resembling the upright fibers of a carpet. Previously, polymer brushes have been grown on static microcantilevers, and the deflection of the sensors used to detect phenomena such as changes in solvent quality,^{30,31} pH,³¹ and temperature,^{31,32} as well as the presence of glucose in solution,³³ and of saturated toluene vapor in nitrogen.³⁴ Recently, a thick, uniform film of poly(methyl methacrylate) (PMMA) has been grown directly from the surface of nanocantilever sensors via surface initiated atom transfer radical polymerization (SI-ATRP). (Nano letters paper) Upon exposure to chemical vapors the SI-ATRP PMMA-coated nanocantilever exhibited strong positive shifts in resonance frequency, demonstrating that mass loading, which induces a decrease in the resonant frequency, was not the dominant response mechanism. However, these studies did not examine other underlying mechanistic questions remain such as whether mass-loading would be the dominant response mechanism for a nanocantilever coated with a

rubbery polymer, and what sections of the nanocantilever would be the most sensitive to the sorption of vapor molecules.

In this study, surface initiated atom transfer radical polymerization (SI-ATRP) was used to grow thick, uniform films of two rubbery polymers, poly(methyl acrylate) (PMA), and poly(n-butyl methacrylate) (PBMA) on resonant nanocantilever chemical vapor sensors, which were then exposed to a series of chemical vapors. The response behavior of the nanocantilevers coated with rubbery polymers was compared to that of nanocantilevers coated with SI-ATRP grown films of the glassy polymer, PMMA, and thereafter compared to the calculated frequency shifts expected from mass-loading. Both the direction of the observed frequency shifts and the response time of the sensors were strongly influenced by whether the polymer film was rubbery or glassy.

The importance of stiffness change as a response mechanism was further shown when polymer films were localized to specific sections of the nanocantilever sensors through a chromium masking and passivation scheme to determine which part of the structure was responsible for the experimentally observed responses of the unmasked nanocantilevers. This work has revealed that nanocantilevers coated with SI-ATRP grown films respond to chemical vapors primarily through changes in stiffness, rather than via mass-loading. The importance of stiffness change as a response mechanism therefore should inform the design and coating of nanocantilevers for sensing applications.

RESULTS AND DISCUSSION

I broke up results and discussion into subsections, with results sections first and discussion sections second

SI-ATRP Polymer Films on Unmasked Nanocantilevers

SI-ATRP was used to grow films of PMMA (88 nm thick), PMA (110 nm thick), and PBMA (108 nm thick) on nanocantilever sensors, as shown in **Figure 1**. The thickness of the polymer brush films on the nanocantilevers was determined using scanning electron microscopy (SEM). Ellipsometry was also used to measure the thickness of PMMA and PBMA films grown on flat substrates (silicon wafer with a 30 nm gold film on top of a 10 nm chromium adhesion layer), but that technique was not used for PMA because of that film's greater surface roughness. The roughness of the PMA film was attributed to a lower polymer chain graft density compared to the PMMA and PBMA films because, previously, polymer film dimpling has been observed upon the drying and collapse of the brush, which lead to the formation pinned micelles on the surface, composed of a number polymer chains.^{35, 36} PMMA is a glassy polymer (bulk T_g = 105 °C), while PMA (bulk T_g = 5 °C) and PBMA (bulk T_g = 15 °C) are rubbery at the operating temperature of the nanocantilever (approximately 30 °C).³⁷ Briefly, the polymer films were grown by first forming a self assembled monolayer (SAM) of Bis(2-[2'-bromoisobutyryloxy]ethyl)disulfide (BiBOEDS), an

ATRP polymerization initiator, which spontaneously binds to the gold via the disulfide. The polymerization conditions were such that no sacrificial initiator (unbound initiator in the solution) was necessary to control the reaction, so polymerization only occurred on the gold, BiBOEDS-functionalized surface. The PMMA and PBMA were grown at room temperature for 10 h and 20 h, respectively, while the PMA film was grown at 50 °C for 48 h, as detailed in the Methods section. An elevated temperature was necessary for the reaction to proceed, but increasing the reaction temperature further was undesirable because the thiol bond labile above 60 °C, which can result in chain termination due to thiol desorption.³⁸ Dropcast polymer films of PMMA, PMA, and PBMA were also applied to nanocantilevers for comparison to the corresponding SI-ATRP polymer films.

The self-sensing piezoresistive nanocantilevers used in this study were 2.5 µm long bilayer structures of silicon nitride (100 nm thick) with the top layer comprising a 30 nm gold film, over a 10 nm chromium adhesion layer. The gold was used as an etch mask in fabrication and then for the actuation of vibration and the readout of the frequency during sensor operation.²² Bare nanocantilevers had an average resonance quality factor (Q) of 120 in ambient conditions, which remained unchanged within the standard deviation of the initial Q when coated with a 2-10 nm dropcast polymer film, with 10 nm being approximately the maximum film thickness possible for a dropcast film. **Figure S1**, in the Supplementary Information, shows that nanocantilevers coated with an SI-ATRP grown PMMA film (SI-PMMA) had an average Q of 100, while nanocantilevers with an SI-ATRP grown PMA film (SI-PMA) had an average Q of 90, and nanocantilevers coated with an SI-ATRP grown PBMA film (SI-PBMA) had an average Q of 50. Three to eight cantilevers with each coating were used to calculate the average Q.

Response of Unmasked Nanocantilever to Chemical Vapors

Nanocantilever sensors were exposed to 400 s pulses of a series of chemical vapors at 0.02 P/P^o (where P is the partial pressure and P^o the saturated vapor pressure) in a background of laboratory air (1.10 ± 0.15 ppth water vapor). The chemical vapors were selected to include non-polar, polar, aromatic, and halogenated compounds. The resonant frequencies of nanocantilevers were tracked using a phase-locked loop (PLL), enabling the real-time measurement of frequency shifts due to the sorption of chemical vapors.²² Bare nanocantilevers and nanocantilevers coated with dropcast films of PMMA, PMA, and PBMA were tested along with nanocantilevers coated with SI-PMMA, SI-PMA, and SI-PBMA, as shown in **Figure 2**. The responses of nanocantilevers coated with dropcast PMA and PBMA are not shown for clarity, but they were on the same order of magnitude of the responses of nanocantilevers with the dropcast PMMA (D-PMMA) film. All nanocantilevers coated with SI-ATRP grown polymer films exhibited responses to all of the chemical vapors. Nanocantilevers coated with the glassy SI-PMMA exhibited positive shifts in resonance frequency when exposed to polar vapors, as previously

described, (my Nano Letters paper) while the nanocantilevers coated with SI-PMA and SI-PBMA exhibited negative frequency shifts upon exposure to all chemical vapors.

The response time of nanocantilevers coated with SI-ATRP grown polymer films was determined as the time necessary for the sensor to reach 90% of its equilibrium response upon exposure to $0.02P/P^0$ of each tested vapor. Sensors coated with SI-PMA and SI-PBMA responded to all vapors within 50 s, while SI-PMMA coated nanocantilevers responded within 50 s for non-polar vapors, but required up to 1700 - 2600 s to reach 90% of equilibrium when exposed to polar vapors (Figure 3). The linearity of the sensor responses with respect to the concentration of toluene, isopropanol, and ethyl acetate was also tested in the range of 0.005 – 0.08 P/P^0 . Unlike SI-PMMA, (REF Nano Letters) nanocantilevers coated with both SI-PMA and SI-PBMA responded linearly to 400 s pulses of each chemical vapor. Nanocantilevers coated with SI-PMA and SI-PBMA also responded linearly to chloroform vapor, which induced the largest responses of any the vapor set.

Modeling of the Frequency Shift Caused by Mass Loading

To model the NEMS frequency shifts due to analyte mass loading, it was assumed that the polymer uniformly coats the top surface of the NEMS, with the additional mass absorbed into the polymer calculated according to the partition coefficient of each polymer/vapor pair. Partition coefficients were derived from the frequency shifts of quartz crystal microbalances (QCMs) coated with SI-ATRP grown polymer films. The resulting mass-induced frequency shifts were calculated using an analytical elastic continuum model for the polymer-coated cantilever; further details appear in the Methods section. The calculated relative frequency shifts ($\Delta f/f_0$) due to mass loading for a nanocantilever coated with 100 nm SI-PMMA ranged from -0.47 to -3.8×10^{-5} for hexane and chloroform, respectively, for SI-PMA -0.06 to -0.20×10^{-5} for heptane and chloroform, respectively, and for SI-PBMA -0.06 to -0.89×10^{-5} for heptane and chloroform, respectively. The comparison of calculated and experimental relative frequency shifts is presented in Table 1.

Chromium Masked Nanocantilevers

Nanocantilevers with an additional masking layer of chromium on top of the gold surface were fabricated to study the effects of localizing SI-ATRP polymer films to sections of the nanocantilever structure. The chromium mask was applied to the nanocantilever tip (Cr-tip), legs and base (Cr-legs), or only base (Cr-base) via an additional electron-beam lithography step conducted prior to the nanocantilever release etch step. Additionally, prior to formation of the polymerization BiBOEDS SAM, the chromium was passivated with a SAM of n-hexylphosphonic acid. Without this treatment, significant polymer film growth (>10 nm) was measured on flat chromium surfaces via ellipsometry, and was visible in SEM images of chromium-masked

cantilevers. Chromium passivation was tested by comparing the ratio of the thickness of an SI-PMMA brush film grown on flat gold and passivated-chromium substrates. All substrate-pairs for comparison studies underwent identical SAM formation steps, and were exposed to polymerization conditions together in the same reaction vial to minimize any differences in processing. The ratio of the thickness of the SI-PMMA films on gold and passivated-chromium substrates was measured as 20:1 by ellipsometry. When the n-hexylphosphonic acid SAM was formed prior to conducting SI-ATRP on chromium-masked nanocantilevers, no polymer was visible on the chromium-masked regions of the nanocantilevers while smooth, translucent polymer films have grown on the exposed gold, as shown in [Figure 4](#). A similar high specificity of film growth was also observed for SI-PBMA ([Figure 5](#)), but SI-PMA was unable to be sufficiently localized to the gold for use in this study. The SI-PMMA films on the chromium-masked nanocantilevers was 74 nm thick, with the SI-PBMA films were 63 nm thick. Upon coating the chromium-masked nanocantilevers with SI-ATRP polymer films, the average shift in resonance frequency was within the standard deviation of the average resonance frequency of the uncoated nanocantilevers, though there was a slight increase in the average resonance frequency of the Cr-tip and Cr-base sensors (polymer grown on the clamped end), and a slight decrease in the resonance frequency of the Cr-legs sensors (polymer grown on the free end).

Chromium-masked nanocantilevers with SI-PMMA ([Figure 6](#)) and SI-PBMA ([Figure 7](#)) films were exposed to 400 s pulses of a series of chemical vapors at 0.02 P/P₀, with the sensor responses of single, representative cantilevers. At least three nanocantilevers of each chromium-masking geometry and polymer coating were tested, and the representative chromium-masked sensors were from a single fabrication and polymerization batch to minimize processing differences. Chromium-masked nanocantilevers without polymer films responded to the chemical vapors similarly to bare, unmasked nanocantilevers. Of the chromium-masked nanocantilevers with an SI-PMMA film, the Cr-tip sensors responded more strongly than the Cr-legs and the Cr-base sensors. Of the Cr-masked nanocantilevers with an SI-PBMA, the responses of the Cr-legs sensor were weaker than the Cr-tip and Cr-base sensors.

The Contribution of Stiffness to the Experimental Resonant Frequency Shifts

The calculated frequency shifts due to mass-loading were one to two orders of magnitude smaller than the frequency shifts observed during vapor exposure experiments, indicating that another mechanism must be responsible for the remainder of sensor responses. Additionally, because mass-loading decreases the resonance frequency, the positive shifts in resonance frequency observed for SI-PMMA coated sensors must be due to different response mechanism. The resonant frequency of a nanocantilever is a function of the mass and stiffness, where the change in relative frequency can be described by,

$$\frac{\Delta f}{f_0} = \frac{\Delta k}{2k} - \frac{\Delta m_{eff}}{2M_{eff}} \quad (1)$$

where Δf is the change in frequency, f_0 is the fundamental resonance frequency, k is the spring constant, Δk is the change in spring constant, M_{eff} is the NEMS effective mass, and Δm_{eff} is the change in effective mass.²⁷ Since mass-loading cannot account for the experimentally observed frequency shifts, the vapor sorption into the polymer films must be changing the spring constant of the nanocantilever, either stiffening the sensor, as with SI- PMMA coated nanocantilevers, or softening the sensor, as with SI-PMA and SI-PBMA coated nanocantilevers. Previously, the frequency shifts of micro- and nanocantilever sensors, which could not be explained by mass loading, have been attributed to changes in sensor stiffness, as detailed in the introduction, though further study is required to develop a complete understanding of underlying causes of these changes in spring constant.

These results are a reminder that caution must be employed whenever mass-loading occurring on a micro- or nanoresonator is calculated directly from measured frequency shift. Changes in spring constant should be taken into account when one or more continuous monolayers of vapor molecules are adsorbed on the sensor surface (as occurs with the bare nanocantilevers), or when the nanocantilever is coated with a continuous polymer film.³⁹

Effect of Polymer Glass Transition Temperature on Sensor Behavior

The glass transition temperature (T_g) of a polymer denotes the temperature at which the material undergoes a phase change from a glassy state to a rubbery state. Below the T_g , the polymer is in a glassy state in which the polymer chains are locked into a single configuration, unable to easily move past each other, leading to a stiff material with a slow diffusion constant. Conversely, the rubbery state is characterized by significantly increased chain mobility, a softer bulk material, and an increased diffusion coefficient for vapor molecules. The polymers PMMA and PMA were chosen for this comparison study because of they represented chemically similar, but physically different sorptive materials, with PMMA being glassy and PMA being rubbery at 30 °C. The only chemical difference between PMA and PMMA is that PMMA has a single extra methyl group per monomer, which prevents the PMMA polymer chains from easily slipping past each other and is responsible for PMMA's greater T_g . A second rubbery polymer, PBMA, was included in these experiments because it was determined that PMA was a poor candidate for localized polymerization procedure. PBMA has a greater affinity toward non-polar analytes than PMMA or PMA due to the n-butyl group in each monomeric unit of the polymer.

When chemical vapors sorb into the polymer films, changes occur in film properties such as thickness and Young's modulus, both of which are affected polymer chain orientation.

Comparing the responses of the SI-ATRP PMMA and SI-ATRP PMA coated nanocantilevers to chemical vapors, it is seen that the affect of the penetrant vapor molecules on sensor response is dependent on whether the polymer brush is glassy or rubbery. For a glassy polymer, the configuration of the chains in the polymer brush is locked, so a small number of penetrant molecules may cause the film to stiffen like a swollen gel. In contrast, the individual chains of the rubbery polymers are able to slide past each other, allowing the chains to accommodate the penetrant molecules, which may be plasticizing the film. Given the high Young's modulus of silicon nitride of (~110 GPa) vs. those of the polymers (measured by atomic force microscopy (AFM) nanoindentation as 8 GPa for a 150 nm dry PMMA brush⁴⁰ and 50-60 MPa for 50 nm dry PMA brush³⁵). Further work, such as nanoindentation of polymer brush films during exposure to chemical vapors, is required to elucidate any changes occurring in Young's modulus.

While nanocantilevers coated with rubbery SI-PMA and SI-PBMA films had lower Q values than cantilevers coated with dropcast PMMA and SI-PMMA films, this reduction in Q did not negatively impact the sensor responses to chemical vapors at the concentrations tested. For applications requiring trace detection, the choice of polymer film thickness must be balanced to maximize vapor capture while retaining a sufficient Q to measure small shifts in resonance frequency in order to optimize the minimum detectable level (MDL).

Nanocantilevers coated with rubbery polymer films of SI-PMA and SI-PBMA responded quickly to chemical vapors because the diffusion of vapor molecules in rubbery polymers is Fickian, as the relative mobility of the penetrant molecules is slower than the polymer chain mobility.⁴¹ Unlike rubbery polymers, glassy polymers such as PMMA are known to exhibit non-Fickian diffusion characterized by a delayed relaxation of the polymer chains (two stage sorption), which can greatly increase the time required for the film to reach a new equilibrium state.⁴²⁻⁴⁵ Due to the slow chain relaxation, glassy polymers can also exhibit history effects, such that the order of chemical vapor exposures can impact the shape and magnitude of an individual response. Given that sensor response magnitude of cantilevers coated glassy and rubbery polymer films is similar, rubbery polymer films are preferred due to their faster response time.

Localization of Polymer Films on Nanocantilever Sensors

This work demonstrates a method for highly selective deposition of localized polymer films on nanostructures post-fabrication, protecting the polymer from potentially damaging processing steps such as plasma etches. High quality polymer films are essential for vapor detection, especially for the discrimination between vapors where an array of sensors coated with a variety of chemically distinct polymer films is employed,⁴⁶ and to study the response mechanisms behind the observed frequency shifts. The localization of the polymer film directs the absorption of chemical vapors to the sensor, or the most sensitive part of the sensor, rather than allowing a portion of the vapor molecules to be lost by absorption on non-sensitive areas,

which would be detrimental for a trace detection application. This bottom up technique is amenable to wafer-scale production and adaptation to other surface initiated polymerization techniques.²⁹ While PMMA and PBMA were successfully localized to the gold regions of the nanocantilever, the PMA brush grew on the chromium mask as well. It is believed the failure of the chromium passivation was due to desorption of the n-hexylphosphonic acid SAM during the 48 hr, 50 °C PMA polymerization reaction. Chromium was chosen for the masking layer because of its adherence to gold and its resistance to the plasma etch used to release the nanocantilevers from the substrate. A number of passivation SAMs were tested including multiple silanes, carboxylic acids, and phosphonic acids, with n-hexyl phosphonic acid exhibiting superior performance compared to all other SAMs tested. Phosphonic acid SAMs have been studied previously on titania⁴⁷ and alumina,⁴⁸ and it has also been shown that alkane thiols and alkane carboxylic acid SAMs can be formed simultaneously on adjacent gold and alumina surfaces.⁴⁹ By first protecting the chromium regions with the n-hexyl phosphonic acid SAM, subsequent exposure to BiBOEDS resulted in the initiator self assembling only on the bare gold surface.

The responses of nanocantilevers coated with localized polymer films indicate that vapor sorption on the legs and base of the sensors is the primary source of the observed frequency shifts. For chromium masked nanocantilevers coated with SI-ATRP PMMA, the Cr-Tip sensors responded more strongly to chemical vapors than the Cr-Legs or Cr-Base sensors. Additionally, of the chromium masked nanocantilevers coated with SI-ATRP PBMA, the Cr-Legs sensors produced weak responses to chemical vapors compared to the Cr-Tip and Cr-Base sensors. Modeling of the shape of the nanocantilever's fundamental resonance mode showed that mass-loading from vapor absorption on the sensor's legs had only a weak effect on resonant frequency; a hundred times smaller than mass loading on the tip. Conversely, changes in sensor stiffness have the greatest affect on resonant frequency if they occur near the clamped end of the nanocantilever where the majority of the bending occurs.

CONCLUSION

Resonant nanocantilevers have a number of desirable qualities necessary for incorporation into highly miniaturized chemical vapor detection systems, including their small size, extreme sensitivity, and adaptability to various chemical targets. There has been a need for a method to deposit thick, uniform polymer films on nanocantilevers to both enhance vapor sorption and to develop a thorough understanding of the mechanisms behind the observed sensor responses. The challenge of depositing high-quality polymer films was overcome using SI-ATRP, and was demonstrated by growing approximately 100 nm thick films of PMMA, PMA, and PBMA on nanocantilevers. Nanocantilevers were exposed to a series of seven non-polar and polar chemical vapors to test their response speed and magnitude. While nanocantilevers coated with the glassy SI-PMMA film exhibited positive shifts in resonant frequency upon exposure to polar

vapors, sensors coated with the rubbery SI-PMA and SI-PBMA films exhibited negative shifts in resonance frequency for both non-polar and polar vapors. The responses of nanocantilevers coated with all SI-ATRP grown polymer films were one to two orders of magnitude larger than expected by mass loading alone, and were attributed to the stiffening or softening of the polymer films. Nanocantilevers coated with SI-PMA and SI-PBMA responded to all vapors within 50 s, but nanocantilevers coated with SI-PMMA required up to 2600 s to respond to polar vapors. Additionally, the bottom-up nature of SI-ATRP enabled the localization of polymer films to chosen sections of each nanocantilever by using a chromium mask, passivated with a n-hexylphosphonic acid SAM, which restricted the self assembly of the BiBOEDS polymerization initiator to the uncovered gold surface. Nanocantilevers were fabricated with three different mask geometries, Cr-tip, Cr-legs, and Cr-base, to determine what are of the sensor was the most sensitive to vapor sorption. Localization of the polymer film was achieved for SI-PMMA and SI-PBMA, but not for SI-PMA due to the elevated temperature and long polymerization time required to grow a film a sufficiently thick film. Nanocantilevers with the Cr-legs mask and both SI-PMMA and SI-PBMA films exhibited reduced responses to chemical vapors compared to nanocantilevers with Cr-tip and Cr-base masks. The sensor responded maximally when vapor sorption occurred on the legs and base of the sensors, providing further evidence that changes in nanocantilever spring constant dominate the observed responses. These results show that for resonant nanocantilevers coated with thick, continuous polymer films, both vapor sorption and bending at the clamped end must be maximized to enhance sensitivity. Additionally, localized polymer coating could be applied in trace detect situations where mass loading and stiffening would compete to impede sensitivity. By coating nanocantilever chemical vapor sensors with rubbery polymer brush films, the sensors respond rapidly and strongly to changes in stiffness, making it a competitive technology for incorporation into highly-miniaturized detections systems. Furthermore, this work can be applied to all resonant NEMS sensors, enabling localization of target binding to specific areas on the resonator, enabling quantitative mass-loading calculation from frequency shifts, and maximizing resonator sensitivity by preventing the activation of competing response mechanisms.

METHODS

Cantilevers Fabrication

The fabrication of silicon nitride nanocantilevers with integrated piezoresistive readouts has been described in detail previously.^{22, 50} Briefly, cantilever and bondpad shapes were patterned with electron beam lithography onto a 100 nm thick SiN layer on a silicon substrate, followed by gold film deposition, and then liftoff. Dry plasma etching was then used to release the cantilevers. The gold overlayer served as both etch mask during fabrication and later as a piezoresistive transducer.⁵¹ Chromium masked nanocantilevers were fabricated by first defining the bondpad and nanocantilever in gold, followed by a second electron beam lithography step to

define the chromium areas, again followed by resist liftoff and then a release etch. Nanocantilevers had a typical fundamental resonance frequency of 10-12 MHz and quality (Q) factors of 120 in ambient conditions. Unmasked nanocantilevers had a capture area of $1.5 \mu\text{m}^2$. Resonance was actuated thermoelastically.⁵² Nanocantilever sensors were operated with home-built, LabView controlled, electronics⁵¹ which tracked each sensor's resonance frequency using parallel, independent phase-locked loops.

Surface chemistry

Materials

Methyl methacrylate (MMA), methyl acrylate (MA), and n-butyl methacrylate (BMA) (all containing 10-100 ppm MEHQ inhibitor), HQ/MEHQ inhibitor removal column packing, poly(methyl methacrylate) (PMMA; $T_g = 105 \text{ }^\circ\text{C}$; $MW = 35,000$; $\rho = 1.20 \text{ g/mL}$), poly(methyl acrylate) (PMA; $T_g = 5 \text{ }^\circ\text{C}$; $MW = 40,000$; $\rho = 1.22 \text{ g/mL}$), and poly(n-butyl methacrylate) (PBMA; $T_g = 15 \text{ }^\circ\text{C}$; $MW = 180,000$; $\rho = 1.07 \text{ g/mL}$) were purchased from Scientific Polymer Products, Inc. Bis(2-[2'-bromoisobutyryloxy]ethyl)disulfide (BiBOEDS) (>90%) was purchased from ATRP Solutions. Methanol (anhydrous, 99.8%), n,n,n',n'',n''-pentamethyldiethylenetriamine (PMDETA), copper (I) bromide (CuBr) (98%), copper (II) bromide (CuBr₂) (99.999%), and 2,2'-bipyridyl (2-bipy) (>99%) were purchased from Aldrich. CuBr was purified by stirring with glacial acetic acid for 24 hrs at room temperature, followed by rinsing with ethanol and diethyl ether, and then drying overnight in vacuum. Purified CuBr was stored in a vacuum desiccator until use. Absolute ethanol was purchased from Decon Laboratories, Inc. Regent grade hexane, heptane, toluene, ethyl acetate, chloroform, tetrahydrofuran, and isopropanol were purchased from VWR, and were used to produce analyte vapors. All chemicals were used as received unless otherwise stated. Ultrapure, deionized water (18 M Ω /cm) was used for all syntheses. All QCMs and the QCM actuator were purchased from International Crystal Manufactures (ICM, Inc.)

Formation of SAMs

Solutions for SAM formation were prepared in 20 ml scintillation vials, consisting of 5 mM n-hexylphosphonic acid or BiBOEDS in absolute ethanol. Typically, each vial contained 2.5 – 5 mL of solution, which was sufficient to fully immerse the substrate. Solutions were stored in the dark to prevent potential degradation of the SAM forming molecules, particularly of the BiBOEDS, due to UV light.

Flat gold substrates were fabricated by evaporation of 30 nm gold film on silicon over a 10 nm chromium adhesion layer. Flat chromium substrates were fabricated by evaporation of a 30 nm chromium film on silicon, and were stored in air such that a native oxide was formed. All flat substrates, nanocantilevers, and QCMs were first thoroughly washed with hexane, acetone, tetrahydrofuran, and absolute ethanol, and then dried with compressed air. Organic

contaminants were removed using an 8 min ozone plasma etch (XX machine), followed by rinsing with deionized water (18 MΩ/cm), thorough drying with compressed air, and immediate immersion in the pre-prepared ethanol solution of either n-hexylphosphonic acid or BiBOEDS. To aid in the handling of the delicate QCMs, a sample holder consisting of an NMR tube cap with a slit cut with a razor blade was employed. A single QCM was slid into the slit, so that the cap could be handled with tweezers (see Supplemental Information for a photograph of the QCM holder).

Substrates were soaked in each solution for at least 36 h to ensure the formation of an ordered SAM. Substrates were then rinsed with absolute ethanol and dried with compressed air. Substrates were characterized and then either immersed in a second SAM-formation solution or immediately prepared for use in a polymerization reaction. Unmasked nanocantilevers were not immersed in the n-hexylphosphonic acid solution.

ATRP of PMMA

Polymerization of MMA was conducted by water-accelerated SI-ATRP.⁵³ Neat MMA was first passed through an inhibitor removal column. The purified MMA was either used immediately, or was stored in sealed vials that were placed in a freezer until use. A two necked round bottom flask was charged with 7.5 mg purified MMA, 6 mL methanol, and 1.5 mL deionized water. The flask was sealed with septa and then the solution sonicated while sparging with nitrogen or argon for 45 min. The catalyst components, 258 mg of CuBr and 114 mg 2-bipy, were then added to the solution, which was then simultaneously sonicated and sparged for 30-45 min until the catalyst dissolved. Substrates were suspended with a flat alligator clip in a 20 mL scintillation vial equipped with a small stir bar and a septum. The clip was attached to a wire that was sufficiently long to bend over the rim of the vial, and was held in place with the septum. The vial was purged with nitrogen or argon for at least 45 min before introduction of the solution. The reaction solution was transferred via syringe from the round bottom flask to the vial containing the suspended substrate to prevent contact with oxygen. The reaction was allowed to proceed at room temperature with stirring and a constant inert gas purge. At the desired time (e.g. 20 h for a 90 nm thick film) the substrate was removed and thoroughly rinsed with tetrahydrofuran, methanol, and absolute ethanol.

ATRP of PMA

Polymerization of MA was conducted by bulk SI-ATRP,⁵⁴ and the reaction parameters adjusted from the original publication such that polymer growth occurred at 50 °C to prevent desorption of the BiBOEDS SAM. MA was first passed through an inhibitor removal column. A round bottom flask was charged with 23 g MA (excess to account for evaporation during the long polymerization) and 432 mg PMDETA. The flask was sealed with a septum, and then the solution

was sonicated while sparging with argon for 1 h. A large test tube fitted with a magnetic stir bar was charged with 257 mg CuBr and 15 mg CuBr₂. The substrate was suspended in the test tube with a flat clip that was wired to a metal needle. The needle was pierced through the septum which was then used to seal the test tube, allowing the substrate height to be controlled (see Supplemental Information for a photograph of the set up). The pointed tip of the needle was wrapped in parafilm to seal it and to prevent accidental injury and prevent oxygen contamination. Substrate suspension allowed the solution to be stirred without damaging the substrate. The tube was purged continuously with argon. The test tube was maintained at 50 °C by emersion in an oil bath for the duration of the reaction. The sparged solution was transferred to the test tube using a syringe. Care was taken to prevent solution from contacting the substrate, which was kept suspended above the liquid. After stirring the solution for 1 h at 50 °C to dissolve the catalyst, the substrate was lowered into the reaction solution. The reaction was allowed to proceed for 48 hrs, which resulted in a 100 nm thick PMA film. The solution was exposed to air to stop the polymerization. Substrates were rinsed with chloroform, methanol, and absolute ethanol.

ATRP of PBMA

Polymerization of BMA was conducted by water accelerated SI-ATRP.⁵⁵ Neat BMA was first passed through an inhibitor removal column, and then used immediately. A two necked round bottom flask was charged with 10 mL purified BMA, 9 mL isopropanol, and 1 mL deionized water. The flask was sealed with septa and then the solution sonicated while sparging with argon for 45 min. The catalyst components, 52 mg of CuBr and 127 mg 2-bipy, were then added to the solution, which was then simultaneously sonicated and sparged until the catalyst dissolved (30-45 min). The remainder of the reaction proceeded as for ATRP of PMMA, with a typical reaction time of 12 h producing a 100 nm thick PBMA film.

Dropcast Polymer Films

Polymer solutions for creating dropcast films on nanocantilevers were made by first making a concentrated solution by sonicating approximately 100 mg polymer in 20 mL toluene until the polymer beads were dissolved, which was then diluted 5 mM. A 10 µL micropipette was used to apply a 1.5 µL droplet of the dilute PMMA solution to the chip containing nanocantilever sensors, which was allowed to evaporate naturally. This dropcasting procedure resulted in 2-10 nm thick polymer films.

Characterization

Films were characterized using ellipsometry and scanning electron microscopy (SEM). Polymer film thickness was measured with a Gaertner L166C ellipsometer, equipped with HeNe (633 nm wavelength) laser, at a 70° angle of incidence. The optical constants of the flat gold

substrates were measured prior to formation of the initiator SAM. Both initiator SAM and polymer film thickness were measured. The refractive index both the n-hexylphosphonic acid and BiBOEDS SAMs was assumed to be 1.46. The refractive index of PMMA assumed to be 1.49, the index of PMA to be 1.48, and the index of PBMA to be 1.48, based on values provided by Scientific Polymer Products, Inc for bulk polymers. The thickness of the initiator SAM measured between 0-2 Å. SEM (ZEISS 1550 VP FESEM) was used to verify the quality of nanocantilever fabrication and the quality of the SI-ATRP grown polymer films.

Vapor Exposure Experiments

The nanocantilevers were exposed to analyte vapors using an automated vapor delivery system controlled by LabView.⁵⁶ At least three sensors of each type (e.g. unmasked nanocantilevers with dropcast PMMA films, Cr-legs nanocantilevers with SI-BPMA films) were tested. The analytes (hexane, toluene, heptane, ethyl acetate, chloroform, tetrahydrofuran, and isopropanol) were delivered at a concentrations of 0.005-0.08 P/P° (partial pressure divided by saturated vapor pressure), and each exposure consisted of 70 s of pure carrier gas, 400 s of analyte vapor exposure, followed by 630 s of carrier gas to purge the system. For single concentration experiments, a run consisted of five exposures to each analyte at 0.02 P/P° . For linearity experiments, five exposures per concentration per analyte were delivered in the order 0.03, 0.01, 0.048, 0.005, 0.08, and 0.02 P/P° to prevent possible hysteresis from affecting linearity profile. The response times of the nanocantilevers were determined by running the sensors “open-loop” and measuring the error signal, rather than tracking the resonance frequency with a PLL,²⁸ The nanocantilevers were housed in a brass chamber with an internal volume of 100 mL. Between one and four sensors were tested in each experimental run, and all sensors were broken in prior to data collection by multiple exposures to each analyte over a period of 12-24 h. Temperature was not controlled, but was stable at 21 ± 1 °C.

Nanocantilever Sensor Data Analysis

Nanocantilever frequency data was corrected for baseline drift prior to extraction of sensor responses using OriginLab (Version 7.5). The baseline-corrected frequency data was then imported into MATLAB (Mathworks, Version R22008b) and the sensor responses extracted using custom scripts. Baseline noise was computed as the standard deviation of drift-corrected baseline frequency over a period of 10 s prior to sensor response. Signal to noise ratio was calculated conservatively as the average response divided by three times the baseline noise. Nanocantilever sensor response data reported in figures and tables were recorded from single, representative sensors. Some variation was observed between individual sensors of each type, but it did not distort the reported trends.

Determination of Partition Coefficients (could move this to SI)

Partition coefficients (K) were determined by measuring the mass uptake of PMMA films applied to quartz crystal microbalances (QCMs). Each QCM was cleaned with hexane, acetone, and methanol before measurement of its initial resonance frequency, $F_{o,i}$. Polymer films were prepared either by spraycoating the QCM with a solution of PMMA, PMA, or PBMA in tetrahydrofuran (160 mg / 20 mL) using an airbrush, or by SI-ATRP, as described above. All coated QCMs were stored in a closed, but not sealed, container for at least 24 hrs after film formation to aid evaporation of any solvent trapped in the films. Before data collection QCMs were broken-in by exposing them to a randomized series of vapor exposures for 12-18 hrs.

QCMs were exposed to analyte vapors with an automated vapor delivery system.⁵⁶ Five exposures of the seven vapors at each of the five concentrations ($P/P_o = 0.01, 0.02, 0.04, 0.06, 0.08$) were conducted in an order randomized for both analyte identify and concentration. After an initial purge of 500 s, each exposure was 400 s in duration, with a 700 s purge between exposures. The change in resonance frequency due to polymer coating, $\Delta F_{polymer}$, was calculated as the difference of the resonance frequency before and after coating. The frequency change due to each vapor exposure, $\Delta F_{analyte}$, was calculated as the difference in frequency between the QCM during exposure relative to the baseline frequency. The baseline frequency was calculated as the average frequency during the 20 s prior to the specific vapor exposure, and the frequency during exposure was calculated as the average frequency between 350 and 398 s after the exposure had begun.

The calculation of the partition coefficient from the QCM frequency shift data has been described previously.⁵⁷ Briefly, first a line with a forced zero is fitted versus concentration data. The slope of this fit is then converted into a partition coefficient by,

$$K_{eq} = \frac{\rho R T m * 10^6}{M_w \Delta F_{polymer} P_{atm}} \quad (2)$$

Where R is the ideal gas constant ($1 \text{ atm mol}^{-1} \text{ K}^{-1}$), ρ is the density (g mL^{-1}) of the polymer, T is the temperature (K), m is the slope of $\Delta F_{analyte}$ versus concentration (Hz/ppth in air), M_w is the molecular weight (g mol^{-1}) of the analyte, $\Delta F_{polymer}$ (Hz) is the frequency shift due to polymer coating, and P_{atm} is the atmospheric pressure (atm). The density of PMMA used in the K_{eq} calculations was 1.20 g/mL for QCMs with both spraycoated and SI-ATRP grown films.

Modeling

As described above, the fractional frequency shift is related to the effective mass of the resonator. Rewriting Eqn. (XX), we find

$$\Delta f = \frac{f_0}{2M_{eff}} \Delta m_{eff}. \quad (3)$$

The change in effective mass caused by analyte absorption is position-dependent, as molecules absorbed closer to the cantilever base participate less in resonant motion and so have a smaller inertial effect. This dependence is directly related to the resonance mode shape as follows:

$$\delta m_{eff}(x) = \delta m(x) \phi^2(x), \quad (4)$$

where $\delta m(x)$ is the differential mass absorbed at position x along the length of the cantilever, and $\phi^2(x)$ is the normalized mode shape function.⁵⁸ $\delta m(x)$ is derived from the measured partition coefficient:

$$\delta m(x) = \frac{K_{eq} P M_w}{\rho R T} A(x) dx. \quad (5)$$

Here P is the partial analyte vapor pressure delivered to the device (typically 0.02 x saturation vapor pressure) and $A(x)$ is the cross-sectional area of the polymer at length position x . To determine the effective mass Δm_{eff} added to a portion of the cantilever (e.g., the legs only or the head only), Eqn. (XX) was integrated over the respective length. The mode shape function was determined by modeling the cantilever head and legs as connected elastic beam segments⁵⁹ and solving the resulting differential equations using a Mathematica script.

SUPPLEMENTARY INFORMATION

Tabulated response data for chromium-masked nanocantilevers, tabulated partition coefficient values for polymer films, nanocantilever resonance quality factors, sensor linearity, and the change in f_0 upon coating of chromium-masked nanocantilevers with SI-ATRP grown polymer films is available.

FIGURES

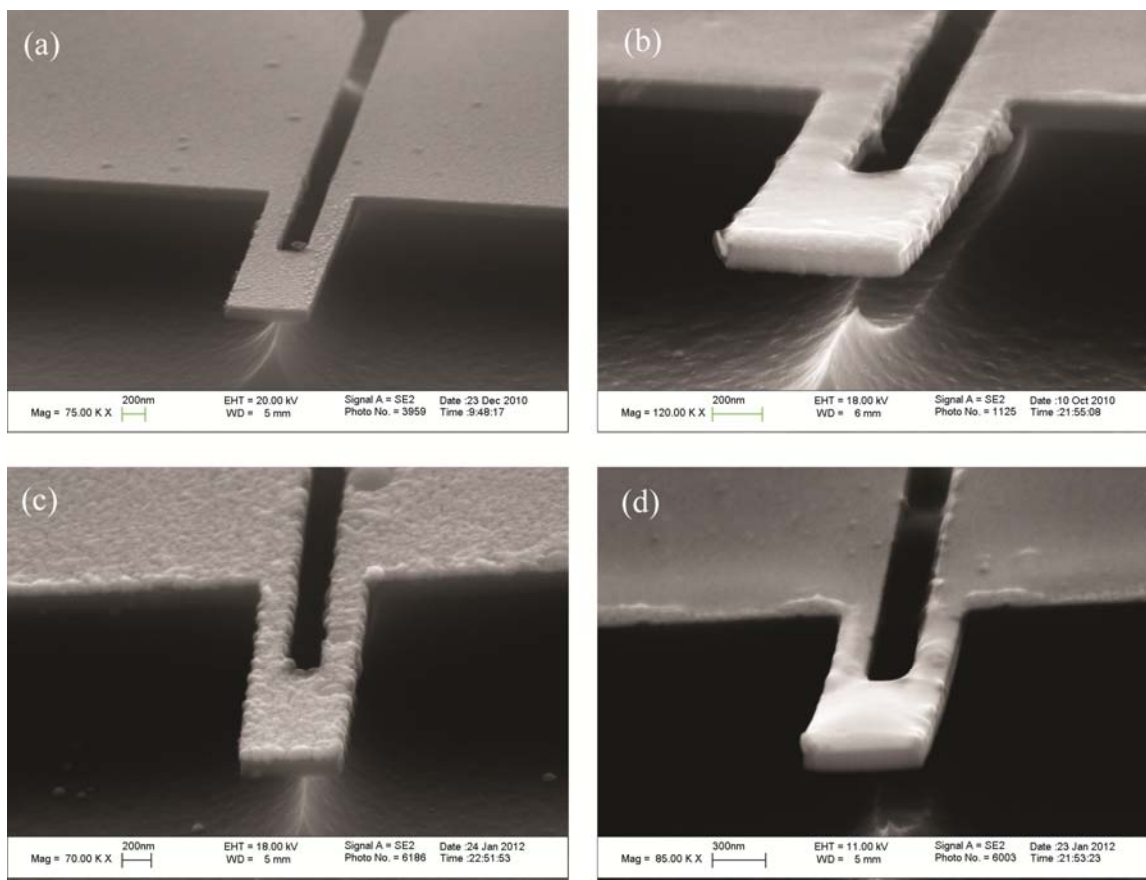


Figure 1: SEM images of unmasked nanocantilevers: as fabricated (a), coated with 88 nm SI-PMMA (b), coated with 110 nm SI-PMA (c), and coated with 108 nm SI-PBMA (d).

NOTE: ACS Nano wants lineart figure in eps format (1200 dpi), which does no import well into Word, so gifs have been substituted in this manuscript.

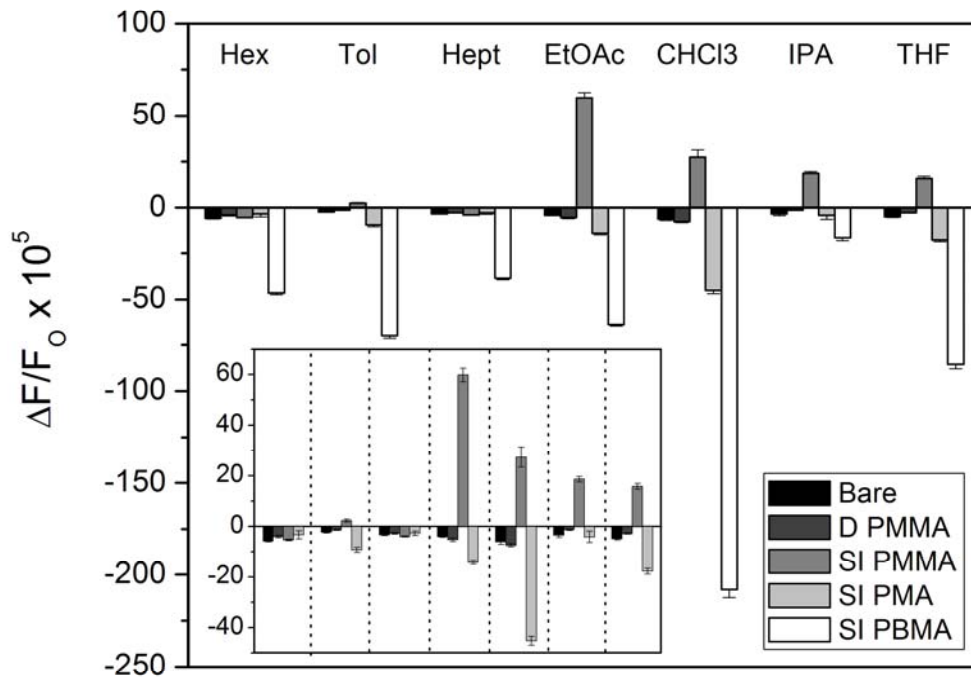


Figure 2: Responses of unmasked nanocantilevers to 400 sec pulses of a series of chemical vapors at a concentration of 0.02 P/P°. Nanocantilevers coated with glassy SI-PMMA responded positively to polar vapors, while nanocantilevers coated with rubbery SI-PMA and SI-PBMA responded negatively to all vapors.

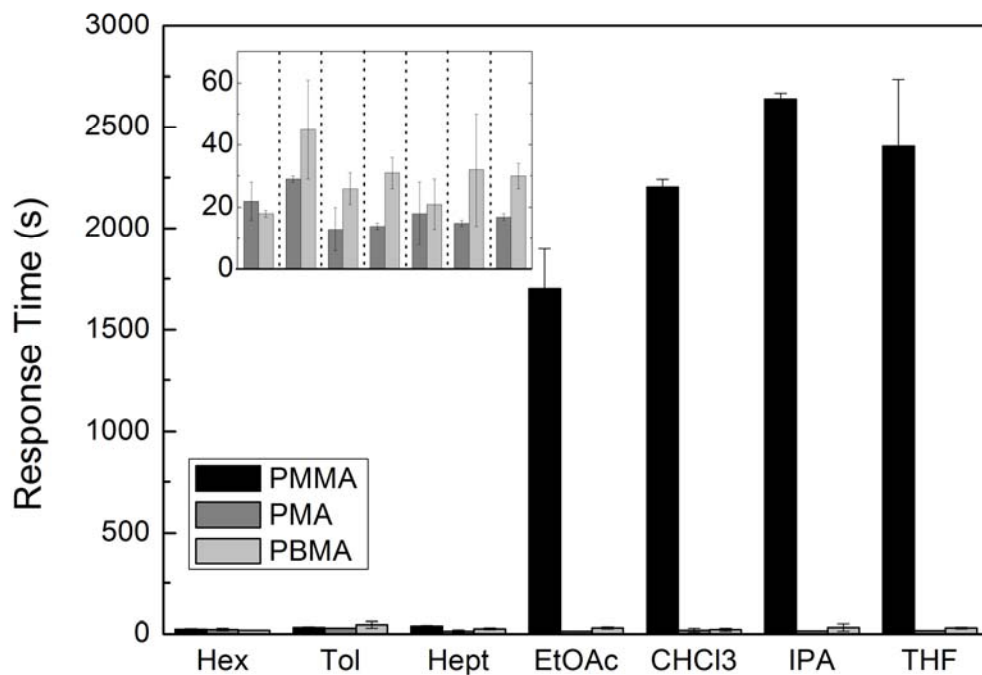


Figure 3: Nanocantilevers coated with rubbery SI-PMA and SI-PBMA responded to all vapors within 50 s, while nanocantilevers coated with glassy SI-PMMA required long exposures to reach equilibrium with polar vapors.

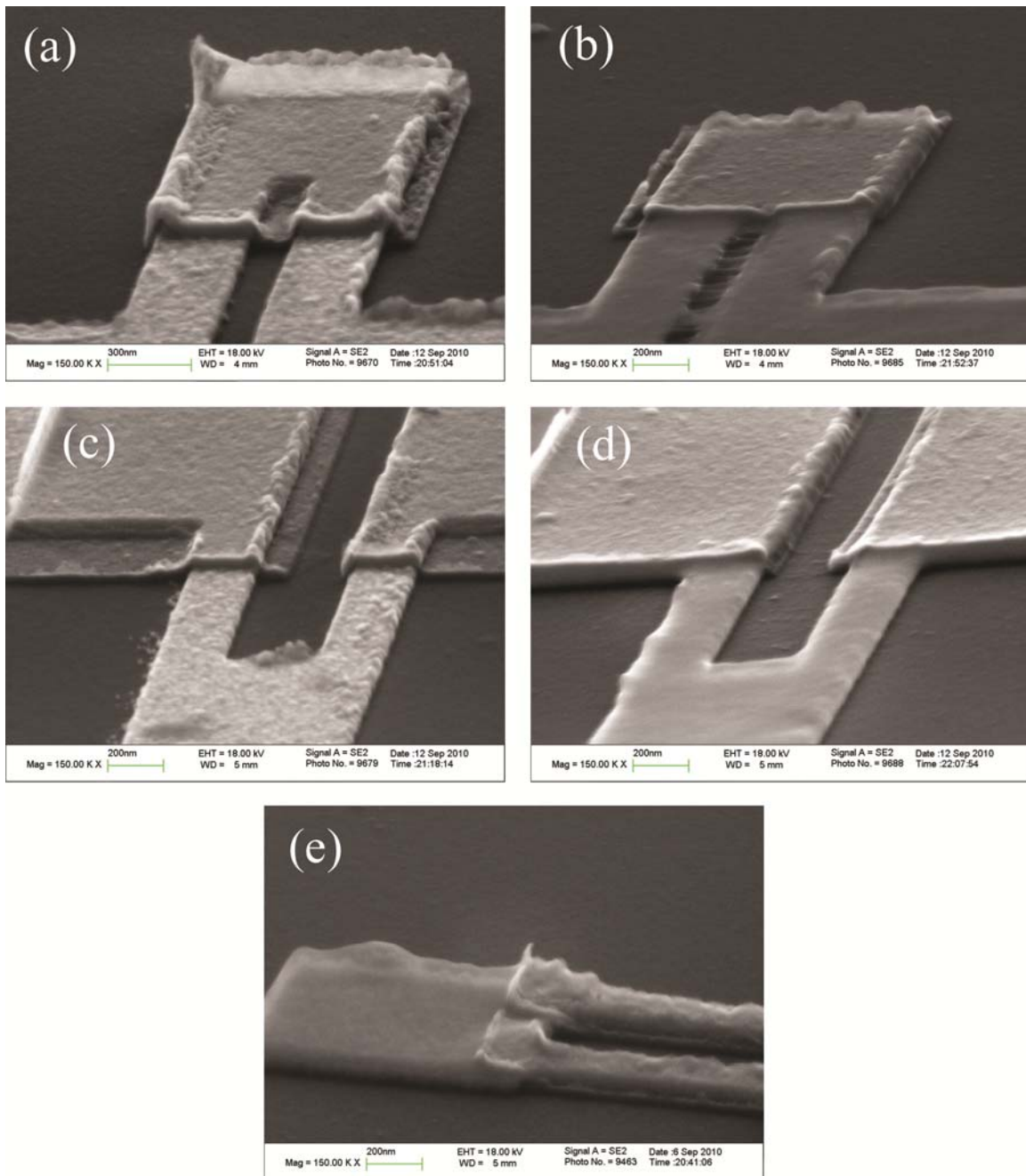


Figure 4: SEM images of unsuspended chromium-masked nanocantilevers before and after selectively coating the exposed gold with SI-PMMA: Cr-tip before (a) after (b) polymerization, Cr-base before (c) and after (d) polymerization, and Cr-legs after (e) polymerization, where the smooth translucent PMMA film is visible on the exposed gold, while the chromium-masked legs remain bare.

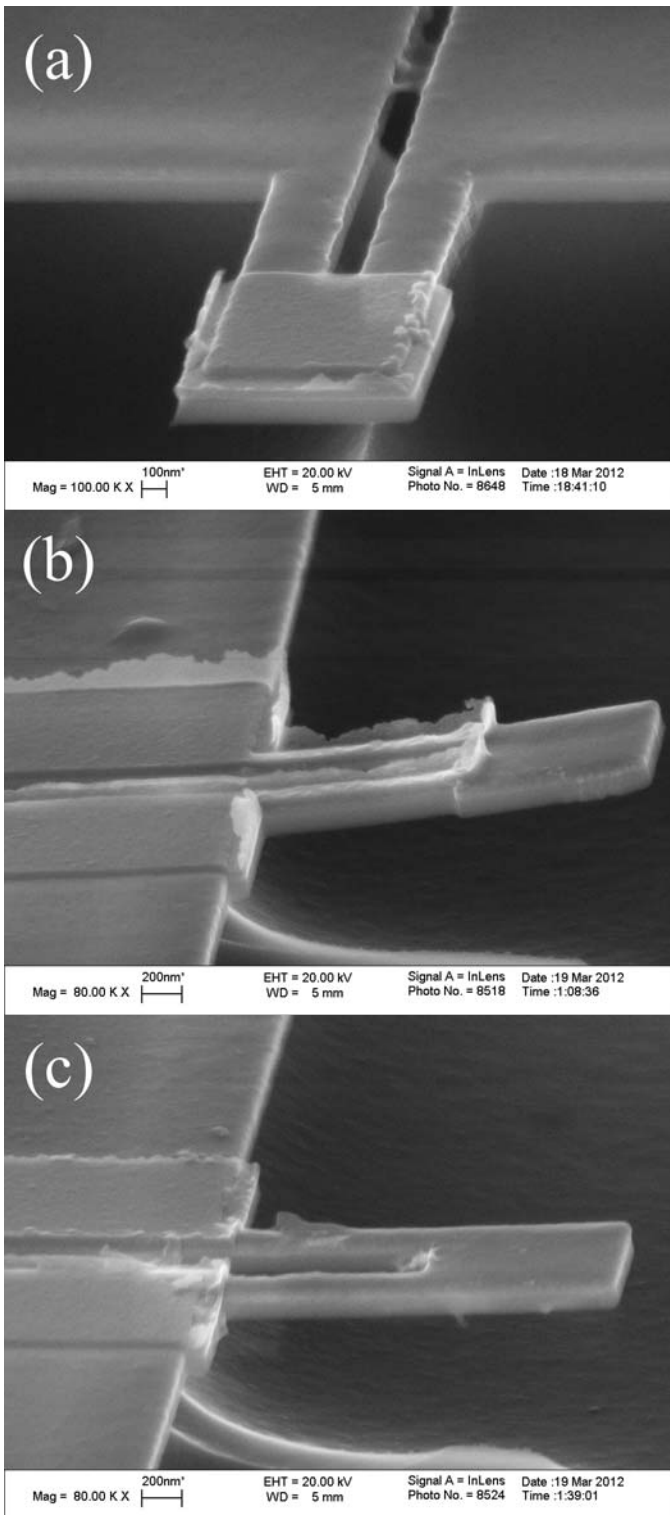


Figure 5: SEM images of chromium-masked nanocantilevers with localized films of SI-PBMA on the exposed gold regions: Cr-tip (a), Cr-legs (b), and Cr-base (c).

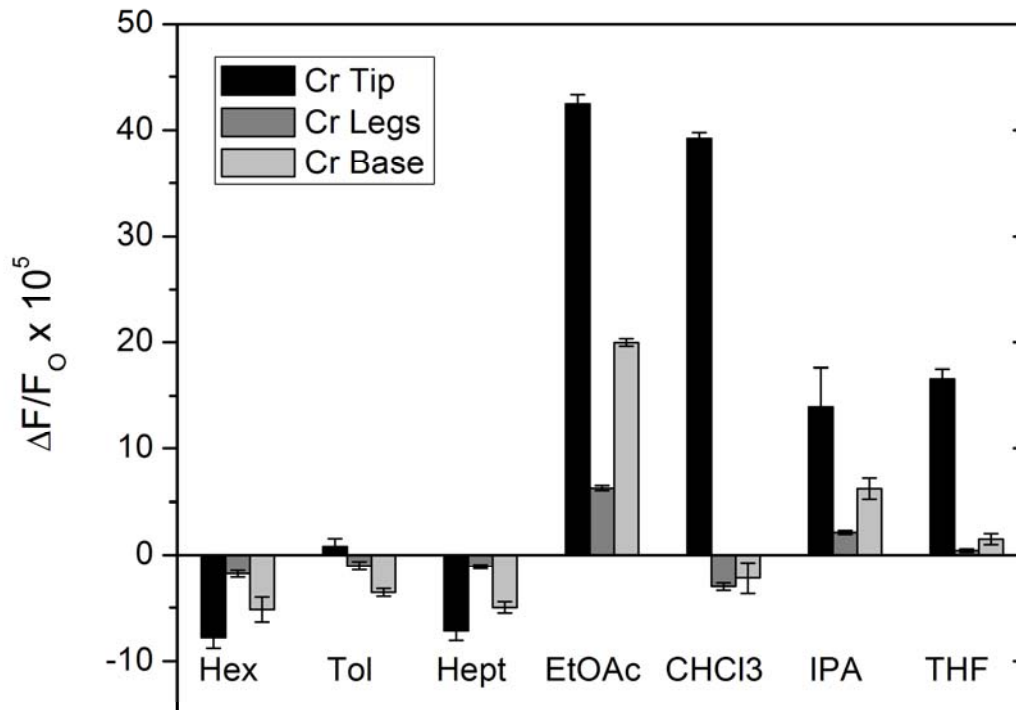


Figure 6: Responses of chromium-masked nanocantilevers coated with localized films of glassy SI-PMMA to a series of chemical vapors presented at 0.02 P/P^o. Cr-tip nanocantilevers showed the greatest responses and Cr-legs nanocantilevers showed the smallest responses, indicating that mass-loading does not dominate the response.

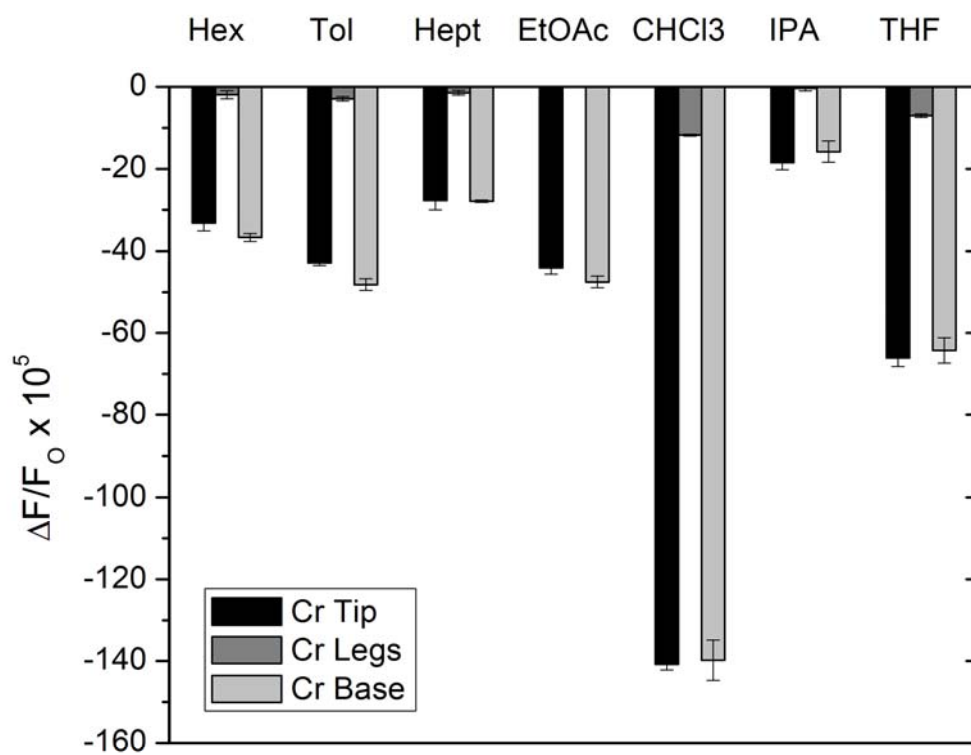


Figure 7: Responses of chromium-masked nanocantilevers coated with localized films of rubbery SI-PBMA to a series of chemical vapors presented at 0.02 P/P^o. Cr-tip nanocantilevers exhibit much smaller responses than Cr-legs and Cr-base nanocantilevers, indicating that vapor sorption on the clamped end is essential for strong responses,

Table 1: Comparison of Experimentally Measured Frequency Shifts and Calculated Frequency Shifts Due to Mass Loading for Unmasked Nanocantilever Sensors

<i>Responses of Nanocantilevers: $\Delta f/f_0 \times 10^5$</i>						
Vapor	SI-PMMA		SI-PMA		SI-PBMA	
	Experimental	Calculated	Experimental	Calculated	Experimental	Calculated
Hexane	-5.30 ± 0.26	-0.47	-3.32 ± 1.59	-0.13	-46.45 ± 1.08	-0.13
Toluene	2.37 ± 0.54	-1.07	-9.21 ± 0.99	-0.14	-69.67 ± 1.31	-0.20
Heptane	-3.96 ± 0.21	-0.28	-2.72 ± 0.85	-0.06	-38.55 ± 0.86	-0.07
Ethyl acetate	59.80 ± 2.65	-0.61	-14.22 ± 0.78	-0.16	-63.57 ± 0.75	-0.43
Chloroform	27.40 ± 3.95	-3.80	-45.14 ± 1.72	-0.20	-208.12 ± 4.40	-0.89
Isopropanol	18.60 ± 1.03	-0.23	-4.10 ± 2.28	-0.06	-16.55 ± 1.59	-0.18
Tetrahydrofuran	15.80 ± 1.13	-0.78	-17.75 ± 1.13	-0.13	-85.40 ± 2.56	-0.24

REFERENCES

1. Lewis, P. R.; Manginell, P.; Adkins, D. R.; Kottenstette, R. J.; Wheeler, D. R.; Sokolowski, S. S.; Trudell, D. E.; Byrnes, J. E.; Okandan, M.; Bauer, J. M.; Manley, R. G.; Frye-Mason, C., Recent advancements in the gas-phase MicroChemLab. *Sensors Journal, IEEE* **2006**, *6* (3), 784-795.
2. Rock, F.; Barsan, N.; Weimar, U., Electronic nose: Current status and future trends. *Chemical Reviews* **2008**, *108* (2), 705-725.
3. Covington, E.; Bohrer, F. I.; Xu, C.; Zellers, E. T.; Kurdak, C., Densely integrated array of chemiresistor vapor sensors with electron-beam patterned monolayer-protected gold nanoparticle interface films. *Lab Chip* **2010**, *10* (22), 3058-3060.
4. Lu, C. J.; Steinecker, W. H.; Tian, W. C.; Oborny, M. C.; Nichols, J. M.; Agah, M.; Potkay, J. A.; Chan, H. K. L.; Driscoll, J.; Sacks, R. D.; Wise, K. D.; Pang, S. W.; Zellers, E. T., First-generation hybrid MEMS gas chromatograph. *Lab Chip* **2005**, *5* (10), 1123-1131.
5. Albert, K. J.; Lewis, N. S.; Schauer, C. L.; Sotzing, G. A.; Stitzel, S. E.; Vaid, T. P.; Walt, D. R., Cross-reactive chemical sensor arrays. *Chemical Reviews* **2000**, *100* (7), 2595-2626.
6. Ibañez, F. J.; Gowrishetty, U.; Crain, M. M.; Walsh, K. M.; Zamborini, F. P., Chemiresistive vapor sensing with microscale films of gold monolayer protected clusters. *Analytical chemistry* **2006**, *78* (3), 753-761.
7. Jian, R. S.; Huang, R. X.; Lu, C. J., A micro GC detector array based on chemiresistors employing various surface functionalized monolayer-protected gold nanoparticles. *Talanta* **2012**, *88*, 160-167.
8. Snow, E. S.; Perkins, F. K.; Houser, E. J.; Badescu, S. C.; Reinecke, T. L., Chemical Detection with a Single-Walled Carbon Nanotube Capacitor. *Science* **2005**, *307* (5717), 1942-1945.
9. Robinson, J. A.; Snow, E. S.; Perkins, F. K., Improved chemical detection using single-walled carbon nanotube network capacitors. *Sens. Actuator A-Phys.* **2007**, *135* (2), 309-314.
10. Grate, J. W., Acoustic wave microsensor arrays for vapor sensing. *Chemical Reviews* **2000**, *100* (7), 2627-2647.
11. Grate, J. W.; Rose-Pehrsson, S. L.; Venezky, D. L.; Klusty, M.; Wohltjen, H., Smart sensor system for trace organophosphorus and organosulfur vapor detection employing a temperature-controlled array of surface acoustic wave sensors, automated sample preconcentration, and pattern recognition. *Analytical chemistry* **1993**, *65* (14), 1868-1881.
12. Wang, L.; Fine, D.; Dodabalapur, A., Nanoscale chemical sensor based on organic thin-film transistors. *Applied Physics Letters* **2004**, *85* (26), 6386-6388.
13. Chen, P. C.; Ishikawa, F. N.; Chang, H. K.; Ryu, K.; Zhou, C., A nanoelectronic nose: a hybrid nanowire/carbon nanotube sensor array with integrated micromachined hotplates for sensitive gas discrimination. *Nanotechnology* **2009**, *20* (12), 8.
14. Pinnaduwege, L. A.; Ji, H. F.; Thundat, T., Moore's law in homeland defense: An integrated sensor platform based on silicon microcantilevers. *IEEE Sens. J.* **2005**, *5* (4), 774-785.
15. Lavrik, N. V.; Sepaniak, M. J.; Datskos, P. G., Cantilever transducers as a platform for chemical and biological sensors. *Review of Scientific Instruments* **2004**, *75* (7), 2229-2253.
16. Lang, H. P.; Baller, M. K.; Berger, R.; Gerber, C.; Gimzewski, J. K.; Battiston, F. M.; Fornaro, P.; Ramseyer, J. P.; Meyer, E.; Güntherodt, H. J., An artificial nose based on a micromechanical cantilever array. *Anal. Chim. Acta* **1999**, *393* (1-3), 59-65.
17. Chapman, P. J.; Vogt, F.; Dutta, P.; Datskos, P. G.; Devault, G. L.; Sepaniak, M. J., Facile Hyphenation of Gas Chromatography and a Microcantilever Array Sensor for Enhanced Selectivity. *Analytical chemistry* **2006**, *79* (1), 364-370.
18. Datar, R.; Kim, S.; Jeon, S.; Hesketh, P.; Manalis, S.; Boisen, A.; Thundat, T., Cantilever Sensors: Nanomechanical Tools for Diagnostics. *Mrs Bulletin* **2009**, *34* (6), 449-454.
19. Yang, Y. T.; Callegari, C.; Feng, X. L.; Ekinici, K. L.; Roukes, M. L., Zeptogram-scale nanomechanical mass sensing. *Nano Lett.* **2006**, *6* (4), 583-586.
20. Chiu, H. Y.; Hung, P.; Postma, H. W. C.; Bockrath, M., Atomic-Scale Mass Sensing Using Carbon Nanotube Resonators. *Nano Lett.* **2008**, *8* (12), 4342-4346.
21. Jensen, K.; Kim, K.; Zettl, A., An atomic-resolution nanomechanical mass sensor. *Nat. Nanotechnol.* **2008**, *3* (9), 533-537.

22. Li, M.; Tang, H. X.; Roukes, M. L., Ultra-sensitive NEMS-based cantilevers for sensing, scanned probe and very high-frequency applications. *Nat. Nanotechnol.* **2007**, *2* (2), 114-120.
23. Eom, K.; Park, H. S.; Yoon, D. S.; Kwon, T., Nanomechanical resonators and their applications in biological/chemical detection: Nanomechanics principles. *Phys. Rep.-Rev. Sec. Phys. Lett.* **2011**, *503* (4-5), 115-163.
24. Tamayo, J.; Ramos, D.; Mertens, J.; Calleja, M., Effect of the adsorbate stiffness on the resonance response of microcantilever sensors. *Applied Physics Letters* **2006**, *89* (22), 3.
25. Ramos, D.; Tamayo, J.; Mertens, J.; Calleja, M.; Zaballos, A., Origin of the response of nanomechanical resonators to bacteria adsorption. *Journal of Applied Physics* **2006**, *100* (10), 3.
26. Lee, D.; Kim, S.; Jung, N.; Thundat, T.; Jeon, S., Effects of gold patterning on the bending profile and frequency response of a microcantilever. *Journal of Applied Physics* **2009**, *106* (2), 024310.
27. Thundat, T.; Chen, G. Y.; Warmack, R. J.; Allison, D. P.; Wachter, E. A., Vapor Detection Using Resonating Microcantilevers. *Analytical chemistry* **1995**, *67* (3), 519-521.
28. Li, M.; Myers, E. B.; Tang, H. X.; Aldridge, S. J.; McCaig, H. C.; Whiting, J. J.; Simonson, R. J.; Lewis, N. S.; Roukes, M. L., Nanoelectromechanical Resonator Arrays for Ultrafast, Gas-Phase Chromatographic Chemical Analysis. *Nano Lett.* **2010**, *10* (10), 3899-3903.
29. Barbey, R.; Lavanant, L.; Paripovic, D.; Schuwer, N.; Sugnaux, C.; Tugulu, S.; Klok, H. A., Polymer Brushes via Surface-Initiated Controlled Radical Polymerization: Synthesis, Characterization, Properties, and Applications. *Chemical Reviews* **2009**, *109* (11), 5437-5527.
30. Bumbu, G. G.; Wolkenhauer, M.; Kircher, G.; Gutmann, J. S.; Berger, R., Micromechanical cantilever technique: A tool for investigating the swelling of polymer brushes. *Langmuir* **2007**, *23* (4), 2203-2207.
31. Abu-Lail, N. I.; Kaholek, M.; LaMattina, B.; Clark, R. L.; Zauscher, S., Micro-cantilevers with end-grafted stimulus-responsive polymer brushes for actuation and sensing. *Sensors and Actuators B-Chemical* **2006**, *114* (1), 371-378.
32. Bradley, C.; Jalili, N.; Nett, S. K.; Chu, L. Q.; Forch, R.; Gutmann, J. S.; Berger, R., Response Characteristics of Thermoresponsive Polymers Using Nanomechanical Cantilever Sensors. *Macromol. Chem. Phys.* **2009**, *210* (16), 1339-1345.
33. Chen, T.; Chang, D. P.; Liu, T.; Desikan, R.; Datar, R.; Thundat, T.; Berger, R.; Zauscher, S., Glucose-responsive polymer brushes for microcantilever sensing. *J. Mater. Chem.* **2010**, *20* (17), 3391-3395.
34. Bumbu, G. G.; Kircher, G.; Wolkenhauer, M.; Berger, R.; Gutmann, J. S., Synthesis and characterization of polymer brushes on micromechanical cantilevers. *Macromol. Chem. Phys.* **2004**, *205* (13), 1713-1720.
35. Lemieux, M.; Minko, S.; Usov, D.; Stamm, M.; Tsukruk, V. V., Direct measurement of thermoelastic properties of glassy and rubbery polymer brush nanolayers grown by "grafting-from" approach. *Langmuir* **2003**, *19* (15), 6126-6134.
36. Koutsos, V.; van der Vegte, E. W.; Hadziioannou, G., Direct view of structural regimes of end-grafted polymer monolayers: A scanning force microscopy study. *Macromolecules* **1999**, *32* (4), 1233-1236.
37. Scientific Polymer Products, Inc.
38. Saha, S.; Bruening, M. L.; Baker, G. L., Facile Synthesis of Thick Films of Poly(methyl methacrylate), Poly(styrene), and Poly(vinyl pyridine) from Au Surfaces. *ACS Applied Materials & Interfaces* **2011**, *3* (8), 3042-3048.
39. Liu, T.; Pihan, S.; Roth, M.; Retsch, M.; Jonas, U.; Gutmann, J. S.; Koynov, K.; Butt, H. J.; Berger, R., Frequency Response of Polymer Films Made from a Precursor Colloidal Mono layer on a Nanomechanical Cantilever. *Macromolecules* **2012**, *45* (2), 862-871.
40. Tranchida, D.; Sperotto, E.; Chateauminois, A.; Scholnherr, H., Entropic Effects on the Mechanical Behavior of Dry Polymer Brushes During Nanoindentation by Atomic Force Microscopy. *Macromolecules* **2011**, *44* (2), 368-374.
41. Felder, R. M.; Huvad, G. S.; Fava, R. A., 17. Permeation, Diffusion, and Sorption of Gases and Vapors. In *Methods in Experimental Physics*, Academic Press: 1980; Vol. Volume 16, Part C, pp 315-377.
42. Berens, A. R.; Hopfenberg, H. B., Diffusion of organic vapors at low concentrations in glassy PVC, polystyrene, and PMMA. *Journal of Membrane Science* **1982**, *10* (2-3), 283-303.

43. Sanopoulou, M.; Petropoulos, J. H., Systematic Analysis and Model Interpretation of Micromolecular Non-Fickian Sorption Kinetics in Polymer Films. *Macromolecules* **2001**, *34* (5), 1400-1410.
44. Ferrari, M.-C.; Piccinini, E.; Giacinti Baschetti, M.; Doghieri, F.; Sarti, G. C., Solvent-Induced Stresses during Sorption in Glassy Polycarbonate: Experimental Analysis and Model Simulation for a Novel Bending Cantilever Apparatus. *Industrial & Engineering Chemistry Research* **2008**, *47* (4), 1071-1080.
45. De Angelis, M. G.; Sarti, G. C., Solubility of Gases and Liquids in Glassy Polymers. *Annual Review of Chemical and Biomolecular Engineering* **2011**, *2* (1), 97-120.
46. Lewis, N. S., Comparisons between mammalian and artificial olfaction based on arrays of carbon black-polymer composite vapor detectors. *Accounts of Chemical Research* **2004**, *37* (9), 663-672.
47. Gawalt, E. S.; Avaltroni, M. J.; Koch, N.; Schwartz, J., Self-Assembly and Bonding of Alkanephosphonic Acids on the Native Oxide Surface of Titanium. *Langmuir* **2001**, *17* (19), 5736-5738.
48. Goetting, L. B.; Deng, T.; Whitesides, G. M., Microcontact Printing of Alkanephosphonic Acids on Aluminum: Pattern Transfer by Wet Chemical Etching. *Langmuir* **1999**, *15* (4), 1182-1191.
49. Laibinis, P. E.; Hickman, J. J.; Wrighton, M. S.; Whitesides, G. M., Orthogonal Self-Assembled Monolayers: Alkanethiols on Gold and Alkane Carboxylic-Acids on Alumina. *Science* **1989**, *245* (4920), 845-847.
50. Yang, Y. T.; Ekinici, K. L.; Huang, X. M. H.; Schiavone, L. M.; Roukes, M. L.; Zorman, C. A.; Mehregany, M., Monocrystalline silicon carbide nanoelectromechanical systems. *Applied Physics Letters* **2001**, *78* (2), 162-164.
51. Bargatin, I.; Myers, E. B.; Arlett, J.; Gudlewski, B.; Roukes, M. L., Sensitive detection of nanomechanical motion using piezoresistive signal downmixing. *Applied Physics Letters* **2005**, *86* (13), 3.
52. Bargatin, I.; Kozinsky, I.; Roukes, M. L., Efficient electrothermal actuation of multiple modes of high-frequency nanoelectromechanical resonators. *Applied Physics Letters* **2007**, *90* (9), 3.
53. Jones, D. M.; Huck, W. T. S., Controlled surface-initiated polymerizations in aqueous media. *Adv. Mater.* **2001**, *13* (16), 1256-1259.
54. Matyjaszewski, K.; Miller, P. J.; Shukla, N.; Immaraporn, B.; Gelman, A.; Luokala, B. B.; Siclován, T. M.; Kickelbick, G.; Vallant, T.; Hoffmann, H.; Pakula, T., Polymers at interfaces: Using atom transfer radical polymerization in the controlled growth of homopolymers and block copolymers from silicon surfaces in the absence of untethered sacrificial initiator. *Macromolecules* **1999**, *32* (26), 8716-8724.
55. Xu, C.; Wu, T.; Drain, C. M.; Batteas, J. D.; Fasolka, M. J.; Beers, K. L., Effect of block length on solvent response of block copolymer brushes: Combinatorial study with block copolymer brush gradients. *Macromolecules* **2006**, *39* (9), 3359-3364.
56. Severin, E. J.; Doleman, B. J.; Lewis, N. S., An investigation of the concentration dependence and response to analyte mixtures of carbon black/insulating organic polymer composite vapor detectors. *Analytical Chemistry* **2000**, *72* (4), 658-668.
57. Briglin, S. M.; Freund, M. S.; Tokumar, P.; Lewis, N. S., Exploitation of spatiotemporal information and geometric optimization of signal/noise performance using arrays of carbon black-polymer composite vapor detectors. *Sensors and Actuators B-Chemical* **2002**, *82* (1), 54-74.
58. Hanay, M. S.; Kelber, S.; Naik, A. K.; Chi, D.; Hentz, S.; Bullard, E. C.; Colinet, E.; Duraffourg, L.; Roukes, M. L., Single-protein nanomechanical mass spectrometry in real time. *Nat Nano* **2012**, *7* (9), 602-608.
59. Timoshenko, S.; Young, D. H.; Weaver, W., *Vibration Problems in Engineering*. 4 ed.; Wiley: New York, 1974.

Nanocantilever Chemical Vapor Sensors Coated with Localized Rubbery and Glassy Polymer Brush Films: Sensing Changes in Stiffness

Supplementary Information

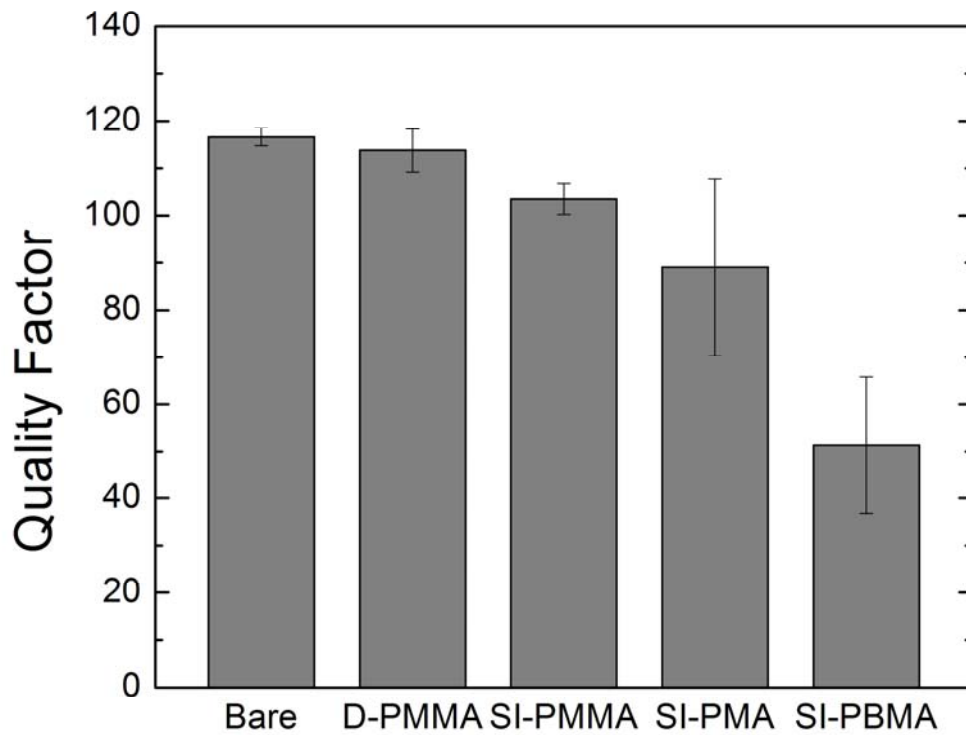


Figure S1: The resonance quality factor is changes little upon coating nanocantilevers with D-PMMA and SI-PMMA films, but decreases when the nanocantilevers are coated with rubbery SI-PMA and SI-PBMA films.

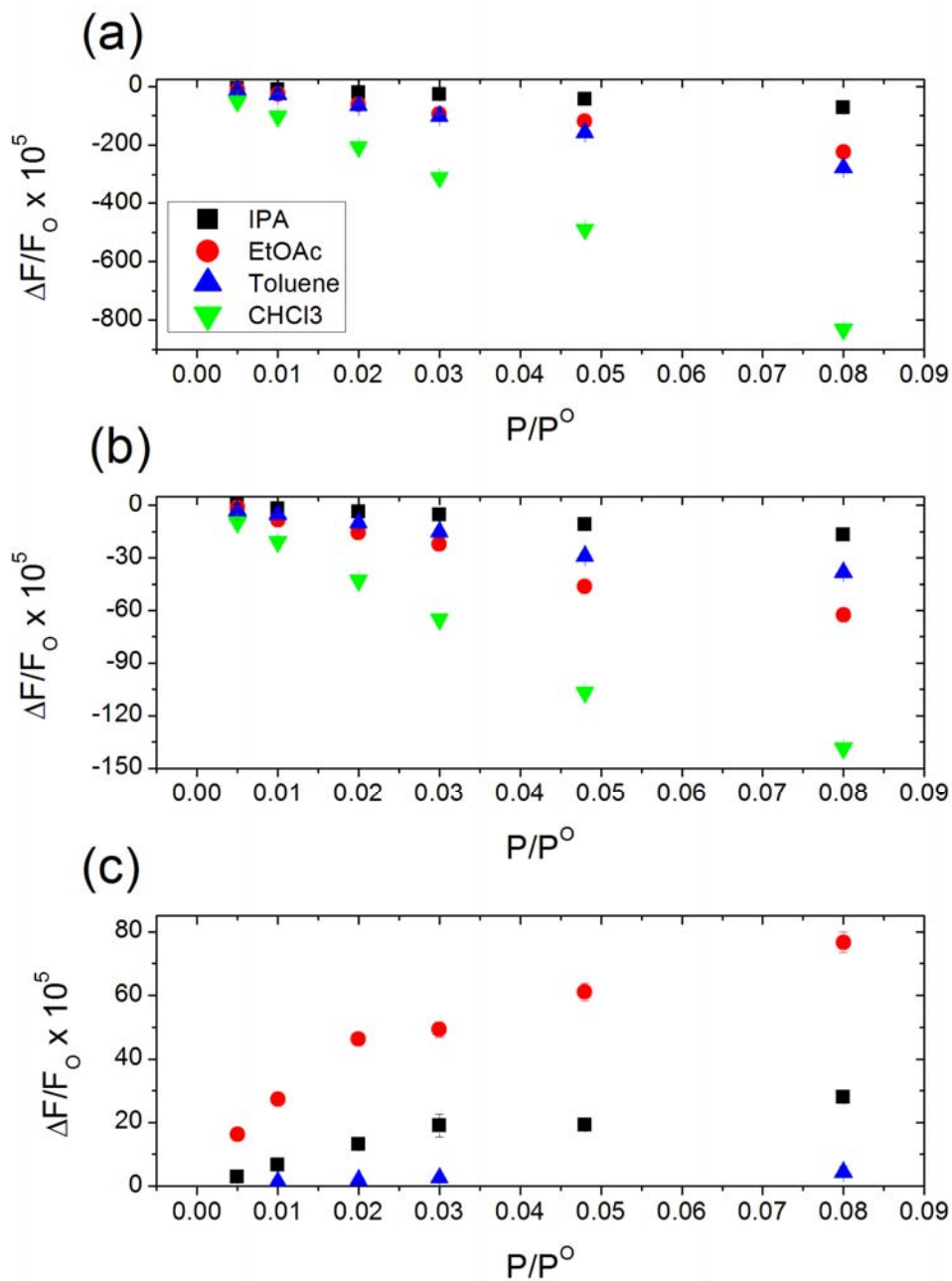


Figure S2: Linearity of sensor responses with respect to vapor concentration for unmasked nanocantilever coated with SI-PBMA (a), SI-PMA (b), and SI-PMMA (c).

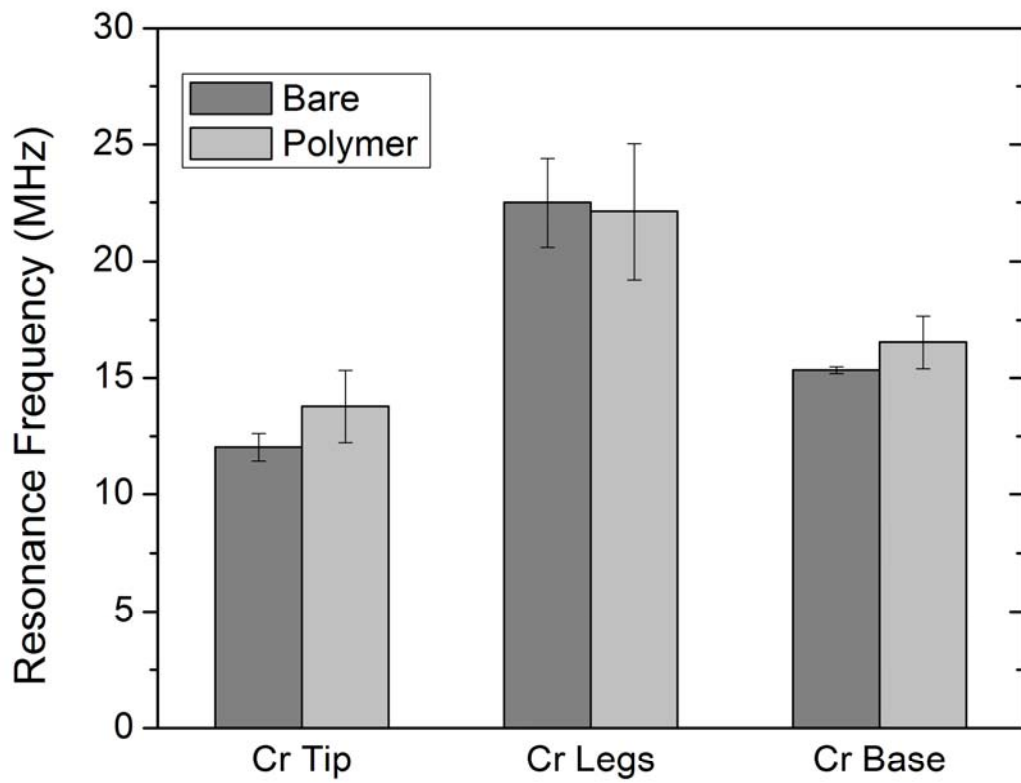


Figure S3: Average change in resonance frequency upon coating chromium-masked cantilevers with SI-ATRP grown polymer films.

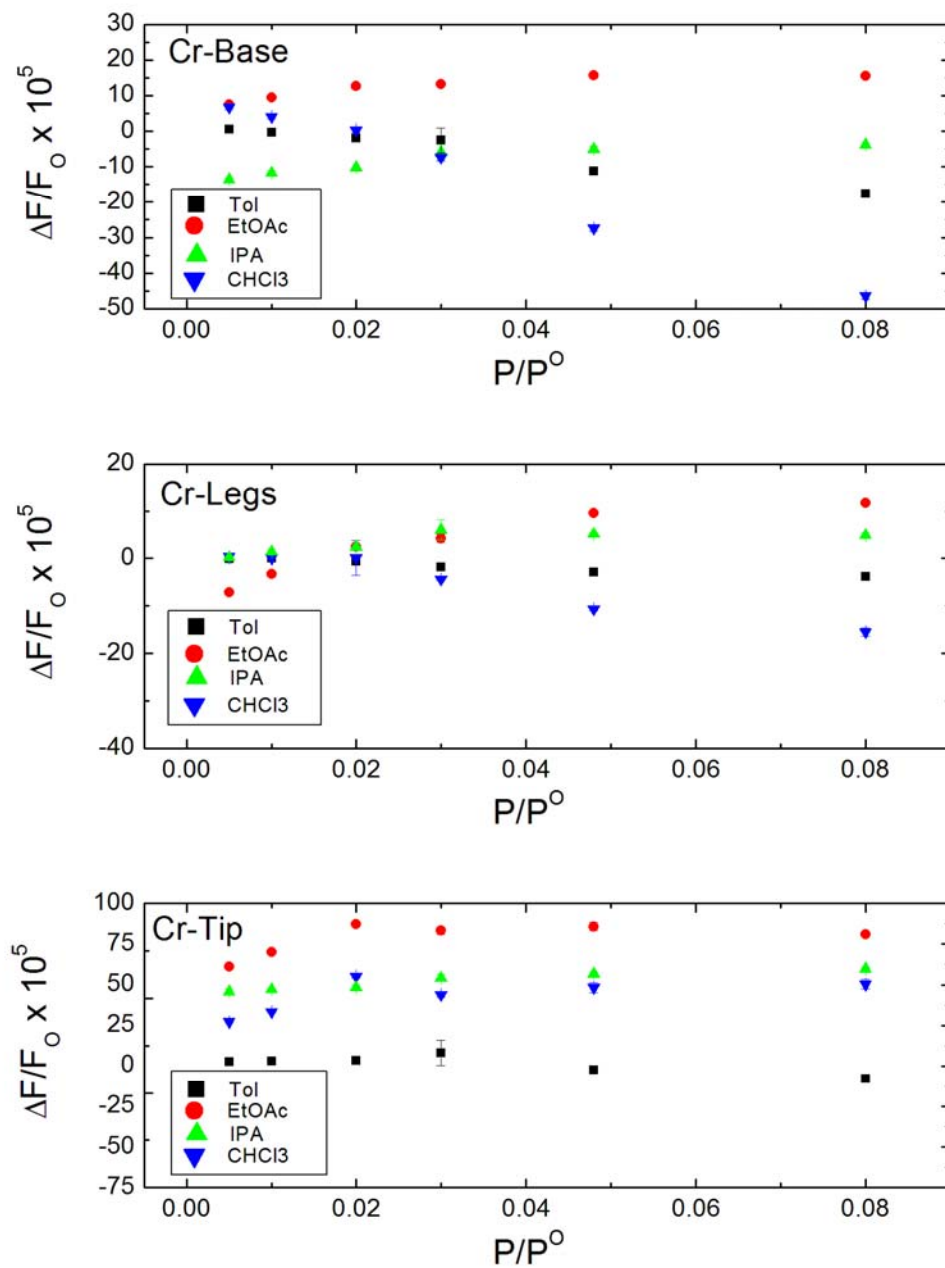


Figure S4: Linearity of sensor responses with respect to vapor concentration for chromium-masked nanocantilevers coated with localized SI-PMMA films.

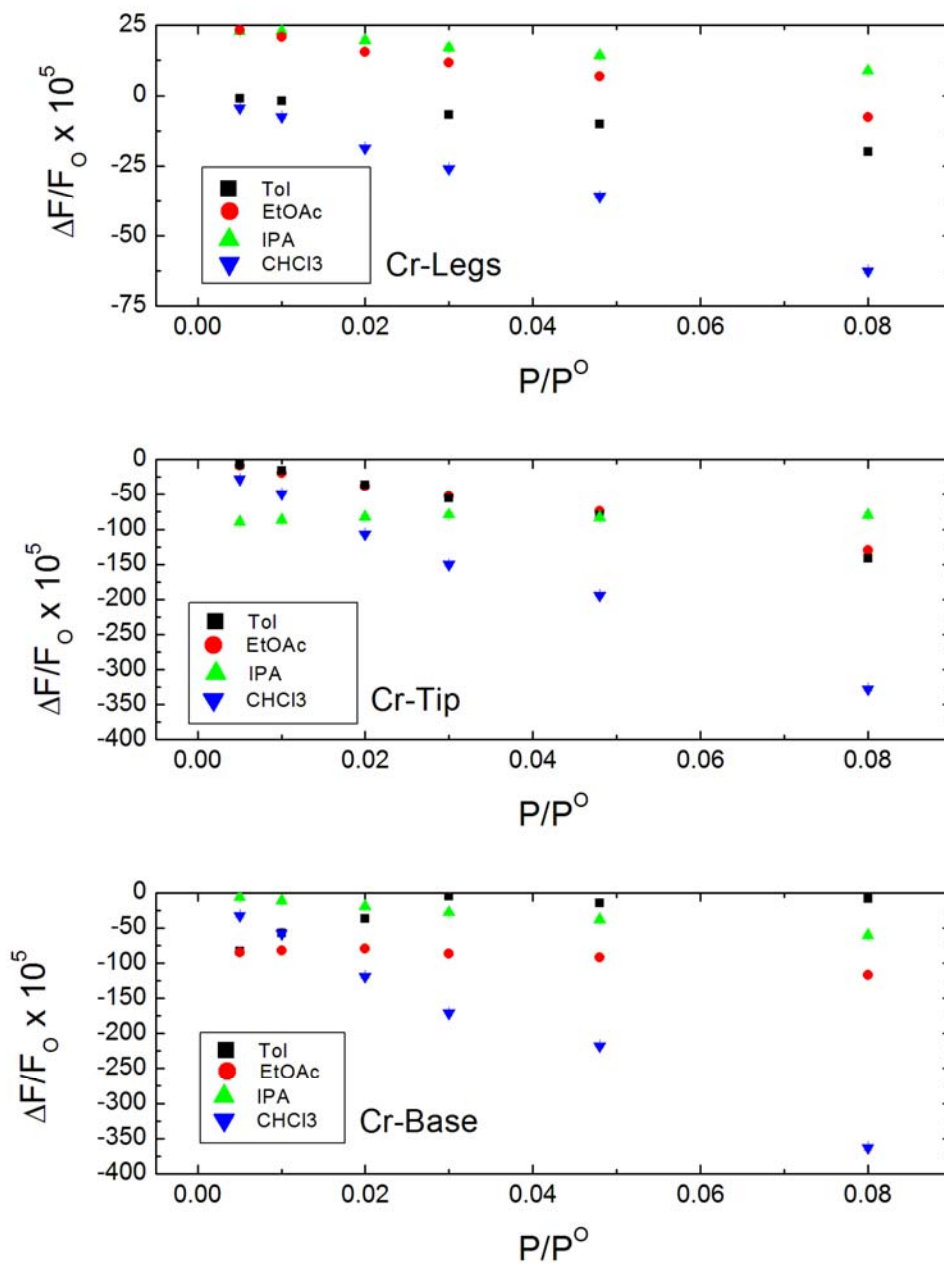


Figure S5: Linearity of sensor responses with respect to vapor concentration for chromium-masked nanocantilevers coated with localized SI-PBMA films.

Table S1: Relative frequency shifts of chromium-masked nanocantilevers coated with localized SI-PMMA films exposed to vapors at 0.02 P/P⁰.

Responses of Nanocantilevers: $\Delta f/f_0 \times 10^5$			
Vapor	Cr-Tip	Cr-Legs	Cr-Base
Hexane	-7.78 ± 0.99	-1.79 ± 0.31	-5.19 ± 1.18
Toluene	0.82 ± 0.72	-1.03 ± 0.39	-3.57 ± 0.37
Heptane	-7.17 ± 0.87	-1.11 ± 0.193	-4.99 ± 0.53
Ethyl acetate	42.50 ± 0.79	6.25 ± 0.25	19.96 ± 0.35
Chloroform	39.25 ± 0.54	-3.02 ± 0.36	-2.20 ± 1.47
Isopropanol	13.96 ± 3.67	2.13 ± 0.18	6.19 ± 1.00
Tetrahydrofuram	16.58 ± 0.94	0.42 ± 0.17	1.52 ± 0.52

Table S2: Relative frequency shifts of chromium-masked nanocantilevers coated with localized SI-PBMA films exposed to vapors at 0.02 P/P⁰.

Responses of Nanocantilevers: $\Delta f/f_0 \times 10^5$			
Vapor	Cr-Tip	Cr-Legs	Cr-Base
Hexane	-33.24 ± 1.88	-1.93 ± 1.00	-36.72 ± 0.94
Toluene	-42.90 ± 0.58	-2.95 ± 0.51	-48.11 ± 1.38
Heptane	-27.81 ± 2.26	-1.46 ± 0.58	-27.95 ± 0.27
Ethyl acetate	-44.09 ± 1.52	0.27 ± 0.56	-47.46 ± 1.40
Chloroform	-140.80 ± 1.36	-11.80 ± 0.19	-139.87 ± 4.92
Isopropanol	-18.49 ± 1.77	-0.39 ± 0.66	-15.81 ± 2.57
Tetrahydrofuram	-66.07 ± 2.07	-7.06 ± 0.46	-64.24 ± 3.10

Table S3: Partition coefficients for dropcast and SI-ATRP grown polymer films.

Partition Coefficients (K_{eq})						
Vapor	Bulk PMMA	SI-PMMA	Bulk PMA	SI-PMA	Bulk PBMA	SI-PBMA
Hexane	105	40	56	41	165	145
Toluene	525	375	220	256	2047	2014
Heptane	308	90	160	76	362	384
Ethyl acetate	108	280	47	102	438	399
Chloroform	46	200	19	44	875	853
Isopropanol	1037	350	593	106	400	446
Tetrahydrofuram	57	115	21	57	402	376

Annual Report (April 2013)

Development of Structural Steel with Higher Blast Resistance: Influence of Cold Rolling, Pearlite Volume Fraction and Grain Size

Hamouda Ghonem

Mechanics of Materials Research Laboratory
Department of Mechanical, Industrial and Systems Engineering
University of Rhode Island, Kingston RI 028821
ghonem@egr.uri.edu

Prepared for: DHS Center of Excellence for Explosive Detection, Mitigation and Response

Objectives

The research work in the Mechanics of Materials Research Laboratory (MMRL), as part of the blast mitigation group of the DHS Center of Excellence, focuses on identifying deformation and damage mechanisms of the reinforcing low carbon steel (LCS) phase of civil structures subjected to blast loadings. For this purpose, an extensive program has been carried out to examine various microstructure factors which influence the dynamic behavior, as well as, post-impact performance of LCS. These include prior deformation (by cold rolling), second phase particles (variation of pearlite volume fraction by heat treatment) and grain size (grain refinement through severe plastic deformation).

The first task in this work has dealt with identification of the deformation mechanisms in LCS associated with plate impacts. This has been achieved through the use of a light gas gun (designed and built in the MMRL as part of the DHS program). Results of this work have provided knowledge of the two rate controlling mechanisms, slip and mechanical twinning, and their relation with blast severity. In conjunction with this work, the critical stress required for twin initiation has been identified through the use of a Split Hopkinson Pressure Bar apparatus (SHPB, designed and built in the MMRL as part of the DHS program) at cryogenic temperatures. This critical stress has been implemented in a numerical model in order to predict twin volume fraction (TVF) as a function of impact pressure. TVF is shown to increase with impact pressure and post-impact testing has shown an increase in TVF is associated with a decrease in residual life. Furthermore, the critical twinning stress has also been explicitly modeled as a function of prior deformation by cold rolling of the as-received LCS which is shown to suppress twin formation during plate impact experiments and increase the critical stress twinning. ***Results of this work conclude that post-impact performance of LCS measured in terms of residual life, can be significantly improved by prior cold rolling.***

The second task of this work has examined the role of second phase particles, in particular the volume fraction of pearlite colonies, on the relative significance of the thermal and athermal stress components in relation to the overall flow behavior of the material. This has been achieved through a series of high strain rate tests carried out on the SHPB over temperatures ranging from 20 to 650°C. Results of this work have been analyzed in terms of thermal and athermal flow stress components for both the as-received LCS (9% pearlite volume fraction) and heat treated LCS (0% pearlite volume fraction). The thermal stress component, a function of only temperature and strain rate, arises from the interaction of dislocations with short range barriers, (phonons, forest dislocations, dislocation jogs and kinks and Peierls-Narbarro resistance to dislocation motion) is shown to be independent of pearlite volume fraction. On the other hand, the athermal stress component, which arises from the interaction of dislocations with long range barriers (grain boundaries, precipitates, second phase particles) is strongly influenced by the pearlite volume fraction, a second phase particle of the LCS studied. A decrease in pearlite volume fraction decreases the athermal stress component. The athermal component is a function of strain and as stated,

micro structural parameters. The total flow stress is the summation of the thermal and athermal stress components, which is also shown a decrease with the decrease in pearlite volume fraction. ***These results point out to a route for optimizing the pearlite volume fraction of the LCS in order to increase its flow resistance under dynamic loading conditions.***

The third part of this work aims at determining the influence of grain size on the evolution of the flow stress components under dynamic impact loading. For this, the constitutive behavior of the athermal stress component, developed previously as an explicit function of strain and pearlite volume fraction, will be examined as a function of the grain size. In order to achieve this goal, the coarse grain LCS (40-50 μm) will be subjected to severe plastic deformation (SPD) to produce ultra-fine grain (UFG) LCS (10-1 μm). The dynamic response of UFG steel will then be examined following the approach used in the second task described above. The SPD process to refine the steels grain size is achieved through the use of an equal channel angular press (ECAP). For this purpose, an ECAP die has been designed and built to produce UFG steel bars with up to a 1 inch cross section. These bars, with different grain size, will be used to generate specimens which will be tested dynamically using the available gas gun and SHPB. ***The outcome of the research work in this task is to identify the optimum grain size and pearlite volume fraction to achieve the highest possible impact load resistance of LCS.***

A brief review of the three research tasks mentioned above and their major outcomes are described in the following sections. This is followed by a list of publications and conferences, and students supported in this program. Also, attached are the papers published as part of this program.

Summary of Research

This section provides an overview and major outcomes of the three tasks examined by the MMRL group during the period 2012-2013.

Task I: Role of Cold Rolling on Impact Resistance

As mentioned above, work in this task has dealt with identification of the deformation mechanisms in LCS associated with plate impact using a light gas gun. An important result of the work performed within the frame work of this task, in the past two years, is that the high strain rate deformation of LCS occurs by two processes; dislocation slip and mechanical twinning (see Figure 1a). Furthermore, it was established that as the impact stress is increased, the volume fraction of twins increases. This increase in TVF is shown to be detrimental to the overall fracture energy during post-impact loading, as the twin boundaries play a significant role in crack propagation direction. One method, cold rolling (pre-straining), which has been shown to suppress twin nucleation, can be easily implemented into steel manufacturing processes. An inherent feature in the cooling process after hot rolling I-beams is a heterogeneous distribution of dislocations. By implementing a final cold rolling procedure into the manufacturing process, a network of mobile dislocations can be homogeneously dispersed throughout the substructure. It is shown in the current work that the plastic deformation taking place during high impact loading, in prior cold rolled material, is accommodated entirely by dislocation slip in a uniform fashion, as shown in Figure 1b. The cold rolling processes is quantified in terms of the amount of pre-strain from the original condition, i.e. the change in thickness relative to the original thickness.

A set of plate impact tests were completed at room temperature on 1% and 20% pre-strained samples. As shown in Figure 2, similar TVFs are produced in the 1% pre-strained material as in the as-received steel, but this requires double the impact stress. This will be shown to be a result of an increase in the stress required to nucleate, rather than a change in the twin growth process.

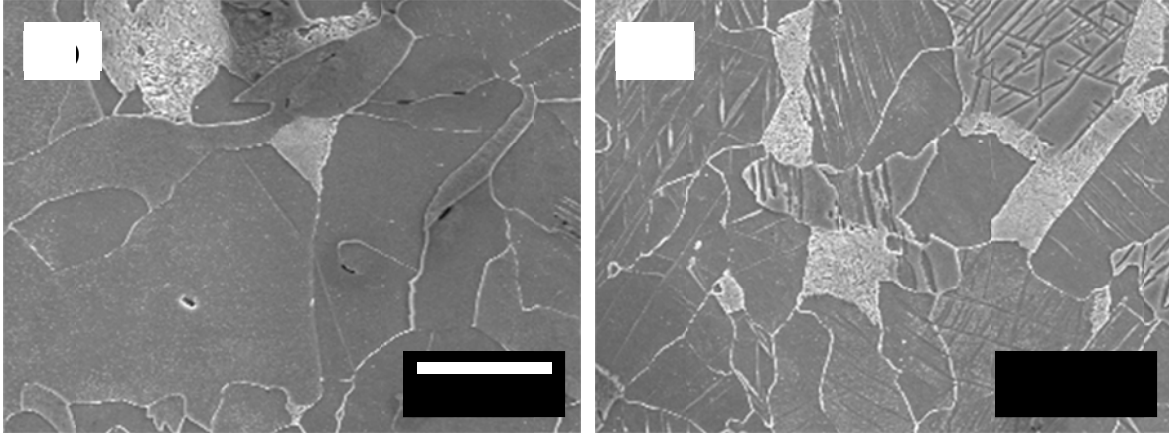


Figure 1: (a) Scanning electron micrograph of the as-received, hot rolled LCS deformed by an 11GPa plate impact, showing the presence of mechanical twins. (b) Scanning electron micrograph of LCS which has been pre-strained to 1% and deformed by an 11GPa plate impact, showing no mechanical twins present.

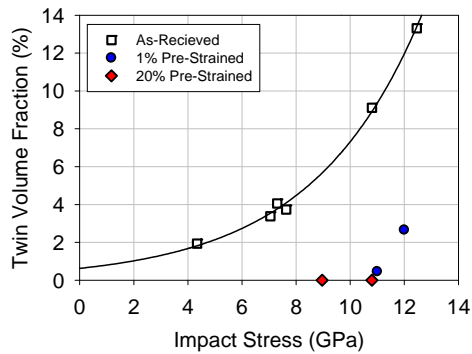


Figure 2: Twin volume fraction as a function of impact stress during room temperature plate impacts for the as-received, 1%, and 20% pre-strained LCS.

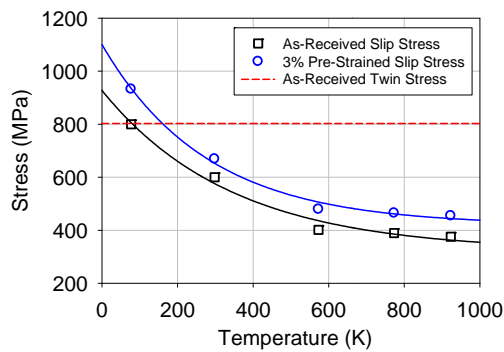


Figure 3: Slip stress and twin stress as a function of temperature, at a strain rate of $1.6 \times 10^3 \text{ s}^{-1}$. Note the solid blue and solid black lines are the minimum stress required to deform slip in the 3% pre-strained and as-received LCS, respectively, and the dashed red line is the minimum stress required for twin nucleation. For a given temperature condition, the lowest stress (slip or twin) defines the dominant deformation mode.

Tests at -196°C (77K) using the SHPB are performed in order to determine the relationship between twinning stress and the level of pre-strain. These tests were done on as-received and 3% pre-strained specimens at strain rates ranging from 8×10^2 up to $7 \times 10^3 \text{ s}^{-1}$. Figure 4 shows that the flow stress increases with strain rate and is higher for the 3% pre-strained specimen coinciding with the increase in the initial yield strength as shown in Figure 3.

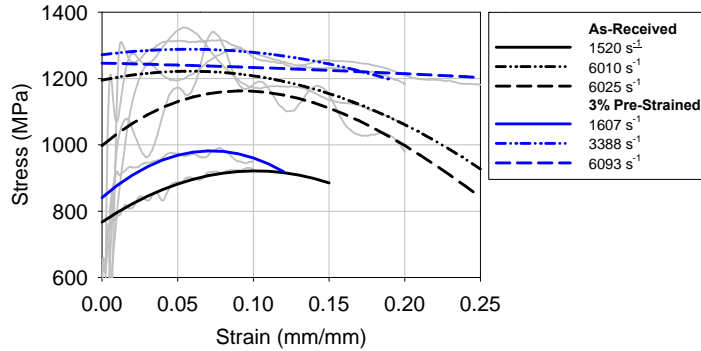


Figure 4: Typical stress-strain curves of LCS tested at -196°C (77K) using the SHPB. Note the black lines correspond to the as-received LCS and the blue lines correspond to the 3% pre-strained LCS. The strain rates are indicated in the legend.

The recovered specimens from these tests were sectioned and examined using optical and scanning electron microscopy to determine if mechanical twins are observed (see Figure 5 and 6). From this, the stress required for twin nucleation is determined for the corresponding strain rate.

As shown in Figure 5, the as-received LCS displays a clear transition from pure slip deformation at low strain rate to that of slip and twinning at higher strain rate. This is not evident in the 3% pre-strained LCS deformed at low temperature where no twins are present at either strain rate. In addition, Figure 6b shows some evidence that dynamic recovery is present and could be a possible explanation for the lack of strain hardening at the higher rates. The data from these tests was then extrapolated to higher strain rates and a larger range of pre-strain utilizing a relation between pre-strain and corresponding material hardness and dislocation density. These results are shown in Figure 7.

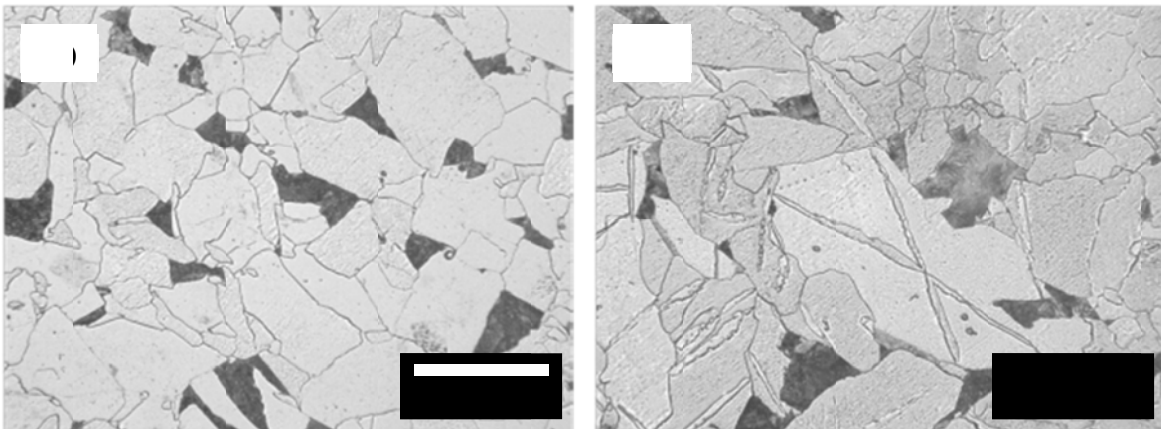


Figure 5: Typical optical micrographs of as-received LCS deformed at -196°C (77K) at strain rates of (a) 1520 s^{-1} and (b) 6010 s^{-1} .

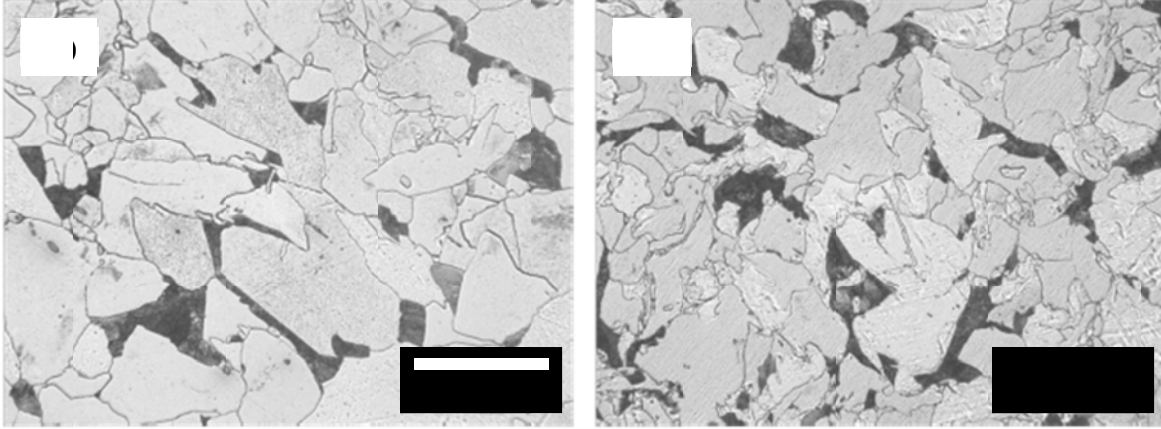


Figure 6: Typical optical micrographs of 3% pre-strained LCS deformed at -196°C (77K) at strain rates of (a) 1187 s^{-1} and (b) 6093 s^{-1} .

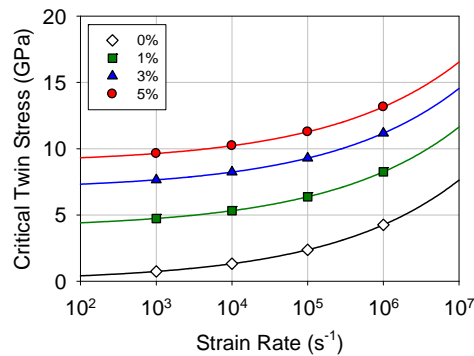


Figure 7: Critical stress required for twin nucleation as a function of strain rate for pre-strain conditions ranging from 0% (as-received LCS) to 5%, as indicated in the legend.

From Figure 7 it is clear that the initial increase in twinning stress between as-received and 1% pre-strained material is sufficient to prevent twin nucleation in low temperature SHPB testing, or significantly delay the onset and reduce the available energy to grow twins in the strain rate range for plate impacts at 10^5 s^{-1} . The absence of the twins during plate impacts of cold rolled LCS infers that deformation develops in a homogeneous uniform fashion without localized high stress regions. This is an important aspect when selecting materials for applications where impact or explosive loading could be introduced. Reducing regions of high stress concentration by introducing a homogeneous substructure allows for a uniform state of deformation throughout the material, making stress analysis and design more feasible and predictable. Therefore, cold rolling can be used as an effective means of improving dynamic impact resistance. Further testing is being conducted to validate the effectiveness of cold rolling on the post-impact integrity of the material in terms of energy to failure and crack initiation.

The work described above including full details of the deformation mechanisms and related model to predict twin volume fraction as a function of impact load and pre-straining is documented in a journal paper which is submitted to the Journal Material Science and Engineering in April 2013.

Task II: Role of Pearlite Colonies on Dynamic Flow Stress

The flow stress of LCS is examined within a range of strain rates and temperature conditions to identify the role of pearlite colonies on the dynamic flow stress. Testing in the dynamic regime is completed using a SHPB. The flow stress is generally analyzed in terms of two basic components; thermal and athermal. The thermal component is viewed as solely dependent on temperature and strain rate and is a resultant of dislocations interactions with short range barriers including phonons, Peierls-Nabarro, forest dislocations, dislocation jogs and kinks. The athermal component of stress, which is independent of temperature and strain rate, is considered to be a result of dislocation interactions with long range barriers including grain boundaries, precipitates and second phase particles. The latter parameter, in the case of LCS, is governed by micro-structural parameters such as pearlite volume fraction and grain size.

The explicit role of pearlite volume fraction on the dynamic response of LCS has been characterized by examining flow stress parameters generated using a series of SHPB tests, at strain rates ranging from 10^2 to 10^4 s⁻¹ and testing temperatures of 20, 300, 500 and 650°C. The materials studied are as-received coarse grained low carbon steel, composed of α -ferrite and pearlite phase having a 9% volume fraction, and a LCS comprised of spheriodized carbides dispersed within a ferrite matrix and 0% pearlite phase. The removal of pearlite in the latter material was achieved by a two-stage heat treatment in which the as-received material, seen in Figure 8a, is brought to 750°C, just above the austenizing temperature for a length of time and then quickly quenched in an ice-brine water solution, resulting a ferrite-fine pearlite microstructure. This material is then heated to 720°C, held for 2 hours, followed by a slow furnace cooling and its microstructure is shown in Figure 8b.

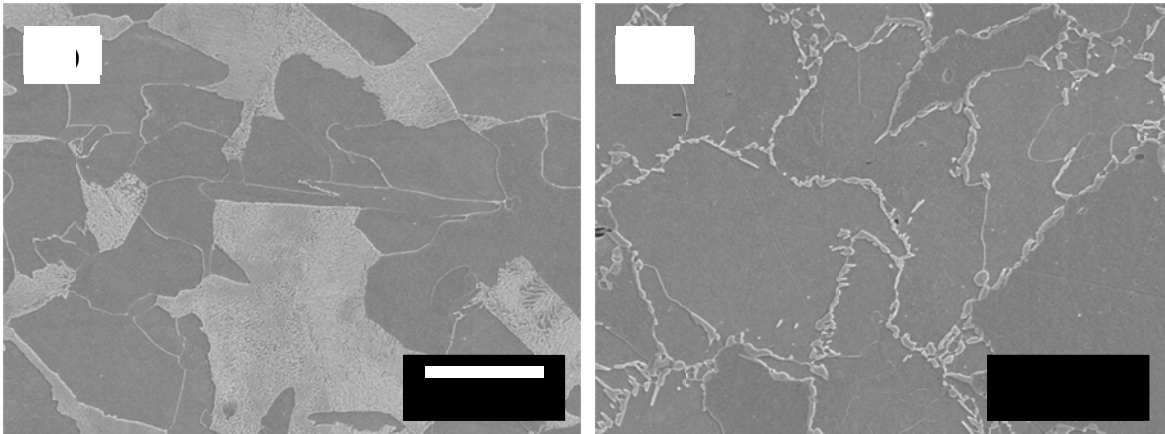


Figure 8: Scanning electron micrograph of the (a) as-received LCS (dark regions are ferrite grains and light regions are pearlite colonies) and (b) heat treated LCS (dark regions are ferrite grains and light regions are spheriodized carbides located along boundaries).

Typical stress-strain curves generated from SHPB testing are shown in Figure 9a for the as-received and 9b for the heat treated material. The effect of temperature on LCS is shown in Figure 9c, indicating that for the same strain rate, the flow stress decreases as the temperature increases. Figure 9d, on the other hand, shows that for the same temperature, the flow stress increases as the strain rate increases.

Results of these tests have been analyzed to identify and compare the thermal and athermal stress components in both the as-received and heated materials. The thermal stresses are shown in Figures 10a and 10b, for the as-received and heat treated LCS, respectively. These figures indicate that the removal of the pearlite colonies, have no affect on the thermal stress. On the other hand, Figures 10c and 10d show a 16% decrease in the athermal stress component with the removal of the pearlite colonies. This relationship with pearlite volume fraction is illustrated in Figure 11.

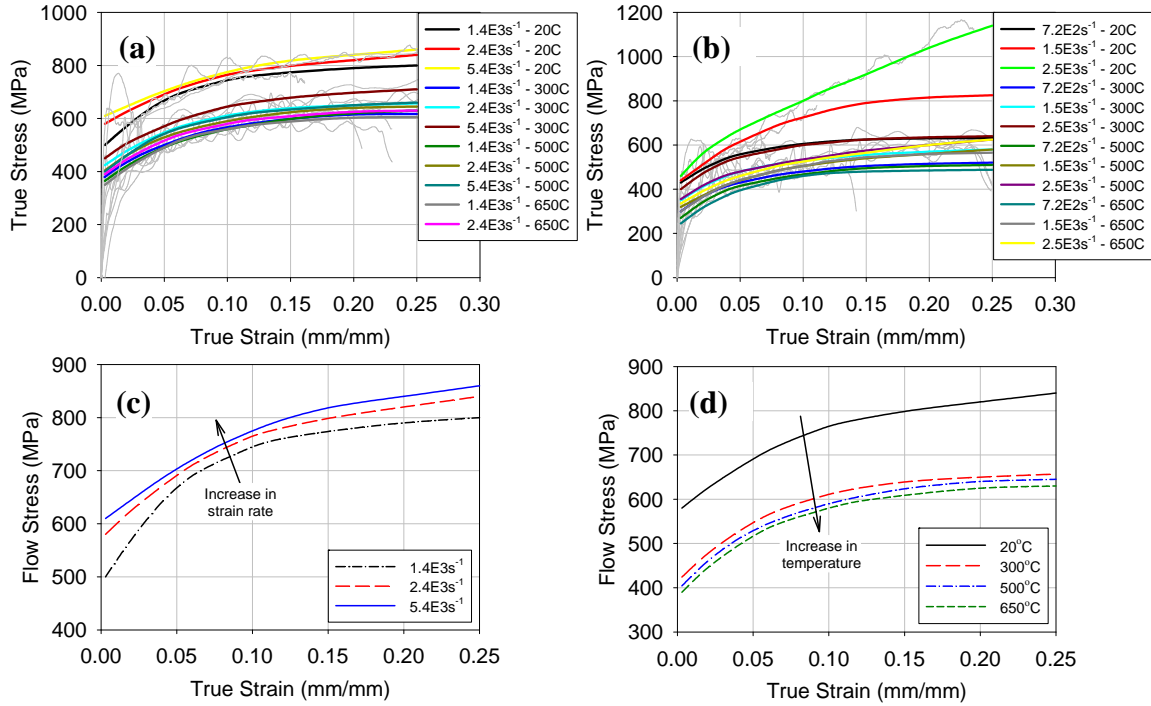


Figure 9: Stress-strain curves for (a) as-received LCS and (b) heat treated LCS at various strain rates and temperatures. Stress-strain curve for as-received LCS at (c) a constant temperature of 20°C, showing stress increases with the increase in strain rate and (d) at a constant strain rate of $2.4 \times 10^3 \text{ s}^{-1}$, showing that stress decreases with the increase in temperature.

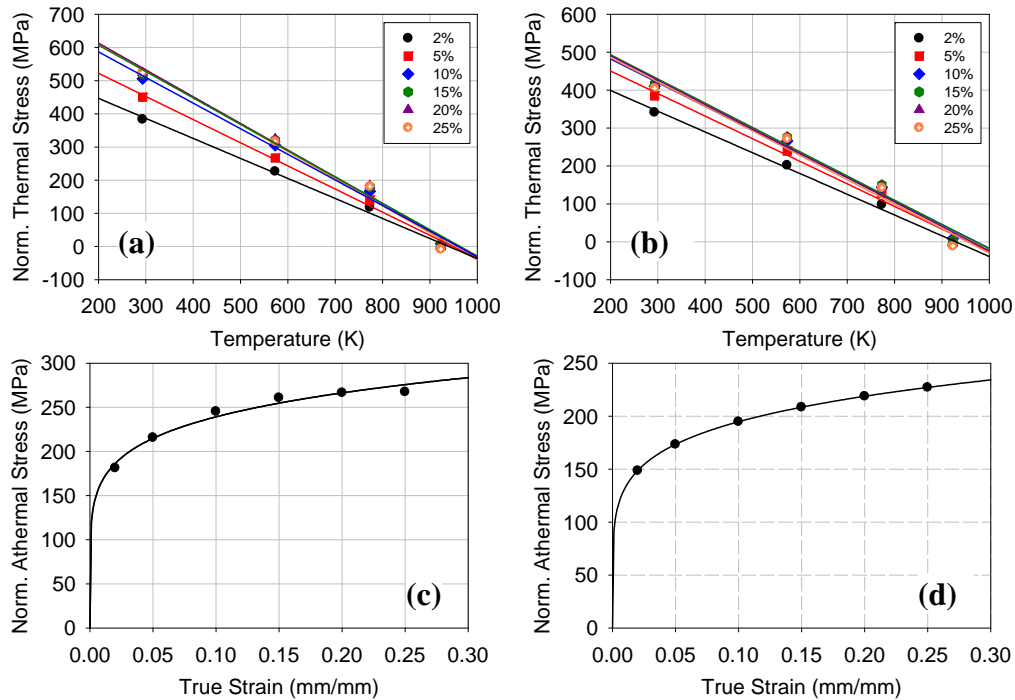


Figure 10: The normalized thermal stress versus temperature for the (a) as-received and (b) heat treated LCS for different strain values (indicated in the legend). The normalized athermal stress versus strain for the (c) as-received and (d) heat treated LCS.

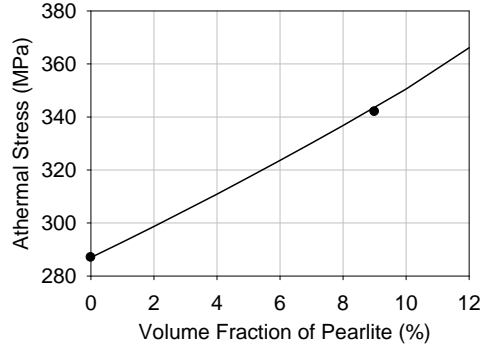


Figure 11: The athermal stress as a function of pearlite volume fraction, where the 0% and 9% pearlite volume fractions correspond to the heat treated and as-received LCS, respectively.

Furthermore, a constitutive flow model based on the linear summation of thermal and athermal stress components is developed. Results of the dynamic stress strain tests shown above were utilized to identify the model parameters. The model outcomes in terms of flow stress-strain relationship for different temperatures and strain rates are generated and plotted in Figure 12 which shows close correlation with experimental results.

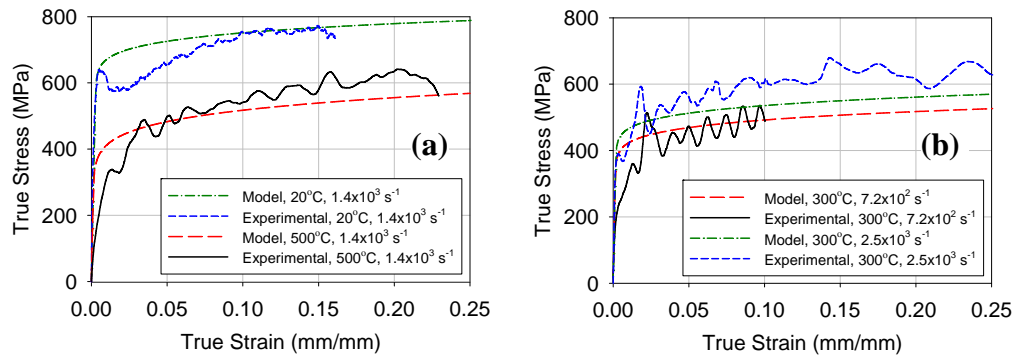


Figure 12: Typical stress-strain curves for (a) as-received LCS at 20°C and 500°C at a strain rate of $1.4 \times 10^3 s^{-1}$ and (b) heat treated LCS at 300°C at strain rates of $7.2 \times 10^2 s^{-1}$ and $2.5 \times 10^3 s^{-1}$, as indicated in the plot legends, for experimental tests and the corresponding numerical simulations. These illustrate the model's ability to capture the sensitivity due to variation in strain rate, temperature and pearlite volume fraction.

The work described above including full details of the dynamic flow constitutive behavior of the LCS as a function of pearlite volume fraction (0%, 9%, 20% and 60%) is documented in a journal paper which is submitted to the Journal Material Science and Engineering in April 2013.

Task III: Role of Grain Size on Dynamic Flow Stress

This study focuses on identifying explicitly the relationship between the athermal component of the dynamic flow stress and grain size. This knowledge will allow the development of more accurate constitutive flow equations capable of predicting the material deformation response under dynamic loading. The experimental portion of this work will be achieved by developing ultra-fine grained (UFG) LCS by severe plastic deformation (SPD). An SPD approach, with the ability to transition to large scale production, is the equal channel angular pressing (ECAP) which consists of two main components: a 100 ton hydraulic press and a high strength ECAP die with a 90° angle channel (see Figure 13). This channel

is built to accept either a billet with a 1 x 1 inch or 0.5 x 0.5 inch cross section. The extreme shear strain caused by traversing the channel, in multiple passes, results in heavily formed dislocation networks organized in sub grain structures. The aim of the current experimental work is to refine a 6 in³ coarse grained LCS bar (40-50 μm) to an ultra fine grain size (10-1 μm).

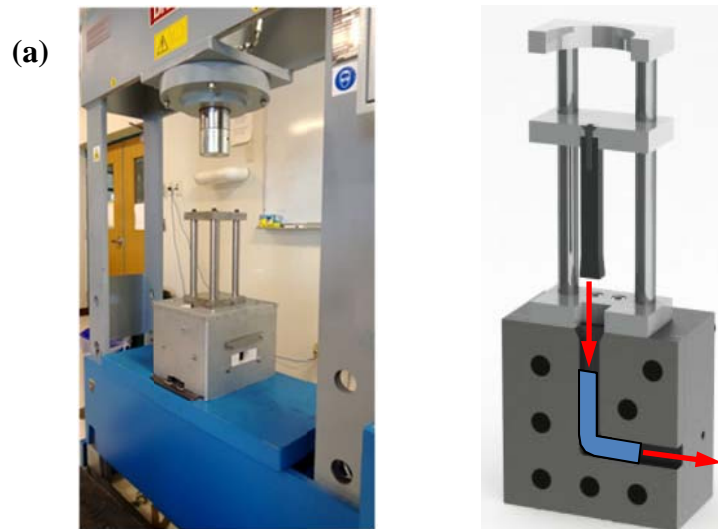


Figure 13: (a) UFC facility established at the MMRL consisting of a 100 ton hydraulic press with a 90° channel ECAP die. (b) A cross-sectional view of the ECAP die illustrating the direction of the billet extrusion during the SPD process.

The grain refinement, using the ECAP processing technique, requires several passes with a specified rotation of the billet during each pass. This rotation will result in a final microstructure that has equiaxed refined grains that are evenly distributed through the thickness. It is expected that the refined grained billet will show an increase in yield strength, a decrease in the hardening coefficient and a loss of ductility. In order to optimize the post-ECAP'ed material, for improved strength while still retaining ductility characteristics, a post-ECAP annealing procedure has been devised and will be implemented. This process will remove residual stresses existing in the material and allow for a more equilibrated state, thus recovering much of the original ductility, with a limited loss of the grains refinement.

This task work is currently underway and it is expected that a journal paper on the dynamic flow stress behavior of LCS as a function of grain size be written and submitted by June 30, 2013.

Accomplishments

Research efforts have been made in order to improve upon the manufacturing low carbon structural steel to provide an increase in its overall blast resistance. The following accomplishments have been made between the period of August 2012-April 2013:

- Dynamic deformation of LCS is studied utilizing recently designed and built SHPB
- Athermal and thermal components of flow stress and model parameters are determined for as-received coarse grain LCS
- A heat treatment process is carried out to remove pearlite structure from LCS, resulting in a LCS with 0% pearlite volume fraction
- Flow stress behavior of LCS is determined as an explicit function of pearlite volume fraction

- Athermal and thermal components of flow stress and model parameters of coarse grain as-received (9% pearlite volume fraction) and heat treated (0% pearlite volume fraction) LCS are determined from experimental dynamic stress-strain curves obtained using SHPB
- Flow stress behavior of LCS is successfully modeled as an explicit function of pearlite volume fraction
- A processing path is realized for optimized LCS with improved dynamic impact resistance by tailoring pearlite volume fraction via heat treatments

List of Publications Journal Publications

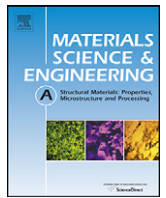
- K. Maciejewski, Y. Sun, O. Gregory and H. Ghonem, "Time-Dependent Deformation of Low Carbon Steel at Elevated Temperatures," *J Material Science and Engineering A*, Volume 534, 2012, 147-156. (pdf attached)
- Y. Sun, K. Maciejewski, H. Ghonem, "Simulation of Viscoplastic Deformation of Low Carbon Steel Structures at Elevated Temperatures," *J Materials Engineering and Performance*, Volume 21, Issue 7, 2012, 1151-1159. (pdf attached)
- W. Visser, Y. Sun, O. Gregory, G. Plume, C-E. Rousseau, H. Ghonem, "Deformation Characteristics of Low Carbon Steel Subjected to Dynamic Impact Loading," *Material Science and Engineering A*, Volume 528, Issue 27, October 2011, 7857-7866. (pdf attached)
- J. Spirdione, K. Maciejewski, H. Ghonem, "Role of Pearlitic Colonies to the High Strain Rate Response of Low Carbon Steel at Elevated Temperatures," *J Material Science and Engineering A*, April 2013. (submitted)
- W. Visser, J. Spirdione, K. Maciejewski, H. Ghonem, "Deformation Twinning in Cold Rolled Low Carbon Steel," *J Material Science and Engineering A*, April 2013. (submitted)

Conferences

- J. Spirdione, W. Visser, K. Maciejewski, H. Ghonem, "Significance of Pearlite Colonies on Dynamic Deformation of Low Carbon Steel," *Material Science and Technology Conference*, David L. Lawrence Convention Center, Pittsburgh, PA, October 10, 2012.
- W. Visser, J. Spirdione, K. Maciejewski, H. Ghonem, "Effects of Pre-Strain on Impact Deformation Mechanisms of Low Carbon Steel," *Material Science and Technology Conference*, David L. Lawrence Convention Center, Pittsburgh, PA, October 10, 2012.
- W. Visser, Y. Sun, H. Ghonem, "Twin Influence on Post-Impact Deformation of Low Carbon Steel," *SEM Annual Conference and Exposition on Experimental and Applied Mechanics*, Mohegan Sun, Uncasville, CT, June 16, 2011.
- W. Visser, G. Plume, C. Rousseau, O. Gregory, H. Ghonem, "Deformation Criterion of Low Carbon Steel Subjected to High Speed Impacts," *Proceedings of the IMPLAST 2010 Conference*, Society for Experimental Mechanics, Inc., Providence, RI, October 14, 2010. (pdf attached)
- K. Maciejewski, Y. Sun, O. Gregory, H. Ghonem, "Deformation and Hardening Characteristics of Low Carbon Steel at Elevated Temperature," *Material Science and Technology Conference*, David L. Lawrence Convention Center, Pittsburgh, PA, October 8, 2008.

Students Supported

- Kimberly Maciejewski, PhD Candidate
- Justin Spirdione, Masters Student
- William Visser, PhD Candidate



Time-dependent deformation of low carbon steel at elevated temperatures

Kimberly Maciejewski^a, Yaofeng Sun^a, Otto Gregory^b, Hamouda Ghonem^{a,*}

^a Department of Mechanical Engineering and Applied Mechanics, University of Rhode Island, Kingston, RI 02881, USA

^b Department of Chemical Engineering, University of Rhode Island, Kingston, RI 02881, USA

ARTICLE INFO

Article history:

Received 20 November 2010
 Received in revised form 26 August 2011
 Accepted 10 November 2011
 Available online 30 November 2011

Keywords:

Low carbon steel
 Structural steel
 Non linear kinematic hardening
 Strain rate sensitivity
 Microstructure
 High temperature
 Finite element

ABSTRACT

This paper focuses on the microstructure and deformation properties of structural steel at elevated temperatures. The amounts and morphology of carbides present were monitored as a function of thermal exposure parameters. It was observed that as the temperature approaches the ferrite-austenite phase transformation (727 °C), considerable diffusion of cementite plates and abnormal grain growth occurs. A viscoplastic constitutive model has been employed to simulate the flow behavior of the steel. Monotonic and cyclic tests were carried out to determine the kinematic and isotropic hardening parameters required for full identification of the model variables. Results of the model were compared with those obtained experimentally. The material parameters were shown to be sensitive to the microstructure and temperature. Variation in carbide amounts and morphology in the post thermal exposed specimens result in differences in the kinematic hardening, as compared to the as received material. Furthermore, the temperature sensitivity of the isotropic hardening is indicated by the presence a cyclic hardening/softening transition in the temperatures 600–700 °C. Validity of the model in capturing time dependent behavior of the structural steel is examined using a sequentially coupled thermal-stress finite element analysis of single steel beam. Results of this simulation are discussed in terms of effects of temperature and strain-rate sensitivity on the material's viscoplastic deformation response.

© 2011 Elsevier B.V. All rights reserved.

1. Introduction

Accurate characterization and simulation of the deformation response of structural steel is an important concern in establishing a damage criterion for the design of civil structures. In general, design requirements to resist thermal exposures resulting from direct fire are thought of in the context of life safety and not in terms of life-cycle performance. On the other hand, post-thermal exposure performance criteria for such structures may require serviceability and reuse. Under this condition, structure designs must be based on the ability of the structure to provide optimum fire resistance. This can be achieved through the utilization of the material plastic and viscoplastic response in a manner as to not compromise the integrity of the entire structure. The current state of knowledge concerning the deformation behavior of loaded structures focuses on the final state of the structure rather than the detailed knowledge of the transient effects leading to the progressive failure of the structure. The lack of this knowledge is due to the fact that failure events under thermal exposure are a highly coupled phenomenon. That depends in large on the mechanical and thermal

properties of the reinforcing phase. In almost all existing critical facilities, and for years to come, structural low carbon steel is the prime reinforcing material. The variations in the loading rate associated with thermally exposed structure can alter the plastic flow characteristics of the steel. In addition, thermal exposure can reach temperature levels capable of introducing significant changes in the steel's microstructure and mechanical properties.

The mechanical behavior of various metals and alloys can be quite complex at high temperature where interactions of time- and temperature-dependent processes take place. The general approach to simulate steel response under fire conditions is the use of power law stress-strain equations [1]. Other studies [2] have modeled the deterioration in the material strength with increasing temperature by a set of nonlinear stress-strain-temperature relationships using a Ramberg-Osgood equation in which creep effects are implicitly included. This model includes the temperature dependent nonlinear material behavior, variations in temperature distributions both along and across each steel member within a structure, as well as, the effects of thermal strains and residual stresses. These types of strain-rate independent plasticity formulas, do not account for the interactive effects of plasticity and viscous flow, hardening or load rate sensitivity occurring under combined load and temperature environment, see for example, the work of Outinen et al. [3] on structural steel S355 and Makelainen et al. on high-strength structural steel S420M [1]. Another approach is the

* Corresponding author. Tel.: +1 401 874 2909; fax: +1 401 874 2925.
 E-mail address: ghonem@egr.uri.edu (H. Ghonem).

use of a continuously nonlinear stress–strain curves applied to sub-segments with different temperatures. The average temperature of each subsegment is used to determine the appropriate stress–strain curve, and its average strain is used to find a tangent modulus from this curve. This approach, in addition to the requirement of a monotonic stress–strain database at varying temperatures and strain rates, is difficult to integrate within a complex structure [4]. Tan et al. [5] have incorporated strain reversal into their modeling of steel structures, allowing one to analyze steel frames subjected to unloading or cooling of the structure. The program can analyze steel frames subjected either to increasing external loads at ambient temperature or constant external loads at elevated temperature. The factors affecting the structural behavior at elevated temperature include temperature-dependent material nonlinearity, geometric nonlinearity, thermal gradient, and the creep effect.

The work presented in this paper aims at describing the structural steel behavior under thermal exposure in terms of a unified flow formulation that takes into consideration the evolution of hardening features of the steel as a function of temperature and exposure time. These formulations, that couple the time dependent plastic response, are based on an internal state variable model incorporating kinematic and isotropic hardening variables. Thus, the model is capable of describing the material response under variable strain rate conditions. The first part of this paper explores the evolution of microstructure as a function of both time and temperature. This metallurgical study is aimed at investigating the amount and morphology of the iron carbide phase and grain size as a function of exposure time and temperature. Understanding these characteristics will lead to critical post thermal exposure conditions for mechanical testing. Mechanical tests carried out at post thermal and elevated temperatures for identification of the model parameters will be described in the second part of this paper. The third part of the paper will describe various numerical applications including, uniaxial simulations in one dimensional strain-controlled loading scenarios and a finite element model of a single beam exposed to varying temperature and loading scenarios.

2. Material characterization

The material used in this study is A572 grade 50 steel which has the following nominal composition (in wt%): 0.23 max Carbon, 0.005–0.05 Columbium, 1.35 max Manganese, 0.04 max Phosphorus, 0.40 max Silicon, 0.05 max Sulfur, 0.01–0.15 Vanadium, 0.015 max Nitrogen, iron remaining [6]. The microstructure of the as-received steel is typical of normalized steel, consisting of pearlite colonies and alpha-ferrite equiaxed grains, as seen in Fig. 1a. An important factor influencing time dependent deformation of the steel is the morphological changes in the grain size and carbides of the starting material. Evolution of microstructure was monitored as a function of temperature, ranging from 300 °C to 700 °C, and time, from 0 to 200 min. The upper temperature level was selected to be below the ferrite-austenite phase transformation temperature of 727 °C, thus upon quenching the heat treated specimen, the microstructure will remain as a ferrite-cementite microstructure. The heat treatments were carried out in air environment using coupons measuring 0.75 in. × 0.75 in. × 0.03 in. The treatment procedure was performed in a vertical furnace in which each specimen was heated at an average rate of 105 °C/min to the desired temperature followed by quenching in ice salt water bath following the various exposure times. Microstructural features were evaluated using quantitative stereology techniques. The grain size was determined using the mean intercept method [7] and is reported as a mean intercept length. The volumetric percent of pearlite was also calculated as a function of temperature and exposure time.

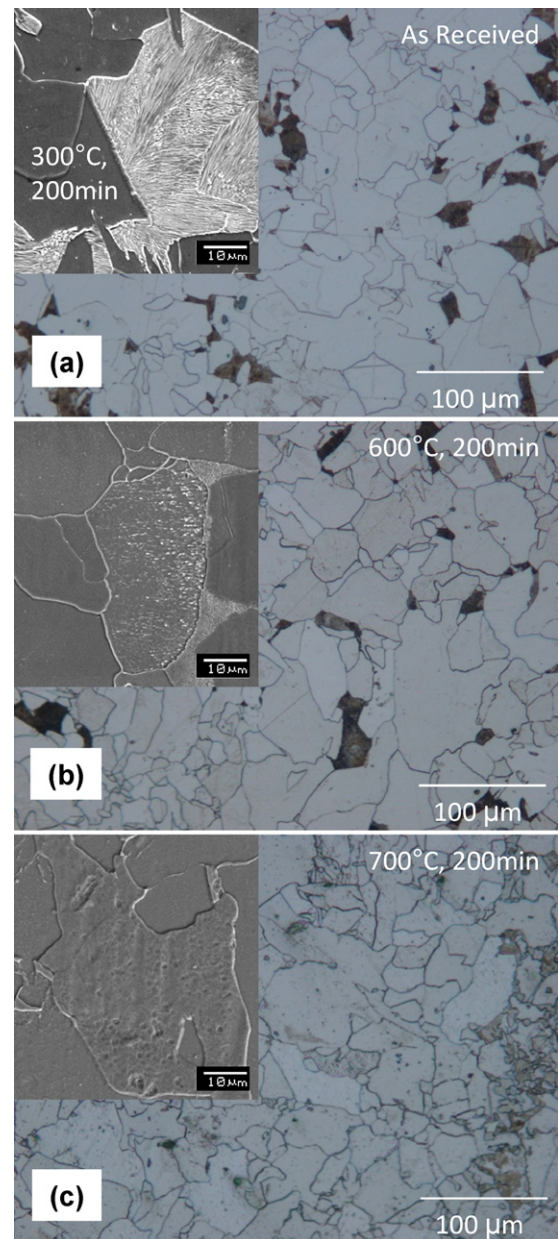


Fig. 1. Micrographs of (a) as received low carbon steel and a specimen heat treated at 300 °C, (b) 600 °C and (c) 700 °C for 200 min (all samples are etched for 5 s with 5 vol% nital).

Results of these heat treatment experiments showed that at temperatures in the range of 300–727 °C, iron carbide can change from a plate-like habit or lamella (Fig. 1a), as in the case of pearlite, to a spheroidized habit (Fig. 1b and c), depending on thermal exposure conditions. Fig. 2a shows that the volume percent of pearlite in samples exposed to temperatures 600 °C and below did not notably vary from the as received condition. Analysis of the 700 °C samples, while indicated the presence of the alpha-ferrite grains, shows that the volume of pearlite colonies decreased to around 2%. Furthermore, Fig. 2a shows that for the same temperature the exposure time does not have a significant effect in the amount of pearlite (the points at 700 °C are plotted for exposure times greater than 1 min). Depending on time and temperature carbon particles go into solution, thus decreasing the amount of pearlite colonies present. Scanning electron microscopy was used to observe these grains at a higher magnification as shown in Fig. 1b and c.

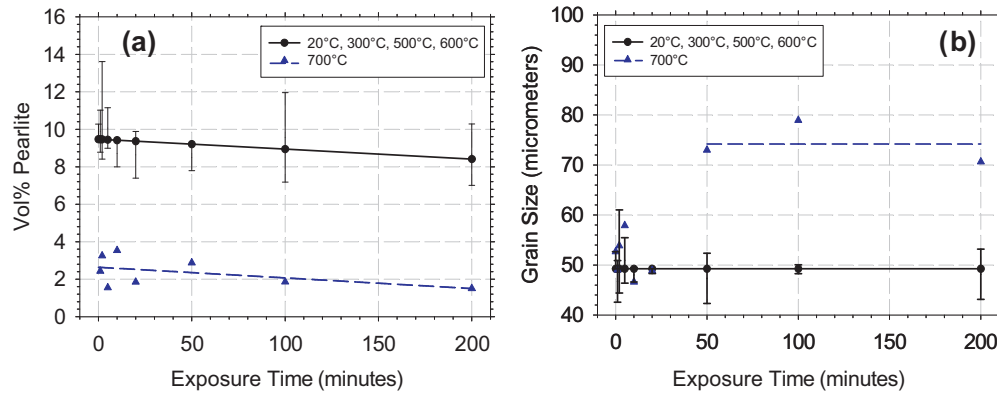


Fig. 2. The effects of temperature and time on volume percent pearlite and grain size. (a) Exposure time vs. volume percent pearlite, and (b) exposure time vs. grain size. The points at 700 °C are plotted for exposure times greater than 1 min, the 0 min condition corresponds to the as received material.

Some grains heat treated at 600 °C and 700 °C showed evidence of spheroidization.

The heat treatments did not result in significant grain growth at temperature exposures below 600 °C, as seen in Fig. 2b. The average grain size following thermal exposures at 300 °C, 500 °C, and 600 °C is fairly steady around about 50 μm. These results are consistent with those observed by Gayle et al. [8], which did not show microstructural changes at or below 500 °C. At There is an increase in the grain size for the longer exposure times for the 700 °C sample. At 700 °C, however, the average grain size increased with exposure time showing an average size of 74 μm. The 700 °C specimens also show evidence of a bimodal distribution which generally results from the pinning of grain boundaries by impurities thus preventing diffusion across boundaries [9,10].

The results described above, indicate that the thermal exposures can be grouped into three categories. The first category includes the as-received, 300 °C and 500 °C, which represents the condition of equiaxed grains with pearlite colonies. The second category belongs to the 600 °C condition which shows pearlite colonies and evidence of spheroidization. The third category is limited to the 700 °C which shows spheroidized particles of carbon with the absence of pearlite colonies and a bimodal grain size. As a result, modeling of the constitutive behavior of the material under consideration will focus on the three conditions; as received, 600 °C and 700 °C. The first step is to outline the viscoplastic model which will be applied in this analysis. This is described in the following section.

3. Non-linear kinematic hardening model

Several unified material constitutive models exist in literature. These models account for the combined effects of plastic and creep deformation response by including terms that account for the evolution of isotropic and kinematic hardening parameters during the loading history of the material, see refs. [11–14]. The non-linear kinematic hardening model applied in the current work has the advantage that it requires the determination of a limited number of material variables and accounts for deformation recovery and thus capable of modeling the strain-rate sensitivity of the material. The model is formulated on the assumption that a viscoplastic potential, Ω , exists in the stress space. A particular form of the viscoplastic potential is given as [15]:

$$\Omega = \frac{K}{\alpha(n+1)} \exp\left(\alpha \left\langle \frac{\sigma_v}{K} \right\rangle^{n+1}\right) \quad (1)$$

where K , n , and α are material parameters that characterize the rate sensitivity. To describe the viscoplastic behavior, the concept

of time-dependent overstress or viscous stress is used. This is given as:

$$\sigma_v = |\sigma - X| - R - k \quad (2)$$

The variable σ signifies the applied stress tensor and k is a temperature dependent material constant representing the initial size of the elastic domain. R and X are hardening variables corresponding to isotropic stress or drag stress and kinematic stress or back stress tensor. The relation between the plastic flow and the viscoplastic potential is determined by means of the normality rule [12,13,16]:

$$\dot{\varepsilon}_p = \left\langle \frac{\sigma_v}{K} \right\rangle^n \exp\left(\alpha \left\langle \frac{\sigma_v}{K} \right\rangle^{n+1}\right) \text{sign}(\sigma - X) \quad (3)$$

The rules governing the evolution of the kinematic and the isotropic hardening variables are described below. Here it should be mentioned that the low carbon steel under consideration, as will be detailed later, exhibits strain rate sensitivity which is important in loading scenarios involving variable force distributions arising from thermal distributions [17]. As such, it is necessary to incorporate recovery terms into the hardening laws. The kinematic hardening term, measured by the back stress X , is expressed as a sum of a linear, X_2 , and non-linear, X_1 , time-dependent term [18,19]:

$$X = X_1 + X_2 \quad (4)$$

The general forms of back stress including strain hardening, dynamic recovery and static recovery terms are written as [15,20,21]:

$$\dot{X}_1 = C_1(a_1\dot{\varepsilon}_p - X_1|\dot{\varepsilon}_p|) - \beta_1|X_1|^{r_1-1}X_1 \quad (5)$$

$$\dot{X}_2 = C_2(a_2\dot{\varepsilon}_p - X_2|\dot{\varepsilon}_p|) - \beta_2|X_2|^{r_2-1}X_2 \quad (6)$$

where C , a , β , and r are material-dependent parameters.

The slow evolution of microstructure associated with cyclic hardening or softening of the material can be described by the isotropic hardening variable, R , which is the difference in the saturation position after a loading cycle and that corresponding to the monotonic loading for the same plastic strain. This is governed by the following relationships:

$$\dot{R} = b(Q - R)|\dot{\varepsilon}_p| \quad (7)$$

$$Q = Q_{\max}(1 - e^{-\mu q}) \quad (8)$$

$$q = \max(|\varepsilon_p|, q) \quad (9)$$

where Q and b are the limiting values of the isotropic hardening variable. Q is the saturation limit of R , while the constant, b , is a temperature and material-dependent parameter describing how fast R reaches Q . This latter parameter can be either a positive value, indicating cyclic hardening, or a negative value, indicating

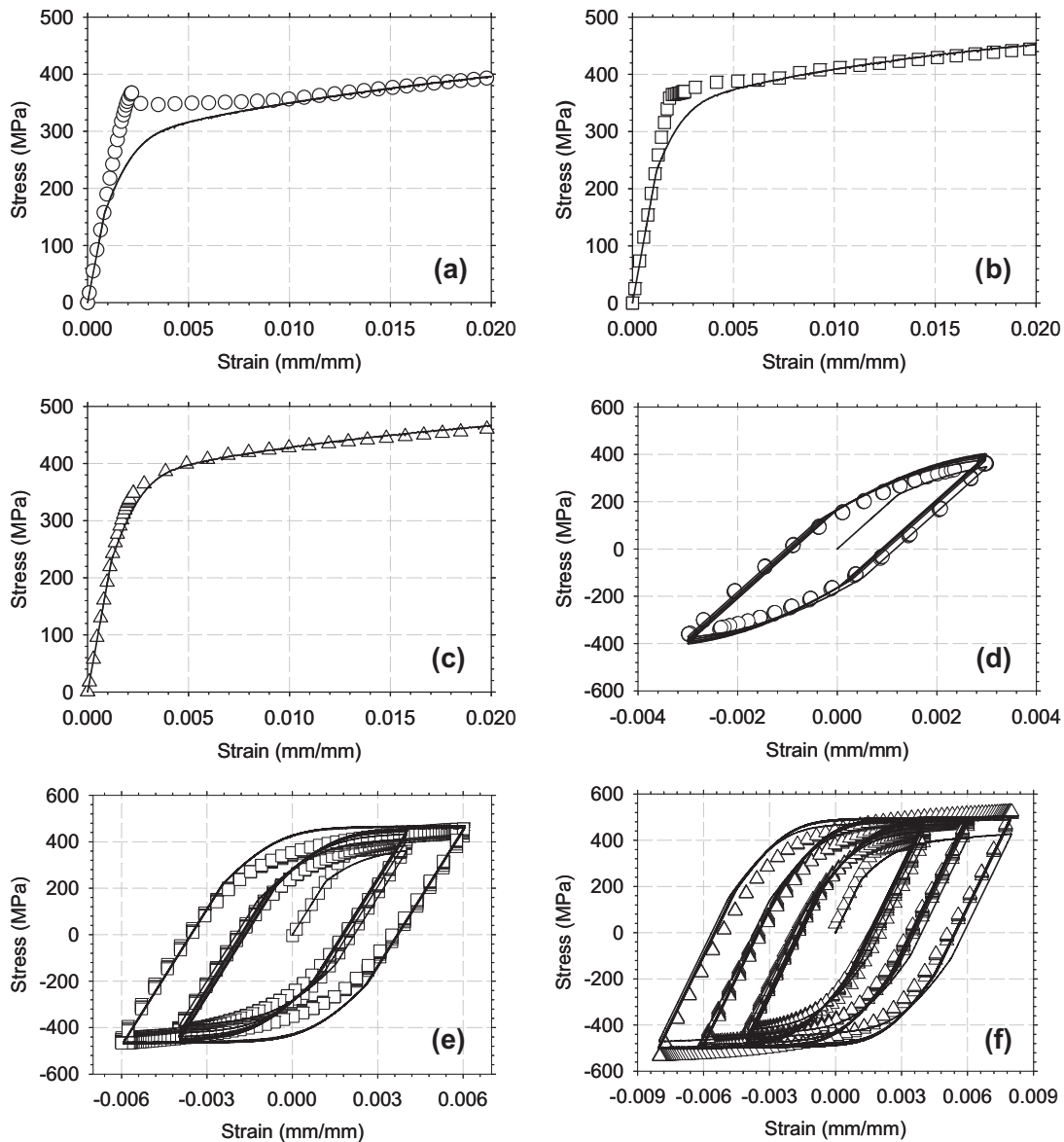


Fig. 3. Comparison between experimental (Symbol) and numerical (Solid line) monotonic stress–strain curves for (a) as received, (b) post-600 °C thermal exposure, and (c) post-700 °C thermal exposure low carbon steel tested at room temperature. Comparison between experimental and numerical cyclic stress–strain loops at various strain ranges for low carbon steel for the following test conditions at room temperature, (d) as received, (e) post-600 °C thermal exposure, (f) post-700 °C thermal exposure.

cyclic softening. Q_{\max} is the maximum value of Q , and q is the maximum strain achieved during loading, which memorizes the previous plastic strain range [22].

4. Experimental determination of model constants

A series of strain-controlled tests were carried out on A572 Grade 50 Low Carbon Steel, at both room and high temperature, to determine the various material parameters described above in order to fully identify the non-linear kinematic hardening model. The testing was performed on cylindrical hourglass type specimens with an overall length of 4.5 in., a gage length of 1 in. and a gage diameter of 0.4375 in. The mechanical testing was carried out using a servo hydraulic test machine, equipped with a heat induction unit for the high temperature tests. The strain was measured with a quartz rod extensometer. A monotonic test is carried out, at a strain rate of $5 \times 10^{-6} \text{ s}^{-1}$, to determine the modulus, E , and yield stress,

k , of the material. Results of this rate at various loading conditions are shown in Figs. 3a–c and 4a.

A series of strain-controlled fully reversed cyclic stress–strain tests ($R = -1$) are performed, until peak stress saturation is reached, at a strain rate of $5 \times 10^{-6} \text{ s}^{-1}$. The strain range of these tests varied from $\pm 0.2\%$ to $\pm 1\%$ strain. The cyclic stress–strain curves at various test conditions are shown in Figs. 3d–f and 4b, c. These loops are employed to generate the isotropic and kinematic hardening, as well as, viscosity and recovery parameters, which are described below.

4.1. Isotropic hardening parameters

The slow internal changes described by isotropic stress occurs over a large number of cycles and is a function of accumulated plastic strain, corresponding to the difference in the maximum stress of the current cycle and the maximum stress of the first loop associated with the monotonic stress–strain curve. Assuming the increase

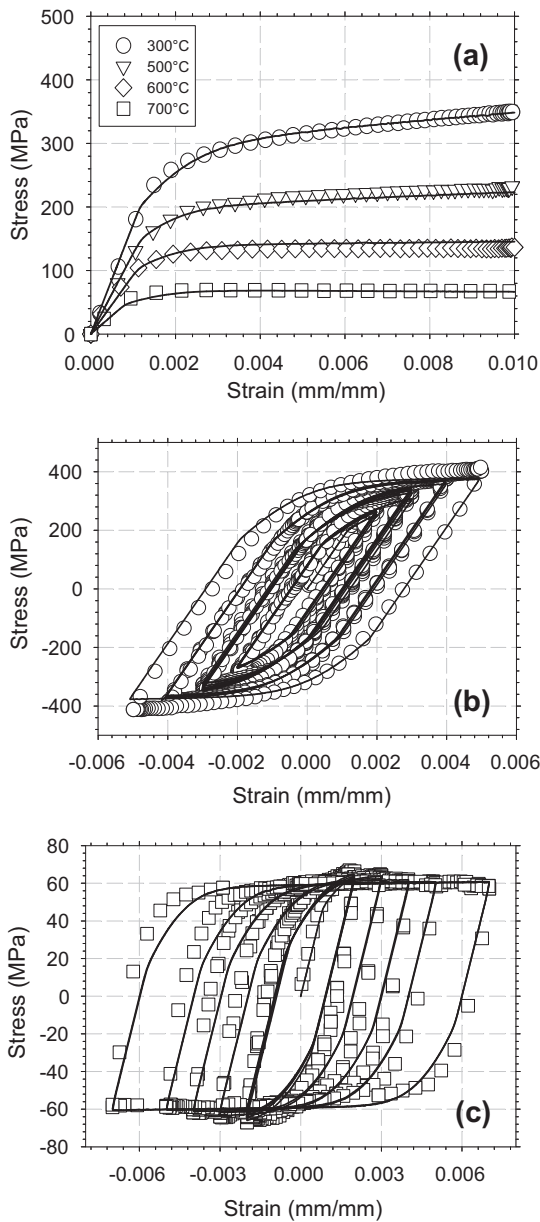


Fig. 4. Comparison between experimental (Symbol) and numerical (Solid line) monotonic stress–strain curves for (a) as received tested at high temperatures. Comparison between experimental and numerical cyclic stress–strain loops at various strain ranges for as received low carbon steel tested at (b) 300 °C and (c) 700 °C.

in maximum stress, σ_M , occurs only due to isotropic hardening, R , the following relationship can be determined, see Nouailhas [15,23]:

$$\frac{R}{Q} = \frac{\sigma_M - \sigma_{M0}}{\sigma_{MS} - \sigma_{M0}} = (1 - e^{-bp}) \tag{10}$$

where σ_M , σ_{MS} , σ_{M0} correspond to the maximum stress of cycle M , the maximum stress of the saturated cyclic loop and the first loop respectively. The accumulated plastic strain, p , is defined by $p = |\varepsilon_p| = 2N\Delta\varepsilon_p$. N is the number of cycles and ε_p is the sum of plastic strain in tension and compression. The material parameter, b , is determined by fitting of the above equation to the experimental R/Q vs. p data as shown below in Fig. 5a for high temperature test conditions at 300 °C. Q_{max} and μ in Eq. (8) are calculated by fitting this equation to the experimental Q vs. q data as shown in Fig. 5b. Where $Q_{max} = \sigma_{MS} - \sigma_{M0}$ and q is the maximum strain achieved during loading, in this case $q = \Delta\varepsilon^p/2$.

4.2. Kinematic hardening parameters

For each strain range, the hardening of the material in the first cycle of the cyclic stress–strain loops is assumed to be related to the kinematic hardening only and the accumulated plastic strain p is equal to the plastic strain ε_p . The kinematic stress corresponds to the center of the linear part of the first reversible cyclic loop at each strain range. As discussed earlier kinematic stress is expressed as the sum of two terms, each a function of plastic strain through integration of Eqs. (5) and (6) X can be represented as follows:

$$X = a_1(1 - e^{-C_1\varepsilon_p}) + a_2(1 - e^{-C_2\varepsilon_p}) \tag{11}$$

where a_i , the asymptotic value of X_i , and C_i , the rate at which X_i reaches a_i , are obtained from curve fitting of experimental X vs. ε_p data as shown below in Fig. 6.

4.3. Viscous stress parameters

To describe the time-dependent viscous stress terms, n and K , a strain-controlled monotonic stress–relaxation test is performed. A typical relaxation test at 300 °C is shown in Fig. 7a. During the periods of holding at a constant total strain, the stress as a function of time is acquired, as shown in Fig. 7b. Under constant strain conditions during hold time, the plastic strain rate can be written as $\dot{\varepsilon}_p = -\dot{\sigma}/E$. Where the stress rate is determined from the stress vs. hold time graph shown in Fig. 7b and E is the modulus.

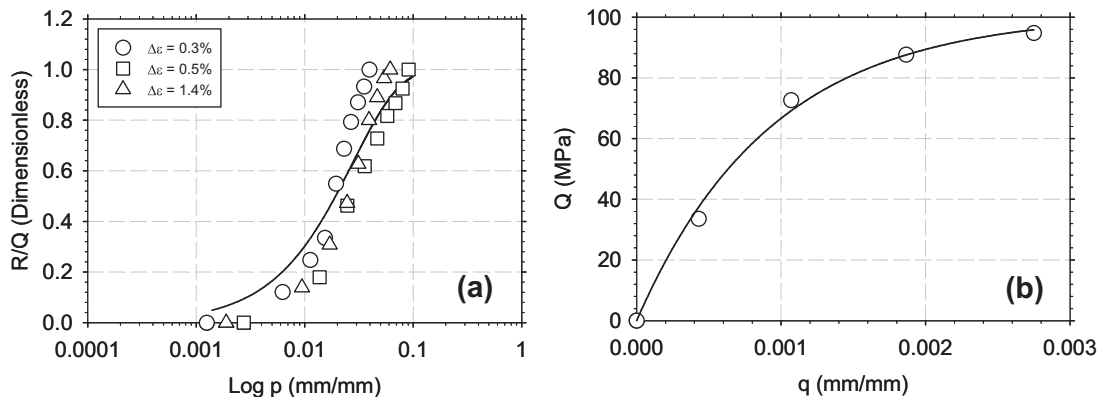


Fig. 5. (a) Fit of Eq. (10) (Solid line) to experimental (Symbol) R/Q vs. \log accumulated plastic strain for low carbon steel for at 300 °C. (b) Fit of Eq. (8) (Solid line) to experimental (Symbol) Q vs. q for low carbon steel for at 300 °C.

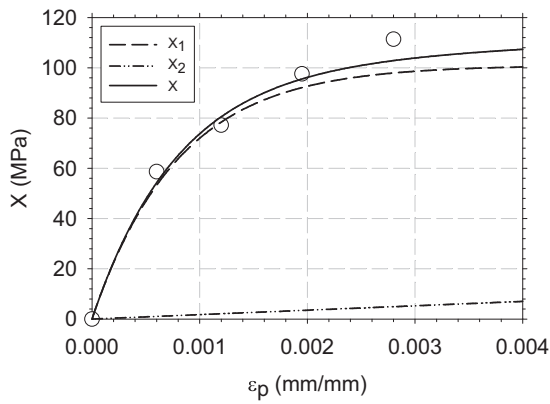


Fig. 6. Fit of Eq. (11) (Lines) to experimental (Symbol) kinematic stress vs. plastic strain for low carbon steel at 300 °C.

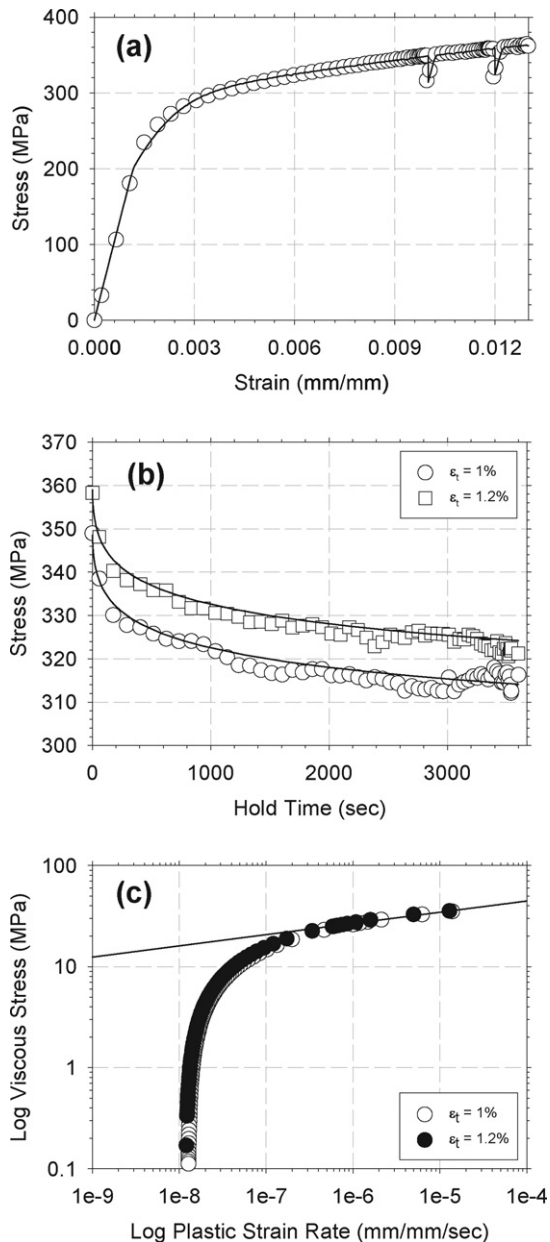


Fig. 7. Comparison of experimental (Symbol) and numerical (Solid line) (a) relaxation stress vs. strain curve and (b) relaxation stress vs. hold time at constant strain values for low carbon steel at 300 °C. (c) Fit of Eq. (13) (Solid line) to experimental (Symbol) log viscous stress vs. log plastic strain rate for low carbon steel at 300 °C.

The viscous stress can be expressed in terms of plastic strain rate by rearranging the equation for plastic flow, given by Eq. (3), to the form:

$$\log(\sigma - \sigma_i) = \frac{1}{n} \log\left(-\frac{\dot{\sigma}}{E}\right) + \log K \quad (12)$$

For arbitrary values of σ_i , one can plot $\log \sigma_v$ vs. $\log \dot{\epsilon}_p$. The parameters n and K are determined from fitting the linear part of the curve (Fig. 7c). An average of n and K is taken for different values of ϵ_t . The material constant, α , is taken to be the saturation limit of viscous stress for high plastic strain rates. This constant is determined by fitting Eq. (3) to the experimental viscous stress vs. plastic strain rate at a high plastic strain rate. The low strain rates are captured by the time-dependent behavior of the material. The most sensitive terms reflecting the lower strain rates are the static recovery terms in Eqs. (5) and (6), these are discussed in the next paragraph.

4.4. Recovery parameters

As discussed earlier, the kinematic stress includes a dynamic and static recovery terms expressed by the last two parts in Eqs. (5) and (6); respectively. The dynamic recovery term represents processes for by passing or penetrating barriers at comparable rates and occurs during deformation. The material constants for dynamic recovery are defined in Eq. (11). On the other hand, the static recovery describes the microstructural rearrangement in the absence of deformation. It is a temperature and time-dependent function representing climb or diffusion-assisted processes for the relief of stress fields. The static recovery term requires the knowledge of the parameters, β_i and r_i in Eqs. (5) and (6). For this purpose, the back stress can be expressed by rearranging Eq. (2) to the form:

$$X(t) = \sigma(t) - R - k - \sigma_v \quad (13)$$

where $\sigma(t)$ is the linear portion of the experimental stress vs. time curve from Fig. 7b (at large values of time) and the terms R , k , and σ_v , are constants with respect to time at a constant value of plastic strain. The time-dependent back stress can also be obtained by integrating Eqs. (5) and (6) with respect to time. Assuming a linear recovery term ($r_1 = r_2 = 1$), the integration yields:

$$X(t) = \frac{C_1 a_1 |\dot{\epsilon}_p|}{C_1 |\dot{\epsilon}_p| + \beta_1} (1 - e^{-(C_1 |\dot{\epsilon}_p| + \beta_1)t}) + \frac{C_2 a_2 |\dot{\epsilon}_p|}{C_2 |\dot{\epsilon}_p| + \beta_2} (1 - e^{-(C_2 |\dot{\epsilon}_p| + \beta_2)t}) \quad (14)$$

By plotting $X(t)$ using Eq. (13) and curve fitting the plot to Eq. (14), initial estimate of the parameters β_1 and β_2 which along with r_1 and r_2 , are optimized with stress–strain data at various strain rates [24].

The material parameter determination procedure, described above, has been applied at two post-thermal exposure conditions (specimens tested at 20 °C that has seen prior thermal exposure at 600 °C and 700 °C for 200 min and quenched). These will be termed here as post-thermal exposure tests, as well as, as received steel at temperatures ranging from 20 to 700 °C (these will be termed high temperature tests). The material parameters for each condition in these two categories are listed in Table 1.

5. Simulation and validation of the model

Modeling was achieved by carrying out a simultaneous integration of the set of viscoplastic constitutive Eqs. (2)–(9) described above and using the material constants listed in Table 1. The model application to different loadings including post thermal exposure

Table 1

Material parameters for A572 Grade 50 low carbon steel tested at 20 °C that has seen prior thermal exposure at 600 °C and 700 °C for 200 min and quenched, and as received steel tested at temperatures ranging from 20 °C to 700 °C.

Thermal history	Post 600 °C	Post 700 °C	20 °C	300 °C	500 °C	600 °C	700 °C
E (GPa)	196	196	188	172	127	93	58
k (MPa)	101	101	100	71	27	11	3
a_1 (MPa)	120	150	137	96	54	36	22
C_1	1411	1411	1411	1411	1411	1411	1411
a_2 (MPa)	820	1120	1864	1753	1111	566	175
C_2	1.15	1.15	1.15	1.15	1.15	1.15	1.15
b	78	78	78	78	78	78	78
Q_{\max} (MPa)	113	113	86	78	31	1	-10
μ	1447	1447	1447	1447	1447	1447	1447
n	14	14	14	14	14	14	14
K (MPa)	351	351	155	349	304	227	107
α	5.50E+06	5.50E+06	5.50E+06	5.00E+06	1.00E+05	4.50E+00	9.90E-01
β_1 (Pa ^{2.58})	1.00E-21	1.00E-21	1.00E-21	9.90E-20	1.00E-15	1.00E-15	1.00E-15
β_2 (Pa ^{2.15})	4.60E-26	4.60E-26	4.60E-26	2.10E-16	1.00E-12	1.00E-12	1.00E-12
r_1	2.58	2.58	2.58	2.58	2.58	2.58	2.58
r_2	2.15	2.15	2.15	2.15	2.15	2.15	2.15

and high temperatures conditions are compared with the corresponding experimental curves, see Figs. 3a–c and 4a. These results show that the outcomes of the employed non linear kinematic hardening model is in good agreement with the experimental stress–strain curves. It is clear from this comparison that the model results do not capture the Lüders phenomena with an upper and lower yield as seen in the experimental curves at room temperature, see Fig. 3a. The two post thermal exposure conditions tested at room temperature (Fig. 3b and c) show an increase in hardening as compared to the as received condition. This increase is apparent in the material constants in which the asymptotic values of the kinematic hardening parameters (constant a_2 in Table 1) are higher for the post thermal exposure conditions. These variations can be explained by the fact that the steel specimens that have been exposed to 600 °C and 700 °C for 200 min microstructures revealed spheroidization indicating more carbon solute atoms in the ferrite matrix, which would act as short range barriers for dislocations. This microstructure also revealed a bimodal grain size distribution, where the grain boundaries would act as long range barriers for dislocations which would in turn reflect on the hardening characteristic of the microstructure. In addition to the monotonic testing at room temperature, high temperature tests are performed and results are shown in Fig. 4a. This figure shows that the hardening, as indicated by the tangential slope of the curve, decreases as temperature increases. This trend reaches a limit at 700 °C where the material shows a perfect plastic response. One can relate this behavior to the dissolution of the pearlite colonies which are the main hardening phase in the material. It should be noted that the condition of spheroidization would not be present at high temperature, this would only occur during the quenching from high temperature.

Furthermore, fully reversed strain-controlled loading case studies were simulated and compared to those obtained experimentally as shown in Figs. 3d–f and 4b, c. The peak stresses for all conditions agree well between the numerical and experimental curves. The plastic strain ranges agree better at lower temperature conditions than higher temperature conditions. Between the temperatures of 600 °C and 700 °C there is a transition between cyclic hardening and cyclic softening behavior as the sign of the Q_{\max} parameter changes from positive to negative (see Table 1). This could be attributed to dissolution of pearlite colonies at 700 °C; the lack of a hardening phase results in cyclic softening.

Case studies for monotonic strain-controlled loading at variable strain rates ranging from 5E–7 to 5E–4 s⁻¹ were performed and compared to those obtained experimentally as seen in Fig. 8. The model can illustrate both strain rate independent and dependent

behavior. At 300 °C the low carbon steel is strain rate independent. Above this temperature, the low carbon steel is increasingly strain rate sensitive. The recovery terms become more influential at higher temperatures. The saturation of the stress vs. strain curve at high strain rates is captured by the material parameter, α , which decreases with increasing temperature (see Table 1). The good agreement between the slow strain rates at the varying temperatures is greatly influenced by the static recovery terms. Table 1 shows that the terms β_1 and β_2 increase with temperature. Thus, there is more recovery at higher temperature.

Generally for all cases, the non-linear kinematic hardening model is capable of modeling low carbon steel. It cannot only capture the effects of variable loading, but also variable temperature conditions.

6. Applications

The one dimensional internal state variable (ISV) model previously described has been extended to a two dimensional UMAT subroutine, incorporating temperature-dependent material constants. These temperature-dependent constants consist of E , k , a_1 , a_2 , Q_{\max} , K , α , β_1 , and β_2 . The formula used to fit the temperature-dependent material constants is given as:

$$C = A \times \tanh \left(- \left(\frac{T}{T_0} \right)^B \right) + C_0 \quad (15)$$

where C is the fitted material constant and T is the temperature, A , B , T_0 , and C_0 , are fitting parameters which are listed in Table 2.

This two dimensional model has been utilized to describe the combined effects of temperature and rate sensitivity on a single steel beam. The simulation of a single steel beam was performed using a commercial finite element program ABAQUS. The geometry

Table 2

Parameters in Eq. (15) for temperature-dependent material constants, E , k , a_1 , a_2 , Q_{\max} , K , α , β_1 , and β_2 .

Constant	A	T_0	C_0	B
E	187,850.1	742	187,743.8	2.8
k	100.6	520.8	99.6	2.3
a_1	137.4	621.3	137.5	1.6
a_2	1830.5	619.1	1864.3	3.9
Q_{\max}	97.7	558	86.1	4.1
K	351.7	720.1	351.5	5.4
α	5.50E+06	437.3	5.50E+06	6.4
β_1	-1.00E-15	443	2.70E-27	18.8
β_2	-1.00E-12	443	3.20E-24	18.8

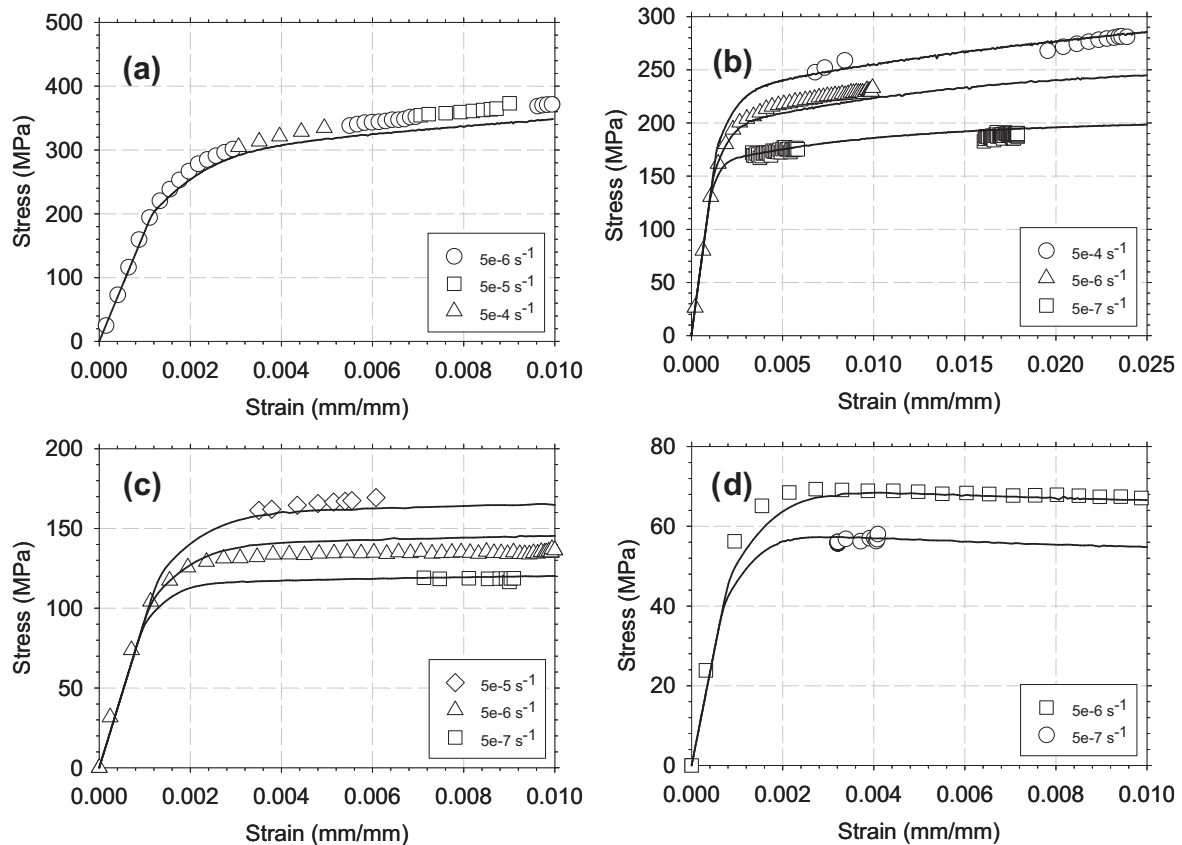


Fig. 8. Comparison of experimental (Symbol) and numerical (Solid line) monotonic stress–strain curves at multiple strain rates for low carbon steel for the following test conditions at (a) 300°C, (b) 500°C, (c) 600°C, and (d) 700°C.

models were built in ABAQUS/CAE. The two dimensional UMAT code for the ISV model was written and employed for the steel material. A single steel beam model, seen in Fig. 9, was built to illustrate effects of loading rate and temperature on the beam deflection. The two-dimensional beam is 3 m long and 0.2 m high. The elements are all plain strain elements. Each element has a size of 0.1 m long, 0.02 m high. The beam was fixed at both ends. Uniform temperature field was applied to the beam. Two temperature cases, 300°C and 700°C, were studied. Uniform pressure ramping up with time was also applied on the beam. Two study cases of pressure ramping rate were investigated. They are 1.5 MPa/min and 0.15 MPa/min. A combination of 2 temperature cases and 2 pressure ramping rates makes 4 simulation cases using single steel beam model.

Four simulation cases were run using the single steel beam model, and their beam deflections were output for comparative analysis. The four curves in Fig. 10 show the evolution of the maximum beam deflections along with the ramping pressure. Fig. 10a shows the beam deflections from 2 simulation cases at the same temperature of 300°C but at two different pressure ramping rates; Fig. 10b from another 2 simulation cases at the temperature

700°C. Low carbon steel exhibits both temperature and strain rate dependence. Fig. 10 emphasizes these dependencies. At elevated temperatures the strength increasingly degrades, as shown in Fig. 10c by the degradation of the peak stress. Fig. 10c also shows that the strain rate sensitivity increases with increasing temperature. Below a critical temperature, between 300°C and 500°C, the steel is rate-independent, while above this value, the steel is rate dependent. This shows the importance of a model which exhibits temperature and strain rate-dependencies.

At the temperature 300°C (Fig. 10a), the beam deflection is not dependent on the pressure ramping rate, however it shows the dependence of pressure ramping rate at the temperature 700°C (Fig. 10b). The comparison accounts for the effect of strain-rate sensitivity on structural deformation. It is implied that 300°C is below the transition temperature of the material strain-rate sensitivity, and 700°C is above that (as implied in Fig. 10c). If we compare the beam deflections under the same pressure load but at the two different temperatures, it is obvious that the beam deflection is larger at the higher temperature 700°C. The higher temperature reduces the strength of the material steel or the stiffness of the steel beam.

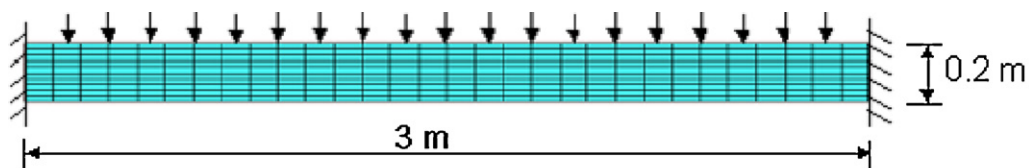


Fig. 9. Single steel beam model.

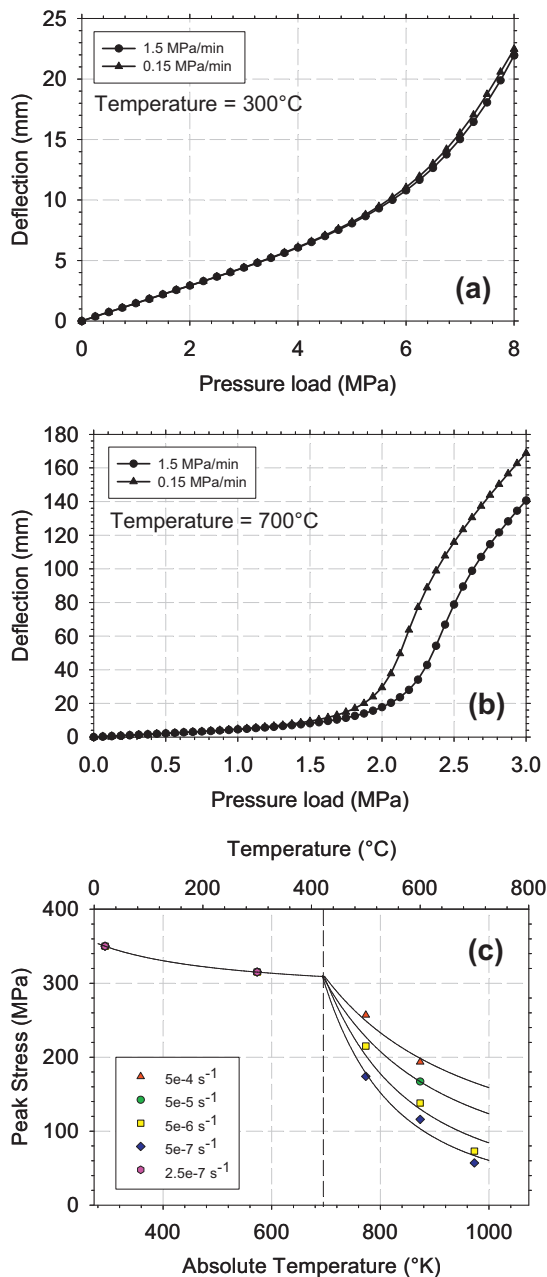


Fig. 10. Beam deflection vs. pressure load at two loading rates at (a) 300 °C and (b) 700 °C. (c) Experimental (Symbol) and curve fit to an Arrhenius equation (Solid lines) of temperature and strain rate dependency of peak stress at a tensile strain 0.5%.

7. Summary and conclusions

The work in this paper has examined the microstructure variations and deformation response of the low carbon steel subjected to post thermal exposure and elevated temperature conditions. Changes in the grain size as well as amounts and morphology of carbides present were monitored as a function of temperature, ranging from room temperatures up to 700 °C for exposure times up to 200 min. Furthermore, a viscoplastic constitutive model has been employed to simulate the flow behavior of the steel in the temperature ranges mentioned above and a series of monotonic and cyclic tests were carried out to determine the parameters required for full identification of the model variables. The main conclusions of this study can be summarized as follows:

1. The grain size, measuring 50 μm , did not show changes for all thermal exposure conditions below 600 °C. The 600 °C and 700 °C specimens show evidence of a bimodal distribution. The as received material and those that have been heat treated at temperatures 600 °C and below, show no changes in the amount of pearlite colonies present while the condition at 700 °C shows the absence of pearlite colonies. In addition, spheroidized particles of carbon have been observed at specimens exposed to 600 °C and 700 °C.
2. An Internal State Variable model, incorporating temperature-dependent material constants, static and dynamic recovery terms, based on non-linear kinematic hardening formulations to describe the viscoplastic flow behavior of low carbon structural steel under variable thermal conditions has been examined. Validity of the fully formulated constitutive model has been established through comparison with corresponding experimental results.
3. Monotonic and cyclic tests were performed at both room temperature and high temperature in order to provide data to determine material dependent parameters for a non-linear kinematic hardening model. The material parameters are shown to be not only responsive to variations in temperature, but microstructure as well. Microstructure sensitivity is seen through differences in the kinematic hardening for the mechanical testing at room temperature which suggest that the spheroidized carbide particles and bimodal grain size distribution in the post thermal exposed specimens act as barriers for dislocations. Furthermore, between the temperatures of 600 °C and 700 °C there is a transition between cyclic hardening and cyclic softening behavior, thus indicating the temperature sensitivity of the isotropic hardening.
4. The temperature and rate sensitivity of low carbon steel has been examined using a finite element analysis of a steel-beam. This has been implemented with a sequentially coupled thermal-stress analysis under variable loading and temperature scenarios. The predicted deformation shows that it is necessary to consider the time-dependent plastic deformation in the steel-beam subjected to elevated temperature.

Acknowledgments

This work has been funded by FM Global and the Department of Homeland Security Center of Excellence: Explosives Detection, Mitigation, and Response at the University of Rhode Island.

References

- [1] P. Makelainen, J. Outinen, J. Kesti, *Journal of Constructional Steel Research* 48 (1998) 47–57.
- [2] H.A. Saab, D.A. Nethercot, *Engineering Structures* 13 (1991) 371–382.
- [3] J. Outinen, J. Kesti, P. Makelainen, *Journal of Constructional Steel Research* 42 (3) (1997) 161–169.
- [4] S.R. Najjar, I.W. Burgess, *Engineering Structures* 18 (1) (1996) 77–89.
- [5] K.H. Tan, S.K. Ting, Z.F. Huang, *Journal of Structural Engineering* 128 (1) (2002) 105–114.
- [6] J. Cattan, *Steel Industry Embraces A992*, Modern Steel Construction, 1999.
- [7] G.F. Vander Voort, *Metallography Principles and Practice*, McGraw-Hill, New York, USA, 1984.
- [8] F.W. Gayle, R.J. Fields, W.E. Luecke, S.W. Banovic, T. Foecke, C.N. McCowan, D.J. McColskey, T.A. Siewert, *Mechanical and Metallurgical Analysis of Structural Steel*, NIST NCSTAR 1-3, Federal Building and Fire Safety Investigation of the World Trade Center Disaster, 2005, September.
- [9] W.D. Callister Jr., *Materials Science and Engineering an Introduction*, 7th ed., John Wiley and Sons, Inc., York, PA, USA, 2007.
- [10] G.E. Dieter, *Mechanical Metallurgy*, McGraw-Hill, USA, 1986.
- [11] D.C. Stouffer, L.T. Dame, *Inelastic Deformation of Metals Models, Mechanical Properties and Metallurgy*, John Wiley and Sons, Inc., New York, 1996.
- [12] M. Yaguchi, Y. Takahashi, *JSME International Journal Series A* 42 (1) (1999).
- [13] J.L. Chaboche, G. Rousselier, *Transactions of the ASME, Journal of Pressure Vessel Technology* 105 (1983) 123–133.

- [14] J.L. Chaboche, G. Rousselier, *Transactions of the ASME, Journal of Pressure Vessel Technology* 105 (1983) 159–164.
- [15] D. Nouailhas, *International Journal of Plasticity* 5 (1989) 501–520.
- [16] J.L. Chaboche, *International Journal of Plasticity* 5 (1989) 247–302.
- [17] Y.C. Wang, T. Lennon, D.B. Moore, *Journal of Constructional Steel Research* 35 (1995) 291–322.
- [18] J.L. Chaboche, K. Dang Van, G. Cordier, *Proceedings of the Fifth International Conference on SMIRT, Div. L, Berlin, Germany, 1979.*
- [19] J.L. Chaboche, *International Journal of Plasticity* 7 (1991) 661–678.
- [20] W. Prager, *Journal of Applied Physics* 20 (3) (1949) 235–241.
- [21] P.J. Armstrong, C.O. Frederick, *A Mathematical Representation of the Multiaxial Bauschinger Effect*, Berkeley Nuclear Laboratories, Report RD/B/N731, 1996.
- [22] A.S. Zaki, H. Ghonem, *Proceeding of the ASME 2000 Design, Reliability, Stress Analysis and Failure Prevention Conference*, Baltimore, Maryland, USA, September 10–13, 2000.
- [23] D. Nouailhas, *Proceedings of the Second International Conference on Constitutive Laws for Engineering Materials: Theory and Application*, Tuscon, Arizona, USA, January 5–8, 1987, pp. 717–724.
- [24] J. Lemaitre, J.L. Chaboche, *Mechanics of Solid Materials*, Cambridge University Press, Cambridge, United Kingdom, 1990.

Simulation of Viscoplastic Deformation of Low Carbon Steel Structures at Elevated Temperatures

Y. Sun, K. Maciejewski, and H. Ghonem

(Submitted November 19, 2010; in revised form June 17, 2011)

The deformation response of a low carbon structural steel subjected to high temperature simulating fire conditions is generated using a viscoplastic material constitutive model which acknowledges the evolution of the material hardening parameters during the loading history. The material model is implemented in an ABAQUS subroutine (UMAT) which requires the determination of the material constants as a function of temperature. Both the temperature dependency and strain-rate sensitivity of the material parameters have been examined by the analysis of a single steel beam and a steel-framed structure subjected to temperatures ranging from 300 to 700 °C. Sequentially coupled thermal-stress analysis is applied to a structure under simulated fire condition. Results of this analysis show that above a transitional temperature, the deformation of the steel is strain-rate dependent. The combined effect of heat flux and loading rate on the complex deformation of a two-story steel structure is examined and the significance of employing a viscoplastic material model is discussed.

Keywords finite element analysis, hardening, internal state variables, strain-rate sensitivity, structural steel, viscoplasticity

1. Introduction

With the advancement of computation technology, engineers tend to adopt more advanced thermal and mechanical simulation techniques to assess the safety and reliability of engineering structures. Advanced numerical analysis allows less simplifications or assumptions for the description of material constitutive behavior, geometric modeling, real boundary conditions and loading, hence leading to a more realistic prediction of the stress/deformation in the studied engineering structure. For example, the deformation response prediction of steel-framed structures under fire conditions was done based on an elasto-plastic beam-column formulation (Ref 1, 2); the non-uniform profile of temperature across section of frame members was considered in Ref 3; the creep strain model was included in the simulation of steel frames in fire (Ref 4); nonlinear analyses for three-dimensional steel frames in fire was presented in Ref 5, 6, but without taking into account the strain-rate sensitivity of the steel material at elevated temperature and nonlinear temperature distribution both across section of steel frames and along length of beam column.

In this study, viscoplastic constitutive equations (Ref 7, 8) are used to describe the nonlinear behavior of low carbon steel at elevated temperatures. The material parameters in the viscoplastic constitutive equations are modeled as a function of temperature and implemented in ABAQUS subroutine UMAT.

Y. Sun, K. Maciejewski, and H. Ghonem, Mechanics of Materials Research Laboratory, Department of Mechanical Engineering and Applied Mechanics, University of Rhode Island, Kingston, RI 02881. Contact e-mail: ghonem@egr.uri.edu.

The UMAT code is verified by the simulation of tensile tests of monotonic displacement loading at different temperatures and of a fatigue test of cyclic displacement loading. The simulation of single steel beam is conducted to show the effect of loading rate and temperature on the beam deflection. Furthermore, sequentially coupled thermal-stress simulation technique is employed in the finite element analysis of a three-dimensional steel-framed structure. Transient heat transfer analysis is first conducted to obtain the temperature distribution on the steel frames as a function of time. Nodal temperature results from heat transfer analysis are then transferred for structural response analysis. The main focus of this article is to study the influence of the mechanical behaviors of the steel material on the deformation response of steel structures.

2. Viscoplastic Constitutive Equations

The model described in this section is based on unified constitutive equations in the manner developed by Chaboche and Rousselier (Ref 7, 9). This model formulated on the assumption that a viscoplastic potential, Ω , exists in the stress space. A particular form of the viscoplastic potential is (Ref 8):

$$\Omega = \frac{K}{\alpha(n+1)} \exp\left(\alpha \left\langle \frac{\sigma_v}{K} \right\rangle^{n+1}\right), \quad (\text{Eq 1})$$

where K , n , and α are material parameters that characterize the rate sensitivity. To describe the viscoplastic behavior, the concept of time-dependent overstress or viscous stress, σ_v , is used. This is given as:

$$\sigma_v = J(\sigma - X) - R - k, \quad (\text{Eq 2})$$

where the tensor X represents the kinematic hardening stress, R and k are scalar variables corresponding to the isotropic hardening stress and the initial yield stress, respectively, and $J(\sigma - X)$, is Von Mises second invariant defined by:

$$J(\sigma_{ij} - X_{ij}) = \left(\frac{3}{2} (\sigma'_{ij} - X'_{ij}) : (\sigma'_{ij} - X'_{ij}) \right)^{1/2} \quad (\text{Eq 3})$$

where σ' and X' are the deviatoric parts of the applied stress tensor, σ , and the back stress tensor, X , respectively. The scalar k is a temperature-dependent material constant representing the initial size of the elastic domain. Throughout this development, the total strain is partitioned into an elastic component and an inelastic component. The unified viscoplastic equations incorporate the plastic and creep components simultaneously in an inelastic or viscoplastic strain component denoted by ε_p throughout the rest of this article (Ref 7, 9, 10). The relation between plastic flow and the viscoplastic potential is determined by means of the normality rule:

$$d\varepsilon_p = \frac{\partial \Omega}{\partial \sigma_{ij}} = dp \frac{3}{2} \frac{(\sigma'_{ij} - X'_{ij})}{J_2(\sigma'_{ij} - X'_{ij})}, \quad (\text{Eq 4})$$

where the dp is the accumulated plastic strain rate, which is given in terms of effective plastic strain as:

$$dp = \left(\frac{2}{3} d\varepsilon_p d\varepsilon_p \right)^{1/2} = \left\langle \frac{J_2(\sigma - X) - R - k}{K} \right\rangle^n \times \exp \left(\alpha \left\langle \frac{J_2(\sigma - X) - R - k}{K} \right\rangle^{n+1} \right) \quad (\text{Eq 5})$$

The kinematic hardening terms, measured by the back stress X , describes the internal changes during each inelastic transient. Two terms of back stress describing the phenomena of the Bauschinger effect will be considered here. The first term, X_{ij}^1 , is the short-range hardening effect, which is a fast saturated variable. The second term, X_{ij}^2 , is a quasi-linear variable describing the long-range hardening effect. Hence, the back stress is defined as:

$$X_{ij} = X_{ij}^1 + X_{ij}^2 \quad (\text{Eq 6})$$

where each term is described by a general form as (Ref 7, 8):

$$\dot{X}_{ij}^i = c_i \left(\frac{2}{3} a_i \dot{\varepsilon}_{ij}^p - X_{ij}^i \dot{p} \right) - \beta_i \left| J(X_{ij}^i) \right|^{r_i-1} X_{ij}^i \quad (\text{Eq 7})$$

The first term describes the strain hardening as a function of X , plastic strain rate and accumulated plastic strain rate. The second term represents processes for bypassing or penetrating barriers at comparable rates and is termed dynamic recovery. The third term, which is strongly temperature dependent, describes the time-recovery or static-recovery as a function of X . c , α , β , and r are material-dependent parameters and $J(X_{ij})$ is the second invariant of X_{ij} .

The slow evolution of microstructure associated with cyclic hardening or softening of the material can be described by the isotropic hardening variable, R , which is the difference in the saturation position after a loading cycle and that corresponding to the monotonic loading for the same plastic strain. This is governed by the following equations:

$$\dot{R} = b(Q - R)\dot{p} \quad (\text{Eq 8})$$

$$Q = Q_{\max}(1 - e^{-\mu q}) \quad (\text{Eq 9})$$

$$q = \max(|\varepsilon_p|, q) \quad (\text{Eq 10})$$

where Q and b are the limiting values of the isotropic hardening variable. Q is the saturation limit of R while the constant,

b , is a temperature and material-dependent parameter describing how fast R reaches Q . This latter parameter can be either a positive value, indicating cyclic hardening, or a negative value, indicating cyclic softening. Q_{\max} is the maximum value of Q , and q is the maximum strain achieved during loading, which memorizes the previous plastic strain range (Ref 11).

3. Model's Material Parameters

The material employed in this study is A572 Grade 50 Low Carbon Steel and its microstructure which is shown in Fig. 1, includes pearlite colonies and α -ferrite equiaxed grains. The average grain size is 53 μm (ASTM 5). Volume fraction of the pearlite phase is 10%.

A series of strain-controlled tests were carried out on the as-received steel, at both room and high temperature, to determine the various material parameters described above in order to fully identify the nonlinear kinematic hardening model. The mechanical testing was carried out using a servo hydraulic test machine, equipped with a heat induction coil for the high temperature tests. The strain was measured with a quartz rod extensometer.

A monotonic test is carried out, to determine the modulus, E , and yield stress, k , of the material. Results of this rate at various loading conditions are shown in Fig. 2(a). A series of strain-controlled fully reversed cyclic stress-strain tests (fatigue stress ratio = -1) are performed at strain ranges varying from $\pm 0.2\%$ to $\pm 1\%$ strain. A typical cyclic stress-strain curve at 300 $^\circ\text{C}$ is shown in Fig. 2(b). These loops are employed to generate the isotropic and kinematic hardening, as well as, viscosity and recovery parameters.

The isotropic hardening parameter, b , is determined from the evolution of the peaks of the cyclic stress-strain curves (Fig. 2b) Q_{\max} and μ are calculated from the difference in the peak stress of the first cycle and the saturated cycle as a function of the maximum plastic strain achieved during loading (Ref 8, 11–13). The kinematic stress corresponds to the center of the linear part of the first reversible cyclic loop at each strain

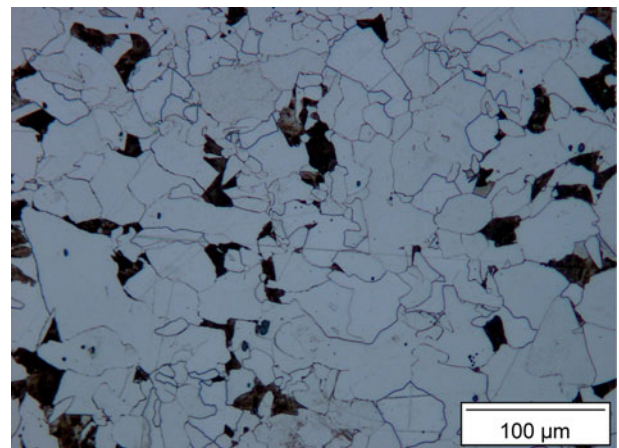


Fig. 1 Optical micrograph of as-received A572 Grade 50 steel etched for 5 s in 5 vol.% nital. The microstructure is typical of normalized steel, consisting of pearlite colonies (dark phase) and α -ferrite (light phase) equiaxed grains. The pearlite colonies have a volume fraction of 10% and the grain size is 53 μm (ASTM 5)

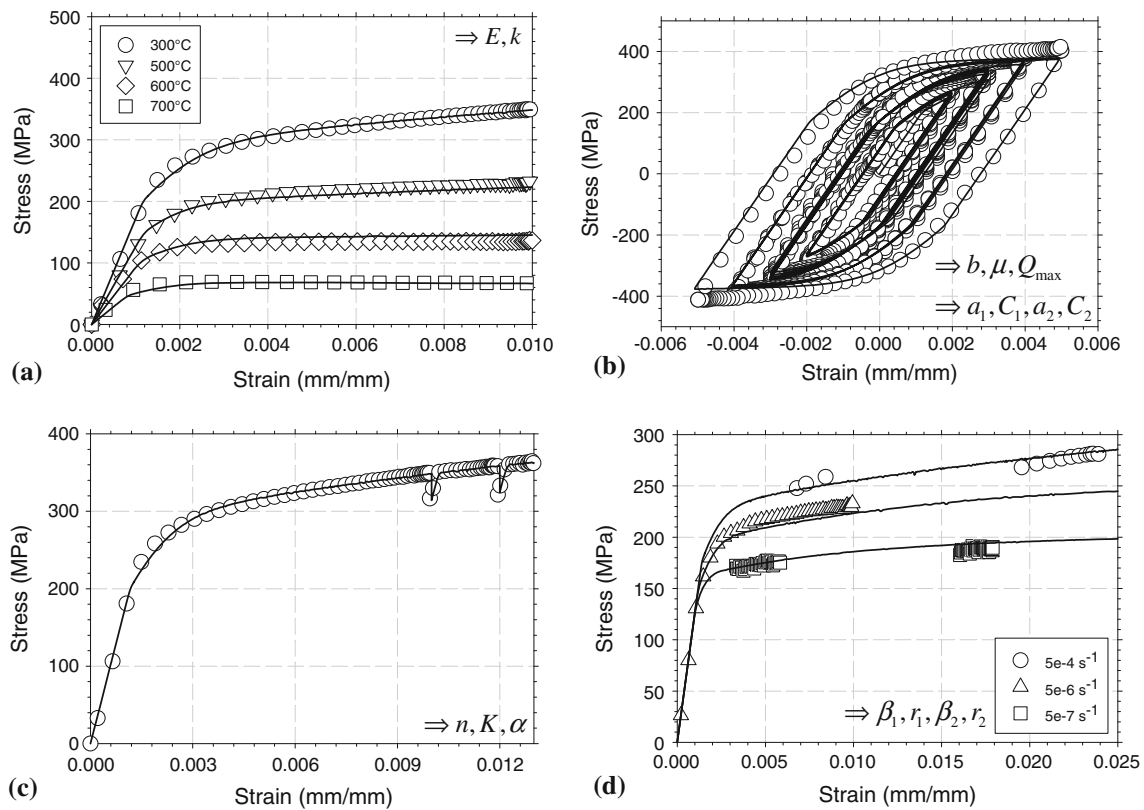


Fig. 2 Experimental (symbol) and numerical (solid line) stress-strain curves for low carbon steel tested. (a) Monotonic stress-strain curves, (b) cyclic stress-strain curves at 300 °C, (c) relaxation stress-strain curves at 300 °C, and (d) monotonic stress-strain curves at multiple strain rates at 500 °C. These curves are used to determine the material parameters specified on the graphs

range (Fig. 2b). This stress is determined as a function of plastic strain to determine the materials parameters a_1 , c_1 , a_2 , and c_2 .

To describe the time-dependent viscous stress term, a strain-controlled monotonic stress-relaxation test is performed, as seen in Fig. 2(c). For this, during the periods of holding at a constant total strain, the stress and stress rate as a function of time is acquired. This is used to obtain the viscous stress in terms of plastic strain rate, from which, n and K , strain-rate sensitive parameters must be determined (Ref 8, 10, 14). The material constant, α , is taken to be the saturation limit of viscous stress for high-plastic strain rates.

Time-dependent recovery parameters, β_1 , β_2 , are determined from the linear portion of the stress time curve. In this region it is assumed that R , k and viscous stress are constant and the time-dependent stress is only coming from the time-dependent back stress. These parameters, β_1 , β_2 , r_1 and r_2 , are optimized with stress-strain data at various strain rates. Strain-rate sensitivity tests (Ref 14) are performed in which a specimen is loaded monotonically in strain control at multiple strain rates as shown in Fig. 2(d).

The material parameter determination procedure, described above, has been applied to as-received steel tested at temperatures ranging from 20 to 700 °C, and is further detailed in Ref 8, 10–14. The material constants from the above procedure are shown in Table 1 for each temperature condition.

Several of the material constants, as described above, are temperature dependent. The material constants have been determined for five different temperatures, ranging from room

temperature to 700 °C. A linear interpolation to the material constants is generally used to extend a constitutive model working for any temperature, which may be less accurate. A nonlinear form better describes the temperature span, and the formula used to fit the temperature-dependent material constants is given below:

$$C = A * \tanh\left(-\left(\frac{T}{T_0}\right)^m\right) + C_0, \quad (\text{Eq 11})$$

where C and T represent a material constant and temperature, respectively, A , m , T_0 , and C_0 are unknown parameters which are figured out by curve fitting to $C - T$ data.

Figure 3 shows two examples of the curve fitting to the temperature-dependent Young's modulus and strain-rate sensitivity coefficient using the Eq 11.

The saturation of material constants at lower temperature was captured by the hyperbolic tangent function of temperature. The saturation values are defined by the parameters, A and C_0 . The sensitivity of the material constant change with temperature is defined by the exponent, m . The reference temperature, T_0 , defines the temperature at the middle of the transitional segment of the curve. The parameters for temperature-dependent material constants are listed in Table 2.

The temperature-dependent and independent material constants are used to fully define the viscoplastic constitutive model. This model is then implemented in finite element software to describe the material behavior under varying loading and temperature conditions.

Table 1 Material parameters for as-received A572 Grade 50 low carbon steel tested at temperatures ranging from 20 to 700 °C

Temperature	20 °C	300 °C	500 °C	600 °C	700 °C
E , GPa	188	172	127	93	58
k , MPa	100	71	27	11	3
a_1 , MPa	137	96	54	36	22
C_1	1411	1411	1411	1411	1411
a_2 , MPa	1864	1753	1111	566	175
C_2	1.15	1.15	1.15	1.15	1.15
b	78	78	78	78	78
Q_{\max} , MPa	86	78	31	1	-10
μ	1447	1447	1447	1447	1447
n	14	14	14	14	14
K , MPa	155	349	304	227	107
α	$5.5E+06$	$5.0E+06$	$1.0E+05$	$4.5E+00$	$9.9E-01$
β_1 , Pa ^{2.58}	$1.0E-21$	$9.9E-20$	$1.0E-15$	$1.0E-15$	$1.0E-15$
β_2 , Pa ^{2.15}	$4.6E-26$	$2.1E-16$	$1.0E-12$	$1.0E-12$	$1.0E-12$
r_1	2.58	2.58	2.58	2.58	2.58
r_2	2.15	2.15	2.15	2.15	2.15

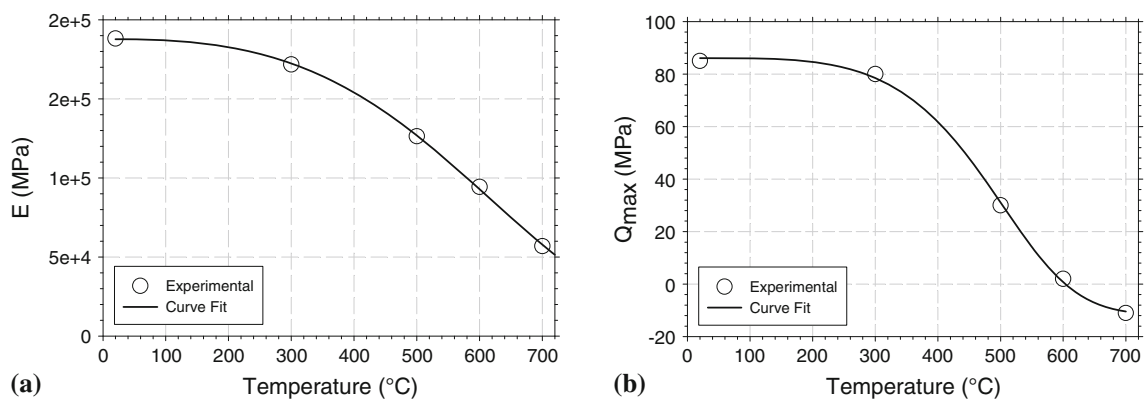


Fig. 3 Modeling of temperature-dependent material constants. (a) Young's modulus and (b) isotropic hardening coefficient, Q_{\max}

Table 2 Parameters in Eq 11 for temperature-dependent material constants

Constant	A	T_0	C_0	m
E	187850.1	742.0	187743.8	2.8
k	100.6	520.8	99.6	2.3
a_1	137.4	621.3	137.5	1.6
a_2	1830.5	619.1	1864.3	3.9
Q_{\max}	97.7	558.0	86.1	4.1
K	351.7	720.1	351.5	5.4
α	$5.5E+06$	437.3	$5.5E+06$	6.4
β_1	$-1.0E-15$	443.0	$2.7E-27$	18.8
β_2	$-1.0E-12$	443.0	$3.2E-24$	18.8

4. Validation of UMAT Code

The viscoplastic constitutive equations have been implemented into ABAQUS through a subroutine UMAT. A finite element model of uniaxial fatigue specimen was built to simulate the experimental tensile and fatigue tests. A comparison of experimental and numerical stress-strain curves is used to examine the implementation of the simulation model. A quarter 3D finite element model is shown in Fig. 4. The

diameter of the cylindrical specimen is 6.35 mm and the gage length is 10 mm. The block element with eight nodes was used to mesh the geometry model. Nodes on the bottom plane were fixed in vertical direction, and symmetry boundary conditions were applied to the nodes on two side planes. To simulate the tensile tests, nodes on the top plane were subjected to a displacement ramping from 0 to 0.1 mm within 2000 s. Four simulation cases were done by assigning four different uniform temperatures to the whole model. The predicted stress-strain curves are shown in Fig. 5 and compared with the experimental results which show good agreement.

The quarter cylinder model was also used for the simulation of a fatigue test at 300 °C. A cyclic displacement loading (see Fig. 6a) was applied to the nodes on the top plane.

The magnitude of applied displacement equals the value that the gage length of the model times the strain that the element was subjected to. The displacement loading shows three strain ranges, $\pm 0.2\%$, $\pm 0.3\%$, and $\pm 0.4\%$. Four cycles were run under strain range $\pm 0.2\%$, six cycles under strain range $\pm 0.3\%$, and three cycles under strain range $\pm 0.4\%$. The cyclic test of three strain ranges used the same loading strain rate of 5×10^{-6} mm/mm/s. The period of one cycle under strain range $\pm 0.2\%$ is 1600, 2400 s under strain range $\pm 0.3\%$, and 3200 s under strain range $\pm 0.4\%$. The element stresses in vertical direction were output and plotted with the strains in the

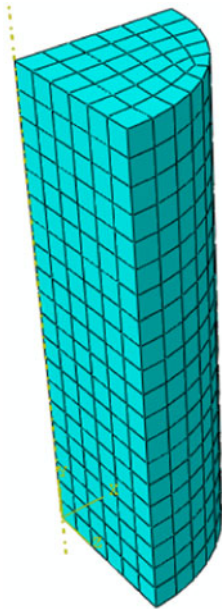


Fig. 4 FE model for tensile tests

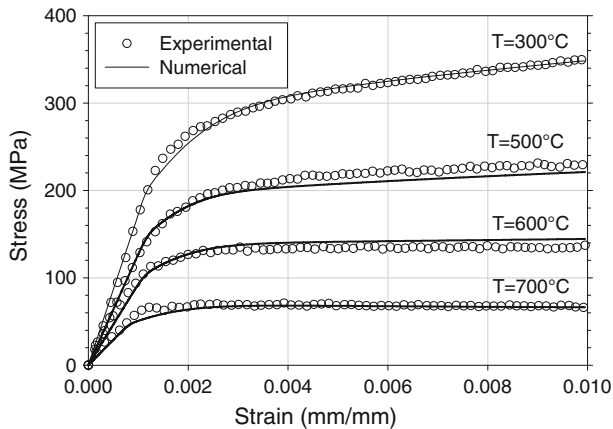


Fig. 5 Numerical and experimental stress-strain curves

same direction. Both experimental and numerical hysteresis stress-strain curves are shown in Fig. 6(b). The good agreement of experimental and numerical stress-strain curves validates the implementation of the UMAT code.

5. Finite Element Analysis and Results

5.1 Simulation of Single Steel Beam

Numerical simulations were conducted using two finite element models, a simple model of single steel beam and a complex model of steel-framed structure. Simulation of single steel beam model (Fig. 7) was built to examine effects of loading rate and temperature on the beam deflection.

The two-dimensional beam is 3 m long and 0.2 m high. The element type of plain strain was assigned to all elements. Each element has a size of 0.1 m long, 0.02 m high. Uniform temperature field was applied to the beam and two temperature cases, 300 and 700 °C, were studied. Uniform pressure ramping up with time was also applied on the beam. Two cases of pressure ramping rate were investigated; 1.5 and 0.15 MPa/min.

The beam deflections from the four simulation cases described above are compared in Fig. 8, which shows the evolution of the maximum beam deflections along with the ramping pressure.

Figure 8(a) compares the beam deflections generated at 300 °C for two different pressure ramping rates, while Fig. 8(b) shows the comparison at 700 °C. At the temperature 300 °C, the beam deflection is not dependent on the loading rate; however, it shows dependency at the temperature 700 °C. This result indicates that the 300 °C is below the transition temperature of the material strain-rate sensitivity. If we compare the beam deflections under the same pressure load but at the two different temperatures, it becomes obvious that the beam deflection is larger at 700 °C. The higher temperature reduces the strength of the material steel or the stiffness of the steel beam.

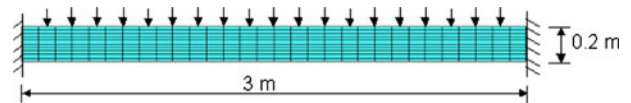


Fig. 7 Single steel beam model

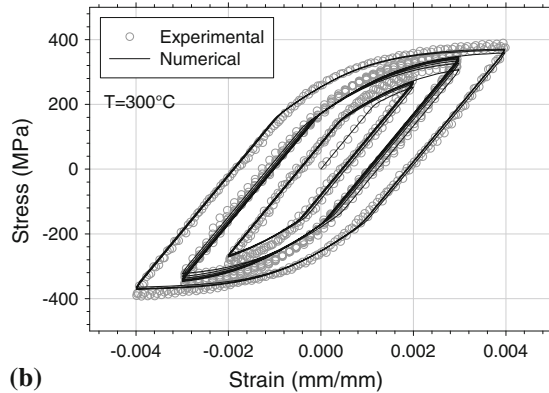
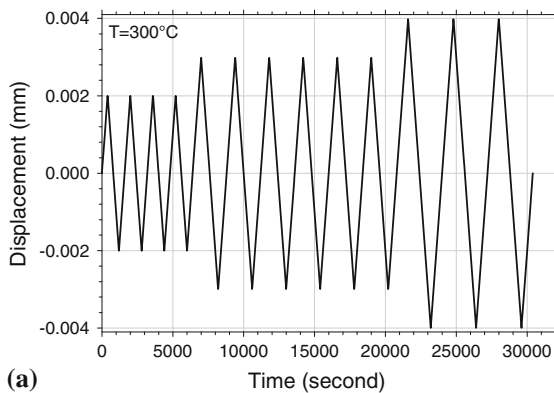


Fig. 6 (a) Cyclic strain loading in fatigue tests and (b) experimental and numerical hysteresis stress-strain curves at 300 °C

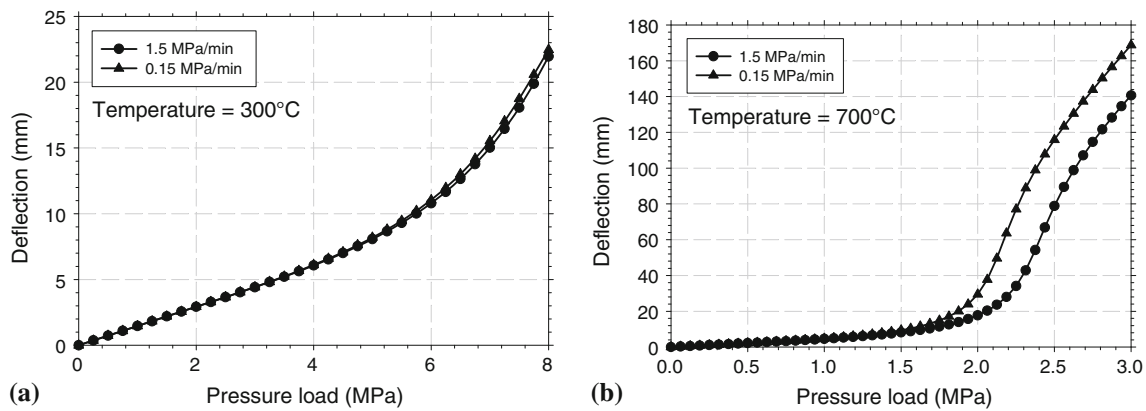


Fig. 8 Beam deflection at two loading rates (a) at temperature 300 °C and (b) at temperature 700 °C

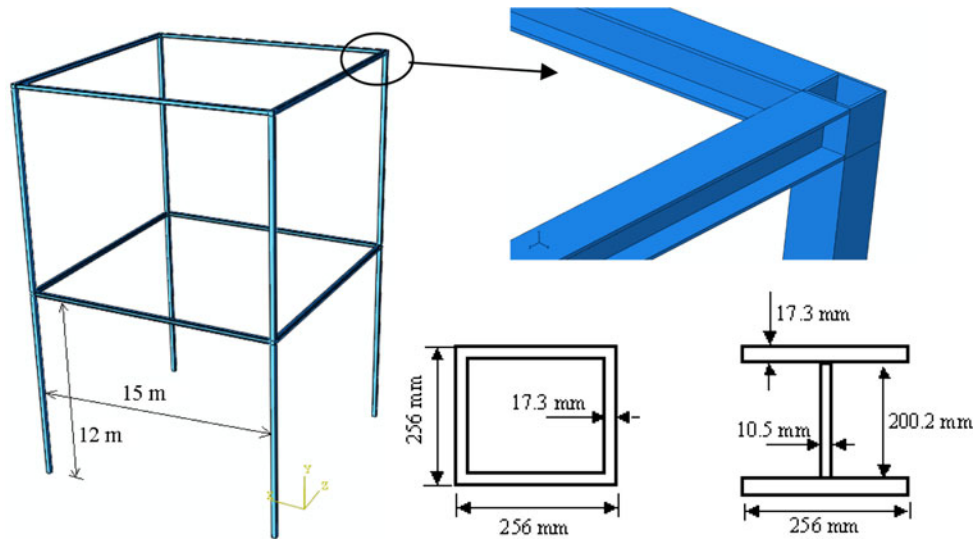


Fig. 9 FE model of a 3D steel-framed structure under fire condition

5.2 Simulation of Steel-Framed Structure Under Fire Condition

Finite element analysis of steel-framed structures under fire condition uses a sequentially coupled thermal-stress analysis (Ref 15). In this analysis, a transient heat transfer analysis is first performed to obtain temperature distribution history, and then a stress/deformation analysis is conducted to obtain structural deformation. Nodal temperatures are calculated in the transient heat transfer analysis and stored as a function of time in the heat transfer result file. The stress analysis uses the same geometry model with the same meshing as the heat transfer analysis. The temperature fields for the stress analysis are coupled with temperature results from transient heat transfer analysis.

A three-dimensional model of a multi-story structure was built, the dimensions of which are shown in Fig. 9.

The structure has two cells with eight box-shape columns and eight I-shape beams. Each column is 12 m high and each beam is 15 m long. The dimensions of the column and beam cross sections are shown in Fig. 9. We consider the beams and columns to be integral. Eight-node block elements were used to mesh the structure as shown in Fig. 10.

The element size is 0.5 m in longitude direction of beam and column, and <0.04 m in their transverse direction. The total number of elements is 19,136.

5.2.1 Heat Transfer Analysis. The finite element model was first employed to conduct transient heat analysis. The material properties required for heat transfer analysis are shown in Table 3.

The element type was set as DC3D8 for heat transfer analysis. The room temperature 25 °C was assigned to the steel-frame structure as the initial condition. A surface heat flux of 16 kW/m² was applied on the bottom plane of one beam in the first floor, and 24 kW/m² on the side plane of its connected column in order to simulate the appearance of a fire in the cell (see Fig. 11).

The heat transfer duration is 1 h. The calculated temperatures at all nodes and at different time are stored in the output file of heat transfer analysis. The output frequency of nodal temperatures is 0.2 Hz.

Figure 12 shows the temperature distribution after 1 h of heat transfer. The non-uniform temperatures across the sections of steel frames were observed.

The higher temperature occurred to the positions near the surface where external heat flux was applied. Within 1 h, the

heat spread was confined in the mid cell of the first floor. Positions far away from the surface where the heat flux came in almost maintained their initial temperature of 25 °C. Figure 13 and 14 show the temperature history at seven points on the heated beam's and column's cross sections, respectively.

The temperature at the monitored positions increases with time since the continuous heat flow increase the thermal energy of the structure. For the beam, the temperatures at points B1 and B2 are higher than those at points B3, B4, and B5, and much higher than those at points B6 and B7. For the column, the temperatures at points C1 and C2 are higher than those at points C3, C4, and C5, and much higher than those at C6 and C7. Although B1 and B2 are on the same heat flux surface, their temperatures are different. The temperature at B1 is higher than that at B2 because the position B2 is nearer to the web, which is the heat transfer path.

5.2.2 Stress/Deformation Analysis. In the stress/deformation analysis, the element type was changed from heat transfer type to stress analysis type C3D8, while the geometry

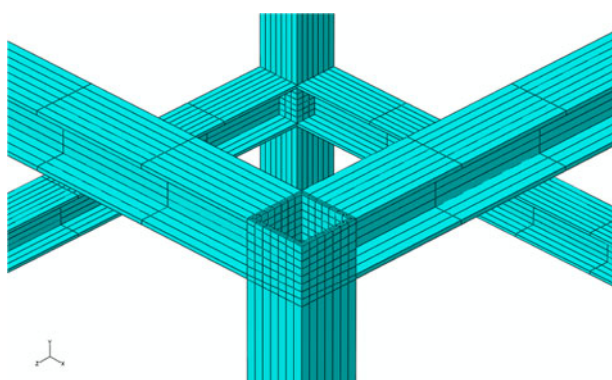


Fig. 10 Meshing of FE model of 3D steel-framed structure

Table 3 Material properties for heat transfer analysis

Mass density	Thermal conductivity	Specific heat
7800 kg/m ³	50 J/m ² °C	470 W/kg °C

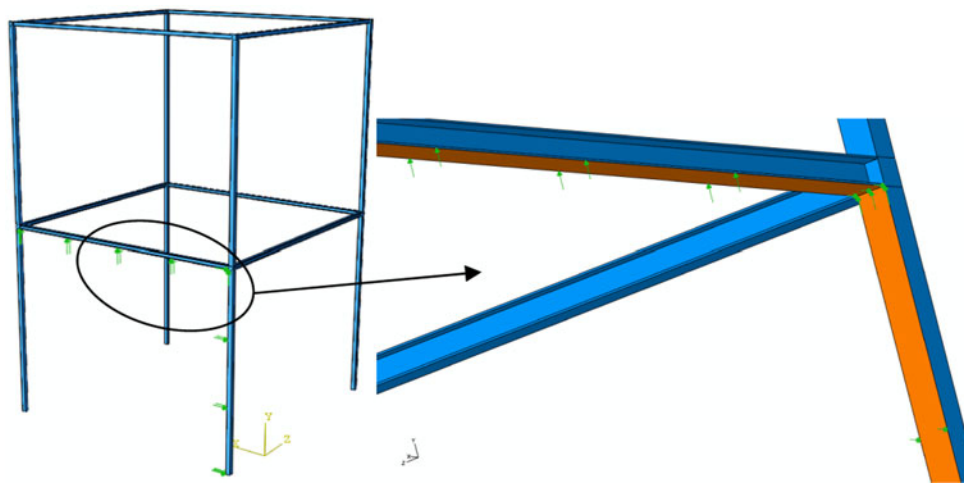


Fig. 11 Surface heat flux as thermal loading applied to the structure

remained the same. The developed UMAT was used as the material model. The four columns were fixed at their roots. A uniform pressure was applied on all beams and temperature field was assigned to the whole structure. The simulation consists of three loading steps. The first step is to increase the uniform pressure from 0 to 0.04 MPa in 10 s, while keeping the temperature constant at 25 °C. In the second step, the maximum pressure loading is maintained and the temperature field is coupled with the results obtained from the transient heat transfer analysis, and hence the duration of step 2 is 60 min. In the third step, both the pressure and temperature distribution in the structure is held constant for 30 min. Therefore, static stress/deformation analysis was performed with a time period of 90 min plus 10 s. The maximum time increment is 0.5 s. The control setting for the nonlinear effect of large displacement was activated in the simulation. The displacement, strain, and stress results along with time were output from the stress analysis.

The final deformation of the three-dimensional two-story structure from the stress analysis using the viscoplastic constitutive model, discussed above, was examined. Among the four beams of the first floor, the beam subjected to the heat flux deflected more than other beams as expected. Figure 15 shows the deflection history of two beams at the first floor (see Fig. 10).

The heated beam refers to the beam which had the heat flux applied to it, and the non-heated beam is a beam neighboring the heated beam. In the 10 s of load step 1, the deflections of the two beams increase quickly due to the increasing pressure load. In this step, the two beams achieved the same amount of deflection due to geometrical symmetry, the same loading condition, and uniform structural temperature. In load step 2, the deflection of the heated beam does not increase at the beginning although its temperatures increase. It is concluded that the beam's deflection starts to increase when the applied load/stress becomes larger than the strength of the beam. The applied load did not change but the beam's strength degraded with the increase of temperature. When the strength of the heated beam degraded below its stress level, the inelastic strain occurred as shown in Fig. 16, and the beam's deflection started to increase slowly initially and then faster with the continuously increasing of the beam's temperature.

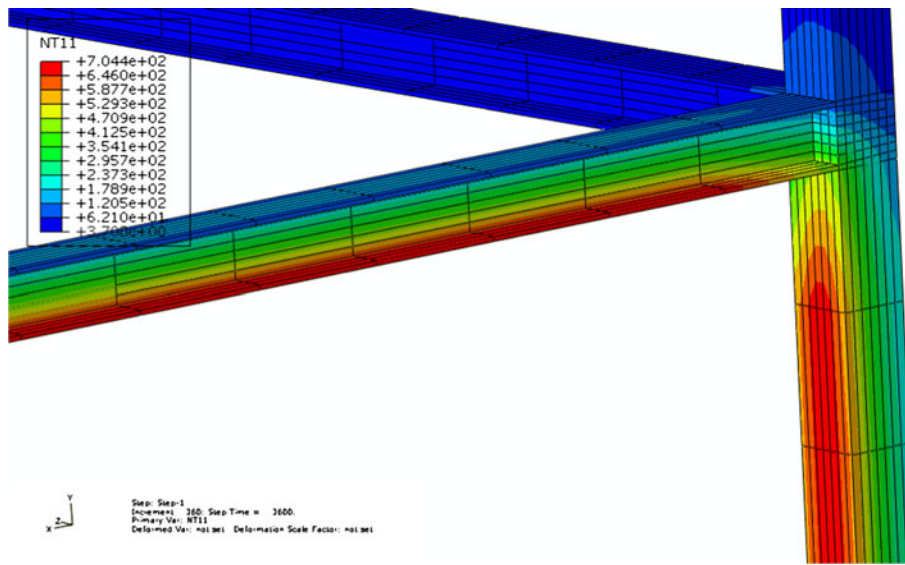


Fig. 12 The final temperature distribution in the structure

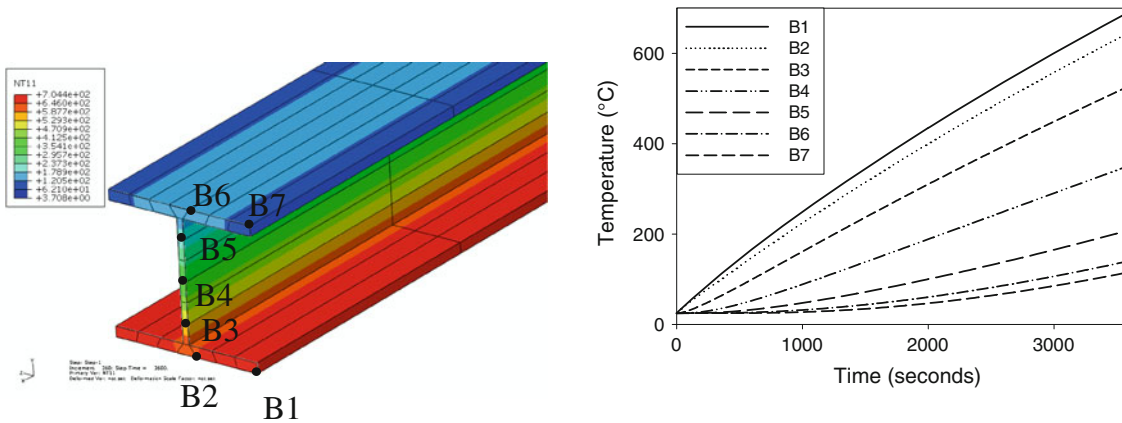


Fig. 13 Temperature history of seven points on the beam's cross section

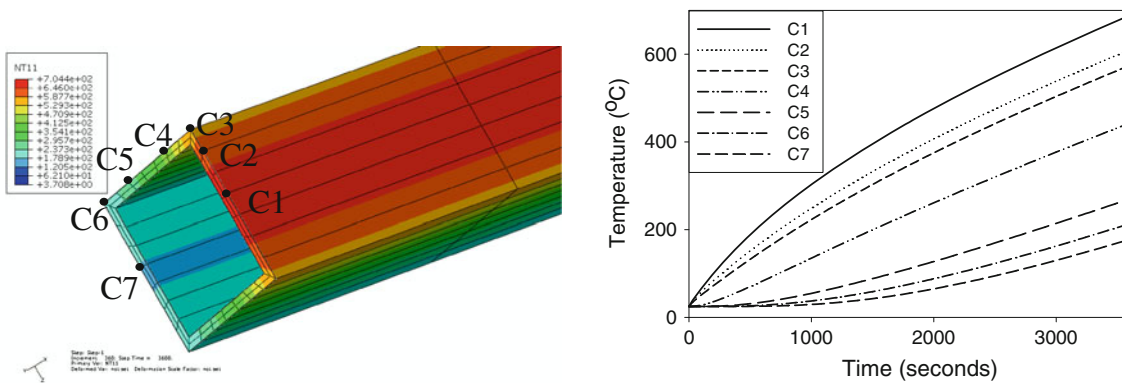


Fig. 14 Temperature history of seven points on the column's cross section

In load step 3, the applied loading and the temperature distribution did not change (actually the applied stress relaxed as shown in Fig. 16), but the heated beam's deflection continued to

increase. The deflection increase in load step 3 was attributed to the creep deformation (that is, material strain-rate sensitivity) at elevated temperatures, which can be shown in Fig. 16.

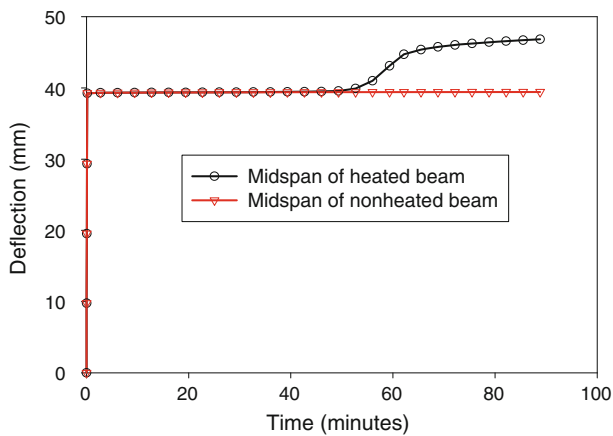


Fig. 15 The deflection history at the midspan of the heated and non-heated beams

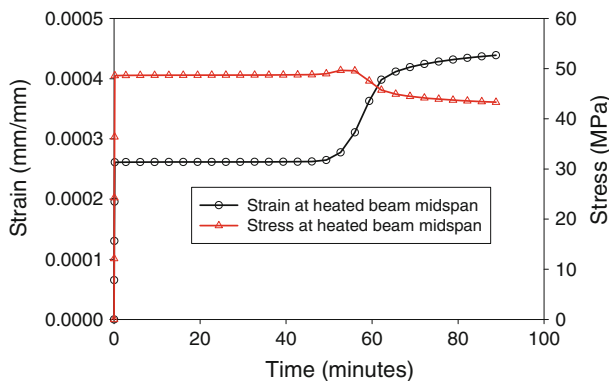


Fig. 16 Strain and stress history at the midspan of the heated beam

6. Conclusions

The work in this article describes a viscoplastic constitutive model that has been employed to simulate the flow behavior of structural steel A572 Grade 50 steel at elevated temperatures. The material constants of the model have been fitted as a function of temperature, thus allowing the implementation of the corresponding constitutive equations in a UMAT subroutine of the ABAQUS platform. The validation of the UMAT has been carried out by comparing the experimental data with those obtained from the numerical simulations under the same applied load conditions. The finite element analysis of a three-dimensional steel-framed structure under fire condition has been performed using a simulation strategy of sequentially coupled thermal-stress analysis. The general conclusions of this study can be listed as follows:

1. The nonlinear material behavior of the low carbon structural steel at elevated temperatures can be captured by unified constitutive equations, which consist of a nonlinear kinematic hardening model and a hyperbolic function for the modeling of temperature-dependent material constants.

2. The steel shows a transition temperature for the time-dependent plastic deformation. The strain-rate sensitivity transition is indicated by the trend of temperature-dependent material constants.
3. The heat transfer analysis of the 3D steel-frame structure shows the temperature distributed nonlinearly across the sections of the steel frame and along the length of beams and columns.
4. As the temperature increases, large bending or buckling deformation could occur to the steel-frame structure as a result of the degradation of the material's strength below the applied stress level.
5. The time-dependent material behavior contributes to the structure's bending or buckling when the applied temperature is higher than the strain-rate sensitivity transition temperature.

References

1. J.Y. Liew, L.K. Tang, T. Holmaas, and Y.S. Choo, Advanced Analysis for the Assessment of Steel Frames in Fire, *J. Constr. Steel Res.*, 1998, **47**, p 19–45
2. P. Makelainen, J. Outinen, and J. Kesti, Fire Design Model for Structural Steel S420M Based Upon Transient-State Tensile Test Results, *J. Constr. Steel Res.*, 1998, **48**, p 47–57
3. G.Q. Li and S.C. Jiang, Prediction to Nonlinear Behavior of Steel Frames Subjected to Fire, *Fire Saf. J.*, 1999, **32**, p 347–368
4. Y.C. Wang, T. Lennon, and D.B. Moore, The Behavior of Steel Frames Subject to Fire, *J. Constr. Steel Res.*, 1995, **35**, p 291–322
5. P. Kumar, V.V. Nukala, and D.W. White, A Mixed Finite Element for Three-Dimensional Nonlinear Analysis of Steel Frames, *Comput. Methods Appl. Mech. Eng.*, 2004, **193**, p 2507–2545
6. S.R. Najjar and I.W. Burgess, A Nonlinear Analysis for Three-Dimensional Steel Frames in Fire Conditions, *Eng. Struct.*, 1996, **18**(1), p 77–89
7. J.L. Chaboche and G. Rousselier, On the Plastic and Viscoplastic Constitutive Equations—Part I: Ruled Developed with Integral Variable Concept, *Trans. ASME J. Press. Vessel Technol.*, 1983, **105**, p 123–133
8. D. Nouailhas, Unified Modeling of Cyclic Viscoplasticity: Application to Austenitic Stainless Steels, *Int. J. Plast.*, 1989, **5**, p 501–520
9. J.L. Chaboche and G. Rousselier, On the Plastic and Viscoplastic Constitutive Equations—Part II: Application of Integral Variable Concepts to the 316 Stainless Steel, *Trans. ASME J. Press. Vessel Technol.*, 1983, **105**, p 159–164
10. J.L. Chaboche, Constitutive Equations for Cyclic Plasticity and Cyclic Viscoplasticity, *Int. J. Plast.*, 1989, **5**, p 247–302
11. A.S. Zaki and H. Ghonem, Modeling the Ratcheting Phenomenon in an Austenitic Steel at Room Temperature, *Proceeding of the ASME 2000 Design, Reliability, Stress Analysis and Failure Prevention Conference* (Baltimore, MA), 2000
12. K. Maciejewski, Y. Sun, O. Gregory, and H. Ghonem, Deformation and Hardening Characteristics of Low Carbon Steel at Elevated Temperature, *Material Science and Technology Conference and Exhibition* (Pittsburgh, PA), October 2008
13. D. Nouailhas, A Viscoplastic Modelling Applied to Stainless Steel Behavior, *Proceedings of the Second International Conference on Constitutive Laws for Engineering Materials: Theory and Application*, January 5–8 (Tuscon, AZ), 1987, p 717–724
14. J. Lemaitre and J.L. Chaboche, *Mechanics of Solid Materials*, Cambridge University Press, Cambridge, 1990
15. ABAQUS Inc. *ABAQUS Standard User's Manual*, 6.6 ed., 2006

Deformation Criterion of Low Carbon Steel Subjected to High Speed Impacts

W. Visser, G. Plume, C-E. Rousseau, O. Gregory*, H. Ghonem
92 Upper College Road, Kingston, RI 02881
Department of Mechanical Engineering
*Department of Chemical Engineering
University of Rhode Island

Abstract

A study has been carried out to examine effects of blast loading on the microstructure deformation response of A572 Grade 50 low carbon structural steel. Symmetrical planar impact experiments have been carried out using a single stage gas gun to drive projectiles to velocities between 200 and 500 m/sec resulting in low to moderate shock loading of disc type steel specimens. Longitudinal stress histories of the impacted specimens were captured at the back face of the loaded specimens with the use of manganin gages. A constitutive model was employed to numerically simulate the particle velocity at the impact surface as well the pressure distribution across the specimens as a function of impact duration. An analytical approach utilizing a deformation model was used to link twin volume fraction to blast severity. Post-mortem analysis was carried out on the impacted specimens with the use of optical and scanning microscopy in order to correlate the severity of the impacts with development of twinning within the microstructure. A comparison between the analytically calculated and experimentally measured twin volume fraction was used to optimize the material and deformation models and establish a correlation between impact pressure and deformation response of the steel under examination.

Introduction

Impact loading of steel is a subject that has been studied widely for structural applications and material characterization. It has been established that high strain rate loading of steel will result in a change of both microstructural and mechanical properties which individually affect the residual life of the material. Vast amounts of research has been done in order to assess blast loading and deformation effects, much of it being on steel as it is a primary reinforcing phase of structures. Research in blast analysis, while in general utilizes the finite element technique to provide solutions for the dynamic response of the structures [1], requires implementation of microstructure constitutive models is required to accurately capture changes in mechanical properties during high strain rate loading.

In order to replicate the pressure profile and high strain rate deformation caused by explosive loading and recover large intact specimens, various techniques exist of which Field et al. [2] provide a detailed review. To achieve the highest velocities, above 1km/s, two and three stage gas guns are used. These techniques are typically used for obtaining Hugoniot curves, measuring spall strength, post-impact mechanical testing, and measuring phase change, the latter of which is the concern of the work presented herein.

The phase change of the material is of particular interest in material investigation and has been incorporated into analytical modeling in order to predict deformation response. De Resseguier and Hallouin [3] studied iron disks of different thickness submitted to shock loading by means high-power laser pulses. Post shock studies of the iron microstructure revealed significant twin formation. Using a constitutive twinning model proposed by Johnson and Rohde [4] accurate predictions of twin volume fraction and elastic-plastic response of the material have been made. Johnson and Rohde [4] proposed a mathematical model to describe deformation by slip and twinning based upon the laws of mass and momentum conservation. Plate impact experiments were used to examine shock-loaded iron and analytically predict twin volume fraction in recovered specimens as a function of impact stress.

The objective of this study is to establish the effect of moderate shock loading up to strain rates of 10^5 s^{-1} , on the microstructure deformation mechanisms of low carbon steel. This objective will be achieved by identifying a deformation criterion based on microstructure response to blast loading. This will be examined by subjecting discs of low carbon steel to high velocity impact loading using a light gas gun. Impact specimens will be analyzed

by measurement of microstructural variations and mechanical properties. Attempts will be made to study the deformation pattern in steel using material and deformation models. Results of this analysis will be linked with the experimental work in order to assess the validity of the approach. In this paper, we present the experimental procedure used to impact the steel specimens and experimental observations of microstructure. In addition, numerical methods and analytical modeling of dynamic deformation based on slip and twinning are described, and results are compared with experimental findings.

Material and Experimental Procedure

The as received microstructure of A572 grade 50 low carbon steel is body center cubic structure which consists of primarily α -ferrite phase with colonies of pearlite; Figure 1. Preparation of all specimens was done by mechanical polishing to 1 micron and chemical etching using 5% nital solution for 8 seconds. [5]

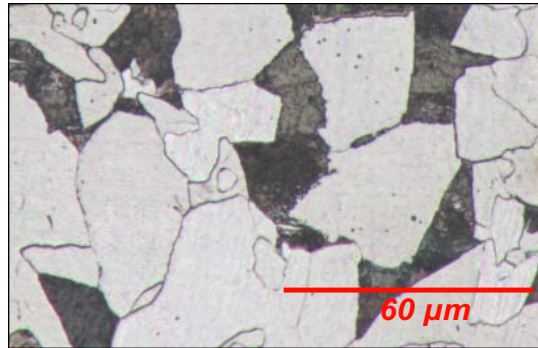


Figure 1. Micrograph of as received A572 grade 50 structural steel.

This material was prepared into round discs by electro discharge machining (EDM) and tested by subjecting it to different impact loads using a single stage light gas gun.

A series of five plate impact experiments have been carried out using a single stage light gas gun. Fixed back conditions were employed in order to minimize energy loss and provide means for recovering post impact specimens. Figure 2 provides an illustration of the experimental gas gun and target set up. The projectile measurements are 31.75mm diameter and 3mm thick, while the target disk and backing plate measurements are 57.15mm diameter and 6mm thick. The target dimensions allowed for tensile specimens to be machined from deformed specimens for post impact mechanical testing.

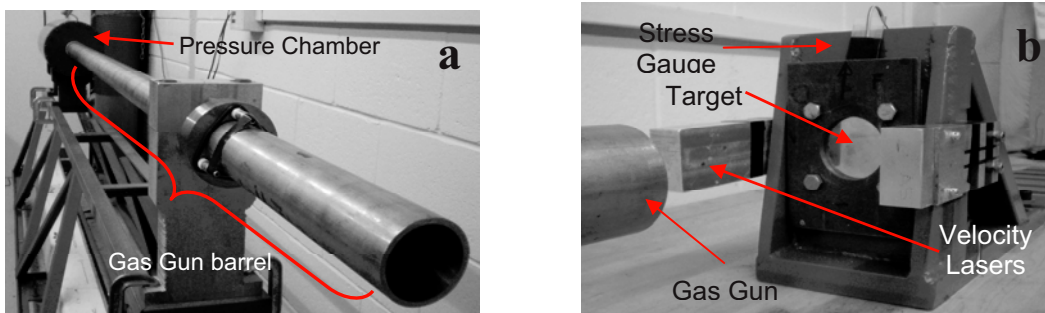


Figure 2. Photograph of a.) the experimental light gas gun and b.) the target and fixed back holder

Projectile velocities ranging from 200 to 500 m/sec were measured using two lasers which were mounted perpendicular to the projectile and in front of the target. Input pressure was used to control projectile velocities and magnitude of impact loads. Longitudinal stress histories were recorded using manganin stress gauges bonded centrally between the back surface of the target disk and a steel backing plate. Figure 3 shows a typical stress vs. time record obtained from the back surface of the target disk during an impact.

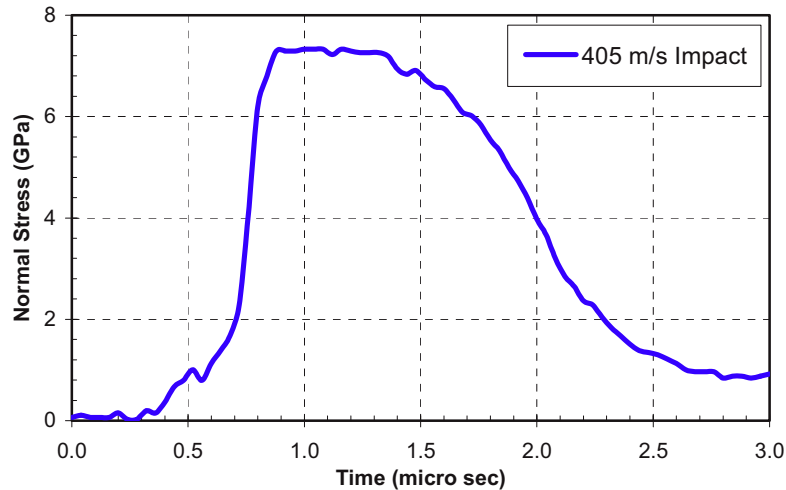


Figure 3. Impact Stress recorded with manganin gauge at the back surface of target disk during a 405 m/s impact

The curve from figure 3 will be compared to numerical results and used as a reference for optimizing simulation parameters. As a reference, particle velocity profiles of the target impact surface will be used as an input into analytical constitutive equations.

Experimental Results

Post impact target specimens revealed plastic deformation in the impacted area and back surface as well as increase in total diameter. The area of impact was discolored suggesting a large and rapid increase in temperature on the front surface during impact; Figure 4.



Figure 4. Impacted steel target specimen and deformed projectile

Specimen surfaces were ground flat using a surface grinder under coolant, and polished and etched. Optical microscopy was conducted on post impact test specimens and the results show the presence of mechanical twins within the α -ferrite grains; see Figure 5. Micrographs of the cross-section just below the impact surface showed a lack of twins, which is evidence that temperature rise was high enough to suppress twin formation in the contact region.

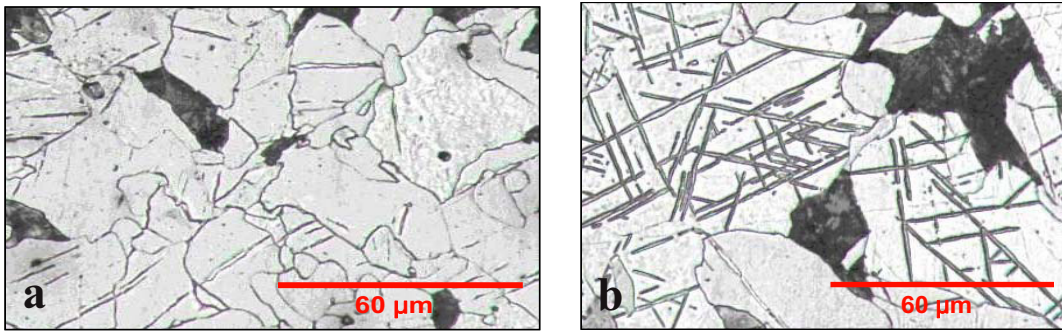


Figure 5. Example of optical micrographs of post impact steel specimens a.) 7 GPa peak stress yielding 3.4% twins, b.) 9 GPa peak stress yielding 4.3% twins.

Results of these optical micrographs show that all of the twins are of lenticular shape, which is indicative of the mechanism by which the twins form. The majority of the grains have parallel twins extending between grain boundaries. However, there are also large amounts of twin-twin interaction in which twins terminate at other twins, or continue through the intersections, which suggests formation on multiple planes. Volume fraction of the twins was calculated using ASTM E562-05, standard test method involving systematic manual point count method. This count provides an average estimation of twin volume fraction which was correlated to impact stress, as illustrated in Figure 6. Figure 6 and Figure 8 show that twin volume fraction and macro hardness are both positively correlated to impact stress.

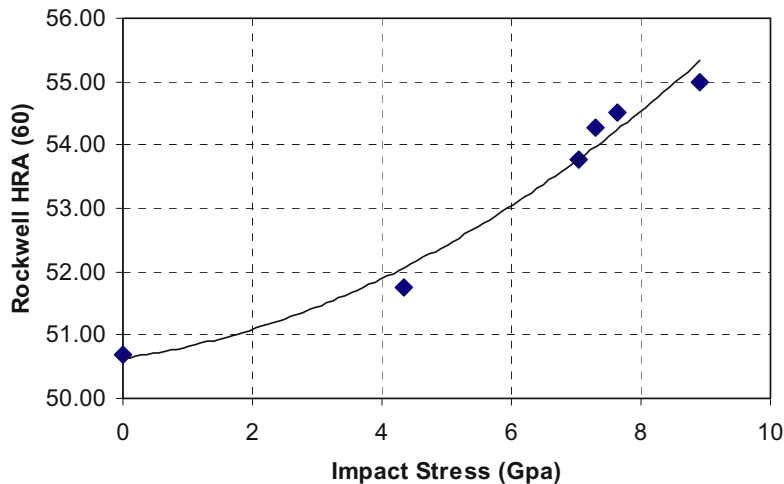


Figure 6. Post-impact macro hardness as a function of impact stress

The increase in hardness, which indicates an increase in yield strength of the material, can be attributed to strain hardening, as described by Maciejewski [5], and to twin-matrix interfaces, which provide additional barriers for further dislocation slip. There may exist a unique relationship between the twinning and hardness properties, however since hardness also increases in the absence of twinning, no attempt has been made from this study to examine the unique relationship between hardness and twinning.

Numerical and Analytical Analysis

Finite element simulation using Abaqus dynamic explicit analysis was used to model plate impacts. Simulation of impact conditions provides knowledge of impact wave parameters as well as a description of the blast related stress distribution within the impacted steel. Inputs parameters for boundary and loading conditions are obtained from experimental procedures. From the simulation, the longitudinal stress distribution is matched with experimental stresses recorded. Once good correlation exists between numerical and experimental outputs, particle velocity history at the impact surface is extracted from numerical results and used as an input for

analytical modeling of twin volume fraction as a function of impact loading. In order to obtain stress histories in accordance with experimental results, parameters for a rate dependent model were required. The built in Johnson-Cook material model [6] was used to express the equivalent Von-Mises tensile flow stress as a function of the equivalent plastic strain, strain rate, and temperature. Values for constants were optimized using a room temperature stress-strain curve of the as received material [5]. Numerical stress history of the target specimen during impact show comparable profiles to experimental impact results. In this profile, three important components which must be captured accurately, pressure rise time, impact duration, and maximum stress, all exhibit good fits with experimental data. Figure 7 shows a numerically generated stress profile during impact at the back surface of the target specimen compared with experimental results.

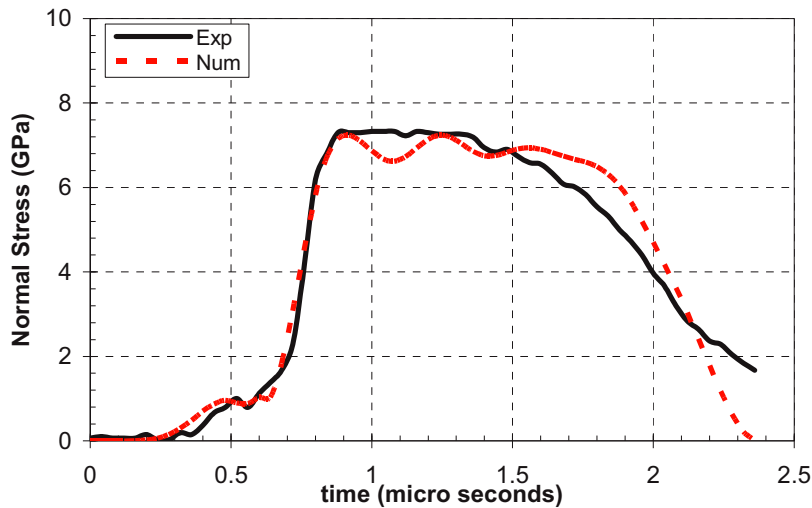


Figure 7. Experimental and numerical stress history at the back of the target specimen.

Cross slip and dislocation coalescence proposed by Sleswyk provides a basis for a mechanistic model governing twin formation and has been confirmed by Mahajan [8]. The model proposed by Johnson and Rohde [4] incorporates slip and twinning mechanisms described [7,8] and accurately calculates twin volume fraction of low carbon b.c.c. steel for the given loading conditions. In order to analytically predict twin volume fractions, a modified form of a model based on the work of Johnson and Rohde [4] was applied here. Lenticular shape of twins suggests formation by progressive shear of the lattice [7] in which slip must be present in order for twin formation to occur [8]. Johnson and Rohde [4] examined shock-loaded iron in order to analytically predict twin volume fraction in recovered specimens. They state that twin formation is based upon proportional shear of the lattice rather than local shuffling of the atoms and twin formation is preceded by corresponding dislocation multiplication. The assumptions and observation from this study are described in the constitutive model in which total plastic strain is composed of both dislocation slip and deformation twinning, and the twin volume fraction and growth rate are functions of corresponding shear stress. The dynamic response and deformation twinning of low carbon steel under impact loading is described by the laws of mass and momentum conservation. Analytical twin volume fractions were calculated using this model for each impact condition using a critical shear stress criterion. An average bulk material value was determined and compared to experimental results; see Figure 8.

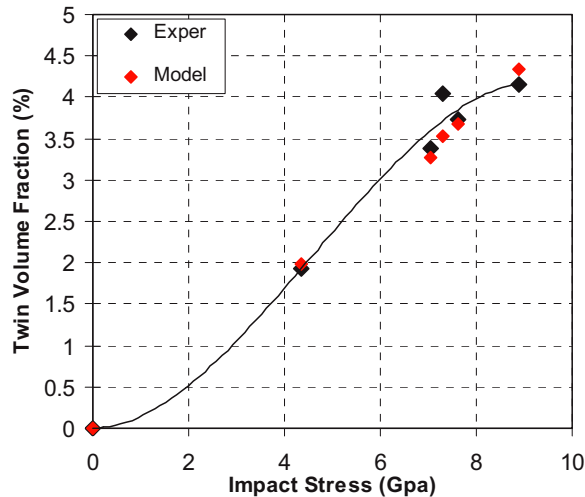


Figure 8. Comparison of experimentally measured and analytically computed twin volume fraction as a function of impact stress.

Analytical model predictions show similar trends to experimental measurements for the given stress range. The linearity of the experimental and calculated data in Figure 8 apparently deviates from this trend at higher stresses as the twins begin to saturate in the material, or other deformation mechanisms begin to play a role. While the relationship between impact stress and twin volume fraction may be satisfied within the given conditions, shear banding and phase transformation have been observed to occur at extremely high pressures [9,10], and the criteria may no longer be valid. Further study of the material at higher stresses and strain rates are needed to develop the relationship further and set limits for its accuracy.

Conclusions

The objective of the study is to present a correlation between high rate impact and microstructure variation of low carbon steel. Five plate impact experiments were carried out and post impact microscopy shows deformation mechanisms occurring during shock loading of low carbon b.c.c. steel. The coupling of numerical simulations and the analytical constitutive model act as a tool for defining impact history and predicting post-impact microstructure. Results of this study can be briefly summarized as follows:

1. Impact experiments indicated that slip and mechanical twinning are two competing deformation mechanisms occurring during high rate loading of b.c.c. low carbon steel.
2. A direct and unique relationship between impact stress and volume fraction of twins has been experimentally established.
3. Microscopic observations of lenticular deformation twins formed on multiple planes within each grain indicate the twinning mechanism. This formation mechanism was used as a basis for selection of an analytical model aiming at predicting twin volume fraction.
4. The analytical model incorporates both slip and twinning mechanisms and accurately calculated twin volume fraction. This model was coupled with a rate dependent model implemented into numerical procedures and was capable of capturing deformation response and twin formation during impacts for the given stress range.

Acknowledgements

This project has been fully funded by the Department of Homeland Security Center of Excellence: Explosives Detection, Mitigation, and Response at the University of Rhode Island.

References

1. Liew. "Survivability of steel frame structures subject to blast and fire." *Journal of Constructional Steel Research*. 64 (2008) 854-866.

2. Field, Walley, Proud. "Review of experimental techniques for high rate deformation and shock studies." *International Journal of Impact Engineering*. 30 (2004) 725-775.
3. De Resseguier, Hallouin. "Stress relaxation and precursor decay in laser shock-loaded iron." *J. Appl. Phys.* 84.4 (1998) 1932-38.
4. Johnson, Rohde. "Dynamic deformation twinning in shock-loaded iron." *J. Appl. Phys.* 42.11 (1971) 4171-82.
5. Maciejewski, Sun, Gregory, Ghonem. "Time-Dependent Deformation of Low Carbon Steel at Elevated Temperature." (Submitted for Publication)
6. Johnson, Cook. "A constitutive model and data for metals subjected to large strains, high strain rates and high temperatures." In: *Proceedings of the Seventh International Symposium on Ballistic*, La Hague, Netherlands. (1983) 541-547.
7. Wasilewski. "Mechanism of bcc twinning: Shear or shuffle?" *Metallurgical Transactions*. 1 (1970) 2641-2643.
8. Mahajan. "Interrelationship between slip and twinning in B.C.C. crystals." *Acta Metallurgica*. 23 (1975) 671-684.
9. Dougherty, Cerreta, Pfeif, Trujillo, Gray. "The impact of peak shock stress on the microstructure and shear behavior of 1018 steel." *Acta Materialia* 55 (2007): 6356-6364.
10. Firrao. "Mechanical twins in 304 stainless steel after small-charge explosions." *Materials Science and Engineering*. A 424 (2006) 23-32.



Deformation characteristics of low carbon steel subjected to dynamic impact loading

W. Visser^a, Y. Sun^a, O. Gregory^b, G. Plume^a, C-E. Rousseau^a, H. Ghonem^{a,*}

^a Department of Mechanical Engineering, University of Rhode Island, Kingston, RI 02881, USA

^b Department of Chemical Engineering, University of Rhode Island, Kingston, RI 02881, USA

ARTICLE INFO

Article history:

Received 26 November 2010
Received in revised form 19 May 2011
Accepted 23 June 2011
Available online 29 June 2011

Keywords:

Low carbon steel
Shock
Impact loading
Twinning
Post-impact

ABSTRACT

The effects of impact loading on changes in microstructure have been studied in low carbon steel. Low to moderate shock loading tests have been carried out on steel specimens using a single stage gas gun with projectile velocities ranging from 200 to 500 m/s. Stress history at the back face of the target specimen and projectile velocity prior to impact were recorded via manganin stress gauges and velocity lasers, respectively. A Johnson–Cook constitutive material model was employed to numerically simulate the material behavior of low carbon steel during impact and obtain the particle velocity at the impact surface as well the pressure distribution across the specimens as a function of impact duration. An analytical approach was used to determine the twin volume fraction as a function of blast loading. The amount of twinning within the α -ferrite phase was measured in post-impact specimens. A comparison between experimental and numerical stress histories, and analytical and experimental twin volume fraction were used to optimize the material and deformation models and establish a correlation between impact pressure and deformation response of the steel under examination. Strain rate controlled tensile tests were carried out on post-impact specimens. Results of these tests are discussed in relation to the effects of impact loading on the yield and ultimate tensile strength as well as the hardening and strain energy characteristics.

© 2011 Elsevier B.V. All rights reserved.

1. Introduction

Impact loading of steel is a subject that has been studied widely for structural applications and material characterization. It has been established that high strain rate loading of steel will result in a change of both microstructural and mechanical properties which individually affect the residual life of the material. Vast amounts of research has been done in order to assess blast loading and deformation effects, much of it being on steel as it is a primary reinforcing phase of structures. Research in blast analysis, while in general utilizes the finite element technique to provide solutions for the dynamic response of the structures [1], requires implementation of microstructure constitutive models required to accurately capture changes in mechanical properties during high strain rate loading.

In order to replicate the pressure profile and high strain rate deformation caused by explosive loading and recover intact specimens suitable for further testing and analysis, various techniques exist of which Field et al. [2] provide a detailed review. Some basic techniques which are of main concern to material characterization are drop weight testing, split Hopkins pressure bar, Taylor

impacts, plate impacts, and explosive loading. While SHPB tests produce elastic–plastic wave propagation, the maximum strain rates achieved are typically in the range of 10^4 s^{-1} . Plate impact tests are often used to replicate explosive loading due to the fact that the strain rates, greater than 10^4 , and planar shock waves achieved clearly simulate that of explosive shock wave loading. During plate impacts at high velocities, a state of one-dimensional strain is produced until lateral release waves from the edge of the projectile and target specimen reach the center of the impact area. To achieve the highest velocities, above 1 km/s, two and three stage gas guns are used. These techniques are typically used for obtaining Hugoniot curves, measuring spall strength, post-impact mechanical testing, and measuring phase change, the latter of which is the concern of the work presented herein.

An important aspect in the post-impact analysis of materials is the phase change of the microstructure, which is generally incorporated into analytical modeling in order to predict deformation response. Recent studies, by Gregory et al. [3], of recovered pipe bomb fragments provided basis for characterization of plain carbon-steel subject to high rate deformation. They observed metallurgical variations of the steel in order to estimate explosive loading severity. It was found that explosive loading resulted in elongation in grains in both the α -ferrite and pearlite phases, intersecting slip bands and cross slip, as well as mechanical twin

* Corresponding author. Tel.: +1 401 874 2909; fax: +1 401 874 2925.
E-mail address: ghonem@egr.uri.edu (H. Ghonem).

formation. Firrao et al. [4] subjected stainless steel to plane shock wave loading by means of spherical plastic explosives with varying charge weights and varying charge-target distances. Changes in microstructure on the impact surface included oxidations, partial melting at grain boundaries, isolated slip bands, and mechanical twins in areas around fragment impact points. Changes through the thickness of the specimen were limited to mechanical twins in discontinuous layers bordering the exposed surface, but never across the entire thickness. Through X-ray analysis it was found that dislocation density remains unchanged, proving that deformation by dislocation slip, and subsequently plastic yielding, was not reached, which is also evident through measurement of thickness variations. Based upon observed twinning and estimated explosive pressures, Firrao et al. [4] were able to calculate critical stress required for twinning, and proved that twin nucleation occurs prior to yielding. De Resseguier and Hallouin [5] studied iron disks of different thickness submitted to shock loading by means high-power laser pulses. Post-shock studies of the iron microstructure revealed significant twin formation. Using a constitutive twinning model proposed by Johnson and Rohde [6] accurate predictions of twin volume fraction and elastic–plastic response of the material have been made [5,7]. They used plate impacts to examine shock-loaded iron and analytically predict twin volume fraction in recovered specimens as a function of impact stress. Atroshenko et al. [8] examined the strengthening properties of materials, including copper, aluminum, titanium, and steel, due to spherical loading by means of explosives, and uniaxial loading using a light gas gun. The strength of the material was measured as a function of distance from the impact using microhardness measurements. In all materials except aluminum, microstructure refinement and increases in hardness occurred. Smida and Bosansky [9] provide experimental and fractographical analysis of ferritic structural steel in order to provide a correlation between the role of deformation twins and mode of fracture. Tensile and Charpy impact tests were carried out and the occurrence of deformation twins on the fracture surface were studied. Murr et al. [10] observed profuse mechanical twinning in Tantalum when subjected to shock wave deformation of magnitudes up to 45 GPa. From post-impact testing, shock hardening was observed which have been attributed to twins as barriers to plastic deformation.

Deformation in BCC materials by means of shock loading is described as being composed of the competing mechanisms of slip and twinning. Murr et al. [10] rationalize that critical twinning stress is highly dependent upon and directly proportional to the stacking-fault energy. Their work examined twin formation during shock loading and twinning effect on the post-shock mechanical response of Tantalum. Murr et al. found that twinning was more predominant at the impact surface than at the back surface. Post-shock testing consisted of quasi-static and dynamic compression tests as well as microhardness measurements. The rationale of slip–twinning transition was explained through experimental observations and a mechanistic model proposed by Armstrong and Worthington. A model was presented to predict the critical threshold stress for twin initiation which is based upon the Swegle–Grady relationship, grain-size and temperature. Meyers et al. [11,12] recognize the fact that twin initiation and growth is closely tied to dislocation motion which is highly strain rate and temperature sensitive. They note that twinning can have two significant effects upon plastic deformation; it increases the work hardening rate by creating more barriers, effectively subdividing the grains, and it contributes to plastic deformation due to twinning shear. Meyers briefly describes the effects of strain rate, temperature, grain size, texture, and stress state effects upon twinning nucleation. The model used is based upon a similar theory for FCC material in Murr's study of Tantalum [10], in which dislocation pile-ups are a key aspect to twin nucleation. Equations for critical shear stress for

twinning are presented for BCC, FCC, and HCP materials, all of which are dependent upon strain rate, temperature, and the Hall–Petch relation for grain size. They describe that the twins per grain is a function of stress which is independent of temperature and strain rate and the amount of twins will increase monotonically with increasing stress. The evident common aspect in all these works is the twin formation in steel during high strain rate loading. A correlation, however, does not exist between blast conditions, i.e. strain rate and stress state, and twin volume fraction, from which a unique criteria defining material integrity can be established. This criterion is the objective of this study. For this purpose, the effect of blast loading up to strain rates of 10^5 s^{-1} , on the microstructure deformation mechanisms of low carbon steel will be examined. Discs of low carbon steel were subjected to high velocity impact loading using a light gas gun. Impact specimens were analyzed by measurement of microstructural variations and mechanical properties. Attempts are made to study the deformation pattern in steel using material and deformation models. Results of this analysis are linked with the experimental work in order to assess the validity of the approach. Prediction of impact loading conditions will be achieved through a relationship between twin volume fraction and impact stress history and linked to post-impact mechanical properties. An experimental procedure was used to impact low carbon steel specimens and experimental observations of microstructure. In addition, numerical methods used and means of obtaining accurate results are described. An analytical model of dynamic deformation based upon slip and twinning is described and results are compared with experimental findings.

2. Material and experimental procedure

The as received microstructure of the low carbon steel, as shown in Fig. 1, consists of primarily α -ferrite phase with colonies of pearlite. The pearlite colonies are made of α ferrite and Fe_3C cementite lamellas; Fig. 1. Average grain size is $50 \mu\text{m}$ with 9% volume fraction of the pearlite phase. Tensile tests of as received material showed yield strength of the material to be 348 MPa at 0.2% offset at room temperature with a Young's modulus of 197 GPa. Preparation of all specimens was done by mechanical polishing to $1 \mu\text{m}$ and chemical etching using 5% nital solution. This material was prepared into round discs by electro discharge machining and tested by subjecting it to different impact loads using a single stage light gas gun. A series of five plate impact experiments have been carried out using a single stage light gas gun; Fig. 2a. Fixed back conditions, Fig. 2b, were employed in order to minimize energy loss and provide means for recovering post-impact specimens; Fig. 2c provides a schematic of the experimental set up. The projectile measurements are 31.75 mm diameter and 3 mm thick, while the target disk and backing plate

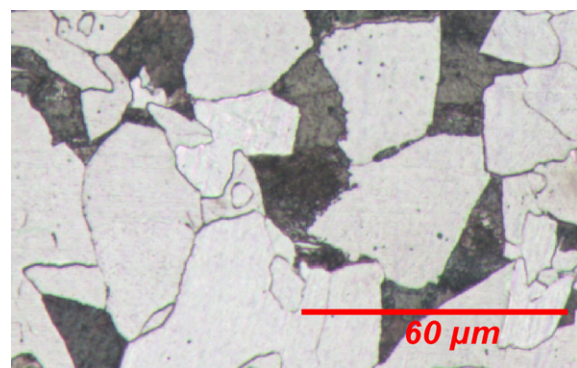


Fig. 1. Optical Micrograph of as received A572 grade 50 structural steel. Lighter grains are α -ferrite, and darker grains are pearlite.

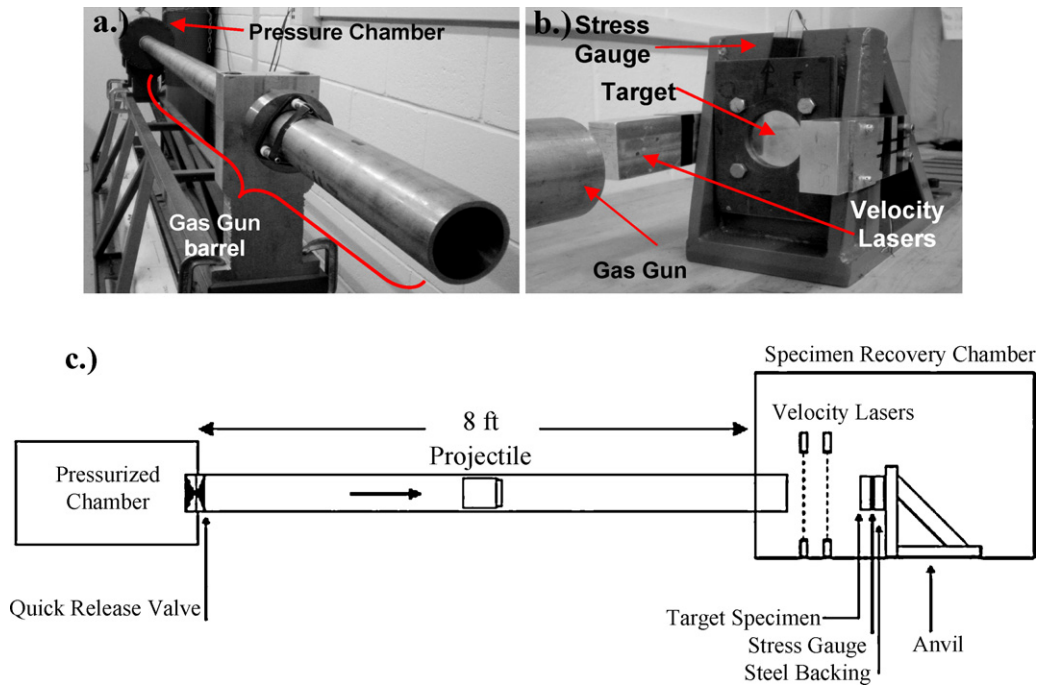


Fig. 2. (a.) Photograph of experimental gas gun. (b.) Fixed back apparatus for plate impact tests. (c.) Schematic of gas gun and target apparatus.

measurements are 57.15 mm diameter and 6 mm thick. The target dimensions allowed for tensile specimens to be machined from deformed specimens for possible mechanical testing.

Projectile velocities ranging from 200 to 500 m/s were measured using two lasers which were mounted perpendicular to the projectile and in front of the target. Input pressure was used to control projectile velocities and magnitude of impact loads. Input pressure of Helium gas was used to control projectile velocities and achievable stress levels. Longitudinal stress histories were recorded using manganin stress gauges bonded centrally between the back surface of the target disk and a steel backing plate.

Typical results of normal stress versus time curves are shown in Fig. 3, for the five different impact velocities. These curves, generated from data recorded from the back surface of the impacted target disk, are characterized by four distinct features; the elastic precursor, the plastic wave, the peak stress level and duration, and the unloading wave. The Hugoniot elastic limit, σ_{HEL} , which is the

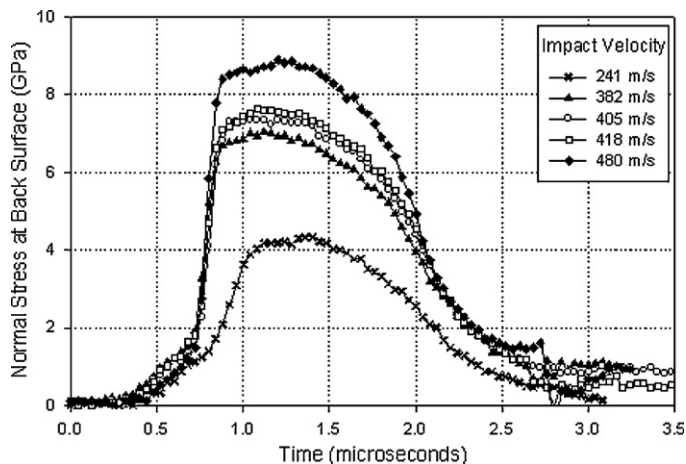


Fig. 3. Impact stress data recorded at the back surface of target disk.

amplitude of the initial elastic wave, is related to the shear stress, τ , through the relation:

$$\sigma_{HEL} = 2\tau \left[\frac{1-\nu}{1-2\nu} \right] \quad (1)$$

where ν is Poisson's ratio. From the impact stress–time histories, the elastic limit for all curves is reached at 1 GPa. A σ_{HEL} of 1 GPa corresponds to a 0.285 GPa maximum resolved shear stress, and for shear stress greater than this, it is suggested that dislocation slip accommodates plastic deformation [6].

The time between impact and that at which the stress gauge at the back surface begins to register the elastic wave can be estimated using the velocity of the elastic precursor. The wave speed of the elastic precursor, $C_{Elastic}$, is described as [13]:

$$C_{Elastic} = \sqrt{\frac{E(1-\nu)}{\rho(1+\nu)(1-2\nu)}} \quad (2)$$

where E , and ρ are the elastic modulus and material density, respectively. Using the calculated elastic wave speed with a 6 mm thick specimen, the elastic wave will reach the back surface in 1.03 μ s. If the projectile and target are of the same material, identical waves will simultaneously propagate in both. The projectile will stay in contact with the specimen until the elastic wave in the projectile reflects off of the free surface and returns to the contact surface. The projectile and target will remain in contact for the time duration, $t_{Contact}$, determined as [13]:

$$t_{Contact} = \frac{2L_p}{C_{Elastic}} \quad (3)$$

where L_p is the projectile thickness. Since the projectile is half the thickness of the target specimen, they will separate in the same time the elastic wave reaches the back of the target, at 1.03 μ s.

Each of the stress–time curves shown in Fig. 3 will be compared to that obtained numerically as will be detailed in a later section, for the same impact condition and will be used as a reference for obtaining particle velocity at the impact surface. Simulated particle velocity of the target impact surface will be used as an input into analytical constitutive equations formulated as the basis of the

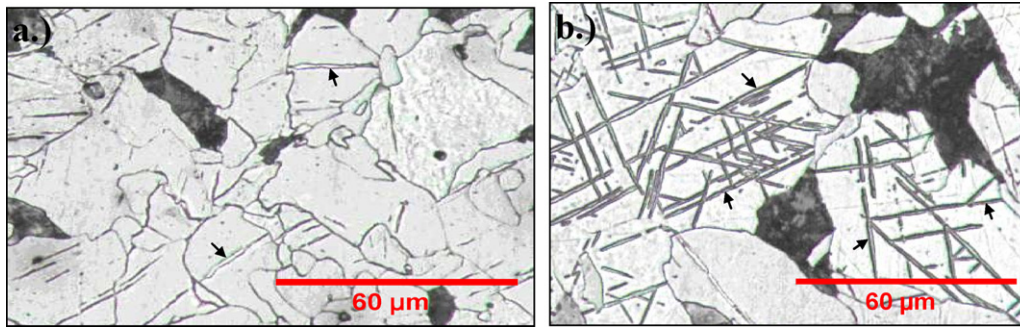


Fig. 4. Example of optical micrographs of post-impact steel specimens: (a.) 7 GPa peak stress yielding 3.4% twins, (b.) 9 GPa peak stress yielding 4.3% twins. Lighter grains are α -ferrite, and darker grains are pearlite; black arrows indicate deformation twins.

Johnson and Rohde, in order to calculate twin volume fraction as a function of local shear stress and time.

3. Experimental results

Post-impact target specimens show that plastic deformation took place in the impacted area and back surface as accompanied with an increase in total diameter of the target disk. The area of impact was discolored suggesting a large and rapid increase in temperature on the front surface during impact. Specimen surfaces were ground flat using a surface grinder under coolant, and polished and etched. Optical microscopy was conducted on post-impact test specimens and the results show the presence of mechanical twins within the α -ferrite grains; see Fig. 4. Micrographs of the cross-section just below the impact surface showed a lack of twins, which suggests that the temperature rise was high enough to suppress twin formation in the contact region.

Results of these optical micrographs show that all of the twins are of lenticular shape, which is indicative of the mechanism by which the twins form. The majority of the grains have parallel twins extending between grain boundaries. However, there are also large amounts of twin–twin interaction in which twins terminate at other twins, or continue through the intersections, which suggests formation on multiple planes [14]. Volume fraction of the twins was calculated using ASTM E562-05, standard test method involving systematic manual point count method [15]. This count provides an average estimation of twin volume fraction which was correlated to impact stress, as shown in Table 1. Fig. 5 shows that macro hardness is also positively correlated to impact stress.

The increase in hardness, which indicates an increase in yield strength of the material, can be attributed to strain hardening [16], and to presence of twin–matrix interfaces, which provide additional barriers for further dislocation slip. There may exist a unique relationship between the twinning and hardness properties, however, since hardness also increases in the absence of twinning, no attempt has been made in this study to examine the unique relationship between hardness and twinning.

4. Numerical and analytical analysis

The analysis of the impact process will be carried out first by calculating the particle velocity for each impact condition. This velocity will then be utilized to calculate the corresponding deformation field and corresponding twin volume fraction.

Table 1
Peak impact stress and measured twin volume fraction.

Impact stress (GPa)	0.00	4.34	7.05	7.63	7.30	8.90
Mean twin V_f (%)	0.00	1.93	3.38	3.73	4.05	4.16

4.1. Particle velocity simulation

Dynamic-explicit finite element simulation was used to model plate impacts. Simulation of impact conditions provides knowledge of impact wave parameters as well as a description of the blast related stress distribution within the impacted steel. Input parameters for boundary and loading conditions are obtained from experimental procedures. From the simulation, the longitudinal stress distribution is matched with experimental stresses recorded. Once good correlation exists, particle velocity at the impact surface is extracted from numerical results and used as an input for analytical modeling of twin volume fraction as a function of impact loading. In order to obtain stress histories in accordance with experimental results, parameters for a rate dependent model were required. For this purpose, the Johnson–Cook (JC) constitutive model [17] was used to express the equivalent Von-Mises tensile flow stress as a function of the equivalent plastic strain, strain rate, and temperature. This stress is expressed as [13,17]:

$$\sigma = \underbrace{(A + B\varepsilon^n)}_{\text{Strain hardening}} \underbrace{\left[1 + C \ln\left(\frac{\dot{\varepsilon}}{\dot{\varepsilon}_0}\right)\right]}_{\text{Strain rate effect}} \underbrace{\left[1 - \left(\frac{T - T_r}{T_m - T_r}\right)^m\right]}_{\text{Temperature dependency}} \quad (4)$$

where σ is the Von-Mises tensile flow stress, which is the applied stress in the loading direction for the uniaxial tensile test case; ε is the equivalent plastic strain, which equals the strain in the loading direction for the uniaxial tensile test case; A , B and n are material constants to characterize the strain hardening behavior of the material; C is the material constant to describe the strain rate effect; m is the material constant to describe the temperature dependency. Values for material constants, Table 2, were optimized

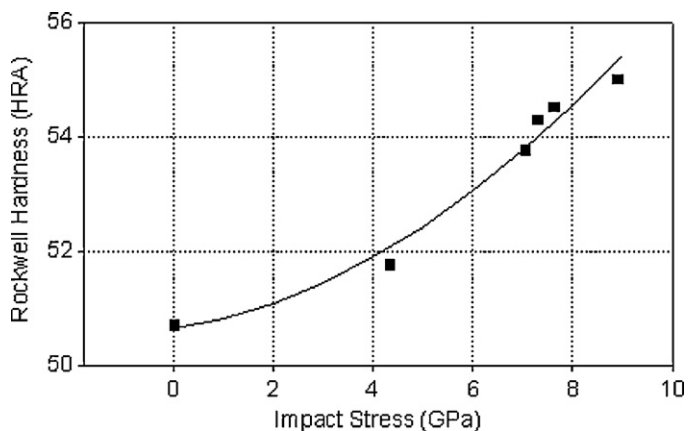


Fig. 5. Post-impact macro hardness (measured in Rockwell A scale with a major load of 60 kg) as a function of impact stress.

Table 2
Material properties and JC model constants for use in finite element simulation.

Young's modulus	Poisson's ratio	Density	Inelastic heat fraction	Specific heat
200 GPa	0.3	7850 kg/m ³	0.864	0.465 kJ/(kg K)
<i>A</i>	<i>B</i>	<i>C</i>	<i>n</i>	<i>m</i>
348	900	0.032	0.434	1

using a room temperature stress–strain curve of the as received material obtained from the work of Maciejewski et al. [16]; see Fig. 6.

Once the parameters for Eq. (4) are optimized, simulation of the plate impact is preceded. To obtain comparable σ_{HEL} during simulation, the constant *A* is adjusted from the static to the dynamic yield strength of the material. In this simulation, symmetry of the impacted test specimen permits simulation of only one quarter of the specimen, as illustrated in Fig. 7a; however, model boundary and loading conditions replicate that of the actual experiment, as illustrated in Fig. 7b. Step time period was 3 μs and included adiabatic heating effects. The model was symmetrically bounded on edges to prevent rotation and translation on the cross-sectional areas. The displacement and rotation of the surface of the backing plate was fixed in the axial direction corresponding to experimental setup. The temperature of the parts and the velocity of the projectile were defined as a predefined field. The mesh is standard hex type element CD38R with 12,416 and 1,848 elements in the target and flyer plate, respectively, and is approximately 1 mm \times 1 mm on the surface and refined to 0.375 mm in the axial direction.

Numerical stress history of the target specimen during impact shows comparable profiles to experimental impact results. In this profile, three important components which must be captured accu-

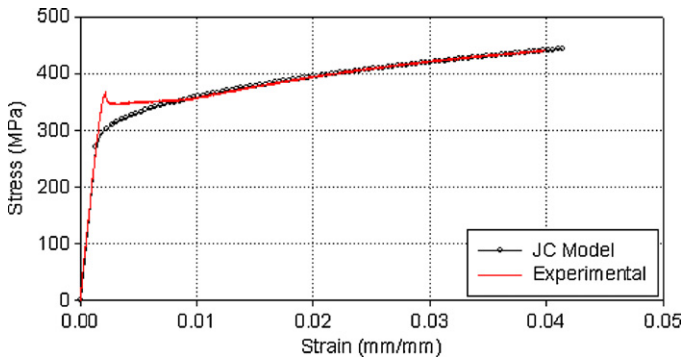


Fig. 6. Stress–strain curve of as received material plotted with JC model output. The curve was obtained at room temperature with a strain rate of 50^{-6} s^{-1} .

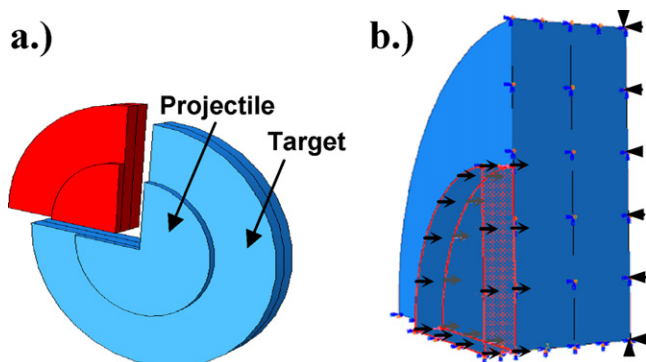


Fig. 7. (a.) Quarter plate model of axis-symmetrical target disk, and (b.) predefined velocity field imposed on projectile and fixed back boundary conditions on target.

rately, pressure rise time, impact duration, and maximum stress, all exhibit good fit with experimental data. Fig. 8 shows numerically generated stress profiles during impact at the back surface of the target specimen compared with experimental results.

Results show good correlation between rise time, peak stress, and σ_{HEL} amplitude. Linear and quadratic bulk viscosity parameters in the dynamic explicit step were adjusted in order to reduce noise in the numerical solution. Furthermore, the linear and quadratic bulk viscosity parameters damp high frequency ringing and smear the shock front across several elements to prevent collapse under high velocity gradients. Once good agreement between numerical and experimental stress–time curves is achieved, the simulated maximum particle velocity at the front surface of the specimen can be used as an input for calculation of twin volume fraction. An approach to carry out these calculations is described in the following section.

4.2. Twin volume fraction calculation

The twin region can be simply described as an area of stacking faults enclosed by partial dislocations. Two ways in which this can occur are discussed by Wasilewski [18]. Wasilewski suggests that twins can form by progressive shear of the parent lattice or by a close atomic shuffle within the lattice, both of which will end in the same arrangement within the twinning planes; Fig. 9. Twinning by progressive shear of the parent lattice will produce a shear offset, of which plastic deformation results, Fig. 9a, while a local rearrangement or shuffle will produce no shear offset, Fig. 9b. It is assumed that formation of the twin by homogeneous shear will produce a shear offset equal to kh , where k is the strength of the simple shear, also known as the *twinning shear*, and h is the average thickness of the twin lamella. For bcc crystals the twinning is most readily formed on the $\{112\}$ planes in the (111) direction which has a twinning shear equal to $1/\sqrt{2}$ [6]. The two modes can be distinguished by observation of the shape of the twins formed. Twins by shear will be lenticular in shape while those created by shuffle will be prismatic [18]. Based upon the characteristic lenticular shape of the twins formed in this study, they are assumed to be produced by progressive shear of the parent lattice, as in opposition to the theory of atomic shuffle.

From the works of Wasilewski [18] and Johnson and Rohde [6], it is inherent that twins form by local rearrangement of atoms resulting in a shear offset, as opposed to local shuffling. In order to analytically predict twin volume fraction, these two points are considered and a modified form of a deformation model based on the work of Johnson and Rohde [6] was therefore applied here. This deformation model incorporates slip and twinning mechanisms previously described [18–20] and will be used to calculate twin volume fraction in the material for the given loading conditions. The assumptions and observation from these previous studies are described in the constitutive model in which total plastic strain is composed of both dislocation slip and deformation twinning, and the twin volume fraction and growth rate are functions of corresponding shear stress. The dynamic response and deformation twinning of low carbon steel under impact loading is described by

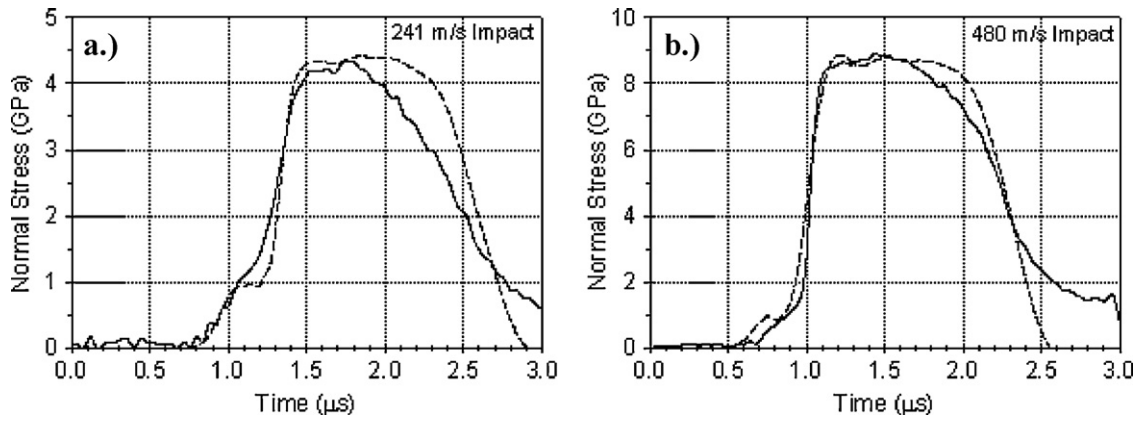


Fig. 8. Experimental (solid line) and numerical (dashed line) stress history data matching for two impact cases. Graph legends pertain to projectile velocity.

the laws of mass and momentum conservation, which are written as:

$$\frac{\rho_0}{\rho^2} \frac{\partial \rho}{\partial t} + \frac{\partial u}{\partial X} = 0 \tag{5}$$

$$\rho_0 \frac{\partial u}{\partial t} + \frac{\partial \sigma}{\partial X} = 0 \tag{6}$$

where ρ_0 is initial density, ρ is an evolved density, and u is particle velocity during impact at time t at a distance of X from the impact surface. The stress, σ , component can be defined by a contact pressure P , and shear stress τ , and is expressed as:

$$\sigma = P + \frac{4}{3} \tau \tag{7}$$

where

$$P = \rho(C + Su)u \tag{8}$$

and

$$\dot{\tau} = \mu(\dot{\epsilon}_t - 2\dot{\gamma}) \tag{9}$$

where μ is shear modulus, C and S are wave speed constants, and ϵ_t is total strain in the wave direction and is given by:

$$\epsilon_t = 1 - \frac{\rho_0}{\rho} \tag{10}$$

γ is the plastic shear strain on the plane of maximum shear stress described as the summation of slip and twinning strains:

$$\gamma = \gamma_s + \gamma_{tw} \tag{11}$$

Plastic strain due to twinning, and that due to slip are expressed as:

$$\gamma_{tw} = k(\alpha - \alpha_0) \tag{12}$$

$$\gamma_s = \frac{1}{2} \epsilon_t - 2k\alpha - \alpha_0 - \frac{\tau_s}{\mu} \tag{13}$$

respectively, where k is twinning shear, α is the volume fraction of twins, α_0 is initial twin volume fraction, and τ_s is the shear stress required for slip. Volume fraction of twinned material is given by:

$$\alpha = \left(\alpha_0^{1/m} + \frac{1}{t_c} \int_0^t v(\tau) dt \right)^m \tag{14}$$

where t_c is characteristic time, which is a constant controlling the rate of twin density, and $m=3$ is for growth of twins both through the thickness and radial directions. The dimensionless growth rate of twins, $v(\tau)$, is expressed as:

$$v(\tau) = \frac{\tau}{\tau_T} - 1 \quad \tau \geq \tau_T \tag{15}$$

where τ_T is shear stress required for twinning. This set of equations provides a method of calculating twin volume fraction as a function of shear stress. The results of this model in terms of average twin volume fraction versus impact stress are compared with experimental results, and are shown in Fig. 10.

Analytical model predictions show similar trends to experimental measurements for the given stress range. The linearity of the experimental and calculated data in Fig. 10 apparently deviates

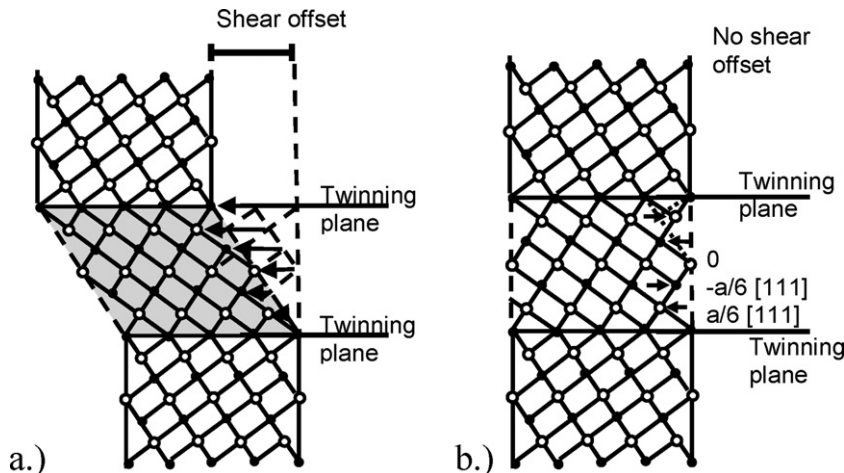


Fig. 9. (a.) Twin formation by progressive shear of the parent lattice, and (b.) twin formed by successive alternating “shuffle” of atoms by sequence $+a/6[1 \bar{1} 1]$, $-a/6[1 \bar{1} 1]$, 0 [18].

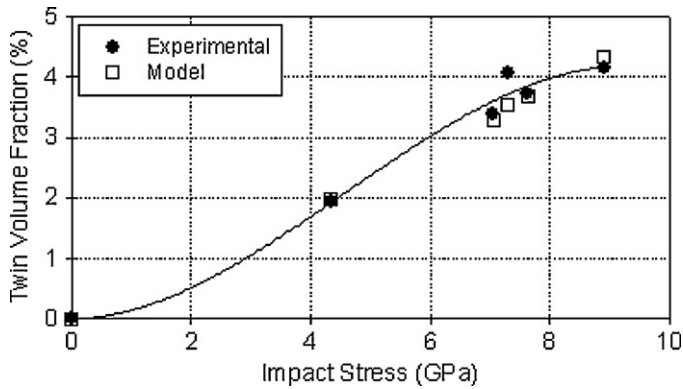


Fig. 10. Comparison of experimentally measured and analytically computed twin volume fraction within α -ferrite grains as a function of impact stress.

from this trend at higher stresses as the twin volume fraction seems to saturate in the material, or other deformation mechanisms begin to dominate. While the relationship between impact stress and twin volume fraction may be satisfied within the given conditions, shear banding and phase transformation have been observed to occur at extremely high pressures [4,21], and the criteria may no longer be valid. Further study of the material at higher stresses and strain rates are underway by the authors in order to extend the deformation criterion and set limits for its applicability.

5. Post-impact residual strength

The influence of twin volume fraction on the residual strength of the material is examined through strain rate controlled monotonic tensile tests and has been compared to the response of the as-received condition. For this purpose, post-impact steel discs were ground and polished flat to a nominal thickness of 3 mm and cut into dog-bone specimens. Geometry and dimensions of the specimen as being cut from the impacted disc are illustrated in Fig. 11. Testing was carried out at room temperature using a servo hydraulic mechanical test system and strain values were recorded using a knife edge extensometer mounted in the gauge section of the test specimen. Testing of as-received material was carried out at two strain rates; $10^{-5}/s$ and $20^{-5}/s$. Results show no strain rate dependency at this rate and temperature. All post-impact specimens were tested at $20^{-5}/s$.

It was observed that as-received specimens began necking at 20% strain, while the post-impact specimens began necking in the range of 10–20%, depending on the impact stress history. Engineer-

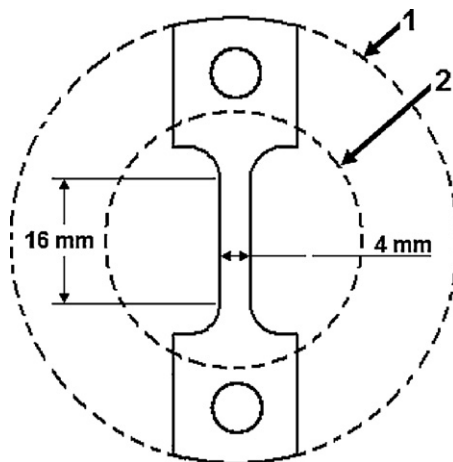


Fig. 11. Tensile specimen (3 mm thick) cut from impact region 2, of target disk 1.

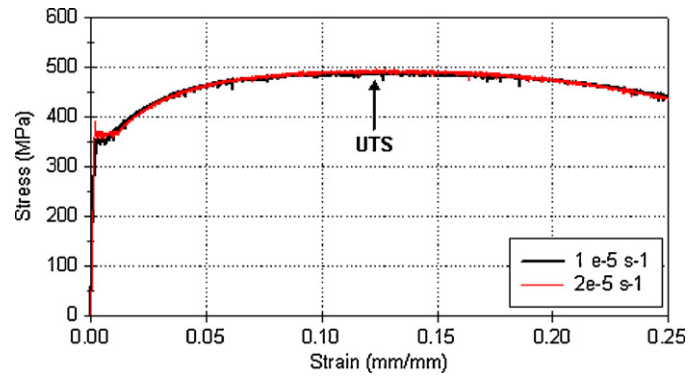


Fig. 12. Stress–strain curves of as-received material tested at strain rates of $10^{-5}/s$ and $20^{-5}/s$.

ing stress–strain curves for the as-received material are presented in Fig. 12. These curves show clear upper and lower yield points, Lüders extension [22] and serrated plastic flow resembling characteristics of Portevin–Le Châtlier effects [23]. Despite the serrated characteristics, the amplitude of serration is minimal in comparison to the magnitude of the general stress level, and is considered insignificant in the overall analysis of the curves. Engineering stress–strain curves of the post-impact tensile specimens, categorized by impact velocity and volume fraction of twins, are presented in Fig. 13.

Post-impact mechanical response of the material showed an increase in yield strength and slight increase in the ultimate strength, and a decrease in the work hardening. A comparison between yield and UTS for different twin volume fractions is shown in Fig. 14.

This figure shows that as twin volume fraction increases, the yield stress approaches the ultimate strength of the material. The convergence of these curves indicates that the plastic hardening characteristics are becoming less prominent. Figs. 14 and 15 suggest that an increase in twin volume fraction results in a decrease in the ability of the material to store defects during post-impact plastic deformation, which is represented by the loss in work hardening [21] and in the loss of available strain energy up to UTS. Furthermore, quantitative and qualitative interpretation of mechanisms governing elastic–plastic response and instability of the material can be made by comparing the as-received and post-impact stress–strain characteristics.

The as-received and the post-impact stress–strain curves both exhibit serrated flow characteristics which have been observed and reported in low carbon and stainless steels [22,24]. Post-impact specimens lack an upper and lower yield point and are characterized by presence of serrations. These serrations can occur in the event of an increase in dislocation density or velocity or both [25]. This increase can be attributed to dislocations within deformation bands locking and unlocking and can be distinguished by three different profiles; type-A, type-B, and type-C [25,26], as illustrated in Fig. 16. Type-A serrations are characterized by periodically spaced yield points which increase in size and spacing with further straining. This process is controlled by the formation and propagation of deformation bands along the gauge section [26]. Increases in stress are due to large solute atmospheres which prevent unpinning of dislocations, while the creation of new dislocations suddenly decreases the stress. Each successive deformation band requires higher stress to activate. Type-B serrations are characterized by quickly fluctuating peaks and valleys lying along the general level of the stress–strain curve. In this case, in contrast to type-A, the serrations are the result of the propagation of deformation bands rather than formation of new bands. In order to maintain the applied strain rate, an increase in dislocation density,

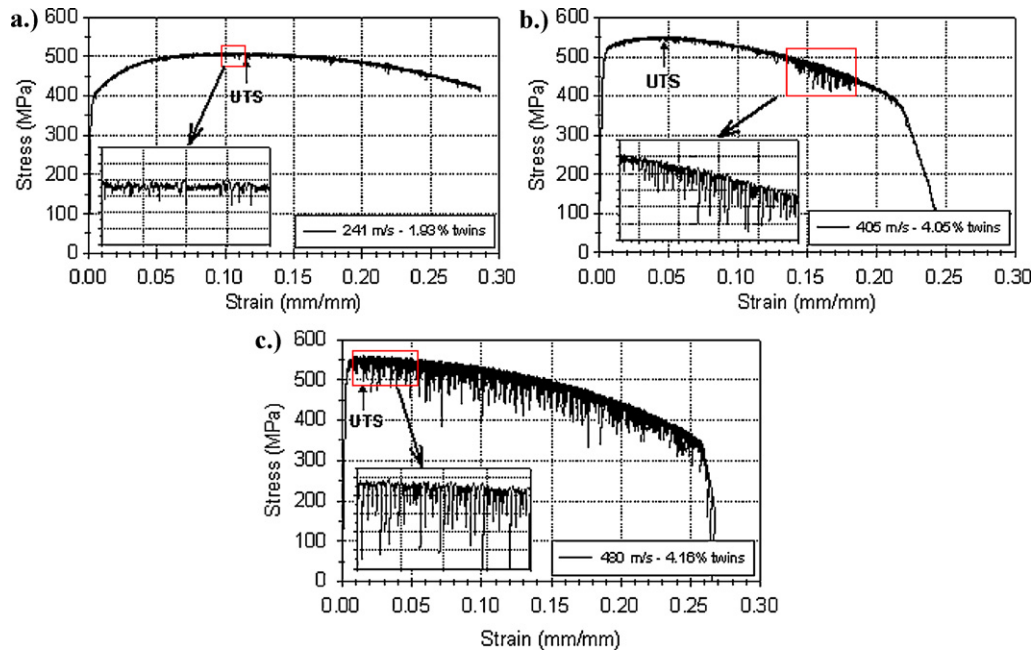


Fig. 13. Stress–strain curves of post-impact steel specimens. Graph legends pertain to projectile velocities at which the steel was impacted and resultant twin volume fraction. Inset graph shows detailed view of serration characteristics.

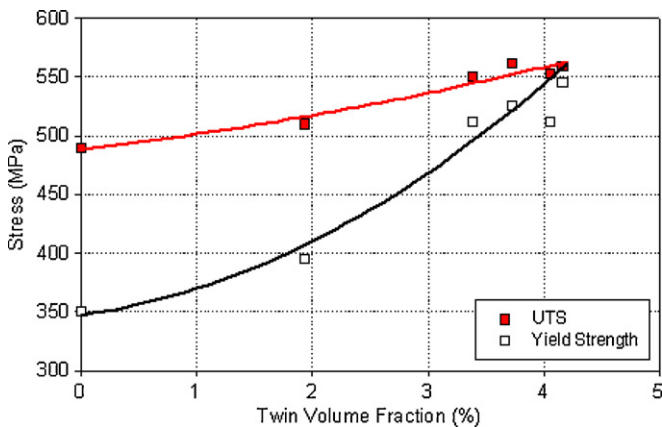


Fig. 14. Ultimate tensile strength and yield stress of post-impact tensile specimens as a function of twin volume fraction.

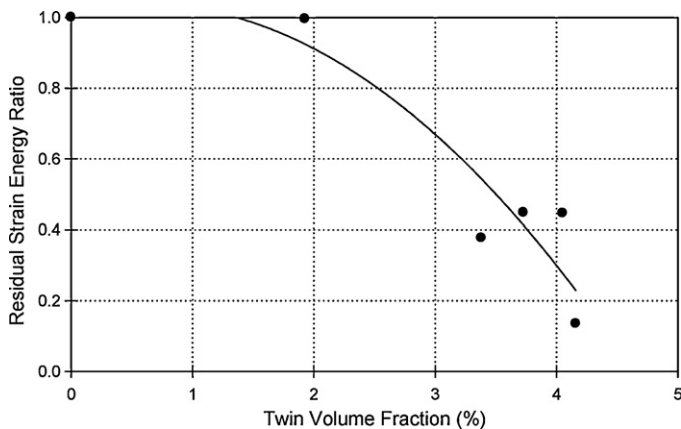
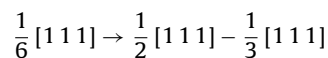


Fig. 15. Residual strain energy ratio versus twin volume fraction. The ratio is in reference to the as-received condition with no twins. Strain energy is measured as area under the curve up to strain at UTS.

and in turn, a decrease in average dislocation velocity results in segregation of solute atoms. The slow moving dislocations become locked rapidly until the stress increases and breaks the dislocation free again, thus allowing the band to propagate. This process continues within the deformation band until it has run through the entire gauge section or has encountered another band [25]. Type-C serrations are characterized by distinct yield drops occurring below the general level of the stress–strain curve. This process is controlled by unlocking of pinned dislocations. Inhomogeneous deformation due to stress concentrations created at barriers, such as grain or twin boundaries, result in localized regions of a higher strain rate. This creates additional drag on the atmosphere of dislocations and in turn, frees dislocations and reduces the stress. The sudden availability of mobility decreases the average dislocation velocity in the deformation band and sets up a condition for solute atoms to relock the dislocations and repetition of the process [25].

The type-C load drops, as well as the general softening behavior characterizing the post-impact stress–strain curves can be attributed to Sleswyk's emissary dislocation mechanism [28]. As Fig. 4b shows, several of the twins, while lenticular shaped, have blunted ends. This is evidence that the twinning shear is accommodated by slip in the matrix [24]. The incoherent twin boundary can be schematically visualized in Fig. 17. During tensile testing, slip in the matrix can emanate from available dislocations which make up the incoherent twin boundary; Fig. 17(a). This dislocation boundary supports a high energy configuration surrounding the twin. As further straining continues, the matrix accommodates plastic deformation by slip of these dislocations upon dissociation of every third dislocation:



as shown in Fig. 17(b). A $\frac{1}{2} [111]$ total dislocation glides away from the twin, leaving behind a $\frac{1}{3} [111]$ complementary dislocation, and drastically lowers the configuration energy. Thus, as further plastic deformation continues, the energy is reduced locally allowing for dislocation pile-ups to break through the twin boundary, as can be seen in the stress reduction of Fig. 13c. If the matrix is

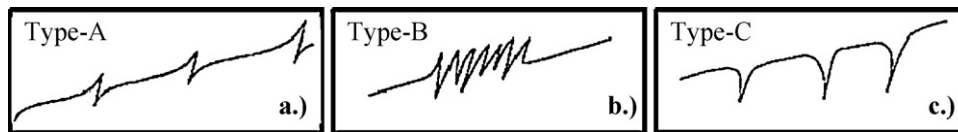


Fig. 16. Typical segments of a stress–strain profile with (a.) type-A, (b.) type-B, and (c.) type-C serrations.

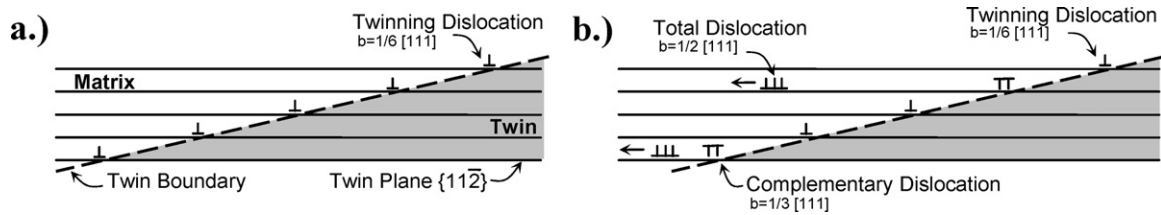


Fig. 17. (a.) Incoherent twin boundary composed of twinning dislocations on $\{112\}$ planes, and (b.) dissociation of twinning dislocation as the matrix accommodates slip [24].

not able to accommodate the shear, then a crack may develop in the twin boundary region. The cracking can be seen in Fig. 18, as they are formed both along the ferrite–pearlite interface, and within the ferrite grains [27], both which occur parallel to the twinning direction. This suggests that the presence of twins in the microstructure influences the not only the elastic–plastic response, but also the characteristics of the failure mechanism.

The as-received tensile curves show type-B serrations occurring from the onset of yield through the entire plastic stress–strain curve. Post-impact specimens with less than 4% twins also exhibit type-B serrated flow with a random minority of type-C load drops, as shown in detail in the inset of Fig. 13a. Fig. 13b shows, as the

volume fraction of twins increases to 4%, the stress–strain curve transitions from type-B to type-C serrations upon further straining [25]. A detailed view of the type-B to type-C transition is shown in the inset of Fig. 13b. Although this transition is after the UTS, it still acts as an indication that twin interactions are becoming a dominant mechanism for locking mobile dislocations. As the volume fraction of twins increases further, as shown in Fig. 13c, the majority of the serrations are of type-C.

Since type-C serrations occur from unlocking of pinned dislocations, the transition from B to C could suggest that the material has reached a point where all stored dislocations are locked up due to the presence of twinned regions [21]. During post-impact straining, the networks of locked dislocations between twinned regions break free, causing successive load drops. This change in stress–strain characteristics suggests that the material has transitioned to a point of instability when 4% or more twins exist in the microstructure.

6. Conclusions

The objective of the study is to present a correlation between high rate impact and microstructure variation of low carbon steel. Five plate impact experiments were carried out and post-impact microscopy shows deformation mechanisms occurring during shock loading of low carbon b.c.c. steel. The coupling of numerical simulations and the analytical constitutive model acts as a tool for defining impact history and predicting post-impact microstructure. Results of this study can be briefly summarized as follows:

1. A direct and unique relationship between impact stress and volume fraction of twins has been experimentally established.
2. Microscopic observation of impact specimens indicate that slip and mechanical twinning are two competing deformation mechanisms occurring during high rate loading of low carbon steel. The lenticular shape of the twins indicates that the twin formation mechanism is by progressive shear of the parent lattice. As impact stress increases, another twinning plane becomes active, and results in large amounts of intergranular twin–twin interactions.
3. Based on microscopic observations, an analytical twinning model aiming at predicting twin volume fraction incorporating both slip and twinning mechanisms has been applied and shown to accurately calculate twin volume fraction. This model was coupled with a rate dependent model implemented into numerical procedures and was capable of capturing deformation response and twin formation during impacts for the given stress range.

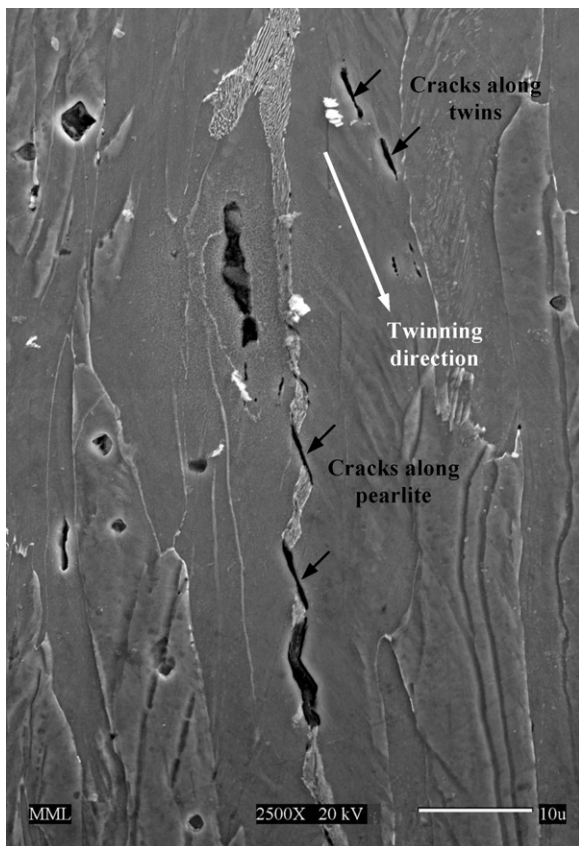


Fig. 18. SEM micrograph of necked region in post-impact tensile specimen. Cracking occurred along the ferrite–pearlite and twinning interfaces during post-impact tensile testing. All of the cracks within this region are oriented in the twinning direction, suggesting that twins play a role during fracture.

4. Quantitative analysis of the post-impact stress–strain curves clearly shows an increase in both yield and ultimate strength, which indicates an increase in stored dislocations in the microstructure as a result of impact loading. However, while the yield and UTS both benefit from shock loading, the available strain energy is drastically reduced; up to 87%. If this trend is extrapolated further, it will show that the yield and ultimate tensile strength converge, thus eliminating available energy.
5. It is apparent that as the shock loading is increased, new twinning planes are activated. Qualitative analysis provides insight into the dislocation–twinning interaction during plastic deformation. Low impacted specimens reveal small fluctuations in stress–strain response representing that of type-B serrations. At higher impact levels, the presence of multiple twinning planes and twin–twin interactions results in the transition of type-B serrations to type-C load drops during plastic deformation. This suggests that twin–twin interactions play a significant role in controlling plastic deformation, which is responsible for instability within the microstructure.
6. The twins play an important role in the direction of cracking during failure. They provide new interfaces at which cracks may initiate and propagate, and also control the direction of crack propagation.

Acknowledgment

This project has been funded by the Department of Homeland Security Center of Excellence: Explosives Detection, Mitigation, and Response at the University of Rhode Island.

References

- [1] J.Y. Richard Liew, *Journal of Constructional Steel Research* 64 (2008) 854–866.
- [2] J.E. Field, S.M. Walley, W.G. Proud, H.T. Goldrein, C.R. Siviour, *International Journal of Impact Engineering* 30 (2004) 725–775.
- [3] O. Gregory, J. Oxley, J. Smith, M. Platek, H. Ghonem, E. Bernier, M. Downey, C. Cumminskey, *Materials Characterization* 61 (3) (2010) 347–354.
- [4] D. Firrao, P. Matteis, G. Scavino, G. Ubertaini, M.G. Ienco, G. Pellati, P. Piccardo, M.R. Pinasco, E. Stagno, R. Montanari, M.E. Tata, G. Brandimarte, S. Petralia, *Materials Science and Engineering A* 424 (2006) 23–32.
- [5] T. De Resseguier, M. Hallouin, *Journal of Applied Physics* 84 (4) (1998) 1932–1938.
- [6] J.N. Johnson, R.W. Rohde, *Journal of Applied Physics* 42 (11) (1971) 4171–4182.
- [7] J.W. Taylor, *Journal of Applied Physics* 36 (10) (1965) 3146–3150.
- [8] S.A. Atroschenko, N.S. Naumova, S.A. Novikov, *International Journal of Impact Engineering* 33 (2006) 62–67.
- [9] T. Smida, J. Božanský, *Materials Science and Engineering A* 287 (2000) 107–115.
- [10] L.E. Murr, M.A. Meyers, *Acta Materialia* 45 (1) (1997) 157–175.
- [11] M.A. Meyers, O. Vöhringer, V.A. Lubarda, *Acta Materialia* 49 (2001) 4025–4039.
- [12] M.A. Meyers, D.J. Benson, O. Vöhringer, B.K. Kad, Q. Xue, H.-H. Fu, *Materials Science and Engineering A* 322 (2002) 194–216.
- [13] V. Panov, Ph.D. Thesis, Cranfield University, 2005.
- [14] S. Mahajan, *Metallurgical Transactions A* 12A (1981) 379–386.
- [15] L. Jiang, J. Jonas, R. Mishra, A. Luo, A. Sachdev, S. Godet, *Acta Materialia* 55 (2007) 3899–3910.
- [16] K. Maciejewski, Y. Sun, O. Gregory, H. Ghonem, *International Journal of Steel and Iron Research* (2011), in press.
- [17] G.R. Johnson, W.H. Cook, *Proceedings of the Seventh International Symposium on Ballistic*, La Hague, Netherlands, 1983, pp. 541–547.
- [18] R.J. Wasilewski, *Metallurgical Transactions* 1 (1970) 2641–2643.
- [19] J.W. Christian, S. Mahajan, *Progress in Materials Science* 39 (1995) 1–157.
- [20] S. Mahajan, *Acta Metallurgica* 23 (1975) 671–684.
- [21] L.M. Dougherty, E.K. Cerreta, E.A. Pfeif, C. Trujillo, G.T. Gray, *Acta Materialia* 55 (2007) 6356–6364.
- [22] E. Pink, S. Kumar, *Materials Science and Engineering A* 201 (1995) 58–64.
- [23] K. Renard, S. Ryelandt, P.J. Jacques, *Materials Science and Engineering A* 527 (2010) 2969–2977.
- [24] Reed-Hill, E. Robert, *Physical Metallurgy Principles*, 2nd ed., Nostran, New York, 1973, pp. 611–660.
- [25] D. Fahr, *Analysis of stress–strain behavior of type 316 stainless steel*, ORNL/TM-4292, 1973, Oak Ridge National Laboratory Report.
- [26] P. Rodriguez, *Bulletin of Material Science* 6 (4) (1984) 653–663.
- [27] N. Narasaiah, K.K. Ray, *Materials Science and Engineering A* 392 (2005) 269–277.
- [28] A.W. Sleeswyk, *Acta Metallurgica* 10 (1962) 803–812.

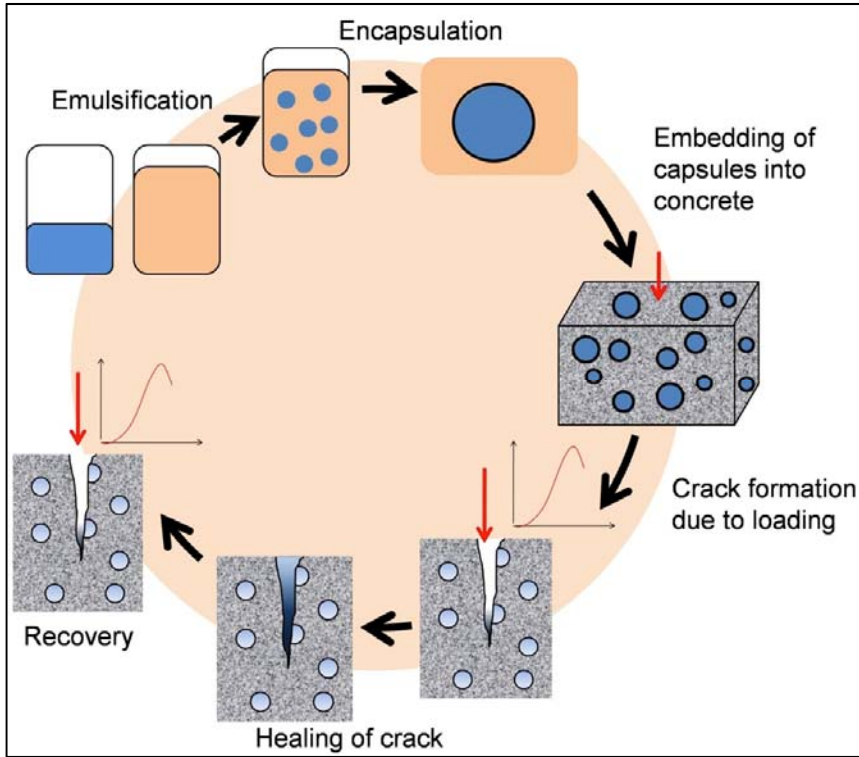


Figure 2. Overall concept used in this study.

3. Accomplishments:

- (i) Samples with capsules located only in regions where concrete experiences tension recover flexural strength more (58% versus 25%) after initial damage than in samples where capsules are distributed throughout.

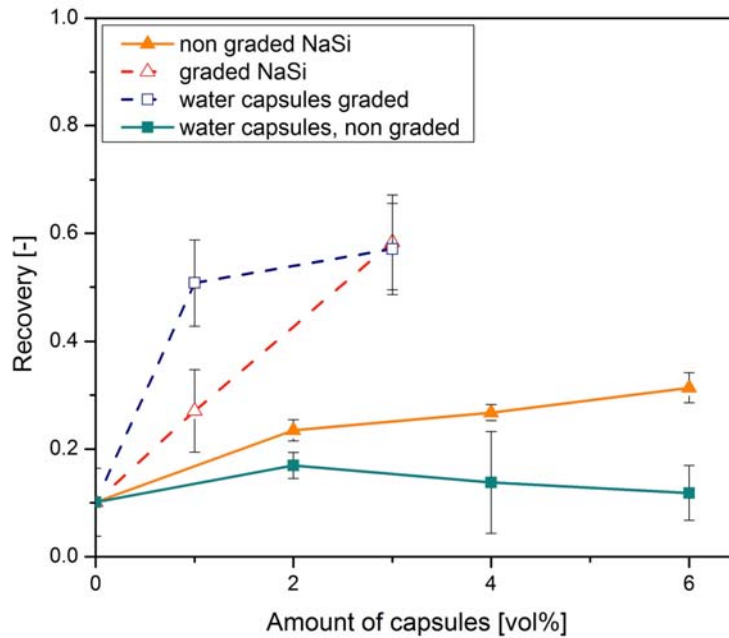


Figure 3. Flexural strength recovery after taking sample to point of incipient failure, then waiting 7 days after which the same sample is retested.

- (ii) Water containing capsules appear to be as efficient as those containing sodium silicate solution
- (iii) Capsules do not break during mixing, but only upon crack initiation.

These experiments are detailed in the attached MS thesis by Svenja Reinke.

(iv) Currently fabricating capsules that are loaded with magnetic particles and calcium nitrite, a strong anti-corrosion agent. These particles will migrate to rebars upon application of an axially directed current to the rebars. This is the MS thesis topic for Lennart Kleinfeldt.

4. Students Supported: Svenja Reinke, Lennart Kleinfeldt

5. Transition Partners: CEMEX – Brugg, Switzerland

6. Publications:

- (i) Self-healing Concrete, M. Pelletier, T. Bhattacharya, A. Bose, submitted to Journal of Concrete Research, in review (2013).
- (ii) Optimization of Autonomous Healing Properties of Concrete Using Microcapsules with Healing Agents, S. Reinke, L. Lozeau, A. Shukla, R. Brown, A. Bose, Journal of Concrete Research, to be submitted (2013)

7. Presentations

- (i) Self-healing Concrete, S. Reinke, T. Bhattacharya, A. Shukla, R. Brown, A. Bose, DHS Center Annual Review, Kingston, April 2012.

POLYUREA/POLYURETHANE MICROCAPSULES BASED
SELF HEALING CONCRETE

BY

SVENJA KRISTIN REINKE

A DISSERTATION SUBMITTED IN PARTIAL FULFILLMENT OF THE
REQUIREMENTS FOR THE DEGREE OF
MASTER OF SCIENCE
IN
CHEMICAL ENGINEERING

UNIVERSITY OF RHODE ISLAND

2012

Library Rights Statement

In presenting this thesis in partial fulfillment of the requirements for an advanced degree at the University of Rhode Island, I agree that the Library shall make it freely available for inspection. I further agree that permission for copying, as provided for by the Copyright Law of the United States (Title 17, U.S. Code), of the thesis for scholarly purposes may be granted by the Librarian. It is understood that any copying or publication of this thesis for financial gains shall not be allowed without my written permission.

I hereby grant permission to the University of Rhode Island Library to use my thesis for scholarly purposes.

Signature

Date

MASTER OF YOUR DEGREE THESIS

OF

SVENJA KRISTIN REINKE

APPROVED:

Thesis Committee:

Major Professor _____

DEAN OF THE GRADUATE SCHOOL

UNIVERSITY OF RHODE ISLAND
2012

ABSTRACT

In self healing concrete, the propagation of cracks in the material is prevented by embedded microcapsules containing an aqueous self healing agent. By adding an encapsulated aqueous solution the effect of autonomous healing of concrete is increased. Microscope studies lead to the conclusion that the capsules do not break upon the mixing process in the mortar production and the solution is released upon cracking. Moreover, reflective microscope tests with colored capsules inside mortars have shown that the capsules release their content when cracks occur. The water reacts with unreacted calcium-hydroxide and calcium silicate particles which are present in concrete and forms a CSH gel which seals the crack. Thus, a large portion of strength can be recovered. The self healing technology has been improved by selective capsule distribution to achieve a recovery of up to 58 %. SEM images gave first insights into how the capsules appear inside a concrete like environment. Calcium nitrite containing capsules are working well for corrosion inhibition, by releasing calcium nitrite as a protective layer around the reinforcement bars. The presented technology is an important contribution to the development of smart, high-performance construction materials.

ACKNOWLEDGMENTS

It is a pleasure to thank those who made this thesis and my experience at the University of Rhode Island possible. I owe my deepest gratitude to Prof. Arijit Bose. This thesis would not have been accomplished without my major professor Arijit Bose. I am heartily thankful for the encouragement, guidance and support from the initial to the final level. I appreciated that I always got the feeling that I can rely on you as a scientific expert and on your never ending support. I also would like to thank Prof. Arno Kwade who has been an inspiration and guidance throughout my entire university time. Dankeschön dafür, dass Sie mich bei all meinen universitären Projekten durchgehend mit großem Engagement unterstützt haben.

Furthermore, I would like to thank Triparna Bhattacharyya who introduced me into the topic of self healing concrete, life at the University of Rhode Island and the department of chemical engineering and made her support available in a number of ways. I am also strongly indebted to Lindsay Lozeau who helped me enormously and I know that without her this work combined with my industrial experience would have not been possible. I like to thank Nicholas Heeder for his endurance in helping me with the mechanical testing.

I like to deeply thank Prof. Richard Brown and Prof. Arun Shukla for their support and several discussions. I like to mention Amitesh Saha, Hari Katepalli and Indrani Chakraborty who helped me if possible.

I like to thank Sigrid Berka, Prof. Stefan Scholl, Prof. Michael Greenfield and Anne-Kathrin Kaiser from the international office of the Technical University Braunschweig for helping me with making my little American dream true.

I am thankful for my friends in Germany and all the new ones I met during my studies. You helped a lot in making this experience unforgettable and I appreciate that you are there for me in good and in challenging times.

I would have not been able to manage my life and be the person I am without the love and support of my family and Marcel. I owe you my deepest thank you for your support and for letting me go to find myself and to explore the wide world in Braunschweig, Edinburgh and finally in Rhode Island far away from home. Ich danke Euch von ganzem Herzen und mit all meiner Liebe. Ich bin sehr froh, dass es Euch gibt!

TABLE OF CONTENTS

ABSTRACT.....	1
TABLE OF CONTENTS.....	vi
LIST OF FIGURES	ix
LIST OF DIAGRAMS.....	xi
CHAPTER 1	1
INTRODUCTION	1
CHAPTER 2	4
REVIEW OF LITERATURE	4
2.1 Introduction into Concrete Science	4
2.1.1 Historical Overview.....	5
2.1.2 Introduction into Cement Science	6
2.1.3 Weaknesses and Strengths of Concrete Materials.....	12
2.1.4 Flexural Strength of Reinforced Concrete.....	13
2.2 Techniques for Self healing in Cementitious Materials	17
2.3 Encapsulation Methods	20
CHAPTER 3	25
METHODOLOGY.....	25
3.1 Production	26
3.1.1 Polyurea/Polyurethane Microcapsules.....	26
3.1.2 Mortar Samples.....	30
3.2 Characterization.....	33
3.3 Performance.....	35
3.3.1 Determination of Recovery in Flexural Strength.....	35

3.3.2 Corrosion Test	36
CHAPTER 4	38
FINDINGS	38
4.1 Production	38
4.1.1 Water Capsules	38
4.1.2 Calcium Nitrite Capsules	41
4.1.3 Sodium Silicate Capsules	41
4.2 Characterization.....	44
4.2.1 Capsules.....	45
4.2.2 Characterization of Mortar Samples.....	57
4.3 Performance.....	61
4.3.1 Water Capsules as Reference.....	61
4.3.2 Capsule Distribution inside Mortar Samples.....	63
4.3.3 Recovery of Mortar Samples with PEG Capsules.....	66
4.3.4 Sodium Silicate as Self healing agent.....	67
4.3.5 Corrosion Test	70
CHAPTER 5	76
CONCLUSION	76
APPENDICES	80
REFERENCES.....	80
POSTERS.....	86
LITERATURE REVIEW FOR PELLETIER [6] AND BHATTACHARYYA [7]	87
VALIDATION OF SET-UP FOR CORROSION MEASUREMENT	102
BIBLIOGRAPHY	104

LIST OF TABLES

Table 2.1: Risk and probability of corrosion dependent on open circuit potential	16
Table 2.2: schematic summary of influence of monomer on shell parameters, taken from [29]	24
Table 3.1: Overview over chemicals used for encapsulation	28
Table 3.2: Composition of solutions O1, O2 and W1 to prepare approximately 20 ml of capsules	29
Table 3.3: Variations in monomer chemistry to standard method	29
Table 3.4: Solutions for chemical stability test	34
Table 3.5: Tests to obtain high yield of sodium silicate capsules	42
Table 3.6: Tests for altering (lowering) pH of sodium silicate solution	43
Table 4.1: Tests to obtain high yield of sodium silicate capsules	42
Table 4.2: Tests for altering (lowering) pH of sodium silicate solution	43
Table 4.3: Optical microscope images for stability test of capsules without PEG	50
Table 4.4: Optical microscope images for stability test of capsules without PEG	51
Table 4.5: Optical microscope images for stability test of capsules with PEG	52
Table 4.6: Optical microscope images for stability test of capsules with PEG	53
Table 4.7: Optical microscope images for shake test to check mechanical stability of different kinds of capsules	55
Table A.1: Results compression strength, data taken from Bhattacharyya [7]	88
Table A.2: Results for validation of corrosion set-up	103

LIST OF FIGURES

Figure 2.1: Schematic of cement production	7
Figure 2.2: Schematic of changes in the components and their amounts with increasing temperature, source [16].....	9
Figure 2.3: Stresses in concrete for flexural loading with and without reinforcement bars	14
Figure 2.4: Cross section of flexural loaded bar with a rectangular cross section.....	15
Figure 2.5: Principle of microcapsule based self healing concrete.....	19
Figure 3.1: Overview of mechanism on the basis of recovery of strength	25
Figure 3.2: Sketch of capsule preparation.....	27
Figure 3.3: Set-up of graded samples with capsules placed where tension acts	31
Figure 3.4: Set-up of corrosion samples	32
Figure 3.5: Set-up of three point bend test for mortar samples.....	36
Figure 3.6: Set-up of corrosion experiment with mortar samples.....	37
Figure 4.1: Emulsion without monomer, no capsule formation and with no catalyst (the capsules are very fragile based on their stability is shown in 4.2.1.4).....	39
Figure 4.2: PEG test on wall formation with different Polyethylene glycols as second monomer and PEG dioleate as second surfactant	40
Figure 4.3: Optical microscopy images of capsules with different aqueous contents .	46
Figure 4. 4: Microscopy images of capsules containing pure water	46
Figure 4.5: Fluorescence images in comparison with optical microscopy, with water soluble color	47

Figure 4.6: Optical microscopy images of capsules inside wet mortar after mortar preparation including mixing	56
Figure 4.7: Images of cracked area with colored capsules, done with reflective microscope	58
Figure 4.8: SEM images of capsules inside mortar samples at different magnifications	59
Figure 4.9: Images taken with reflective microscope of steel wires in different mortar samples taken after corrosion test	75
Figure A.1: SEM images of polyurea/polyurethane microcapsules made by interfacial polymerization [7].....	98
Figure A.2: Set-up corrosion test, M. Pelletier [6].....	99

LIST OF DIAGRAMS

Diagram 4.1: XRD results for dry capsules	48
Diagram 4.2: XRD of mortar samples with and without capsules.....	60
Diagram 4.3: Recovery of flexural strengths of mortar samples with sodium silicate and water capsules.....	62
Diagram 4.4: Load at first failure for graded and non-graded water as well as sodium silicate capsules dependent on total amount of capsules in mortar samples.....	63
Diagram 4.5: Load at second failure for graded and non-graded water as well as sodium silicate capsules dependent on total amount of capsules in mortar samples ...	64
Diagram 4.6: Recovery of flexural strength with comparison of graded and non-graded mortar samples, plotted in dependence of total amount of capsules in mortar sample	65
Diagram 4.7: Recovery of flexural strength of capsules with pure water content.....	67
Diagram 4.8: Recovery of flexural strength for mortar samples with graded sodium silicate capsules, non-graded and non-graded with sodium silicate/calcium nitrite capsules	68
Diagram 4.9: Overview of recovery for different mortar samples with capsules with a core of sodium silicate, water and combination of calcium nitrite and sodium silicate based on amount of capsules.....	69
Diagram 4.10: Corrosion of steel wires in different solutions	71
Diagram 4.11: Circuit potential for a) plain steel wire, mortar sample b) without capsules, c) calcium nitrite and sodium silicate capsules and d) and e) calcium nitrite capsules in different concentrations.....	73

Diagram A.1: Compressive strength in dependence for reference samples without capsules and with 2 vol% capsules, data taken from Bhattacharyya [7]	87
Diagram A.2: Dynamic strength tested with Split Hopkinson pressure bar, data taken from Bhattacharyya [7]	90
Diagram A.3: Maximum load at three point bend test for samples with different amounts of capsules, data taken from [6, 7].....	91
Diagram A.4: Recovery of flexural strength at different capsule loadings from 0 vol% to 6 vol%, data taken from [6, 7]	92
Diagram A.5: Mass change due to water absorption tested by Bhattacharyya [7] after compression and without compression	94
Diagram A.6: Potential progress in dependence of time for samples with 2 vol % sodium silicate capsules and for reference samples without any capsules, diagram has been taken from [6] and been adapted	100
Diagram A.7: Validation lines for corrosion set-up, comparison of determined voltage of set-up and voltage measured with calibrated voltmeter.....	102

CHAPTER 1

INTRODUCTION

The demands for construction materials increase constantly and improvement of existing materials is required in order to fulfill the needs of the future to provide high-performance, smart and environmental friendly solutions for buildings and infrastructure, among others. Cementitious materials are the most widely used construction materials worldwide [1]. Furthermore, Jonkers [2] predicts that concrete, a cement based material, will continue to be the most important building material for infrastructure. Concrete is used extensively for its high compressive strength [3]. It can withstand compressive load well but fails easily under tension [4]. Reinforcement bars are added to the concrete structure to increase the tensile strength [5]. It is well known that tiny cracks on the surface of the concrete make the whole structure vulnerable due to water ingress. This in turn results in corrosion of the steel reinforcement bars which are used to support the construction to better withstand tensile load. This leads to a reduction of the lifespan of a concrete structure and repairs can cost time and money. Moreover, it is often very difficult to gain access to the structure where repairs are needed. In self healing concrete, the propagation of cracks is prevented [6]. Thus, self healing concrete has a huge significance in everyday life to make infrastructure and housing safer and longer lasting by protecting the material from damage due to weather and cyclic loadings. Furthermore, by increasing the lifetime of the construction, less concrete has to be produced, resulting in both lower

emission of CO₂ and saving natural resources and energy as well as lessening the economic impact from regular maintenance and repair. The production of concrete is very energy consuming. The implementation of self healing concrete on a large scale is of high interest of the industry. The self healing approach presented in this work is based on embedded microcapsules containing a healing agent. The agent is released when a crack causes the capsules to rupture. The healed material recovers a large portion of its original flexural strength [6, 7]. But more needs to be known about the properties of the capsules and about the self healing mechanism. In order to implement and improve the technology it is essential to find out how the interfacial polymerization works to develop a production method for large yield of capsules containing specific healing agents. Moreover, it is investigated how the distribution of capsules within the concrete sample affects strength and recovery. Graded samples with selective capsules distribution are prepared and tested for flexural strength and recovery. Samples under flexural stress fail at the opposite side of loading and capsules are needed where failure occurs in order to self heal the concrete structure. This way the self healing can be realized with fewer capsules in total. It has been observed that capsules can reduce the initial strength as they act as stress concentrators. By adding less capsules in total but with a selective distribution it is going to be examined if the self healing can be improved. Additionally, encapsulation of different healing agents and their ability to inhibit corrosion will also be tested. This work provides important information about the capsule production, its scale-up, characterization of the capsules and their properties inside concrete like materials and the performance of the capsules as a self healing product and a corrosion inhibitor.

Thus, it gives a good foundation for the implementation of microcapsule based self healing concrete.

CHAPTER 2

REVIEW OF LITERATURE

This section gives a short introduction into the science of concrete and presents common self healing approaches for concrete materials. Microcapsule based self healing concrete is emphasized. Therefore, the general mechanism of encapsulation via interfacial polymerization is also introduced. For a more detailed description of concrete science Mindess et al. [8] is recommended. More information about self healing mechanisms is given in [9], and the mechanisms of encapsulation are described in [10].

2.1 Introduction into Concrete Science

Concrete is an artificial construction material composed of a binding material with embedded particles or aggregates. It develops its properties by hydration of the cement [17]. The Latin word “concretus” means “to grow together”. The binder is a mixture of hydraulic cement and water. According to the British standard [17] cement can be defined as a hydraulic binder, which means it is a “finely ground inorganic material which, when mixed with water, forms a paste which sets and hardens by means of hydration reactions and processes and which, after hardening, retains its strength and stability even under water”. Additionally, coarse and fine aggregates such as sand and gravel and optional admixtures are added to the cement plus water to form

concrete [12, 15, 17]. Admixtures are materials added during the mixing process of concrete in small amounts compared to the mass of cement to change and optimize the properties of the fresh or hardened concrete. Aggregates are granular mineral materials put into concrete. They can be natural, artificial or recycled. The water/cement ratio which is the ratio of water present in the fresh concrete and not absorbed by the aggregates and the cement content by mass in fresh concrete is an important parameter for strength development of concrete. A mixture of just water, cement and optional admixtures is named cement paste. By adding sand, thus a material composed of cementitious binder, fine aggregated, water and admixtures, mortar is made. Concrete is mortar with aggregates. [17]

2.1.1 Historical Overview

The use of cementitious materials goes back many years BC. Felder-Casagrande et al [11] date the first use of mortar back to 22,600 years ago. They come to the conclusion that mortar was already used in Turkey 22,600 years ago based on a ^{14}C measurement. Nevertheless, Felder-Casagrande et al admit that the historic determined period of the sample would be 10.000 years ago [11]. Nevertheless, it is known that the Egyptians built the pyramids with gypsum mortar in 3000 BC [12]. They already prepared systems of uniting blocks and stones with a mortar out of sand and a cementitious material similar to present concrete solutions [13]. Gypsum is calcium sulfate with two molecules of crystallized water $\text{CaSO}_4 \cdot 2\text{H}_2\text{O}$ [12]. The Greeks conducted further development of cement and the Romans were finally able to build very durable structures out of a material similar to concrete [12, 13]. They also

used milk and animal blood for additives. It was not known how to make high quality mortar the following years until the end of the Middle Ages [12, 13]. The word “cement” turns up first in the Middle Ages in Batman Uppon Bartholome’s book “De Proprietatibus Rerum”: “Lyme is called calx, & is a stone burnt; by meddeling thereof with sand and with water, cement is made” [14]. John Smeaton discovered hydraulic lime in 1756 [12]. According to him his discovery is an “artificial stone” similar in strength and durability as Portland stone [15]. Bry Higgins patented the use of hydraulic cement for external use of mortar and James Parker made a patent for natural hydraulic cement, Parker cement, in the 18th century [12]. Further development has been done including Joseph Aspdin’s patent of Portland cement [12], which is made by calcinations of chalky lime and fine ground clays, and Isaac Johnson’s discovery of manufacturing tricalcium silicate (C3S), cement as we know it today, in the 19th century. Portland cement is the cement used today. It is made according to the patent of Joseph Aspdin. The beginning of the 20th century is characterized by improvement of cement manufacturing and further development of additives and admixtures. [12 - 16]

2.1.2 Introduction into Cement Science

The paragraph gives an overview for a better understanding of the concepts and characteristics of cement and the hydration process. It starts with the production of cement wherein the main components of cement are introduced. Then, the basic

concepts of the hydration process which is essential for the characteristic strength of cementitious materials are presented.

2.1.2.1 Production of Portland Cement

Concrete gets a strong solid by the cement which is a hydraulic binder. It is a material used to bind particles together whereby the fine inorganic cement particles form a paste which sets and hardens when mixed with water because of chemical reactions [13]. Cement is made out of clinker. The raw materials: steel ore, clay and limestone in the right proportions make the clinker and this is then the main component of cement [13].

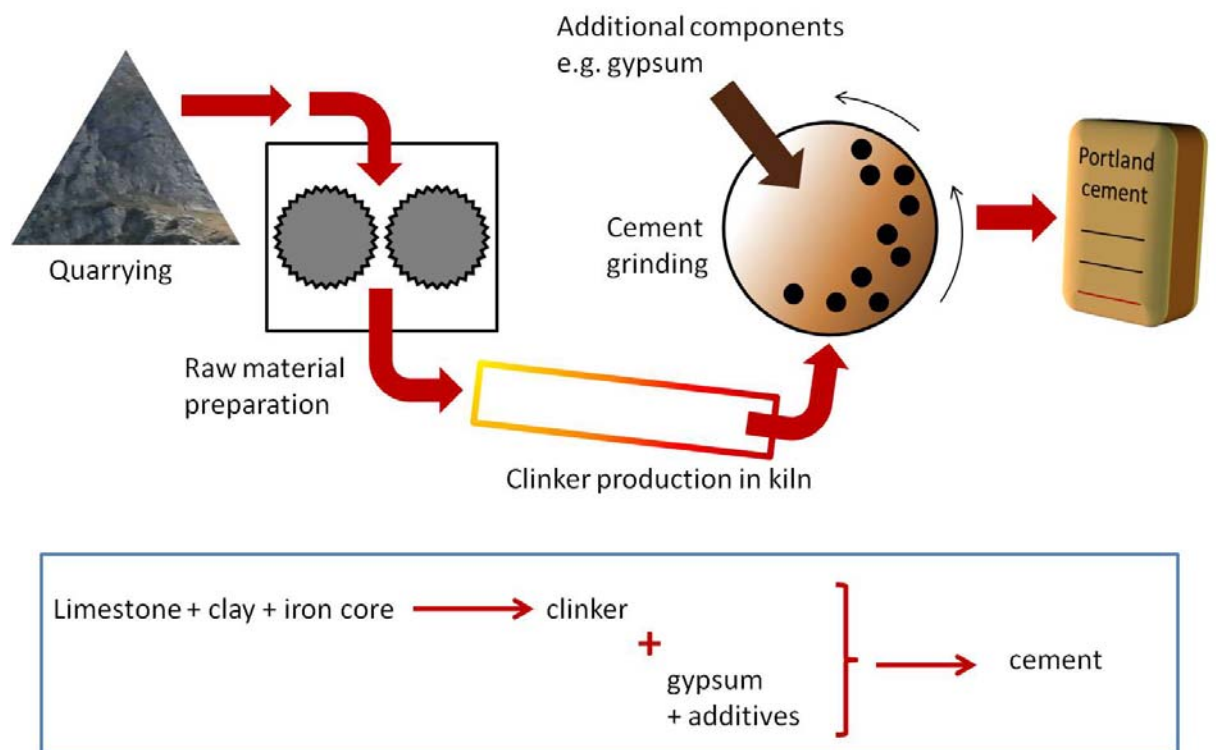


Figure 2.1: Schematic of cement production

Thus, cement is composed of common materials: sand, lime and water [16]. Figure 2.1 gives a general overview over the steps in the cement production. First of all, the raw materials have to be prepared: the big particles from the limestone and clay quarry are crushed into smaller and homogenous particles, same for the steel ore. According to Aïtcin [18] the first grinding is essential to favor the solid/solid reactions inside the kiln at 1450°C which results in the formation of alite, belite, and the interstitial phase. The main components of the raw materials of the cement production are: calcium carbonate (CaCO_3), silica (SiO_2), aluminum oxide (Al_2O_3) and ferric oxide (FeO_3). The next step is the production of clinker. Clinker is mainly made of hydraulic calcium silicates ($(\text{CaO})_3\text{SiO}_2$ and $(\text{CaO})_2\text{SiO}_2$), tricalcium aluminate ($(\text{CaO})_3\text{Al}_2\text{O}_3$) and tetracalcium aluminoferrate ($(\text{CaO})_4\text{Al}_2\text{O}_3\text{Fe}_2\text{O}_3$) [13, 16] whereby calcium silicates and calcium aluminate dominate the structure of cement [16].

Table 2.1: Chemical abbreviations of cement components

Component name	Composition	Abbreviation
Calcium oxide (lime)	CaO	C
Silicon dioxide (silica)	SiO_2	S
Aluminum oxide (alumina)	Al_2O_3	A
Steel (III) oxide	Fe_2O_3	F
Calcium silicate hydrate gel	$(\text{CaO})_x \cdot \text{SiO}_2 \cdot y\text{H}_2\text{O}$	CSH
Tricalcium silicates	$(\text{CaO})_3\text{SiO}_2$	C3S
Dicalcium silicates	$(\text{CaO})_2\text{SiO}_2$	C2S
Tricalcium aluminate	$(\text{CaO})_3\text{Al}_2\text{O}_3$	C3A
Tetracalcium aluminoferrate	$(\text{CaO})_4\text{Al}_2\text{O}_3\text{FeO}_3$	C4AF

The chemical compositions mentioned have common abbreviation in cement technology which are presented in table 2.1. The process of making clinker is called

“pyroprocessing” and the main component is the rotating kiln where the raw materials are heated up to a temperature of around 1450°C and burnt [18]. Figure 2.2 illustrates the change of components and their amounts in the clinker with increasing time and temperature [16].

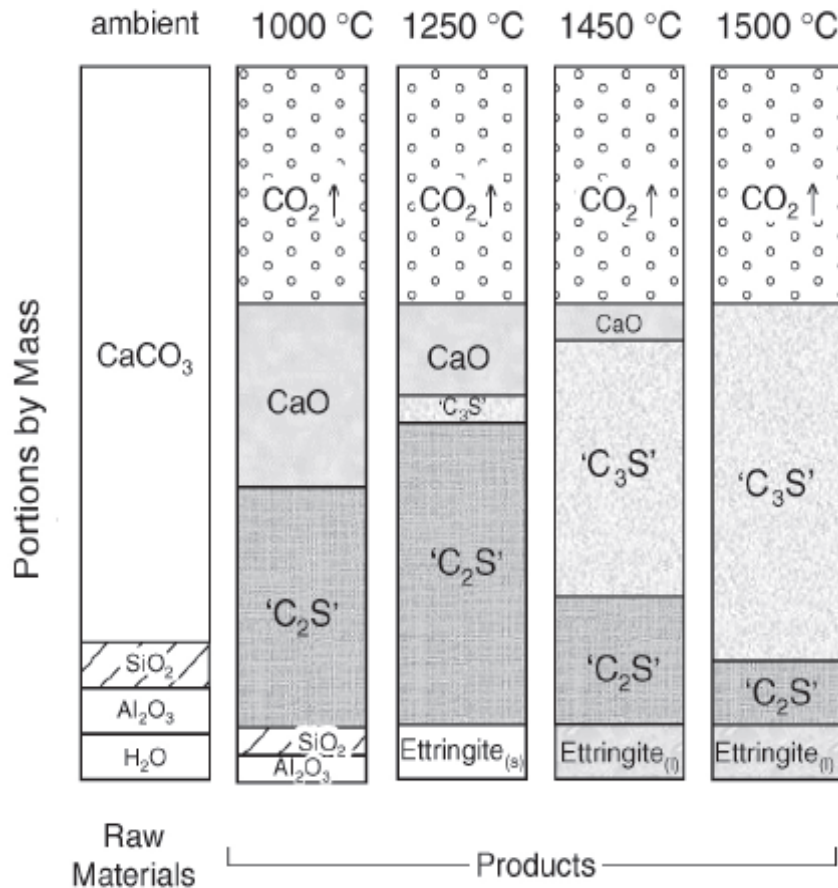


Figure 2.2: Schematic of changes in the components and their amounts with increasing temperature, source [16]

The raw components are slowly decomposed. Calcium carbonate CaCO_3 reacts to form calcium oxide CaO and carbon dioxide CO_2 . The calcium oxide reacts further to dicalcium silicate C_2S which becomes tricalcium silicate C_3S at higher temperatures of over 1250°C. Additionally, there is formation of liquid aluminate and Ettringite at

about 1450°C. This pyroprocess is the most energy and money consuming step in the cement production as high temperatures are needed. To finally get Portland cement gypsum, calcium sulfate dihydrate, is added to the clinker and the mixture is ground. According to Aitcin [18] the second grinding is needed to activate the reactivity of the clinker. Ordinary Portland cement only contains Portland clinker and gypsum [18]. Other kinds of Portland cement have additional components such as fly ash or slag. The properties like chemical structure, particle size and quantity and proportion, respectively of the synthetic materials, calcium silicates, tricalcium aluminate and tetracalcium ferroaluminate give the cement its properties [12, 13, 16, 18].

2.1.2.2. Hydration process

The hydration process is the chemical conversion of the powder cement in combination of water into a stone like solid. The hydration reaction goes through different states whereby heat is generated. The first phase of the hydration process is called pre-induction period and is short [16]. When water is added to the cement, part of the cement grains dissolve and there is formation of compounds in solution. More precisely, it is the dissolution of C3S. Thus, the oxygen ions on the surface of the C3S lattice react with the water to form hydroxide ions which are combined with calcium ions. This leads to the dissolution of material from the C3S [16]. The chemical reactions in the first phase of hydration are [16]:



Meanwhile, silicates from the lattice dissolve according to the following:



The dissolved components are forming a 'CSH' gel:



The reason why gypsum is added to the clinker in Portland cement is to slow down this first phase in order to avoid rapid setting of the cement. The gypsum works by the formation of aluminate and sulfoaluminate phases, the so-called Ettringite phase, in a reaction with gypsum and tricalcium aluminate [16]. It is formed until the saturation concentration is reached. The following period, the induction period, is characterized by a slowdown of the reaction. The exact reasons for the slowdown are not well known [16]. One hypothesis is that the CSH layer rapidly covers the surface of the dissolving C3S. The layer gets more permeable over time and the reaction accelerates after this period [16]. Another reason could be the saturation of the mixture or supersaturating of the solution with calcium hydroxide as well as formation of two types of CSH [16]. The third phase is the acceleration stage where nucleation and growth of the hydration products and rapid hydration of C3S followed by slowly hydration of C2S [16]. The C3S reacts to form calcium hydroxide and a CSH gel on the surface of the cement particle. The hydration of C3A continues and the ferrite phase reacts with C3A which leads to formation of crystals and an interconnected network. Further information about the theories of the second period can be found in literature, e.g. [16, 13]. The higher the concentration of solid hydration products, the slower the reaction is due to diffusion limitation. Nevertheless, the hydration process and the gel formation continue for weeks [16]. After 28 days 85-90% of the maximum

strength is reached. The hydration products lead to stiffness, setting and hardening of the cementitious material over time. Heat is generated in the hydration process, especially in the first few days. Concrete with early strength usually heats up more which has to be kept in mind and either used as an advantage or needs to be limited [17]. As the hardened material is lower in volume compared to fresh concrete shrinkage occurs which can lead to the development of cracks which has to be avoided. [12, 16]

2.1.3 Weaknesses and Strengths of Concrete Materials

A list of weaknesses and strengths of concrete is given in Gambhir [3]. It is pointed out that concrete is widely used in construction because it is most economical in the long run compared to other engineering materials. Besides, concrete mainly consists of locally available materials. Moreover, concrete is cheap and fire resistant and develops high compressive strength. Concrete is durable and can be as hard as natural stone from which it got its name: artificial stone. In combination with steel reinforcement bars it can be used in numerous applications. An important property of cement is its hydraulicity; thus, the ability to set and remain insoluble under water [15] without weakening for a long time. Concrete can be easily formed in different shapes and sizes thanks to its flowability before hardening [3, 4, 13] and the molds can be reused after the concrete has solidified. In wet state concrete can be pumped and easily sprayed on as well as filled into fine cracks to repair tiny cracks. As a construction material concrete does not need surface treatment unless special requirements are

wished such as water repellent concrete. And usually concrete requires easy and little maintenance if not cracked [3]. On the other hand, a main weakness is that concrete has low tensile strength. Steel reinforcement bars, fibers or meshes are used to increase the tensile strength of the concrete structure. But if cracks are developed and water can penetrate through the concrete towards the steel reinforcement bars, corrosion happens and weakens the concrete structure. Cracks can also develop due to freeze and thaw cycles, drying shrinkage or moisture movement because fresh concrete shrinks on drying and hardened concrete expands on wetting. Additionally, contraction and expansion occur due to temperature changes which can lead to cracks. Consequently, cracks should be avoided or repaired to increase the performance of the concrete structure. But external repair is often costly and difficult. [3, 12]

2.1.4 Flexural Strength of Reinforced Concrete

As seen in figure 2.3 compression and tension is acting in a concrete sample stressed by flexural loading like in a three point bend test. Because concrete has such low tensile strength but good compressive strength it fails due to the tension.

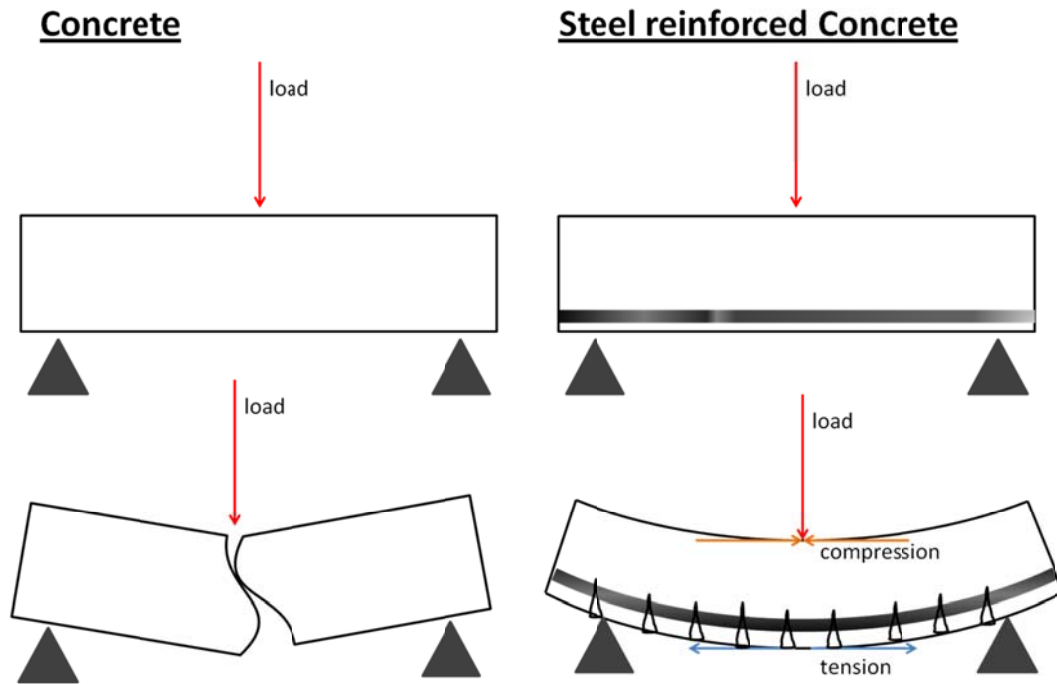


Figure 2.3: Stresses in concrete for flexural loading with and without reinforcement bars

Tension is acting in the opposite side of loading, whereas the side where the flexural load is applied is compressed. Steel reinforcement bars are added to the concrete structure to increase the tensile strength and to avoid failure. Reinforced concrete can usually carry the service load even if there are some cracks on the tension side. Nevertheless, it is important that the concrete is still able to protect the reinforcement bars. The mortar used in this project has a compressive strength of up to 19 MPa [6, Appendix]. Ultra-high-strength concrete can have compressive strength over 150 MPa [12]. Whereas the tensile strength of concrete is usually only about 1/10 of its compressive strength for normal-strength concrete and even lower for high-strength concrete [12]. Steel has tensile strength of some hundreds of MPa [25]. Thus, steel reinforcement bars, fibers or meshes can take some of the tensile strength to improve the stability of the concrete structure. The steel reinforcement bars provide

the tensile strength for the concrete structure whereas the concrete gives the protective environment for the steel against chemical destruction which is shown in the next section.

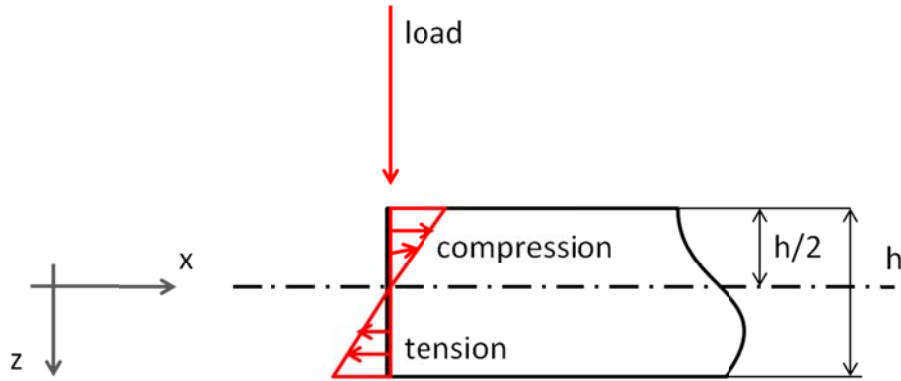


Figure 2.4: Cross section of flexural loaded bar with a rectangular cross section

The cross section of a flexural loaded bar is shown in figure 2.4. The internal stresses are directly dependent on the coordinate z as shown in equation 1.

$$\sigma(x) = \frac{M_B(x)}{I} \cdot z \quad (1)$$

with

$$I_{yy} = \frac{w \cdot h^3}{12} \quad (2)$$

with the width (w), height (h) and momentum M_B . The z -axis is in the plane where no stresses are acting and is called the neutral axis. The neutral axis lies in the center of gravity of the cross section. For specimen with rectangular cross sections this axis is at the half of the height $h/2$. As a conclusion, at the bottom part tension is acting and in the top part of the sample compression during flexural loading and the concrete fails due to tension, thus on the bottom part.

2.1.5 Corrosion of Reinforcement Bars

Under normal conditions the concrete is highly alkaline at a pH of 13.0 to 13.8, and ordinary steel reinforcement bars are surrounded by a nanometer thick protective layer to protect it from corrosion. The high alkalinity results mainly out of calcium hydroxide formed during the hydration process. The passive layer principally consists of iron ions and is formed spontaneously. The protective layer can be destroyed by carbonation of concrete or by the presence of chloride ions. If calcium hydroxide reacts with carbon dioxide from the environment calcium carbonate is formed which leads to a decrease of pH and the protective alkaline nature is changed. This process is called carbonation. Thus, carbonation is the neutralization of alkalinity of concrete by carbon dioxide of the atmosphere. At a pH of around 9 the passive film is no longer stable. Chloride ions at high concentrations at the surface of the reinforcement bars can locally destroy the passive layer. Corrosion occurs if the protective layer is destroyed and water and oxygen are at the surface of the reinforcement bars. The degree of corrosion can be determined by measuring the open circuit potential using a gel-filled epoxy calomel reference electrode. Table 2.1 shows the risk and probability of corrosion dependent on the open circuit potential. [25, 26]

Table 2.1: Risk and probability of corrosion dependent on open circuit potential [26]

Open circuit potential [mV]	Risk of corrosion	Probability of risk of corrosion
> -125 > -200	Low	10 %
-126 to -275 -350 to -200	Intermediate corrosion risk	
< -276 < -350	High	<90%
< -426 < -500	Severe corrosion	

2.2 Techniques for Self healing in Cementitious Materials

The ability to heal, regenerate and repair, respectively without any further external treatment is called self healing [19]. Various self healing mechanisms can be observed in nature such as the self healing phenomena of damaged tree skins or that human wounds heal themselves [1]. Even cementitious materials show autonomous healing of cracked areas. To enhance the autonomous self healing mechanism different self healing approaches are examined including fiber, bacteria and microcapsule based self healing concrete. This section serves as a short introduction into the different approaches. A more detailed summary of the work done on microcapsule based self healing concrete is given in the appendix and encapsulation methods are presented in chapter 2.3 based on the review by Kondo [20].

According to Jonkers [2] microcracks, which are cracks up to 0.2 mm do generally not directly impair the safety and strength of a concrete construction. Moreover, it can be seen that the microcracks heal themselves to a certain degree which is called ‘autonomous’ healing. Jonkers explains the autonomous healing of cementitious materials with non-reacted cement particles in the concrete matrix which react with water penetrating through the cracks resulting in closure of the microcracks. A CSH gel similar to the one formed during hydration (which has been discussed in paragraph 2.1.2.2) is formed and seals the microcrack. Based on the state of the art the autonomous healing of cementitious materials can additionally be explained with formation of calcium carbonate or calcium hydroxide, blocking the cracks by particles or the swelling of the CSH gel and therefore the expansion of the hydrated

cementitious matrix [1]. The self healing products such as presented in this paragraph are inspired by biologic systems [21]. They increase the effect of autonomous healing and the recovery of strength by healing upon trigger like load or heat, etc.

One approach is to use hollow fibers to store healing agents. The fibers are embedded in the concrete matrix. In theory, the fibers, which are e.g. out of glass, are brittle and break upon cracking, release the healing agent, seal the crack and therefore, inhibit the propagation of the cracks. Alkali-silica solutions and epoxy resins have been used as healing agent in the work by Mihashi [22]. The mechanism of storing and releasing the healing agent upon cracking has been proven and the approach has been shown as feasible. Another approach of self healing concrete is embedding of bacteria and nutrients into the concrete which seal the crack by microbiological precipitation of calcium carbonate whereas the bacterial cell membrane acts as the nucleation site [1]. As soon as cracks occur and water penetrates through the material the bacteria spores are activated and the bacteria consume calcium lactate which has been put in encapsulated form inside the concrete. The bacteria spores can stay in the concrete for more than 200 years without being destroyed. They germinate and grow upon contact with water. Thereby, it produces insoluble limestone which seals the crack. According to Jonkers [2] one disadvantage is that the cost for the described self healing approach is about the double of that of conventional concrete. Nevertheless, Jonkers justifies the technology with the decreased maintenance costs and consequently savings in the long term. Another disadvantage is that the clay pellets with the self healing agent uses 20% of the volume and as this volume is usually filled

with harder aggregates the concrete is about 25% weaker in compression than conventional concrete. [1, 2]

A new approach is to introduce microcapsules into the concrete which contain a healing agent and release their content upon crack formation to seal microcracks and prevent the propagation of the cracks. The approach is based on the work by the Sottos group [21] who started using microcapsules for self healing polymers. The principle of microcapsule based self healing concrete proposed by Pelletier [6] and Bhattacharyya [7] is shown in figure 2.5. The embedded microcapsules contain sodium silicate and water and are ruptured upon crack formation. They release the healing agent and due to capillary forces the solution is released into the microcrack [6, 7].

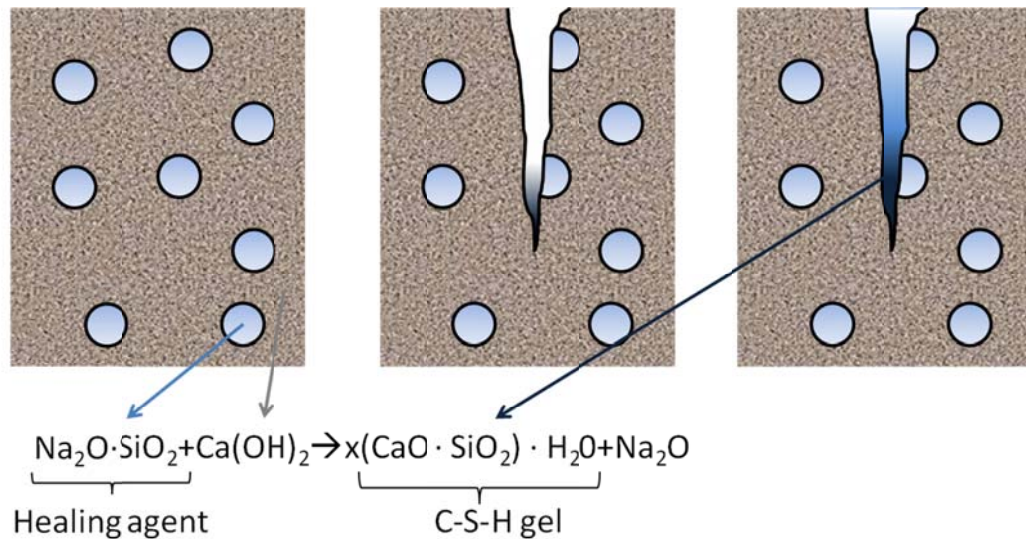


Figure 2.5: Principle of microcapsule based self healing concrete

The sodium silicate reacts with calciumhydroxide to CSH gel which hardens and has similar properties to cement. A detailed description of CSH gel formation in cement is given in paragraph 2.1.2.2. The capsule based self healing concrete has been

investigated at the University of Rhode Island and is followed up in this work. Pelletier [6] started exploring sodium silicate as a self healing agent and proposed an encapsulation method based on interfacial polymerization and the work of Frère [23] and Saihi [24] on encapsulating aqueous solutions. Furthermore, it has been investigated by Pelletier [6] in how far the embedded sodium silicate solution capsules can increase the self healing effect and if it can be used as a corrosion inhibitor. Bhattacharyya [7] did further tests on the ability of partial strength recovery at flexural, dynamic as well as compressive load and the influence of capsule amount in a mortar samples as well as the influence of capsule size. The recovery of the flexural strength increases with increasing capsule loading but the initial load decreases due to the addition of capsules [6]. With the introduction of capsules weakness points are added to the concrete structure. Furthermore, preliminary tests with sodium silicate capsules as corrosion inhibitor on iron wires have been conducted. The results which have been a basis for this work can be found in the appendix. Detailed information are also given in the thesis by Pelletier [6] and Bhattacharyya [7].

2.3 Encapsulation Methods

Microcapsules, which are small spheres with a diameter of around 1 μm to several hundred μm , can be formed using various methods. In general, it is first needed to disperse the core material into a continuous phase (this process is the emulsification) and secondly, a wall material has to be formed around the dispersed droplets (the microencapsulation process). A general division is made between

physical and chemical methods for encapsulation. Physical methods include spray drying, fluidized bed coating, spinning disk and solvent evaporation among others [10, 20]. The starting point for physical methods is a polymer and solely shape formation takes place. On the other hand, suspension and emulsion polymerization as well as dispersion and interfacial polymerization are chemical encapsulation methods. The chemical methods are characterized by having prepolymers or monomers as a starting point which chemically reacts to a polymer shell at the interface between the two phases of the dispersion. Chemical methods are described in more detail as they are used because of their easy adaption to a wide variety of applications and because of the fact that a chemical encapsulation method is used in this work. [20, 10]

One way of polymer formation to prepare capsules is **emulsion polymerization**. In that process the monomer is added drop wise to the stirred polymerization medium containing the core material and an emulsifier. Primary nuclei are formed in the aqueous medium and polymer molecules are produced. However, according to Dubey et al [10] lipophilic materials are more suitable for encapsulation with this technique. But the advantage is that the technique is easy to adapt for capsule sizes of just some nanometers up to millimeters. [10]

Interfacial polymerization uses the fact that compounds having active hydrogen atoms such as $-OH$, $-NH$ and $-SH$ dissolved in an aqueous phase can react with polyacid chlorides or polyisocyanates which are dissolved in an organic phase. The reaction takes place at the interface of these two phases and this leads to

encapsulation of the core material. As there are a lot of possible combinations of two monomers many different polymers can be formed. Two interfacial polymerization methods are introduced here: the interfacial polycondensation and the in situ polymerization. [20]

Interfacial polycondensation is one of the interfacial polymerization methods. Two complementary monomers are needed for this technique. The polycondensation takes place at the interface of two immiscible phases each having one of the two complementary monomers which are polymerized. The encapsulated core material has to be present in the dispersed phase and for emulsification an appropriate emulsifier has to be used. If the monomer is not soluble in the dispersed phase the monomer precipitates around the droplets to form a polymer shell. Usually, the polycondensation reaction takes place on the organic phase of the interface. The aqueous soluble monomer has to be transported through the interface and the already formed polymer shell to the oil side where the polymerization takes place. This monomer transport is dependent on the pH, the aqueous phase, temperature and the chemistry of the organic phase as well as the surfactants. This method can be used for a variety of polymers such as polyamides, polyureas, polyurethanes and polyesters and a large scale of droplet sizes and capsule kinds can be achieved with this method. [20, 10]

The second example for interfacial polymerization is **in situ polymerization**. In this method only one monomer, either water soluble or oil soluble is used. The

reaction takes place at the interface between the organic and the water phases at elevated temperatures and with help of a catalyst. [20]

Polyurethanes are per definition polymers which contain urethane linkages in the main polymer chain. Polyurethane can be formed by a reaction between diisocyanate $O=C=N-R$ and a diol $HO-R-OH$. Polyesters, polycarbonates and polyethers are examples for diols. Isocyanates are chemicals with an extremely reactive group $-N=C=O-$. An isocyanate with two reactive isocyanate groups is called diisocyanate. Diisocyanates can be classified into two categories: aromatic and aliphatic diisocyanates. Diphenylmethanes and toluene diisocyanate belong to the group of aromatic diisocyanates; whereas, hexamethylene diisocyanate is an example for an aliphatic diisocyanate. Besides the mentioned reaction using an alcohol to form polyurethanes, isocyanates can react with an amide to form **polyurea**. Isocyanate reacts with water to form an unstable product and the reacts further on to get an amine. Thus, diisocyanate and water gives polyurea; whereas, the combination of diisocyanate with polyethylene glycol would form polyurethane. [28]

The chemistry of the monomers strongly influences the properties of the polyurea/polyurethane shell. Dependent on the monomer chemistry of the isocyanate, aromatic or aliphatic polyurethanes can be produced. Aromatic polyurethanes are more susceptible to ultraviolet light but more thermal resistant compared to aliphatic polyurethanes. But the thermooxidation resistance is mainly influenced by the type of the long-chain diol. Polyesters are more thermooxidative stable than polyethers. The

hydrolysis resistance is also dependent on the long-chain diol. Ether groups show a better resistance than ester groups. And the less polar the diol is, which means the longer the chain, the more phase separated the polyurethane is.

Table 2.2: schematic summary of influence of monomer on shell parameters, taken from [29]

Parameter	Polyester based TPU	Polycaprolactone based TPU	Polyether based TPU
Hydrolysis resistance	--	-	++
Microbial stability	--	--	+
Adhesion strength	+	++	-
Thermooxidative resistance	+	+	-
Low temperature flexibility	o	+	++
Mechanical properties	++	++	+
Oil and grease resistance	++	+	-
Injectability (cycle time)	+	++	o

(++ excellent; + good ; o acceptable; - poor ; -- very poor)

Thus, polyether is more phase separating than polyester. The oil and solvent resistance is just the opposite the higher the polarity the better the oil resistance. Table 2.2 shows a schematic overview over the parameters of the shell dependent on the monomer chemistry. [29, 30]

CHAPTER 3

METHODOLOGY

This paragraph shows the methods and materials used in the framework of this work. Figure 3.1 gives an overview over the general procedure based on the example of the recovery of strength. In all tests to produce capsules, the first step is the emulsification of an aqueous phase into an oil phase. The aqueous droplets are then encapsulated via interfacial polymerization [6, 7]. Subsequently, the capsules are embedded in mortar samples.

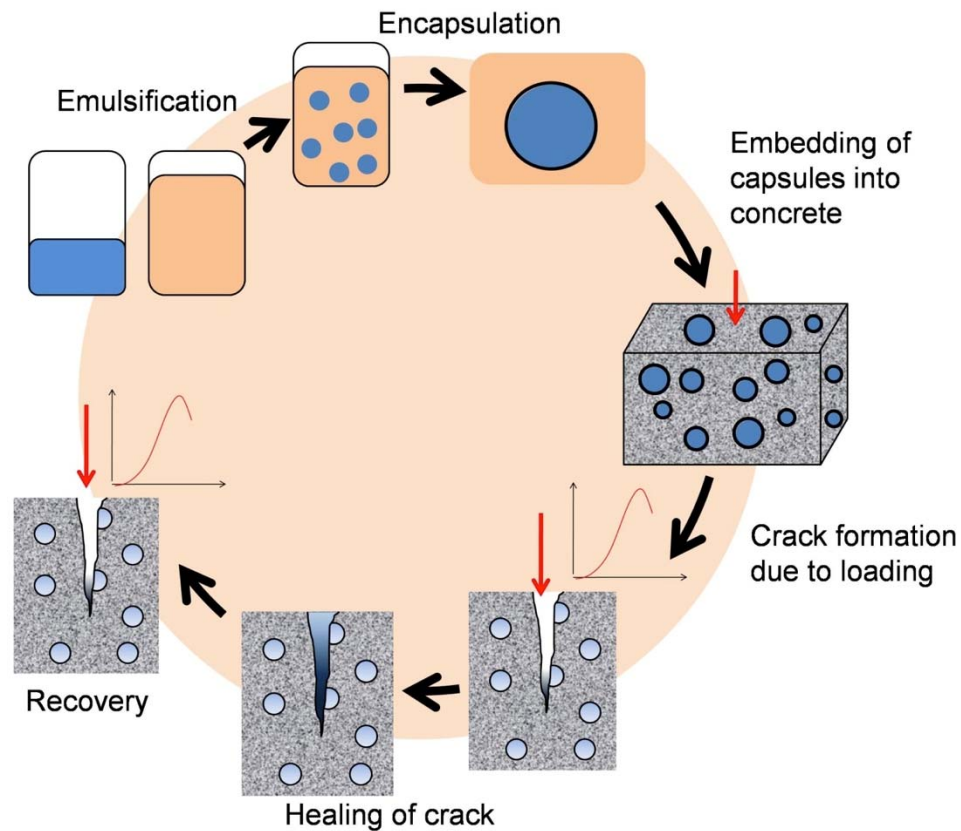


Figure 3.1: Overview of mechanism on the basis of recovery of strength

After curing, a crack propagating through the mortar sample is caused by loading. As the crack causes the capsules to rupture, the aqueous healing solution is released and according to the proposal by Pelletier [6] a CSH gel is formed by the sodium silicate of the healing agent and calcium hydroxide particles in the cement [6, 7]. The cracked mortar samples are retested after an appropriate healing time in order to test the recovery. A healing time of 7 days has been chosen as appropriate [6, 7]. The different steps of capsule production, mortar sample preparation and performance testing with the three point bend and the corrosion test are explained in the following in more detail. Furthermore, characterization methods are introduced.

3.1 Production

As shown in figure 3.1 capsules are prepared via interfacial polymerization. Afterwards they are embedded inside mortar samples. The production of the capsules and the mortars are described in the next paragraphs.

3.1.1 Polyurea/Polyurethane Microcapsules

The synthesis of the polymer microcapsules is adapted from Saihi et al. [24] and first introduced for preparation of microcapsules for self healing concrete in Pelletier [6] where a detailed description can be found. Figure 3.2 gives an overview over the process of capsule preparation. As figure 3.2 shows the first step is to prepare three solutions, O1, O2 and W1. Afterwards a water-in-oil emulsion with solution W1 in O1 is formed and subsequently O2 is added to start the shell formation and shell

growth. W1 is the aqueous solution which is used as dispersed phase in the continuous oil phase, O1, which is a mixture of organic phase with surfactants. O2 is a solution of organic phase with the monomer and catalyst needed for encapsulation. All chemicals used for encapsulation with the standard method are summed up in table 3.1. In the standard method, the surfactants Span 85 and PEG dioleate are used in order to get a stable emulsion. Toluene is taken as the organic continuous phase of the water-in-oil emulsion. DI water acts as the dispersed phase and as a basis of the aqueous core material. The catalyst used is dibutyl tin dilaurate. The standard method uses Basonat F 200 WD, a cross-linking agent from BASF, as the oil soluble monomer.

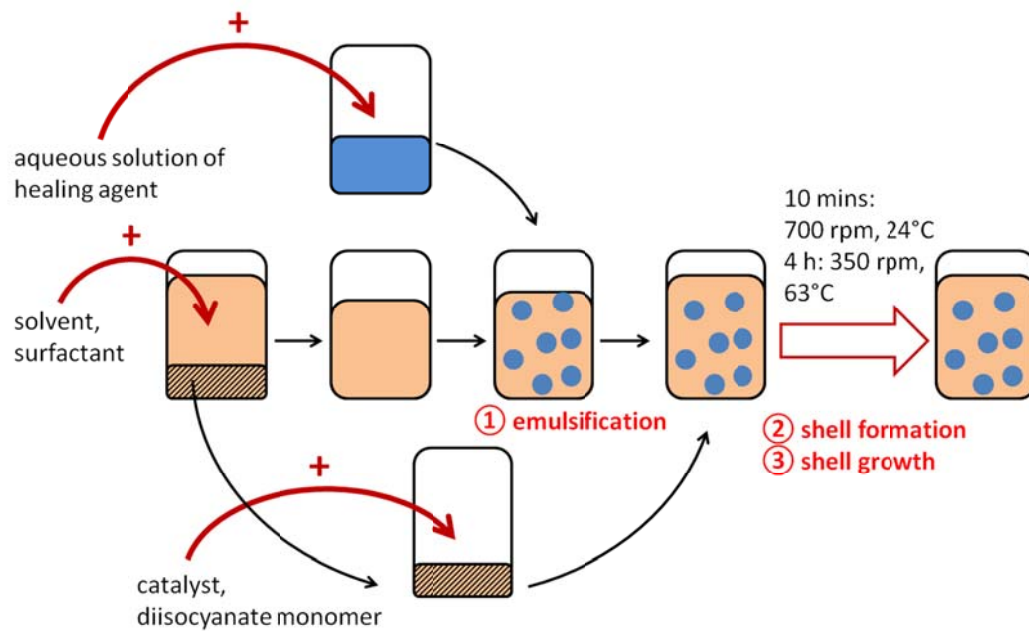


Figure 3.2: Sketch of capsule preparation

Table 3.1: Overview over chemicals used for encapsulation

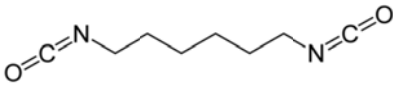
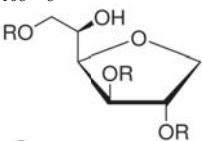
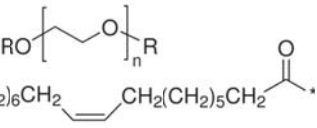
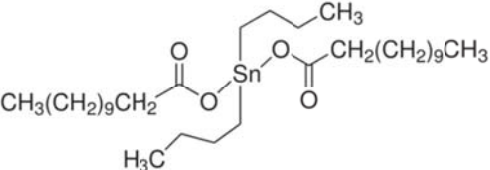
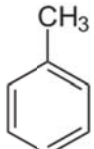
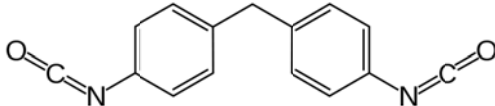
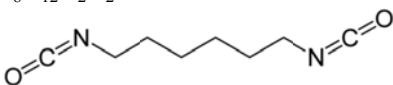
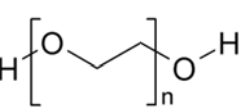
Name	Chemical structure	Function	Comments
Basonat F 200 WD (BASF)	$C_8H_{12}N_2O_2$ 	Monomer, according to BASF crosslinking agent with main component HMDI	Solvent free polyisocyanate, BASF confidential ingredients
Span 85 = Sorbitan trioleate (Sigma Aldrich)	$C_{60}H_{108}O_8$  $R = \text{CH}_2(\text{CH}_2)_5\text{CH}_2\text{CH}=\text{CHCH}_2(\text{CH}_2)_6\text{CH}_3$	Surfactant, maybe part of membrane structure (according to FTIR data by Saihi et al [24])	Tests have been done with different amounts of Span 85: capsule formation possible without Span 85, with less or more, but poor quality
PEG dioleate (Sigma Aldrich)	$C_{20}H_{40}O_4$  $R = \text{CH}_3(\text{CH}_2)_6\text{CH}_2\text{CH}=\text{CHCH}_2(\text{CH}_2)_5\text{CH}_2\text{C}(=\text{O})\text{O}-$	Second surfactant	Role of PEG dioleate has not been investigated in the framework of this work; PEG dioleate is used as 2 nd surfactant according to Saihi et al [24]
Dibutyltin dilaurate (Sigma Aldrich)	$C_{32}H_{64}O_4\text{Sn}$ 	Catalyst	
Toluene (Sigma Aldrich)	$C_6H_5CH_3$ 	Solvent for emulsification	Requirements for oil phase: Solvent needs to be immiscible with water but monomer, catalyst and surfactant have to be soluble in solvent
MDI = Methylene diphenyl diisocyanate	$C_{15}H_{10}N_2O_2$ 	Alternative monomer instead of Basonat	
HMDI	$C_8H_{12}N_2O_2$ 	Alternative monomer instead of Basonat	
PEG	$C_{2n}H_{4n+2}O_{n+1}$ 	Water soluble alternative monomer	First tests with PEG 600 show encapsulation but not as strong as without PEG, further tests should be conducted

Table 3.2 gives an overview over the amounts used to prepare approximately 20 ml of water or calcium nitrite capsules.

Table 3.2: Composition of solutions O1, O2 and W1 to prepare approximately 20 ml of capsules

Solution	Composition
O1	• 90 ml toluene, • 4.2 ml Span 85, • 2.1 ml PEG dioleate After preparation of O2 (less solution in total is left)
O2	• 15 ml O1, • 0.6832 ml Basonat, • 0.047 ml Dibutyl tin dilaurate
W1	• 30 ml DI water, • core material

In this work variations with other monomers, such as methylene diphenyl diisocyanate (MDI) and hexamethylene diisocyanate (HMDI) instead or in combination with Basonat are tested. The variations of the standard method tested in this work are shown in table 3.3.

Table 3.3: Variations in monomer chemistry to standard method

Test	Organic phase monomer	Water phase monomer	Comments/Source
Standard method	Basonat F 200 WD	-	Based on Saihi et al [24] and Pelletier [6]
HMDI as monomer	HMDI	-	Basonat main component is HMDI according to BASF information
MDI as monomer	MDI	-	Based on Saihi et al [24]
Basonat and HMDI	Basonat and HMDI	-	Minimum cross linking agent needed [23]
Basonat and PEG	Basonat	PEG 400 and PEG 600	Interfacial polycondensation between two complementary monomers, theory described in section 2.3 and [30]
HMDI and HMDA	HMDI	HMDA	

Besides using different diisocyanate monomers, which is the oil soluble monomer and which leads to in situ polymerization, the influence of a second monomer in the water phase has been tested. PEG with a molecular weight of 400 and 600 has been tested as the water soluble monomer complementary to Basonat and a mixture of both PEG molecular monomers 400 and 600 has been used. Having two complementary monomers gives interfacial polycondensation with polymerization of the two complementary polymers like PEG and MDI.

3.1.2 Mortar Samples

The mortar samples are prepared according to the standard procedure of ASTM C-109 and described in Pelletier [28, 6]. For six 2-inch-cubes 242 ml of DI water are slowly mixed with 500 g of Portland cement for 30 seconds. After having added 1375 g of Ottawa Sand C-109 an additional mixing of 30 seconds at slow speed is carried out and more mixing for 30 seconds on medium speed is realized. The mixture is set aside for 75 seconds. Meanwhile, the sides of the mixing bowl are scraped. After an additional mixing time of 60 seconds at medium speed the mixture is set aside for 75 seconds again. If requested, capsules are added to the mixture and the final step is to mix for 15 seconds on medium speed. The mortar mixture is filled into molds. The molds have to be filled equally and it has to be ensured that each mold is fully filled with mortar. The mortars harden in the molds for 24 hours and are removed from the molds after 1 day. The samples are submerged into water for 2 days and are

cured for 28 days in a humid air environment. Further tests such as three-point bend testing can be conducted after 28 days of curing time.

3.1.2.1 Graded Mortar Samples

Graded mortar samples have been prepared according to the sketch shown in figure 3.3. The capsules have been placed where tension occurs and no capsules have been placed in the rest of the sample. As explained in section 2.1.4 the bottom half is under tension and the top part under compression. As concrete has low tensile strength but high compressive strength it fails in the tension part when loaded by flexural stress. Thus, the capsules are placed in the bottom part of the mortar sample. The mortar samples are 50% filled with capsule containing mortar with different capsule loading from 2 vol% to 6 vol% and 50% with mortar without capsules.

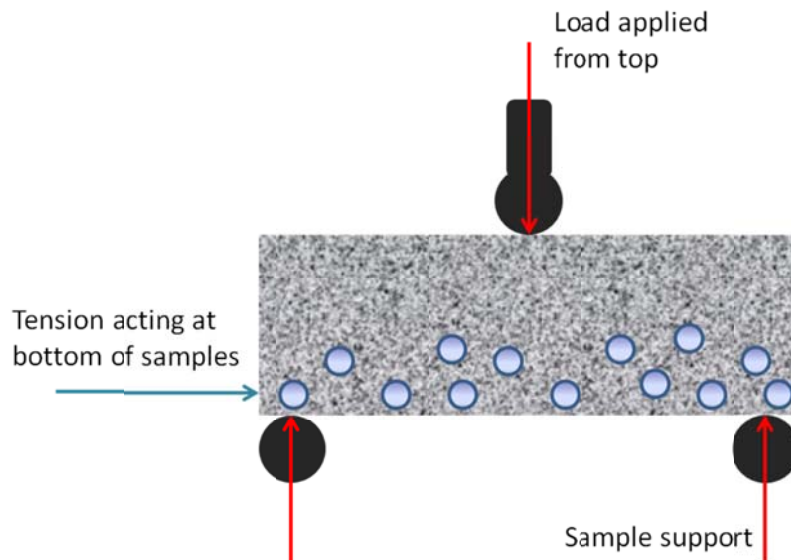


Figure 3.3: Set-up of graded samples with capsules placed where tension acts

Consequently, the total amount of capsules is 1 vol% in the case where the bottom part is filled with 2 vol% of capsules; it is 2 vol% in total for the 4 vol% of capsules at the bottom part and 3 vol% in total in the third case with a bottom part of mortar with a capsule loading of 6 vol% of capsules, respectively. The recovery of flexural strength of the graded samples is determined with the three-point-bend test which is described in chapter 3.3.1.

3.1.2.2 Mortar Samples for Corrosion Tests

The mortars for the corrosion samples are prepared according to paragraph 3.1.2 and the ASTM standard C-109 [31]. The first 50% of the molds are filled and three steel wires are equally put into the mortar. The molds are fully filled afterwards.



Figure 3.4: Set-up of mortar samples for corrosion test

The set-up of the samples is shown in figure 3.4. The steel wires are protected with duct tape for approximately 1 cm just at the place where the wire is entering the mortar sample in order to avoid that the wires corrode outside the concrete samples.

The curing of the mortar samples is done as described in paragraph 3.1.2. The samples

are cracked with the three point bend test. The crack is induced above the steel wire through the sample down to the wire. It has to be made sure that the NaCl salt water is able to penetrate from the surface of the mortar sample to the surface of the wire. Subsequently, a centrifuge tube which has been cut is tightly attached on top of the mortar sample the way it is shown in figure 3.4. The tube is sealed to the mortar sample with rubber sealant. The rubber sealant needs two days to harden. Afterwards, the entire sample has been covered with duct tape as shown in figure 3.4 on the right hand side.

3.2 Characterization

Besides the techniques mentioned in the previous paragraphs, other characterization methods have been used to get information about the nature of the capsules and their influence on mortar samples. For further information literature about analytical instruments are recommended, e.g. the “Handbook of Analytical Instruments” by Khandpur [32]. Various microscope techniques have been used to investigate the optical properties of the capsules including optical microscopy, fluorescence microscopy, Scanning Electron Microscopy (SEM) and reflective microscopy. In order to get information about the crystallinity as well as the impact on the crystallinity of the capsules on mortar samples X-Ray diffraction (XRD) has been conducted. XRD is an X-Ray scattering technique and can provide information about the crystal structure [33]. Mortar samples with and without capsules have been analyzed to get information about the samples and whether the capsules influence the

crystallinity of the mortar samples. XRD has also been done on pure polyurea capsules. The permeability of microcapsules is strongly dependent on the degree of crystallinity - an increase in the degree of crystallinity results in a decrease of permeability [34].

To examine the chemical and mechanical stability of the capsules stability tests have been done. The chemical stability towards alkaline solutions has been tested by suspending the capsules in different solutions shown in the table 3.4 for 7 days in total. The capsules have been imaged after 5 minutes, 1 hour, 24 hours and 7 days. It has been investigated if the capsules break or if still capsules are visible under the optical microscope.

Table 3.4: Solutions for chemical stability test

Test	Sample #	pH	Addition of approx.
Stability in aqueous solution at different pH	1.1, 3.1	1.0	20 vol% HCl solution
	1.2, 3.2	7.0	DI water
	1.3	9.0	20 vol% NaOH solution
	3.3, 1.4	10.0	33 vol% NaOH solution
	3.4, 1.5	10.5	50 vol% NaOH solution
	3.5	11.0	56 vol% NaOH solution
Stability in sodium silicate solutions at different concentrations	2.1, 4.1	11.5	1.6 wt% NaSi solution
	2.2, 4.2	11.75 -12.0	6 wt% NaSi solution
	2.3, 4.3	12.5	17 wt% NaSi solution
	2.4, 4.4	13.0	25 wt% NaSi solution
	2.5, 4.5	13.5	33 wt% NaSi solution

Besides the chemical stability, the mechanical stability of the capsules has been tested. For the mechanical stability test the capsules are imaged with the optical microscope. After that, they are exposed to vigorous shaking and they are imaged again. It is observed if the capsules or emulsion droplets (if no capsule formation took place) respectively break upon the mechanical stress.

3.3 Performance

The influence of the capsules inside mortar samples and their performance for self healing purposes and corrosion inhibition has been examined. Additional to the preliminary tests by Pelletier [6] and Bhattacharyya [7], the influence of capsules on flexural strength has been tested with focus on the influence of selective capsule distribution inside the mortar samples and the flexural strength with capsules of different aqueous agents. By using pure water capsules the contribution of the healing agent, the sodium silicate powder, has been determined. Furthermore, corrosion tests have been conducted.

3.3.1 Determination of Recovery in Flexural Strength

The cured mortar samples are loaded with the three-point bend test to measure the flexural strength. This is the point of incipient failure. If recovery is tested a load is applied until an initial crack is formed. The samples are healed for 7 days and retested

under the same conditions. The three-point-bend test was used to examine the flexural strength of the mortar samples. The set-up can be seen in figure 3.5.

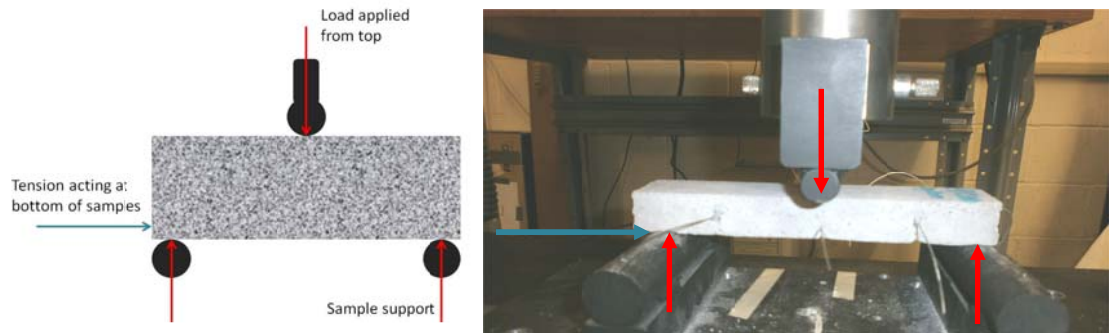


Figure 3.5: Set-up of three point bend test for mortar samples

The sample specimen is hold by two supports and load is applied from the top. Thus, tension is acting on the bottom side of the sample where failure occurs first. The speed of the applied load is kept constant and the extension and force is measured. As soon as the load drops by an amount of 25% of its maximum load the application of load is stopped and the sample is removed automatically done by the Instron machine. By known dimensions of the sample the maximum load in [Pa] can be calculated by dividing the force with dimensions of [N] by the area [m²].

3.3.2 Corrosion Test

The set-up for the corrosion test is shown in figure 3.6. The figure has a sketch of the corrosion experiment (a) and photos of the sample (c) as well as the whole set-up (b). A 0.5 M NaCl salt solution is filled in the centrifuge tube on top of the mortar sample and the potential between the steel wire inside the mortar sample and a reference electrode inside the salt solution is measured and recorded by a computer. The

measurement is started as soon as the NaCl water solution is added. The potential is measured for up to 7 days.

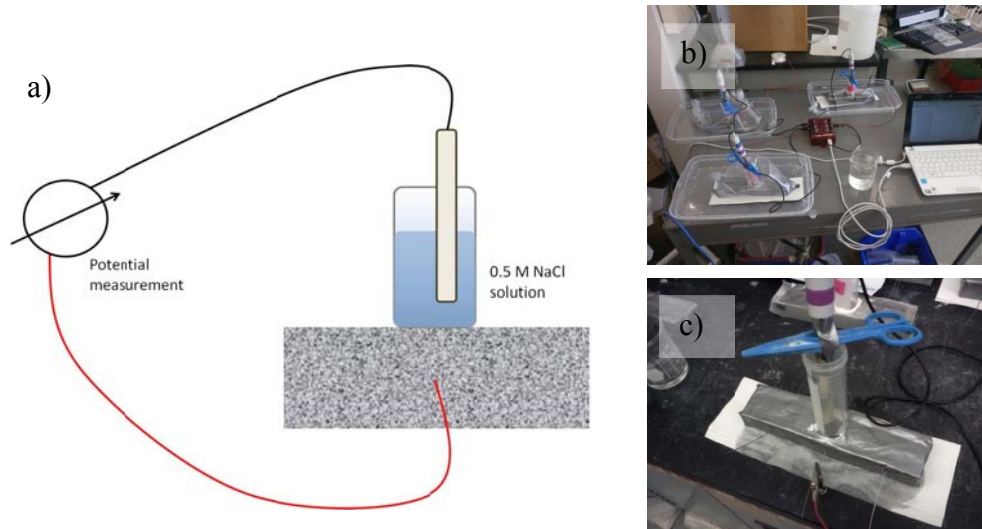


Figure 3.6: Set-up of corrosion experiment with mortar samples

As a preliminary test the corrosion of the steel wires in different solutions outside mortar samples is investigated. For this preliminary test, the steel wires used for the corrosion test described above are tested in 0.5 M salt solution, 6.25 wt% and 12 wt% calcium nitrite solution and a 25 wt% sodium silicate solution.

CHAPTER 4

FINDINGS

4.1 Production

Different aqueous solutions have been encapsulated with the method described in paragraph 3.1.1 which is based on Pelletier [6], Frère [23] and Saihi et al [24]. Pure water has been encapsulated to examine the influence of the healing agent on the recovery and the general impact of capsules inside mortar samples. The influence of the water capsules are compared to the impact of sodium silicate capsules. Calcium nitrite dissolved in water was used because of its well known corrosion inhibition effects.

4.1.1 Water Capsules

The preparation of the water capsules has been conducted based on paragraph 3.1.1. The aqueous phase contained pure DI water solely. The capsules have been made to get information about the influence of the healing agent, e.g. sodium silicate, and the contribution of the capsules inside the mortar samples. To investigate the capsules several microscope techniques have been used among others. The yield was approximately 20 vol% of the total liquid amount, significantly higher than the yield for sodium silicate capsules achieved by Pelletier [6] and Bhattacharyya [7]. It was

found out that the yield is directly dependent on the amount of emulsion. A higher yield of emulsion compared to sodium silicate has been achieved with water, calcium nitrite and with various dyes dissolved in water. Different monomers have been used for encapsulation. Based on the work of Pelletier [6] Basonat F200 WD, a cross-linking agent from BASF, has been used as the oil soluble monomer. Besides, tests with hexamethylene diisocyanate (HMDI) and diphenylmethylen diisocyanate (MDI) as the oil soluble monomer have been done. But Basonat showed the best quality in terms of strength and durability of the capsule membrane. Consequently, Basonat has been used for the encapsulation for the tests described in this framework. It has also been tried out to produce capsules without any monomer. But as expected and shown in figure 4.1 on the left no capsules are formed without monomer and just an emulsion is produced.

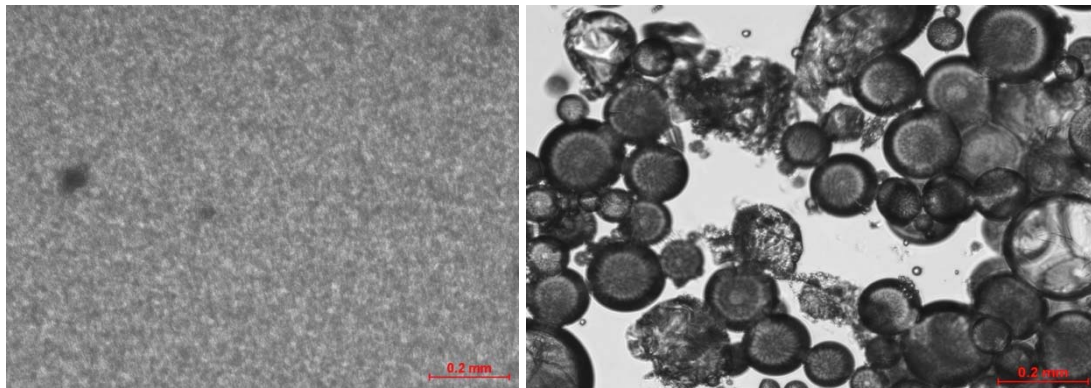


Figure 4.1: Emulsion without monomer, no capsule formation and with no catalyst (the capsules are very fragile based on their stability is shown in 4.2.1.4)

Capsules without dibutyltin dilaurate which is used as catalyst were produced. The image is shown in figure 4.1. A stability test conducted according to section 3.2 (results are discussed in paragraph 4.2.1.4) showed that these capsules break upon

mechanical stress. If capsules break in the stability test it can be assumed that the polymer shell is thin and fragile. It could be that the capsules are more fragile because of different chemical properties.

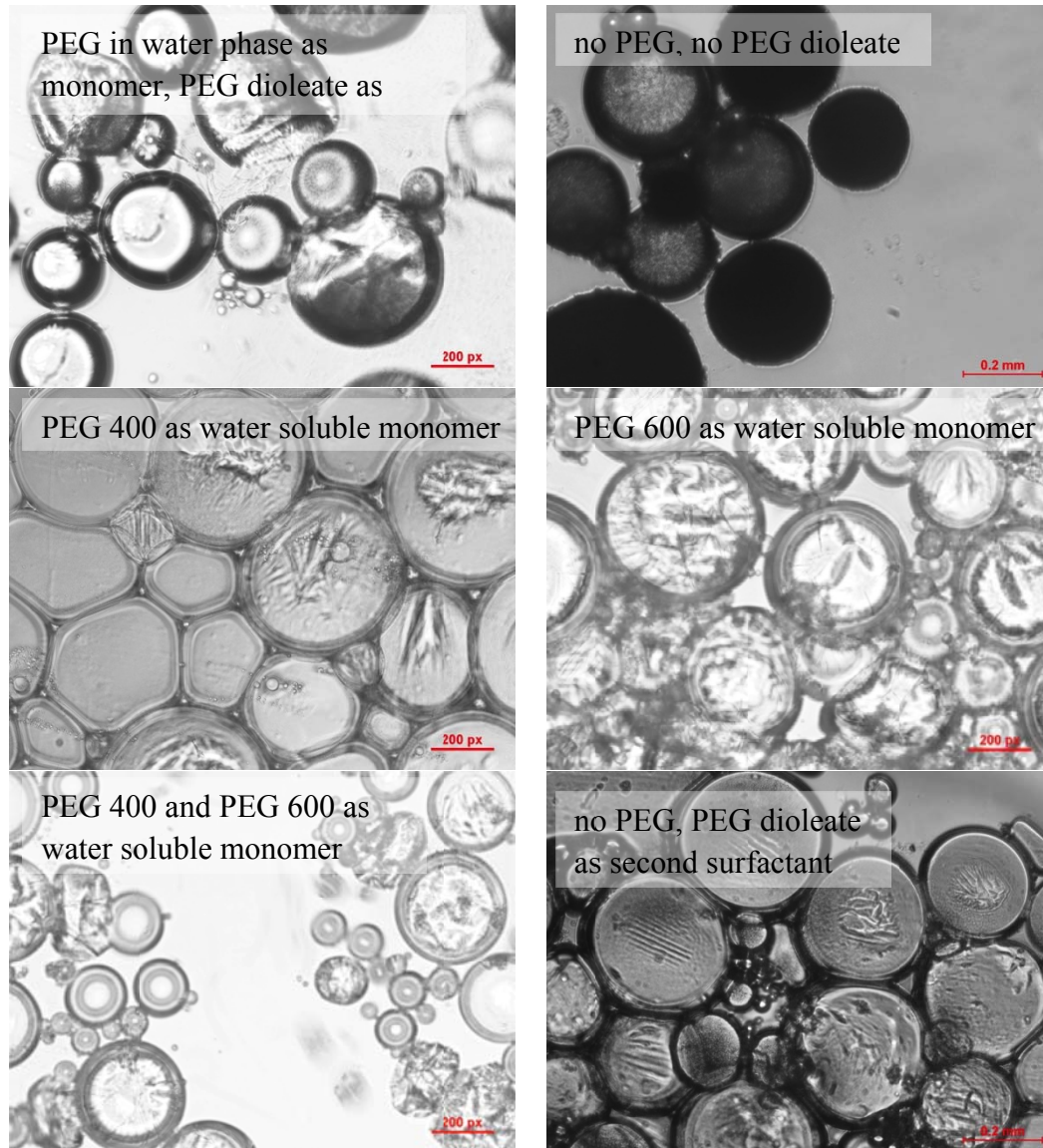


Figure 4.2: PEG test on wall formation with different Polyethylene glycols as second monomer and PEG dioleate as second surfactant

Furthermore, it is assumed that polymerization took place but either it was not completely polymerized or the thickness of the shell was small which leads to thin and fragile capsules which break upon low mechanical stress. Besides the capsules with

Basonat as the only monomer, capsules with PEG as a second monomer have been produced. PEG at different molecular weights and no PEG nor PEG dioleate at all have been tested. No significant difference can be seen under the optical microscope as seen in figure 4.2. As no significant improvement has been observed, the performance tests have been conducted with the procedure described in paragraph 3.1.1. As shown in paragraph 4.2.1.4 the capsules with no PEG dioleate are fragile and break easily.

4.1.2 Calcium Nitrite Capsules

The encapsulation of calcium nitrite was successful in different weight ratios of calcium nitrite. Capsules with an amount of 6.25 wt% and 12 wt% have been made with a good yield of up to 20 vol% compared to the total amount of liquid (solvent and water).

4.1.3 Sodium Silicate Capsules

The encapsulation of an aqueous solution of sodium silicate has been successfully conducted like described in [6] and [7] and shown in figure 3.2. Nevertheless, it has been found out that the method suggested by Pelletier [6] leads to a very low yield for sodium silicate capsules.

Table 4.1: Tests to obtain high yield of sodium silicate capsules

Approach	Justification and source	Observation
Increase of temperature	Increase temperature leads to better diffusion of molecules through membrane [23]	No change
Increase time for polyurea/ polyurethane shell growth (up to 12 hours)	Increasing time allows better and entire shell growth [23]	No change in between hour 0 and 6, after 12 hours stuck to the ground
Decrease of pH with nitric acid until ca. pH 10.8	Dependence of yield on pH has been observed in preliminary tests, possibility of lowering as well as altering pH are discussed further down in this paragraph in table 4.2	Higher yield, not as high as water, CaNi capsules
Using different amounts of NaSi and also dropping pH at lower concentrations of sodium silicate		At low NaSi concentration (max. 5 wt% of NaSi) slightly better yield, but capsules very fragile
Sodium silicate gel formation, suspending, dropping pH of NaSi gel in water to 8-9		Encapsulation didn't work out, stuck to ground, probably too dense and change of viscosity
Addition of water droplets at lower pH while shell growth		No significant change
Use of liquid NaSi instead of solid NaSi which is dissolved in DI water		
Adding PEG to water, with/without PEG dioleate as 2 nd surfactant	Formation of polyurethane via interfacial condensation possible [23]	Results are described in the 4.1.1 paragraph in more detail
Addition of more catalyst	Catalyst is needed for polymerization reaction [23, 24]	Stable droplets observed which are a good emulsion or very fragile capsules
Alteration of monomer	Various papers such as [23, 24] show encapsulation with other monomers	As described in 4.1.1 it was possible to encapsulate with alternative monomers, but high yield has not been obtained

The yield of capsules is less than 2 vol% based on the total amount of liquid (water and solvent) whereas the yield with just water and calcium nitrite is up to 20 vol% of capsules based on the total amount of water and solvent. Table 4.1 sums up the different tests done in order to obtain a high yield sodium silicate capsule solution. The observations described in table 4.1 show that it was not possible to obtain sodium silicate in the same high yield as water and calcium nitrite capsules with the methods of table 4.1. According to Saihi et al [24] the reaction takes place between the diisocyanate and the water in the aqueous phase. By adding sodium silicate the pH increases to 14. Therefore, tests with encapsulation of aqueous solutions at different pH have been done and showed that the yield decreases at high pH. The pH can be dropped until a pH of 10.7 before gel formation of the silicate starts. The gel cannot be encapsulated by the method used. Table 4.2 is a list of experiments done to try to decrease the pH in order to increase the yield of capsule formation. But as well known and described in literature, e.g. [35], it is not possible to obtain an aqueous sodium silicate solution at lower pH than 10.7 without gel formation and the methods described in table 4.1 and table 4.2 do not show remarkable improvement.

Table 4.2: Tests for altering (lowering) pH of sodium silicate solution

Method	Observation
Addition of alcohol (MeOH) in different amounts and combinations with nitric acid to drop pH of NaSi solution	MeOH has no effect on pH or gel formation and as pH drops underneath 10.7 gel formation takes place
Use of liquid sodium silicate in different concentrations and addition of acid	As soon as pH decreases lower than 10.7 gel formation takes place

It has been observed that the emulsification step in the interfacial polymerization is the leading factor determining the yield of capsules. The shells of the capsules are forming at the emulsion droplet's interface [20]. In the case of sodium silicate an equilibrium of three layers, an oil layer on top, a very small emulsion layer in the middle and a water layer at the bottom, can be observed. Whereas, with pure water and calcium nitrite just two layers are formed: An oil layer on top and an emulsion layer at the bottom. As described in paragraph 2.3 and 3.1.1 the polymer shell forms around the emulsion droplets. Thus, there is just capsule formation where emulsion is. If the emulsion layer is small, the yield of capsules is low. Consequently, the yield for sodium silicate containing capsules is poor. The amount of surfactant [36] and amount of salt [37] have a crucial effect on the emulsification. Further investigation on how to increase the emulsification layer and shift the equilibrium to a two phase system with a high amount of emulsion have to be done in order to obtain high yields of sodium silicate capsules.

4.2 Characterization

Various characterization methods have been used to obtain information about the capsules and their properties inside mortar samples. The characterization of the capsules is presented first, followed by the observations and discussions of properties of the capsules inside mortar samples.

4.2.1 Capsules

The capsules have been mainly examined with focus on their strength. Microscope techniques have been used for investigation of capsule formation, stability. Fluorescence microscopy can provide information of chemistry of core material.

4.2.1.1 Optical Microscope

Figure 4.3 shows optical microscope images of the capsules. It can be seen that a shell has been formed. The size distribution is large with capsules in the order of up to 800 microns and very small capsules with a diameter of 10 microns or less. Figure 4.3 shows that capsule formation has been successful with all the different aqueous solutions tested (pure water, calcium nitrite, sodium silicate and a mixture of sodium silicate and calcium nitrite). Furthermore, it can be seen that in the case of encapsulation with sodium silicate (images at bottom of figure 4.3) the capsules float in residues which are an indication that polymerization also took place in the bulk of the oil phase as well as at the interface between water droplets and oil. This observation along with the poor yield supports the fact that due to poor yield of the emulsification polymerization does not take place just on the interface as the formed interfacial area is smaller than available monomer for polymerization. Thus, it has to be investigated how to increase the quantity of the emulsion layer.

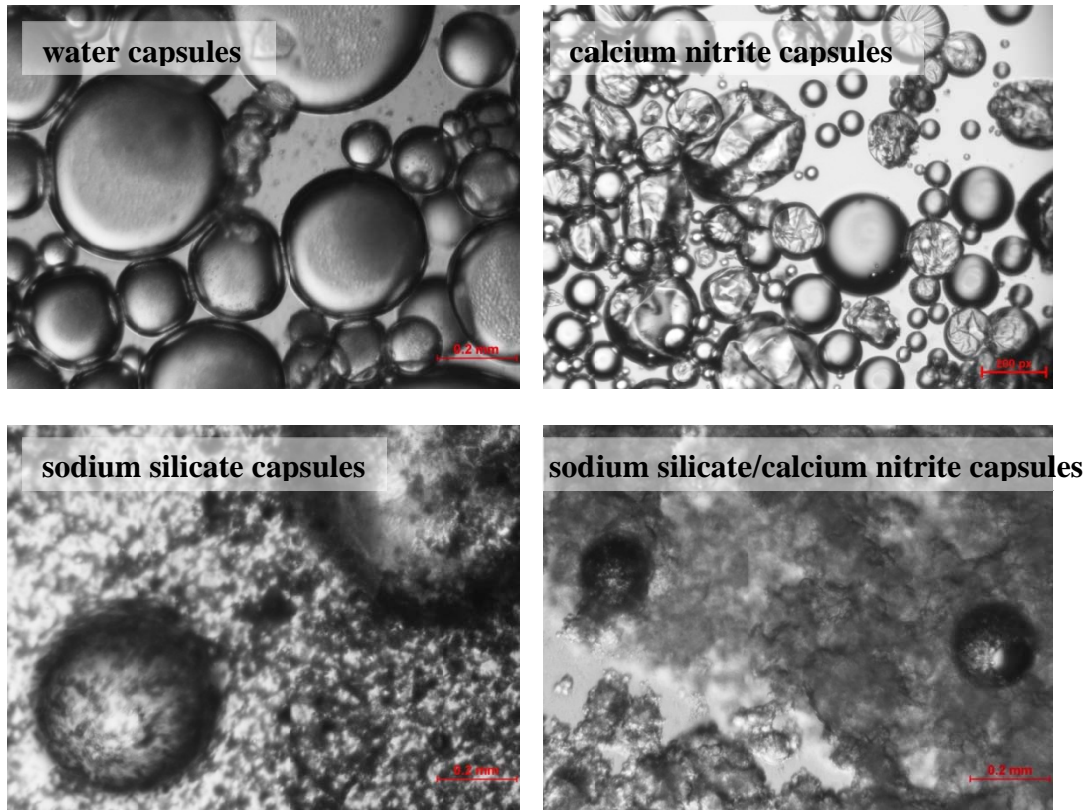


Figure 4.3: Optical microscopy images of capsules with different aqueous contents

Figure 4.4 shows images of water capsules done with the optical microscope at different magnifications with focus on the shell. They show the shell formation around the water droplets. Additionally, it can be seen that small droplets are formed besides the major capsules.

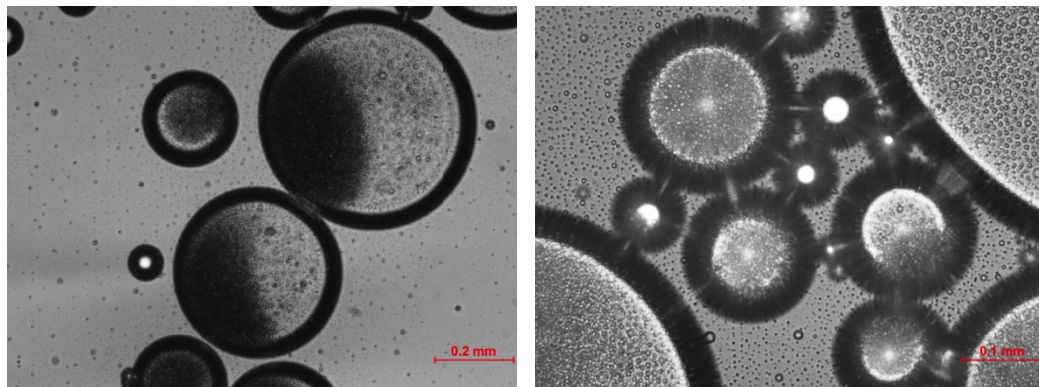


Figure 4. 4: Microscopy images of capsules containing pure water

The lights seen in the membrane are because of the light of the optical microscope and are just imagine objects. In order to get information about the nature of the small droplets and whether they are water, oil or air bubbles, fluorescence microscopy has been done.

4.2.1.2 Fluorescence Microscopy

Fluorescent dye has been added to the water phase in order to show that a water-in-oil emulsion has been formed and that the whole amount of water has been successfully encapsulated. The fluorophor (4,6 carboxyfluorescein) is water soluble. The experiment has been conducted without healing agent. Figure 4.5 shows the water capsules under the optical microscope with and without fluorescence.

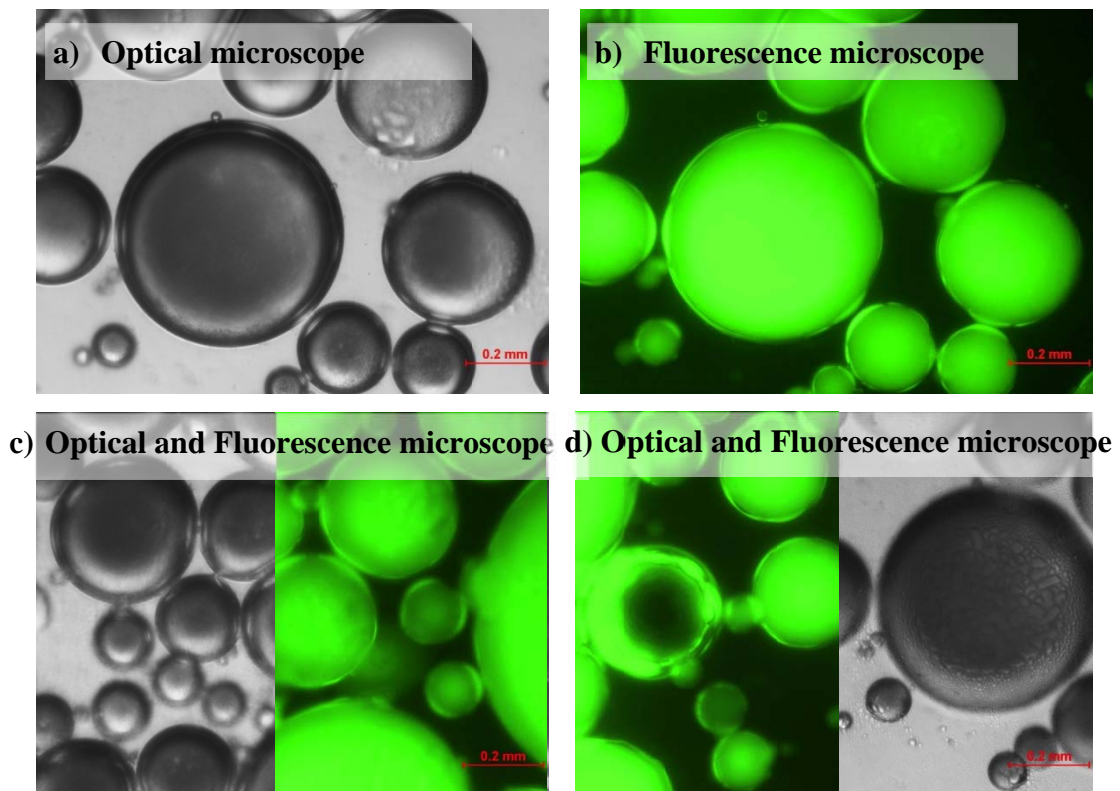


Figure 4.5: Fluorescence images in comparison with optical microscopy, with water soluble dye

It can be clearly seen that the water phase containing just water soluble fluorophor is fully encapsulated. No fluorescence could be seen outside capsules. It can be assumed that just water is encapsulated and the solvent stays outside the capsules.

4.2.1.3 Crystallinity

As the permeability of the capsule membrane is a crucial property for the application of the capsules as self healing enhancement factors it has been tested. As described in paragraph 3.2 the permeability is dependent on the degree of crystallinity of the polymer shell [34].

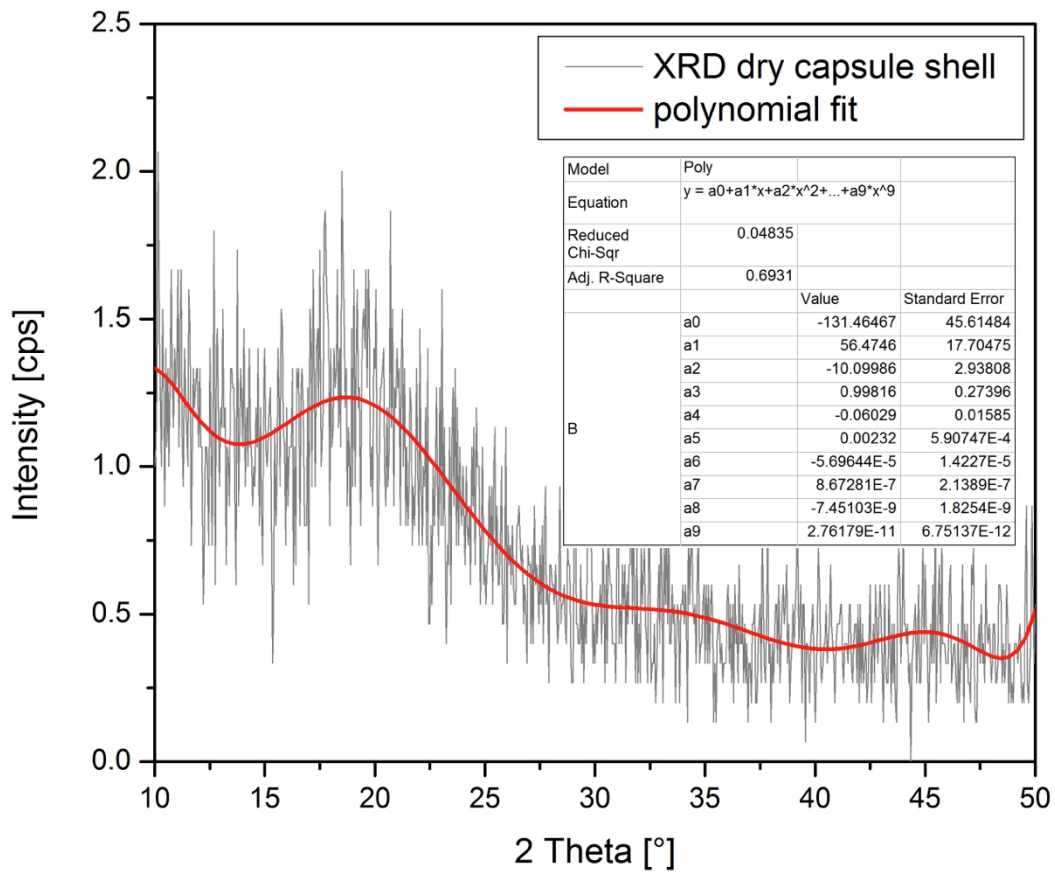


Diagram 4.1: XRD results for dry capsules

Thus, X-Ray diffraction of dry capsules has been done. The result is shown in diagram 4.1. The diagram 4.1 indicates that the capsules are amorphous. There is an indication for the characteristic peak of polyurethane in the range of $15^\circ < 2\theta < 25^\circ$ [34] but the peak partly disappears in the noise. The maximum intensity is with 2 cps not high.

4.2.1.4 Stability of Capsules

To examine the stability of the polyurea and polyurethane microcapsules inside alkaline solutions tests with capsules with a) produced with the standard method described in 3.1 (without PEG), and b) with PEG as a second monomer, are dispersed in alkaline solutions at different pH. The capsules are imaged after 5 minutes, 1 hour, 24 hours and 7 days. The images are shown in table 4.3 to table 4.6. Table 4.3 shows the images of polyurea capsules which are exposed to aqueous solutions at different pH for 1 week. The pH of the solution has been adjusted with sodium hydroxide (NaOH) and hydrogen chloride (HCl). As the capsules are highly hydrophobic they agglomerate upon exposure to an aqueous solution as seen in table 4.3 if not dispersed with a dispersant. The capsules are not destroyed even after a week inside the alkaline solution. Also in comparison to water capsules at pH 7.0 the capsules do not differ in appearance. But it can be seen that the membrane gets thin compared to the images of capsules seen in figure 4.1. It could be that the membrane is permeable and surrounding water gets inside the capsule which leads to swelling of the capsules.

Table 4.3: Optical microscope images for stability test of capsules without PEG

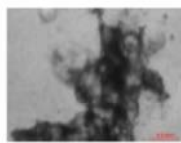
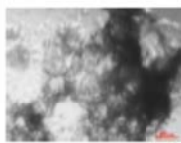
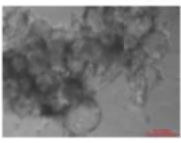
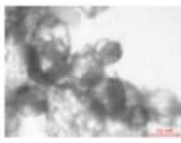
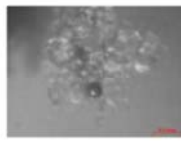
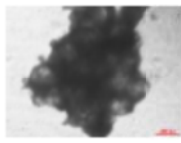
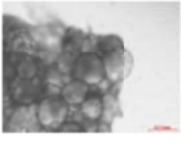
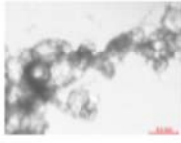
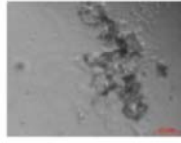
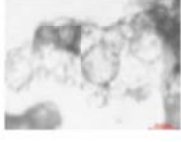
Sample	5 minutes	1 hour	24 hours	7 days
1: pH 1.0				
2: pH 7.0				
3: pH 9.0				
4: pH 10.0				
5: pH 10.5				

Table 4.4 shows polyurea capsules from the same batch as in table 4.3 immersed into sodium silicate solutions at different concentrations. In comparison to table 4.3 it can be clearly seen that sodium silicate solution has a greater destroying effect on the capsules than alkaline water. After 1 week there are no capsules anymore (images without capsules are marked in red). The remaining polyurea shells can be seen but they are clearly broken. It seems like the capsules are already affected after a very short time of 5 minutes.

Table 4.4: Optical microscope images for stability test of capsules without PEG

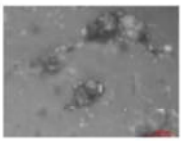
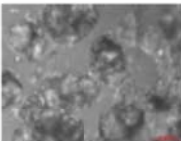
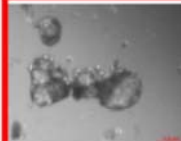
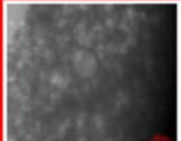
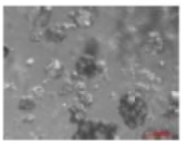
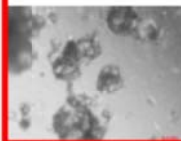
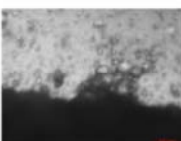
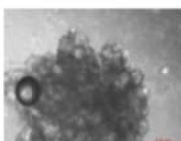
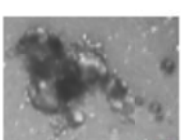
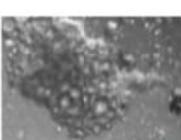
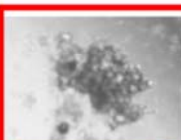
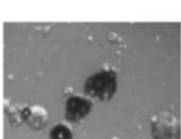
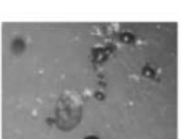
Sample	5 minutes	1 hour	24 hours	7 days
1: pH 11.5				
2: pH 12.0				
3: pH 12.5				
4: pH 13.0				
5: pH 13.5				

Table 4.5 shows the tests done with polyurethane capsules (with PEG as second monomer) immersed to alkaline water and high acid water. In general, it can be seen that the capsules are stable. The microscope images indicate that the capsules inside the aqueous solution of pH 1 break after 1 hour. Thin shells can be seen after 1 hour but the capsules are not stable anymore. It could be that very low pH destroys the capsules. It is also hard to distinguish the image taken after 5 minutes for sample 5.

But as all the other images of sample 5 clearly show capsules it can be assumed that the capsules done with PEG do not break at high alkaline solutions.

Table 4.5: Optical microscope images for stability test of capsules with PEG

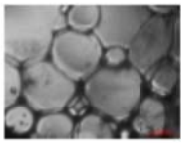
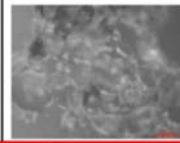
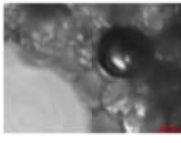
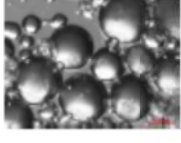
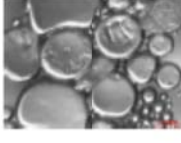
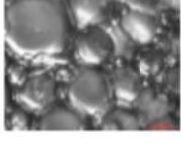
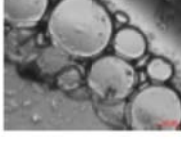
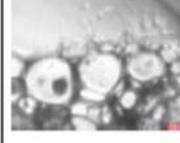
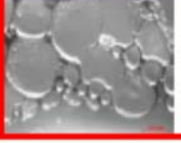
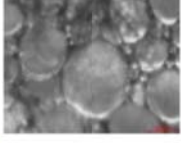
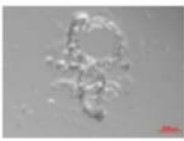
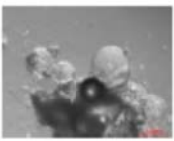
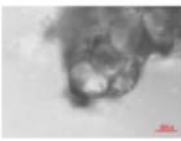
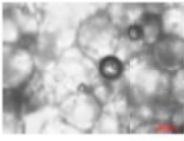
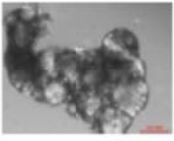
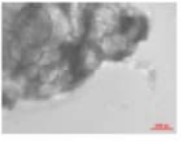
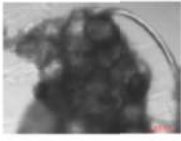
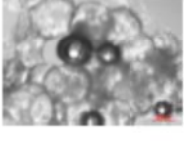
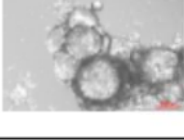
Sample	5 minutes	1 hour	24 hours	7 days
1: pH 1.0				
2: pH 7.0				
3: pH 10.0				
4: pH 10.5				
5: pH 11				

Table 4.6 shows the polyurethane capsules from the same batch as in table 4.5 exposed to sodium silicate solutions. It can be clearly seen that the effect of the sodium silicate is more significant than the one of the alkaline solution from table 4.5. It can be seen that sodium silicate solutions at high pH (over 12) have a negative effect leading to breakage of the polyurethane capsules.

Table 4.6: Optical microscope images for stability test of capsules with PEG

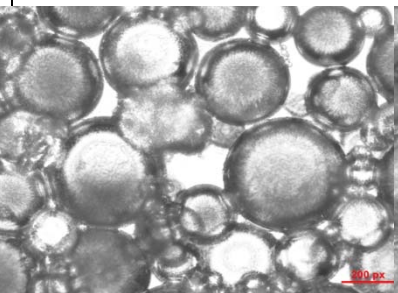
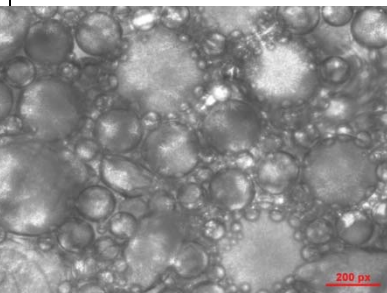
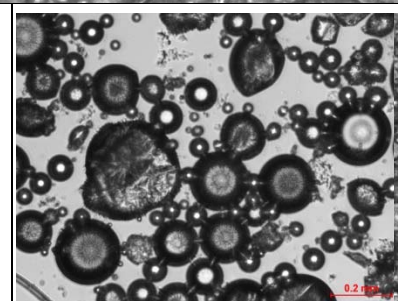
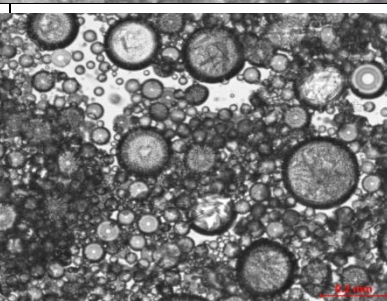
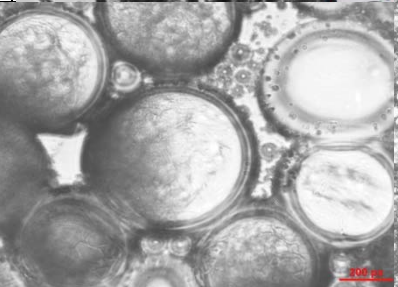
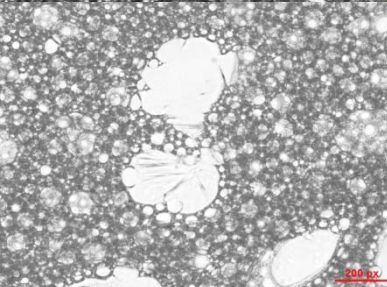
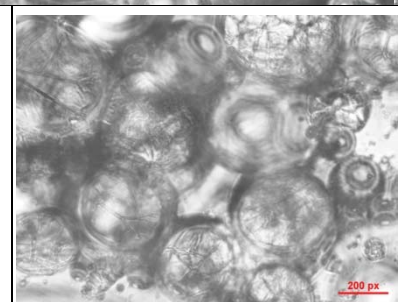
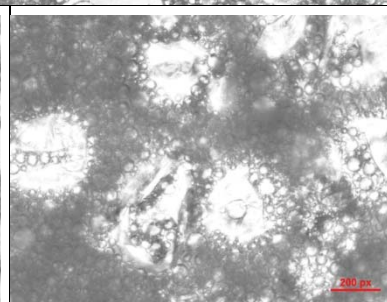
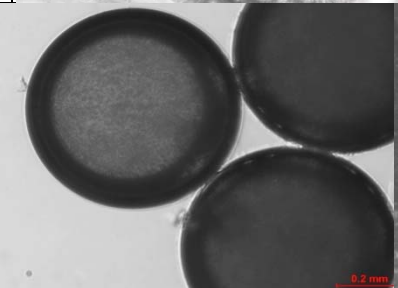
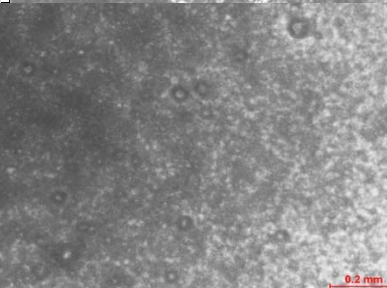
Sample	5 minutes	1 hour	24 hours	7 days
1: pH 11.5				
2: pH 11.75				
3: pH 12.0				
4: pH 13.0				
5: pH 13.5				

In summary, it can be concluded that the capsules do not break due to exposure to alkaline solutions but that they are destroyed in high pH sodium silicate solutions after being immersed for at least 7 days. Furthermore, the destruction of the capsules exposed to high alkaline sodium silicate solutions could also explain the low yield of sodium silicate capsules. Because in addition to the fact that the amount of emulsion is lower for sodium silicate emulsions compared to water and calcium nitrite, sodium silicate in high amounts could lead to breakage of the polyurea and polyurethane capsules. It seems like the difference between the polyurea (prepared according to

paragraph 3.1) and polyurethane (with PEG as 2nd monomer) on the chemical stability is not significant.

As an easy and fast determination of the mechanical stability of the capsules a shake test where the capsules are imaged before and after gently shaking has been done. Table 4.7 lists the results of the stability test. It can be clearly seen that the capsules without PEG dioleate but PEG as a second monomer and without any PEG are very fragile. Shaking leads to breakage of the droplets. In another test, the capsules have been observed over a time period of over 1 week and no phase separation which is typical for an emulsion after that time has occurred. A reference sample with an emulsion has been also tested and consequently it can be assumed that indeed capsule formation took place.

Table 4.7: Optical microscope images for shake test to check mechanical stability of different kinds of capsules

Test	Image before shaking	Image after shaking
<p>normal procedure: there are mechanical stable capsules, only very large capsules break upon hard shaking</p>		
<p>No catalyst: images do not allow clear conclusion, it seems like capsule formation but less stable but fragile</p>		
<p>no PEG dioleate, with PEG 400: Any reasonably-sized capsules left after the shake tests seem distorted in shape and texture. Capsules are very fragile.</p>		
<p>with PEG 600: similar observations as with PEG 400</p>		
<p>no PEG dioleate, no PEG: These are not capsules, simply an emulsion. Shaking vigorously only broke the pseudo-capsules</p>		

The tests indicate that the capsules are fragile upon mechanical stress but membrane formation took place. The capsules at standard preparation method and the ones without catalyst seem to be the most stable capsules. It is surprising that it is possible to get capsules without catalyst. It could be that the polymerization is an auto-polymerization between the diisocyanate and water where no catalyst is needed. Further investigation on the chemical reactions taken place when the wall is formed have to be conducted.

4.2.1.5 Capsules in wet mortar

Figure 4.6 shows capsules in wet mortar after the preparation of mortar. It is obvious that the capsules are not broken due to the mixing process to repair mortar samples. Therefore, it can be assumed that the capsules inside the wet mortar samples are still intact.

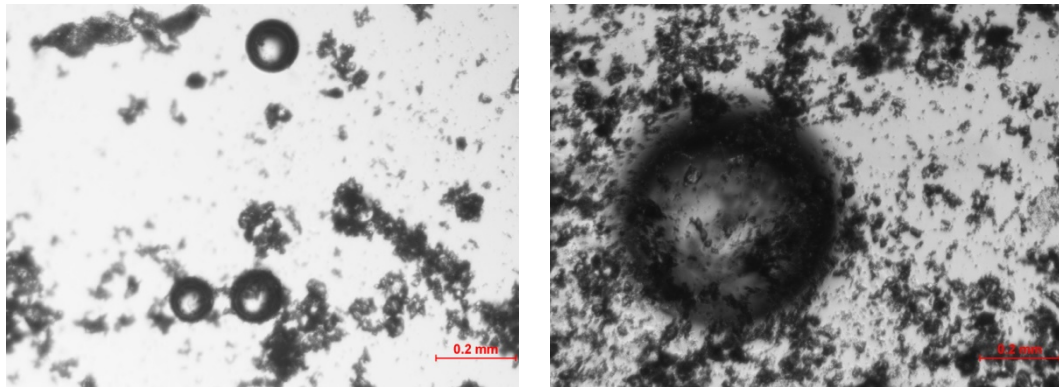


Figure 4.6: Optical microscopy images of capsules inside wet mortar after mortar preparation including mixing

4.2.2 Characterization of Mortar Samples

In order to examine the self healing mechanism and to show how the technology works, mortar samples with capsules have been investigated. A main question to answer is if the capsules are broken or not inside the hardened mortar samples.

4.2.2.1 Optical Investigation of Capsules inside Mortar Samples

The cracked area of the mortar samples has been investigated with the reflective microscope. Figure 4.7 shows the images. Circular holes are visible on the surface. To show if the holes are air or capsules on the surface, capsules with red dye solution have been imbedded inside the mortar samples. Red dye can be seen and show that the holes have been capsules and also that the capsules release the dye selective upon cracking. According to the images of figure 4.7 it can be assumed that the capsules are not destroyed due to preparation of mortar and that they can release their content upon cracks.

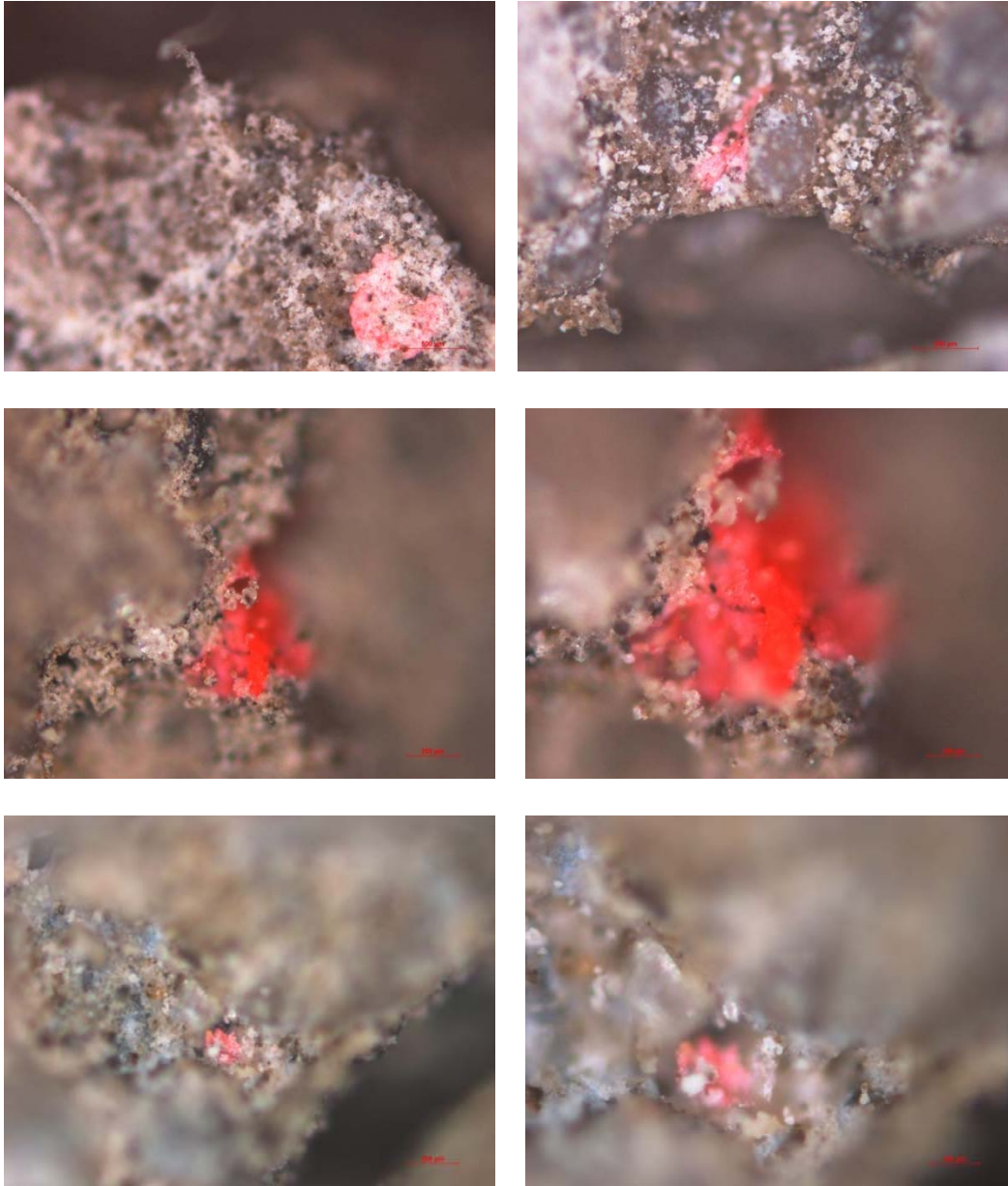


Figure 4.7: Images of cracked area with colored capsules

SEM images of the capsules inside mortar at the cracked area are shown in figure 4.8

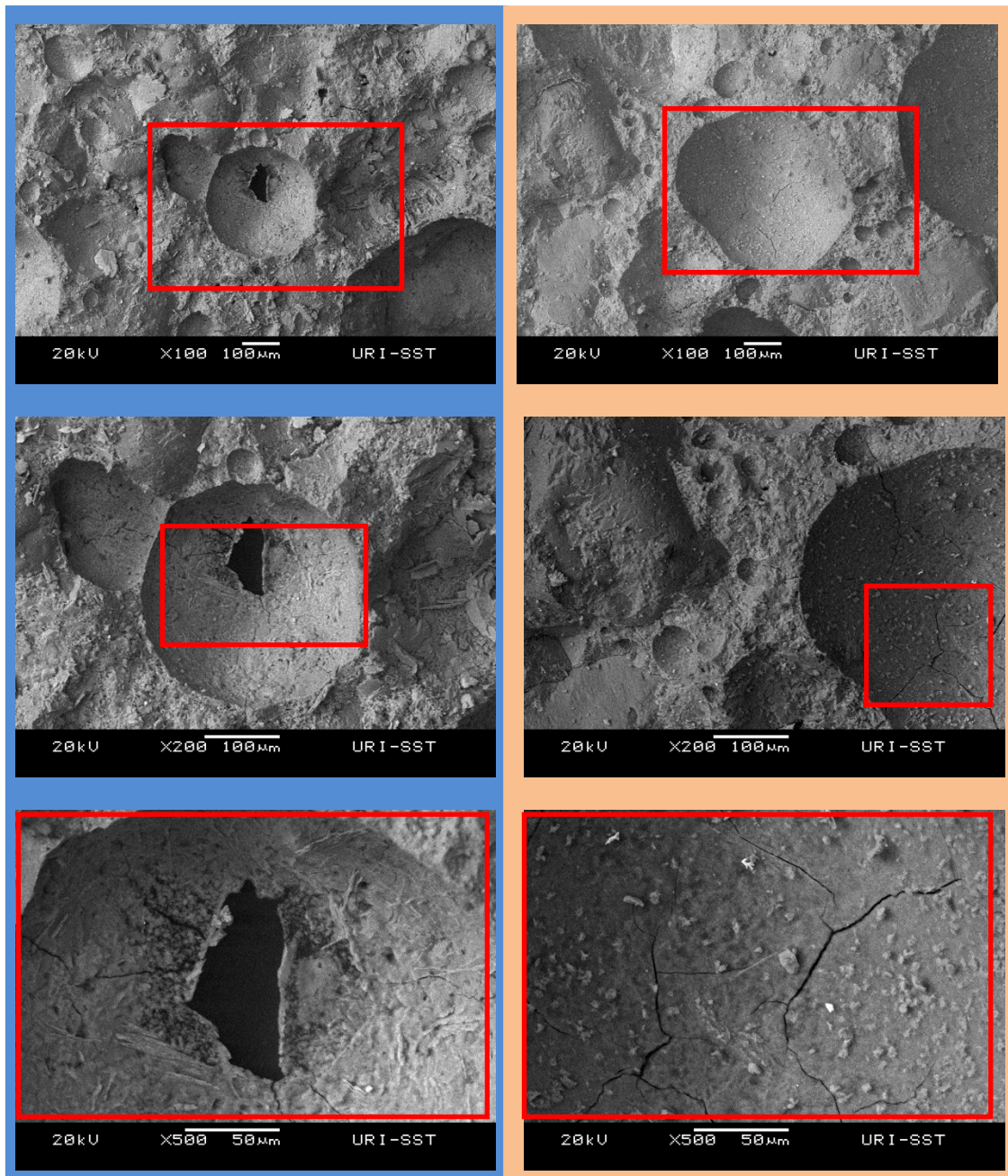


Figure 4.8: SEM images of capsules inside mortar samples at different magnifications

Figure 4.8 shows two capsules inside mortar at different magnifications. The left side has images of a capsule with a hole inside. It could be that the capsule broke inside the mortar due to stress because of hydration or loads while inside the mortar sample or

due to the impact of the loading of the crack. The images on the right show another capsule with a close up of the inner shell. Tiny cracks in the shell can be seen.

4.2.2.2 Crystallinity

The influence of the capsules on the crystal structure of the mortar samples has been investigated with X-Ray diffraction. Mortar samples with and without capsules have been examined and can be compared. As seen in diagram 4.2 the location of major peaks are the same (location of peaks are marked). Thus, there is no significant difference visible. Thus, the capsules do not affect the crystalline structure of the mortar at such low amounts of capsules. The intensity can vary from sample to sample due to the diversity of mortar.

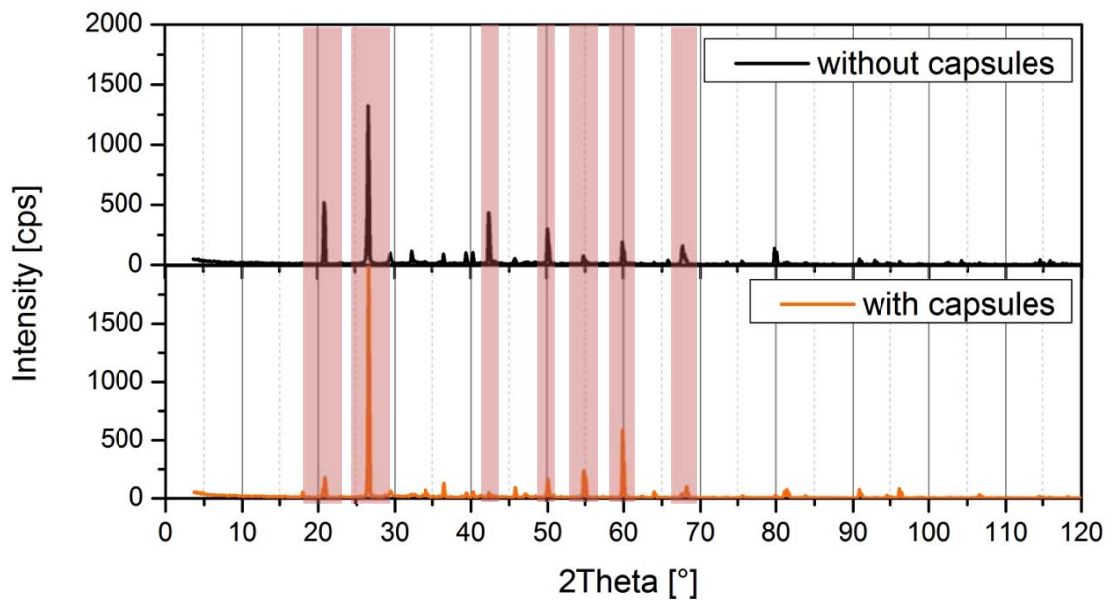


Diagram 4.2: XRD of mortar samples with and without capsules

4.3 Performance

The performances of the capsules as a self healing enhancer and as a corrosion inhibitor are discussed in the following chapter. The determination of self healing ability is based on the recovery of flexural strength measured with the three point bend test.

4.3.1 Water Capsules as Reference

In order to get information about the contribution of the presence of capsules and the contribution of the self healing agent, e.g. sodium silicate, capsules with just water as the aqueous phase have been prepared and tested. Diagram 4.3 shows the recovery of flexural strength of mortar samples with different amounts of capsules. It can be seen that the samples with capsules show better recovery than the control samples without capsules. As described in paragraph 3.3.1 the samples are loaded until failure, the load is stopped and the samples are allowed to heal for 7 days until they are loaded again and the second load of failure is measured. The recovery is determined by dividing the second maximum load at failure by the first maximum load at failure. The recovery is measured for different amount of capsules and compared to the reference samples without any capsules. The samples with sodium silicate inside the aqueous solution show slightly better recovery. However, due to limited repetitions and because of the versatility and inhomogeneous nature of concrete inaccuracies can occur.

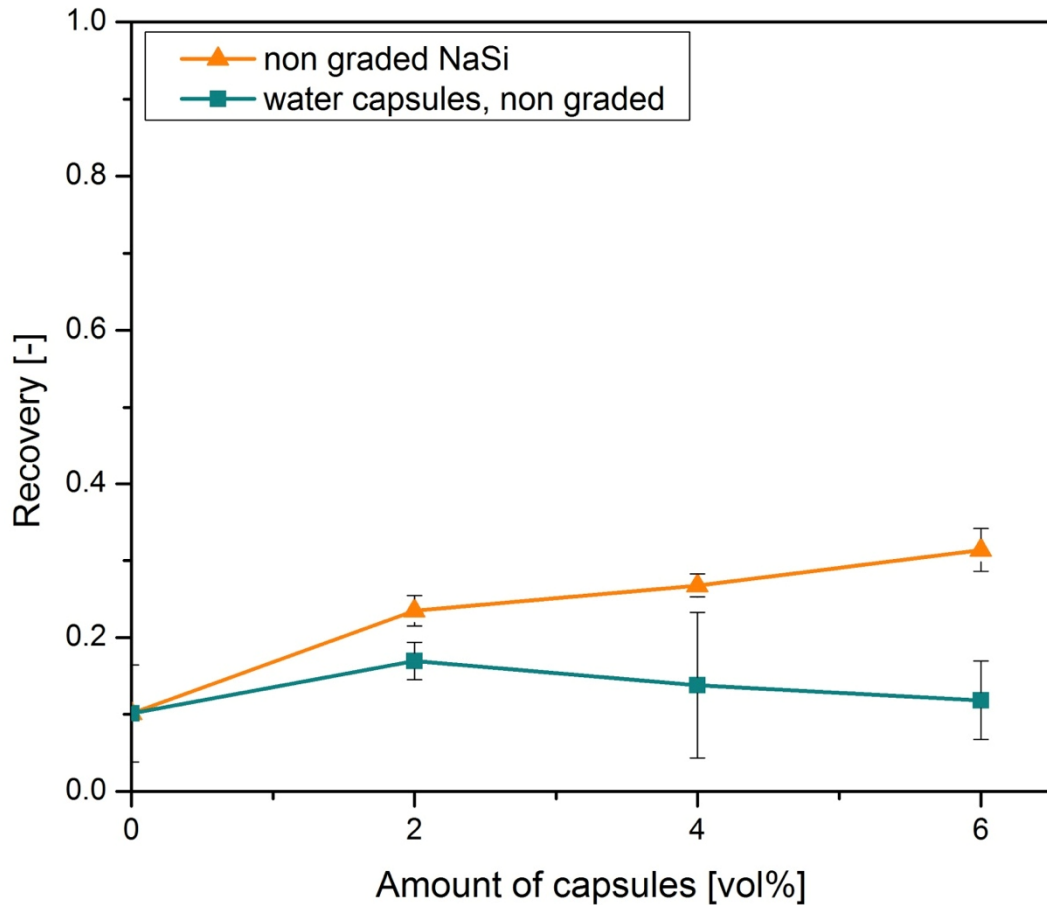


Diagram 4.3: Recovery of flexural strengths of mortar samples with sodium silicate and water capsules

Therefore, the results should be regarded with caution. Nevertheless, it can be concluded that the capsules have a positive effect on the recovery of flexural strength of concrete. And it seems like it is the extra supply of water which leads to better recovery and not just the sodium silicate. The encapsulated water could be released upon crack and react with not reacted calcium hydroxide and silicate particles in the concrete to form a solid CSH gel which heals the crack.

4.3.2 Capsule Distribution inside Mortar Samples

As described in paragraph 2.1.4 and 3.1.2.1 the tensile strength acts on the opposite side of the applied load by flexural loading. As concrete has lower tensile strength than compressive strength the samples break on the tension side. Thus, capsules are placed on the bottom side of the mortar samples where cracks occur. As seen in diagram 4.4 the initial load is decreased compared to the reference samples without capsules which can be explained with introduction of weakness points by addition of capsules.

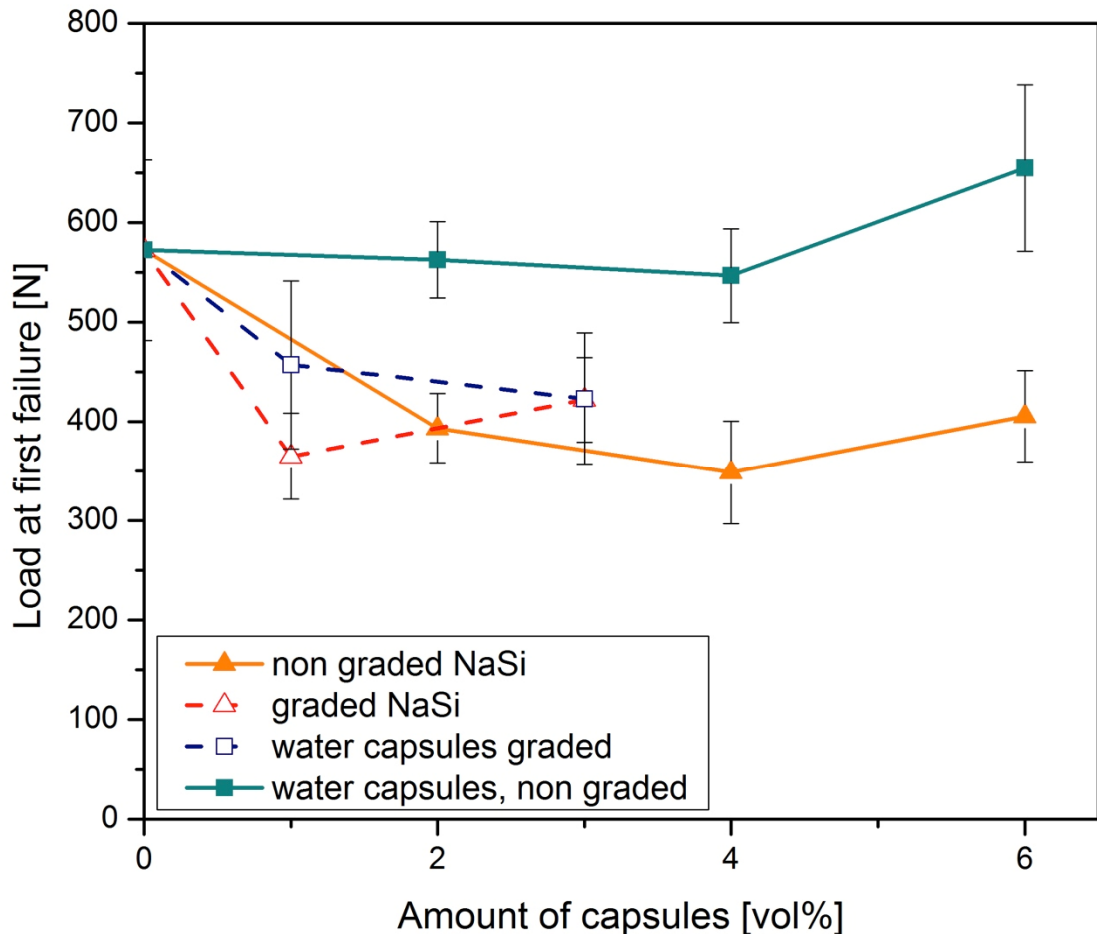


Diagram 4.4: Load at first failure for graded and non-graded water as well as sodium silicate capsules dependent on total amount of capsules in mortar samples

But the load at first failure is not dependent on the total amount of capsules in the sample. The load at first failure is the load before microcracks are developed deliberately and the agent of the capsules is released. Thus, the number concentration of capsules does not have a significant influence on the load at first failure. The healing is initiated after the microcracks rupture the capsules and the capsule content is released. After the healing period of 7 days the load at second failure is measured which is shown in diagram 4.5. It can be seen that the second load is higher for the graded samples with selective distribution of capsules.

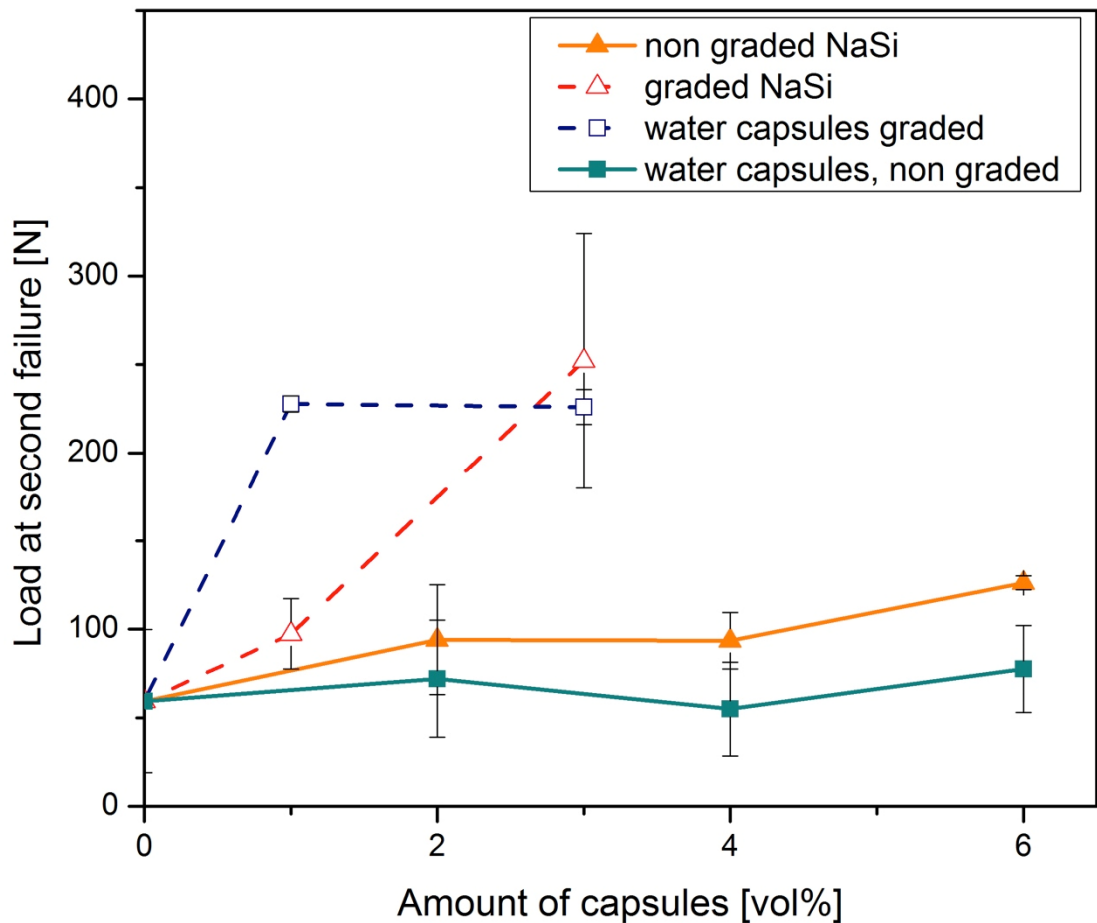


Diagram 4.5: Load at second failure for graded and non-graded water as well as sodium silicate capsules dependent on total amount of capsules in mortar samples

The loads at second failure divided by the one at first failure gives the recovery. The recovery of the graded and non-graded samples in dependence of the total amount of capsules in the mortar samples is shown in diagram 4.6. Samples with water and with sodium silicate have been examined.

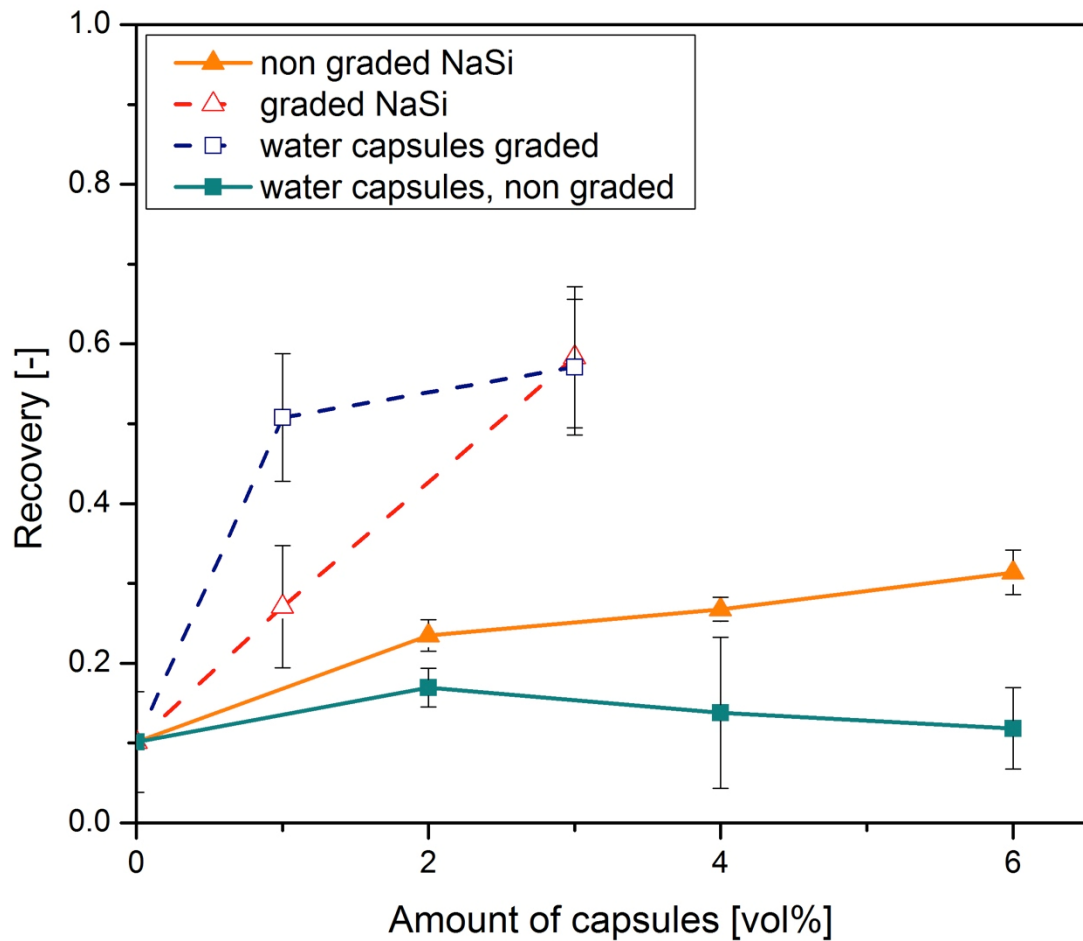


Diagram 4.6: Recovery of flexural strength with comparison of graded and non-graded mortar samples, plotted in dependence of total amount of capsules in mortar sample

As seen in diagram 4.6 the recovery for the graded samples is higher than for the non-graded samples. The difference is even more drastic at higher total amount of capsules. This can be explained with an increase in load at second failure shown in diagram 4.6. It indicates that there is more healing in the graded samples because more

of the initial load can be recovered. As discussed before there is no remarkable difference between the water and sodium silicate samples to allow conclusions about the influence of the healing agent. It is very probable that as mentioned before the extra supply of water leads to the enhanced recovery.

4.3.3 Recovery of Mortar Samples with PEG Capsules

The recovery of the flexural strength for the polyurethane capsules made with PEG as second monomer in comparison to the water capsules in polyurea shell done with the standard method (without PEG) and the graded samples with water capsules (without PEG) are depicted in diagram 4.7. As seen in diagram 4.7 the difference between the capsules with and without PEG is not significant. Consequently, the recovery does not vary for the capsules with and without PEG. Thus, as expected, the capsules show very similar behavior in terms of self healing. It is obvious that the graded samples show significantly better recovery than the non-graded samples. The difference between graded and non-graded samples has been discussed in paragraph 4.3.2.

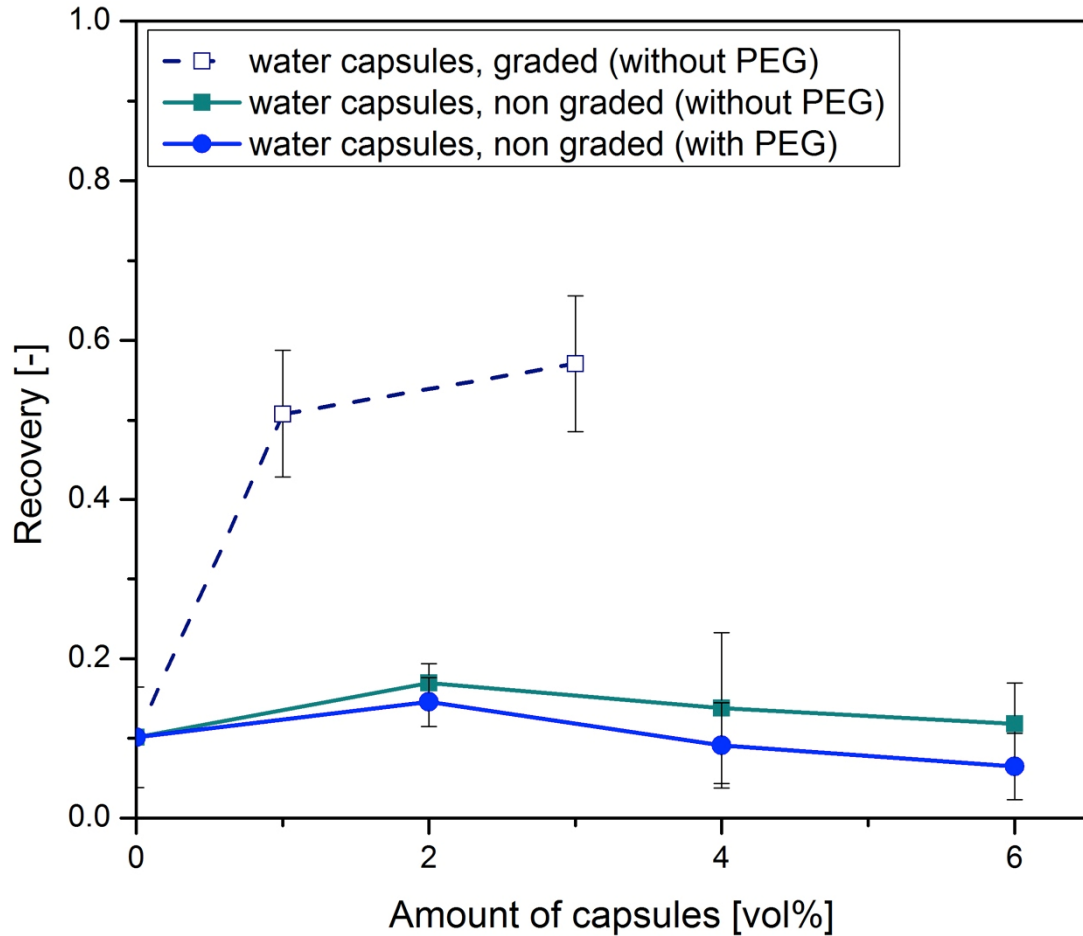


Diagram 4.7: Recovery of flexural strength of capsules with pure water content

4.3.4 Sodium Silicate as Self healing agent

As shown in paragraph 4.4.1 and 4.4.2 there is no significant difference between the effect on recovery and self healing between water capsules and with encapsulated sodium silicate solution. Besides sodium silicate, a mixture of sodium silicate and calcium nitrite, which is investigated as a corrosion inhibitor, has been tested. Diagram 4.8 shows the results for the recovery of the flexural strength. It can be seen that the capsules with a mixture of sodium silicate and calcium nitrite show

less recovery than the sodium silicate capsules. Nevertheless, there is not enough data available to make conclusions at this point.

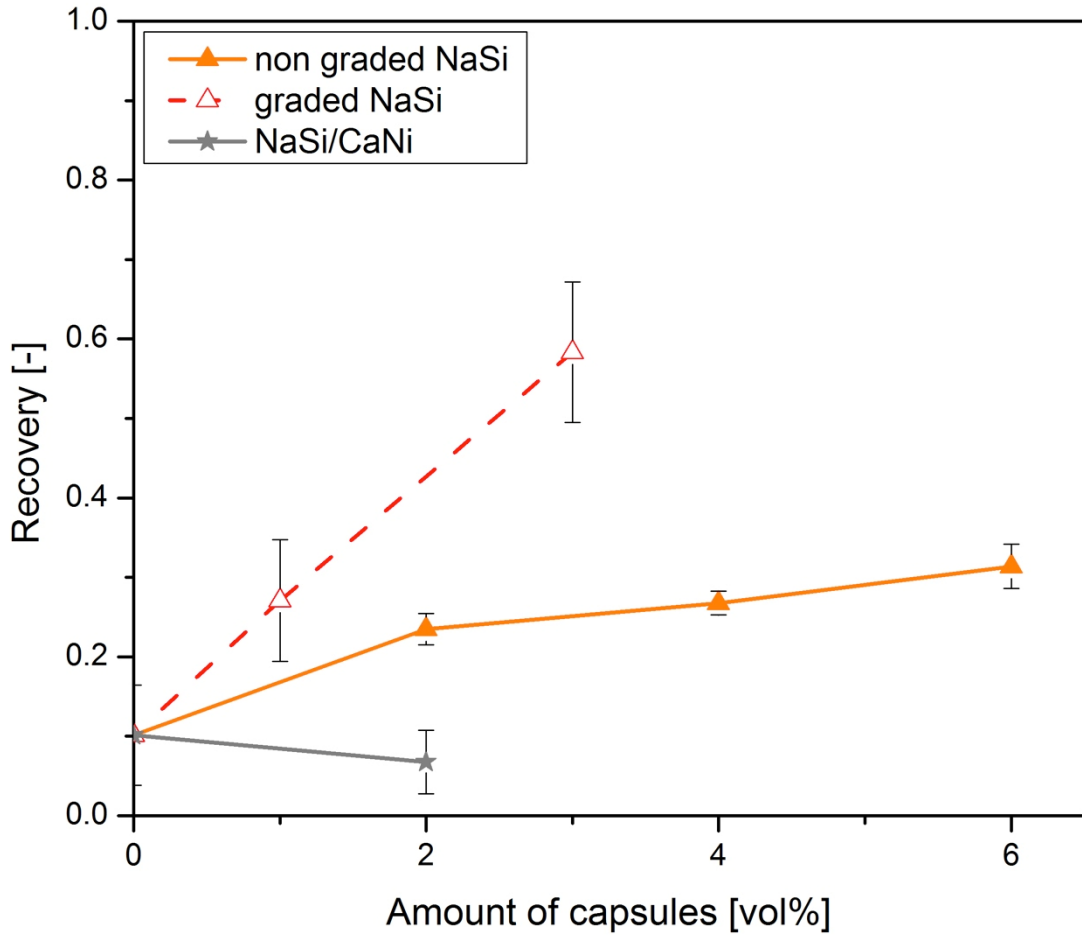


Diagram 4.8: Recovery of flexural strength for mortar samples with graded sodium silicate capsules, non-graded and non-graded with sodium silicate/calcium nitrite capsules

As discussed in paragraph 2.1.2.2 the CSH gel is formed by mixing water and cement.

As mentioned in paragraph 2.2 non-reacted calcium hydroxide particles in the concrete structure can react with water and form a solid and healing CSH gel. By adding encapsulated water which can be released upon microcracks extra water is provided which can enhance the autonomous healing of concrete and can be used to increase the self healing effect.

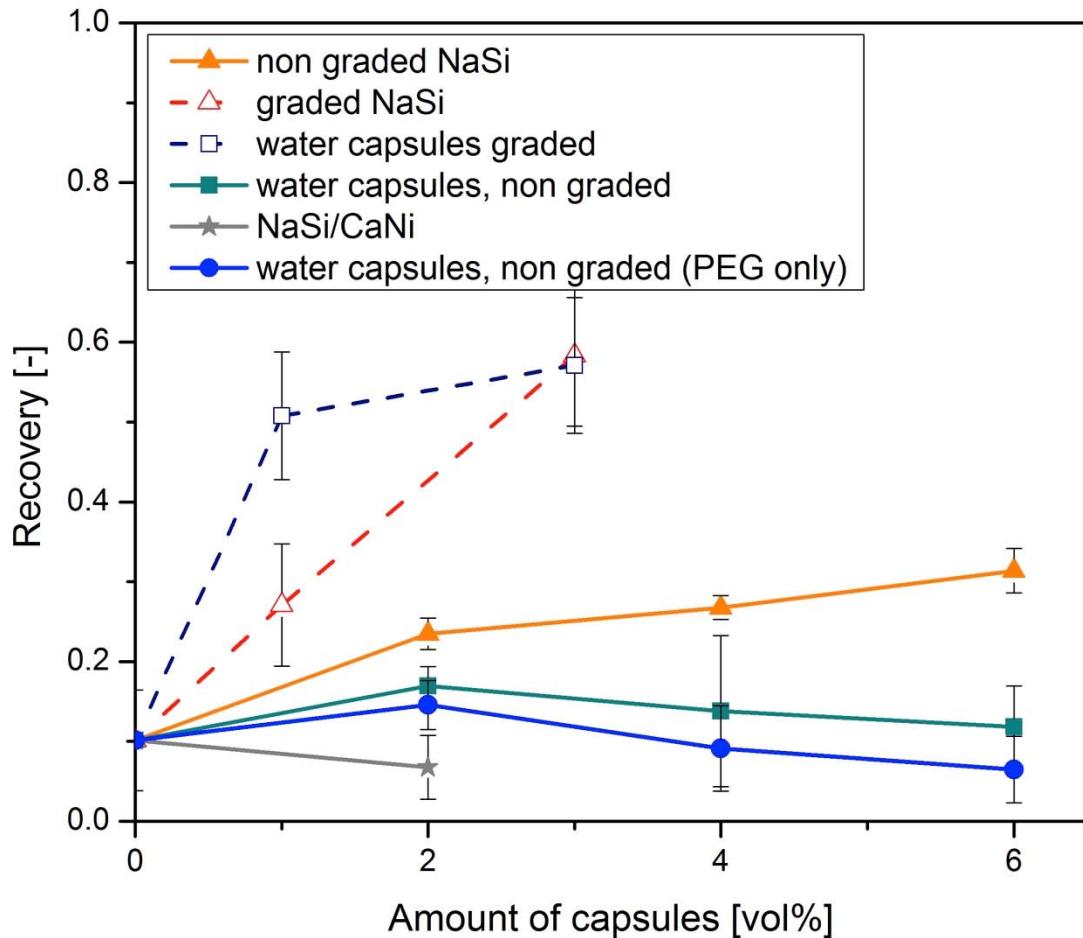


Diagram 4.9: Overview of recovery for different mortar samples with capsules with a core of sodium silicate, water and combination of calcium nitrite and sodium silicate based on amount of capsules

According to the data available the extra water has a positive effect on the self healing and it is not the dissolved sodium silicate. It can be assumed that there are enough non-reacted particles inside the concrete which can react later and seal cracks.

Furthermore, it can still be assumed that the formation of a CSH gel leads to the increase in recovery which supports Pelletier [6] and Bhattacharyya [7] describing the self healing effect as a formation of CSH gel.

4.3.5 Corrosion Test

Calcium nitrite is a well known corrosion inhibitor. The calcium nitrite is encapsulated and its ability to inhibit corrosion due to cracks in concrete is investigated inside mortar samples. Prior to the tests the set-up is validated and the corrosion of the steel wires outside mortar is examined. The steel wires from the mortars are imaged with a reflective microscope after corrosion to have a closer look at what happened inside the mortar samples. The results for validation of the new established set-up can be found in the appendix.

4.3.5.1 Corrosion of Steel Wires outside Mortar

As described in paragraph 3.3.2 a preliminary test to investigate the corrosion behavior of the steel wires outside mortar is made by exposure of the wires to different solutions and measurement of the voltage. Table 2.2 lists the risk and probability of corrosion dependent on open circuit potential. Diagram 4.9 shows the measured circuit potential for the wires in different solutions with time. It can be seen that there is no significant difference between the two calcium nitrite solutions. Thus, it seems that a concentration of 6.25 wt% is already sufficient for the corrosion inhibition effect and helps to build a protection layer and more calcium nitrite does not have an increase in corrosion inhibition. The potential of the wire in sodium silicate is in between the ones with calcium nitrite and NaCl solution. The potential curve of the salt solution of 0.5 M NaCl shows the lowest potential which is associated with severe corrosion. According to the table severe corrosion takes place at a potential of -0.46 to -0.5 Volts. It can be seen in diagram 4.9 that the steel wire inside the NaCl salt solution already

shows severe corrosion after a few seconds. The wires in calcium nitrite solution stay in low corrosion state or even less for the whole measurement period of 7 hours.

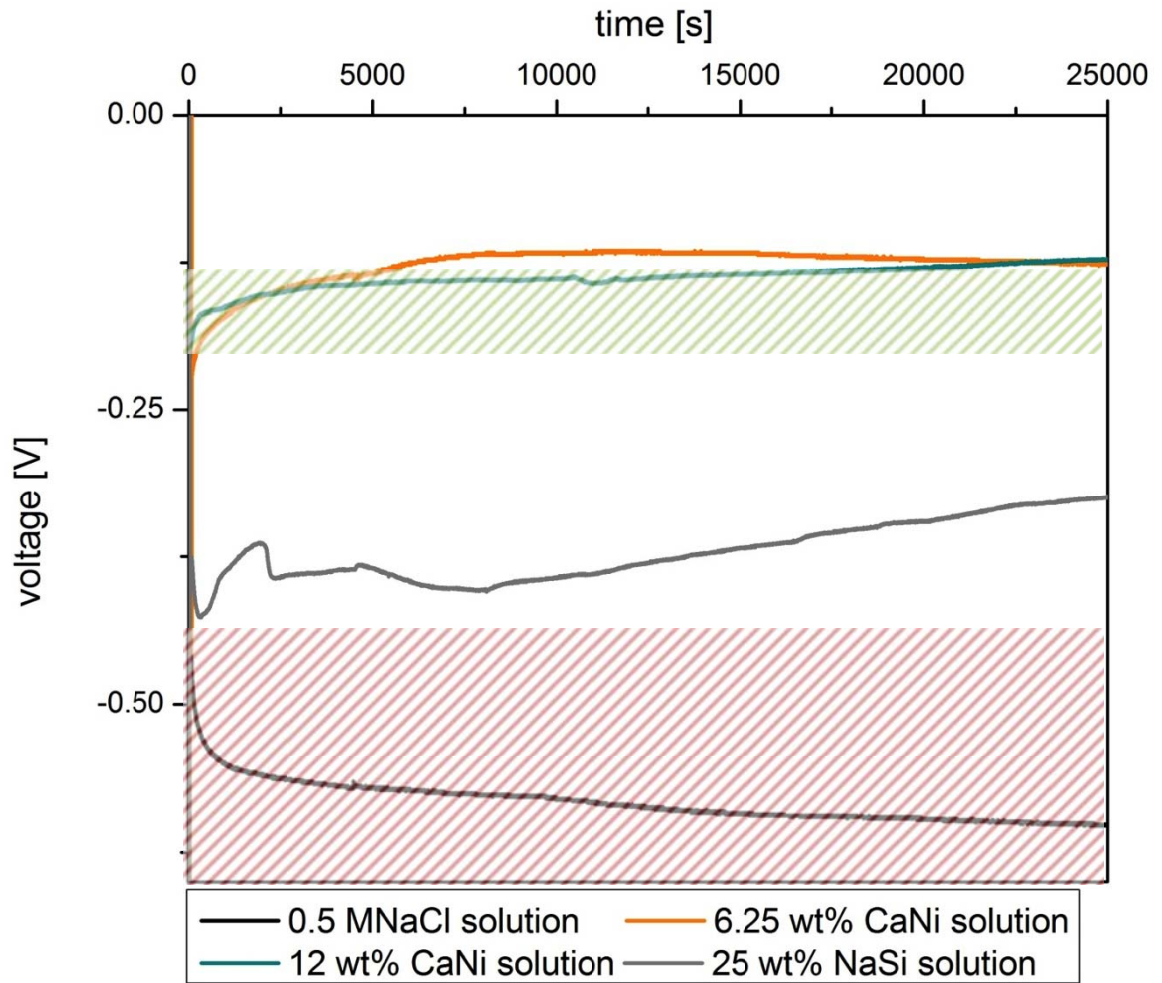


Diagram 4.10: Corrosion of steel wires in different solutions

The wire in sodium silicate solution is in between of intermediate and high risk of corrosion. As a conclusion, diagram 4.9 implies that 0.5 M NaCl leads to severe corrosion of the steel wires whereas calcium nitrite has an inhibition effect on the corrosion of the steel wires. Thus, further tests with the calcium nitrite as a corrosion inhibitor have been conducted and are presented in the following.

4.3.5.2 Corrosion Experiments with Mortar Samples

To investigate the corrosion inhibition of encapsulated calcium nitrite solution the results of calcium nitrite in different concentrations (d and e) are compared to the potential of a plain steel wire (a) and mortar samples without capsules (b) , and calcium nitrite and sodium silicate capsules (c). The mortar samples with the capsules have been cracked prior to testing to introduce a crack from the surface of the mortar sample which is exposed to NaCl salt water and the steel wire. After cracking the samples have been sealed so that the salt water can just enter the mortar from the top surface of the mortar sample above the wire location. The corrosion test has been started after the sealing has been set. Figure 3.4 shows the set-up of the mortar samples for the corrosion test. For starting the test, 0.5 M NaCl has been added to the cylinder on top of the mortar sample which allowed the salt solution to penetrate through the mortar sample.

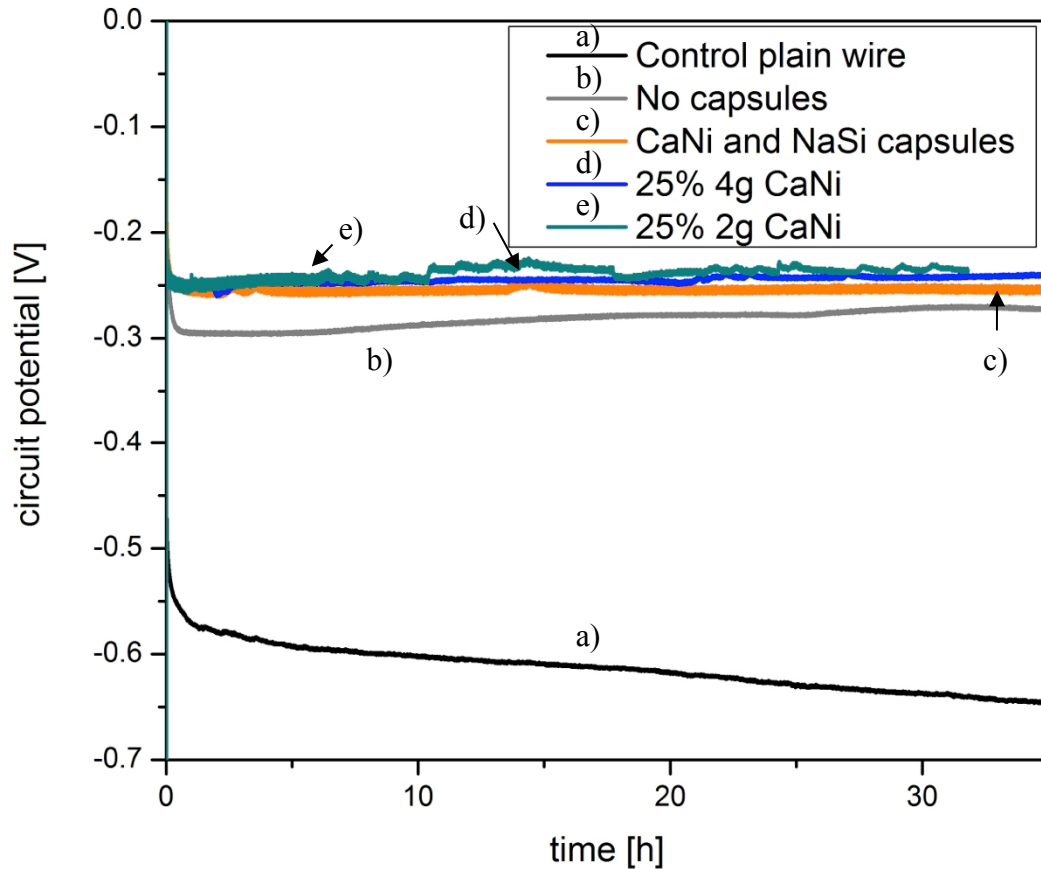


Diagram 4.11: Circuit potential for a) plain steel wire, mortar sample b) without capsules, c) calcium nitrite and sodium silicate capsules and d) and e) calcium nitrite capsules in different concentrations

The results for the corrosion experiment according to paragraph 3.3.2 for the mortar samples with and without capsules are shown in diagram 4.10. It can be clearly seen that the control sample with the steel wire not embedded in mortar has the highest negative potential with less than -0.5 V. Thus, according to table 2.1 the wire outside mortar is severe corroded. The typical circuit potential of steel in NaCl salt water is at -0.62 V which basically agrees with the results shown in diagram 4.10. A gradual increase of voltage indicates passive layer formation. It occurs in the mortar samples but not on the plain wire. The most significant increase is with the sample without capsules. It could be that because of calcium and silicate molecules naturally available

in concrete formation of a small passive layer is formed which is then gradually build up until the end of the test. It seems like this process needs time. Whereas, with the capsules this process can happen faster as more calcium nitrite and sodium silicate molecules, respectively are available upon crack of the capsules. Furthermore, it can be seen that the best corrosion inhibition can be realized with a pure calcium nitrite solution. However, the tested concentration changes do not have any differences. The mixture of sodium silicate and calcium nitrite has a slightly smaller corrosion inhibition. The results shown in diagram 4.10 are in very good agreement with the findings of chapter 4.4.5.2.

The steel wires have been investigated with the reflective microscope after the corrosion test and the images are shown in figure 4.9. It can be seen at the black and/or brown spots that corrosion took place. Furthermore, it can be seen that the samples for N3 which are the ones with calcium nitrite capsules show least signs of corrosion. The image on the bottom right shows that crystals, probably with calcium nitrite formed around the steel wire. It may have acted as a corrosion inhibitor and therefore the diagram 4.10 can be explained with formation of a protective layer around the wire.

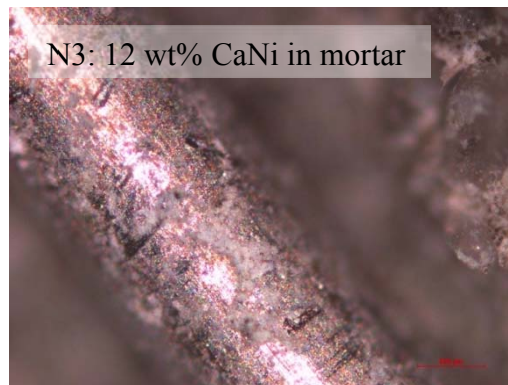
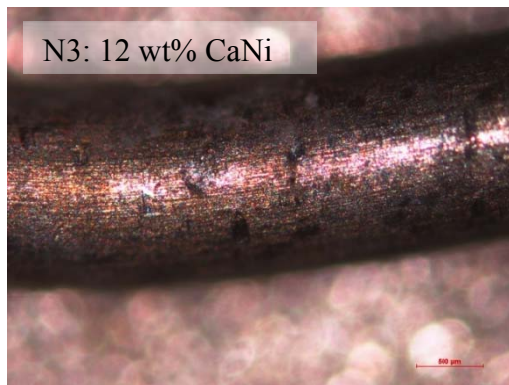
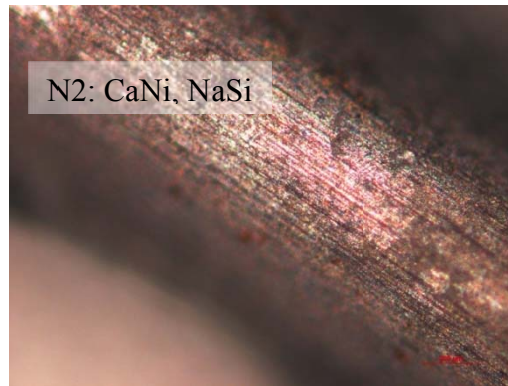


Figure 4.9: Images taken with reflective microscope of steel wires in different mortar samples taken after corrosion test

CHAPTER 5

CONCLUSION

Three main aspects have been examined: The production of capsules with different aqueous core materials and investigation of the chemistry with a focus on variation and improvement of capsule properties. Furthermore, the capsules have been characterized with regard to their properties and stability in and outside of mortars. Finally, the performance based on the self healing capability and corrosion inhibition has been determined. Emphasis has been put on the improvement of self healing performance by selective capsule distribution. The results are an important basis for industrial implementation and improvement of the microcapsule based enhancement technology for concrete. With the findings a scale-up can be realized and a big step towards understanding of the interaction of capsules and concrete has been made.

In the production part of this work it was possible to encapsulate pure water, calcium nitrite and water soluble color as well as fluorescence dye with a large yield and in a scale-up. Furthermore, an aqueous sodium silicate solution has been successfully encapsulated and it has been found out that the reason for the poor yield is the emulsification step. Because of the introduction of sodium silicate salt and the consequently drop in pH a three phase equilibrium with a small emulsion layer is formed. Further tests have to be conducted to realize a change of the equilibrium phases towards a two phase equilibrium with a large emulsion layer. It is assumed that by changing surfactants, the amount of surfactant, salts and temperature it should be possible to get a high yield of sodium silicate capsules.

The capsules have been characterized with focus on the mechanical and chemical stability whereby they have been observed with a variety of microscope technologies. Additionally their properties inside mortar have been investigated. First of all, it has been found out that the capsule production method developed by Pelletier [6] at the University of Rhode Island leads to capsules with the highest stability and that this method is most suitable for the application of self healing concrete among all tested methods including the use of different monomers, amounts of surfactant and catalyst. Nevertheless, encapsulation of aqueous solutions with the standard method introduced by Pelletier [6] but with different monomers was successful, too. Microscope studies lead to the conclusion that the capsules do not break upon the mixing process in the mortar production. Moreover, reflective microscope tests with colored capsules have proofed that the capsules release their content when cracks occur. SEM images gave first insights into how the capsules appearance is inside a concrete like environment. Unbroken capsules inside mortars have been seen under the SEM. More precise data on the stability of the microcapsules could be gotten by testing the strength of the capsules with a nanoindenter.

The performance of the microcapsules in concrete like materials based on self healing and corrosion inhibition has been examined. It has been shown that the performance can be improved by having less microcapsules but with targeted placement and distribution of capsules within the concrete sample. The graded samples with selective capsules placement showed a recovery of up to 58% with a total capsule amount of 3 vol% inside the mortar samples. In comparison to that, a maximum recovery of 31% is achieved with non-graded samples (with a total capsule amount of 6 vol%). Thus, the recovery and consequently the self healing effect can be improved by selective

distribution of capsules in the areas where the sample fails and microcracks occurs. Furthermore, essential information about the technology which leads to the positive effect of increased recovery has been found. It has been shown that indeed the extra supply of encapsulated water with or without sodium silicate which can be released upon need lead to a significant better recovery of strength. It is assumed that by adding encapsulated water which is release when cracks occur the autonomous healing process is remarkable enhanced. The water reacts with not reacted calcium-hydroxide and silicate particles which are present in concrete and forms a CSH gel which seals the cracks. In terms of corrosion inhibition it was found out that calcium nitrite capsules are working best for corrosion inhibition. Probably by releasing calcium nitrite protective layer around the steel wires is formed and the corrosion effect is minimized. For easy, fast and reliable corrosion testing an interface between computer and the physical world has been established and validated. The validation of the set-up carried out showed that the set-up for corrosion testing of mortar samples established in the framework of this project is reliable and can be easily used. The data of up to 8 samples at a time can be logged and saved.

Overall, it can be said that the technology of encapsulated healing and corrosion inhibition materials can enhance the lifetime of concrete structures. The method of encapsulation is easy and cheap and therefore very well suitable for concrete industry. As mentioned, further development on capsule preparation and investigation towards the fully understanding of the technology and processes carried out while capsules formation and while self healing and corrosion inhibition have to be done in the future. In order to scale-up the process for industrial use it is recommended to substitute the toluene with another appropriate solvent which is less harmful.

This work provides an essential basis for the self healing enhancement and corrosion inhibition of concrete which can provide longer lasting concrete. This would lead to less concrete production, less repair costs. Therefore, the developed concrete is consequently better in terms of economic issues and environmental protection.

APPENDICES

REFERENCES

1. Introduction:

- [1] **M. Wu, B. Johannesson, M. Geiker**, A review: Self healing in cementitious materials and engineered cementitious composites as a self healing material, Construction and Building Materials 28, 571 – 583, 2012
- [2] Self healing concrete, Interview with **Dr. Henk Jonkers**, TU Delft, Ingenia Issue 46, March 2011
- [3] **M. L. Gambhir**, Concrete Technology, third edition, The McGraw-Hill Companies, Civil Engineering Series, 2004
- [4] **K. Kovler, N. Roussel**, Properties of fresh and hardened concrete, Cement and Concrete Research, Volume 41, Issue 7, July 2011, Pg 775-792
- [5] **R. Dodge Woodson**, Concrete Structures – Protection, Repair and Rehabilitation, Butterworth-Heinemann, Elsevier Inc., 2009
- [6] **M. Pelletier**, Self healing Concrete, Master's thesis, University of Rhode Island, 2010
- [7] **T. Bhattacharyya**, Self healing in Concrete Materials, Master's thesis, University of Rhode Island, 2011

2. Theoretical background

[8] **Mindess, Young, Darwin**, Concrete, Prentice Hall, 2003

[9] **S. K. Ghosh**, Self healing Materials: Fundamentals, Design Strategies, and Applications, John Wiley & Sons, 2009

[10] **R. Dubey, T. C. Shami, K. U. B. Rao**, Microencapsulation Technology and Applications, Defense Science Journal, Vol. 59, No 1, January 2009, pp. 82 – 95, 2009

2.1 Introduction into Concrete Science

[11] **Felder-Casagrande, Wiedemann, Reller**, The calcination of limestone – Studies on the past, the presence and the future of a crucial industrial process, Journal of Thermal Analysis, Vol. 49, 971 – 978, 1997

[12] **Zongjin Li**, Advanced concrete Technology, John Wiley & Sons, Inc., 2011

[13] Editor: **P. C. Hewlett**, Leas's chemistry of Cement and Concrete, 4th edition, Butterworth Heinemann, 2001

[14] **Batman Uppon Bartholome**, His Booke De Proprietatibus Rerum, Imprinted by Thomas Caft Dwelling by Paules wharfe, London, 1582, found in: <http://books.google.de>, last access 06/12/2012, 11:30

[15] **J. Aspdin**, British Patent #5022, October 21, 1824, found in [16]

[16] **D. MacLaren**, Mary-Ann White, Cement: Its Chemistry and Properties, Journal of Chemical Education, Vol. 80 No. 6 June 2003

[17] **BS 12:1996**: Specifications for Portland cement, British standard, 15th edition, 1996 and European Standard EN-206-1: Specification, performance, production and conformity, 2000

[18] **P.C. Aïtcin**, **Libros del curso** “Ingeniería de los Cementantes Hidráulicos”; Doctorado en Ingeniería de Materiales de Construcción y Estructuras; Cuerpo académico de Tecnología del Concreto; 2005; p. 608

2.2 Techniques for Self healing in Cementitious Materials

[19] **M. Q. Zhang**, **M.Z. Rong**, Self healing Polymer and Polymer Composites, Practical and Applied Considerations, John Wiley & Sons. Copyright, 2011

[20] **T. Kondo**, Microcapsules: Their Science and Technology, Part 1. Various Preparation Methods

[21] **N. Sottos**, **S. White**, **I. Bond**, Introduction: self healing polymers and composites, J. R. Soc. Interface (2007) 4, 347–348

[22] **H. Mihashi**, **H. Y. Kaeko**, **T. Nishiwaki**, **K. Otuska**, Fundamental study on development of intelligent concrete characterized by self healing capability for

strength, *Trans Jpn Concr Inst* 2000, 22 (2): 441-50, source not present and reviewed by author, but cited in [19]

[23] **Y. Frère, L. Danicher, P. Gramain**, Preparation of Polyurethane microcapsules by interfacial Polycondensation, *Eur. Polym. J.* Vol 34, No. 2, pp. 193-199, 1988

[24] **D. Saihi, I. Vromn, S.Giraud, S. Bourbigot**, Microencapsulation of ammonium phosphate with a polyurethane shell. Part II. Interfacial polymerization technique, *Reactive & Functional Polymers* 66, pp. 1118-1125, 2006

2.3 Microcapsule based Self healing Concrete

[25] **L. Bertolini, B. Elsener, P. Pedferri, R. Polder**, Corrosion of Steel in Concrete, Prevention, Diagnosis, Repair, Wiley-VCH, 2004

[26] **H.-W. Song, V. Saraswathy**, Corrosion Monitoring of Reinforced Concrete Structures - A Review. *International Journal of Electrochemical Science*, 2007. **2**: p. 1-28

[27] **ASTM C1585-04**, Standard Test Method for Measurement of Rate of Absorption of Water by Hydraulic-Cement Concretes, 2004

[28] **M. Ionescu**, Chemistry and Technology of Polyols for Polyurethanes, iSmithers Rapra Publishing, 2005

[29] **merquinsa**, polyurethane types, pdf file found on homepage,
<http://www.merquinsa.com/whats/FPPUtypes1.pdf>, last access 8/15/2012, 8:42 AM

[30] **Wittebecker, E. L., Morgan, P. W.**, Interfacial Polycondensation. I., Journal of Polymer Science, volume XL, 289-297, 1959

3 Methods and Materials

[31] **ASTM C-109/C 109-M**, Standard Test Method for Compressive Strength of Hydraulic Cement Mortars (Using 2-in. or [50-mm] Cube Specimens), 2005

[32] **R.S. Khandpur**, Handbook of Analytical Instruments, McGraw-Hill Handbooks, 2006

[33] **B. E. Warren**, X-Ray diffraction, Dover publication, 1990

[34] **S.K. Yadav, Kartic C. Khilar, A.K. Suresh**, Release rates from semi-crystalline polymer microcapsules formed by interfacial polycondensation, Journal of Membrane Science 125, 213-218, 1997

4 Results and Discussion

[35] **J. Nordström, E. Nilsson, P. Jarvol, M. Nayeri, A. Palmqvist, J. Bergenholtz, A. Matic**, Concentration- and pH-dependence of highly alkaline sodium silicate solutions, Journal of Colloid and Interface Science 356, 37-45, 2011

[36] **B.P. Binks**, Emulsion type below and above the CMC in AOT microemulsion systems, *Colloids and Surfaces A: Physicochemical and Engineering Aspects*, 71, 167-172, 1993

[37] **J. Zhang, L. Li, J. Wang, H. Sun, J. Xu, D. Sun**, Double Inversion of Emulsions Induced by Salt Concentration, *Langmuir*, 28, 6769-6775, 2012

POSTERS

Self-Healing Concrete

Svenja Reinke (s.reinke@tu-bs.de), Lindsay Lorenz, Arijit Bose (bosea@egr.uri.edu), Richard Brown, Arun Shukla
University of Rhode Island, Department of Chemical Engineering, Department of Mechanical, Industrial and Systems Engineering

Abstract

Concrete is a material used widely in construction for its high compressive strength per small unit cost. But due to environmental exposure and repeated cyclic loadings, it develops cracks that reduce its strength. In self-healing concrete, the propagation of cracks is prevented by embedded microcapsules with an aqueous self-healing agent to prolong lifetime. The agent is released when a crack causes the capsules to rupture. The healed material recovers a large portion of its original flexural strength. We are now investigating how the distribution of capsules within the concrete sample affects strength and recovery, using both static and dynamic loading tests. Encapsulation of different healing agents and their ability to inhibit corrosion will also be tested. Furthermore, alternative production of custom made capsules is being explored.

Polyurethane Capsules - Interfacial Polymerization of Water-in-Oil Emulsion

- With water (as reference)
- Calcium nitrite (corrosion inhibitor)
- Sodium silicate (self healing ability)

Optical light microscopy

a) Water capsules
b) sodium silicate capsules in fresh cement

Fluorescence microscopy

With water soluble color

Corrosion Experiment

Calibration:

Corrosion of plain steel wire (without cement sample):

- Calibration successful, system and set-up are reliable
- Better corrosion inhibition of cement samples compared to plain steel wire
- Poor reproducibility for measurement of cement samples (dependence of crack width has to be regarded)
- No big differences between different samples

Testing Concrete Samples

- Reference samples without capsules
- Test 2: Load to initial failure and testing of recovery after 1 week

Dependency on rate [mm/min] of load applied by Instron machine
Graded samples better recovery than reference sample

Further Samples: Graded samples 2 vol%, 6 vol% with water, with sodium silicate

Encapsulation

Embedding of capsules into cement (cured for 28 days)

Crack formation due to loading

Recovery

Healing of crack

$$\text{Na}_2\text{O} \cdot \text{SiO}_2 + \text{Ca}(\text{OH})_2 \rightarrow \text{CaO} \cdot \text{SiO}_2 \cdot \text{H}_2\text{O} + \text{Na}_2\text{O}$$

Sodium silicate powder → C-S-H gel
Cement x=2, 3

Future Work

- Further exploration of self-healing mechanism by investigation of fractured area, formed C-S-H gel
- Properties of capsule (strength and durability)
- Scale up
- Indirect tensile test and blast load

[1] T. Bhattacharyya, Self Healing in Concrete Materials, Master's thesis, 2011. [2] M. Pelletier, A. Bose, Self-healing Concrete, Submitted to Journal of Concrete Research, 2011

Self-Healing Concrete

Svenja Reinke, Triparna Bhattacharyya, Michelle Pelletier, Arun Shukla, Richard Brown, Arijit Bose
s.reinke@tu-bs.de and bosea@egr.uri.edu
University of Rhode Island, Department of Chemical Engineering, Department of Mechanical, Industrial and Systems Engineering

Abstract

Concrete is a material used widely in construction for its high compressive strength per small unit cost. But due to environmental exposure and repeated cyclic loadings, it develops cracks that reduce its strength. In self-healing concrete, the propagation of cracks is prevented by embedded microcapsules with an aqueous self-healing agent to prolong lifetime. The agent is released when a crack causes the capsules to rupture. The healed material recovers a large portion of its original flexural strength. We are now investigating how the distribution of capsules within the concrete sample affects strength and recovery, using both static and dynamic loading tests. Encapsulation of different healing agents and their ability to inhibit corrosion will also be tested. Furthermore, alternative production of custom made capsules is being explored.

Technical Approach

Self-healing mechanism
= localized and targeted release of healing agent to recover strength

$\text{Na}_2\text{O} \cdot \text{SiO}_2 + \text{Ca}(\text{OH})_2 \rightarrow \text{CaO} \cdot \text{SiO}_2 \cdot \text{H}_2\text{O} + \text{Na}_2\text{O}$
Sodium silicate powder → C-S-H gel
Cement x=2, 3

Polyurethane Capsules
Interfacial polymerization of water-in-oil emulsion [2]

Water
Without healing agent (as reference)

Calcium nitrite
Corrosion inhibitor

Sodium silicate
Self healing ability → formation of C-S-H gel

Compressive strength [1]

Flexural strength [1,2]

Dynamic strength [1]

Relevance

- Concrete is most extensively used construction material worldwide → huge significance in everyday life
- To make infrastructure safer and longer lasting
- Protection of materials from damage due to weather and cyclic loadings
- Production of less concrete, resulting in both lower emission of CO₂ and saving natural resources and energy
- Lessening economic impact from regular maintenance and reconstruction

Accomplishments Through Current Year

Capsule loading [1,2]

Water absorption [1]

- No remarkable influence of capsule under very high dynamic load and compression [1]
- Significant increase of yield of capsules per amount emulsion
- Encapsulation of different aqueous solutions (water, sodium silicate, calcium nitrite) successful

Opportunities for Transition to Customer

- Implementation of self-healing concrete on a large scale in high interest of industry (CEMEX, BASF)
- Scale up will be investigated.

Future Work

- Capsule distribution within the concrete sample
- Corrosion testing with calcium nitrite
- Alternative way to prepare capsules; Membrane emulsification to get a smaller size distribution of capsules

- Further exploration of self-healing mechanism by investigation of fractured area, formed C-S-H gel
- Properties of capsule (strength and durability)
- Investigate alternative method of capsule preparation and scale up

Publications Acknowledging DHS Support

[1] T. Bhattacharyya, Self Healing in Concrete Materials, Master's thesis, 2011
[2] M. Pelletier, A. Bose, Self-healing Concrete, Submitted to Journal of Concrete Research, 2011

This material is a United States Government work and, as such, is in the public domain in the United States of America.

Summary of work on capsule based self healing concrete done at the University of Rhode Island by Pelletier [6] and Bhattacharyya [7]

1. Compressive Strength

Bhattacharyya tested the influence of capsules under compressive load [7]. 2 vol% of capsules have been used filled with an aqueous sodium silicate solution and have been compared to samples without capsules as a reference. Two tests have been done. At the first test (Test a) the samples have been compressed and resulting maximum loads have been measured.

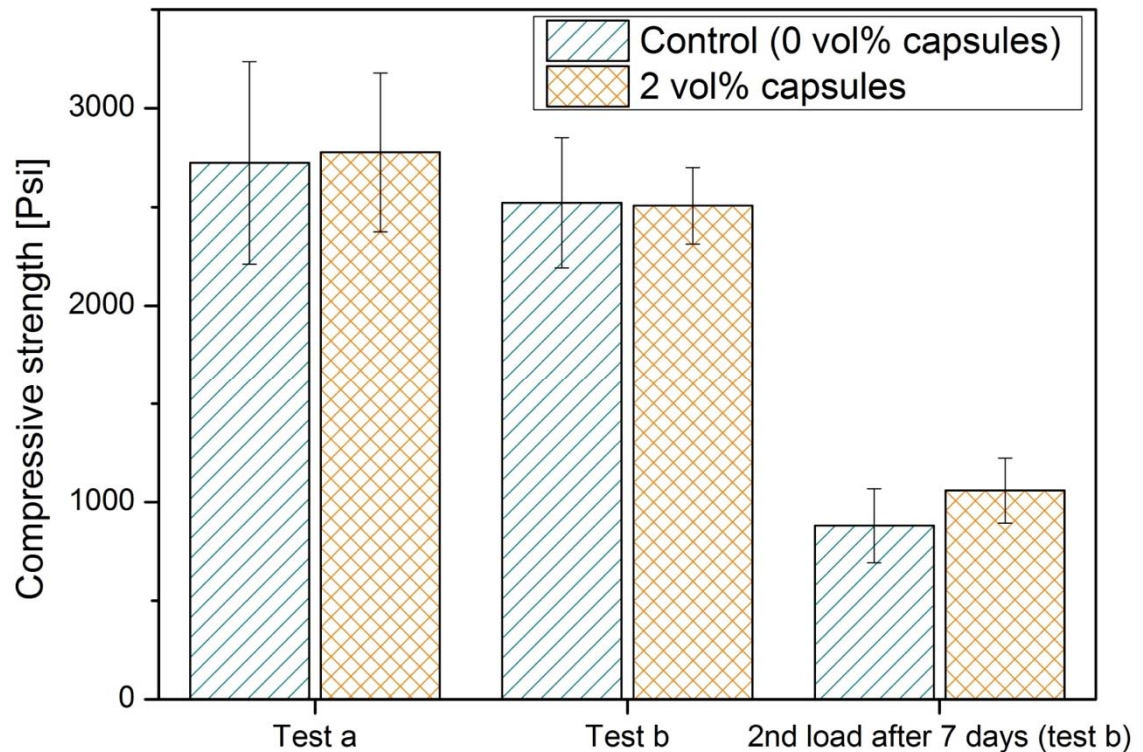


Diagram A.1: Compressive strength in dependence for reference samples without capsules and with 2 vol% capsules, data taken from Bhattacharyya [7]

The maximum load is the load when first failure occurs. At a second test (Test b) the recovery of flexural strength has been examined. The recovery can be expressed by the ratio of second load by first load. Therefore, the samples have been loaded until first failure, have been cured for 7 days and reloaded until final failure. The results are shown in diagram A.1. Three samples have been tested in each test and the diagram shows the average values with error bars. The diagram shows that there is no significant influence of the capsules on the compressive strength of the mortar samples.

Table A.1: Results compression strength, data taken from Bhattacharyya [7]

Sample		Compressive strength and standard deviation First load		Compressive strength and standard deviation Second load	
		[Psi]	[MPa]	[Psi]	[MPa]
Control	Compressive strength	2777	19	X	
	Standard deviation [%]	403	3		
Capsules (2vol%)	Compressive strength	2724	19		
	Standard deviation [%]	513	4		
Control	Compressive strength	2522	17	880	6
	Standard deviation [%]	330	2	188	1
Capsules (2vol%)	Compressive strength	2507	17	1058	7
	Standard deviation [%]	194	1	165	1

There is a slight increase in recovery of strength for the capsule samples with 42.2 % compared to 34.89 % for the control samples without capsules. Nevertheless, the difference in the recovery should be regarded with caution as the maximum load varies from sample to sample as seen in the range of error bars. Additionally, the load is with over 2500 Psi. Therefore it is very probable that the influence of the capsules

cannot be seen at such high loads [7]. Table A.1 gives an overview over the results Bhattacharyya determined in [Psi].

2. Dynamic Strength

Bhattacharyya also tested the behavior of capsules under dynamic load. The test has been conducted with a Split Hopkinson pressure bar (SHPB). Mortar samples with a diameter of 2 inches and a height of 0.5 inch have been prepared. The SHPB is usually used for ductile materials and not for brittle materials such as concrete. Nevertheless, a first estimation can be made with the test. The diagram A.2 shows the results taken from Bhattacharyya [7]. According to the diagram there is no remarkable difference between the samples containing 2 vol% of capsules and the control samples without capsules. But the results should be evaluated carefully because first - as mentioned before - the SHPB is usually used for ductile materials and secondly the sample size was too small to provide representative predictions of the influence of the capsules on the dynamic strength. As the capsule amount has just been 2 vol% and the samples have been small, it is not possible to make sure that the capsules have been distributed enough to ensure sufficient influence on the dynamic strength of the mortar samples.

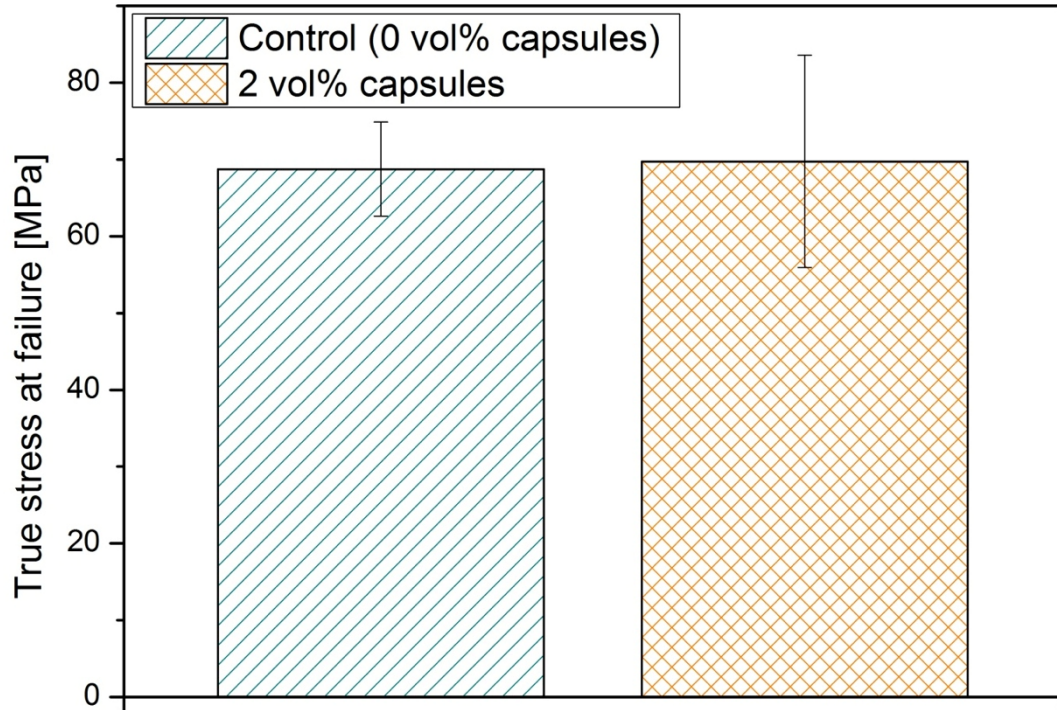


Diagram A.2: Dynamic strength tested with Split Hopkinson pressure bar, data taken from Bhattacharyya [7]

3. Flexural Strength

The flexural strength and the recovery of the flexural strength have been measured with the three point test which is explained in more detailed in paragraph 3.3. The mortar samples have been made according to paragraph 3.1. The preparation procedure is taken from Pelletier [6] and Bhattacharyya [7]. After 28 days of curing the samples have been stressed until first failure which has been indicated with a rapid decrease in load dependent on extension of the Instron machine. The failure was not a final breakage. In contrast, tiny microcracks lead to the abrupt decrease in load and the samples have not been broken into pieces. The samples have been healed for 7 days whereby they have been stored in a closed plastic bag. They have been stressed

again under the same conditions as the first loading. This procedure has been repeated a second time for samples with a capsule loading of 2 vol%, 4 vol% and 6 vol% after 7 days of healing. By dividing the second by the first maximum load the recovery can be calculated. The recovery 2 is the 3rd load divided by the 2nd load.

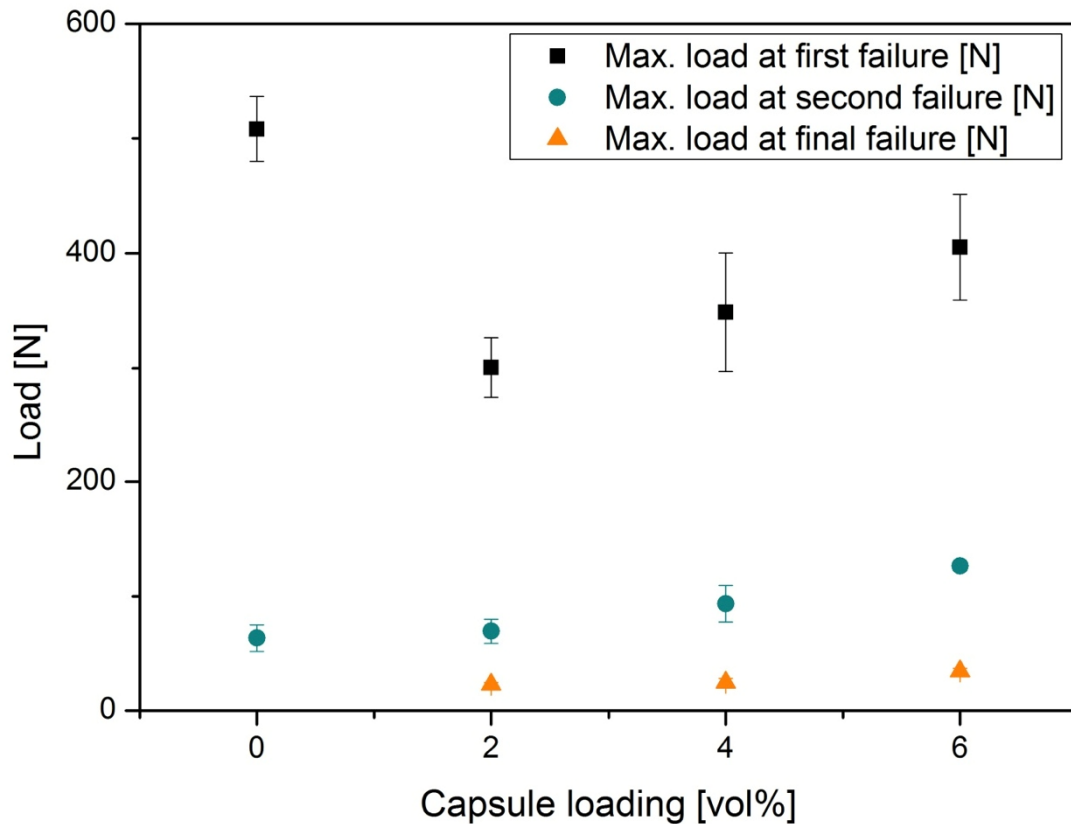


Diagram A.3: Maximum load at three point bend test for samples with different amounts of capsules, data taken from [6, 7]

Diagram A.3 shows the maximum loads for the initial failure, second loading and the final failure. It can be seen that the load increases with increasing amount of capsules from 2 to 6 vol%. The loads for the reference samples without capsules have a higher

maximum load. The decrease of load at introduction of capsules in the mortar samples can be explained with the input of weakness points.

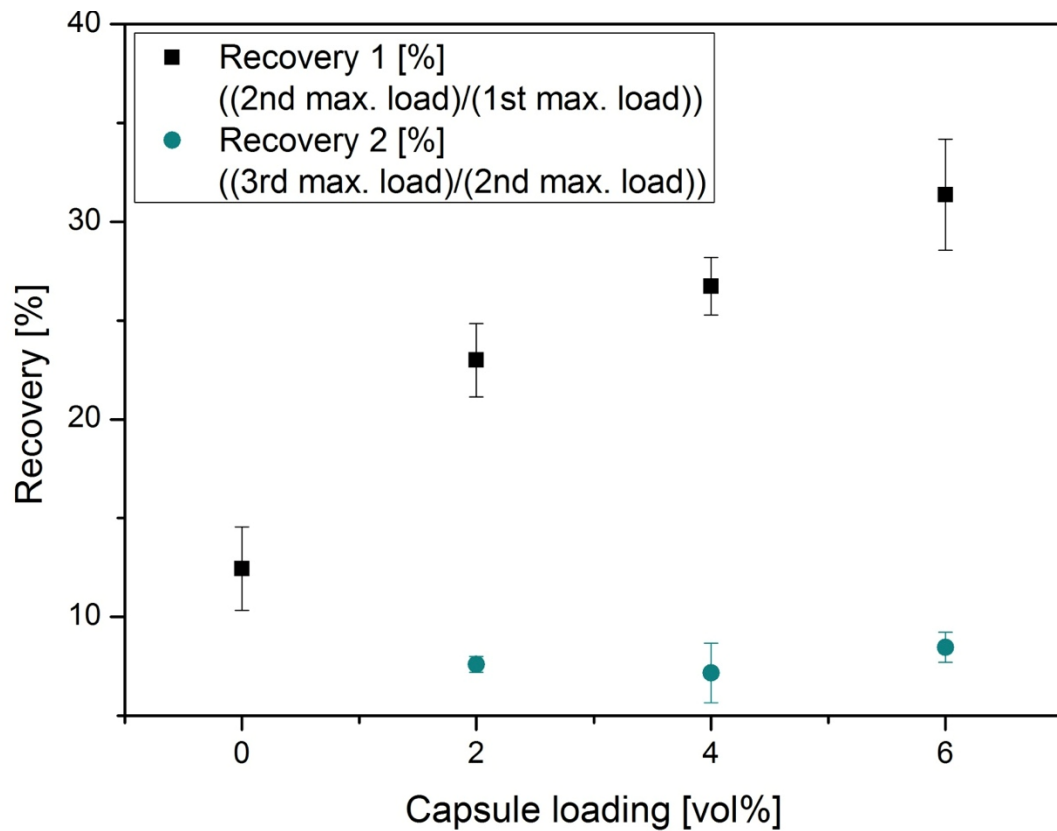


Diagram A.4: Recovery of flexural strength at different capsule loadings from 0 vol% to 6 vol%, data taken from [6, 7]

Diagram A.4 shows the results for the recovery of the flexural strength. It can be clearly seen that the recovery increases significantly with increasing capsule loading. The recovery for no capsules of 12 % can be explained with autonomous healing which has been discussed in paragraph 2.2. For the samples containing 2 vol% of capsules the recovery 1 is 23-24%, the samples with 4 vol% capsules has an average recovery of 27-28% whereas the samples which contained about 6% by volume of the

capsules show a recovery of 31% to 34%. Bhattacharyya [7] explained the increase in recovery with a healing process taken place in the healing period. It is said that the broken samples release the sodium silicate which leads to formation of the calcium silicate hydrate (CSH) gel and consequently sealing the crack tip. Thus, according to Bhattacharyya [7] the samples regain some strength. Furthermore, Bhattacharyya [7] mentions that as polyurethane acts elastically, the capsules may absorb a small portion of the load. The recovery 2 does not change significantly with capsules amount which can be because the sample is broken along the same crack line again and consequently most of the capsules on that plane have already been broken and have already released the healing agent [7].

4. Water Absorption

To investigate the effect of capsules on water absorption Bhattacharyya [7] tested the water absorption by a measurement based on the ASTM C1585-04 [27]. The mortar samples have been prepared and cured for 28 days according to paragraph 3.2. The samples have then been dried in a vacuum chamber for 6 hours at 30°C and four side faces of the cubic samples have been sealed with ductile tape and the top side has been loosely covered with Parafilm which has been tied tightly with an elastic band. The mass of the samples has been measured prior to exposure to water, after 60s, 5min, 10min, 20min, 30min, 60min, 2hr, 3hr, 4hr, 5hr, 6hr, 1day, 2 days, 3 days, 4 days, 5 days, 6 days, a week and 8 days and the change in mass has been determined.

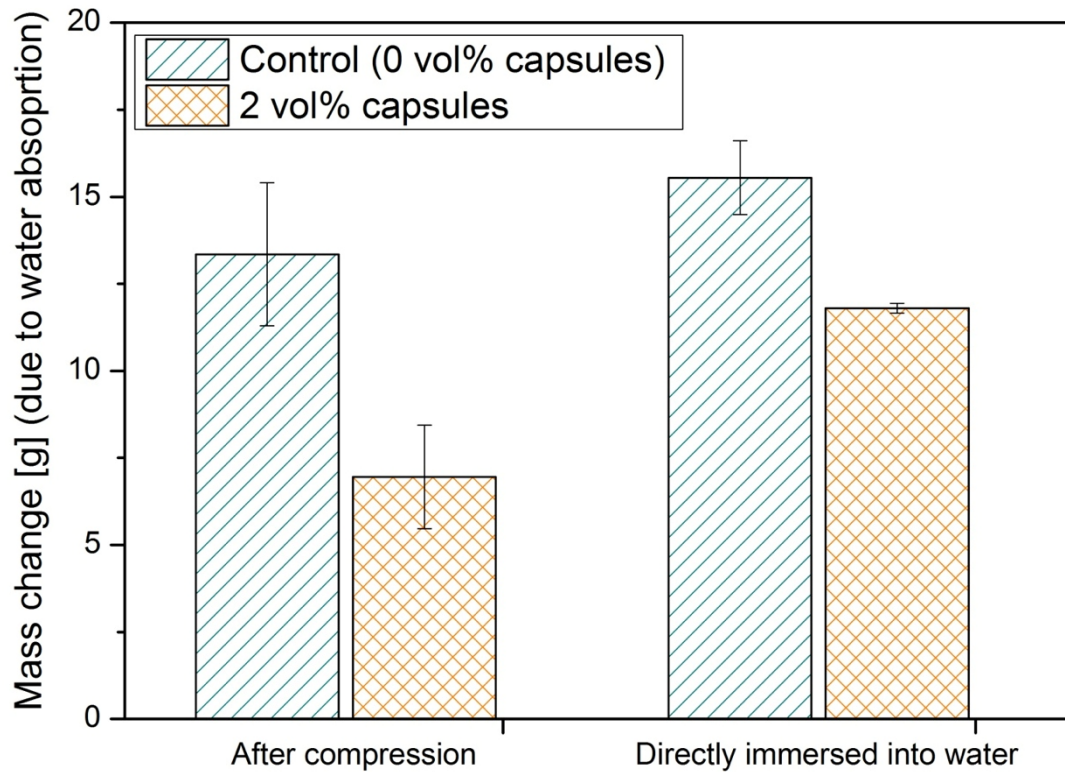


Diagram A.5: Mass change due to water absorption tested by Bhattacharyya [7] after compression and without compression

In a second test the samples have been compressed, cured for a week and then the water absorption has been tested with the method described above. A detailed description of the test and results can be found in Bhattacharyya [7]. Diagram A.5 shows the mass change due to water absorption after compression and without compression for the reference samples, mortar samples without capsules, and mortar samples with 2 vol % of capsules. It can be seen that the samples with capsules absorb less water compared to the control samples. Bhattacharyya proposed that reduced porosity is the reason for a reduction in water absorption. The test of water absorption after compression showed rapid increase in mass due to water absorption for the first

10 to 20 minutes and the mass increased until saturation was reached. Bhattacharyya explained this phenomenon with additional voids due to cracks. It is said that the capsules containing samples show less water absorption in the end because of formation of a CSH gel and reduction of porosity and permeability. The reduced porosity was already proposed as the corrosion inhibitory effect by Pelletier [6]. [7]

5. Capsule Production

Pelletier established a method for encapsulation of an aqueous sodium silicate. The polyurethane microcapsules with an aqueous sodium silicate solution have been made via interfacial polymerization. Pelletier [6] developed a method for the preparation of the polyurethane microcapsules based on Saihi et al [24]. The method developed by Pelletier [6] is presented below. Paragraph 2.4 gives a better overview over the theory of interfacial polymerization.

Preparation of Solutions O1, O2, W1

1) Solution O1:

- Measure 90 ml of toluene in a beaker
- Add 4.2 ml of Span 85 and 2.1 ml of PEG dioleate with a pipette
- Stir solution until homogeneous mixture is formed (use e.g. magnet stirrer)

2) Solution O2:

- Take 15 ml of solution O1 with a pipette and put it into another beaker

- Add 47 μ l of Dibutyltin dilaurate to 15 ml with a pipette, mix solution so that homogeneous solution is formed
- Add 0.7 ml of Basonat (while mixing; homogeneous solution has to be formed), the Basonat can be added drop by drop.
- Mix solution O2 until homogeneous mixture is formed

3) Solution W1

- 30 ml water
- If needed: Add water soluble core material (such as sodium silicate, color, calcium nitrite) to water

Emulsification

Solution O1 is placed on a magnet stirrer and stirring rate is increased to up to 1400 rpm. Do not increase stirrer rate if spilling occurs. Add solution W1 slowly while mixing. Cover beaker with aluminum foil to avoid spilling and massive evaporation of toluene. Increase stirrer rate and form emulsion. In general, the higher the stirrer rate, the smaller the capsules size. The emulsion is visible as a whitish solution. The formation of emulsion can be checked under the microscope. Stir at high stirring rate (up to 1400 rpm) for 5 minutes to ensure formation of emulsion.

Wall formation

Decrease stirrer rate to 700 rpm. Add solution O2 slowly to mixture and stir at 700 rpm for 10 minutes.

Shell growth

Decrease stirrer rate to 350 rpm and increase temperature to 63°C. Stir emulsion for 4 hours at 63°C.

Test for Capsule Formation

The following fast and easy test shows whether shell formation already took place or if the liquid is still an emulsion without polymer shell: Place a little drop of solution on microscope slide. If emulsion breaks it can be seen and a difference can be noticed. Further analysis if shell formed can be made with optical microscope. Polymer shell can be usually seen as slightly wrinkled membrane around water droplets. Do droplets burst easily and fast: shell formation has not taken place entirely. The capsules should not break if capsule solution is centrifuged at 500 rcf (139 rpm) for 2 minutes.

Washing

Capsules should be at least washed once with toluene to remove surfactants and residues. After decantation add toluene to capsule solution and centrifuge 2 minutes at 500 rcf. Remove toluene layer at top and do washing step again if necessary. The washing step should be repeated as long as toluene layer is not transparent and colorless but yellowish. Washing with another solvent is highly recommended.

Bhattacharyya [7] pictured the microcapsules under the SEM. The SEM images are shown in figure A.1.

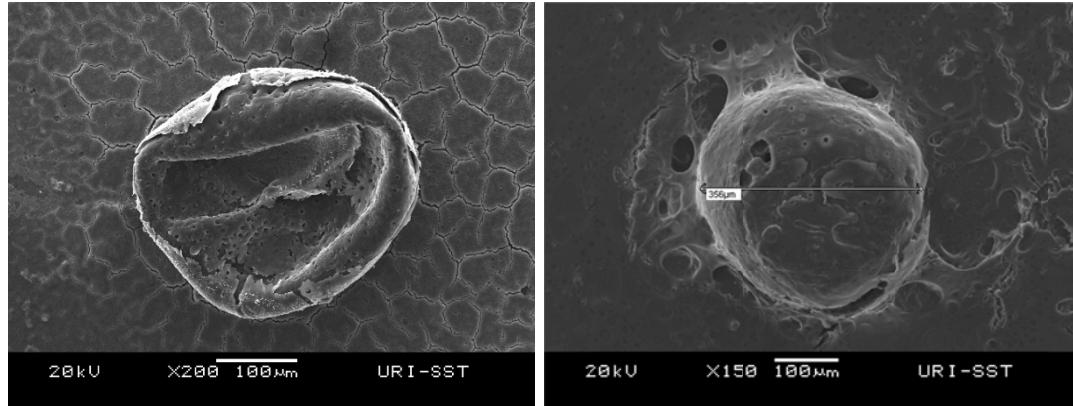


Figure A.1: SEM images of polyurea/polyurethane microcapsules made by interfacial polymerization [7]

They show an entire capsule on the right hand side and a broken capsule on the left hand side.

6. Corrosion Inhibition

To increase the tensile strength of concrete reinforcement bars are introduced into the concrete structure. The reinforcement bars are susceptible to corrosion if not protected. Pelletier [6] did preliminary tests on the ability of corrosion inhibition with help of sodium silicate capsules. Samples with 2 vol% of capsules filled with an aqueous sodium silicate solution and reference samples without capsules have been tested. A detailed description of the samples preparation is given Pelletier [6].



Figure A.2: Set-up of corrosion test, set-up used by Pelletier

The set-up Pelletier [6] used can be seen in figure A.2. Pelletier used iron wires to investigate the corrosion effect. Samples with three iron wires have been put into the mortar samples as seen in the figure on the right hand side. The mortar samples have been cracked so that sodium chloride water can penetrate through the sample to get into contact with the wire. The potential which is an indication for the progress of corrosion has been measured with a voltmeter. As shown in table 2.1 severe corrosion happens in the control samples without capsules significantly faster than in the samples with 2 vol% capsules. Table 2.1 gives an overview over the areas of risk and classification of corrosion dependent on the open circuit potential [26].

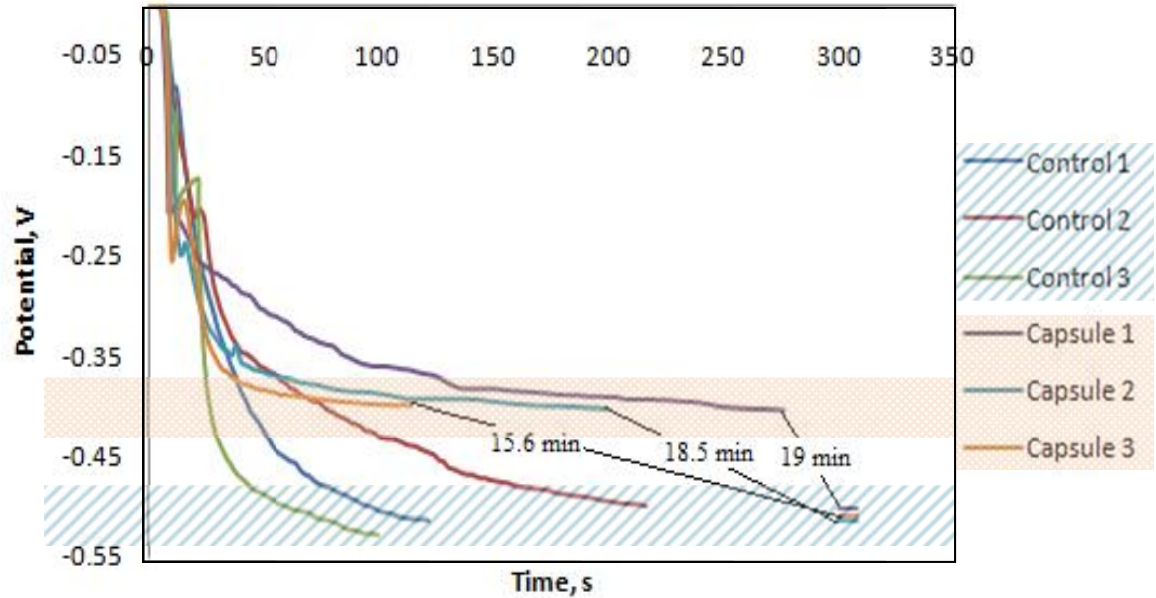


Diagram A.6: Potential progress in dependence of time for samples with 2 vol % sodium silicate capsules and for reference samples without any capsules, diagram has been taken from [6] and been adapted

Three repetitions have been made for the samples with capsules and for the reference samples. The results are shown in diagram A.6 [6]. It can be seen that the potential decreases more rapidly for the control samples without capsules compared to the samples with 2 vol% of sodium silicate capsules.

Pelletier [6] proposed two mechanism of corrosion inhibition. One proposal is that the samples are stressed during the three point bend test and the capsules rupture and release the healing agent. Consequently, it could be that some of the sodium silicate will attract to the positive ions present on the metal and deposit on the metals surface. Pelletier stated that the formation of a passive film on the surface of the metal will protect it from corrosion. Another mechanism according to Pelletier is the reduced

water transport through the concrete matrix due to reduced porosity, decreased interconnectivity and healed cracks because of the release of the healing agent. This would slow down the ingress of chlorides and leads to reduction of the corrosion rate.

[6]

VALIDATION OF SET-UP FOR CORROSION MEASUREMENT

The corrosion is measured with the set-up shown in figure 3.6 and described in paragraph 3.3.2. To investigate the degree of corrosion the potential between a reference electrode and the steel wire inside the mortar samples is measured. Prior to the mortar experiments the new set-up has to be validated.

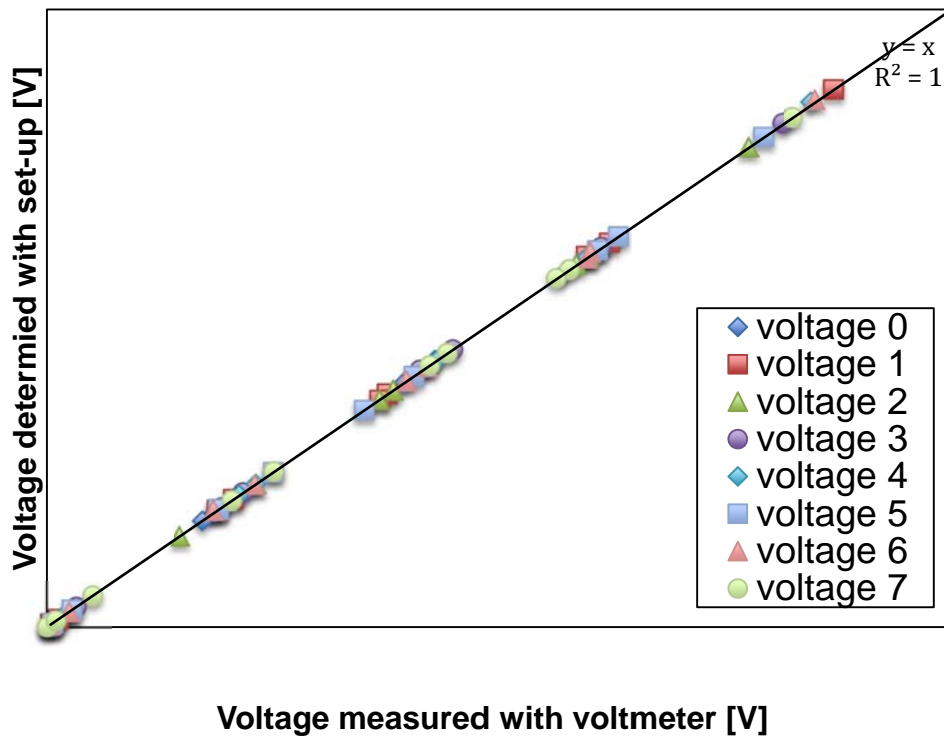


Diagram A.7: Validation lines for corrosion set-up, comparison of determined voltage of set-up and voltage measured with calibrated voltmeter

The validation line can be seen in diagram A.7. It is visible that the set-up is very accurate. The set-up has 8 channels and all channels 0-7 are checked. The results are shown in diagram A.7. Additionally, table A.2 shows that the deviation of the slope from 1 is less than 1 % for every channel and that the coefficient of determination is

higher than 0.9999 for all channels. Consequently, it can be said that the system is reliable.

Table A.2: Results for validation of corrosion set-up

channel	slope of validation line	deviation of slope from 1 [%]	R² [-]
0	1.0048	0.48	1
1	1.0038	0.38	1
2	1.0031	0.31	1
3	1.0047	0.47	0.9999
4	1.0048	0.48	1
5	1.0032	0.32	1
6	1.0062	0.62	1
7	1.0026	0.26	1

BIBLIOGRAPHY

AÏTCIN, P.C., 2005. Libros del curso “Ingeniería de los Cementantes Hidráulicos”; Doctorado en Ingeniería de Materiales de Construcción y Estructuras. Cuerpo académico de Tecnología del Concreto.

ASPDIN, J., 1824. An Improvement in the Mode of Producing an Artificial Stone. Great Britain:

ASTM C109 / C109M - 11B, 2011. ASTM C109 / C109M - 11b Standard Test Method for Compressive Strength of Hydraulic Cement Mortars (Using 2-in. or [50-mm] Cube Specimens).

BARTHOLOMAEUS, A., 2003. Batman vppon Bartholome his booke De proprietatibus rerum, newly corrected, enlarged and amended: with such additions as are requisite, vnto euery seuerall booke: taken fourth of the most approued authors, the like heretofore not translated in English. Profitable for all estates, as well for the benefite of the mind as the bodie. 1582. Ann Arbor, Michigan: University of Michigan, Digital Library Production Service.

BERTOLINI, L., ELSENER, B., PEDEFERRI, P. and POLDER, R.B., 2003; 2005. Corrosion of Steel in Concrete. Wiley-VCH Verlag GmbH & Co. KGaA

BHATTACHARYYA, T., 2011. Self healing in concrete materials.

BINKS, B.P., 1993. Emulsion type below and above the CMC in AOT microemulsion systems. 71(2), pp. 167.

BLEZARD, R.G., 2003. 1 - The History of Calcareous Cements. Lea's Chemistry of Cement and Concrete (Fourth Edition). 4th edn. Oxford: Butterworth-Heinemann, pp. 1.

BRITISH PATENT, 1996. BS 12:1996, Specifications for Portland Cement. Great Britain.

DUBEY, R., 2009. Microencapsulation Technology and Applications. Defence Science Journal, 59(1).

FELDER-CASAGRANDE, S., WIEDEMANN, H.G. and RELLER, A., 1997. The calcination of limestone — Studies on the past, the presence and the future of a crucial industrial process. Volume 49(2), pp. 971-978.

FRÈRE, Y., DANICHER, L. and GRAMAIN, P., 1998. Preparation of polyurethane microcapsules by interfacial polycondensation. Kidlington, ROYAUME-UNI: Elsevier.

GAMBHIR, M.L., 2004. Concrete Technology. 3rd edn. New Delhi: The McGraw-Hill Companies.

GHOSH, S.K., 2008; 2009. Self-Healing Materials: Fundamentals, Design Strategies, and Applications. Self-Healing Materials. Wiley-VCH Verlag GmbH & Co. KGaA, pp. 1-28.

GLASSER, F.P., 2003. 5 - The Burning of Portland Cement. Lea's Chemistry of Cement and Concrete (Fourth Edition). 4th edn. Oxford: Butterworth-Heinemann, pp. 195.

HEWLETT, P., 2004. Lea's Chemistry of Cement and Concrete. forth edn. Oxford UK: Butterworth-Heinemann.

HISTORICAL STANDARD, 2004. ASTM C1585-04 Standard Test Method for Measurement of Rate of Absorption of Water by Hydraulic-Cement Concretes.

IONESCU, M., 2005. Chemistry and Technology of Polyols for Polyurethanes. Shawbury, Shrewsbury, Shropshire, UK: iSmithers Rapra Publishing.

JACKSON, P.J., 2003. 2 - Portland Cement: Classification and Manufacture. Lea's Chemistry of Cement and Concrete (Fourth Edition). 4th edn. Oxford: Butterworth-Heinemann, pp. 25.

JONKERS, H.M., THIJSEN, A., MUYZER, G., COPUROGLU, O. and SCHLANGEN, E., 2010. Application of bacteria as self-healing agent for the development of sustainable concrete. Ecological Engineering, 36(2), pp. 230.

KHANDPUR, R.S., 2006. Handbook of Analytical Instruments. 1st edn. New York, NY: McGraw-Hill Professional.

KONDO, T., 2001. Microcapsules: Their Science and Technology Part I. Various Preparation Methods. Journal of Oleo Science, 50(1), pp. 1-11.

KOVLER, K. and ROUSSEL, N., 2011. Properties of fresh and hardened concrete. 41(7), pp. 775.

LAWRENCE, C.D., 2003. 4 - The Constitution and Specification of Portland Cements. Lea's Chemistry of Cement and Concrete (Fourth Edition). 4th edn. Oxford: Butterworth-Heinemann, pp. 131.

LI, Z., 2011. Advanced Concrete Technology. John Wiley & Sons, Inc.

MACLAREN, D.C. and WHITE, M.A., 2003. Cement: Its Chemistry and Properties. Journal of chemical education, 80(6), pp. 623.

MACPHEE, D.E. and LACHOWSKI, E.E., 2003. 3 - Cement Components and Their Phase Relations. Lea's Chemistry of Cement and Concrete (Fourth Edition). 4th edn. Oxford: Butterworth-Heinemann, pp. 95.

MERQUINSA, Polyurethane Types.

<http://www.merquinsa.com/whats/FPPUtypes1.pdf>, last access 8/15/2012, 8:42 AM

MIHASHI, H., KANEKO, Y., NISHIWAKI, T. and OTSUKA, K., 2000. Fundamental study on development of intelligent concrete characterized by self-healing capability for Strength. 22, pp. 441-450.

MINDESS, S., YOUNG, J.F. and DARWIN, D., 2002. Concrete. Upper Saddle River, NJ 07458, U.S.A.: Prentice Hall.

NORDSTRÖM, J., NILSSON, E., JARVOL, P., NAYERI, M., PALMQVIST, A., BERGENHOLTZ, J. and MATIC, A., 2011. Concentration- and pH-dependence of highly alkaline sodium silicate solutions. 356(1), pp. 37.

ODLER, I., 2003. 6 - Hydration, Setting and Hardening of Portland Cement. Lea's Chemistry of Cement and Concrete (Fourth Edition). 4th edn. Oxford: Butterworth-Heinemann, pp. 241.

PELLETIER, M.M., 2010. Self-healing concrete.

SAIHI, D., VROMAN, I., GIRAUD, S. and BOURBIGOT, S., 2006. Microencapsulation of ammonium phosphate with a polyurethane shell. Part II. Interfacial polymerization technique. Reactive and Functional Polymers, 66(10), pp. 1118.

SIMS, I. and BROWN, B., 2003. 16 - Concrete Aggregates. Lea's Chemistry of Cement and Concrete (Fourth Edition). 4th edn. Oxford: Butterworth-Heinemann, pp. 907.

SONG, H. and SARASWATHY, V., 2007. Corrosion Monitoring of Reinforced Concrete Structures - A Review. 2(1), pp. 1-28.

SOTTOS, N., WHITE, S. and BOND, I., 2007. Introduction: Self-healing polymers and composites. 4, pp. 347-348.

WAGH, S.J., DHUMAL, S.S. and SURESH, A.K., 2009. An experimental study of polyurea membrane formation by interfacial polycondensation. 328(12), pp. 246.

WARREN, B.E., 1990. X-Ray diffraction.

WOODSON, R.D., 2009. Chapter 6 - Materials and methods for repair and rehabilitation. Concrete Structures. Boston: Butterworth-Heinemann, pp. 61.

WU, M., JOHANNESSON, B. and GEIKER, M., 2012. A review: Self-healing in cementitious materials and engineered cementitious composite as a self-healing material. 28(1), pp. 571.

YADAV, S.K., RON, N., CHANDRASEKHARAM, D., KHILAR, K.C., SURESH, A.K. and NADKARNI, V.M., 1996. Polyureas by interfacial polycondensation: Preparation and properties. Journal of Macromolecular Science, Part B, 35(5), pp. 807-827.

ZHANG, J., LI, L., WANG, J., SUN, H., XU, J. and SUN, D., 2012. Double Inversion of Emulsions Induced by Salt Concentration. *Langmuir*, 28(17), pp. 6769-6775.

ZHANG, M.Q. and RONG, M.Z., 2011. Frontmatter. *Self-Healing Polymers and Polymer Composites*. John Wiley & Sons, Inc., pp. i-xii.

April 5, 2013

Title: Structural Response to Non-ideal Explosions

Sponsor: Department of Homeland Security Science & Technology Directorate (DHS/S&T) Explosives Center of Excellence (COE) through URI and NEU.

PI: J.E. Shepherd, **Student Researchers:** J. Damazo

Objective and Summary of Activities in 2012–2013

Gaseous detonation experiments were performed in the Explosion Dynamics Laboratory at the California Institute of Technology to investigate the effect of internal explosions on surrounding structures. Detonations were used as a model to simulate the pressure and heat loadings caused by non-ideal explosions. The overall project objective is to develop the capability to predict the degree of damage induced by a non-ideal explosion in tubes and to investigate methods to mitigate the extent of this damage. The objective of testing in 2012-2013 was to obtain systematic data on pressure, heat transfer, and boundary layer interaction using a range of combustible mixtures. This was accomplished and the work is currently being written up and will form the basis of J. Damazo's PhD dissertation and subsequent journal articles. We anticipate Damazo's PhD will be awarded in June 2013.

Highlighted Accomplishments

1. Completed the experimentation in the gaseous detonation tube facility to document visual, pressure, and heat flux measurements for a range of mixture fuels, diluents, and initial pressures.
2. Carried out non-ideal explosion experiments examining the gas dynamics of reflected shock and detonation waves inside tubes with closed end.
3. Applied analytical boundary layer theory to the case of a propagating detonation and compared predictions to heat flux measurements.
4. Used short exposure, high frame-rate schlieren photography to record the first movies of planar reflection of gaseous detonations.
5. Analyzed time-of-arrival signals from pressure and optical measurements and determined the source of the previously documented discrepancies between ideal zero-thickness detonation reflection theory and experiments. Applied a finite-thickness reaction zone model to explain observed reflected wave speeds.

Details

In order to predict damage, pressure and thermal loadings to the structure must be understood sufficiently well to create models that can be incorporated into structural dynamics simulations. In the earlier phases of this project (summarized in Karnesky et al., 2013), we created an idealized pressure load based on one-dimensional gas dynamics and a zero-thickness model of a detonation wave. Experiments on thin-wall tubes and structural simulations with LS-DYNA were used to validate the loading model that described the pressure field before and after detonation reflection from a closed end. Although our model was highly successful in making quantitative predictions of plastic deformation, significant discrepancies between pressure and wave speed were observed. In order to improve the loading model, we needed to understand the sources of these discrepancies, which we initially had attributed as being due to viscous effects, i.e., reflected shock wave-boundary layer interaction, that were neglected in our initial modeling efforts. We also had neglected thermal loads in our initial models and did not have any data to validate proposed thermal models.

For these reasons, we developed new experiments to specifically examine the reflection process in sufficient detail that we could determine thermal loads, viscous interaction effects, and the effect of detonation structure. An extensive set of tests was carried out for incident detonation and shock waves in a variety of test gases using a test fixture instrumented with pressure and heat flux gauges. Because pressure and thermal loads are greatest in locations of wave reflection, the measurement gauges were clustered near an end-wall wall where the waves underwent planar reflection. The experimental facility was designed to allow for optical access to the reflection event. High-speed schlieren images were captured using a Specialised Imaging SIMD16 set to record 16 frames at 750,000 pictures per second (pps) and 20 ns exposure time. With these measurement techniques, the gas dynamics of reflected shock and detonation waves were observed.

The goals of the detonation tube experiments are to measure the wall pressure and heat flux loading caused by either a reflecting shock or detonation wave. To observe this flow, we use a schlieren imaging system to visualize the incident and reflected waves. The speed of the detonation wave is 2-3 km/s implying any visualization system must have exposure times on the order of tens of nanoseconds and a frame-rate on the order of 500,000 frames per second (fps).

The experiments were carried out in the GALCIT detonation tube (Fig. 1), a special-purpose facility which was designed and built at Caltech specifically to carry out experimentation on detonation waves. The facility consists of a 288-mm diameter tube with a special ignition system at one end and square (150 x 150 mm) test section with optical access at the other end. The ignition system uses a combination of electrical (capacitor discharge into an exploding wire) and chemical (a short section of an acetylene-oxygen mixture) energy to create a nearly planar detonation wave. The detonation propagates away from the point of ignition towards the test section at the constant theoretical Chapman—Jouguet (CJ) velocity. The Taylor—Zel'dovich (TZ) expansion wave trails the detonation and gradually brings the fluid to rest. Once the detonation impinges upon the test section's closed end, a reflected shock wave propagates into the TZ expansion at a non-constant speed. The detonation facility is 7.6 m in length implying that the effects of the TZ expansion are relatively slow so that near the end wall at times immediately following the reflection event, we may approximate the reflected shock as propagating into a steady and spatially uniform flow.

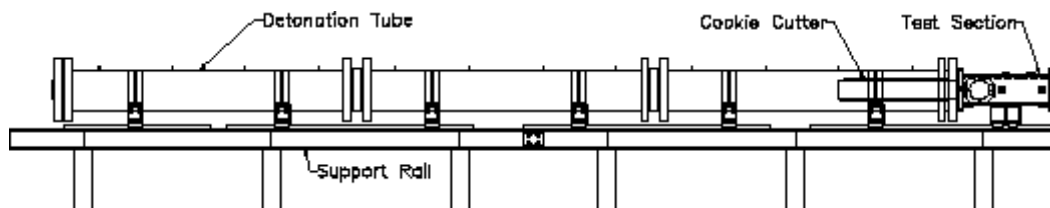


Figure 1. Diagram of experiment used in detonation experiments; the tube and test section are 7.6 m in length.

A “splitter” plate parallel to the horizontal walls and with a sharp leading edge is inserted into the test section to raise the location of the boundary layer into the center of the observation windows. This splitter plate was instrumented with 12 PCB 113B26 pressure transducers and 12 surface junction thermocouples identical to those employed by Sanderson and Sturtevant (Rev Sci Inst 73(7), 2781-7, 2002) for measuring heat flux inside the test section. The thermocouple signals are amplified by a TriTek Model 205B instrumentation amplifier with a response time of 7.5 μ s to a unit step input. The spectral method employed by Sanderson and Sturtevant is used for reducing the heat flux data. A Z-type schlieren system is used to visualize the incident detonation and shock wave reflection. The schlieren system consists of a Photogenic PL1000DRC flashlamp combined with a Specialised Imaging SIMD16 intensified CCD camera. To satisfy the low exposure time, high frame-rate requirement, the SIMD16 was operated with a shutter speed of 20 ns and an intra-frame time of 1.27 μ s (corresponding to a frame-rate of approximately 775,000 fps). This allows sixteen images to be taken in quick succession and was used to visualize the incoming detonation and the reflected shock wave for each test.

Stoichiometric hydrogen-oxygen and ethylene-oxygen mixtures of various initial pressure and dilutions were used to study the effects of composition on the dynamics of the reflected shock. Figure 2 shows pressure signals from two detonations of stoichiometric hydrogen-oxygen at an initial pressure of 25 kPa. Data from two experiments with identical initial conditions were plotted to illustrate the repeatability in the experiment. These pressure signals allow us to properly assess the pressure loading to the tube wall as a function of time and distance from reflection. We are also able to examine the wave time-of-arrival at each location and thereby determine wave speeds. Time-of-arrival data with a range associated with the rise time of the pressure signals is plotted for each pressure signal in Fig. 2 as vertical dashed black lines. We see that the characterization of the arrival time range is especially important for the reflected shock due to the observed rise time that is approximately 10 times longer than the rise time associated with the incident detonation.

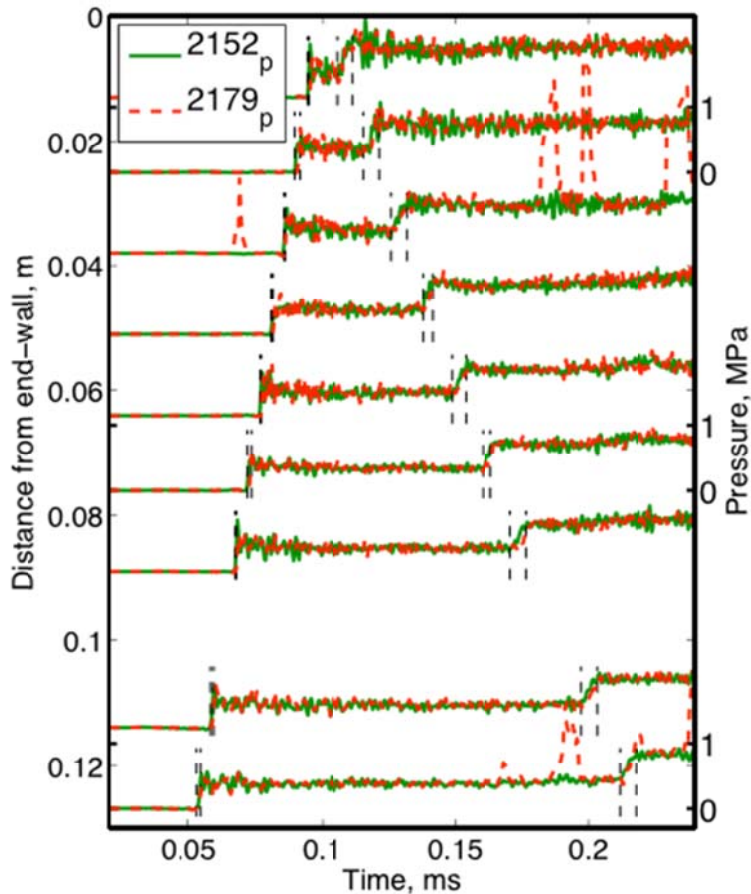


Figure 2. Pressure data from two experiments of stoichiometric hydrogen-oxygen at an initial pressure of 25 kPa. The dashed black lines represent range of time characterizing the rise time for incident and reflected wave arrival.

The schlieren video for shot 2152 (the red line of figure 2) is shown in figure 3(a). Sixteen frames are shown and are given chronologically in left-to-right, top-to-bottom. Each frame shows the same 30 mm wide field of view. The detonation is initially seen to propagate towards the end-wall located at the right-edge of the frame. The detonation impinges upon this wall in frame 7. Frames 8-16 then show the reflected shock wave propagating back to the left. There is a great deal of information regarding the gas dynamics of detonation reflection that can be learned from these images. Focusing the analysis on the wave location in each image, we can complement the pressure measurement arrival data. Processing the data in each frame, we are able to determine the wave location and quantify the uncertainty

due to the smearing of the front location because of the three-dimensional cellular structure of the detonation. Combining this data with the arrival data obtained from the pressure signals, we can construct the space-time diagram shown in Fig. 3(b). Detonation arrival data are shown in red and reflected shock arrival data are shown in blue. The dashed lines correspond to the one-dimensional theory described in our journal publication, Karnesky et al. (2013). The solid lines correspond to a polynomial fit to the arrival data of the form

$$X_{\text{det}} = U_{\text{det}}(t_0 - t)$$

$$X_{\text{sh}} = U_{\text{sh}}(t - t_0) + \frac{1}{2}a_{\text{sh}}(t - t_0)^2$$

U_{det} and t_0 , with error bars, are determined from the detonation data and U_{sh} and a_{sh} are fit to the reflected shock data. Numbers for the specific experiment shown in Figs. 2 and 3 are given in Table 1.

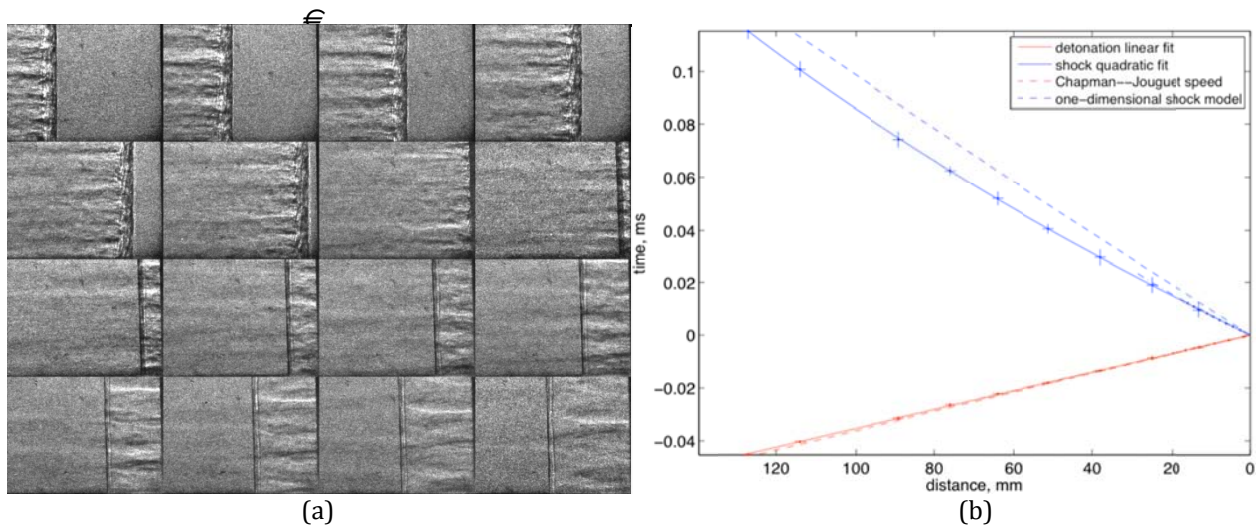


Figure 3. (a) Sixteen schlieren images obtained from a single detonation experiment of stoichiometric hydrogen-oxygen at an initial pressure of 25 kPa. Images are read left-to-right, top-to-bottom. Each frame is 30 mm wide. (b) Pressure and image data are combined to assemble a detailed picture of detonation wave reflection. A polynomial fit is employed to show that the reflected wave speed at the wall is substantially faster than predicted by an ideal one-dimensional reflection model.

Examining Fig. 3(b) and Table 1, we observe that the reflected wave speed is substantially under-predicted near the wall by the highly idealized zero-thickness model of detonation reflection. This is true in every experiment we performed and the discrepancy is far outside of any measurement uncertainty. After considering various possibilities, we believe that the source of this discrepancy is that the ideal model does not consider the finite reaction zone structure of the detonation wave. The ideal model of reflection considers a detonation wave that is infinitely thin, appearing to be a sharp jump in properties from reactants directly to combustion products. Real detonation waves consist of a non-reacting shock wave followed by a finite-thickness reaction zone. In addition, as observed in Fig. 3 the detonation wave is not precisely planar and the flow behind the wave is three-dimensional due to the instability of the detonation wave as manifested by the transverse shock waves (commonly referred to as cellular structure). Setting aside the three-dimensional structure of the wave (which can only be addressed through numerical simulation), we consider a one-dimensional model of detonation wave as a non-reacting shock followed by a zone of chemical reaction. The rates of chemical reaction and energy release determine the structure and thickness of the reaction zone. The initial portion of the reaction zone is termed the induction zone and is a region where radicals are increasing exponentially in concentration but the energy release is small so that the thermal properties of the gas are those behind the initial non-reacting shock. At the downstream end of the induction zone, there is a narrow zone of large energy release followed

by a slow approach to equilibrium – this is the classical ZND model of detonation structure.

Considering the reflection of the finite-thickness model of the detonation, we observe that immediately after leading shock wave reflects from the wall it will encounter shocked but un-reacted gas. The reaction will occur very quickly behind the reflected shock because the temperature and pressure are already so high within the reaction zone and are increased further by the reflected shock. As a consequence, the induction zone explodes almost instantly when the reflected shock wave moves into it. Approximating the explosion process as a detonation in the shocked but un-reacted gas in the induction zone, we obtain an estimate of the initial reflected shock speed that is in much better agreement with the measured values, as shown in the last column of Table 1.

Mixture	p_0 , kPa	Measured U_{sh} , m/s	Zero Thickness U_{sh} , m/s	Finite Thickness U_{sh} , m/s
H2-O2	25 kPa	1389 ± 6	1049	1393
		% difference from experiment:	24.5%	0.3%

Table 1. Reflected shock speeds as determined from the experiment, a zero thickness detonation model, and a finite thickness detonation model. The thermodynamic states and wave speeds are found using the Shock and Detonation Toolbox (Browne et al. GALCIT Technical Report FM2006-006, 2008).

Summary

A systematic experimental investigation of detonation reflection has been performed. The pressure and heat flux was measured behind an incident detonation and reflected shock wave for a range of compositions and initial pressures. High-speed schlieren images were obtained showing the interactions of the reflected shock wave with the transverse wave structure as well as the boundary layer set up by the incident detonation. Very minimal disruption of the reflected shock is observed due to interaction with the incident wave boundary layer. The lack of significant reflected shock wave bifurcation verifies earlier results with single images and conclusively rules out shock-wave boundary layer interaction as a significant factor in detonation reflection for a wide range of mixtures. Detailed analysis was carried out on the time-of-arrival data gathered from the pressure signals and schlieren photographs. These measurements confirmed the previously noted mismatch between the reflected shock speed and zero thickness model of detonation reflection. In addition, the data analysis revealed that a very high initial reflected shock velocity and rapid deceleration is responsible for the disagreement between the experimental data and zero-thickness model proposed by Karnesky et al. The high initial reflected shock speed can be explained by considering the finite thickness of the reaction zone and the interaction of the reflected shock wave with the induction zone region, resulting in a rapid explosion of the induction zone region. Modeling this explosion as the detonation of shocked but un-reacted gas as computed with the ZND detonation model yields very good agreement for the initial reflected shock speed.

Publications and Presentations

1. J. Damazo, J. Odell, and J. E. Shepherd. *Boundary Layer Profile Behind Gaseous Detonation as it Affects Reflected Shock Wave Bifurcation*. Proceedings of the 42nd AIAA Fluid Dynamics Conference, New Orleans, June 25-28, 2012. (Conference proceedings paper and presentation)
2. J. Damazo and J. E. Shepherd. *Planar Reflection of Detonation Waves*. Proceedings of the 65th Fall Meeting of the American Physical Society's Division of Fluid Dynamics, San Diego, November 18-20, 2012. (Conference proceedings paper and presentation)
3. J. Karnesky, J. Damazo, K. Chow-Yee, A. Rusinek, J. E. Shepherd "Plastic Deformation due to Reflected Detonation" *International Journal of Solids and Structures*, 50:97-110, 2013.

Experimental Investigation of Blast Mitigation for Target Protection

S. F. Son^a, A. J. Zakrajsek^a, E. J. Miklaszewski^a, D. E. Kittell^a, J. L. Wagner^b, D. R. Guildenbecher^b

^aPurdue University, West Lafayette, IN 47906, USA

^bSandia National Laboratories, Albuquerque, NM 87185, USA

Introduction

Blast waves, whether from conventional munitions or improvised explosive devices, pose a major risk to people and property throughout the world [2]. Engineering methods to protect individuals and structures vary widely due to the diverse range of threats and potential situations. This chapter focuses narrowly on the protection of high-valued structures and other large targets where removal from the threat zone is often impossible. In these situations, methods are needed to dissipate and reflect incoming blast waves and mitigate damage potential.

Any proposed mitigation method must be evaluated for effectiveness, and while steady advances in computational physics have been made in this area, experimentation remains crucial. Therefore, this chapter emphasizes experimental methods for evaluation of blast mitigation, both from a practical and fundamental standpoint. In addition, some of the capabilities of current computational methods are highlighted. The chapter begins with a review of the underlying physics. This is followed by a brief overview of experimental methods. Finally, the remainder of the chapter is dedicated to recent experimental and computational results for a potential configuration involving protective water sheets.

Physics of blast waves

Detonation releases a large amount of energy in a small volume, and in an unconfined gaseous environment, such as air, energy interactions quickly give rise to a blast wave expanding in all directions. At a fixed point away from the detonation, a near-instantaneous in-

crease in the static pressure is followed by a period of rapid pressure decay. Depending on the conditions of the blast and the distance from the source, the static pressure may eventually fall below atmospheric. Finally, with sufficient time, pressure equilibrates back to atmospheric.

Figure 1 illustrates a typical blast profile. The initial pressure rise is due to a shock wave whose properties are well approximated using the Rankine-Hugoniot relations [3]. The shock *overpressure*, Δp , defined as the instantaneous peak static pressure minus the ambient pressure, typically peaks during the passage of the leading shock. The time period of positive static pressure is defined as the *positive pulse duration*. The *impulse* is defined as the area under the pressure curve during the positive pulse duration. Finally, the negative pulse duration and negative impulse are typically much longer and smaller than the positive pulse. Effects of the negative pulse are often assumed negligible for blast mitigation design.

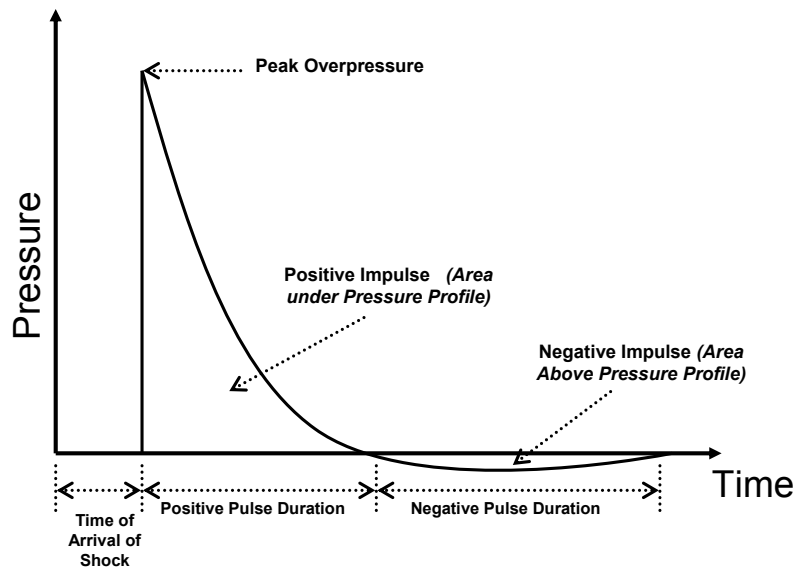


Figure 1: Typical static pressure profile of a blast wave measured at a fixed point in space.

In general, a lower overpressure and impulse leads to greater blast-wave survivability. Theoretical analyses of blast waves have

been completed by a number of authors, with classic analytic expressions provided by Taylor [4, 5], Sedov [6], and others. In agreement with common experience, all of these analyses show a strong decrease in overpressure and impulse with increasing distance from the source. Therefore, it is clear that an effective defense against the damaging effects of a blast wave is to separate the source of the blast and the target. For this reason, high-value targets, such as the White House, embassies, large ships, and so on, often have established perimeters with restricted access for individuals and vehicles. However, such perimeters cannot be made infinitely large and are particularly challenging to implement for existing structures in urban settings. In some cases adequate standoff distances are simply not possible. For this reason, novel and cost effective methods are needed to protect such structures and their inhabitants. This is the focus of the remainder of the chapter.

Experimental methods

Explosive Field-Tests

The literature includes a large number of proposed blast mitigation methods. Examples include barriers of soil, concrete, foams sprays, polycarbonate, steel, etc. Evaluation of the effectiveness of these methods requires quantification of the change in overpressure and impulse to the target compared to an un-mitigated blast. This is most often achieved via field-tests involving actual explosives, which is the focus of the first half of this section. However, explosive blast testing is expensive and lacks repeatability necessary to resolve fundamental phenomena. Diagnostics that can be applied in the field are also limited. For this reason, fundamental investigations of mitigation mechanisms have recently been performed in more controlled environments, such as pressure-driven shock tubes, which is the focus of the second half of this discussion.

At a test range, an explosive charge of known quantity is placed some distance away from a target, and blast loading experiments are conducted with and without the proposed mitigant in-place. Pressure transducers are used to measure the overpressure, positive pulse duration, and impulse. The time scales of interest are often on the order of milliseconds to microseconds, during which time the ther-

mal and mechanical loading can be significant. Fast pressure transducers are required, which can stand-up to this harsh environment. Among the various commercially available configurations, pressure transducers based on the piezoelectric principle are most often utilized. These transducers contain piezoelectric crystals that convert mechanical stress into an electrical signal and are sensitive to rapid changes in overpressure.

To obtain quality measurements, the experimentalist must take care to properly select and configure pressure transducers. In any flow measurement, proper placement and orientation of pressure transducers are crucial. Where the flow is parallel to the sensing surface, the transducer measures the static pressure. In blast measurements, this is most often achieved with a ruggedized probe shaped like a pencil with the pointed end facing the incoming blast wave. The design allows the wave to propagate with minimal distortions along the side of the probe, which contains the sensing element. Alternatively, a pressure transducer may be orientated with its sensing element facing the incoming blast wave. In this orientation, the sensor quantifies the reflected overpressure, which can be related to the incident overpressure assuming idealized shock relations [3]. Regardless of the orientation, additional care must be taken to ensure that measurements are unaffected by mechanical vibrations, thermal stress, and line losses. Industrial transducer suppliers can assist with these issues, which tend to be transducer specific.

In addition to pressure measurements, optical techniques, such as high-speed imaging, Schlieren, and shadowgraphy, have been applied to image the shock waves in an experiment [7]. These techniques are equally applicable to shock tube experiments or blast experiments.

Shock Tube Experiments

The shock tube is a basic instrument often used for shock attenuation research relevant to blast mitigation [8-18]. In addition, shock tubes are commonly utilized in aerodynamics [19-23], fluid dynamics [24-29], shock physics [30-32], and combustion experiments [33, 34]. As is shown in Fig. 2a, the basic components of a shock tube include a high pressure driver section (region 4) and a low pressure driven section (region 1), which are initially divided by a diaphragm [1]. Upon rupture of the diaphragm (Fig. 2b), a normal shock wave is formed in response to the instantaneous pressure difference between the driver and driven sections. With continuing time, the shock wave propagates downstream resulting in a high-speed, shock-induced flow with velocity u_2 , which is often utilized in fluid

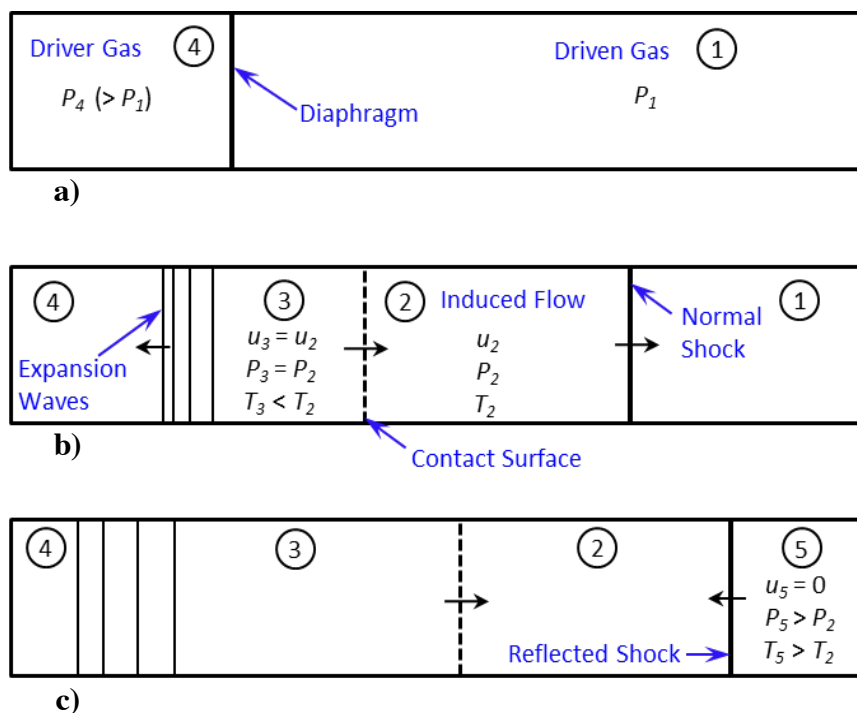


Figure 2. Illustration of basic shock tube principles. Both the figure and accompanying text are after Anderson [1]: a) initial conditions, b) following the rupture of the diaphragm, and c) following reflection of the normal shock from the end-wall.

dynamics experiments. Upstream of region 2, a contact surface separates the driver and driven gases. The contact surface moves at a velocity u_3 equal to u_2 . Across the contact surface the pressure is equal, but there is a discontinuity in temperature and entropy. Expansion waves form causing pressure in the driver gas to continuously vary between regions 3 and 4. Depending on the initial conditions in the shock tube, the expansion waves may propagate to the left or to the right. Eventually, the normal shock will reach the end of the tube resulting in a reflected shock wave as is shown in Fig 2c. To match the end-wall boundary condition, the reflected shock must completely slow the flow in region 5 to a velocity of zero [1]. To obtain high temperatures, chemical kinetics experiments are commonly performed in this region of twice-shocked flow.

Many studies have used shock tubes to evaluate the use of porous materials for blast mitigation [8-13]. Several other experiments have measured the effects of compressible foam placed upstream of a wall in the path of a normal shock wave [8-10]. The foam results in a decrease in reflected shock strength, although, importantly, the pressure at the back wall is amplified significantly in comparison to experiments without foam. Tests with rigid porous materials placed upstream of shock tube end-walls also indicate an increase in end-wall pressure compared to the baseline case [11]. However, this increase appears to be less than that in deformable foam experiments [10]. In addition, experiments have demonstrated the attenuation of detonation waves traveling along porous walls [12] and walls lined with foams [13].

The use of solid particles for blast mitigation has also been tested in shock tube experiments [14-17], where the general configuration involves placing gas-solid mixtures upstream of incident normal shock waves. Based on the data of Sommerfeld [14], Aizik et al. [15] gave a correlation for shock attenuation in dilute gas-solid mixtures, which they claimed to be valid for particle volume fractions less than 1%. The use of denser particle mixtures has also been evaluated. For example, streamwise-thin particle curtains with dense particle volume fractions of 20% have resulted in modest shock attenuation [16] and streamwise-thick, granular filters consisting of packed particle beds have led to significant shock attenuation [17].

Water sheets in the path of normal shock waves have also been tried for mitigation purposes [18]. In comparison to undisturbed shocks, the shocks transmitted through the water sheets were diminished. However, as a result of subsequent compression waves and impinging water droplets, the peak end-wall pressures in experiments with water sheets were up to ten times higher than those without water and the impulses were up to two times higher [18].

The above discussion demonstrates the complexities and tradeoffs associated with shock attenuation techniques. For example, a reduction in shock strength is often accompanied with an increase in peak pressure that occurs more gradually.

Although many studies have focused on the attenuation of planar shock waves in shock tubes, little work has been aimed at understanding the physical mechanisms involved in mitigating the expanding blast waves associated with real detonations. New data are required to enable effective blast mitigation methods. Towards this end, experiments have been conducted for water sheets subjected to blasts from an explosively driven shock tube, which is the subject of the remainder of this chapter.

Mitigation using unconfined water sheets

As discussed above, an explosion yielding a blast wave can cause catastrophic damage to people and property. To mitigate damage from such an event, a number of investigators have proposed the use of water in various configurations. Water sprays, attached barriers, and sheets could be explored. In this investigation, an unconfined free-flowing water-sheet, with an approximate thickness of 0.3 cm, is experimentally examined using an explosively driven shock tube at three different standoff distances. This differs somewhat from the shock tube experiments described above and is meant to simulate an explosive blast profile. The results presented in this section show that the water-sheet mitigates the initial peak overpressure and impulse of the blast. Further insights into the underlying physics are revealed by a numerical simulation using Sandia's CTH hydrocode [35].

Water is an attractive material for use as a blast mitigant because it is often readily available [36]. Previous investigations have fo-

cused on blast mitigation by water sprays or confined masses of water [36, 37] with mixed success as quantified by the peak overpressure and impulse mitigation. An alternative geometry is that of a free-flowing water sheet forming a shield around the object to be protected. A few numerical models have considered this geometry [38, 39], and their results indicate that water sheets may effectively limit the peak overpressure of the blast. However, there are limited experimental data to validate these findings. Meekunnasombat *et al.* [18] considered liquid layers in a confined vertical shock tube, and their experiments highlighted the advantageous behavior of multiple layers of water. However, it is unclear if their results can be extended to the case of the unconfined water sheet, which is the likely geometry for practical blast mitigation. In addition, Bremond and Villermaux [40] considered the breakup of a thin soap film under normally incident shock loading. However, it is unclear if the physical breakup mechanisms revealed in their investigation can be extended to the thicker water sheets considered here.

The aim of this work is to study the blast mitigating potential associated with a sheet of water. To elucidate the fundamental physics, an experimental investigation is coupled with a numerical model. The following two sections focus on the experimental configuration and results, respectively. Numerical results are presented in subsequent section. The results presented here form an initial starting point to determine the feasibility of water sheets as a possible blast mitigant.

Experimental configuration for water sheets

Explosively driven shock tube

Experiments were conducted in an open field, with an explosively driven shock tube, and a custom fabricated water sheet generator. A schematic of the experimental configuration is shown in Fig. 3. The explosively driven shock tube is used to produce a relevant laboratory size blast wave. Previous work has shown that this configuration yields a blast profile similar to open field explosive tests, and the shock tube directs the energy from the blast in one direction allowing for the use of less explosive as compared to a conventional open field explosive test [41, 42].

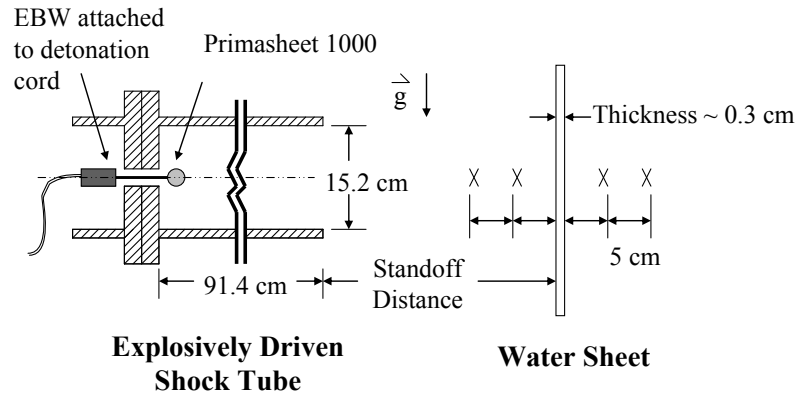


Figure 3. Experimental configuration for investigation of blast loading of an unconfined water sheet. The out of plane water sheet dimension is roughly 70 cm, while the in plane height is 30 cm. The “X’s” indicate the location of the static pressure gauges which are positioned along the centerline of the shock tube.

In an experiment, the explosively driven shock tube is loaded with 3 grams of Primasheet 1000. Primasheet 1000 is a pentaerythritol tetranitrate (PETN) based plastic explosive consisting of approximately 63% PETN powder. Initiation of the PETN plastic sheet explosive is achieved by a combination of detonation cord (PETN powder) and an explosive bridge wire (EBW) detonator (RP-502 EBW) charged by a firing set, see Fig 3.

The shock tube consists of a detonation chamber and a high explosive chamber. The two chambers are bolted together to protect the cables, test apparatus, and other equipment from the fragments produced by the aluminum detonator cap. A small hole links the two chambers and allows for passage of detonation cord. By changing the distance of the shock tube from the water sheet (defined as the *standoff distance*), the characteristics of the incident shock wave are altered. Decreasing the standoff distance increases the overpressure at the water sheet.

Water sheet generator and pressure gauges

A water sheet is generated with a custom fabricated water sheet generator, operating at a constant flow rate of approximately 56 L/min, producing a sheet approximately 0.3 cm thick. In the ab-

sence of blast loading, the sheet is continuous and displays surface perturbations, which likely arise from turbulent or capillary instabilities. In an experiment, the incoming blast wave is approximately normal to the water sheet.

Due to space constraints near the water sheet, typical pencil gauges cannot be placed at the locations marked in Fig. 3 without disrupting the water flow. Instead, PCB 113A22/113B22 piezoelectric dynamic pressure sensors were threaded into custom fabricated plates orientated to measure the static pressure of the blast. The experimental configuration includes two pressure gauges placed in front and two behind the water sheet, as shown in Fig 3. As the water sheet standoff distance is varied from one experiment to the next, the pressure gauges are repositioned to maintain the distances with respect to the water sheet shown in Fig. 3.

Shadowgraphy visualization

In select experiments, the shock wave is visualized using the high-speed shadowgraphy technique described in [43]. Videos are recorded at 11,494 fps and an exposure of 26 μ s using a Vision Research Phantom v7.3 digital high-speed camera and an Oriel 1000 W xenon arc lamp. The field of view is approximately 53 by 53 cm and is recorded on a 171 by 171 pixel region of the CCD.

Water sheet experimental results

Experiments were performed at three different standoff distances: 20 cm, 31 cm, and 41 cm (distance from exit of shock tube to water sheet). To verify repeatability, all experiments were performed three times. Further repetition of experimental conditions was cost prohibitive, as is often the case in explosive field measurements.

Pressure measurements

Figure 4 shows the free field pressure traces taken without the water sheet. Additionally, tabulated values for all free field distances measured are shown in Table 1. Figure 5 displays the pressure traces from an experiment with a water sheet at a 31 cm standoff distance. Note the significantly lower peak pressures at distances behind the water sheet (36 and 41 cm). Other standoff distances produce similar results. Table 2 summarizes the pressure measurements after the wa-

ter sheets, for all three standoff distances considered. In this table, the peak overpressure is taken as the highest recorded static pressure during the transient experiment. The standard error is calculated between the three experiments performed at each condition.

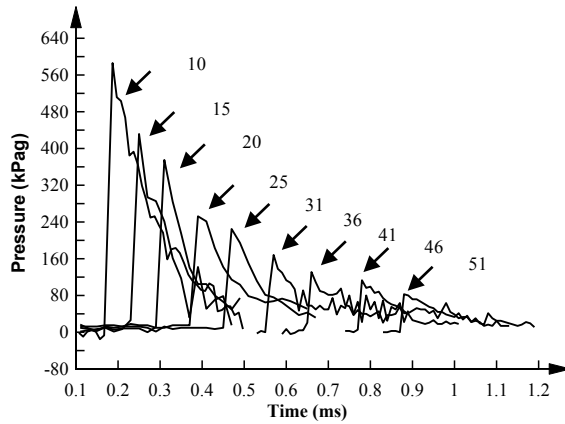


Figure 4. Free field experimental pressure traces. Numbers indicate the distances in cm between the exit of the shock tube and the pressure gauge.

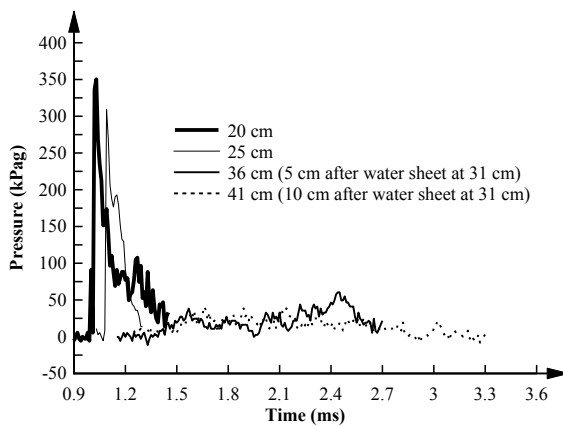


Figure 5. Pressure trace of a blast test with a water sheet at a 31 cm standoff distance. Numbers indicate the distances in cm between the exit of the shock tube and the pressure gauge.

Table 1. Free field (no water sheet) experimental shock wave parameters. Uncertainties indicate the standard error.

Pressure Gauge Standoff Distance (cm)	Peak Over-pressure (kPa)	Impulse (kPa-ms)	Positive Pulse (ms)
10	586 ± 29	60 ± 9	0.2 ± 0.1
15	436 ± 18	35 ± 8	0.2 ± 0.1
20	389 ± 15	32 ± 5	0.3 ± 0.1
25	253 ± 21	32 ± 3	0.3 ± 0.1
31	203 ± 19	19 ± 5	0.2 ± 0.1
36	169 ± 3	19 ± 4	0.3 ± 0.1
41	130 ± 1	18 ± 2	0.3 ± 0.1
46	117 ± 4	18 ± 1	0.4 ± 0.1
51	88 ± 6	12 ± 1	0.3 ± 0.1

Table 2. Initial experimental shock wave parameters 5 and 10 cm after the water sheets. Uncertainties indicate the standard error.

Water Sheet Standoff Distance (cm)	5 cm after Water Sheet		
	Peak Over-pressure (kPa)	Impulse (kPa-ms)	Positive Pulse (ms)
20	60 ± 8	18 ± 3	0.3 ± 0.1
31	31 ± 4	5 ± 2	0.3 ± 0.1
41	26 ± 5	6 ± 2	0.4 ± 0.1
Water Sheet Standoff Distance (cm)	10 cm after Water Sheet		
	Peak Over-pressure (kPa)	Impulse (kPa-ms)	Positive Pulse (ms)
20	53 ± 6	12 ± 3	0.3 ± 0.1
31	27 ± 8	4 ± 0.3	0.3 ± 0.1
41	23 ± 3	6 ± 0.4	0.4 ± 0.1

Pressure trace after water sheet

The experimental results show that the unconstrained free flowing water sheet significantly reduces the initial overpressure and impulse of the blast. This is best illustrated in Fig. 5. At the 31 cm water-sheet standoff distance the peak overpressure is reduced by 82% and the impulse is reduced by 75% as measured by the pressure gage placed 5 cm behind the water sheet. These results show qualitative agreement with previous work with water shields [38, 39].

The pressures measured downstream of the water sheet also show a somewhat unexpected increase in the pressure at a finite time following the passage of an initial shock wave. Some pressure traces showed this rise in the pressure more distinctly. For example, figure 6 highlights the pressures measured downstream of the water sheet at 31 cm. Based on the distances between the measurement points and the delay time between the initial pressure rise, it is found that the initial transmitted wave propagates at approximately sonic conditions. The second pressure increase, which occurs sometime after the passage of the sonic wave, travels at subsonic velocity. The source of this behavior is currently not understood. Possible causes may be impact of liquid water on the pressure gauges or passage of high-pressure products released after the sheet fragments.

This phenomena is somewhat similar to the rise in pressure sometimes observed during shock wave reflections from porous foams [10]. However, unlike a foam, the water sheet does not contain regular voids. For this reason, wave propagation mechanisms are likely to be distinctly different between the foam and water sheet configurations, and more work is needed to understand this phenomena.

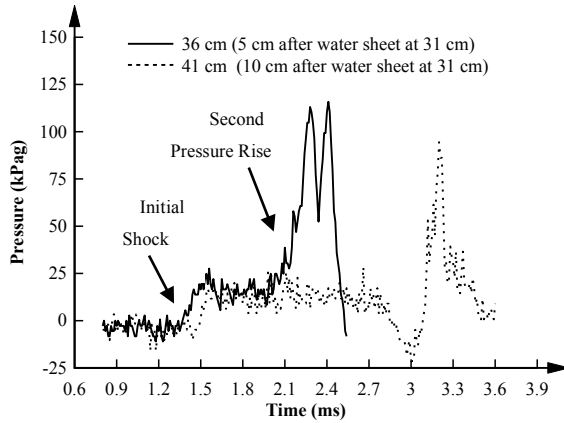


Figure 6. Pressure trace of gauges 5 and 10 cm behind the water-sheet at a 31 cm standoff distance.

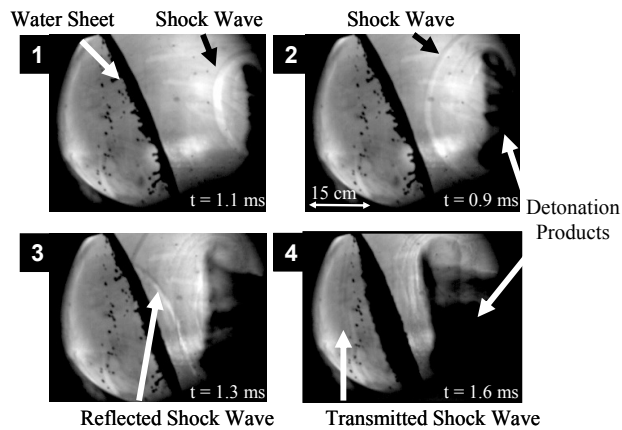


Figure 7. High speed shadowgraphy of a blast loaded water-sheet at a 31 cm standoff distance.

Shadowgraphy visualization

The shock wave interaction with the water-sheet was visualized using shadowgraphy. Select images from a high-speed shadowgraphy video are shown in Fig. 7, where the flow is right to left. The video is taken without pressure gauges which tend to obstruct the observation of the incident, reflected, and transmitted shock waves.

The reflected wave seen in the third image is due to the impedance differences between the air and water [44]. In the fourth image a weak transmitted shock wave is observed. The disruption of the water sheet is also seen.

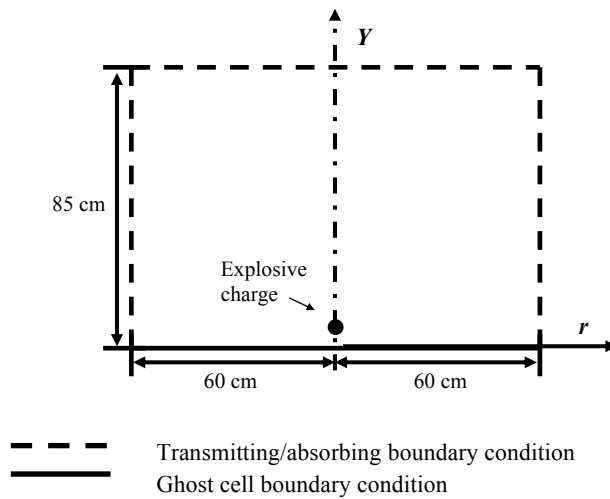


Figure 8. CTH simulation geometry and boundary conditions.

Numerical simulation

Exploratory numerical simulations were completed utilizing Sandia's hydrocode, CTH. CTH is a multi-material, large deformation, strong shock wave, solid mechanics code developed at Sandia National Laboratories [35]. In what follows, the CTH model is first validated using the free field conditions and is then used to qualitatively study the interaction of the shock wave and water sheet. This is meant to demonstrate what is possible with these types of simulations and does not represent a final study. The utility of these types of simulations to interpret the experimental results is demonstrated.

For simplicity, the explosively driven shock tube was not modeled in this study. Rather, an open field charge model was employed; nevertheless, as shown below the model qualitatively captures the physical phenomena. The geometry and boundary conditions are shown in Fig. 8. The model is axisymmetric with a spherical open field charge of PETN. The bottom boundary condition is set to allow

the pressure to be zero in the ghost cells and to later remove all material from that ghost cell. This boundary condition ensures that mass does not enter the mesh but is allowed to leave. The remaining three boundary conditions use a sound speed based absorbing/transmitting condition to approximate an infinite or semi-infinite medium. Here mass can flow into and out of the mesh.

The explosive charge is assumed to follow the Jones–Wilkins–Lee (JWL) equation-of-state (EOS) for PETN. Since the experimental explosive is comprised of 63% PETN, the model mass is scaled to allow the use of the JWL EOS. The explosive charge is detonated using a history variable reactive burn (HVRB) model. The HVRB is a pressure–based model used to treat shock induced initiation that grows to a detonation for heterogeneous explosive material [13]. When the HVRB is used, the equations of state for the unreacted and reacted phases are usually the Mie-Grüneisen and JWL equations of state [45]. Atmospheric air was modeled at an initial absolute pressure of 100 kPa using a tabulated SESAME EOS. The SESAME EOS Library is a standardized, computer-based library of thermodynamic properties developed by Los Alamos National Laboratory [46]. Fixed nodes are included in the CTH model to match the experimental free field pressure gauge locations. The mass of PETN used in the model (48.4 grams) was determined by comparing the predicted pressure to the experimental pressures and adjusting the mass until reasonable agreement was obtained. It should be noted that the mass of the PETN used in the model is an order of magnitude larger than the experiment value. This difference can be attributed to the fact that a shock tubes is used in the experiment to focus the blast in one direction. Figure 9 compares the free field pressure traces between the final CTH model and the experimental results. The average percent difference between the peak overpressure is 7.8% and the average percent difference between the impulses is around 20%. Perhaps some of the difference from experiment and calculations observed in the width of the positive pulse close to the water sheet could be due to not modeling the focusing effect of the shock tube.

To model the water-sheet, adaptive mesh refinement was used with a radially symmetric mesh. Spatial blocks were divided into 256 zones and had up to four levels of refinement. This resulted in a

maximum resolution of 195 microns near any moving interface, reaction zone, or region of steep pressure gradient. Note, results from the adaptive mesh was similar to initial calculations using a fixed Eulerian mesh, except that the water sheet became more jagged during the later stages of break-up with adaptive meshing.

Liquid water is modeled with the Mie-Grüneisen EOS. The water sheets are assumed to be initially smooth with a thickness of 0.3 cm. Furthermore, the sheets are assumed to be infinite (stretching across CTH domain) to eliminate effects caused by diffraction of the shock wave around the water sheet, and to better isolate the interaction of the shock wave and water sheet. In addition, it should be noted that the CTH models do not include surface tension effects which may play a significant role in the physical breakup process. Because of these simplifications, the simulation results are considered for qualitative insight into the physical phenomena, rather than quantitative predictions.

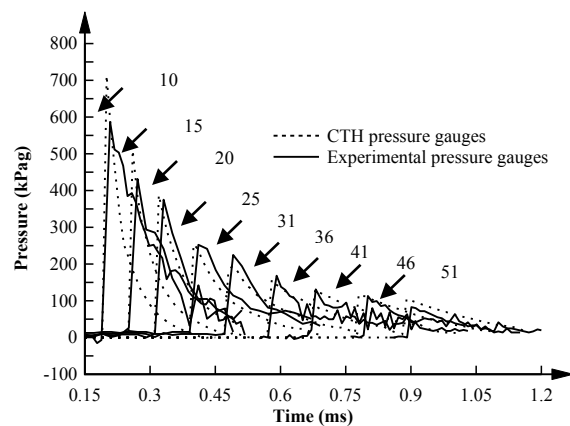


Figure 9. Comparison of CTH pressure traces vs. experimental pressure traces. Numbers indicate the distances in cm between the exit of the shock tube and the pressure gauge.

Figure 10 shows predicted contours of pressure at select time intervals. Due to the impedance mismatch at the air-water interface, a significant portion of the initial shock reflects off the water-sheet and

only a weak shock wave is initially transmitted. Comparison with Fig. 8 reveals many qualitative similarities between simulation and experiment including the reflected wave, transmission of a weak shock wave, and fragmentation of the sheet.

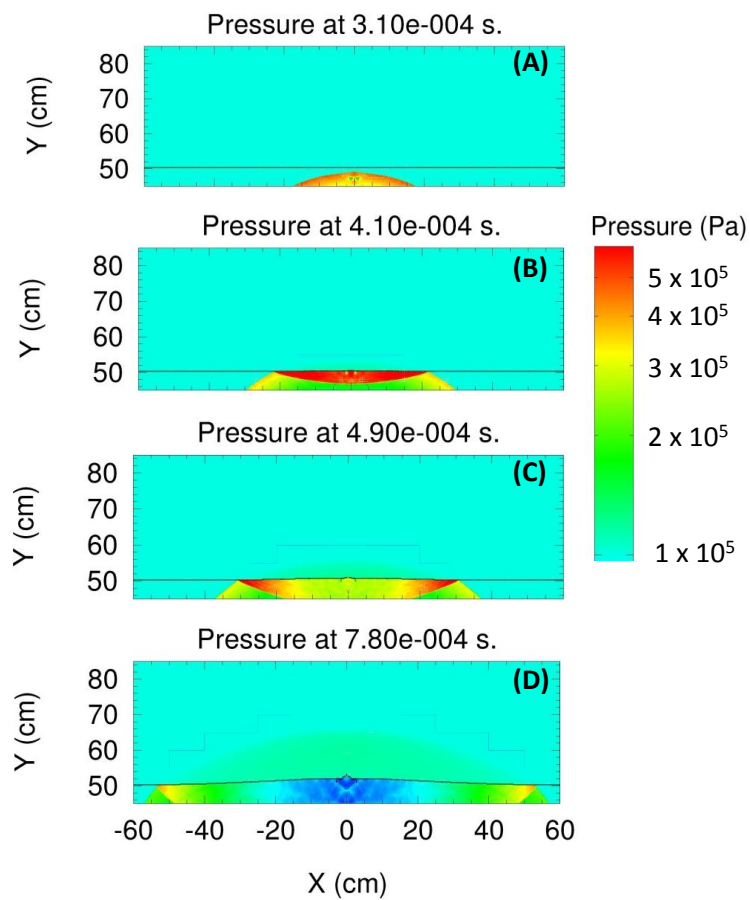


Figure 10. Simulation results showing absolute pressure for shock wave interaction with the water-sheet at the 20 cm standoff distance. (A) initial shock wave reaches the water-sheet, (B) reflection of a shock wave off the

surface of the water-sheet, (C) development of weak transmitted shock wave behind the intact water-sheet, and (D) water-sheet breakup.

Figure 11 shows pressure results from the CTH model at 5 and 10 cm after the water-sheet at a 20 cm standoff distance. This can be qualitatively compared to experimental results presented in Fig 6. Both the experimental and numerical results show the initially transmitted pressure wave. However, the simulation does not capture a distinct second rise in pressure. Note, the pressure fluctuations seen in the simulation results, particularly near the centerline, are thought to be a result of water passing through the domain resulting in an unphysical, numerical artifact. These differences between simulations and experiments highlight the importance of coupled experimental and numerical efforts. Further work is needed to fully understand the experimentally observed pressure profile.

Discussion of water sheet mitigation

As discussed by Henderson et al. [44], when a blast wave first contacts a water-sheet, a large portion of the incident energy is reflected back towards the source due to the impedance mismatch at the air-water interface. The remaining energy, which is transmitted through the water sheet, forms the observed weak shock wave and the resulting initial pressure rise. For the experimental conditions considered here, the initial blast overpressure is mitigated by as much as 80%. This indicates that a water sheet may be an effective emergency blast mitigant.

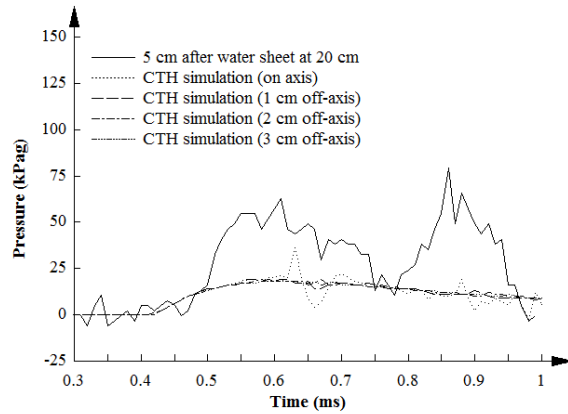


Figure 11. Comparison between CTH and experimental pressure traces 5 cm after the water-sheet at a 20 cm standoff distance.

However, a second rise in pressure is observed, resulting in a greater overall peak overpressure behind the water sheet. As discussed above, experimental and numerical results are insufficient to elucidate the source of this behavior and further work is needed. Such work could include investigations in a pressure-driven shock tube as discussed in the first half of this chapter. Such an investigation would be particularly advantageous due to the well-controlled environment and the resulting ability for quantitative optical diagnostics.

Conclusions

Blast loaded objects undergo complex fluid-structure interactions. These interactions introduce a large range of length-scales and physical phenomena, which complicate first-principle models and numerical simulation. For this reason, experimental investigations of blast mitigants are vital to the determination of their effectiveness. In addition, fundamental experimental results can be used to guide model improvements.

This chapter has discussed the most relevant experimental methods, including large-scale blast loading experiments and fundamental shock-tube experiments. In addition, an example investigation of blast mitigation via a water-sheet is presented. Initial results from the experimental investigation reveal significant blast mitigation at certain conditions. However, more work is needed to elucidate the

relevant physical phenomena such that predictive models can be developed. This is highlighted by a comparison with numerical simulation.

The further development of this, and other blast mitigation methods, requires a three pronged approach. Further blast loading experiments are required to identify optimal conditions and quantify effectiveness. Furthermore, fundamental experiments, such as those conducted in pressure-driven shock-tubes, are needed to visualize and quantify the details of the complex interaction of a shock-wave with the proposed mitigant. Finally, these efforts must be closely integrated with numerical simulations to aid in development of predictive models. Simulations may possibly be improved with true fluid modeling of the water sheet and full simulation of the shock tube.

Acknowledgements

We would like to thank the Department of Homeland Security and the Center of Excellence for Explosive Detection, Mitigation and Response, Sponsor Award No. 080409/0002251. Additionally, special thanks to Matthew Massaro and Jesus Mares who assisted with experiments.

Sandia National Laboratories is a multi-program laboratory managed and operated by Sandia Corporation, a wholly owned subsidiary of Lockheed Martin Corporation, for the U.S. Department of Energy's National Nuclear Security Administration under contract DE-AC04-94AL85000.

References

- [1] Anderson, J. A., 1990, *Modern compressible flow: with historical perspective*, Mc-Graw Hill.
- [2] National Research Council, 1995, *Protecting Buildings from Bomb Damage: Transfer of Blast-Effects Mitigation Technologies from Military to Civilian Applications*, The National Academies Press.
- [3] Needham, C. E., 2010, *Blast Waves*, Springer, Heidelberg.

- [4] Taylor, G., 1950, "The formation of a blast wave by a very intense explosion. I. Theoretical discussion," *Proceedings of the Royal Society of London Series A, Mathematical and Physical Sciences*, **201**(1065), pp. 159-174.
- [5] Taylor, G., 1950, "The Formation of a Blast Wave by a Very Intense Explosion. II. The Atomic Explosion of 1945," *Proceedings of the Royal Society of London. Series A. Mathematical and Physical Sciences*, **201**(1065), pp. 175-186.
- [6] Sedov, L. I., 1959, *Similarit and Dimensional Methods in Mechanics*, Academic Press, New York.
- [7] Settles, G. S., 2006, *Schlieren and shadowgraph techniques: Visualizing phenomena in transparent media*, Springer-Verlag, Berlin.
- [8] Monti, R., 1970, "Normal shock wave reflection on deformable solid walls," *Meccanica*, **5**(4), pp. 285-296.
- [9] Gelfand, B. E., Gubanov, A. V., and Timofeev, E. I., 1983, "Interaction of shock waves in air with a porous screen," *Fluid Dynamics*, **18**(4), pp. 561-566.
- [10] Skews, B. W., Atkins, M. D., and Seitz, M. W., 1993, "The impact of a shock wave on porous compressible foams," *Journal of Fluid Mechanics*, **253**pp. 245-265.
- [11] Levy, A., Ben-Dor, G., Skews, B. W., and Sorek, S., 1993, "Head-on collision of normal shock waves with rigid porous materials," *Experiments in Fluids*, **15**(3), pp. 183-190.
- [12] Radulescu, M. I., and Lee, J. H. S., 2002, "The failure mechanism of gaseous detonations: experiments in porous wall tubes," *Combustion and Flame*, **131**(1-2), pp. 29-46.
- [13] Teodorczyk, A., and Lee, J. H. S., 1995, "Detonation attenuation by foams and wire meshes lining the walls," *Shock Waves*, **4**(4), pp. 225-236.
- [14] Sommerfeld, M., 1985, "The unsteadiness of shock waves propagating through gas-particle mixtures," *Experiments in Fluids*, **3**(4), pp. 197-206.
- [15] Aizik, F., Ben-Dor, G., Elperin, T., Igra, O., Mond, M., and Groenig, H., 1995, "Attenuation law of planar shock waves propagating through dust-gas suspensions," *AIAA Journal*, **33**(5), pp. 953-955.

- [16] Wagner, J., Beresh, S., Kearney, S., Trott, W., Castaneda, J., Pruett, B., and Baer, M., 2012, "A multiphase shock tube for shock wave interactions with dense particle fields," *Experiments in Fluids*, **52**(6), pp. 1507-1517.
- [17] Britan, A., Ben-Dor, G., Igra, O., and Shapiro, H., 2001, "Shock waves attenuation by granular filters," *International Journal of Multiphase Flow*, **27**(4), pp. 617-634.
- [18] Meekunnasombat, P., Oakley, J., Anderson, M., and Bonazza, R., 2006, "Experimental study of shock-accelerated liquid layers," *Shock Waves*, **15**(6), pp. 383-397.
- [19] Selberg, B., and Nicholls, J., 1968, "Drag coefficient of small spherical particles," *AIAA Journal*, **6**(3), pp. 401-408.
- [20] Takayama, K., and Itoh, K., 1986, *Shock Waves and Shock Tubes; Proceedings of the Fifteenth International Symposium*, Sanford University Press.
- [21] Igra, O., and Takayama, K., 1993, "Shock Tube Study of the Drag Coefficient of a Sphere in a Non-Stationary Flow," *Proceedings of the Royal Society of London. Series A: Mathematical and Physical Sciences*, **442**(1915), pp. 231-247.
- [22] Jourdan, G., Houas, L., Igra, O., Estivalezes, J.-L., Devals, C., and Meshkov, E. E., 2007, "Drag coefficient of a sphere in a non-stationary flow: new results," *Proceedings of the Royal Society A: Mathematical, Physical and Engineering Science*, **463**(2088), pp. 3323-3345.
- [23] Wagner, J., Beresh, S., Kearney, S., Pruett, B., and Wright, E., 2011, "Shock Tube Investigation of Unsteady Drag in Shock-Particle Interactions."
- [24] Haas, J.-F., and Sturtevant, B., 1987, "Interaction of weak shock waves with cylindrical and spherical gas inhomogeneities," *Journal of Fluid Mechanics*, **181**pp. 41-76.
- [25] Brouillette, M., 2002, "THE RICHTMYER-MESHKOV INSTABILITY," *Annual Review of Fluid Mechanics*, **34**(1), pp. 445-468.
- [26] Jacobs, J. W., and Krivets, V. V., 2005, "Experiments on the late-time development of single-mode Richtmyer--Meshkov instability," *Physics of Fluids*, **17**(3), pp. 034105.
- [27] LEINOV, E., MALAMUD, G., ELBAZ, Y., LEVIN, L. A., BEN-DOR, G., SHVARTS, D., and SADOT, O., 2009,

- "Experimental and numerical investigation of the Richtmyer–Meshkov instability under re-shock conditions," *Journal of Fluid Mechanics*, **626**pp. 449-475.
- [28] Motl, B., Oakley, J., Ranjan, D., Weber, C., Anderson, M., and Bonazza, R., 2009, "Experimental validation of a Richtmyer–Meshkov scaling law over large density ratio and shock strength ranges," *Physics of Fluids*, **21**(12), pp. 126102.
- [29] Orlicz, G. C., Balakumar, B. J., Tomkins, C. D., and Prestridge, K. P., 2009, "A Mach number study of the Richtmyer–Meshkov instability in a varicose, heavy-gas curtain," *Physics of Fluids*, **21**(6), pp. 064102.
- [30] Skews, B. W., 1967, "The shape of a diffracting shock wave," *Journal of Fluid Mechanics*, **29**(02), pp. 297-304.
- [31] SUN, M., and TAKAYAMA, K., 2003, "Vorticity production in shock diffraction," *Journal of Fluid Mechanics*, **478**pp. 237-256.
- [32] Tanno, H., Itoh, K., Saito, T., Abe, A., and Takayama, K., 2003, "Interaction of a shock with a sphere suspended in a vertical shock tube," *Shock Waves*, **13**(3), pp. 191-200.
- [33] Michael, J. V., and Sutherland, J. W., 1986, "The thermodynamic state of the hot gas behind reflected shock waves: Implication to chemical kinetics," *International Journal of Chemical Kinetics*, **18**(4), pp. 409-436.
- [34] Masten, D. A., Hanson, R. K., and Bowman, C. T., 1990, "Shock tube study of the reaction hydrogen atom + oxygen .fwdarw. hydroxyl + oxygen atom using hydroxyl laser absorption," *The Journal of Physical Chemistry*, **94**(18), pp. 7119-7128.
- [35] Crawford, D., 2012, CHT Shock Physics, 14 December 2011, <http://www.sandia.gov/CTH/>.
- [36] Kailasanath, K., Tatem, P. A., and Mawhinney, J., 2002, "Blast Mitigation Using Water -- A Status Report."
- [37] Schwer, D., and Kailasanath, K., 2006, "Blast Mitigation by Water Mist (3) Mitigation of Confined and Unconfined Blasts."
- [38] Cheng, M., Hung, K., and Chong, O., 2005, "Numerical study of water mitigation effects on blast wave," *Shock Waves*, **14**(3), pp. 217-223.

- [39] Shin, Y. S., Lee, M., Lam, K. Y., and Yeo, K. S., 1998, "Modeling mitigation effects of watershield on shock waves," *Shock and Vibration*, **5**(4), pp. 225-234.
- [40] BREMOND, N., and VILLERMAUX, E., 2005, "Bursting thin liquid films," *Journal of Fluid Mechanics*, **524**pp. 121-130.
- [41] Freiwald, D. A., 1972, "Approximate Blast Wave Theory and Experimental Data for Shock Trajectories in Linear Explosive-Driven Shock Tubes," *Journal of Applied Physics*, **43**(5), pp. 2224-2226.
- [42] Alley, M. D., 2009, "Explosive blast loading experiments for TBI scenarios: Characterization and mitigation," M.S. Thesis, Purdue University, West Lafayette.
- [43] Settles, G., 2006, "High-speed imaging of shock waves, explosives, and gunshots," *American Scientist*, **94**(1), pp. 22-31.
- [44] Henderson, L. F., Jia-Huan, M., Akira, S., and Kazuyoshi, T., 1990, "Refraction of a shock wave at an air--water interface," *Fluid Dynamics Research*, **5**(5-6), pp. 337-350.
- [45] Todd, S. N., Anderson, M. U., and Caipen, T. L., 2011, Springer New York.
- [46] Lyon, S. P., Johnson, J. D., and Group T-1, SESAME: The Los Alamos National Laboratory equation of state database, 20 November 2011, http://t1web.lanl.gov/doc/SESAME_3Ddatabase_1992.html.

ANNUAL REPORT 2013

Self Healing Materials for Autonomic Mitigation of Blast Damage

Faculty PIs: Nancy R. Sottos and Scott R. White
 Graduate Student: Jason F. Patrick
 Undergraduate Student: Laura K. Richardson

The Beckman Institute for Advanced Science and Technology
 University of Illinois at Urbana-Champaign
 Urbana, IL 61801

Objective

This document summarizes research conducted at the University of Illinois at Urbana-Champaign (UIUC) over the past four years, in regards to the development of self-healing materials for autonomic mitigation of blast-induced damage. The goal of this project is to develop self-healing composite systems for mitigation of blast damage over a variety of platforms including civil based infrastructure and aerospace vehicles. The intended outcome of this research will not only address issues directly related to protection and recovery of blast-induced damage but also contribute to scientific advancements in the realm of polymer composites. A concise list of research accomplishments motivated by the aforementioned objectives is provided below:

Tasks Accomplished

Prior (Aug. 2009 - July 2010)

- Selection of ideal composite sandwich panel system with regards to blast mitigation performance and realistic integration of self-healing technology.
- Incorporation of bio-inspired microvascular networks into cellular materials to deliver expansive foam healing chemistries suitable for rapid, macro-scale blast damage recovery in polymeric foam sandwich core materials.

(Aug. 2010 - July 2011)

- Demonstration of self-healing in a commercial, polyisocyanurate (PIR) foam core using a 3-pt. Single Edge Notched Bend (SENB) mode-I fracture test under quasi-static loading conditions (*Published manuscript* [1]).
- Development of “sacrificial fiber” technology for fabrication of microvascular, fiber-reinforced polymer (FRP) composites (*Published manuscripts* [2, 3]).

(Aug. 2011 - July 2012)

- Extension of the patented “sacrificial fiber” vascularization (VaSC) procedure to encompass conventional 2D woven FRP composite laminate systems.
- Development of a mechanical testing protocol for evaluation of self-healing performance in 2D woven microvascular composites (*Manuscript in preparation*).

Recent (Aug. 2012 - April 2013)

- Demonstration of recovery in interlaminar delamination resistance of 2D woven FRP composites via microvascular delivery of a two-part healing chemistry. (*Details I-a*).
- Attainment of multiple *in-situ* self-healing cycles for mode-I fracture repair in vascularized fiber-reinforced composites via active, pressurized fluid delivery (*Details I-b, Submitted manuscript [4]*).
- Assessment of structural impact of vascularization process on interlaminar fracture resistance in 2D woven composite laminates. (*Details II*).

Summary

Our first milestone was to develop initial specifications for a self-repairing material system based on modern structural requirements for blast resistant composite structures. We completed a comprehensive survey of state-of-the-art materials and potential failure modes for blast resistant composite structures [5-10]. Based on our review of the literature in this area, we identified 3D woven composite sandwich structures as primary candidates for integration of microvascular, self-healing functionality [11-15]. The unique architecture of 3D woven sandwich panels is favorable for seamless integration of current self-healing technology with little impact on initial mechanical properties. Novel composite sandwich panel configurations such as Transonite[®] make use of 3D woven E-glass composite skins separated by a polymeric foam core and rigidly connected by through thickness fiber insertions. These panels have been shown to withstand 5 lbs of C4 explosive detonated at a mere 3 ft standoff distance. Depending on the through thickness fiber stitching density, primary failure modes after shock loading include delamination of the face sheets from the core, microcracking in the 3D woven composite face sheets, and fracture proliferation throughout the foam core.

In our initial work [1], we focused primarily on core damage and the development of a self-healing polymeric foam. Blast events predominantly cause the foam core to fracture, significantly reducing structural stiffness and sandwich efficiency of the composite system [10]. Self-healing of core damage will enable recovery of mechanical integrity and result in enhanced resistance to multiple blast events. Conventional polyurethane (PUR) and polyisocyanurate (PIR) foam cores are condensation materials prepared from organic polyisocyanates, polyols, catalysts, surfactants, and a foaming or blowing agent [16]. In typical foam formulations, the polyisocyanate compound is referred to as Part A whereas the remaining materials constitute Part B. Our strategy was to incorporate a vascular network in a closed-cell PIR foam, whereby Parts A and B were sequestered in separate channels of a 3pt. single edge notch bend (SENB) specimen. Upon quasi-static loading and subsequent crack propagation, the healing agents were released and polymerized on contact to regenerate the foam scaffold. Healing efficiencies in excess of 100% were realized through proper selection of the material system and optimization of delivery parameters. The reactive nature of the PUR foam chemistry provided for rapid healing kinetics, with over 75% recovery in both stiffness and fracture toughness in 1 hr at room temperature. Another attractive feature of this system was the volumetric expansion of the healing chemistry, demonstrating the ability

to repair macro-scale fractures comparable to damage induced by blast events. Additionally, multiple damage-healing cycles were attained without sacrifice to healing efficiency or structural integrity.

During the second phase of this project, we developed a technique [2,3] for vascularizing (VaSC) fiber-reinforced polymer (FRP) composites to provide a means for circulation of liquid healing agents throughout the structural composite sandwich panel face sheets. This now patented “sacrificial fiber” technology (See Appendix) is capable of producing complex vascular networks in a variety of FRP composite reinforcements, providing a conduit for bioinspired dynamic functionality in a multitude of engineering applications. While the initial VaSC demonstration was performed in 3D woven composites, we decided to first pursue self-healing in more conventional 2D woven FRP laminate systems to gain a deeper understanding of the viscous fluid mixing dynamics and healing reaction kinetics involved. A mechanical evaluation procedure based on mode-I interlaminar delamination in a Double Cantilever Beam (DCB) specimen geometry has been developed to accurately assess healing performance. Through careful selection of a two-part epoxy based healing chemistry, and improved fluid distribution to the fracture plane via pressure-based delivery through interpenetrating networks, multiple damage-healing cycles exceeding 100% recovery have been achieved. Additionally, we have shown the VaSC procedure actually increases interlaminar delamination resistance compared to unvascularized composite laminates.

Upon completion of the current research efforts pertaining to self-healing characterization in 2D woven systems, investigation into the damage mechanisms and microvascular based recovery in 3D woven FRP composites subjected to impact will commence. Subsequent work will focus on the total integration of microvascular foam core and composite face sheet components (2D/3D) into a state-of-the-art self-healing structural sandwich panel.

Students Supported



Jason F Patrick

PhD candidate in Civil Engineering at UIUC
(emphasis in mechanics & materials)



Laura K Richardson

Senior in Aerospace Engineering at UIUC
(interest in structural aircraft design)

Transition Partners



Industrial weaving of “sacrificial fibers” to produce 3D non-crimp orthogonal (3WEAVE™) microvascular composite textile preforms.



Melt-spinning of catalyst infused poly(lactic acid) “sacrificial fibers” for vascularizing a wide range of polymeric materials.

Patents

1. Esser-Kahn, H. Dong, P.R. Thakre, J.F. Patrick, N.R. Sottos, J.S. Moore, S.R. White, “Micro-Vascular Materials and Composites for Forming the Materials”
US Patent No. 13/416,002 (*Published* March 14, 2013), UIUC.
2. J.F. Patrick, K.R. Hart, N.R. Sottos, J.S. Moore, S.R. White, “Self-Healing Composite Materials and Micro-Vascular Composites for Forming the Materials”
US Patent No. 13/416,002 (*Filed* December 20, 2012), UIUC.

Publications

1. A. Esser-Kahn, P. Thakre, H. Dong, J. Patrick, V. Vlasko-Vlasov, N. Sottos, J. Moore, and S. White, Three-Dimensional Microvascular Fiber-Reinforced Composites, *Advanced Materials*, **23**, 3654-3658 (2011).
2. H. Dong, A. Esser-Kahn, P. Thakre, J. Patrick, N. Sottos, S. White, J. Moore, Chemical Treatment of Poly(lactic acid) Fibers to Enhance the Rate of Thermal Depolymerization, *Applied Materials and Interfaces*, **4**, 503-509 (2012).
3. J. Patrick, N. Sottos, S. White, Microvascular Based Self-Healing Polymeric Foam, *Polymer*, **53**, 4231-4240 (2012).
4. A. King, J. Patrick, N. Sottos, S. White, G. Huff, J. Bernhard, Microfluidically Switched Frequency Reconfigurable Slot Antennas, *Submitted to IEEE Antennas and Wireless Propagation Letters* (2012).
5. J. Patrick, K. Hart, B. Krull, C. Diesendruck, N. Sottos, S. White, J. Moore, Self-Healing in Fibre Reinforced Composites via Bioinspired Microvascular Networks, *Submitted to Nature Materials* (2013).
6. B. Krull, J. Patrick, N. Sottos, S. White, Overhead Automatic Optical Crack Tracking for E-glass Composite Double Cantilever Beam (DCB) Specimens, *In Preparation for Experimental Mechanics* (2013).

Presentations

1. J. Patrick, D.J. Fairfield, N. Sottos, S. White, Microvascular Based Self-Healing Polymeric Foam. 3rd International Conference on Self-healing Materials, Bath, UK, June 2011.
2. J. Patrick, K. Hart, S. White, N. Sottos, J. Moore, Microvascular Based Self-Healing 2D Woven Composites. American Society of Composites 27th Technical Conference, Arlington, TX, October 2012.
3. J. Patrick, K. Hart, B. Krull, C. Diesendruck, J. Moore, N. Sottos, S. White, Self-Healing of Woven Composite Laminates via Bioninspired Microvascular Networks. 4th International Conference on Self-healing Materials, Ghent, BE, June 2013.

Details I-a: Self-healing 2D Woven Microvascular Composites

In order to assess microvascular-based healing performance in a 2D woven FRC laminate, the Double Cantilever Beam (DCB) mode-I interlaminar fracture test was selected with relevant experimental parameters depicted in Figure 1a [17-19]. An 8-harness (8H) satin weave (9 oz./yd², E-glass) fabric reinforcement was chosen due its prevalence in composite structures, and more importantly the stable crack growth resistance (R-curve) behavior (Figure 1b) exhibited during DCB testing under displacement controlled loading [18-20]. The predominantly constant R-curve provides a suitable basis for using the tensile opening (mode-I) strain energy release rate (G_I) as a metric to quantify healing efficiency [21, 22] according to:

$$G_I = \frac{3P\delta}{2ba} \quad (1)$$

where P is the applied load, δ is the load-line displacement, b is specimen width, and a is delamination length (Note: $a = a_0 + \Delta a$).

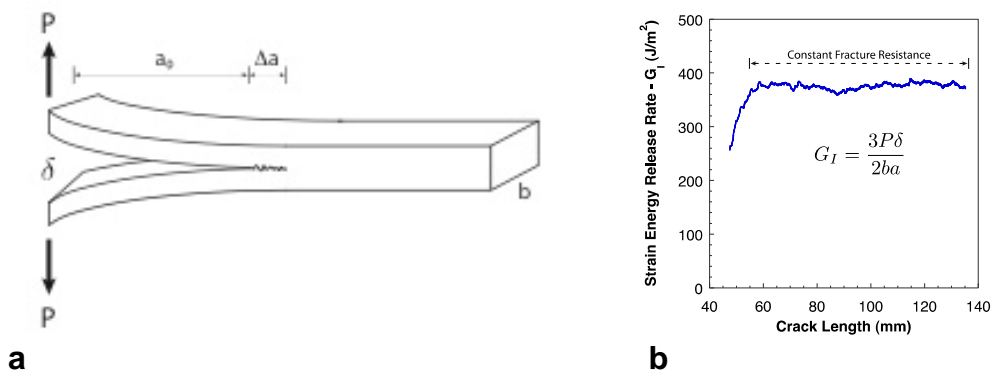


Figure 1. (a) Schematic of Double Cantilever Beam (DCB) mode-I fracture specimen; (b) Experimental crack growth resistance (R-curve) behavior for 2D woven 8-harness satin (9 oz./yd²) E-glass composite (Note: fracture along warp direction).

DCB samples were quasi-statically loaded under displacement (δ) control at a rate of 5 mm/min. Illuminating the translucent, E-glass composite samples from below enhanced visual observation of crack propagation using both top and side mounted CCD cameras. Delamination length measurements were determined in 5 mm increments, per ASTM D-5528, from images taken every 1 seconds. Corresponding mode-I strain energy release rates (G_I) were calculated according to Equation (1).

Based on the success of self-healing in polymer systems via microvascular delivery of a two-part epoxy [11-15], a dual-channel 2D woven fiber-reinforced composite DCB specimen was designed (Figure 2). Equipped with new capabilities in network architecture as a result of the VaSC technology [2], undulating through-thickness microchannels were incorporated via stitching to ensure rupture and fluid release upon interlaminar crack advance. The longitudinally ‘parallel’ channels were placed in close proximity (5mm) to accommodate diffusive mixing of actively delivered (pumped) liquid healing agents. As an extension of the ‘parallel’ design (Figure 3a), a more complex ‘herringbone’ vascular architecture was constructed to further promote in-situ mixing of reactive healing agents and increase delamination recovery (Figure 3b).

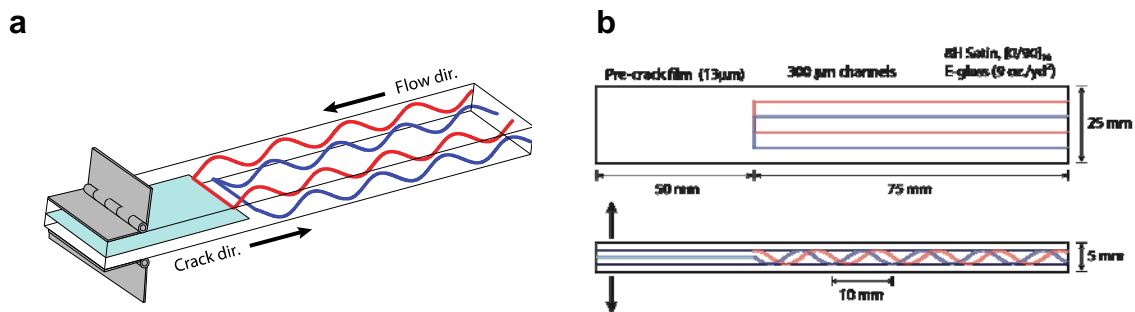


Figure 2. (a) Dual channel (red/blue) self-healing microvascular DCB concept; (b) Physical sample dimensions and layup details for composite fabrication.

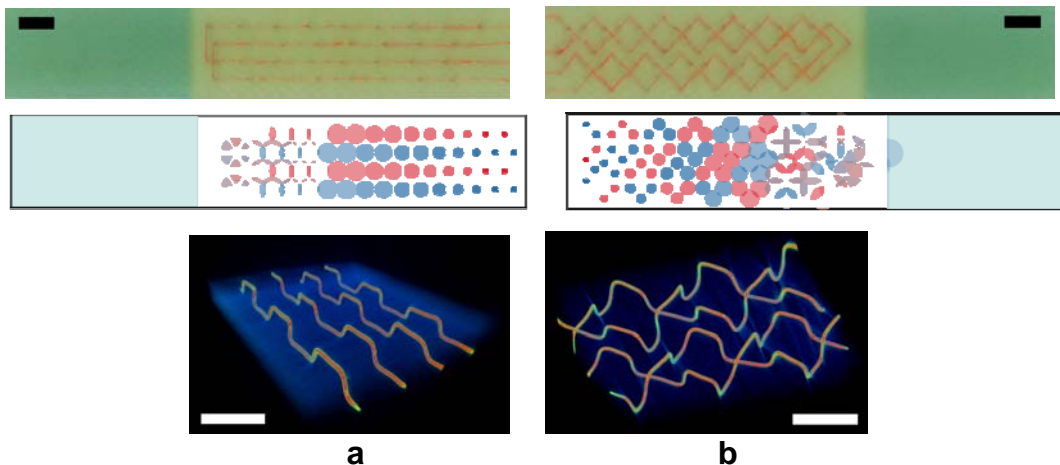


Figure 3. Microvascular network configurations investigated (a) Parallel (b) Herringbone; (Top): pre-vascularized composite samples showing embedded 300 μm “sacrificial fibers”; (Middle): idealized two-part liquid healing agent distributions on fractured surfaces; (Bottom): post-vascularized x-ray computed tomographic (μCT) images of liquid gallium-indium filled networks revealing internal channel structures (scale bars = 10mm).

Details I-b: Multiple Cycles of *In-situ* Damage Recovery

In-situ self-healing tests were conducted by first filling the dual-vascular networks with their respective healing agents (epoxy resin R , amine hardener H) from pressurized reservoirs connected via tubing to micro-dispense tips embedded in the channel orifices. The DCB samples were loaded until the delaminating crack ruptured the first set of vascular channels. Thereafter, the channels were pressurized to deliver a constant total volumetric flow rate (100 μL) of healing agents at a stoichiometric ratio of 2R:1H to the fracture plane. Loading continued as healing agents were concurrently delivered until reaching a preset incremental crack length (Δa), upon which the pressure induced flow was stopped and the sample unloaded (Figure 4).

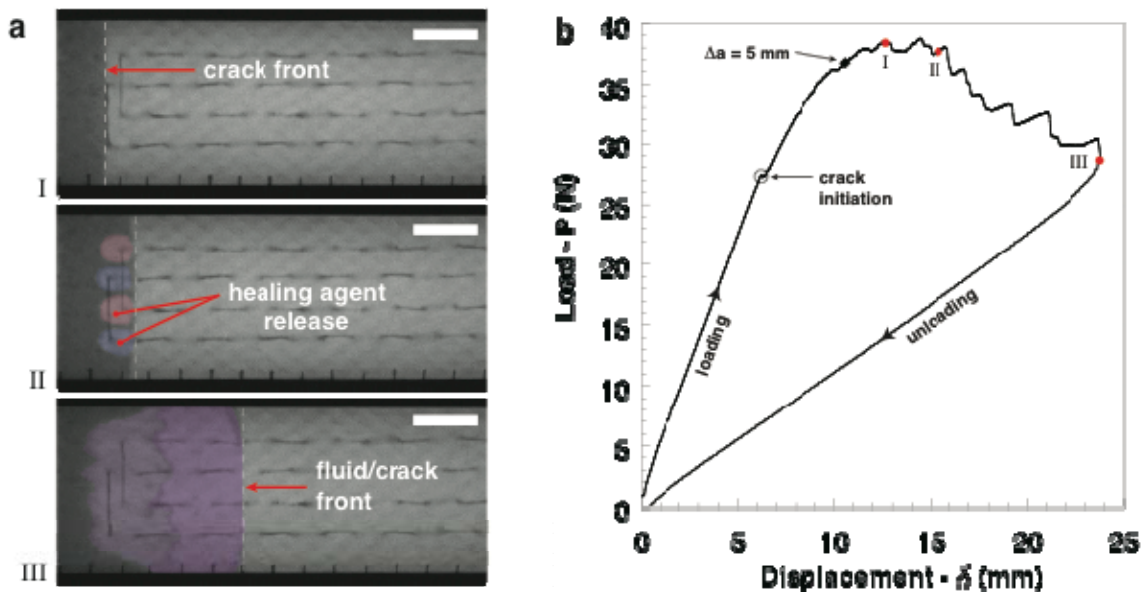


Figure 4. *In-situ* healing agent delivery (a) Overhead optical images of healing agent delivery in a parallel vascularized DCB during loading and crack advance (I-III) (scale bars = 10mm) (b) Representative load-displacement plot for virgin self-healing DCB sample showing typical fracture behavior at various stages (4a) of *in-situ* pressurized healing agent delivery.

Healing took place at 30°C for 48 hours with a slight static pressure head on the fluid reservoirs to maintain free-flowing vasculature [11-12]. The sample was then reloaded from the same initial pre-crack length (a_0) without pressurized fluid delivery, until the crack front again reached virgin material and pressurized delivery of healing agents was reactivated. Loading continued until reaching the next, preset crack length and again the sample was unloaded and allowed to heal under the same conditions. A total of four loading cycles were conducted for preset incremental crack lengths of: $\Delta a = 30, 50, 70, 95$ mm. A representative load-displacement history for all four cycles is shown in Figure 5a. Corresponding healing efficiencies (η_G), or recovery in mode-I strain energy release rate (Figure 5b), was appropriately quantified in this study by [17, 21-23]:

$$\eta_G \equiv \frac{G_I^{\text{Healed}}}{G_I^{\text{Virgin}}} \quad (2)$$

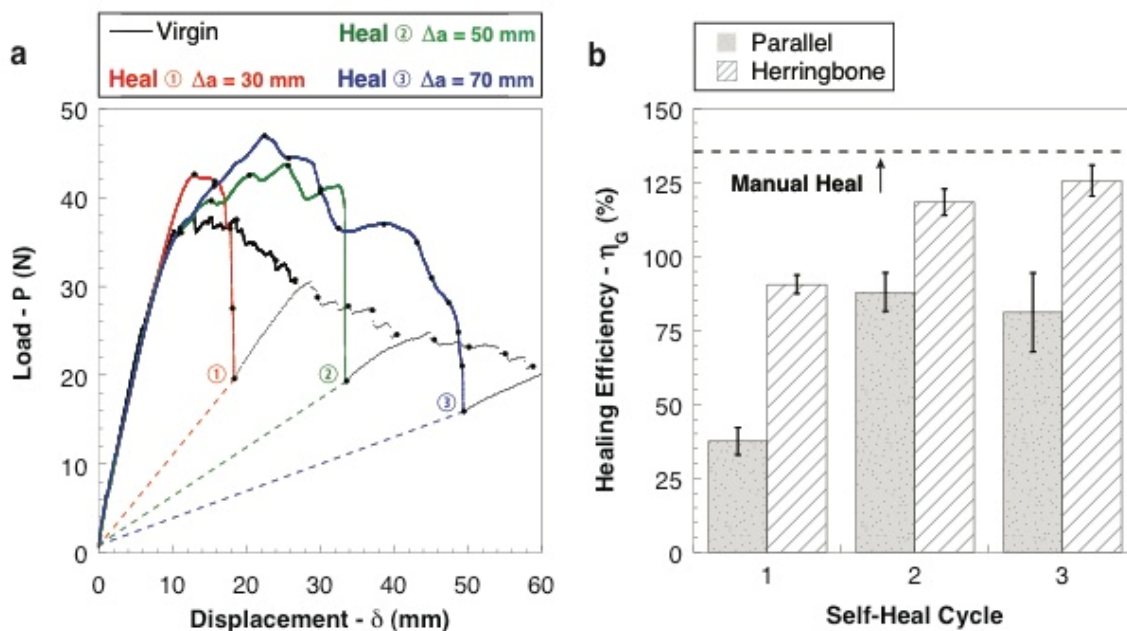


Figure 5. Self-healing results **(a)** Representative multiple cycle (48 h, 30°C) load-displacement data for an *in-situ* self-healing DCB specimen (herringbone). **(b)** Average healing efficiencies calculated according to Equation (2) for each vascular pattern at a component delivery ratio of 2-parts epoxy resin (R) to 1-part amine based hardener (H) by volume. (Note: dashed line indicates average healing efficiency of manually repaired samples with pre-mixed healing agents; vertical error bars represent the standard error from three samples tested).

Both sets of data illustrate excellent mechanical recovery in all three cycles of *in-situ* microvascular based self-healing. Immediately apparent is the increased performance (>100% recovery in virgin strength) of the herringbone vascular network over the parallel configuration due to improved fluid interspersion in the fracture plane (Figure 3). Importantly, the herringbone architecture approaches the maximum values established by pre-mixed, manually repaired tests. Vascularized DCB samples also exhibited a propensity for continued damage-recovery provided that sufficient supply of healing agents remained in external reservoirs.

Scanning electron micrographs of the fracture plane from successive regions of an *in-situ* self-healing DCB sample (herringbone) after three consecutive self-healing cycles are provided in Figure 6. A representative image from a region ($\Delta a = 0-30$ mm) experiencing three self-healing events features an accumulation of polymerized, solid material indicated by the presence of raised hackle marks. A lower amount of solid polymer is observed in the two heal cycle region ($\Delta a = 30-50$ mm) where underlying, debonded glass fibers are clearly visible. The presence of ruptured glass fibers provides another contribution to damage recovery by increasing the surface area for adhesive bonding of healing agents. Finally, in a representative single heal cycle region ($\Delta a = 50-70$ mm), a portion of the fracture surface is overlaid with only partially polymerized healing agents (smooth surface), providing direct evidence for lower healing in regions of close proximity to the crack front.

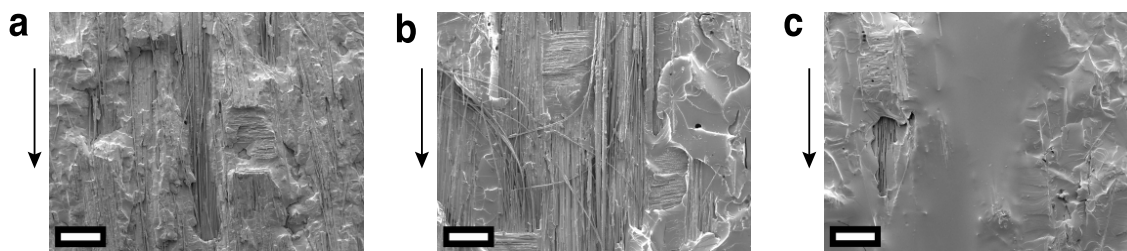


Figure 6. Scanning electron micrographs (SEM) from successive regions of an *in-situ* DCB sample (herringbone - 2R:1H) after three consecutive self-healing cycles (scale bars = 300 μ m) **(a)** $\Delta a = 0 - 30$ mm (3 heals); **(b)** $\Delta a = 30 - 50$ mm (2 heals); **(c)** $\Delta a = 50 - 70$ mm (1 heal).

Details II: Effect of Vascularization on Mode-I Fracture Resistance

Additionally, the effect of the VaSC process on G_I was assessed to ensure no appreciable loss in crack-growth resistance is incurred. Table 1 provides a summary of the results for neat (no channels), treated (VaSC thermal conditions, no channels), and both the parallel and herringbone vascular configurations. The VaSC treated samples show a slight (4%) reduction in G_I compared to the neat case, however the parallel and herringbone specimens exhibit a respective 3 and 10% increase over the neat crack-growth resistance. Scanning electron micrographs provided in Figure 7 reveal the fracture resistance mechanisms operative in our self-healing composites. Comparison of the plain, woven 8H satin fabric (7a, left) with a neat composite fracture surface (7b, middle) illustrates the presence of polymer matrix debonding from the E-glass reinforcement during fracture and ruptured fibre-bridging providing supplementary crack growth resistance [19]. Fracture toughness is further enhanced by the presence of vascular inclusions (7c, right) which invoke crack blunting mechanisms previously reported in the literature [24]. Thus, the presences of microvascular networks actually serve to increase the resistance to interlaminar, mode-I fracture over conventional ‘pristine’ composites.

Table 1. Effect of vascularization (VaSC) process on mode-I crack growth resistance

DCB sample type	G_I (J/m ²)	Normalized
Neat (36 h RT + 2 h 121°C + 3 h 177°C)	488 \pm 8.4 ^a	1.00 ^b
Treated (neat + 36 h 200°C @ 12 torr vacuum)	471 \pm 11.2	0.96
VaSC – Parallel (treated + channels)	502 \pm 3.4	1.03
VaSC – Herringbone (treated + channels)	537 \pm 15.1	1.10

^a one standard deviation, ^b by average neat value

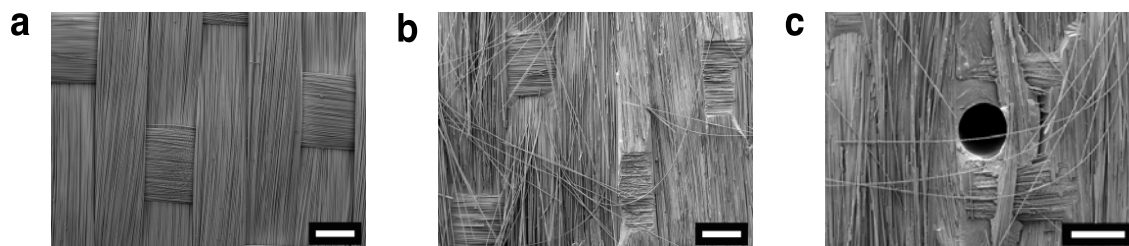


Figure 7. SEM interlaminar region characterization (a) plain 8H satin E-glass reinforcing fabric (b) neat DCB fracture surface showing fiber-bridging and matrix debonding phenomena; (c) ruptured empty, through-thickness channel along fractured DCB mid-plane (scale bars = 300 μm).

While these latest experimental findings mark the first true demonstration of multiple cycles of *in-situ* microvascular self-healing in a FRC via active delivery of a two-part epoxy, additional research is required to unravel the governing physics and reach full self-healing potential. Current spectroscopic investigations including confocal Raman and fluorescence are being conducted in order to determine fluid interspersions in the fracture plane as a result of varying network configuration and ensuing mixing/degree of polymerization attained. This in-depth characterization study will provide useful information for optimization of future microvascular designs under a variety of composite geometry and loading conditions. More advanced network fabrication procedures to create these optimal, multiscale vascular structures are also being pursued including state-of-the-art 3D printing and laser micromachining techniques [25, 26]. Another ongoing research endeavor is determining the effect of vascular features and/or VaSC processes employed to produce these dynamic composites, on the in-plane mechanical integrity of the native structural material [27]. A series of standardized mechanical tests [28-29] will be conducted in order to develop a comprehensive understanding of the material response.

Once the 2D FRC vascular self-healing systems are well understood, our research efforts will move towards developing similar damage-healing protocols for 3D woven microvascular composites subjected to energetic impact. The ultimate goal of our anticipated research and development program is to combine the stand alone microvascular FRC and polymer foam self-healing technologies into a single composite structural sandwich panel capable of unprecedented, autonomic blast protection.

REFERENCES

1. J. Patrick, N. Sottos, S. White, Microvascular Based Self-Healing Polymeric Foam, *Polymer*, **53**, 4231-4240 (2012).
2. A. Esser-Kahn, P. Thakre, H. Dong, J. Patrick, V. Vlasko-Vlasov, N. Sottos, J. Moore, and S. White, Three-Dimensional Microvascular Fiber-Reinforced Composites, *Advanced Materials*, **23**, 3654-3658 (2011).
3. H. Dong, A. Esser-Kahn, P. Thakre, J. Patrick, N. Sottos, S. White, J. Moore, Chemical Treatment of Poly(lactic acid) Fibers to Enhance the Rate of Thermal Depolymerization, *Applied Materials and Interfaces*, **4**, 503-509 (2012).
4. J. Patrick, K. Hart, B. Krull, C. Diesendruck, J. Moore, N. Sottos, S. White, Self-Healing in Fibre Reinforced Composites via Bioinspired Microvascular Networks, *Submitted: Nature Materials* (2013).

5. J. Baucom, M. Zikry. Evolution of Failure Mechanisms in 2D and 3D Woven Composite Systems under Quasi-static Perforation. *Journal of Composite Materials*, **45**, 1651-1674 (2003).
6. J. LeBlanc, A. Shukla, C. Rousseau, A. Bogdanovich. Shock Loading of three-dimensional woven composite materials. *Composite Structures*, **79**, 344-355 (2007).
7. J. Grogan, S. Tekalur, A. Shukla, A. Bogdanovich, A. Coffelt. Ballistic Resistance of 2D and 3D Sandwich Composites. *Journal of Sandwich Structures and Materials*, **9**, 283-302 (2007).
8. J. Patrick, "Fundamental Characteristics of 3-D GFRP Pultruded Sandwich Panels." *M.S. Thesis*, Department of Civil and Environmental Engineering, North Carolina State University, Raleigh, NC (2007).
9. A. Bogdanovich, M. Mohamed, Three-Dimensional Reinforcements for Composites, *SAMPE Journal*, **45(6)**, 2-20 (2009).
10. S. Tekalur, A. Bogdanovich, A. Shukla. Shock loading response of sandwich panels with 3-D woven E-glass composite skins and stitched foam core. *Composites Science and Technology*, **69**, (2009).
11. A. Hamilton, N. Sottos, S. White, Pressurized vascular systems for self-healing materials, *Journal of the Royal Society Interface*, **9(70)**, 1020–1028 (2012).
12. A. Hamilton, N. Sottos, S. White, Self-healing of internal damage in synthetic vascular materials, *Advanced Materials*, **22**, 5159–5163 (2010).
13. C. Hansen, S. White, N. Sottos, J. Lewis, Accelerated Self-healing via ternary interpenetrating microvascular networks, *Advanced Functional Materials*, **21**, 4320-4326 (2011).
14. C. Hansen, W. Wu, K. Toohey, N. Sottos, S. White, J. Lewis, Self-healing materials with interpenetrating microvascular networks, *Advanced Materials*, **21**, 4143–4147 (2009).
15. K. Toohey, C. Hansen, N. Sottos, J. Lewis, S. White, N. Sottos, Delivery of two-part self-healing chemistry via microvascular networks, *Advanced Functional Materials*, **19**, 1399–1405 (2009).
16. M. Kapps, S. Buschkamp, The production of rigid polyurethane foam, Technical Report, Bayer Material Science, (2004).
17. M. Kessler, S. White, Self-activated healing of delamination damage in woven composites, *Composites A*, **32**, 683–699 (2001).
18. J. Whitney, C. Browning, W. Hoogsteden, A Double Cantilever Beam Test for Characterizing Mode I Delamination of Composite Materials, *Journal of Reinforced Plastics and Composites*, **1**, 297-313 (1982).
19. ASTM International, ASTM D5528: Standard Test Methods for Mode I Interlaminar Fracture Toughness of Unidirectional Fiber-Reinforced Polymer Matrix Composites (2007).
20. N. Alif, L. Carlsson, L. Boogh, Effect of weave pattern and crack propagation direction on mode I delamination resistance of woven glass and carbon composites, *Composites Part B*, **29**, 603-611 (1998).
21. S. White, N. Sottos, P. Geubelle, J. Moore, M. Kessler, S. Sriram, E. Brown, S. Viswanathan, Autonomic healing of polymer composites, *Nature*, **409**, 794–797 (2001).
22. E. Brown, Use of the tapered double-cantilever beam geometry for fracture toughness measurements and its application to the quantification of self-healing, *Strain Analysis for Engineering Design*, **46**, 167–186 (2011).
23. J. Rule, E. Brown, N. Sottos, S. White, J. Moore, Wax-Protected Catalyst Microspheres for Efficient Self-Healing Materials, *Advanced Materials*, **17**, 205-208 (2005).
24. A. Kousourakis, A. Mouritz, M. Bannister, Interlaminar properties of polymer laminates containing internal sensor cavities. *Composite Structures*, **75**, 610–618 (2006).
25. J. Miller, K. Stevens, M. Tang, B. Baker, D. Nguyen, D. Cohen, E. Toro, A. Chen, P. Galie, X. Yu, R. Chaturvedi, S. Bhatia, C. Chen, Rapid casting of patterned vascular networks for perfusable engineered three-dimensional tissues. *Nature Materials*, **11**, 768–774 (2012).
26. M. Focke, D. Kosse, C. Müller, H. Reinecke, R. Zengerle, F. Stetten, Lab-on-a-Foil: microfluidics on thin and flexible films. *Lab on a Chip*, **10**, 1365–1386 (2010).
27. A. Kousourakis, M. Bannister, A. Mouritz, Tensile and compressive properties of polymer laminates containing internal sensor cavities, *Composites A*, **39**, 1394-1403 (2008).
28. ASTM International, ASTM D3039: Standard Test Methods for Tensile Properties of Polymer Matrix Composite Materials (2008).
29. ASTM International, ASTM D7264: Standard Test Methods for Flexural Properties of Polymer Matrix Composite Materials (2007).
30. A. King, J. Patrick, N. Sottos, S. White, G. Huff, J. Bernhard, Microfluidically Switched Frequency Reconfigurable Slot Antennas, *Submitted: IEEE Antennas and Wireless Propagation Letters* (2012).

APPENDIX

The recently patented process (Figure A1) designated ‘Vaporization of Sacrificial Components’ (VaSC), integrates a commercially available biopolymer fiber into existing textile composite reinforcement manufacturing techniques to imbue FRP composites with three-dimensional vasculature.

In VaSC a robust, chemically treated [2, 3] thermoplastic monofilament deemed ‘sacrificial fiber’ is directly woven into composite textile reinforcement (Fig. A1a). Upon subsequent epoxy resin infusion (Fig. A1b), vacuum/pressure compaction, and elevated temperature post-curing, the fibers sublimate via thermal depolymerization leaving behind high fidelity, inverse replica vascular features (Fig. A1c). The resulting vascularized composite permits the circulation of fluids (Fig. A1d) through its internal structure, providing a conduit for dynamic functionality. In addition to self-healing capability, vascular composites also accommodate multiphysical properties such as thermal regulation and electromagnetic modulation [30] via a simple substitution of fluids.

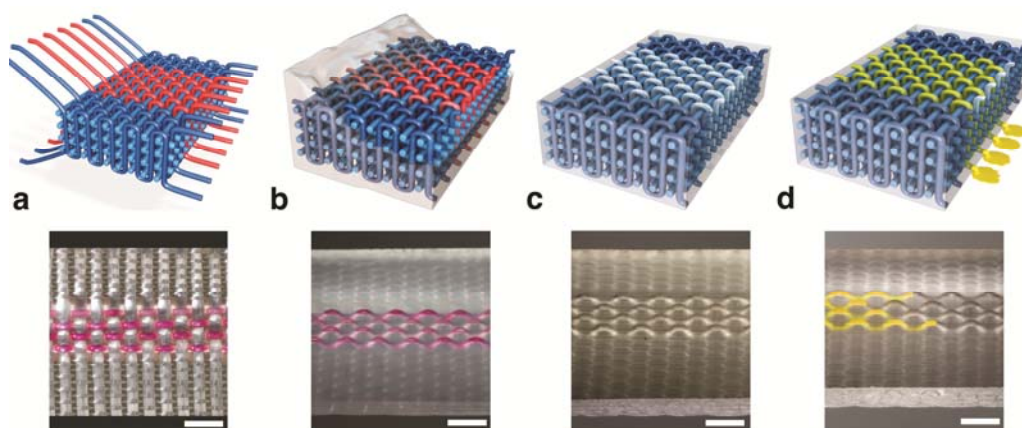


Figure A1. VaSC fabrication procedure. **(a)** ‘sacrificial fibers’ (red) woven into glass reinforcing fabric; **(b)** infiltration of polymer resin into composite preform; **(c)** matrix solidification and subsequent thermal depolymerization resulting in vascularized structural composite; **(d)** fluid filled (yellow) microchannels (scale bars = 5 mm). Image from Esser-Kahn et al. [2].

The initial VaSC demonstration was performed in 3D woven fiber reinforced composites (FRC), mainly to showcase the commercial practicality and complex geometric possibilities in vascular design [2, 9], although the technique is amendable to a variety of reinforcement architectures.

Stress Attenuation by Means of Particulates
Carl-Ernst Rousseau
Mechanical Engineering; University of Rhode Island

Objective:

The objective of this work is to identify effective means of stress wave mitigation. Traditional shielding techniques have consisted in heavy and voluminous metallic barriers that are effective but cumbersome. The focus has naturally shifted to composites, as they possess lower densities and, though not as sturdy as metals, have resilience capabilities approaching them. The approach associated with composites has also been highly empirical. For instance, consecutive tests performed on two equivalent types of fibrous composites will indicate which one is more appropriate to a *specific* shielding task. However, what specific aspect of the material's microstructure ensures this outcome? We endeavor to answer those questions by launching stress waves within these materials and note instances of absorption, reflection, or deflection that reduce or eliminate damage. We aim to do so not only for composites, but also for metals, as we explicitly target the influence of porosity, inclusions, impurities, cell or grain boundaries, and sizes. Finally, complete description of materials for dynamic, stress wave, and shock study or prediction is frequently associated with knowledge of the Hugoniot conditions. For any material, the latter representation is the result of numerous experimental studies. Last year, we had expressed the hope of being able to develop a technique whereby the Hugoniot can be obtained from the amalgamation of data pertaining to a single experiment. We are pleased to report that the success of the first set of experiments concluded in the last month redounded to the credit of our methodology. Consequently, we will soon be able to provide a complete dynamic representation of a material through the medium of two single experiments, where traditionally, several dozens were required by means of the traditional methodologies.

Significance to DHS:

The work performed, its extension and future ramifications are highly relevant to DHS' aim of protection of infrastructure and citizenry. Indeed full comprehension of mechanisms of failure and of its prevention, will allow engineers working in the security field to base choices on sound scientific grounds, and be better able to combine materials characteristics in order to fabricate more effective shields. Also, experimental techniques developed during the course of this study will allow for the application of speedier and more efficient gathering of experimental outcomes, both for ourselves and others in the broader scientific community who elect to use the techniques we have developed.

Accomplishments:

Within this past year, we have authored two papers associated with this work, one is under review, and three others will be submitted presently. Two conference publications have been accepted and will be presented in June 2013. We have successfully concluded our collaboration

with the Lawrence Livermore National Lab on identifying the sources of failure initiation in metals. One high school physics teacher, three undergraduate students. One Master's student will complete his studies in August, and one Ph.D. student working on this DHS project will receive his degree this month.

Task 1. Effect of microstructure on failure

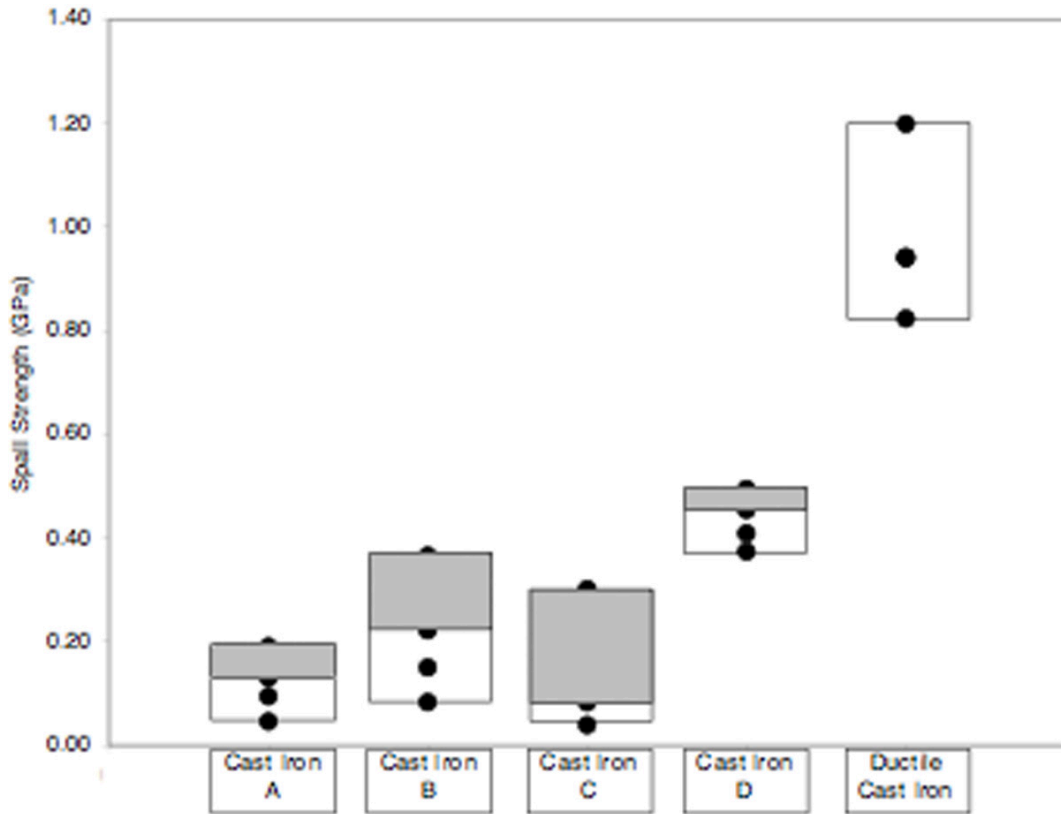
Plate impact experiments were conducted in a vacuum chamber evacuated to 10 torr with the use of a 50 mm bore single stage helium driven gas gun. The impactors and tested specimens were 45 mm in diameter, and respectively 5 mm and 10 mm thick. For all experiments, a 20 mm thick polycarbonate backing window was used. PVC sabots were used to carry the impactors down the 2 meter long gun barrel while specimens were supported, awaiting impact, by means of small PVC rings that were temporarily bonded to a metal sample holder. In order to help attain better impact planarity, sabots were designed such as to impact the specimen before they fully exited the barrel of the gun. Flyer velocities were captured by means of two laser detectors positioned 12.7 mm and 38.1 mm from the specimen's front face. Velocity was inferred from the time between interruptions and the distance between the two detectors. 50 Ω manganin stress gauges were embedded between the back surfaces of the test samples and 20 mm thick polycarbonate backing windows with the use of Buehler Epo-Thin Epoxy. A digital oscilloscope was used to capture the output signal of the stress gauge power supply and the laser detectors.

Impacted specimens were captured for post mortem analysis utilizing a soft recovery technique by means of clay bricks coupled with a shock absorbing catch box. Recovered specimens were cut through the thickness in order to expose the spall plane for analysis. Cut specimens were ground and polished to a 1 micron finish for clearer viewing under scanning electron and optical microscopes.

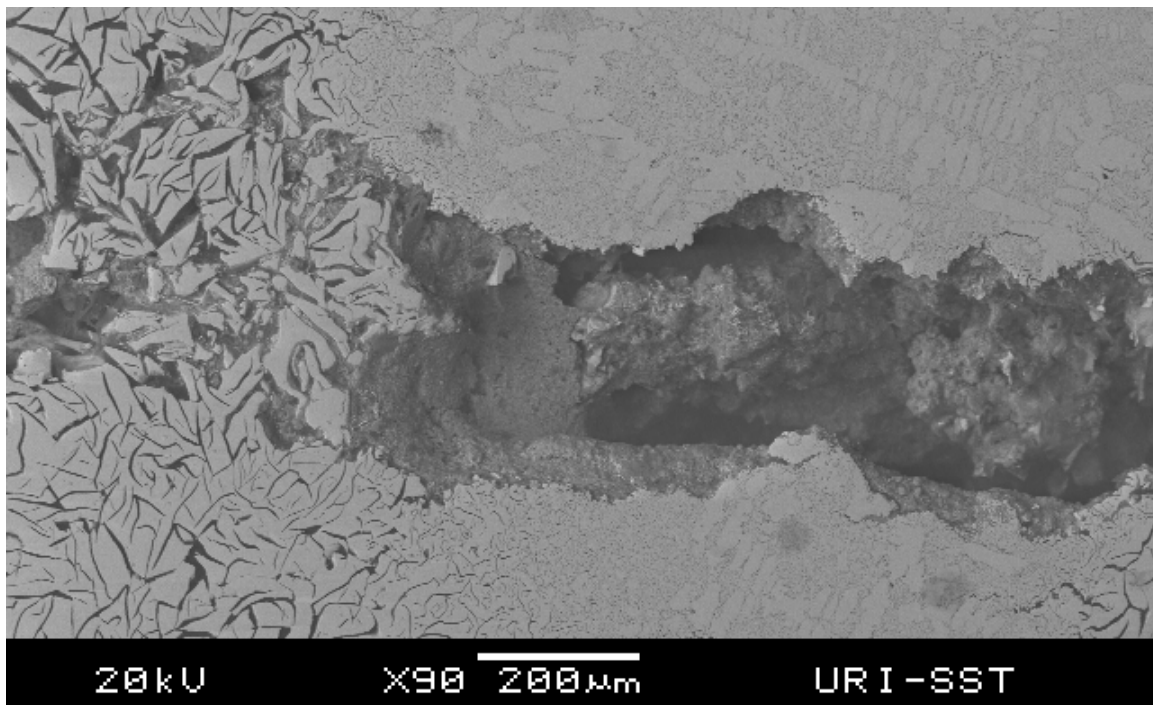
Four separate experiments were conducted covering an impact velocity range of 100-300 m/s for each respective casting. Results from these experiments suggested a strong correlation between the magnitudes of the calculated spall strengths and the damage level initiated. Upper end values of spall strength were found for cases where complete spall fracture occurred, while minor damage levels associated with incomplete fracture produced the lower range. A summary of the resulting spall strengths determined for each respective casting can be found in the figure, below. The shaded regions within this figure indicate experiments where the test samples exhibited complete spall fracture and therefore were not able to be imaged as described in the previous section.

SEM and optical micrographs of recovered samples demonstrated that the initiation of failure is strongly linked to the debonding of graphite from the metal matrix. In cases where graphite existed in the form of coarse flakes, spall plains exhibited large initiated cracks along graphite-matrix interfaces, as noted in the micrographs of the recovered samples from experiments on castings A-C. The relative length of the graphite within each respective casting demonstrated a link to the spall strengths determined, where castings A-C tested with much lower values than casting D which was composed of smaller graphite flakes. In agreement with this observation,

the small surface area shared by the graphite nodules and metal matrix in the ductile cast iron resulted in much higher strength values for this material than found for the gray cast irons. The subsequent coalescence of the initiated microcracks required propagation into the metal matrix to form a completed fracture plane. The small range of strengths exhibited by cast iron D indicates that this process can be completed with minimal additional energy in cases where the spacing between graphite flakes is relatively small. This observation is further supported by considering a SEM micrograph of a recovered sample from casting D impacted at 190 m/s found in the figure below. Within this micrograph graphite of type VII A4 and VII D8 can be noted respectively on the left and right. In the case of the coarse distribution of graphite, the material partially retained its integrity, however, a large spall plane can be noted in the case of the fine distribution. A pearlitic metal matrix is noted to provide an increase in tensile strength through the final stages of spall fracture as indicated by the higher strengths found for casting B in comparison to castings A and C. This observation is in agreement with quasi-static testing of cast irons in literature where it is commonly noted that free ferrite can significantly reduce a castings tensile strength.



Results from this investigation suggest a strong correlation between the magnitudes of calculated spall strengths and the damage level initiated where an increased amount of energy is required to generate completed fracture planes. The morphology of graphite within cast irons has been shown to strongly affect the material's spall strength. Initiation of spallation is linked to the debonding of graphite from the metal matrix. The subsequent coalescence of initiated cracks into a complete fracture plane is correlated to both the microstructural components of the metal matrix and comparative spacing of the graphite phase. In cases where graphite spacing is relatively small, this process can be completed with minimal additional energy. A metal matrix of pearlite has been linked to increased tensile strength in castings, helping to prevent the coalescence of initiated cracks in the formation of complete spall fracture planes.



Task 2. New method for predicting stress attenuation within materials by ultrasonic means

The ultrasonic pulse-echo immersion technique consists of sending a mechanical pulse in the ultrasonic frequency range to a material and analyzing several echoes reflected from the material in order to calculate the longitudinal wave speed and attenuation coefficient of the material under test.

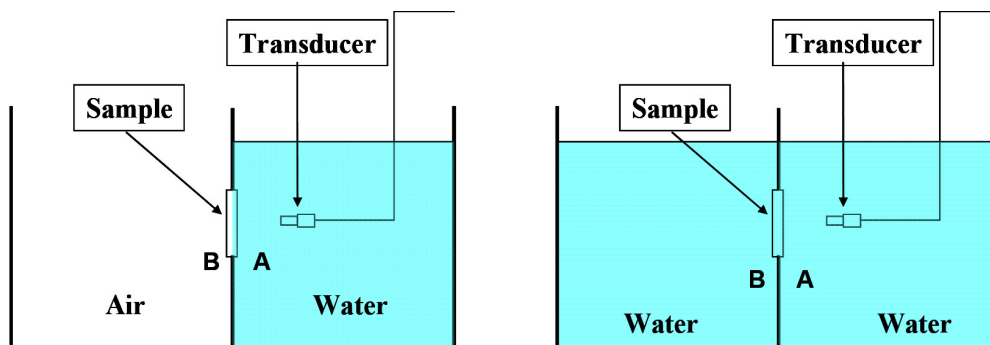
The mechanical pulse is created by an ultrasonic transducer that is based on the piezoelectric effect of a crystal. The main characteristic of the immersion technique is that the pulse is not transmitted directly from the transducer to the material but rather through a liquid (water, in the present case) in which the solid material is immersed and that acts as a coupler between transducer and material. The material sample is immersed in the liquid and placed perpendicularly to the transducer to facilitate the analysis and calculations.

We will designate the generated wave as (V_0), the front wall reflection as (V_0'), and the multiple reflections or echoes from back wall of the solid material as (V_1), (V_2), ... (V_n). In the pulse-echo immersion technique, V_1 and V_2 are used to calculate the longitudinal wave speed and the attenuation coefficient of the material. The magnitudes of these echoes are, based on the assumptions that 1) reflection and transmission of the pulse occur at the water-sample interface, 2) attenuation of the pulse occurs only within the solid material, and 3) the beam is spreading. Variables R_A , R_B , T_A , T_B are actually functions representative of the reflection and transmission coefficients of faces A (front) and B (back), respectively, and D is representative of the divergence of the wave. The wave attenuation can thus be expressed as: $\alpha = (1/2h) \ln [(V_1/V_2 R_A R_B (D_1/D_2))]$, where h is the material thickness.

The reflection coefficients depend on the impedances of both the material to be tested and the liquid medium. The erroneous assumption frequently made in experimentation is the two media form a perfectly bonded interface. Our experiments have proven that this assumption does not hold, leading to significant errors in the attenuation coefficient calculation. The effect is particularly pronounced for materials that have low affinity to water, such as teflon specimens or urethane-based products frequently used in composites.

In order to resolve the problems associated with the traditional ways of calculating the attenuation coefficient of a material, we have developed a new experimental method that considers the reflection coefficients in both faces to be unknown and possibly different. Traditional means of experimentation, on the other hand incorrectly regard both facial conditions as being identical. Our methodology allows measurement of both reflection and attenuation coefficients simultaneously. The method can be extended to any material and guarantees the correct measurement of attenuation.

The next stage of this research will correlate this “true” attenuation to the material’s internal friction and stress mitigation.



Task 3. Improved methodology for determining material Hugoniot

At present we have just successfully established a methodology for determining material's Hugoniot based on a set of two experiments. Conventional experimentation requires several dozens tests to establish the dynamic state of a material. Much work needs to be done to refine the methodology, which was initially undertaken by Doctoral Candidate G. Plume. As he received his degree this month, doctoral student M. Goni will undertake those improvements. We, thus propose to continue refining this work for another year as a means of completely establishing dynamic states of novel, mitigating materials.



Doctoral candidate Gifford Plume at work on Task 1.



Master's recipient Bhaskar Ale at work on the initial stages of Task 2.

Papers Published:

Plume, G., Rousseau, C.-E., April 5, 2012, "Investigation into the Spall Strength of Cast Iron." International Journal of Nonlinear Science and Numerical Simulations, Vol. 13, Issue 2, pp. 195199, (doi: 10.1515/IJNSNS.2011.098).

Ale, B., Rousseau, C.-E., "Dynamic attenuation and compressive characterization of syntactic foams", Engineering Materials and Technology, In-Press 2013.

Collaboration

Effect of porosity on the performance of cast iron with Lawrence Livermore National Laboratory

Graduate Students

Gifford Plume (May 2013); Miguel Goni (August 2013); Michael Franzblau (May 2013)

Undergraduate Students

Christian Mejia (May 2014); Jose DeFaria (May 2012); Sameer Saran (May 2014)

Annual Performance Report

2012-2013

Development of Novel Composite Materials & Structures for Blast Mitigation

Arun Shukla¹, Nate Gardner², Payam Fahr², Emad Makki², Jefferson Wright²

¹ Principal Investigator, Simon Ostrach Professor

² Students, Dynamic Photomechanics Laboratory

Department of Mechanical, Industrial and Systems Engineering

University of Rhode Island, Kingston, RI 02881

Submitted to Department of Homeland Security (DHS)

Objective

The current investigations aim to develop novel material systems and sandwich structures that can withstand shock wave (air-blast) loadings and effectively mitigate the blast overpressures. The study also focuses on the response of these material systems and sandwich structures in extreme (temperature) environments.

Summary

A shock tube apparatus was utilized to generate a controlled shock loading on the specimens (Fig. 1a). It has an overall length of 8 m, consisting of a driver, driven and muzzle section. The high-pressure driver section and the low pressure driven section are separated by a diaphragm. By pressurizing the high-pressure section, a pressure difference across the diaphragm is created. When this difference reaches a critical value, the diaphragm ruptures. This rapid release of gas creates a shock wave, which travels down the tube to impart a dynamic loading on the specimen. The driver gas is helium and the driven gas is ambient air.

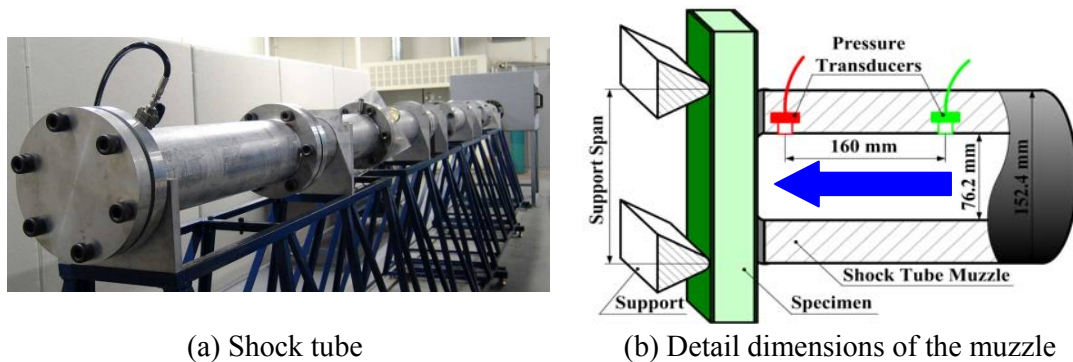


Fig. 1: Shock tube apparatus

Fig. 1b shows the detailed dimensions of the muzzle and locations of the specimen and the pressure sensors (PCB102A). The sensors are mounted at the end of the muzzle section to measure the incident pressure and the reflected pressure during the experiment. The final muzzle diameter is 0.076 m (3 in). The distance between the two sensors is 0.160 m and the distance between the second sensor and the end of the muzzle is ~ 0.020 m. The specimen was placed in the supports and positioned close to the end of the muzzle. These support fixtures ensure clamped boundary conditions with a span of 0.203 m (8 in) by 0.203 m (8 in). A typical pressure profile obtained from the transducer closest to the specimen (~ 0.020 m away) can be seen in Fig. 2. It should be noted that both pressure transducers were utilized to obtain the shock wave history, i.e. incident / reflected pressure and incident / reflected velocity. However, only the pressure transducer closest to the specimen was utilized to obtain the pressure applied on the specimen.

The Digital Image Correlation (DIC) technique was also used to measure the full-field, in-plane and out-of-plane displacements. The DIC arrangement is shown in Fig. 3. Initially the camera records an image of the specimen in its un-deformed state. A second picture is then taken after the specimen has deformed. The two images are then compared in order to calculate the in-plane and out-of-plane displacements of the specimen. A random speckle

pattern is applied on the specimen and each speckle is individually tracked in order to obtain the in-plane and out-of-plane displacements.

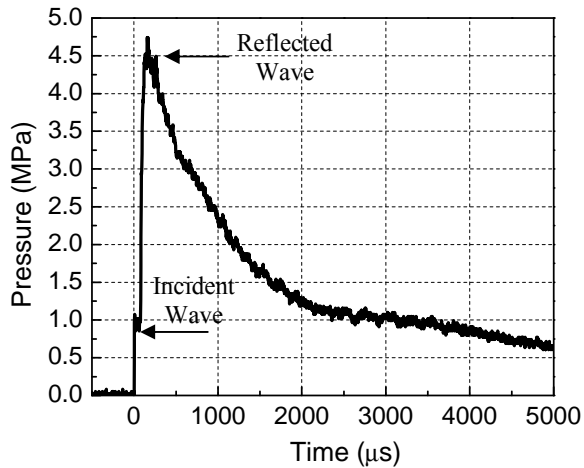


Fig. 2: Typical pressure profile from transducer closest to the specimen

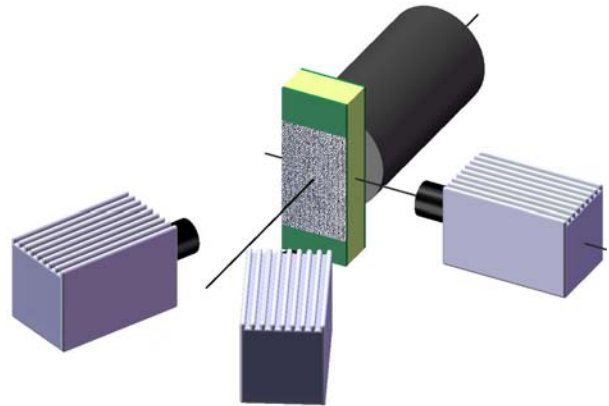


Fig. 3: High-speed photography systems

Accomplishments

Task 1: Dynamic Response of Laminated Safety Glass Panel subjected to Shock Loading under Extreme Environments

Laminated Safety Glass (LSG) is a composite material that combines the unique properties of glass with the benefits of a tough but highly elastic organic material (PVB) interlayer (materials having both advantages of the organic materials such as the light-weight, flexibility and of the inorganic materials such as the high strength, heat-stable, and chemical resistance). The objective of this study is to investigate the blast performance of (LSG) panel, coated with XO-Armor® protective films on both (front / back) faces, and to mitigate the blast loading at extreme environments which was investigated experimentally using the shock tube apparatus. A 3D-Digital Image Correlation (DIC) technique is used to obtain the out-of-plane deflection, in-plane strain developed, and the velocity of the back face, accordingly to understand the failure mechanism during shock wave event. The results show that the coated protective films play a crucial role in the dynamic behavior of (LSG) panels when they are subjected to a blast loading. Effects of temperatures on thermoplastic films will change the mechanical properties, therefore, changing the dynamic response of the glass structure overall. The results indicated that at high temperature the strength of specimen was decreased and accordingly it behaves more ductile. However, for low temperature the panel behaves more brittle where the material strength was increased in this condition. Moreover, the efficiency and energy analyses will be developed to calculate the amount of energies that are absorbed and reflected by the system structure during the blast event.

Task 2: Blast Response of Nano-Scale Core-Shell Rubber (CSR) toughened Sandwich Composites

The dynamic behavior of two types of sandwich composites made of E-Glass Vinyl-Ester (EVE) face sheets and Corecell™ A500 foam was studied using a shock tube apparatus. The core material and thickness, as well as overall specimen dimensions were held constant,

with the only difference arising in the resin system used during the infusion. The non-core-shell rubber toughened resin system (Non-CSR) consisted of a vinyl-ester resin only; while the CSR toughened resin consisted of the same vinyl-ester resin, but with Kane Ace MX-153 nano-scale core-shell rubber particles added to the mixture. Prior to shock tube testing, the quasi-static and dynamic constitutive behavior of the face sheets (tensile/compressive) and foam (compressive) was evaluated. During the shock tube testing, high-speed photography coupled with the optical technique of Digital Image Correlation (DIC) was utilized to capture the real-time deformation process as well as mechanisms of failure. Post-mortem analysis was also carried out to evaluate the overall blast performance of these configurations. Results indicated that adding nano-scale core-shell rubber (CSR) particles to sandwich composites, aids in dispersing the initial shock wave loading, thus reducing the overall deflection, strain, and velocity and improving the overall blast resistance of the structure.

Task 3: Experimental and Numerical study of Foam Filled Corrugated Core Steel Sandwich Structures Subjected to Blast Loading

In this study, the influence of foam infill on blast resistivity of corrugated steel core sandwich panels was investigated experimentally and numerically through high speed photography and Finite Element Methods, respectively. After verifying the finite element model numerically studies were conducted to investigate the effect of face sheet thickness (1, 3 and 5 mm), corrugated sheet thickness (0.2 mm, 0.6 mm and 1 mm) and boundary conditions (Simple Supported and Encastre supported on sides) on blast performance. Experimental and FEM results were found to be in good agreement with R^2 values greater than 0.95. Results showed that the addition of foam infill reduced both the back face deflections and front face deflections by more than 50% at 3 ms after blast loading at a weight expense of only 2.3%. However, increasing face sheet thickness and corrugated sheet thickness decreased the benefit obtained from foam filling in the sandwich structure. Foam infill benefits were more prominent for simple supported edge case than encastre supported edge case.

Task 4: Corrugated Structures to improve Thermal and Blast Mitigation (Collaboration with the University of Connecticut)

Blast loading experiments on corrugated steel sandwich panels were being conducted using a shock tube apparatus configured for extreme temperatures in conjunction with high-speed digital image correlation (DIC) photography. A syntactic filler material was developed to fill the corrugated panels and is being experimentally evaluated in order to understand its contributions in enhancing thermal resistivity and blast response under rapid dynamic loading. Preliminary results show that the syntactic filler material mitigates back-face deformation. Two experimental series were performed for this study. At room temperature, the performance of the filler material was investigated comparing empty and filled panels at a low pressure. High temperature experiments were performed by heating the back face of filled panels to 500°C. A temperature differential of at least 350°C was observed over a duration of 20 minutes, at which point a shock load was impinged on the specimen.

Details

Task 1: Dynamic Response of Laminated Safety Glass Panel subjected to Shock Loading under Extreme Environments

Laminated Safety Glass (LSG) is a composite material that combines the unique properties of glass with the benefits of a tough but highly elastic organic material (PVB) interlayer as shown in (materials having both advantages of the organic materials such as the light-weight, flexibility and of the inorganic materials such as the high strength, heat-stable, and chemical resistance). The objective of this study is to investigate the blast performance of (LSG) panel that is coated with XO-Armor® protective films on both (front / back) faces as shown in (Fig.4(a)), and to mitigate the blast loading at extreme environments were conducted using the shock tube apparatus.

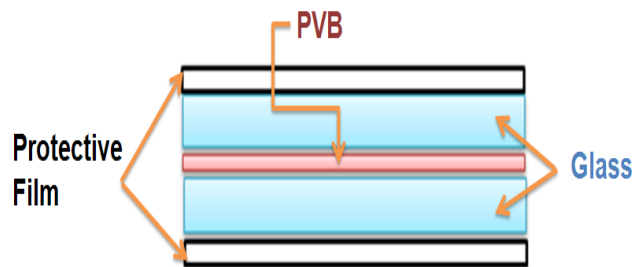


Fig.4 (a): Schematic of Glass Structure System

Material Details

As shown in Fig.4 (b), the sandwiched glass panel consists of two clear glass panels made out of soda-lime-silica glass which are bonded by a polyvinyl butyral (PVB) interlayer. This bonding process takes place utilizing heat and pressure treatment. The PVB layer has good bonding strength, is optically clear and does not diminish the optical properties of the glass panel.

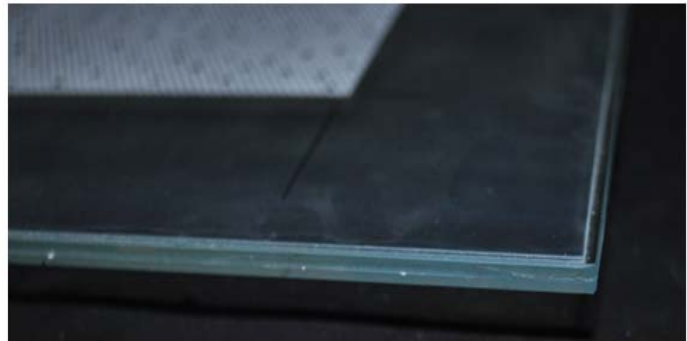


Fig.4 (b): LSG-Panel with XO-Armor® Protective

The laminated sandwiched glass panel is made by adhering a protective film from XO ARMOR® on both of the outer faces of the sandwiched glass panel. The protective film is 0.279 mm thick and a special adhesive XO® bond was used to adhere the protective film onto both of the faces of the sandwiched glass panel. The specimen is 305 mm long×305 mm wide×7.0 mm thick. According to the ASTM (D-882) standard test method for tensile properties of thin plastic sheeting, a simple test was performed at strain rate of 6×10^{-4} (ϵ/s) to obtain the following physical properties as shown in Table 1.

Modulus of Elasticity (Gpa)	3.5
Yield Strength (Mpa)	85
Ultimate Tensile Strength (Mpa)	181
Elongation (%)	150
Break Strength (lbs/inch)	295

Table 1: Tensile properties of XO ARMOR® protective film.

High and Low Temperature Experimental Setup for Shockwave Loading

Panels are tested at room temperature, at (0 °C, -8 °C) for low temperatures, and at (50 °C, 80 °C) for high temperatures (Gulf Countries). During the experiments, a special environmental chamber is designed to heat up and cool down the panels to required temperatures prior to blast loading. For testing the specimen under high temperature, a thermally insulated enclosure was designed around the support fixture as shown in Fig.5(a).



Fig.5 (a): Thermally insulated enclosure

A heating element was utilized to heat the internal environment and a circulation fan was used to ensure proper air-circulation Fig.5(b). By adjusting the output power of the heating element, various uniform (steady state) temperatures in the heating chamber were achieved.

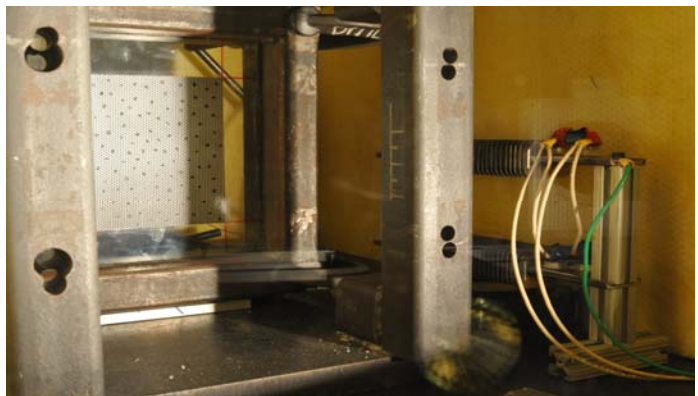


Fig.5 (b): Heating setup

Lab View software has been used for recording and plotting the temperature-time calibration for both (high / low) setups. To perform the experiment at a steady state temperature of 80 °C, a typical temperature-time plot for a specimen is shown in Fig.6. The specimen was heated for approximately 180 min. and then was subjected to shock-wave loading. In the last 20 Minutes from the calibration process, temperature had a minimal incremental increase (< 1 °C) between the insulated enclosure chamber and the center of the specimen.

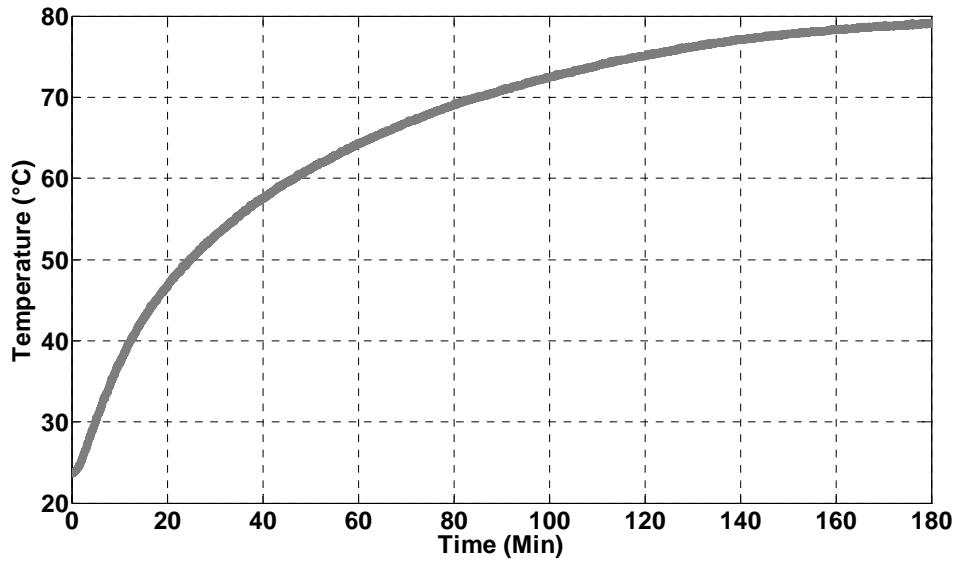


Fig.6: A typical heating calibration plot of 80 °C

For low temperature testing, the specimen was cooled down inside a cooling freezer for about an hour up to a maximum temperature of (-20 °C), where the panel was kept in between and covered by two plastic pages filled with a frozen liquid of an antifreeze (coolant) to continue cooling the entire panel outside the cooling freezer as shown in Fig.7. Once this was achieved, the specimen was quickly moved to the support fixture inside the shock-tube facility and the specimen ready for the blast. The environmental heat will increase the temperature of specimen uniformly, where the panel was held

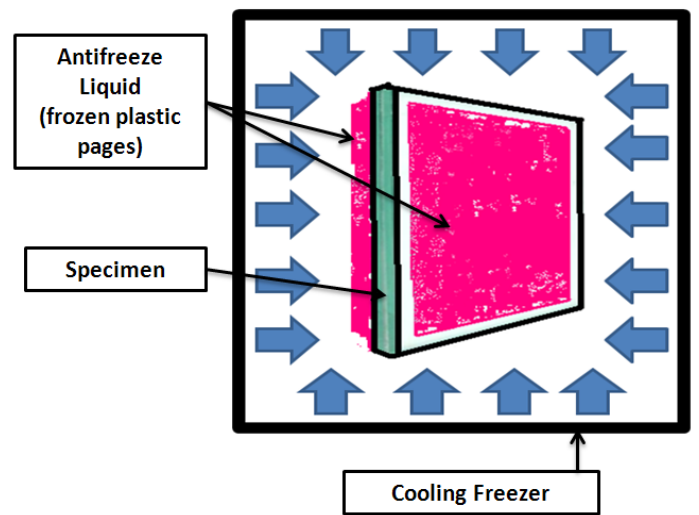


Fig.7: Schematic of panel sandwiched between two anti-freeze frozen plastic bags in cooling freezer.

in room temperature at different periods of time, in order to achieve different specific designed low temperatures as shown in Fig.8.

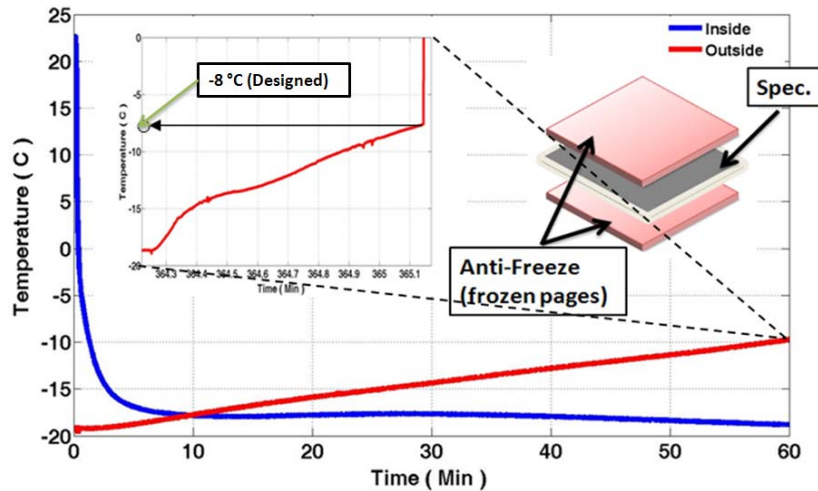


Fig.8: A typical cooling calibration plot of -8 °C

Blast Pressures Subjected to Specimen in Shock Tube Experiments

The square flat plate specimens utilized in this experimental study are held under fully clamped boundary conditions prior to blast loading. The dynamic loading is applied over a central circular area of 76.2 mm in diameter. The diameter of the driver and driven section is 0.15 m. The final muzzle diameter is 0.07 m. Two pressure transducers are mounted at the end of

the muzzle section measure the incident shock pressure and the reflected shock pressure during the experiment. All of the specimens are subjected to the same level of incident pressure in this experiment. A typical pressure profile obtained at the transducer location closer to the specimen is shown in Fig. 9, where the reflected velocity for the panel was about 350 m/s.

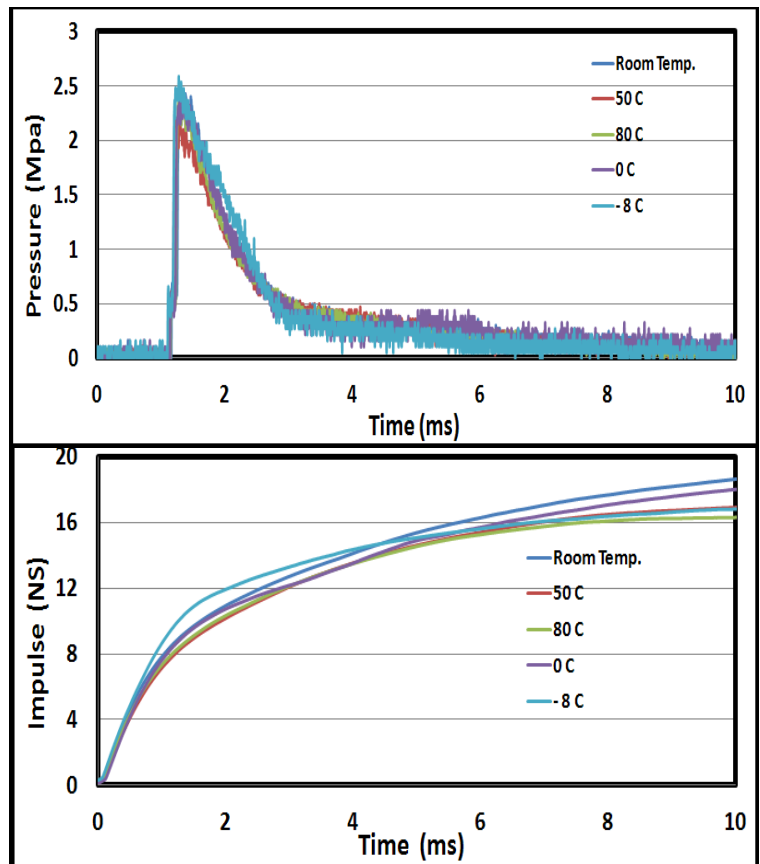


Fig.9: A typical pressure profiles and there calculated impulses temperatur

Digital Image Correlation (DIC) Analysis

A 3D-Digital Image Correlation (DIC) technique is used to obtain the out-of-plane deflection, in-plane strain developed, and the velocity of the back face, accordingly to understand the failure mechanism during shock wave event. Cameras are Photron SA1 high-speed digital camera and are used at a frame-rate of 20,000 fps with an image resolution of 512×512 pixels for one second time duration. These cameras are synchronized to make sure that the images and data can be correlated and compared.

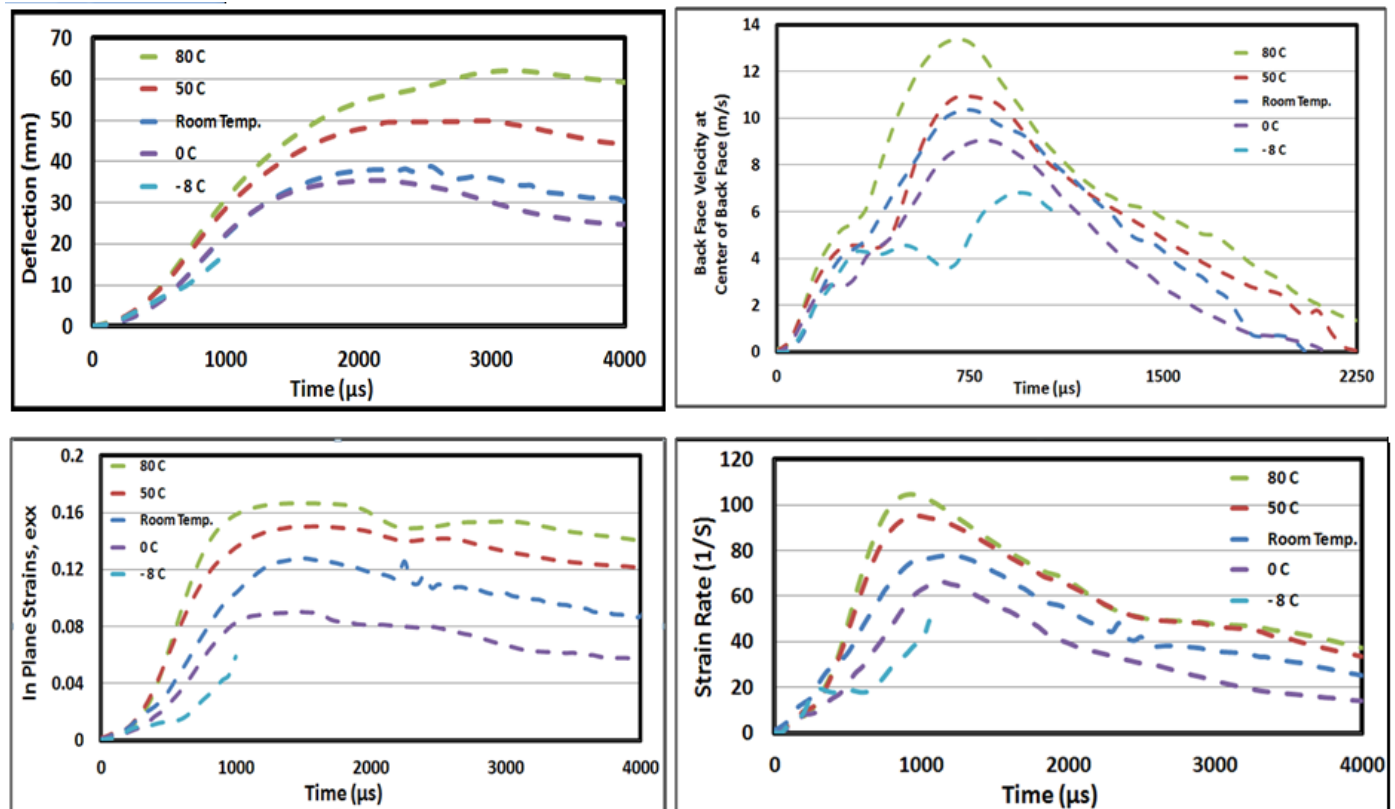
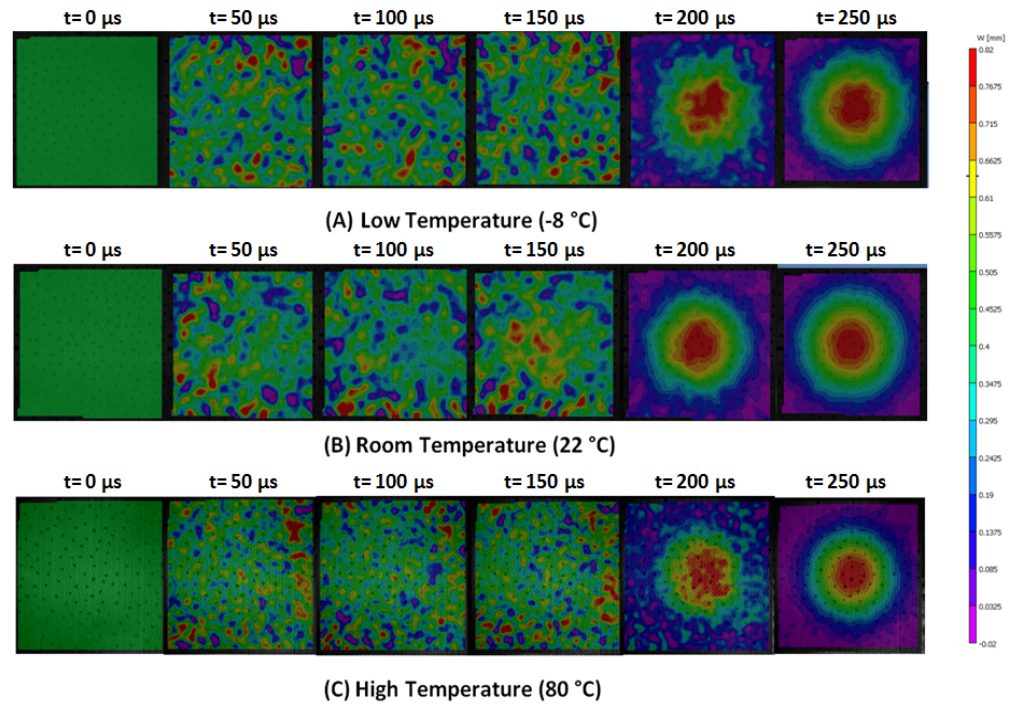


Fig.10: Time- out of plane deflection, in-plane strain developed, strain rate, and the velocity of the back face at (room, high, low) temperature

The deflection on the back face of the specimen during the fluid structure interaction between the gas and the specimen is shown in Fig. 11. The shock wave impinged on the specimen at $t=0 \mu\text{s}$. Circular deflection contours on the back face begins to appear at $t=50 \mu\text{s}$ showing that the stress wave has



propagated through the specimen. The transient deflection contours on the back

Fig.11: Deflection of the back face during fluid structure interaction time for room, high and low

face evolve with time. As shown in Fig.11, after a critical time interval ($\sim 150\text{--}200 \mu\text{s}$) the non-uniform loading disappears and a uniform loading is achieved. At high temperature, it takes a longer time for the stress wave to propagate and stabilize due to lower wave speeds resulting in a longer fluid structure interaction time ($\sim 200 \mu\text{s}$) than that of room and low temperature.

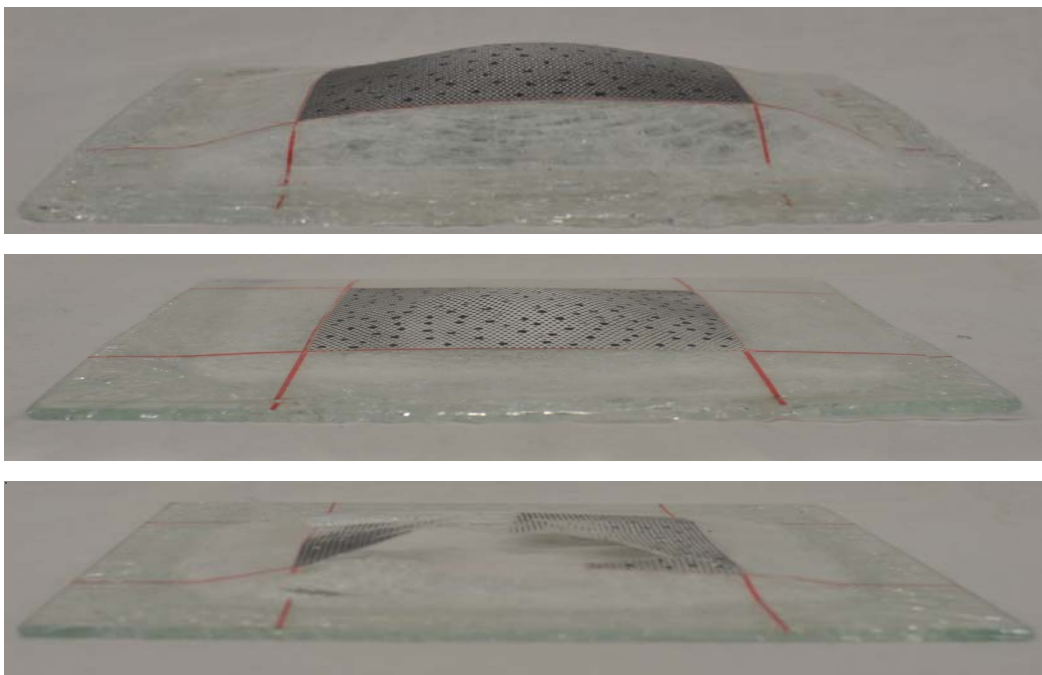


Fig.12: Post-mortem images of samples at (room, high, low) temperature

The center-point of full-field analysis was chosen and out of plane deflection and in-plane strain data were extracted at this point for better understanding of blast mitigation properties as shown in Fig.10. At ($\sim 0-450 \mu\text{s}$), specimens at different temperatures had a deflection of 5 mm with about $0.02 \text{ } \epsilon/\text{s}$ in- plane- strain in such away panels have the same trend of deflection. After this time, the protective film was behaving mechanically at different environments and reaches higher deflections at high temperatures which, results in overall better dynamic response of the glass structure changing behavior. For instant at $80 \text{ } ^\circ\text{C}$, the laminated sandwich glass panel shows a maximum deflection of 60 mm at $t=3\text{ms}$ whereas at room temperature, the specimen has a maximum deflection of 40 mm at the same period of time. So that, the laminated sandwich glass panel did not fail catastrophically and had further deflection according to the required temperature which resulted in higher in-plane strains. However at low temperature, the specimen shows a deflection of only 15 mm with a through hole formation at $t=1000 \mu\text{s}$, the panel behaves more brittle. In contracts at high temperature, there was no through hole formation and specimens behave more ductile and deflect /absorb more energy. Also, the in-plane strain history for the panel over an extended time at different temperatures is shown Fig. 10. The back face velocity of center point deflection was calculated and the specimen at $80 \text{ } ^\circ\text{C}$ had a maximum velocity of about 13.8 m/s at $t=750 \mu\text{s}$. Initially the specimen has zero velocity and as the stress wave propagates through the panel structure, the back face center point will deflects until the event ends where the velocity goes to zero again with an extended time of (3 ms) as shown in (Fig.10). Figure 12 indicates that as the temperature increases, the protective film expand more and will absorb more energy.

Task 2: Blast Response of Nano-Scale Core-Shell Rubber (CSR) toughened Sandwich Composites

1. Introduction

Sandwich structures have very important applications in naval and aerospace industry. Due to their construction they have many advantages that include high strength/weight ratio, high stiffness/weight ratio, and energy absorption capabilities. Sandwich structures consist of two thin, stiff face sheets, usually of the same thickness, separated by a lightweight, thicker core. The face sheets carry almost all of the bending and in-plane loads, while the core helps to stabilize the face sheets and defines the flexural stiffness and out-of-plane shear and compressive behavior. When sandwich structures are subjected to high-intensity impulse loadings, such as air blasts, the core materials play a crucial role in the dynamic behavior and overall structural response. Their properties assist in dispersing the mechanical impulse that is transmitted into the structure, and thus protect anything located behind it [1-3].

Common cores are made of metallic and non-metallic honeycombs, cellular foams, balsa wood, PVC, truss and lattice structures. Extensive research exists in the literature regarding the dynamic response of sandwich structures consisting of the various core materials and geometric structures [3-9]. These studies have indicated that advanced sandwich structures can potentially have significant advantages over monolithic plates of equivalent mass in absorbing the blast energy, whether in air or underwater. Apart from the various core materials and structures, the face sheet also plays an important role in the blast mitigation properties of the structure. In fact, the face sheet is the part of the structure which is directly exposed to the blast loading.

For marine applications, fiber-composite (face sheet) materials are commonly based on epoxies and other thermosetting polymers. This is due to the fact that these thermosetting polymers are highly cross-linked resulting in materials which exhibit good elevated temperature resistance and low creep. However, their high cross-link densities cause them to be relatively brittle in nature. This limits their applications as structural materials, as they have a poor resistance to crack initiation and growth. To overcome this deficiency and increase toughness, a commonly used method is the addition of a second dispersed particulate phase (during infusion). This second dispersed particulate phase can either be initially soluble in the epoxy resin and which then phase separates during curing to form or it can be of pre-formed particles. For the phase-separable tougheners, both rubbers (carboxyl-terminated butadiene-acrylonitrile (CBTN) [10, 11]) and thermoplastics [12-14] have been investigated. Pre-formed particles that have been studied include ceramic particles (glass [15, 16], alumina [17], or silica [18,19]), metal particles (aluminum [18]), polymers [20, 21] and core-shell rubber particles [22-27].

The behavior of rubber toughened and core-shell rubber toughened epoxy resin has been extensively studied in the literature [10,11, 22-27]. The core-shell rubber particles consist of two parts, a core which is rubber for impact resistance, and a shell which is a co-polymer compatible with epoxy resin. Note for these investigations, most of these rubber particles were on the micro-scale level. Results of these investigations indicated that the addition of rubber particles to epoxy resins can aid in increasing the fracture toughness, lap shear / T-peel strength, and fatigue resistance, as well as allow for no loss of T_g or thermal

properties (during infusion process), consistent morphology and a wide cure window. Therefore, the addition of rubber particles to current resin systems allows the once-brittle by nature resin to become toughened and subsequently more impact resistant.

Due to the improvement in mechanical properties, these rubber toughened epoxies can be used as the matrices for fiber-reinforced composite systems. However, the addition of these tougheners or pre-formed rubber particles, in the concentrations required to sufficiently enhance the toughness, can significantly increase the viscosity of the matrix resin. Also, conventional pre-formed particles generally have a particle diameter larger than the inter-fiber spacing, and particles are filtered out during infusion. This has led to the development of nano-scale rubber particles [27], defined as rubber particles less than 100 nm in diameter, since these particles will flow between the fibers during infusion [28].

Even though the behavior of rubber toughened epoxy systems has been extensively investigated in the literature, investigations regarding the behavior of glass-fiber reinforced composites and sandwich structures are limited. Therefore, the current study will investigate the influence of nano-scale core-shell rubber (CSR) particles [Kane Ace MX 153] on the behavior and performance of E-glass vinyl-ester (EVE) composite panels and sandwich structures. It will expand upon the authors' previous work [29-31], for which the blast performance of sandwich composites made of E-Glass Vinyl-Ester (EVE) face sheets and Corecell™ A-series foam was studied. The quasi-static and dynamic constitutive behaviors of the face sheets (both with and without CSR) and foam core material were first studied using a Split Hopkinson Pressure Bar (SHPB) device. The sandwich composites were then fabricated and subjected to shock wave loading generated by a shock tube. Both sandwich composites consisted of identical materials, core thickness and overall dimensions, with the only difference arising in the resin system. The non-coreshell rubber toughened resin system (Non-CSR) consisted of a vinyl-ester resin only; while the CSR toughened resin consisted of the same vinyl-ester resin, but with Kane Ace MX-153 nano-scale coreshell rubber particles added to the mixture. The shock pressure profiles and real-time deformation images were carefully analyzed to reveal the failure mechanisms of these sandwich composites. Digital Image Correlation (DIC) analysis was implemented to investigate the real-time deflection, strain and velocity of the back face of the specimens. Post-mortem analysis was also carried out to evaluate the overall blast performance of these sandwich structures.

2. Material and Specimen

2.1 Skin (Face sheet) and Core Materials

The face sheet materials that were utilized in this study are E-Glass Vinyl Ester (EVE) composites. The woven roving E-glass fibers of the face sheet materials were placed in a quasi-isotropic layout [0/45/90/-45]_s. The fibers were made of the .610 kg/m² areal density plain weave. The resin system used consisted of Ashland Derakane Momentum 8084, Ashland Derakane Momentum 411-200, and Kaneka Kane Ace MX153 (Coreshell Rubber) with the front and back skins (face sheets) consisting of identical layups and materials. Both composite panels consisted of 55% volume fraction of glass (fiber). Fig. 13 shows a schematic of the sandwich composite with skin and core materials.

Ashland Derakane 8084 is an elastomer modified epoxy vinyl ester resin designed to offer increased adhesive strength, superior resistance to abrasion and severe mechanical stress, while giving greater toughness and elongation. Ashland Derakane 411-200 is an epoxy vinyl ester resin based on Bisphenol-A epoxy that is specifically formulated for use in vacuum infusions. Kaneka Kane Ace MX153 is a 33% concentrate coreshell rubber (CSR) toughening agent in unmodified liquid epoxy resin based on Bisphenol-A. The CSR of Kane Ace MX153 is based on a lower T_g rubber component which provides more toughening than standard CSR compositions. MX153 is stable and the CSR remains completely dispersed under normal handling, formulating and curing conditions. Fig. 14 shows an SEM image of nano-scale core-shell rubber particles [27].

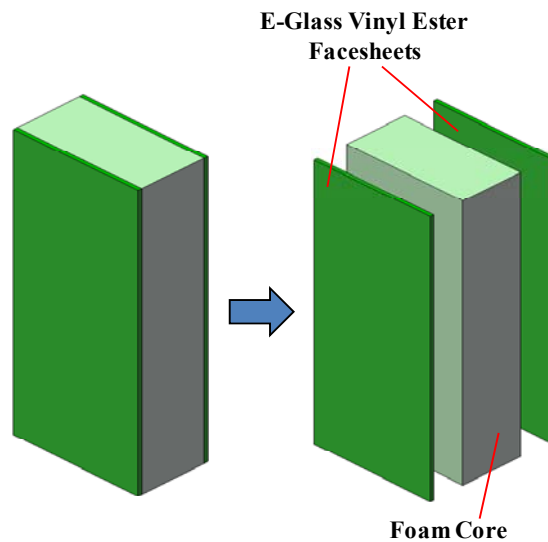


Fig. 13: Schematic of sandwich composite with skin and core

Due to the fact that resin viscosity is important during the infusion process (VARTM), the Ashland Derakane Momentum 411-200 was added to the Ashland Derakane Momentum 8084 in order to counteract the high viscosity of the Kaneka Kane Ace MX153. The dynamic viscosities of the Ashland Derakane 8084, 411-200 and Kaneka Kane Ace MX153 are 360 mPa-s (25°C), 210 mPa-s (25°C), and 20,000 mPa-s (50°C), as given from the manufacturer's data [32-34]. For this investigation a mixture of 48 % Ashland Derakane 8084, 48 % Ashland Derakane 411-200 and 4 % Kaneka Kane Ace MX 153 nano-scale core-shell rubber (CSR) particles was used to fabricate the CSR toughened composite face sheets and sandwich panels.

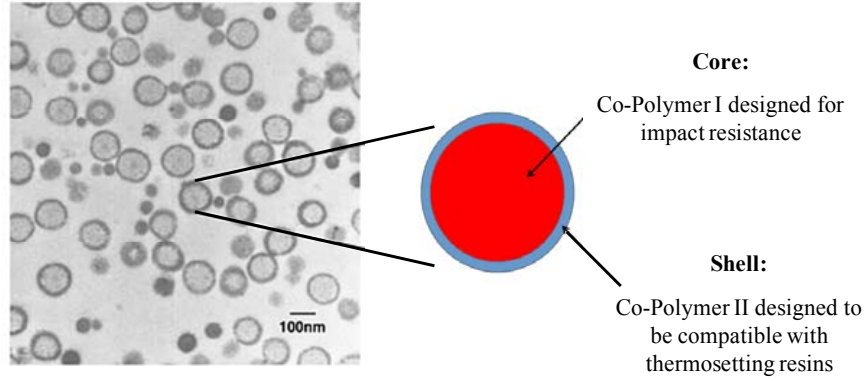


Fig. 14: SEM image of nano-scale core-shell rubber (CSR) particles [27].

The core material used in the present study is Corecell™ A500, which is a styrene acrylonitrile (SAN) foam manufactured by Gurit SP Technologies specifically for marine sandwich composite applications. Table 2 lists important material properties of the foam from the manufacturer’s data [35], as well as the material properties of the face sheet [29]. The material properties of the face sheet and the core materials were determined using proper ASTM standards, D 3410 and D 1621 respectively. The SEM images of the A500 foam cell microstructure can be seen in Fig. 15.

Table 2: Quasi-static material properties of foam core [35] and EVE face sheet [29]

	Nominal Density, ρ (kg/m ³)	Compressive Modulus, E (MPa)	Compressive Strength, σ_y (MPa)	Acoustic Impedance (kg/m ² s)	Wave
A500	92	64	0.9	7.7×10^4	
E-Glass Vinyl-Ester Composite	1800	13600 [longitudinal] 3900 [transverse]	220	4.9×10^6 [longitudinal] 2.6×10^6 [transverse]	

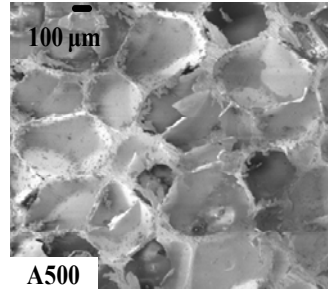


Fig.15: Cell microstructure of A500 foam core layer [35]

2.2 Core-shell Rubber (CSR) Toughened Sandwich Composites

Vacuum Assisted Resin Transfer Molding (VARTM) process was utilized to fabricate the sandwich specimens. During the VARTM process, the sandwich specimens were infused under the same conditions, i.e. temperature, humidity, and vacuum pressure (760 mmHg (1 atm)), with the same volume of resin. The overall dimensions for the samples were approximately 102 mm wide, 254 mm long and 48 mm thick. The foam core itself was approximately 38 mm thick, while the skin thickness was approximately 5 mm.

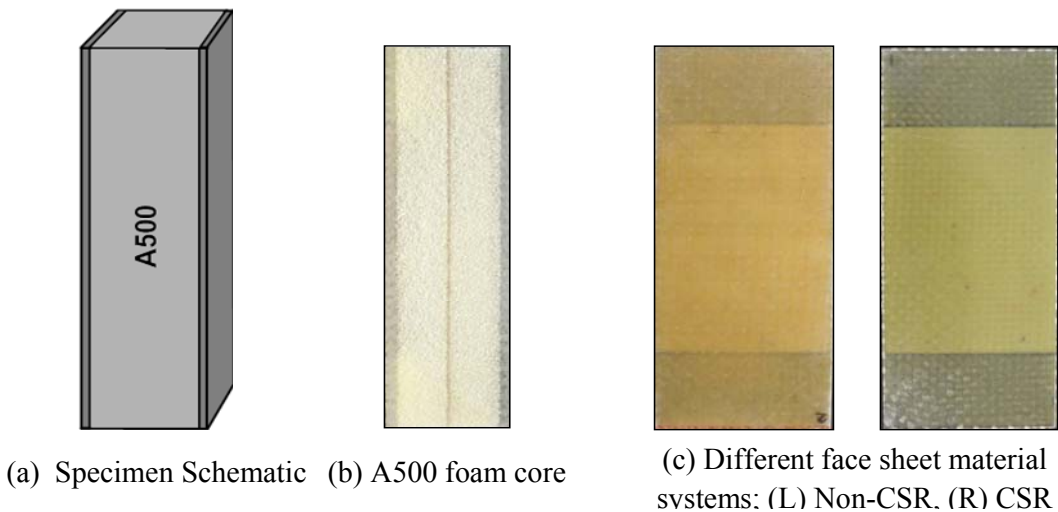


Fig.16: Specimen design and face sheet configurations

For the sandwich composites utilized in this study, two different resin systems were used; one configuration utilized a simple vinyl-ester resin system, while the other configuration utilized the same vinyl-ester resin system but with nano-scale core-shell rubber (CSR) toughening. The sandwich composite panels can be seen in Fig. 16. Both configurations consisted of one core layer of foam, A500. Since the core material and thickness, as well as overall specimen dimensions were identical, with the only difference arising in the resin system used during the infusion, the areal density of the two configurations was within 3%, i.e. the areal density of the Non-CSR toughened sandwich composite was 19 kg/m^2 , and the CSR toughened sandwich composite was 18.5 kg/m^2 .

3. Experimental Setup and Procedure

3.1 Quasi-Static Loading

The quasi-static loading was implemented by a screw-driven testing machine (Instron 5582), as shown in Fig. 17. For the quasi-static tensile and compressive tests on the face sheet materials, the proper ASTM standards for polymer matrix composite materials were used, ASTM D3039/D3039M - 08 (tensile) and ASTM D3410/D3410M - 03 (compressive). The experimental set-up consisted of the Instron 5582 testing machine, an extensometer (25.4 mm gage section) and a data acquisition system, along with a Wheatstone bridge high-strain indicator and oscilloscope (Tektronix TDS 3014). Note for the tensile experiments, two strain gages (C2A-13-250LW-350, Vishay Micro-measurements) were placed on the panels to ensure no shear loading is being applied. These gages were placed longitudinally and centered approximately in the middle of the specimen (length), centered 5 mm from the right and left side. For the compressive tests both gages were placed longitudinally, one gage on each side of the panel (front and back). Specimens were loaded with a constant crosshead rate of 2 mm/min and 1.5 mm/min for the tensile and compressive tests respectively. For the tensile loading, an extensometer was utilized to obtain the exact deformation of the specimen, while under compressive loading the machine compliance was subtracted from the total deformation to obtain the exact deformation of the specimen. Specimen dimensions were approximately 25.4 mm wide, 254 mm long and 5 mm thick (tensile) and 25.4 mm wide, 152 mm long and 5 mm thick (compression). For the transverse compressive loading of the face sheet material, circular specimens with a diameter of approximately 12.7 mm, and thickness of 5 mm were used. Specimens were loaded with a constant crosshead rate of 0.25 mm/min.

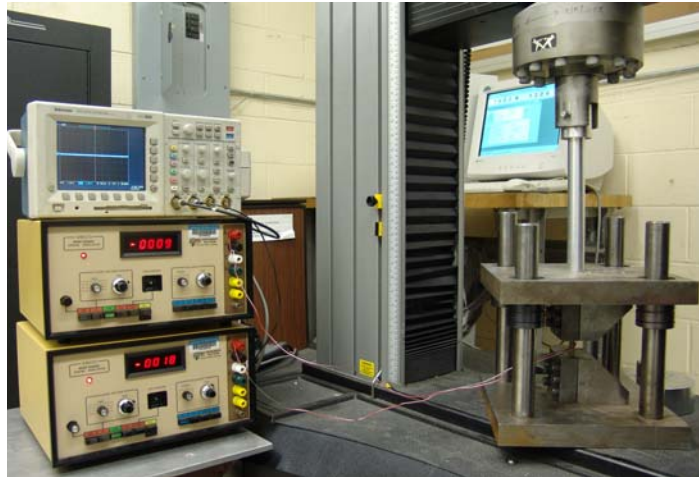
For the quasi-static compressive tests of the core material, the proper ASTM standard for rigid cellular plastics (foam) was used, ASTM D1621 – 04a. Specimens were loaded with a constant crosshead rate of 2.5 mm/min. Specimen dimensions were approximately 25.4 mm wide, 25.4 mm long, and approximately 12.7 mm thick.



(a) Instron 5582 tensile experimental set-up (face sheets)



(b) Close up of specimen, along with extensometer and strain gages



(c) Instron 5582 compressive experimental set-up (face sheets)

Fig. 17: Quasi-static experimental set-

3.2 Drop Weight Impact Tower

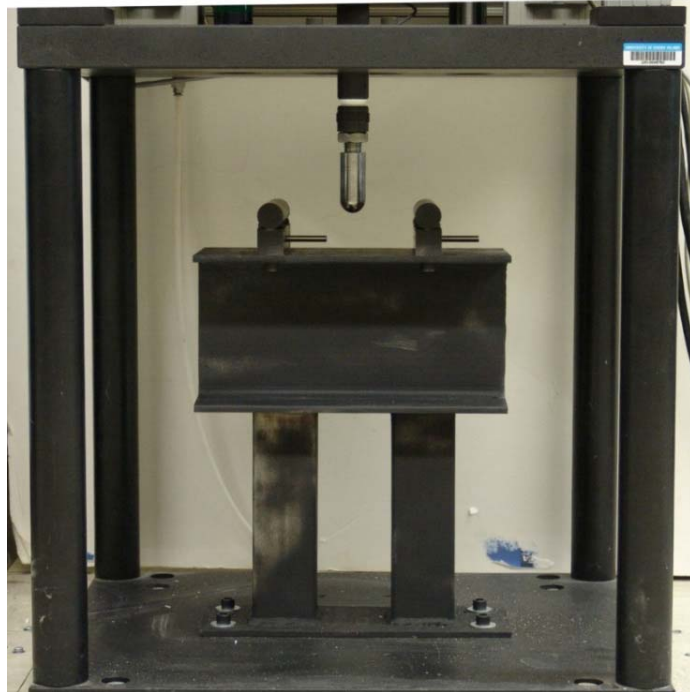
The dynamic loading was implemented by a drop weight impact tower apparatus (Instron 9210), as shown in Fig. 18. To investigate the dynamic impact behavior of the face sheets, the proper ASTM standard for polymer matrix composite materials was utilized (ASTM D 7136/D 7136M - 07). The Dynatup 9210 used is outfitted with a medium weight crosshead and is capable of producing 4.6-300 Joules of energy. The maximum impact velocity that can be achieved is 5 m/s. The drop tower is equipped with a data acquisition system. The data acquisition system includes a velocity detector, a piezoelectric tup for measuring loads, a signal conditioning amplifier, and a computer with an A/D board. The velocity detector is capable of measuring impact velocity as well as rebound velocity.

Normally specimens are held within the drop tower enclosure during experiments. To allow the use of an environmental chamber or testing of specimens too large to fit in the enclosure, the 9210 can be modified. Specimens that do not fit in the enclosure can be fixed

within the support base, outside of the enclosure. A simple support fixture was built that resides in the support base (see Figure 18b). Note the span width between supports is approximately 152 mm, which is identical to the simple support span in the shock loading experiments. The positioning of the specimen outside of the enclosure also allowed the specimen to be oriented in such a way that a high speed photography system could be employed during testing. The use of the high-speed photography system was to ensure proper results, i.e. duration of event (prior to impacting support fixture), no slipping of the specimen, and proper loading (center).



(a) Instron Dynatup drop weight tower



(b) Simple support fixture

Fig. 18: Drop Weight Impact Experimental

To perform an experiment several steps must be taken. The crosshead mass and drop height must be determined. Given that highest energy output was to be used the cross head was loaded with the maximum weight. All weights are stamped with their mass. The additional mass of the crosshead, reaction plate, reaction plate bolts, tup, tup bolts, and striker were taken into account. The mass of the crosshead, reaction plate and bolts are labeled from the manufacturer. The tup, tup bolt and striker were weighed to determine their mass. Table 3 shows the mass of all components contributing to the impact.

Component	Reaction plates and bolts	44 KN (10,000) lb tup and bolt	25.4 mm (1in) hemispherical striker	Crosshead	Weights	Total Mass
Mass (kg)	1.39	0.85	0.31	4.79	11.16	19.5

Table 3: Mass of drop-weight components contributing to impact

Both face sheet materials were subjected to approximately 150 J of a low velocity impact with a 25.4 mm (1in) diameter hemispherical striker installed on the tup. Given the impact energy and known mass of the drop weight, the drop height, h , was determined by

$$h = \frac{E}{mg} \quad (1)$$

where E is the desired energy, m is the mass of the drop weight, and g is the acceleration due to gravity.

After the drop height was determined, the drop tower velocity was tested. The specimen was placed in the fixture and the cross head was lowered until it came into contact with the specimen. The velocity sensor must be adjusted so that the velocity flag attached to the crosshead is in line with the bottom of the sensor. With the sensor adjusted, the number indicated on the scale was taken as a datum point and the calculated drop height was set from the datum. The crosshead was raised to the appropriate height and the specimen removed. A velocity test was then completed to ensure that the proper velocity was reached. Impact velocities were checked against a calculated velocity determined by

$$v = \sqrt{2gh} \quad (2)$$

Before experiments were performed, the data acquisition system was configured. Each tub has a calibration factor that must be input into the software. The system was configured using the correct calibration factor for the 10,000 lb tup. After the calibration factor was entered, the sampling rate was properly chosen. The sampling rate will determine if the entire event is captured. The data acquisition system will record 8192 data points regardless of the sampling rate, therefore it is important to know the duration of the impact event. For the given study, the event duration was approximately 12 ms. A sampling rate of 410kHz was chosen as this corresponds to 20 ms allowing for a proper margin of safety. Figure 19 shows a specimen placed in the simple supports with the hemispherical impactor in contact with the specimen.



Fig. 19: Specimen placed in simply-supported conditions for drop weight impact event

3.3 Split Hopkinson Pressure Bar (SHPB)

A Split Hopkinson Pressure Bar (SHPB) is the most common device for measuring dynamic constitutive properties of materials. For the current investigation two different SHPB systems were utilized; solid incident-solid transmission bar for high-impedance materials and a solid incident-hollow transmission bar (Modified SHPB) for low-impedance materials. Due to the low-impedance of Corecell™ foam material, dynamic experiments for the core materials were performed with a modified SHPB device with a hollow transmission bar to increase the transmitted signal intensity. A sketch of the modified SHPB device and typical pulse profiles are given in Fig. 20. It has a 304.8 mm-long striker, 1600 mm-long incident bar and 1447 mm-long transmission bar. All of the bars are made of a 6061 aluminum alloy. The nominal outer diameters of the solid incident bar and hollow transmission bar are 19.05 mm. The hollow transmission bar has a 16.51 mm inner diameter. At the head and at the end of the hollow transmission bar, end caps made of the same material as the bar were press fitted into the hollow tube. By applying pulse shapers, the effect of the end caps on the stress waves can be minimized. The details of the analysis and derivation of equations for analysis of experimental data can be found in ref [36].

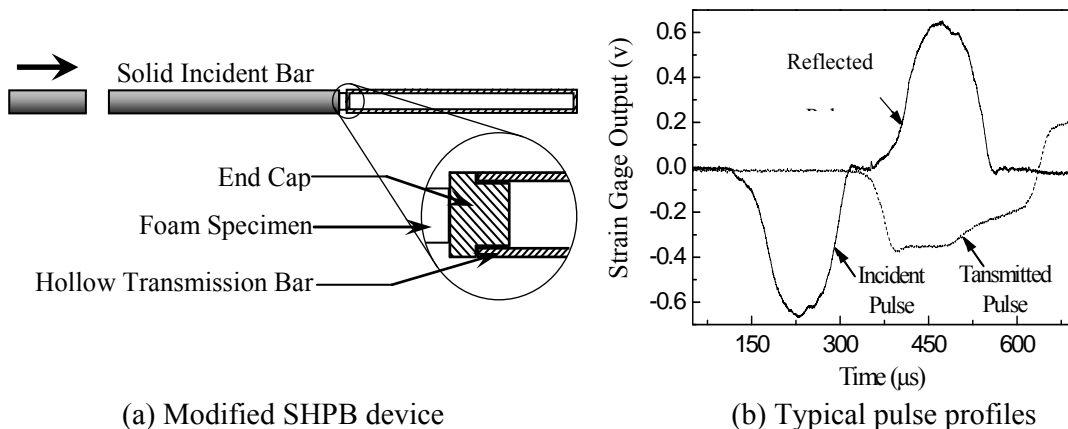


Fig. 20: Sketch of modified SHPB device with hollow transmission bar and typical pulse profiles

Due to the high-impedance of the EVE composite face sheets, dynamic experiments were performed with a normal SHPB device (solid incident-solid transmission). . It has a 203.2 mm-long striker, 1600 mm-long incident bar and 1447 mm-long transmission bar. All of the bars are made of Maraging steel. The nominal outer diameters of the solid incident bar and solid transmission bar are 12.7 mm.

3.4 Shock Tube

The shock tube apparatus used to obtain the controlled dynamic loading is shown in Fig. 21(a). Shock tubes offer the advantages of plane wave fronts, wave parameters that are easily controllable and repeatable, and uniform loading over shock tube muzzle diameter [37]. A complete description of the shock tube and its calibration can be found in ref. [38]. In principle, the shock tube consists of a long rigid cylinder, divided into a high-pressure driver section and a low pressure driven section, which are separated by a diaphragm. By pressurizing the high-pressure driver section, a pressure difference across the diaphragm is created. When this pressure differential reaches a critical value, the diaphragm ruptures. The subsequent rapid release of gas creates a shock wave, which travels down the shock tube to impart shock loading on the specimen at the muzzle end.

When the shock wave impacts the specimen located at the end of the muzzle, the wave is reflected at a higher pressure than that of the incident shock pressure. The theoretical detail on the equations for shock tubes has been previously established in the literature and is briefly discussed in the following section [39]. There are four basic theoretical assumptions which are used to describe the gas flow in shock tube:

1. The gas flow is one-dimensional.
2. The gas is ideal and has constant specific heats.
3. Heat transfer and viscosity effects are neglected.
4. Diaphragm rupture is instantaneous and does not disturb the subsequent gas flow.

Using conservation of energy, mass, and momentum as described by Wright [39], the following relationships for pressure, temperature and density across a shock front can be derived:

$$\frac{P_2}{P_1} = \frac{2\gamma M_1^2 - (\gamma - 1)}{\gamma + 1} \quad (3)$$

$$\frac{T_2}{T_1} = \frac{\{2\gamma M_1^2 - (\gamma - 1)\} \{(\gamma - 1)M_1^2 + 2\}}{(\gamma + 1)^2 M_1^2} \quad (4)$$

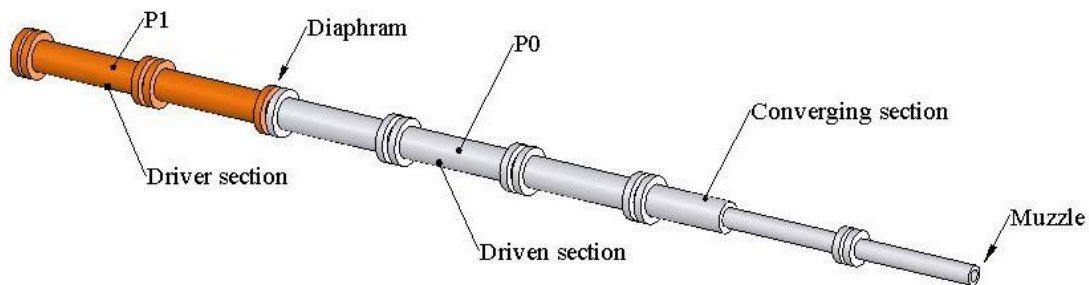
$$\frac{\rho_2}{\rho_1} = \frac{M_1^2 (\gamma + 1)}{(\gamma - 1)M_1^2 + 2} \quad (5)$$

where, P_1 , T_1 and ρ_1 , are pressure, temperature and density ahead of the shock front and, P_2 , T_2 and ρ_2 , are the pressure, temperature and density behind the shock front, γ is the adiabatic gas constant, and M_1 is the mach number of the shock wave relative to the driven gas. The pressure imparted on the specimen can be controlled by varying the above parameters in equations 1, 2, and 3. Different gases, such as nitrogen, and helium, were used in the shock

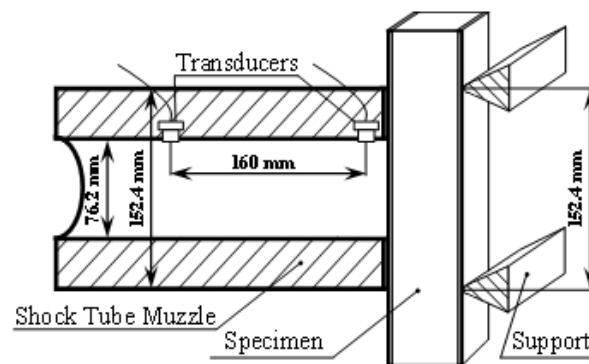
tube and it was found that helium is the most suitable gas to replicate blast loading conditions and also offered the added advantage of repeatability.



(a) Shock tube facility at URI



(b) Schematic of shock tube



(c) Detailed dimensions of the muzzle

Fig. 21: Shock tube apparatus

The shock tube apparatus utilized in the present study has an overall length of 8 m, consisting of a driver, driven, converging and muzzle section. The diameter of the driver and driven section is 0.15 m. The final muzzle diameter is 0.07 m. Fig. 21(b) shows detailed dimensions and locations of the muzzle, specimen, supports and the pressure sensors (PCB102A). The sensors are mounted at the end of the muzzle section to measure the incident pressure and the reflected pressure during the experiment. The final muzzle diameter is 0.076 m. The distance between the two sensors is 0.160 m and the distance between the second sensor and the end of the muzzle is ~ 0.020 m. The specimen was placed in the supports and

positioned close to the end of the muzzle. These support fixtures ensure simply supported boundary conditions with a 0.152 m span.

3.5 High Speed Photography Systems

Two high-speed photography systems were used in the present study, as shown in Fig. 22. A high-speed 3-D Digital Image Correlation (DIC) system, consisting of two high-speed digital cameras [Photron SA1], was placed facing the back side of the specimen to obtain the real-time full-field in-plane strain, along with out-of-plane deflection and velocity of the back face sheet. A randomized speckle pattern was placed directly on the back face sheet of the sandwich composite to ensure good contrast of the images. Another high-speed digital camera, [Photron SA1], was placed perpendicular to the side surface of the specimen to capture the side-view deformation images and mechanisms of failure. A framing rate of 20,000 fps was utilized which gives an interframe time of approximately 50 μ s.

The Digital Image Correlation (DIC) technique is utilized to capture the real-time full-field response of the back face of the sandwich composite panels. It is a non-intrusive, optical technique which allows for the capturing of the real-time dynamic response of sandwich composites through the use of high-speed photography and specialized software (PFV). In order to capture the three-dimensional response of the specimens, two cameras must be used in stereo configuration. This means the cameras must be calibrated and have synchronized image recording throughout the entire blast event. The calibration of the cameras is performed by placing a grid containing a known pattern of points (dots) in the exact location as to where the specimen will be placed during the experiment. This grid is then translated and rotated both in and out-of-plane, while manually recording a series of images. Due to the fact that the grid pattern has predetermined spacing, the coordinates of the center of each point (dot) is extracted from each image. Since the coordinate location of each dot is extracted uniquely for each camera, this allows for a correspondence of the coordinate system between cameras (Tiwari et al. [40]). DIC post-processing is performed utilizing the image pairs that are recorded during the blast loading event. Using VIC-3D software package, as distributed by Correlated Solutions, common pixel subsets of the randomized speckle pattern are matched between the deformed images and the un-deformed image. By matching the pixel subsets of the random speckle pattern, the three-dimensional location of distinct points on the face of the panel throughout time is obtained. This technique has been applied as a full-field measurement technique in many applications, including shock loading (Tiwari, et al. [41])

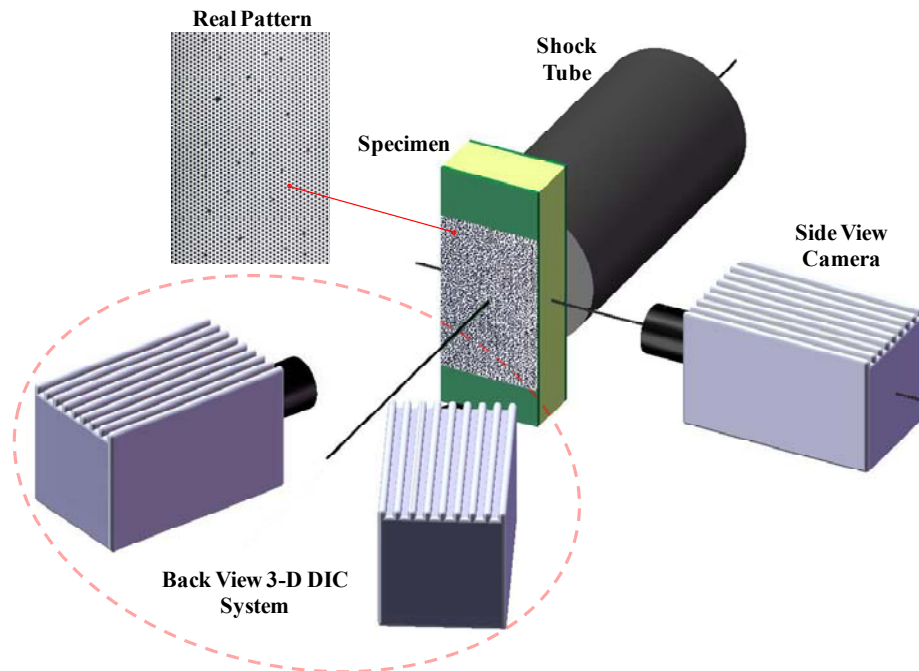


Fig. 22: High-speed photography set-up (Back-view DIC and side-view)

3.6 Experimental Procedure and Parameters

An initial series of experiments was conducted for both configurations and three samples were tested for each. This was followed by a second set of experiments, in which two specimens were tested for each configuration. Two different loading conditions were applied. For the first set of experiments, a simply stacked diaphragm of 5 plies of 10 mil mylar sheets with a total thickness of 1.27 mm was utilized to generate an impulse loading on the specimen with an incident peak pressure of approximately 1.0 MPa, a reflected peak pressure of approximately 5.0 MPa and a wave speed of approximately 1000 m/s. A typical pressure profile obtained from the transducer closest to the specimen (~ 0.02 m away) can be seen in Fig. 23. It should be noted that both pressure transducers were utilized to obtain the shock wave history, i.e. incident / reflected pressure and incident / reflected velocity. However, only the pressure transducer closest to the specimen was used to obtain the pressure applied on the specimen.

For the second set of experiments, a simply stacked diaphragm of 1 ply of 10 mil mylar sheets with a total thickness of 0.254 mm was utilized to generate an impulse loading on the face sheets only, with an incident peak pressure of approximately 0.3 MPa, a reflected peak pressure of approximately 1 MPa, and a wave speed of approximately 650 m/s. Due to the authors previous work [29-31], the experiments corresponding to the loading conditions with an incident peak pressure of 1.0 MPa will be presented and discussed in detail, while the face sheet experiments corresponding to the lower loading conditions (incident peak pressure 0.3 MPa) will be utilized to better evaluate the performance and failure mechanisms of the sandwich structures.

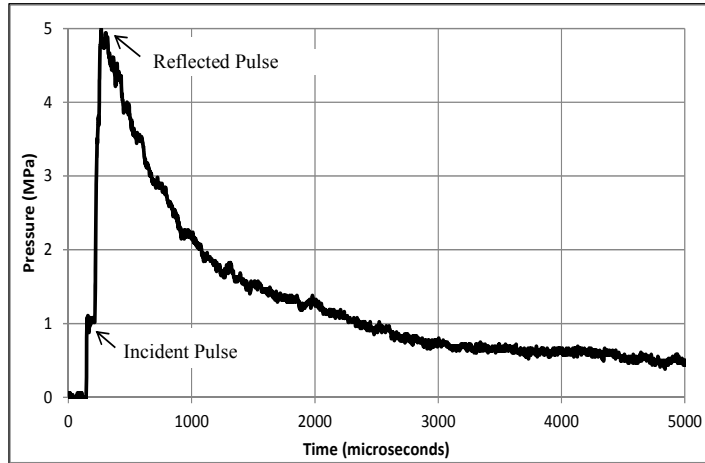


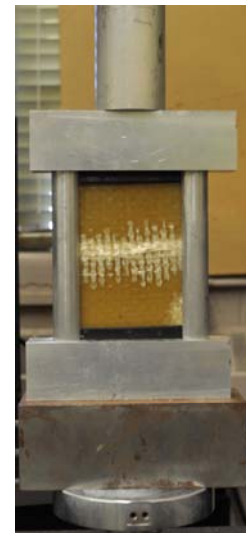
Fig. 23: Incident and reflected pressure profile

3.7 Residual Compressive Strength Measurements

Following the blast loading experiments, residual strength measurements of the face sheet materials were taken. The compressive strength was chosen as the residual strength parameter for this investigation. It is generally the most severely affected by impact regarding all of the mechanical properties given that the major mode of impact damage is most often delamination. Delamination is extremely detrimental to the residual compressive strength. The equipment used to measure the residual strength consisted of an Instron 5585 screw-driven testing machine, and a special compression fixture, Fig. 24, designed to be similar to that described in [42] and ASTM standard D 7137/ D7137M – 07.



(a) Instron 5582 compressive residual strength experimental set-up (pre-damaged face sheets)



(b) Close up of pre-damaged specimen in compressive fixture

Fig. 24: Compressive residual strength experimental set-up

The compression fixture consists of two rigid blocks connected by two .22.2 mm diameter guide rods. During the experiment, the compressive load was applied to the sample through the top block. The top block was free to slide up or down on the guide rods. The guide rods were used to ensure proper alignment of the load. The sample was loaded in two 4.8 mm deep slots, in between the two blocks. The fit in the slots was tight to provide clamped edge conditions on the loaded edge of the sample. The vertical edges of the sample were supported laterally by anti-buckling guides.

The fixture was placed into the loading frame of the Instron 5582 testing machine and the post damaged panels were loaded with a constant crosshead rate of 1.25 mm/min until failure. Data from this test consisted of the maximum load the plate could withstand before failure.

4. Experimental Results and Discussion

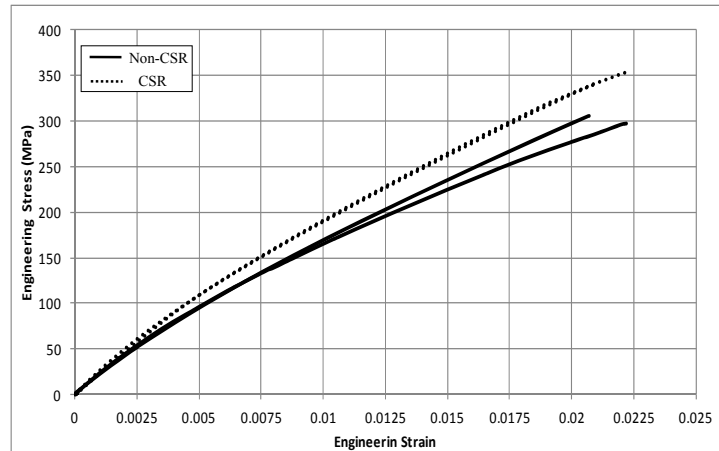
4.1 Constitutive Behavior of Face sheet and Core Material

4.1.1 Quasi-Static Behavior

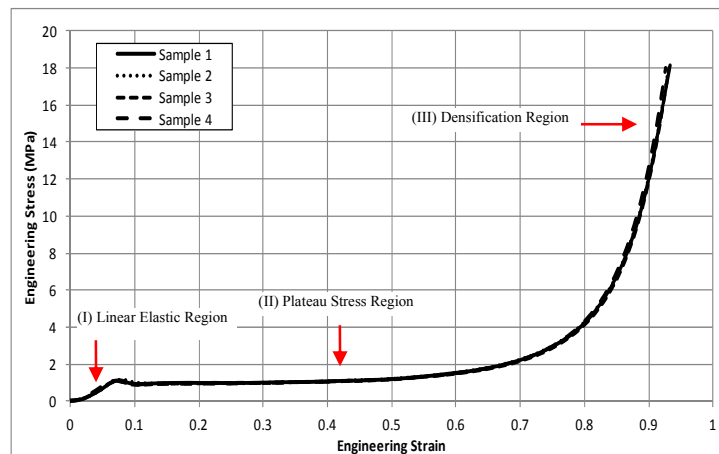
The quasi-static behavior of the face sheet and core materials were first investigated using an Instron 5582 screw-driven testing machine. The compressive properties of the A500 foam, as well as the tensile and compressive properties of the two composite face sheet panels (Non-CSR and CSR toughened) was studied to better understand the individual behavior of all of the constituents used in the sandwich composite structure. Understanding the individual properties of each material will allow for a better understanding of the entire material system, i.e. sandwich structure. Due to the fact that during a shock wave loading event the face sheet materials exhibit very little compression (transverse and longitudinally), only the tensile behavior of the face sheet material will be presented here, as shown in Fig. 25(a). The compressive behavior of the A500 foam core material can be observed in Fig. 25(b).

For the tensile behavior of the face sheets, it can be observed that the CSR toughened composite exhibits a stiffer behavior in comparison to the Non-CSR composite panel. The average tensile Young's Modulus, E , and ultimate tensile strength, U_T , was approximately 14.5 GPa and 300 MPa for the Non-CSR and 16 GPa and 350 MPa for the CSR toughened face sheet respectively. Therefore it can be concluded that the overall tensile strength and stiffness increases approximately 10% for the CSR toughened face sheet over the Non-CSR face sheet.

For the quasi-static compressive behavior of the foam core, the stress-strain curves show three deformation regions; (I) the linear elastic region, (II) the plateau stress (plastic yielding) region and (III) the densification region [43]. It can be observed that the plateau stress of the A500 foam is approximately 0.88 MPa.



(a) Quasi-static behavior of the different composite face sheets (Non-CSR and CSR)



(b) Quasi-static behavior of the Corecell™ A500 foam

Fig. 25: Quasi-static behavior of composite face sheets (tensile) and A500 foam core (compressive)

4.1.2 Drop Weight Impact

Both types of composite panels were subjected to low velocity high mass (LVHM) impact events using an Instron Dynatup 9210 drop weight tower apparatus. The specimens were simply-supported, across a 152 mm span (identical support conditions and span length as in shock tube experiments). The 19.4 kg mass was released from a drop height of 75 cm, achieving a maximum impact velocity of 3.8 m/s and a total impact energy of ~ 150 J. Load data and velocity data were recorded by a data acquisition system, and the total energy absorbed during the impact event was obtained through the data collected. Fig. 26 shows the total energy absorbed during the 150 J impact event.

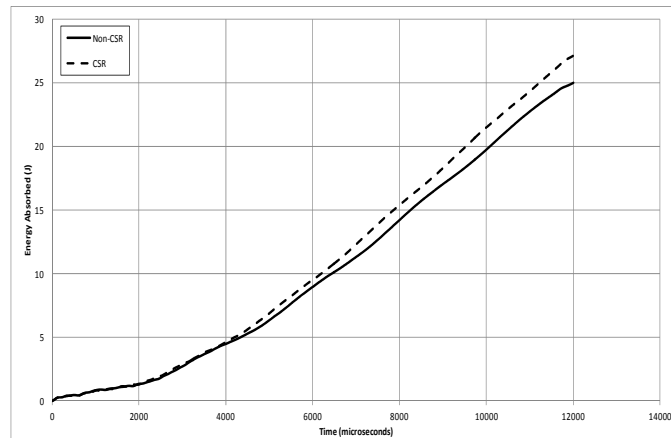
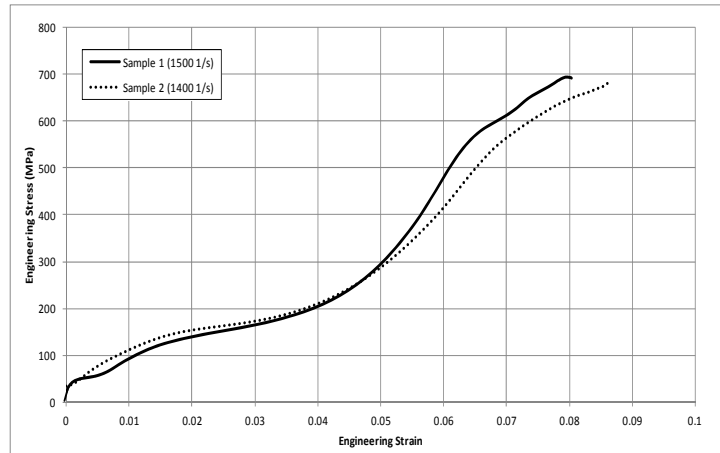


Fig. 26: Total energy absorbed for both composite face sheets during drop weight impact event

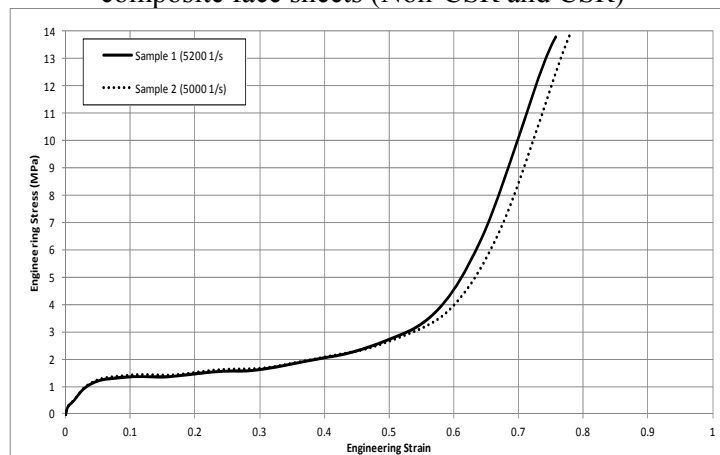
4.1.3 Split Hopkinson Pressure Bar

The high strain rate behavior of the face sheet and core materials was investigated using a SHPB apparatus. For the dynamic behavior of the face sheet materials, Fig. 27(a), it can be observed

Fig. 27(b) shows the dynamic behavior of the A500 foam core material. Note, the stress-strain curves also show the three deformation regions, as they did under quasi-static loading, even though the densification region is much harder to achieve under dynamic loading conditions. The high strain rate yield stress and plateau (flow) stress of the A500 foam is much higher than its quasi-static yield and plateau stresses, approximately 100% (1.60 MPa and 0.88 MPa respectively). The improvement of the mechanical behavior from quasi-static to high strain-rates in this core material, as well its long stress plateaus, signifies its ability to absorb large amounts of energy under high strain-rate dynamic loading. Therefore, it shows great potential in being used as a core material in sandwich structures subjected to high intensity air blasts



(a) High strain rate behavior of the different composite face sheets (Non-CSR and CSR)



(b) High strain rate behavior of the Corecell™ A500 foam

Fig. 27: High strain rate compressive behavior of composite face sheets and A500 foam core

4.2 Blast Response of Core-shell Rubber (CSR) Toughened Sandwich Composites

4.2.1 Real time deformation

The real-time observations of the transient behavior for both types of configurations subjected to shock wave loading are shown in Fig. 28. The shock wave (pressure wave) propagates from the right side of the image to the left side and some detailed deformation mechanisms are pointed out in the figures. It should be noted that the time scheme used to represent the images in each configuration is identical. Therefore for both of the configurations investigated, the images are correlated based on the same time per frame. This

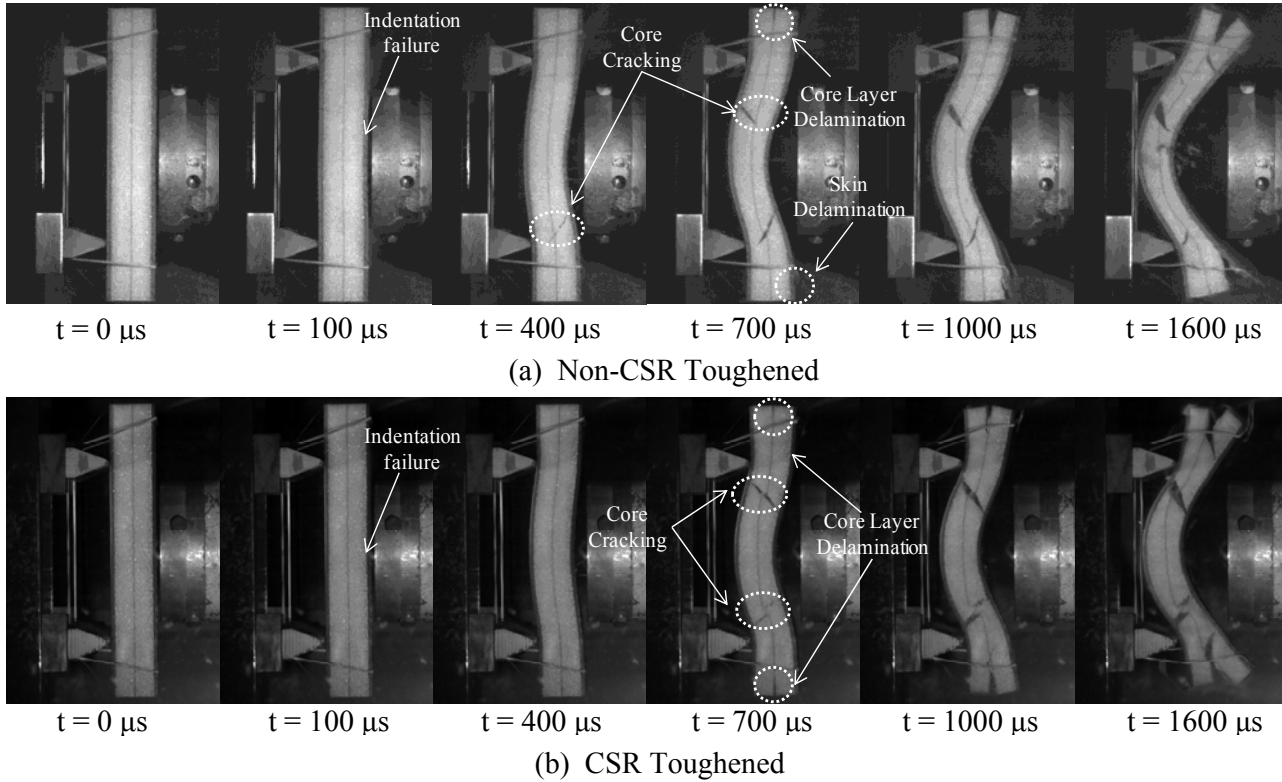
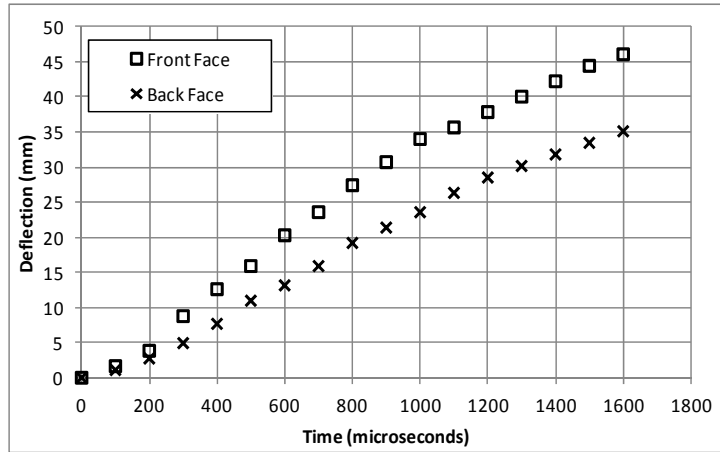


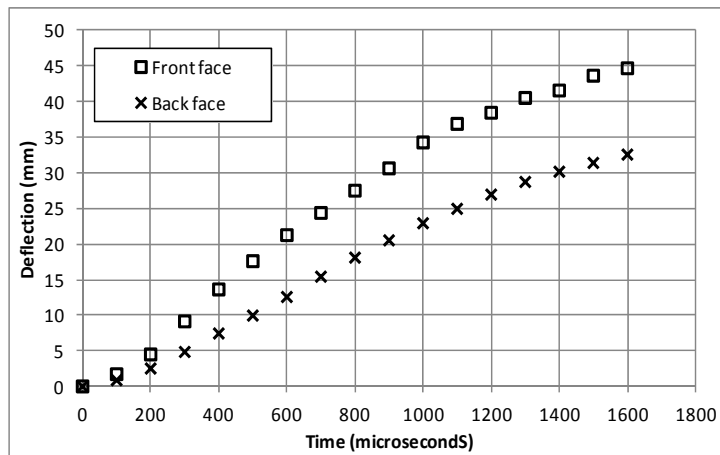
Fig. 28: High-speed images for (a) Non-CSR and (b) CSR toughened sandwich composites

4.2.2 Deflection

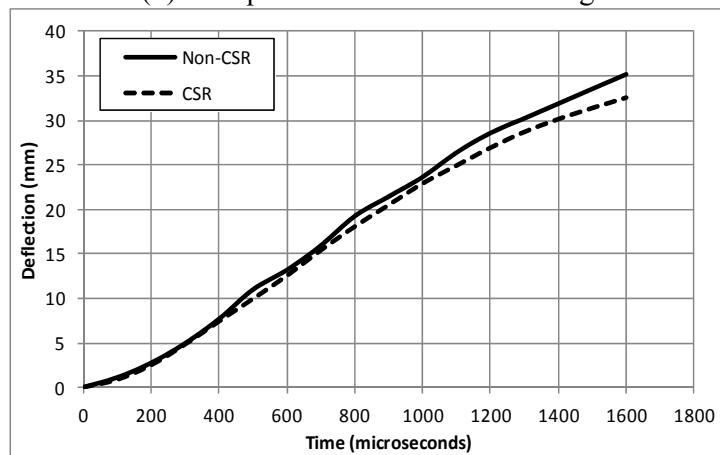
The mid-point deflection of each sandwich panel and all of its constituents was obtained from the high-speed images and a typical response can be seen in Fig. 29. For both configurations studied, the midpoint deflection of the front face (front skin) and back face (back skin) of the specimen was plotted. For the sandwich composite without core-shell rubber (Non-CSR), as shown in Fig 29 (a), it is evident that at $t = 1600 \mu\text{s}$ the front face deflects to approximately 46 mm, while the back face sheet deflects approximately 35 mm. Therefore the difference between the deflection of the front face and deflection of the back face signifies the total amount of compression observed in the core. Therefore, it can be concluded that the core compressed approximately 11 mm, which is 30% of its original thickness (38 mm).



(a) Mid-point deflection of Non-CSR toughened



(b) Mid-point deflection of CSR toughened



(c) Comparison of back face deflections for both configurations

Fig. 29: Mid-point deflections of both configurations

For the core-shell rubber (CSR) toughened sandwich composite, as shown in Fig 29(b), it is evident that at $t = 1600 \mu\text{s}$ the front face deflects to approximately 45 mm, while the back face sheet deflects approximately 32 mm. Therefore the difference between the deflection of the front face and deflection of the back face signifies the total amount of compression observed in the core. Therefore, it can be concluded that the core compressed approximately 12mm, which is 30 % of its original thickness (38 mm).

4.2.3 Digital Image Correlation (DIC) Analysis

Utilizing the Digital Image Correlation (DIC) technique, the full-field deflection (W), in-plane strain (ϵ_{yy}) and particle velocity (dW/dt) of the back face sheet of each configuration were generated. Fig. 30 – Fig. 33 show the full-field results for the back face sheet of both configurations respectively. Fig. 30 shows the full-field out-of-plane deflection (W) during the initial fluid-structure interaction ($t \leq \sim 250 \mu\text{s}$, [22]), with an emphasis on the shape of the loading, as indicated by the localized areas of larger deflection. For the Non-CSR toughened sandwich composites, as shown in Fig. 30a, by $\sim t = 100 \mu\text{s}$, the loading can be observed as a circular region in the center of the back face sheet. For the CSR toughened sandwich composites, as shown in Figures 30b, by $t = 100 \mu\text{s}$ the loading is more dispersed across the back face sheet, resulting in up to two or even three areas of localized deflection (loading). Therefore, it can be concluded that utilizing CSR, and thus introducing nano-scale rubber particles into the composites, aids in dispersing the initial loading on the structure, resulting in up to three areas of localized deflection (loading) on the back face sheets.

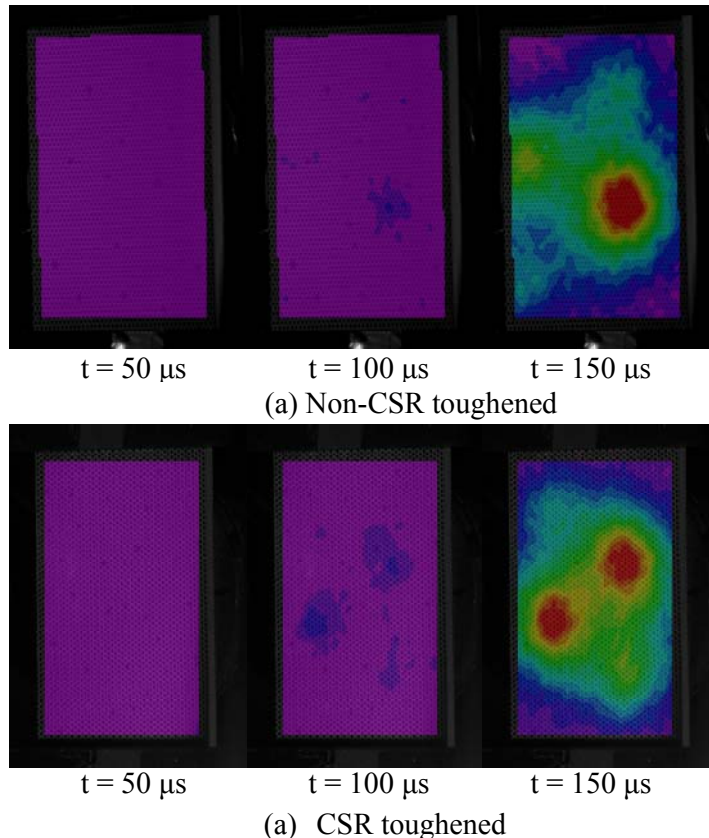


Fig. 30: Localized areas of larger deflections (loading) during fluid-structure interaction

Fig. 31 shows the full-field out-of-plane deflection (W) for both configurations. Note the scale ranges from 0 mm (purple) to 42 mm (red). It is evident from the figure that the back face of both core configurations exhibits limited out-of-plane deflection prior to $t = 400 \mu\text{s}$. Between $t = 400 \mu\text{s}$ and $t = 1600 \mu\text{s}$, both of these configurations continue to bend and exhibit deflections. For the sandwich composite with equivalent core layer thickness, as shown in Fig. 31a, it can be observed that at $t = 1600 \mu\text{s}$, the central region of the panel has deflected approximately 33 mm. When using sandwich composites with equivalent core layer mass (Fig. 31b), it can be seen that at $t = 1600 \mu\text{s}$, the central region of the panel has deflected approximately 41 mm. Therefore, it can be concluded that when using a core configuration with equivalent layer thickness, the deflection across the central region of the back face sheet is reduced approximately 20%.

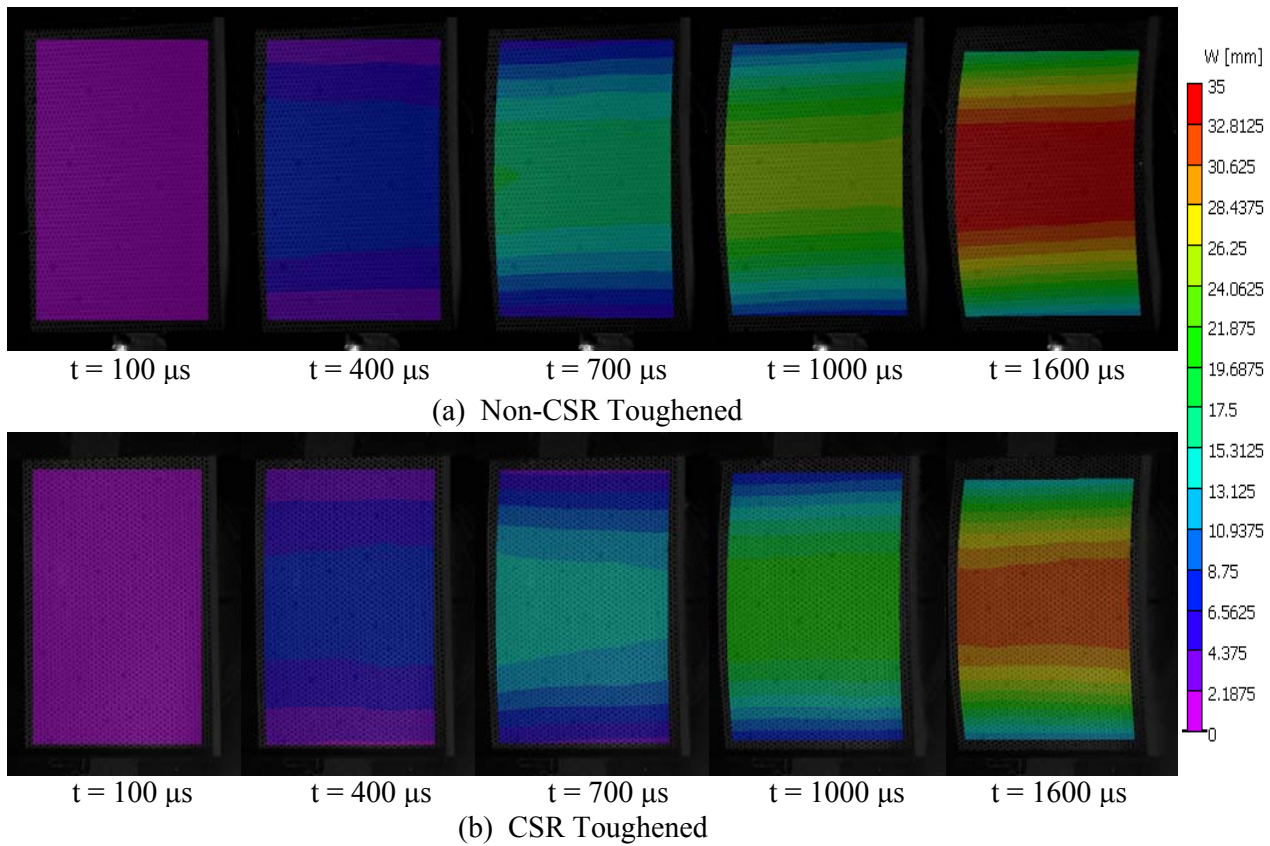


Fig. 31: Full-field out-of-plane deflection (W) of both configurations

The full-field, in-plane strain (ϵ_{yy}) is shown in Fig 32 for both configurations with a scale of 0 (purple) to .025 (red), or 0% to 2.5% respectively. It can be observed in the figure that the back face of both core configurations exhibits very minimal in-plane strain (ϵ_{yy}) prior to $t = 100 \mu\text{s}$. Between $t = 100 \mu\text{s}$ and $t = 1600 \mu\text{s}$, both of these configurations continue bending and the in-plane strain values continue to increase. For the sandwich composite with equivalent core layer thickness, as shown in Fig. 32a, it can be observed that at $t = 1600 \mu\text{s}$, the central region of the panel exhibits an in-plane strain of approximately .022, or 2.2%. When using sandwich composites with equivalent core layer mass (Fig. 32b), it can be seen that at $t = 1600 \mu\text{s}$, the central region of the panel exhibits an in-plane strain of approximately .024, or 2.4%. Therefore, it can be concluded that when using a core configuration with equivalent layer thickness, the maximum in-plane strain across the central region of the back face sheet reduced approximately 8%.

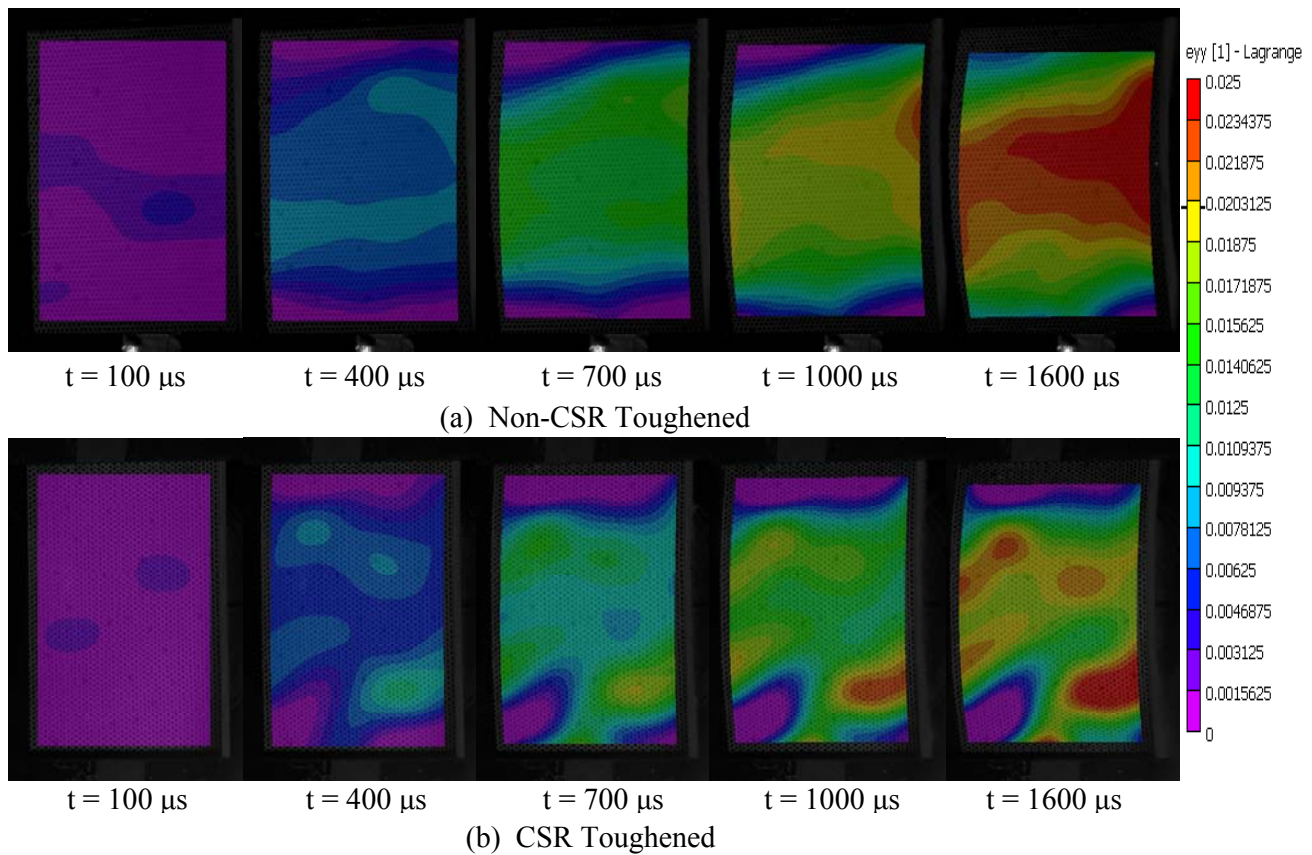


Fig. 32: Full-field in-plane strain (ϵ_{yy}) of both configurations

Figure 33 shows the full-field out-of-plane velocity (dW/dt) for both configurations. Note the scale ranges from 0 mm/s (purple) to 35,000 mm/s (red), or 0 m/s to 35 m/s. For the sandwich composites with equivalent core layer thickness, as shown in Fig. 33a, the back face exhibits a large out-of-plane velocity ($\sim 25\%$ of its maximum) by $t = 100 \mu\text{s}$. At $t = 400 \mu\text{s}$, the central region of the back face has reached an out-of-plane velocity of approximately 30 m/s. By $t = 700 \mu\text{s}$ the velocity has reached a maximum value of 31 m/s, and reduced back to approximately 30 m/s. From $t = 700 \mu\text{s}$ and onward, the velocity continues to decrease from 30 m/s to 22 m/s ($t = 1000 \mu\text{s}$) and finally down to 7 m/s ($t = 1600 \mu\text{s}$). For the sandwich composites with equivalent core layer mass, as shown in Fig. 27b, the back face exhibits a larger out-of-plane velocity ($\sim 40\%$ of its maximum) by $t = 100 \mu\text{s}$. At $t = 400 \mu\text{s}$, the central region of the back face has reached an out-of-plane velocity of approximately 31 m/s. By $t = 700 \mu\text{s}$ the velocity has reached a maximum values, 34 m/s, and reduced to 33 m/s. From $t = 700 \mu\text{s}$ and onward, the velocity continues to decrease from 33 m/s to 29 m/s ($t = 1000 \mu\text{s}$) and finally down to 20 m/s ($t = 1600 \mu\text{s}$).

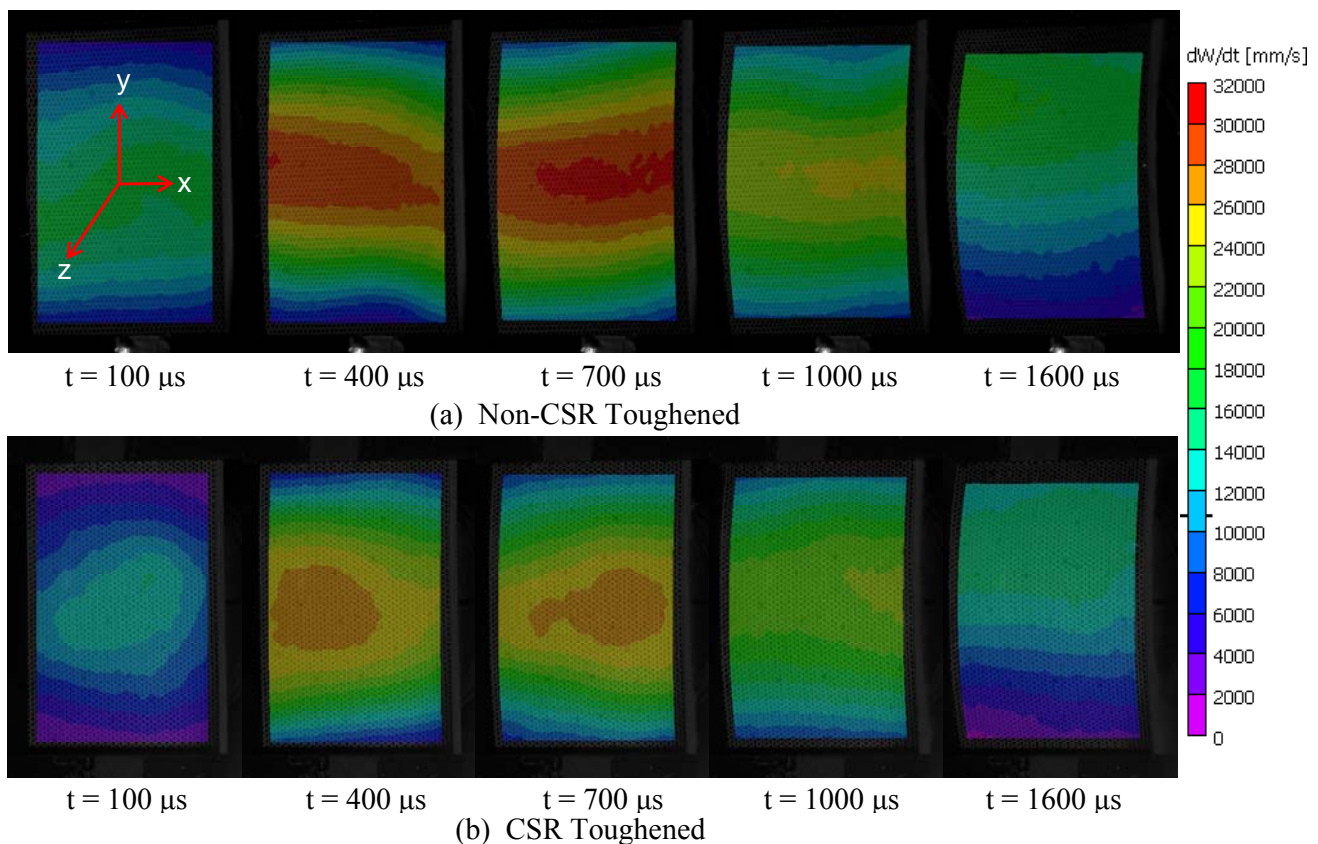


Fig. 33: Full-field out-of-plane velocity (dW/dt) of both configurations

Therefore it can be concluded that when using a sandwich composites with equivalent core layer thickness, the maximum back face velocity is approximately 8% smaller than the sandwich composite with equivalent core layer mass. Also note, the velocity of the panel at $t = 1600 \mu\text{s}$ is approximately 65% smaller as well, i.e 20m/s and 7 m/s respectively.

Using the point inspection tool from the Digital Image Correlation (DIC) software, a point directly in the center of the back face of each specimen was chosen. The out-of-plane deflection (W) showed excellent agreement with the results generated utilizing the high-speed images and therefore only the in-plane strain (ϵ_{yy}) and out-of-plane velocity (dW/dt) results are shown. Fig. 34 and Fig. 35 show the in-plane strain and out-of-plane velocity values obtained. Looking at the in-plane strain values (Fig. 34) it can be seen that at $t = 1600 \mu\text{s}$, the maximum in-plane strain value at the central point of the back face sheet for the sandwich composite with equivalent core layer thickness is approximately 0.0225, or 2.25%. When using a sandwich composite with equivalent core layer mass, it can be seen that at $t = 1600 \mu\text{s}$, the maximum in-plane strain value at the central point of the back face sheet is approximately 0.0245, or 2.45%. Therefore it can be concluded that when using sandwich composites with equivalent core layer mass, the maximum in-plane strain across the central region of the back face sheet is reduced 8% in comparison to the sandwich composites with equivalent core layer mass.

Fig. 35 shows the out-of-plane velocity (dW/dt) for both configurations. For the sandwich composite with equivalent core layer thickness, the maximum velocity is reached at $t = 500 \mu\text{s}$ and is approximately 31 m/s. For the sandwich composite with equivalent core layer mass, the maximum velocity is reached at approximately the same time, $t = 500 \mu\text{s}$, but the velocity is larger (34 m/s). Therefore it can be concluded that when using sandwich composites with equivalent core layer mass, the maximum out-of-plane velocity across the central region of the back face sheet is reduced 8% in comparison to the sandwich composites with equivalent core layer mass.

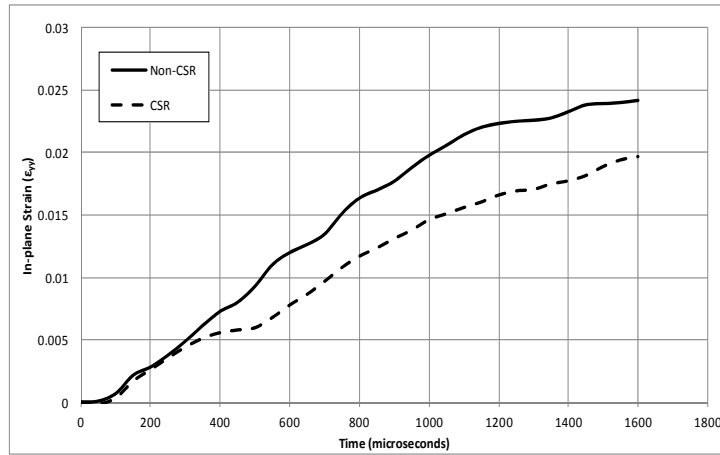


Fig.34: In-plane strain (ϵ_{yy}) of both configurations

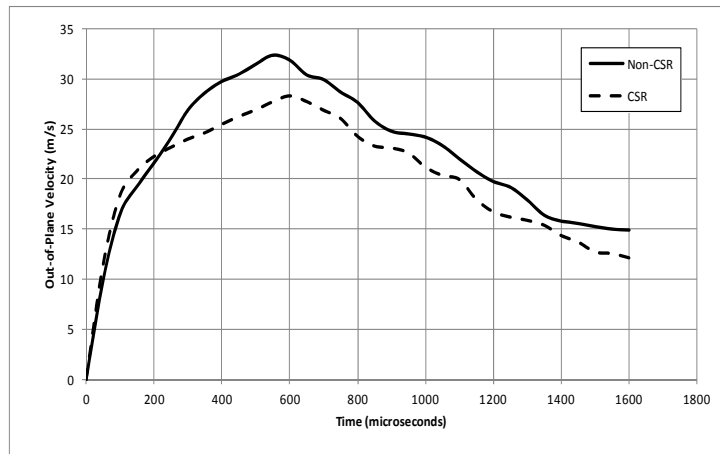


Fig. 35: Out-of-plane velocity (dW/dt) of both configurations

In order to provide a more comprehensive understanding on the behavior response of the sandwich panels during the shock wave loading, the individual face sheets were subjected to blast wave loading as well. The Digital Image Correlation (DIC) technique was applied to the face sheet experiments (incident peak pressure 0.3 MPa). For this investigation full-field analysis was also carried out, as well as line-inspection. Since the behavior of the face sheets during the initial fluid structure interaction was similar to that of the sandwich composites, only the line-inspection analysis will be presented here. Utilizing the line-inspection tool from the Digital Image Correlation (DIC) software, a longitudinal line directly in the center of the back face of each specimen was chosen, and the results were extracted, as shown in Fig. 36.

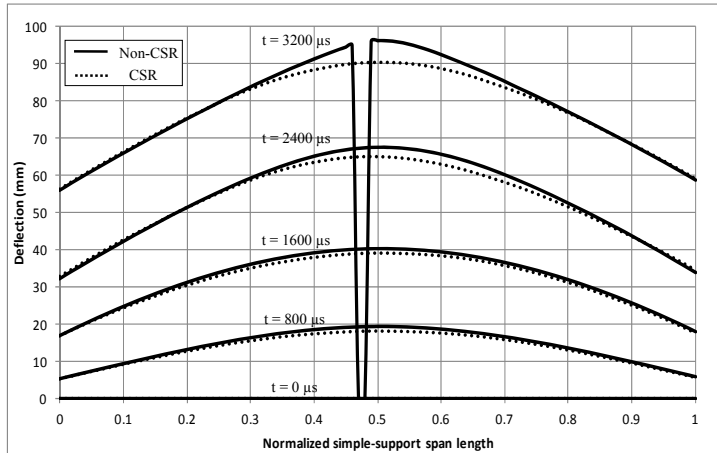
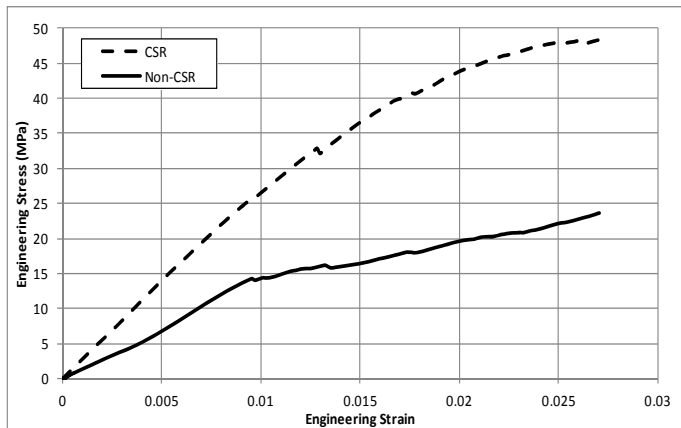


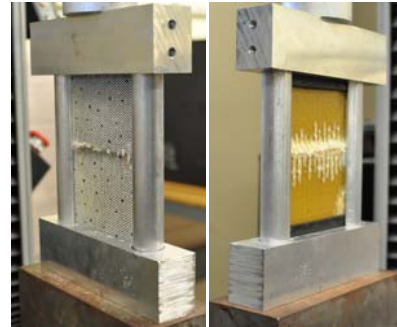
Fig. 36: Longitudinal line-inspection analysis across central region of back face for both composite face sheet systems

4.2.4 Residual Compressive Strength

After the blast loading event occurred on the face sheets, both types of composite face sheets were subjected to post-blast residual compressive strength measurements. The results of these tests are shown in Fig. 37.



(a) Residual compressive strengths of both types of composite face sheets



(b) Non-CSR Toughened



(c) CSR Toughened

Fig. 37: Residual compressive strength of both types of composite face sheets after being subjected to high intensity blast loading (incident peak pressure 0.3 MPa)

4.2.5 Post-mortem Analysis

After the quasi-static (Drop-weight) and dynamic events (SHPB and Shock Tube) occurred, the damage patterns were visually examined and recorded using a high resolution digital camera and are shown in Fig. 38 - Fig. 41. The damage patterns of both types of composite face sheets subjected to a 150 J drop-weight impact event are shown in Fig. 38.

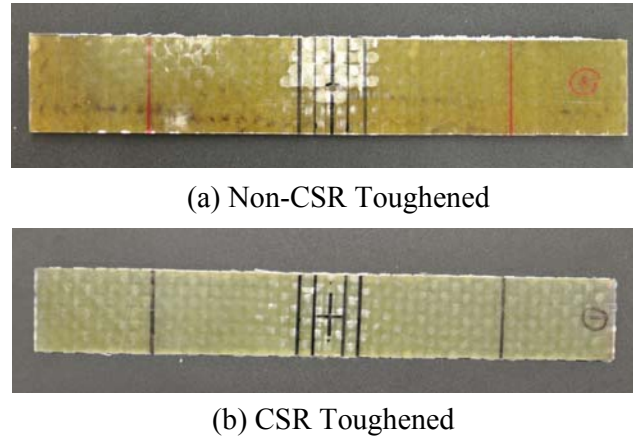


Fig. 38: Visual examination of both composite face sheets after being subjected to 150 J impact

Fig. 39 shows the damage patterns of composite face sheets subjected to a strain rate of 10^3 (~ 5000 1/s) using a Split Hopkinson Pressure Bar apparatus.

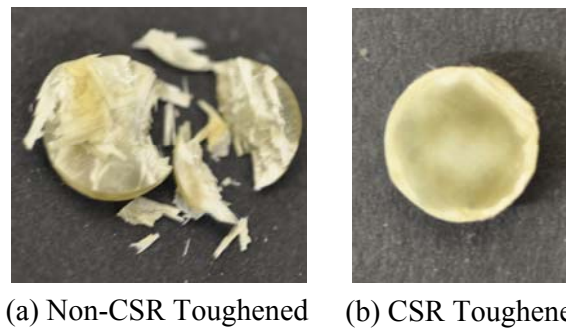


Fig. 39: Visual examination of both composite face sheets after being subjected to high strain-rate loading (SHPB)

The damage patterns of both types of sandwich composite panels subjected to an incident peak pressure of 1.0 MPa, a reflected peak pressure of 5.0 MPa, and an incident velocity of 1000 m/s using the shock tube apparatus are shown in Fig. 40.

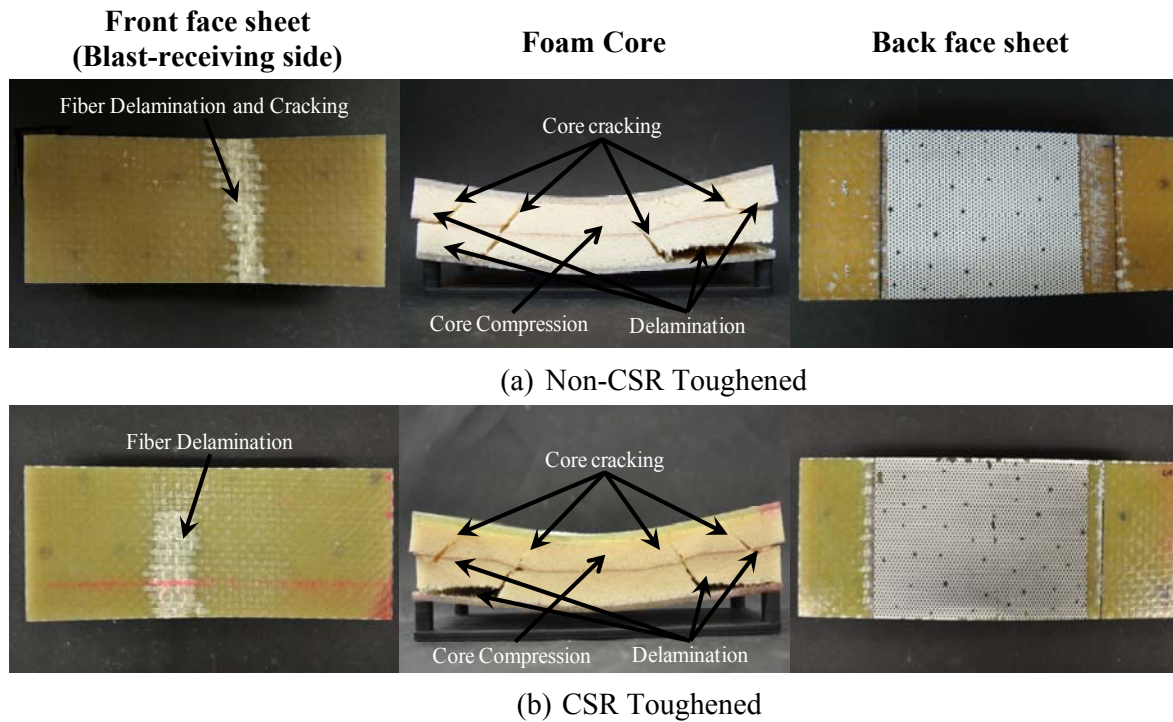
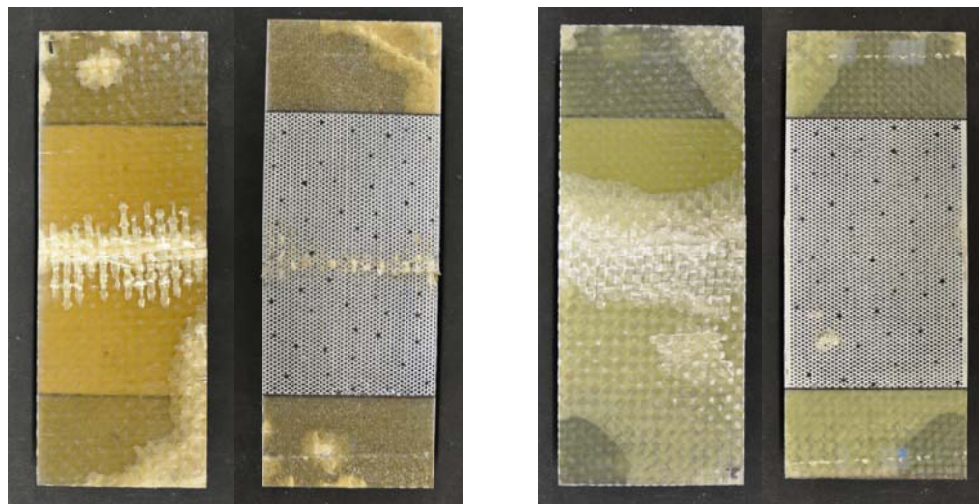


Fig. 40: Visual examination of both configurations after being subjected to high intensity blast load (incident peak pressure 1.0 MPa)

Fig. 41 shows the damage patterns of both types of composite face sheets subjected to an incident peak pressure of 0.3 MPa, a reflected peak pressure of 1.0 MPa, and an incident velocity of 650 m/s using the shock tube apparatus.



(a) Non-CSR Toughened Composite; (L) Front face sheet, (R) Back face sheet (b) CSR Toughened Composite; (L) Front face sheet, (R) Back face sheet

Fig. 41: Visual examination of both composite face sheets after being subjected to

5. Conclusions

The following is the summary of the investigation:

- (1) Core-shell rubber particles (CSR) have a significant effect on the quasi-static and dynamic behavior of composite materials and sandwich structures. It was observed that the addition of 4% CSR to E-glass Vinyl-Ester (EVE) composite face sheets increased the tensile strength (~10%) and drop-weight impact resistance (~10%). After the dynamic loading, such as SHPB and shock wave loading, the CSR toughened face sheets maintained structural integrity, while the Non-CSR face sheets did not.
- (2) The dynamic stress-strain response is significantly higher than the quasi-static response for the Corecell™ A500 foam studied. The increase in the yield strength from quasi-static response to dynamic response, along with the longer stress plateau, indicates that this core material shows great potential in absorbing large amounts of energy.
- (3) Two types of sandwich composites were fabricated, one with the addition of nano-scale core-shell rubber (CSR) particles during infusion, and one without (Non-CSR). The core material and thickness, as well as overall specimen dimensions were held constant. Results indicated that the addition of nano-scale core-shell rubber (CSR) particles to the panels allows for an increase in blast performance. By dispersing the initial loading, the CSR toughened sandwich composites exhibit lower amounts of out-of-plane deflection and velocity, as well as in-plane strain, approximately 8%, 12% and 20% respectively.

6. Acknowledgement

The authors kindly acknowledge the financial support provided by Dr. Yapa D. S. Rajapakse, under Office of Naval Research Grant No. N00014-04-1-0268. The authors acknowledge the support provided by the Department of Homeland Security under Cooperative Agreement No. 2008-ST-061-ED0002. Authors thank Gurit SP Technology and Specialty Products Incorporated (SPI) for providing the material as well as Dr. Stephen Nolet and TPI Composites for providing the facility for creating the composites used in this study.

7. References

- [1] Xue Z. and Hutchinson JW (2003) Preliminary assessment of sandwich plates subject to blast loads. *Int J Mech Sci*, 45, 687-705.
- [2] Fleck NA and Deshpande VS (2004) The resistance of clamped sandwich beams to shock loading. *J Appl Mech*, 71, 386-401.
- [3] Dharmasena KP, Wadley HNG, Xue Z and Hutchinson JW (2008) Mechanical response of metallic honeycomb sandwich panel structures to high-intensity dynamic loading. *Int J Imp Eng*, 35 (9), 1063-1074.
- [4] Zhu F, Zhao L, Lu G and Wang Z (2008) Deformation and failure of blast loaded metallic sandwich panels – Experimental investigations. *Int J Imp Eng*, 35 (8), 937-951.

- [5] Nurick GN, Langdon GS, Chi Y and Jacob N (2009) Behavior of sandwich panels subjected to intense air blast: part 1- Experiments. *Comp Stru*, 91 (4), 433 – 441.
- [6] Tagarielli VL, Deshpande VS and Fleck NA (2008) The high strain rate response of PVC foams and end-grain balsa wood. *Comp B*, 39, 83–91.
- [7] Radford DD, McShane GJ, Deshpande VS and Fleck NA (2006) The response of clamped sandwich plates with metallic foam cores to simulated blast loading. *Int J Sol Struc*, 44, 6101-612.
- [8] McShane GJ, Deshpande VS, and Fleck NA (2007) The underwater blast resistance of metallic sandwich beams with prismatic lattice cores. *J Appl Mech*, 74, 352 – 364.
- [9] McShane GJ, Radford DD, Deshpande VS and Fleck NA (2006) The response of clamped sandwich plates with lattice cores subjected to shock loading. *European J Mech – A: Solids*, 25, 215-229.
- [10] Kinloch AJ, Shaw SJ, Tod DA, Hunston DL (1983) Deformation and fracture behaviour of a rubber-toughened epoxy: 1. Microstructure and fracture studies. *Polymer*, 24 (10): 1341-1354
- [11] Yee AF, Pearson RA (1986) Toughening mechanisms in elastomer-modified epoxies *Journal of Material Science*, 21: 2462-2474
- [12] Bucknall CB and Partridge IK (1983) Phase separation in epoxy resins containing polyethersulphone *Polymer*, 24 (5): 639 – 644
- [13] Kinloch AJ, Yuen ML, Jenkins SD (1994) Thermoplastic-toughened epoxy polymers *Journal of Material Science* 29: 3781-3790
- [14] Johnsen BB, Kinloch AJ, Taylor AC (2005) Toughness of syndiotactic polystyrene/epoxy polymer blends: microstructure and toughening mechanisms, *Polymer* 46: 7352-7369.
- [15] Broutman LJ, Sahu S (1971) The effect of interfacial bonding on the toughness of glass filled polymers. *Mater Sci Eng*, 8: 98-107.
- [16] Spanoudakis J, Young RJ (1984) Crack propagation in a glass particle- filled epoxy resin - Part 1, *J Mater Sci*, 19: 473-486.
- [17] McGrath LM, Parnas RS, Lenhart JL, King S (2006) Fracture toughness of alumina-epoxy composites. *Poly Mater Sci Eng, Preprints*, 94: 683 – 684.
- [18] Griffiths R, Holloway D (1970) The fracture energy of some epoxy resin materials, *J Mater Sci*, 5 (4): 302-307.
- [19] Hsieh TH, Kinloch AJ, Masania K, Sohn Lee J, Taylor AC, Sprenger S (2010) The toughness of epoxy polymers and fiber composites modified with rubber microparticles and silica nanoparticles. *J Mater Sci*, 45: 1193 – 1210.
- [20] Dixon DG, Harris SJ, Dempster M, Nicholls P (1998) Effect of PEEK fibers and powder on joints made with high temperature adhesive, *J Adhesion*, 65 (1- 4): 131-162.

- [21] Kinloch AJ, Taylor AC (2002) The toughening of cyanate-ester polymers –Part I – Physical modification using particles, fibers and woven mats. *J Mater Sci*, 37: 433-460.
- [22] Lin KF, Shieh YD (1998) Core-Shell Particles Designed for Toughening the Epoxy Resins: I. Preparation and Characterization of Core-Shell Particles, *J Appl Poly Sci*, 69: 2069-2078.
- [23] Lin KF, Shieh YD (1998) Core-shell particles designed for toughening the epoxy resins: II. Core-shell particle toughened epoxy resins, *J Appl Poly Sci*, 70: 2313 -2322.
- [24] Becu L, Maazouz A, Sautereau and Gerard JF (1997) Fracture behavior of epoxy polymers modified with core-shell rubber particles, *Journal of Applied Polymer Science*, 65 (12): 2419-2431.
- [25] Yan C, Xiao KQ, Ye L, and Mai YW (2002) Numerical and experimental studies on the fracture behavior of rubber toughened epoxy in bulk specimen and laminated composites. *Journal of Material Science*, 37 (5): 921-927
- [26] Giannakopoulos G ,Masania K, and Taylor AC (2011) Toughening of epoxy using core-shell particles. *Journal of Material Science*, 46 (2): 327-338.
- [27] Kaneka Texas Corporation, <http://www.kanekatexas.com/MX>
- [28] Kinloch AJ, Mohammed RD, Taylor AC, Sprenger S and Egan D (2006) The interlaminar toughness of carbon-fibre reinforced plastic composites using ‘hybrid-toughened’ matrices. *Journal of Material Science* 41(15): 5043-5046.
- [29] Gardner N, Wang E, Shukla A (2011) Performance of functionally graded sandwich beams under shock wave loading. *Composite Structures*, DOI 10.1016/j.compstruct.2011.12.006.
- [30] Wang E, Gardner N, Shukla A. The blast resistance of sandwich composites with stepwise graded cores. *International Journal of Solids and Structures* 2009; 46: 3492-3502.
- [31] Gardner N, Wang E, Kumar P, Shukla A. Blast mitigation in a sandwich composite using graded core with polyurea interlayer. *Experimental Mechanics* 2011. DOI 10.1007/s11340-011-9517-9.
- [32] Derakane 8084 Material Data Sheet, www.ashland.com
- [33] Derakane 411-200 Material Data Sheet, www.ashland.com
- [34] Kaneka Kane Ace MX 153Material Data Sheet, <http://www.kanekatexas.com>
- [35] Corecell™ A-Series Foam Material Data Sheet, <http://www.gurit.com/corecell-foam.aspx>. Accessed 20 Sept 2011.
- [36] Chen W, Zhang B, Forrestal MJ. A split Hopkinson bar technique for low impedance materials. *Experimental Mechanics* 1998; 39 (2): 81–85.
- [37] Kumar P, LeBlanc J, Stargel D and Shukla A. Effect of plate curvature on blast response of aluminum panels. *Impact Engineering* 2012; Accepted

- [38] LeBlanc J, Shukla A, Rousseau C, Bogdanovich A. Shock loading of three-dimensional woven composite materials. *Composite Structures* 2007; 79: 344- 355.
- [39] Wright J. Shock tubes. New York: John Wiley and Sons Inc, 1961.
- [40] V. Tiwari, M.A. Sutton, S.R. McNeill, Assessment of High-speed Imaging Systems for 2D and 3D Deformation Measurements: Methodology Development and Validation, *Experimental Mechanics* 2007; 47: 561-579.
- [41] V. Tiwari, M.A. Sutton, S.R. McNeill, S. Xu, X. Deng, W.L. Fourney, D. Bretall, Application of 3D Image Correlation for Full-Field Transient Plate Deformation Measurements During Blast Loading, *International Journal of Impact Engineering* 2009; 36; 862-874.
- [42] Wu HT and Springer GS. Impact induced stresses, strains, and delaminations caused by impact on composite plates. *Journal of Composite Materials* 2008; 22: 533
- [43] Gibson LJ, Ashby MF. *Cellular Solids: Structures and Properties*. New York: Pergamon Press, Inc., 1988.
- [44] Wang, E. Blast resistance and energy mitigation behavior of sandwich composite materials. Ph.D Dissertation, University of Rhode Island, 2010.

Task 3: Experimental and Numerical study of Foam Filled Corrugated Core Steel Sandwich Structures Subjected to Blast Loading

1. INTRODUCTION

A major consideration in the design of military vehicles is their resistance to explosive blast loading. With the fast development of modern military technology, monolithic plates are continuing to fall behind the desired levels of blast protection. Sandwich structures with cellular solid cores, such as metallic foams and honeycomb structures, have shown superior weight specific stiffness and strength properties compared to their monolithic counterparts in blast resistant structural applications. Their cellular microstructure allows them to undergo large deformation at nearly constant nominal stress and thus absorb more energy [1, 2, 3]. To date, the effect of foam filling on blast mitigation of corrugated core sandwich panels under shock loads has not been fully understood. In this study to clarify the foam infill influences on blast resistivity of corrugated steel core sandwich panels, with and without foam filling, shock tube experiments and Finite Element Method (FEM) were used to investigate the phenomenon. In addition, monolithic face sheets and foam core sandwich panels were tested and analyzed to validate the FEM. More studies were numerically conducted to investigate the effect of face sheet thickness and corrugated sheet thickness under two different boundary conditions, namely simply supported and encastre supported. In order to see the effect of corrugated core rigidity soft, medium, and hard core cases were studied numerically utilizing both filled and empty conditions under blast loading.

In recent years, a number of micro-architected materials have been developed to use as cores in sandwich panels. These include pyramidal cores [4, 5, 6], diamond celled lattice cores [7], corrugated cores [8], hexagonal honeycomb cores [9], foam cores [10], and square honeycomb cores [11]. The benefits of sandwich construction depend on core topology. Core designs that afford simultaneous crushing and stretching resistance are preferred. One of the most preferred practical core topologies in blast resistant sandwich panel construction is the corrugated metallic core. These cores provide manufacturing advantages, as well as high strength, in both the normal and longitudinal directions of the structures [7, 12, 13].

Sandwich structures have various energy dissipation mechanisms, such as bending and stretching of the face sheet, as well as compression and shear of the core. This is especially pertinent in the case of impulsive loading, wherein the interstices in the metal cellular core can provide adequate space for the large plastic deformation, which is an efficient mechanism to dissipate the energy produced by blast impact [14-17]

During blast loading, the cellular solid core can absorb more than one half of the initial kinetic energy imparted to face sheet of the sandwich plate. This is due to crushing in the early stages of deformation, prior to significant overall bending and stretching, without unduly reducing the separation between the face sheets. High crushing strength and energy absorption per unit mass of the core is therefore important [21].

Wakabayashi et al. conducted experiments that suggest that low-density materials may provide the most effective blast mitigation [24]. In recent years, sandwich structures with strong face sheets and lightweight cores have become central structural components for blast mitigation. Polymeric foams offer unique structural, impact, thermal and acoustic properties, which make them an excellent choice as core materials to obtain low density blast resistive sandwich structures [2, 25] Based on these ideas, a lot of research on blast mitigating layered sandwich structures has been performed in recent years, using foam cores with different wave impedances to minimize shock effect [26, 27, 28].

Studies on metallic sandwich panels subjected to air blasts [17, 8] indicate that sandwich plates with high ductility and high energy absorption capacity per unit areal mass show good performance. Liang et al. [29] and Wei et al. [30] studied the behavior of metallic sandwich cores with varying strengths and found that soft cores (those in which the core is much less stiff than the sandwich panels' faces) reduce the momentum transferred, thus providing better mitigation for blast loading. For metallic structures, energy absorption in metallic lattice cores is through large scale plasticity, shear and compressive buckling, and eventual tearing of core walls and face sheets [25].

Another possible application of structural foams is for use as a filler material inside cellular metallic core sandwich structures. It is possible to obtain a new sandwich structure by combining these two cores' shock absorption advantages and decrease the transmitted shock load due to differing acoustic impedances. Moreover, foam filling stabilizes the core cell walls against buckling and increases the strength of the core. Vaziri et al. [21] studied two different types of PVC foam filled stainless steel honeycomb and folded core sandwich plates using FEM under various restrictions. They found no clear advantage or disadvantage implemented by foam filling for structural purpose under quasi static and impact loading.

Jhaver R. and Tippur H. [31] investigated syntactic foam filled aluminum honeycomb composites compression response by experimental and computational methods. They obtained considerable increases in elastic modulus and plateau stress through foam filling the honeycomb composites. Murray G. et al. studied polymer filled aluminum honeycomb structures to investigate the filling effect on damping using numerical methods with experimental validations. It was found that high damping improvements in the filled honeycomb explained the significant strain energy in the polymeric infill due to the Poisson's mismatch between the honeycomb and the infill [32]. Yungwirth et al. showed that low modulus elastomer infill in pyramidal lattice truss metallic core increased the impact energy absorption capacity [33]. Other studies have had success improving the impact resistance of honeycomb cores by fully or partially filling the cells of the honeycomb [34-37].

2. EXPERIMENTAL PROCEDURE

2.1 SPECIMEN PREPARATION

In this study, corrugated steel core sandwich structures were produced with low carbon steel face sheets and galvanized low carbon steel sinusoidal shape corrugations in a four-layer match-up. A schematic of the sandwich panels is shown in Figure 42.

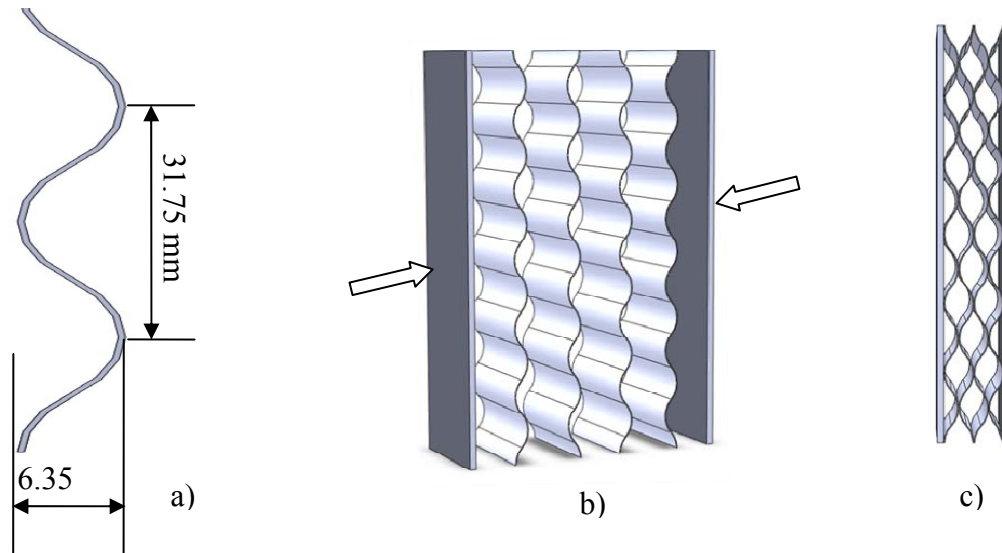


Fig. 42 (a) Corrugated core sheet dimensions (b) Manufacturing procedure of corrugated steel core sandwich structures (c) Final sandwich panel side view.

The face sheets had lateral dimensions of 50.8 x 203.2 x 3.2 mm. The sinusoidal corrugated sheet reference dimensions are shown in Figure 1a. Thickness of the corrugated sheet was 29 gauges (0.44 mm) with galvanization. The corrugation sheets and the face sheets were bonded to each other with epoxy adhesive G/Flex (West System Inc.). The tensile adhesion strength of this material was 20 MPa. Three different sandwich panel configurations (See Figure 43) were subjected to blast loading with simply supported boundary conditions.

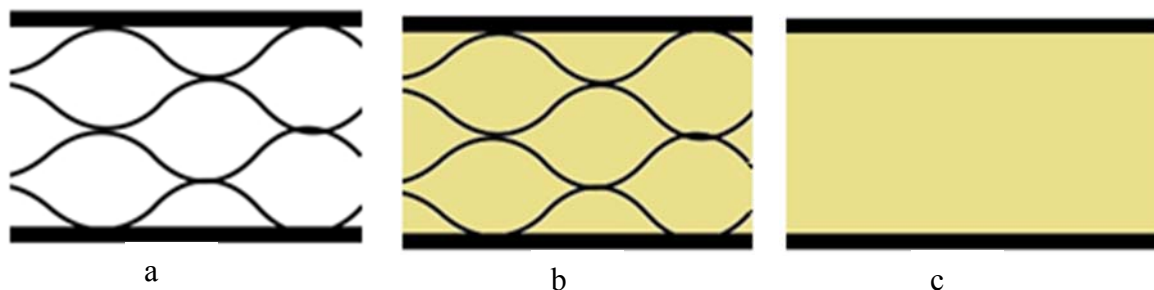


Fig. 43: Schematics of the experimental sandwich panels
(a) Empty corrugated steel core sandwich panel
(b) Foam filled corrugated steel core sandwich panel
(c) Foam core sandwich panel

2.2 SHOCK LOADING PROCEDURE

A shock tube apparatus was used to generate shock waves with planar wave fronts. A photograph of the shock tube used in these studies can be seen in Figure 44. A typical shock tube produced pressure profile is shown in Figure 45. Two pressure transducers (PCB102A) were mounted at the end of the muzzle section to record the incident and reflected pressure profiles. The first pressure sensor was mounted 20 mm away from the muzzle, and the second was mounted 180 mm away (160 mm separation from the first pressure sensor). The final muzzle inner diameter was 38.1 mm (See Figure 46). The incident peak pressure of the shock wave was chosen to be 5.5 MPa in the current study.



Fig. 44: Shock tube apparatus

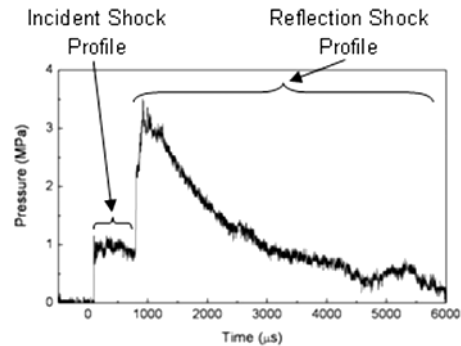


Fig. 45: Typical experimental pressure profile [38]

The specimen was placed onto a simply supported boundary condition fixture with a 152.4 mm span. The flat front face of the specimen was set normal to the axis of the shock tube with the face completely covering the muzzle. A diagram of this set up can be seen in Figure 46. At least three specimens of each type were subjected to experiments to ensure repeatability.

A high speed photography system was utilized to capture the motion of the specimens in order to determine their deformation and damage propagation. The lens axis of the camera was set perpendicular to the shock tube as shown in Figure 46. The camera used was a Photron SA1 high-speed digital camera, which has the ability to capture images at a framing rate of 20,000 frames per second with an image resolution of 512x512 pixels for a 3 millisecond time duration.

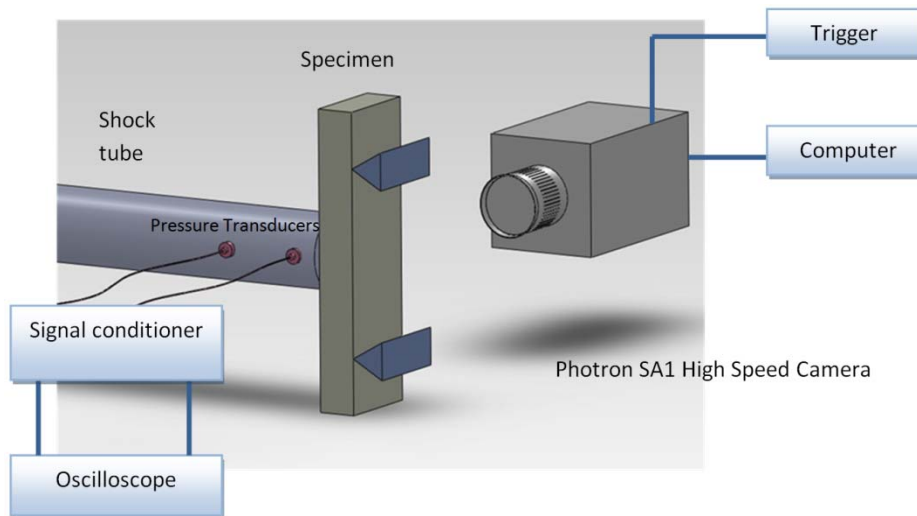


Fig. 46: High speed camera side view deflection measurement

3. NUMERICAL PROCEDURE

Dynamic explicit 3D FEA analyses of the sandwich panels subjected to a blast load were performed using Abaqus/Explicit finite element software . During analysis nonlinear geometry was accounted for, and simulated for a duration of 3 ms . All required field outputs such as displacements, strains, stress, etc., and history outputs such as energy, are defined in this module.

3.1 Finite Element Model

A model was created to render simple and encastre supported (along the back face's short edges) corrugated steel core sandwich panels 203 x 50.8 x 25.34 mm, subjected to blast loading. In the model, each layer section was accepted as a homogenous sheet with a prescribed thickness. Corrugated layers are accepted as shells defined by their mid plane. In the model, interactions between the corrugated core and the front and back face sheets are taken as surface-to-surface contacts under the penalty contact method and finite tangential sliding. The shear stress limit is described as 20 MPa.

The sandwich panel was subjected to a pressure-time profile as seen in Figure 47b. This pressure-time profile was taken from the shock tube experiments.

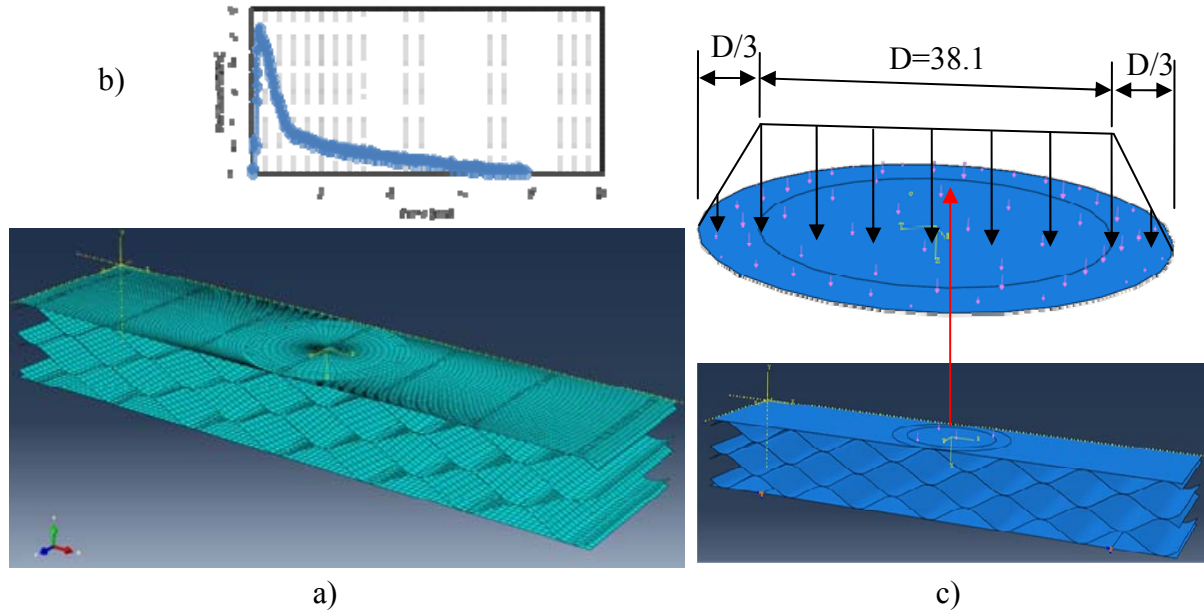


Fig. 47: (a) Shock load distribution function and applied pressure area
 (b) Applied shock load pressure-time profile (c) FEM model

This shock pressure profile is described in Abaqus software as a tabular data. It was applied to the specimen front face as a non-uniform function (Figure 47c) of area. This variation in shock pressure induced by the shock tube was observed experimentally and validated numerically by Kumar et al. [38]. For FEM simulations, the specimen was symmetrically aligned with the center of the shock tube, and the distance between the supports was fixed at 152.4 mm.

3.2 Material Properties

The material properties of the corrugated steel sheets and face sheets are: elasticity modulus (E) 205 GPa, poisson ratio (ν) 0.29, density (ρ) 7.85 g/cm³, and one-dimensional acoustic wave impedance $Z = \rho \cdot \sqrt{\frac{E}{\rho}}$ is 3962x10⁴ kg/m²s.

A Johnson Cook material model with strain hardening was applied in Abaqus as the material model. Johnson Cook parameters in the analysis for the material are given in Table 4.

The yield stress is, therefore, expressed as

$$\bar{\sigma} = [A + B(\bar{\epsilon}^{pl})^n] \left[1 + C \ln \left(\frac{\dot{\bar{\epsilon}}^{pl}}{\dot{\epsilon}_0} \right) \right] (1 - \hat{\theta}^m)$$

where $\bar{\sigma}$ is the yield stress at nonzero strain rate, $\bar{\epsilon}^{pl}$ is the equivalent plastic strain, $\dot{\epsilon}_0$ is the quasi static strain rate, $\dot{\bar{\epsilon}}^{pl}$ is the equivalent plastic strain rate, and A , B , C , n and m are material constants [39]. $\hat{\theta}$ is the nondimensional temperature ratio and set to zero in this paper.

A (MPa)	B (MPa)	n	C	m	$\dot{\epsilon}_0 (s^{-1})$
220	499.87	0.228	0.017	0.917	1

Table 4: Johnson Cook Parameters for low carbon steel used in FEM analysis [40]

General purpose humidity cured Polyurethane (PU), of density 0.0446 g/cm³ and Elasticity modulus 0.24 MPa, foam was used. General mechanical properties were found using quasi static compression tests, and high strain rate (3000 /s) properties were found via Split Hopkinson Pressure Bar experiments (See Figure 487) (41) and are shown in Figure 48.

PU foam material shows non-linear, hyperelastic behavior and is extremely compressible. The porosity permits very large volumetric changes. Polyurethane foams under large strains were modeled as compressible hyperelastic solids, if their time dependent mechanical properties and hysteresis are ignored. These materials can deform elastically to large strains, up to 90% strain in compression and are intended for finite strain applications. For PU foams, an Ogden strain energy potential [39] can be applied. In all FE analysis, a Poisson's ratio, $\nu=0$ was used.

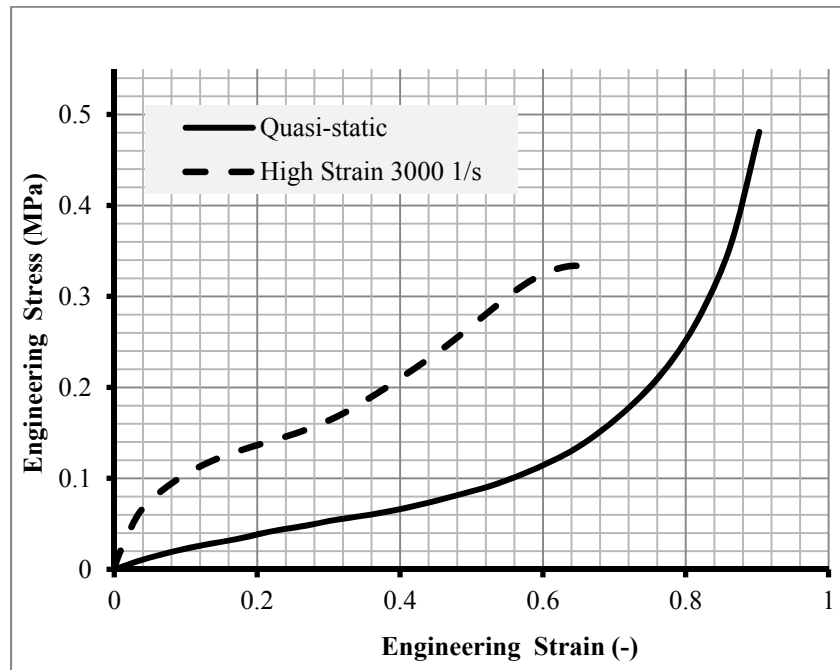


Fig. 48: Quasi Static and High-Strain Rate Compression Properties of the Polyurethane Foam

4. EXPERIMENTAL RESULTS AND DISCUSSION

4.1 Applied Pressure and impulses

The average peak value of the shock pressure subjected to specimens was 5.5 MPa. The specimens' average mass was 616.2 g, 491.9, and 630.4 g for empty corrugated steel core sandwich panels, foam core sandwich panels, and foam filled corrugated steel core sandwich panels respectively. The impulse imparted onto the specimen can be calculated from the detected reflected pressure. These pressure profiles can be considered to be the same as the pressure applied to the plates [42]. $P_R P_0$

4.2 High Speed Photography Measurements

The real time observations of the deformation of each type of specimen are shown in Figures 49, 51 and 53.

4.3 Empty corrugated steel core sandwich specimen response

The side view history of the empty specimen shows different compression behavior over the entirety of the metallic corrugated core (See Figure 49) during the loading. The beginning of the Back Face Deflection (BFD) occurred 0.25 ms after the initial Front Face Deflection (FFD) of the specimen, which implies a coupled response.

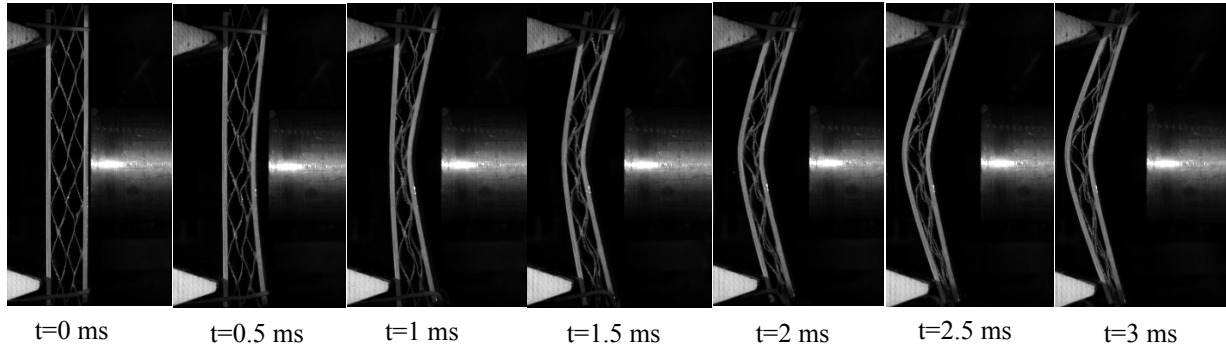


Fig. 49: Unfilled corrugated steel core sandwich panel high speed images during shock loading

Core compression and bending/stretching stages can be clearly observed by using core compression/time curves. In Figure 12, the core compression variation over time is given for the empty corrugated steel core sandwich panel. It is clearly seen that, from rest to 1.25 ms, core compression increased. After this time, compression of the core remained stable without change, but the front and back faces continued to deflect. This is indicative of the sandwich panel's global bending. The average core compression strain rate increased very quickly up to 1800 1/s at 1.25 ms and then remained stable until the end of the compression stage (See Figure 50).

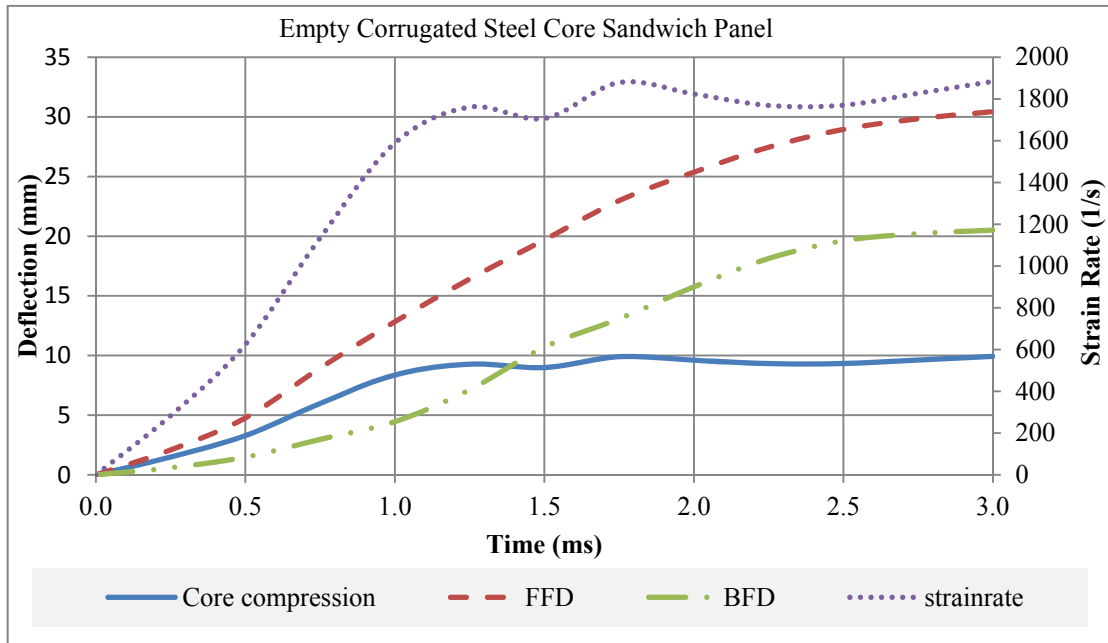


Fig. 50: Core compression, FFD (Front Face Deflection) and BFD (Back Face Deflection) in empty corrugated steel core sandwich panels.

4.4 Foam Core Sandwich Panels

High speed side view camera images, recording the deflections of foam core sandwich panels, are given in Figure 51. After the shock wave impinged upon the specimen, the weak foam core did not resist the front face motion enough to decrease its velocity until 0.25 ms. As seen in Figure 52, the back face started its motion after this time. This behavior is called "slapping" [18, 19].

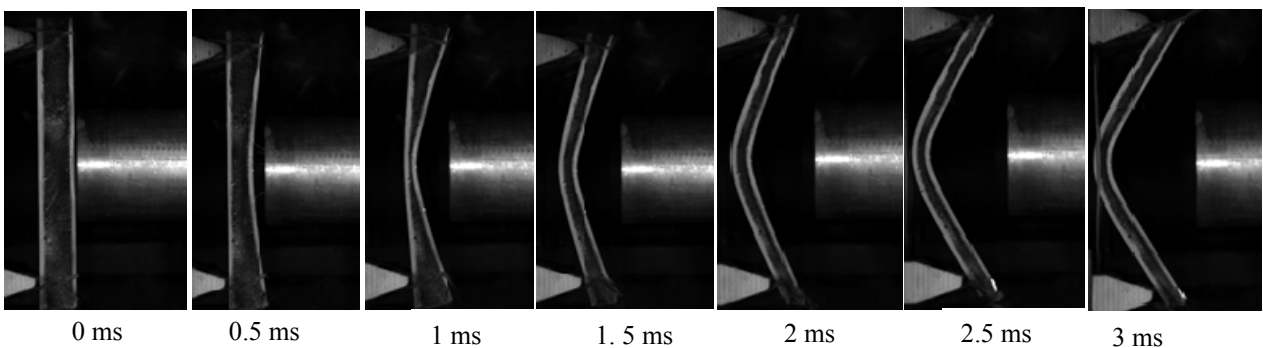


Fig. 51: High Speed Images of the foam core sandwich specimen

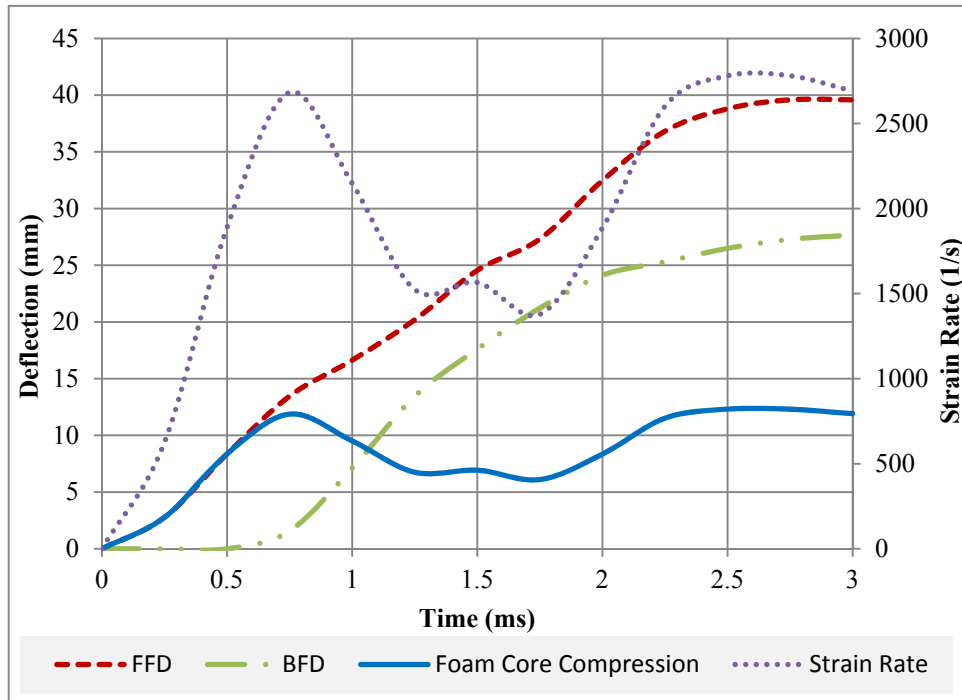


Figure 52. FFD, BFD, Foam Core compression and Strain rate of core in foam core sandwich panels

4.5 Foam Filled Corrugated Steel Core Sandwich Panels

The foam filling caused very large changes in specimen behavior when compared to that of the empty and foam core specimens. This behavior can be seen in Figure 53, which shows high speed side view camera images. Core compression in the foam filled case is decreased when compared to empty and foam core sandwich panels. The BFD starts almost at the same time with FFD. In Figure 54, variations of the velocities of both faces are given. The slope of both the front and back face velocities show the same magnitude, except two durations between 0.5-1 ms and 2-2.5 ms. The front face started deflecting initially, but after only 0.25 ms the BFD began. During the 0.25 ms to 0.75 ms time period core compression can be observed. Between 1 ms and 2 ms the FFD increased more than the BFD, thus causing an increase in the core compression. After this time, both the BFD and FFD started to decrease, and the core decompressed. This reaction occurred over much less time than the empty corrugated steel core and foam core sandwich panels. This shows that even by employing a weak, elastic foam filling the properties of the core increased. In this case, the obtained maximum strain rate in the core was much lower than that of both the empty and foam core cases, and was calculated to be 582 1/s around 2 ms (See Figure 55). The compression percentage at this time was 14.6%. This means that the foam did not exhibit high strain rate behavior in the foam filled corrugated core sandwich panel under blast loading. It is obviously seen that the foam filling increased bending rigidity and core compression strength.

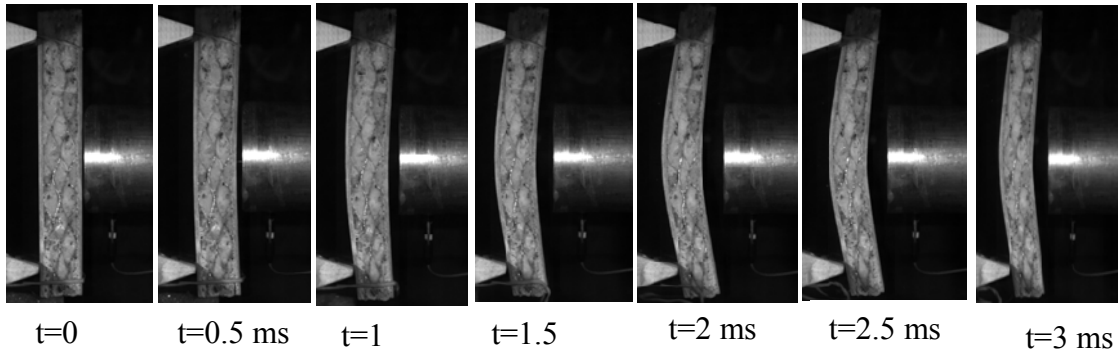


Figure 53. High Speed Images of the fully foam filled corrugated core sandwich specimen

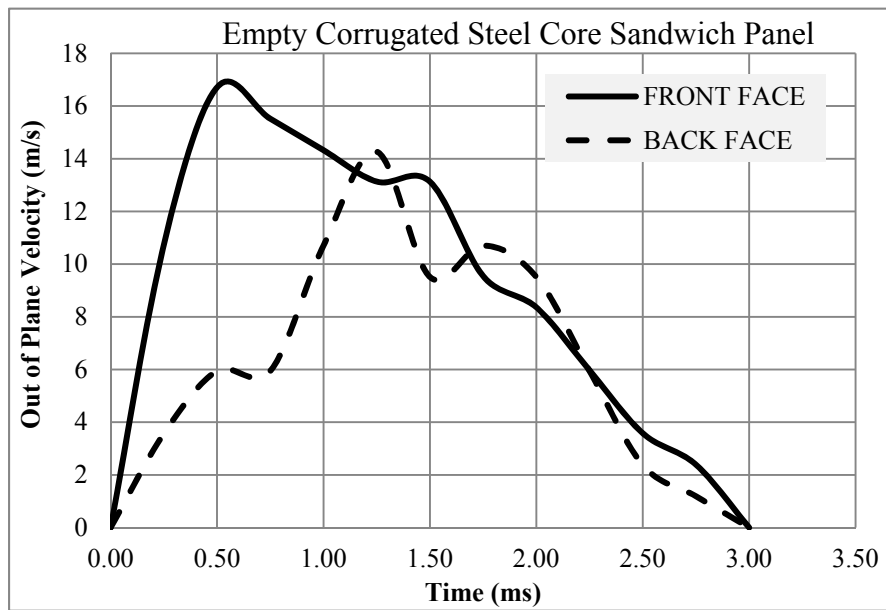


Figure 54. Variations of the velocities of both faces

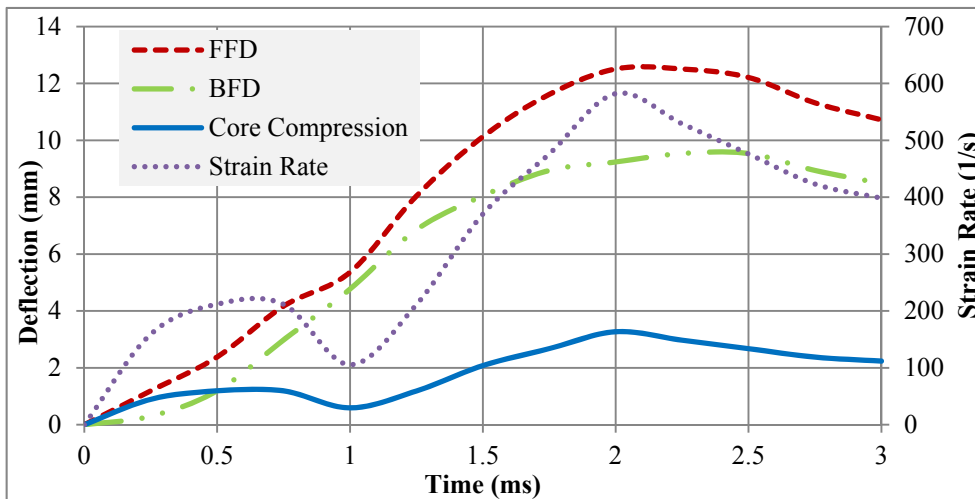


Fig. 55: FFD, BFD, Core Strain Rate and Core Compression variation after shock loading during captured time period

4.6 Comparison of Experimental Mid Span Deflections of the Sandwich Panels

Figure 56 shows back face and front face mid span deflections. It is clearly seen that both FFD and BFD results of the foam filled corrugated steel core sandwich panel are smaller than the empty and foam core sandwich panels, while its mass exceeds that of the empty sandwich panel by just 2.30%. The benefits of the corrugated steel core sandwich panel and foam core sandwich panels are combined by foam filling of corrugated steel core interstices.

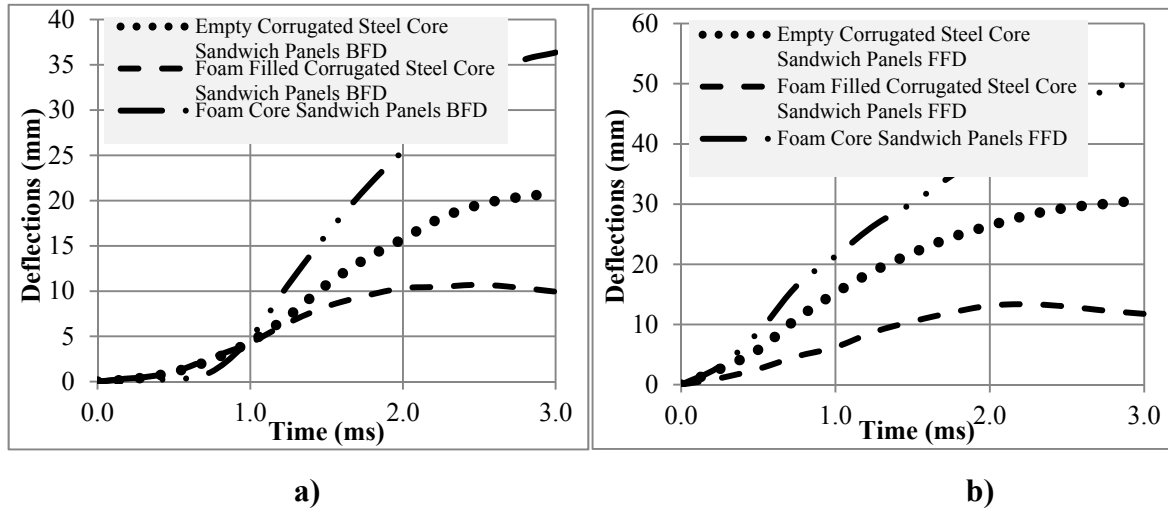


Fig. 56: Shock tube experiments' results a) Average Back Face Deflections (BFD) b) Average Front Face Deflections (FFD).

5. NUMERICAL RESULTS AND DISCUSSIONS

5.1 Validation of Numerical Solutions

To verify the material properties, boundary and contact conditions in the FEM were compared to the shock tube experimental results for the face sheet; foam core sandwich panel, empty corrugated steel core sandwich panel, and foam filled corrugated steel core sandwich panels. Comparative results can be seen in Figures 57, 58, 59 and 60.

The Pearson's correlation coefficient R^2 were calculated using equations given in [45] as a means to evaluate the model's accuracy. The correlation coefficient is a measure of accuracy of the linear relationship between the experimental and predicted data. The predictability of the finite element model over both the front and back faces of the four different experimental designs is shown in Table 5.

Table 5: Predictability of the Model for the Deflection of the Panel Configurations

	Face Sheet	Foam Filled Corrugated Steel Core Sandwich Panels		Foam Core Sandwich Panels		Empty Corrugated Steel Core Sandwich Panels	
		FFD	BFD	FFD	BFD	FFD	BFD
R^2	0.9766	0.9549	0.980	0.980	0.984	0.992	0.9986

The correlation coefficient R^2 under all cases is 0.95 or higher, indicating that the trends of both the experimental results and the finite element model are well aligned. All models are accepted with good agreement and can be used to further investigate the influences of the foam and thicknesses of the face sheets and core sheets. See Figures 56-59 for experimental and FEM deflection comparisons.

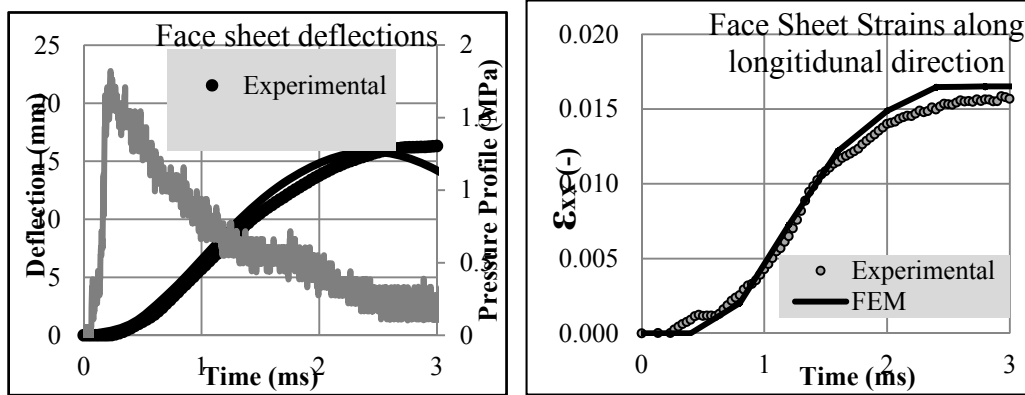


Fig 57: Experimental and FEM comparisons of Face Sheet a) Face sheet deflections. b) Longitudinal strains

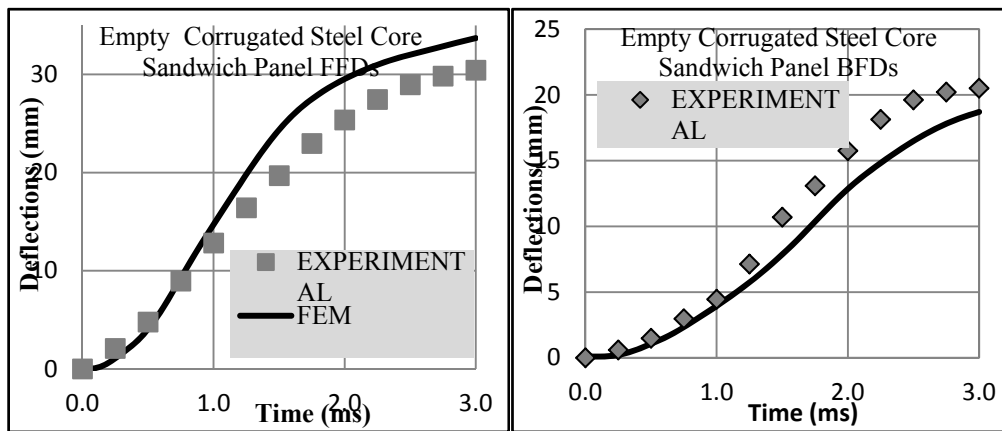


Fig. 58: FEM and Experimental Empty Corrugated Steel Core sandwich specimen a) Front Face Deflection b) Back Face Deflection.

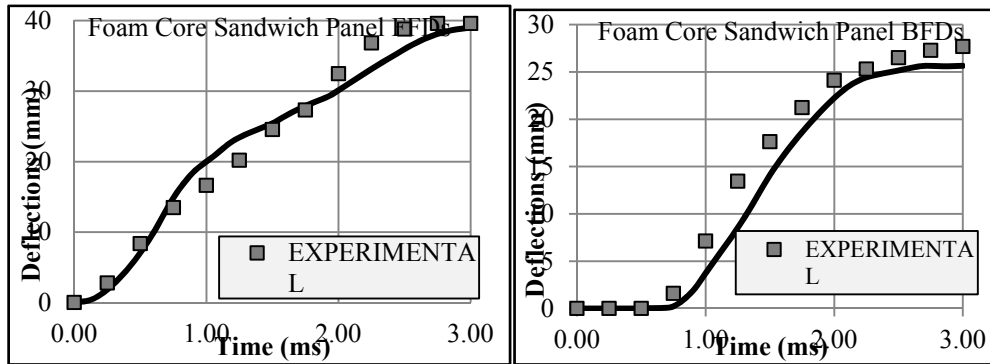


Fig. 59: FEM and Experimental foam core sandwich specimen a) Front Face Deflection b) Back Face Deflection.

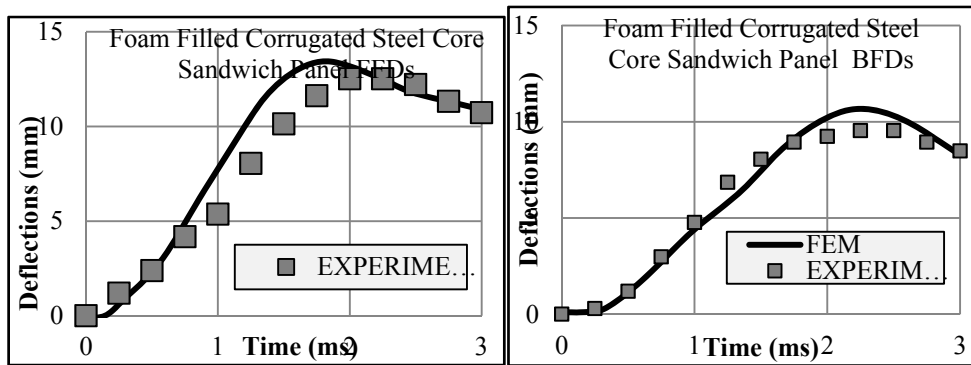


Fig 60: FEM and Experimental Foam Filled corrugated steel core sandwich specimen a) Front Face Deflection b) Back face deflection.

5.2 Investigation of Face Sheet Thickness - Corrugated Core Sheet Thickness and Boundary Conditions effects on Foam Filling Contribution

Face sheet thickness, corrugated steel sheet thickness, and boundary condition effects (see Figure 61) were investigated using FEM simulations. All variables' values are given in Table 6. Sandwich panel length, width, and core thickness are accepted as constants in the FEM simulations as 184.24 x 50.8 x 20.6 mm as well as applied shock pressure. By adding the foam filling, the masses of specimens changed by a very small amount. For example the maximum variation of mass was 3.8% in the 0.2 mm Core Sheet Thickness (CST) and 1 mm Face Sheet Thickness (FST) case. However, by changing FST and CSTs, the mass was increased 4 times in the 5 mm FST - 1 mm CST case as compared to the 1 mm FST - 0.2 mm CST case. Unit mass deflections were calculated for comparison to one another (See Table 7). Totally, 36 runs were performed to understand each of the parameter's influences on the behavior of the sandwich panel.

Table 6. Investigated parameters in FEM simulations of empty and foam filled corrugated steel core sandwich panels.

Boundary Condition	Face Sheet Thickness (mm)	Corrugated Sheet Thickness (mm)
Simple Supported	1, 3, 5	0.2, 0.6, 1
Encastre	1, 3, 5	0.2, 0.6, 1

Table 7. Calculated Masses of FEM models for the empty corrugated steel core sandwich panels

FST (mm)	1			3			5			
	CST (mm)	0.2	0.6	1	0.2	0.6	1	0.2	0.6	1
Empty Sandwich Panel Mass(g)		209	332	462	502	628	754	794	920	1050

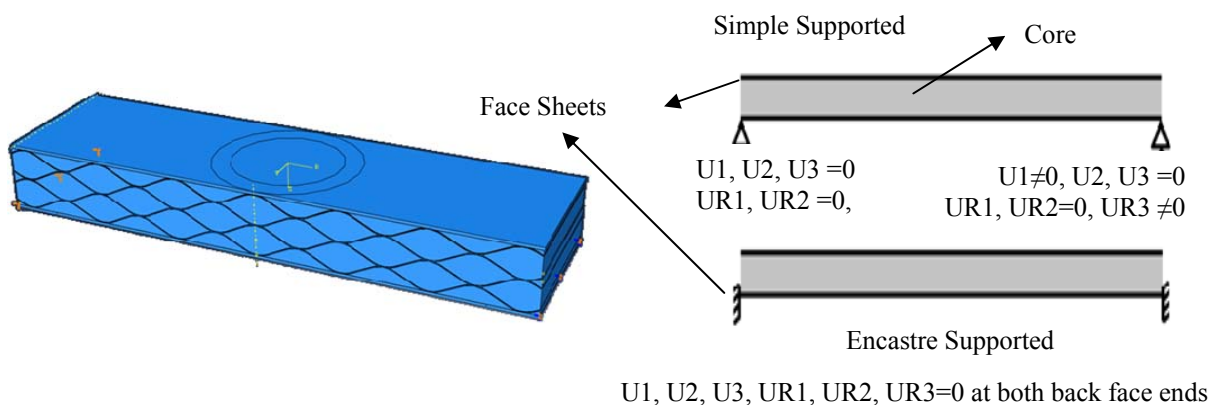


Fig. 61: Boundary conditions used in FEM simulations

5.3 Front Face Deflections (FFDs)

Figures 62, 63 and 64 show the behavior of the 1, 3 and 5 mm FST sandwich panels under different CST and boundary conditions for the empty corrugated steel core and foam filled corrugated steel core cases.

All FFDs were obtained from the FEM simulations at the front face center point of the specimens. In all these cases, the FFD of the specimens decreased with the incorporation of foam filling. It can be seen from Figures 61, 62 and 63, that the foam filling's contribution to mitigating FFD and BFD is lessened with the increase of the CST. From these figures, it can be observed that the Simple Supported (SS) sandwich panels show more deflection than Encastre Supported (ES) sandwich panels in all cases.

The foam filling decreased all FFDs, except in the cases of the 1 mm CST, in which cases it became the predominant influence on the core through increased bending resistivity. In these cases the filled and empty specimens' FFDs are close in both simple and encastre supported boundary conditions.

The foam filling effects on the FFD increased when reducing both the FSTs and CSTs. The biggest FFD reduction due to foam filling was obtained by up to 48%, in the 1 mm FST - 0.6 mm CST case. It can be clearly seen that, by increasing the FST, the foam filling effect is reduced.

Table 8 shows mid span deflection differences in front face unit mass deflections between empty corrugated steel core sandwich panels and foam filled corrugated steel core sandwich panels. In almost all cases the mid span deflection differences were positive. This means that foam filling reduced front face deflection. The differences were very low in some panels, such as 5 mm FST and 1 mm CST, which was the most massive sandwich structure used. These sandwich panels were not affected by foam infill. We can say, by increasing the FSTs and CSTs, that the benefits of the foam infill were reduced. This situation can be explained by the increase in core strength and the increase in the face sheet bending rigidity, which increases the transmitted blast load to the back face without corrugated steel core densification.

Table 8. Front Face Unit Mass Deflection Differences (mm/g) between empty corrugated steel core specimens and foam filled corrugated steel core specimens.

FST (mm)	1						3						5						
CST (mm)	0.2		0.6		1		0.2		0.6		1		0.2		0.6		1		
Time (ms)	SS	ES	SS	ES	SS	ES	SS	ES											
0.00	0.000	0.000	0.000	0.000	0.000	0.000	0.000	0.000	0.000	0.000	0.000	0.000	0.000	0.000	0.000	0.000	0.000	0.000	0.000
0.30	0.029	0.029	0.012	0.012	0.005	0.005	0.002	0.002	0.001	0.001	0.001	0.001	0.001	0.001	0.000	0.000	0.000	0.000	0.000
0.60	0.073	0.072	0.038	0.038	0.013	0.013	0.011	0.011	0.004	0.004	0.002	0.002	0.002	0.002	0.002	0.001	0.000	0.000	0.000
0.90	0.091	0.087	0.050	0.049	0.016	0.015	0.025	0.025	0.008	0.008	0.002	0.002	0.003	0.003	0.003	0.003	0.000	0.000	0.000
1.20	0.096	0.101	0.061	0.055	0.016	0.015	0.030	0.033	0.010	0.010	0.002	0.001	0.005	0.005	0.003	0.003	0.000	0.000	0.000
1.50	0.101	0.097	0.071	0.056	0.015	0.013	0.033	0.040	0.011	0.012	0.003	0.000	0.007	0.007	0.003	0.002	0.000	0.000	0.000
1.80	0.107	0.109	0.079	0.057	0.015	0.011	0.035	0.042	0.012	0.014	0.003	-0.001	0.009	0.010	0.004	0.003	0.000	0.000	0.000
2.10	0.114	0.104	0.087	0.061	0.016	0.012	0.038	0.042	0.013	0.015	0.002	-0.001	0.011	0.011	0.005	0.004	0.000	0.000	0.000
2.40	0.119	0.112	0.099	0.061	0.018	0.015	0.044	0.042	0.013	0.016	0.001	0.000	0.014	0.014	0.005	0.004	0.000	0.000	0.000
2.70	0.110	0.108	0.113	0.060	0.022	0.015	0.050	0.042	0.013	0.017	0.001	0.001	0.017	0.017	0.005	0.004	0.000	0.000	0.000
3.00	0.098	0.102	0.125	0.058	0.026	0.011	0.058	0.040	0.013	0.018	0.001	0.001	0.020	0.019	0.006	0.003	0.000	0.000	0.000

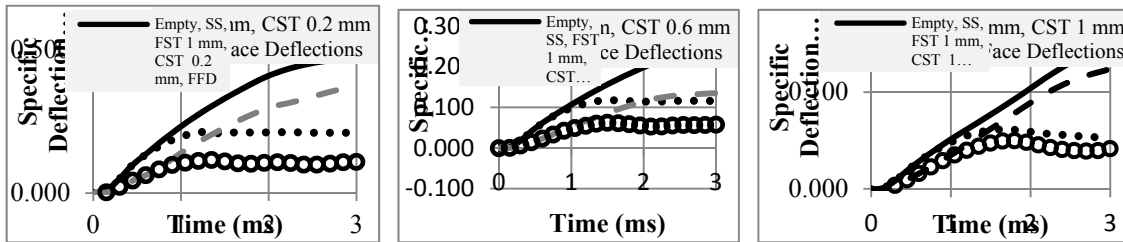


Fig. 62: FFDs depend on CST, BC and Foam filling in 1 mm FST sandwich panels a) CST 0.2 mm b) CST 0.6 mm c) CST 1 mm

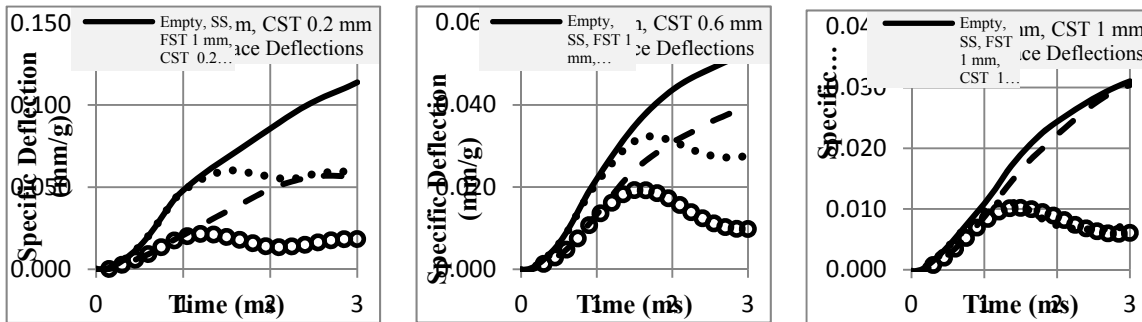


Fig. 63: FFDs depend on CST, BC and Foam filling in 3 mm FST sandwich panels a) CST 0.2 mm b) CST 0.6 mm c) CST 1 mm

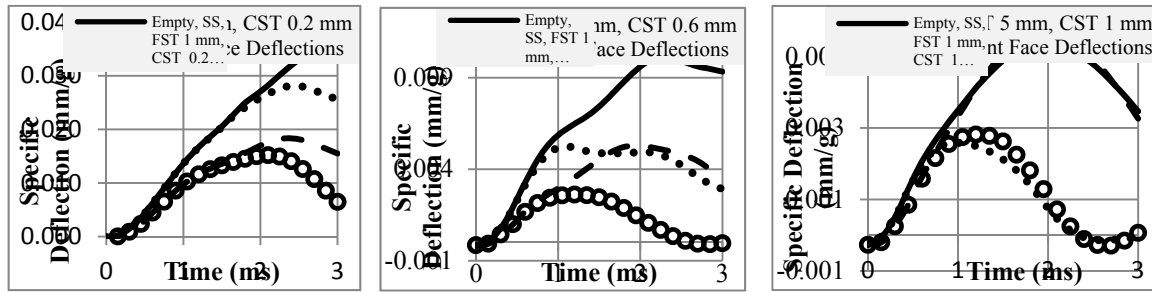


Fig. 64: FFDs depend on CST, BC and Foam filling in 5 mm FST sandwich panels a) CST 0.2 mm b) CST 0.6 mm c) CST 1 mm

5.4 Back Face Deflections (BFDs)

All of the obtained BFDs from FEM simulations can be seen in Figures 64, 65 and 66. In sandwich panels, and armor in general, the smallest BFD is the premier desirable characteristic in most cases. Table 9 shows BFD differences between empty corrugated steel core sandwich panels and foam filled corrugated steel core sandwich panels under shock loading.

In most of the investigated sandwich panel cases, BFDs were reduced by foam filling. The biggest reduction of BFDs was observed in the 1 mm FST - 0.6 mm CST foam filled sandwich panels. However, in the thickest face sheet condition (FST 5 mm), foam filling did not change the BFDs. The FST and CST increase reduced the influence of the foam infill on mitigating deflection. Encastre boundary conditions produced less BFDs than simple supported in almost all cases.

Table 9: Back face deflection difference between empty corrugated steel core specimen and foam filled corrugated steel core specimens

FST (mm)	1						3						5						
	0.2		0.6		1		0.2		0.6		1		0.2		0.6		1		
Time (ms)	SS	ES	SS	ES	SS	ES	SS	ES	SS	ES	SS	ES	SS	ES	SS	ES	SS	ES	
0.00	0.000	0.000	0.000	0.000	0.000	0.000	0.000	0.000	0.000	0.000	0.000	0.000	0.000	0.000	0.000	0.000	0.000	0.000	0.000
0.30	-0.002	-0.002	0.000	0.000	0.001	0.001	0.000	0.000	0.000	0.000	0.000	0.000	0.000	0.000	0.000	0.000	0.000	0.000	0.000
0.60	-0.005	-0.002	-0.006	-0.004	0.003	0.003	-0.004	-0.004	0.001	0.000	0.001	0.001	0.000	0.000	0.000	0.000	0.000	0.000	0.000
0.90	0.015	0.021	0.003	0.005	0.005	0.004	-0.011	-0.009	0.001	0.001	0.002	0.001	-0.001	-0.001	0.000	0.000	0.000	0.000	0.000
1.20	0.034	0.027	0.013	0.009	0.006	0.004	-0.008	-0.002	0.002	0.000	0.002	0.000	-0.003	-0.002	0.001	-0.001	0.000	-0.001	0.000
1.50	0.043	0.020	0.023	0.012	0.005	0.001	-0.005	0.003	0.002	-0.001	0.002	-0.001	-0.005	-0.002	0.002	-0.001	0.000	-0.001	0.000
1.80	0.059	0.021	0.034	0.010	0.006	0.000	-0.001	0.004	0.002	-0.002	0.002	-0.002	-0.006	0.000	0.002	-0.001	0.000	-0.001	0.000
2.10	0.069	0.023	0.045	0.009	0.008	0.000	0.004	0.003	0.001	-0.002	0.001	-0.001	-0.005	0.002	0.003	0.000	0.000	0.000	0.000
2.40	0.067	0.020	0.056	0.009	0.010	0.001	0.008	0.004	0.000	-0.002	0.001	-0.001	-0.004	0.004	0.003	0.001	0.000	0.000	0.000
2.70	0.066	0.019	0.067	0.010	0.012	0.002	0.015	0.003	0.001	-0.002	0.001	0.000	-0.002	0.003	0.004	0.000	0.000	0.000	0.000
3.00	0.058	0.025	0.079	0.009	0.014	0.001	0.022	0.003	0.002	-0.002	0.001	-0.001	-0.001	0.003	0.004	0.000	0.000	0.000	0.000

It can be observed from this table that foam filling is more effective in thinner FST core sandwich panels. The biggest reduction in BFD, of 48%, was obtained in 1 mm FST- 0.6 mm CST simple supported case. Furthermore, an increase in the CST caused a reduction of the foam filling effects.

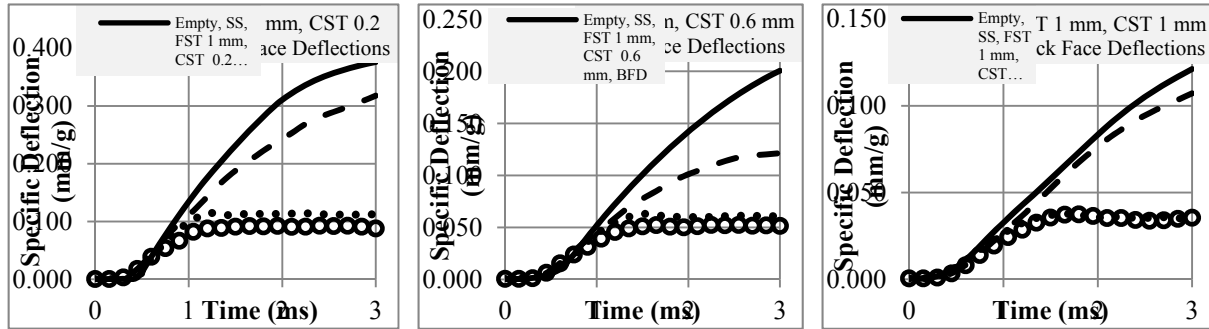


Fig. 65: BFDs depend on CST, BC and Foam filling in 1 mm FST sandwich panels a) CST 0.2 mm b) CST 0.6 mm c) CST 1 mm

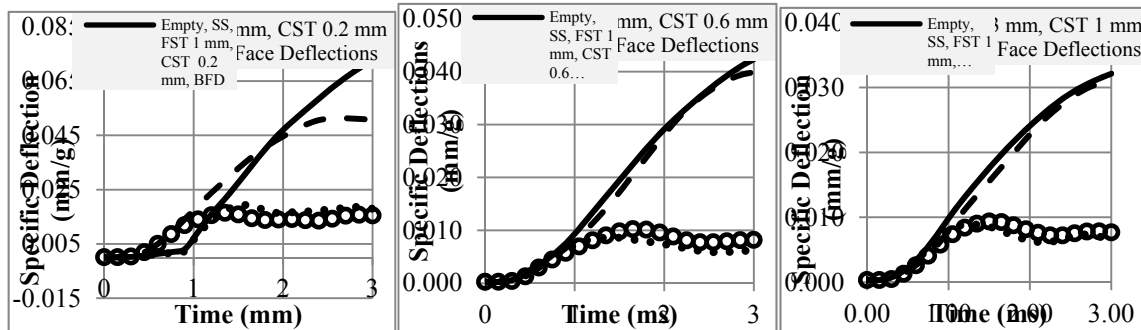


Fig. 66: BFDs depend on CST, BC and Foam filling in 3 mm FST sandwich panels a) CST 0.2 mm b) CST 0.6 mm c) CST 1 mm

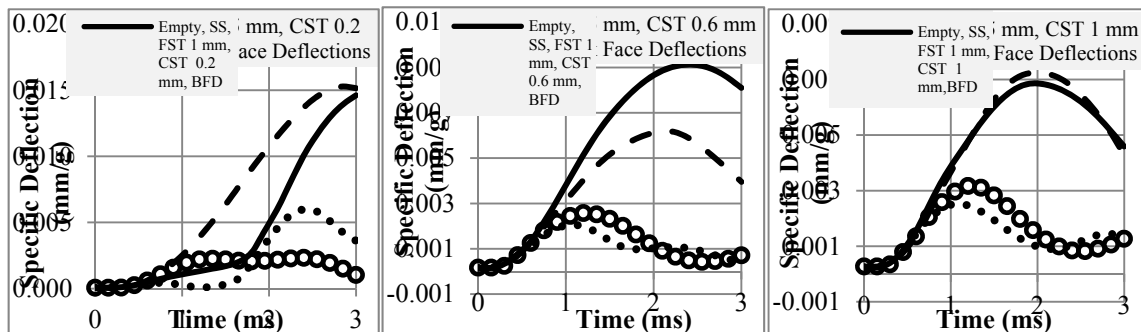


Fig. 67: BFDs depend on CST, BC and Foam filling in 5 mm FST sandwich panels a) CST 0.2 mm b) CST 0.6 mm c) CST 1 mm

6. CONCLUSIONS

The main scope of this study is to develop a sandwich structure with improved performance under shock loading at room temperatures. To achieve this purpose, metallic corrugated core sandwich panels with polymeric foam filling are developed.

Corrugated metallic core sandwich panels are very good blast resistive sandwich structures. They absorb blast energy due to the plastic deformation of their corrugated cores. However, they are relatively heavy when compared to polymeric foam core sandwich structures. If the weight of the panels can be decreased without reducing blast resistive performance, or performance increased without greatly increasing weight, the materials could be a good alternative in manufacturing, construction, navy, army, and automotive industries. Foam filling inside the cellular metallic core intercedes can be expected to cause some structural benefits, although they are not understood completely. Therefore, this study aimed to discover the effects of foam filling, face sheet thickness, and core cell wall thickness under simple supported and encastre boundary conditions on blast loaded metallic core sandwich panels. Obtained results are summarized as follows:

- 1) The first behavior of the corrugations before the plastic deformation is elastic buckling and bending. To increase the buckling resistivity and bending rigidity of the corrugations, foam filling are applied between cells. The foams increased the buckling and bending rigidity of the core. Experimental and FEM results show that the foam filling increased the blast resistivity of the sandwich panels.
- 2) Foam filling decreased FFD and BFDs by more than 50% of the empty corrugated steel core case. The difference between the impedance of the steel and the foam was very big. This causes dissipation and scattering of the shock pressure wave.
- 3) Strong, soft, and slapping core collapses were observed, and although aspected the hard core of these three had the highest back face deflection of the three. The most rigid core, i.e. the fully foam filled core, showed the least back face deformation. Core compression by the foam infill is reduced up to 77.5%. It is observed that foam infill raised the load carrying capacity of the metallic cellular core and the bending rigidity of the sandwich panel by improving core cell wall buckling resistivity and bending rigidity. This improvement increased the core compression strength.
- 4) FEM simulations matched very well with the experimental results. The Johnson Cook material model for steels and the Ogden material model for low density closed-cell polyurethane foams can be used in FEM solutions.
- 5) FEM simulations showed that foam filling effects changed with face sheet thickness, corrugated sheet thickness, and boundary conditions. In all cases, foam filling reduced the front face deflections.
- 6) Increasing face sheet thickness and corrugated sheet thickness was reduced the foam filling effect in the sandwich structure.

- 7) The encastre boundary conditions show fewer front face deflections than the simple supported case.
- 8) In the encastre boundary conditions, the Face Sheet Thickness is more effective than the Corrugated Sheet Thickness This means that the face sheet properties are more dominant than the core properties in fully clamped edge conditions in the metallic core sandwich panels under shock loading.
- 9) Front face and back face deflections were reduced by foam filling by more than 50% around maximum deflection time, while increasing the mass of the panel by only 2.30%.

REFERENCES

1. Zhu F. and Lu G. A Review of Blast and Impact of Metallic and Sandwich Structures. *Electronic Journal of Structural Engineering. Special Issue: Loading on structures.* (2007) 92-101.
2. Gibson, L.J., and Ashby, M.F. *Cellular solids: structure and properties* (2.nd edition), Cambridge University Press, (1997) Cambridge.
3. Hanssen, A.G., Enstock, L., and Langseth, M. Close-range blast loading of aluminium foam panels, *International Journal of Impact Engineering* (2002) 27:593–618.
4. Dharmasena [K. P.](#), Wadley [H.N.G.](#), Williams [K.](#), Xue [Z.](#), Hutchinson [J. W.](#) "Response of metallic pyramidal lattice core sandwich panels to high intensity impulsive loading in air" *International Journal Of Impact Engineering* (2011) 38:275-289.
5. Dharmasena [K.P.](#), Queheillalt [D.T.](#), Wadley [H.N.G.](#), Dudt [P.](#), Chen [Y.](#), Knight [D.](#), Evans [A.G.](#), Deshpande [V.S.](#) [Dynamic compression of metallic sandwich structures during planar impulsive loading in water.](#) *European Journal Of Mechanics A-Solids* (2010) 29 (1): 56-67
6. [Wadleya](#) H., [Dharmasena](#) K., Chen [Y.](#), Dudt [P.](#), Knight [D.](#), Charette [R.](#), Kiddy [K.](#) Compressive response of multilayered pyramidal lattices during underwater shock loading. *International Journal of Impact Engineering* (2008) 35(9): 1102-1114
7. Fleck N.A. and Deshpande V.S. The resistance of clamped sandwich beams to shock loading. *Journal of applied mechanics*, (2004);71:386-401.
8. Xue ZY, Hutchinson JW. A comparative study of impulse-resistant metal sandwich plates. *Int J Impact Eng* (2004) 30(10):1283-305.
9. Theobald, M. D.; Langdon, G. S.; Nurick, G. N., Pillay S., Heyns, A. Merrett, R. P. [Large inelastic response of unbonded metallic foam and honeycomb core sandwich panels to blast loading.](#) *Composite Structures*, (2010) 92 (10):2465-2475
10. Langdon G.S., von Klemperer C.J., Rowland B.K., Nurick G.N. The response of sandwich structures with composite face sheets and polymer foam cores to air-blast loading: Preliminary experiments. *Engineering Structures* (2012) 36:104-112.

11. H.J. Rathbun , D.D. Radford , Z. Xue, M.Y. He, J. Yang , V. Deshpande , N.A. Fleck , J.W. Hutchinson , F.W. Zok, A.G. Evans .Performance of metallic honeycomb-core sandwich beams under shock loading. *International Journal of Solids and Structures* (2006) 43:1746–1763.
- 12 . Valdevit L., Wei Z., Mercer C., Zok F.W., Evans A.G. Structural performance of near-optimal sandwich panels with corrugated cores. *International Journal of Solids and Structures* (2006) 43(16): 4888-4905.
- 13 .Qiu, X., Deshpande, V.S., Fleck, N.A. Finite element analysis of the dynamic response of clamped sandwich beams subject to shock loading. *Euro. J. Mech. A/Solids* (2003)22:801–814.
14. Cui X., Zhao L., Wang Z., Zhao H., Fang D. Dynamic response of metallic lattice sandwich structures to impulsive loading. *International Journal of Impact Engineering* (2012) 43: 1-5.
15. Evans AG, Hutchinson JW, Ashby MF. Multifunctionality of cellular metal systems. *Prog Mater Sci* (1998) 43(3):171-221.
16. Hutchinson JW, Xue ZY. Metal sandwich plates optimized for pressure impulses. *Int J MechSci* 2005;47(4-5):545-569.
17. Xue ZY, Hutchinson JW. Preliminary assessment of sandwich plates subject to blast loads. *Int J MechSci* 2003;45(4):687-705.
18. Tilbrook M.T., Deshpande V.S. and Fleck N.A. Underwater blast loading of sandwich beams: Regimes of behaviour. *International Journal of Solids and Structures*, 46(2009) 3209-3221.
19. Tilbrook M.T., Deshpande V.S., Fleck N.A. The impulsive response of sandwich beams:Analytical and numerical investigation of regimes of behaviour. *Journal of the Mechanics and Physics of Solids*, 54 (2006) 2242–2280.
21. Vaziri A., Xue Z. and Hutchinson J.W. Metal Sandwich plates with polymer foam filled cores. *Journal of Mechanics of Materials and structures*, (2006) 1(1):95-125.
20. Rabczuk T., Kim J.Y., Samaniego E. and T. Belytschko. Homogenization of sandwich structures. *Int. J. Numer.Meth.Engng*, (2004); 61:1009–1027.
22. [Schimizze](#) B., [Son](#) S. F., [Goel](#) R., [Vechart](#) A. P., [Young](#) L. An experimental and numerical study of blast induced shock wave mitigation in sandwich structures. (2013) [74 \(1\)](#):1–9.
23. Zhuang S., Ravichandran G., Grady D.E. An experimental investigation of shock wave propagation in periodically layered composites. *Journal of the Mechanics and Physics of Solids*.51 (2003) 245 – 265.
24. T. Homae, K. Wakabayashi, T. Matsumura, and Y. Nakayama .Reduction Of Explosion Damage Using Sand Or Water Layer. *Shock Compression Of Condensed Matter* (2007): Proceedings of the Conference of the American Physical Society Topical Group on Shock Compression of Condensed Matter. Date: 24–29 June 2007. AIP Conf. Proc. 955, pp. 1289-1292; doi:<http://dx.doi.org/10.1063/1.2832958> (4 pages), Waikoloa (Hawaii).

25. S. Avachat and M. Zhou. Effect of Face sheet Thickness on Dynamic Response of Composite Sandwich Plates to Underwater Impulsive Loading. [Experimental Mechanics](#) (2012) 52(1): 83-93
26. Gardner N., Wang E., Shukla A. Performance of functionally graded sandwich composite beams under shock wave loading. *Composite Structures* (2012) 94: 1755–1770.
27. Li Y, Ramesh KT, Chin ESC. Dynamic characterization of layered and graded structures under impulsive loading. *Int J Solids Struct.* (2001);38(34–35):6045–61.
28. Wang E, Gardner N, Shukla A. The blast resistance of sandwich composites with stepwise graded cores. *Int J Solids Struct.* (2009) 46:3492–502.
29. Liang YM et al. The response of metallic sandwich panels to water blast. *J ApplMech Trans Asme* (2007) 74(1):81–99.
30. Wei Z et al The resistance of metallic plates to localized impulse. *J MechPhys Solid.* (2008) 56(5):2074–2091.
31. Jhaver R. and Tippur H. Characterization and modeling of compression behavior of syntactic foam-filled honeycombs. *Reinforced Plastics and Composites* (2010) 29(21):3185-3196.
32. Murray G., Gandhi F. and Hayden E. Polymer-filled honeycombs to achieve a structural material with appreciable damping. *Journal of Intelligent Material Systems and Structures* (2012) 23(6):703–718.
33. Yungwirth C. J., Radford D.D., Aronson M., Wadley H.N.G. Experiment assessment of the ballistic response of composite pyramidal lattice truss structures. *Composites: Part B* 39 (2008) 556–569.
34. Wu, C.L., Weeks, C.A. and Sun, C.T. Improving Honeycomb-Core Sandwich Structures for Impact Resistance, *Journal of Advanced Materials* (1995) 26(4): 41–47.
35. Resewski, C. and Buchgraber, W. Properties of New Polyimide Foams and Polyimide Foam Filled Honeycomb Composites, *Material Wissenschaft und Werkstofftechnik* (2003) 34(4): 365–369.
36. Vaidya, U.K., Ulven, C., Pillay, S. and Ricks, H. Impact Damage of Partially Foam-filled Co-injected Honeycomb Core Sandwich Composites, *Journal of Composite Materials* (2003) 37(7): 611–626.
37. Vaidya, U.K., Kamath, M.V., Mahfuz, H. and Jeelani, S. Low Velocity Impact Response of Resin Infusion Molded Foam filled Honeycomb Sandwich Composites, *Journal of Reinforced Plastics and Composites* (1998) 17(9): 819–849.
38. Kumar P., LeBlanc J., Stargel D., Shukla A. Effect of plate curvature on blast response of aluminum panels. *International Journal of Impact Engineering* (2012)46:74-85
39. Abaqus Analysis user manual, Vol. III (Materials), Dassault Systemes Simulia Corp., Providence, RI, USA, 2010.

40. Schever, L. Optional Strain-Rate Forms for the Johnson Cook Constitutive Model and the Role of the Parameter Epsilon 0. 6th European LsDyna User' Conference, Frankenthal 2007, Session Impact, 1-14.
41. Gardner N., Wang E., Kumar P. and Shukla A. Blast Mitigation in a Sandwich Composite Using Graded Core and Polyurea Interlayer. *Experimental Mechanics* (2012) 52:119–133
42. [Jackson](http://www.sciencedirect.com/science/article/pii/S1359836810001460) M. and [Shukla](#) A. Performance of sandwich composites subjected to sequential impact and air blast loading. *Composites Part B: Engineering* (2011) 42:155–166.
43. Dharmasena K. P., Wadley H.N.G., Williams K., Xue Z., Hutchinson J. W. Response of metallic pyramidal lattice core sandwich panels to high intensity impulsive loading in air. *International Journal of Impact Engineering* (2011) 38:275-289.
44. Kambouchev N., Radovitzky R. and Noels L. Fluid-Structure Interaction Effects in the Dynamic Response of Free-Standing Plates to Uniform Shock Loading. *Journal of Applied Mechanics* (2007)74:1042- 1045.
45. Hou QY, Wang JT. A modified Johnson–Cook constitutive model for Mg–Gd–Y alloy extended to a wide range of temperatures. *Computational Materials Science* (2010) 50:147–152.

Task 4: Corrugated Structures to improve Thermal and Blast Mitigation (Collaboration with the University of Connecticut)

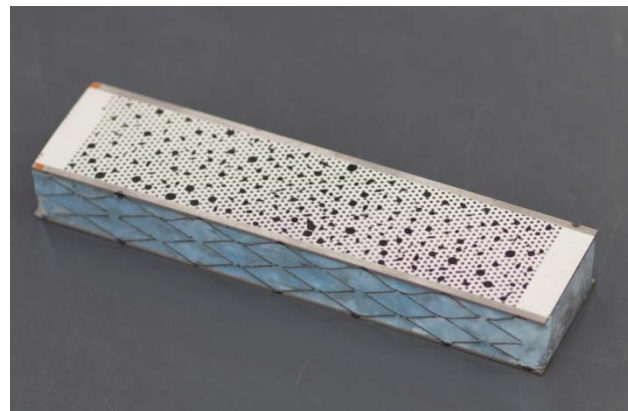
Material details

Each specimen was composed of two 1018 steel face sheets with dimensions of 203.2mm length, 50.8mm width, and 1.6mm thickness. The core was constructed by stacking four layers of G90 corrugated galvanized steel sheets, with a thickness of 0.29mm. The corrugated sheets were cut using a machining process, that ensured uniform width and perpendicularity while preserving the corrugation radii of curvature. The specimen was constructed by spot welding each node on both sides of the panel (as shown in Fig. 68(a)). An empty sandwich panel weighs 376 grams.

A syntactic filler material was designed utilizing a two part platinum silicone and A20/1000 Glass Bubbles by 3M Company. Quasi-static compression tests showed a foam-like behavior when the silicone contained 30% Glass Bubbles, by weight. By using these hollow microspheres, the density of the silicone was lowered and thermal resistivity was improved. The mass of a filled corrugated sandwich panel was 481.8 grams. Fig67(b) shows a filled sandwich structure along with a random speckle pattern used for the Data Image Correlation technique.



(a)



(b)

Fig. 68 Corrugated Sandwich Panels

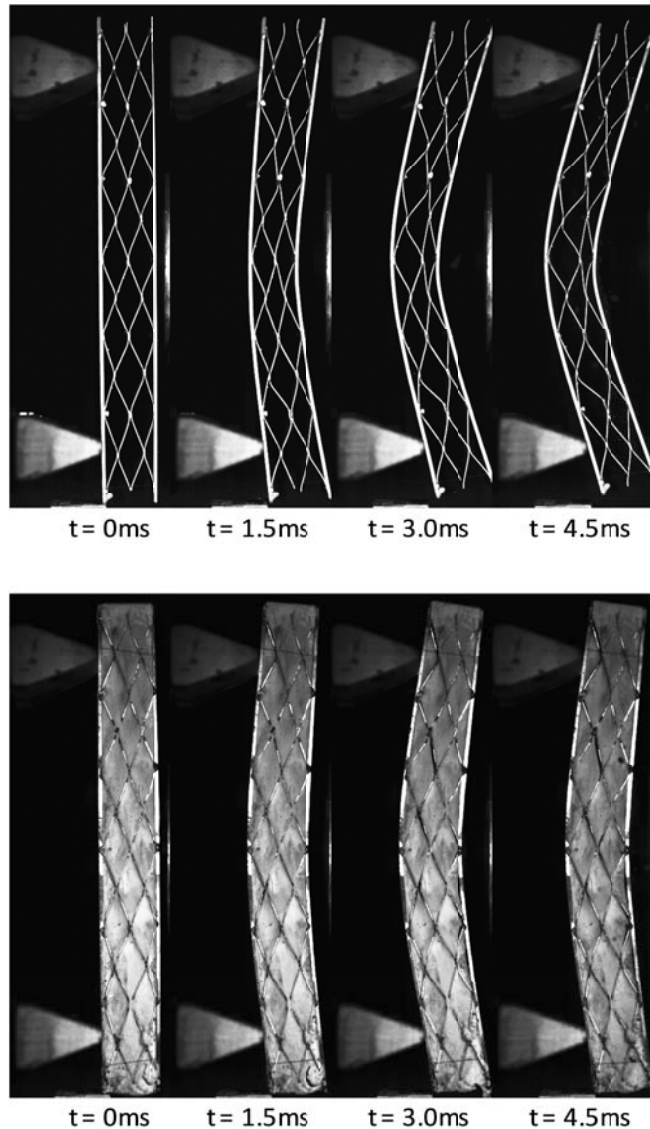
Real-Time Deformation and Analysis

The real-time observations of the transient behavior for both empty and filled corrugated sandwich panels subjected to shock wave loading are shown in Fig. 69. The shock wave propagates from the right side of each frame to the left side and both cases are compared within the same reference time period, where $t=0\text{ms}$ corresponds to the moment before shock loading.

Onset of core compression in the empty corrugated sandwich panel began by approximately 1.5ms, accompanied by front and back face deformations. The front face sheet deflected more than the back and buckling could be seen along the corrugation that was joined to the back face. By 3.0ms core compression was pronounced along the central region of the specimen and several welds had failed due to shear effects. Maximum deflection, of 17mm, was obtained by 4.5ms.

The filled corrugated structure showed very little core compression throughout the entire event. Delamination of the filler from the corrugation is observed as well as local failure at the welds, primarily where the core was joined to the face sheets. Maximum deflection, of 12mm, occurred around 3.0ms and by 4.5ms, the specimen had already started to rebound.

A plot of the back face deflection can be seen in Fig 70. Because the filler material added weight to the specimen overall, the result for the filled case has been normalized with respect to the aerial density of the empty sandwich panel. The back face of the filled specimen began to deflect almost immediately whereas the empty corrugation experienced a brief delay until about 0.25ms. During this time, the front face of the empty specimen deflected, compressing the core. Despite the added mass of the filler, even when normalized, the deflections were less with the presence of the filler material.



imens

Macroscopic Post-Mortem Analysis

Permanent deformation of the corrugated steel sandwich panels were visually inspected and documented using a digital camera, as seen in Fig. 70.

The first series of experiments were performed at room temperature (RT) and a predetermined low pressure (LP) of 1.25-MPa. This was done to understand the performance of both the empty (E) and filled (F) specimens; they have been designated

RTLTP-E and RTLTP-F. The following series compared filled specimens at a higher pressure (HP) of 1.7-MPa, and at both room temperature and a high temperature (HT) of 500°C.

After experiencing a shock loading the RTLTP-E specimen exhibited plastic deformation in the front and back face sheets of 16.7mm and 11.9mm respectively. The core permanently compressed by 8% of its original width in the central region of the specimen. Welds at the outer edges along the central axis showed signs of shearing and core buckling was visible in the central region where the shock impinged on the specimen.

The *post-mortem* condition of the filled specimens, RTHP-F, RTHP-F, and HTFP-F, showed little signs of core compression; however, plastic deformation was apparent in the face sheets. The RTLTP-F specimen showed evidence of delamination of the filler material from the corrugation; however, since the filler is not bonded to the corrugation, it is assumed that this failure mechanism does not contribute to energy dissipation. What the filler does offer is resistance to core buckling and a larger area for applied forces to act. Delamination occurred between the front face sheet and the core via breakage of welds.

The RTHP-F specimen was investigated using higher pressure and endured greater plastic deformation as compared to the low pressure trial. The front face sheet delaminated along its edges, but was still attached at the center. The back face sheet experienced delamination, but this occurred in the central region and was still attached at the edges. Permanent deformation of the front and back face sheets were 15.1mm and 13.5mm, respectively.

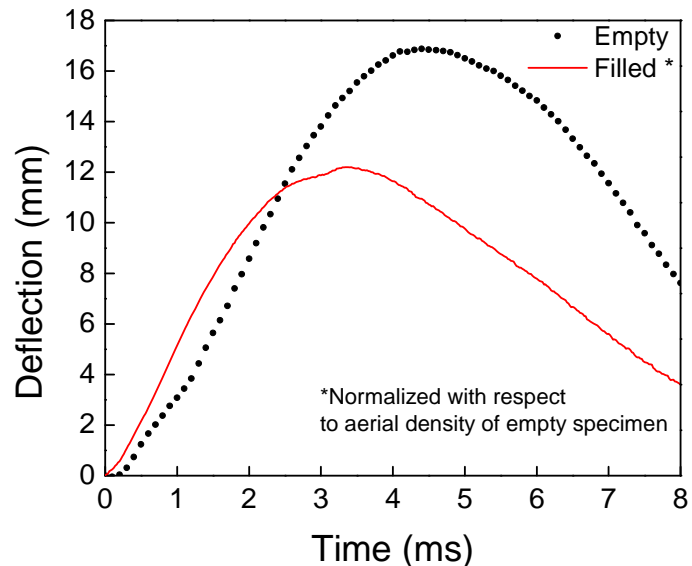


Fig. 70 Deflections of filled and unfilled

The HTHP-F specimen was investigated at a higher temperature. The back face of the specimen was heated to $\sim 500^{\circ}\text{C}$ (932°F) for a duration of twenty minutes. The back face temperature reached steady state after six minutes while the front face temperature reached a maximum of $\sim 150^{\circ}\text{C}$ (302°F) before a shock load was applied. Fig. 72 shows a plot of the front and back face temperature profiles during preliminary heating.

During this time a layer of the filler material in contact with the heated face sheet had turned white. This was a result of the silicone decomposes into silica (or silicon dioxide) along with the emission of carbon dioxide and carbon monoxide. The post mortem specimen showed major deflection and delamination of both front and back face sheets. The corrugated core appeared to be plastically deformed, but was actually held by the welds on the outer edge of the back face sheet, which remained intact. Inner core delamination was present due to a shearing of spot welds.

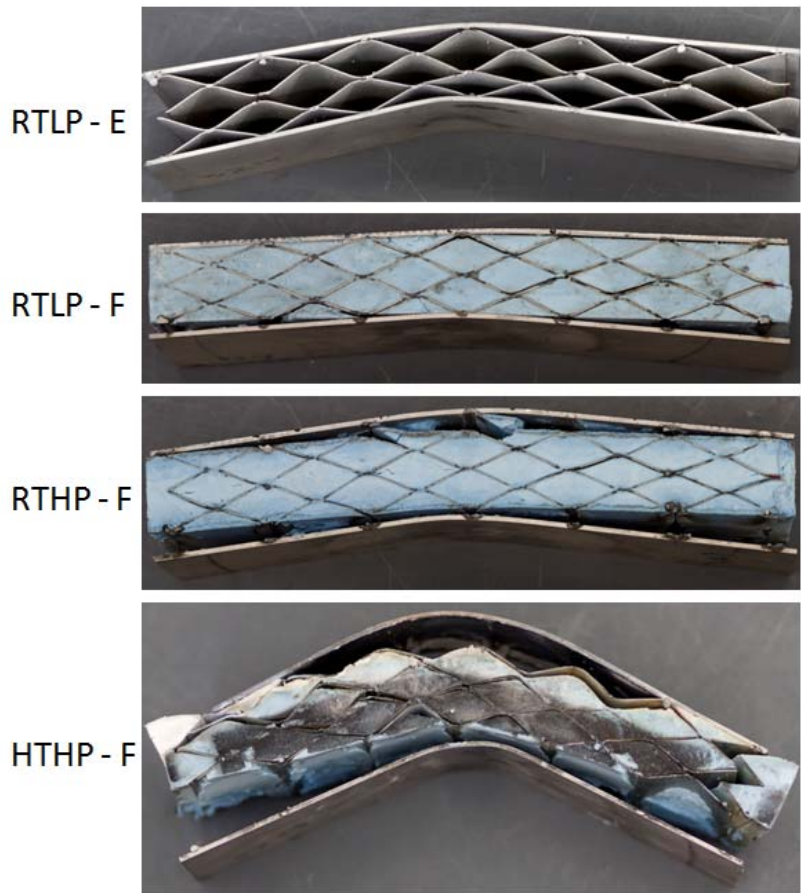


Fig. 71 Post-mortem images of samples

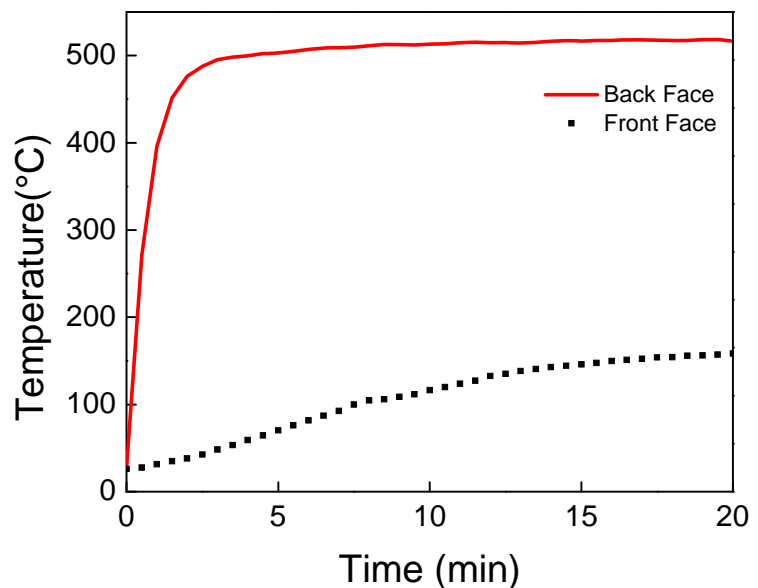


Fig. 72 Thermal profile of HTHP-F during heating

Task 5: Collaboration with Industry / Transition to Customer

Novel material systems and sandwich structures, including but not limited to laminated glass panels, corrugated steel armor, and sandwich composites with a functionally graded foam core (Fig. 73) were designed and fabricated to withstand blast loadings and mitigate blast overpressures. Technical collaboration with XO Armor[®], Specialty Products Inc., Gurit SP Technology, 3M Company, and TPI Composites helped in facilitating sample preparation. This effort also aligns with the mission of DHS to transition technology and allow for a unified effort to protect our homeland.



Fig. 73 Collaborations with Industry



Fig. 74: Novel material systems fabricated with help from Industry

Students Supported

1. Sandeep Abotula (Ph.D)
2. Nate Gardner (Ph.D)
3. Emad Makki (Ph.D)
4. Jefferson Wright (M.S)
5. Payam Fahr (M.S)
6. Chris Shillings (Undergraduate)



Fig. 75: Students working on shock tube experiments

Journal Publications

1. E. Wang, N Gardner and A. Shukla, "The Blast Resistance of Sandwich Composites with Stepwise Graded Cores", *International Journal of Solid and Structures*, 46, 3492-3502, 2009.
2. E. Wang and A. Shukla, "Analytical and Experimental Evaluation of Energies during Shock Wave Loading", *International Journal of Impact Engineering*, 1188-1196, 2010.
3. M. Jackson, A. Shukla, "Performance of Sandwich Composites Subjected to Sequential Impact and Air Blast Loading", *Composites: Part B*, 42, 155–166, 2011.
4. P. Kumar and A. Shukla, "Dynamic Response of Glass Panels Subjected to Shock Loading", *Journal of Non-Crystalline Solids*, Vol. 357 (24), 3917-3923, 2011.
5. E. Wang, J. Wright and A. Shukla, "Analytical and Experimental Study on the Fluid Structure Interaction During Air Blast Loading", *Journal of Applied Physics*, Vol. 110, 114901-1 – 114901-12, 2011.
6. N. Gardner, E. Wang, P. Kumar and A. Shukla, "Blast Mitigation in a Sandwich Composite Using Graded Core and Polyurea Interlayer", *Experimental Mechanics*, Vol. 52, 119-133, 2012.
7. N. Gardner, E. Wang and A. Shukla, "Performance of Functionally Graded Sandwich Composite Beams under Shock Wave Loading", *Composite Structures*, Vol. 94 (5), 1755–1770, 2012
8. E. Wang and A. Shukla, "Blast Performance of Sandwich Composites with In-Plane Compressive Loading", *Experimental Mechanics*, Vol. 52, 49-58, 2012.
9. P. Kumar, J. LeBlanc, D. Stargel and A. Shukla, "Effect of Plate Curvature on Blast Response of Aluminum Panels", *International Journal of Impact Engineering*, Vol. 46, 74-85, 2012.
10. E. Wang, N. Gardner, S. Gupta and A. Shukla, "Fluid-Structure Interaction and its Effect on the Performance of Composite Structures under Air-Blast Loading", *Journal of Multiphysics*, Vol. 6(3), 2012
11. "Effect of plate curvature on blast response of carbon composite panels," with P. Kumar and D. Stargel, *Composite Structures*, Vol. 99, pp. 19-30, 2013.

Conference Proceedings

1. E. Wang, N. Gardner and A. Shukla, "Experimental Study on the Performance of Sandwich Composites with Stepwise Graded Cores Subjected to a Shock wave Loading", *SEM Annual Conference and Exposition on Experimental and Applied Mechanics*, Albuquerque, New Mexico, June 1-4, 2009.
2. N. Gardner, "Blast Performance of Sandwich Composites with Discretely Layered Core", *SEM Annual Conference and Exposition on Experimental and Applied Mechanics*, Albuquerque, New Mexico, June 1-4, 2009.

3. S.A. Tekalur, E. Wang, M. Jackson and A. Shukla, "Failure Behavior and Energy Absorption of Sandwich Composites under Dynamic Loading", SEM Annual Conference and Exposition on Experimental and Applied Mechanics, Albuquerque, New Mexico, June 1-4, 2009.
4. E. Wang and A. Shukla, "Evaluation of Incident, Reflected and Deformation Energies During Blast Experiments", SEM Annual Conference and Exposition on Experimental and Applied Mechanics, Albuquerque, New Mexico, June 1-4, 2009.
5. N. Gardner and A. Shukla, "The Blast Response of Sandwich Composites With a Functionally Graded Core", SEM Annual Conference and Exposition on Experimental and Applied Mechanics, Indianapolis, Indiana, June 7-10, 2010.
6. N. Gardner and A. Shukla, "The Blast Response of Sandwich Composites With a Functionally Graded Core and Polyurea Interlayer", SEM Annual Conference and Exposition on Experimental and Applied Mechanics, Indianapolis, Indiana, June 7-10, 2010.
7. E. Wang and A. Shukla, "The Blast Response of Sandwich Composites with In-Plane Pre-Loading". SEM Annual Conference and Exposition on Experimental and Applied Mechanics, Indianapolis, Indiana, June 7-10, 2010.
8. P. Kumar and A. Shukla, "Blast Loading Response of Glass Panels", SEM Annual Conference and Exposition on Experimental and Applied Mechanics, Indianapolis, Indiana, June 7-10, 2010.
9. E. Wang and A. Shukla, "Core Deformation of Sandwich Composites under Blast Loading", SEM Annual Conference and Exposition on Experimental and Applied Mechanics, Indianapolis, Indiana, June 7-10, 2010.
10. E. Wang and A. Shukla, "Blast Response of Sandwich Composites using Digital Image Correlation Technique", 9th International Conference on Sandwich Structures (ICSS9), Caltech, Pasadena, California, June 14 - 16, 2010.
11. E. Wang and A. Shukla, "Performance of Pre-Stressed Sandwich Composites Subjected to Shock Wave Loading", 14th International Conference on Experimental Mechanics (ICEM 14), Poitiers, FRANCE July 4-9, 2010.
12. N. Gardner and A. Shukla, "The Blast Resistance of Sandwich Composites with a Functionally Graded Core and Polyurea Interlayer", IMPLAST 2010, SEM Fall Conference, Providence, RI, October 12-14, 2010.
13. P. Kumar and A. Shukla, "Dynamic Response of Glass Panels Subjected to Shock Loading", IMPLAST 2010, SEM Fall Conference, Providence, RI, October 12-14, 2010.
14. N. Gardner and A. Shukla, "The Blast Response of Sandwich Composites with Graded Core: Equivalent Core Layer Mass vs. Equivalent Core Layer Thickness", SEM Annual Conference and Exposition on Experimental and Applied Mechanics, Uncasville, Connecticut, June 13 - 16, 2011.

15. P. Kumar and A. Shukla, "Dynamic Response of Shock Loaded Architectural Glass Panels", SEM Annual Conference and Exposition on Experimental and Applied Mechanics, Uncasville, Connecticut, June 13 - 16, 2011.
16. P. Kumar and A. Shukla, "Effect of Curvature on Shock Loading Response of Aluminum Panels", SEM Annual Conference and Exposition on Experimental and Applied Mechanics, Uncasville, Connecticut, June 13 - 16, 2011.
17. P. Kumar and A. Shukla, "Blast Response of Architectural Glass Panels", SEM Annual Conference and Exposition on Experimental and Applied Mechanics, Uncasville, Connecticut, June 13 - 16, 2011.
18. P. Kumar, D. Stargel and A. Shukla, "Response of Curved Carbon Composite Panels to Shock Loading," European Conference on Composite Materials, 24-28 June, 2012, Venice, Italy